

Oil & Natural Gas Technology

DOE Award No.: DE-FC26-03NT41779

Gas Storage Technology Consortium

Final Report

September 30, 2003 to September 30, 2010

Prepared by:

Joel L. Morrison

Elizabeth Wood

Barbara Robuck

Submitted by:

The Pennsylvania State University

The EMS Energy Institute

University Park, PA 16802

Prepared for:

United States Department of Energy
National Energy Technology Laboratory

December 21, 2010



Office of Fossil Energy

DISCLAIMER

This report was prepared as an account of work sponsored by an agency of the United States Government. Neither the United States Government nor any agency thereof, nor any of their employees, makes any warranty, express or implied, or assumes any legal liability or responsibility for the accuracy, completeness, or usefulness of any information, apparatus, product, or process disclosed, or represents that its use would not infringe privately owned rights. Reference herein to any specific commercial product, process, or service by trade name, trademark, manufacturer, or otherwise does not necessarily constitute or imply its endorsement, recommendation, or favoring by the United States Government or any agency thereof. The views and opinions of the authors expressed herein do not necessarily state or reflect those of the United States Government or any agency thereof.

ABSTRACT

The EMS Energy Institute at The Pennsylvania State University (Penn State) has managed the Gas Storage Technology Consortium (GSTC) since its inception in 2003. The GSTC infrastructure provided a means to accomplish industry-driven research and development designed to enhance the operational flexibility and deliverability of the nation's gas storage system, and provide a cost-effective, safe, and reliable supply of natural gas to meet domestic demand. The GSTC received base funding from the U.S. Department of Energy's (DOE) National Energy Technology Laboratory (NETL) Oil & Natural Gas Supply Program. The GSTC base funds were highly leveraged with industry funding for individual projects.

Since its inception, the GSTC has engaged 67 members. The GSTC membership base was diverse, coming from 19 states, the District of Columbia, and Canada. The membership was comprised of natural gas storage field operators, service companies, industry consultants, industry trade organizations, and academia. The GSTC organized and hosted a total of 18 meetings since 2003. Of these, 8 meetings were held to review, discuss, and select proposals submitted for funding consideration. The GSTC reviewed a total of 75 proposals and committed co-funding to support 31 industry-driven projects. The GSTC committed co-funding to 41.3% of the proposals that it received and reviewed. The 31 projects had a total project value of \$6,203,071 of which the GSTC committed \$3,205,978 in co-funding. The committed GSTC project funding represented an average program cost share of 51.7%. Project applicants provided an average program cost share of 48.3%.

In addition to the GSTC co-funding, the consortium provided the domestic natural gas storage industry with a technology transfer and outreach infrastructure. The technology transfer and outreach were conducted by having project mentoring teams and a GSTC website, and by working closely with the Pipeline Research Council International (PRCI) to jointly host technology transfer meetings and occasional field excursions. A total of 15 technology transfer/ strategic planning workshops were held.

TABLE OF CONTENTS

DISCLAIMER	i
ABSTRACT	ii
TABLE OF CONTENTS.....	iii
LIST OF FIGURES	v
LIST OF TABLES.....	v
INTRODUCTION	1
EXECUTIVE SUMMARY	3
EXPERIMENTAL.....	5
RESULTS & DISCUSSION	6
Consortium Background and Organizational Structure	6
Consortium Membership.....	8
Project Solicitation and Selection Process	9
Project Funding Commitment Overviews.....	11
2004 Funding Commitment Overview	11
2005 Funding Commitment Overview	11
2006 Funding Commitment Overview	15
2007 Funding Commitment Overview	15
2008 Funding Commitment Overview	18
GSTC Technology Transfer	18
Website	20
Technology Transfer/ Strategic Planning Meetings	20
Final Technical Reports.....	22
CONCLUSIONS	26
REFERENCES	27
APPENDICES	28
Appendix A: GSTC Constitution.....	29
Appendix B: GSTC Membership Listing.....	38
Appendix C: 2004, Gas Storage Field Deliverability Enhancement and Maintenance: An Intelligent Portfolio Management Approach, <i>West Virginia University Final Report</i>	41

Appendix D: 2004, Renovation of Produced Waters from Underground Natural Gas Storage Facilities: A Feasibility Study Using Hybrid Constructed Wetland Technology, <i>Clemson University Final Report</i>	114
Appendix E: 2004, Real-Time Wellbore Integrity Monitoring, <i>Colorado School of Mines Final Report</i>	179
Appendix F: 2005, Temperature Effects on Threaded Couplings in Caverns, <i>RESPEC Final Report</i>	208
Appendix G: 2005, New Comprehensive Inventory Analysis Tool, <i>Schlumberger Consulting Services Final Report</i>	303
Appendix H: 2005, Cement Evaluation in Gas Filled Boreholes, <i>Baker Atlas Final Report</i>	474
Appendix I: 2005, Smart Gas: Using Chemicals to Improve Gas Deliverability, <i>Correlations Company Final Report</i>	495
Appendix J: 2005, Wellbore Cement Bond Integrity, <i>University of Texas Final Report</i>	541
Appendix K: 2005, Demonstration-Scale Constructed Wetland System for Treatment of Produced Waters from Underground Gas Storage, <i>Clemson University Final Report</i>	647
Appendix L: 2005, Gas Storage Field Deliverability Enhancement and Maintenance: An Intelligent Portfolio Management Approach, <i>West Virginia University Final Report</i>	685
Appendix M: 2009, Ultrasonic Guided Wave Integrity Analysis Tool for Well Casing, <i>The Pennsylvania State University Final Report</i>	789
Appendix N: 2009, RGD X-Ray Technology Well Bore Inspection and Assessment- A Feasibility Study, <i>Gas Technology Institute Final Report</i>	838

LIST OF FIGURES

Figure 1. Geographic Summary of the GSTC Membership	8
---	---

LIST OF TABLES

Table 1. Summary of GSTC Funding Meetings	12
Table 2. GSTC Projects Funded in 2004	13
Table 3. GSTC Projects Funded in 2005	14
Table 4. GSTC Projects Funded in 2006	16
Table 5. GSTC Projects Funded in 2007	17
Table 6. GSTC Projects Funded in 2008	19
Table 7. Summary of Strategic Planning and Technology Transfer Meetings.....	21
Table 8. Summary of GSTC's 2004 and 2005 Project Final Report Submittals	23
Table 9. Summary of GSTC's 2006 and 2007 Project Final Report Submittals	24
Table 10. Summary of GSTC's 2008 and 2009 Project Final Report Submittals	25

INTRODUCTION

Gas storage plays a critical role in meeting the demand for natural gas in the U.S. by buffering the fluctuations in natural gas production, transmission, and end use demand. Producers, transmission and distribution companies, marketers, and end users all benefit directly from the load balancing function of storage. During periods of low natural gas demand, natural gas is injected into storage reservoirs. The natural gas is withdrawn from the reservoir during periods of high demand. Depleted gas reservoirs, salt cavern reservoirs, and aquifer reservoirs are the principal types of storage reservoirs.

To address the underground natural gas storage needs of the domestic natural gas industry the Gas Storage Technology Consortium (GSTC) was established in 2003 through a Cooperative Agreement between the U.S. Department of Energy's (DOE) National Energy Technology Laboratory (NETL) Oil & Natural Gas Supply Program and The Pennsylvania State University (Penn State). The day-to-day management activities of the GSTC are has been preformed by Penn State's EMS Energy Institute. The GSTC receives base funding from NETL Oil & Natural Gas Supply Program.

The primary focus of the GSTC was to provide a means to accomplish industry-driven research and development designed to enhance the operational flexibility and deliverability of the nation's natural gas storage systems; thereby, providing a cost-effective, safe, and reliable supply of natural gas to meet domestic demand. Consortium technology development was conducted in the general areas of well-bore and reservoirs, operations, mechanical, and salt caverns. Consortium members elected an executive council that was charged with reviewing projects for consortium co-funding. Projects were submitted by GSTC members and were funded on an annual basis. Proposals had to address improving the production performance of gas storage and provide significant cost sharing. The process of having industry members develop, review, and select projects for funding ensured that the GSTC conducted research that was relevant and timely to the gas storage industry. The scope of Penn State's activities included managing the process of attracting and maintaining consortium members, soliciting proposals with NETL

guidance and oversight, awarding and monitoring subcontracts to members to accomplish the selected technical works, and disseminating the results of the technical work via meetings and final reports.

Since its inception, the GSTC has engaged 67 members. The GSTC membership base was diverse, coming from 19 states, the District of Columbia, and Canada. The membership was comprised of natural gas storage field operators, service companies, industry consultants, industry trade organizations, and academia. The GSTC organized and hosted a total of 18 meetings since 2003. Of these, 8 meetings were held to review, discuss, and select proposals submitted for funding consideration. The GSTC reviewed a total of 75 proposals and committed co-funding to support 31 industry-driven projects. The GSTC committed co-funding to 41.3% of the proposals that it received and reviewed. The 31 projects had a total project value of \$6,203,071, of which the GSTC committed \$3,205,978 in co-funding. The committed GSTC project funding was represented an average program cost share of 51.7%. Project applicants provided an average program cost share of 48.3%.

In addition to the GSTC co-funding, the consortium provided the domestic natural gas storage industry with a technology transfer and outreach infrastructure. The technology transfer and outreach were conducted by having project mentoring teams and a GSTC website, and by working closely with the Pipeline Research Council International (PRCI) to jointly host technology transfer meetings and occasional field excursions. A total of 15 technology transfer/ strategic planning workshops were held.

EXECUTIVE SUMMARY

The Gas Storage Technology Consortium (GSTC) worked with the domestic underground natural gas storage industry to enhance the operational flexibility and deliverability of the nation's natural gas storage systems. Gas storage plays a critical role in meeting the demand for natural gas in the U.S. by buffering the fluctuations in natural gas production, transmission, and end use demand. Producers, transmission and distribution companies, marketers, and end users all benefit directly from the load balancing function of storage. GSTC was established in 2003 through a Cooperative Agreement between the U.S. Department of Energy's (DOE) National Energy Technology Laboratory (NETL) Oil & Natural Gas Supply Program and The Pennsylvania State University (Penn State). The period of performance for this Cooperative Agreement was September 30, 2003 to September 30, 2010. This report represents the final technical report for the GSTC and its associated activities.

The GSTC management duties were conducted by Penn State's EMS Energy Institute located at Penn State's University Park campus in central Pennsylvania. The scope of Penn State's activities included managing the process of attracting and maintaining consortium members, soliciting proposals with NETL guidance and oversight, awarding and monitoring subcontracts to members to accomplish the selected technical works, and disseminating the results of the technical work via meetings and final reports.

The primary focus of the GSTC was to provide a means to accomplish industry-driven research and development designed to enhance the operational flexibility and deliverability of the nation's natural gas storage systems; thereby, providing a cost-effective, safe, and reliable supply of natural gas to meet domestic demand. Consortium technology development was conducted in the general areas of well-bore and reservoirs, operations, mechanical, and salt caverns. Consortium members elected an executive council that was charged with reviewing projects for consortium co-funding. Projects were submitted by GSTC members and were funded on an annual basis. Proposals had to address improving the production performance of gas storage and provide significant cost

sharing. The process of having industry members develop, review, and select projects for funding ensured that the GSTC conducted research that was relevant and timely to the gas storage industry.

Since its inception, the GSTC has engaged 67 members. The GSTC membership base was diverse, coming from 19 states, the District of Columbia, and Canada. The membership was comprised of natural gas storage field operators, service companies, industry consultants, industry trade organizations, and academia. The GSTC organized and hosted a total of 18 meetings since 2003. Of these, 8 meetings were held to review, discuss, and select proposals submitted for funding consideration. The GSTC reviewed a total of 75 proposals and committed co-funding to support 31 industry-driven projects. The GSTC committed co-funding to 41.3% of the proposals that it received and reviewed. The 31 projects had a total project value of \$6,203,071, of which the GSTC committed \$3,205,978 in co-funding. The committed GSTC project funding was represented an average program cost share of 51.7%. Project applicants provided an average program cost share of 48.3%.

In addition to the GSTC co-funding, the consortium provided the domestic natural gas storage industry with a technology transfer and outreach infrastructure. The technology transfer and outreach were conducted by having project mentoring teams and a GSTC website, and by working closely with the Pipeline Research Council International (PRCI) to jointly host technology transfer/ strategic planning meetings and occasional field excursions. A total of 15 technology transfer/ strategic planning meetings were held.

EXPERIMENTAL

In this program, the Penn State was responsible for the establishment and the day-to-day management activities of the Gas Storage Technology Consortium. Experimental work was conducted by the projects that the GSTC co-funded and reported accordingly in the quarterly and final reports. No experimental work was performed as a part of Penn State's management duties.

RESULTS & DISCUSSION

This report represents the final technical report for the GSTC and its associated activities. The report covers the GSTC activities conducted from September 30, 2003 to September 30, 2010. The results and discussion section of the final report provides a comprehensive discussion of the following:

- ✓ Consortium Background and Organizational Structure
- ✓ Consortium Membership
- ✓ Project Solicitation and Selection Process
- ✓ GSTC Meeting Summary
- ✓ GSTC Project Funding Commitment and Project Expenditure Summaries
- ✓ GSTC Technology Transfer

Consortium Background and Organizational Structure

The GSTC was established in 2003 through a DOE Cooperative Agreement with Penn State. In 2003, the EMS Energy Institute at Penn State was operating two industry-driven consortia - the Consortium for Premium Carbon Products from Coal (CPCPC) and the Stripper Well Consortium (SWC). The administrative infrastructure and EMS Energy Institute's demonstrated track record to operate such consortia enabled the rapid establishment and launching of the GSTC and its associated activities.

The GSTC operational model was similar to CPCPC and SWC in that Penn State's primary responsibility was to establish an industrial partnership that would serve as a focal point to address technical concerns of the industry. In CPCPC, the membership was focused in the production of premium carbon products from coal. In the SWC, the membership was focused on developing new technologies to improve the production performance from domestic oil and gas stripper wells. Using these models, Penn State worked with the natural gas industry, particularly the underground storage sector, to identify and address the technical concerns of enhancing the operational flexibility and deliverability of the nation's natural gas storage systems.

The governing document for the GSTC organizational structure is the GSTC Constitution, which is provided in Appendix A. The Constitution was approved by NETL and the GSTC membership prior to commencing GSTC-related activities. The Constitution provided clear direction in the GSTC's mission, membership, executive council and consortium director, amending the constitution, program funding, publications and conferences, finances, and intellectual property rights policy for the consortium. Per the NETL Cooperative Agreement with Penn State, Penn State was responsible for the management of the consortium. The scope's of Penn State's responsibilities included overseeing the process of recruiting and maintaining the consortium membership base, developing technical request-for-proposals (RFPs) with industry and NETL guidance, soliciting and compiling technical proposals that were received from the GSTC RFP, compiling and disseminating incoming proposals for the GSTC executive council and program sponsors, awarding and monitoring subcontracts, collecting and disseminating GSTC project reports to the consortium membership and program sponsors, organizing and hosting technology transfer meetings and events, developing and updating a GSTC web site, and serving as an industry network organization for the U.S. underground natural gas storage industry.

Each GSTC member appointed a representative to the technical advisory committee, which served as a technical steering committee for the consortium. The technical advisory committee nominated representatives to serve on the GSTC executive council. After the nomination process, the GSTC technical advisory committee elected 9 members to the GSTC executive council. The executive council's primary responsibility is to assist the consortium in reviewing proposals and recommending to NETL which proposals should receive GSTC co-funding. The executive council was comprised of 9 voting members, the GSTC Director (non-voting), the NETL appointed GSTC Program Manager (non-voting) and a representative from the Pipeline Research Council International (PRCI), also a non-voting council member.

Proposals were solicited through a competitive RFP process from the GSTC membership. In addition to the NETL base funding, PRCI provided additional funding to those

selected projects that PRCI deemed as being strategically important to the industry. By leveraging the NETL and PRCI funding streams, the GSTC was able to co-fund 31 projects over a 7 year timeframe.

Consortium Membership

The GSTC membership was comprised of natural gas storage field operators, service companies, industry consultants, industry trade organizations, and academia. The GSTC membership base was diverse, coming from 19 states, the District of Columbia, and Canada. A total of 67 members were engaged in the GSTC activities since 2003. Figure 1 provides a geographic summary of the GSTC membership. A detailed listing of the GSTC membership is provided in Appendix B.

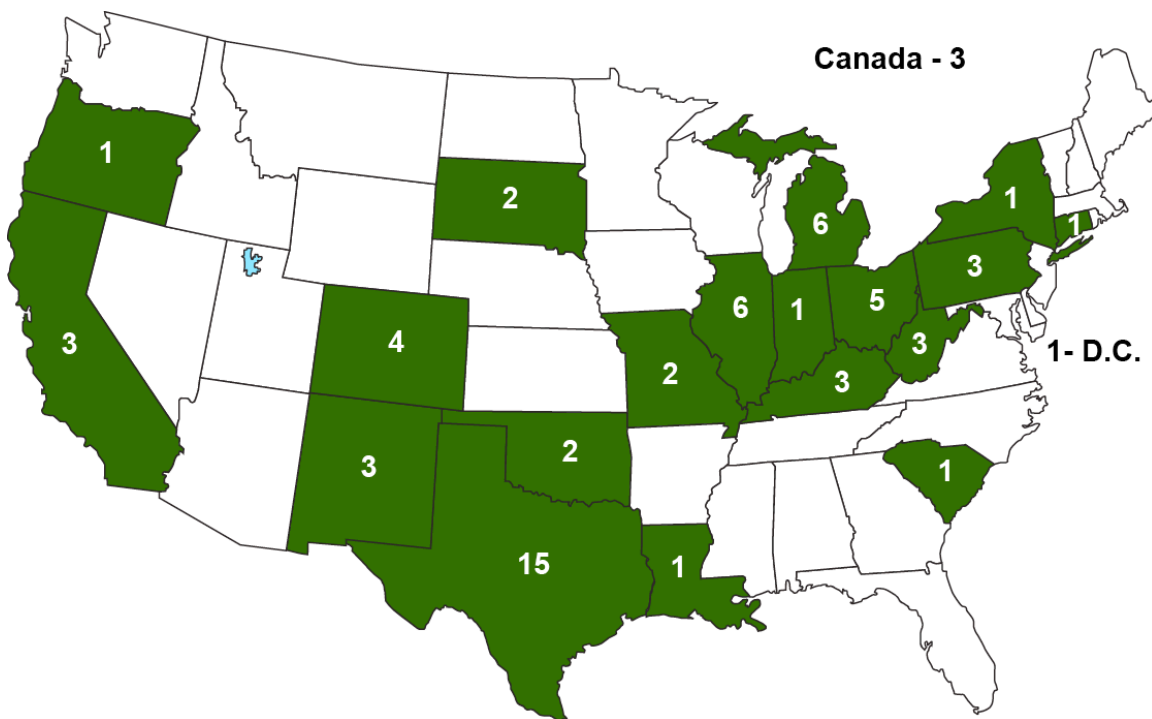


Figure 1. Geographic Summary of the GSTC Membership

Project Solicitation and Selection Process

The GSTC conducted 8 project solicitations using a RFP process that were co-developed by recommendations from the GSTC membership, PRCI, and NETL. Although the RFP language and priorities varied slightly with each funding cycle, the overall research focus areas were centered on the following:

Mechanical. Examples include, but are not limited to, investigations that address pipe and well casing integrity, the improvement of downhole leak detection, the development of new casing evaluation tools, the development/ evaluation of advanced metallurgy/ materials for use in well casing and casing repairs, cement bonding, delta-temperature effects on casing, use of “smart pipe” concepts for well casing, corrosion mitigation and quantification, removal techniques for scales, fines, salts, asphalts, and techniques to remediate damage through stimulation/ recompletion/ workover of existing wells.

Well-Bore and Reservoir. Examples include, but are not limited to, investigations that address reservoir characterization, consider new approaches to modeling of gas cycling and inventory verification, develop techniques to maintain and improve injectivity and deliverability, and expand existing aquifers and reservoirs.

Operations. Examples include, but are not limited to, investigations that address handling of produced water, techniques to minimize/mitigate water encroachment, cost effective multiphase wellhead measurement systems, design criteria for facility sizing to meet variable demand, and best practices associated with product quality shipped/delivered. In addition, applied research into the development/ evaluation of low-cost salt inhibitors to mitigate salt precipitation within the reservoir, well, and pipeline systems are being sought.

Salt Cavern. Examples include, but are not limited to, investigations that address salt cavern stability and growth rates, interconnectivity and best practices techniques for management of caverns.

The GSTC utilized an innovative proposal review and selection process. Members seeking project co-funding from the GSTC were required to submit a technical proposal to the consortium and, in addition, were required to make a formal presentation to the consortium membership, which provided the membership and the applicant ample time and dialogue to review and discuss the merit of the funding request. In the proposal phase, the GSTC issued a technical RFP and allowed for a nominal 60-day submission period. The GSTC RFPs were sent to consortium members, provided to industrial trade organizations, sent out via e-mail to numerous listservs, and posted to the GSTC website. All proposals were required to provide a minimum of 40% cost share to the project. Cost share in the form of cash and/or in-kind was allowable provided that cost share was project specific and occurred in the period of performance of the anticipated grant. A typical RFP required the following proposal sections:

- ✓ Cover sheet (1 page),
- ✓ Public executive summary (1 page),
- ✓ Project description (5 pages),
- ✓ Project schedule (1 page),
- ✓ Anticipated results (2 pages),
- ✓ Project budget (1 page) to the GSTC
- ✓ Biographical Sketch (1 page/ person)
- ✓ Cost Share Commitment Letters (40% required)
- ✓ Letters of Support (recommended)

After the proposals were received, they were compiled and sent to the GSTC executive council and program sponsors for review prior to the GSTC meeting where they would be reviewed and discussed. The members of the GSTC technical advisory committee were provided the public executive summary for each proposal.

Applicants seeking co-funding from the GSTC were also required to make a nominal 20-minute presentation to the GSTC membership that was immediately followed by a 10-minute question and answer period. After the project proposals were reviewed and presented, and the applicant addressed questions from the GSTC membership and executive council, the council deliberated to recommend which proposals should be funded. Applicants were notified within 1-2 weeks after the conclusion of the meeting if their proposal was selected for GSTC co-funding.

Project Funding Commitment Overviews

The description of the GSTC funding commitments is provided below. A tabular summary of the number of funding commitments and funding breakdown by year is provided in Table 1.

2004 Funding Commitment Overview. In 2004, the GSTC issued a single RFP to solicit proposals for co-funding consideration. A total of 17 proposals were submitted and reviewed at the GSTC membership meeting in Morgantown, WV on June 9-10, 2004. From the 17 proposals, the Executive Council recommended that GSTC provided co-funding to support 4 projects. A total of 4 projects were selected for GSTC co-funding in 2004.

These 2004 GSTC-funded projects are summarized in Table 2. Table 2 summarizes the funding awarded and the funding expended during the project. Cost share is expressed as the amount of funding provided by the applicant to the total project cost. The project “Evaluation of Compact Separators for Gas Storage Field Control” was not completed nor were project funds expended.

2005 Funding Commitment Overview. In 2005, the GSTC issued two RFPs to solicit proposals for co-funding consideration. In the first round of funding, 12 proposals were submitted and reviewed at the GSTC membership meeting in Houston, TX on February 2-3, 2005. From these proposals, the Executive Council recommended that GSTC provided co-funding to support 5 projects. In the second round of funding, 5 proposals were submitted and reviewed at the GSTC membership meeting in Pittsburgh, PA on August 30-31, 2005. From these proposals, the Executive Council recommended that GSTC provided co-funding to support 3 projects. A total of 8 projects were selected for GSTC co-funding in 2005.

These 2005 GSTC-funded projects are summarized in Table 3. Table 3 summarizes the funding awarded and the funding expended during the project. Cost share is expressed as

Table 1. Summary of GSTC Funding Meetings.

Date	Location	# Proposals Submitted	# Projects Funded	Project Funding %
June 9-10, 2004	Morgantown, WV	17	4	23.5
February 2-3, 2005	Houston, TX	12	5	41.7
August 30-31, 2005	Pittsburgh, PA	5	3	60.0
February 21-22, 2006	San Diego, CA	15	8	53.3
May 16-17, 2007	Buffalo, NY	9	4	66.7
November 6-7, 2007	Portland, OR	5	2	40.0
April 17-18, 2008	Chicago, IL	2	1	50.0
October 21-22, 2008	Washington, DC	10	4	40.0
Proposals/ Project Total		75	31	41.3

Table 2. GSTC Projects Funded in 2004.

Project Title	Applicant Name	Funding Awarded				Funds Expended			
		Applicant	GSTC	Total Project	% Cost Share	Applicant	GSTC	Project Total	% Cost Share
Gas Storage Field Deliverability Enhancement and Maintenance: An Intelligent Portfolio Management Approach	West Virginia University	\$78,317	\$104,850	\$183,167	42.8	\$78,433	\$98,783	\$177,217	44.3
Evaluation of Compact Separators for Gas Storage Field Fluid Control	Colorado Engineering Experiment Station	\$33,200	\$50,000	\$83,200	39.9	\$0	\$0	\$0	0.0
Renovation of Produced Waters from Underground Natural Gas Storage Facilities: A Feasibility Study Using Hybrid Constructed Wetland Technology	Clemson University	\$64,981	\$97,486	\$162,467	40.0	\$80,575	\$97,468	\$178,043	45.3
Real Time Well Bore Integrity Modeling	Colorado School of Mines	\$136,800	\$172,198	\$308,998	44.3	\$136,800	\$120,760	\$257,560	53.1
TOTAL		\$313,298	\$424,534	\$737,832	42.5	\$295,808	\$317,011	\$612,820	48.3

Table 3. GSTC Projects Funded in 2005.

Project Title	Applicant Name	Funding Awarded				Funds Expended			
		Applicant	GSTC	Total Project	% Cost Share	Applicant	GSTC	Project Total	% Cost Share
Temperature Effects on Threaded Couplings in Caverns	RESPEC	\$63,560	\$87,340	\$150,900	42.1	\$66,687	\$87,340	\$154,027	43.3
New Comprehensive Inventory Analysis Tool	Schlumberger Consulting Services	\$81,900	\$119,800	\$201,700	40.6	\$83,703	\$119,800	\$203,503	41.1
Cement Evaluation in Gas Filled Borehole	Baker Atlas	\$81,120	\$117,000	\$198,120	40.9	\$45,369	\$91,521	\$136,891	33.1
Smart Gas: Using Chemicals to Improve Gas Deliverability	Correlations Company	\$74,884	\$112,325	\$187,209	40.0	\$74,884	\$112,325	\$187,209	40.0
Wellbore Cement Bond Integrity	University of Texas	\$171,027	\$252,721	\$423,748	40.4	\$179,415	\$249,582	\$428,997	41.8
Demo-Scale Constructed Wetland System for Treatment of Produced Waters from Underground Gas Storage	Clemson University	\$89,732	\$134,537	\$224,269	40.0	\$89,879	\$134,537	\$224,416	40.0
Gas Storage Field Deliverability Enhancement and maintenance: An Intelligent Portfolio Management Approach	West Virginia University	\$82,361	\$127,156	\$209,517	39.3	\$86,924	\$126,556	\$213,481	40.7
Scale Remediation Using Sonication: Pre-Commercial Test Project	TechSavants, Inc.	\$366,762	\$175,000	\$541,762	67.7	\$401,250	\$175,000	\$576,250	69.6
Total		\$1,011,346	\$1,125,879	\$2,137,225	47.3	\$1,028,111	\$1,096,661	\$2,124,774	48.4

the amount of funding provided by the applicant to the total project cost. All projects that received funding approval were completed.

2006 Funding Commitment Overview. In 2006, the GSTC issued a single RFP to solicit proposals for co-funding consideration. A total of 15 proposals were submitted and reviewed at the GSTC membership meeting in San Diego, CA on February 21-22, 2006. From these proposals, the Executive Council recommended that GSTC provided co-funding to support 8 projects. A total of 8 projects were selected for GSTC co-funding in 2006.

These 2006 GSTC-funded projects are summarized in Table 4. Table 4 summarizes the funding awarded and the funding expended during the project. Cost share is expressed as the amount of funding provided by the applicant to the total project cost. All of the projects that received funding approval were completed except for the project “Protocol Evaluation for Scale Prevention and Remediation in Gas Storage Reservoirs and Formulations” which was terminated in the early stage of the research.

2007 Funding Commitment Overview. In 2007, the GSTC issued two RFPs to solicit proposals for co-funding consideration. In the first round of funding, 9 proposals were submitted and reviewed at the GSTC membership meeting in Buffalo, NY on May 16-17, 2007. From these proposals, the Executive Council recommended that GSTC provided co-funding to support 4 projects. In the second round of funding, 5 proposals were submitted and reviewed at the GSTC membership meeting in Portland, OR on November 6-7, 2007. From these proposals, the Executive Council recommended that GSTC provided co-funding to support 2 projects. A total of 6 projects were selected for GSTC co-funding in 2007. These 2007 GSTC-funded projects are summarized in Table 5. Table 5 summarizes the funding awarded and the funding expended during the project. Cost share is expressed as the amount of funding provided by the applicant to the total project cost. The project “RGD X-Ray Technology Well Bore Inspection and Assessment – A Feasibility Study” was not completed nor were project funds expended.

Table 4. GSTC Projects Funded in 2006.

Project Title	Applicant Name	Funding Awarded				Funds Expended			
		Applicant	GSTC	Total Project	% Cost Share	Applicant	GSTC	Project Total	% Cost Share
State-of-the Art Assessment of Alternative Casing Repair Methods	Edison Welding Institute	\$30,000	\$45,000	\$75,000	40.0	\$29,964	\$44,638	\$74,602	40.2
Wellbore Cement Bond Integrity	Univ. of Texas at Austin	\$161,332	\$237,951	\$399,283	40.0	\$236,350	\$174,172	\$410,523	42.4
Brine String Integrity-Case History Survey and Model Evaluation	PB Energy Storage Services	\$18,512	\$27,768	\$46,280	40.0	\$16,537	\$24,805	\$41,342	40.0
Predicting and Mitigating Salt Precipitation	Correlations Company	\$80,000	\$120,000	\$200,000	40.0	\$80,000	\$120,000	\$200,000	40.0
Technology Feasibility Evaluation of Non-Intrusive Optical Detection, Monitoring and Preliminary Characterization of Casing Cement Leaks for Gas Wells	URS Group	\$17,010	\$39,310	\$56,320	30.0	\$20,961	\$39,305	\$60,266	34.0
Effects of Tensile Loading on the Remaining Strength of Corroded Casing	Kiefner and Associates	\$103,920	\$155,880	\$259,800	40.0	\$85,144	\$127,716	\$212,860	38.8
Protocol Evaluation for Scale Prevention and Remediation in Gas Storage Reservoirs and Formulations	Colorado School of Mines	\$165,000	\$237,600	\$402,600	41.0	\$0	\$6,879	\$6,879	0
Storage Field Wellbore Flow Data Containing Water and Hydrates	Colorado Engineering Experiment Station	\$30,833	\$23,878	\$54,711	56.4	\$30,833	\$23,878	\$54,711	56.3
Total		\$606,607	\$887,387	\$1,493,994	40.6	\$499,789	\$561,393	\$1,061,183	47.1

Table 5. GSTC Projects Funded in 2007.

Project Title	Applicant Name	Funding Awarded				Funds Expended			
		Applicant	GSTC	Total Project	% Cost Share	Applicant	GSTC	Project Total	% Cost Share
Evaluation of Magnetic Pulse Welding (MPW) for Improved Casing Repair	Edison Welding Institute	\$60,750	\$90,000	\$150,750	40.3	\$60,750	\$90,000	\$150,750	40.3
RGD X-Ray Technology Well Bore Inspection and Assessment - A Feasibility Study	Gas Technology Institute	\$237,257	\$80,755	\$318,012	74.6	\$0	\$0	\$0	0.0
Penetration Power of Ultrasonic Guided Waves for Piping and Well Casing Integrity Analysis	The Pennsylvania State University	\$73,281	\$85,000	\$158,281	46.3	\$75,050	\$85,000	\$160,050	46.9
Smart Gas: Using Chemicals to Improve Gas Deliverability-Phase II	Correlations Company	\$113,000	\$37,000	\$150,000	75.3	\$182,000	\$37,000	\$219,000	83.1
Gas Storage Facility Design Under Uncertainty	University of Texas at Austin	\$47,862	\$61,320	\$109,182	40.0	\$41,200	\$60,396	\$101,597	40.5
Predicting and Mitigating Salt Precipitation - Phase II	Correlations Company	\$25,000	\$25,000	\$50,000	50.0	\$25,000	\$25,000	\$50,000	50.0
Total		\$557,150	\$379,075	\$936,225	59.5	\$384,000	\$297,396	\$681,397	56.4

2008 Funding Commitment Overview. In 2008, the GSTC issued two RFPs to solicit proposals for co-funding consideration. In the first round of funding, 2 proposals were submitted and reviewed at the GSTC membership meeting in Chicago, IL on April 17-18, 2008. From these proposals, the Executive Council recommended that GSTC provided co-funding to support 1 project. In the second round of funding, 10 proposals were submitted and reviewed at the GSTC membership meeting in Washington, DC on October 21-22, 2008. From these proposals, the Executive Council recommended that GSTC provided co-funding to support 4 projects. A total of 5 projects were selected for GSTC co-funding in 2008.

These 2008 GSTC-funded projects are summarized in Table 6. Table 6 summarizes the funding awarded and the funding expended during the project. Cost share is expressed as the amount of funding provided by the applicant to the total project cost. All projects that received funding approval were completed.

GSTC Technology Transfer

The primary focus of the GSTC was to provide a means to accomplish industry-driven research and development designed to enhance the operational flexibility and deliverability of the nation's natural gas storage systems. Technology transfer played a key role in achieving this focus.

The GSTC technology transfer activities can be broken down into the following categories:

- ✓ Electronic communication using web-based technology,
- ✓ Organizing and hosting membership meetings dedicated to technology transfer,
and
- ✓ Compiling and distributing final technical project reports.

Table 6. GSTC Projects Funded in 2008.

Project Title	Applicant Name	Funding Awarded				Funds Expended			
		Applicant	GSTC	Total Project	% Cost Share	Applicant	GSTC	Project Total	% Cost Share
Testing for the Dilation Strength of Salt	RESPEC	\$85,500	\$102,265	\$187,765	45.5	\$85,502	\$102,265	\$187,767	45.5
Temperature Logging as a Mechanical Integrity Test (MIT) for Gas-Filled Caverns	RESPEC	\$49,065	\$73,957	\$123,022	39.9	\$49,064	\$72,124	\$121,188	40.5
Extension of a Method to Validate the Remaining Strength of Corroded Casing to Additional Cases	Kiefner and Associates	\$68,158	\$88,212	\$156,370	43.6	\$56,585	\$83,176	\$139,761	40.5
RGD X-Ray Technology Well Bore Inspection and Assessment - A Feasibility Study	Gas Technology Institute	\$237,257	\$49,669	\$286,926	82.7	\$210,929	\$49,668	\$260,597	81.0
Ultrasonic Guided Wave Integrity Analysis Tool for Well Casing	The Pennsylvania State University	\$68,712	\$75,000	\$143,712	47.8	\$68,712	\$74,998	\$143,710	47.8
Total		\$508,692	\$389,103	\$897,795	56.7	\$470,792	\$382,231	\$853,023	55.2

Website. The GSTC began its Web site in March 2004. The web site address was <http://www.energy.psu.edu>. The site provided an important venue for technology transfer, recruitment, and member communication. The Web site gave members the opportunity to benefit from meetings and other projects, even if they were unable to attend GSTC events. During the course of the project, the secure member section of the Web site gave members access to all quarterly and final reports as well as meeting documents such as agendas and presentations.

The GSTC Website had executive summaries from current and past projects available for members and the general public to view. In addition, the Web site contained membership lists, GSTC and industry news, requests for proposals, and meeting information. The Web site was heavily visited with over 123,000 total hits from March 1, 2004 through September 30, 2010. During that timeframe, the Web site had an average of 3,700 visitors per year and over 28,000 files downloaded.

Technology Transfer/ Strategic Planning Meetings. The GSTC membership held a limited number of strategic planning meetings to plan its activities and numerous meetings to discuss the status of on-going projects and results from projects that were completed. These meetings are summarized in Table 7.

A limited number of strategic planning meetings were held to plan the GSTC changes and to make programmatic changes when needed. A total of 4 strategic planning meetings were held. Numerous technology transfer meetings were held. A total of 5 meetings were held solely for the purpose of having the GSTC membership review the status of on-going projects and to review the project results of recently completed projects. In addition, 6 additional meetings combined the review of on-going projects and the presentation of new proposed projects. A total of 15 meetings had technology transfer review for the GSTC membership.

Table 7. Summary of Strategic Planning and Technology Transfer Meetings.

Date	Location	Meeting Purpose
December 4, 2003	State College, PA	Strategic Planning
March 2, 2004	Houston, TX	Strategic Planning
September 9, 2004	State College, PA	Strategic Planning – Executive Council
February 2-3, 2005	Houston, TX	Technology Transfer & Proposal Review
August 30-31, 2005	Pittsburgh, PA	Technology Transfer & Proposal Review
November 7-8, 2006	Pittsburgh, PA	Technology Transfer
October 4, 2006	San Francisco, CA	Technology Transfer
November 6-7, 2007	Portland, OR	Technology Transfer & Proposal Review
November 19, 2007	Morgantown, WV	Technical Transfer/ Software Training
September 17, 2008	Boulder, CO	Strategic Planning
April 17-18, 2008	Chicago, IL	Technology Transfer & Proposal Review
October 21-22, 2008	Washington, DC	Technology Transfer & Proposal Review
November 19, 2009	Pittsburgh, PA	Technology Transfer
April 29, 2009	Morgantown, WV	Technology Transfer
September, 22, 2010	Kansas City, MO	Technology Transfer

Final Technical Reports. At the conclusion of each project, a final technical report was prepared by the applicant and then submitted to NETL and Penn State for review. Upon NETL and Penn State acceptance, the final report was distributed to the GSTC membership via a secure web portal on the GSTC website. Final payment to the project was then made. Tables 8-10 provide a summary of when the final reports were submitted to NETL. A limited number of final reports were not submitted to NETL and are therefore included in Appendices C-N of this report.

Table 8. Summary of GSTC's 2004 and 2005 Project Final Report Submittals.

Project Title	Company Name	Final Report Submitted
2004 Funded Projects		
Gas Storage Field Deliverability Enhancement and Maintenance: An Intelligent Portfolio Management Approach	West Virginia University	Included in this report
Renovation of Produced Waters from Underground Natural Gas Storage Facilities: A Feasibility Study Using Hybrid Constructed Wetland Technology	Clemson University	Included in this report
Real Time Well Bore Integrity Modeling	Colorado School of Mines	Included in this report
2005 Funded Projects		
Temperature Effects on Threaded Couplings in Caverns	RESPEC	Included in this report
New Comprehensive Inventory Analysis Tool	Schlumberger Consulting Services	Included in this report
Cement Evaluation in Gas Filled Borehole	Baker Atlas	Included in this report
Smart Gas: Using Chemicals to Improve Gas Deliverability	Correlations Company	Included in this report
Wellbore Cement Bond Integrity	University of Texas	Included in this report
Demo-Scale Constructed Wetland System for Treatment of Produced Waters from Underground Gas Storage	Clemson University	Included in this report
Gas Storage Field Deliverability Enhancement and maintenance: An Intelligent Portfolio Management Approach	West Virginia University	Included in this report
Scale Remediation Using Sonication: Pre-Commercial Test Project	TechSavants, Inc.	07/01/08 – 09/30/08 GSTC Quarterly Report

Table 9. Summary of GSTC's 2006 and 2007 Project Final Report Submittals.

Project Title	Company Name	Final Report Submitted
2006 Projects		
State-of-the Art Assessment of Alternative Casing Repair Methods	Edison Welding Institute	01/01/09 – 03/31/09 GSTC Quarterly Report
Wellbore Cement Bond Integrity	Univ. of Texas at Austin	01/01/09 – 03/31/09 GSTC Quarterly Report
Brine String Integrity-Case History Survey and Model Evaluation	PB Energy Storage Services	07/01/08 – 09/30/08 GSTC Quarterly Report
Predicting and Mitigating Salt Precipitation	Correlations Company	01/01/09 – 03/31/09 GSTC Quarterly Report
Technical Feasibility Evaluation of Non-Intrusive Optical Detection, Monitoring and Preliminary Characterization of Casing Cement Leaks for Gas Wells	URS Group	01/01/09 – 03/31/09 GSTC Quarterly Report
Effects of Tensile Loading on the Remaining Strength of Corroded Casing	Kiefner and Associates	10/01/08 – 12/31/08 GSTC Quarterly Report
Storage Field Wellbore Flow Data Containing Water and Hydrates	Colorado Engineering Experiment Station	04/01/08 – 06/30/08 GSTC Quarterly Report
2007 Projects		
Evaluation of Magnetic Pulse Welding (MPW) for Improved Casing Repair	Edison Welding Institute	07/01/08 – 09/30/08 GSTC Quarterly Report
Penetration Power of Ultrasonic Guided Waves for Piping and Well Casing Integrity Analysis	The Pennsylvania State University	07/01/08 – 09/30/08 GSTC Quarterly Report
Smart Gas: Using Chemicals to Improve Gas Deliverability-Phase II	Correlations Company	01/01/09 – 03/31/09 GSTC Quarterly Report

Table 10. Summary of GSTC’s 2008 and 2009 Project Final Report Submittals.

Project Title	Company Name	Final Report Submitted
2008 Projects		
Gas Storage Facility Design Under Uncertainty	University of Texas at Austin	10/01/09 – 12/31/09 GSTC Quarterly Report
Predicting and Mitigating Salt Precipitation - Phase II	Correlations Company	01/01/09 – 03/31/09 GSTC Quarterly Report
Testing for the Dilation Strength of Salt	RESPEC	01/01/10 – 03/31/10 GSTC Quarterly Report
2009 Projects		
Temperature Logging as a Mechanical Integrity Test (MIT) for Gas-Filled Caverns.	RESPEC	07/01/10 – 09/30/10 GSTC Quarterly Report
Extension of a Method to Validate the Remaining Strength of Corroded Casing to Additional Cases	Kiefner and Associates	07/01/10 – 09/0/10 GSTC Quarterly Report
RGD X-Ray Technology Well Bore Inspection and Assessment-A Feasibility Study	Gas Technology Institute	Included in this report
Ultrasonic Guided Wave Integrity Analysis Tool for Well Casing	The Pennsylvania State University	Included in this report

CONCLUSIONS

Since its establishment in 2003, Penn State has worked with the U.S. underground natural gas storage industry to develop an industry-driven consortium that worked to enhance the operational flexibility and deliverability of the nation's gas storage system, and provide a cost-effective, safe, and reliable supply of natural gas to meet domestic demand. The GSTC base funding, which was provided by NETL, was highly leveraged with industry funding.

Since 2003, the GSTC has engaged 67 members. The GSTC membership base was diverse, coming from 19 states, the District of Columbia, and Canada. The membership was comprised of natural gas storage field operators, service companies, industry consultants, industry trade organizations, and academia. The GSTC organized and hosted a total of 18 meetings since 2003. Of these, 8 meetings were held to review, discuss, and select proposals submitted for funding consideration. The GSTC reviewed a total of 75 proposals and committed co-funding to support 31 industry-driven projects. The GSTC committed co-funding to 41.3% of the proposals that it received and reviewed. The 31 projects had a total project value of \$6,203,071, of which the GSTC committed \$3,205,978 in co-funding. The committed GSTC project funding was represented an average program cost share of 51.7%. Project applicants provided an average program cost share of 48.3%.

In addition to the GSTC co-funding, the consortium provided the domestic natural gas storage industry with a technology transfer and outreach infrastructure. The technology transfer and outreach were conducted by having project mentoring teams and a GSTC website, and by working closely with PRCI to jointly host technology transfer meetings and occasional field excursions. A total of 15 technology transfer workshops were held.

The GSTC completed its activities on September 30, 2010.

REFERENCES

This final report does not cite any references.

APPENDICES

The final report has 14 appendices, which contain GSTC administrative documents (Appendices A and B) and individual project final reports, which were not previously submitted to NETL (Appendices C-N).

Appendix A: GSTC Constitution

Appendix B: GSTC Membership Listing

Appendix C: 2004, Gas Storage Field Deliverability Enhancement and Maintenance: An Intelligent Portfolio Management Approach, *West Virginia University*

Appendix D: 2004, Renovation of Produced Waters from Underground Natural Gas Storage Facilities: A Feasibility Study Using Hybrid Constructed Wetland Technology, *Clemson University*

Appendix E: 2004, Real-Time Wellbore Integrity Monitoring, *Colorado School of Mines*

Appendix F: 2005, Temperature Effects on Threaded Couplings in Caverns, *RESPEC*

Appendix G: 2005, New Comprehensive Inventory Analysis Tool, *Schlumberger Consulting Services*

Appendix H: 2005, Cement Evaluation in Gas Filled Boreholes, *Baker Atlas*

Appendix I: 2005, Smart Gas: Using Chemicals to Improve Gas Deliverability, *Correlations Company*

Appendix J: 2005, Wellbore Cement Bond Integrity, *University of Texas*

Appendix K: 2005, Demonstration-Scale Constructed Wetland System for Treatment of Produced Waters from Underground Gas Storage, *Clemson University*

Appendix L: 2005, Gas Storage Field Deliverability Enhancement and Maintenance: An Intelligent Portfolio Management Approach, *West Virginia University*

Appendix M: 2009, Ultrasonic Guided Wave Integrity Analysis Tool for Well Casing, *The Pennsylvania State University*

Appendix N: 2009, RGD X-Ray Technology Well Bore Inspection and Assessment-A Feasibility Study, *Gas Technology Institute*

Appendix A
GSTC Constitution

CONSTITUTION FOR GAS STORAGE TECHNOLOGY CONSORTIUM

Article I

Name and Purpose:

Section 1. The name of this organization shall be the Gas Storage Technology Consortium (GSTC).

Section 2. The mission of the GSTC is to assist in the development, demonstration and commercialization of technologies to improve the integrity, flexibility, deliverability, and cost-effectiveness of the nation's underground natural gas (hydrocarbon) storage facilities. Moreover, the projects selected will primarily focus on demonstration of technologies to preserve and improve the deliverability of and management of existing conventional underground storage reservoirs and salt cavern storage facilities, and secondarily focus on research to develop man-made storage systems and other non-traditional methods in close proximity to demand centers. Its functions shall pertain to natural gas science and engineering, and the dissemination of new information to the scientific community, industry and the general public. The specific research focus will be identified in the Requests for Proposals (RFPs).

The organization shall serve its Members by guiding, stimulating, and aiding their efforts to:

- i) Formulate research, development, and technology assessment goals;
- ii) Create a supporting infrastructure for conducting research and development that will increase knowledge of and expand the technological base for natural gas (hydrocarbon) storage; and
- iii) Promote and enhance the dissemination of research results and technology transfer to storage operators for the benefit of the nation.

Section 3. The GSTC and Members who are not participants in a project are not liable in any way for any activities under a given project.

Article II

Membership:

Any individual, firm, partnership, association, institution, university or corporation engaged in natural gas (hydrocarbon) storage, or engaged in research and development of technologies associated with natural gas (hydrocarbon) storage, or a user of natural gas (hydrocarbon) storage services is eligible for Membership in the GSTC Consortium.

Section I. Membership in the GSTC shall be at one of three Membership levels:

- i) Full Memberships are defined as those Members from any individual firm, partnership, institution, or corporation directly engaged in the production and service of the natural gas (hydrocarbon) industry, or individuals and institutions engaged in research and development associated with natural gas (hydrocarbon) or users of natural gas (hydrocarbon) services and who have provided an annual membership fee of \$1,000 per year. Full Members are entitled to designate one (1) voting representative to the Technical Advisory Committee, receive periodic

communications, to compete for a seat on the Executive Council, to sponsor or propose a project for Consortium funding, and to receive quarterly and final technical reports. Full Members are eligible to have up to two (2) people in attendance at meetings. Full Members are eligible to receive research funding from the Consortium. Annual membership fees for full members are subject to change at the discretion of the Executive Council. No meeting fee will be assessed to full members.

- ii) Affiliate Members are defined as those Members from associations and professional societies. Affiliate Members are entitled to designate one (1) voting representative to the Technology Advisory Committee, and to receive periodic communications. Affiliate Members are eligible to have up to two (2) people in attendance at meetings. Affiliate Members are not eligible to receive research funding from the GSTC Consortium, may not be elected to the Executive Council, nor are they eligible to receive technical reports. If however, an Affiliate member provides co-funding in support of a specific project, the Affiliate member is eligible to receive the technical reports associated with the specific project and may be eligible for appointment to the Executive Council as provided in Section III. The annual membership fee for Affiliate Membership is \$500 per year and is subject to change at the discretion of the Executive Council. No meeting fee will be assessed to affiliate members.
- iii) University Members are defined as any university or college that is engaged in research and development technologies associated with natural gas (hydrocarbon) storage. No membership fee will be assessed to University Members. University Members are entitled to designate (1) voting representative to the Technical Advisory Committee, receive periodic communications, to compete for a seat on the Executive Council, to sponsor or propose a project for Consortium funding, and to receive quarterly and final technical reports. University Members will be assessed a meeting fee of no more than \$100 per day to cover expenses associated with their attendance at meetings.

Section 1a. Full, Affiliate, and University Membership

- i) Application for Full, Affiliate and University Membership shall be submitted to the Director whose responsibility it shall be to ensure their completeness and compliance with provisions of the consortium's constitution.
- ii) Upon receipt of Membership fee, the member(s) shall immediately exercise all rights, privileges and responsibilities of Membership. In the case of a University or College, the membership fee is waived.
- iii) Calendar year shall mean January 1 through December 31.

- iv) Voting on consortium issues by the Technical Advisory Committee will only be by those members in attendance.

Section 1b. Full, Affiliate or University Members may withdraw from the Consortium upon thirty (30) days written notice to the Consortium Director. Membership fees are nonrefundable.

Article III

Organization and Officers:

The GSTC shall be governed and managed by an Executive Council and the Consortium Director.

Section 1. The Executive Council shall be the policy making body of the Consortium. The Executive Council shall establish an overall research and development plan for the GSTC, approve and issue requests for proposals to Full Members and University Members to fulfill research and development priorities, establish review procedures for research proposals, select proposals to be funded by the Consortium based upon the relevance to the established goals and objectives of the Consortium, and perform the duties necessary to achieve the GSTC mission. The director and various committees derived from the GSTC Membership shall be utilized as deemed necessary by the Executive Council to achieve these and other Executive Council goals.

Section 1a. The Executive Council shall be composed of:

- i) Nine (9) voting members elected by the Technical Advisory Committee;
- ii) The GSTC Director who shall be a non-voting member presiding over the Council;
- iii) A representative from the National Energy Technology Laboratory (NETL) who shall be a non-voting member of the Council;
- iv) A representative from the Pipeline Research Council International (PRCI) shall be a non-voting member of the Council;
- v) A maximum of two (2) university members;
- vi) A minimum of 5-storage operators - storage operator in this context is defined as a U.S. based operator that files an EIA (Energy Information Administration) 191 form;
- vii) Executive Council can be expanded as per Article III, sections 2c and 2d.

Section 1b. With the advice and consent of the Executive Council representatives, the GSTC Director shall set the time, place and agenda of the Executive Council meetings and shall preside over these meetings. Every effort will be made to hold meetings in various geographical locations throughout the country. Whenever possible, telephone conferencing will be scheduled to conduct meetings. Executive Council Members shall be responsible for their own travel and other expenses associated with the performance of their responsibilities.

Section 1c. Representatives of the Executive Council who are unable to attend the Executive Council meeting shall notify the Director as far in advance as possible. An Executive Council Member can vote in absentia provided it is done in a written form, however Executive Council Members must be present to vote on the selection of proposals to be funded by the Consortium.

Section 2. The Technical Advisory Committee shall provide research ideas, and aid the Executive Council in developing and implementing technology transfer plans for the GSTC. The Technical Advisory Committee shall advise both the Executive Council and the Director regarding the relevance and the scientific merit of the Constitution research and development programs.

Section 2a. The Technical Advisory Committee shall be composed of one (1) voting representative from each Full, Affiliate and University GSTC Membership.

Section 2b. The Technical Advisory Committee shall elect nine (9) representatives to serve on the Executive Council. In the initial year, the Technical Advisory Committee shall elect five (5) representatives who shall serve a two-year term and four (4) who shall serve a one-year term. Thereafter, the Technical Advisory Committee shall elect either four (4) or five (5) representatives each year to replace outgoing representatives. No representative can serve two consecutive terms except the one-year term representatives elected in 2004. In the event an Executive Council Representative is unable to fulfill their full term of office, the Consortium Director and the NETL Representative will convene the Technical Advisory Committee to elect a new representative to complete the unfinished term. Voting will be by electronic ballot and election by a simple majority of the voting members.

Section 2c. With the consent of the Technical Advisory Committee, the Executive Council may be expanded to eleven (11) voting Members pending a simple majority vote of the Technical Advisory Committee. The eleven members Executive Council must be composed of no less than six (6) Gas Storage Operators.

Section 2d. With the consent of the Technical Advisory Committee pending a simple majority vote and approval of the NETL representative, the Executive Council may be expanded to include those member(s), that provide co-funding to the Consortium. The Full or Affiliate member shall be a non-voting member of the Executive Council. Terms of Full or Affiliate members so elected as non-voting members of the Executive

Council will be determined on a case-by-case basis by the GSTC Director and the Council Representative from NETL.

Section 3. The GSTC Director shall be the chief representative of the Consortium and shall be responsible for the administration of its affairs. The Director may represent the Consortium in situations where a single representative of the Consortium is appropriate. The Director may interact with public and private funding sources to secure and maintain funding necessary to meet the long-term goals of the Consortium.

Section 3a. As the GSTC Administrator, the Director shall implement the decisions of the Executive Council, and oversee the daily operations of the Consortium. The Director will establish and enforce computerized and other necessary communication systems among all Consortium Members. Under the direction of the Executive Council, the Director, in accordance with Articles III Section 4 and Articles V and VII, will operationally manage Consortium funding. The Director will have authority to establish and maintain research reporting procedures using Department of Energy guidelines where applicable. The Director may publicize the GSTC and its research results utilizing publications, research reviews, and any other means approved by the Executive Council. The Director will make recommendations to the Executive Council to aid it in setting policy for the GSTC.

Section 3b. The Director shall be appointed by the College of Earth and Mineral Sciences with the approval of the Pennsylvania State University, and serves at the pleasure of The Pennsylvania State University. It is the responsibility of the University to provide staff and facilities for the conduct of the Director's duties and responsibilities as provided in the Constitution.

Section 3c. The Director will schedule at least one Executive Council meeting per year at places and times set by the Director with the approval of the Executive Council representatives. The Director will prepare the agenda for Executive Council meetings from items submitted by the representatives of the Executive Council and the Technical Advisory Committee. The Director shall preside over the Executive Council meetings and arrange for minutes of the meetings to be recorded and distributed to all Members. Attendance by a majority of the representatives of the Executive Council shall constitute a simple majority of voting members for the conduct of business at scheduled meetings. In the event that specific items of Consortium business require a vote of the Executive Council and it is impractical to convene a full Executive Council meeting, the Director will poll the Executive Council Membership by telephone, computer, or other means. The Director in consultation with the Executive Council, shall schedule Technology Transfer meetings and Technology Advisory Committee meetings, at a minimum of one meeting per year.

Section 4. Administrative costs in support of the Director and Director's office will be borne by the Consortium and shall not exceed the management funding provided to The Pennsylvania State University through the DOE Cooperative Agreement.

Article IV.

Amending the Constitution:

Section 1. The Consortium Constitution can be amended only at the recommendation of the Executive Council. All amendments must comply with the Pennsylvania State University and the DOE Cooperative Agreement. Recommended changes to the Constitution must be first approved by a two-thirds majority vote of the Executive Council and subsequently approved by a two-thirds vote of the consortium membership.

Section 1a. Any GSTC member may propose a change in the Constitution by petition to the Consortium Director. The Director shall submit the proposed amendment or change to each representative of the Executive Council at least thirty (30) days prior to the next meeting of the Executive Council.

Article V

Program Funding:

Section 1. The GSTC Director will solicit proposals from the Full and University Members of the Consortium on an annual basis. A fully executed membership agreement must be in place and current prior to accepting a proposal for review.

Section 2. A minimum 40% co-funding is required for each proposal submitted to the GSTC Consortium. The 40% co-funding is calculated as 40% of the total cost of the proposed project. The Consortium does encourage collaboration among the GSTC Members. Full Members, University Members and any other participants in proposed research projects are encouraged to provide additional co-funding for each proposal submitted to the Consortium for review. All co-funding must be supported by appropriate documentation and will be subject to review as part of the complete proposal package.

Section 3. Proposals from non-US Full and University members may be accepted and funded, provided that 75% of the total cost, based on actual costs, is conducted in the U.S.

Section 4. The Consortium Director shall receive proposals from the Full and University Members and distribute the proposals to the Executive Council fourteen (14) days before the Consortium meeting.

Section 5. The Executive Council is the final decision making body for approval of all projects funded by the GSTC.

Section 6. The GSTC Director will notify all applicants of their funding status in writing within fourteen (14) days of the Executive Council decision.

Section 7. For each research project funded through the Consortium, the Executive Council will appoint a small (2-4) member ad-hoc committee consisting of GSTC Members to help provide technical guidance during the conduct of the work. Members are precluded from appointment to ad-hoc committees for a project co-funded by the member's corporate or university affiliation. Technical progress will be reviewed periodically at Consortium meetings.

Article VI.

Publications and Conferences:

Section 1. Overview Articles will be used to promote and describe, in non-technical terms, the activities of the GSTC. The preparation, presentation and publication of overview articles for GSTC projects shall remain the responsibility of The Pennsylvania State University. GSTC Members shall be provided with the opportunity to review any overview papers or presentations containing any of the results of the GSTC funded projects and are free to distribute overview articles.

Section 2. Presentations. Full Members and University Members may present technical papers on their GSTC funded projects provided the Consortium is acknowledged for its funding and provided that said Presentations do not contain any proprietary information subject to non-disclosure restrictions.

Section 3. Publications. Subject to the following restrictions, Full and University Members shall be free to publish the results of the GSTC funded projects provided they maintain the confidentiality of Gas Storage Technology information, where it has been clearly marked "Confidential" in the initial proposal funded by the GSTC:

- i) All such publications shall be consistent with deliverables and statement of work approved by the Executive Council and contained in the subaward/subcontract issued by The Pennsylvania State University;
- ii) DOE shall be given the right to review and comment on all publications pursuant to Section 4.18 of DOE Cooperative Agreement No. DE-FC26-03NT41779; and
- iii) Parallel to the DOE review period, the Executive Council shall have the right to review and comment upon any such publications and to the extent practical; and
- iv) The DOE and the Executive Council shall have 30 days to provide comments to the Consortium Director. The Consortium Director will distribute comments to the author of the publication. Authors shall give any such comments due consideration.

Section 4. The GSTC Director shall be responsible for the preparation of all guidelines for technical reports and publications that have been approved by the Executive Council.

Article VII.

Finances:

Section 1. The Pennsylvania State University will serve as fiscal agent for the Consortium. As such, the Pennsylvania State University will represent the Consortium in fiscal matters and have the ultimate accounting and financial reporting duties and the sole legal authority to enter into contracts and to administer and expend funds on behalf of the Consortium. Periodically a summary of the total value of the GSTC consortium will be posted to the Consortium website and will be available only to current members.

Article VIII.

Intellectual Property Rights Policy for Gas Storage Technology Consortium:

Section 1. Pursuant to Chapter 18 of Title 35 of the United States Code, commonly known as the Bayh-Dole Act, as enacted by the Department of Energy (DOE) in DEAR 952-227-11, any domestic small business firm or nonprofit organization conducting research under Consortium funding (Research Party) may elect to retain title to any invention conceived of or first actually reduced to practice by its employees in the course of or under the research conducted with Consortium funding. Title to these inventions will be subject to DOE patent policies, including retention by the Government of a license for Government use and march-in rights, and U.S. competitiveness and manufacture requirements. The Consortium will petition the DOE for a class waiver of ownership rights to any inventions conceived or first actually reduced to practice by employees of entities other than domestic small business firms and nonprofit organizations. Information that results from the research and development conducted with Consortium funding and that would be trade secret or commercial or financial information that is privileged or confidential if the information had been obtained without Federal support, may be protected from public disclosure for up to five years after development of the information, but shall be available to Consortium Members during the period of protection.

Appendix B
GSTC Membership Listing

GSTC Membership Listing **(September 30, 2003 – September 30, 2010)**

1. Ameren Corporation, *IL*
2. American Gas Association (AGA), *DC*
3. AOPL C/O Enterprise Products, *MI*
4. Atmos Energy, *TX*
5. Baker Atlas, *MI*
6. Baker Petrolite, *TX*
7. Basic Systems, Inc., *OH*
8. Boardwalk Pipeline Partners, *KY*
9. Buckeye Pipe Line Company, *TX*
10. C-Fer Technologies, *Canada*
11. California Energy Commission, *CA*
12. CenterPoint Energy, *MO*
13. Citizens Gas & Coke Utility, *IN*
14. Clemson University, Dept. of Environmental Engineering & Earth Sciences, *SC*
15. Colorado Engineering Experiment Station, *CO*
16. Colorado School of Mines, *CO*
17. Columbia Gas Transmission, LLC , *WV*
18. Consumers Energy, *MI*
19. Correlations Company, *NM*
20. Dominion Delivery, *OH*
21. Dominion Transmission, Inc., *WV*
22. DTE Energy/Mich Con, *MI*
23. Duke Energy Gas Transmission, *TX*
24. Edison Welding Institute, Inc. (EWI), *OH*
25. El Paso Corporation, *CO*
26. Enbridge Gas Distribution, *Canada*
27. Enstor Operating Co., LLC, *TX*
28. Equitans, LP, *PA*
29. Furness Newburge, Inc., *KY*
30. Gas Technology Institute, *IL*
31. Gemini Solutions, Inc., *TX*
32. Gulf South Pipeline, *LA*
33. Halliburton Energy Services, *MI*
34. IMPACT Technologies LLC, *OK*
35. Isotech Laboratories, Inc., *IL*
36. Kiefner and Associates, Inc., *OH*
37. Kinder Morgan, Inc., *IL*
38. Marathon Pipe Line , *OH*
39. National Fuel Gas Supply Corporation, *NY*
40. New Mexico Tech, *NM*
41. NGS Energy LP, *CT*
42. NITEC, LLC., *CO*
43. NW Natural, *OR*

44. ONEOK Gas Storage, LLC , *OK*
45. Pacific Gas & Electric Company, *CA*
46. Panhandle Energy, *TX*
47. PB Energy Storage Services, *SD*
48. PII North America, Inc., *TX*
49. Pipeline Research Council International, Inc. PRCI, *IL*
50. RESPEC, *SD*
51. Schlumberger Data & Consulting Services, *PA*
52. Shell Pipeline Company, *TX*
53. Southern California Gas Co. (Sempra Energy), *CA*
54. Spectra Energy Transmission, *TX*
55. TechSavants, Inc., *NM*
56. Texas A&M University, Petroleum Eng. Dept., *TX*
57. Texas Gas Transmission, LLC, *KY*
58. The Pennsylvania State University, EMS Energy Institute, *PA*
59. TransCanada Pipelines Ltd. (ANR Pipelines), *MI*
60. TransGas Limited, *CANADA*
61. University of Illinois, The Board of Trustees, *IL*
62. University of Missouri, Rolla, *MO*
63. University of Texas-Austin, *TX*
64. URS Corporation, *TX*
65. Well Dynamics, Inc., *TX*
66. West Virginia University, *WV*
67. Williams Gas Pipeline, *TX*

Appendix C
2004, Gas Storage Field Deliverability Enhancement and Maintenance:
An Intelligent Portfolio Management Approach,
West Virginia University Final Report

Gas Storage Field Deliverability Enhancement and Maintenance: An Intelligent Portfolio Management Approach.

First Year Final Report

Reporting Start Date: September 1, 2004

Reporting End Date: December 31, 2005

Report prepared by:

Shahab D. Mohaghegh, Ph.D.

Principal Investigator

Petroleum & Natural Gas Engineering

West Virginia University

Morgantown, WV 26506

Telephone: 304.293.7682 Ext. 3405

Fax: 304.293.5708

Email: Shahab@wvu.ed

Reporting Issue Date: February 2006

Subcontract No. 2805-WVU-DOE-1779

Report prepared for:

GSCT Consortium Director

PSU/Energy Institute

The Pennsylvania State University

C211 Coal Utilization Laboratory

University Park, PA 16802-2309

Telephone: 814.865.0531

Fax: 814.685.3248

Email: jlm9@psu.edu

DISCLAIMER

This report was prepared as an account of work sponsored by an agency of the United States Government. Neither the United States Government nor any agency thereof, nor any of their employees, makes any warranty, expressed or implied, or assumes any legal liability or responsibility for the accuracy, completeness, or usefulness of any information, apparatus, product, or process disclosed, or represents that its use would not infringe privately owned rights. Reference herein to any specific commercial product, process, or service by trade name, trademark, manufacturer, or otherwise does not necessarily constitute or imply its endorsement, recommendation, or favoring by the United States Government or any agency thereof. The views and opinions of authors expressed herein do not necessarily state or reflect those of the United States Government or any agency thereof.

ABSTRACT

Portfolio management, a common practice in the financial market, is essentially an optimization problem that attempts to increase return on investment. The objective this project is to apply the state-of-the-art in optimum portfolio management to the gas storage field in order to optimize the return on investment associated with well remedial operations.

Each year gas storage operators spend hundreds of thousands of dollars on workovers, re-completions, and re-stimulations of storage wells in order to battle the decline in deliverability due to well damage with time. A typical storage field has tens if not hundreds of production wells. Each well will respond to a remedial operation in its own unique way that is a function of a set of uncontrollable parameters such as porosity and permeability and a set of controllable parameters such as completion and stimulation practices.

The objective of this project is to identify the combination of best candidate wells for the remedial operations that will result in the most successful program each year, and consequently provides the highest return on investment. The project deliverable is a Windows-based software application that would perform the analysis and provide the list of wells and their corresponding remedial operation for each year base on the budget constraints identified by the user.

The state-of-the-art in intelligent systems application that is currently being used extensively in the Wall Street is the methodology to achieve the objectives of this proposed project. This methodology includes a hybrid form of artificial neural networks, genetic algorithms and fuzzy logic. The principal investigator of this project is a pioneer in application of intelligent systems in the oil and gas industry and has a successful track record in developing intelligent applications for our industry.

Columbia Gas Transmission Corporation will be the industry partner of this project and will cooperate with the research and development team in order to ensure successful completion of the project.

At the end of the first year of the project the database was completed. The database includes modules for interpretation of gas storage wells pressure test data as it is demonstrated in this report.

TABLE OF CONTENTS

Abstract	3
Table of Content	4
List of Figures	5
Introduction	7
Executive Summary	8
Experimental	9
Results & Discussions	10
Conclusions	72

LIST OF FIGURES

Figure 1. Well-bore data retrieved from a file 13

Figure 2. Correction of Wrong API number in data 14

Figure 3. Data addition and refinement for Well-bore Data 15

Figure 4. Multiple Data Entries in Completion Table 17

Figure 5. Well-bore data retrieved from a file 18

Figure 6. Data addition and refinement for Completion Data 19

Figure 7. Perforation data retrieved from a file 21

Figure 8. Data addition and refinement for Perforation Data 22

Figure 9. Perforation data retrieved from a file 24

Figure 10. Different formats of Nitrogen Amount 26

Figure 11. Data addition and refinement for Stimulation Data 28

Figure 12. Tubing head pressure profile for multi-point test 32

Figure 13. Bottom-hole pressure profile for multi-point test 32

Figure 14. Flow test 1 – Delta pressure squared vs. time 33

Figure 15. Flow test 2 – Delta pressure squared vs. time 33

Figure 16. Extended flow test – Delta pressure squared vs. time 34

Figure 17. Log-log graph 34

Figure 18. Gas properties simulator 35

Figure 19. Calculation of true skin 36

Figure 20. Calculation of true skin from build up test 37

Figure 21. Retrieving flow rate of an open flow test 39

Figure 22. Data addition and refinement for well test data 40

Figure 23. Screen shot of database showing different tables 41

Figure 24. Main Screen of software 42

Figure 25. Browsing through the well-bore data 43

Figure 26. Well-bore tab 45

Figure 27. Completion tab 46

Figure 28. Perforation tab 47

Figure 29. Stimulation tab 48

Figure 30. Well-test tab 49

Figure 31. Adding a complete new Well – well-bore tab 50

Figure 32. Adding a complete new Well - completion tab 51

Figure 33. Adding a complete new Well – entering data for wellbore 52

Figure 34. Adding a complete new Well – entering data for perforation 52

Figure 35. Adding a complete new Well – entering data for stimulation 53

Figure 36. Adding a complete new Well – entering data for well test 53

Figure 37. Result of adding a complete new well 54

Figure 38. Editing well data 56

Figure 39. Editing completion data 57

Figure 40. Saving completion data 58

Figure 41. Saved completion data 59

Figure 42. Deleting perforation record 60

Figure 43. Finding a well 61

Figure 44. Retrieving the data..... 62

Figure 45. Well-test Analysis Option in well-test tab 63

Figure 46. Show Chart – Peak Day Rate 63

Figure 47. Show Chart – Absolute Open Flow 64

Figure 48. Well Test analysis – Showing types of tests 65

Figure 49. Well Test analysis – zoomed 65

Figure 50. Well-tests selected for analysis 66

Figure 51. Well-tests selected to find value of ‘n’ 66

Figure 52. Draw a line to find value of ‘n’ 67

Figure 53. Calculating value of ‘n’ 67

Figure 54. Calculating C, PDR & AOF 68

Figure 55. C, PDR & AOF values saved in the database 68

Figure 56. Selecting Ohio County 69

Figure 57. Selecting wells according to stimulation year 70

Figure 58. Offset wells 70

Figure 59. Selecting Well Parameters 71

Figure 60. Result of the wells & parameters selected 71

INTRODUCTION

Each year Gas Storage operators spend hundreds of thousands of dollars to combat the inevitable decline in the deliverability of their production wells. The decline in deliverability with time has two major contributors. The first contributor is geology and reservoir characteristics that are uncontrollable parameters. The second sets of parameters that contribute to the decline are associated with well damage that is addressed by well remedial operations such as workovers, re-completions, and re-stimulation of the producing wells. The parameters associated with these remedial operations can be controlled by the operator.

It is a fact that every well will respond to a specific remedial operation in a unique way. For example the deliverability of well “A” will increase two folds if a proper restimulation is performed on it while the same operation performed on well “B” will result in little or no deliverability enhancement. Same is true for workovers. Finding the best candidate for restimulation or workover, each year, from among the tens or hundreds of wells is a challenging task. Consider another situation where well “C” will have a 70% increase if a restimulation is performed but it would have a 65% increase if a far less expensive workover is performed. Obviously performing a workover instead of a restimulation on well “C” would be more economical this year.

EXECUTIVE SUMMARY

Portfolio management, a common practice in the financial market, is essentially an optimization problem that attempts to increase return on investment. The objective this project is to apply the state-of-the-art in optimum portfolio management to the gas storage field in order to optimize the return on investment associated with well remedial operations.

Each year gas storage operators spend hundreds of thousands of dollars on workovers, re-completions, and re-stimulations of storage wells in order to battle the decline in deliverability due to well damage with time. A typical storage field has tens if not hundreds of production wells. Each well will respond to a remedial operation in its own unique way that is a function of a set of uncontrollable parameters such as porosity and permeability and a set of controllable parameters such as completion and stimulation practices.

The objective of this project is to identify the combination of best candidate wells for the remedial operations that will result in the most successful program each year, and consequently provides the highest return on investment. The project deliverable is a Windows-based software application that would perform the analysis and provide the list of wells and their corresponding remedial operation for each year base on the budget constraints identified by the user.

The state-of-the-art in intelligent systems application that is currently being used extensively in the Wall Street is the methodology to achieve the objectives of this proposed project. This methodology includes a hybrid form of artificial neural networks, genetic algorithms and fuzzy logic. The principal investigator of this project is a pioneer in application of intelligent systems in the oil and gas industry and has a successful track record in developing intelligent applications for our industry.

Columbia Gas Transmission Corporation will be the industry partner of this project and will cooperate with the research and development team in order to ensure successful completion of the project.

At the end of the first year of the project the database was completed. The database includes modules for interpretation of gas storage wells pressure test data as it is demonstrated in this report.

EXPERIMENTAL

No experimental work was performed during this project.

RESULTS & DISCUSSIONS

This is the detail report of the progress made so far in the above mentioned project, which consists of following components:

- 1- Project Overview
- 2- Data made available and it's format
- 3- Database & Software

PROJECT OVERVIEW

The objective of this project is to apply state-of-the-art intelligent, optimum portfolio management to the gas storage field in order to optimize the return on investment associated with well remedial operations. Columbia Gas Transmission Corporation is the industry partner in this project and provided us with very valuable data and in-depth knowledge about their gas storage field operations.

The data in very crude form was provided to the research and development team in the last week of March, 2005. The team extracted valuable data and organized it in a form of database, with generic make up in order to be reusable. Windows-based software was developed which can help the user in viewing and later populating the data with easy to use interface. One of its modules provides the user with all the valid stimulations required as an input for Neural Network.

DATA MADE AVAILABLE AND IT'S FORMAT

The research and development (R & D) team was initially provided data in MS excel worksheets. On further request some pdf files with well schematics, well test files and well summary files were provided but still the required data especially relating to stimulations and well-tests was so scarce that the team in July, 2005 went to the Columbia Transmission Corporation Office in Charleston, WV to get more information. Retrieval of data from different files and thousands of microfiche was taking so long at the office that it was decided that West Virginia University lab facilities will be used to read thousands of microfiche. So for the next few weeks the team concentrated its efforts on data collection. That data could be segregated into five main tables, each relating to specific characteristic features of the gas storage wells. The five characteristic features are below:

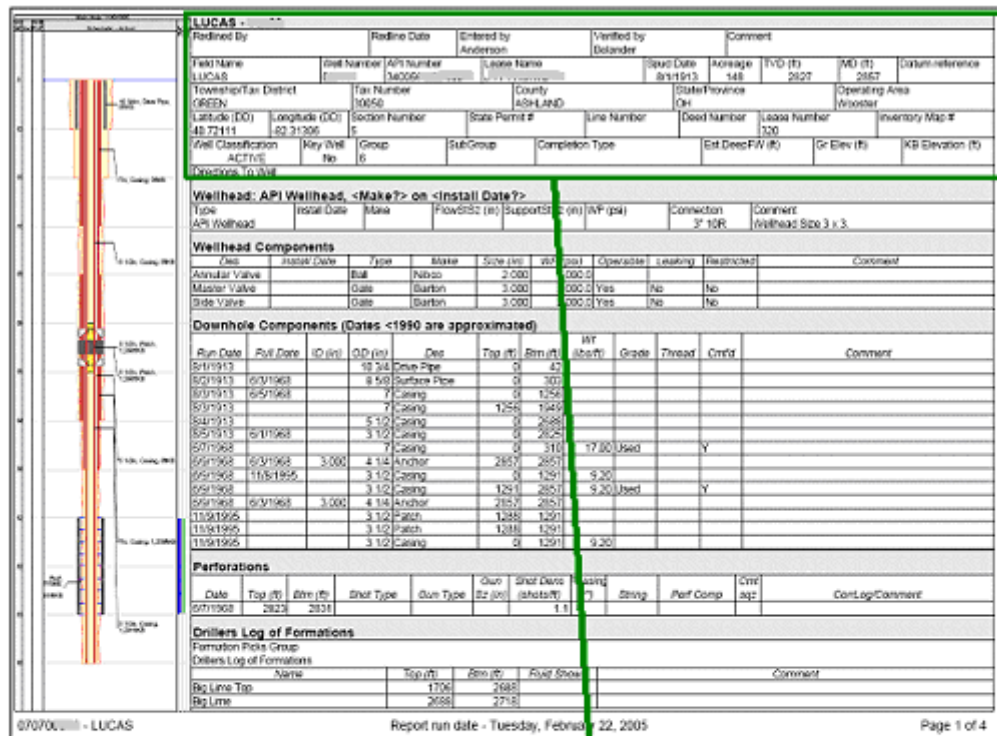
- 1- Well-bore data
- 2- Completion Data
- 3- Perforation Data
- 4- Stimulation Data
- 5- Well-Test Data

WELL BORE DATA

It includes basic features of the well like location, depth, well name ... etc. Data about well-bore was retrieved mostly from well schematics and well summary reports. The data already provided by Columbia Transmission Corporation was also verified. The complete list of the data type retrieved is below

1. API Number
2. Field Name
3. Well
4. Lease Name
5. Classification
6. Latitude (Lat)
7. Longitude (Long)
8. Section
9. Township
10. County
11. State
12. Operator
13. Total Vertical Depth
14. Formation

Picture of one of the form from which this data was retrieved is on next page



LUCAS - 000000									
Redlined By		Redline Date		Entered by		Verified by		Comment	
Anderson				Anderson		Bolander			
Field Name		Well Number		API Number		Lease Name		Spud Date	
LUCAS		340056		340056				8/1/1913	
Township/Tax District		Tax Number		County		State/Province		Acreage	
GREEN		30050		ASHLAND		OH		148	
Latitude (DD)		Longitude (DD)		Section Number		State Permit #		Line Number	
40.72111		-82.31306		5					
Well Classification		Key Well		Group		SubGroup		Completion Type	
ACTIVE		No		6					
								Est. DeepFW (ft)	

Fig1. Well-bore data retrieved from a file

The tables contained many minor mistakes like wrong Well API number length and many spelling mistakes. A picture of this correction is below:

1	A	B	C	D	E	F	G	H	I	J	K
	Field Name	Well	Lease Name	API	Classification	Latitude	Longitude	Section	Township	County	State
32	LUCAS	03897	*SYLVIA C. KROUT, ET AL*	34-005-93897	ACTIVE	40.6961	-82.3058	17	GREEN	ASHLAND	OH
33	LUCAS	03912	P. SHAFFER #1	34-005-602660000	SPECIAL	40.7133	-82.24	1	GREEN	ASHLAND	OH
34	LUCAS	03921	G. W. HINER #2	34-005-93921	ACTIVE	40.7383	-82.2719	34	VERMILLION	ASHLAND	OH
35	LUCAS	03926	JOHN BUSLER #1	34-005-602650000	ACTIVE	40.7106	-82.2358	12	GREEN	ASHLAND	OH
36	LUCAS	03929	D. KICK #1	34-005-93929	ACTIVE	40.7103	-82.2611	10	GREEN	ASHLAND	OH
37	LUCAS	03931	W. E. GUTHRIE #1	34-005-93931	ACTIVE	40.6889	-82.3047	17	GREEN	ASHLAND	OH
38	LUCAS	03932	H. J. TRUMPOWER #1	34139601180000	ACTIVE				MONROE	RICHLAND	OH
39	LUCAS	03935	J. O. ANDREWS #2	34-005-93935	ACTIVE				GREEN	ASHLAND	OH
40	LUCAS	03939	M. A. MAURER #1	34-005-93939	ACTIVE				VERMILLION	ASHLAND	OH
41	LUCAS	03945	*RUSSEL J. LIFER, ET UX*	34-005-93945	ACTIVE				GREEN	ASHLAND	OH
42	LUCAS	03946	C. SMITH #1	34005602420000	ACTIVE	40.6703	-82.3339	19	GREEN	ASHLAND	OH
43	LUCAS	03950	G. W. PURVINE #1	34139601230000	ACTIVE	40.6736	-82.3453	24	MONROE	RICHLAND	OH
44	LUCAS	03953	J. H. ROWE #1	34139201590000	ACTIVE	40.6761	-82.3417	24	MONROE	RICHLAND	OH
45	LUCAS	03963	WM. & MARY BRENNSTUHL #1	34-005-93963	ACTIVE	40.6228	-82.2925	9	HANOVER	ASHLAND	OH
46	LUCAS	03967	J. F. MANG #1	34005602590000	ACTIVE	40.6983	-82.3061	8	GREEN	ASHLAND	OH
47	LUCAS	03969	J. & E. PARR #1	34-005-93969	ACTIVE	40.6739	-82.3375	19	GREEN	ASHLAND	OH
48	LUCAS	03972	J. H. ROWE #2	34-139-93972	ACTIVE	40.6797	-82.3408	24	MONROE	RICHLAND	OH
49	LUCAS	03976	W. & M. APPLGATE #1	34-139-93976	ACTIVE	40.6836	-82.3494	13	MONROE	RICHLAND	OH
50	LUCAS	03978	A. & C. GUTHRIE #1	34-005-93978	ACTIVE	40.6806	-82.3356	19	GREEN	ASHLAND	OH
51	LUCAS	03983	E. & M. OSWALD #1	34139601590000	ACTIVE	40.6836	-82.345	13	MONROE	RICHLAND	OH
52	LUCAS	03995	S. E. MCKENLEY #1	34-005-93995	ACTIVE	40.7378	-82.2231	36	VERMILLION	ASHLAND	OH
53	LUCAS	03997	W. & M. APPLGATE #2	34-139-93997	ACTIVE	40.6856	-82.3536	13	MONROE	RICHLAND	OH
54	LUCAS	04008	H. & M. MCGUIRE #1	34005216200000	ACTIVE	40.6983	-82.2614	10	GREEN	ASHLAND	OH

Wrong API Number length

1	Field Name	Well	API	Classification	Latitude	Longitude	Section	Township	County	State	Operator
32	LUCAS	03897	34-005-93897	ACTIVE	40.6961	-82.3058	17	GREEN	ASHLAND	OH	Columbia Gas Transmissi
33	LUCAS	03912	34-005-60266	SPECIAL	40.7133	-82.24	1	GREEN	ASHLAND	OH	Columbia Gas Transmissi
34	LUCAS	03921	34-005-93921	ACTIVE	40.7383	-82.2719	34	VERMILLION	ASHLAND	OH	Columbia Gas Transmissi
35	LUCAS	03926	34-005-60265	ACTIVE	40.7106	-82.2358	12	GREEN	ASHLAND	OH	Columbia Gas Transmissi
36	LUCAS	03929	34-005-93929	ACTIVE	40.7103	-82.2611	10	GREEN	ASHLAND	OH	Columbia Gas Transmissi
37	LUCAS	03931	34-005-93931	ACTIVE	40.6889	-82.3047	17	GREEN	ASHLAND	OH	Columbia Gas Transmissi
38	LUCAS	03932	34-139-60118	ACTIVE	40.6736	-82.3478	24	MONROE	RICHLAND	OH	Columbia Gas Transmissi
39	LUCAS	03935	34-005-93935	ACTIVE		-82.247	2	GREEN	ASHLAND	OH	Columbia Gas Transmissi
40	LUCAS	03939	34-005-93939	ACTIVE		-82.2375	25	VERMILLION	ASHLAND	OH	Columbia Gas Transmissi
41	LUCAS	03945	34-005-93945	ACTIVE		-82.3017	17	GREEN	ASHLAND	OH	Columbia Gas Transmissi
42	LUCAS	03946	34-005-60242	ACTIVE	40.6703	-82.3339	19	GREEN	ASHLAND	OH	Columbia Gas Transmissi
43	LUCAS	03950	34-139-60123	ACTIVE	40.6736	-82.3453	24	MONROE	RICHLAND	OH	Columbia Gas Transmissi
44	LUCAS	03953	34-139-20159	ACTIVE	40.6761	-82.3417	24	MONROE	RICHLAND	OH	Columbia Gas Transmissi
45	LUCAS	03963	34-005-93963	ACTIVE	40.6228	-82.2925	9	HANOVER	ASHLAND	OH	Columbia Gas Transmissi
46	LUCAS	03967	34-005-60259	ACTIVE	40.6983	-82.3061	8	GREEN	ASHLAND	OH	Columbia Gas Transmissi
47	LUCAS	03969	34-005-93969	ACTIVE	40.6739	-82.3375	19	GREEN	ASHLAND	OH	Columbia Gas Transmissi
48	LUCAS	03972	34-139-93972	ACTIVE	40.6797	-82.3408	24	MONROE	RICHLAND	OH	Columbia Gas Transmissi
49	LUCAS	03976	34-139-93976	ACTIVE	40.6836	-82.3494	13	MONROE	RICHLAND	OH	Columbia Gas Transmissi
50	LUCAS	03978	34-005-93978	ACTIVE	40.6806	-82.3356	19	GREEN	ASHLAND	OH	Columbia Gas Transmissi
51	LUCAS	03983	34-139-60159	ACTIVE	40.6836	-82.345	13	MONROE	RICHLAND	OH	Columbia Gas Transmissi
52	LUCAS	03995	34-005-93995	ACTIVE	40.7378	-82.2231	36	VERMILLION	ASHLAND	OH	Columbia Gas Transmissi
53	LUCAS	03997	34-139-93997	ACTIVE	40.6856	-82.3536	13	MONROE	RICHLAND	OH	Columbia Gas Transmissi
54	LUCAS	04008	34-005-21620	ACTIVE	40.6983	-82.2614	10	GREEN	ASHLAND	OH	Columbia Gas Transmissi

Corrected API Number

Fig2. Correction of Wrong API number in data

GRAPHICAL ANALYSIS OF RAW DATA vs. REFINED DATA

WELLBORE DATA														
DATA FIELDS	API Number	Field Name	Well	Lease Name	Classification	Lat	Long	Section	Township	County	State	Operator	Total Vertical Depth	Formation
INITIAL DATA AVAILABLE	430	427	430	430	427	429	430	430	430	430	430	430	425	430
FINAL DATA AVAILABLE	430	430	430	430	430	430	430	430	430	430	430	430	430	430

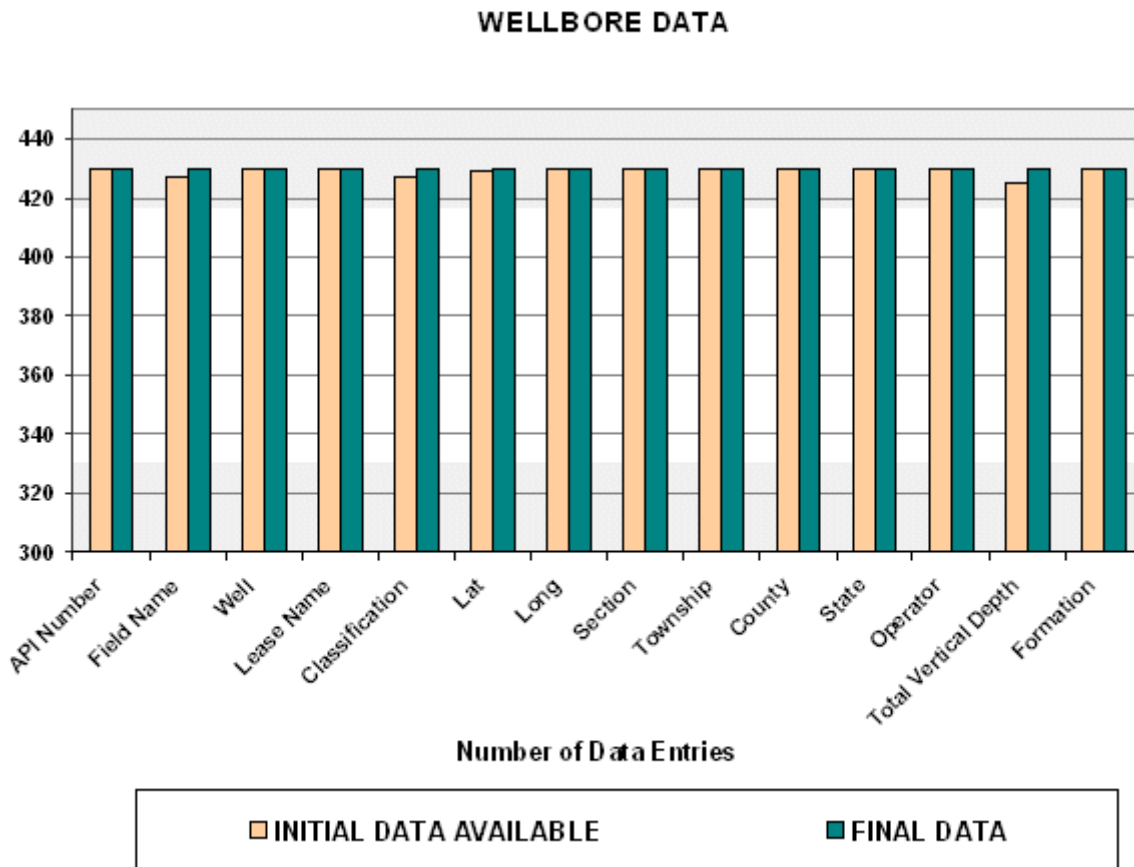


Fig3. Data addition and refinement for Well-bore Data

COMPLETION DATA

Completion data mostly relates to the type and depth of casing/liner/tubing run in the gas storage wells. The data type retained for the database includes following

1. API Number
2. Field Name
3. Well Name (Well)
4. Completion Description (Des)
5. Date Tubing Run (Dt Tm Rn)
6. Outer Diameter (OD)
7. Top of Casing
8. Bottom of Casing(Bot)
9. Casing Weight (Weight)
10. Casing Grade (Grade)

Unfortunately the data was mostly in an excel file and had to be verified with well schematic drawings. This led to the most unusual step in this project as it lead to reduction of valuable data available to us. This was due to the erroneous and multiple data entry originally in the completion table. Identification of the multiple entries and their removal from table was the most focused act of cleaning the data, as omission of desirable records was unacceptable. Following pictures show one of such flawed multiple data entries which were removed.

	A	B	C	D	E	F	G	H	I	J	K	L
1	Field Name	Well	API	Des	DTmRun	OD	Top	Bot	Weight	Grade		
71	LUCAS	00873	34-005-90873	Casing	03-Oct-17	7.00	0	2043	20.00			
72	LUCAS	00873	34-005-90873	Casing	02-Mar-64	5.50	0	2908	17.00	Seamless		
73	LUCAS	01981	34-005-91981	Drive Pipe	01-Nov-24	10.75	0	33	40.00			
74	LUCAS	01981	34-005-91981	Surface Pipe	02-Nov-24	8.63	0	299	24.00			
75	LUCAS	01981	34-005-91981	Casing	03-Nov-24	7.00	1893	1931	20.00			
76	LUCAS	01981	34-005-91981	Casing	04-Nov-24	5.50	0	2681	17.00			
77	LUCAS	01981	34-005-91981	Casing	02-Nov-63	3.50	0	2694	9.20	Used		
78	LUCAS	01981	34-005-91981	Packer	03-Nov-63	5.50	2684	2694		Straight Anchor		
79	LUCAS	01981	34-005-91981	Packer	03-Nov-63							
80	LUCAS	01981	34-005-91981	Packer	03-Nov-63							
81	LUCAS	02008	34-005-92008	Drive Pipe	01-Jul-25							
82	LUCAS	02008	34-005-92008	Surface Pipe	02-Jul-25							
83	LUCAS	02008	34-005-92008	Packer	03-Jul-25	8.63	1829	1839		Larkin Lead B.H.		
84	LUCAS	02008	34-005-92008	Packer	03-Jul-25	8.63	1829	1839				
85	LUCAS	02008	34-005-92008	Casing	03-Jul-25	7.00	1793	1839	20.00			
86	LUCAS	02008	34-005-92008	Packer	04-Jul-25	7.00	2500	2510				
87	LUCAS	02008	34-005-92008	Packer	04-Jul-25	7.00	2500	2510		OVS Midget		
88	LUCAS	02008	34-005-92008	Casing	04-Jul-25	5.50	0	2510	17.00			
89	LUCAS	02008	34-005-92008	Casing	02-Oct-63	5.50	0	2654				
90	LUCAS	02008	34-005-92008	Packer	02-Oct-63	5.50	2551	2561				
91	LUCAS	02008	34-005-92008	Anchor	02-Oct-63	5.50	2561	2571				
92	LUCAS	02008	34-005-92008	Packer	02-Oct-63	5.50	2551	2561				
93	LUCAS	02008	34-005-92008	Anchor	02-Oct-63	5.50	2561	2571				
94	LUCAS	02060	34-005-92060	Casing	01-Oct-25	10.75	0	64	40.00			

Multiple Data Entry

Fig4. Multiple Data Entries in Completion Table

In the completion table the following notations used as casing description were replaced in place of different notations being used to have a standard definition

NOTATION KEPT IN DATABASE	Surface casing
NOTATIONS DISCARDED	Drive pipe
	Driver Pipe
	Swedge
	Two stage

Completion data was mostly re- checked for accuracy from the documents, picture of which is shown below for a Well

LUCAS - **																	
Redlined By		Redline Date		Entered by		Verified by		Comment									
Field Name		Well Number		API Number		Lease Name		Spud Date		Acreage		TVD (ft)		MD (ft)		Datum reference	
Township/Tax District		Tax Number		County		State/Province		Operating Area									
Latitude (DD)		Longitude (DD)		Section Number		State Permit #		Line Number		Deed Number		Lease Number		Inventory Map #			
Well Classification		Key Well		Group		SubGroup		Completion Type		Est DeepFW (ft)		Gr Elev (ft)		KB Elevation (ft)			
Directions To Well																	
Wellhead: API Wellhead, <Make?> on <Install Date?>																	
Type		Install Date		Make		FlowStSz (in)		SupportStSz (in)		WP (psi)		Connection		Comment			
API Wellhead												3" 10R		Wellhead Size 3 x 3.			
Wellhead Components																	
Des	Install Date	Type	Make	Size (in)	WP (psi)	Operate	Leaking	Restricted	Comment								
Annular Valve		Ball	Nibco	2.000	2,000.0												
Master Valve		Gate	Barton	3.000	2,000.0	Yes	No	No									
Side Valve		Gate	Barton	3.000	2,000.0	Yes	No	No									
Downhole Components (Dates <1990 are approximated)																	
Run Date	Pull Date	ID (in)	OD (in)	Des	Top (ft)	Btm (ft)	Wt (lbs/ft)	Grade	Thread	Cmt'd	Comment						
8/1/1913			10 3/4	Drive Pipe	0	42											
8/2/1913	6/3/1968		8 5/8	Surface Pipe	0	303											
8/3/1913	6/5/1968		7	Casing	0	1256											
8/3/1913			7	Casing	1256	1949											
8/4/1913			5 1/2	Casing	0	2688											
8/5/1913	6/1/1968		3 1/2	Casing	0	2825											
6/7/1968			7	Casing	0	310	17.00	Used		Y							
6/9/1968	6/3/1968	3.000	4 1/4	Anchor	2857	2857											
6/9/1968	11/8/1995		3 1/2	Casing	0	1291	9.20										
6/9/1968			3 1/2	Casing	1291	2857	9.20	Used		Y							
6/9/1968	6/3/1968	3.000	4 1/4	Anchor	2857	2857											
11/9/1995			3 1/2	Patch	1288	1291											
11/9/1995			3 1/2	Patch	1288	1291											
11/9/1995			3 1/2	Casing	0	1291	9.20										

Downhole Components (Dates <1990 are approximated)											
Run Date	Pull Date	ID (in)	OD (in)	Des	Top (ft)	Btm (ft)	Wt (lbs/ft)	Grade	Thread	Cmt'd	Comment
8/1/1913			10 3/4	Drive Pipe	0	42					
8/2/1913	6/3/1968		8 5/8	Surface Pipe	0	303					
8/3/1913	6/5/1968		7	Casing	0	1256					
8/3/1913			7	Casing	1256	1949					
8/4/1913			5 1/2	Casing	0	2688					
8/5/1913	6/1/1968		3 1/2	Casing	0	2825					
6/7/1968			7	Casing	0	310	17.00	Used		Y	
6/9/1968	6/3/1968	3.000	4 1/4	Anchor	2857	2857					
6/9/1968	11/8/1995		3 1/2	Casing	0	1291	9.20				
6/9/1968			3 1/2	Casing	1291	2857	9.20	Used		Y	
6/9/1968	6/3/1968	3.000	4 1/4	Anchor	2857	2857					
11/9/1995			3 1/2	Patch	1288	1291					
11/9/1995			3 1/2	Patch	1288	1291					
11/9/1995			3 1/2	Casing	0	1291	9.20				

Fig5. Well-bore data retrieved from a file

ANALYSIS OF RAW DATA vs. REFINED DATA

Please note that multiple data entry was the major reason for the reduction in the refined data from the initial

COMPLETION DATA											
DATA FIELDS	Total Completions Run	API Number	Field Name	Well	Description	Date Tubing Run	OD	Top Casing	Bot	Weight	Grade
INITIAL DATA AVAILABLE	2910	431	431	431	2909	2909	2909	2909	2909	1781	1607
FINAL DATA AVAILABLE	2413	430	431	431	2413	2413	2413	2413	2413	1723	1607

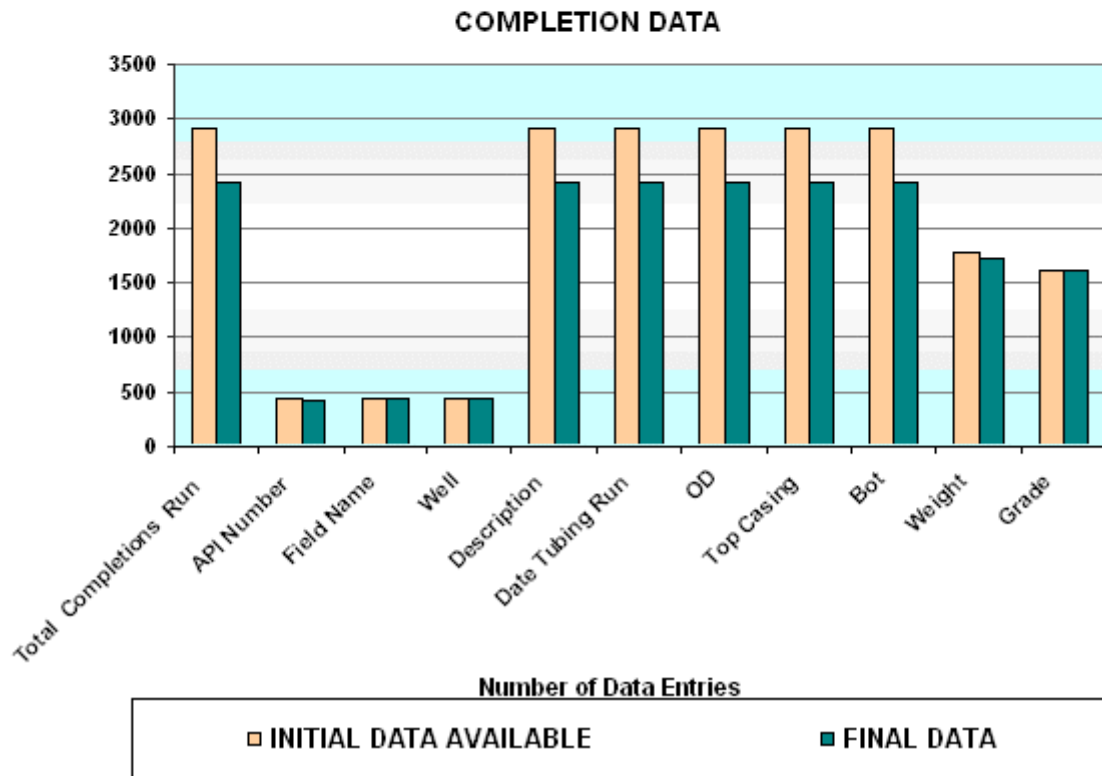


Fig6. Data addition and refinement for Completion Data

PERFORATION DATA

This data set contains mostly all the information relating to the perforations done on the gas storage well like perforation top & bottom depth and shots per feet. Following are the data types included in this type of data set are below

1. Well API Number
2. Field Name
3. Well Name
4. Completion Type
5. Perforation Date (Perf Date)
6. Perforation Top (Perf Top)
7. Perforation Bottom (Perf Btm)
8. Shot Type
9. Shot Per feet (Shot Per ft)

The picture of a document showing this information is shown below

LUCAS - 00											
Redlined By		Redline Date		Entered by Anderson		Verified by Bolander		Comment			
Field Name	Well Number	API Number	Lease Name		Spud Date	Acreage	TVD (ft)	MD (ft)	Datum reference		
LUCAS	00...	340056			8/1/1913	148	2827	2857			
Township/Tax District		Tax Number	County		State/Province	Operating Area			Inventory Map #		
GREEN		30050	ASHLAND		OH	Wooster					
Latitude (DD)	Longitude (DD)	Section Number	State Permit #	Line Number	Deed Number	Lease Number	Inventory Map #				
72111	31306	5									
Well Classification	Key Well	Group	SubGroup	Completion Type		Est DeepFW (ft)	Gr Elev (ft)	KB Elevation (ft)			
ACTIVE	No	8									
Directions To Well											
Wellhead: API Wellhead, <Make?> on <Install Date?>											
Type	Install Date	Make	FlowStSz (in)	SupportStSz (in)	WP (psi)	Connection	Comment				
API Wellhead						3" 10R	Wellhead Size 3 x 3.				
Wellhead Components											
Des	Instal Date	Type	Make	Size (in)	WP (psi)	Operable	Leaking	Restricted	Comment		
Annular Valve		Ball	Nibco	2.000	2,000.0						
Master Valve		Gate	Barton	3.000	2,000.0	Yes	No	No			
Side Valve		Gate	Barton	3.000	2,000.0	Yes	No	No			
Downhole Components (Dates <1990 are approximated)											
Run Date	Full Date	ID (in)	OD (in)	Des	Top (ft)	Btm (ft)	WT (lbs/ft)	Grade	Thread	Cmt/ft	Comment
8/1/1913			10.34	Drive Pipe	0	42					
8/2/1913	8/3/1968		8.58	Surface Pipe	0	303					
8/3/1913	8/5/1968		7	Casing	0	1256					
8/3/1913			7	Casing	1256	1949					
8/4/1913			5.12	Casing	0	2638					
8/5/1913	8/1/1968		3.12	Casing	0	2625					
8/7/1968			7	Casing	0	310	17.00	Used		Y	
8/9/1968	8/3/1968	3.000	4.14	Anchor	2857	2857					
8/9/1968	11/8/1995		3.12	Casing	0	1291	9.20				
8/9/1968			3.12	Casing	1291	2857	9.20	Used		Y	
8/9/1968	8/3/1968	3.000	4.14	Anchor	2857	2857					
11/9/1995			3.12	Patch	1288	1291					
11/9/1995			3.12	Casing	1288	1291					
11/9/1995			3.12	Casing	0	1291	9.20				
Perforations											
Date	Top (ft)	Btm (ft)	Shot Type	Gun Type	Gun Sz (in)	Shot Dens (shots/ft)	Phasing (°)	String	Perf Comp	Cmt sqz	Comment
8/7/1968	2823	2831				1.1					
Drillers Log of Formations											
Formation Picks Group											
Drillers Log of Formations											
Name	Top (ft)	B	Fluid Shows	Comment							
Big Lime Top	1706										
Big Lime	2658										

070700323 - LUCAS

Report run date

y, February 22, 2005

Page 1 of 4

Perforations											
Date	Top (ft)	Btm (ft)	Shot Type	Gun Type	Gun Sz (in)	Shot Dens (shots/ft)	Phasing (°)	String	Perf Comp	Cmt sqz	Comment
8/7/1968	2823	2831				1.1					

Fig7. Perforation data retrieved from a file

ANALYSIS OF RAW DATA vs. REFINED DATA

PERFORATION DATA										
DATA FIELDS	Total Perforations	API Number	Field Name	Well Name	Completion Type	Perf Date	Perf Top	Perf Bottom	Shot Type	Shot Per ft
INITIAL DATA AVAILABLE	392	57	57	57	48	392	392	392	209	383
FINAL DATA AVAILABLE	392	57	57	57	48	392	392	392	209	383

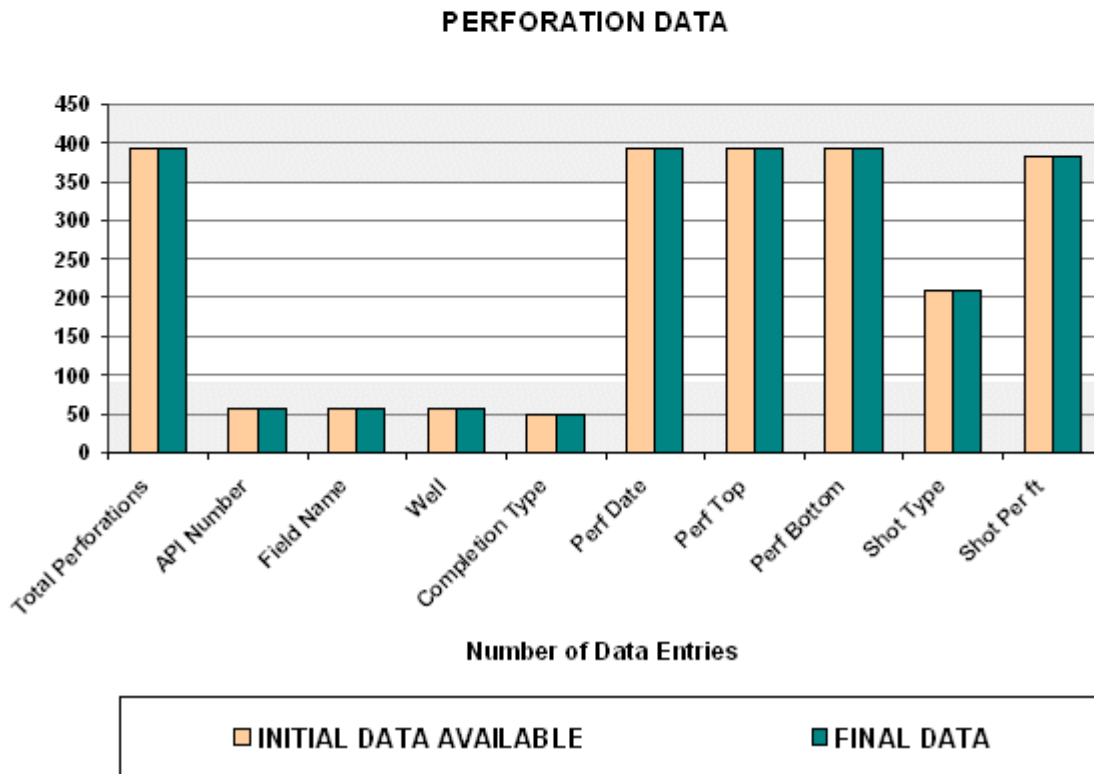


Fig8. Data addition and refinement for Perforation Data

STIMULATION DATA

Stimulation data is the one of the most significant dataset about the storage wells. Because of this it was very important that we have maximum records of valid stimulations. Following data type is used to represent stimulation

1. API Well Number
2. Well Name
3. Size of String
4. Stimulation From
5. Stimulation To
6. No Of Shots
7. Fractured by
8. Stimulation Type
9. Stimulation Date
10. Water
11. Acid
12. Gel
13. Foam
14. Nitrogen
15. Alcohol
16. Cushion
17. Flush
18. Sand Quantity
19. Sand Type
20. Injection Rate
21. Total Fluid
22. Breakdown Pressure
23. ISIP

Unfortunately initially we didn't have much data about the stimulations being done in this Lucas field. With this in mind every record with Columbia Transmission Corporation was carefully examined. The largest source of stimulation data came from the thousands of microfiche with some data being found in well summary reports. Following is a picture of data in well summary reports.

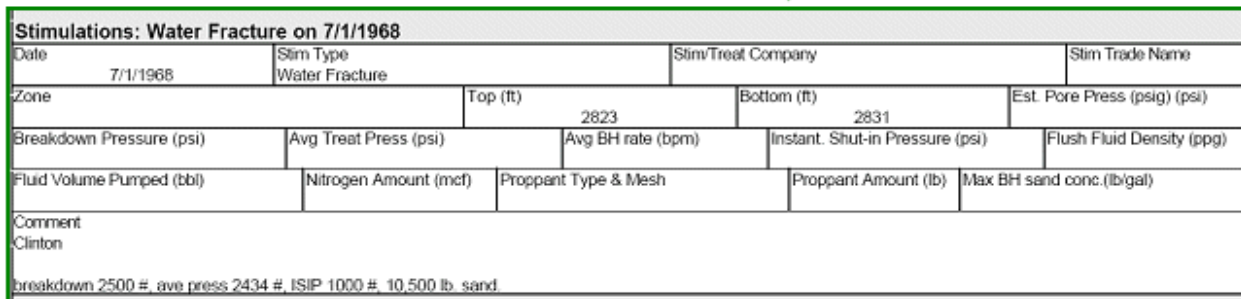
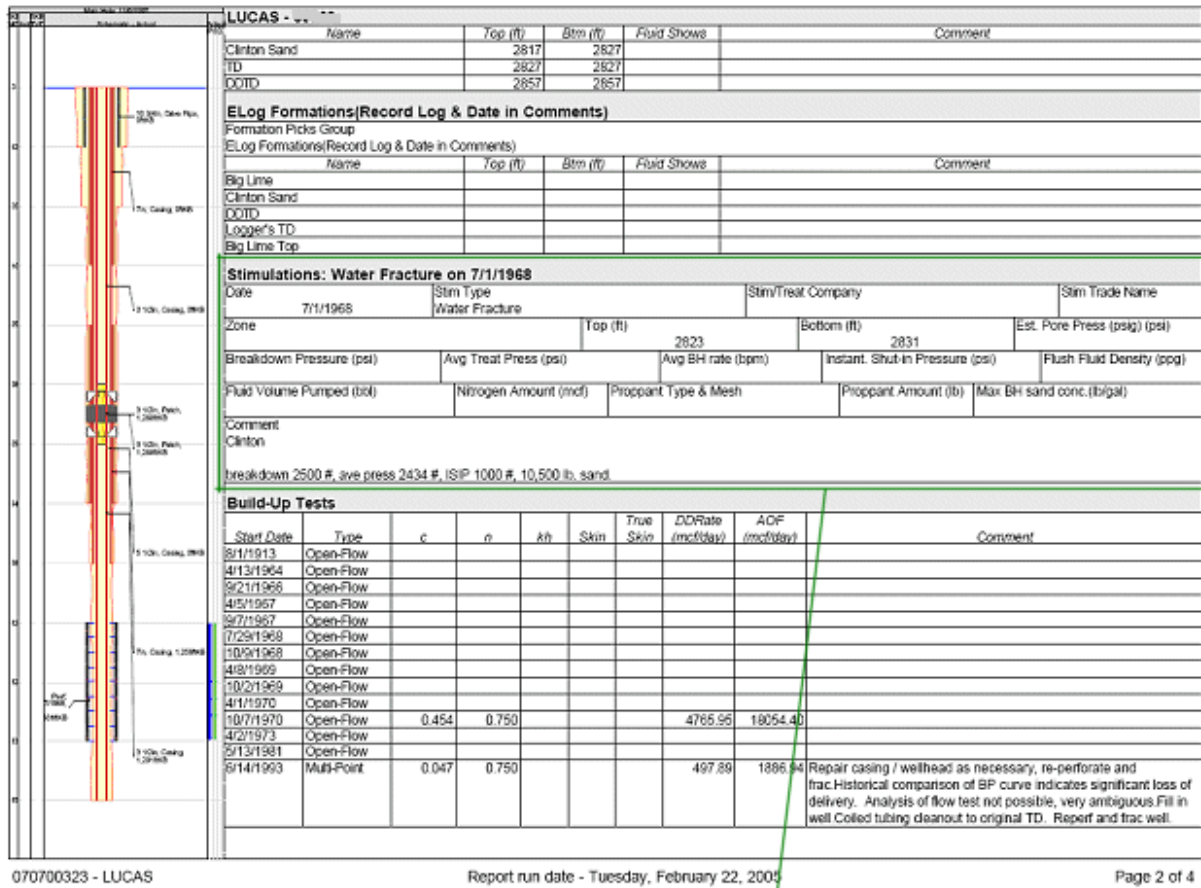
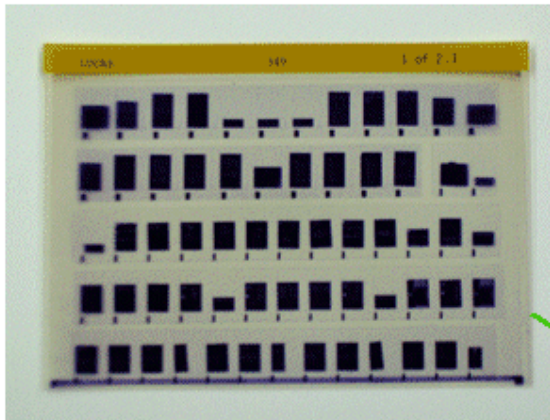


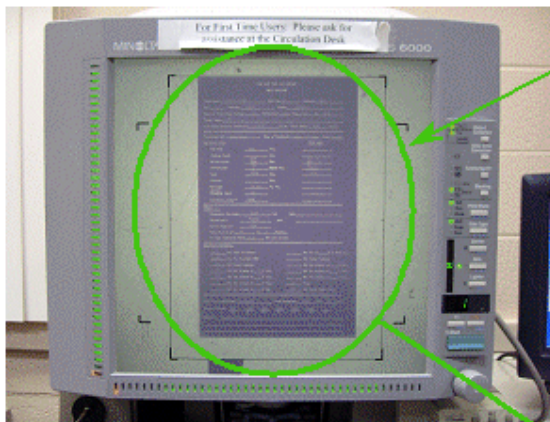
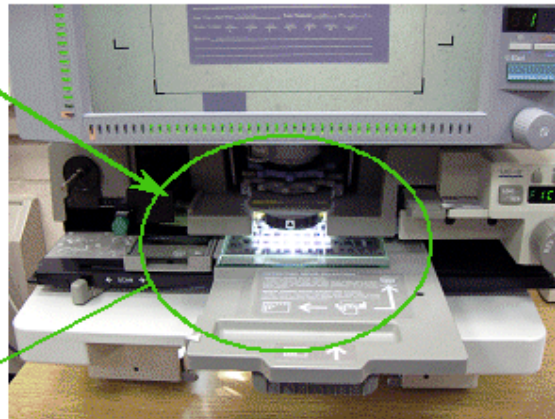
Fig9. Perforation data retrieved from a file

MICROFICHE TO DATABASE



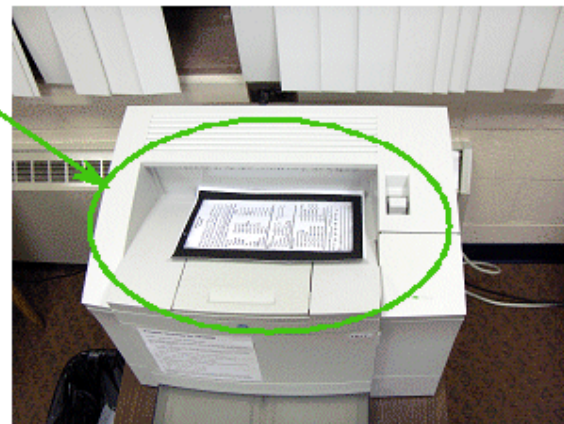
Each Microfiche contained dozens of documents from invoices to valuable stimulation and well-test data

Microfiche were read by digital Microfilm scanners



Each scanned image of the microfiche was searched and read for valuable data

Prints were taken of the documents containing data



API Number	SizeOfString	StimFrom	StimTo	NoOfShots	Fractureby	Type	St
34-005-01272	4.5	2062	2906	8	Dowell Inc.	Water-Gel	117
34-005-02420	4.5	2759	2764	11	Dowell Inc.	Water-Gel	123
34-005-02887	4.5	2804	2810	13	Dowell Inc.	Water-N2	6
34-005-02889	4.5	2838	2845	12	Dowell Inc.	Water-N2	7
34-005-02889	4.5	2820	2828	10	Dowell Inc.	Water-N2	60
34-005-02897	4.5	2863	2860	12	Halliburton Co.	Water-Gel	73
34-005-02901	4.5	2723	2748	12	Halliburton Co.	Water-Gel	60
34-005-02907	3.5	2023	2045	13	Halliburton Co.	Water-Gel	7
34-005-02909	4.5	2796	2814	5	Halliburton Co.	Water-Gel	73
34-005-02909	4.5	2809	2814	6	Halliburton Co.	Water-Gel	73
34-005-02911	4.5	2785	2805	13	Halliburton Co.	Water-Gel	90
34-005-02960	4.5	2911	2921	13	Dowell Inc.	Water-Gel	107
34-005-10516	5.5	2568	2608		Halliburton Co.	Viss-Frac	127
34-005-10517	5.5	2559	2590		Dowell Inc.	Water-N2	57
34-005-10518	5.5	2580	2622		Dowell Inc.	Petro-Gel	127
34-005-10519	5.5	2674	2832		Halliburton Co.	Water-N2	97
34-005-10520	5.0	2905	2964		Dowell Inc.	Water-Gel	17
34-005-10527	5.5	2886	2901		Dowell Inc.	Water-N2	8
34-005-10533	5.5	2627	2653		Dowell Inc.	Petro-Gel	12
34-005-10538	5.5	2804	2844		Dowell Inc.	Petro-Gel	127
34-005-10540	5.5	2860	2905		Dowell Inc.	Water-N2	67

Data was entered in the database

The following notations were used in place of different notations being used in the tables

NOTATIONS USED IN DATABASE	WATER GEL FRAC	PETRO GEL FRAC	FOAM FRAC	NITRO SHOT	WATER/N2 FRAC	WATER FRAC	10/20 SAND
NOTATIONS THAT WERE REPLACED	Gelled water frac	Petro gel	Foam	Shot	Water / N2	water	10/20
	Water Gel	Petro Gel Petro gel fracture	foam Frac foam fracture		Water N2 Fracture Water nitrogen		Sand 10/20
					Water/N2 assist Water Fracture w/N2 assist		

All records of Nitro-shots were discarded for this database as they have no stimulation parameters on record and are part of history now plus they also damage the well. Above all they will tend to degrade the Neural Network.

GRAPHICAL ANALYSIS OF RAW DATA vs. REFINED DATA

STIMULATION DATA																								
DATA FIELDS	Total Stimulations	API Number	Well	Size Of String	Stim From	Stim To	No Of Shots	Fractured by	Type	Stim Date	Water	Acid	Gel	Foam	N2	Alcohol	Cushion	Flush	Sand Quantity	Sand Type	Injection Rate	Total Fluid	Breakdown Pressure	ISIP
INITIAL DATA AVAILABLE	32	32	32	32	32	32	32	32	32	32	0	0	0	0	0	0	0	0	32	32	25	0	27	24
FINAL DATA AVAILABLE	390	430	430	308	388	388	166	354	370	391	85	293	294	157	249	21	277	302	368	266	263	317	181	345

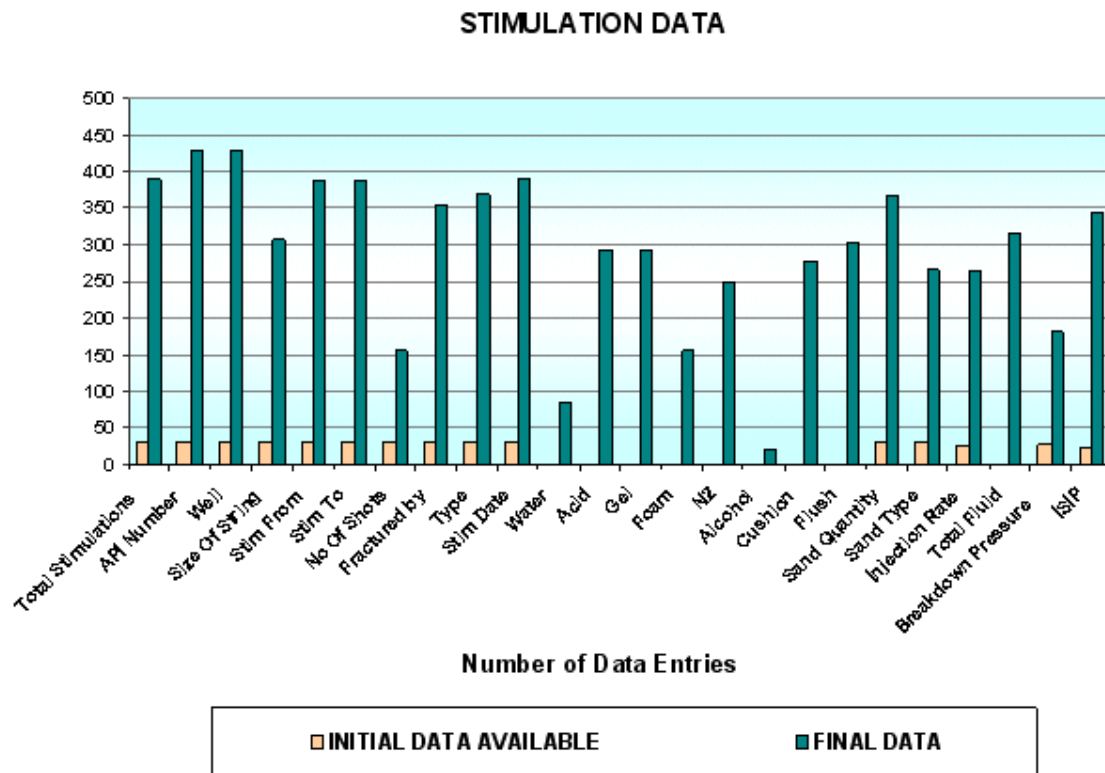


Fig11. Data addition and refinement for Stimulation Data

WELL TEST DATA

Well-test data is the most extensive dataset that our R & D team worked on. It has the max amount of records nearly 3365 and 29 data types that control every aspect of a well-test. The data type selected for a well-test representation consists of following

1. Well API Number
2. Field Name
3. Test Date
4. Test Type
5. Time 1
6. Field Pressure 1
7. Flowing Pressure 1
8. Rate 1
9. Time 2
10. Field Pressure 2
11. Flowing Pressure 2
12. Rate 2
13. Time 3
14. Field Pressure 3
15. Flowing Pressure 3
16. Rate 3
17. Time Extended
18. Field Pressure Extended
19. Flowing Pressure Extended
20. Rate Extended
21. kh
22. Skin
23. True Skin
24. Non Darcy Co-efficient
25. n Value
26. C Value
27. Delta Pressure Squared
28. Peak Day Rate
29. Absolute Open Flow

Lot of data was missing in this dataset so it was decided that values of n, C, PDrate & AOF will be interpreted manually and on the other side work on software will continue to automatically do this interpretation procedure with little input from user. This program will be discussed in great detail latter.

ESTIMATION OF n, C, PEAK DAY RATE & ABSOLUTE OPEN FLOW

EMPIRICAL APPROACH

SINGLE/OPEN FLOW TESTS

The values used for point 1 and 2 are from different well-tests

1- Find ΔP^2

$$3- \frac{1}{n} = \frac{\log(\bar{p}^2 - p_{wf}^2)_2 - \log(\bar{p}^2 - p_{wf}^2)_1}{\log q_2 - \log q_1} \quad (\text{Where } q \text{ is in MMcfD})$$

$$4- C = \frac{q_g}{(\bar{p}^2 - p_{wf}^2)^n} \quad (\text{Where } q \text{ is in McfD})$$

$$5- AOF = C(1150^2 - 0^2)^n \quad \text{McfD}$$

$$6- PDRate = (C \times 250,000)^n \quad \text{McfD}$$

MULTI-POINT TESTS

Estimation of n, C, PD rate & AOF:

1- Same as above except that the points used are from the same test

NOTE: The n, C, PD rate & AOF values for more than 400 well-tests were manually calculated

ESTIMATION OF KH, SKIN, TRUE SKIN, NON-DARCY COEFFICIENT

- 1- From extended draw-down test plot ($P_i - P_{wf}$) vs. time on log-log paper. Draw unit-line for un-stimulated wells and half-slope line for Stimulated wells. Find end of well-bore storage effects after 1-1/2 log time cycle
- 2- Find values of viscosity, z-factor, compressibility of storage gas at different pressure assuming Gas gravity = 0.585 & temperature = 75 F = 535 R

DRAW-DOWN TEST

- 1- Plot P_{wf}^2 vs. time
- 2- Draw straight line after pseudo-steady state starts
- 3- Find slope m and P^2 1hr
- 4-
$$kh = \frac{1637qTzu}{m}$$
- 5-
$$S = 1.151 \left[\frac{P^2 - P^2_{1hr}}{m} - \log \left(\frac{k}{\phi \mu c r_w^2} \right) + 3.23 \right]$$
- 6- Plot skin vs. flow-rate. It should be a straight line
- 7- Slope of this line is D
- 8- Find True Skin (S') at $q=0$.

BUILD-UP TEST

- 1- Plot P_{wf}^2 vs. $(tp+dt)/dt$ on semi-log paper
- 2- Draw straight line after well-bore storage effects diminishes
- 3- Find slope m and P^2 1hr
- 4-
$$kh = \frac{1637qTzu}{m}$$
- 5-
$$S = 1.151 \left[\frac{P^2_{1hr} - P^2}{m} - \log \left(\frac{k}{\phi \mu c r_w^2} \right) + 3.23 \right]$$
- 6- Plot skin vs. flow-rate. It should be a straight line
- 7- Slope of this line is D
- 8- Find True Skin (S') at $q=0$.

We require time, flow-rate & Bottom hole pressure from the data which is present in two txt files as bottom hole & surface recording files. The flow rates are at Wellhead so we match the bhp & THP with time.

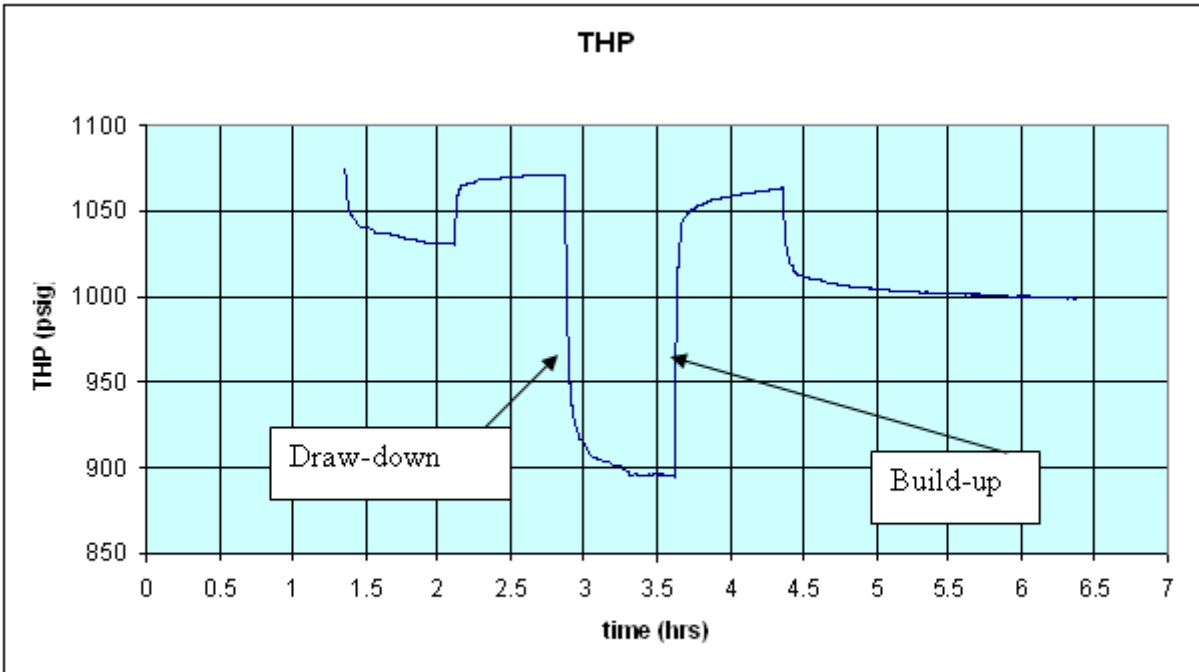


Fig12. Tubing Head Pressure profile for Multi-point test

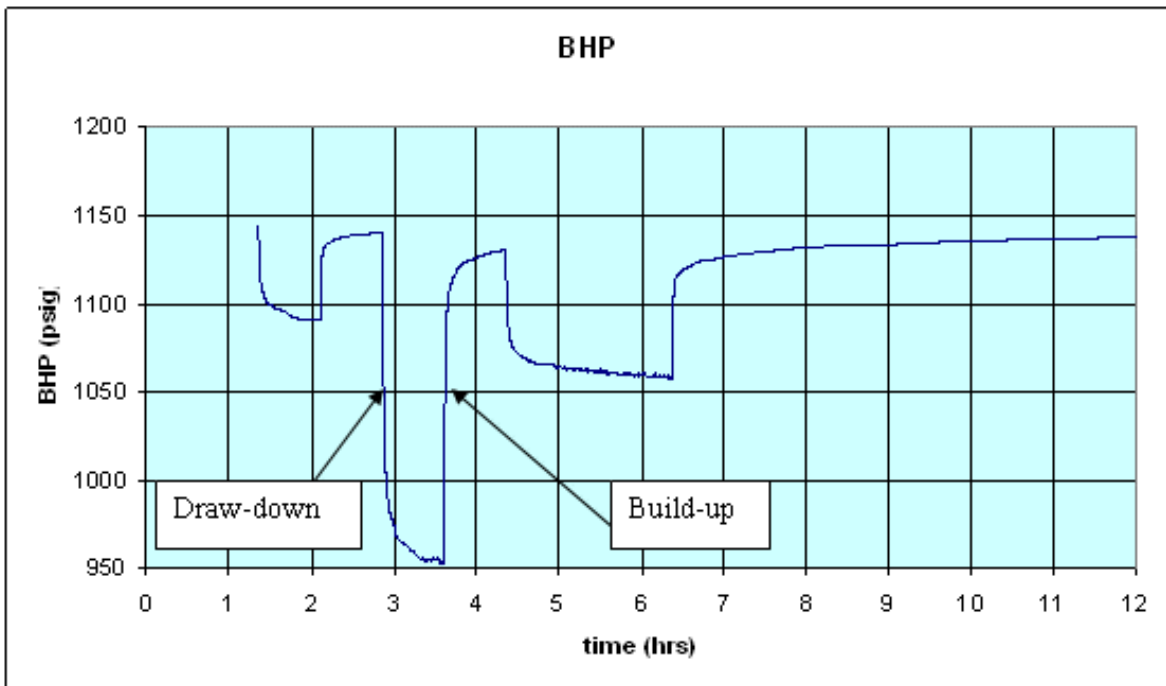


Fig13. Bottom Hole Pressure profile for Multi-point test

The multipoint-test data is divided into Draw-down & build-up test and each one is analyzed separately.

DRAW-DOWN TEST

Analysis of drawdown tests was done as described above and following graphs were obtained

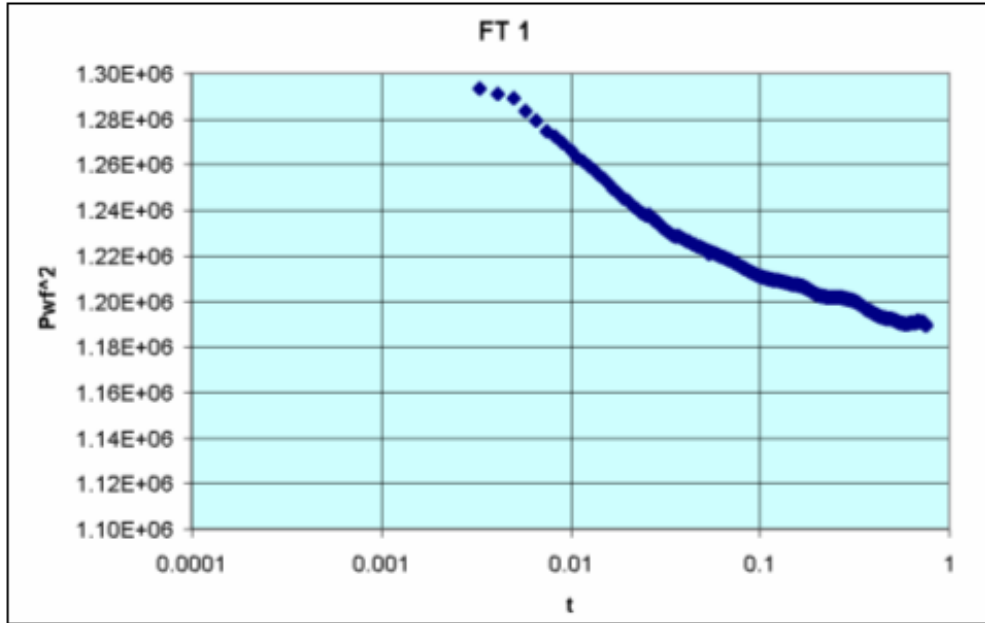


Fig14. Flow Test 1 – Delta pressure squared vs. time

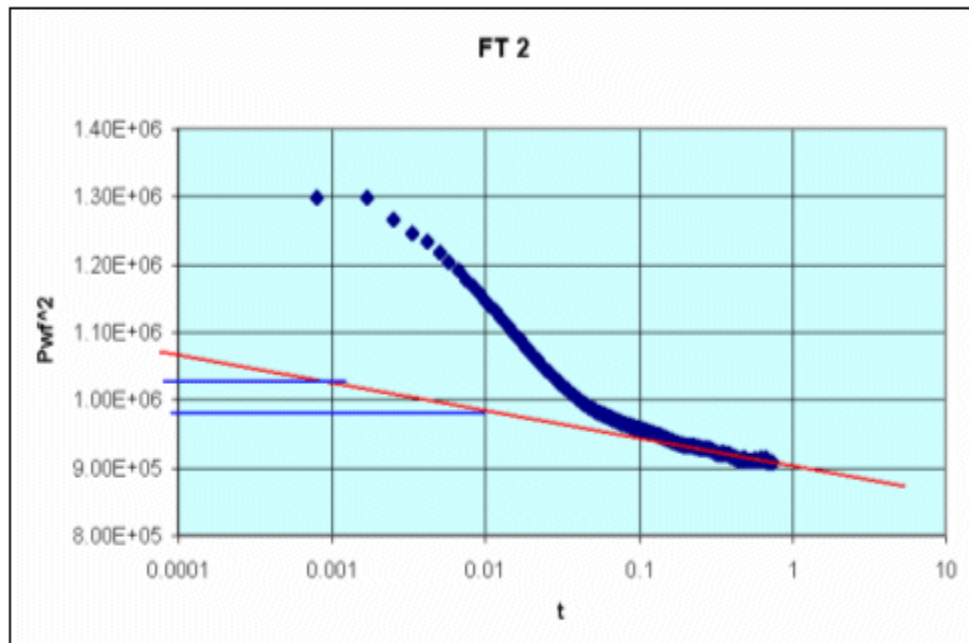


Fig15. Flow Test 2 – Delta pressured squared vs. time

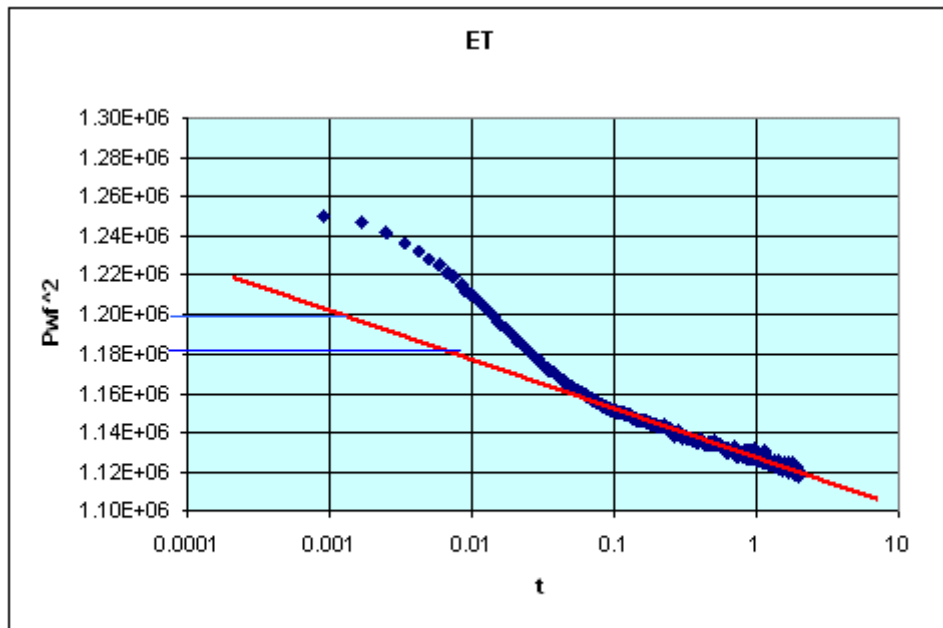


Fig16. Extended Flow Test – Delta pressured squared vs. time

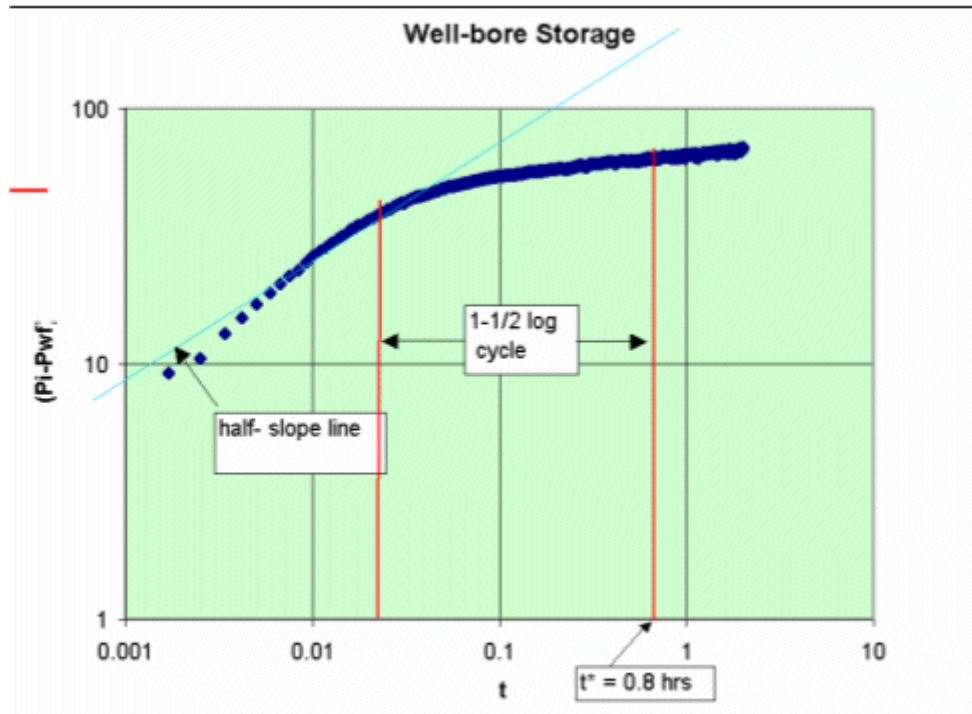


Fig17. log-log graph

For well-tests after fracture half-slope line is drawn and for un-simulated wells unit slope line is drawn to find end of well-bore effects and start of pseudo-steady state.

Gas production Simulator was used to find the values of viscosity, z-factor and compressibility of storage gas at different pressure assuming Gas gravity = 0.585 & Temperature = 75 F = 535 R that are also used by Columbia Trans.

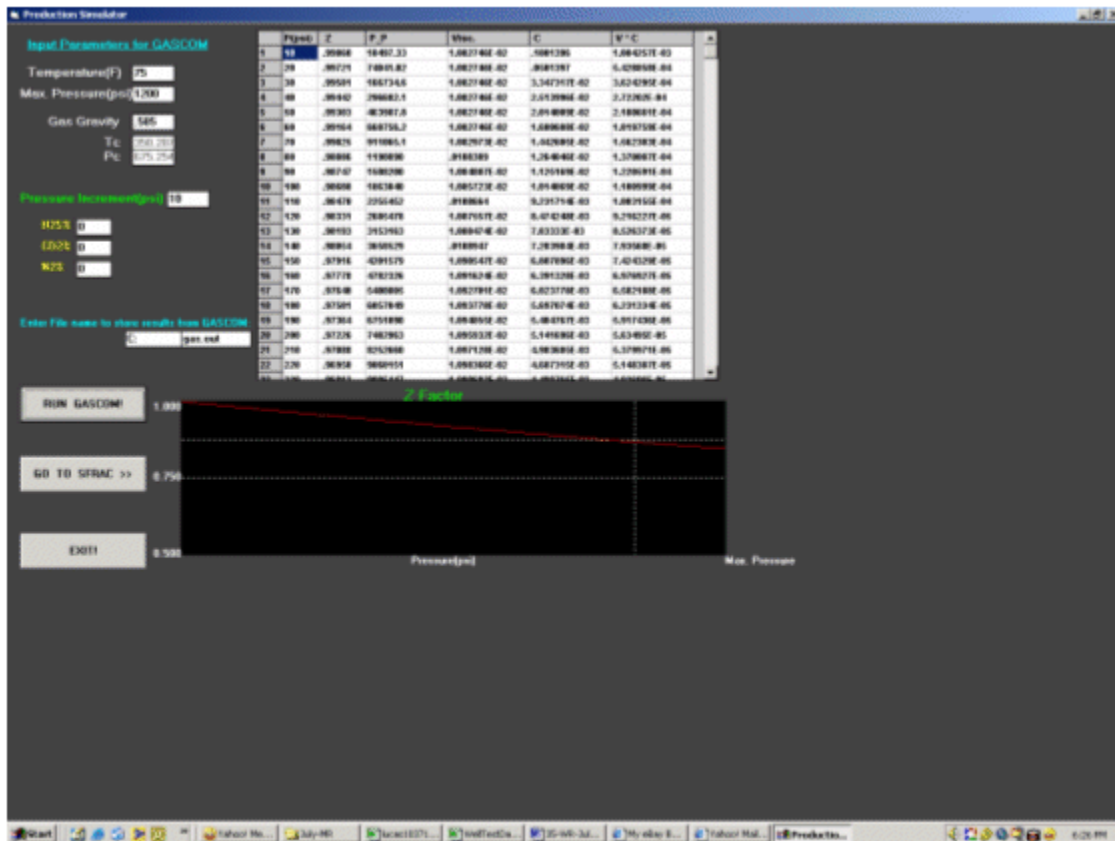


Fig18. Gas properties Simulator

The slope from P_{wf}^2 vs. time on semi-log graph was used to find kh & then skin. The three values of skin were plotted on Q vs. S graph and extrapolated to Q = 0 to get True skin (S').

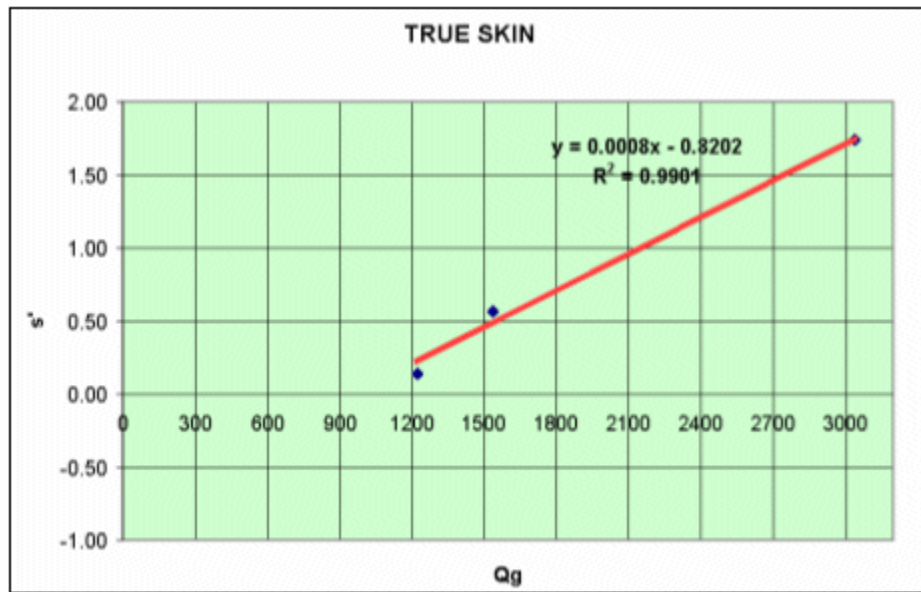


Fig19. Calculation of True skin

DRAW-DOWN TEST RESULTS

	FLOW TEST 1	FLOW TEST T2	EXTENDED TEST
porosity	0.14	0.14	0.14
rw	0.1458333	0.1458333	0.1458333
Ct	1.02E-03	1.08E-03	1.04E-03
Uav	1.28E-02	1.26E-02	1.27E-02
Zav	0.8558691	0.8635354	0.859119
P	1143	1140	1127.3
Qav	1223.8668	3038.7039	1536.1134
Tav	533	533	533
h	10	10	10
m	2.00E+04	5.40E+04	2.20E+04
kh	5.86E+02	5.36E+02	6.67E+02
k	5.86E+01	5.36E+01	6.67E+01
plhr ²	1.185E+06	9.000E+05	1.128E+06
S	0.14	1.74	0.57
S'	-0.8202		
D	0.0008		

BUILD-UP TEST

In build-up tests, the slope drawn for Horner plot is after the time when well-bore storage effects were found to be minimum from previous draw-down test. This slope is then used to find the values of kh & skin. The True skin is found the similar way as in draw-down test.

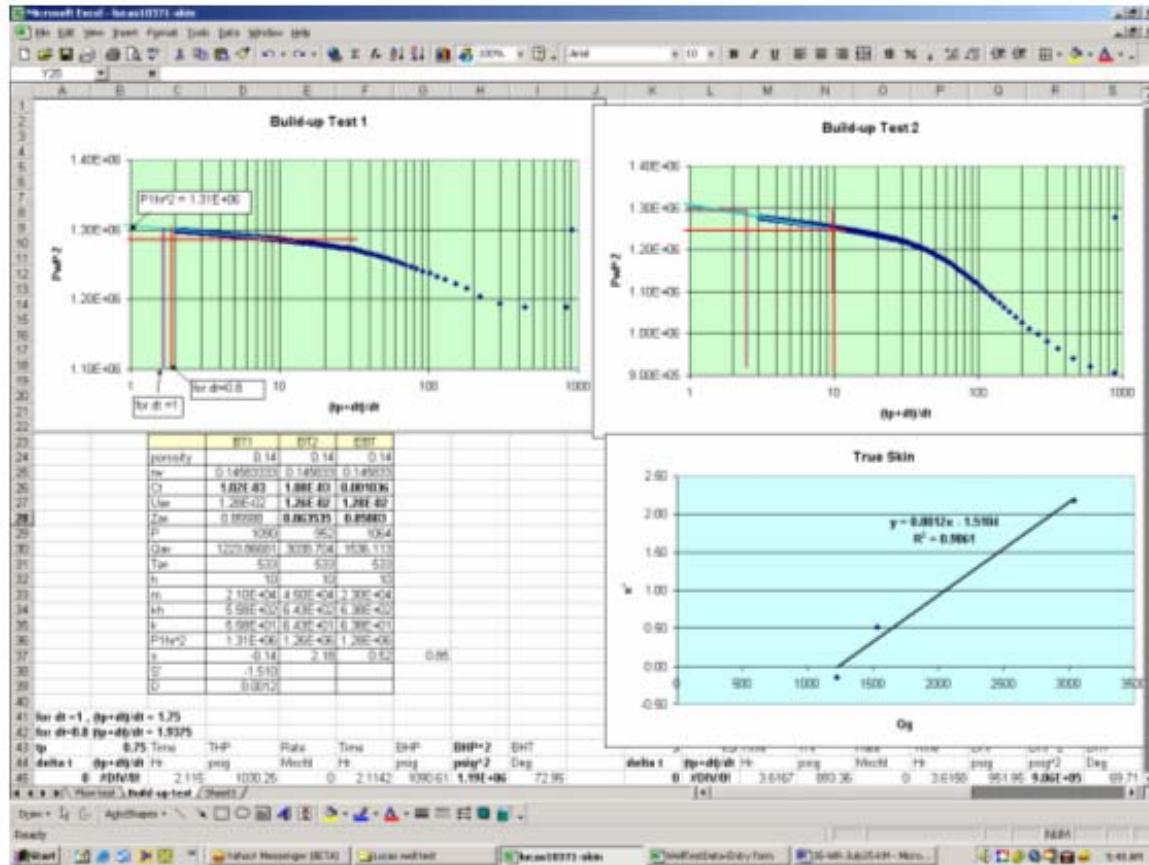


Fig20. Calculation of True skin from Build-up test

BUILD-UP TEST RESULTS

	BUILD-UP TEST 1	BUILD-UP TEST 2	EXTENDED BUILD-UP TEST
porosity	0.14	0.14	0.14
rw	0.14583333	0.145833	0.145833
Ct	1.02E-03	1.08E-03	0.001036
Uav	1.28E-02	1.26E-02	1.28E-02
Zav	0.85588	0.863535	0.85803
P	1090	952	1064
Qav	1223.86681	3038.704	1536.113
Tav	533	533	533
h	10	10	10
m	2.10E+04	4.50E+04	2.30E+04
kh	5.58E+02	6.43E+02	6.38E+02
k	5.58E+01	6.43E+01	6.38E+01
Plhr²	1.31E+06	1.26E+06	1.28E+06
s	-0.14	2.18	0.52
S'	-1.510		
D	0.0012		

AVERAGED RESULTS

	DRAW-DOWN	BUILD-UP	AVERAGE	ACTUAL
S'	-0.8202	-1.510	-1.165	-1.17
D	0.0008	0.0012	0.0010	.00126

Due to large errors corresponding to estimating skin and kh values manually, it was decided that for time being these values will not entered in the database.

Following are some pictures of the documents to show the different format in which the data was present in files and microfiche.

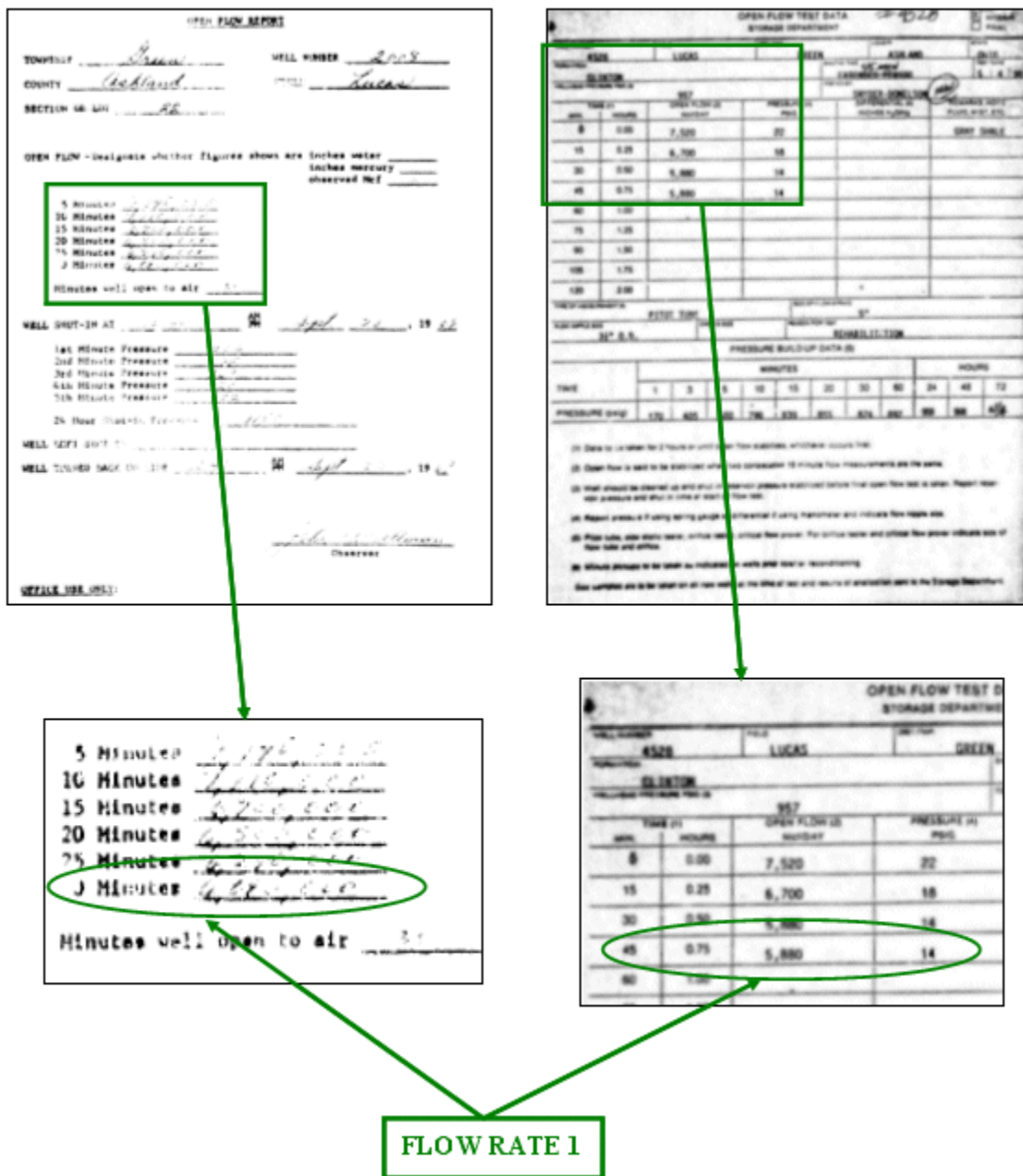


Fig21. Retrieving flow-rate of an open-flow test

GRAPHICAL ANALYSIS OF RAW DATA vs. REFINED DATA

WELL TEST DATA																															
DATA FIELDS	Total Well-Tests	API Number	Field Name	Well	Test Date	Test Type	Time 1	Field Pressure 1	Flowing Pressure 1	Rate 1	Time 2	Field Pressure 2	Flowing Pressure 2	Rate 2	Time 3	Field Pressure 3	Flowing Pressure 3	Rate 3	Time Extended	Field Pressure Ext	Flowing Pressure Ext	Rate Ext	kh	Skin	True Skin	Non Darcy Coefficient	n-value	C-value	Delta P Squared	Peak Day Rate	Absolute Open Flow
INITIAL DATA AVAILABLE	3223	431	431	431	3223	3223	3223	3223	3223	3223	347	347	347	347	292	292	292	292	345	345	345	345	191	182	163	163	916	916	916	916	916
FINAL DATA AVAILABLE	3365	431	431	431	3365	3365	3365	3365	3365	3365	347	347	347	347	292	292	292	292	345	345	345	345	194	185	166	166	1362	1362	1362	1362	1362

WELL TEST DATA

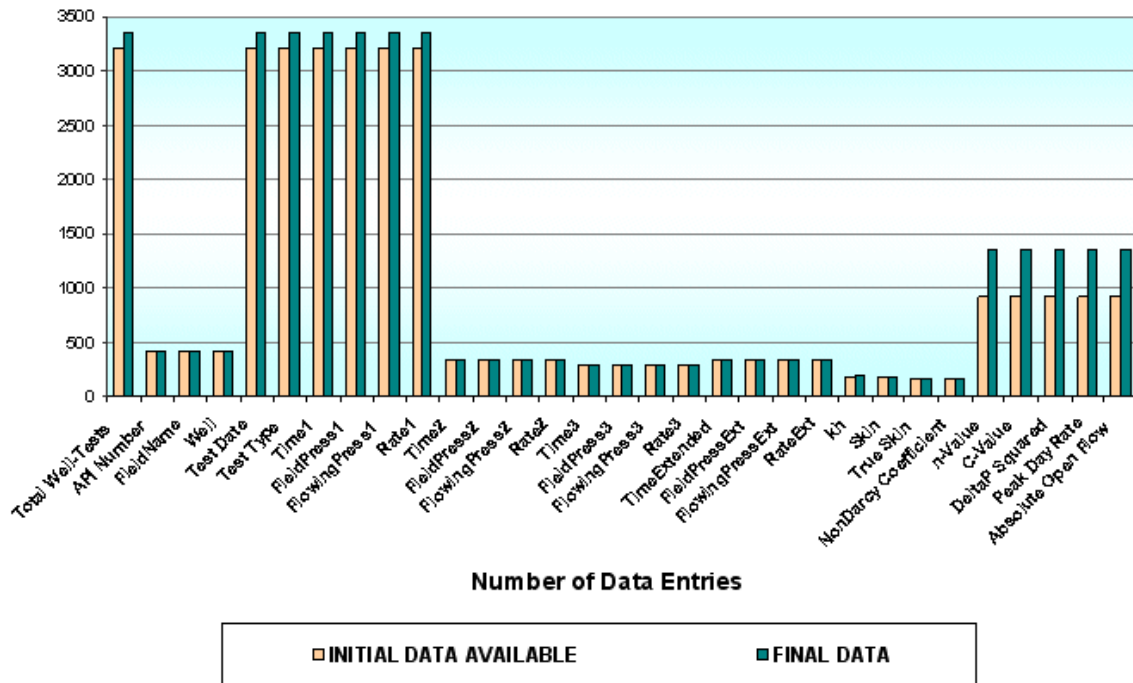


Fig22. Data addition and refinement for well test data

DATABASE & SOFTWARE

SOFTWARE BASICS

This software allows you to add/edit well data in the database and choose the data that you want to look at, for a selected well. It also has a Well Test Analysis tool which calculates the well deliverability parameters like n, C, Peak Day rate & Absolute Open Flow

The database for this software consists of five tables

1. Well bore Data
2. Completion Data
3. Perforation Data
4. Stimulation Data
5. Well Test Data

The **API number** of a well is the primary key in this database so it must be known before adding a record and cannot be duplicated

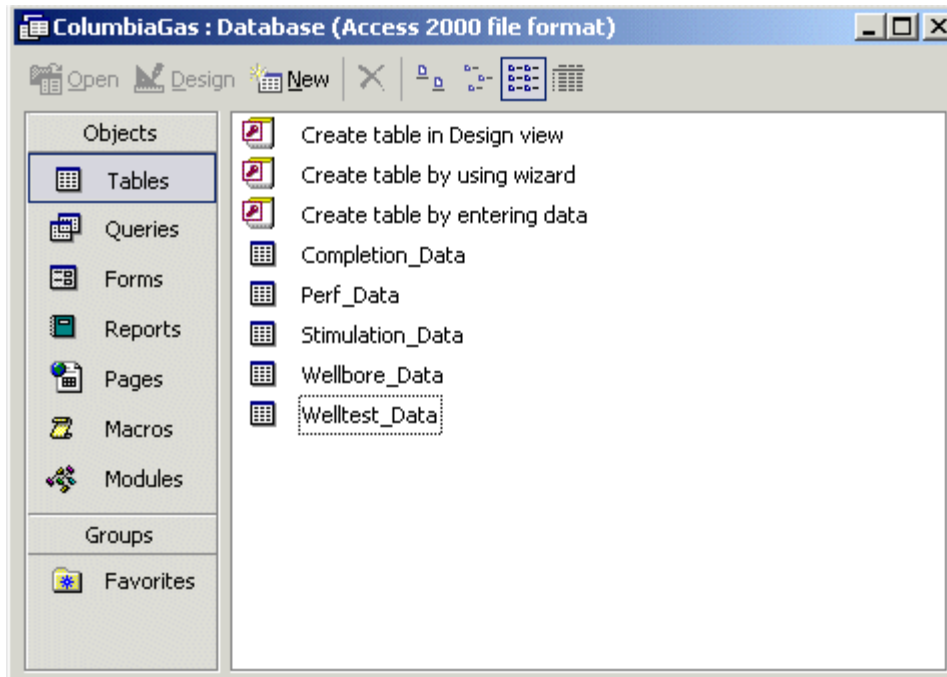


Fig23. Screen shot of database showing different tables

The software starts with the main menu screen with six options



Fig24. Main Screen of software

Editing / Viewing Data



To edit/view well data or do a Well Test Analysis

Select Well Data



To choose the well data that you want to look at for selected wells

Exit



To Exit from the Program

Tutorial



To open the Help file / Tutorial for this program

About



To get general information about the developing of thus project

EDIT / VIEW WELL DATA

This screen has all the well data in the form of five tabs (for five database tables) that can be edited / viewed or a Well Test Analysis can be performed in the Well Test tab

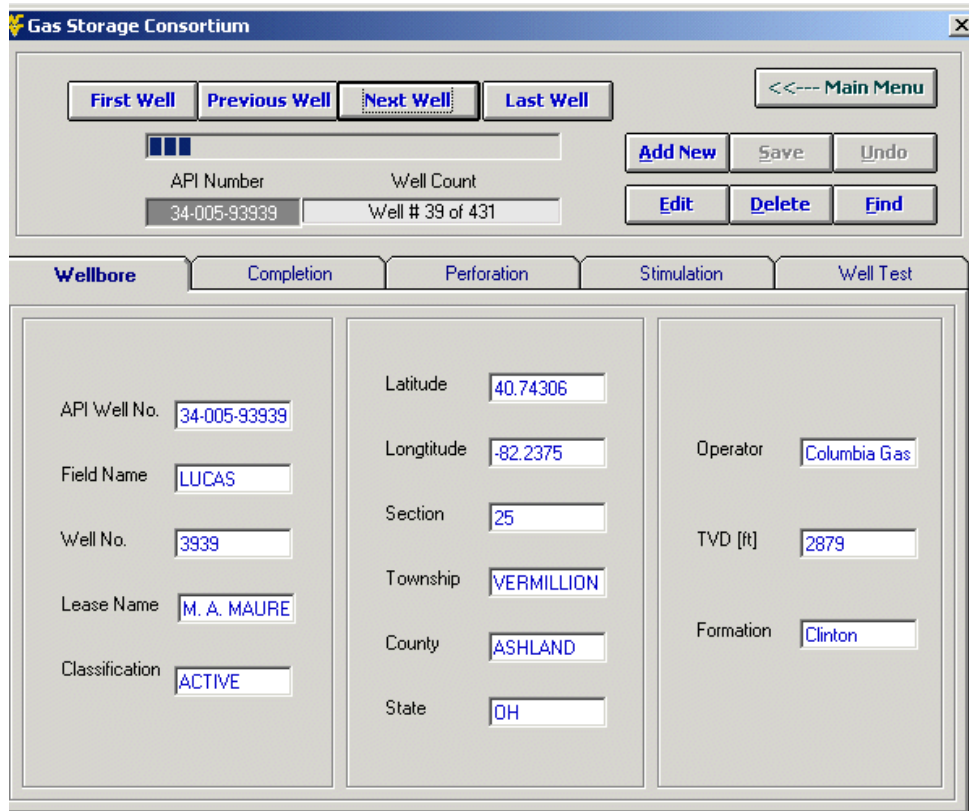
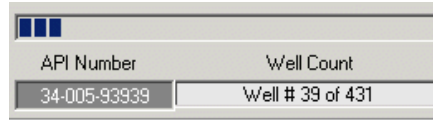


Fig25. Browsing through the well-bore data

To browse between different wells

To move to the first well, previous well, next well & the last well in the record click on the button assigned to it. The records are assorted in ascending order according to well number

API Number & Well Count

The progress bar shows the relative position of the record and well count shows the current well position in the well bore database out of the total records. The API number of the current well is also displayed

Back to main menu

Takes you back to the very first screen of the program

Editing Tools

These buttons will help you to add a new record, edit or delete it or find a well for which you want the data to be retrieved if you know its API number

DIFFERENT TABS

WELL BORE

Wellbore	Completion	Perforation	Stimulation	Well Test
API Well No. <input type="text" value="34-005-93939"/>		Latitude <input type="text" value="40.74306"/>		
Field Name <input type="text" value="LUCAS"/>		Longitude <input type="text" value="-82.2375"/>	Operator <input type="text" value="Columbia Gas"/>	
Well No. <input type="text" value="3939"/>		Section <input type="text" value="25"/>	TVD [ft] <input type="text" value="2879"/>	
Lease Name <input type="text" value="M. A. MAURE"/>		Township <input type="text" value="VERMILLION"/>	Formation <input type="text" value="Clinton"/>	
Classification <input type="text" value="ACTIVE"/>		County <input type="text" value="ASHLAND"/>		
		State <input type="text" value="OH"/>		

Fig26. Well-bore tab

This tab contains all the data pertaining to the name, location & some main features of the current well

COMPLETION

Field Name	Value	OD (in)	Value
Field Name	LUCAS	OD (in)	7
Well No.	326	Top (ft)	0
Description	Casing	Bottom (ft)	75
Date Tubing Run	11/2/1969	Weight (lbs/ft)	17.00
	MM/DD/YYYY	Grade	SMLS USED

Buttons: First Completion, Previous Completion, Next Completion, Last Completion

Fig27. Completion tab

This tab contains all the data relating to different completion run in the well

To browse between different Completions

Buttons: First Completion, Previous Completion, Next Completion, Last Completion

To move to the first completion, previous completion, next completion & the last completion in the record, click on the button assigned to it. The completions are assorted in ascending order according to date tubing run for current well

PERFORATION

The screenshot shows a software interface with five tabs: Wellbore, Completion, Perforation, Stimulation, and Well Test. The 'Perforation' tab is selected and displays 'Perforation # 2 of 3'. The form contains the following data:

Field Name	LUCAS	Perforation Top [ft]	2,371
Well No.	12058	Perforation Bottom [ft]	2,407
Perforation Type	Set-Thru	Shot Type	size. 50 / Glass
Perforation Date	5-Sep-1981 MM/DD/YYYY	Shots Per foot	1.0

At the bottom of the form are four navigation buttons: 'First perforation', 'Previous Perforation', 'Next Perforation', and 'Last Perforation'.

Fig28. Perforation tab

To browse between different Perforations



To move to the first perforation, previous perforation, next perforation & the last perforation in the record, click on the button assigned to it. The perforations are assorted in ascending order according to perforation date for current well

STIMULATION

Wellbore	Completion	Perforation	Stimulation	Well Test	
Stimulation # 1 of 1					
Well No.	3932	Type	Water-N2	Flush [bbls]	30
Size of String (in)	3.5	Water [bbls]	50	Sand Quantity [lbs]	8000
Stim From [ft]	2906	Acid [bbls]	2.4	Sand Type	20/40
Stim To [ft]	2928	Gel [bbls]	125	Injection Rate [bbls/min]	13
No of Shots	44	Foam [bbls]	0.07	Total Fluid [bbls]	229.87
Fractured by	Dowell Inc.	N2 [Mcf]	50	Summary Total [bbls]	175
Date	8/2/1966 MM/DD/YYYY	Alcohol [bbls]	2.4	Break-down Pr. [psi]	2000
		Cushion [bbls]	20	ISIP [psi]	1000
<input type="button" value="First Stimulation"/> <input type="button" value="Previous Stimualtion"/> <input type="button" value="Next Stimulation"/> <input type="button" value="Last Stimulation"/>					

Fig29. Stimulation tab

To browse between different Stimulations

<input type="button" value="First Stimulation"/>	<input type="button" value="Previous Stimualtion"/>	<input type="button" value="Next Stimulation"/>	<input type="button" value="Last Stimulation"/>
--	---	---	---

To move to the first stimulation, previous stimulation, next stimulation & the last stimulation in the record, click on the button assigned to it. The stimulations are assorted in ascending order according to stimulation date for current well

WELL TEST

Wellbore	Completion	Perforation	Stimulation	Well Test																				
WellTest # 10 of 11																								
Well Test																								
	Time [hrs]	Field Pr. [psi]	Flow Pr. [psi]	Rate [McfD]																				
First Reading	0.75	639	605	254																				
Second Reading	0.75	639	545	460																				
Third Reading	0.75	627	580	337																				
Extended Time	3	627	567	312																				
<table border="0" style="width: 100%;"> <tr> <td>Field Name</td> <td colspan="4">LUCAS</td> </tr> <tr> <td>Well No.</td> <td colspan="4">3585</td> </tr> <tr> <td>Test Date</td> <td colspan="4">6/23/1993</td> </tr> <tr> <td>Test Type</td> <td colspan="4">Multi-Point</td> </tr> </table>					Field Name	LUCAS				Well No.	3585				Test Date	6/23/1993				Test Type	Multi-Point			
Field Name	LUCAS																							
Well No.	3585																							
Test Date	6/23/1993																							
Test Type	Multi-Point																							
kh [md-ft]	132	NonDarcyCo-eff	3.05200	DeltaP ² [psi ²]	250000																			
Skin	-2.14	n Value	0	PD Rate [McfD]	570																			
True Skin	-3.10	C Value	1	ADF [McfD]	1328																			
<input checked="" type="radio"/> PD Rate <input type="radio"/> ADF																								
<input type="button" value="Show Chart"/> <input type="button" value="Well Test Analysis"/>																								
<input type="button" value="First WellTest"/> <input type="button" value="Previous WellTest"/> <input type="button" value="Next WellTest"/> <input type="button" value="Last WellTest"/>																								

Fig30. Well-test tab

To browse between different Well Tests

First WellTest	Previous WellTest	Next WellTest	Last Welltest
-----------------------	--------------------------	----------------------	----------------------

To move to the first well test, previous well test, next well test & the last well test in the record, click on the button assigned to it. The well tests are assorted in ascending order according to well test date for current well

Adding a new data

One can add a complete new well or just only a new well-bore/completion/perforation/stimulation/well-test data by following method

Adding a complete new well data

- 1- Click on the Add New button while keeping your well bore tab as active

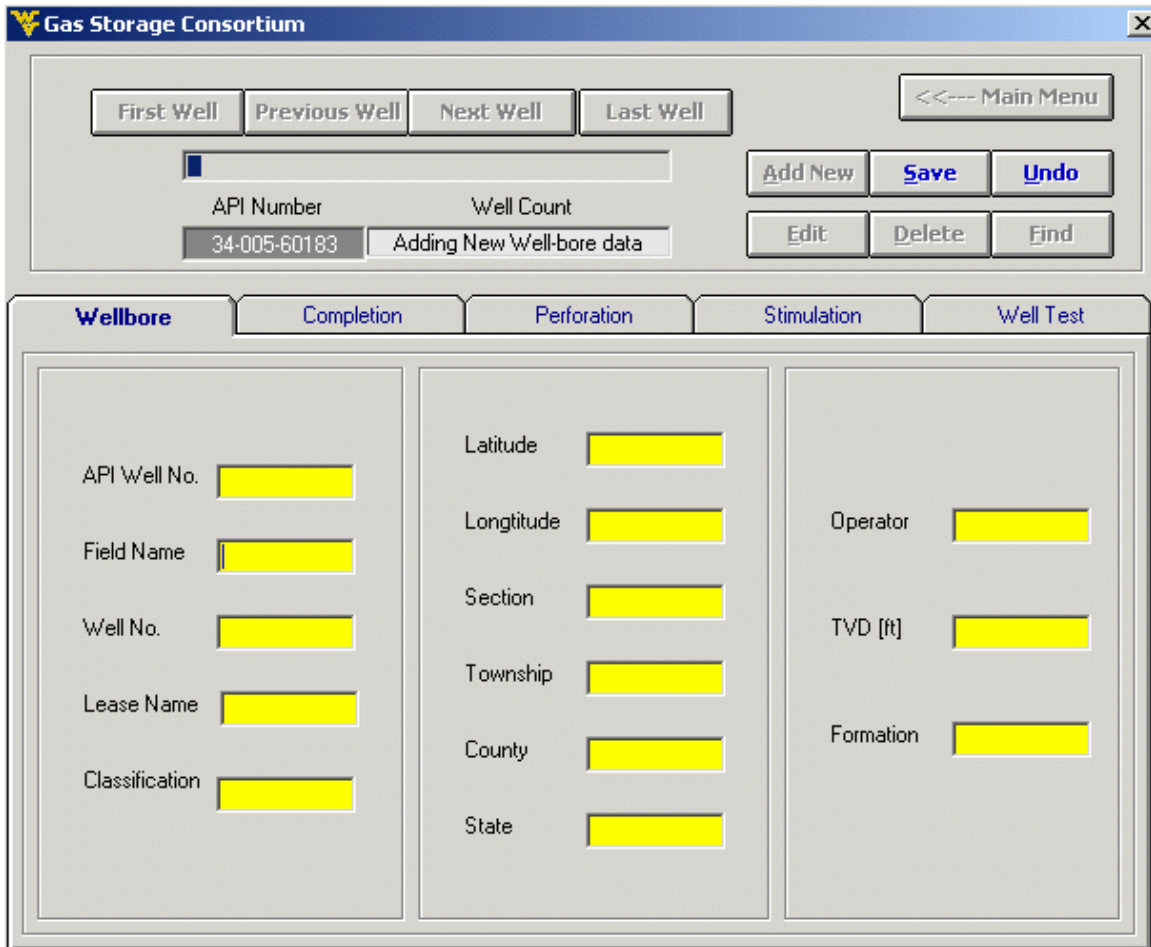
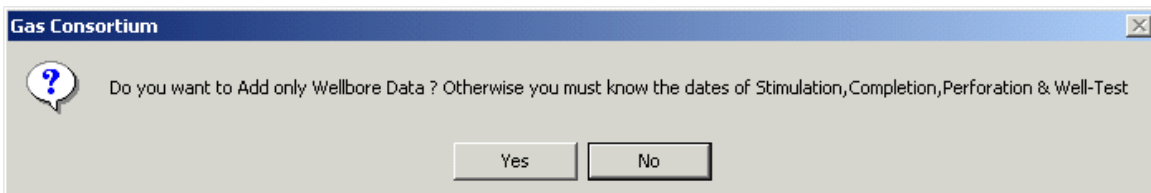


Fig31. Adding a complete new Well – well-bore tab

The following messages will pop-up. If you want to add the complete new well-bore data then click No button .

If you don't have the dates of Stimulation, Completion, Perforation & Well-Test data then click Yes and then add them one-by one



Following screen appears if No is clicked

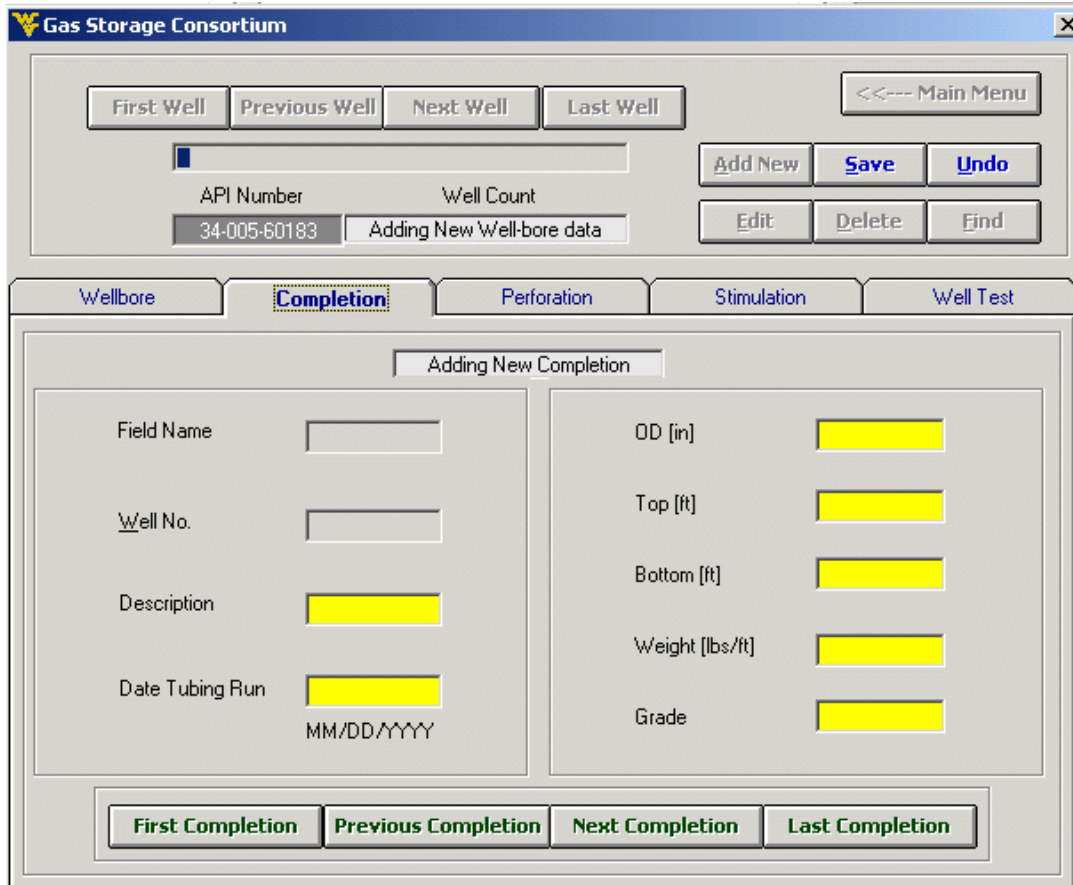


Fig32. Adding a complete new Well - completion tab

The background color of text boxes of all tabs including well-bore tab will be yellow indicating that they are ready for entering data

- 2- Enter the data in all the tabs. The dates for completion, perforation, stimulation & well test job should be known

Fig33. Adding a complete new Well – entering data for wellbore

Fig34. Adding a complete new Well – entering data for perforation

Gas Storage Consortium

First Well Previous Well Next Well Last Well <<--- Main Menu

API Number 34-005-60183 Well Count Adding New Well-bore data

Add New Save Undo Edit Delete Find

Wellbore Completion Perforation **Stimulation** Well Test

Adding New Stimulation

Well No. Type Flush [bbbs]

Size of String (in) 3 Water [bbbs] Sand Quantity [lbs]

Stim From [ft] 1670 Acid [bbbs] Sand Type

Stim To [ft] 1680 Gel [bbbs] Injection Rate [bbbs/min]

No of Shots 20 Foam [bbbs] Total Fluid [bbbs]

Fractured by KAM N2 [Mcf] Summary Total [bbbs]

Date 09/26/2004 Alcohol [bbbs] Break-down Pr. [psi]

MM/DD/YYYY Cushion [bbbs] ISIP [psi]

First Stimulation Previous Stimulation Next Stimulation Last Stimulation

Fig35. Adding a complete new Well – entering data for stimulation

Gas Storage Consortium

First Well Previous Well Next Well Last Well <<--- Main Menu

API Number 34-005-60183 Well Count Adding New Well-bore data

Add New Save Undo Edit Delete Find

Wellbore Completion Perforation Stimulation **Well Test**

Adding New Well Test

Well Test

	Time [hrs]	Field Pr. [psi]	Flow Pr. [psi]	Rate [McfD]
First Reading				
Second Reading				
Third Reading				
Extended Time				

Field Name Well No. Test Date 09/26/2005 Test Type

Well Test
 PD Rate
 AOF

Show Chart Well Test Analysis

kh [md-ft] NonDarcyCo-eff DeltaP² [psi²]

Skin n Value PD Rate [McfD]

True Skin C Value AOF [McfD]

First WellTest Previous WellTest Next WellTest Last WellTest

Fig36. Adding a complete new Well – entering data for well test

3- Click the Save button 

RESULT OF ADDING A COMPLETE NEW WELL DATA

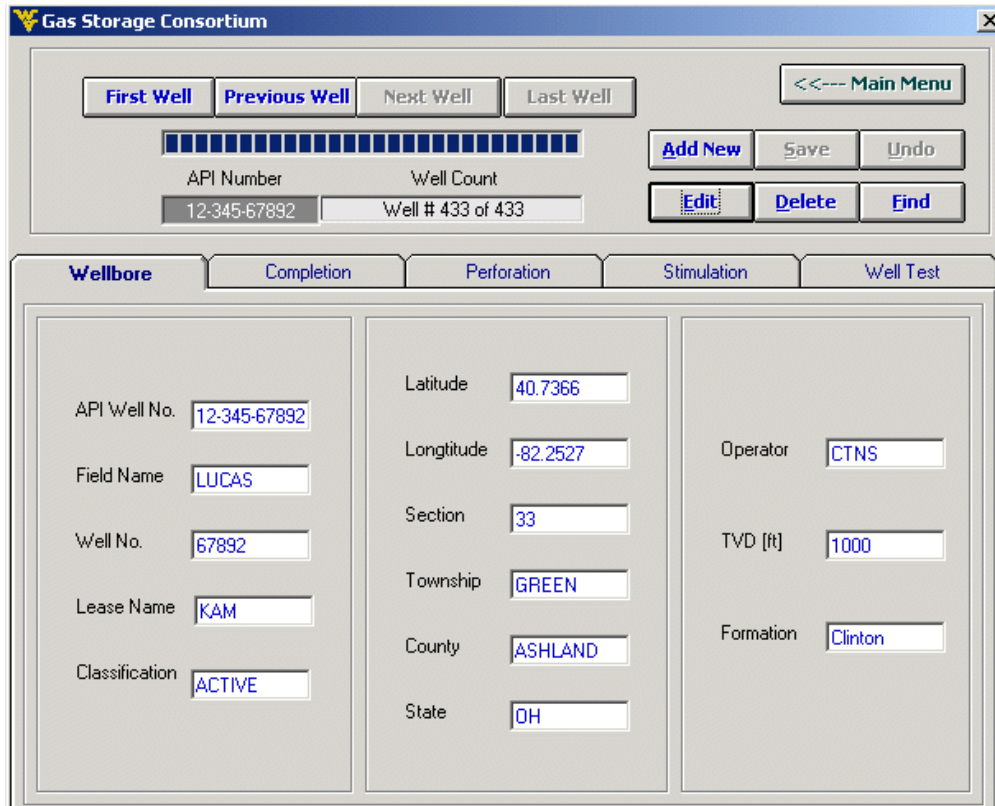
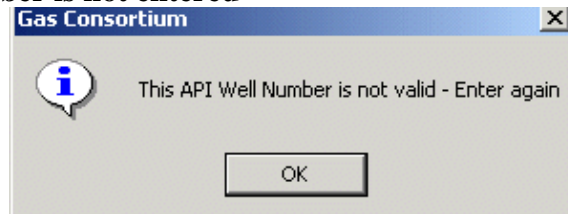


Fig37. Result of adding a complete new well

Warnings – If API Number is not entered



Warnings – If API Number entered is already in the database

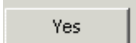


ADDING ONLY WELL-BORE/COMPLETION/PERFORATION/ STIMULATION/ WELL-TEST DATA

- 1- Click on the Add New button  while keeping that tab active for which you want to add the data.

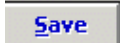
Only for well-bore tab following message pops-up



Click Yes  button to add only Well-bore data

The background color of all text boxes of that tab will be yellow indicating that they are ready for entering data

- 2- Enter the data. The dates for completion, perforation, stimulation & well test job should be known

- 3- Click the Save button 

Editing data

One can edit complete well or just only a new well-bore/completion/perforation/ stimulation/well-test data by following methods

Editing a complete well data

- 1- Click on the Edit button  while keeping your well bore tab as active

Following screen pops-up



Select accordingly

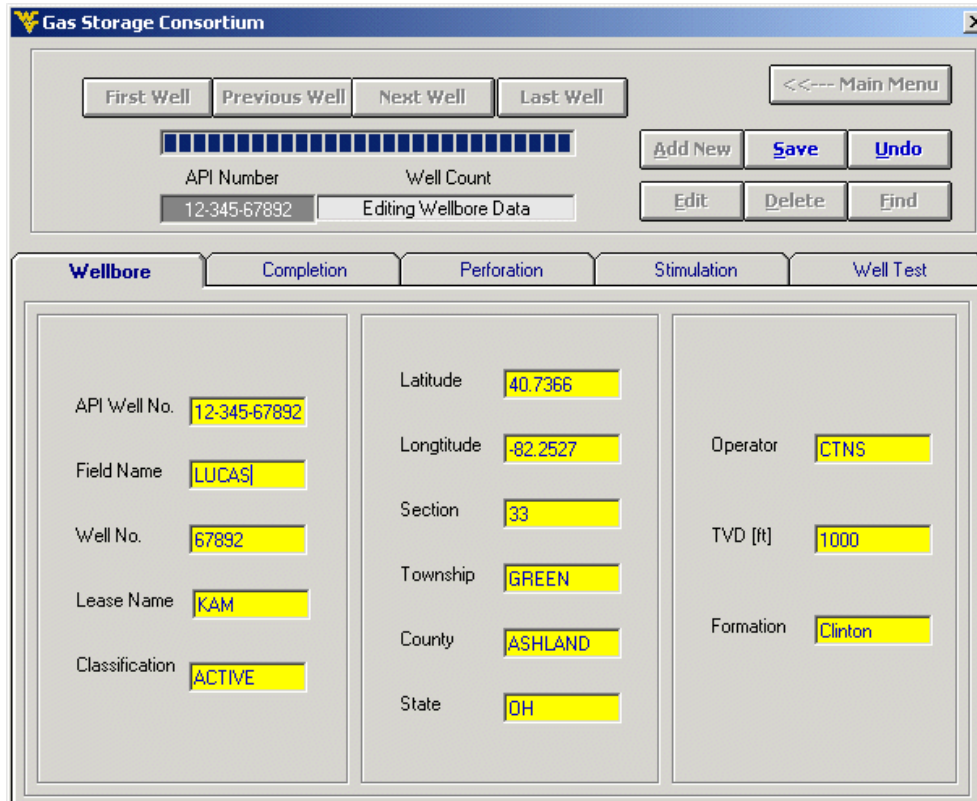


Fig38. Editing well data

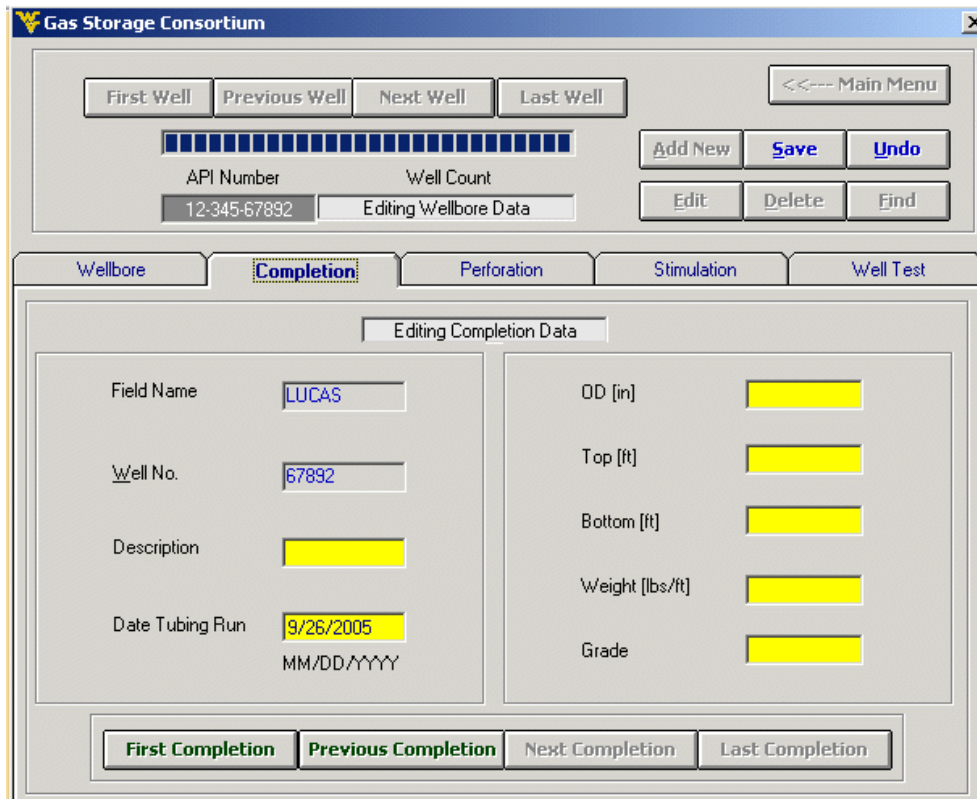


Fig39. Editing completion data

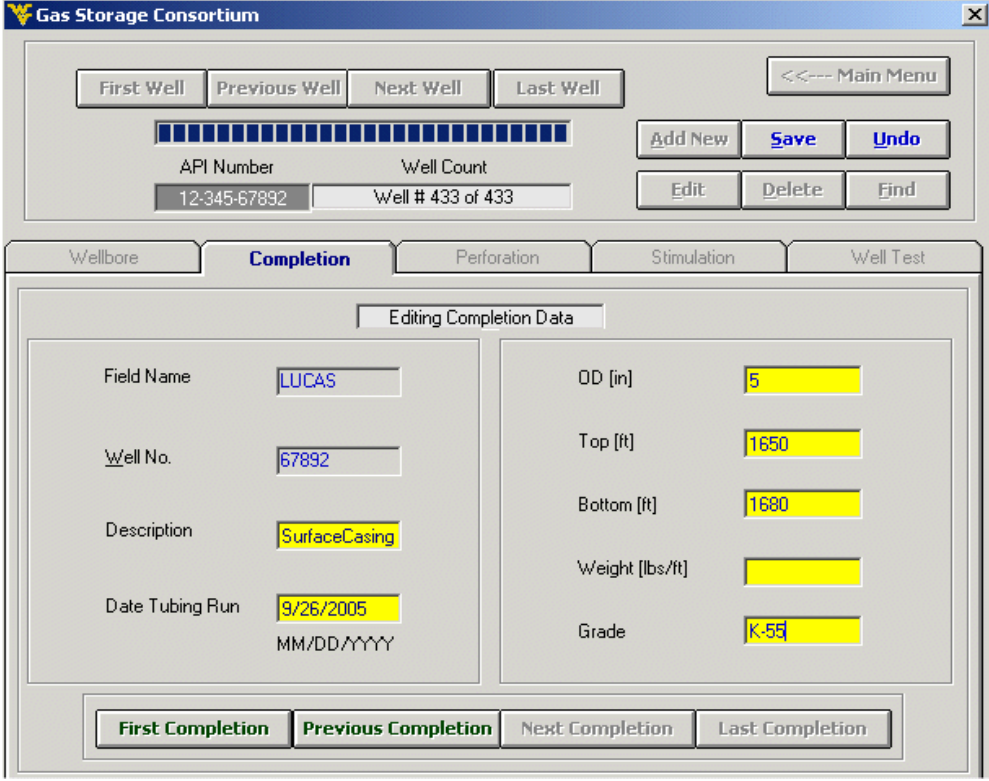
The background color of text boxes of all tabs including well-bore tab will be yellow indicating that they are ready for entering data

2- Enter the data in all the active tabs. The dates for completion, perforation, stimulation & well test job should be known

3- Click the Save button 

EDITING ONLY COMPLETION/PERFORATION/ STIMULATION/WELL-TEST DATA

- 1- Click on the Edit button  while keeping that tab active for which you want to edit the data except well bore tab



The screenshot shows a software window titled "Gas Storage Consortium". At the top, there are navigation buttons: "First Well", "Previous Well", "Next Well", "Last Well", and "Main Menu". Below these are "Add New", "Save", and "Undo" buttons. A progress bar and "API Number" (12-345-67892) and "Well Count" (Well # 433 of 433) are also present. The main area has tabs for "Wellbore", "Completion", "Perforation", "Stimulation", and "Well Test". The "Completion" tab is active, showing a form titled "Editing Completion Data". The form has two columns of fields. The left column includes "Field Name" (LUCAS), "Well No." (67892), "Description" (SurfaceCasing), and "Date Tubing Run" (9/26/2005). The right column includes "OD (in)" (5), "Top (ft)" (1650), "Bottom (ft)" (1680), "Weight (lbs/ft)", and "Grade" (K-55). At the bottom of the form are buttons for "First Completion", "Previous Completion", "Next Completion", and "Last Completion".

Fig40. Saving completion data

The background color of all text boxes of that tab will be yellow indicating that they are ready for entering data

- 2- Enter the data. The dates for completion, perforation, stimulation & well test job should be known
- 3- Click the Save button 

RESULT OF EDITING ONLY COMPLETION DATA

The screenshot shows a software window titled "Gas Storage Consortium" with a close button (X) in the top right corner. The interface includes a navigation bar with buttons for "First Well", "Previous Well" (highlighted), "Next Well", and "Last Well", along with a "<<--- Main Menu" button. Below this is a progress indicator and a summary section showing "API Number: 12-345-67892" and "Well Count: Well # 433 of 433". Action buttons include "Add New", "Save", "Undo", "Edit", "Delete", and "Find". A tabbed interface at the bottom has tabs for "Wellbore", "Completion" (selected), "Perforation", "Stimulation", and "Well Test". The "Completion" tab shows "Completion # 1 of 1" and a data entry form with the following fields:

Field Name	LUCAS	OD [in]	5
Well No.	67892	Top [ft]	1650
Description	SurfaceCasing	Bottom [ft]	1680
Date Tubing Run	9/26/2005 MM/DD/YYYY	Weight [lbs/ft]	
		Grade	K-55

At the bottom of the window, there are buttons for "First Completion", "Previous Completion" (highlighted), "Next Completion", and "Last Completion".

Fig41. Saved completion data

DELETING DATA

One can delete complete well or just only delete completion/perforation/ stimulation/well-test data by following methods

Deleting a complete well data

- 1- Click on Delete button  while keeping your well bore tab as active

Editing only completion/perforation/ stimulation/well-test data

- 1- Click on Delete button  while keeping that tab active of which you want to delete the data except well bore tab

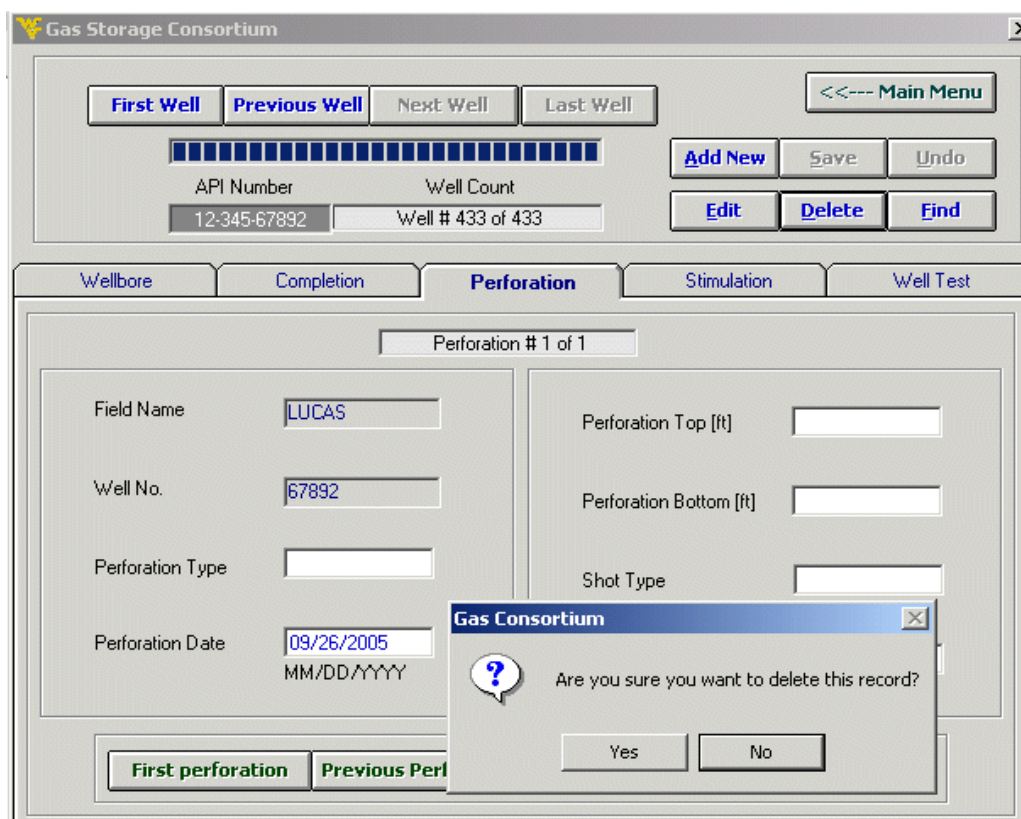
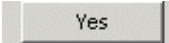


Fig42. Deleting perforation record

You will be greeted with the above message to make sure that delete button is not accidentally pressed

- 2- Click on yes  if you want the selected record to be deleted

UNDO THE EDIT / ADD OPERATION

To undo the edit or add operation before they can be saved click undo button



FINDING A WELL

Follow the following procedure to find a well for which you have some idea of its API well number

Click on Find button



The following screen is displayed

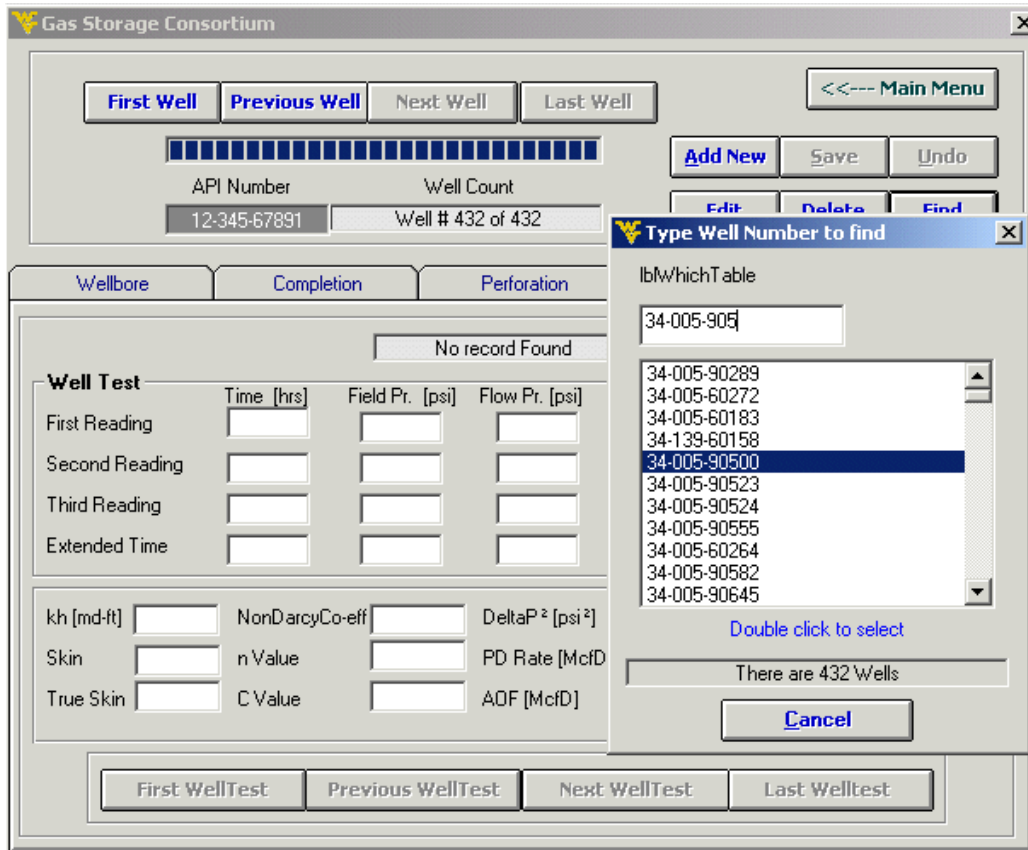


Fig43. Finding a well

1- Type the API number to find the well and then double click it in the list

If the API number is found then the message below is displayed and the data for that well is retrieved

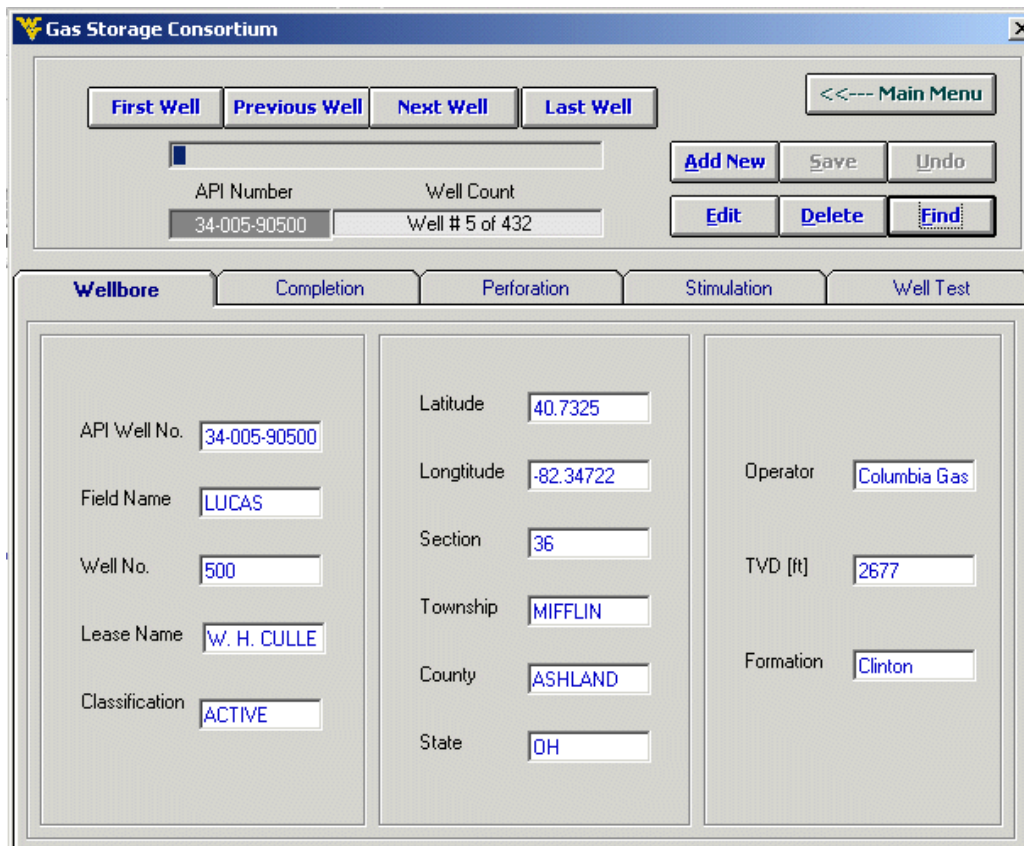
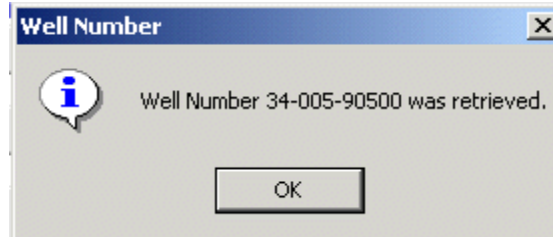


Fig44. Retrieving the data

WELL TEST ANALYSIS

To do the well test analysis on the well and to draw graph of Peak day rate and Absolute open flow use the option / command buttons below

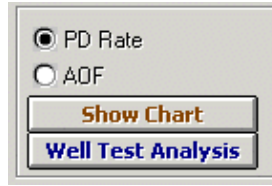


Fig45. Well-test Analysis Option in well-test tab

PEAK DAY / AOF GRAPH

Select **PD rate** / **AOF** option button and click **Show Chart** button . The following screens will appear according to the option selected

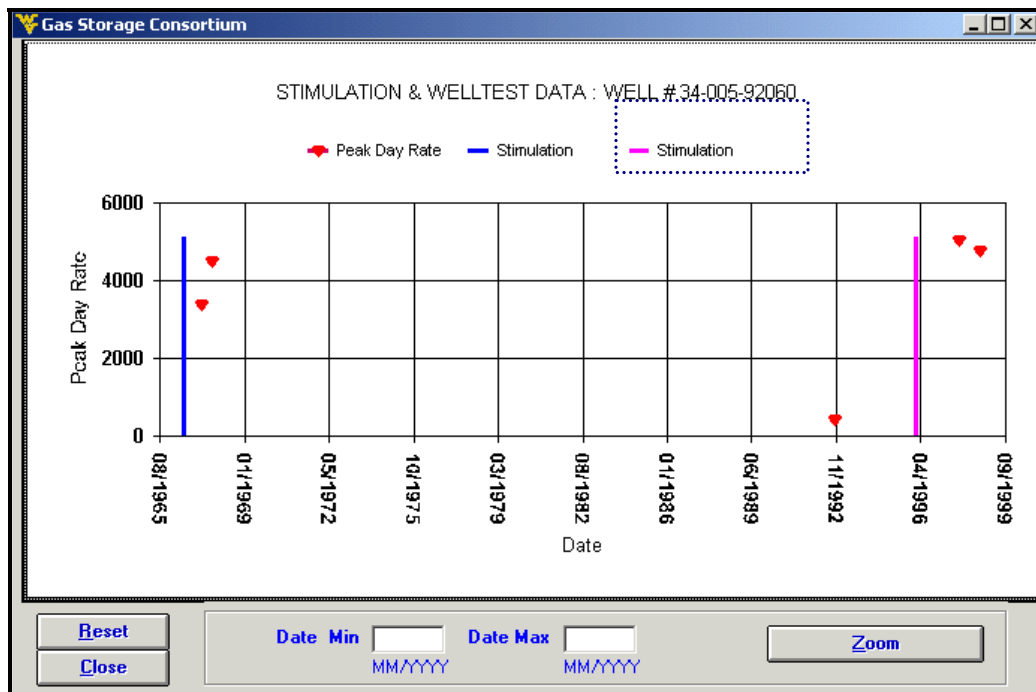


Fig46. Show Chart – Peak Day Rate

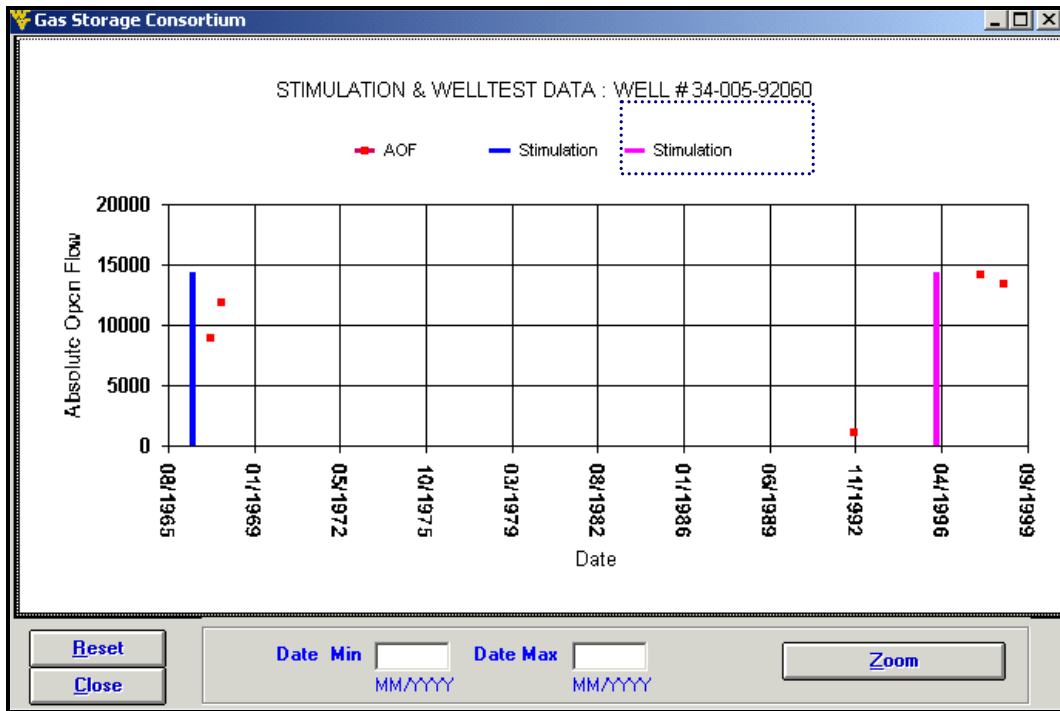


Fig47. Show Chart – Absolute Open Flow

WELL TEST ANALYSIS TOOL

Click the **Well Test Analysis** button  and the following screen will pop up indicating different types of well tests that have done on the selected well

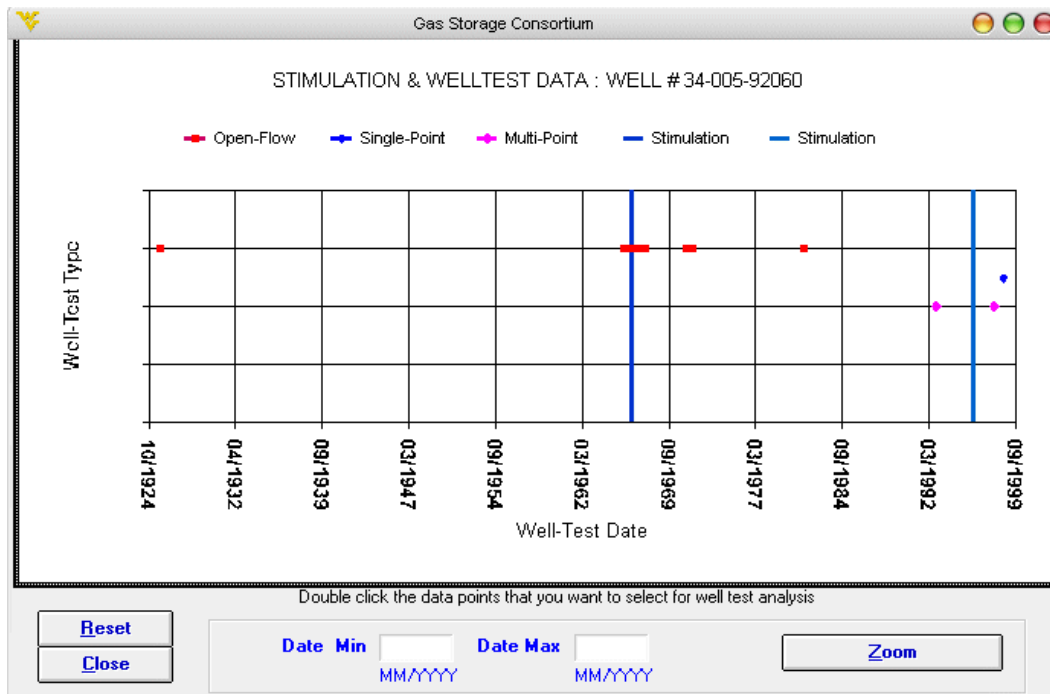


Fig48. Well Test analysis – Showing types of tests

To zoom the screen, type minimum and maximum date and press **Zoom** button. The screen will be zoomed between the dates typed

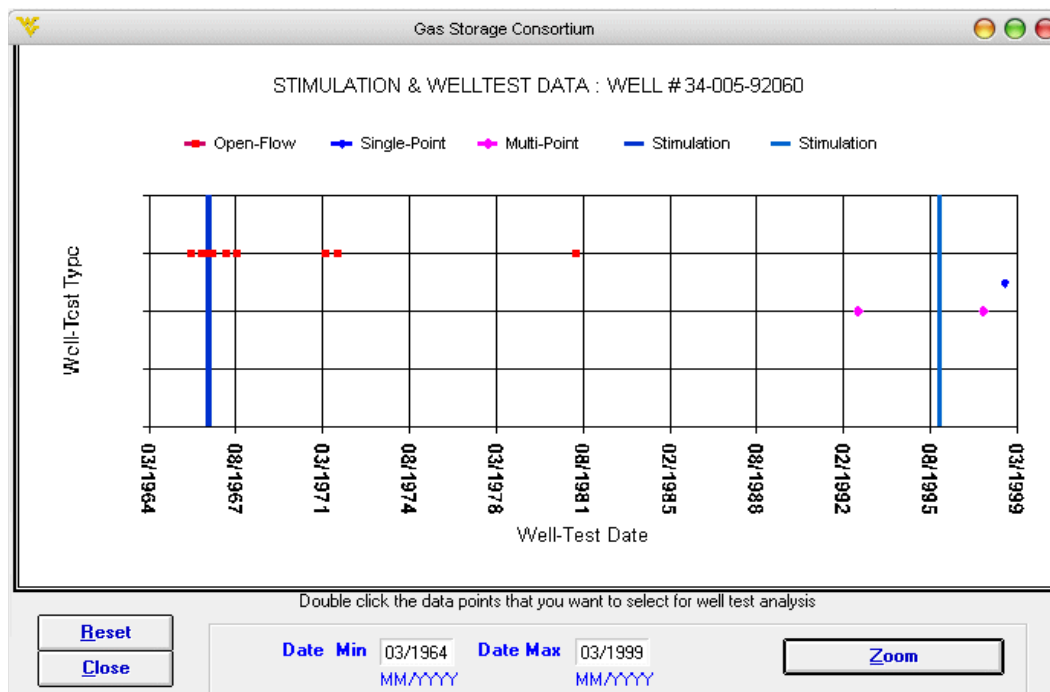


Fig49. Well Test analysis – zoomed

SELECTING WELL TESTS TO PLOT

Double click on the data points that you want to select for well test analysis. These points will be added in the Selected Well Tests list box.

You can remove the points from Selected Well Tests list box by selecting the well tests and then press Remove points button

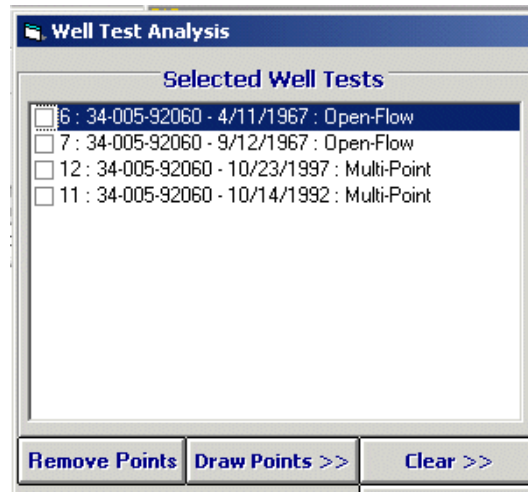


Fig50. Well-tests selected for analysis

Select the well tests that you want to draw and draw them by clicking 'Draw Points' button

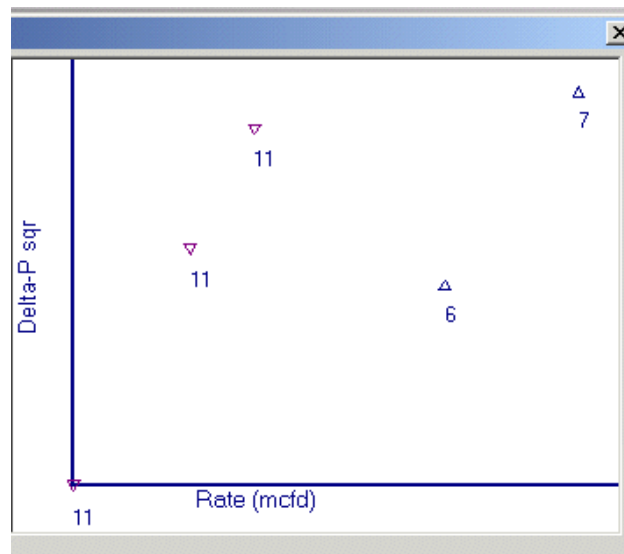


Fig51. Well-tests selected to find value of 'n'

CALCULATING SLOPE 'N'

Draw a line in the picture box keeping left mouse button held down

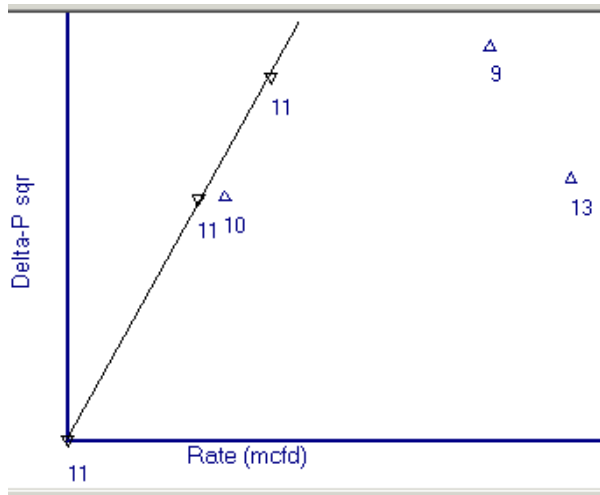


Fig52. Draw a line to find value of 'n'

Press Calculate n button to find the slope the drawn line

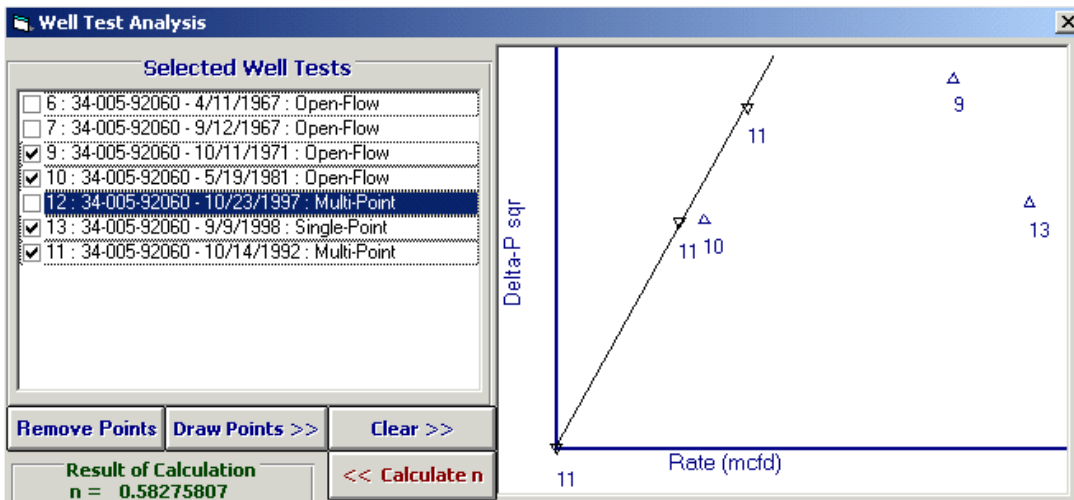


Fig53. Calculating value of 'n'

CALCULATING C, PEAK DAY, AOF

Press the **Calculate C, PDrate, AOF** button to find these values

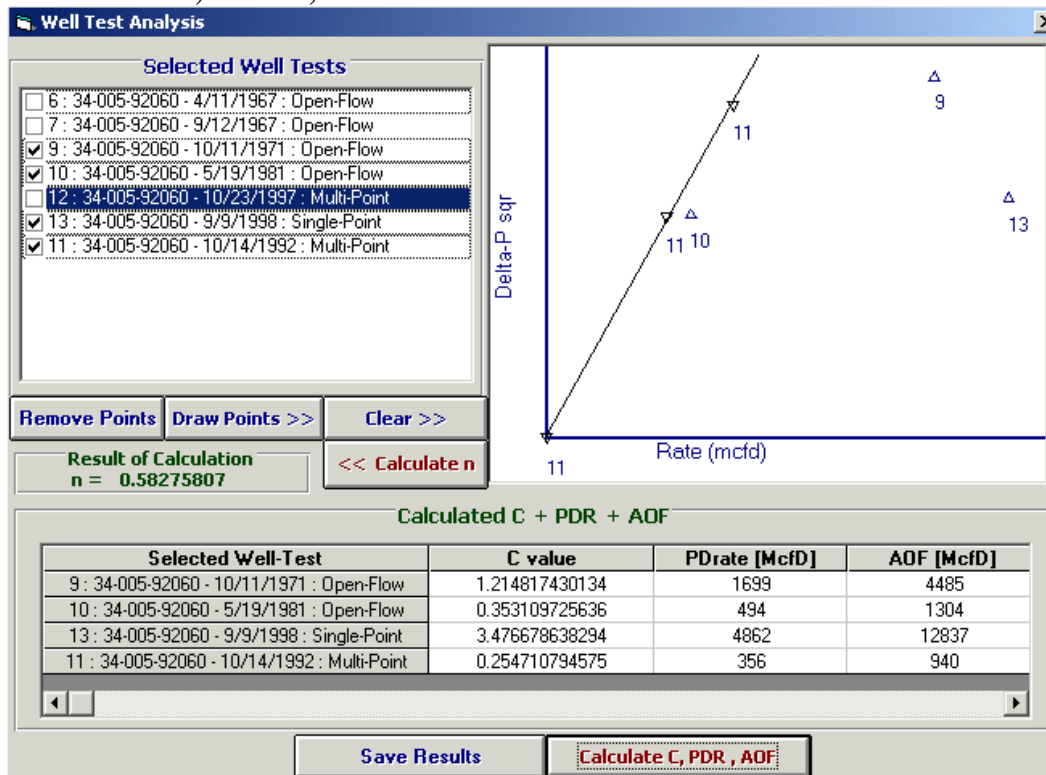


Fig54. Calculating C, PDR & AOF

SAVING THE WELL DELIVERABILITY PARAMETERS CALCULATED

To save the results click the **Save Results** button. The new calculated well deliverability parameters would be added in the database

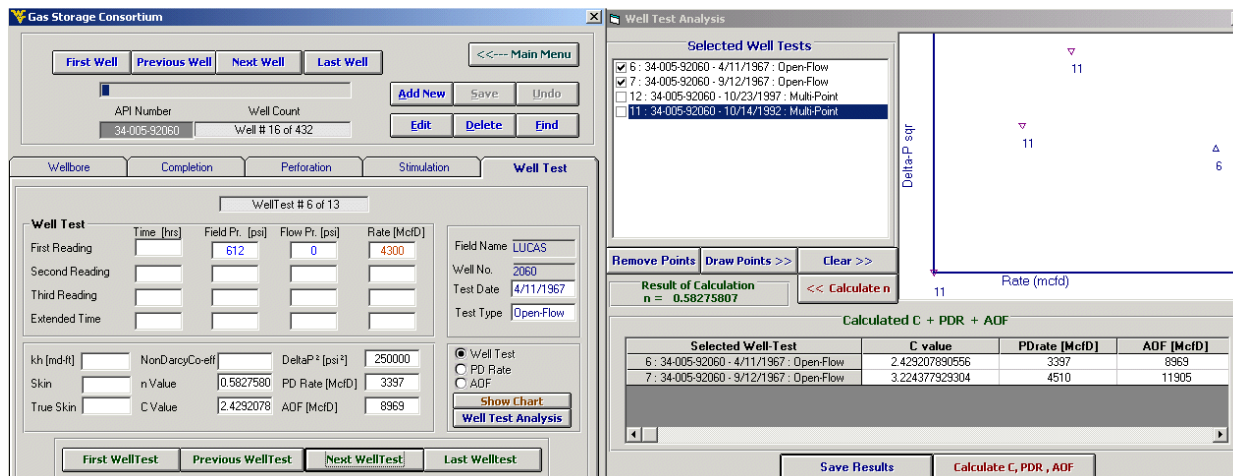


Fig55. C, PDR & AOF values saved in the database

SELECT WELL DATA

In this form the user can choose to select the data of the wells that he wants to look at. Following are a few ways he can choose the data

SELECTING A WELL BY STATE /COUNTY

The user selects the state first and then the county. All the wells will be selected for that county in the selected wells list box

The screenshot shows a software interface with two main sections: 'SELECT' and 'SELECTED WELLS'.
 In the 'SELECT' section, there is a dropdown menu for 'STATE' with 'OHIO' selected. Below it is a list box for 'COUNTY' containing 'ASHLAND' and 'RICHLAND'. A 'Reset' button is located at the bottom of this section.
 In the 'SELECTED WELLS' section, there is a list box titled 'API Well Number' containing a list of well numbers: 34-005-01272, 34-005-02420, 34-005-02887, 34-005-02889, 34-005-02897, 34-005-02901, 34-005-02907, 34-005-02909, 34-005-02911, 34-005-02960, 34-005-10044, 34-005-10516, and 34-005-10517. The first item, 34-005-01272, is selected. A 'Select All' button is located at the bottom of this section.

Fig56. Selecting Ohio County

SELECTING A WELL BY STIMULATION YEAR

The user can select the option button for stimulated year and input the year values. If Select Wells button is clicked then all the wells that have been stimulated between these years will be shown in the selected wells list box

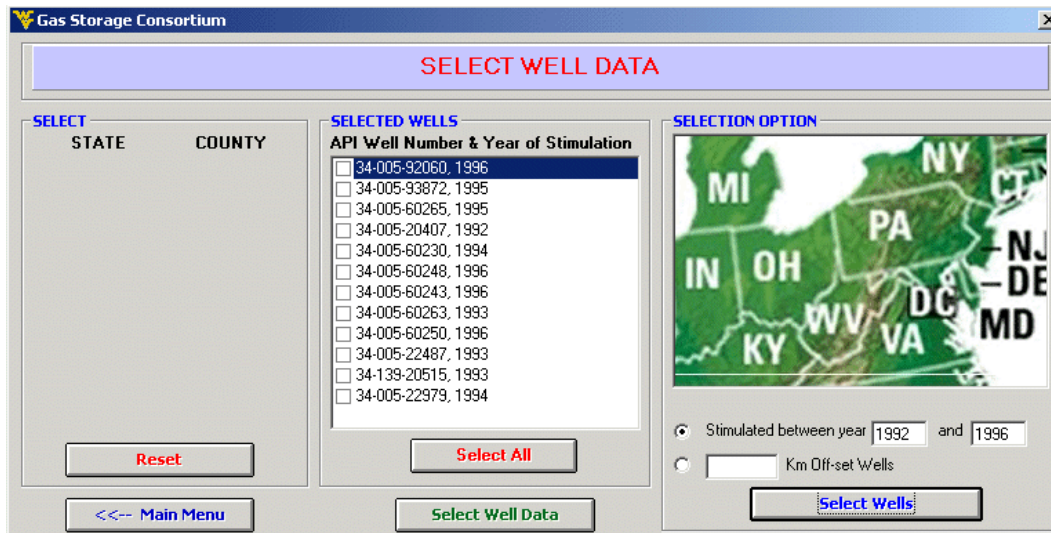


Fig57. Selecting wells according to stimulation year

SELECTING OFFSET WELLS TO A WELL

The user selects the offset option and the well near which he wants to find the off-set wells, and then enters the distance of off-set in kilometers. If Select Wells button is clicked then all the wells that are off-set of the selected well will be shown in the selected wells list box

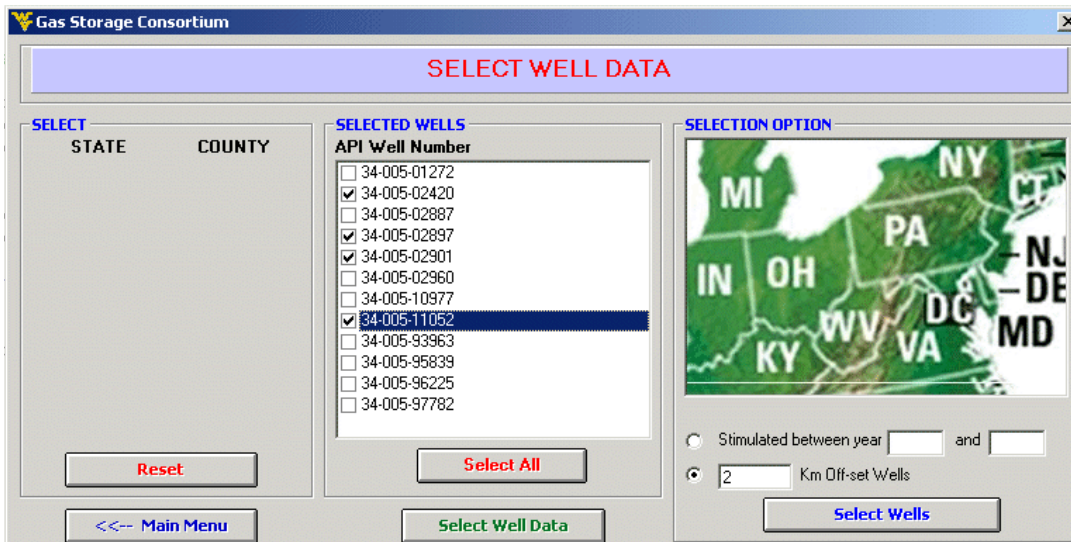


Fig58. Offset wells

SELECTING WELL DATA TO DISPLAY

When the wells for which the user want the data to be retrieved have been selected, click the Select Well Data button  and select the parameters

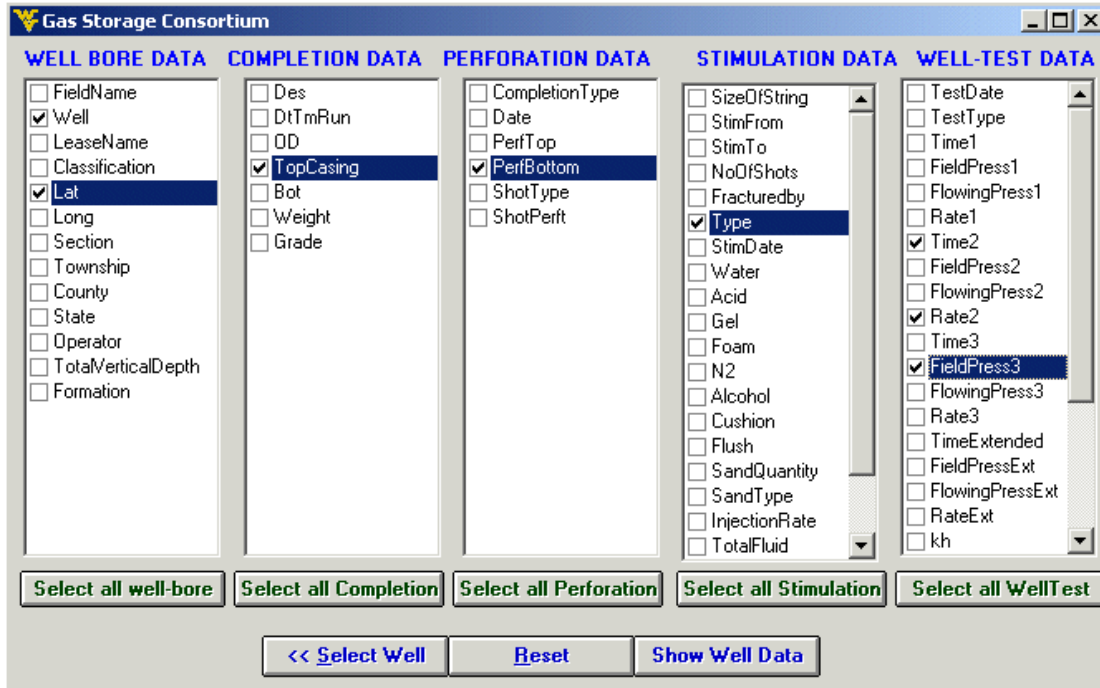


Fig59. Selecting Well Parameters

Click Show Well Data  to retrieve the data

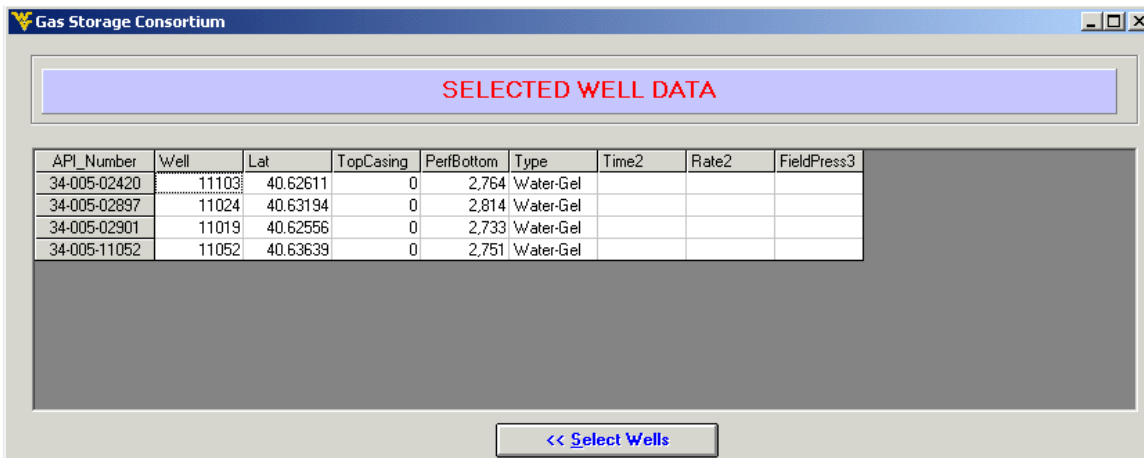


Fig60. Result of the wells & parameters selected

CONCLUSIONS

The first year of the project was completed successfully. A database software application was developed that included a module for gas storage well test interpretation. This software package was compiled and together with a user manual was included as part of this report. The software package is included in the accompanying CD.

Appendix D
2004, Renovation of Produced Waters from Underground Natural Gas
Storage Facilities: A Feasibility Study Using Hybrid Constructed
Wetland Technology,
Clemson University Final Report

Renovation of Produced Waters from Underground Natural Gas Storage Facilities: A Feasibility Study Using Hybrid Constructed Wetland Technology

Final Report

September 1, 2004 – December 31, 2005

Submitted by:

**James W. Castle (PI), Ph.D., Associate Professor, Clemson University
John H. Rodgers Jr. (Co-PI), Ph.D., Professor, Clemson University
Brenda M. Johnson, Graduate Research Assistant, Clemson University
Laura E. Ober, Graduate Research Assistant, Clemson University
Scott Brame, Research Associate, Clemson University**

January 30, 2006

**Gas Storage Technology Consortium
Subaward #2808-CU-DOE-1779**

**Clemson University
340 Brackett Hall
Clemson, SC 29634**

Disclaimer

“This report was prepared as an account of work sponsored by an agency of the United States Government. Neither the United States Government nor any agency thereof, nor any of their employees, makes any warranty, express or implied, or assumes any legal liability or responsibility for the accuracy, completeness, or usefulness of any information, apparatus, product, or process disclosed, or represents that its use would not infringe privately owned rights. Reference herein to any specific commercial product, process, or service by trade name, trademark, manufacturer, or otherwise does not necessarily constitute or imply its endorsement, recommendation, or favoring by the United States Government or any agency thereof. The view and opinions of authors expressed herein do not necessarily state or reflect those of the United States Government or any agency thereof.”

Abstract

The use of hybrid constructed wetland treatment systems offers an innovative approach for handling water produced from natural gas storage. Materials such as chlorides, metals, hydrocarbons, and corrosion inhibitors are often of concern in these waters. Specifically designed constructed wetland treatment systems have been used to treat each of these constituents independently, but this technology has not been demonstrated for produced waters from gas storage fields. Specific objectives of this study were: (1) to characterize produced waters; (2) to compare National Pollutant Discharge Elimination System (NPDES) standards in several situations where produced waters may be discharged or reused; (3) to design, construct, and monitor the performance of a pilot-scale constructed wetland system for treatment of water produced from gas storage fields; (4) to evaluate treatment effectiveness and performance of the pilot-scale system; and (5) to confirm design characteristics (hydrosol, hydroperiod, vegetation, sizing, etc.) for field-scale constructed wetland treatment systems. Statistical data regarding the composition of gas storage produced waters were gathered and tabulated from industry and literature. Several gas storage companies provided actual samples of produced water for analysis. NPDES permits were obtained for Ohio, Pennsylvania, New York, and West Virginia, and these permits were compiled into a single model (comprehensive) permit that was utilized for treatment performance criteria for targeted constituents. A pilot-scale constructed wetland treatment system was designed, constructed, and allowed time to stabilize. Simulated produced waters treated by the pilot-scale system were formulated and mixed. Four experiments were completed in which Experiment 1 (fresh produced water), Experiment 2 (brackish produced water), Experiment 3 (saline produced water), and Experiment 4 (hyper-saline produced water), were run through the appropriate modules of the hybrid constructed wetland treatment system. As samples were collected during each of these experiments, analyses were performed and results were compared to the model NPDES permit. Design parameters were developed and refined to accomplish remediation of the specific produced waters. Data obtained during this study indicate that the pilot-scale hybrid CWTS provided effective treatment of simulated natural gas storage produced waters.

Table of Contents

DISCLAIMER	ii
ABSTRACT	iii
INTRODUCTION	1
EXECUTIVE SUMMARY	3
EXPERIMENTAL	5
Task 1: Characterize Produced Waters	5
Task 2: Obtain Discharge Permits and Develop Treatment Performance Goals	5
Task 3: Design and Construct Hybrid Treatment System	6
Task 4: Evaluate Treatment Effectiveness and Performance of the Pilot-Scale System	10
Task 5: Confirm Design Characteristics	11
RESULTS AND DISCUSSION	11
Task 1: Characterize Produced Waters	11
Task 2: Obtain Discharge Permits and Develop Treatment Performance Goals	12
Task 3: Design and Construct Hybrid Treatment System	12
Task 4: Evaluate Treatment Effectiveness and Performance of the Pilot-Scale System	15
Experiment 1: Simulated Freshwater	16
Metals	16
Toxicity	18
Experiment 2: Simulated Brackish Water	18
Metals	18
Toxicity	21
Experiment 3: Simulated Saline Water	22
Metals	22
Toxicity	29
Experiment 4: Simulated Hyper-Saline Water	30
Metals	30
Toxicity	37
Oil-in-Water Data	38
General Water Chemistry	38
Task 5: Confirm Design Characteristics	38
Oil/Water Separator	38
Reverse Osmosis System	39
Simulated Brackish Water II	39
Metals	39
Toxicity	43
Oil-in-Water Data	43
General Water Chemistry	44
CONCLUSIONS	44

REFERENCES CITED 46
OTHER PERTINENT PUBLICATIONS 46
APPENDIX: General Water Chemistry Data..... 48

List of Tables

Table 1. Targeted constituents, inflow concentrations, and chemical sources for simulated produced water..... 5
 Table 2. Model (comprehensive) NPDES Permit for discharge of natural gas storage produced waters. 7
 Table 3. Analytical methods for parameters monitored from the pilot hybrid constructed wetland treatment system..... 10
 Table 4. Stages and processes of the hybrid constructed wetland treatment system..... 14

List of Figures

Figure 1. Schematic of the hybrid pilot-scale constructed wetland treatment system for water produced from natural gas storage..... 4
 Figure 2. Pilot-scale constructed wetland treatment system..... 8
 Figure 3. Reverse Osmosis System..... 15
 Figure 4. Experiment 1: Simulated freshwater metal analysis for cadmium performed by AA. 16
 Figure 5. Experiment 1: Simulated freshwater metal analysis for zinc performed by ICP 17
 Figure 6. Experiment 2: Simulated brackish water metal analysis for cadmium performed by AA..... 18
 Figure 7. Experiment 2: Simulated brackish water metal analysis for copper performed by AA..... 19
 Figure 8. Experiment 2: Simulated brackish water metal analysis for lead performed by AA..... 20
 Figure 9. Experiment 2: Simulated brackish water metal analysis for zinc performed by ICP. 21
 Figure 10. Experiment 3: Saltwater module and RO permeate results for simulated saline water metal analysis of cadmium performed by ICP..... 22
 Figure 11. Experiment 3: Freshwater module (post-RO System) for simulated saline water metal analysis of cadmium performed by ICP..... 23
 Figure 12. Experiment 3: Saltwater module and RO permeate results for simulated saline water metal analysis of copper performed by ICP..... 24
 Figure 13. Experiment 3: Freshwater module (post-RO System) for simulated saline water metal analysis of copper performed by ICP..... 25
 Figure 14. Experiment 3: Saltwater module and RO permeate results for simulated saline water metal analysis of lead performed by ICP. 26
 Figure 15. Experiment 3: Freshwater module (post-RO System) for simulated saline water metal analysis of lead performed by ICP. 27
 Figure 16. Experiment 3: Saltwater module and RO permeate results for simulated saline water metal analysis of zinc performed by ICP. 28

Figure 17. Experiment 3: Freshwater module (post-RO System) for simulated saline water metal analysis of zinc performed by ICP.	29
Figure 18. Experiment 4: Saltwater module and RO permeate results for simulated hypersaline water metal analysis of cadmium performed by ICP.	30
Figure 19. Experiment 4: Freshwater module (post-RO System) for simulated hypersaline water metal analysis of cadmium performed by ICP.	31
Figure 20. Experiment 4: Saltwater module and RO permeate results for simulated hypersaline water metal analysis of copper performed by ICP.	32
Figure 21. Experiment 4: Freshwater module (post-RO System) for simulated hypersaline water metal analysis of copper performed by ICP.	33
Figure 22. Experiment 4: Saltwater module and RO permeate results for simulated hypersaline water metal analysis of lead performed by ICP.	34
Figure 23. Experiment 4: Freshwater module (post-RO System) for simulated hypersaline water metal analysis of lead performed by ICP.	35
Figure 24. Experiment 4: Saltwater module and RO permeate results for simulated hypersaline water metal analysis of zinc performed by ICP.	36
Figure 25. Experiment 4: Freshwater module (post-RO System) for simulated hypersaline water metal analysis of zinc performed by ICP.	37
Figure 26. Oil/Water Separator for Experiment 3.	39
Figure 27. Newly constructed Oil/Water Separator to be used in Experiment 4.	39
Figure 28. Results for simulated brackish water II metal analysis of cadmium performed by ICP.	40
Figure 29. Results for simulated brackish water II metal analysis of copper performed by ICP.	41
Figure 30. Results for simulated brackish water II metal analysis of cadmium performed by ICP.	42
Figure 31. Results for simulated brackish water II metal analysis of cadmium performed by ICP.	43

Appendix: Tables

Table 1. General Water Chemistry Results for Experiment 1: Batch 1 (Simulated Fresh Produced Water)	49
Table 2. General Water Chemistry Results for Experiment 1: Batch 2 (Simulated Fresh Produced Water)	50
Table 3. General Water Chemistry Results for Experiment 2: Batch 1 (Simulated Brackish Produced Water)	51
Table 4. General Water Chemistry Results for Experiment 2: Batch 2 (Simulated Brackish Produced Water)	52
Table 5. General Water Chemistry Results for Experiment 3: Batch 1 (Simulated Saline Produced Water)	53
Table 6. General Water Chemistry Results for Experiment 3: Batch 2 (Simulated Saline Produced Water)	54
Table 7. General Water Chemistry Results for Experiment 4: Batch 1 (Simulated Hyper-Saline Produced Water)	55

Table 8. General Water Chemistry Results for Experiment 4: Batch 2 (Simulated Hyper-Saline Produced Water) 56
Table 9. General Water Chemistry Results for Simulated Brackish Produced Water II..... 57

Introduction

One of the highest priorities identified by the Gas Storage Technology Consortium (GSTC) is the investigation of new approaches for handling produced water. Produced waters pose a challenge for treatment because they vary greatly in their composition. Expansion of existing gas storage fields and development of new fields are limited by the high costs associated with wastewater treatment and disposal. Currently there are two common methods for handling produced water. The first method is to transport the produced water to specialized treatment facilities followed by surface discharge of the treated water, and the second is to reinject the water to the subsurface. While volumes of produced water are increasing, conventional treatment methods are becoming exponentially more costly as surface discharge and re-injection regulations under the National Pollutant Discharge Elimination System (NPDES) and Clean Water Act (CWA) grow more stringent. Finding new approaches for handling produced waters is essential for continued operation of many existing storage fields and for the development of new storage capacities.

Water produced from gas storage facilities may be generated in relatively high volumes and contain a variety of constituents that limit disposal or reuse of the water. Materials such as chlorides, hydrocarbons, and corrosion inhibitors are of concern in these waters. Although salinity of some produced waters may be low enough to meet NPDES discharge limits, concentrations of other constituents in these waters may preclude discharge, resulting in a need for treatment or disposal. Generic parameters such as biochemical oxygen demand (BOD) and chemical oxygen demand (COD) may be targeted for treatment. Specifically designed constructed wetland treatment systems (CWTS) have been used to treat various constituents independently, but this technology has not been demonstrated for produced waters from gas storage fields. Wetlands possess unique reactions not occurring in other aquatic or terrestrial systems. Constructed wetlands can be poised or buffered to ensure that desired reactions (transfers and transformations) affecting the constituents targeted for treatment proceed at predictable rates over long periods of time (decades).

The use of CWTS is a readily implemented approach with the potential to reduce the costs of handling water produced from gas storage fields. The proposed approach offers the following specific advantages:

1. low construction cost;
2. low operational and maintenance costs;
3. reliability; and
4. flexibility in design, so the approach is applicable to many gas storage fields.

The purpose of the current research is to develop a low cost and readily implemented hybrid CWTS for treating produced water as part of a system integrated with surface facilities of gas storage fields. The approach is applicable to a wide range of waters produced from gas storage, as the composition and volumes of waters generated vary greatly among storage fields. A pilot-scale study serves to decrease uncertainties and confirm design features for future, field-scale constructed wetland treatment systems.

The pilot-scale study provides data regarding the feasibility of this approach for treating gas storage produced waters of various compositions. Specific objectives of this pilot-scale study are:

1. To characterize several produced waters;
2. To compare NPDES standards in several situations where produced waters may be discharged or reused;
3. To design, construct, and monitor the performance of a pilot-scale constructed wetland treatment system for treatment of water produced from gas storage fields;
4. To evaluate treatment effectiveness and performance of the pilot-scale system; and
5. To confirm design characteristics (hydrosol, hydroperiod, vegetation, sizing, etc.) for future field-scale constructed wetland treatment systems.

A hybrid CWTS capable of effectively and consistently treating simulated produced waters in compliance with NPDES standards was designed and tested at a pilot-scale.

The major expected benefit of investigating CWTS technology for the handling of water produced from gas storage is significantly decreased costs for produced water management, which could potentially lead to expansion of existing storage fields. In addition, new geographic areas may be opened up for development of gas storage fields in light of the anticipated economic advantages.

Executive Summary

The first objective of this investigation was to characterize water produced from natural gas storage (Task 1). Two steps were involved with produced water characterization: 1) analysis of actual produced waters, and 2) statistical analysis of produced water composition data. To help accomplish the first step, sampling kits were sent to various natural gas storage facilities in order to obtain samples of actual produced waters for analysis. The second step in the characterization of produced water was the statistical analysis of data provided by various gas storage facilities. These data, which were obtained from industry members of the Gas Storage Technology Consortium, were statistically analyzed and compared using the Statistical Analysis System (SAS Institute, 2002). Based on results from analyses of these data, characteristics of the produced waters tend to cluster into four groups (based primarily on chloride concentrations):

- 1.) fresh - characterized by low chloride concentrations (≤ 400 - $2,500$ mg/L);
- 2.) brackish - characterized by medium chloride concentrations ($2,500$ - $15,000$ mg/L);
- 3.) saline - characterized by high chloride concentrations ($15,000$ - $40,000$ mg/L); and
- 4.) hyper-saline - characterized by extremely high chloride concentrations ($\geq 40,000$ mg/L).

The data gathered from the statistical analysis of produced waters were utilized to formulate simulated produced waters. By using simulated produced waters, the specific characteristics of the water entering the system are known. When these characteristics are compared with those of the treated water leaving the system, the constituents removed by the system can be determined more accurately.

In order to develop reasonable treatment performance goals for the constructed wetland treatment systems (CWTS), the second objective of this research project was to obtain NPDES permits and to develop treatment performance goals based on these permits (Task 2). This objective required contacting various State regulatory and USEPA offices in Ohio, Pennsylvania, New York, and West Virginia, as well as gathering information from industry contacts in West Virginia and Pennsylvania. Concurrent with the work on this task, the USEPA released a website (USEPA, 2004) for easy access of NPDES permits which provided additional information. After analysis of approximately 50 NPDES permits from the aforementioned states, a model (comprehensive) permit was generated.

The third objective of the investigation was to design, construct, and monitor the performance of a pilot-scale constructed wetland system for treatment of water produced from gas storage fields (Task 3). The design of the hybrid CWTS includes five major components (or modules): (1) the produced water is retained in a detention basin; (2) the produced water is passed through an API oil/water separator; (3) the water from the oil/water separator progresses through two saltwater wetland cells in series containing quartz-sand hydrosol and *Spartina alterniflora*; (4) the water from the saltwater cells is held in a second detention basin until passing through a reverse osmosis (RO) system; (5) if the water no longer shows toxicity to receiving system biota, it is directly discharged; if the water is still toxic, it is passed through a freshwater wetland system. Each module

has a different function in the treatment of produced water. Depending on the salinity of the produced water as well as the oil and grease concentration present in the water, various modules in this process may be bypassed. For example, the RO system will be used only for water with greater than 4,000 mg/L chlorides. The design for the pilot-scale system is shown in Figure 1.

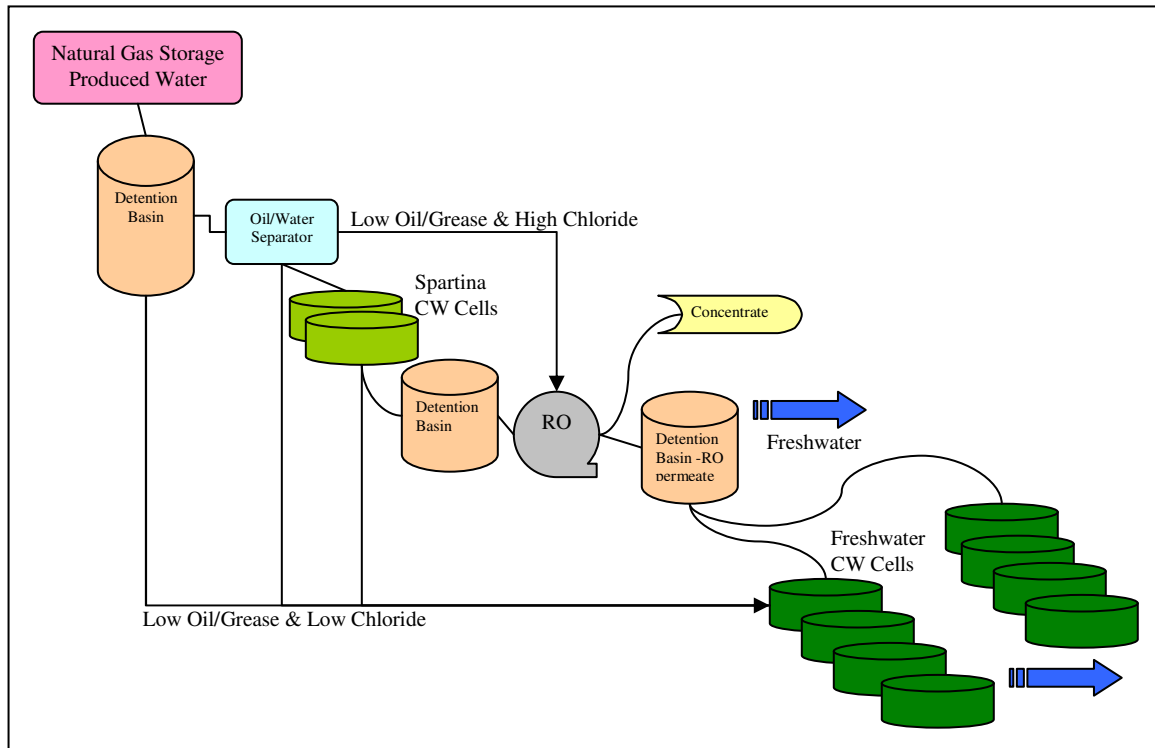


Figure 1. Schematic of the hybrid pilot-scale constructed wetland treatment system for water produced from natural gas storage. CW = constructed wetland; RO = reverse osmosis system.

Task 4 was to evaluate treatment effectiveness and performance of the pilot-scale CWTS. Standard operating procedures (SOPs) for analysis of water samples as well as sampling procedures were developed and confirmed. The first two experiments, Experiment 1 (simulated fresh produced water) and Experiment 2 (simulated brackish produced water), were run through only the freshwater wetland portion of the hybrid CWTS due to their low oil/grease and low chloride concentrations. For Experiment 3 (simulated saline produced water) and Experiment 4 (simulated hyper-saline produced water) it was necessary to run the water through the entire hybrid CWTS due to high oil/grease and high chloride concentrations (>4,000 mg/L chlorides). As water samples were collected, standard operating procedures for their analysis were followed and modified accordingly to optimize results. Task 5 was to confirm design characteristics (hydrosol, hydroperiod, vegetation, sizing, etc.) for a demonstration-scale CWTS. Task 6 involved report preparation and documentation of results for transfer of the technology.

Experimental

Task 1: Characterize Produced Waters

Produced waters were characterized in Task 1 in order to determine realistic composition of water for use in the pilot-scale CWTS. Approximately 4,000 records of produced waters provided by several natural gas storage companies were analyzed using the Statistical Analysis System (SAS Institute, 2002). The results were grouped into four categories of water composition (fresh, brackish, saline, and hyper-saline) using primarily the median and quartiles of chloride concentrations (Table 1). Six targeted constituents are listed in Table 1, which are representative of produced water composition for the purpose of evaluating treatment effectiveness. These constituents were used in Task 4 to formulate simulated waters for treatment in the pilot-scale CWTS. The chemical source of each constituent is also listed in Table 1.

Table 1: Targeted constituents, inflow concentrations, and chemical sources for simulated produced water.

Constituent	Chemical Source	Fresh Target Inflow	Brackish Target Inflow	Saline Target Inflow	Hyper-Saline Target Inflow
		(mg/L)	(mg/L)	(mg/L)	(mg/L)
Cadmium	CdCl ₂	0.02	0.41	0.8	1.21
Copper	CuCl ₂ ·2H ₂ O	0.02	1.68	3.34	5
Lead	PbCl ₂	0.1	5.47	6.84	10.2
Zinc	ZnCl ₂	0.1	23	45.9	69
Oil/Grease	Motor Oil	3	19	49	78
Chlorides	CaCl ₂ , NaCl, MgCl ₂ ·6H ₂ O	<400-2,500	2,500-15,000	15,000-40,000	>40,000

The utilization of simulated waters has many benefits. Simulated waters allow for a complete knowledge of system input, which in turn allows for a better comparison with system output. Simulated waters are also more cost effective for preliminary, pilot-scale experiments. The simulated natural gas storage produced waters are designed to closely replicate the composition of actual waters as shown by statistical analysis of the data and are in agreement with published data (Pope and Pope, 1999; USEPA, 2004; Veil et al., 2004).

Task 2: Obtain Discharge Permits and Develop Treatment Performance Goals

NPDES permits were obtained from a variety of sources including industry and government websites, the United States Environmental Protection Agency (USEPA), and natural gas storage companies. Several USEPA offices were contacted, including those

in Ohio, Pennsylvania, New York, and West Virginia, to obtain sample permits. While these data were gathered, the USEPA released a website (USEPA, 2004), providing easier access to NPDES permits. These NPDES permits were carefully examined and used to create a list of possible constituents of concern and a range of surface discharge limits for the constituents found in produced waters. This information was used to create a model NPDES permit for the project (Table 2). Values included in this table, when shown in the format X-Y, illustrate the range of values found for constituents of concern in various NPDES permits. This model permit delineates viable output or performance goals to apply to the hybrid constructed wetland treatment system for each of the constituents of concern.

Task 3: Design, Construct and Monitor Hybrid Treatment System

The first step of treatment involved storage of the simulated produced water in a 3780 L (1000 gallon) detention basin, allowing time for some solids to settle. From the detention basin the water was pumped by a Fluid Metering, Inc.® (FMI) piston pump to an American Petroleum Institute (API) oil/water separator at a rate of 149 mL/min. For this pilot study, the API oil/water separator was 116.8 cm (46 in) long by 55.9 cm (22 in) wide by 30.4 cm (12 in) deep. The body of the separator was fiberglass with a skimmer and baffle of Plexiglas. The water leaving the oil/water separator entered a pilot-scale saltwater wetland.

The second step utilized two saltwater wetland cells (Figure 1) with quartz sand hydrosol and planted with both tall and short forms of *Spartina alterniflora*. The purpose of these cells was to remove any residual oil and grease from the produced water in order to prevent fouling of the reverse osmosis (RO) membrane. These cells provided an opportunity for retained organics to be oxidized and for precipitation of various metal compounds. The water leaving the pilot-scale saltwater wetland cells drained into a detention basin prior to treatment by the RO system. If the produced water is not saline (i.e. <4,000 mg/L as chlorides), then steps two and three could be omitted.

The third step targeted salt removal through the use of an RO system. The RO system was utilized when Experiment 3 (saline water) and Experiment 4 (hyper-saline water) passed through the CWTS. The primary purpose of the RO system was to decrease chloride concentration and total dissolved solids (TDS) concentrations in saline waters to a tolerable level for the freshwater wetland and aquatic life. This system was run in batches and the post-treatment water was collected in a detention basin before being pumped into the freshwater wetland portion of the treatment system at a rate of 97.2 mL/min.

The pilot-scale freshwater CWTS was designed to remove metals and organic compounds that remain after passing through the API oil/water separator, the saltwater wetland cells, and the RO system. The freshwater system may also be used independently (i.e., bypassing the *Spartina* cells and RO) for treatment of waters with less than 4,000 mg/L chloride concentrations. The freshwater wetland system served as a final clean-up or polishing step. Its primary purpose is to ensure that the post-treatment

Table 2: Model (comprehensive) NPDES Permit for discharge of natural gas storage produced waters.

CONSTITUENT	LIMITS	UNITS	CONSTITUENT	LIMITS	UNITS
PH	6-9	SU	OIL & GREASE	15	mg/L
BOD5(20°C)	29-57	mg/L	CARBON, TOTAL ORGANIC (TOC)	5	mg/L
CBOD5	25	mg/L			
COD	170-292	mg/L	BENZENE	0.06-2.88	µg/L
SOLIDS, TOTAL DISSOLVED	500	mg/L	TOLUENE	0.028-5.0	µg/L
SOLIDS, TOTAL SUSPENDED	30-70	mg/L	ETHYLBENZENE	0.142-5.0	µg/L
ALKALINITY/ACIDITY	alkalinity<acidity		ORTHO-XYLENE	5	µg/L
			XYLENE, META & PARA	0.01-100	µg/L
BARIUM	154	mg/L	BTEX	< 5.0	µg/L
CHLORIDES	5,000	mg/L			
CHLORINE, TOTAL RESIDUAL	0.038	mg/L	NAPHTHALENE	0.2	mg/L
CHROMIUM, TOTAL	0.1-100	µg/L	1,1,1-TRICHLORO-ETHANE	0.05	mg/L
COPPER, TOTAL	0.37-1.0	mg/L	1,2-DICHLOROPROPANE	0.196	µg/L
CYANIDE, TOTAL	0.4	mg/L	ETHYLENE GLYCOL	50	µg/L
FLUORIDE, TOTAL	30	mg/L	PAH	2.8-12.2	mg/L
IRON, TOTAL	0.6-9.4	mg/L			
LEAD, TOTAL	2.6-400	µg/L	TOXICITY	Zero discharge of water containing toxic substances in concentrations that are toxic to human, animal or aquatic life.	
MANGANESE, TOTAL	1-4.4	mg/L			
MERCURY, TOTAL	0.004	mg/L			
NICKEL, TOTAL	2	mg/L			
NITROGEN, AMMONIA TOTAL (AS N)	1.5-6.6	mg/L			
PHOSPHOROUS, TOTAL	1	mg/L			
SULFIDE, TOTAL	0.21-1.0	mg/L			
TIN, TOTAL	50	µg/L			
ZINC, TOTAL	0.4-5.0	mg/L			

Note: Limits are based on New York, Ohio, Pennsylvania, and West Virginia NPDES permits.



Figure 2. Pilot-scale constructed wetland treatment System (CWTS) for water produced from natural gas storage. The smaller photograph shows the system in its early stage of construction. The two trains on the left are the freshwater wetland cells that form the final stage of treatment. The two trains of wetland cells on the right contain *Spartina alterniflora*, which is used for the treatment of saline water. The larger photograph shows the CWTS in June 2005 following the successful establishment and growth of the wetland plants.

water is non-toxic. In the pilot-scale freshwater wetland system, there were two parallel trains consisting of four cells. Each cell was contained within a 121.9 cm (48 in) long by 77.5 cm (30.5 in) wide by 63.5 cm (25 in) deep, 378 L (100 gal) Rubbermaid[®] tub. The four cells in series provided adequate sampling locations and prevent “short circuiting” (water passing through without adequate treatment). The cells were connected by PVC pipe fittings and approximately 30 cm long segments of 3/4” poly-tubing. The PVC pipe fittings were designed to maintain surface flow and were placed 6 cm below the top of each Rubbermaid[®] tub.

Each of the freshwater wetland cells (Figure 2) consisted of three macrofeatures: hydrosol, macrophytes, and a hydroperiod. The first two cells in each train contained reducing hydrosol (sediment collected from 18 Mile Creek, SC, amended with clay and organic materials) and were planted with *Schoenoplectus californicus* C.A. Meyer (California bulrush). The final two cells in each train contained oxidizing hydrosol (quartz sand) and were planted with *Typha latifolia* L. (broadleaf cattail). Each cell contained approximately 140 L (37 gal) of water (not including pore water). By maintaining a flow rate of 97.2 mL/min, the hydroperiod or hydraulic retention time

(HRT) of the CWTS was maintained at 24 hours per cell or 96 hours for the entire freshwater system.

Upon the completion of the design and construction of the hybrid CWTS, monitoring of the CWTS began. Experiment 1, fresh produced water, was run through the freshwater wetland portion of the CWTS for four weeks. Two batches of simulated produced water were needed to run the experiment for this length of time. Water samples were collected progressively throughout the system according to the hydraulic retention time at the onset of the experiment and once in the middle of the experiment (following the mixing of the second batch of water).

Upon the completion of Experiment 1, well-water with a chloride concentration of approximately 2,500 mg/L and containing no oil or metals was run through the freshwater system to allow the plants to acclimate to the level of chlorides characteristic of Experiment 2, simulated brackish produced water. In Experiment 2, two batches of brackish produced water were pumped through the system over the course of four weeks. Based upon the concentrations of constituents found in the simulated produced water, Experiment 2, brackish produced water, was run through only the freshwater wetland portion of the CWTS. Again, samples were collected progressively throughout the system according to the hydraulic retention time at the onset of the experiment, and once in the middle of the experiment (following the mixing of the second batch of water).

To allow the plants in the freshwater system to acclimate to the level of chlorides expected in the permeate from RO in Experiment 3, well-water with a chloride concentration of approximately 1,500 mg/L and containing no oil or metals was run through the freshwater system for one week. Then well-water with no amendments was run through the freshwater system until this module was required for Experiment 3. Experiment 3 utilized the entire hybrid CWTS, including the API oil/water separator and the RO system, due to the concentrations of constituents found in this category of water. Samples were collected progressively throughout the system according to the hydraulic retention time at the onset of the experiment, and once in the middle of the experiment (following the mixing of the second batch of water).

The level of chlorides expected to reach the freshwater system during Experiment 4, simulated hyper-saline produced water, was expected to be similar to that found for Experiment 3. For this reason, well-water with no amendments was run through the freshwater system between Experiment 3 and Experiment 4. Experiment 4 utilized the entire hybrid CWTS; however, for this final experiment, a new oil/water separator was built and used in place of the API oil/water separator from the previous experiment. Samples were collected progressively throughout the system according to the hydraulic retention time at the onset of the experiment, and once in the middle of the experiment (following the mixing of the second batch of water).

Task 4: Evaluate Treatment Effectiveness and Performance of the Pilot-Scale System

As samples were collected throughout the experiments, the treatment effectiveness and performance were evaluated. Samples were analyzed for the parameters listed in Table 3 according to the associated standard operating procedures.

Table 3: Analytical methods for parameters monitored from the pilot hybrid constructed wetland treatment system.

Parameter	Method	Method Detection Limit
Temperature	Direct Instrumentation: YSI Model 52	0.5°C
pH	Direct Instrumentation: Orion Model 420A	0.01
Conductivity	Direct Instrumentation: YSI 30	0.1 µS/cm
Alkalinity	Standard Methods: 2320 B	2 mg/L as CaCO ₃
Hardness	Standard Methods: 2340 C	2 mg/L as CaCO ₃
DO ¹	Direct Instrumentation: YSI Model 52	0.1 mg/L
COD ²	Closed reflux colorimetry (HACH- modified from Standard Methods: 5220 D)	3 mg/L
BOD ³	Standard Methods: 5210 B	0.1 mg/L
Chloride	High: HACH Drop Count Titration Method	500 mg/L
	Low: HACH colorimetric method 8207	25 mg/L
Sulfate	Standard Methods: 4500 E	1 mg/L
Metals	Atomic Absorption Spectrometry (AA)	Cd-0.002 mg/L Cu-0.010 mg/L Pb-0.050 mg/L Zn-0.005 mg/L
	Inductively Coupled Plasma-Atomic Emissions Spectrometry (ICP-AES): USEPA 200.8	Cd-0.010 mg/L Cu-0.010 mg/L Pb-0.015 mg/L Zn-0.010 mg/L
TDS ⁴	Standard Methods: 2540 C	0.1 mg/L
TSS ⁵	Standard Methods: 2540 D	0.1 mg/L
Oil and Grease	Flourometer	1.0 mg/L
Bulk Redox	Standard Voltmeter, Accumet® calomel reference electrode, and <i>in situ</i> platinum-tipped electrodes (Faulkner et al., 1989).	±10mV

¹ Dissolved Oxygen

² Chemical Oxygen Demand

³ Biological Oxygen Demand

⁴ Total Dissolved Solids

⁵ Total Suspended Solid

Task 5: Confirm Design Characteristics

Upon completion of Experiment 1 and Experiment 2 excessive separation of oil was observed in the detention basin. For the remaining experiments, the waters were continuously mixed with a submersible pump in the initial detention basin. This reduced the settling of solids and the separation of the oil fraction, allowing a more representative sample to be pumped into the CWTS.

After Experiment 3, it was noted that a more effective oil/water separator was needed. The new model is approximately 122 cm (48 in) long by 61 cm (24 in) wide by 40.6 cm (16 in) deep. It incorporates some of the same baffle concepts as the initial oil/water separator but also utilizes dissolved air flotation, turbulence reduction, and filtering to separate the oil from the water.

Upon completion of Experiments 1 through 4, a second simulated brackish water was processed through the system. Experiment 1 showed no toxicity in inflow or outflow, and Experiment 2 showed toxicity in both the inflow and outflow. Thus a water with concentrations set at the minimum NPDES permit limits for the constituents of concern (Tables 1 and 2) was needed to assess the capabilities of the freshwater wetland module. This water was called Simulated Brackish Water II.

Results and Discussion

Task 1: Characterize Produced Waters

The composition of produced waters associated with natural gas production and storage varies greatly depending upon the geologic formation from which it originates, the extraction method utilized in the natural gas production process, and the treatment chemicals selected for the process. Data provided by several gas storage facilities show wide ranges of values for many produced water constituents. Chloride concentrations and total solids show the largest range in values from non-detect to 384,000 mg/L and non-detect to 494,000 mg/L, respectively. In order to characterize the produced waters, they were divided into four general categories based upon statistical analysis:

- 1.) fresh - low chloride concentrations (≤ 400 -2,500 mg/L),
- 2.) brackish - medium chloride concentrations (2,500-15,000 mg/L),
- 3.) saline - high chloride concentrations (15,000-40,000 mg/L), and
- 4.) hyper-saline - extremely high chloride concentrations ($\geq 40,000$ mg/L).

Separate experiments conducted in Task 4, using simulated produced water, are defined by each of these four categories.

Chlorides play a major role in the character of produced water. Based on data provided by several major gas storage companies, it was determined that chlorides in produced waters are composed primarily of 47% sodium chloride (NaCl), 47% calcium chloride (CaCl₂), and 6% magnesium chloride (MgCl₂).

Based on statistical analysis and literature review, a large variety of metals may be present in produced waters (USEPA, 2000; Veil et al., 2004). Many of these metals are present in concentrations that are toxic to receiving system biota. This toxicity consequently leads to failure to meet NPDES permit limits. It is not feasible to study in great depth every metal present in produced waters. Due to time and cost, four metals, cadmium (Cd), copper (Cu), lead (Pb), and zinc (Zn), were chosen based on their presence in produced waters, toxicity to receiving system biota, and cost of experimentation.

In order to create the simulated produced waters, it was necessary to define the inflow concentrations of Cd, Cu, Pb and Zn. For the first (fresh) simulated produced water, the range of each metal concentration typically found in produced waters was examined and then compared to the risk-based concentration. The targeted inflow metal concentrations were chosen primarily based upon the risk to *Ceriodaphnia dubia* in 7-day toxicity experiments, which is referred to as the lowest observable effect concentration (LOEC), in the USEPA's ECOTOX database (USEPA, 2002). Metal concentrations for the other three experiments were determined by the published values for each metal. Simulated hyper-saline produced water was determined by the maximum published values, simulated saline water metal concentrations were determined by the 75th percentile, and simulated brackish water metal concentrations by the median. The goal was to test for the lowest effluent concentration that can be achieved by the system below the NPDES permitted level for the widest range of Cd, Cu, Pb, and Zn concentrations.

Task 2: Obtain Discharge Permits and Develop Treatment Performance Goals

A model NPDES permit (Table 2) was created from approximately fifty NPDES permits that were issued by Ohio, Pennsylvania, New York, and West Virginia. The tabulated permits were issued for various oil and gas industrial purposes including oil field services, natural gas transmission, petroleum refining, oil and gas general permitting, and industrial wastewater pollution control. These permits were utilized to create an initial list of constituents of concern and to provide an objective treatment output concentration for each constituent. The comprehensive model permit served as a means of measuring the success of the hybrid constructed wetland treatment system to effectively remove the constituents of concern. If the discharge from the system failed to meet the standards outlined in the model permit, necessary adjustments were made to fine tune the system until it was capable of meeting these requirements.

Task 3: Design, Construct and Monitor Hybrid Treatment System

The major components of the design plan included a detention basin, an API oil/water separator, two saltwater wetland cells, an RO system or nanofiltration unit, and two trains of four freshwater wetland cells each. The first two of the four freshwater wetland cells contained hydrosol that created a bulk reducing environment which promoted the removal of metals and sulfates by the following processes: precipitation of metals, sorption, plant uptake, and biodegradation (Table 4). In order to create a reducing

environment, the hydrosol must possess a sediment oxygen demand greater than the rate at which oxygen is supplied to the system. This can be accomplished by using a hydrosol with high clay content and a relatively high amount of labile organic matter. When hydrosol of this type is combined with plants that do not greatly oxygenate the rhizosphere, a reducing environment capable of the aforementioned removal processes can be established. The final two freshwater wetland cells contained hydrosol that created a bulk oxidizing environment which promoted the removal of water soluble organics and metals through oxidative processes including biodegradation, sorption, plant uptake, and precipitation (Table 4). A bulk oxidizing environment is accomplished through hydrosol with high sand content and little to no organic matter combined with plants that have high radial oxygen loss in the rhizosphere.

Due to the detrimental effects of high chloride concentrations on the growth and survival of the freshwater plants chosen for the CWTS, an RO system was included in the design for any produced water containing chloride concentrations greater than 4,000 mg/L. RO systems are capable of removing chlorides, TDS, and many other constituents; however, RO membranes are sensitive to oil and grease. In order to extend the life of the RO membrane (prevent membrane fouling and subsequent failure of the RO system), two saltwater wetland cells were added to the system as a method of pretreatment to the RO system. These cells were planted with *Spartina alterniflora*, a saltwater macrophyte, as a means of ensuring the removal of residual oil and grease that may not have been adequately removed by the API oil/water separator. These saltwater cells also provided additional benefits, such as an environment conducive to the precipitation of various metal compounds.

Table 4: Stages and processes of the hybrid constructed wetland treatment system

	Stage of Treatment		Processes		Constituents Removed
	Detention Basin	→	Settling, Precipitation	→	Solids
	Oil/Water Separator	→	Gravity/Density Settling	→	Solids & Oil
	Spartina Cells (Oxidizing)	→	Sorption, Biodegradation, Sedimentation, Precipitation	→	Oil & Grease, Water Soluble Organics
	Detention Basin	→	Settling, Precipitation	→	Solids
	RO System	→	Membrane – Reverse Osmosis	→	TDS: Chlorides, Hardness, Salts, Metals, & Sulfates
	Detention Basin	→	Settling, Precipitation	→	Solids
	Schoenoplectus Cells (Reducing)	→	Precipitation, Sorption, Plant Uptake, Biodegradation	→	Metals
	Typha Cells (Oxidizing)	→	Precipitation, Sorption, Plant Uptake, Biodegradation	→	Water Soluble Organics, Metals

Task 4: Evaluate Treatment Effectiveness and Performance of the Pilot-Scale System

Analytical methods to complete Task 4 were chosen (Table 3), standard operating procedures were written for each method, and a sampling plan was written prior to initiation of the experiments to ensure adequate and representative sampling and analysis.

The system was loaded according to the concentrations outlined in Table 1 for each experiment. The salts and metals were weighed in the laboratory. The specific gravity of the Shell™ Rotella T™ Multigrade SAE 15W-40 oil was found to be approximately 0.87 g/mL as determined by weighing a 50 mL volume on a laboratory balance. From this specific gravity, the appropriate concentration of oil and grease for each batch of water was measured by volume. The constituents were added to 1000 gallons of well-water for each batch. The water was mixed for 24 hours using a submersible pump to allow the salts to dissolve and organics to partition into the water. Following mixing, the simulated produced waters for Experiments 1 and 2 were given 24 hours to settle, before being pumped into the treatment system. It was assumed that by allowing time to settle, the simulated produced water would be more representative of actual produced water. For Experiment 3 and Experiment 4, the simulated produced waters were mixed continuously to prevent separation of oil from water in the initial detention basin.

In Experiments 1 (simulated fresh water) and 2 (simulated brackish water), the freshwater wetland system was the primary component utilized for treatment of produced water (PW). The water was pumped directly from the 1000 gal detention basin into each of the two freshwater wetland trains at a rate of 97.2 mL/min, in order to maintain a 24 hr hydraulic retention time for each wetland cell.

These freshwater wetlands are capable of processing a maximum of 4,000 mg/L chlorides due to the sensitivity of the macrophytes to chlorides. NPDES permits require chloride concentrations to be below 5,000 mg/L. Since the chloride concentrations in Experiment 1, fresh produced water (400 mg/L chlorides), and Experiment 2, brackish produced water (2,500 mg/L chlorides), are both below this limit, it was not necessary to send these waters through all the stages of the hybrid constructed wetland system. By bypassing the oil/water separator, the two saltwater wetland cells, and the RO system in cases where the chloride concentrations are relatively low, both time and money can be saved.



Figure 3: Reverse Osmosis System.

Experiment 3, saline produced water (15,000 mg/L chlorides), and Experiment 4, hyper-saline produced water (40,000 mg/L chlorides), used the entire hybrid CWTS. The water was pumped from the initial 1000 gal detention basin into the oil/water separator at a rate of 149 mL/min to maintain a 24 hour hydraulic retention time for each of the saltwater cells and a 22 hour hydraulic retention time for the oil/water separator. From the second saltwater cell (Spartina 2), the water was collected in a 550 gallon detention basin. From this first 550 gallon detention basin,

the water progressed through an RO system (Figure 3). Permeate from the RO system was collected in a second 550 gallon detention basin, while the concentrate was collected and treated separately. Permeate collected in the second 550 gallon detention basin became the inflow to the freshwater wetlands, being pumped into each of the two freshwater wetland trains at a rate of 97.2 mL/min, in order to maintain a 24 hr hydraulic retention time for each cell.

All of the metal analyses were conducted at Clemson University. Cadmium, copper and lead for Experiments 1 and 2 were analyzed by Atomic Absorption Spectrometry (AA-5100, Perkin-Elmer Corporation). For Experiments 1 and 2, zinc was analyzed by Inductively Coupled Plasma-Atomic Emission Spectrometry (ICP-AES, Spectro Flame Modula EOP, Spectro Analytical Inc.). All four metals for Experiment 3 and Experiment 4 were analyzed by Inductively Coupled Plasma-Atomic Emission Spectrometry (ICP-AES, Spectro Flame Modula EOP, Spectro Analytical Inc.).

Experiment 1: Simulated Freshwater

Metals

For Experiment 1, metal concentrations were loaded at approximately 0.02 mg/L Cd, 0.02 mg/L Cu, 0.1 mg/L Pb, and 0.1 mg/L Zn. Both Cu and Pb concentrations were below current detection limits of the AA utilized for analysis. The results for Cd are shown in Figure 4, and the results for Zn are shown in Figure 5.

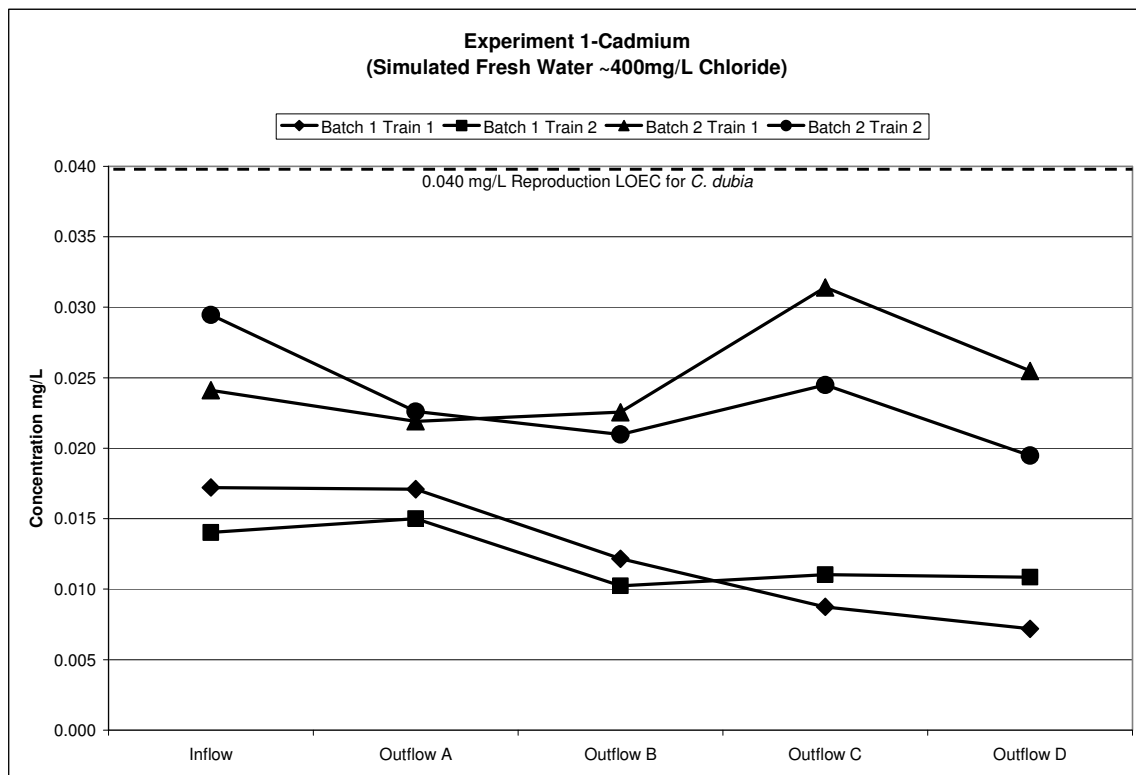


Figure 4. Experiment 1: Simulated freshwater metal analysis for cadmium performed by AA.

Cadmium was not found in any of the NPDES permits for the pertinent EPA regions; however, cadmium is found in produced waters at high concentrations and therefore is regulated by the NPDES permit limit that calls for zero toxicity. For this reason, the lowest observable effect concentration (LOEC) for reproduction of *C. dubia* was utilized as a target outflow concentration (USEPA, 2002). The inflow vs. final outflow concentrations for Batch 1: Train 1 and Train 2 were 0.017/0.007 mg/L and 0.014/0.011 mg/L respectively. For Batch 2: Train 1 and Train 2, the inflow vs. final outflow concentrations were 0.024/0.026 mg/L and 0.030/0.020 mg/L respectively. As shown in Figure 4, all Cd inflow and outflow concentrations for Experiment 1 fell below the target outflow limit.

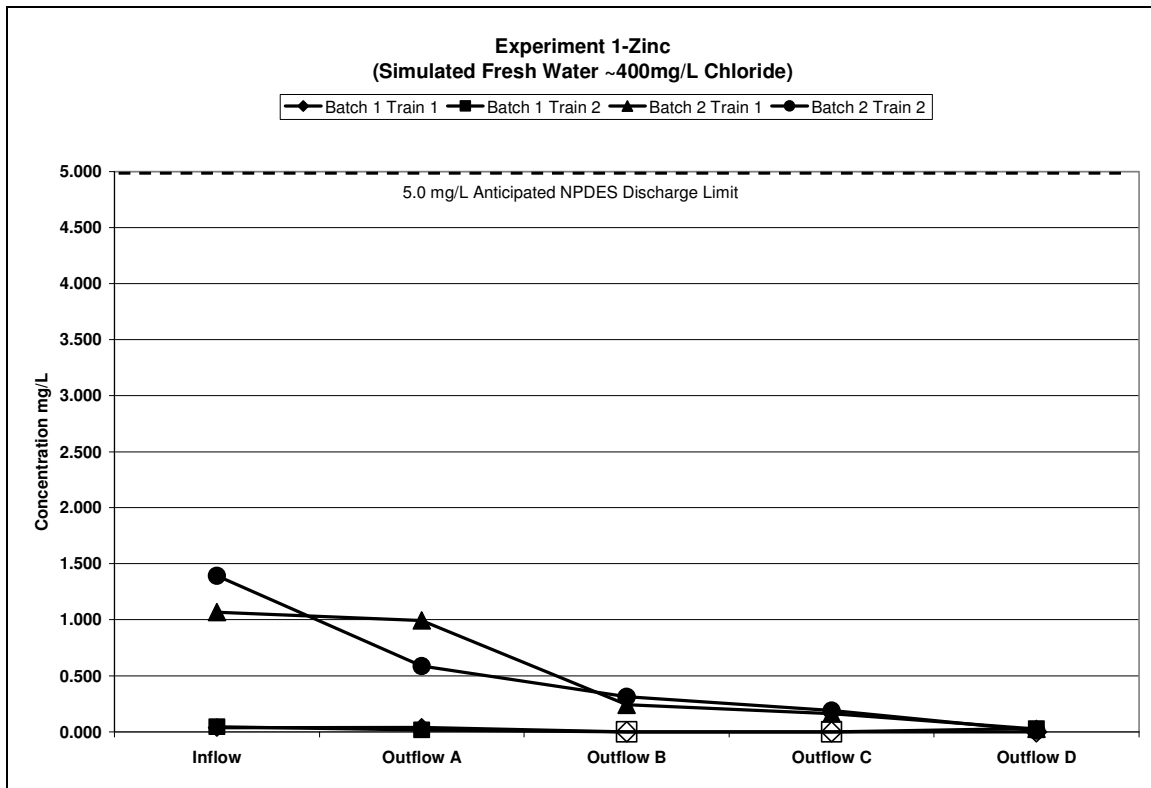


Figure 5. Experiment 1: Simulated freshwater metal analysis for zinc performed by ICP.

Zinc was loaded at a concentration of approximately 0.1 mg/L. The open symbols in Figure 5 indicate outflow values that were below the current detection limit of 10 µg/L. The inflow concentration of Batch 2 increased by an order of magnitude due to a calculation error. However, this error did not prove to have a significant effect on the final outflow concentration. The inflow vs. final outflow concentrations for Batch 1: Train 1 and Train 2 were 0.035 mg/L/non-detect and 0.044/0.029 mg/L respectively. For Batch 2: Train 1 and Train 2, they were 1.070/0.025 mg/L and 1.390/0.011 mg/L respectively. As shown in Figure 5, all inflow and outflow Zn concentrations for Experiment 1 fell below the anticipated NPDES limit. The “Anticipated NPDES Discharge Limit” is the outflow goal defined by the model NPDES permit (Task 2: Table 2).

Toxicity

For Experiment 1, 7-day toxicity tests were performed with *C. dubia* on inflow and final outflow waters from each batch and train. There was no significant difference between the controls and the inflow for mortality or reproduction. There was a significant increase in reproduction of *C. dubia* in the outflow of both trains when compared to the inflow and control results. Waters from Experiment 1 were not toxic to *C. dubia*.

Experiment 2: Simulated Brackish Water

Metals

For Experiment 2, metal concentrations were loaded at approximately 0.41 mg/L Cd, 1.68 mg/L Cu, 5.47 mg/L Pb, and 23 mg/L Zn.

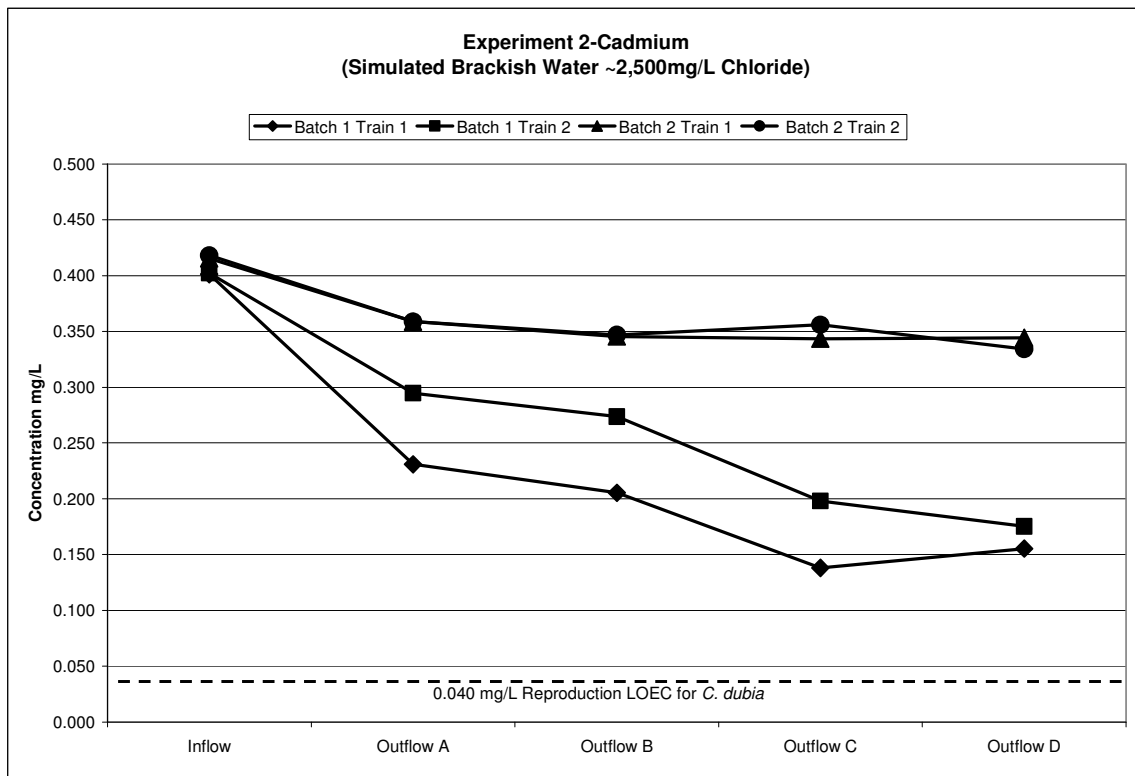


Figure 6. Experiment 2: Simulated brackish water metal analysis for cadmium performed by AA.

The inflow vs. final outflow cadmium concentrations for Batch 1: Train 1 and Train 2 were 0.401/0.155 mg/L and 0.402/0.175 mg/L. For Batch 2: Train 1 and Train 2, they were 0.415/0.344 mg/L and 0.418/0.334 mg/L respectively. As shown in Figure 6, all outflow Cd concentrations for Experiment 2 were greater than the target outflow limit. This indicates that further adjustments need to be made to the system in order to optimize it for the removal of Cd.

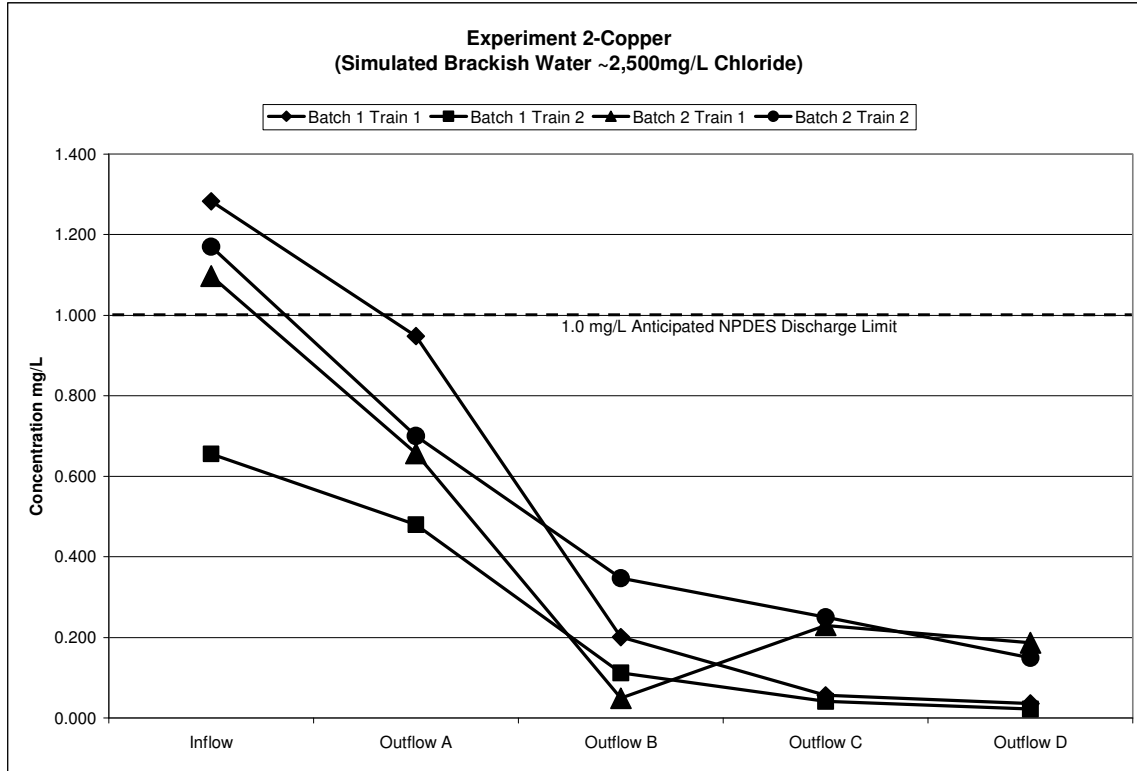


Figure 7. Experiment 2: Simulated brackish water metal analysis for copper performed by AA.

The NPDES permits for the regions examined provided a NPDES discharge limit of 1.0 mg/L for Cu. Two of the data points for Batch 1: Train 2 were lost due to a computer error during original analysis and were performed later on the ICP-AES. The inflow vs. final outflow concentrations for Batch 1: Train 1 and Train 2 were 1.283/0.036 mg/L and 0.656/0.022 mg/L. For Batch 2: Train 1 and Train 2, inflow vs. outflow concentrations were 1.097/0.187 mg/L and 1.170/0.149 mg/L respectively. As shown in Figure 7, all outflow Cu concentrations for Experiment 2 fell below the anticipated NPDES limit.

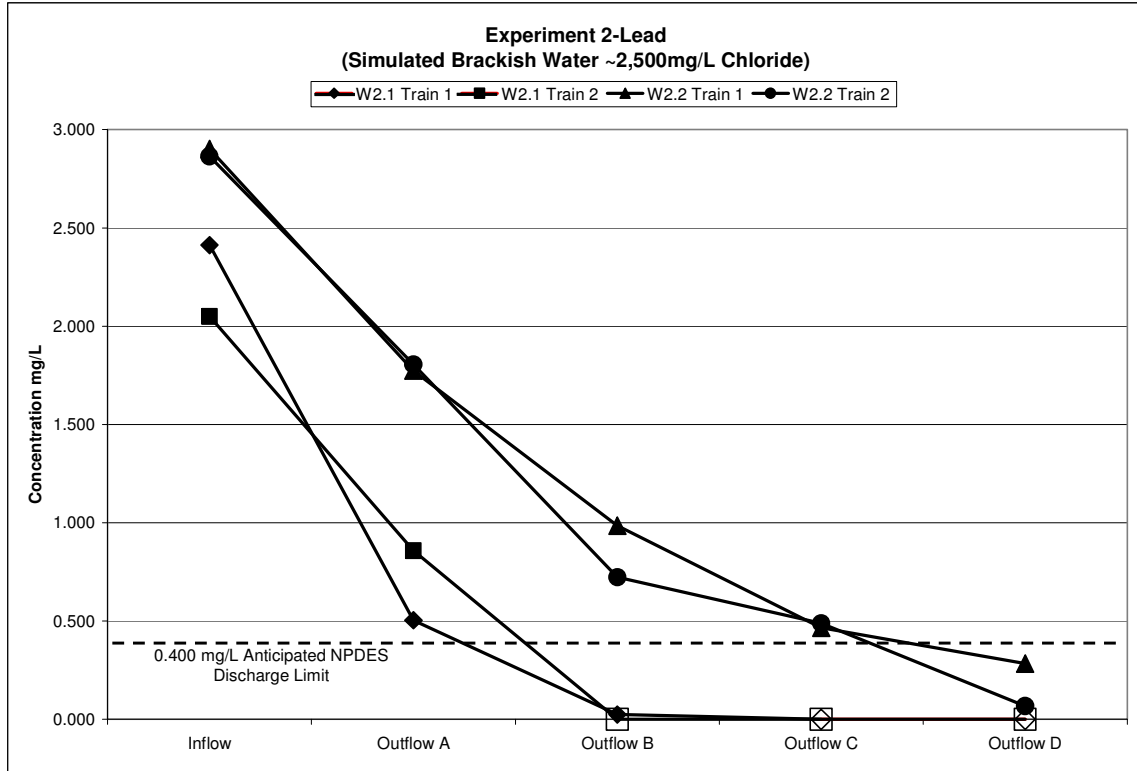


Figure 8. Experiment 2: Simulated brackish water metal analysis for lead performed by AA.

The NPDES permits for the regions examined provided a NPDES discharge limit of 0.400 mg/L for Pb. The open symbols in Figure 8 indicate values that were below the detection limit of the instrument used. The inflow vs. final outflow concentrations for Batch 1: Train 1 and Train 2 were 2.413/non-detect mg/L and 2.049/non-detect mg/L. For Batch 2: Train 1 and Train 2, they were 2.901/0.284 mg/L and 2.864/0.068 mg/L respectively. As shown in Figure 8, all outflow Pb concentrations for Experiment 2 fell below the anticipated NPDES limit.

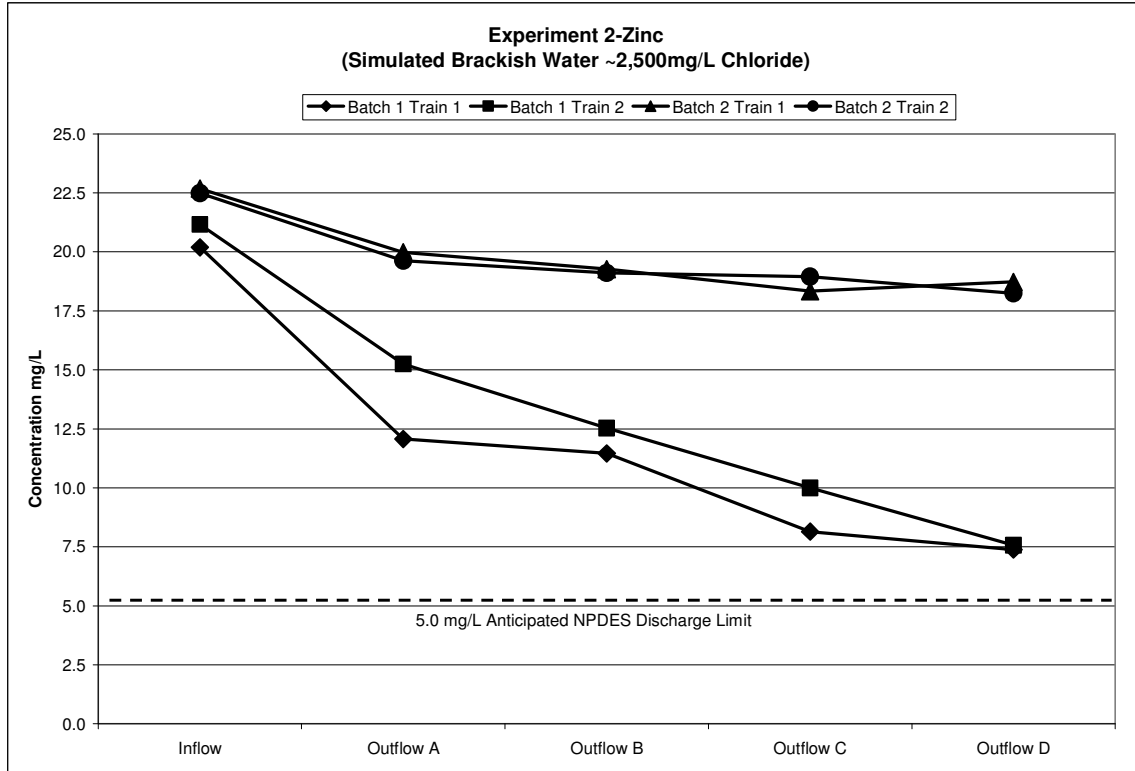


Figure 9. Experiment 2: Simulated brackish water metal analysis for zinc performed by ICP.

The NPDES permits for the regions examined provided a NPDES discharge limit of 5.0 mg/L for Zn. The inflow vs. final outflow concentrations for Batch 1: Train 1 and Train 2 were 20.19/7.39 mg/L and 21.16/7.57 mg/L. For Batch 2: Train 1 and Train 2, they were 22.68/18.73 mg/L and 22.49/18.25 mg/L respectively. As shown in Figure 9, all outflow Zn concentrations for Experiment 2 were greater than the anticipated NPDES limit. This indicates that further adjustments need to be made to the system in order to optimize it for the removal of Zn.

Toxicity

In Experiment 2, 7-day toxicity tests utilizing *C. dubia* were performed only on the waters from Batch 1 because of time constraints. Experiment 2: Batch 1 showed total mortality after 24 hours in 100%, 50%, and 5% final outflow water. From these preliminary screening tests, two full tests were run at 2.5% and 1.2% water for mortality and reproduction effects data, respectively. At the 2.5% dilution there was full mortality for the inflows to both trains, while there was no significant effect on mortality in the outflows from either of the two trains. At the 1.2% Dilution Train 1 shows significantly lower reproduction of *C. dubia* than the control in both inflow and outflow, while Train 2 shows significantly lower reproduction of *C. dubia* in the inflow but no significant difference between the control and the outflow.

Experiment 3: Simulated Saline Water

Metals

For Experiment 3, metals were loaded at concentrations of approximately 0.8 mg/L Cd, 3.34 mg/L Cu, 6.84 mg/L Pb, and 45.9 mg/L Zn.

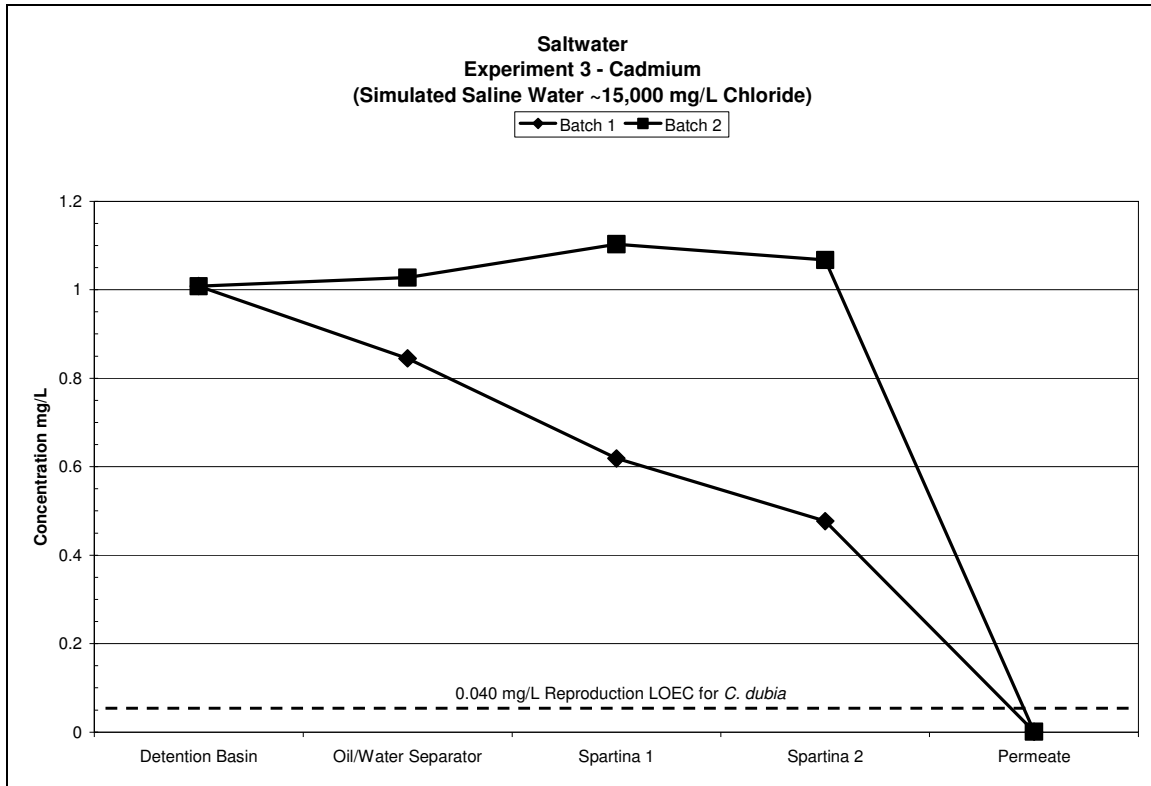


Figure 10. Saltwater module and RO permeate results for Experiment 3: Simulated saline water metal analysis of cadmium performed by ICP. The saltwater module is that portion of the hybrid constructed wetland treatment system occurring before the RO system (i.e., all points except “permeate”). The RO permeate is the outflow water from the RO system that is then pumped into the two freshwater wetland trains. For each batch of water in the above graph, the RO permeate concentration is the average of the inflow concentrations for each of the two freshwater wetland trains.

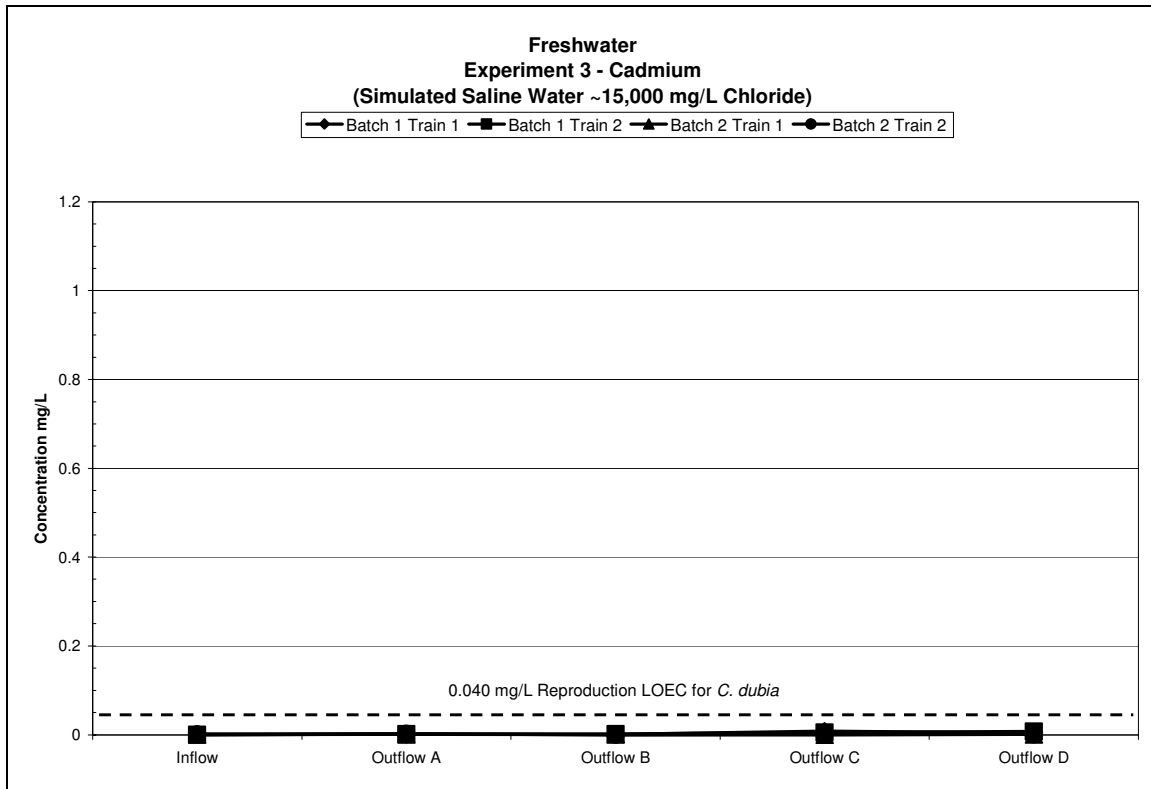


Figure 11. Freshwater module (post-RO system) results for Experiment 3: Simulated saline water metal analysis of cadmium performed by ICP.

The inflow cadmium concentrations to the entire hybrid CWTS were 1.008 mg/L and 1.0076 mg/L for Batch 1 and Batch 2, respectively, of the simulated saline produced water. As shown in Figure 10, the Cd concentrations decreased as the water flowed through the saltwater portion of the hybrid CWTS and the RO system took the concentrations below the target outflow limit. The inflow vs. final outflow concentrations for Batch 1: Train 1 and Train 2 of the freshwater system were 0.0017/0.0041 mg/L and 0.0001/0.0072 mg/L. For Batch 2: Train 1 and Train 2, they were 0.0004/ 0.0010 mg/L and 0.0011/0.0020 mg/L, respectively. As shown in Figure 11, the inflow water to each freshwater wetland train had low concentrations of Cd due to removal by the RO system. The inflow water to the freshwater system was below the target outflow limit based on the LOEC for reproduction of *C. dubia*. As the water flowed through the freshwater system, it remained below the target outflow limit.

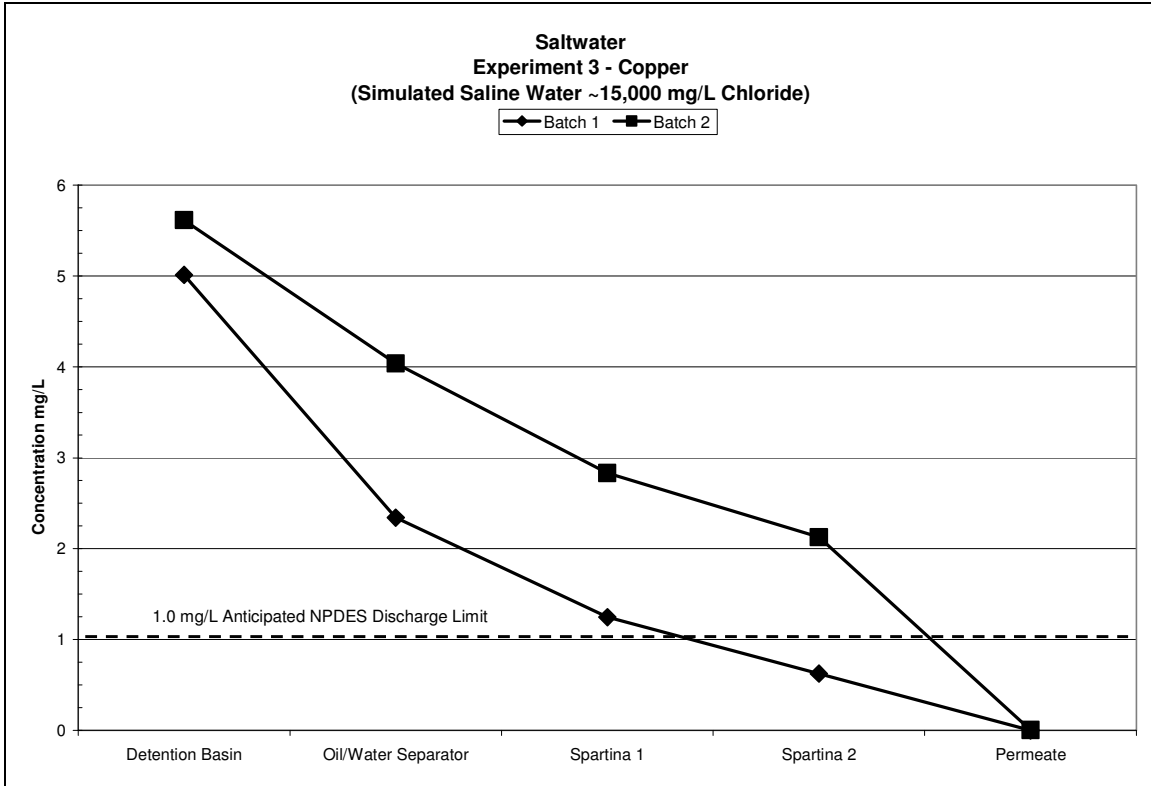


Figure 12. Saltwater module and RO permeate results for Experiment 3: Simulated saline water metal analysis of copper performed by ICP. The saltwater module is that portion of the hybrid constructed wetland treatment system occurring before the RO system (i.e., all points except “permeate”). The RO permeate is the outflow water from the RO system that is then pumped into the two freshwater wetland trains. For each batch of water in the above graph, the RO permeate concentration is the average of the inflow concentrations for each of the two freshwater wetland trains.

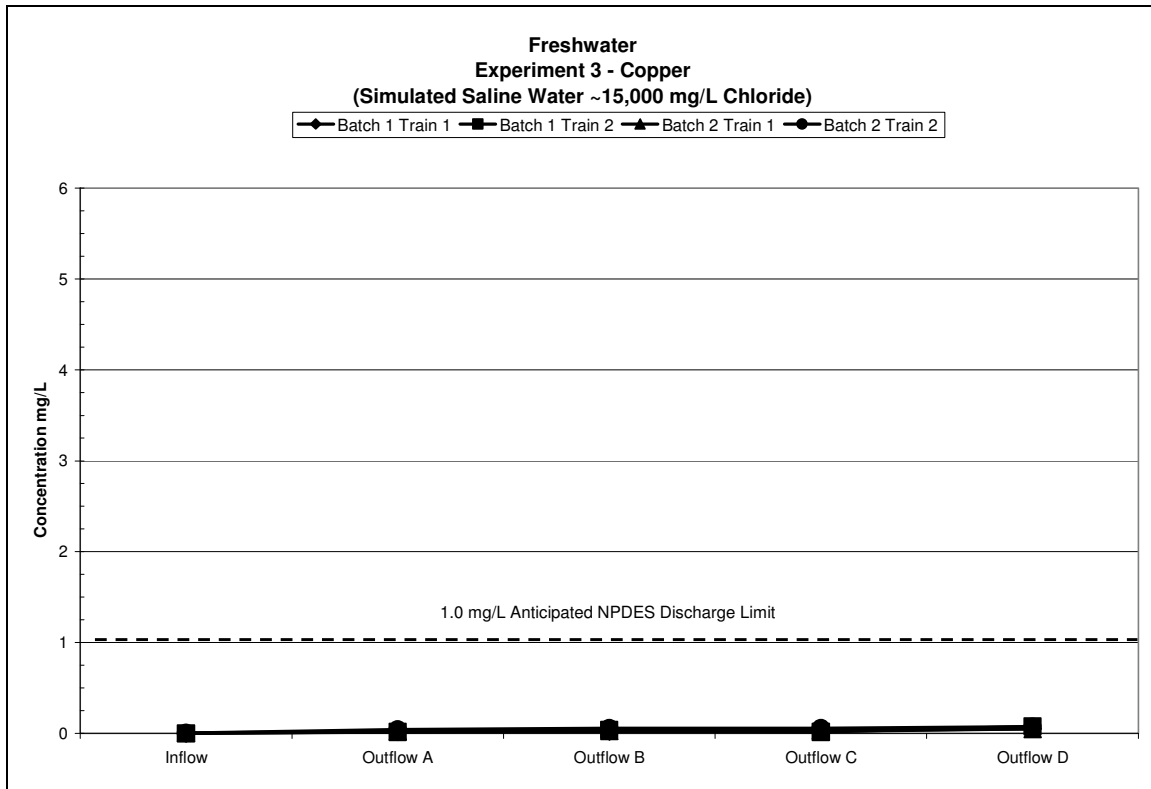


Figure 13. Freshwater module (post-RO system) results for Experiment 3: Simulated saline water metal analysis of copper performed by ICP.

The NPDES permits for the regions examined provided a NPDES discharge limit of 1.0 mg/L for Cu. The inflow concentrations to the entire hybrid constructed wetland system were 5.012 mg/L and 5.616 mg/L for Batch 1 and Batch 2 respectively. As shown in Figure 12, the Cu concentrations decreased as the water flowed through the saltwater portion of the hybrid CWTS, and the RO system took the concentrations below the target outflow limit set by the model NPDES permit. The inflow vs. final outflow concentrations for Batch 1: Train 1 and Train 2 of the freshwater system were 0.0005/0.0512 mg/L and 0.0009/0.0779 mg/L. For Batch 2: Train 1 and Train 2, they were 0.0050/0.0478 mg/L and 0.0050/0.0732 mg/L, respectively. As shown in Figure 13, all water samples for both batches of water collected after the RO system, the permeate (outflow from the RO system) through the outflow from Trains 1 and 2, met the NPDES discharge limit of 1.0 mg/L for copper.

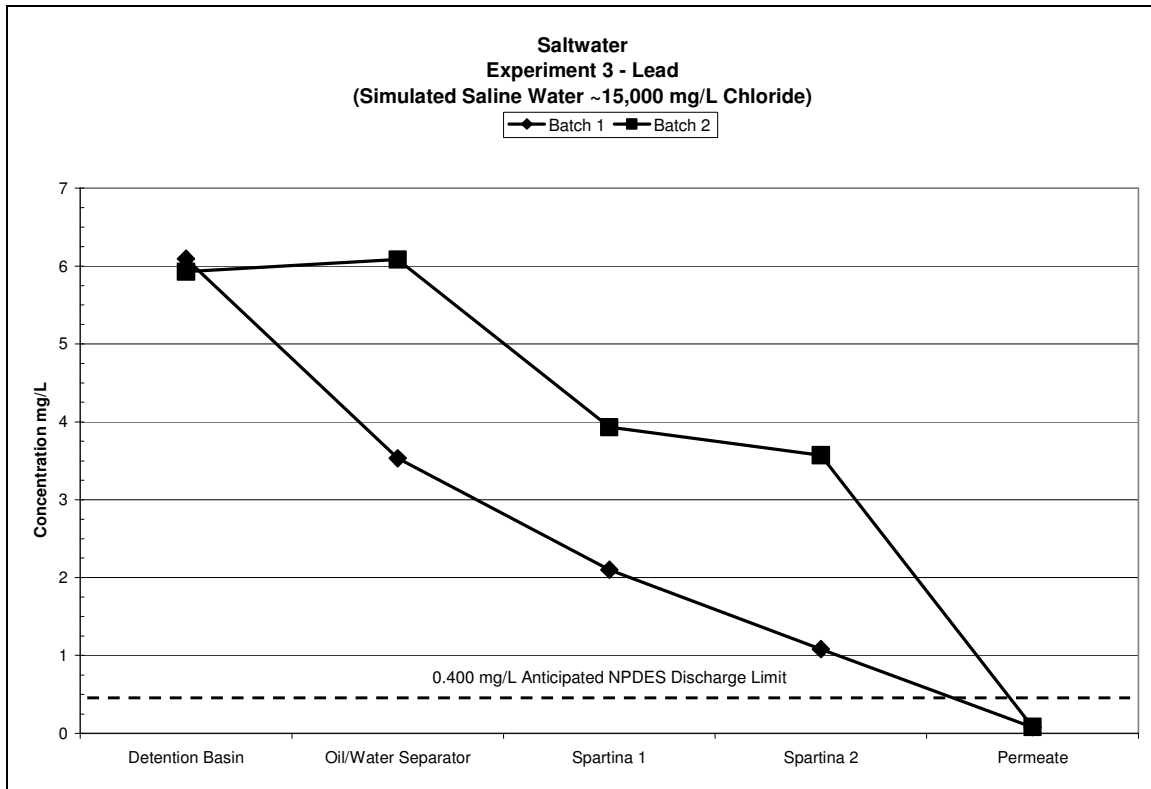


Figure 14. Saltwater module and RO permeate results for Experiment 3: Simulated saline water metal analysis of lead performed by ICP. The saltwater module is that portion of the hybrid constructed wetland treatment system occurring before the RO system (i.e., all points except “permeate”). The RO permeate is the outflow water from the RO system that is then pumped into the two freshwater wetland trains. For each batch of water in the above graph, the RO permeate concentration is the average of the inflow concentrations for each of the two freshwater wetland trains.

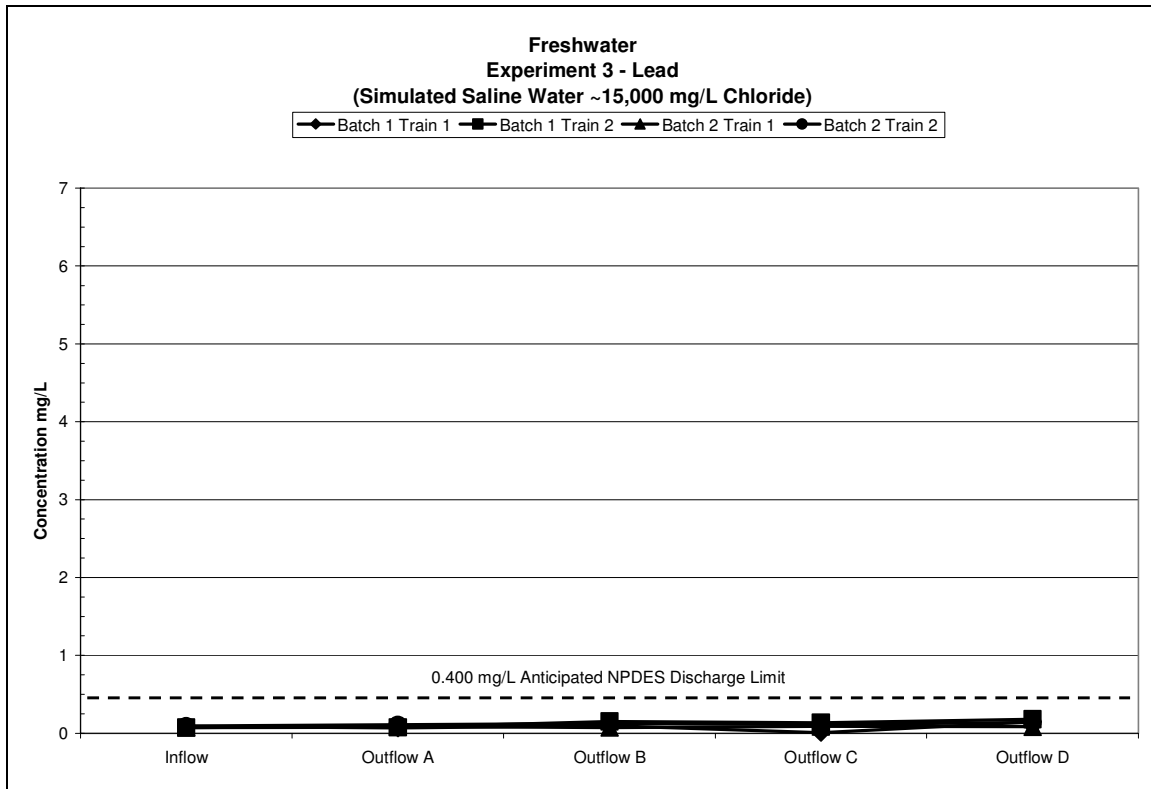


Figure 15. Freshwater module (post-RO system) results for Experiment 3: Simulated saline water metal analysis of lead performed by ICP.

The NPDES permits for the regions examined provided a NPDES discharge limit of 0.400 mg/L for Pb. The inflow concentrations to the entire hybrid constructed wetland system were 6.096 mg/L and 5.928 mg/L for Batch 1 and Batch 2, respectively. As shown in Figure 14, the Pb concentrations decreased as the water flowed through the saltwater portion of the hybrid CWTS and the RO system took the concentrations below the target outflow limit set by the model NPDES permit. The inflow vs. final outflows for Batch 1: Train 1 and Train 2 of the freshwater system were 0.0870/0.1455 mg/L and 0.0737/0.1795 mg/L. For Batch 2: Train 1 and Train 2, they were 0.0724/0.0821 mg/L and 0.0919/0.1365 mg/L, respectively. As shown in Figure 15, all water samples for both batches of water collected after the RO system, the permeate (outflow from the RO system) through the outflow from trains 1 and 2 met the NPDES discharge limit of 0.400 mg/L for lead.

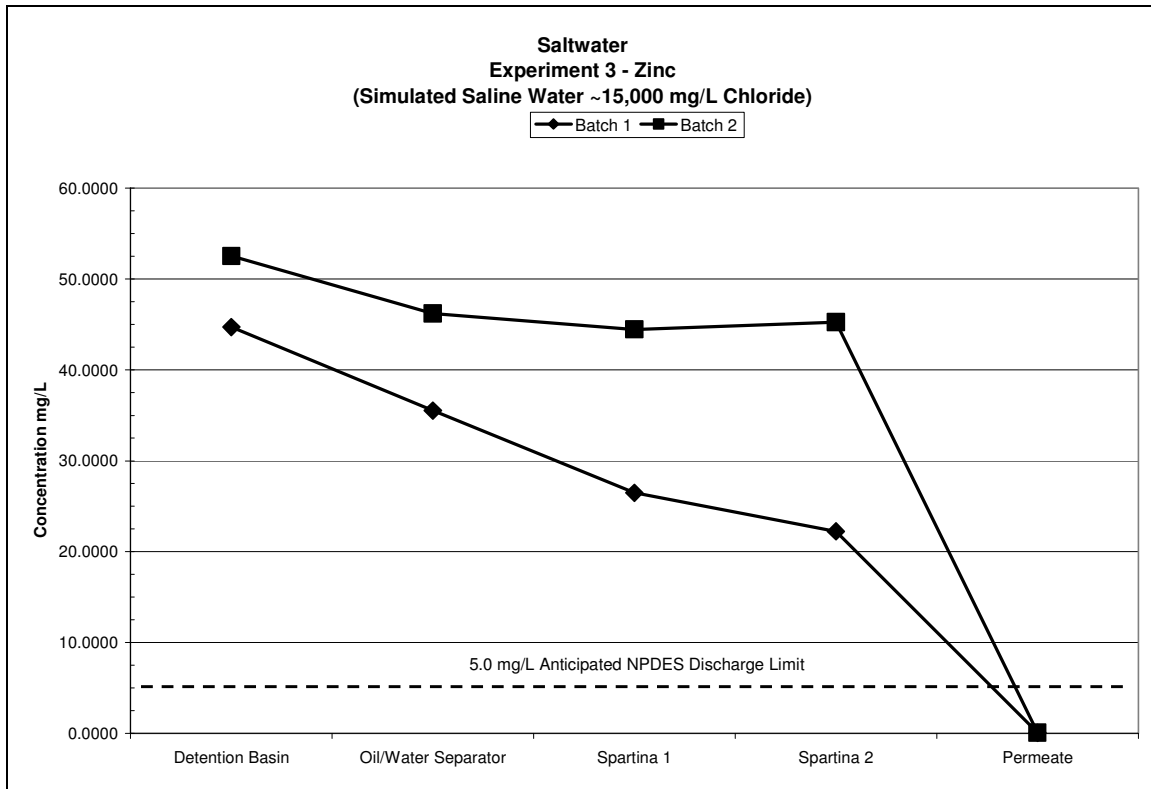


Figure 16. Saltwater module and RO permeate results for Experiment 3: Simulated saline water metal analysis of zinc performed by ICP. The saltwater module is that portion of the hybrid constructed wetland treatment system occurring before the RO system (i.e., all points except “permeate”). The RO permeate is the outflow water from the RO system that is then pumped into the two freshwater wetland trains. For each batch of water in the above graph, the RO permeate concentration is the average of the inflow concentrations for each of the two freshwater wetland trains.

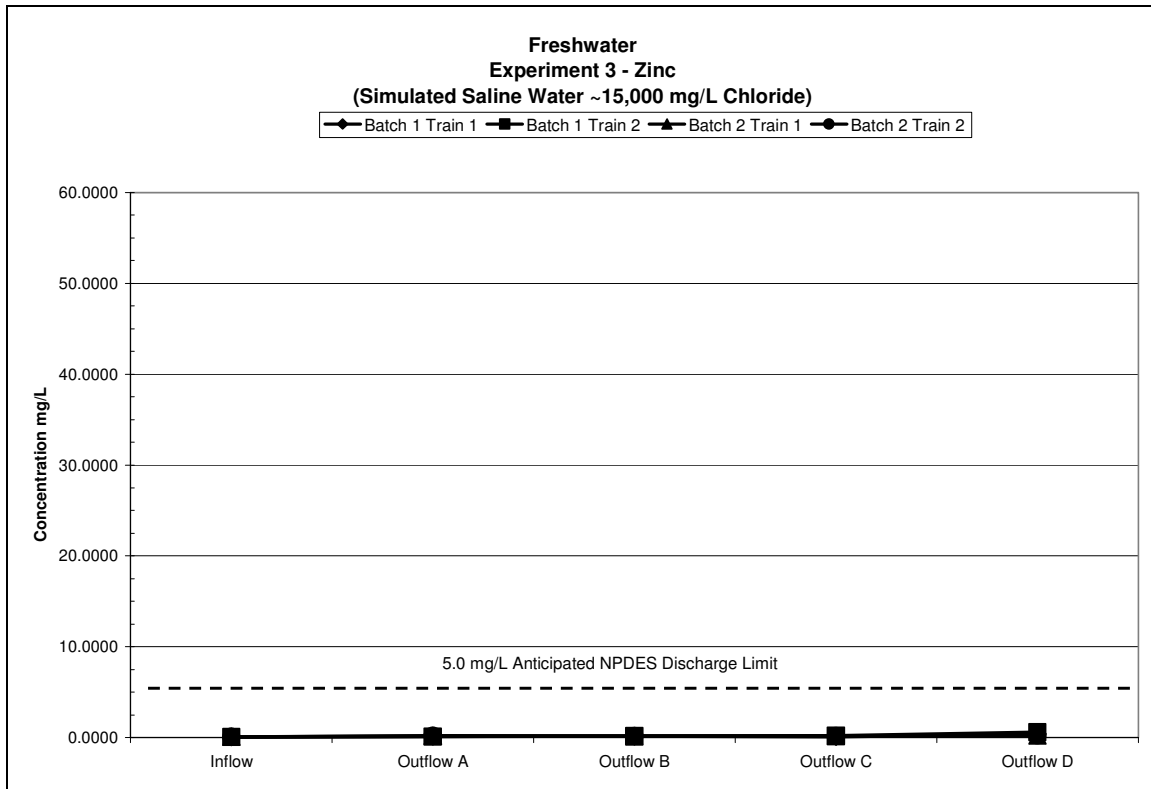


Figure 17. Freshwater module (post-RO system) results for Experiment 3: Simulated saline water metal analysis of zinc performed by ICP.

The NPDES permits for the regions examined provided a NPDES discharge limit of 5.0 mg/L for Zn. The inflow concentrations to the entire hybrid constructed wetland system were 44.7340 mg/L and 52.5340 mg/L for Batch 1 and Batch 2, respectively. As shown in Figure 16, the Zn concentrations decreased as the water flowed through the saltwater portion of the hybrid CWTS, and the RO system took the concentrations below the target outflow limit set by the model NPDES permit. The inflow vs. final outflow concentrations for Batch 1: Train 1 and Train 2 of the freshwater system were 0.0656/0.4025 mg/L and 0.0696/0.5895 mg/L. For Batch 2: Train 1 and Train 2, they were 0.0881/0.2482 mg/L and 0.0928/0.2568 mg/L, respectively. As shown in Figure 17, all water samples for both batches of water collected after the RO system, the permeate (outflow from the RO system) through the outflow from trains 1 and 2, met the NPDES discharge limit of 5.0 mg/L for zinc. Like the results for cadmium, copper, and lead, the low concentrations of zinc in the RO permeate support the proposed fine-tuning of the RO system for increased volumes of permeate and decreased amounts of concentrate.

Toxicity

In Experiment 3, 7-day toxicity tests utilizing *C. dubia* were performed only on the waters from Batch 2 due to time constraints. Experiment 3: Batch 2 samples from the saltwater module (detention basin, oil/water separator outflow, Spartina cell 1 outflow, and Spartina cell 2 outflow) were diluted to 3% sample water: 97% moderately hard water to prevent interference in toxicity results from chlorides. These waters showed total mortality after 24 hours. In the freshwater system, the inflow to Train 2 showed total

mortality after 24 hours. The inflow to Train 2 was also found to have a low pH which is likely the cause of these results. The outflow from Train 2 showed significantly decreased reproduction of *C. dubia* but no significant difference in mortality from the control. Train 1 showed no significant difference in reproduction or mortality of *C. dubia* from the control.

Experiment 4: Simulated Hyper-Saline Water

Metals

For Experiment 4, metals were loaded at concentrations of approximately 1.21 mg/L Cd, 5.0 mg/L Cu, 10.2 mg/L Pb, and 69.0 mg/L Zn.

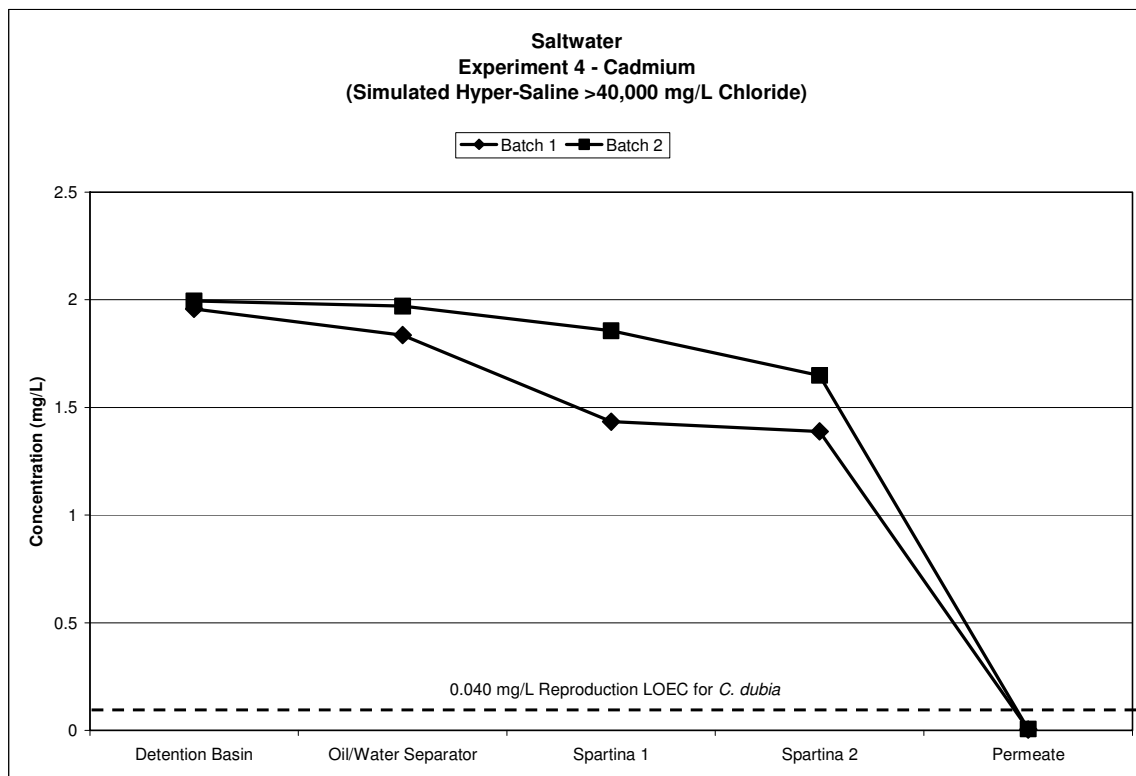


Figure 18. Saltwater module and RO permeate results for Experiment 4: Simulated hyper-saline water metal analysis of cadmium performed by ICP. The saltwater module is that portion of the hybrid constructed wetland treatment system occurring before the RO system (i.e., all points except “permeate”). The RO permeate is the outflow water from the RO system that is then pumped into the two freshwater wetland trains. For each batch of water in the above graph, the RO permeate concentration is the average of the inflow concentrations for each of the two freshwater wetland trains.

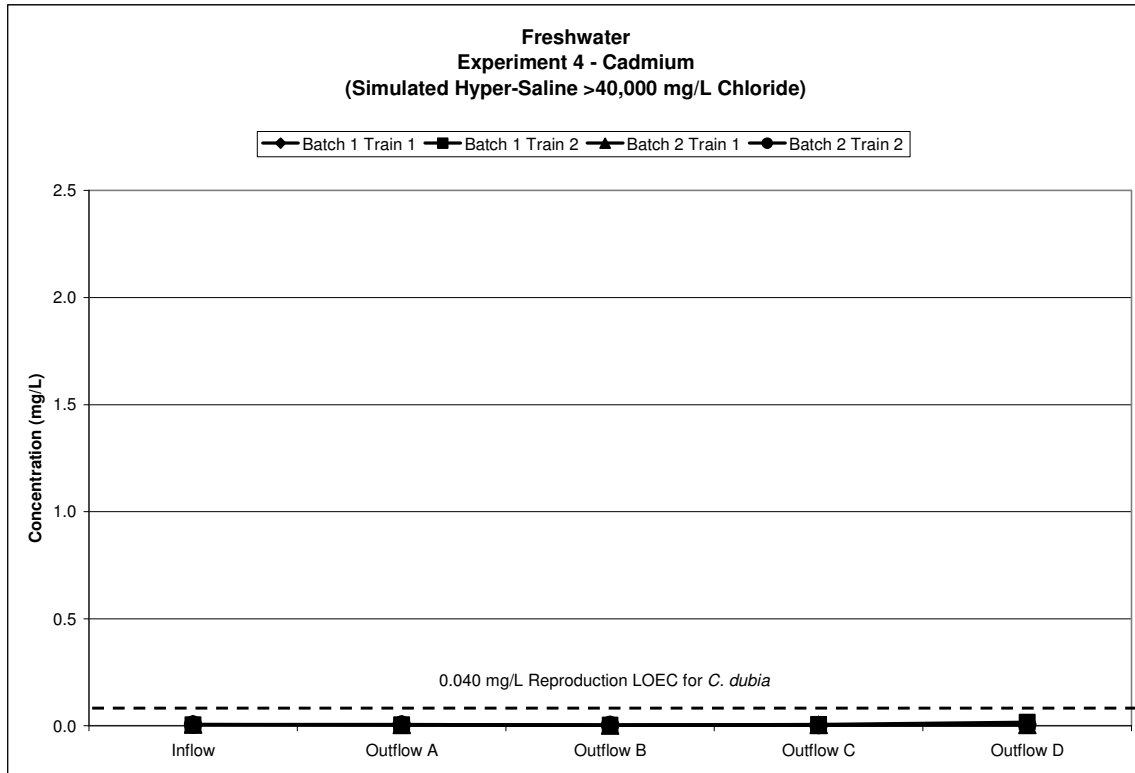


Figure 19. Freshwater module (post-RO system) results for Experiment 4: Simulated hyper-saline water metal analysis of cadmium performed by ICP.

The inflow cadmium concentrations to the entire hybrid CWTS were 1.958 mg/L and 1.994 mg/L for Batch 1 and Batch 2, respectively, of the simulated hyper-saline produced water. As shown in Figure 18, the Cd concentrations decreased as the water flowed through the saltwater portion of the hybrid CWTS. The inflow vs. final outflow concentrations for Batch 1: Train 1 and Train 2 of the freshwater system were 0.0069/0.0076 mg/L and 0.0059/0.0168 mg/L. For Batch 2: Train 1 and Train 2, they were 0.0062/0.0039 mg/L and 0.0055/0.0043 mg/L, respectively. As shown in Figure 19, the inflow water to each freshwater wetland train had low concentrations of Cd due to removal by the RO system. The inflow water to the freshwater system was below the target outflow limit based on the LOEC for reproduction of *C. dubia*. As the water flowed through the freshwater system, it remained below the target outflow limit.

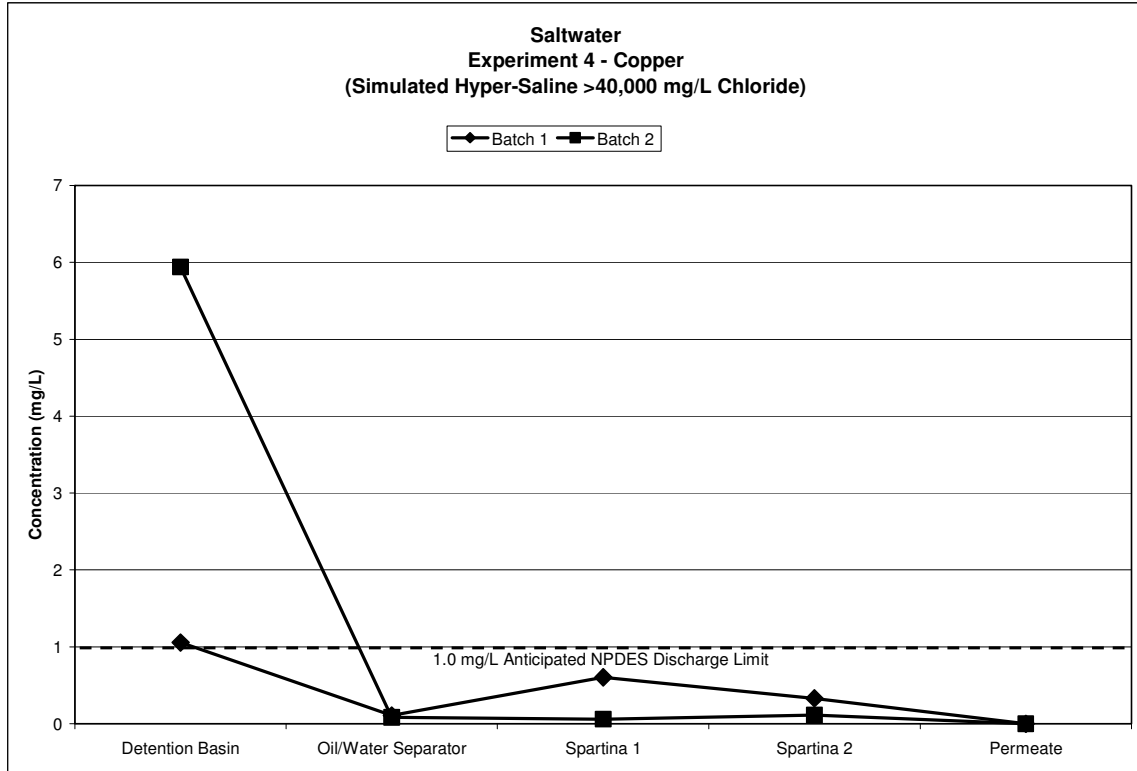


Figure 20. Saltwater module and RO permeate results for Experiment 4: Simulated hyper-saline water metal analysis of copper performed by ICP. The saltwater module is that portion of the hybrid constructed wetland treatment system occurring before the RO system (i.e., all points except “permeate”). The RO permeate is the outflow water from the RO system that is then pumped into the two freshwater wetland trains. For each batch of water in the above graph, the RO permeate concentration is the average of the inflow concentrations for each of the two freshwater wetland trains.

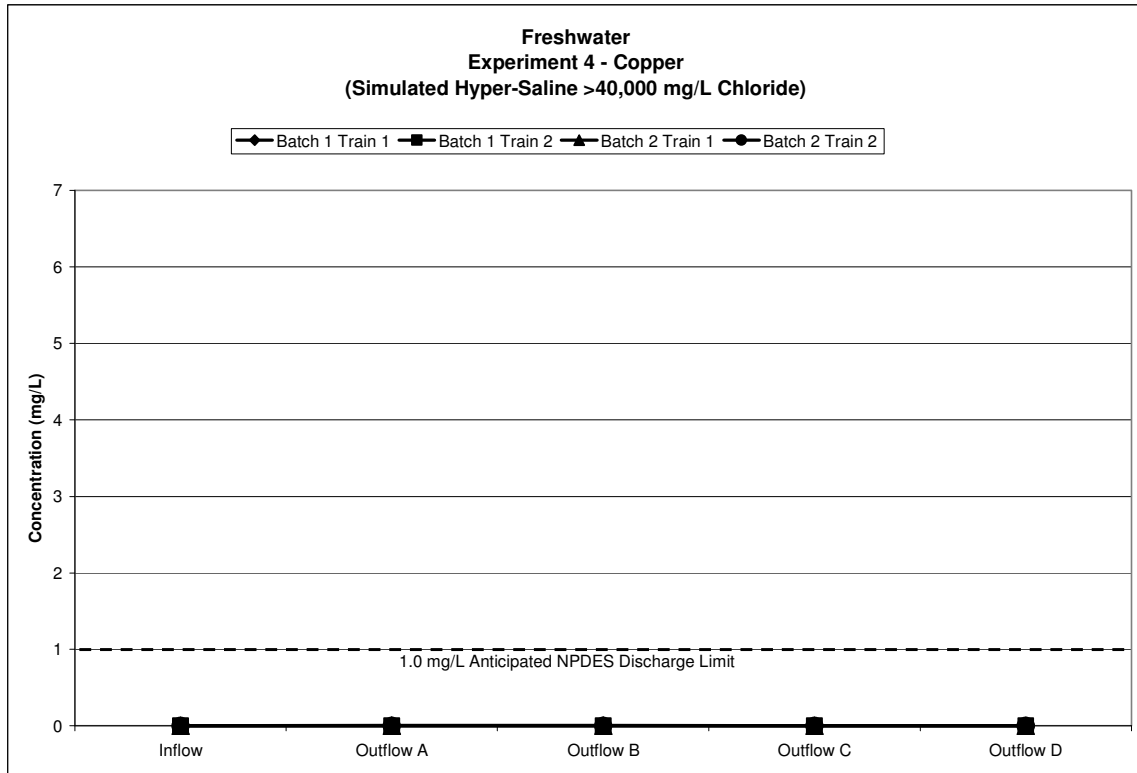


Figure 21. Freshwater module (post-RO system) results for Experiment 4: Simulated hyper-saline water metal analysis of copper performed by ICP.

The NPDES permits for the regions examined provided a NPDES discharge limit of 1.0 mg/L for Cu. The inflow concentrations to the entire hybrid constructed wetland system were 1.056 mg/L and 5.940 mg/L for Batch 1 and Batch 2, respectively. As shown in Figure 20, the Cu concentrations decreased to levels below the target outflow limit set by the model NPDES permit as the water flowed through the oil/water separator and into the saltwater portion of the hybrid CWTS. As the water continued through the system into the saltwater portion and through the RO system, the copper concentrations remained below the target outflow limit set by the model NPDES permit. The inflow vs. final outflow concentrations for the entire freshwater system were below method detection limits. As shown in Figure 21, all water samples for both batches of water collected after the oil/water separator, including water samples from the saltwater wetland cells, the RO system, and the freshwater wetland cells, met the NPDES discharge limit of 1.0 mg/L for copper.

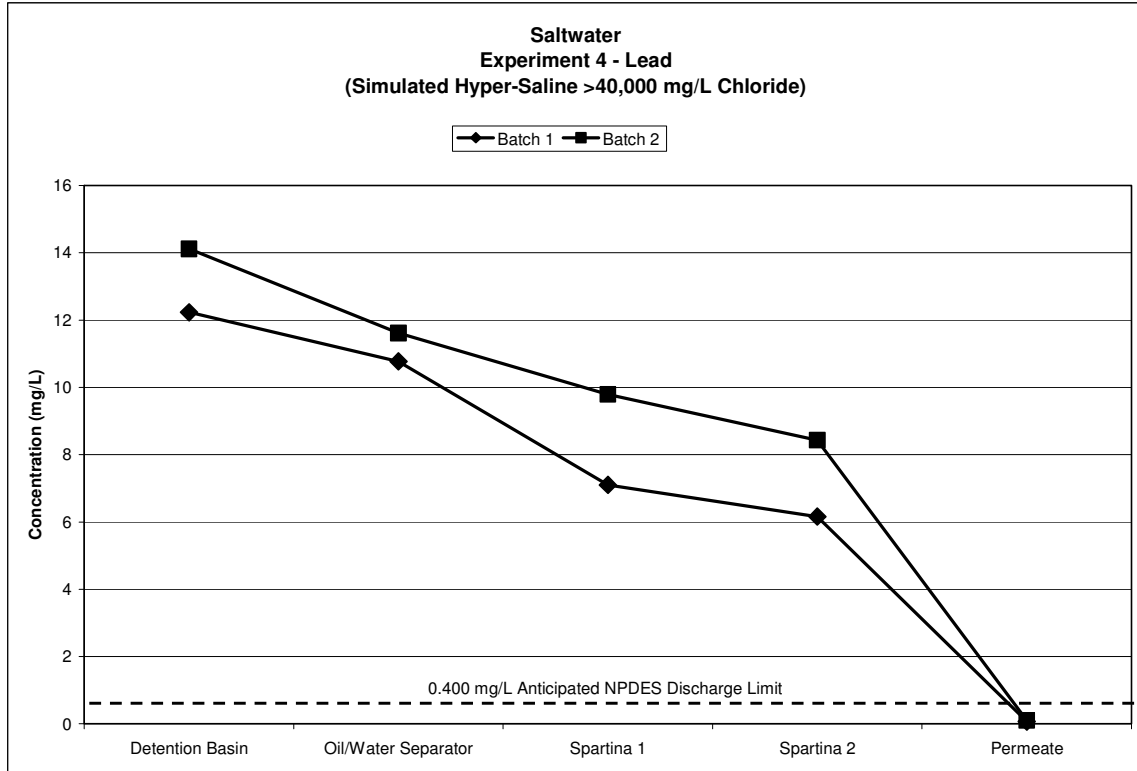


Figure 22. Saltwater module and RO permeate results for Experiment 4: Simulated hyper-saline water metal analysis of lead performed by ICP. The saltwater module is that portion of the hybrid constructed wetland treatment system occurring before the RO system (i.e., all points except “permeate”). The RO permeate is the outflow water from the RO system that is then pumped into the two freshwater wetland trains. For each batch of water in the above graph, the RO permeate concentration is the average of the inflow concentrations for each of the two freshwater wetland trains.

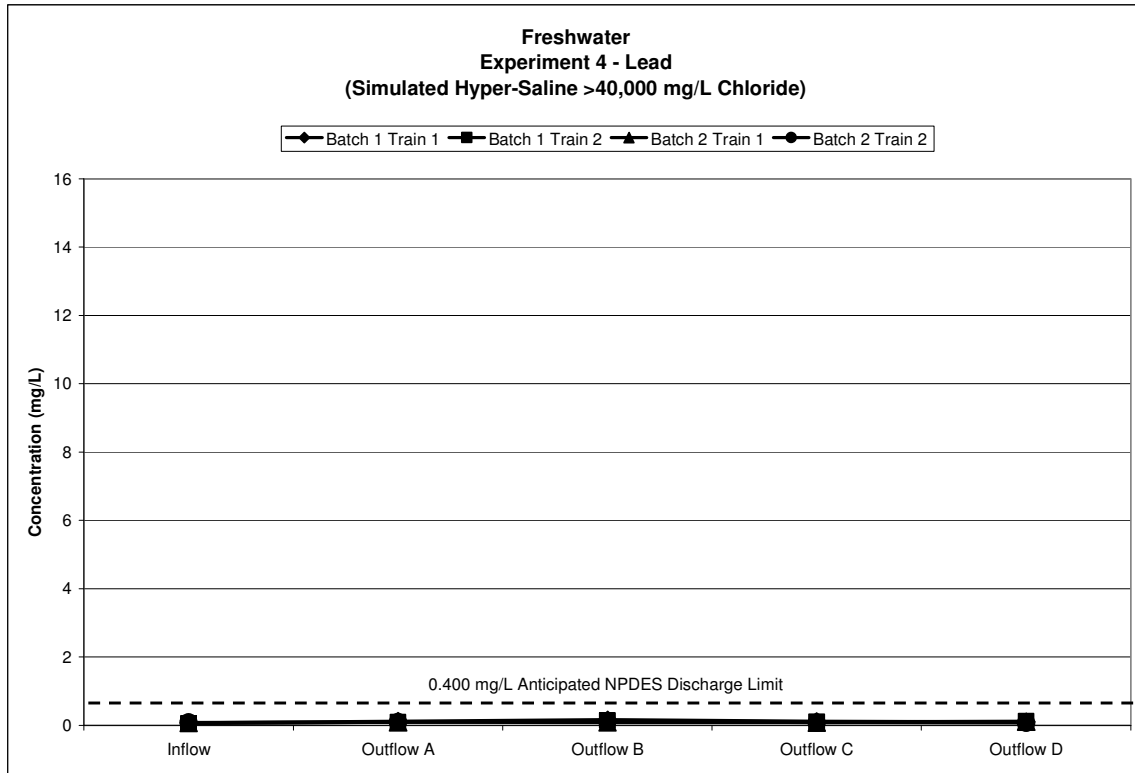


Figure 23. Freshwater module (post-RO system) results for Experiment 4: Simulated hyper-saline water metal analysis of lead performed by ICP.

The NPDES permits for the regions examined provided a NPDES discharge limit of 0.400 mg/L for Pb. The inflow concentrations to the entire hybrid constructed wetland system were 12.23 mg/L and 14.11 mg/L for Batch 1 and Batch 2 respectively. As shown in Figure 22, the Pb concentrations decreased as the water flowed through the saltwater portion of the hybrid CWTS, and the RO system took the concentrations below the target outflow limit set by the model NPDES permit. The inflow vs. final outflows for Batch 1: Train 1 and Train 2 of the freshwater system were 0.0683/0.0974 mg/L and 0.0510/0.1130 mg/L. For Batch 2: Train 1 and Train 2, they were 0.0679/0.1005 mg/L and 0.0847/0.0703 mg/L, respectively. As shown in Figure 23, all water samples for both batches of water collected after the RO system, the permeate (outflow from the RO system) through the outflow from trains 1 and 2 met the NPDES discharge limit of 0.400 mg/L for lead.

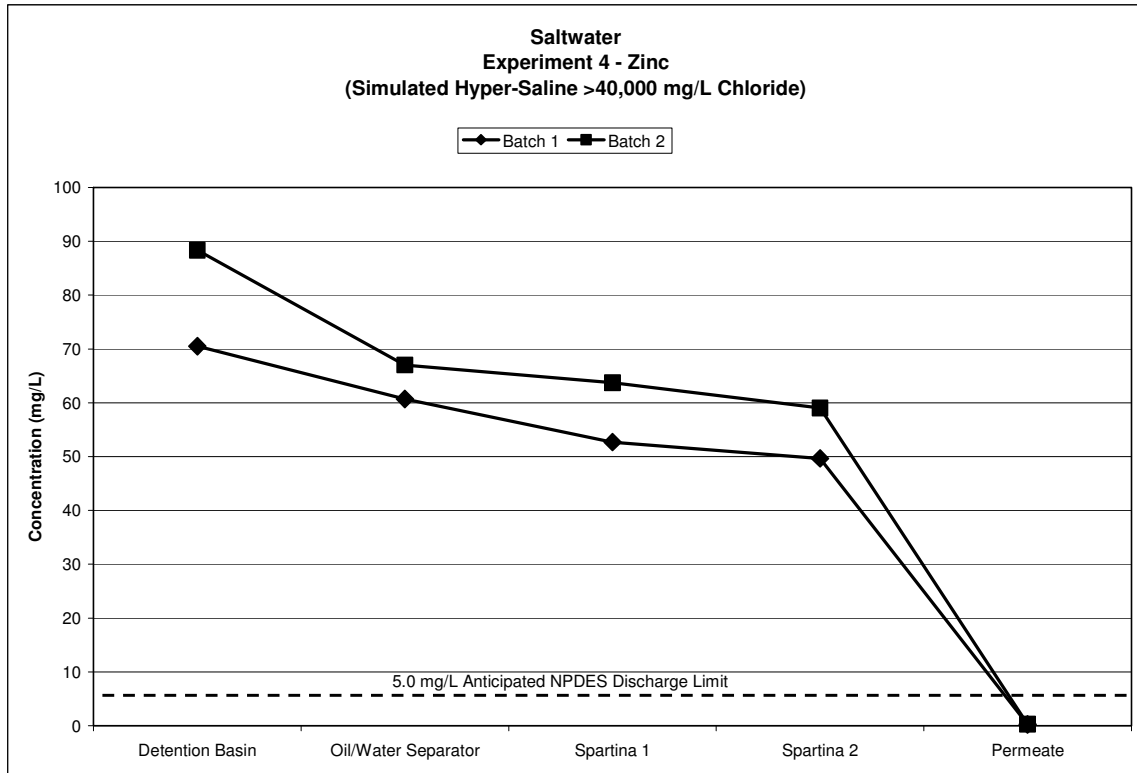


Figure 24. Saltwater module and RO permeate results for Experiment 4: Simulated hyper-saline water metal analysis of zinc performed by ICP. The saltwater module is that portion of the hybrid constructed wetland treatment system occurring before the RO system (i.e., all points except “permeate”). The RO permeate is the outflow water from the RO system that is then pumped into the two freshwater wetland trains. For each batch of water in the above graph, the RO permeate concentration is the average of the inflow concentrations for each of the two freshwater wetland trains.

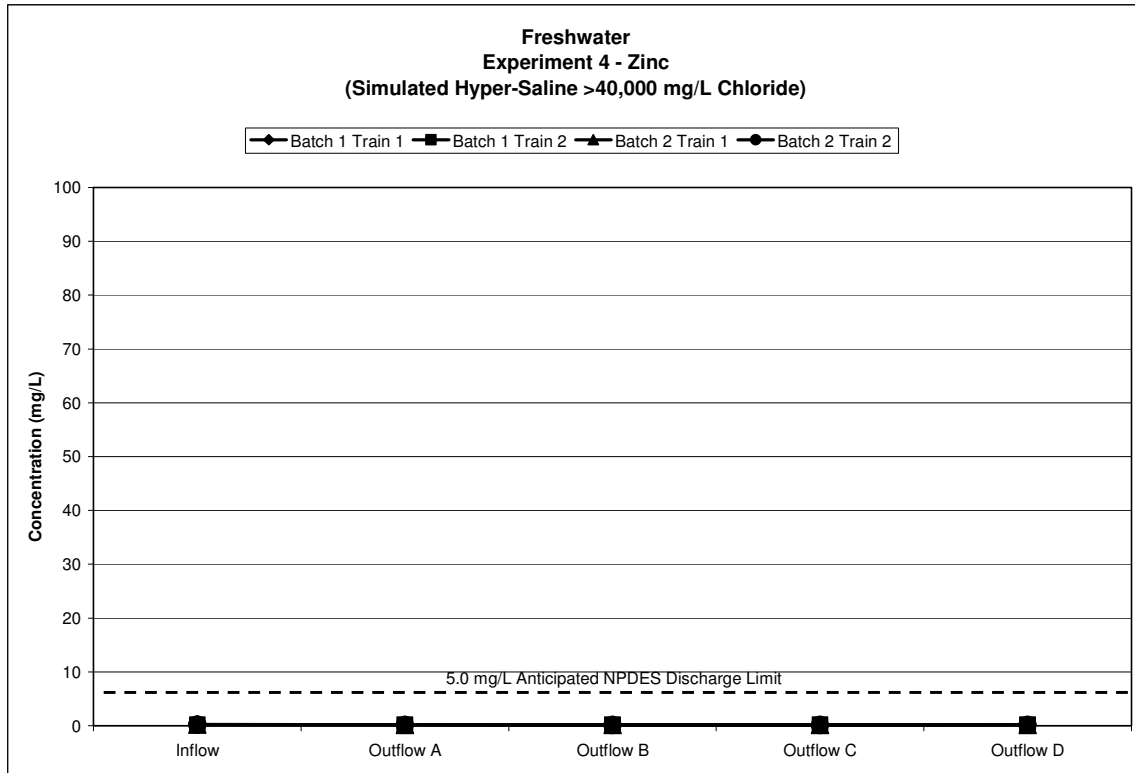


Figure 25. Freshwater module (post-RO system) results for Experiment 4: Simulated hyper-saline water metal analysis of zinc performed by ICP.

The NPDES permits for the regions examined provided a NPDES discharge limit of 5.0 mg/L for Zn. The inflow concentrations to the entire hybrid constructed wetland system were 70.5 mg/L and 88.3 mg/L for Batch 1 and Batch 2 respectively. As shown in Figure 24, the Zn concentrations decreased as the water flowed through the saltwater portion of the hybrid CWTS and the RO system took the concentrations below the target outflow limit set by the model NPDES permit. The inflow vs. final outflow concentrations for Batch 1: Train 1 and Train 2 of the freshwater system were 0.2498/0.1915 mg/L and 0.2346/0.1958 mg/L. For Batch 2: Train 1 and Train 2, they were 0.2368/0.1789 mg/L and 0.2361/0.1750 mg/L respectively. As shown in Figure 25, all water samples for both batches of water collected after the RO system, the permeate (outflow from the RO system) through the outflow from trains 1 and 2 met the NPDES discharge limit of 5.0 mg/L for zinc. Like the results for cadmium and lead, the low concentrations of zinc in the RO permeate support the proposed fine-tuning of the RO system for increased volumes of permeate and decreased amounts of concentrate.

Toxicity

In Experiment 4, 7-day toxicity tests utilizing *C. dubia* were performed on both the waters from Batch 1 and Batch 2. Experiment 4 samples from the saltwater module were diluted to 1.2% sample water, 98.8% moderately hard water to prevent chloride interference in toxicity results. In Experiment 4, both Batch 1 and Batch 2, showed survival of *C. dubia* as significantly less than the controls in each component of the

saltwater module. There was total mortality of *C. dubia* in both the detention basin water and oil/water separator outflow, and none of the organisms in either batch produced offspring.

The water tested in the freshwater module was run at 100% sample water for both experiments. The outflow from these wetland cells showed no significant differences in mortality or reproduction of *C. dubia* when compared to the control for both batches of water.

Oil-in-Water Data

Oil-in-water was measured by Turner Designs Hydrocarbon Instruments TD500 Handheld Oil in Water Meter. The methods used were adapted from Standard Methods fluorometric determination of oil-in-water. Measurements taken using this instrument indicate that the method has some interference, possibly from algae present in the water column.

General Water Chemistry

General water chemistry data provide an overview of the characteristics of each category of water as it flows through the system. To adequately assess the effectiveness of the system, each category of water was run through the CWTS for four weeks. For each category, two batches of water were mixed and analyzed. The general water chemistry results for each experiment and batch are shown in the Appendix.

Task 5: Confirm Design Characteristics

Task 5 focuses on confirming design characteristics and modifying the system to optimize performance.

Oil/Water Separator

The oil/water separator was one of the modules that was modified to improve performance. High values of oil-in-water were measured in the outflow from the Spartina 1 and Spartina 2 wetland cells during Experiment 3. While interference by algae may be the cause of the high concentrations of oil in water found in the outflows from these cells, visual inspection of the system suggested that the original oil/water separator (Figure 26) was not adequately removing the oil and grease from the water. Due to the detrimental effect excess hydrocarbon concentrations may have on the macrophytes, *Spartina alterniflora*, in the saltwater wetland cells and on the RO membrane, it was deemed necessary to make some adaptations to the oil/water separator in preparation for Experiment 4. In response to the above results and observations, a new oil/water separator was designed, built, and tested at a bench-scale. The new model incorporated some of the same baffle concepts used by the original oil/water separator and also utilized dissolved air flotation, turbulence reduction, and filtering techniques to separate the oil from the water. Following the successful removal of oil at the bench-scale by the new model, a pilot-scale oil/water separator was built with this design (Figure 27) and was incorporated into the hybrid CWTS for Experiment 4 in place of the previously used API oil/water separator.



Figure 26: Oil/Water Separator used in Experiment 3.



Figure 27: Newly constructed Oil/Water Separator used in Experiment 4.

Reverse Osmosis System

The RO system also presents an opportunity for fine tuning the system and improving the system efficiency. Since the metal concentrations in the RO permeate are below the target outflow limits set forth in the NPDES permits, it may be beneficial to adjust the RO system (e.g. use less restrictive membranes) and allow more dissolved solids through, thus utilizing the freshwater wetland to its full potential. Also, by adjusting the RO system to create a larger volume of permeate, a smaller volume of concentrate is generated. Concentrate is the wastewater produced by the RO system requiring costly disposal. Since the freshwater system is capable of handling up to 4,000 mg/L chlorides, the RO system could be fine-tuned to produce a larger volume of permeate with higher concentrations of chlorides and metals. The freshwater system would then be used for decreasing the metal concentrations below the target outflow limits. By reducing the volume of concentrate and increasing the use of the freshwater system for metal removal, there is improved efficiency of the hybrid CWTS.

Simulated Brackish Water II

Metals

For Experiment 5, metals were loaded at concentrations emulating those of the model NPDES permit limit of approximately 0.37 mg/L Cu, 0.4 mg/L Pb, and 1.3 mg/L Zn. A concentration of 0.04 mg/L was used for Cd based on the lowest observable effect concentration (LOEC) for reproduction of *C. dubia* (USEPA, 2002). This experiment utilized the detention basin, the oil/water separator, and the freshwater module.

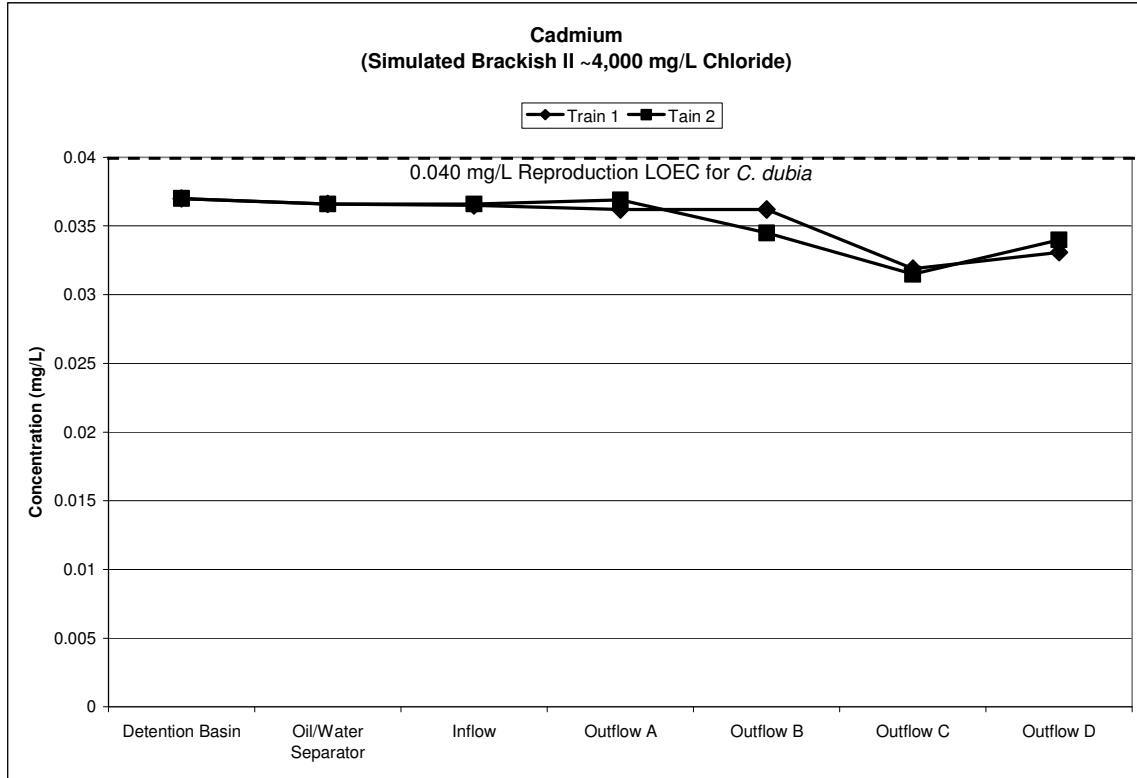


Figure 28. Results for simulated brackish water II metal analysis of cadmium performed by ICP.

The inflow cadmium concentration to the entire hybrid CWTS was 0.037 mg/L for the simulated brackish II produced water. As shown in Figure 28, the Cd concentrations decreased gradually as the water flowed through the CWTS. The final outflow concentrations for Train 1 and Train 2 were 0.0331 and 0.0340 mg/L, respectively. The inflow water to the freshwater system was below the target outflow limit based on the LOEC for reproduction of *C. dubia*. As the water flowed through the freshwater system, it remained below the target outflow limit.

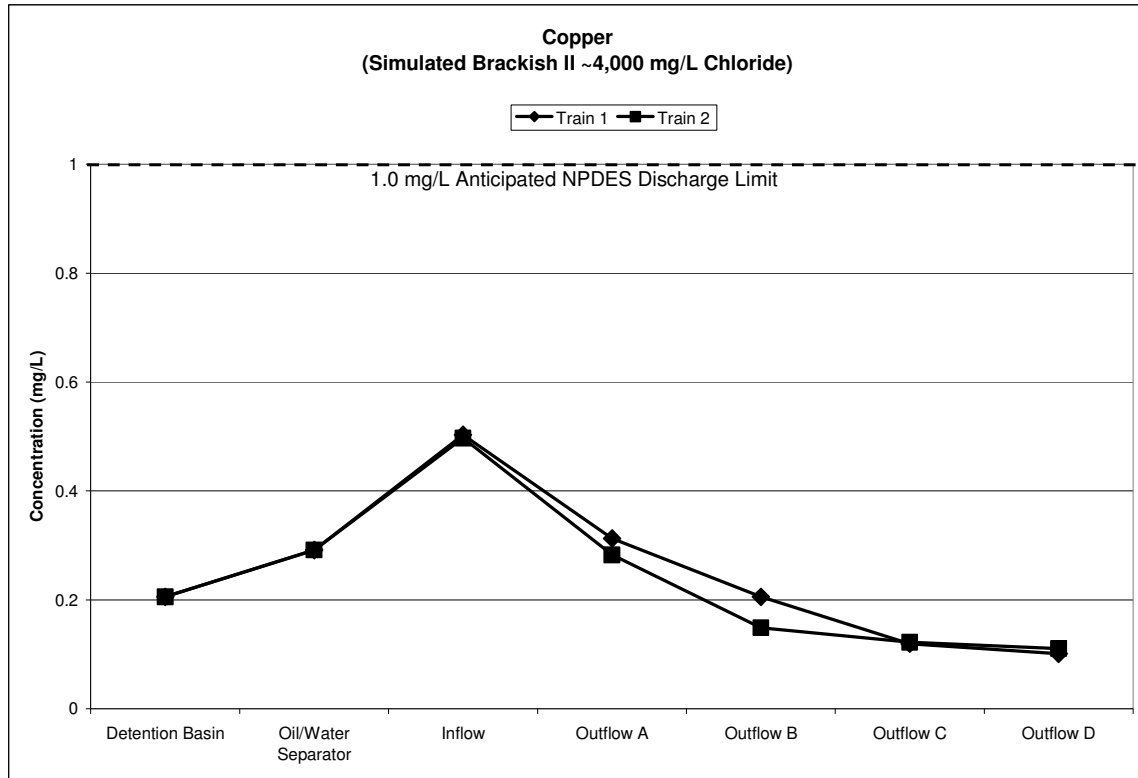


Figure 29. Results for simulated brackish water II metal analysis of copper performed by ICP.

The NPDES permits for the regions examined provided a NPDES discharge limit of 1.0 mg/L for Cu. The inflow concentration to the entire hybrid constructed wetland system was 0.2055 mg/L. The final outflow concentrations for Train1 and Train 2 were 0.1008 and 0.1105, respectively. As shown in Figure 29, the Cu concentrations remained below the target outflow limit set by the model NPDES permit as the water flowed through the oil/water separator and into the freshwater portion of the hybrid CWTS.

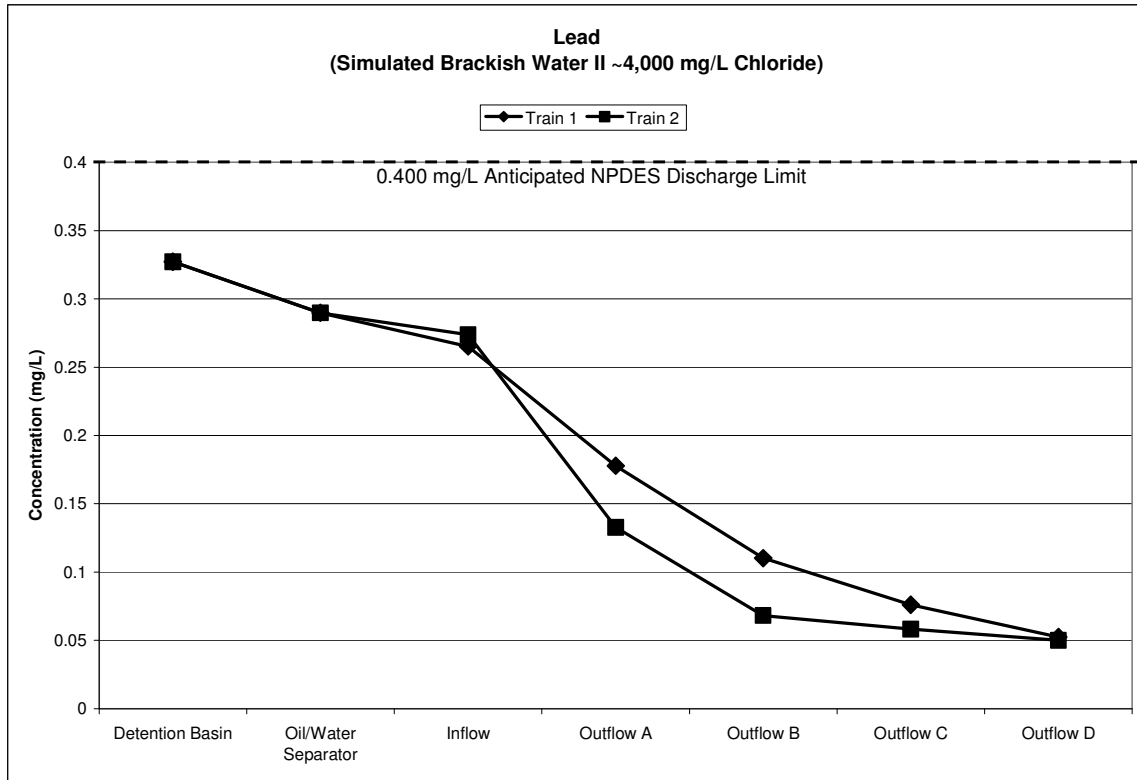


Figure 30. Results for simulated brackish water II metal analysis of lead performed by ICP.

The NPDES permits for the regions examined provided a NPDES discharge limit of 0.400 mg/L for Pb. The inflow concentration to the entire hybrid constructed wetland system was 0.3271 mg/L. The Pb concentrations decreased as the water flowed through the freshwater module. The final outflows for Train 1 and Train 2 were 0.052 and 0.0501 mg/L, respectively. As shown in Figure 30, the Pb concentrations were maintained below the NPDES limit.

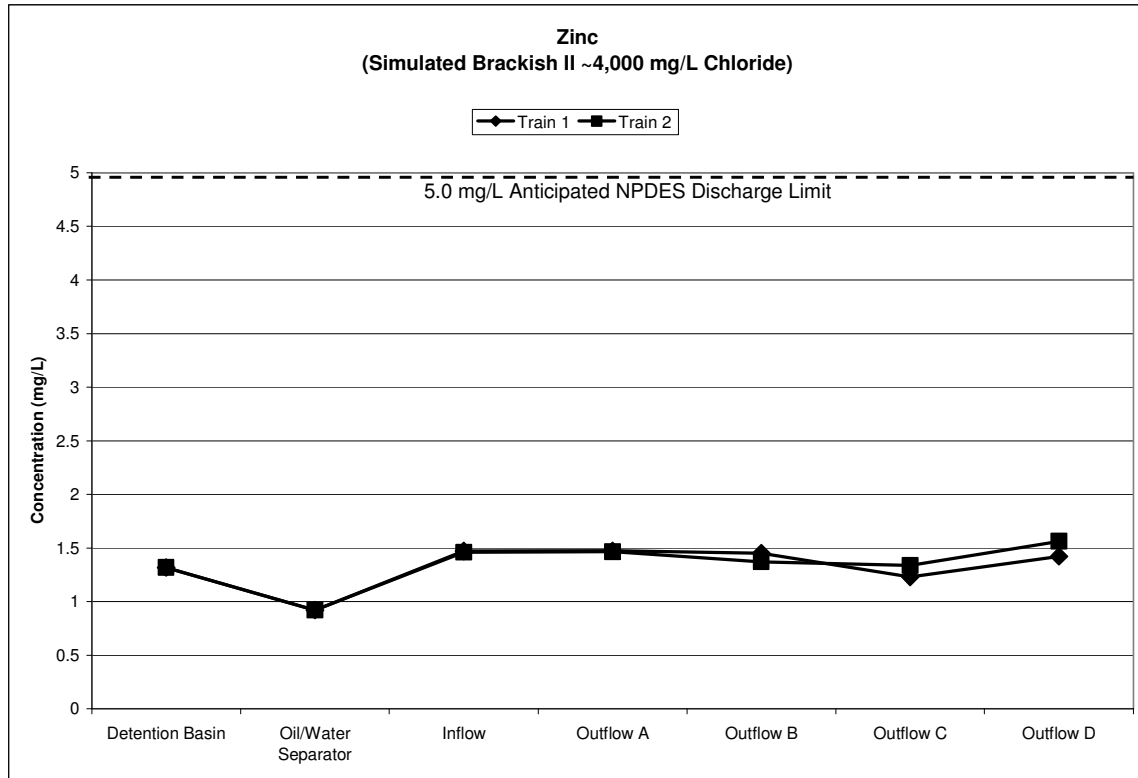


Figure 31. Results for simulated brackish water II metal analysis of zinc performed by ICP.

The NPDES permits for the regions examined provided a NPDES discharge limit of 5.0 mg/L for Zn. The inflow concentrations to the entire hybrid constructed wetland system were 1.318 mg/L. The final outflow concentrations for Train 1 and Train 2 were 1.562 and 1.423mg/L, respectively. As shown in Figure 31, the Zn concentrations were maintained below the NPDES limit.

Toxicity

In Experiment 5, 7-day toxicity tests utilizing *C. dubia* were performed. Experiment 5 samples were diluted to 20% sample water, 80% moderately hard water to reduce possible chloride interference in toxicity results. In Experiment 5 showed survival of *C. dubia* as significantly less than the controls for both inflows into the freshwater module. The outflow from each of the freshwater wetland cells showed no significant differences in mortality. The entire system showed significantly different reproduction of *C. dubia* as compared to the control. This may be due to increased chloride concentrations due to evaporation. As noted in Appendix Table 9, as the water flows through the system the chloride concentration increases, thus using the same dilution the concentration of chlorides in the outflow waters would be greater than the inflow waters.

Oil-in-Water Data

As in the other experiments, oil-in-water was measured by Turner Designs Hydrocarbon Instruments TD500 Handheld Oil in Water Meter. The methods used were adapted from

Standard Methods fluorometric determination of oil-in-water. Measurements taken using this instrument indicate that the method has some interference, possibly from algae present in the water column.

General Water Chemistry

The general water chemistry results for this experiment are shown in the Appendix-Table 9.

Conclusions

During the first quarter of the investigation, produced waters were characterized (Task 1), NPDES standards for treated produced waters were determined (Task 2), and the pilot-scale treatment system was designed and constructed (Task 3). Produced water composition varies widely based upon the geologic formation from which it originates, the extraction method utilized in the natural gas production process, and the treatment chemicals utilized in the process. A model NPDES permit was derived from a number of oil and gas permits issued by the states of Ohio, Pennsylvania, New York, and West Virginia. This model (comprehensive) permit serves as the performance goals for the pilot-scale constructed wetland treatment system. The treatment system is designed to target specific characteristics of natural gas storage produced waters. The design includes an API oil/water separator, saltwater wetland system, RO system, and freshwater wetland system.

During the second quarter of the investigation, Experiments 1 and 2 were completed. These experiments involved running the first two categories of produced water, simulated fresh and brackish, through the freshwater wetland portion of the CWTS. The API oil/water separator, the saltwater wetland cells, and the RO system were bypassed due to the relatively low oil and chloride concentrations found in these two categories of water. In Experiment 1 (simulated fresh produced water), the water showed no toxicity and the concentrations of metals as well as the concentrations of oil were below the limits defined by the model NPDES permit. In Experiment 2 (simulated brackish produced water), both the inflow and the final outflow showed toxicity. This can most likely be attributed to the high concentrations of cadmium and zinc in the final outflow remaining at levels above the model NPDES discharge limits. Copper and lead decreased as the water flowed through the system to concentrations below the model NPDES discharge limits. Oil concentrations remained relatively constant, increasing slightly in the final wetland cell of each train. This may be due to background levels of algae picked up by the fluorometer used to measure oil levels.

Experiment 3 (simulated saline produced water) was completed during the third quarter of the investigation. As water flowed through the oil/water separator and the saltwater portion of the hybrid CWTS, metal concentrations gradually decreased. The RO system reduced metal concentrations to levels below the model NPDES discharge limits (Task 2). The freshwater system maintained metal concentrations below the target outflow limits. By reducing the volume of concentrate and increasing the use of the freshwater system for metal removal, the efficiency of the hybrid CWTS could be improved. In

Experiment 3, the oil/water separator was introduced to decrease the amount of oil entering the saltwater wetland module. Due to high amounts of oil in water found in the water exiting from the original oil/water separator in Experiment 3, a new oil/water separator was designed, built, and tested.

Experiment 4 (simulated hyper-saline produced water) was completed during the fourth quarter of the investigation. As noted earlier, a new oil/water separator was incorporated into the hybrid CWTS for this experiment and proved to be successful at decreasing oil concentrations in the water. As water flowed through the oil/water separator and the saltwater portion of the hybrid CWTS, metal concentrations decreased. The RO system reduced metal concentrations to levels below the model NPDES discharge limits (Task 2), and the freshwater system maintained metal concentrations below the target outflow goals.

During the final four months of the investigation, a fifth experiment was run with simulated brackish water II. This experiment was added to enhance knowledge of the capabilities of the freshwater module. Constituents of concern were added at NPDES permit levels. The system was able to maintain or decrease concentrations of all four metals.

The low concentrations of cadmium, copper, lead, and zinc in the RO permeate from both Experiment 3 and Experiment 4 support the proposed fine-tuning of the RO system for increased volumes of permeate and decreased volumes of concentrate. By reducing the volume of concentrate and increasing the use of the freshwater system for metal removal, the efficiency of the hybrid CWTS could be improved. The new oil/water separator showed greatly improved results compared to the previously used oil/water separator, however, the residual oil contained in the saltwater wetland cells from Experiment 3 continued to flow through the system showing outflow concentrations above the model NPDES discharge limits (Task 2). Another probable cause for unexpectedly high oil-in-water measurements is the presence of algae in the samples; both chlorophyll-a and its phaeophytin derivative fluoresce in the same range as the hydrocarbons measured by the Turner Designs Handheld Oil-in-Water Meter.

Data obtained during the investigation indicate that the pilot-scale CWTS provided effective treatment of simulated natural gas storage produced water. Results are very encouraging as the work moves toward field demonstration of the technology.

References Cited

- Faulkner, S.P., W.H. Patrick, Jr., R.P. Gambrell. 1989. Field Techniques for Measuring Wetland Soil Parameters. *Soil Sci. Soc. Am. J.* 53: 883-890.
- Pope, D. H., and R.M. Pope. 1999. Diagnosis, Treatment, and Monitoring of Microbiologically Influenced Productivity in Natural Gas Storage Facilities. Gas Research Institute, Report GRI-00-0056.
- SAS Institute. 2002. Statistical Analysis System. Version 9. SAS Institute Inc., Cary, North Carolina.
- United States Environmental Protection Agency (USEPA). 2000. EPA Office of Compliance Sector Notebook Project: Profile of the Oil and Gas Extraction Industry. EPA/310-R-99-006.
- United States Environmental Protection Agency (USEPA). 2002. ECOTOX User Guide: ECOTOXicology Database System. Version 3.0. Available: <<http://www.epa.gov/ecotox/>>.
- United States Environmental Protection Agency (USEPA). 2004. National Pollutant Discharge Elimination System: View NPDES Individual and General Permits. Available: <<http://cfpub.epa.gov/npdes/permitissuance/genpermits.cfm>>.
- Veil, A., M.G. Puder, D. Elcock, and R.J. Redweik, Jr. 2004. A White Paper Describing Produced Water from Production of Crude Oil, Natural Gas, and Coal Bed Methane. United States Department of Energy, National Energy Technology Laboratory. Contract W-31-109-Eng-38.

Other Pertinent Publications

- American Public Health Association (APHA), American Water Works Association, and Water Pollution Control Federation. 1998. Standard Methods for Examination of Water and Wastewater, 20th Ed. American Public Health Association, Washington, D.C.
- Gillespie, Jr., W.B., W.B. Hawkins, J.H. Rodgers, Jr., M.L. Cano, and P.B. Dorn. 2000. Transfer and transformations of zinc in constructed wetlands: Mitigation of a refinery effluent. *Ecological Engineering* 14: 279-292.
- Hawkins, W.B., J.H. Rodgers, Jr., A.W. Dunn, P.B. Dorn, and M.L. Cano. 1997. Design and construction of wetlands for aqueous transfers and transformations of selected metals. *Ecotoxicology and Environmental Safety* 36: 238-248.
- Huddleston, G.M. III and J.H. Rodgers, Jr. *in press*. Integrated design of a constructed wetland system for treatment of copper-contaminated wastewater. *Water Environment Research*.
- Huddleston, G.M. III, W.B. Gillespie, Jr., and J.H. Rodgers, Jr. 2000. Using constructed wetlands to treat biochemical oxygen demand and ammonia associated with a refinery effluent. *Ecotoxicology and Environmental Safety* 45:188-193.

- Knight, R.L., R.H. Kadlec, and H.M. Ohlendorf. 1999. The use of treatment wetlands for petroleum industry effluents. *Environmental Science & Tech.* 33: 973-980.
- Mastin, B.J., J.H. Rodgers, Jr. and Y.T. Shah. 2001. Hybrid cavitation/constructed wetland reactors for treatment of chlorinated and non-chlorinated organics. *Chemical Engineering Tech.* 24: 97A-105A.
- Moore, M.T., J.H. Rodgers, Jr., S. Smith, Jr. and C.M. Cooper. 2001. Mitigation of metolachlor-associated agriculture runoff using constructed wetlands in Mississippi, USA. *Agric. Ecosystems and Environ.* 84: 169-176.
- Moshiri, G.A. (ed.). 1993. *Construction Wetlands for Water Quality Improvement*: Lewis Publishers, Ann Arbor, Michigan.
- Murray-Gulde, C., J.E. Heatley, T. Karanfil, J.H. Rodgers, Jr., and J.E. Myers. 2003. Performance of a hybrid reverse osmosis-constructed wetland treatment system for brackish water. *Water Research* 37: 705-713.
- Myers, J.E. 2000. Constructed wetland overview for the petroleum industry. Society of Petroleum Engineers E&P Environmental Conference, Stavanger, Norway (SPE 61181).
- Myers, J.E., L.M. Jackson, R.F. Bernier, and D.A. Miles. 2001. An evaluation of the Department of Energy Naval Petroleum Reserve No. 3 produced water bio-treatment facility. Society of Petroleum Engineers E&P Environmental Conference, San Antonio, TX (SPE 66522).

Appendix: General Water Chemistry Data

Table 1: General Water Chemistry Results for Experiment 1: Batch 1 (Simulated Fresh Produced Water).

Sample	pH	DO (mg/L)	Conductivity (mS/cm)	Temp (°C)	Alkalinity (mg/L)	Hardness (mg/L)	BOD ₅ (mg/L)	Sulfate Conc. (mg/L)	COD (mg/L)	TSS (mg/L)	TDS (mg/L)	Chloride Conc. (mg/L)
1-A Inflow	7.42	9.16	1.4	19.0	12	288	0.82	ND	9.56	8.3	4532	462.5
2-A Inflow	7.36	8.24	1.4	18.6	12	268	ND	ND	4.25	7.9	1562	450
1-A Outflow	6.79	9.41	1.7	19.2	32	340	0.27	ND	10.81	17.1	1162	522.5
2-A Outflow	6.47	8.60	1.9	19.4	16	400	1.60	ND	5.19	14.7	1367	582.5
1-B Outflow	6.73	8.57	2.3	20.2	24	592	0.98	ND	16.75	16	1672	705
2-B Outflow	6.65	8.17	2.2	18.8	30	508	1.40	ND	7.69	7.6	1625	645
1-C Outflow	6.82	9.53	2.5	20.7	20	532	1.17	ND	16.13	8.5	1791	687.5
2-C Outflow	7.19	9.45	2.1	21.5	28	496	1.02	ND	12.69	14.6	1464	602.5
1-D Outflow	7.12	10.30	2.4	20.1	24	456	1.73	ND	12.69	16.2	1709	695
2-D Outflow	7.11	10.30	2.5	20.0	28	540	1.07	ND	5.19	8.2	48	697.5

*ND: Non-Detect

Table 2: General Water Chemistry Results for Experiment 1: Batch 2 (Simulated Fresh Produced Water).

Sample	pH	DO (mg/L)	Conductivity (mS/cm)	Temp. (°C)	Alkalinity (mg/L)	Hardness (mg/L)	BOD ₅ (mg/L)	Sulfate Conc. (mg/L)	COD (mg/L)	TSS (mg/L)	TDS (mg/L)	Chloride Conc. (mg/L)
Equil. Basin	7.05	9.97	1.49	19.9	18	290	1.36	0.00	1.10	0.25	1149	610
1-A Inflow	7.14	9.89	1.50	21.1	12	330	0.86	13.75	0.57	0.55	1132	612.5
2-A Inflow	6.78	9.94	1.50	21.1	16	240	1.69	11.25	1.10	0.75	1116	635
1-A Outflow	6.98	9.54	1.40	21.2	14	340	0.77	11.25	0.04	0.45	1032	575
2-A Outflow	7.00	9.10	1.40	21.8	22	280	0.62	13.75	0.39	4.85	1113	575
1-B Outflow	6.86	9.34	1.40	21.9	22	250	0.76	8.75	0.21	0.95	1145	542.5
2-B Outflow	6.61	9.42	1.40	21.6	46	350	0.64	8.75	0.21	0.35	1181	555
1-C Outflow	6.90	9.78	1.50	23.3	16	290	1.56	8.75	0.57	1.15	1188	590
2-C Outflow	7.13	9.66	1.60	23.0	30	250	1.57	8.75	1.28	9.55	1208	557.5
1-D Outflow	7.24	10.58	1.55	20.1	14	300	2.07	6.25	1.10	0.75	1204	655
2-D Outflow	7.22	11.04	1.56	20.0	18	330	2.20	8.75	1.28	0.85	1244	605

Table 3: General Water Chemistry Results for Experiment 2: Batch 1 (Simulated Brackish Produced Water).

Sample	pH	DO (mg/L)	Conductivity (mS/cm)	Temp (°C)	Alkalinity (mg/L)	Hardness (mg/L)	BOD ₅ (mg/L)	Sulfate Conc. (mg/L)	COD (mg/L)	TSS (mg/L)	TDS (mg/L)	Chloride Conc. (mg/L)
Equil. Basin	7.02	9.50	7.52	~20	14	1360	0.55	4.56	18.34	3.75	5674.5	3260
1-A Inflow	7.06	9.81	7.48	~20	10	1270	0.82	3.80	15.01	1.75	5447.5	2640
2-A Inflow	6.87	9.71	7.47	~20	10	1520	0.68	5.06	13.01	1.75	5782.5	2810
1-A Outflow	6.91	9.20	7.09	~20	22	620	0.91	7.85	8.67	2.85	5043.5	2450
2-A Outflow	6.94	9.30	7.32	~20	20	700	0.64	8.86	12.00	2.65	5369.5	2530
1-B Outflow	7.33	7.74	7.03	~20	26	610	0.44	25.57	10.67	2.15	5086.5	2620
2-B Outflow	7.05	8.26	7.47	~20	22	690	0.67	21.52	21.34	2.25	5459.5	2730
1-C Outflow	7.27	10.10	7.00	~20	24	630	0.91	31.90	11.34	3.25	5166.5	2580
2-C Outflow	7.22	9.90	7.17	~20	22	720	0.87	27.59	10.00	4.45	4297.5	2600
1-D Outflow	7.21	10.61	6.87	~20	18	520	1.43	32.91	9.34	8.65	5147.5	2560
2-D Outflow	7.04	10.13	7.15	~20	16	580	2.75	32.15	17.67	31.75	5454.5	2610

Table 4: General Water Chemistry Results for Experiment 2: Batch 2 (Simulated Brackish Produced Water).

Sample	pH	DO (mg/L)	Conductivity (mS/cm)	Temp (°C)	Alkalinity (mg/L)	Hardness (mg/L)	BOD ₅ (mg/L)	Sulfate Conc. (mg/L)	COD (mg/L)	TSS (mg/L)	TDS (mg/L)	Chloride Conc. (mg/L)
Equil. Basin	7.1	9.18	8.64	20.2	15	1600	0.59	10.38	NA	ND	6855	3050
1-A Inflow	7.1	9.15	8.85	22.2	14	1540	0.6	2.28	31.18	1.4	6657	2920
2-A Inflow	7.06	9.2	8.85	20.6	16	1670	0.46	3.29	30.47	4.5	6830	2950
1-A Outflow	6.92	7.87	8.49	22.2	18	1600	0.35	5.32	29.76	2.1	6491	2950
2-A Outflow	7.02	7.89	8.53	22	18	1630	0.24	8.35	30.47	-0.8	6244	3020
1-B Outflow	7.06	7.82	8.51	20.8	24	1730	0.98	11.90	29.76	1.1	6550	2950
2-B Outflow	6.84	8.91	8.92	21.1	20	1540	0.96	20.51	28.34	1.4	6640	2940
1-C Outflow	7.07	10.66	8.5	21.3	16	1580	0.85	11.65	28.34	1.8	6455	3020
2-C Outflow	7.07	10.45	8.72	17.6	44	1590	1.56	14.18	29.05	1.6	6650	3050
1-D Outflow	7.28	10.53	8.45	17.3	16	1680	1.3	11.14	29.05	3.6	6370	3000
2-D Outflow	7.25	11.04	8.6	19.4	46	1600	1.24	14.68	33.30	6.2	6566	3000

*ND: Non-Detect

Table 5: General Water Chemistry Results for Experiment 3: Batch 1 (Simulated Saline Produced Water).

Sample	pH	DO (mg/L)	Conductivity (mS/cm)	Temp. (°C)	Alkalinity (mg/L)	Hardness (mg/L)	BOD ₅ (mg/L)	Sulfate Conc. (mg/L)	COD (mg/L)	TSS (mg/L)	TDS (mg/L)	Chloride Conc. (mg/L)
Equil. Basin	7.41	8.30	37.82	26	360	10800	8.3	ND	NA	31.2	28708	20000
O/W Sep.	7.15	7.81	33.5	23	260	10000	7.81	ND	NA	5.7	25928	20000
S-1 Outflow	7.00	7.89	28.74	20	260	8400	7.89	ND	NA	12.1	21517	15000
S-2 Outflow	6.81	4.02	26.46	20	220	7600	2.91	ND	NA	8.6	20740	15000
RO Outflow	5.57	8.05	0.281	20	4	6	0.87	ND	NA	1	174	115
1-A Inflow	6.59	9.15	0.176	21	2	16	0.85	ND	3.83	0.1	218	71
2-A Inflow	6.42	9.06	0.176	21	4	16	0.8	ND	7.37	0.2	211	52
1-A Outflow	7.11	10.23	0.248	22	12	38	1.43	ND	8.79	ND	154	83
2-A Outflow	7.12	10.52	0.254	22	12	42	0.96	ND	10.91	ND	162	86
1-B Outflow	7.13	9.42	0.298	21	20	64	1.34	ND	10.20	2.9	181	82
2-B Outflow	7.22	9.27	0.401	21	24	102	1.85	ND	10.91	4.6	252	92
1-C Outflow	7.38	11.64	0.324	21	18	68	3.7	ND	12.33	6.2	202	93
2-C Outflow	7.57	12.15	0.439	21	22	106	4.16	19.11	11.62	8.1	314	103
1-D Outflow	7.41	13.36	0.399	20	18	72	9.39	ND	15.87	11.1	212	92
2-D Outflow	7.41	13.21	0.473	20	22	100	10.05	23.56	18.71	27.5	284	115

*ND: Non-Detect.

*NA: Not Available

Table 6: General Water Chemistry Results for Experiment 3: Batch 2 (Simulated Saline Produced Water).

Sample	pH	DO (mg/L)	Conductivity (mS/cm)	Temp. (°C)	Alkalinity (mg/L)	Hardness (mg/L)	BOD ₅ (mg/L)	Sulfate Conc. (mg/L)	COD (mg/L)	TSS (mg/L)	TDS (mg/L)	Chloride Conc. (mg/L)
Equil. Basin	7.25	8.65	45.20	27.5	22	9000	0.24	18.00	NA	120.75	32811.5	20000
O/W Sep.	7.29	8.92	44.60	21.2	32	11000	0.69	17.69	NA	103.65	32568.5	20000
S-1 Outflow	6.64	7.61	43.30	25.0	30	11000	2.32	18.13	NA	356.65	33047.5	20000
S-2 Outflow	6.72	7.72	43.96	22.2	32	11000	1.10	15.34	NA	64.65	33329.5	20000
1-A Inflow	4.32	8.46	0.2646	26.1	0	14	0.46	ND	ND	51.05	188.5	101
2-A Inflow	5.24	8.34	0.2571	24.0	2	16	0.35	ND	ND	54.75	172.5	98
1-A Outflow	6.99	7.09	0.588	23.3	14	82	0.46	14.56	ND	56.75	406.5	156
2-A Outflow	7.31	6.95	0.602	23.8	12	94	1.20	21.13	ND	55.85	363.5	167
1-B Outflow	7.25	8.03	0.554	23.7	16	104	1.06	27.53	ND	55.05	335.5	153
2-B Outflow	7.21	7.80	0.724	25.3	30	148	1.86	49.25	ND	56.45	441.5	181
1-C Outflow	7.37	8.76	0.554	25.3	20	92	1.90	27.84	ND	56.15	325.5	154
2-C Outflow	6.87	8.19	0.698	26.1	26	132	7.95	49.56	ND	68.75	430.5	180
1-D Outflow	7.22	6.96	0.597	27.2	22	104	2.17	30.03	ND	59.35	368.5	255
2-D Outflow	7.15	6.89	0.744	27.2	20	140	5.32	53.94	ND	63.65	460.5	182

*ND: Non-Detect.

*NA: Not Available

Table 7: General Water Chemistry Results for Experiment 4: Batch 1 (Simulated Hyper-Saline Produced Water).

Sample	pH	DO (mg/L)	Conductivity (mS/cm)	Temperature (°C)	Alkalinity (mg/L)	Hardness (mg/L)	BOD ₅ (mg/L)	Sulfate Conc. (mg/L)	COD (mg/L)	TSS (mg/L)	TDS (mg/L)	Chloride Conc. (mg/L)
Equil. Basin	7.41	7.40	87.7	23.2	42	12000	1.22	44.78	NA	53.55	86726	50000
O/W Sep.	7.38	7.47	81.8	23.2	34	20800	0.15	40.07	NA	6.85	71808	45000
S-1 Outflow	6.55	4.55	69.8	26.2	26	19600	1.15	32.57	NA	7.55	59766	40000
S-2 Outflow	6.40	5.16	70.7	27.7	30	19200	1.75	33.31	NA	14.25	60917	40000
RO Outflow	5.75	7.45	0.975	22.3	ND	ND	ND	ND	NA	2.75	1106	356
1-A Inflow	6.50	8.15	0.725	26.8	6	30	0.37	ND	ND	0.65	444	266
2-A Inflow	6.68	8.16	0.720	27.4	2	30	0.30	ND	ND	1.65	434	262
1-A Outflow	7.22	7.01	0.739	26.3	28	100	6.88	31.54	ND	1.75	507	234
2-A Outflow	7.32	9.93	0.758	27.4	20	94	8.44	17.72	ND	ND	500	236
1-B Outflow	7.26	6.51	0.719	25.4	32	96	5.26	29.63	ND	4.75	511	214
2-B Outflow	7.44	6.05	0.825	27.0	38	132	3.66	38.01	ND	1.75	596	224
1-C Outflow	7.29	6.47	0.665	24.8	32	104	1.44	27.87	ND	5.95	483	195
2-C Outflow	7.54	6.15	0.785	24.9	36	124	1.23	35.81	ND	2.05	599	222
1-D Outflow	7.14	6.44	0.644	26.5	32	96	1.92	25.51	ND	5.05	677	189
2-D Outflow	7.51	7.65	0.736	29.2	34	120	0.95	32.28	ND	1.45	567	205

*ND: Non-Detect.

*NA: Not Available

Table 8: General Water Chemistry Results for Experiment 4: Batch 2 (Simulated Hyper-Saline Produced Water).

								Sulfate				Chloride
Sample	pH	DO (mg/L)	Conductivity (mS/cm)	Temp. (°C)	Alkalinity (mg/L)	Hardness (mg/L)	BOD5 (mg/L)	Conc. (mg/L)	COD (mg/L)	TSS (mg/L)	TDS (mg/L)	Conc. (mg/L)
Equil. Basin	7.61	5.21	99.60	22.3	74	21200	ND	54.01	NA	76.55	82678	50000
O/W Sep.	7.50	6.61	97.40	26.7	34	24000	0.24	49.79	NA	11.75	76606	45000
S-1 Outflow	6.92	7.76	97.00	21.5	32	23600	0.35	45.14	NA	28.05	78150	50000
S-2 Outflow	6.69	6.48	97.20	28.7	30	25600	ND	39.37	NA	41.25	79991	45000
RO Out	6.36	9.26	1.73	21.0	6	28	NA	ND	NA	ND	1390	NA
1-A Inflow	5.41	7.51	0.954	29.0	4	18	1.10	ND	6.80	0.55	545	373
2-A Inflow	5.43	7.50	0.954	29.8	4	20	1.09	ND	6.30	4.05	500	341
1-A Outflow	6.98	5.24	0.831	28.5	14	58	0.87	ND	6.30	0.25	523	417
2-A Outflow	7.28	5.39	0.858	29.1	16	60	1.03	4.58	6.80	1.75	537	287
1-B Outflow	7.25	6.84	0.843	27.2	22	66	1.52	1.90	6.80	2.05	543	253
2-B Outflow	7.17	6.03	0.906	27.8	28	86	0.91	10.49	7.30	2.85	585	266
1-C Outflow	7.09	5.87	0.96	27.3	20	70	0.49	1.48	7.30	3.45	616	318
2-C Outflow	7.23	5.79	1.013	28.3	12	86	1.74	9.51	7.30	3.15	646	301
1-D Outflow	7.30	7.80	0.932	27.3	28	72	1.57	2.75	7.80	4.15	608	295
2-D Outflow	7.59	8.17	1.00	27.7	4	86	1.58	9.37	7.80	4.25	670	320

*ND: Non-Detect.

*NA: Not Available

Table 9: General Water Chemistry Results for Simulated Brackish Produced Water II.

		DO	Conductivity	Temp.	Alkalinity	Hardness	BOD5	Sulfate	COD	TSS	TDS	Chloride
Sample	pH	(mg/L)	(mS/cm)	(°C)	(mg/L)	(mg/L)	(mg/L)	Conc.	(mg/L)	(mg/L)	(mg/L)	Conc.
								(mg/L)				(mg/L)
Equil. Basin	8.03	5.21	9.97	22.3	20	1600	1.82	7.46	30.00	5.7667	5921	3500
O/W Sep.	7.33	6.61	10.80	22.2	20	1500	1.68	6.16	35.00	0.6667	5998	3675
1-A Inflow	7.08	7.51	9.48	22.4	18	1600	1.17	11.74	30.00	3.2667	6068	3950
2-A Inflow	7.05	7.50	9.35	22.6	20	1500	0.98	7.75	30.00	2.1667	6182	3600
1-A Outflow	7.08	5.24	9.71	55.6	20	1500	1.17	7.90	45.00	2.7667	6195	3725
2-A Outflow	6.95	5.39	8.51	22.6	18	1100	1.01	7.32	75.00	5.7667	6136	3500
1-B Outflow	6.78	6.84	8.94	21.8	22	1600	2.60	9.78	55.00	7.0667	6465	3600
2-B Outflow	6.98	6.03	9.38	22.2	26	1700	1.47	17.32	55.00	6.0667	7026	3825
1-C Outflow	7.40	5.87	10.45	22.6	28	1800	1.50	20.94	15.00	3.4667	7032	3950
2-C Outflow	7.30	5.79	10.11	22.5	22	2000	1.10	17.03	15.00	3.4667	7008	3975
1-D Outflow	7.16	7.80	9.91	22.3	28	1900	2.42	19.49	20.00	2.7667	7355	3950
2-D Outflow	7.09	8.17	9.97	22.2	26	1900	1.02	20.36	15.00	2.7667	7309	3950

Appendix E
2004, Real-Time Wellbore Integrity Monitoring,
Colorado School of Mines Final Report

Real-time Wellbore Integrity Monitoring

FINAL Report

Reporting Period Start Date: September 1, 2004
Reporting Period End Date: December 31, 2005

Principal Author:
Professor L. G. Chorn

Issue Date: May, 2006

DOE Award Number:
2809-CSM-DOE-1779

Colorado School of Mines
Department of Petroleum Engineering
1500 Illinois Street
Golden, CO 80401

Subcontractor:
WellDynamics Inc.
445 Woodline Drive
Spring, Texas 77386

DISCLAIMER:

“This report was prepared as an account of work sponsored by an agency of the United States Government. Neither the United States Government nor any agency thereof, nor any of their employees, makes any warranty, express or implied, or assumes any legal liability or responsibility for the accuracy, completeness, or usefulness of any information, apparatus, product, or process disclosed, or represents that its use would not infringe privately owned rights. Reference not necessarily constitute or imply its endorsement, recommendation, or favoring by the United States Government or any agency thereof. The views and opinions of authors expressed herein do not necessarily state or reflect those of the United States Government or any agency thereof.”

Abstract

This report describes the work done under DOE Award Number 2809-CSM-DOE-1779, for the Gas Storage Technology Consortium during the period from October 1, 2004 through December 31, 2005, addressing the application of continuous pressure and temperature monitoring hardware to assess the integrity of tubing and casing in wells linking reservoirs used for natural gas storage with surface facilities.

The principal investigator, a graduate student, and representatives of WellDynamics, Inc performed the work described in this report. Successful results were achieved in the following subtasks:

- Compute and validate the theoretical pressure drop in a flowing wellbore during production operations, if the wellbore has pressure integrity, using OLGA™, a multiphase flow simulator.
- Acquire data sets (different wellbore architectures, reservoir conditions, and flow rates) from gas storage field operators to calibrate a multiphase flow model using Dun and Ros correlations for dry gas vertical flow.
- Develop a database of simulation results for use in model development leading to a nomograph for tubing integrity.
- Modify OLGA™ to predict flowing tubing pressure losses in vertical and deviated wellbores for a range of perforation sizes, tubing diameters, flow rates, gas compositions, and wellhead temperatures and pressures.
- Develop a nomograph for field operators to use pressure/temperature/flow rate data to evaluate tubing integrity.
- Identify suitable hardware for real time data acquisition.

Based on the results of these subtasks, it is clear that gas storage field operators may use this approach to monitor wellbore integrity in some architectures above a threshold flow rate.

Unsatisfactory results were obtained for the following subtasks:

- Identification of a suitable sensor hardware assembly with a low drift rate for permanent installation.

Based on the outcome of this subtask, gas storage field operators will not be able to permanently install pressure/temperature sensors at bottomhole to apply these results. Sensors may be run-in on a wireline to acquire an instantaneous measurement for integrity analysis.

Details of the research are provided in the body of the report.

Table of Contents

Abstract.....	3
Computational Work.....	7
Background.....	7
No-Leak Nomograph Development.....	8
OLGA™ calculations.....	12
Effect of Perforation(s) on Wellbore Pressure Profile.....	12
Using OLGA™ to Calculate Effect of Tubing Perforations on Wellbore Pressure Losses.....	13
Field Data Set Acquisition.....	15
Description of Field Data.....	15
Hardware testing.....	16
Results.....	18
Computational.....	18
Hardware.....	23
Electronics.....	23
Sensor Drift Testing.....	23
Interpretation of Results.....	25
Summary.....	26

List of Graphical Materials

Figure 1. Fraction of flowing tubing pressure loss associated with gravity head, as a function of flow rate and wellhead pressure	10
Figure 2. Effect of wellhead flow rate on OLGA –predicted wellhead temperature (R)	12
Figure 3. Maximum gas loss through a perforation at 100 feet (overburden pressure = 60 psi) given a perforation diameter (y-axis) and local tubing pressure (x-axis)	13
Figure 4. Maximum gas loss through a perforation at 250 feet (overburden pressure = 150 psi) given a perforation diameter (y-axis) and local tubing pressure (x-axis)	13
Figure 5. Solidworks™ layout drawing illustrating the clamp-on style low cost monitoring mandrel	16
Figure 6. Example of error in computed versus measured pressure drop as a function of gas flow rate	18
Figure 7. Frictional and leak pressure losses as a function of wellhead Reynolds number for a 0.25-inch diameter perforation at 100 feet below the wellhead	19
Figure 8. Frictional and leak pressure losses as a function of wellhead Reynolds	

number for a 0.5-inch diameter perforation at 100 feet below the wellhead	19
Figure 9. Frictional and leak pressure losses as a function of wellhead Reynolds number for a 0.75-inch diameter perforation at 100 feet below the wellhead	20
Figure 10. Frictional and leak pressure losses as a function of wellhead Reynolds number for a 1.00-inch diameter perforation at 100 feet below the wellhead	20
Figure 11. Effect of perforation size on pressure loss in a 6.336-inch diameter wellbore	21
Figure 12. Effect of perforation on frictional pressure drop in a 2.441-inch diameter tubing	21
Figure 13. Effect of perforation diameter in a 2.441-inch tubing on pressure loss ...	22
Figure 14. Effect of perforation diameter in a 2.441-inch tubing as a function of tubing pressure	22
Figure 15. Downhole pressure/temperature electronics package	23
Figure 16. Schematic diagram of piezo-resistive sensor	24
Figure 17. Histogram of pressure residuals collected for the sensor calibration test Indicating significant drift of the piezo-resistive unit	25

List of Tables

Table 1. Gas Composition for simulations (based on a gas composition provided by a GSTC member)	15
Table 2. Field data parameter ranges	16
Table 3. Outline specifications for low cost monitoring unit	16
Table 4. Threshold parameter values for detection of tubing perforations in gas wells via pressure drop measurements	26

Introduction

Mechanical failures, water-loading, scale deposition and sand production in wellbore tubulars in long-lived natural gas storage reservoirs and salt domes represents a loss of efficiency in injection and withdrawal. Wellbore reliability is a priority for operators and state regulators.

The underground natural gas storage industry has an outstanding safety record and is striving to maintain its record by seeking out new, comprehensive methods to monitor tubular status. Testing presently requires extended shut-ins of wells and reservoirs to stabilize the system and then monitor the wellhead pressure; or running a wellbore caliber tool in the wellbore. Both of these techniques are expensive and subject to inaccurate results.

Conveniently, the petroleum industry has recently experienced dramatic advances in wellbore monitoring and flow control through the linkage of sensors at the reservoir – wellbore interface with remotely actuated valves. The sensors provide real-time data (pressure, temperature, fluid property, and flow rate) to the operator who can adjust subsurface valve settings to control oil, gas, and water influx to the well. “Downhole” sensors have longevity and reliability in high temperature, high pressure, and corrosive environments. Drift in absolute measurement value remains problematic. The ability to observe conditions in the wellbore with relatively inexpensive sensors offers the underground gas storage operator the tool to monitor the reservoir-to-surface link and demonstrate system reliability. Efficient wellbore performance is demonstrated by matching predicted “no-leak” pressure differentials between the wellhead and the formation to measured data.

Application of this technology to the natural gas storage industry’s wellbore management issue requires the following technology advances:

- a non-isothermal transient flow gas well model with compositional phase behavior to predict pressure and temperature profiles between the well perforations and the wellhead under different flow rates;
- testing of downhole flow sensors (P and T) for their differential measurement sensitivity.

This research program delivers a predictive analysis tool to the Gas Storage industry that allows low cost, reliable testing capabilities.

Computational Work

Background

As part of the cost share structure of the research program Scandpower provided a limited license for the use of OLGA™, a multiphase tubing flow simulator with heat transfer and fluid property calculation capability. OLGA™ is the industry standard flow simulation tool developed collaboratively by Scandpower and several members of the international petroleum industry, using extensive databases of flowing well conditions.

OLGA™ was installed on a single user Windows operating system computer with a 1.2 Megahertz processor and 512K memory. Mr. Ryan London, M.S. candidate in Petroleum Engineering, began testing the software with example problems provided by Scandpower. A member of Scandpower's technical staff visited Colorado School of Mines and provided a brief user introduction session for Mr. London and the PI.

The simulator is designed to handle two and three-phase flow conditions in vertical and horizontal tubing configurations. One-dimensional, multiphase flow regimes accurately represented in OLGA™ include mist, annular, wavy, and slug flows for hydrocarbon and aqueous liquid phases flowing simultaneously with natural gas. The computational scheme subdivides the tubular along the axis of flow into segments and solves for pressure, temperature, phase velocities, and phase saturations. Heat transfer and phase properties are modeled at each time step along the tubular axis. The user can subdivide the tubular as finely or grossly as desired, but finer gridding results in dramatic increases in computation time.

Conservation of mass and momentum equations are solved using an analytic structure described by Ansara, A.M., et al¹,

$$-\left[\frac{dp}{dz}\right]_c = \left[\frac{g\rho_c}{g_c} + \frac{f_c V_c^2 \rho_c}{2g_c d(1-2\delta)}\right]$$

$$-\left[\frac{dp}{dz}\right]_l = \left[\frac{g\rho_l}{g_c} + \frac{2f_{lF} V_{sl}^2 (1-E)^2 \rho_l}{64g_c d \delta^3 (1-2\delta)^3} - \frac{f_c V_c^2 (1-2\delta) \rho_c}{2g_c d \delta (1-\delta)}\right]$$

where variable nomenclature is standard for fluid dynamics. Subscripts refer to phases in the tubular. OLGA™ solves these simultaneous equations sequentially up the wellbore to forecast wellhead pressure and temperature.

Prediction of gas density and viscosities are required to predict pressure loss per unit distance. Both gas properties vary with temperature and pressure. As a consequence, any wellbore

¹ Ansara, A.M., et al¹, "A Comprehensive Mechanistic Model For Upward Two-Phase Flow in Wellbores," SPEPF, (1994).

modeling attempt requires property correlations or an equation of state. Accuracy in the density prediction is particularly critical to the successful pressure loss calculation.

No-Leak Nomograph Development

OLGA™ is a valuable modeling tool but represents a very large investment for gas storage operators. As a consequence, one goal for this project was the development of a simple, yet accurate vertical gas flow simulation tool. Mr. London developed a Visual Basic program that utilized the Duns and Ros Method to predict pressure gradient in a flowing well. The Basic program was fine-tuned against OLGA™ predictions over a wide variety of wellbore architecture and flow rate combinations.

The London program uses standard relationships for estimating fluid properties and multiphase flow relationships, as described below.

For fluid properties estimation, the user has the option of entering gas composition, specific gravity, or specific gravity and pseudo-critical properties. The molecular weight, if given specific gravity, is:

$$MW = 28.964 * \text{specific gravity} \quad (1)$$

Pseudo-critical temperature and pressure are:

$$T_{PC} = 169.2 + (349.5 * \text{specific gravity}) - (74 * \text{specific gravity}^2) \quad (2)$$

$$P_{PC} = 756.8 - 131 * \text{specific gravity} - 3.6 * \text{specific gravity}^2 \quad (3)$$

Reduced pseudo-critical properties are computed by dividing wellhead temperature and pressure by T_{PR} and P_{PR} , respectively.

The gas Z-factor must be computed by iteration. The initial Z_{guess} is set to one and the iteration proceeds as follows:

$$\rho_{PR} = (0.27 * P_{PR}) / (T_{PR} * Z_{\text{guess}}) \quad (5)$$

$$Z = 1 + C_1 * \rho_{PR} + C_2 * \rho_{PR}^2 - C_3 * \rho_{PR}^5 + C_4$$

where :

$$C_1 = 0.3265 - 1.07 / T_{PR} - 0.5339 / T_{PR}^3 + 0.01569 / T_{PR}^4 - 0.05165 / T_{PR}^5 \quad (6)$$

$$C_2 = 0.5475 - 0.7361 / T_{PR} + 0.1844 / T_{PR}^2$$

$$C_3 = 0.1056 * (-0.7361 / T_{PR} + 0.1844 / T_{PR}^2)$$

$$C_4 = 0.6134 * (1 + 0.721 * \rho_{PR}^2) * \rho_{PR}^2 / T_{PR}^3 * e^{(-0.721 * \rho_{PR}^2)}$$

This calculation proceeds until a tolerance of 10^{-5} is reached.

Viscosities and densities are computed from the following relationships:

$$\mu = 1. * 10^{-4} * K * e^{(X * rho^Y)}$$

where :

$$K = (9.379 + 0.01607 * MW) / (209.2 + 19.26 * MW + T_{WH}) * T_{WH}^{1.5} \quad (7)$$

$$X = 3.448 + (986.4 / T_{WH}) + 0.01009 * MW$$

$$Y = 2.447 - 0.224 * X$$

$$rho = 1.4935 * 10^{-3} * P_{WH} * MW / (Z * T_{WH})$$

$$\rho = 144 / 1545 * P_{WH} * MW / (Z * T_{WH}) \quad (8)$$

Confirmation of the consistency of the London program with the results of the more robust OLGATM program provides the gas storage operator with a predictive tool appropriate for withdrawal operation monitoring in a wellbore with no thru-tubing leaks.

By applying the principles of conservation of mass and linear momentum, the steady-state pressure gradient equation is:

$$\left(\frac{dp}{dL} \right)_{total} = \left(\frac{dp}{dL} \right)_{friction} + \left(\frac{dp}{dL} \right)_{hydrostatic} + \left(\frac{dp}{dL} \right)_{acceleration} \quad (9)$$

The acceleration term can be neglected at higher pressures so the last term on the right hand side of equation (1) can be discarded. Given that measurements take place only at the sand face and the wellhead, we will assume an average pressure difference between the two points can be described as:

$$(\Delta p)_{total} = (\Delta p)_{friction} + (\Delta p)_{hydrostatic} \quad (10)$$

where:

$$(\Delta p)_{total} = (p_{bh} - p_{wh})$$

$$(\Delta p)_{friction} = \frac{f \rho L V^2}{D}$$

$$(\Delta p)_{hydrostatic} = \rho g h$$

The density and velocity terms can be accurately calculated from the pressure, temperature, flowrate and pipe characteristics leaving the friction factor the only unknown. There is one equation, and one unknown:

$$\begin{aligned}
(\Delta p)_{friction} &= (\Delta p)_{total} - (\Delta p)_{hydrostatic} \\
(\Delta p)_{friction} &= (p_{bh} - p_{wh}) - \rho gh \\
\frac{f\rho LV^2}{D} &= (p_{bh} - p_{wh}) - \rho gh \\
f_{Method1} &= \frac{[(p_{bh} - p_{wh}) - \rho gh]D}{\rho LV^2}
\end{aligned} \tag{11}$$

This calculation for friction factor assumes that the friction pressure loss term is responsible for all pressure loss remaining after the elevation pressure loss term is accounted for. This term is the average friction factor throughout the length of the pipe at steady state conditions.

Next, the friction factor will be calculated through correlations that approximate the Moody friction factor diagram.

$$\begin{aligned}
f &= f(N_{Re}, \frac{\varepsilon}{D}) \\
N_{Re} &= \frac{\rho DV}{\mu} \\
\rho &= f(p, M_w, z, T) \\
z &= f(p, M_w, T) \\
V &= f(p, Q, D, T) \\
\mu &= f(\rho, M_w, T)
\end{aligned} \tag{12}$$

Therefore, the friction factor is a function of the following variables:

$$f_{Method2} = f(p, T, \varepsilon, D, M_w) \tag{13}$$

If the friction factor calculated using equation (11) is plotted versus the equation (13) approach, the result should be a straight line, the only deviation should be due to averaging, heat losses, and small contributions from the neglected acceleration term.

When a leak does occur, the value for friction factor in Method 1 will rise and be disproportionate to the value for friction factor in Method 2 because of how Method 1 calculates the friction factor. If a leak occurs, the individual pressure components will be:

$$(\Delta p)_{total} = (\Delta p)_{friction} + (\Delta p)_{hydrostatic} + (\Delta p)_{leak} \tag{14}$$

However, equation (11) will still calculate the friction factor based upon:

$$(\Delta p)_{friction} = (\Delta p)_{total} - (\Delta p)_{hydrostatic} \tag{15}$$

Thus, the total pressure drop will increase because of the leak, and Method 1 will errantly allocate the additional pressure drop to the friction term, thereby making the friction factor larger. However, Method 2 relies solely on the value of the pressure and temperature (instead of the difference) and will still be able to successfully calculate the correct friction factor. If Method 1 is

plotted against Method 2 and the points begin to bend upward, the numerical model will have successfully indicated to the operator that a leak has occurred.

The ultimate purpose of modeling the tubing flow regime and fluid properties is to determine the appropriate magnitude of pressure loss associated with frictional losses in the tubing. Frictional losses present themselves as a pressure loss. The pressure difference between the wellhead and the reservoir is a combination of the change in gravity head and the frictional losses. Gravity head calculation is sensitive to the aggregate density of the column of fluid loading the wellbore and exerting a pressure, ρgh , on the bottom of the well, at the reservoir interface. Because we are concerned with a gas-dominated flow, the frictional pressure loss will be quite low. The gravity head as shown in Figure 1 dominates the pressure difference between the wellhead and the reservoir for a dry gas flow. Figure 1 illustrates the magnitude of the gravity head contribution to the pressure difference as a function of wellhead flow rate and wellhead pressure. Wellhead pressure is a proxy for the relative density of the fluid column, assuming temperature gradient and fluid composition (gas and water weight fractions) are held constant.

As expected, the contribution of the frictional losses to the pressure difference is small, ranging from 10 to 35 percent for the field data examined. Any modeling of the wellbore must exhibit accurate density calculations for the fluid column. The addition of water to the gas phase, as a mist, will increase the column density. Data contributed by GSTC members showed only low water fractions, less than a few pounds of water per million standard cubic feet of gas. While gas density can change significantly with pressure and temperature, water density is relatively constant. Consequently, the wellbore flow model calculations assume only the aggregate density based on the weight fraction of water at wellhead conditions plus weight fraction of the gas phase times the empirical relationship for gas density as a function of pressure and temperature.

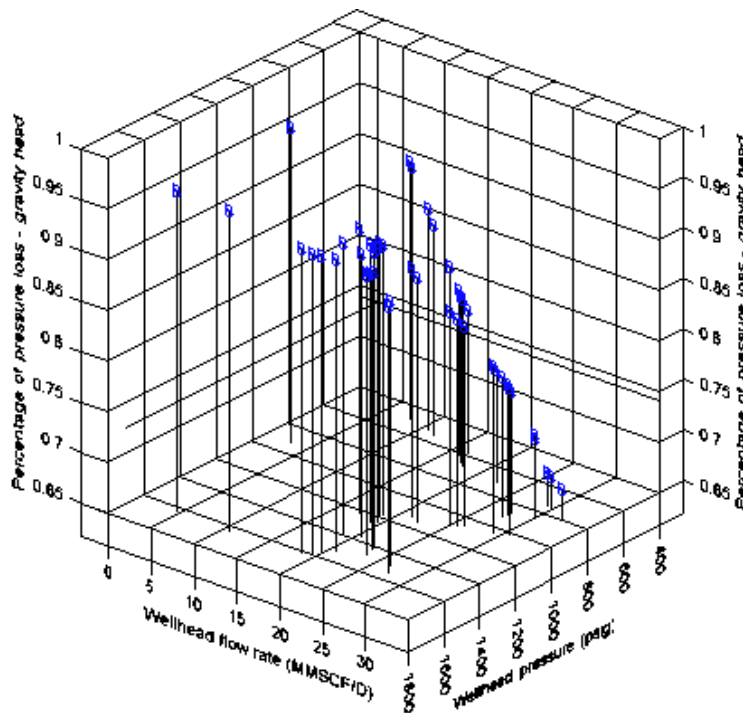


Figure 1. Fraction of flowing tubing pressure loss associated with gravity head, as a function of flow rate and wellhead pressure.

OLGA™ calculations

OLGA™ calculates the flow field profile from the bottom-hole conditions to the surface over small length steps. At each incremental length, coming up the tubing string, new temperature, pressure and fluid properties are computed which reflect volume changes of the gas/water mixture. The user must estimate heat transfer properties of the wellbore in addition to the geothermal gradient. Further, the relative surface roughness of the tubing must be estimated. The combination of these estimates provides for some fine-tuning latitude to match field measurements with computed values.

Figure 2 illustrates the effect of heat transfer and geothermal gradient estimates on the prediction. OLGA™ was run on a field data set with a measured bottomhole temperature of 568 °R and a measured wellhead temperature of 530 °R. The x-axis is the measured wellhead flow rate in MMSCF per day and the y-axis is the OLGA™-computed wellhead temperature. Three wellhead pressures are shown. A perfect agreement between measured and computed would result in a straight-line with a 0° slope at 530°R. The impact of this inaccuracy will be seen in the fluid properties and ultimately in the calculation of the gravity head, ρgh . This causes a limitation in the detection limit of a perforation at low tubing pressures.

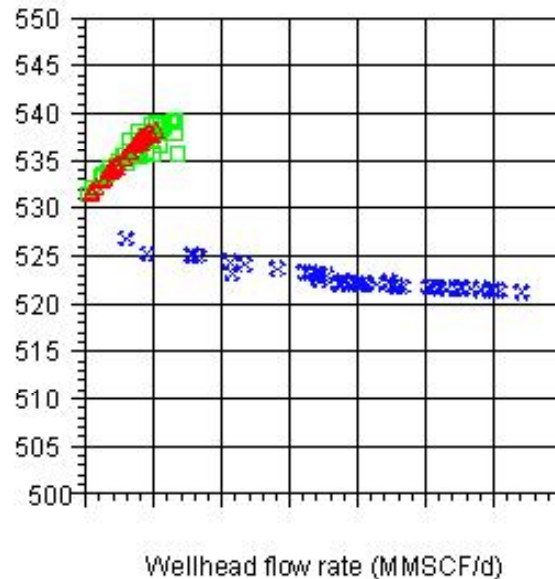


Figure 2. Effect of wellhead flow rate on Olga™-predicted wellhead temperature (°R).

Effect of Perforation(s) on Wellbore Pressure Profile

Small perforations or holes in the tubing will allow the release of gas into shallower zones above the reservoir. The loss of gas volume through the perforation will cause a non-linear pressure decrease in the tubing, deceleration and Joule-Thompson cooling of the gas flow field above the perforation, resulting in a lowered gas pressure at the wellhead.

The amount of gas released to the overburden is a function of tubing pressure, temperature, depth of the perforation (backpressure against outflow), and perforation diameter. There are no known theoretical approaches to estimate the gas flow rate through a perforation. Consequently an attempt was made to estimate the maximum volumetric loss rate using a simple orifice equation. This approach will over-estimate the loss rate since it assumes the orifice is in-line with the principle direction of flow, rather than at a 90° angle to the flow as with a perforation.

The equation² for orifice flow is:

$$Q = C_c A_o \sqrt{\frac{2\Delta p / \rho}{\left(1 - C_c^2 \left(\frac{A_o}{A}\right)^2\right)}}$$

$$C_c = 0.595 + 0.29 \left(\frac{A_o}{A}\right)^{2.5} \quad (16)$$

Examples of the volumetric loss rate, in SCFD, are shown in Figures 3 and 4 for representative tubing diameters, perforation sizes, and wellbore pressures at 100 and 250 feet deep locations. The results of the calculation indicate relatively low gas volumes per day will be lost under conditions typically observed under conditions commonly observed during withdrawal. However, over time, a shallow zone can be significantly pressured up with the “lost” gas resulting in migration updip and potentially release to the surface either through fractures or outcrops.

Using OLGA™ to Calculate Effect of Tubing Perforations on Wellbore Pressure Losses

The present release of OLGA™ incorporates an option to compute the effect of cross-flow between two zones. The option provides the ability to locate the zones vertically, set the size and number of perforations in each zone, and the pressures in the zones.

This option was used to simulate the effect of a tubing perforation near the surface, i.e., at a low backpressure. The depth of the tubing perforation fixes the backpressure by assuming a pressure gradient of 0.6 psi/ft.

One perforation in the tubing was assumed and the flow field computed. Six perforation diameters were considered (0.0625, 0.125, 0.25, 0.5, 0.75 and 1.0 inches) in the study. A matrix of results were compiled, including: bottomhole pressure and temperature, wellhead temperature and pressure, and bottomhole and wellhead flowrates for various wellbore architectures. A single gas composition was used for all simulations. The composition is shown in Table 1.

² E. Shashi Menon, Gas Pipeline Hydraulics, Taylor and Francis Publishers (2005).

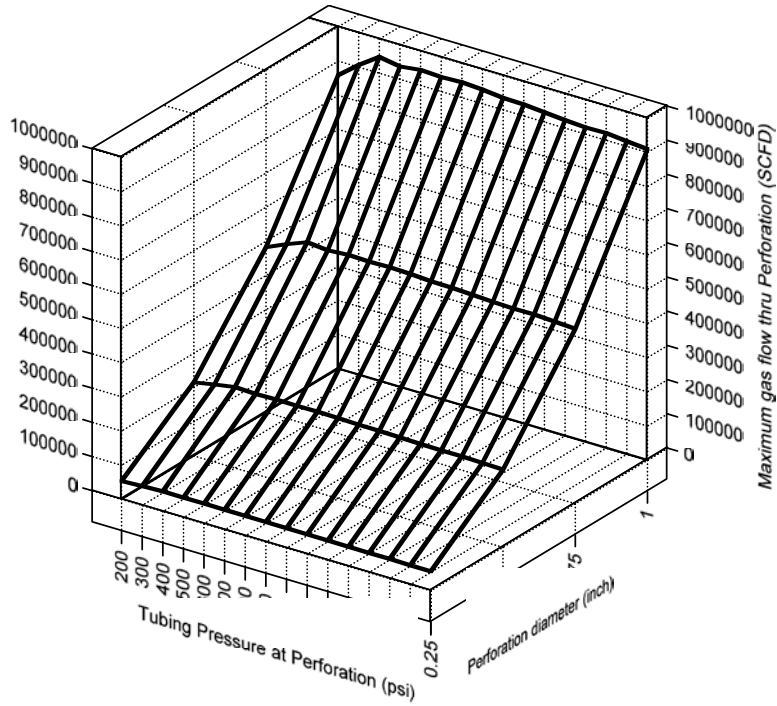


Figure 2. Maximum gas loss through a perforation at 100 feet (overburden pressure = 60 psi) given a perforation diameter (y-axis) and local tubing pressure (x-axis).

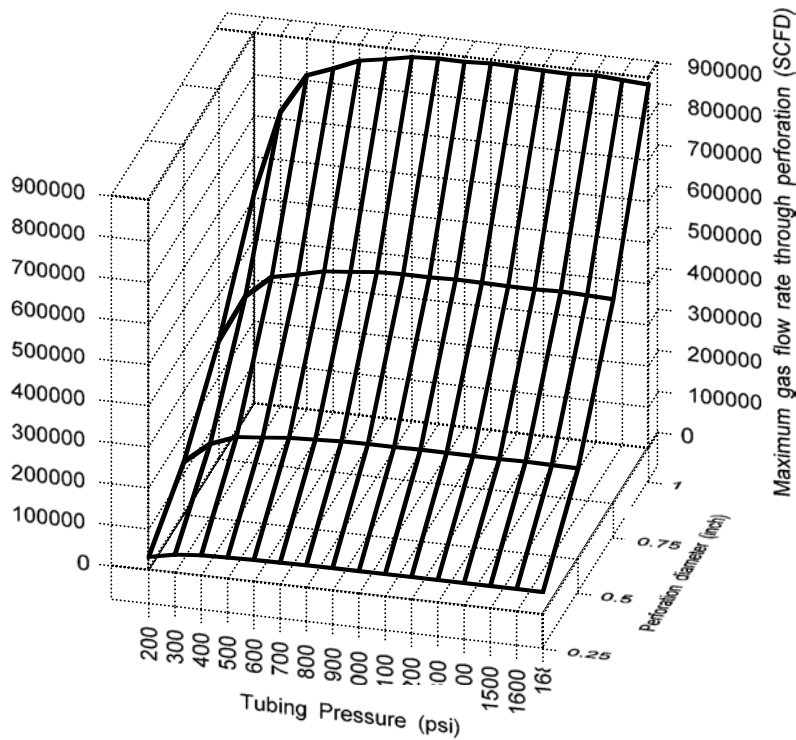


Figure 3. Maximum gas loss through a perforation at 250 feet (overburden pressure = 150 psi), given a perforation diameter (y-axis) and local tubing pressure (x-axis).

Gas Component	Mole Percent Composition
Carbon Dioxide	0.7095
Nitrogen	0.9105
Methane	95.6709
Ethane	2.3638
Propane	0.2499
n-Butane	0.0482
i-Butane	0.031
n-Pentane	0.0069
i-Pentane	0.007
n-Hexane	0.0023

Table 1. Gas Composition for simulations (based on a gas composition provided by a GSTC member)

Field Data Set Acquisition

Members of the Gas Storage Technology Consortium (GSTC) anonymously provided six data sets that were used for simulator calibration and to establish autoclave test conditions for the pressure and temperature sensor package.

The data sets contain hourly surface temperature, pressure and flow rate data over periods from as short as six months to as long as nine years. Reservoir temperatures and pressures are included in the data sets as measured in a shut-in observation well some distance from the well under study.

Description of Field Data

The following table gives the range of parameters within the six data sets.

	Minimum	Maximum
Wellhead tubing diameter	2.041 in	6.366 in
Bottom-hole tubing diameter	2.041 in	7.00 in
Wellhead temperature	530 °R	530 °R
Bottom-hole temperature	530 °R	590 °R
Liquid-Gas ratio (STB/SCF)	0.00	5×10^{-7} (20 lbs/MMSCF)
Wellhead pressure	315 psig	1855 psig
Bottom-hole pressure	349 psig	2084 psig
Measured delta p	33 psig	568 psig
Flow rate (MMSCF/day)	0.279	60.7

Table 2. Field data parameter ranges

All data and calculated results are reported in American engineering units (inches, °R, psig, MMSCF/day, feet/sec, ft/sec, stock tank barrels/standard cubic feet, lb_m/ft^3 , etc.).

Data included 76 measurements with non-zero Gas-Liquid ratios. Analysis indicates that mist flow is the likely flow regime for these two-phase flow situations, but at these low liquid to gas

ratios the presence of water is inconsequential to the pressure loss calculations. Consequently, all OLGA™ simulations were performed with a zero water fraction.

Hardware testing

Research staff at WellDynamics, Inc. developed a qualification program in context with the objectives set out in the research proposal. The basic specifications for the new monitoring system are presented below.

ITEM	DESCRIPTION
Size:	3 ½” and 2 7/8” tubing compatible
Multi-Drop Capability:	6 x Dual
Data Rate:	2 gauges per second
Operating Voltage:	24.0 + 4.0/-12.0 VDC
Operating Temperature:	0° to 125° C, limit 150C
Temperature Accuracy:	± 1° C
Temperature Drift:	< 2° C/year
Pressure Range:	10,000 psi
Pressure Accuracy:	± 0.1% full scale
Pressure Resolution:	< 0.5 psi
Pressure Drift:	< 5.0 psi/year @100° C

Table 3. Outline specifications for low cost monitoring unit

The testing program was designed to address the following critical milestones for the low cost monitoring project;

- To complete the packaging concept for a dual pressure and temperature monitoring unit, with the ability to multi-drop these units in wells with multiple zones,
- Successfully complete a long term test at full rated temperature on the downhole electronics board, and
- Successfully verify the performance of a select piezo-resistive pressure transducer as a replacement to the high cost quartz sensors used in the offshore markets.

Following completion of the final packaging concept, a bench assembly of a fully populated mandrel assembly was executed with several minor design changes. These design changes were largely associated with the chassis and housing for the electronics that required some dimensional adjustment based on minor size discrepancies for the electronic components.

The production drawings were updated following the prototype assembly and new production builds were executed for the start of the full prototype qualification phase as per WellDynamics internal standards for pressure, temperature and vibration.

The production unit is shown in Figure 4, detailing a clamp-on style mandrel with 2 pressure sensors, electrical bus connections (in and out) and a 3rd electrical connection for a position sensor gauge (in wells where flow control systems may be run).

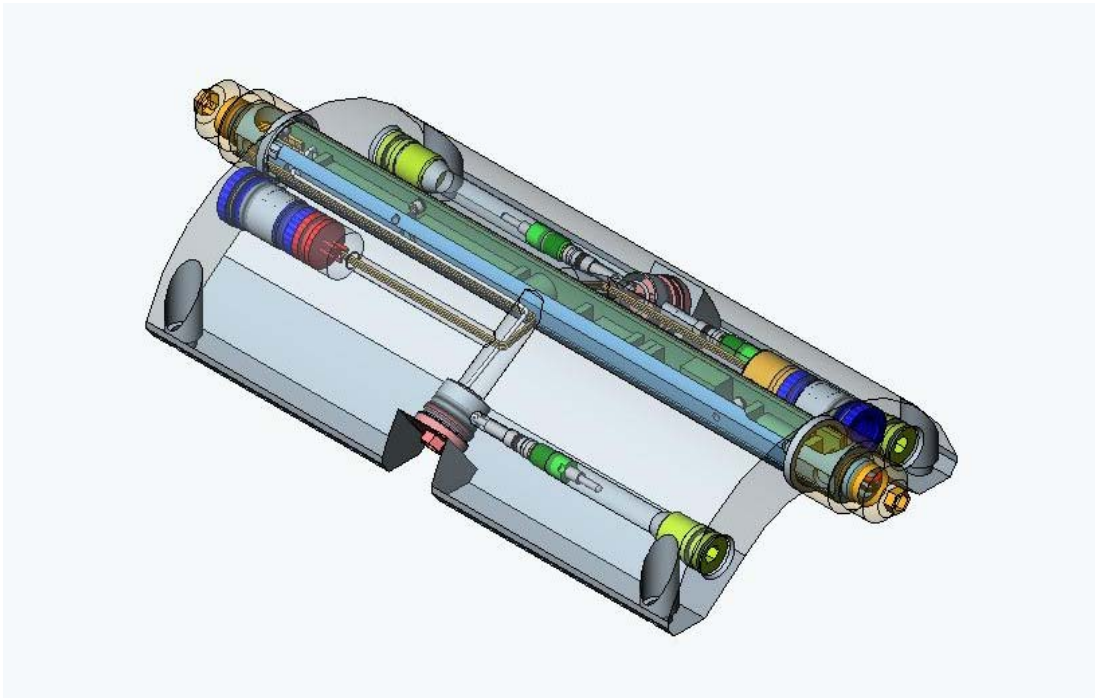


Figure 5: Solidworks™ layout drawing illustrating the clamp-on style, low cost monitoring mandrel.

Results

Computational

The London model was used to predict “no-leak” pressure drops in wellbores. Screenshots from the London model are provided in Appendix A. The model allows the user to select several alternative data input approaches and two computational methods for determining bottomhole pressure, given a wellhead pressure, flowrate, gas composition and temperatures.

The London gas flow model was benchmarked against “no-leak” OLGA™ simulations. The comparative accuracy of the London model was within pressure measurement tolerance. Computed bottom hole pressures were usually within five psig of the pressure measured in the field. The computed pressure difference (bottom hole minus wellhead) was always less than a 2.5 percent error compared to the measurements. Figure 6 shows the percentage error as a function of the wellhead gas flow rate (MMSCF/d) in a 6.34 inch ID wellbore with reservoir depth of approximately 2750 feet.

The error distribution indicates the pressure loss predictions may be inaccurate over the range of flow rates with increasing error magnitude at lower differential pressures. The pressure gauges used may not be sufficiently accurate to measure the small (order 7 percent of the reservoir pressure) differentials observed. Also, the bottom hole pressure was acquired at an offset well and may suffer from non-equilibrium conditions. Also of concern is the accuracy of gas density estimates at low tubing pressure. Errors in density propagate through the gravity head estimate and appear as differences in computed versus measured pressure drop.

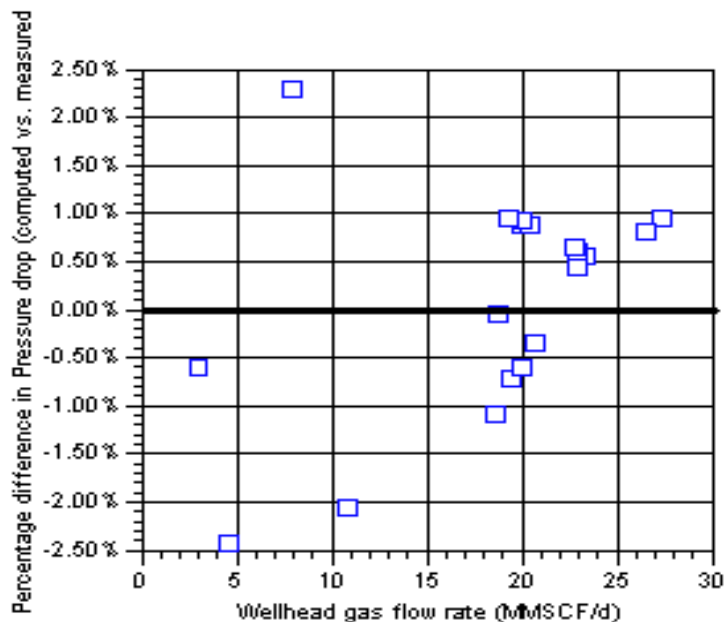


Figure 6. Example of error in computed versus measured pressure drop as a function of gas flow rate.

OLGA was used to simulate the effect of a single tubing perforation under different flowing conditions in the six wellbore architectures described by the field data sets. Approximately

24,000 simulations were performed to understand the combination of variables' effect on the computed pressure loss due to friction and loss of gas through the perforation.

A suite of results for a particular wellbore architecture are shown in Figures 6 through 10 as an illustration of the OLGAs simulations. The total pressure loss (dP) between the wellhead and the reservoir is computed in combination with the gravity head of gas. The total pressure loss minus the gravity head is the flowing or frictional pressure loss of interest. The “no leak” data points are from the London model. The pressure loss estimates correlate well, as expected, with the wellhead gas Reynolds number ($\rho\mu DV/\mu$).

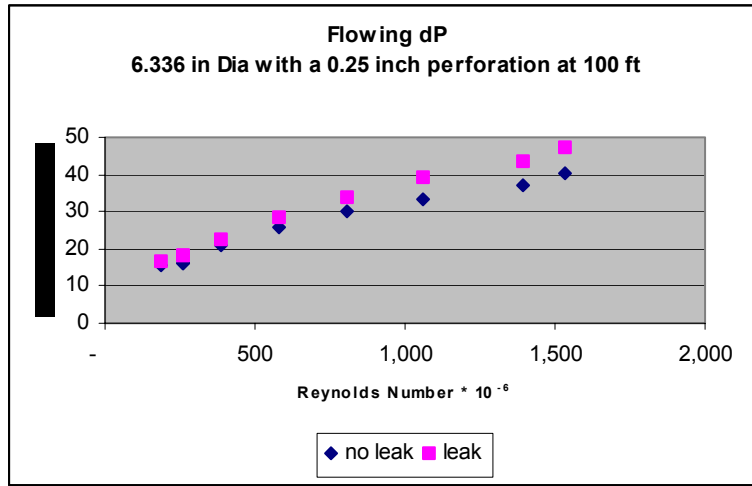


Figure 7. Frictional and leak pressure losses as a function of wellhead Reynolds number for a 0.25-inch diameter perforation at 100 feet below the wellhead.

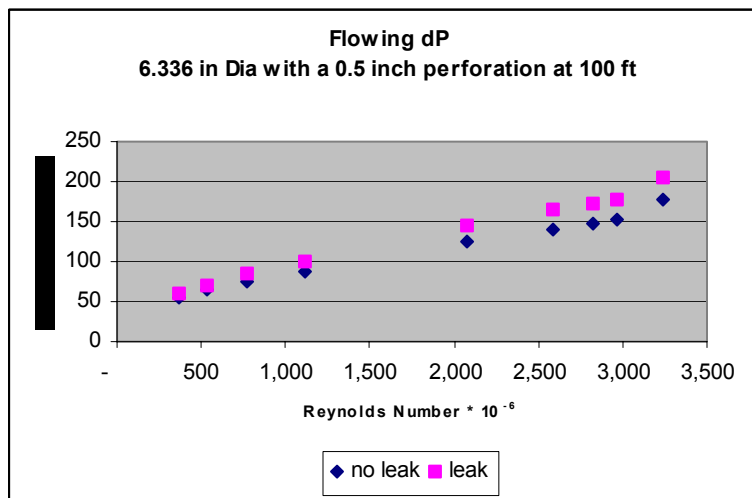


Figure 8. Frictional and leak pressure losses as a function of wellhead Reynolds number for a 0.5-inch diameter perforation at 100 feet below the wellhead.

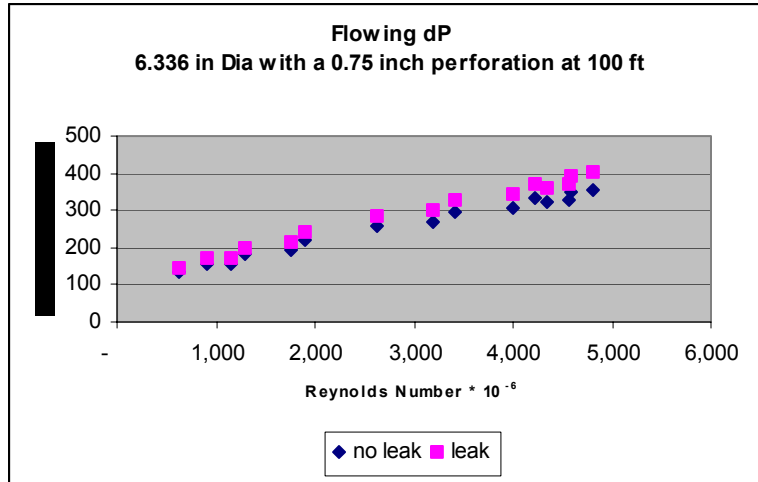


Figure 9. Frictional and leak pressure losses as a function of wellhead Reynolds number for a 0.75-inch diameter perforation at 100 feet below the wellhead.

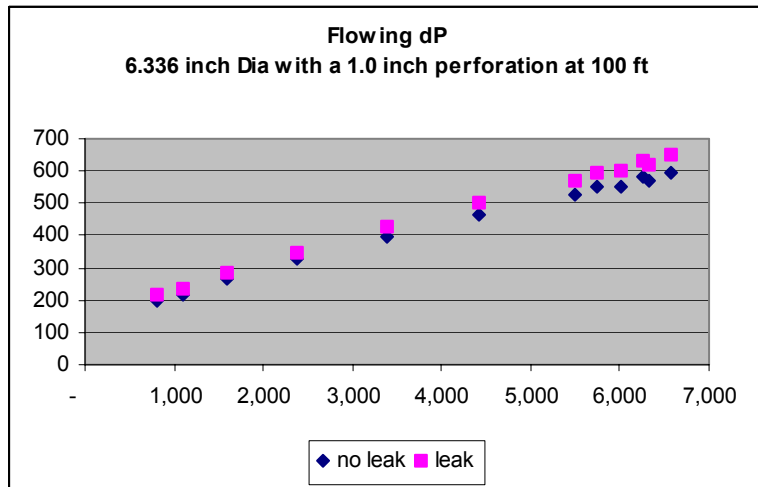


Figure 10. Frictional and leak pressure losses as a function of wellhead Reynolds number for a 1.00-inch diameter perforation at 100 feet below the wellhead.

The “no-leak” frictional pressure losses are a linear function of the wellhead Reynolds number, as expected, for such highly turbulent flows. Incremental pressure losses associated with the existence of a tubing leak are not linear functions of the Reynolds number. This is explained by the orifice calculations and illustrated in Figures 2 and 3. The pressure loss due to a tubing leak is also a function of tubing pressure that is indirectly associated with the gas flow rate in the tubing. Figure 11 shows the effect of perforation diameter on the incremental pressure loss due to a tubing leak. It is clear that above a particular perforation diameter and differential pressure across the perforation, pressure loss due to a tubing perforation is independent of perforation diameter.

We compare the incremental pressure losses due to a tubing leak for a 6.336-inch diameter tubing with a 2.334-inch diameter tubing as a function of Reynolds number in Figure 12. Clearly, the effect is approximately the square of the tubing diameter of the total pressure loss. Consequently, small tubing perforations should be easier to detect in small diameter tubing.

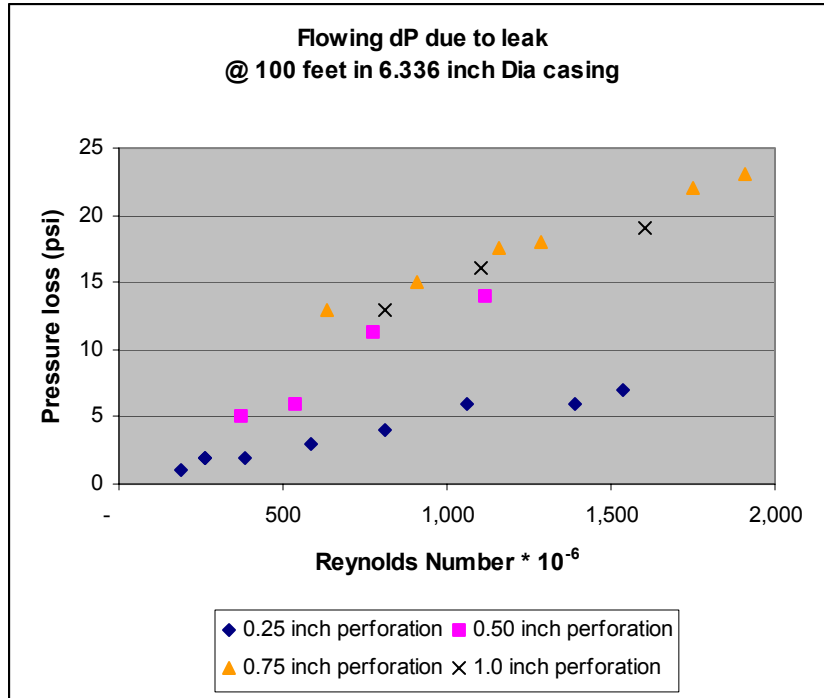


Figure 11. Effect of perforation size on pressure loss in a 6.336-inch diameter wellbore.

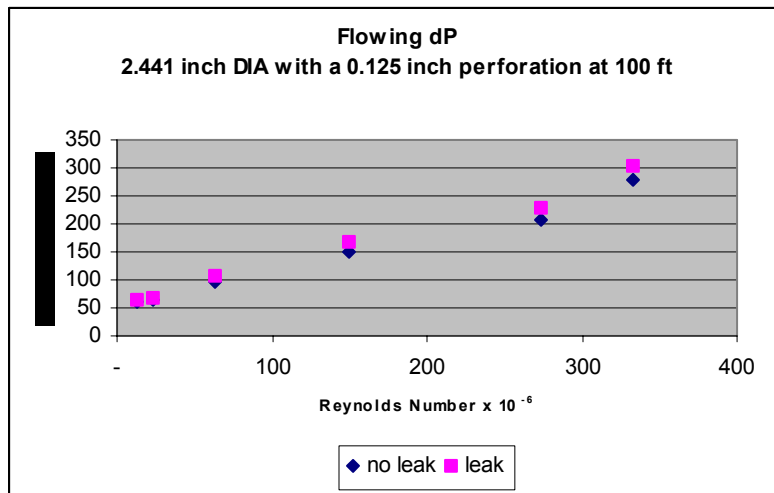


Figure 12. Effect of perforation on frictional pressure drop in a 2.441-inch diameter tubing.

For comparison with Figure 11, we consider the effect of perforation diameter at 100 feet in a 2.441-inch tubing on frictional pressure loss in Figure 13. It is clear that in small diameter tubing, the effect of perforation diameter on frictional pressure loss is independent of perforation size.

All comparisons, to this point, have been made for perforations at 100 feet below the wellhead. The impact on pressure should be at a maximum near the wellhead since backpressure from the formation is low, relative to wellhead pressure. OLGA™ simulations were performed for a suite

of perforation dimensions in a 2.441-inch tubing 250 feet below the wellhead. These results are shown in Figure 14. From this simulation suite, we see that the absolute frictional pressure loss is a strong function of tubing pressure, but is insensitive to perforation dimension.

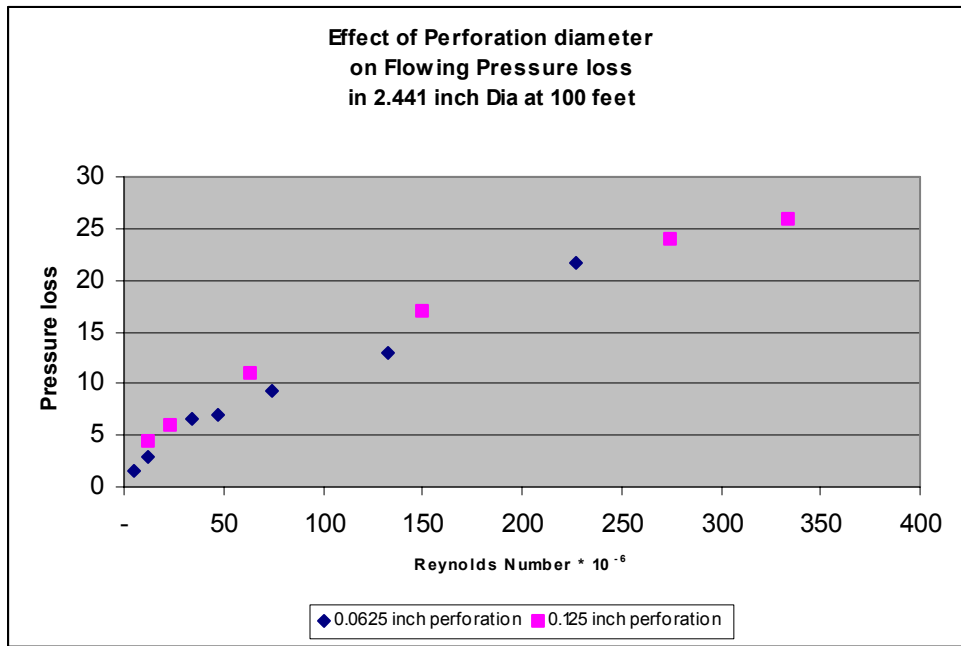


Figure 13. Effect of perforation diameter in a 2.441-inch tubing on pressure loss.

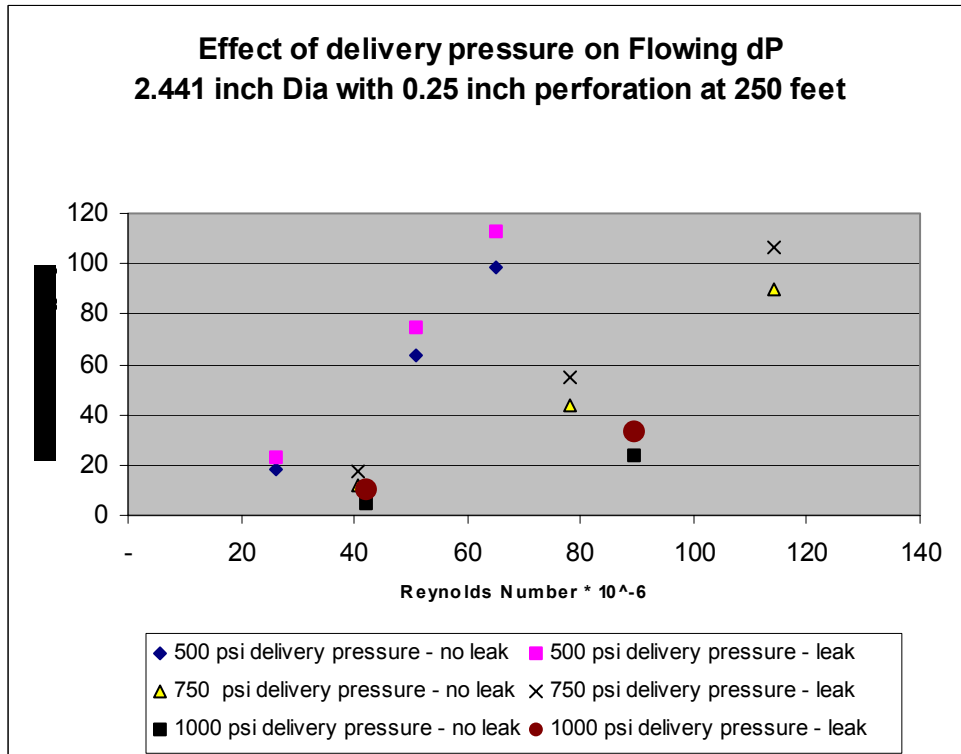


Figure 14. Effect of perforation diameter in a 2.441-inch tubing as a function of tubing pressure.

Hardware

Electronics

The basis of the electronics design was around reducing parts count, reducing assembly time and increasing reliability. The design is based on predominantly through-hole parts based on the fact that solder connections are more reliable and assembly requires less technician experience. Small robust micro-connectors were employed to speed overall assembly time.

The PCB assembly is shown in Figure 15, illustrating its compact size and relatively small number of electronic components.

The electronics were tested at the full rated temperature (125°C) for more than 1 calendar year. The pressure was held at a constant 3,000 psi with cycling at calibration intervals. The reference pressure and temperature system is a quartz-based reference known for both its accuracy and repeatability.

No system failures were recorded during the long-term test.

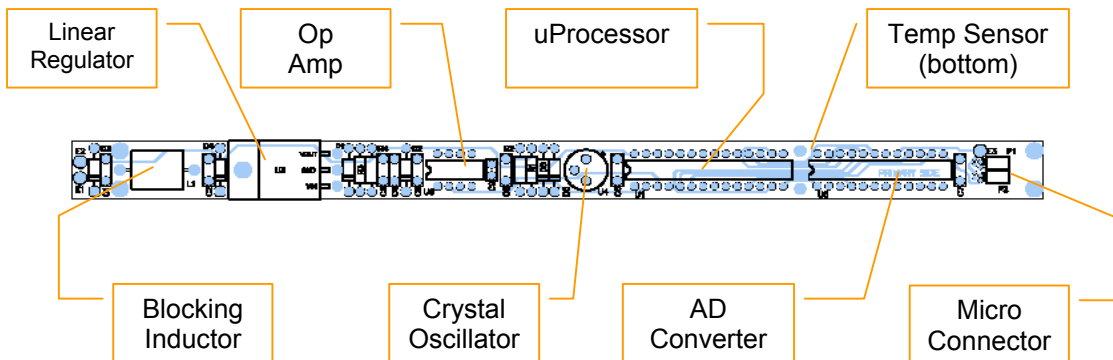


Figure 15. Downhole pressure/temperature electronics package.

Sensor Drift Testing

A collection of piezo-resistive sensors were tested with the electronics assemblies for a long period. These sensors are based on a strain bridge design where the arms of the bridge are of piezo-resistive material as illustrated in Figure 16.

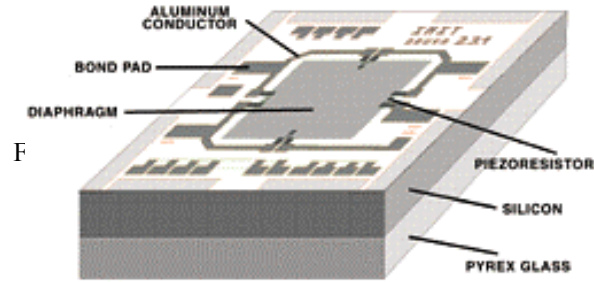


Figure 16. Schematic diagram of piezo-resistive sensor.

The piezo-resistive sensors were meant to be more stable than the first generation bonded counterparts as the strain bridge arms are physically part of the silicon rather than attached (glued).

In excess of 7,000 observations were taken at four temperatures to calculate the sensor coefficients for the test sample. The resulting pressure measurement is expressed as an error in PSI from the control calibration (a quartzdyne) unit.

The sensor was held at 3900 psi and 125°C and calibration data was then collected over four months with the error calculated using the initial coefficients vs. Quartzdyne reference. Note that the histogram “amplitude” indicates number of samples taken for the calibration.

The results for the long-term stability tests were not favourable indicating a drift characteristic well outside the stated specification range. Figure 17 shows the results obtained at the sample points.

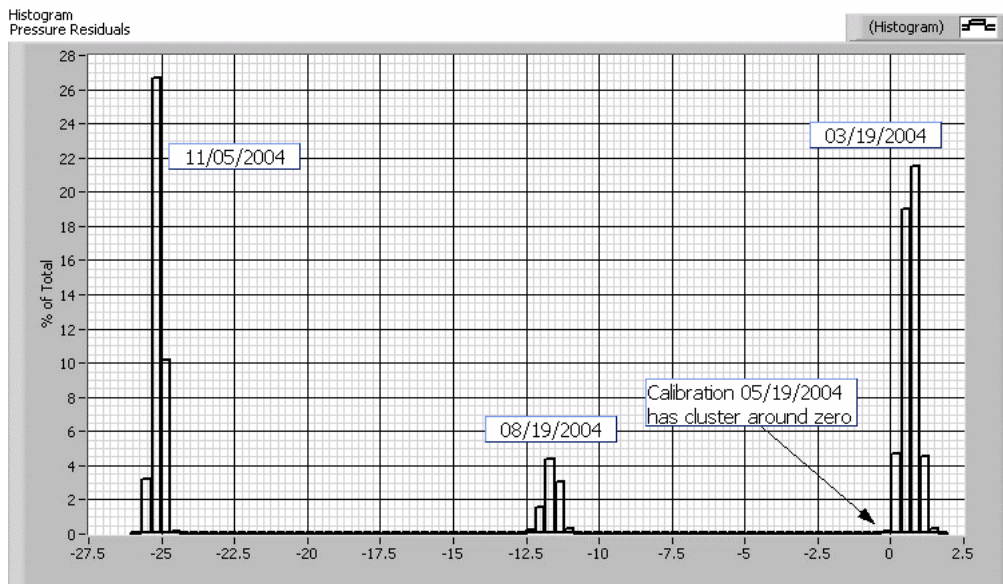


Figure 17. Histogram of pressure residuals collected for the sensor calibration test indicating significant drift of the piezo-resistive unit.

The drift issue has remained unresolved through the duration of this project.

Interpretation of Results

This program has successfully evaluated the effect of a tubing perforation on the frictional pressure loss over a range of wellbore architectures, flow rates, and delivery pressures. The results can be summarized as follows:

- Gas storage field operators can monitor wellbore integrity for wellbores above a particular suite of dimensions, gas flow rates and perforation sizes with existing pressure/temperature sensor technologies via wireline sensor package deployment.
- Gas losses from the wellbore to shallow zones do not exceed 1MMSCFD for perforations less than one-inch in diameter which is relatively easy to observe using this pressure monitoring protocol.
- For wellbore configurations of 2.5-inch diameter and less, the impact of perforations on flows with Reynolds numbers below 50×10^6 and above delivery pressures of 500 psi is below the measurement threshold (10 psia incremental over “no leak” conditions), regardless of the depth of the perforation.
- For perforations with the most serious consequences, shallow and large diameter, existing sensor hardware will provide unequivocal indications at Reynolds number greater than 1×10^7 .
- For perforations located deeper in the wellbore, the incremental frictional pressure losses are small relative to the total losses and can be overlooked, since the incremental loss is a strong function of perforation diameter.
- A nomograph of the combination thresholds of tubing pressure, flow rate and perforation diameter for detection of a tubing perforation is provided in Table 4.
- Deviations in computed (via the London model) versus measured pressures greater than 10 psi should be viewed as suspect and further investigations of wellbore integrity are appropriate, particularly when the deviation cannot be related to the gradual buildup of scale in the wellbore.

For existing hardware sensitivity, we recommend a minimum of a ten psi incremental pressure above the predicted “no leak” pressure differential as the threshold for initiating additional tubing integrity tests. OLGA simulations indicate that the ten psi threshold will be exceeded for perforation dimensions and depths shown below. Note that both a Reynolds number and wellhead pressure threshold are required in the tubing diameters indicated. The operator may assume a linear relationship for Reynolds number and wellhead pressure thresholds for tubing diameters between 2.441 and 6.336 inches.

Tubing diameter (inches)	Perforation Diameter (inches)	Perforation depth (feet)	Reynolds Number $\times 10^{-6}$	Wellhead Pressure (psi)
2.441	0.0625	100	70	500
2.441	0.125	100	50	500
2.441	0.25	250	50	500
2.441	0.25	250	80	750
2.441	0.25	250	120	1000
6.336	0.25	100	2,500	500
6.336	0.5	100	750	500
6.336	0.75	100	400	500
6.336	1.00	100	250	500
6.336	0.5	250	750	1000

Table 4. Threshold parameter values for detection of tubing perforations in gas wells via pressure drop measurements

Summary

The research program has developed a nomograph of threshold flow conditions in standard gas storage wellbore architectures that will allow the operator to use a low cost pressure differential analysis technique to authenticate the integrity of the wellbore. The operator must consider both the Reynolds number and the wellhead pressure in determining the existence, dimension and probable location of a perforation.

The use of a ten psi minimum incremental pressure loss above that predicted by the London model for a “no leak” condition should minimize the occurrence of false positives yet provide enough sensitivity to allow the operator to detect perforations before a great deal of gas is lost to shallower zones.

In a fortuitous sense, the monitoring technique is most sensitive to shallow perforations where the greatest amount of gas is lost for a given perforation dimension and where it will have the largest deleterious effects.

Appendix

London model for gas flow in wellbores with NO perforations

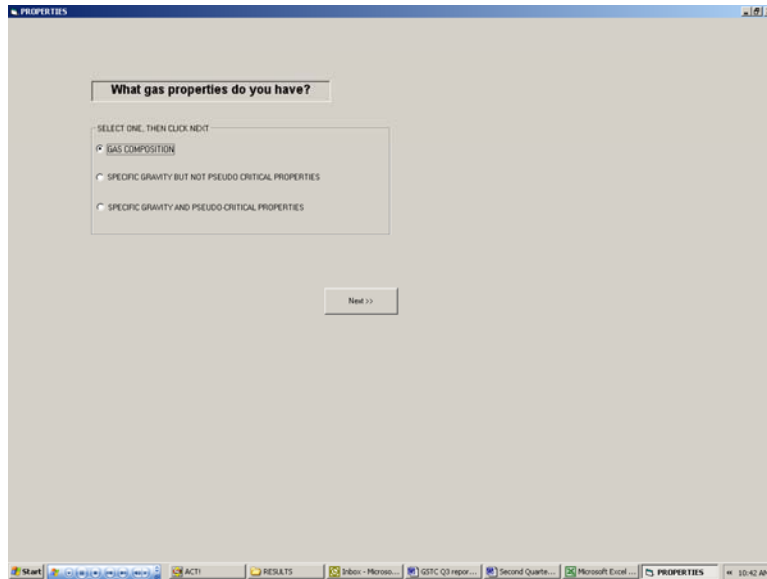


Figure A-1. Initial data input screen for the London gas flow model.

INPUT		OUTPUT	
CARBON DIOXIDE	.7095	MOLECULAR WEIGHT	16.79
NITROGEN	.9105	PSEUDO-CRITICAL PRESSURE	669.75
METHANE	95.6709	PSEUDO-CRITICAL TEMP	349.81
ETHANE	2.3638	SPECIFIC GRAVITY	.5799
PROPANE	.2499	VISCOSITY	.0163
N-BUTANE	.0482	Z	.8507
ISOBUTANE	.031		
N-PENTANE	.0069		
ISOPENTANE	.007		
N-HEXANE	.0023		
PRESSURE	2000		
TEMPERATURE	580		

CLICK HERE TO CALCULATE

NEXT >>

Figure A-2. Gas properties input screen for the London model.

The screenshot displays the 'CULLENDER-SMITH METHOD' software interface. At the top, a table lists the following input parameters and their values:

PRESSURE (WELLHEAD)	3460
TEMPERATURE (WELLHEAD)	580
TEMPERATURE (BOTTOM HOLE)	675
LENGTH OF PIPE (MEASURED DEPTH)	11883
NUMBER OF SECTIONS OF PIPE	2
FLOWRATE (MMSCF/D)	15.67
THETA (DEVIATION FROM VERTICAL)	0
DIAMETER OF PIPE	2.441
SURFACE ROUGHNESS	.00065

Below the table, there are three main buttons:

- A button labeled 'CALCULATE BOTTOM HOLE FLOWING PRESSURE'.
- A button labeled 'PRESS HERE TO OUTPUT RESULTS TO EXCEL AND END PROGRAM'.
- A button labeled 'PRESS HERE TO END PROGRAM'.

At the bottom left, the text 'BOTTOM HOLE FLOWING PRESSURE' is displayed in yellow, followed by a yellow rectangular box representing the calculated output.

Figure A-3. Wellbore architecture input screen and bottomhole pressure calculation output for the London model.

Appendix F
2005, Temperature Effects on Threaded Couplings in Caverns,
RESPEC Final Report

TEMPERATURE EFFECTS ON THREADED COUPLINGS IN CAVERNS

FINAL REPORT
1 May 2005–30 April 2006

by

Kerry L. DeVries
Joel D. Nieland

RESPEC
P.O. Box 725
Rapid City, South Dakota 57709
United States

and

Brian T. Wagg
Jueren R. Xie

C-FER Technologies
200 Karl Clark Road
Edmonton, Alberta
Canada T6N 1H2

February 2007
Revised May 2007

Gas Storage Technology Consortium
Subaward No. 2906-RESPEC-DOE-1779
DOE Award DE-FC26-03NT41779

DISCLAIMER

This report was prepared as an account of work sponsored by an agency of the United States Government. Neither the United States Government nor any agency thereof, nor any of their employees, makes any warranty, express or implied, or assumes any legal liability or responsibility for the accuracy, completeness, or usefulness of any information, apparatus, product, or process disclosed, or represents that its use would not infringe privately owned rights. Reference herein to any specific commercial product, process, or service by tradename, trademark, manufacturer, or otherwise does not necessarily constitute or imply its endorsement, recommendation, or favoring by the United States Government or any agency thereof. The views and opinions of authors expressed herein do not necessarily state or reflect those of the United States Government or any agency thereof.

ABSTRACT

This report documents research performed to identify if gas injection and withdrawal temperatures of typical natural gas well completions could potentially result in failure of the casing through low-frequency cyclic fatigue. Finite element analyses of two salt cavern wells and one reservoir storage well were used to estimate the state of stress in the casing resulting from: (1) casing weight; (2) product pressures; (3) thermally induced stresses; and (4) external ground pressures, including salt creep. The range of stress and temperature conditions determined during simulations of gas service cycles at the lowest casing joint was used as input to another set of finite element models to predict the casing connection response when subjected to cyclic loads caused by pressure and temperature changes. The stress history at critical points in the connections was then used in cyclic fatigue analyses to determine the expected number of cycles the couplings can withstand before failure.

EXECUTIVE SUMMARY

When natural gas is injected or withdrawn from storage, the temperature of the gas flowing through the production casing is almost never in equilibrium with the casing components or the rock mass. As a result, the production casing expands and contracts in response to the temperature fluctuations associated with cavern operation. Expansion and contraction of the casing induces cyclic loads that could have deleterious effects on the integrity of the threaded casing connections. This report documents an assessment that was performed of natural gas storage wells to determine if thermally induced cyclic loads are likely to lead to failure of the well casing. Solution of the well casing problem requires an appropriate description for the structural behavior, thermodynamics, heat transfer, and fluid flow of the gas, casing components, and geologic formation.

The geological setting, well completion practices, and operational use of natural gas storage wells in the United States provide a vast range of well designs and expected well casing loading conditions. Because it is impractical to assess all of the different well casing designs and the performance of the casings in the different geologic settings, this study was limited to the evaluation of three well casings. Candidate well casings were selected after considering which wells are expected to be subjected to the most severe loading conditions, with special consideration given to the most common casing types currently used for salt cavern and reservoir storage wells. The candidate wells selected for evaluation included two salt cavern storage wells having final cemented depths of 579 and 1,494 meters (1,900 and 4,900 feet) and a gas reservoir well drilled into a sandstone formation at a depth of 1,524 meters (5,000 feet). Both salt cavern wells modeled were completed with 340-millimeter-diameter (13³/₈-inch-diameter) K-55 grade casing. The reservoir well used 140-millimeter-diameter (5.5-inch-diameter) J-55 grade production casing.

Two distinct types of finite element models were used: (1) well models that predict the casing loads from ground surface to the casing shoe and (2) connection models that predict the magnitude and location within the connection that is subjected to the most severe cyclic loading. Sources for the loads exerted on the wells modeled in this study include contributions from: (1) casing weight; (2) product pressures; (3) thermal expansion and contraction; and (4) external ground pressures, including salt creep and reservoir compaction. Although not considered by the well models, the effect of casing bending was included in the analyses of the connection models.

Conservative assumptions were made during the well model analyses where possible. These assumptions included modeling the cement as an elastic material that does not fail and using perfectly bonded interfaces between the casing, cement sheath, and adjacent rock formation. Although the axial tensions remained relatively low compared to the strength of the casing during the simulation period of the shallow salt cavern, stresses were predicted to exceed the

tensile strength of the steel casing during the analysis of the deep salt cavern well. Other than the conclusion that creep deformations around the well casing will eventually accumulate to a magnitude that will cause the casing to fail, other possibilities not simulated by the models used in this study include: (1) slip occurs along the steel/cement and/or the cement/salt interface, limiting the axial tensions that can develop in the casing, or (2) failure of the cement occurs, limiting the drag force which is causing the development of tensile stresses in the steel casing. Without physical evidence, it is difficult to identify which possibility is most likely to occur. Regardless, the modeling effort suggests that without slip along the interfaces, failure of the casing, cement, or salt is probable if relatively large vertical creep displacements are present.

For the salt cavern wells, the least-tensile (or most-compressive) vertical stresses are predicted at the beginning of the withdrawal cycle. At this time during the cycle, the temperature of the casing is the warmest and the gas pressure is the greatest. The most-tensile vertical stresses in the salt cavern casing are predicted to occur at the end of withdrawal when the gas temperature is the coolest and the pressure is the lowest. The axial stress at the lowest connection in the shallow salt cavern well was predicted to cycle between 20 and 125 megapascals (MPa) tension (2,900 and 18,100 pounds per square inch (psi)). It was assumed that the cement sheath cannot transmit more than 345 MPa (50,000 psi) to the casing based on supplemental analyses performed during this study. Using this limiting value, the axial stress at the lowest connection in the deep salt cavern well was predicted to cycle between 164 and 345 MPa (23,800 and 50,000 psi).

Because of the slow withdrawal rates assumed for the reservoir well, the temperature of the gas does not become significantly cooler than the storage formation temperature during gas withdrawal. As a result, the least-tensile (or most-compressive) vertical stresses are predicted to occur at the end of withdrawal when the pressure is lowest and the gas temperature is warmest. The most-tensile stresses in the reservoir well casing occur at the end of injection when the temperature is the coolest and the gas pressure is the greatest. Excluding reservoir compaction and bending stresses, the axial stress at the location of the lowest connection in the reservoir well ranges from -1 MPa to 36 MPa (-145 to 5,200 psi).

Models of the threaded connections were used to determine the fatigue life corresponding to the range of axial force and pressure cycles estimated from the well casing models. The first step of the connection analysis consisted of determining the stresses that exist in the connection following the connection make-up procedure. Next, the load cycles predicted at the lowest joint by the well models were imposed to determine the stress and strain distribution in the connection. These stress and strain values were then used to estimate the fatigue life of the connection in terms of the number of injection-withdrawal cycles that can be tolerated. The connection modeling results showed that the stress in localized areas of the connection will exceed the elastic limit of the material, resulting in plastic (unrecoverable) strain; therefore, it

was necessary to adopt a strain-based fatigue criterion that considers the magnitude of plastic strain cycles in the connection.

Based on this conservative analysis, the fatigue life for the reservoir well was estimated to be as short as 235 cycles, or 235 years, assuming an annual pressure cycle. The deep salt cavern casing could withstand approximately 3.7×10^6 pressure cycles, but since the pressure is cycled 12 times per year, the well life is estimated to be 310,000 years. Connection fatigue in the shallow salt cavern well does not appear to be a concern, with a predicted fatigue life of over a million years, assuming 12 pressure cycles per year. Two key uncertainties remain in the analyses that may have significant influence on the estimated fatigue life of the connections. The first is the fatigue performance of the casing and connection materials, which was based on analogous materials. The second uncertainty is how much of the formation movements that occur during pressure and temperature cycles are transferred through the well cement to the casing.

Welding the coupling face to the pipe body in these applications does appear to contribute somewhat to the connection strength, but in some cases, may redistribute the stresses in the connection such that failure occurs in approximately the same number of cycles but in a different location compared to connections without welds. The analyses including the weld did not consider the effects welding may have on local stress concentrations or degradation of the casing and coupling material properties in the heat-affected zone adjacent to the weld.

In conclusion, the predicted thermomechanical response of the well casing during gas storage injection and withdrawal cycles shows that the effects of operating pressure and well temperature changes are minor in comparison to the axial strains imposed by formation movements (i.e., compaction in reservoirs and salt creep in caverns). If the casing loads associated with salt creep and reservoir compaction are not considered, the conservative analyses performed in this study indicate that the minimum number of cycles necessary to cause cyclic fatigue range from about eight hundred to several hundred thousand. This study did not consider the effects of cyclic loading on the integrity of the cement sheath. Fracturing, debonding, and degradation of the cement sheath is a topic for future research.

TABLE OF CONTENTS

1.0 INTRODUCTION	1
1.1 BACKGROUND	1
1.2 OBJECTIVE AND SCOPE.....	1
1.3 REPORT ORGANIZATION	1
2.0 PROJECT OVERVIEW	2
2.1 PROJECT DESCRIPTION.....	2
2.2 CASING LOADS	3
2.2.1 Stresses From Casing Weight	3
2.2.2 Stresses From Product Pressure.....	3
2.2.3 Stresses From Thermal Expansion and Contraction.....	4
2.2.4 Stresses From External Ground Pressure	4
2.2.5 Stresses From Casing Bending.....	5
2.3 OVERVIEW OF APPROACH	5
3.0 CANDIDATE WELL CASING DESCRIPTION	8
4.0 EXPERIMENTAL	16
4.1 SOFTWARE PROGRAMS.....	16
4.1.1 Cavern Thermodynamics Program SCTS	16
4.1.2 Heat Transfer Finite Element Program SPECTROM-41.....	17
4.1.3 Thermomechanical Finite Element Program SPECTROM-32	17
4.1.4 Thermomechanical Finite Element Program ABAQUS	18
4.2 STRATIGRAPHY	18
4.2.1 Salt Dome Cavern Storage	18
4.2.2 Porous Sandstone Reservoir Storage.....	18
4.3 MATERIAL MODELS AND PROPERTIES	19
4.3.1 Steel Casing	19
4.3.2 Threaded Connections	19
4.3.3 Cement Sheath.....	20
4.3.4 Rock Salt	20
4.3.5 Nonsalt Strata	21
4.3.6 Natural Gas	23
4.3.7 Brine.....	23
4.4 IN SITU CONDITIONS.....	23
4.4.1 Stress Distribution.....	24
4.4.2 Temperature Profile.....	24

TABLE OF CONTENTS (Continued)

4.5	GAS PRESSURE CYCLES	24
4.6	FINITE ELEMENT MODELS.....	25
4.6.1	Well Models.....	25
4.6.2	Connection Models	31
5.0	RESULTS AND DISCUSSION OF WELL CASING MODELS	33
5.1	PROBLEM DESCRIPTION	33
5.1.1	Salt Cavern Well Model Simulations	33
5.1.2	Reservoir Well Model Simulations	34
5.2	SALT CAVERN THERMAL SIMULATOR RESULTS	34
5.3	HEAT TRANSFER RESULTS.....	37
5.4	THERMOMECHANICAL RESULTS	47
5.4.1	Stresses From Casing Weight	47
5.4.2	Stresses From Product Pressures	49
5.4.3	Stresses From Thermal Expansion and Contraction	51
5.4.4	External Ground Pressure Considerations.....	51
5.4.5	Total Vertical Stress From Combined Loads.....	54
5.4.6	Stress Condition at the Lowest Casing Connection	54
6.0	RESULTS AND DISCUSSION OF THREADED CONNECTION MODELS.....	57
6.1	INITIAL CONNECTION LOADS	57
6.2	STRAIN-BASED FATIGUE ASSESSMENT CRITERIA.....	58
6.3	RESERVOIR STORAGE CONNECTION RESULTS.....	61
6.4	SALT CAVERN WELL CONNECTION RESULTS	70
6.5	SUMMARY OF FATIGUE LIFE ANALYSES.....	70
7.0	CONCLUSIONS.....	75
8.0	REFERENCES.....	76
APPENDIX A. ADDITIONAL WELL CASING ANALYSES.....		A-1

LIST OF TABLES

TABLE	PAGE
3-1 Well Descriptions and Operating Conditions	15
4-1 Stratigraphic Detail Used in the Numerical Model of Reservoir Well No. 3	19
4-2 Elastic and Thermal Material Properties of Casing Components Used for the Well Models.....	20
4-3 Rock Strata Elastic and Thermal Material Properties	22
5-1 Candidate Well Conditions During the Final Gas Service Cycle Simulated	56
6-1 Material Constants for Fatigue Assessment of J-55 and K-55 Grade Casing	61
6-2 Load Cases for the Reservoir Storage Connection Model.....	63
6-3 Fatigue Life Estimates of the Reservoir Storage Well Connection Model	68

LIST OF FIGURES

FIGURE	PAGE
3-1 Salt Cavern Casing Size Histogram	9
3-2 Salt Cavern Final Cemented Casing Depth Histogram	10
3-3 Casing Schematic of Salt Cavern Well No. 1	12
3-4 Casing Schematic of Salt Cavern Well No. 2	13
3-5 Casing Schematic of Reservoir Storage Well No. 3	14
4-1 Annual Gas Pressure Cycles for the Three Candidate Wells.....	26
4-2 Axisymmetric Finite Element Model of Salt Cavern Well No. 1.....	28
4-3 Axisymmetric Finite Element Model of Salt Cavern Well No. 2.....	29
4-4 Axisymmetric Finite Element Model of Reservoir Storage Well No. 3.....	30
4-5 Schematic of Three-Dimensional Finite Element Connection Model.....	32
5-1 Casing Seat Temperature History for the 610-Meter (2,000-Foot) Shallow Deep Salt Cavern Predicted by SCTS During 60 Gas Service Cycles.....	35
5-2 Casing Seat Temperature History for the 1,524-Meter- (5,000-Foot-) Deep Salt Cavern Predicted by SCTS During 60 Gas Service Cycles.....	36
5-3 Temperature Profile of the Casing in Salt Cavern Well No. 1 During the 60 th Gas Service Cycle	38
5-4 Temperature Profile of the Casing in Salt Cavern Well No. 2 During the 60 th Gas Service Cycle	39
5-5 Temperature Histories at the Casing Seat of the 1,524-Meter- (5,000-Foot-) Deep Reservoir Storage Well No. 3 During Five Gas Cycles.....	40
5-6 Temperature Contours in the Roof Salt Above Salt Cavern Well No. 1 at Various Times Throughout the 5-Year Gas Service Operation.....	42
5-7 Temperature Contours in the Roof Salt Above Salt Cavern Well No. 2 at Various Times Throughout the 5-Year Gas Service Operation.....	43
5-8 Temperature Profiles in the Casing and Salt 12.2 Meters (40 Feet) Above the Casing Shoe of Salt Cavern Well No. 1 During the 60 th Gas Storage Operation Cycle.....	44
5-9 Temperature Profiles in the Casing and Salt 12.2 Meters (40 Feet) Above the Casing Shoe of Salt Cavern Well No. 2 During the 60 th Gas Storage Operation Cycle.....	45
5-10 Temperature Profiles in the Casing and Rock Formation at a Depth of 1,511 Meters (4,960 Feet) During the 5 th Gas Storage Operation Cycle of Reservoir Well No. 3.....	46
5-11 Vertical Stresses in Steel Casings of the Three Candidate Wells Following Well Completion	48

LIST OF FIGURES (Continued)

FIGURE	PAGE
5-12 Incremental Vertical Stresses in the Steel Casings Induced by Product Pressure Changes	50
5-13 Incremental Vertical Stresses in the Steel Casings Induced by Temperature Changes	52
5-14 Two Extremes for Total Vertical Stress in the Steel Casings Predicted During the Last Cycle of the Simulations	55
6-1 Plastic Strain Contours in an 8-Round STC Connection Following Make-Up to API-5B Specifications	57
6-2 Example Results Showing Axial Strain Distribution in a Connection With a Welded Coupling Face	58
6-3 Example Results Showing Axial Strain Distribution in a Connection Without a Welded Coupling Face (Arrows Indicate Locations Where Plastic Strain Concentrations Increase the Likelihood of Fatigue-Related Failures)	59
6-4 Relationship Among Equivalent Strain Amplitude, Mean Stress, and Cycles for J-55 Material Based on Modified Morrow Approach	62
6-5 Relationship Among Equivalent Strain Amplitude, Mean Stress, and Cycles for K-55 Material Based on Modified Morrow Approach	62
6-6 Load Steps for Reservoir Storage Well Connection Model	64
6-7 Axial Strain in Reservoir Well No. 3 for Load Case 1 at the End of Injection (Load Step 2)	65
6-8 Axial Strain in Reservoir Well No. 3 for Load Case 2 at the End of Injection (Load Step 2)	65
6-9 Axial Strain in Reservoir Well No. 3 for Load Case 3 at the End of Injection (Load Step 2)	66
6-10 Axial Strain in Reservoir Well No. 3 for Load Case 4 at the End of Injection (Load Step 2)	66
6-11 Axial Strain in Reservoir Well No. 3 for Load Case 5 at the End of Injection (Load Step 2)	67
6-12 Axial Strain in Reservoir Well No. 3 for Load Case 6 at the End of Injection (Load Step 2)	67
6-13 Fatigue Life for Various Load Cases of the Reservoir Storage Connection Model Assuming 5.1 Centimeters (2.0 Inches) of Formation Movement With Each Gas Cycle	68

LIST OF FIGURES (Continued)

FIGURE	PAGE
6-15 Load Steps for the Connection in Salt Cavern Well No. 1 at a Depth of 567 Meters (1,860 Feet).....	71
6-16 Load Steps for the Connection in Salt Cavern Well No. 2 at a Depth of 1,481 Meters (4,860 Feet).....	71
6-17 Axial Strain in Salt Cavern Well No. 1 Connection at a Depth of 567 Meters (1,860 Feet) at the End of Injection.....	72
6-18 Axial Strain in Salt Cavern Well No. 2 Connection at a Depth of 1,481 Meters (4,860 Feet) at the End of Injection.....	72
6-19 Estimated Fatigue Life for the Salt Cavern Connection Models.....	73
A-1 Predicted Mohr-Coulomb Factor-of-Safety Contours in the Cement Sheath for Different Axial Stress Loads in the Steel Pipe.....	A-4

1.0 INTRODUCTION

1.1 BACKGROUND

When natural gas is injected or withdrawn from subsurface storage facilities, the temperature of the gas flowing through the production casing is almost never in equilibrium with the casing or surrounding rock mass. As a result, the production casing expands and contracts in response to the temperature fluctuations associated with operation. The weakest link for axial tensile loading of a casing string is generally the threaded connection [American Petroleum Institute, 1974]. Expansion and contraction of the casing induce cyclic loads in the connection that could have deleterious effects on the integrity of the connection. This report documents the study performed to determine if thermally induced cyclic loads could lead to failure of well casing connections used for the storage of natural gas in sandstone reservoirs and salt caverns. The report also provides insight into the expected casing loads caused by salt creep and reservoir compaction, assuming the steel casing, cement sheath, and rock mass remain perfectly bonded throughout gas storage operations.

1.2 OBJECTIVE AND SCOPE

The objective of this study is to identify if gas injection and withdrawal temperatures will result in failure through low-frequency cyclic fatigue of typical well completions. To accomplish the objective, finite element analyses were performed of three “typical” well configurations to determine the state of stress in the casing during gas storage operation. The candidate wells included two salt cavern storage wells having final cemented depths of 579 and 1,494 meters (1,900 and 4,900 feet) and a gas reservoir well drilled into a sandstone formation at a depth of 1,524 meters (5,000 feet). Two distinct types of finite element models were used: (1) well models that predict the casing loads from ground surface to the casing shoe and (2) connection models that predict the magnitude and location within the connection that is subjected to the most severe cyclic loading. The approximate number of gas injection and withdrawal cycles permissible before the connections fail is estimated based on the results of the numerical models and fatigue analysis techniques.

1.3 REPORT ORGANIZATION

An overview of the project is given in Chapter 2.0, and descriptions of the three well casing configurations evaluated are provided in Chapter 3.0. The technical approach to the numerical modeling is described in Chapter 4.0. The predicted results of the well models and connection models are provided in Chapters 5.0 and 6.0, respectively. Chapter 7.0 gives a summary of the modeling results and the study conclusions. Cited references are provided in Chapter 8.0. An appendix containing supporting information concludes this report.

2.0 PROJECT OVERVIEW

2.1 PROJECT DESCRIPTION

Under quiescent conditions, casing temperature would not deviate significantly from the in situ temperature of the rock encasing the well. However, gas is often heated above the in situ temperature of the host rock formation during injection by compression. Also, because the gas is almost always stored in a formation warmer than that penetrated by the casing, the gas being withdrawn can exceed the in situ temperature over the length of the casing. The warmer temperature of the gas relative to the casing temperature results in transfer of heat by convection and conduction between the gas and the steel casing. Conduction between the steel casing, cement, and rock formation further alters the temperature field of the casing and surrounding rock formation. During withdrawal to low pressures, the opposite response occurs, as expansion of the gas results in temperatures cooler than the in situ temperature.

Each temperature swing generated by injection and withdrawal of gas causes thermal strain in the casing. Thermal strain (ε) is usually assumed to be linearly related to the temperature change (ΔT) and the coefficient of thermal expansion (α) by the familiar one-dimensional expression:

$$\varepsilon = \alpha \Delta T \quad (2-1)$$

In multidimensional, statically indeterminate situations, Young's modulus and Poisson's ratio become important parameters in determining the magnitude of the thermally induced stresses. The strain caused by thermal expansion or contraction can be significant. For a 610-meter- (2,000-foot-) long steel casing, a 26.67° Celsius (C) (80° Fahrenheit (F)) change in temperature would result in the casing lengthening by about 0.3 meter (1 foot) if the casing were unrestrained. However, bonding between the steel pipe, cement, and rock formation restrains the movement. This restraint produces thermally induced axial loads in the casing. Axial loads are transmitted through the connections and could potentially result in large stresses in the connection because of stress and strain localization effects associated with the complex geometry of the connection.

Under axial loads, the API STC (American Petroleum Institute–Short Threaded and Coupled) casing connections commonly used in gas storage wells will typically fail by either parting caused by tensile rupture at the smallest cross section of the pin (tension) or by a process referred to as “thread jumpout” (tension or compression). The tensile load limit of many API STC connections are approximately 80 percent of the pipe body capacity at yield.

Connection failure may also occur because of fatigue. Cyclic loading associated with the injection and withdrawal cycles in a gas storage facility can impart incremental damage to the connection even at loads well below the yield strength of the pipe body. This accumulated

damage can result in the initiation of cracks in locations where stresses are concentrated because of the loading mechanism or geometry of the connection. One of the key mechanisms that causes cyclic loading in the well casing is the change in wellbore temperature that occurs during the injection-withdrawal cycle. The primary focus of this study is to consider the possibility that these thermally induced cyclic stresses could cause failure of the well casing connections.

2.2 CASING LOADS

In addition to thermally induced loads, the well casing is subjected to other sources of loading that contribute to the total casing load. In most cases, a combination of the various loading mechanisms is most critical to casing and connection performance. The stress analyses performed in this study considered the contributions from (1) casing weight, (2) product pressures, (3) thermal expansion and contraction, (4) external ground (or fluid) pressures, and (5) casing bending. A conservative technical approach was used where possible in calculating the casing stresses. Some of the elements of the conservative analyses are discussed below.

2.2.1 Stresses From Casing Weight

During installation, the final cemented casings in the storage wells hang from the wellhead. Therefore, the lowest portion of the casing is subjected to no stress from the weight of the casing, and the shallowest portion of the casing is subjected to a stress equivalent to the entire weight of the casing. Generally, casing is installed with drilling fluids in the wellbore. Drilling fluids' buoyancy forces support some of the casing weight. For design purposes, it is commonly assumed that the loads in the casing after the cement hardens are identical to the buoyant weight in the cement. For this study, the loads in the casing following cementing were assumed to be equal to the buoyant weight of the steel casing in cement, having approximately the same density as that of drilling mud. Additionally, it was assumed that chemical reactions (i.e., heat of hydration) that occur while the cement hardens do not alter the state of stress in either the casing or cement sheath. In reality, expansion and/or contraction of the cement during curing could alter the stresses in the casing.

2.2.2 Stresses From Product Pressure

The internal pressure in a natural gas storage well varies with depth and is equal to the sum of: (1) the wellhead pressure, (2) the pressure due to the weight of the gas column above the depth of interest in the final cemented casing, and (3) frictional losses. The pressure exerted by the gas on the internal diameter of the casing will increase when compressed gas is injected into the well, raising the pressure in the formation or cavern. Similarly, expansion of the gas during withdrawal will result in a reduction in gas pressure. The gas pressure on the internal diameter of the final cemented casing produces tensile (or less compressive) tangential (hoop) stresses and compressive radial stresses in the casing. If the casing were free to expand,

an increase in the internal pressure would result in outward movement and axial shortening of the casing because of Poisson's effect. Both the outward radial movement and axial shortening are resisted by the bond between the casing and the cement. The stresses generated by a change in product pressure are a function of the material properties of the casing, cement sheath, and the rock formation.

2.2.3 Stresses From Thermal Expansion and Contraction

Rapid gas withdrawal followed by injection of gas heated through compression results in thermal cycling of the cemented casing and surrounding rock formations. The bond with the well cement restricts the casing from elongating as it is heated and from shortening as it is cooled. This constraint leads to axial loads developing within the casing body and connections. The axial load caused by a change in temperature is tensile (or less compressive) if the temperature change results in contraction of the casing. Likewise, the casing becomes more compressive (or less tensile) under conditions that result in thermal expansion of the casing. For this study, it is assumed that the casing, cement sheath, and rock formation are in equilibrium following well completion. Thus thermally induced stresses and strains occur whenever the casing temperature is different than that produced by the geothermal gradient at the depth of interest.

2.2.4 Stresses From External Ground Pressure

External pressures generally act on the final cemented casing and these external pressures produce compressive hoop stresses in the casing. The magnitude of the external pressure cannot be as accurately defined as the internal pressure and, in fact, depends very strongly on the specific geologic conditions adjacent to the casing at the depth of interest. In a salt section, it is generally accepted that the salt formation will develop a relatively uniform loading on the casing equal to the predrilling stress within the salt if no excavations exist near the casing. However, excavations in salt can alter the state of stress at distances exceeding several cavern diameters.

The external loading on the casing in natural gas reservoirs can also be complex. For example, poorly cemented intervals may exist along the casing string; in which case, the in situ fluid (e.g., product or water) will transmit an external pressure directly to the pipe body. In other cases where formation movements (e.g., subsidence) may occur, the external pressure can exceed the weight of the overburden. In any case, the external pressure results in compressive radial and hoop stresses in the casing. The compressive hoop stresses caused by external ground pressure reduce the tensile hoop stresses produced by the internal pressure on the casing. The axial stresses produced by external ground pressure can be tensile or compressive, depending on the specific geologic condition and the interval in the geological column.

In this study, two sources of external ground pressure (loading) were considered: (1) salt creep in the two salt cavern wells and (2) reservoir compaction in the reservoir storage well. As the salt creeps and flows into the cavern, it can drag the casing downward toward the cavern. This stretching of the casing will result in axial tensions. Salt creep also imparts a compressive radial pressure on the outer surface of the casing, further altering the state of stress in the casing. In addition to salt creep, the salt formation responds elastically to changes in cavern pressure. Because salt caverns can be more than 100 meters in diameter and a few hundred meters in height, the elastic response of the rock formation to gas pressure changes can be realized at great distances from the cavern. Thus the external pressures considered in this study for the salt cavern wells include those associated with the elastic and inelastic (creep) behavior of the host salt formation.

For reservoir storage wells, the gas pressure in the storage formation supports some of the overburden weight. When the reservoir pressure is lowered through withdrawal of gas, the overburden support provided by the gas is partially removed. The weight of the overburden rock that was supported by the gas must be supported by the rock within the reservoir. The additional load on the rock results in elastic compaction (shortening) of the formation. The deformations associated with this elastic process are transferred to the steel casing through the cement-rock and cement-steel bonds.

2.2.5 Stresses From Casing Bending

If the final cemented casing hangs perfectly vertical in the wellbore, no bending stresses exist in the casing. However, if the casing is installed in a borehole that deviates from vertical or if the casing deforms laterally by buckling or shearing over time because of formation movements, bending stresses will develop in the casing. Bending stresses cause non-axisymmetric loading of the casing where the total stress may be higher on one side of the connection than on the other. For this study, casing string bending was considered in the reservoir well by assuming it was a directional well with a 9-degree radius of curvature in the build section. However, the salt cavern wells were assumed to be vertical, so bending stresses were not considered in these wells. In addition, buckling and shear-related bending stresses caused by formation movements were not considered in this study.

2.3 OVERVIEW OF APPROACH

Solution to the well casing problems outlined above requires an appropriate description for the thermodynamics, heat transfer, fluid flow behavior of the gas, and the structural behavior of the casing components and geologic formations. Because the geometry and loading of a cemented well are too complex, closed-formed mathematical solutions do not exist that yield answers for the thermomechanical response of the casing. Therefore, numerical modeling was used to predict the well casing responses to the applied loading. Experience, good engineering judgment, and reliable programs are essential for solving the well and connection problems.

A single software program is not available to model all of the processes that contribute to the loadings on the casing and connections. However, the thermal response is usually considered independent of the structural response of the casing and rock formation. Therefore, one-way coupling can be assumed, allowing the temperature fields to be determined by an appropriate heat transfer analysis program and model, which is independent of the structural response. The computed temperature fields can then be used as input for a structural finite element program to compute the thermomechanical response of the casing and surrounding formations.

One approach for evaluating the temperature history of a natural gas storage well is to employ computational fluid dynamics (CFD). The Solution Mining Research Institute recently reviewed the use of CFD to predict the temperature distribution of gas in a salt cavern during injection and withdrawal [Nelson and Van Sambeek, 2003]. However, solution of the problem is much more complex than simply analyzing the flow of gas through the wellbore. The CFD solution requires the modeling of convection cells in the cavern and the boundary layer near the surface of the cavern. The CFD solution is sensitive to the cavern shape and properties of the boundary layer. As a result, CFD have not been routinely used to determine the temperature and pressure of gas in storage and is still being researched. Alternatively, the temperature of the gas in the well and cavern can be predicted by the software program Salt Cavern Thermal Simulator (SCTS) [Nieland, 2004].

The Gas Research Institute funded development of SCTS to provide a means to accurately determine the inventory and temperature of gas storage in salt caverns. SCTS was used in this study to predict the gas temperatures along the length of the salt cavern well casings from the wellhead to the casing shoe. SCTS was also used to compute the average temperature of the gas in the salt caverns. SCTS is limited in that it only assumes radial heat transfer. Further, SCTS does not provide output of the temperature field in the rock formation adjacent to the well or in the salt surrounding the cavern. Therefore, a heat transfer program must be used in conjunction with SCTS to determine the temperature history of the well casing system and host rock formation. For this study, the gas temperatures predicted during injection and withdrawal by SCTS were used as boundary conditions during subsequent heat transfer analyses using the finite element method. For the finite element heat transfer analyses, the temperatures specified along the inner surface of the casing and along the perimeter of the cavern were set to those determined by SCTS for a hypothetical gas storage service cycle. The time-dependent temperature boundary conditions reflect the changing gas temperatures during operation.

Given the temperature field history of the well casing system to be modeled, thermo-mechanical finite element software can be used to predict the stresses and displacements along the entire length of the well casing. The accuracy of the predicted results will depend on the application of appropriate kinematic and pressure/force boundary conditions used to represent the sources of the applied loads. Although the stresses and displacements can be determined at

discrete points by models that represent the well casing from surface to the casing shoe, they do not provide information about the contact force on individual connection threads or the stress distribution within the connection. In this study, three-dimensional finite element models of a threaded connection and short sections of pipe were used to assess the state of stress within the connections. The conditions applied to the connection models were consistent with those determined at the lowest joint location of the two salt cavern wells and one reservoir well evaluated in this study.

The geologic setting, well completion practices, and operational practices of natural gas storage wells in the United States provide a vast range of well designs and expected well casing loading conditions. Because it is impractical to evaluate all of the different well casing designs and the performance of the casings in the different geologic settings, this study was limited to evaluating three well casing configurations. Selection of the three candidate well casings proceeded by compiling well casing records that have been reported in industry surveys, technical publications, and permit applications. Additionally, service contractors and natural gas storage operators were queried to provide additional details regarding the well completion process and storage operating conditions. Candidate well casings were then selected after considering which wells are expected to be subjected to the most severe loading conditions, with special consideration given to the most common casing types currently used for salt cavern and reservoir storage wells. Candidate well descriptions used in this study are described in detail in the next chapter of this report.

3.0 CANDIDATE WELL CASING DESCRIPTION

Two salt cavern wells and one reservoir well are used in this study to assess the impact of thermal cycling on the integrity of the casing and threaded connections. Thermally induced stresses and strains produced in the casing are governed by the temperature of the gas being injected and withdrawn and the in situ temperature of the host formation. An advantage of storing gas in salt caverns is high deliverability. The higher delivery rate of salt caverns is usually accompanied by larger temperature swings of the gas entering and exiting the well compared with reservoir wells. Many salt caverns are designed to allow the cavern to be filled within 20 days and withdrawn in 10 days, with deliverability exceeding 2.01×10^7 normal cubic meters per day (Nm^3/day) (750 million cubic feet per day (MMcfd^1)). Rapid delivery of gas from the salt caverns requires the use of relatively large well casings compared with reservoir wells, which typically have lower deliverability.

Well casing information for salt caverns in the United States was compiled from state regulatory databases and from papers or reports published at technical conferences and symposia. Information regarding 36 caverns was collected, which represent more than half of the natural gas storage caverns currently operated in the United States. The caverns for which data were obtained represent approximately 70 percent of the total salt cavern storage working gas capacity currently developed in the United States. Histograms of the final cemented casing size and depth of the salt caverns are provided in Figures 3-1 and 3-2, respectively. The reported casing depths obtained ranged between 457 and 1,676 meters (1,500 and 5,500 feet). Because only two cavern wells in a salt dome are evaluated in this study, casing depths near the two extremes were chosen. Final cemented casing depths for the shallow and deep salt caverns wells used for this study are 579 and 1,494 meters (1,900 and 4,900 feet), respectively.

Casing sizes for the salt cavern wells vary from 0.1016 to 0.508 meter (4 to 20 inches) in diameter. The most common production casing size used for the salt cavern storage wells is 340 millimeters ($13\frac{3}{8}$ inches), although a significant number of caverns have casings greater than 356 millimeters (14 inches). For the salt cavern wells, 340-millimeter ($13\frac{3}{8}$ -inch) production casings to depths of 579 and 1,493 meters (1,900 and 4,900 feet) were selected for further evaluation in this study. Although the casing grade was not obtained for all of the wells identified, many of wells completed with 340-millimeter- ($13\frac{3}{8}$ -inch-) diameter casing used K-55 grade casing. Therefore, K-55 grade casing was assumed for the salt cavern casings modeled.

Illson and D'Arcy [2004] provide information about casing size and connection types used at 67 depleted reservoir natural gas storage facilities, representing 16 percent of those within the

¹ Natural gas quantities are expressed in terms of normal cubic meters (Nm^3) with reference conditions of 0°C and 0.101325 megapascals (MPa) and in terms of standard cubic feet (scf) with reference conditions of 60°F and 14.73 pounds per square inch (psi). Gas-related computations were made assuming a gas composition of 100 percent methane.

RSI-1546-06-003

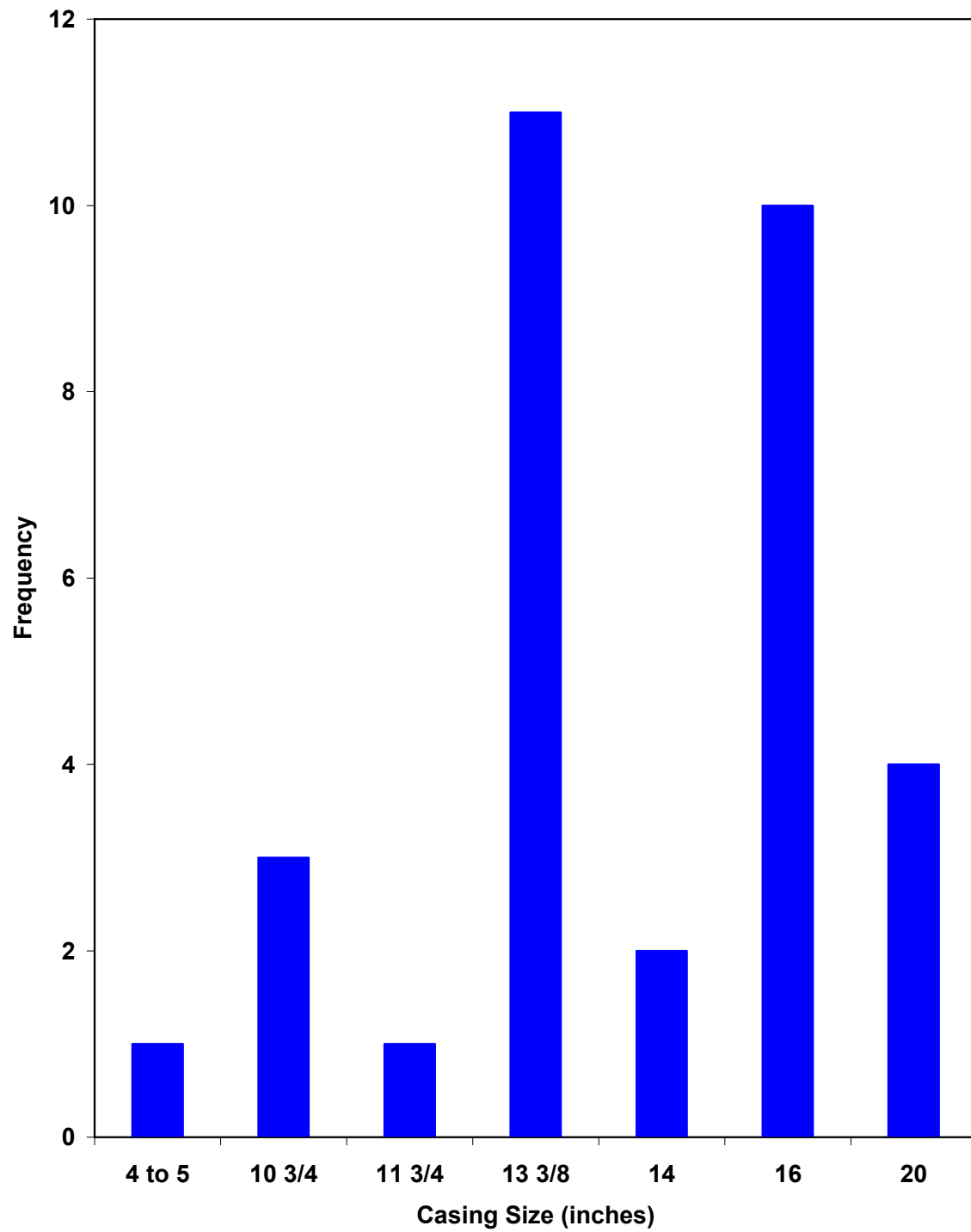


Figure 3-1. Salt Cavern Casing Size Histogram.

RSI-1546-06-004

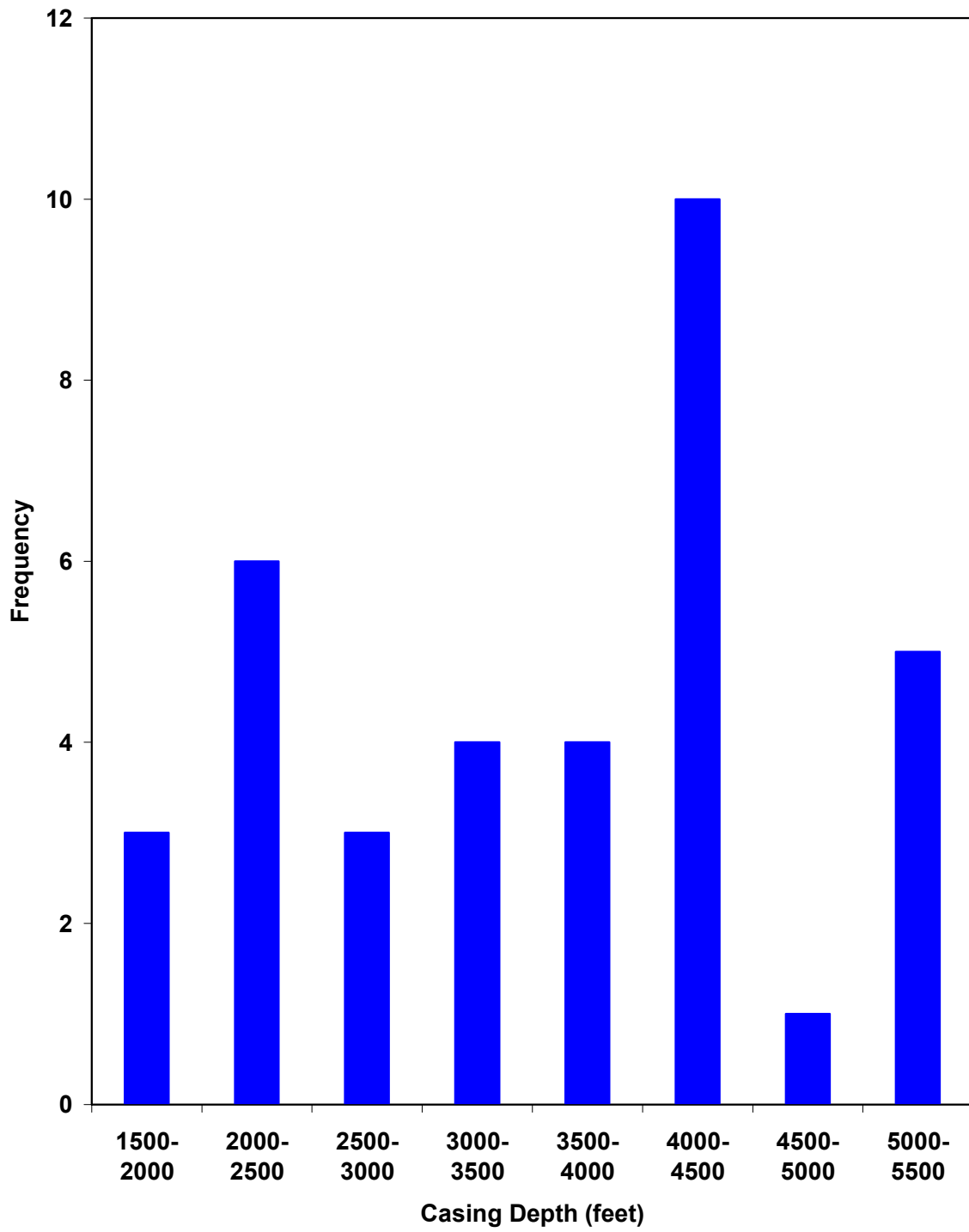


Figure 3-2. Salt Cavern Final Cemented Casing Depth Histogram.

United States. Casing sizes reported ranged between 0.0889 to 0.2731 meter (3.5 to 10.75 inches) in diameter. Based on the results of the survey reported by Illson and D'Arcy [2004], the most common casing size is 140 millimeters (5.5 inches) and the most common grade is J-55. Over 40 percent of the wells in the survey used 140-millimeter (5.5-inch) casing and about 60 percent of the wells used J-55 grade casing. Nearly 95 percent of the connections reported in the survey were API standard 8-R ST&C (8 round, short threaded, and coupled). The most common casing size, grade, and coupling type identified above were used in the thermomechanical evaluations of the reservoir well performed for this study.

Schematics of the three casing configurations evaluated in this study are provided in Figures 3-3 through 3-5. Additional well completion details and operating parameters are provided in Table 3-1. The salt caverns and casings sizes are sufficient to allow complete injection of gas from minimum pressure to maximum pressure in 20 days. Further, the gas can be withdrawn in 10 days without forming hydrates or exceeding a velocity of 30.48 meters (100 feet) per second. As shown in Figure 3-5, the reservoir well includes a 90-degree build section (bend) between 1,219.2 and 1,524.0 meters (4,000 and 5,000 feet) below surface. The 90-degree bend was modeled in this study to provide an additional source of loading that is created in the casing by well deviations. The effects of the cement sheath thickness were not investigated in this study. It was assumed that the cement thickness will have little impact on the results. This assumption was made on the premise that the physical properties of the cement are not significantly different than that of the host rock formation; however, additional analyses would have to be done to confirm this assumption.

As shown in Figures 3-3 through 3-5, the candidate wells are cemented along their entire length. This configuration was chosen because the fully restrained (cemented) case will result in the prediction of the maximum possible axial stress caused by thermal contraction and expansion of the casing. If the casing is only partially cemented, thermally induced stresses and strains will be uniformly distributed over the length of the section that is not cemented and equal to the average stress predicted for the fully restrained case over the same length. However, the cement sheath also limits horizontal deflection and the potential for buckling of the casing. The issue of buckling is believed to be separate from that of thermally induced cyclic fatigue and is not addressed in this study.

The remainder of this report addresses modeling details and results of the modeling effort used to assess the significance of thermal cycling in the gas storage wells. Analysis results include those determined from well models of the casing from the surface to the casing shoe and those results determined from connection models of threaded connections and short sections of pipe.

RSI-1546-05-007

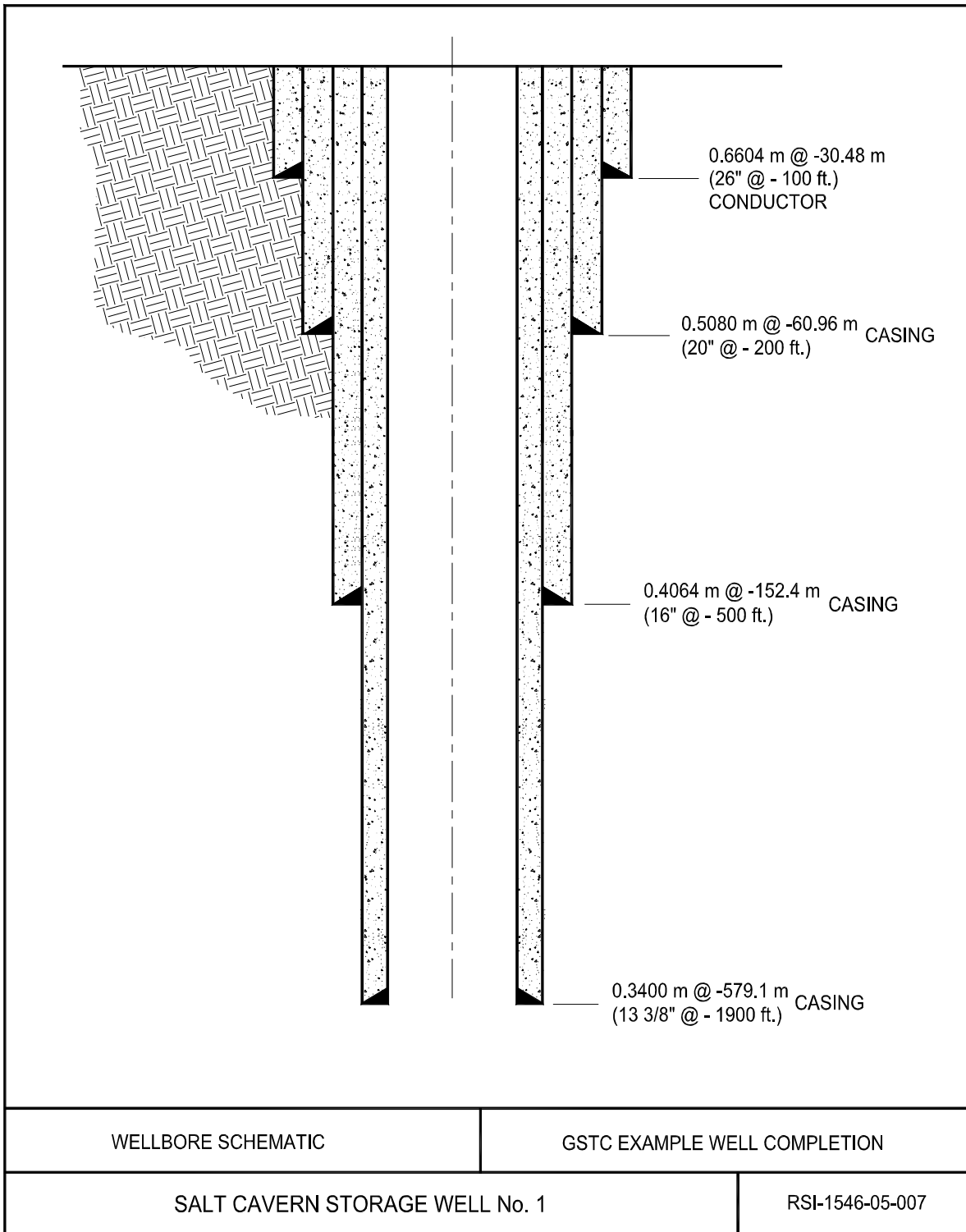


Figure 3-3. Casing Schematic of Salt Cavern Well No. 1.

RSI-1546-05-006

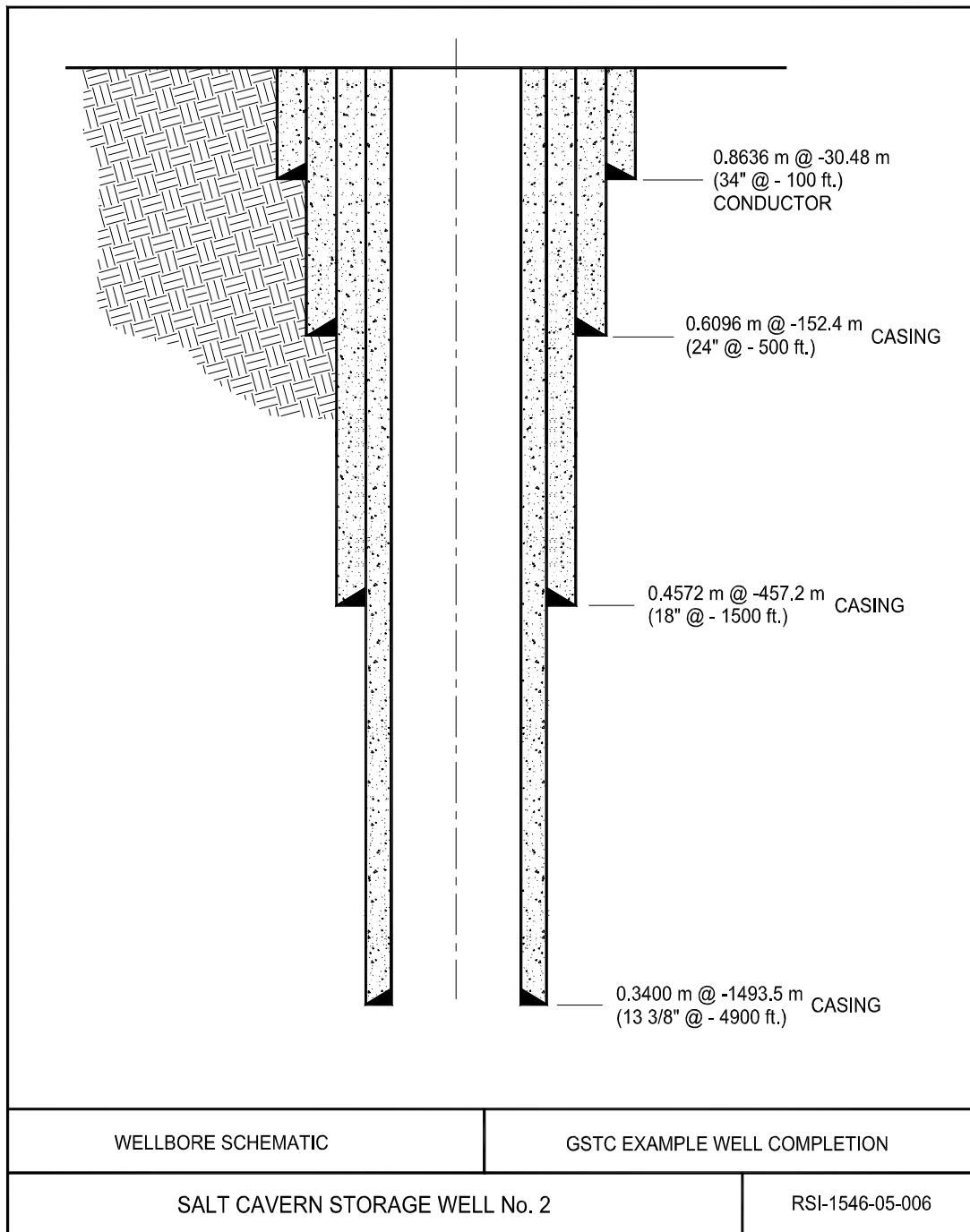


Figure 3-4. Casing Schematic of Salt Cavern Well No. 2.

RSI-1546-06-002

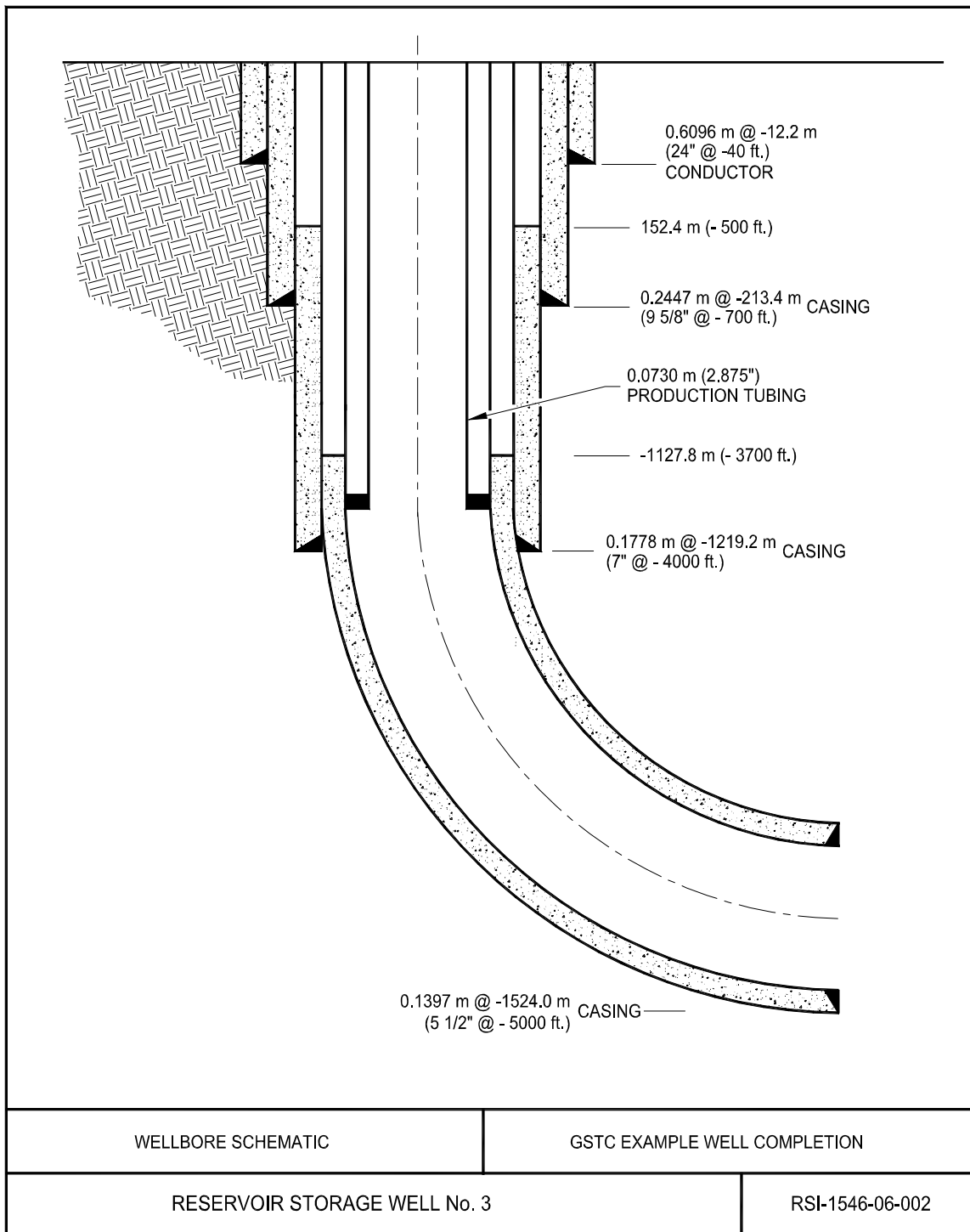


Figure 3-5. Casing Schematic of Reservoir Storage Well No. 3.

Table 3-1. Well Descriptions and Operating Conditions

	Salt Cavern Storage Well No. 1		Salt Cavern Storage Well No. 2		Reservoir Storage Well No. 3	
Final Cemented Casing Depth	579 m	1,900 ft	1,494 m	4,900 ft	1,524 m	5,000 ft
Casing Outer Diameter	0.34 m	13 $\frac{3}{8}$ in	0.34 m	13 $\frac{3}{8}$ in	0.1397 m	5.5 in
Casing Wall Thickness	0.0130 m	0.513 in	0.0130 m	0.513 in	0.0140 m	0.550 in
Casing Weight	107 kg/m	72 lb/ft	107 kg/m	72 lb/ft	23 kg/m	15.5 lb/ft
Casing Yield Strength	379 MPa	55,000 psi	379 MPa	55,000 psi	379 MPa	55,000 psi
Casing Ultimate Strength	655 MPa	95,000 psi	655 MPa	95,000 psi	517 MPa	75,000 psi
Cement Thickness	0.0475 m	1.87 in	0.0475 m	1.87 in	0.0508 m	1.00 in
Injection Temperature	48.89°C	120°F	48.89°C	120°F	21.11°C	70°F
Storage Formation Temperature ^(a)	49.17°C	120.5°F	74.17°C	165.5°F	46.11°C	115°F
Injection Rate	2.84×10^6 Nm ³	106 MMcfd	5.52×10^6 Nm ³	206 MMcfd	1.07×10^6 Nm ³	40 MMcfd
Withdrawal Rate	5.67×10^6 Nm ³	212 MMcfd	1.10×10^7 Nm ³	412 MMcfd	1.07×10^6 Nm ³	40 MMcfd
Minimum Casing Shoe Pressure	3.28 MPa	475 psi	8.45 MPa	1,225 psi	4.14 MPa	600 psi
Maximum Casing Shoe Pressure	11.13 MPa	1,615 psi	28.72 MPa	4,165 psi	22.06 MPa	3,200 psi
Gas Capacity	8.87×10^7 Nm ³	3.2 Bcf	1.90×10^8 Nm ³	7.1 Bcf	2.89×10^8 Nm ³	10.8 Bcf

(a) Storage formation temperatures for salt caverns are given at the cavern midheight.

4.0 EXPERIMENTAL

Numerical methods were used to predict the thermomechanical response of the three candidate wells within the host rock formation. The results of interest are the locations and corresponding times when the maximum and minimum stresses and strains are reached in the casing during the gas service cycle. Based on these extreme conditions, cyclic fatigue analyses were used to determine the expected number of cycles the connections can withstand before failure.

Solution to the problem requires the appropriate software programs and complete definition of the numerical models. Those inputs necessary to completely define the problem are described in this chapter. The steps followed during the assessment include:

1. Compute the temperature of the gas in the casing during natural gas storage operations.
2. Predict the temperature history of the rock formation surrounding the well using a finite element heat transfer program based on the gas temperatures along the length of the casing as boundary conditions.
3. Compute the stresses and strains in the casing during natural gas storage operation using a thermomechanical finite element program.
4. Compute the contact forces and state of stress within the connections using the extreme conditions determined by the thermomechanical analyses of the well models as boundary conditions.
5. Determine the expected number of cycles the connection can withstand before failure is expected using cyclic fatigue analysis.

The computer programs, stratigraphy, constitutive models, material properties, in situ conditions, gas service cycles, and the finite element models used to evaluate the well casings and connections are described below.

4.1 SOFTWARE PROGRAMS

Numerical modeling software was used to model the thermodynamics, heat transfer, structural behavior of the host rock formation, and mechanical behavior of the well casing components. These specialized computer programs are described in the following subsections.

4.1.1 Cavern Thermodynamics Program SCTS

SCTS [Nieland, 2004] is a program developed by PB Energy Storage Services, Inc. (PB ESS) and RESPEC for simulating the thermodynamics and heat transfer related to the storage of

natural gas in underground salt caverns. It accounts for the thermal effects associated with gas compression and expansion; the mass transfer during injection and withdrawal; and the heat transfer between the gas and its surroundings, both in the well and in the cavern.

SCTS was used to determine well casing and cavern temperatures throughout the simulated gas storage operations. SCTS calculates the temperature of the gas at discrete points in the well; however, the program only calculates a single bulk temperature for the gas in the cavern. The well and cavern temperatures as a function of time, determined from SCTS, were applied as boundary conditions to the thermal finite element models to estimate the temperature of the salt surrounding the caverns and/or wells as a function of time.

4.1.2 Heat Transfer Finite Element Program SPECTROM-41

SPECTROM-41 [Svalstad, 1989] is a finite element heat transfer analysis program that was developed by RESPEC to analyze thermal problems in geologic formations. The primary transport process modeled by SPECTROM-41 is conductive heat transfer with fixed, adiabatic, periodic, and convective boundary conditions. SPECTROM-41 has the capability to model complex material properties (including temperature-dependent thermal conductivity) and boundary conditions. SPECTROM-41 was used in this study to simulate the heat transfer between the wells and surrounding rock formation. The results of these calculations were then integrated into the thermomechanical analyses to account for the thermal stresses and strains that are generated by temperature changes in the rock formations and well casings.

4.1.3 Thermomechanical Finite Element Program SPECTROM-32

The finite element program SPECTROM-32 [Callahan et al., 1989] was used to perform the thermomechanical analyses of the well models. SPECTROM-32 is a finite element program developed by RESPEC for the solution of rock mechanics problems. It was designed specifically for the simulation of underground openings and structures. SPECTROM-32 not only has the capability to model the elastic-plastic response that is commonly associated with brittle rock types, but it also has the capability to simulate the viscoplastic behavior that is observed in rock salt. The features and capabilities of SPECTROM-32 required specifically for this analysis include:

- Option for modeling axisymmetric geometries.
- Kinematic and traction boundary conditions.
- Constitutive model for viscoplastic behavior of salt.
- Mohr-Coulomb plasticity constitutive model.
- Peak/residual tension constitutive model.
- Capability to represent arbitrary in situ stress and temperature fields.

4.1.4 Thermomechanical Finite Element Program ABAQUS

The threaded connection analyses were performed using the commercial finite element program ABAQUS, Version 6.5.1 [ABAQUS, Inc., 2005]. Three-dimensional models of complex, multicomponent assemblies can be built in ABAQUS using a variety of modeling elements. Complex operating scenarios can be imposed on the models simulating pressure, load, temperature, displacement, and deformation. Various temperature-, pressure-, and time-dependent behaviors can be used to describe nonlinear material properties under these complex operating scenarios.

4.2 STRATIGRAPHY

Two vastly different host rock formations were considered in the evaluation of the candidate well casing loads. The two salt cavern wells were assumed to be sited in a salt dome rather than a bedded salt formation to maximize the exposure of the casing to salt deformation. The reservoir well was assumed to be sited in a bedded formation and cemented to approximately the same depth as the deeper salt cavern well for comparative purposes. The stratigraphy used for the numerical simulations is described in the following subsections.

4.2.1 Salt Dome Cavern Storage

The two salt cavern wells selected for evaluation were assumed to be located in massive salt domes. Therefore, a simplified all-salt stratigraphy was used for the evaluation of the two salt cavern well casings. Salt domes can be found in Alabama, Louisiana, Mississippi, and Texas, as well as offshore in the Gulf of Mexico. Most of these domes have overlying sediments and caprock of varying thickness. However, it was assumed for this study that the sediments and caprock are relatively thin and sufficiently remote from the casing shoe that they do not have a significant impact on the predicted results in the lower portion of the well casing. Additionally, the gas storage caverns were modeled as being isolated from the edge of the dome and from other caverns.

4.2.2 Porous Sandstone Reservoir Storage

The 1,524-meter- (5,000-foot-) deep reservoir well was assumed to be located in a bedded formation similar to those used for storage in the northeastern United States. The formation is comprised of numerous shale, limestone, anhydrite, dolostone, and sandstone beds. Natural gas is stored in a 30.5-meter-thick (100-foot-thick) sandstone formation between 1,524 and 1,554.5 meters (5,000 and 5,100 feet) below ground surface. To simplify the problem, the rock beds more than 610 meters (2,000 feet) above the gas storage formation were combined into a massive layer that is represented by the predominate formation material, shale. Details of the stratigraphy used in the model of the reservoir well are provided in Table 4-1.

Table 4-1. Stratigraphic Detail Used in the Numerical Model of Reservoir Well No. 3

Stratigraphic Unit	Rock Type	Top (m)	Bottom (m)	Thickness (m)
Overburden	Shale	0	935.1	935.1
Tully	Limestone	935.1	961.9	26.8
Hamilton	Shale	961.9	1,428.9	467.0
Marcellus	Shale	1,428.9	1,486.2	57.3
Onondaga	Limestone	1,486.2	1,500.8	14.6
Needmore	Shale	1,500.8	1,524.0	23.2
Oriskany	Sandstone	1,524.0	1,554.5	30.5
Helderberg	Limestone	1,554.5	1,645.9	91.4

4.3 MATERIAL MODELS AND PROPERTIES

The thermal and structural models of the wells and connections include the casing components, rock strata, and cavern/reservoir fluids. A different constitutive model or material law was used for each material type represented in the conceptual models. Each constitutive model is defined by a set of model parameters that are typically determined from independent laboratory testing of the material being modeled. The model parameters for each of the materials were obtained from the literature. The models and parameters used in the analyses are presented below under separate headings.

4.3.1 Steel Casing

The properties of the casings used for the final cemented strings for each of the candidate wells are listed in Table 4-2. The mechanical behavior of the steel casing was assumed to be linear elastic for the well models. A nonlinear material model was used to describe the behavior of the steel casing for the connection models as described in the next subsection. For the well models, the steel was assumed to be homogeneous and isotropic so its elastic behavior could be characterized using only two elastic parameters.

4.3.2 Threaded Connections

The J-55 and K-55 materials specified for the connection analyses were modeled using the elastic-plastic-thermal-creep constitutive model developed previously by C-FER Technologies based on material coupon tests [Humphreys et al., 1991]. The J-55 material model has a thermal expansion coefficient of $15.6 \times 10^{-6} \text{ K}^{-1}$ ($8.7 \times 10^{-6} \text{ R}^{-1}$) and a Young's modulus of 200 GPa (29,000,000 psi). The yield strength for J-55 was defined on a temperature-dependent basis

and was assumed to be 425 MPa (61,640 psi) at 20°C (68°F), and 405 MPa (58,740 psi) at 200°C (392°F). The K-55 material has a thermal expansion coefficient of $14.4 \times 10^{-6} \text{ K}^{-1}$ ($8.0 \times 10^{-6} \text{ R}^{-1}$), a Young's modulus of 190 GPa (27,557,000 psi), and yield strengths of 427 MPa (61,930 psi) and 370 MPa (68,168 psi) at 20°C (68°F) and 200°C (392°F), respectively.

Table 4-2. Elastic and Thermal Material Properties of Casing Components Used for the Well Models

Material	Property	Value	Units	Reference
Steel Casing	Young's Modulus	206.9	GPa	Riley et al. [1999]
	Poisson's Ratio	0.29	—	Riley et al. [1999]
	Density	7.85	g/cm ³	Incopera [1996]
	Thermal Expansion Coefficient	12.1×10^{-6}	K ⁻¹	Riley et al. [1999]
	Thermal Conductivity	60.52	W/(m-K)	Incopera [1996]
	Specific Heat	435	J/(kg-K)	Incopera [1996]
Cement	Young's Modulus	11.0	GPa	Pfeifle et al. [2000]
	Poisson's Ratio	0.286	—	Pfeifle et al. [2000]
	Density	1.86	g/cm ³	Incopera, [1996]
	Thermal Expansion Coefficient	9.54×10^{-6}	K ⁻¹	Philippacopoulos and Berndt [2000]
	Thermal Conductivity	0.72	W/(m-K)	Incopera [1996]
	Specific Heat	779	J/(kg-K)	Incopera [1996]

4.3.3 Cement Sheath

The cement was also assumed to be a homogeneous, isotropic, linear elastic material. The elastic and thermal properties of cement are provided in Table 4-2.

4.3.4 Rock Salt

When a rate-dependent material is subjected to a deviatoric (shear) stress, it deforms with time (creeps). Although time-dependent deformation occurs in all materials, it is often so small that it can be neglected in most engineering problems. However, the rate-dependent deformation of some geologic materials, such as salt, is significant for the stresses, temperatures, and times of interest in underground storage caverns.

Based on analysis of multistage and other creep data from eight domal salts, Munson [1998] classified the creep of domal salt as forming two distinct groups, either soft or hard, where the

difference is roughly a factor of ten in creep rate between the two groups. Munson [1998] provided estimates for the creep model developed for the Waste Isolation Pilot Plant near Carlsbad, New Mexico, to predict both soft and hard salt behavior. This creep model is referred to as the M-D model. The M-D model is capable of predicting the steady-state and transient creep response of salt over a large range of stress and temperature through the contribution of three micromechanical mechanisms. However, for the range of stress and temperature expected in the salt during natural gas storage, the creep rate predicted by the M-D model is dominated by only one of these mechanisms (the observed and known but undefined mechanism at low temperature and low stress). This mechanism can take on the same functional form as the Norton Power Law [Norton, 1929], after appropriate rearrangement of terms. Whereas the transient nature of salt is an important feature to capture during most numerical modeling studies of natural gas storage caverns, the use of a steady-state creep model such as the Norton Power Law is adequate for the accuracy desired for this study. The Norton Power Law can be expressed as shown below:

$$\dot{\epsilon}_c = A \exp\left(-\frac{Q}{RT}\right) \sigma^n \quad (4-1)$$

For a triaxial compression laboratory creep test, $\dot{\epsilon}_c$ is the axial creep strain, σ is the stress difference, R is the universal gas constant, T is absolute temperature, Q is activation energy, and A and n are material parameters.

To maintain the conservative nature of the analyses, the steady-state properties for the faster creeping salt given by Munson [1998] were used in this study. The corresponding parameter estimates of the Norton Power Law for A , Q , and n are 5.2×10^{-14} MPa⁻ⁿ/year, 10,000 calories/mole, and 5.0, respectively.

In addition to creep, the deformation of salt includes thermoelastic deformation. The thermoelastic properties of salt used for this study are provided in Table 4-3.

4.3.5 Nonsalt Strata

The reservoir storage well is sited in a bedded formation comprised predominately of shale, but also includes limestone and sandstone beds as discussed in Section 4.2.2. The shale and limestone were modeled as linear elastic materials in this study. The sandstone was modeled as a poroelastic material to predict the compaction and expansion of the reservoir caused by pressure changes from gas injection and withdrawal.

The poroelastic model is based on Biot's theory of deformation for porous materials [Biot, 1955]. The poroelastic model accounts for any volumetric straining that may occur because of pore pressure by modifying the total stress tensor (σ_{ij}) as follows:

Table 4-3. Rock Strata Elastic and Thermal Material Properties

Material	Property	Value	Units	Reference
Salt	Young's Modulus	31	GPa	Munson [1998]
	Poisson's Ratio	0.25		Munson [1998]
	Density	2.16	g/cm ³	Dahlstrom [1988]
	Thermal Expansion Coefficient	2.2×10^{-5}	K ⁻¹	Senseny et al. [1992]
	Thermal Conductivity	5.19	W/(m-K)	Callahan [1981]
	Specific Heat	837	J/(kg-K)	Callahan [1981]
Shale	Young's Modulus	20.8	GPa	Croff et al. [1985]
	Poisson's Ratio	0.21		Croff et al. [1985]
	Density	2.56	g/cm ³	Croff et al. [1985]
	Thermal Expansion Coefficient	7.9×10^{-6}	K ⁻¹	Croff et al. [1985]
	Thermal Conductivity	1.39	W/(m-K)	Croff et al. [1985]
	Specific Heat	796	J/(kg-K)	Croff et al. [1985]
Limestone	Young's Modulus	45.8	GPa	Croff et al. [1985]
	Poisson's Ratio	0.27		Croff et al. [1985]
	Density	2.59	g/cm ³	Croff et al. [1985]
	Thermal Expansion Coefficient	6.7×10^{-6}	K ⁻¹	Croff et al. [1985]
	Thermal Conductivity	3.07	W/(m-K)	Croff et al. [1985]
	Specific Heat	743	J/(kg-K)	Croff et al. [1985]
Sandstone	Young's Modulus	20.4	GPa	Croff et al. [1985]
	Poisson's Ratio	0.20		Croff et al. [1985]
	Density	2.29	g/cm ³	Croff et al. [1985]
	Thermal Expansion Coefficient	10.0×10^{-6}	K ⁻¹	Croff et al. [1985]
	Thermal Conductivity	3.40	W/(m-K)	Croff et al. [1985]
	Specific Heat	712	J/(kg-K)	Croff et al. [1985]
	Biot Coefficient	0.7		Economides et al. [1994]

$$\sigma_{ij} = \sigma'_{ij} - \alpha p \delta_{ij} \quad (4-2)$$

where:

σ'_{ij} = the components of the effective stress tensor

α = Biot's constant

p = fluid pressure

δ_{ij} = Kronecker delta.

Table 4-3 lists the thermoelastic properties for the nonsalt rocks modeled in this study.

4.3.6 Natural Gas

Natural gas is modeled in SCTS as a real gas using the American Gas Association's Detail Characterization Method as described by Starling and Savidge [1994]. For this study, the composition of the natural gas was assumed to be 100 percent methane. For the thermomechanical analyses of the two salt cavern wells using SPECTROM-32, gas pressure was applied in the finite element models as tractions along the inside of the casing and the surface of the uncased wellbore and cavern. A linear pressure gradient was assumed for the gas in the well and cavern and is based on the casing seat pressures and bulk cavern gas densities determined by SCTS.

4.3.7 Brine

Because of the very small compressibility of brine (approximately $2.8 \times 10^{-4}/\text{MPa}$ ($1.9 \times 10^{-6}/\text{psi}$)), the increase in brine density associated with the hydrostatic pressure increase over the height of the model is assumed to be negligible (about 0.1 percent change per 305 meters (1,000 feet)). Consequently, the brine density was assumed to be a constant 1.2 g/cm^3 (75 lb/ft^3), resulting in a vertical pressure gradient of 0.0118 MPa/meter (0.52 psi/foot) of depth.

4.4 IN SITU CONDITIONS

Because the creep rate of salt is dependent on temperature and stress, it is important to model temperatures and stresses which are representative of those in the vicinity of the well casings. Also, the magnitude of the thermally induced stresses will depend on the initial in situ temperature for both the salt cavern wells and the reservoir well. The initial stress and temperature distributions used for the numerical models of the well casings are discussed below.

4.4.1 Stress Distribution

Principal in situ stresses are generally assumed to be aligned with a coordinate system that is vertical and horizontal. Assuming that the in situ stress state in salt domes and bedded salt formations is isotropic is generally accepted because most models of salt creep predict that long-term creep removes any differences in the horizontal and vertical stress components. The magnitude of the vertical principal stress is typically assumed to be equal to the weight of the overburden. An initial isotropic state of stress that varies with depth was assumed to exist within the salt formations modeled in this study.

In most nonsalt locations, the magnitudes of the vertical and horizontal principal stresses are not equal. Typically, the two principal horizontal stresses are different from the vertical stress and are also different from each other. The inequality of the principal stresses in most regions is reflected in the regional faulting. However, the axisymmetric representation of the reservoir well numerical model does not allow separate designations for the horizontal stresses. Therefore, the simulations of the reservoir well were performed assuming an isotropic initial state of stress that varies with depth. The initial state of stress within the models before creation of the well is based on an acceleration of gravity of 9.8 m/s^2 (32.15 ft/s^2) and the densities for the overlying strata given in Table 4-3.

4.4.2 Temperature Profile

The temperature profiles used for the analyses of the well models are based on temperatures and temperature gradients reported in the literature. Karably and White [1981] reported geothermal gradients for eight Gulf Coast salt domes ranging from a minimum of 0.01750°C/m (0.0096°F/ft) to a maximum of 0.02935°C/m (0.0161°F/ft). For the salt cavern well models used in this study, a surface temperature of 28.33°C (83°F) and a single temperature gradient of 0.02734°C/m (0.015°F/ft) were assumed.

A surface temperature of 15.56°C (60°F) and temperature gradient of 0.02005°C/m (0.011°F/ft) from ground surface to the reservoir depth of 1,542 meters (5,000 feet) were assumed for the reservoir well model. Using these properties, the temperature at the gas storage depth is 46.11°C (115°F).

4.5 GAS PRESSURE CYCLES

The gas pressure cycles used for the salt cavern well analyses were selected to provide a conservative estimate of the casing loads by using very rapid injection and withdrawal scenarios. The rapid cycles produce the largest temperature range possible for the casing because they reduce the time available for heat transfer to the surrounding rock formation. Repetitive gas injection and withdrawal periods of 20 and 10 days, respectively, were simulated for the two salt cavern well models. The injection and withdrawal rates were adjusted during each cycle in the simulations so that the pressure at the casing shoe was maintained between

the maximum and minimum allowable pressures of 0.001786 and 0.00525 MPa/m (0.85 and 0.25 psi/ft) depth at the casing shoe. The allowable pressure range at the casing shoe was selected because it spans the range used by most natural gas storage caverns in the United States.

Figure 4-1 illustrates the annual pressure cycles used for the salt cavern well models. A total of 60 cycles or 5 years of operation were simulated during the analyses of the well problems to allow sufficient time for the configuration to achieve thermal equilibrium after solution mining of the cavern. A repeatable temperature history was desired for this problem to define the magnitude of the cyclic loading to be specified for the connection analyses.

Deliverability of reservoir storage wells is typically much lower than that of salt caverns. For this study, prolonged injection and withdrawal periods were assumed for the reservoir storage well. The annual pressure cycle used for Reservoir Storage Well No. 3 is illustrated in Figure 4-1. As shown in this figure, the complete cycle requires 1 year with gas injection and withdrawal occurring during 9-month and 3-month periods, respectively. This cycle is intended to represent a storage well that is used for seasonal heating demand during the winter months. Minimum and maximum reservoir formation pressures of 4.14 and 22.06 MPa (600 and 3,200 psi) were specified, respectively. Gas is injected at a temperature of 21.11°C (70°F) and withdrawn at the reservoir storage formation temperature of 46.11°C (115°F).

4.6 FINITE ELEMENT MODELS

Axisymmetric models were used in this study to provide an accurate representation for the well configurations under investigation. A total of six finite element models were developed to complete this study: three well models and three threaded connection models. One well model was developed for each of the three candidate wells under consideration. The connection models were designed to address different casing sizes, connection assemblies (welded and nonwelded), and loading conditions (axisymmetric and nonaxisymmetric). Descriptions of the finite element meshes of the well and connection models are provided in separate sections below.

4.6.1 Well Models

Because the focus of this study was to evaluate casing loads, the selection of the size and shape of the salt storage cavern was arbitrary. However, the displacements caused by salt creep are of primary concern. Cylindrical-shaped caverns having a diameter and height of 60.96 and 304.8 meters (200 and 1,000 feet), respectively, were modeled in this study. The roof of each cavern is located 30.48 meters (100 feet) below the casing shoe depths of 579 and 1,524 meters (1,900 and 4,900 feet). Based on these assumptions, the caverns have a volume of 889,600 m³ (5.6 million barrels) and provide natural gas storage of about 8.6×10^7 Nm³ (3.2 billion cubic feet (Bcf)) for the shallow cavern and 1.9×10^8 Nm³ (7.1 Bcf) for the deeper cavern.

RSI-1546-06-005

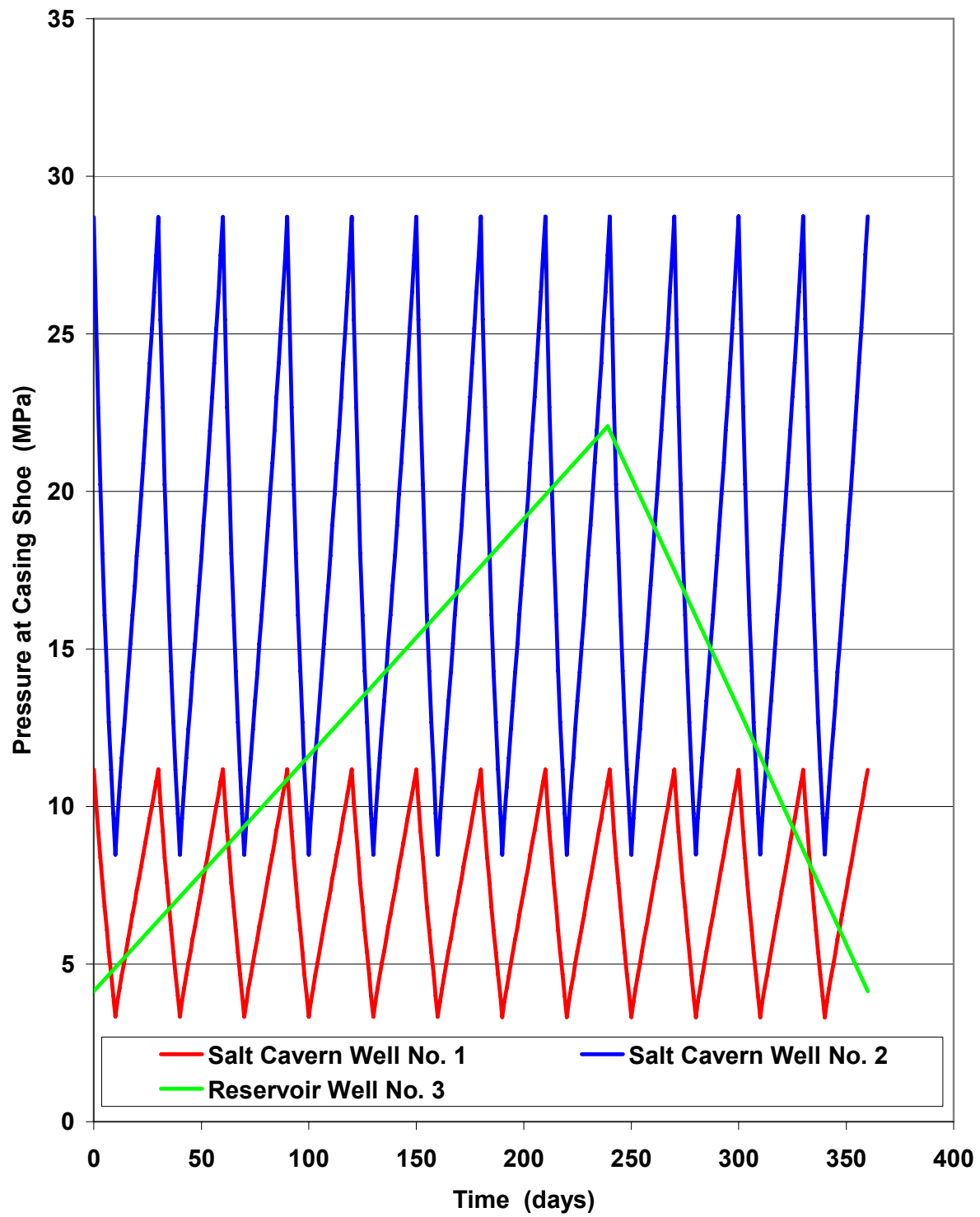


Figure 4-1. Annual Gas Pressure Cycles for the Three Candidate Wells.

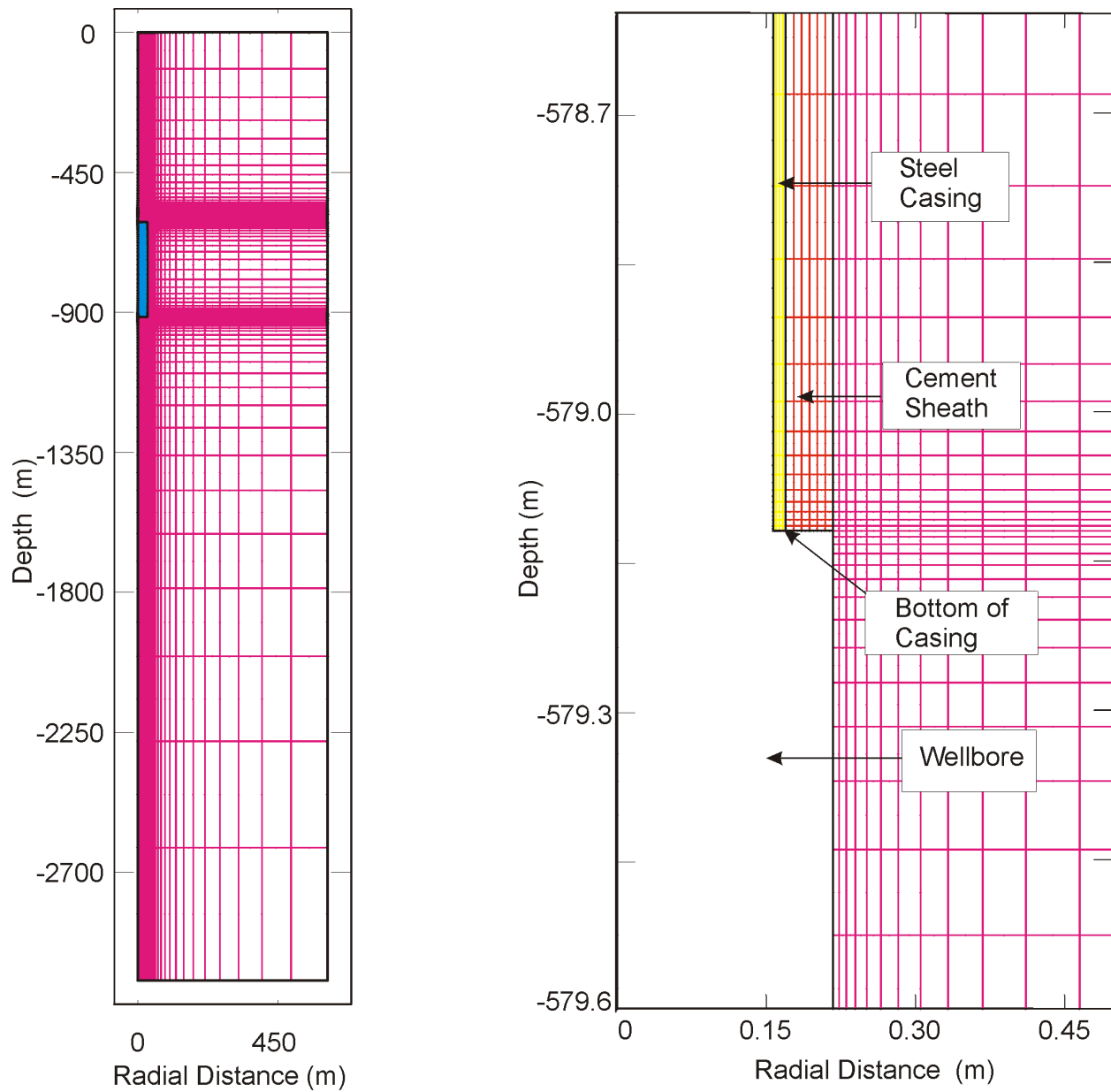
For Salt Cavern Well No. 1, the final cemented casing is seated at a depth of 579 meters (1,900 feet). Figure 4-2 shows the axisymmetric model used for Salt Cavern Well No. 1. The model extends vertically from ground surface to a depth of 3,048 meters (10,000 feet). The model extends laterally 696 meters (2,000 feet) from the center of the well. The extent of the model was selected to isolate the response of the cavern from the influences of the radial and bottom boundaries, which are artificial truncations of the actual horizontal and vertical extents of the salt. Besides the salt and void space of the cavern, the only other components contained in the model are the 340-millimeter- (13³/₈-inch-) diameter steel casing and the 50.8-millimeter (1.87-inch) cement sheath. Surface and intermediate casings are not included in the model because they are sufficiently remote as to have negligible effect on the state of stress in the lower portion of the well, which is of primary concern. The finite element mesh contains 28,533 nodes and 9,372 eight-noded finite elements. The region immediately outside the wellbore and walls of the cavern were very finely subdivided. This extremely fine subdivision was used to accurately represent the high stress and temperature gradients that are anticipated in these areas. This finite element mesh was used for both the heat transfer and thermomechanical analyses of Salt Cavern Well No. 1.

Figure 4-3 shows the axisymmetric model used for Salt Cavern Well No. 2. This model is similar to that used for Salt Cavern Well No. 1 except the top of the cavern is located at a depth of 1,524 meters (5,000 feet) and the cemented casing extends to a depth of 1,494 meters (4,900 feet). The finite element mesh of Salt Cavern Well No. 2 contains 27,933 nodes and 9,174 eight-noded finite elements.

The finite element model of Reservoir Well No. 3 extends from ground surface to a depth of 1,645 meters (5,400 feet). The model extends laterally 696 meters (2,000 feet) from the center of the well. The extent of the model was selected to isolate the response of the well from the influences of the radial and bottom boundaries. The model includes the final cemented casing to a depth of 1,524 meters (5,000 feet) in the stratigraphy identified in Section 4.2.2. Because of the axisymmetric assumption, the 90-degree bend could not be incorporated into the model. Therefore, the casing was assumed to extend to the top of the sandstone storage formation. The mesh used for the analyses of Reservoir Well No. 3 is shown in Figure 4-4. The mesh contains 31,194 nodes and 10,251 eight-noded finite elements. This model was used for both the heat transfer and thermomechanical analyses of Reservoir Well No. 3.

During heat transfer simulations of the three well models, the outer boundaries of the models were insulated and thus no heat was transferred across these boundaries. The gas temperature history in the caverns and/or well was applied to the surface of the cavern and/or well casing of the models to calculate temperatures in the casing and surrounding rock formation. This temperature history was subsequently used in the thermomechanical simulations to account for thermally induced stresses and temperature-dependent behavior of the salt in the models.

RSI-1546-06-006



**Partial View of Mesh
Around Casing**

Figure 4-2. Axisymmetric Finite Element Model of Salt Cavern Well No. 1.

RSI-1546-06-007

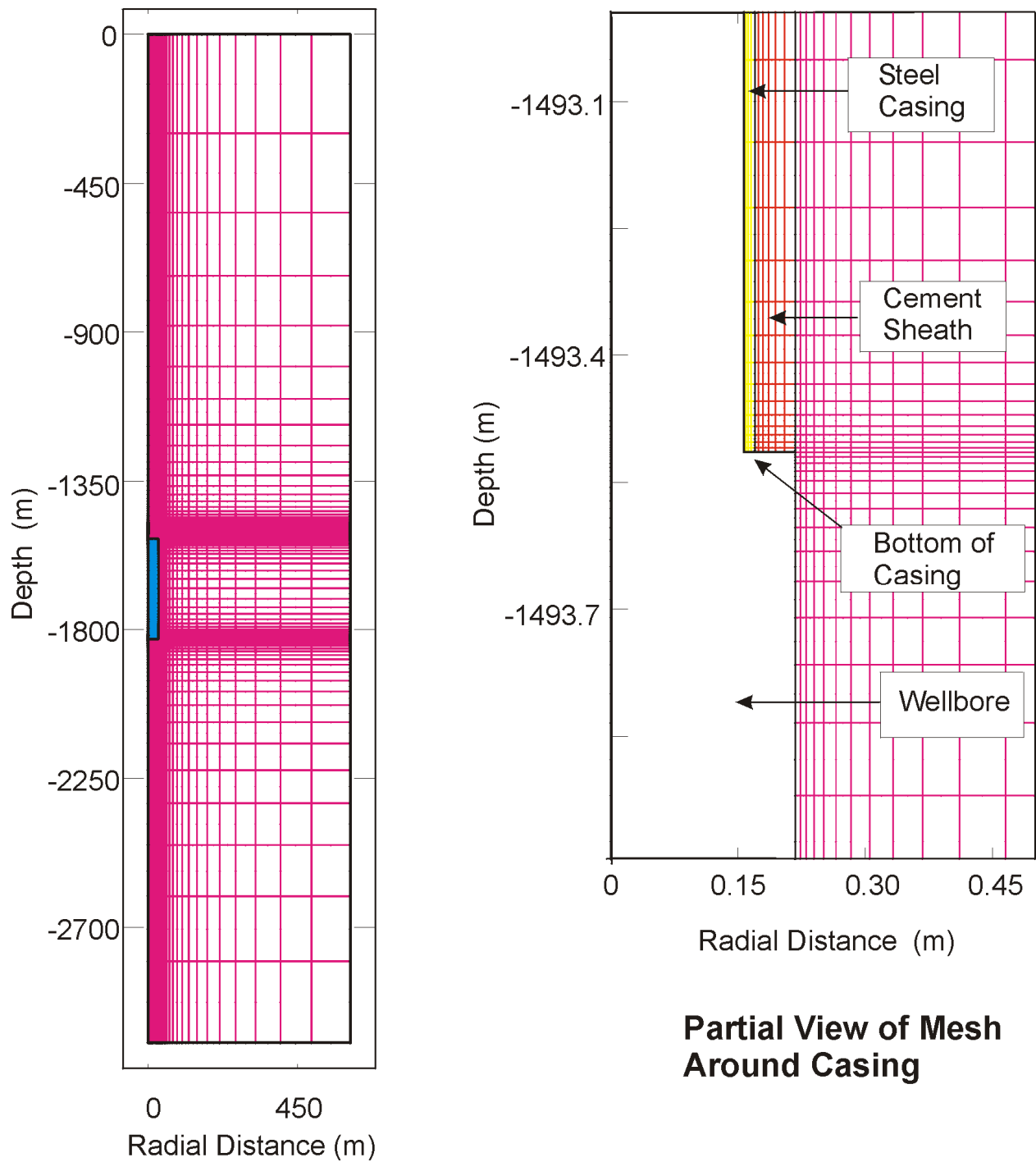


Figure 4-3. Axisymmetric Finite Element Model of Salt Cavern Well No. 2.

RSI-1546-06-008

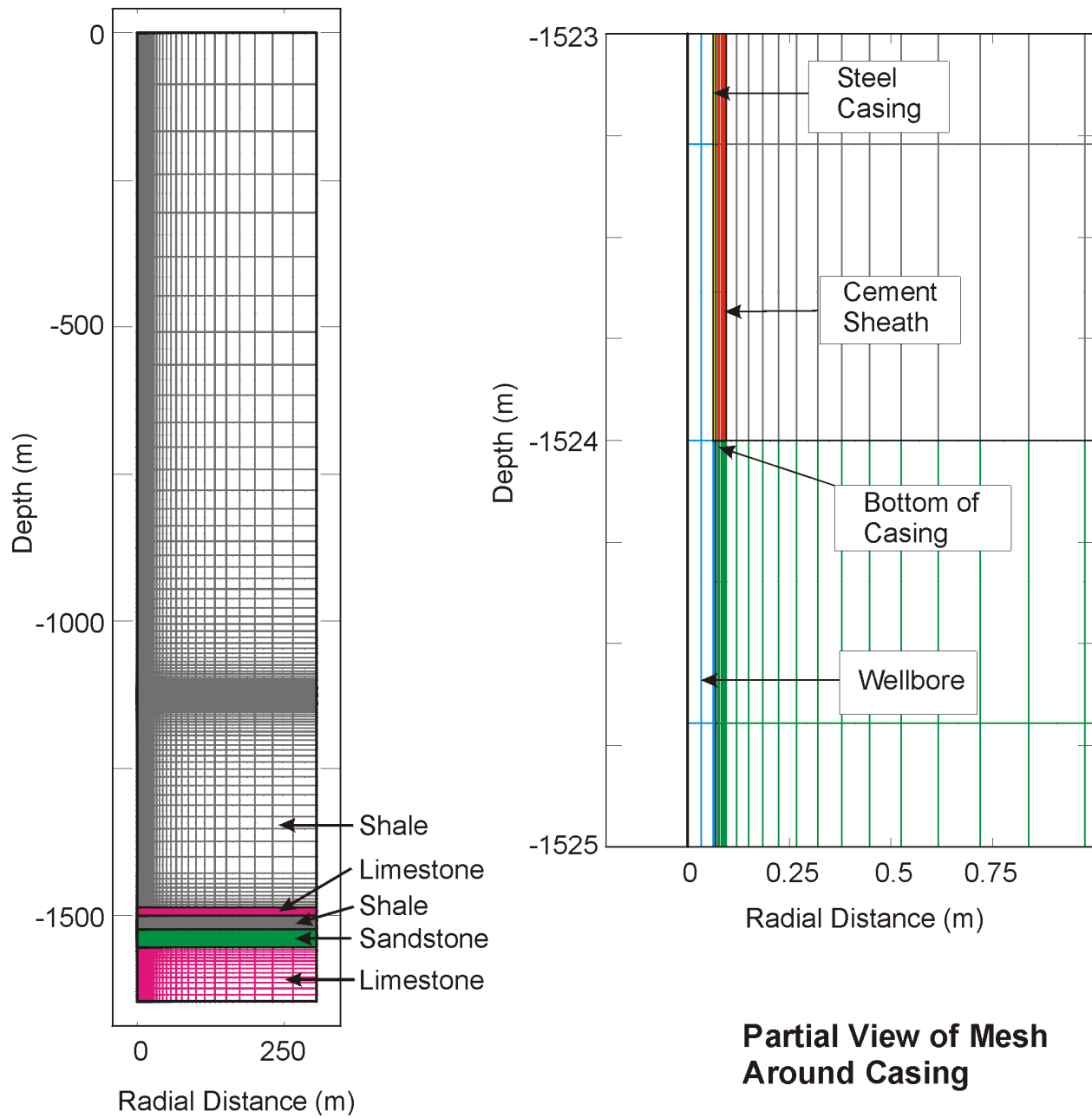


Figure 4-4. Axisymmetric Finite Element Model of Reservoir Storage Well No. 3.

During the thermomechanical simulations, the kinematic boundary conditions specified along the sides of the axisymmetric models were:

- No radial displacement along the centerline.
- No radial displacement along the outer radius.
- No vertical displacement along the bottom surface.

The upper surfaces of the models were free to move in the vertical and horizontal directions.

In the models, normal tractions were specified along the inside diameter of the steel casing to simulate the fluid pressure. For the salt cavern well models, tractions were also specified along the perimeter of the cavern and along the 30.48 meters (100 feet) of open borehole leading into the cavern. The magnitudes of these tractions were set equal to the hydrostatic pressure based on the density of brine during the solution-mining portion of the simulation and based on the respective casing seat pressure and the average cavern gas density during the natural gas storage portion of the simulated history. For the reservoir well model, the tractions along the inside of the steel casing and the pore pressure in the sandstone reservoir were updated to correspond with the downhole pressure.

4.6.2 Connection Models

The casing connections were assumed to conform to the thread profile, thread interference, and coupling length for 8-Round Short Threaded and Coupled (STC) connections as defined by the American Petroleum Institute Recommended Practice API-5B. Connection geometry was assumed to conform to the published nominal dimensions for the 140-millimeter (5.5-inch, 15.5 pound/foot (lb/ft)) and 340-millimeter (13³/₈-inch, 72 lb/ft) casing. The analyses did not consider the effects of manufacturing tolerances on the connection performance. The model included one-half of a coupling and a single pipe pin end with a 127-millimeter (5-inch) length of pipe body extending from the connection as shown in Figure 4-5.

Separate models were developed to analyze axisymmetric and nonaxisymmetric loading scenarios. For the salt cavern well connections, only axisymmetric loading was considered. Both axisymmetric and nonaxisymmetric load conditions were analyzed for the reservoir storage well. The nonaxisymmetric loading condition was necessary to account for the bending stresses caused by the curvature of the casing in the deviated section of the well. For the nonaxisymmetric model, the pipe body end was constrained to a global beam node, at which the axial force and bending moment were applied. A special connection model was also developed for the reservoir storage connection analysis that included the addition of a weld between the coupling face and the pipe body after the connection is made up. Casing deformations, such as shears and buckles that impose bending on the pipe, were not considered.

RSI-1546-06-009

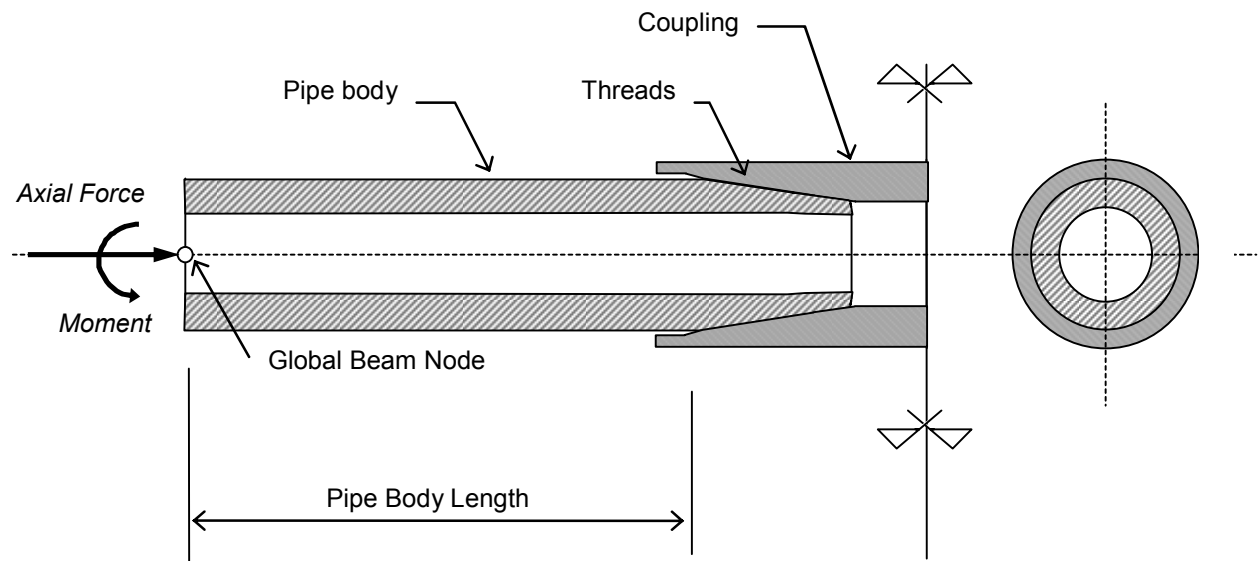


Figure 4-5. Schematic of Three-Dimensional Finite Element Connection Model.

5.0 RESULTS AND DISCUSSION OF WELL CASING MODELS

The axisymmetric finite element models of the three candidate wells described in Chapter 4.0 were used to evaluate the temperature and stress distribution in the steel casing from ground surface to the casing shoe during gas storage operation. The following sections provide a brief description of the well problems and discuss the results of the numerical modeling of the well casings. Results provided during gas storage operation include: (1) gas temperature history and distribution in the well, (2) temperature fields in the casing and rock formation along the wellbore, (3) axial (vertical) stresses in the steel casing, and (4) state of stress at the location of the lowest connection. The stresses and strains determined at the lowest connection in each well were used to define the cyclic loads that were applied to the connection models to determine the potential for cyclic fatigue. Results of the threaded connection modeling are discussed in Chapter 6.0.

5.1 PROBLEM DESCRIPTION

The stress analyses of the well casings considered contributions from (1) casing weight, (2) product pressures, (3) thermally induced stresses, and (4) external ground pressures. The problem descriptions differ for the salt cavern wells and the reservoir well. Descriptions of these two simulations are described separately below.

5.1.1 Salt Cavern Well Model Simulations

The analyses of the two salt cavern well models were initiated assuming a lithostatic state of stress wherein the horizontal stresses are equal to the vertical stress and vary with depth based on the density of salt. Similarly, a linear temperature distribution that varies with depth was also assumed within the modeled region. From this initial condition, the following sequential steps were simulated:

1. Instantaneously drill the 0.4348-meter- (17.12-inch-) diameter well to the depth of the cavern roof.
2. Backfill the well with a compressible, inviscid fluid having the same density as cement.
3. Hang the 340-millimeter (13³/₈-inch) steel casing from ground surface.
4. Update the fluid material in the well annulus to that of hardened cement and simultaneously remove the fluid material in the central hole and apply a traction to the inside diameter of the steel casing to represent the pressure of a column of drilling mud.
5. Simulate solution mining of the cavern by injecting fresh water at a temperature of 21.11°C (70°F) over a 650-day period. The actual models simulate instantaneous excavation of the cavern to its final dimension rather than a progressive enlargement of the

cavern. However, the use of an instantaneous versus incremental mining approach is not expected to have a significant impact on the final stress and temperature fields surrounding the cavern at the end of solution-mining period.

6. Allow the brine-filled cavern to sit stagnant for 446 days. The long stagnant period was included to allow the formation temperature to recover after the extended period of solution mining. The stagnant period was included for modeling convenience because it required less effort than the simulation of additional gas service cycles to obtain a thermal equilibrium.
7. Dewater the cavern in 150 days at maximum gas pressure.
8. Simulate 5 years or 60 gas service cycles.

5.1.2 Reservoir Well Model Simulations

The analysis of the reservoir well model was initiated assuming an initial lithostatic state of stress that varies with depth as described in Section 4.4.1. The initial temperature of the formation was assumed to increase linearly with depth as described in Section 4.4.2. From this initial condition, the following sequential steps were simulated:

1. Instantaneously drill the 190.5-millimeter- (7.5-inch-) diameter well to the top of the storage formation.
2. Backfill the well with a compressible, inviscid fluid having the same density as cement.
3. Hang the 140-millimeter (5½-inch) steel casing from ground surface.
4. Update the fluid material in the well annulus to that of hardened cement and simultaneously remove the fluid material in the central hole and apply tractions along the inner diameter of the steel casing equivalent to that of a column of drilling mud.
5. Update the traction acting along the inside diameter of the steel casing with that produced by natural gas at minimum pressure.
6. Simulate five gas service cycles.

5.2 SALT CAVERN THERMAL SIMULATOR RESULTS

The computer program SCTS was used to determine the temperature range and distribution of the fluid flowing through the casings of the two salt cavern wells. Temperature histories predicted by SCTS for the fluid (either brine or natural gas) in the wells at depths of 579 and 1,494 meters (1,900 and 4,900 feet) are provided in Figures 5-1 and 5-2, respectively. These figures show the complete temperature history starting with solution mining of the caverns using brine. Solution mining of the caverns using brine that is cooler than the in situ temperature lowers the formation temperature in the vicinity of the cavern. However, injection

RSI-1546-06-010

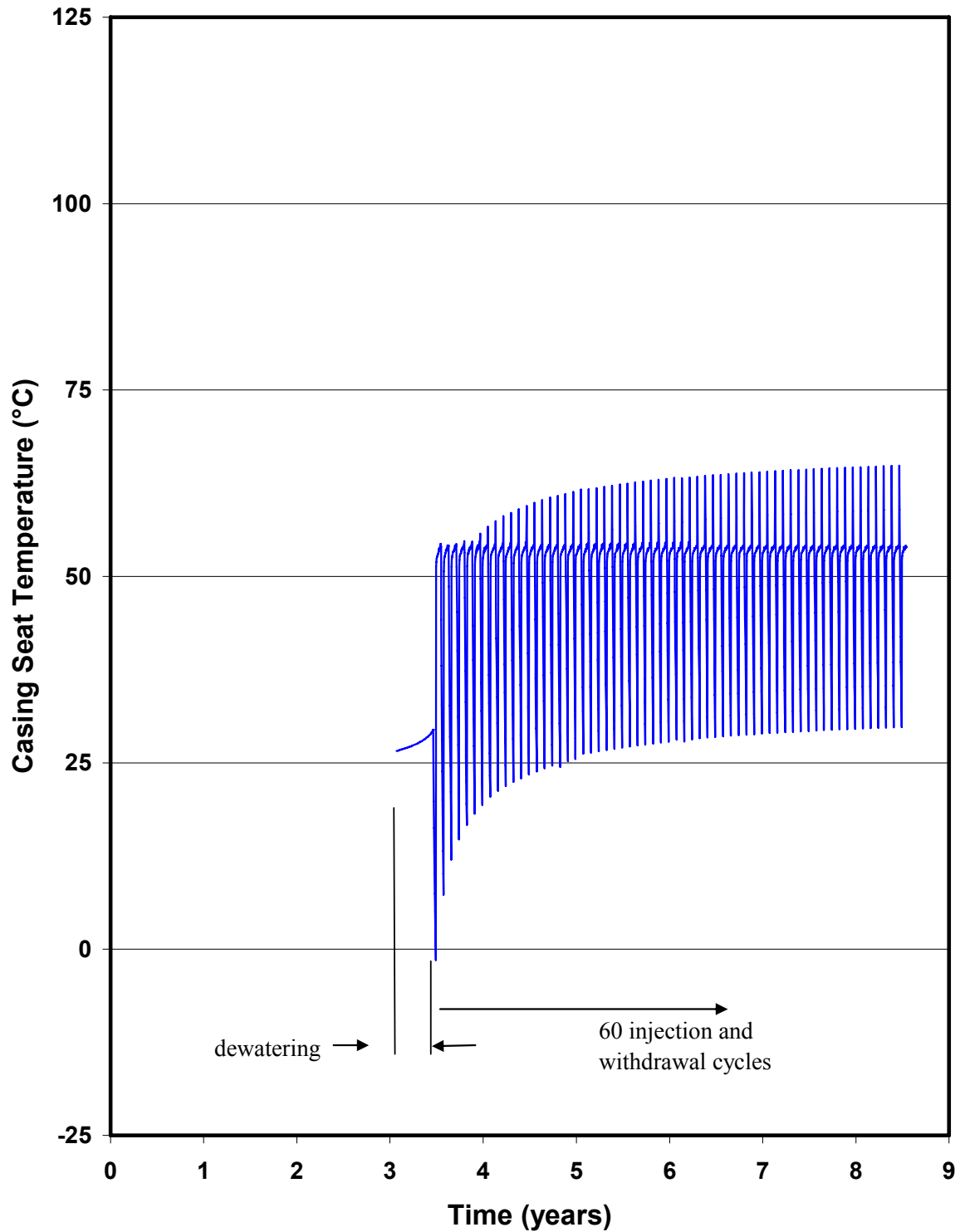


Figure 5-1. Casing Seat Temperature History for the 610-Meter (2,000-Foot) Shallow Salt Cavern Predicted by SCTS During 60 Gas Service Cycles.

RSI-1546-06-011

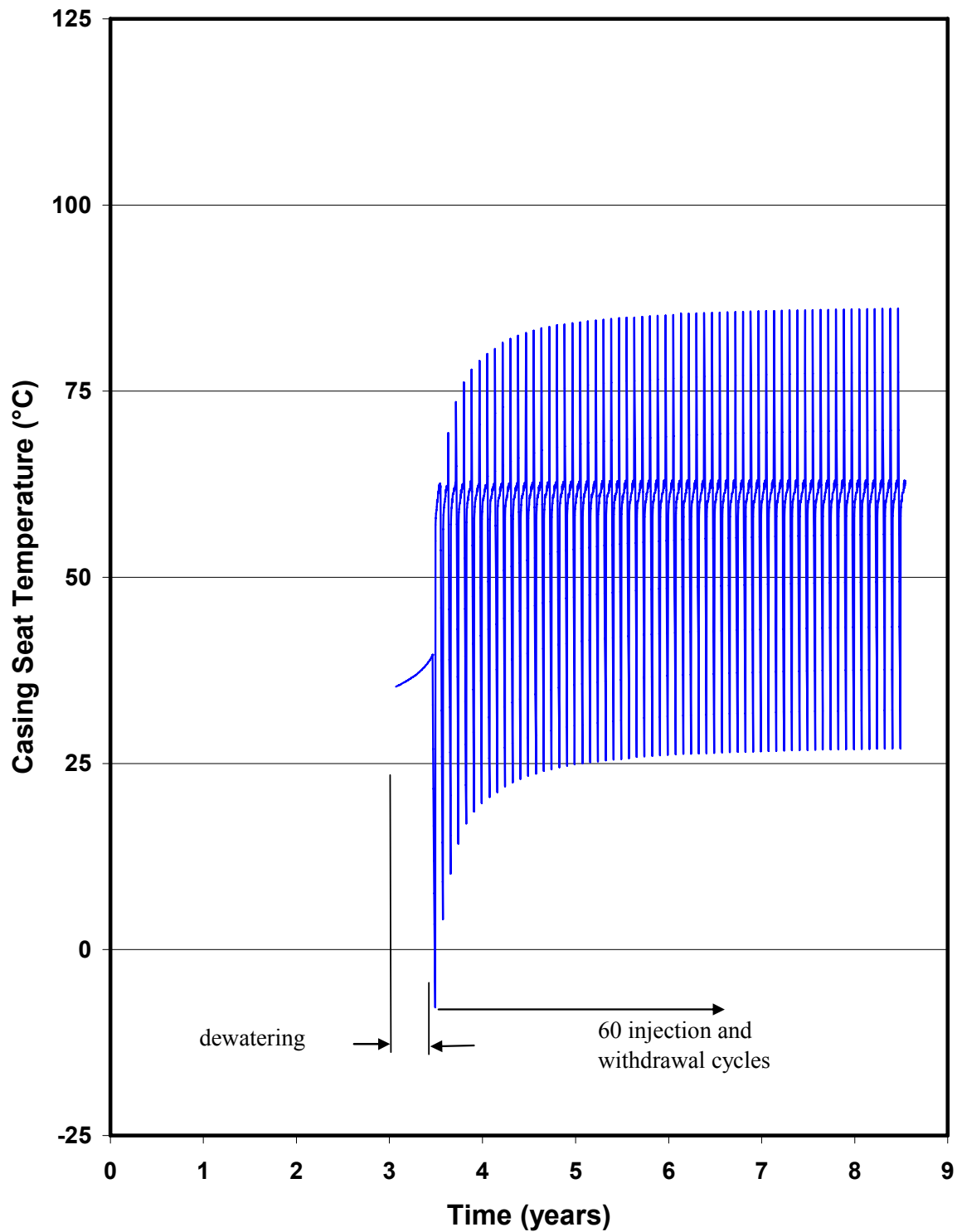


Figure 5-2. Casing Seat Temperature History for the 1,524-Meter- (5,000-Foot-) Deep Salt Cavern Predicted by SCTS During 60 Gas Service Cycles.

of gas at a temperature warmer than the formation temperature results in the gradual increase in the rock formation temperature surrounding the cavern with each successive gas cycle until a new thermal equilibrium is established. As shown in Figures 5-1 and 5-2, about 60 turns of working gas are necessary to provide sufficient time for the formation to obtain a new thermal equilibrium based on the repetitive injection and withdrawal cycles simulated.

In addition to the bulk temperature of the gas in the cavern, temperature histories are provided by SCTS at 15.24-meter (50-foot) increments from the wellhead to the casing shoe. Figure 5-3 illustrates the temperature profile of the gas in the well of Salt Cavern Well No. 1 at the beginning of injection, end of injection, start of withdrawal, and end of withdrawal. During withdrawal, the temperature of the casing quickly approaches that of the gas in the cavern. As a result, the warmest casing temperatures are predicted at the beginning of withdrawal when the pressure is the greatest. As shown in Figure 5-3, the temperature in the well at the beginning of withdrawal is about 10 degrees warmer than that of the casing during injection and 15 degrees warmer than the formation temperature at the cavern midheight of 49.17°C (120.5°F). After the 20-day withdrawal period, the temperature change caused by the decrease in cavern pressure results in the gas temperature becoming significantly lower. At the end of withdrawal, the casing temperature is about 25 degrees cooler than the gas injection temperature. Figure 5-4 is similar to Figure 5-3 except gas temperature profiles are provided for Salt Cavern Well No. 2.

SCTS was developed for the purpose of evaluating salt cavern gas storage operations and is not intended for the evaluation of reservoir storage. Therefore, an alternative method had to be taken to estimate the temperature of the gas in the reservoir storage well. Because of the extended injection and withdrawal periods for the reservoir well, it was assumed that the temperature of the gas remains relatively constant while the gas is flowing. This assumption appears to be valid based on SCTS simulations of salt caverns at low injection rates. Furthermore, the relatively slow flow rates would dictate that the temperature of the gas in the well is constrained between the injection temperature of 21.11°C (70°F) and the gas storage formation temperature of 46.11°C (115°F). Figure 5-5 shows the gas temperature history specified for the five gas service cycles of Reservoir Well No. 3. The gas temperature over the length of the casing was assumed to be equal to the temperature of the gas at the wellhead during injection and equal to the reservoir storage temperature during withdrawal. This approach provides conservative results because the entire casing experiences the maximum possible temperature differential.

5.3 HEAT TRANSFER RESULTS

The computer program SPECTROM-41 was used in this study to simulate the heat transfer between the casing, including the cavern if applicable, and the surrounding rock formation. The results of these calculations were then integrated into the thermomechanical analyses to

RSI-1546-06-012

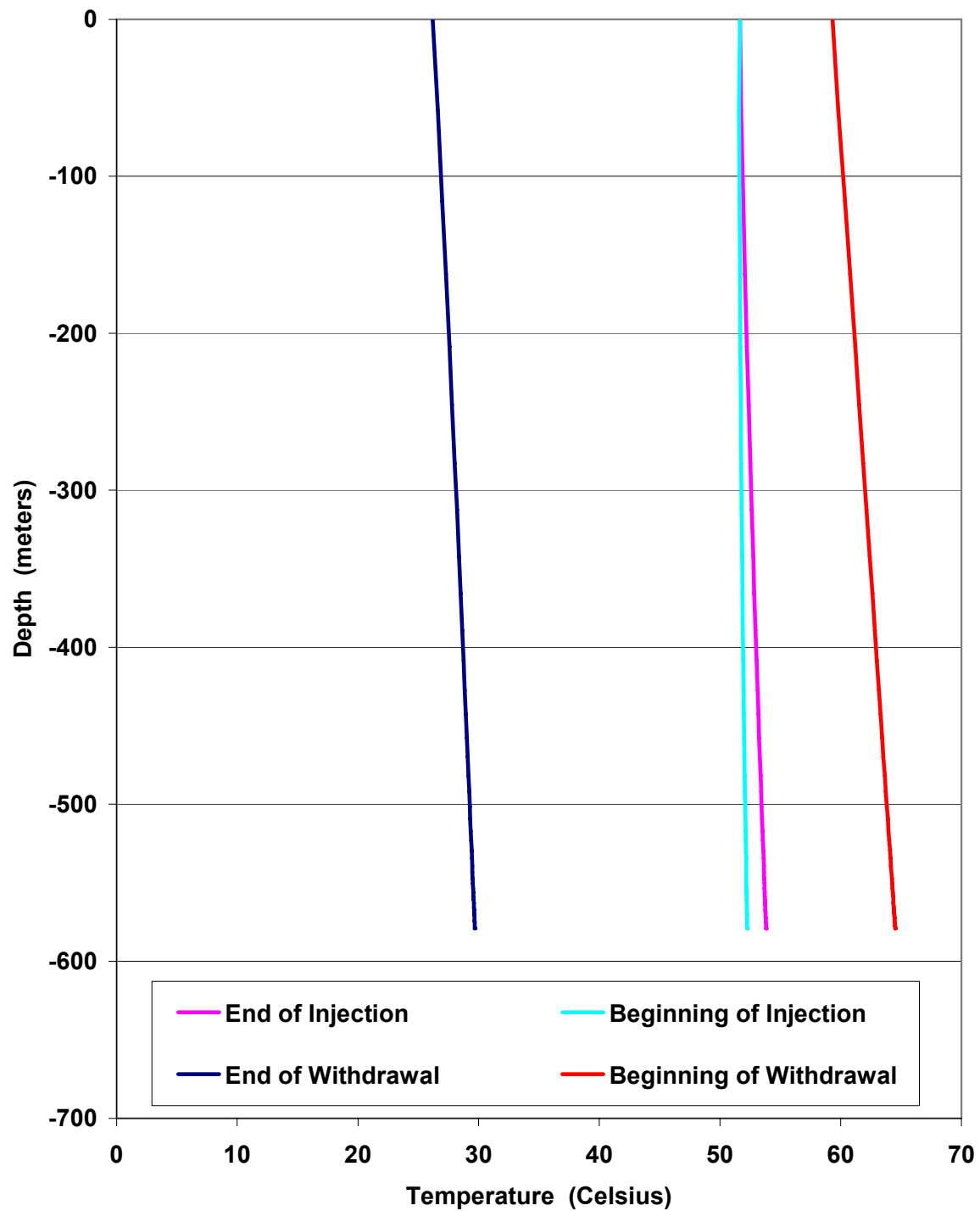


Figure 5-3. Temperature Profile of the Casing in Salt Cavern Well No. 1 During the 60th Gas Service Cycle.

RSI-1546-06-013

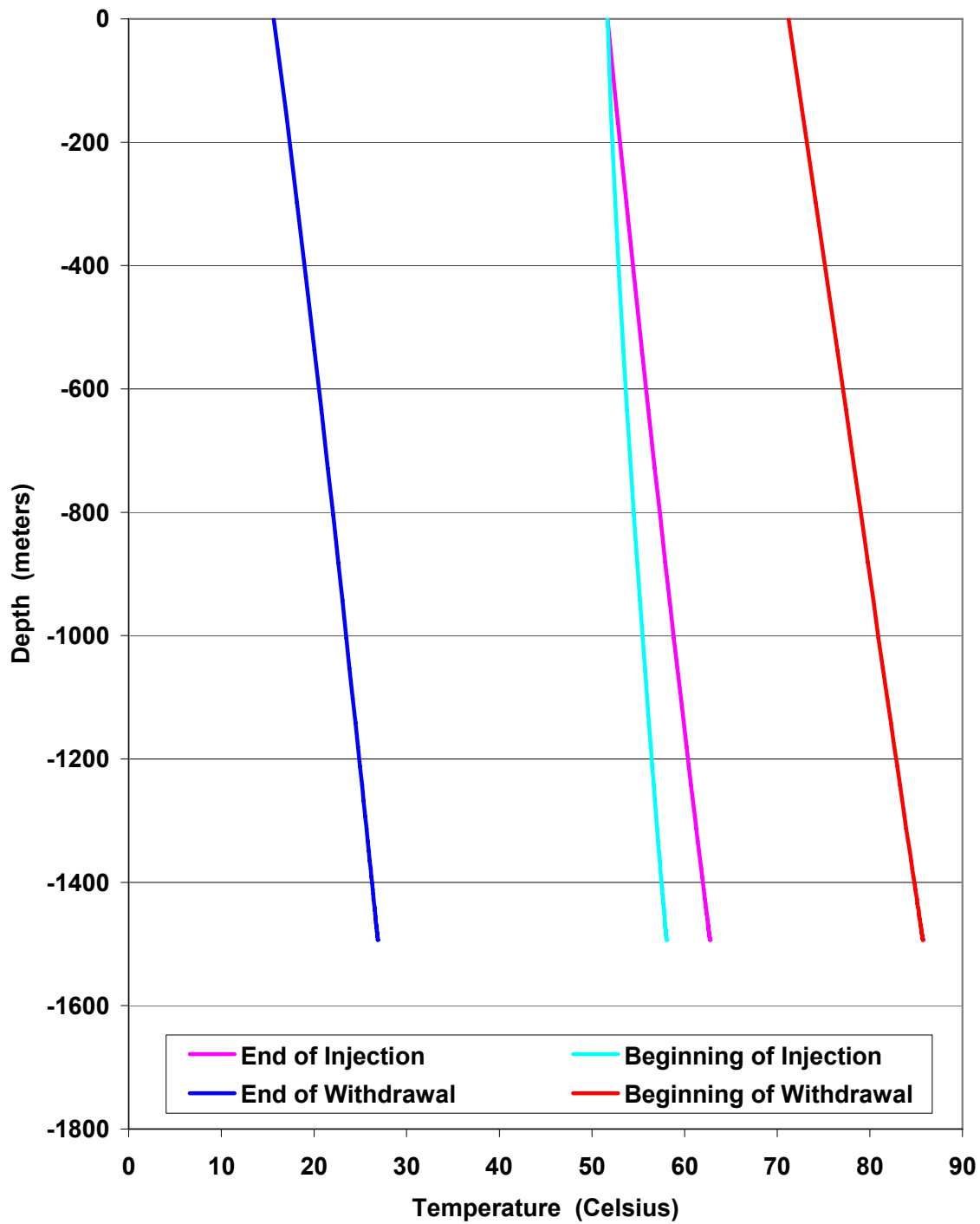


Figure 5-4. Temperature Profile of the Casing in Salt Cavern Well No. 2 During the 60th Gas Service Cycle.

RSI-1546-06-014

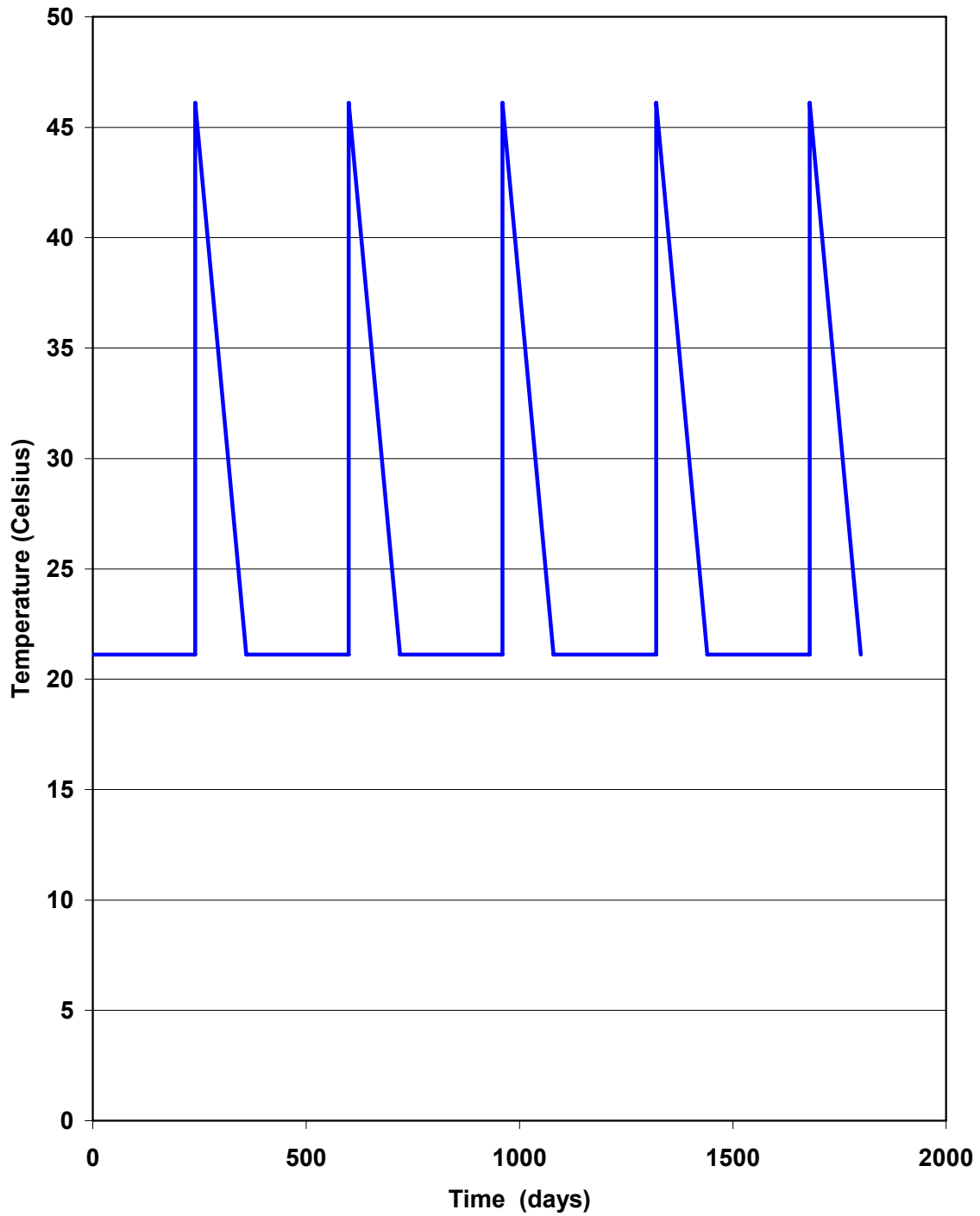


Figure 5-5. Temperature Histories at the Casing Seat of the 1,524-Meter- (5,000-Foot-) Deep Reservoir Storage Well No. 3 During Five Gas Cycles.

account for the thermal stresses and strains that are produced by temperature changes in the casing and rock formation. Because the gas temperature in the casing changes significantly during operation, the simulated gas storage cycles result in both short-term and long-term temperature changes in the casing and host rock formations. The short-term temperature changes only affect the first couple of meters of rock surrounding the casing, and in the case of the salt cavern analyses, the first couple of meters beyond the cavern walls. The long-term temperature changes affect a much larger region and are much more gradual.

Figures 5-6 and 5-7 show temperature contours around the casing shoe of Salt Cavern Wells No. 1 and No. 2, respectively, at various times throughout the 5-year gas storage simulations. These figures show the gradual long-term temperature changes that occur in the salt. Because the surface area and volume of the cavern are much larger than that of the casing, most of the long-term temperature change is caused by heat transfer between the gas in the cavern and the salt surrounding the cavern. The earliest time provided in these figures is following dewatering when the salt around the cavern has been significantly cooled by 2 years of brine production. The remaining three times correspond with when the cavern is at maximum pressure during the 1st and 60th cycle and when the cavern is at minimum pressure during the 60th cycle. After gas operations commence, the salt around the caverns gradually warms throughout the 5-year simulation. Because of the greater depth, the formation temperature is significantly warmer for Salt Cavern Well No. 2; however, the brine injection temperature was the same for both caverns.

Figures 5-8 and 5-9 show the temperatures in the casing and salt as a function of distance from the center of the well at an elevation about 12.2 meters (40 feet) above the casing shoe for Salt Cavern Wells No. 1 and No. 2, respectively. Temperature profiles are provided during the 60th gas service cycle. Profiles are provided at three times during this cycle: (1) end of injection, (2) beginning of withdrawal, and (3) the end of withdrawal. As shown in Figures 5-8 and 5-9, gas temperature changes in the well over a single cycle only affect the first few meters of salt behind the casing.

Because the modeling approach for Reservoir Well No. 3 assumes the gas temperature is constant in the sandstone reservoir, the only temperature changes predicted within the rock formation are those associated with gas flowing through the casing at a temperature different than the in situ temperature. Figure 5-10 provides profiles of temperature versus radial distance from the center of the reservoir well at a depth of 1,511 meters (4,960 feet). Profiles are provided at three times during the 5th gas cycle: (1) end of injection, (2) beginning of withdrawal, and (3) the end of withdrawal. As shown in Figure 5-10, the temperature of the rock within about 15 meters (50 feet) of the casing is lower than the in situ temperature of 45.27°C (113.5°F) at this depth. This is caused by the relatively long periods of continuous gas injection at 21.11°C (70°F).

RSI-1546-06-015

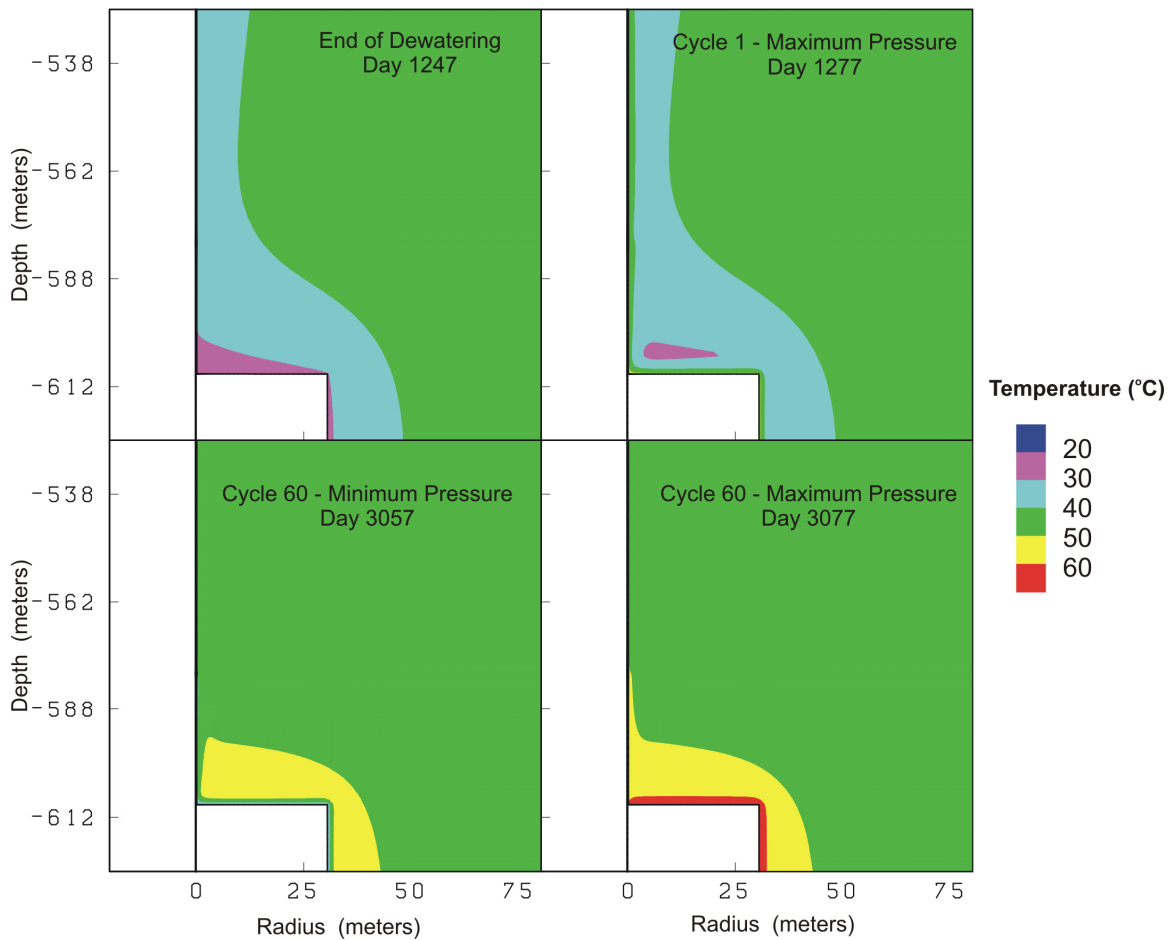


Figure 5-6. Temperature Contours in the Roof Salt Above Salt Cavern Well No. 1 at Various Times Throughout the 5-Year Gas Service Operation.

RSI-1546-06-016

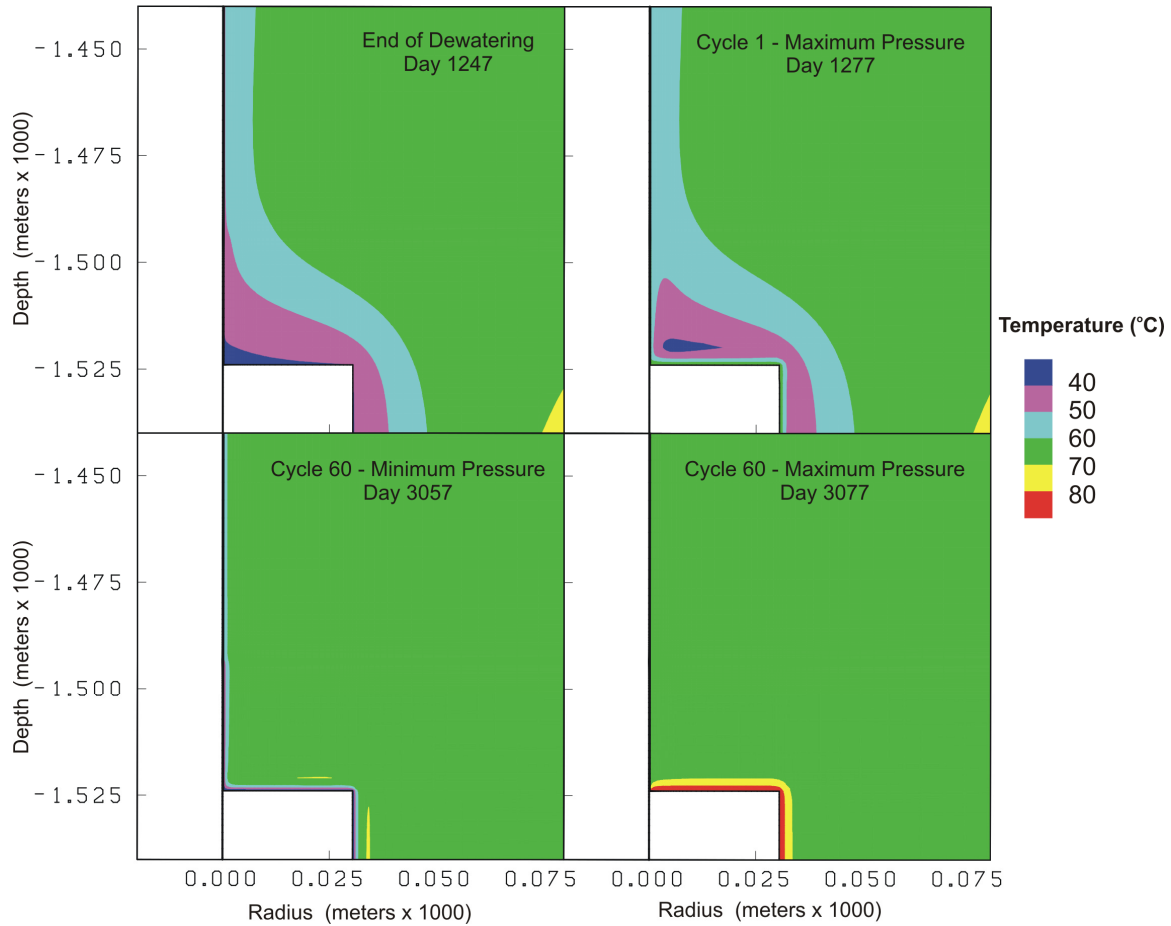


Figure 5-7. Temperature Contours in the Roof Salt Above Salt Cavern Well No. 2 at Various Times Throughout the 5-Year Gas Service Operation.

RSI-1546-06-017

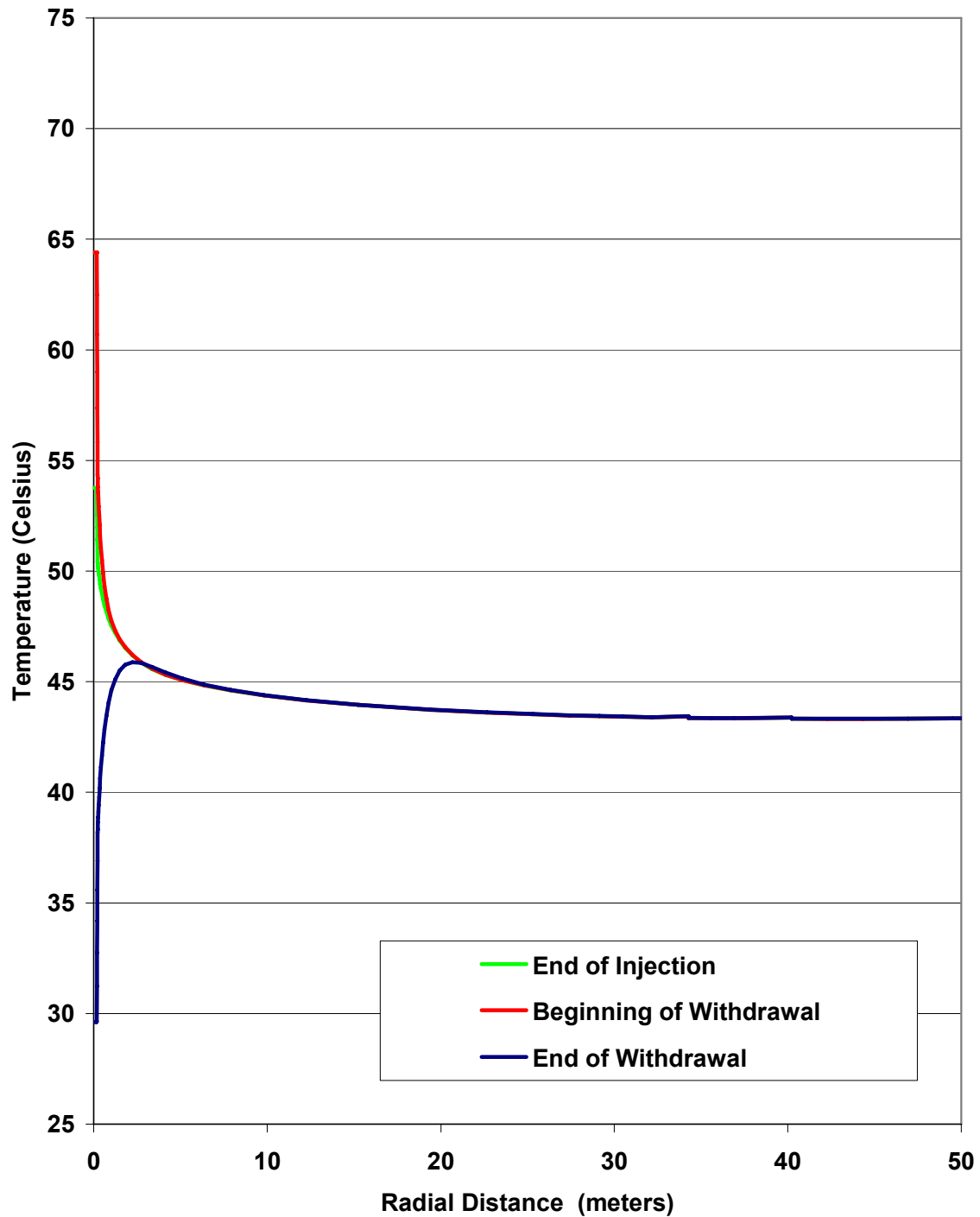


Figure 5-8. Temperature Profiles in the Casing and Salt 12.2 Meters (40 Feet) Above the Casing Shoe of Salt Cavern Well No. 1 During the 60th Gas Storage Operation Cycle.

RSI-1546-06-018

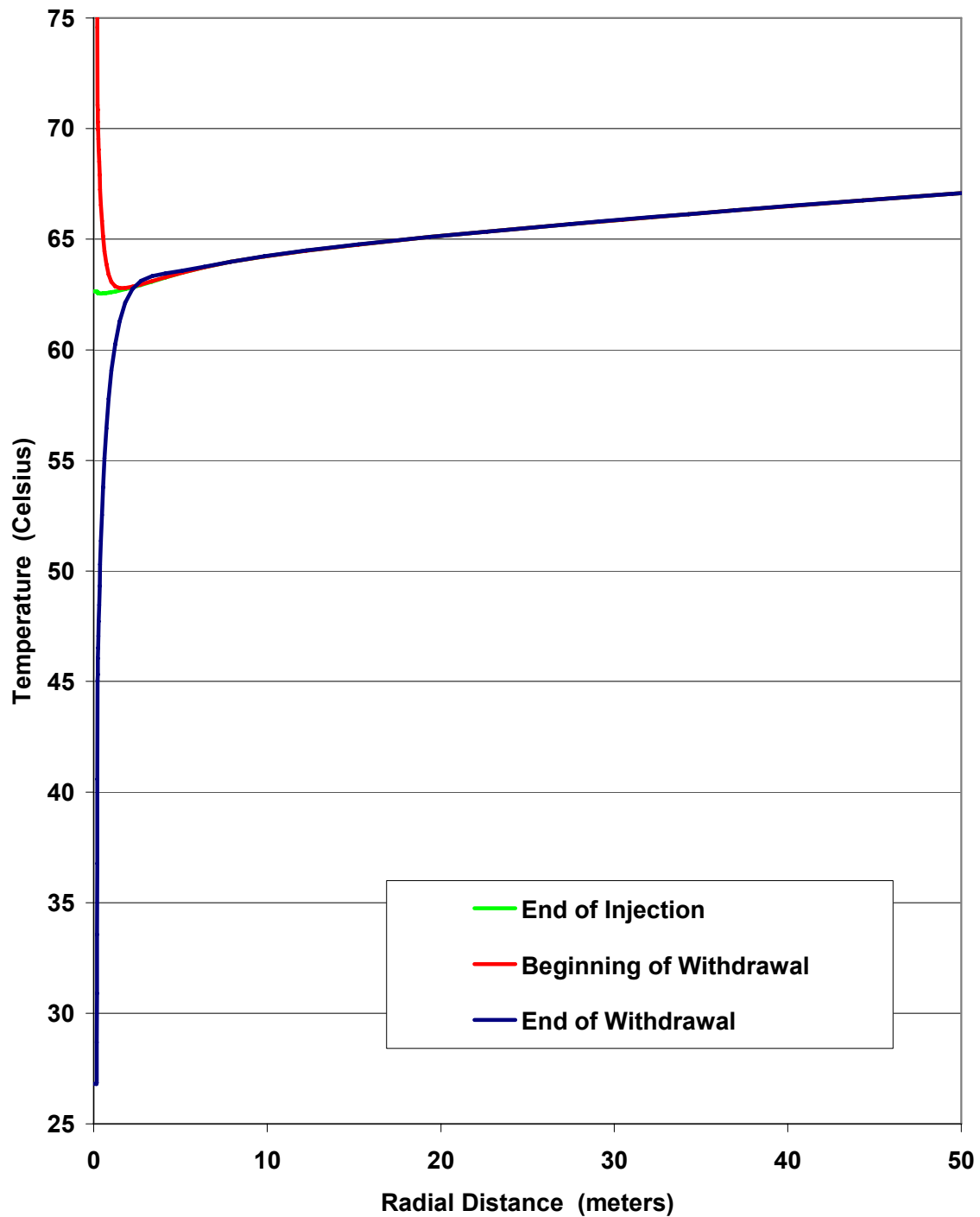


Figure 5-9. Temperature Profiles in the Casing and Salt 12.2 Meters (40 Feet) Above the Casing Shoe of Salt Cavern Well No. 2 During the 60th Gas Storage Operation Cycle.

RSI-1546-06-019

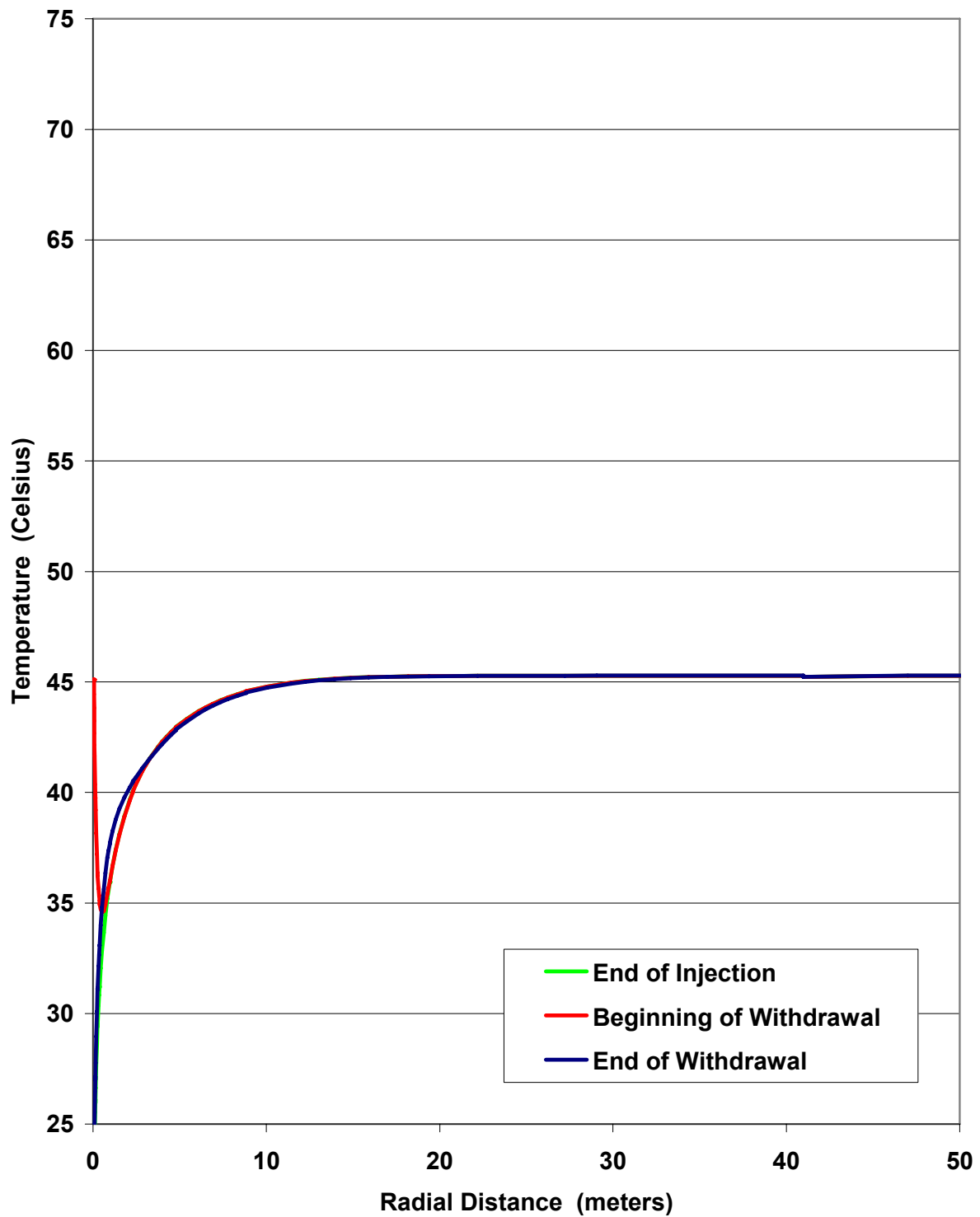


Figure 5-10. Temperature Profiles in the Casing and Rock Formation at a Depth of 1,511 Meters (4,960 Feet) During the 5th Gas Storage Operation Cycle of Reservoir Well No. 3.

5.4 THERMOMECHANICAL RESULTS

SPECTROM-32 was used to predict the structural response of the casing and host rock formation under the various operating conditions. As discussed in Chapter 2.0, the stress analyses performed considered stress contributions from: (1) casing weight; (2) product pressures, (3) thermally induced stresses, and (4) external ground pressures, including salt creep and reservoir compaction. Casing bending was not considered for these thermo-mechanical analyses. Casing bending of the reservoir well was considered during the detailed analyses of the connections provided in Chapter 6.0.

Because the problem modeled includes nonlinear aspects and the loads are not totally independent of each other, superposition of the results is not possible. Nevertheless, elastic solutions were performed to estimate the relative contribution of casing weight, product pressures, and thermally induced stresses to the total stresses induced in the casing of the three wells. Relative contribution was of interest because it provided an indication of the significance of each load type. Of particular interest was the magnitude of thermally induced stresses relative to the total axial stress. For these analyses, salt creep was not modeled, allowing the assumption that each of the casing loads acts independently of the other. However, this assumption did not allow the contribution of external ground pressure caused by salt creep or reservoir compaction to be estimated. Because the casing loads caused by ground pressures are strongly dependent on product pressure and temperature, the relative contribution of ground pressures to the casing load, independent of product pressure and temperature, cannot be determined.

Separate sections are provided below that present the results of the analyses used to estimate the relative contributions of casing weight, product pressure, and thermally induced stresses to the total state of stress expected for each of the three wells. Keep in mind that the results provided are only estimates since the loads are not independent of each other. Predicted results for the total axial stress in the casing from the combined loads of all sources follow a brief discussion regarding external ground pressure issues that were addressed in this study. The state of stress predicted at the lowest casing connection for the three wells concludes this chapter. Unless otherwise specified in this report, negative values are used to indicate compressive stresses in the casing.

5.4.1 Stresses From Casing Weight

For this study, it was assumed that the steel casing was installed with drilling fluid in the wellbore. Further, it was assumed that the drilling fluid was displaced with cement having the same density. Therefore, the drilling fluid and/or cement support some of the weight of the steel pipe through buoyancy; however, the stresses in the cement sheath are equal to that produced by gravitational loading. Figure 5-11 illustrates the vertical (axial) stresses in the steel casing following well completion for the three candidate wells.

RSI-1546-06-020

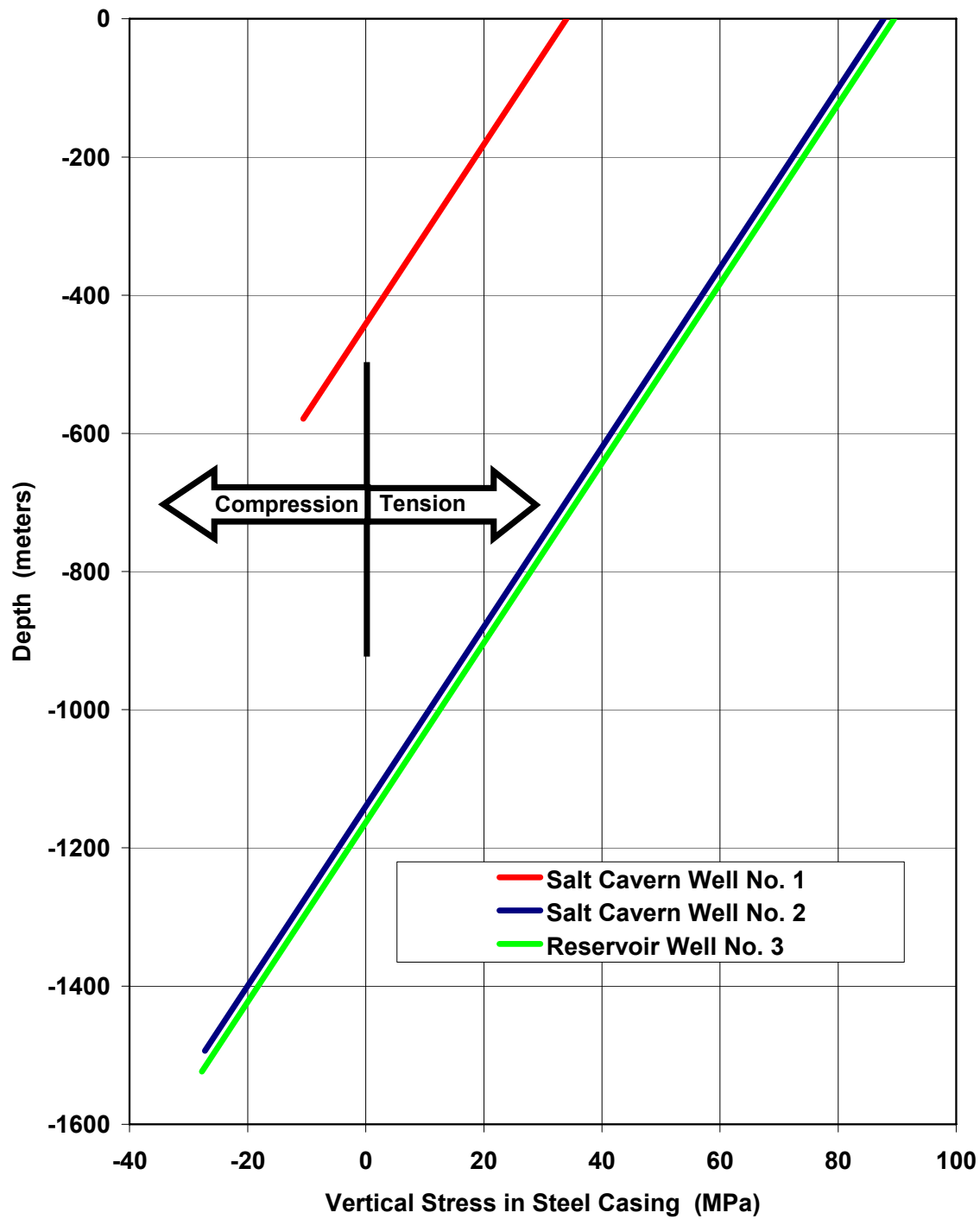


Figure 5-11. Vertical Stresses in Steel Casings of the Three Candidate Wells Following Well Completion.

The vertical stress in the Salt Cavern Well No. 1 casing ranges from 34.03 MPa (4,935 psi) tension at the surface to a maximum compressive stress of -10.55 MPa ($-1,530$ psi) at the casing shoe. The vertical stress in the steel casing as a function of depth for Salt Cavern Well No. 2 and Reservoir Well No. 3 are about the same because the casing lengths differ by only 30.48 meters (100 feet). The stresses in the steel casing of Salt Cavern Well No. 2 range from 87.85 to -27.22 MPa (12,740 to $-3,948$ psi). Likewise, the vertical stresses in Reservoir Well No. 3 range between 89.54 and -27.77 MPa (12,986 and $-4,028$ psi).

5.4.2 Stresses From Product Pressures

Figure 5-12 illustrates the incremental vertical stresses in the steel casing that are produced by changes in gas pressure during storage operation of the three wells. In addition to the pressure change in the well, the predicted results include the elastic response associated with creation of the salt cavern and pressure changes in the salt cavern. Stresses associated with salt creep and pore pressure changes in the sandstone reservoir are discussed in Section 5.4.4. The stresses provided are the incremental stresses from the condition that was predicted to exist following well completion when the casing is full of drilling mud. Thus the stresses provided in Figure 5-12 are the result of replacing the pressure of the drilling mud with that of natural gas during storage plus the response associated with gas pressure changes in the caverns.

Although temperature of the gas and, therefore, the casing and rock, do not remain constant during pressurization and depressurization, isothermal conditions were assumed to compute the incremental stresses associated with changes in product pressure. The results provided in Figure 5-12 are at the two extreme cases of the gas cycle (minimum and maximum pressure) for each respective well. In general, increasing the gas pressure tends to produce a more tensile state of stress along the well axis (vertical stress). However, because of differences in wellhead pressure and fluid density, replacing the drilling mud with natural gas induces both tensile and compressive vertical stresses in the casings, depending on the depth and gas pressure. If the gas pressure is greater than the mud pressure at a given depth, incremental tensile stresses develop in the casing. Likewise, if the gas pressure becomes lower than the pressure exerted by the drilling mud, compressive axial stresses develop in the casing.

The effects of cavern creation and pressure changes in the caverns are evident by the nonlinear responses of the stress profiles in the lower portion of the casings. As shown in Figure 5-12, the curves depicting the incremental vertical stress at maximum and minimum pressure cross within the lower portion of the wells. Thus the lower portion of the casing becomes more tensile at minimum pressure compared to maximum pressure—contrary to the behavior of the rest of the well casing. This occurs because the gas pressure in the cavern pushing upward on the roof of the cavern produces more compression in the roof salt at the higher pressures. Compression of the salt induces incremental compressive stresses and strains in the casing.

RSI-1546-06-021

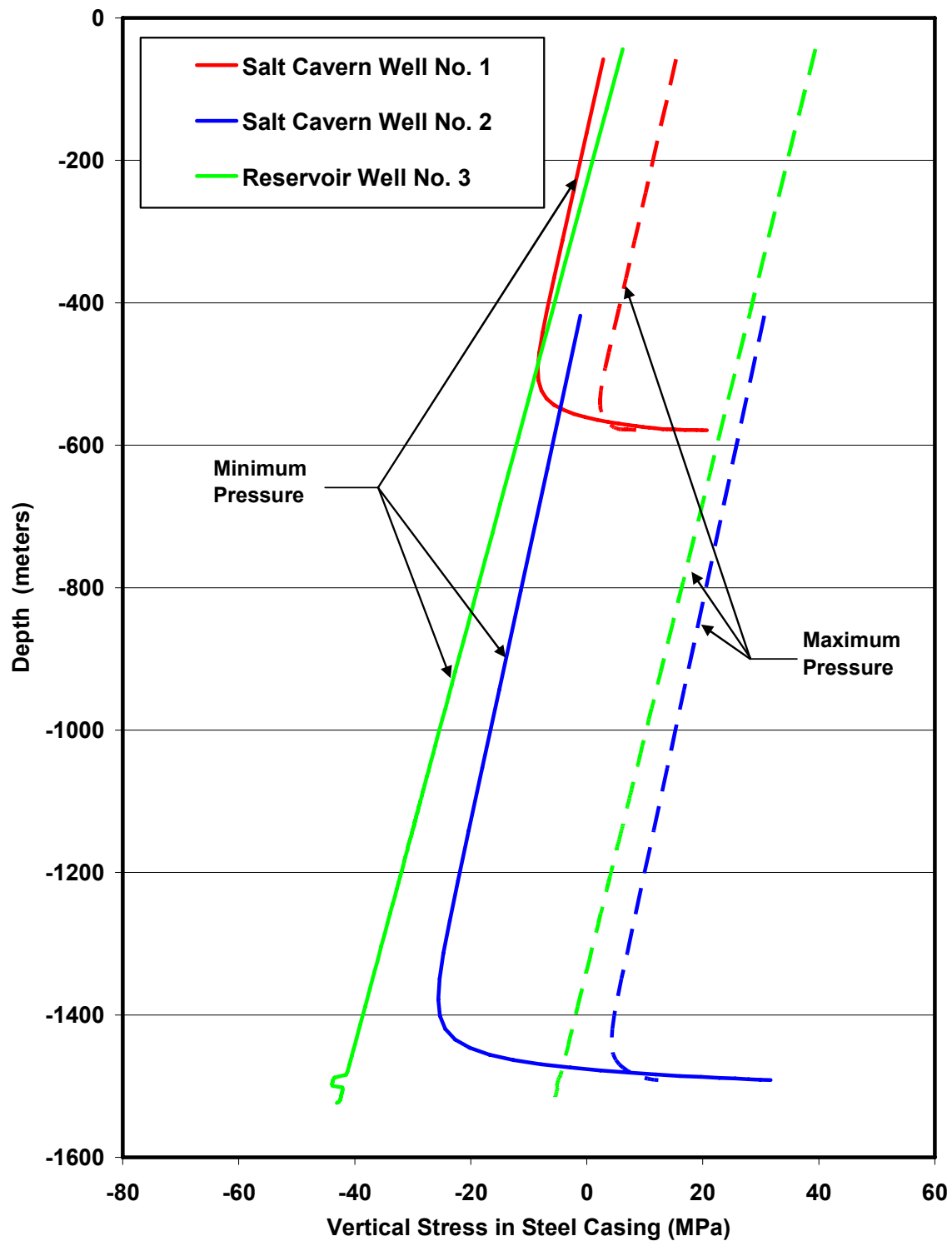


Figure 5-12. Incremental Vertical Stresses in the Steel Casings Induced by Product Pressure Changes.

5.4.3 Stresses From Thermal Expansion and Contraction

Following well completion, the temperature of the well casing is equal to the in situ temperature of the rock formation. An increase in the casing temperature above the in situ temperature results in the vertical stress becoming more compressive. Likewise, if the temperature of the casing becomes less than the in situ temperature, the vertical stress becomes less compressive. Figure 5-13 illustrates the incremental change in vertical stress associated with thermal expansion and contraction when the casings reach the two extremes in temperature during the last cycle of the simulations. In general, the thermally induced stresses become less compressive (or more tensile) with depth.

As shown in Figure 5-13, incremental tensile stresses are predicted when the casing temperatures are coolest during the gas cycle. Conversely, the entire casing becomes more compressive when the temperatures are the warmest in the casing. The influence of the cavern is evident by the nonlinear response of the temperature profiles. This is caused by the long-term temperature change of the rock formation as discussed in Section 5.3. Rock temperatures cooler than the in situ temperature induce compressive (or less tensile) strains in the casing because the salt has a higher coefficient of thermal expansion than the casing components.

5.4.4 External Ground Pressure Considerations

Whenever any underground opening is created, movement of rock toward and into the opening occurs. This is particularly the case for caverns in salt because they are typically large and the salt rock continually creeps. Following well completion, the radial force at the cement/salt interface is less than the initial in situ stress. If no other excavations are present to alter the state of stress, salt creep will increase the radial loading on the casing until it returns to the initial in situ stress. The added radial load will produce incremental radial, tangential, and axial compressive stresses in the casing.

Salt creep can also impart significant tensile loads on the casing. As the salt flows into the cavern, it can drag the casing downward toward the cavern. This stretching of the casing results in axial tensions. Because of material behavior mismatches, shear stresses will develop along the salt/cement interface. The shear stresses could potentially become great enough that the salt could flow along the cement sheath without additional elongation of the casing. However, the results of the two analyses of the salt cavern storage wells indicate that tensile stresses in the lower portion of well continually increase with each cycle. Whereas the axial tensions remain relatively low compared to the strength of the casing during the simulation period of Salt Cavern Well No. 1, stresses were predicted to exceed the tensile strength of the steel casing during the analysis of Salt Cavern Well No. 2. Thus using the conservative modeling approach, assuming that the interfaces remain perfectly bonded, indicates that elongation of the casing caused by salt creep will continue until the casing fails.

RSI-1546-06-022

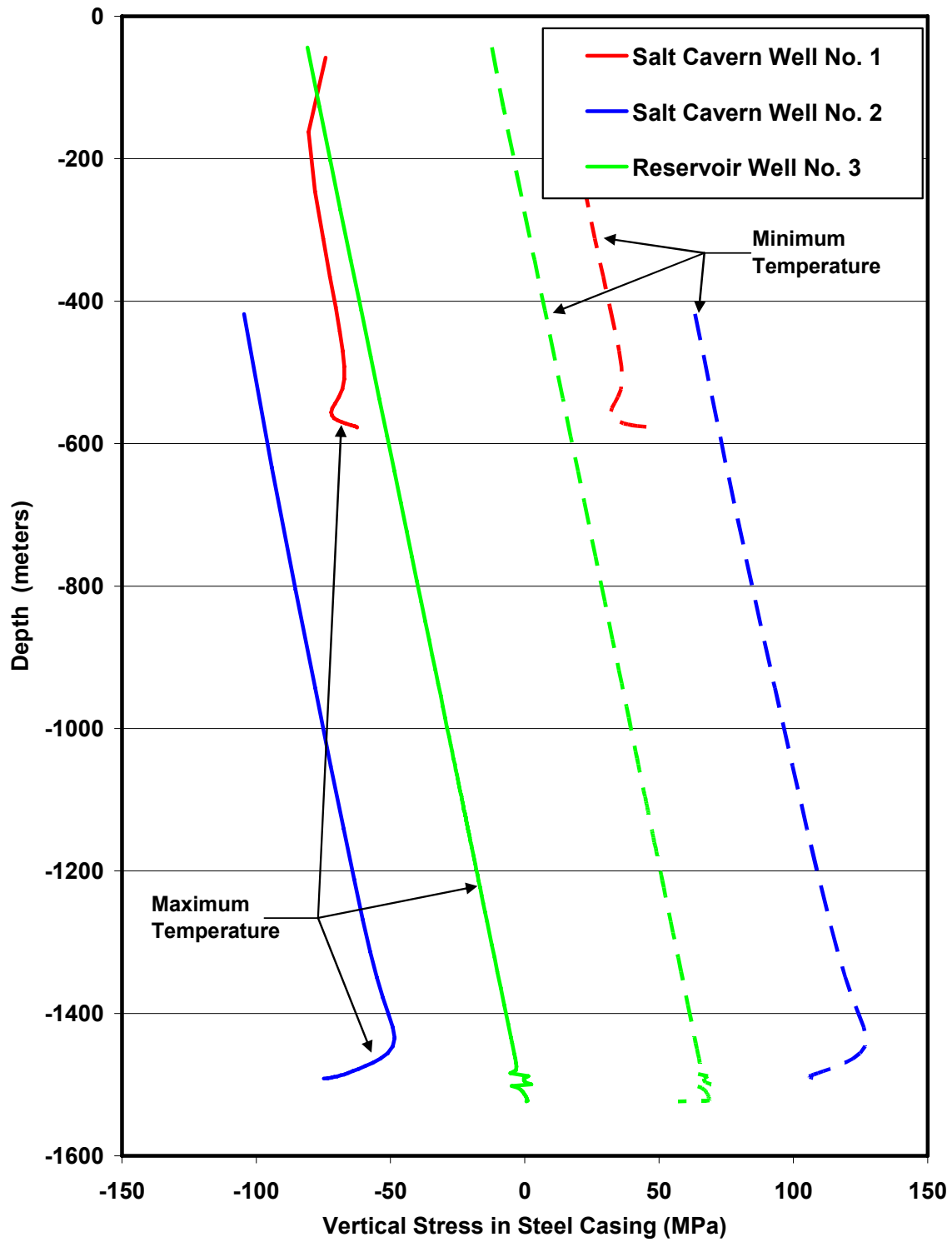


Figure 5-13. Incremental Vertical Stresses in the Steel Casings Induced by Temperature Changes.

RESPEC has considerable experience in modeling the creep deformation around underground openings in salt. Based on this experience and field validation exercises of large-scale tests in salt, it is reasonable to expect that large creep deformations would occur above deep salt caverns such as the one evaluated in this study. Other than the conclusion that creep deformations around the well casing will eventually accumulate to a magnitude that will cause the casing to fail, other possibilities not simulated by the models used in this study include: (1) slip occurs along the steel/cement and/or the cement/salt interface, limiting the axial tensions that can develop in the casing, (2) failure of the cement occurs limiting the drag force which leads to the development of tensile stresses in the steel casing, or (3) the casing seat is located sufficiently away from the cavern such that the well does not experience the large deformations predicted by this study. Little evidence has been reported that casing separations have occurred in brine production, liquid hydrocarbon, or natural gas storage wells in salt caverns in the United States, even for those caverns deeper than 1,524 meters (5,000 feet). Thus it is possible that interface slip or failure of the cement occurs for those well casings that are subject to relatively large vertical creep deformations. However, it is also possible that casing failures have occurred but remain undiscovered or have not been reported.

The modeling approach assuming the casing components and the salt remain perfectly bonded represents the worst-case scenario with regard to predicting axial stress in the casing. An investigation was performed to identify alternative approaches for evaluating the interaction between the casing components and the surrounding rock. The modeling approach had to be capable of predicting the response at the casing scale to include the potential for failure of the cement and slip along the casing interfaces and at the cavern scale to predict changes in the stress field and deformations that extend hundreds of meters from the cavern. The results of this investigation did not reveal a suitable method that was capable of predicting both the near-field and far-field responses. A few details of this investigation are given in Appendix A. The investigation did indicate that failure of the cement will precede failure of the steel pipe. Additionally, the analyses indicate that significant failure occurs within the cement before the tensile stresses in the pipe exceeds 345 MPa (50,000 psi). Based on these results, the maximum axial tensile stress in Salt Cavern Well No. 2 was limited to 345 MPa (50,000 psi) in this study. This tensile limit is unique to the assumptions, modeling approach, and properties used to evaluate the performance of Salt Cavern Well No. 2 and should not be construed as a general limit for cemented casings.

The axisymmetric assumption used for Reservoir Well No. 3 prevented the modeling of the 90-degree bend; thus, the full influence of reservoir compaction could not be determined directly using this model. To provide an estimate for the effects of ground pressure, it was conservatively assumed that the casing will experience the same strains as that of the rock formation. Gas pressures simulated in the sandstone reservoir ranged between 0.41 and 22.06 MPa (600 and 3,200 psi) during the analysis of Reservoir Well No. 3. Because it was assumed that the pressure distribution is uniform within the storage formation, the overburden formations move down uniformly over the entire formation, without bending. As a result, the

sandstone was assumed to expand and contract uniformly in response to pressure changes. The total vertical displacement across the thickness of the sandstone formation was predicted to be about 5.1 centimeters (2 inches). Assuming this deformation is evenly distributed over the 30.48-meter (100-foot) reservoir thickness results in an incremental axial strain of 0.17 percent. This translates to a cyclic stress amplitude in the casing body of 324 MPa (46,990 psi). This result was used to provide a conservative estimate for the casing loads caused by external ground pressures for Reservoir Well No. 3.

5.4.5 Total Vertical Stress From Combined Loads

Axisymmetric finite element models were used to determine the combined loads for the sources identified. The predicted results of interest are the total state of stress in the steel casing and how that stress varies during gas storage operation. Figure 5-14 shows the predicted vertical stresses in the steel casing during the final gas service cycle resulting from the combined loads. The results shown in Figure 5-14 represent the range of conditions that the casing experiences. Thus the stresses in the casing at any given depth fall between the two curves identified for the wells shown in Figure 5-14.

For the salt cavern wells, the least-tensile (or most-compressive) vertical stresses are predicted at the beginning of the withdrawal cycle. At this time during the cycle, the temperature of the casing is the warmest and the gas pressure is the greatest. The most-tensile vertical stresses in the salt cavern casing are predicted to occur at the end of withdrawal when the gas temperature is the coolest and the pressure is the lowest.

Because of the slow withdrawal rates assumed for the reservoir well, the temperature of the gas does not become significantly cooler than the storage formation temperature during the withdrawal phase. As a result, the least-tensile (or most-compressive) vertical stresses are predicted to occur at the end of withdrawal when the pressure is lowest and the gas temperature is warmest. Likewise, the most-tensile stresses in the reservoir well casing occur at the end of injection when the temperature is the coolest and the gas pressure is the greatest. The results for the Reservoir Well No. 3 shown in Figure 5-14 do not include the loads from bending or reservoir compaction. These loads occur in the lower portion of the well that was not included in the axisymmetric model. The loads from bending and reservoir compaction are considered by the connection models as discussed in Chapter 6.0.

5.4.6 Stress Condition at the Lowest Casing Connection

Based on the results shown in Figure 5-14, the largest cyclic loads and the most-tensile states of stress occur at the bottom of the salt cavern well casings. Therefore, it is anticipated that if failure were to occur, it would happen in the lower portion of the casing. The conditions at the lowest joints were selected for further evaluation using the connection models. Table 5-1 provides the predicted stresses in the pipe at the location of the lowest joint in the three

RSI-1546-06-023

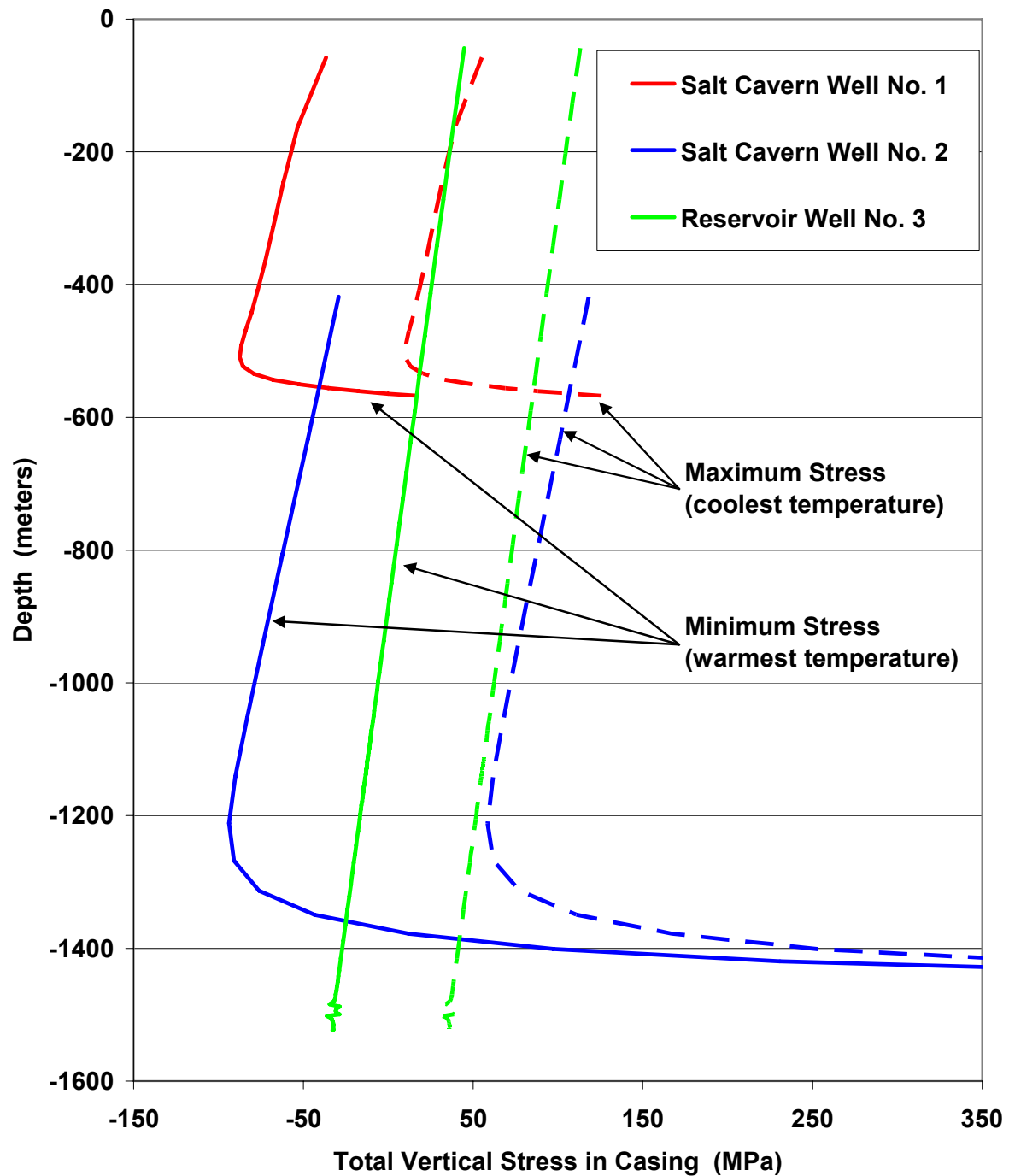


Figure 5-14. Two Extremes for Total Vertical Stress in the Steel Casings Predicted During the Last Cycle of the Simulations.

candidate wells. Stresses are provided at times either immediately preceding or following: (1) the start of injection, (2) the end of injection, and (3) the start of withdrawal. These times provide the maximum range predicted for axial stress in the casing during the final gas service cycle.

Because the model predictions of Salt Cavern Well No. 2 for axial stress exceed the limiting value of 345 MPa (50,000 psi) identified in this study, the axial stress at the start of injection was limited to 345 MPa (50,000 psi), as shown in Table 5-1. As previously mentioned, the maximum axial tensions occur in the lower portion of the salt cavern well casings at the end of withdrawal when the pressure in the cavern is at a minimum pressure and the temperature of the casing is the coolest. The net effect of increasing the casing temperature and pressure in the well and cavern during injection is to produce a more compressive state of stress in the lower portion of the casing. Based on the results of thermomechanical analyses of Salt Cavern Well No. 2, the tensile stress at the lowest connection will be reduced by 110 MPa (15,920 psi) by the time injection is complete. The tensile stress in the casing is reduced even further (an additional 71 MPa (10,295 psi)) during the early stages of withdrawal. These results provide the best available estimates for the range of cyclic loading that is expected for Salt Cavern Well No. 2 and were used in defining the conditions for the connection models for this well.

Table 5-1. Candidate Well Conditions During the Final Gas Service Cycle Simulated

Stage	Internal Pressure		External Pressure		Axial Stress		Casing Temperature	
	MPa	psi	MPa	psi	MPa	psi	°C	°F
Salt Cavern Well No. 1								
Start Injection	3.30	480	9.87	1,430	125.45	18,195	29.61	85
End Injection	11.16	1,620	16.59	2,405	49.88	7,235	49.97	122
Start Withdrawal	11.16	1,620	18.06	2,620	20.14	2,920	64.41	148
Salt Cavern Well No. 2								
Start Injection	8.47	1,230	20.38	2,955	344.74	50,000	26.81	80
End Injection	28.72	4,165	33.33	4,835	234.97	34,080	54.86	131
Start Withdrawal	28.72	4,165	36.41	5,280	163.99	23,785	85.60	186
Reservoir Well No. 3								
Start Injection	4.63	670	21.02	3,050	1.28	185	21.11	70
End Injection	24.66	3,575	25.14	3,645	35.85	5,200	21.11	70
Start Withdrawal	24.66	3,575	27.14	3,935	-32.41	-4,700	46.11	115

(a) Tensile stress in casing limited to the 345-MPa (50,000-psi) maximum.

6.0 RESULTS AND DISCUSSION OF THREADED CONNECTION MODELS

The objective of the connection modeling was to determine the fatigue life corresponding to the axial force and pressure cycles estimated from the casing load analyses given in Chapter 5.0. The first stage of the connection analysis consisted of determining the stresses that exist in the connection following the connection make-up procedure. During the next stage of the analysis, the load cycles estimated in the thermomechanical casing analyses were imposed to determine the stress and strain distribution in the connection. These stress and strain values were then used to estimate the fatigue life of the connection in terms of the number of injection-withdrawal cycles that can be tolerated.

6.1 INITIAL CONNECTION LOADS

The first step in the connection analysis was to model the make-up condition of the API 8-Round STC connection with the magnitude of the interference between the pin and coupling based on the make-up turns specified by Recommended Practice API-5B [American Petroleum Institute, 1999]. Figure 6-1 shows that because of the large amount of initial interference between the pin and coupling resulting from make-up, the stress in localized areas of the connection will exceed the elastic limit of the material, resulting in plastic (unrecoverable) strain.

RSI-1546-06-024

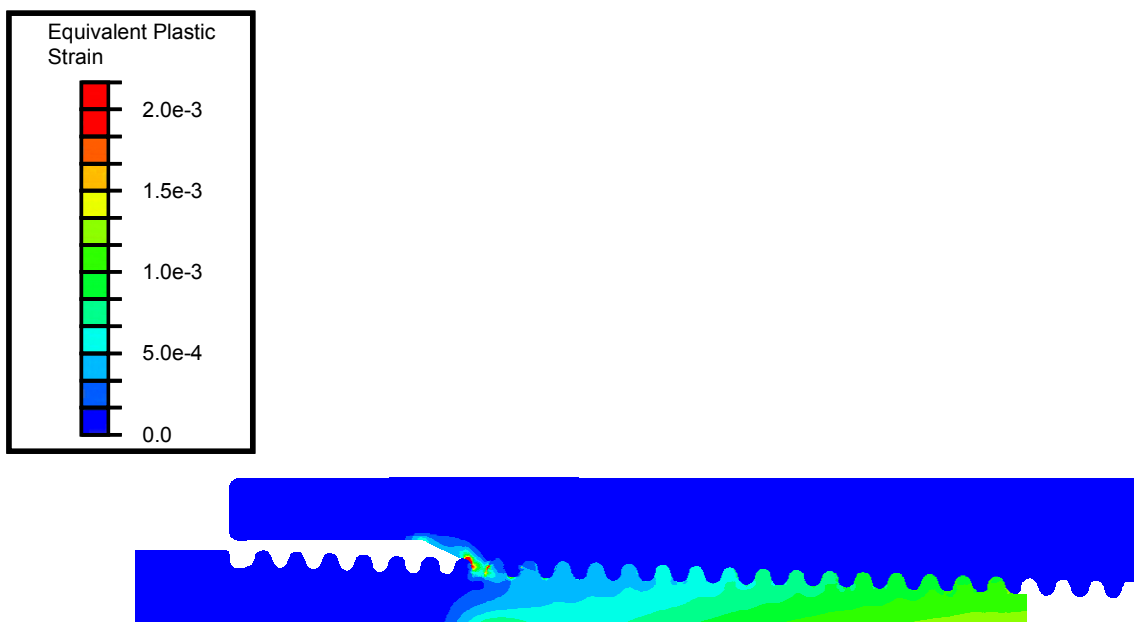


Figure 6-1. Plastic Strain Contours in an 8-Round STC Connection Following Make-Up to API-5B Specifications.

Once the casing is made up and installed in the well, storage operation cycles of gas injection and withdrawal impose temperature and pressure cycles that generate additional plastic strain in localized areas of the connection. Examples of the distribution of the axial strain in the 140-millimeter (5.5-inch, 15.5 lb/ft) J-55 connection at the end of the injection phase are presented for connections with (Figure 6-2) and without (Figure 6-3) the coupling face welded to the pipe body.

RSI-1546-06-025

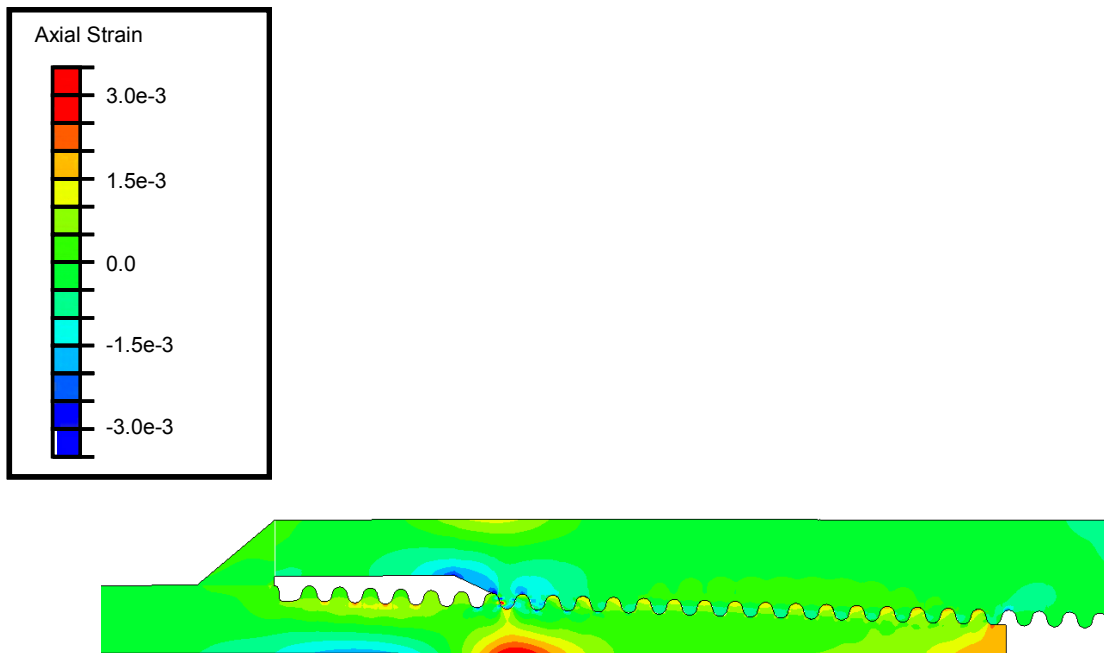


Figure 6-2. Example Results Showing Axial Strain Distribution in a Connection With a Welded Coupling Face.

Figure 6-3 identifies four areas where axial strain is localized: (1) the pin thread root at the first engaged thread, (2) the pin inside diameter (ID) surface underneath the first engaged thread, (3) the outside diameter (OD) surface of the coupling at the coupling entry plane, and (4) the ID surface of the coupling at the coupling entry plane. A multi-axial strain state typically exists at these locations (not just axial strain) both following make-up and under operating conditions. Therefore, the fatigue assessment was based on the multi-axial plastic strain state in these four key locations.

6.2 STRAIN-BASED FATIGUE ASSESSMENT CRITERIA

Traditional stress-based fatigue criteria are intended for situations where the stresses do not exceed the yield strength of the material and no plastic strain occurs. These criteria were considered to be inappropriate for this analysis because of the fact that the imposed stresses

exceed the yield strength of the material in the connection. Therefore, it was necessary to adopt a strain-based fatigue criterion that considers the magnitude of plastic strain cycles in the connection.

RSI-1546-06-026

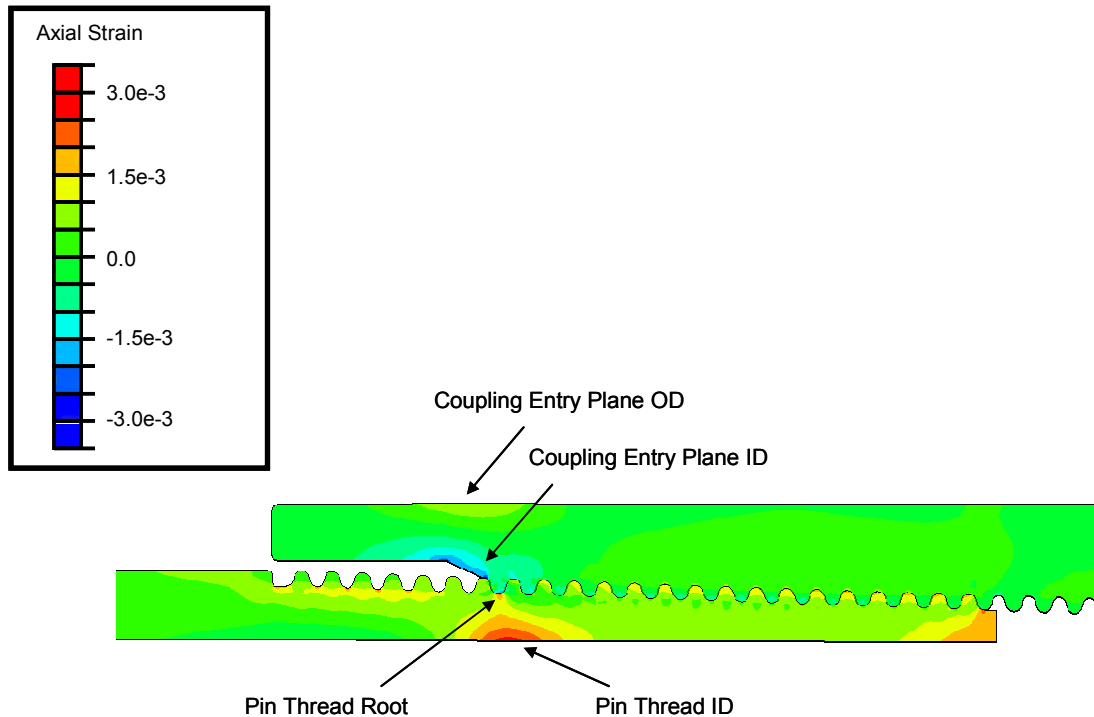


Figure 6-3. Example Results Showing Axial Strain Distribution in a Connection Without a Welded Coupling Face (Arrows Indicate Locations Where Plastic Strain Concentrations Increase the Likelihood of Fatigue-Related Failures).

As noted by Dowling [1998], the development of reliable fatigue prediction methods for multiaxial loading conditions with plastic deformations is currently an area of active research. While reasonable fatigue life estimates are possible for relatively simple situations, significant uncertainty exists as to the best procedure to use for complex nonproportional loading cases (e.g., structural components where the ratios of the principal stresses change and where the principal axes of those stresses may also rotate).

Several strain-based fatigue criteria have been developed for problems involving multiaxial strain. One of the most widely used approaches was developed by Morrow [Dowling, 1998]. The Morrow approach was later modified [Dowling, 1998], resulting in the following relationship among equivalent strain, the number of load cycles, and mean stress:

$$\bar{\epsilon}_a = \frac{\sigma'_f}{E} \left(1 - \frac{\bar{\sigma}_m}{\sigma'_f} \right) (2N_f)^b + \epsilon'_f + (2N_f)^c \quad (6-1)$$

where:

- $\bar{\varepsilon}_a$ = equivalent strain
- σ'_f = true stress at material fracture
- ε'_f = true strain at material fracture
- b = material fatigue constant (elastic slope)
- c = material fatigue constant (plastic slope)
- E = modulus of elasticity
- $\bar{\sigma}_m$ = effective mean stress
- $2N_f$ = number of full cycles.

In this analysis, the static stresses and strains in the critical locations in the connection were entered in the modified Morrow equation to determine the number of load cycles ($2N_f$) that can be tolerated.

The equivalent strain amplitude $\bar{\varepsilon}_a$ describes the multiaxial state of strain existing at one of the critical locations in the casing connection. Several alternative approaches have been proposed for calculating the equivalent strain amplitude based on the strain amplitudes along the principal axes. For this analysis, the general form of equivalent strain amplitude was assumed to be:

$$\bar{\varepsilon}_a = \beta' \sqrt{(\varepsilon_1 - \varepsilon_2)^2 + (\varepsilon_2 - \varepsilon_3)^2 + (\varepsilon_3 - \varepsilon_1)^2} \quad (6-2)$$

where $\varepsilon_1, \varepsilon_2,$ and ε_3 are the principal strain amplitudes and $\beta' = 2/3$ for the octahedral shearing strain and $\beta' = \sqrt{2}/3$ for the von Mises equivalent strain. Sines and Ohgi [1981] have suggested that the octahedral shear strain transformation correlates reasonably well with experimental results.

The material constants $\sigma'_f, \varepsilon'_f, b,$ and c are usually determined through physical tests. The true stress (σ'_f) and true strain (ε'_f) at material fracture were determined for the J-55 and K-55 materials based on C-FER's previous coupon testing programs [Humphreys et al., 1991]. However, these coupon tests did not determine the fatigue constants b and c for these materials.

An extensive review of the literature on fatigue properties of metals was not able to identify specific data for J-55 or K-55 materials. Dowling [1998] provides a general overview of the fatigue performance of various metals. It is reported that the plastic slope c ranges from -0.5 to -0.8 for most engineering metals. Relatively steep elastic slopes, with $b = -0.12$ are common for soft metals (annealed), and shallow slopes, nearer $b = -0.05$, are common for hardened metals.

According to Boller and Seeger [1987a; 1987b], the material CK-35 (which is similar in chemical composition and strength to K-55) shows a fatigue behavior described by $b = -0.075$ and $c = -0.46$. In the absence of any specific fatigue performance data for K-55 material, the values for the CK-35 material were used in this analysis.

The J-55 material is made by thermomechanically forming a sheet into a tube. The resulting microstructure of this material is that of a classic worked steel with evidence of rolling. It is expected J-55 would have a high dislocation density in the manufactured form. Upon cycling, this material is expected to soften as a result of dislocation annihilation, resulting in a cyclic work-hardening coefficient much lower than the monotonic value. This would result in a c value that is larger than the median value of -0.6 , possibly being as high as -0.7 . On the other hand, the b value for J-55 is likely lower than the median value of -0.085 . Therefore, it was assumed that J-55 has a b value of -0.06 for this analysis. Table 6-1 summarizes the material constants used for the fatigue assessment of J-55 and K-55 materials in this report. These values were considered to be the best estimates based on the available data.

Table 6-1. Material Constants for Fatigue Assessment of J-55 and K-55 Grade Casing

Parameter	Units	J-55	K-55
σ'_f	MPa	496	869
ϵ'_f	%	33.6	49.8
b		-0.06	-0.075
c		-0.7	-0.46

The relationships that exist among equivalent strain, mean stress, and number of cycles for J-55 and K-55 materials based on the modified Morrow approach are shown in Figures 6-4 and 6-5, respectively. These figures indicate that pipe constructed of K-55 material should be much more resistant to fatigue than pipes constructed of J-55 material.

6.3 RESERVOIR STORAGE CONNECTION RESULTS

For the reservoir storage application, the casing strings were assumed to be 140-millimeter- (5.5-inch-, 15.5 lb/ft) diameter J-55 with API 8-Round STC connections. Six load cases were defined based on the results of the well models as summarized in Table 6-2.

RSI-1546-06-027

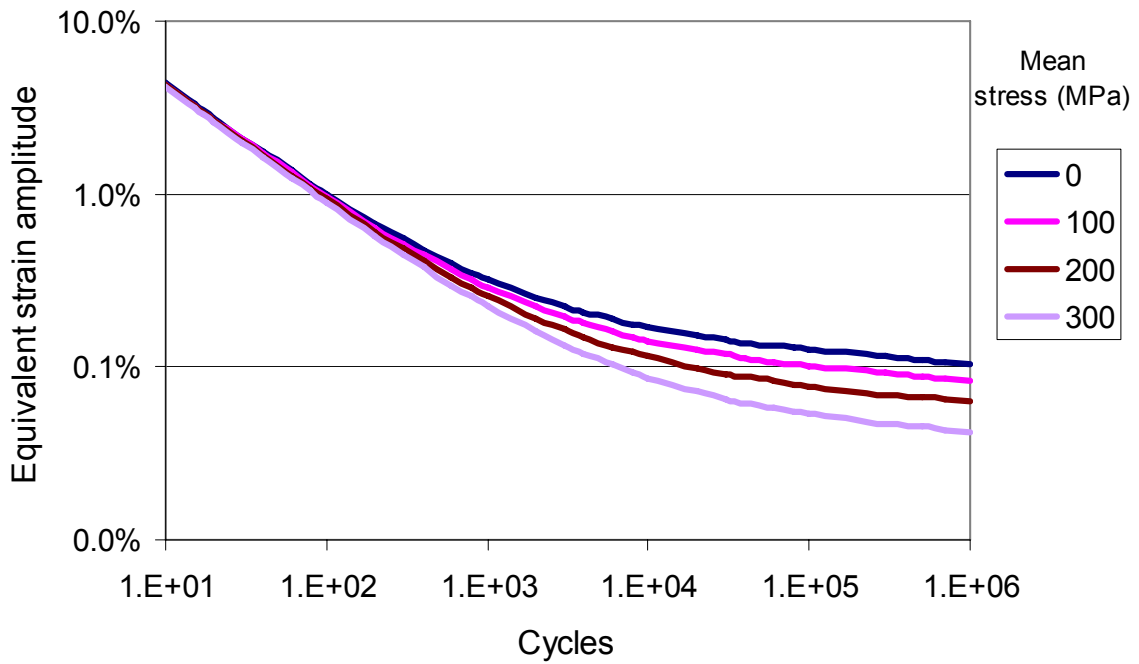


Figure 6-4. Relationship Among Equivalent Strain Amplitude, Mean Stress, and Cycles for J-55 Material Based on Modified Morrow Approach.

RSI-1546-06-028

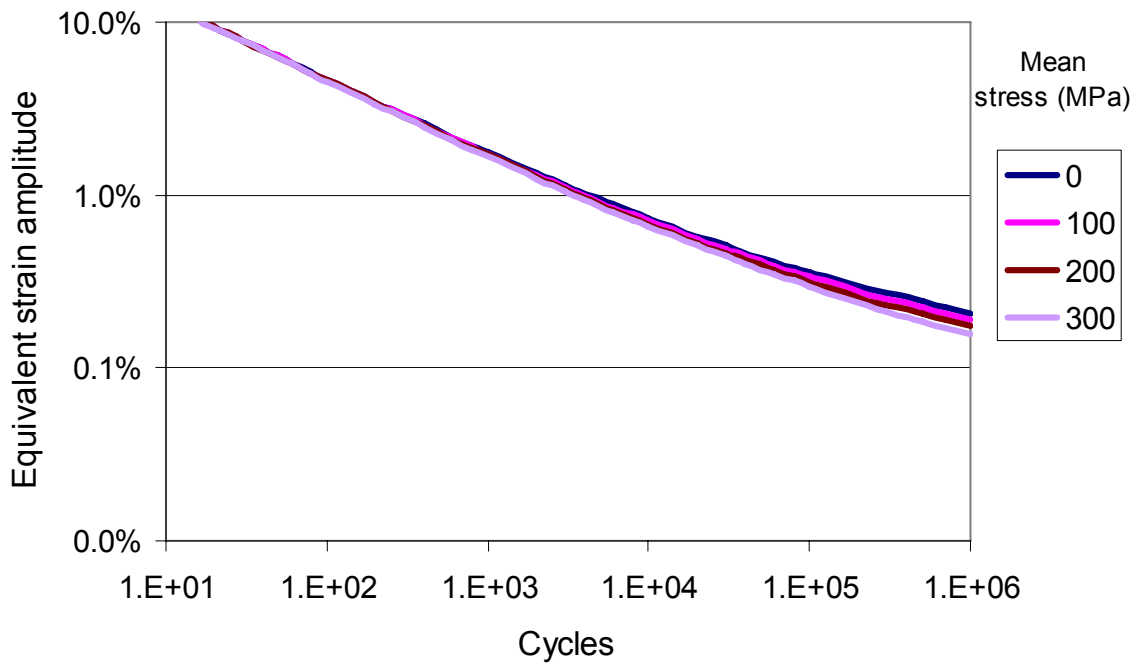


Figure 6-5. Relationship Among Equivalent Strain Amplitude, Mean Stress, and Cycles for K-55 Material Based on Modified Morrow Approach.

Table 6-2. Load Cases for the Reservoir Storage Connection Model

Load Case	Curvature (degrees/30 m)	Incremental Axial Strain (%)	Welded Coupling
1	0	N/A	No
2	9	N/A	No
3	9	-0.17%	No
4	9	0.17%	No
5	9	-0.17%	Yes
6	9	0.17%	Yes

Load Case 1 modeled the simplest case of a straight casing string without welded connections. Load Case 2 considered the impact of well curvature (9° per 30 meters) associated with the build section in the directional well assumed for the reservoir storage facility. Load Cases 3 and 4 considered the incremental longitudinal (axial) strains of 0.17 percent imposed by compaction of the storage reservoir resulting from pore pressure changes during a gas cycle. Load Cases 5 and 6 considered the additional impact of welded connections (weld material connecting the coupling face to the pipe body).

The incremental strain created by pore pressure changes in the sandstone reservoir was superimposed on the loads estimated for the well casing given in Chapter 5.0. The casing strains caused by reservoir expansion/compaction can range from compressive to tensile, depending on the relative movement of the formations in different intervals of the well. As shown in Table 6-2, incremental compressive strains on the casing were simulated by Load Cases 3 and 5 and incremental tensile strains were simulated by Load Cases 4 and 6.

Each load case considered four load steps corresponding to the loading conditions determined previously at: (1) start of injection, (2) end of injection, (3) start of withdrawal, and (4) end of withdrawal, as shown in Figure 6-6. Each load step was defined with a different internal and external pressure, axial force, and temperature.

Figures 6-7 to 6-12 show examples of the results from each of the six load cases analyzed for the reservoir storage well casing at the end of injection (Load Step 2). Figure 6-7 shows a uniform band of strain at the pin thread ID that extends around the inner surface of the pipe for Load Case 1. Comparison of Figures 6-7 and 6-8 shows the effect of the well curvature by the intensification of this strain near the top of the connection and by the corresponding reduction at the bottom. Applying the incremental subsidence-related strains in Load Cases 3 and 4 appear to reduce the axial strain in this area, as shown in Figure 6-9 and 6-10. Welding the coupling tends to intensify the strain in the pin thread ID area, as shown in Figures 6-11

and 6-12. This effect appears to be related to the assumption that the weld isolates the OD of the pin threads that are not engaged from the exterior pressure on the pipe. The pressure in this area was assumed to be equal to atmospheric pressure as a worst-case scenario.

RSI-1546-06-029

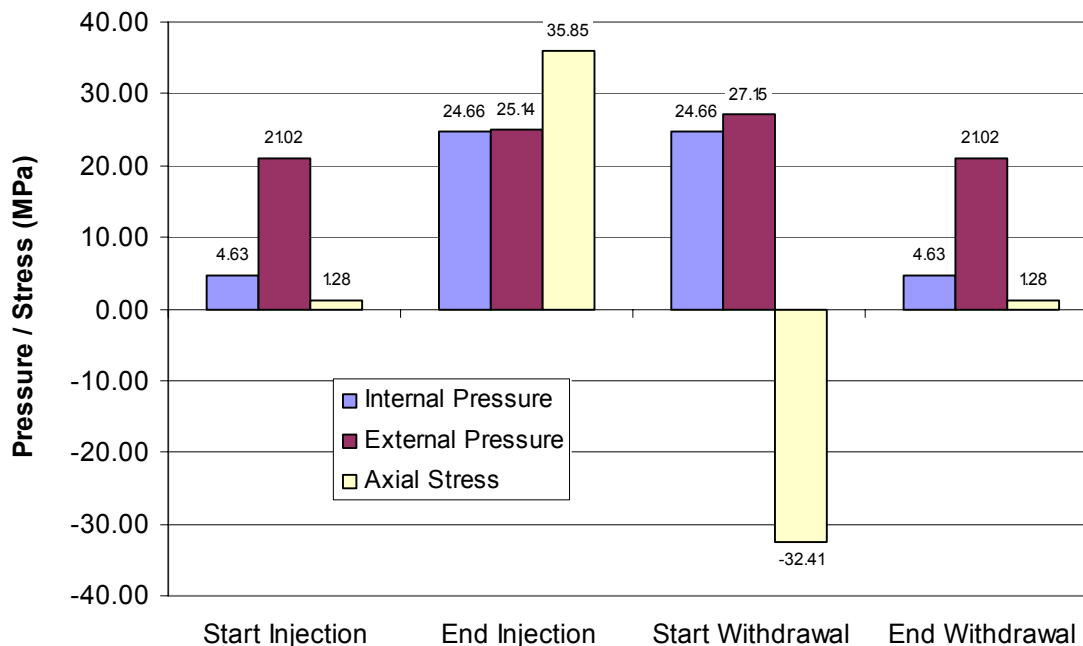


Figure 6-6. Load Steps for Reservoir Storage Well Connection Model.

For each load case, the estimated stress and peak plastic strain values at the four stress localization areas in the connection (Figure 6-3) were tabulated from each of the four load steps. This resulted in 16 combinations of stress and plastic strain in the different areas of the connection during each gas cycle. These stress and strain values were used to estimate the number of cycles to failure for each area in the connection. In each case, the area that was predicted to withstand the lowest number of cycles to failure was considered to be the critical location that would limit the performance of the entire connection. The analysis results showed that the coupling entry plane OD was never the limiting location but that fatigue failures may occur in the other three areas (coupling entry plane ID, pin thread root, and pin thread ID), depending on the combination of stress and strain imposed by the injection-withdrawal cycle.

The results of the fatigue assessment are presented in Table 6-3 and in Figure 6-13. If only the thermally induced and gas pressure induced loads are considered for a straight wellbore (Case 1), the fatigue life is approximately 1,400 cycles, with failures occurring in the coupling entry plane ID. The analysis shows that well curvature (Case 2) reduces the estimated fatigue life to 790 cycles.

RSI-1546-06-030

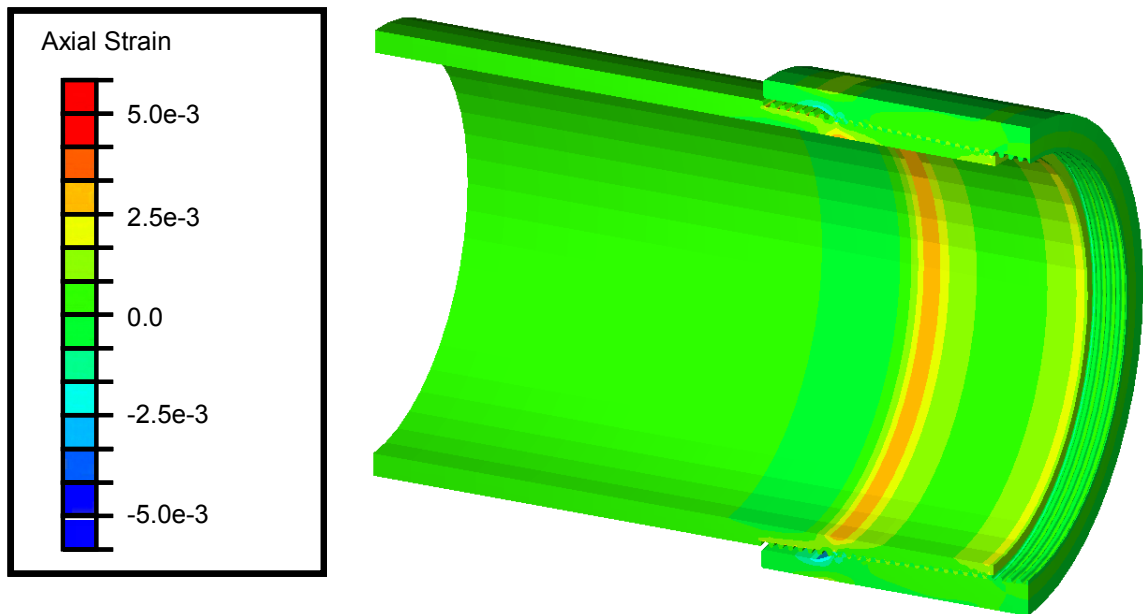


Figure 6-7. Axial Strain in Reservoir Well No. 3 for Load Case 1 at the End of Injection (Load Step 2).

RSI-1546-06-031

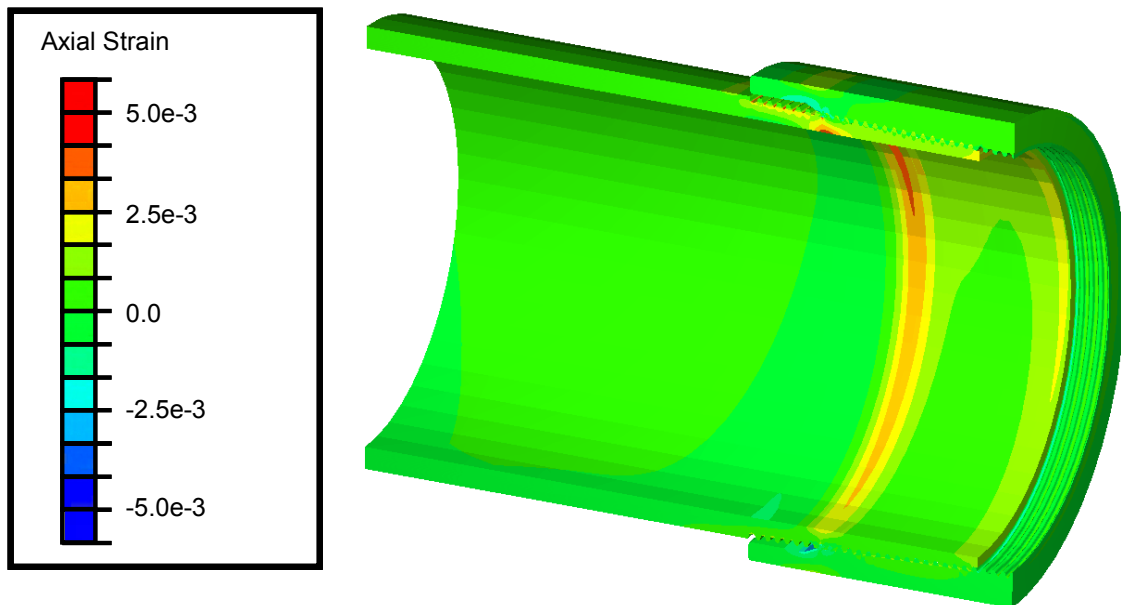


Figure 6-8. Axial Strain in Reservoir Well No. 3 for Load Case 2 at the End of Injection (Load Step 2).

RSI-1546-06-032

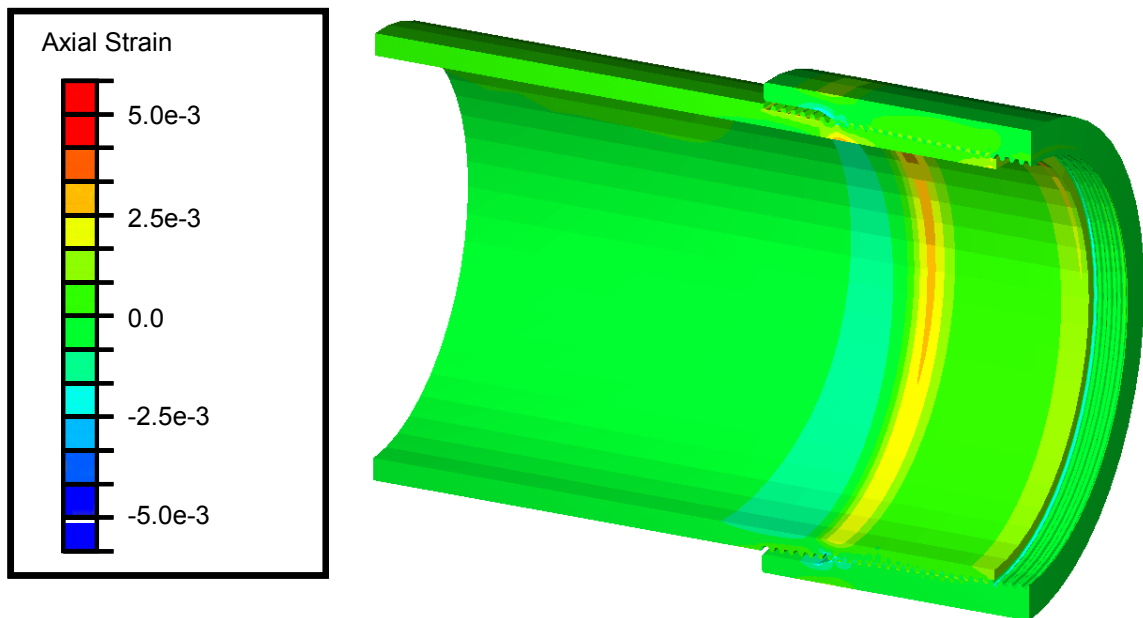


Figure 6-9. Axial Strain in Reservoir Well No. 3 for Load Case 3 at the End of Injection (Load Step 2).

RSI-1546-06-033

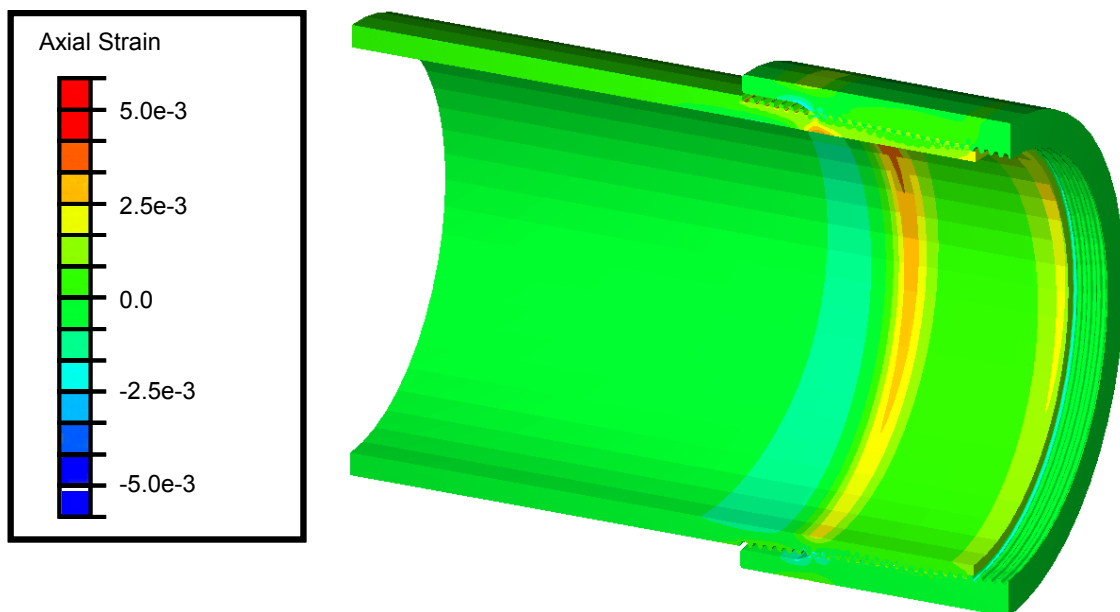


Figure 6-10. Axial Strain in Reservoir Well No. 3 for Load Case 4 at the End of Injection (Load Step 2).

RSI-1546-06-034

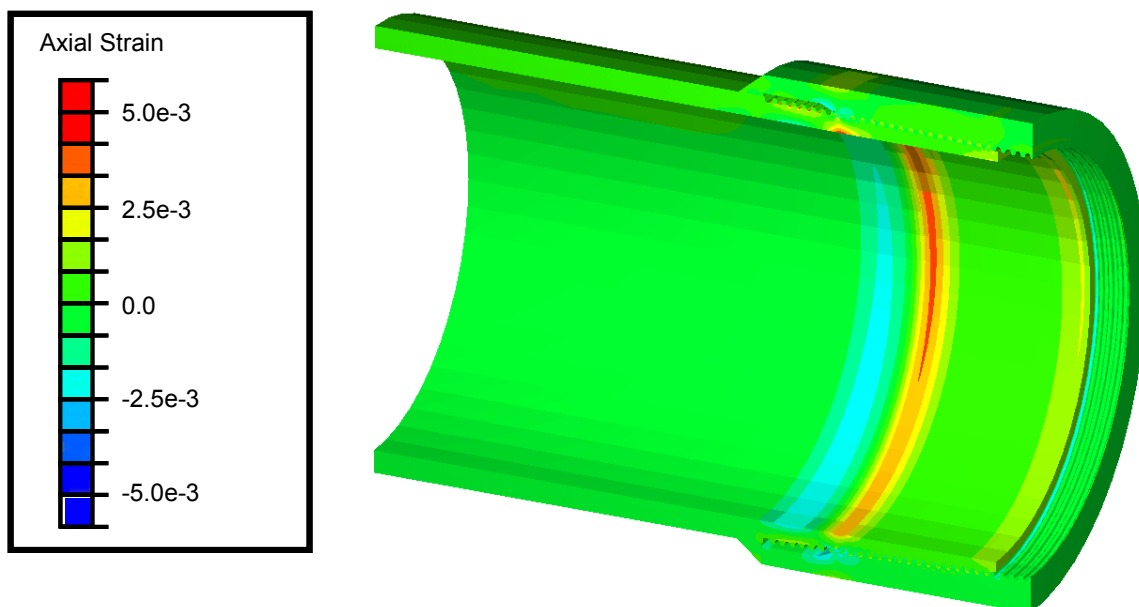


Figure 6-11. Axial Strain in Reservoir Well No. 3 for Load Case 5 at the End of Injection (Load Step 2).

RSI-1546-06-035

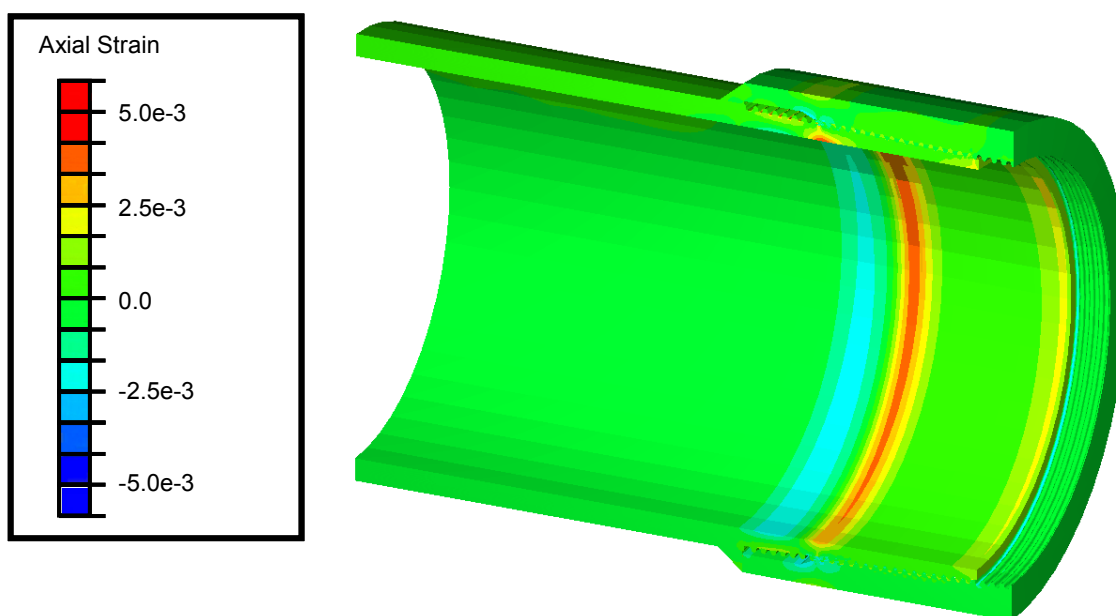
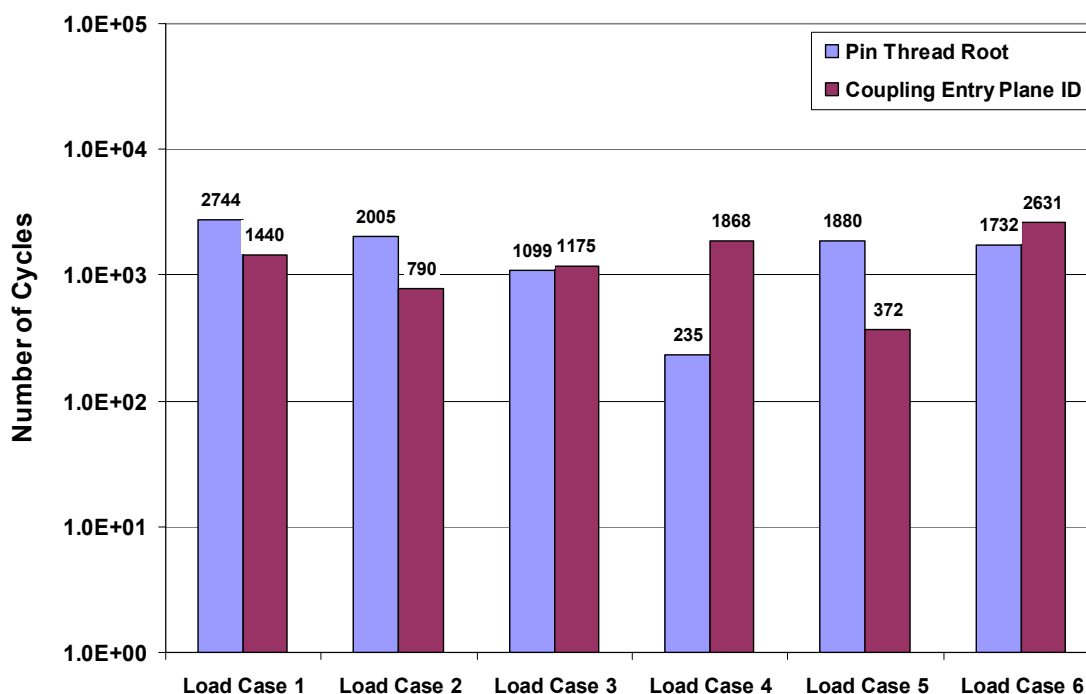


Figure 6-12. Axial Strain in Reservoir Well No. 3 for Load Case 6 at the End of Injection (Load Step 2).

Table 6-3. Fatigue Life Estimates of the Reservoir Storage Well Connection Model

Load Case	Curvature (°/30 meters)	Incremental Axial Strain (%)	Welded Coupling	Fatigue Life Pin Thread (cycles)	Fatigue Life Coupling ID (cycles)
1	0	N/A	No	2,744	1,440
2	9	N/A	No	2,005	790
3	9	-0.17%	No	1,099	1,175
4	9	0.17%	No	235	1,868
5	9	-0.17%	Yes	1,880	372
6	9	0.17%	Yes	1,732	2,631

RSI-1546-06-036

**Figure 6-13.** Fatigue Life for Various Load Cases of the Reservoir Storage Connection Model Assuming 5.1 Centimeters (2.0 Inches) of Formation Movement With Each Gas Cycle.

The analysis shows that where compaction imposes incremental compression on the casing (Case 3), the fatigue life decreases further and the failure location changes to the pin thread root of the connection. Compaction-related tensile strain (Case 4) reduces the fatigue life significantly to its lowest level with failures occurring in the pin thread root after 235 cycles.

These results include significant uncertainty associated with the assumed degree of formation movements caused by pore pressure changes in the reservoir. To evaluate the sensitivity of the results to these assumptions, the analysis was repeated assuming changes in axial casing stress caused by formation movements were reduced by approximately 60 percent. Figure 6-14 shows that the resulting fatigue life estimates increase dramatically for Load Case 4, where the formation movements were assumed to impart incremental tensile strain on the casing. Although Load Case 4 remains the load condition with the shortest estimated fatigue life, it is similar to other load cases and does not stand out as much as when higher load cycles are assumed.

RSI-1546-06-037

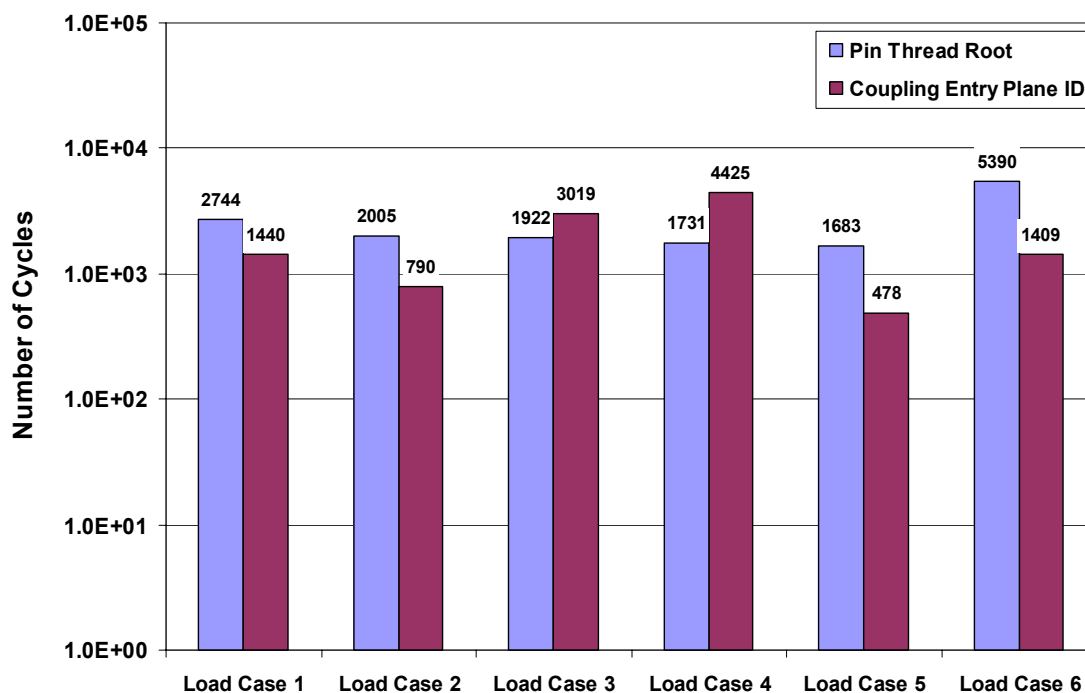


Figure 6-14. Fatigue Life for Various Load Cases of the Reservoir Storage Connection Model Assuming 2.1 Centimeters (0.8 Inch) of Formation Movement With Each Gas Cycle.

Welding the coupling face to the pipe body to strengthen the connection did not significantly change the minimum fatigue life in cases with incremental compaction-related compressive strains (Case 5 = 372 cycles compared to Case 3 = 1,099 cycles). Where compaction-related tensile strains occur, the minimum fatigue life improved with the welded connection (Case 6 = 1,732 cycles compared to Case 4 = 235 cycles). It is important to note that the analyses did not take into consideration the impact of any residual stresses or changes in material properties that may occur due to the welding of the connection.

6.4 SALT CAVERN WELL CONNECTION RESULTS

For the salt cavern application, the casing strings considered 340-millimeter (13 $\frac{3}{8}$ -inch, 72 lb/ft) K-55 API 8-Round STC connections. Connection analyses were performed using the load conditions provided in Chapter 5.0 determined at the lowest joint of the two salt cavern wells. The connection analyses simulated four load steps corresponding to the loading conditions determined at: (1) start of injection, (2) end of injection, (3) start of withdrawal, and (4) end of withdrawal. These load steps are shown in Figure 6-15 for the connection at a depth of 567 meters (1,860 feet) in the well of the shallow cavern (Salt Cavern Well No. 1). Figure 6-16 presents the load steps used for the lowest connection in the deeper cavern well (Salt Cavern Well No. 2). Comparison of Figures 6-15 and 6-16 shows that the deeper well casing involves much higher internal and external pressures and axial force because of the greater depth.

Figures 6-17 and 6-18 show the axial strain distribution at the end of gas injection in the shallow and deep salt cavern well connections, respectively. The strains are evenly distributed around the connections because only axisymmetric loading was assumed for these vertical wells.

Figure 6-19 presents the estimated fatigue life for the two salt cavern well completions. Both cases show that the pin thread root is the most critical location for fatigue failure. The fatigue lives are estimated to be 1.33×10^7 and 3.68×10^6 cycles (1,100,000 years and 310,000 years assuming 12 gas cycles per year) for the shallow and deep well casings, respectively.

6.5 SUMMARY OF FATIGUE LIFE ANALYSES

The fatigue life for the reservoir well was estimated to be as short as 235 cycles, or 235 years, assuming an annual pressure cycle. The deep salt cavern casing could withstand approximately 3.7×10^6 pressure cycles, but since the pressure is cycled 12 times per year, the well life is estimated to be 310,000 years. Connection fatigue in the shallow salt cavern well does not appear to be a concern, with a predicted fatigue life of 1,100,000 years, assuming 12 pressure cycles per year.

The fatigue life of 235 cycles for the reservoir well is believed to be an extremely conservative estimate. This result was obtained assuming that the casing and the sandstone formation strain equally in response to subsidence induced by depressurizing the reservoir formation. In reality, the casing, if cemented to the formation, would resist the ground movement and would experience less strain than that assumed in this study. Another possibility is that slip would occur at the casing interfaces, resulting in lower strains in the casing than the surrounding rock formation. A limited sensitivity analysis showed that the estimated fatigue life can vary significantly, depending on the magnitude of incremental axial

RSI-1546-06-038



Figure 6-15. Load Steps for the Connection in Salt Cavern Well No. 1 at a Depth of 567 Meters (1,860 Feet).

RSI-1546-06-039

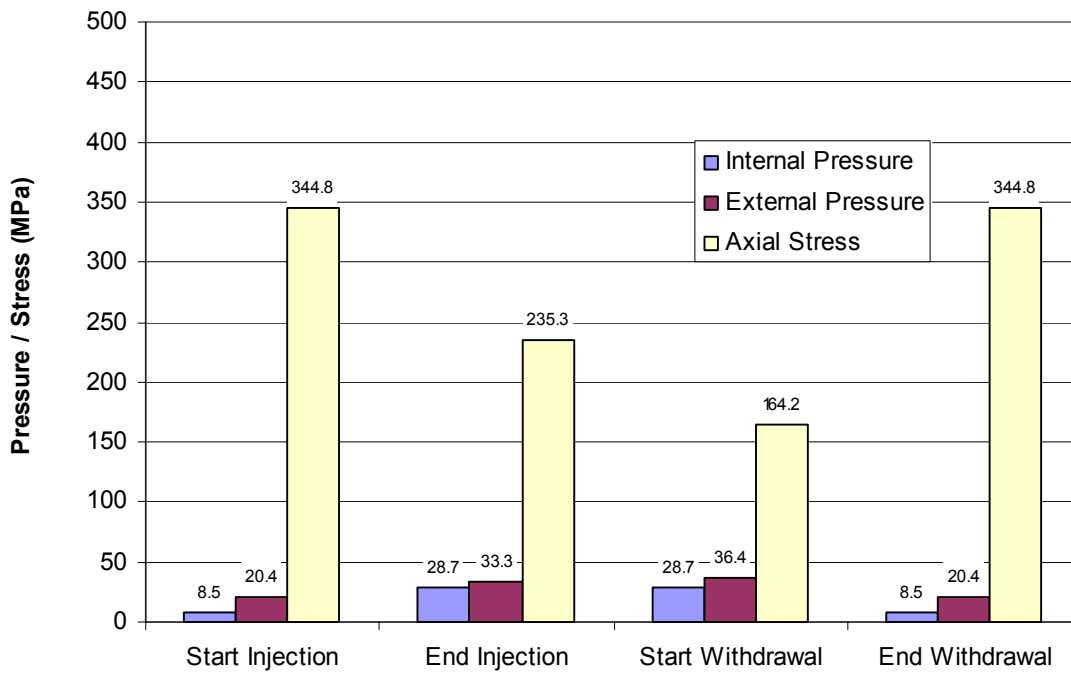


Figure 6-16. Load Steps for the Connection in Salt Cavern Well No. 2 at a Depth of 1,481 Meters (4,860 Feet).

RSI-1546-06-040

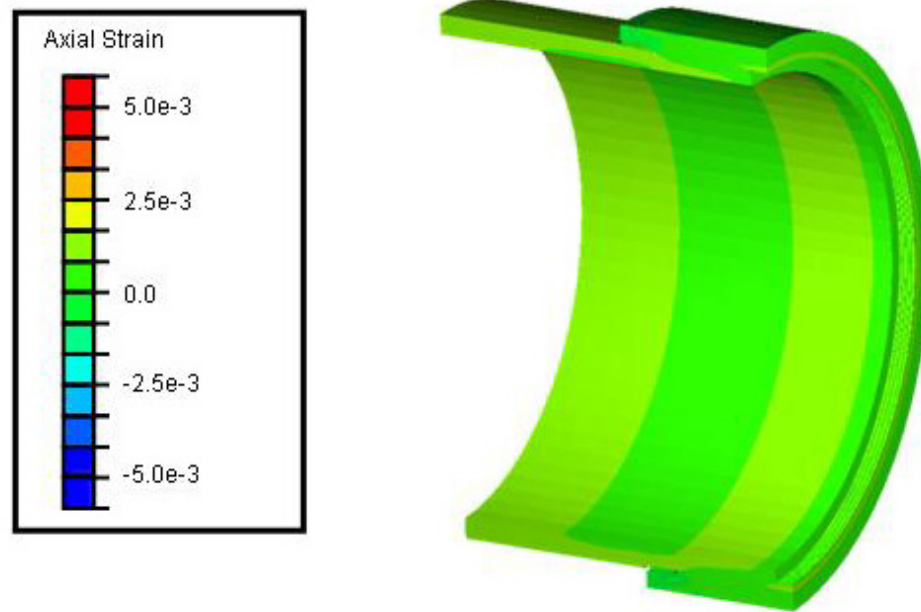


Figure 6-17. Axial Strain in Salt Cavern Well No. 1 Connection at a Depth of 567 Meters (1,860 Feet) at the End of Injection.

RSI-1546-06-041

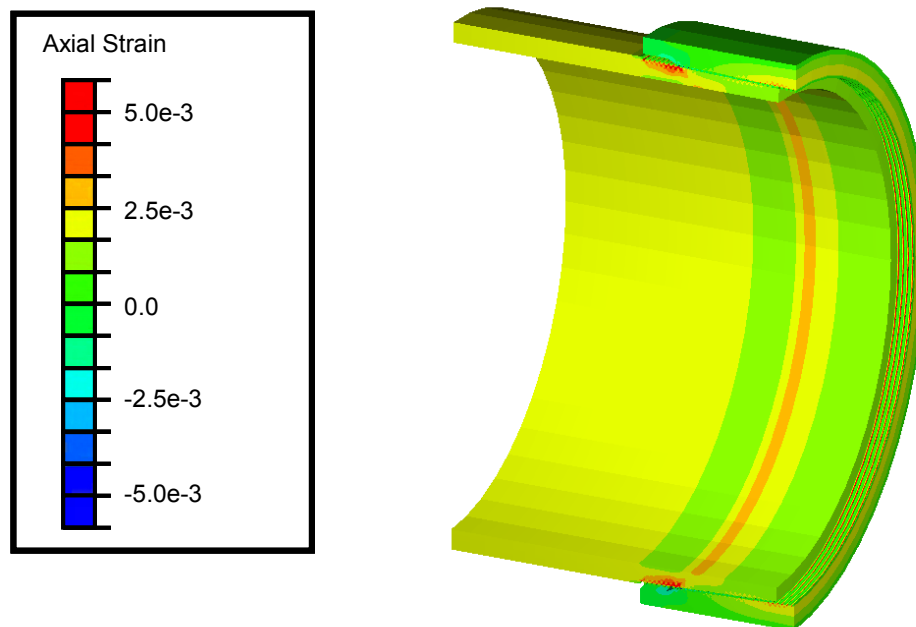


Figure 6-18. Axial Strain in Salt Cavern Well No. 2 Connection at a Depth of 1,481 Meters (4,860 Feet) at the End of Injection.

strain that is assumed to occur because of reservoir compaction. If the incremental axial strain attributable to reservoir compaction is not considered, the fatigue life of the connection increases to 790 cycles.

RSI-1546-06-042

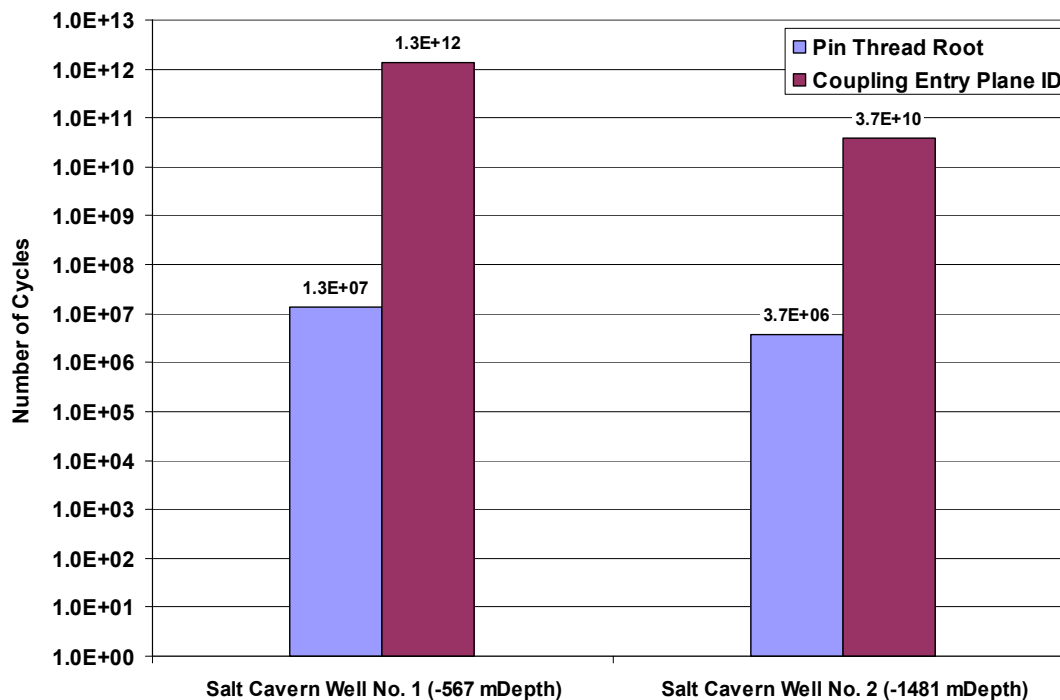


Figure 6-19. Estimated Fatigue Life for the Salt Cavern Connection Models.

Welding the coupling face to the pipe body in these applications does appear to contribute somewhat to the connection strength, but in some cases, may redistribute the stresses in the connection such that failure occurs in approximately the same number of cycles but in a different location compared to connections without welds. The analyses including the weld did not consider the effects welding may have on local stress concentrations or degradation of the casing and coupling material properties in the heat-affected zone adjacent to the weld.

There is a significant amount of uncertainty in the fatigue analysis presented here. This includes uncertainty in the fatigue performance of the connection materials, uncertainty in the effect of corrosion on the connection strength, and uncertainty how the loads (in particular, salt creep and reservoir compaction loads) are transmitted to the well casing. Considering this uncertainty, the minimum estimated fatigue life of 235 years for the reservoir well does not appear to provide a significant margin of safety to ensure adequate storage facility operating life.

The analysis did not consider the occurrence of localized casing strains that may occur because of buckling or shear of the casing that is often associated with large formation

movements. Shear and buckling deformations are common in oilfield production and injection scenarios that cause changes in the reservoir pore pressure. While many of these oilfield applications include very large changes in reservoir pore pressures, resulting in very large formation movements, the smaller pore pressure changes associated with gas storage operations likely cause similar, but smaller, formation movements in the gas storage reservoir and overburden.

Previous analyses of wells subjected to thermal strains and formation movements have shown that if the well cement provides lateral support for the casing, bending strains can be minimal because of buckling in high axial compression environments. However, even a small annular gap between the casing and cement or cement and formation can allow the casing to buckle when subjected to even moderate axial loads, resulting in localized bending strains. These bending strains can be many times greater than the average global strains attributed to thermal or pressure cycling. The effect of gap size on connection performance can be studied parametrically but it is difficult to characterize the actual gap size that might exist in a particular well.

This analysis demonstrated that API 8-Round STC connections may be susceptible to fatigue-related failures in some gas storage applications. Other connection configurations, such as Long Threaded and Coupled (LTC), buttress, and premium (proprietary) connections, are designed by various pipe manufacturers to offer significantly greater strengths. In many cases, the manufacturers report connection strengths that exceed the load capacity of the pipe body. Care must be taken in selecting a specific premium connection because some designs are intended for specific load environments and may not function any better than the 8-Round STC connection in the gas storage well scenario.

Critical pieces of information missing from this analysis of casing performance in gas storage wells are direct measurements of the casing deformations that can be used to verify the loading mechanisms and to help benchmark available models of casing-formation interaction. Conventional multifinger inspection logs can be used to characterize well deformations and provide quantitative measurements of the magnitude and direction of localized casing curvatures caused by formation movements or large casing loads. These logs are sensitive enough to identify casing deformation mechanisms before the deformations are apparent by other means (e.g., gauge rings and downhole video) or cause operational problems (e.g., casing leaks or impaired well access).

7.0 CONCLUSIONS

The analyses of the thermomechanical response of the well casings during gas storage injection and withdrawal cycles show that the effects of operating pressure and well temperature changes are minor in comparison to the axial strains imposed by formation movements (i.e., compaction in reservoirs and salt creep in caverns). Compaction in the candidate reservoir storage wells imposed an estimated 0.17 percent axial strain compared to approximately 0.018 percent strain attributed to the other loading mechanisms. The analysis of the 1,524-meter- (5,000-foot-) deep salt cavern well showed that deformations from salt creep will cause the casing to fail if the casing remains bonded to the salt and the cement does not fail. Even with the assumption that the stress transmitted to the casing is limited to 345 MPa (50,000 psi), the axial strain imposed by the formation movements is approximately 0.17 percent. This is still more than twice the 0.08-percent strain caused by temperature and pressure changes in the well.

The fatigue life of the connections in the reservoir and deep salt cavern wells was estimated to be 235 and 310,000 years, respectively. Although the axial strains imposed by formation movements were about the same for these two wells, the salt cavern well connections can withstand considerably more cycles than the reservoir well connections. This is because the formation movements impart cyclic loads on the reservoir well casing; whereas, salt creep produces monotonically increasing loads. The combined cyclic loads from formation movement and thermal cycling significantly reduce the estimated fatigue life of the reservoir well connection. Connections in both salt cavern wells do not appear to be at risk of cyclic fatigue. Two key uncertainties remain in the analysis that may influence the estimated fatigue life of the connections. The first is the fatigue performance of the casing and connection materials, which was based on analogous materials. The second is how much of the formation movements that occur during pressure and temperature cycles are transferred through the well cement to the casing.

8.0 REFERENCES

- ABAQUS, Inc., 2005.** *User's Manual Version 6.5.1*, Pawtucket, RI.
- American Petroleum Institute, 1974.** "Formulas and Calculations for Casings, Tubing, Drill Pipe, and Line Pipe Properties," *API Bulletin 5C3*, American Petroleum Institute, Washington, DC, March.
- American Petroleum Institute, 1999.** "Gauging and Inspection of Casing, Tubing, and Liner Pipe Threads," *API Bulletin 5B1*, American Petroleum Institute, Washington, DC.
- Biot, M. A., 1955.** "Theory of Elasticity and Consolidation for a Porous Anisotropic Solid," *Journal of Applied Physics*, Vol. 26, No. 2, February, pp. 182–185.
- Boller, C. and T. Seeger, 1987a.** "Materials Data for Cyclic Loading—Part A: Unalloyed Steels," *Materials Science Nomographs*, 42A, Elsevier, New York, NY.
- Boller, C. and T. Seeger, 1987b.** "Materials Data for Cyclic Loading – Part B: Low-Alloy Steels," *Materials Science Nomographs*, 42B, Elsevier, New York, NY.
- Callahan, G. D., 1981.** *Inelastic Thermomechanical Analysis of a Generic Bedded Salt Repository*, ONWI-125, prepared by RE/SPEC Inc., Rapid City, SD, for the Office of Nuclear Waste Isolation, Battelle Memorial Institute, Columbus, OH.
- Callahan, G. D., A. F. Fossum, and D. K. Svalstad, 1989.** *Documentation of SPECTROM-32: A Finite Element Thermomechanical Stress Analysis Program*, DOE/CH/10378-2, prepared by RE/SPEC Inc., Rapid City, SD, for the U. S. Department of Energy, Chicago Operations Office, Argonne, IL, Vol. I and II.
- Croff, A. G., T. F. Lomenick, R. S. Lowrie, and S. H. Stow, 1985.** *Evaluation of Five Sedimentary Rocks Other Than Salt for High-Level Waste Repository Siting Purposes*, Volume 1: Main Report and Appendixes A and B, ORNL/CF-85/2/V1, Oak Ridge National Laboratory for the United States Department of Energy, Washington, DC.
- Dahlstrom, D. J., 1988.** *Thermal Properties Measurements of Avery Island Salt Core*, RSI-0334, prepared by RE/SPEC Inc., Rapid City, SD, for Stone & Webster Engineering Corporation, Boston, MA.
- Dowling, N. E., 1998.** *Mechanical Behavior of Material—Engineering Methods for Deformation, Fracture, and Fatigue*, 2nd ed., Prentice Hall, New Jersey, 830 p.
- Economides, M. J., A. D. Hill, and C. Ehlig-Economides, 1994.** *Petroleum Production Systems*, Prentice Hall PTR, Upper Saddle River, NJ.
- Humphreys, K. J., S. C. Solanki, and R. A. Link, 1991.** *Qualification of Grade-55 Casing for Thermal Recovery Service*, C-FER Project 88-14, prepared by C-FER Technologies, Edmonton, Alberta, Canada, for Joint Industry Members.

Illson, T. F. and C. D'Arcy, 2004. *Wellbore Integrity Assessment-Phase I Industry Survey*, Catalog No. L52134e, prepared by Advantica, Inc., Houston, TX, for Pipeline Research Council International, Inc., Underground Storage Technical Committee, Arlington, VA.

Incopera, D., 1996. *Introduction to Heat Transfer*, 3rd ed., Appendix A, pp. 746–751, John Wiley and Sons, Inc.

Karably, L. S. and R. M. White, 1981. *Geothermal Studies of Seven Interior Salt Domes*, prepared by Law Engineering Testing Company, Marietta, GA, for the Office of Nuclear Waste Isolation, Battelle Memorial Institute, Columbus, OH.

Munson, D. E., 1998. *Analysis of Multistage and Other Creep Data for Domal Salts*, SAND98-2276, Sandia National Laboratories, Albuquerque, NM.

Nelson, P. E. and L. L. Van Sambeek, 2003. *State-of-the-Art Review and New Techniques for Mechanical Integrity Tests of (Gas-Filled) Natural Gas Storage Caverns*, Research Project Report No. 2003-2-SMRI, prepared by RESPEC, Rapid City, SD, for the Solution Mining Research Institute, Encinitas, CA.

Nieland, J. D. 2004. *Salt Cavern Thermal Simulator Version 2.0 User's Manual*, RSI-1760, prepared by RESPEC, Rapid City, SD, for Gas Technology Institute, Des Plaines, IL.

Norton, F. H., 1929. *Creep of Steel at High Temperatures*, McGraw-Hill Book Company, New York, NY.

Pfeifle, T. W., K. D. Mellegard, and N. T. Skaug, 2000. *An Investigation of the Integrity of Cemented Casing Seals With Application to Salt Cavern Sealing and Abandonment*, Research Project Report No. 2000-2-SMRI, prepared by RESPEC, Rapid City, SD, for the Solution Mining Research Institute, Encinitas, CA.

Philippacopoulos, A. J. and M. L. Berndt, 2000. "Characterization and Modeling of Cements for Geothermal Well Casing Remediation," *Geothermal Resources Council Transactions*, Vol. 24, pp. 81–86.

Riley, W. F., L. D. Sturges, and D. H. Morris, 1999. *Mechanics of Materials*, 5th ed., John Wiley & Sons, Inc., New York, NY.

Senseny, P. E., F. D. Hansen, J. E. Russell, N. L. Carter, and J. W. Handin, 1992. "Mechanical Behaviour of Rock Salt: Phenomenology and Micromechanisms," *International Journal of Rock Mechanics and Mining Sciences & Geomechanics Abstracts*, Vol. 29, No. 4, pp. 363–378.

Sines, G. and G. Ohgi, 1981. "Fatigue Criteria Under Combined Stresses and Strains," *Journal of Engineering Materials and Technology*, Vol. 103, pp. 82–90.

Starling, K. E. and J. L. Savidge, 1994. *Compressibility of Natural Gas and Other Related Hydrocarbon Gases*, Report No. 8, 2nd ed., Catalog No. XQ9212, prepared for American Gas Association, Arlington, VA.

Svalstad, D. K., 1989. *Documentation of SPECTROM-41: A Finite Element Heat Transfer Analysis Program*, DOE/CH/10378-1, prepared by RE/SPEC Inc., Rapid City, SD, for the U.S. Department of Energy, Chicago Operations Office, Argonne, IL.

APPENDIX A
ADDITIONAL WELL CASING ANALYSES

APPENDIX A ADDITIONAL WELL CASING ANALYSES

The approach used for solving the well model problems assumed that the casing/cement and cement/salt interfaces remain perfectly bonded. This approach provides a conservative estimate for axial tensions because the casing is forced to displace nearly the same magnitude as the salt. However, the predicted results could be dramatically different if the bond between the material interfaces is broken. The presence of a microannulus, defined as a very small annular gap located between the pipe and the cement sheath, is an example of a condition where the pipe is not bonded to the cement sheath. Even if a microannulus is present, the cement job may be sufficient to form a hydraulic seal and prevent fluid migration behind the pipe under normal production conditions. A microannulus may be caused by several factors, including:

- Thermal expansion of the pipe while the cement cures.
- Thermal contraction of the pipe as a result of fluids cooler than the cement sheath flowing through the pipe.
- Reducing the hydrostatic head of the fluid after holding the pressure on the casing until the cement has set.
- Contaminants, such as grease, on the external surface of the casing.

Interfaces can be modeled numerically as frictional or frictionless contacts. A frictionless contact will only allow normal forces to be transferred across the surface, providing the least conservative estimate for axial tensions in the casing. Attempts were made to model frictional interfaces without success. The scale of the regional well model prevents accurate solution of the interface behavior using convergence criteria based on global equilibrium.

To gain a better understanding of the steel/cement interaction, a finite element analysis was performed to provide an estimate of the maximum tensile load that the cement can impose on the steel pipe. The model developed for this analysis is a cylindrical representation of a 340-millimeter (13 $\frac{3}{8}$ -inch) casing and coupling, surrounded by a 47.5-millimeter- (2-inch-) thick cement sheath within a 1.5-meter- (5-foot-) radius salt mass. The vertical extent of the model was also limited to 1.5 meters (5 feet). Traction forces were applied to the lateral boundaries to represent the confinement of the salt at a depth of about 1,481 meters (4,860 feet).

For this model, it was assumed that the bond has been broken between the steel and the cement and that only the coupling restricts the relative displacement between the two casing components. During the finite element analysis, an axial force was incrementally applied to the steel pipe in an effort to pull the pipe and coupling through the cement sheath. Mohr-

Coulomb factors of safety were monitored in the cement region to identify those regions that failed in shear based on cohesion and friction angles of 8.79 MPa (1,275 psi) and 10 degrees, respectively. Contours of factors of safety in the cement are provided in Figure A-1. As shown in Figure A-1, shear failure of the cement is initiated by the time the axial stress in the pipe reaches 275.81 MPa (40,000 psi). The zone of failure expands as the axial force in the pipe is increased. When the axial load produces 345 MPa (50,000 psi) tension in the steel, the zone of failure extends several inches from the connection and across the thickness of the cement sheath. Based on this result, it would seem unlikely that the cement could transfer an axial load greater than 345 MPa (50,000 psi) because the shear strength of the cement will be greatly deteriorated. This finding is based on the assumptions made in defining the problem, which are perceived as reasonable. Assumptions other than those identified for this problem may impact the results. However, without experimental or field observations, it is not possible to ascertain the physical condition of the cement in a zone experiencing large creep deformations. The 345 MPa (50,000 psi) tensile stress is assumed to be a conservative estimate for the maximum axial tensile stress obtainable in the casing, given the condition that the steel casing has not failed.

RSI-1546-06-043

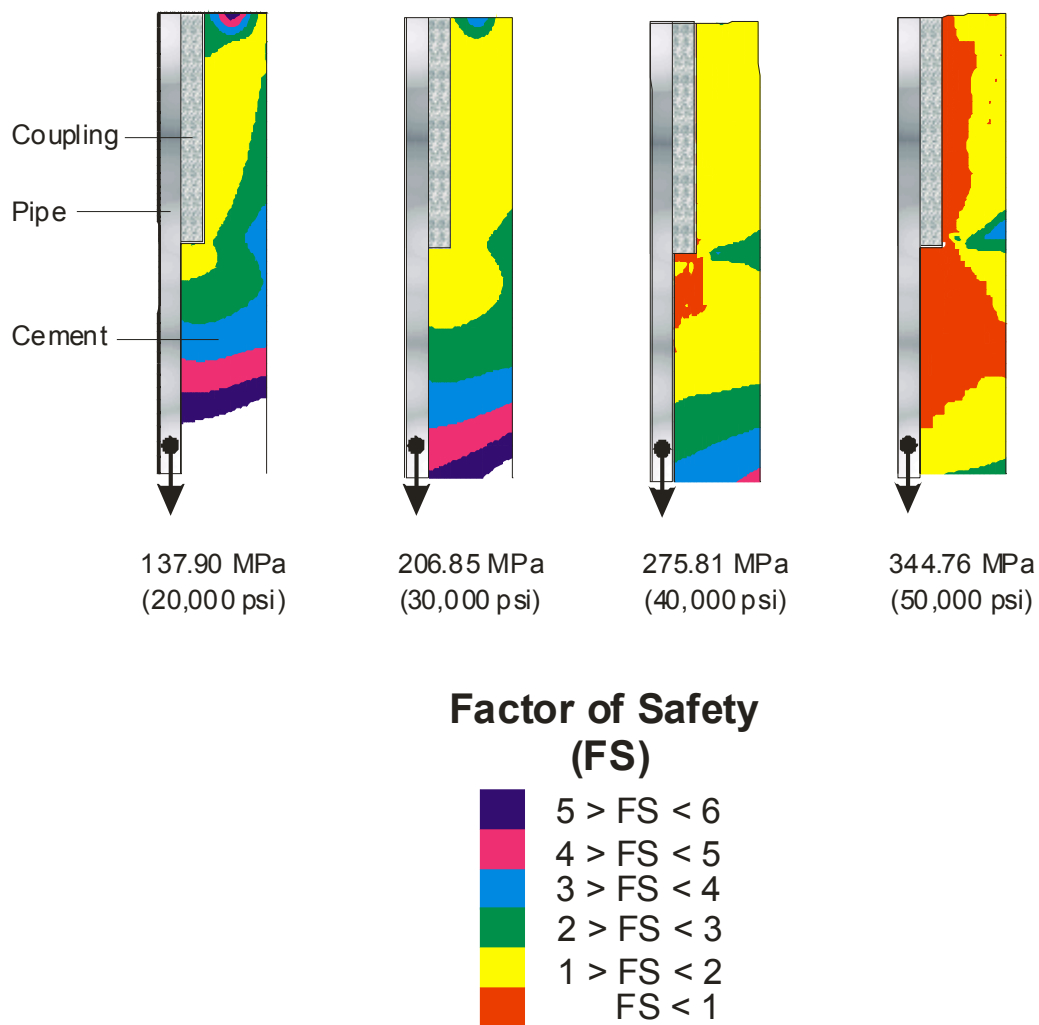


Figure A-1. Predicted Mohr-Coulomb Factor-of-Safety Contours in the Cement Sheath for Different Axial Stress Loads in the Steel Pipe.

Appendix G
2005, New Comprehensive Inventory Analysis Tool,
Schlumberger Consulting Services Final Report

New Comprehensive Inventory Analysis Tool

FINAL TECHNICAL REPORT

1 May 2005 – 31 May 2007

C. M. Boyer II, Project Director, Schlumberger
K. G. Brown, Principle Investigator, Schlumberger
W. K. Sawyer, Principle Consultant, Schlumberger

August 2007

Prime Award No. DE-FC26-03NT41779
Subaward No. 2907-SCS-DOE-1779

Schlumberger
Consulting Services
1310 Commerce Drive
Park Ridge 1
Pittsburgh, PA 15275-1011

DISCLAIMER

This report was prepared as an account of work sponsored by an agency of the United States Government. Neither the United States Government nor any agency thereof, nor any of their employees, makes any warranty, express or implied, or assumes any legal liability or responsibility for the accuracy, completeness, or usefulness of any information, apparatus, product, or process disclosed, or represents that its use would not infringe privately owned rights. Reference herein to any specific commercial product, process, or service by trade name, trademark, manufacturer, or otherwise does not necessarily constitute or imply its endorsement, recommendation, or favoring by the United States Government or any agency thereof. The views and opinions of authors expressed herein do not necessarily state or reflect those of the United States Government or any agency thereof.

ABSTRACT

Inventory analysis is critical to proper management of underground gas storage (UGS) facilities. Often, basic inventory analysis plots (e.g., P/Z vs Inventory) are updated and reviewed once or twice a year, with additional scrutiny being applied if several cycles of data suggests possible inventory problems.

There are over a dozen useful diagnostic plots and techniques available for monitoring inventory and identifying potential causes of lost gas in storage reservoirs. However, many operators have given more and more responsibilities to fewer and fewer personnel in recent years, making truly comprehensive inventory analyses more difficult to accomplish in a reasonable timeframe. In addition, as new storage engineers enter the market to replace the graying retirees, unfamiliarity with the underlying assumptions and limitations inherent in the less known analysis techniques may cause undue hesitation to implement these techniques.

This report summarizes the work performed under contract DE-FC26-03NT41779. The primary objective of this project was to develop a comprehensive inventory analysis software tool that would:

- Allow easy importation of typical storage inventory data,
- Automatically generate pertinent raw data plots and diagnostic plots for the analyst's review and processing of inventory data,
- Provide on-line help that gives an overview of the inventory analysis process and explains the assumptions, applications, limitations, and processes used to analyze specific diagnostic plots, and
- Provide a "toolbox" application that would perform calculations useful in the process of inventory analysis.

This new tool significantly improves operators' ability to effectively monitor inventory and resolve gas loss issues by making inventory analysis processes much more automated and much more comprehensive. It also enhances the analysis process by guiding the engineer to the appropriate analysis techniques and away from the inappropriate analysis techniques via the on-line help tools.

In this report, the software development and design is briefly reviewed, including a summary of the major components of the software and online help features. An example dataset and analysis is presented. Recommendations for future improvements in the software are also discussed.

TABLE OF CONTENTS

DISCLAIMER	I
ABSTRACT	II
TABLE OF CONTENTS	III
LIST OF FIGURES	V
1 INTRODUCTION	1
2 EXECUTIVE SUMMARY	2
2.1 OBJECTIVES	2
2.2 SOFTWARE OVERVIEW	2
2.3 RECOMMENDATIONS	5
3 EXPERIMENTAL	6
3.1 INTRODUCTION	6
3.2 SOFTWARE DEVELOPMENT PLATFORM AND LAYOUT.....	6
3.3 INVENTORY ANALYSIS WORKFLOW	7
3.3.1 <i>Populating Excel Input Template</i>	8
3.3.2 <i>Importing Data to Software</i>	13
3.3.3 <i>Performing Preliminary Calculations</i>	13
3.3.4 <i>Quality Controlling Input/Calculated Data</i>	14
3.3.5 <i>Analyzing Data Using Diagnostic Plots</i>	14
3.3.5.1 Plots to review trends in basic operating data	14
3.3.5.2 Diagnostic plots to identify/quantify gas losses	15
3.3.5.3 Plots to verify that adjustments resolve discrepancies.....	15
3.3.6 <i>Generating Reports</i>	15
3.4 ON-LINE HELP AND REFERENCES.....	16
3.4.1.1 Help: Input Screens	16
3.4.1.2 Help: Analysis Plots	16
3.4.1.3 Help: Toolbox	16

3.4.1.4	Help: Users Manual With Example Problem Tutorial.....	17
3.4.1.5	Help: Inventory Verification Primer	17
3.4.1.6	Help: References	17
3.4.1.7	Help: Storage Inventory and Deliverability Terminology	17
3.4.1.8	Help: Underground Gas Storage Glossary	17
4	RESULTS AND DISCUSSION.....	18
4.1	SOFTWARE DEVELOPED	18
4.2	COST BENEFIT ASSESSMENT	18
5	CONCLUSIONS.....	19
6	REFERENCES	20
7	LIST OF ACRONYMS AND ABBREVIATIONS	21
8	NOMENCLATURE	22

APPENDIX I - SOFTWARE USER'S MANUAL WITH EXAMPLE PROBLEM TUTORIAL

APPENDIX II - INVENTORY ANALYSIS PRIMER

APPENDIX III - LIST OF UNDERGROUND GAS STORAGE REFERENCES

APPENDIX IV - INVENTORY & DELIVERABILITY TERMINOLOGY

APPENDIX V - UNDERGROUND GAS STORAGE GLOSSARY

LIST OF FIGURES

Figure 1: Major windows in the software work area	3
Figure 2: Major windows in the software work area	6
Figure 3: General workflow followed for inventory analysis using new software.....	7
Figure 4: Example input sheet in EXCEL TM template and associated help information....	8

1 INTRODUCTION

Some level of inventory analysis is routinely performed in virtually all gas storage fields, and is a critical to proper management of gas storage facilities. Often, basic inventory analysis plots (e.g., P/Z vs Inventory) are updated and reviewed once or twice a year. If several cycles of data suggests a possible inventory problem, the inventory data and analysis plots are given additional scrutiny. If additional scrutiny suggests significant gas losses, a major study may be initiated, in which inventory is analyzed more comprehensively, usually using two or three analysis techniques (e.g., P/Z vs Inventory analysis and inventory per pound (IPP) analysis).

There are over a dozen useful diagnostic plots and techniques available for monitoring inventory and identifying potential causes of lost gas in storage reservoirs. However, many operators have given more and more responsibilities to fewer and fewer personnel in recent years, making truly comprehensive inventory analyses more difficult to accomplish in a reasonable timeframe. In addition, as new storage engineers enter the market to replace the graying retirees, unfamiliarity with the underlying assumptions and limitations inherent in the less known analysis techniques may cause undue hesitation to implement these techniques. This is indeed unfortunate, since nearly every analysis technique will shed some useful light on inventory and gas loss issues.

Therefore, we proposed development of a user-friendly software package that would: 1) accept typical inventory data available for a field, 2) automatically generate and interactively interpret diagnostic plots, 3) provide on-line help screens summarizing the technical assumptions of each analysis technique, the applicability of the techniques to various types of storage reservoir, the inherent dangers of each technique, and example plots of each technique.

The result of this project is a software package that accomplishes the above objectives. This software significantly improves operators' ability to effectively monitor inventory and resolve gas loss issues by making inventory analysis processes much more automated and much more comprehensive. It also enhances the analysis process by guiding the engineer to the appropriate analysis techniques and away from the inappropriate analysis techniques via the on-line help tools.

2 EXECUTIVE SUMMARY

2.1 Objectives

The primary objectives of this project included:

- Develop and field test a software tool that:
 - Readily accepts inventory data available for a given field and
 - Automatically generates and interactively interprets diagnostic plots
- Develop on-line help tools within the software that provides:
 - The technical reference(s) on which the various inventory analysis technique are based
 - The technical assumptions inherent in each analysis technique
 - The applicability of each technique to various types of storage reservoirs
 - The inherent dangers of each technique
 - Example plots for each technique
 - A “toolbox” that would perform calculations useful for inventory analysis
 - A categorized list of references and technical papers that covers a broad range of underground gas storage topics
 - A glossary of underground gas storage terminology

2.2 Software Overview

This software was developed in the VisualBasic™ programming environment, uses Microsoft ACCESS™ for data storage, employs Microsoft EXCEL™ as a “bridge” between users’ data and the ACCESS™ database, and exports reports to WORD™. EXCEL™ was chosen for use as a template to hold data due to the ubiquitous use of EXCEL™ in the UGS industry. ACCESS™ was chosen due to its excellent data handling and data manipulation capabilities. Use of this software requires the installation of EXCEL™ and WORD™ on the user’s computer, but not ACCESS™.

An EXCEL™ spreadsheet was developed to facilitate transfer of data necessary for inventory analysis from the user to the software. This spreadsheet acts as a “template” to ensure the data types, order, and content are consistent with what the software expects upon import of the data.

There are five major areas or windows in the software work area (**Figure 1**), including:

- A Toolbar window, which contains several toolbars associated with different aspects of inventory analysis calculations and workflow (e.g., BHP and BHP/Z calculations, Inventory Per Pound (IPP) calculations, etc).
- A Data Table window, which displays data from the various tables containing the input and calculated data
- A Workflow window, which shows an outline (in tree structure) of the inventory analysis workflow employed in this software

- A Data/Plotting window, showing data contained in the highlighted table (in the Data Table window) or the diagnostic plot (highlighted in the Workflow window)
- A Plot Feature window, which contains various buttons that allow modification of various plot features.

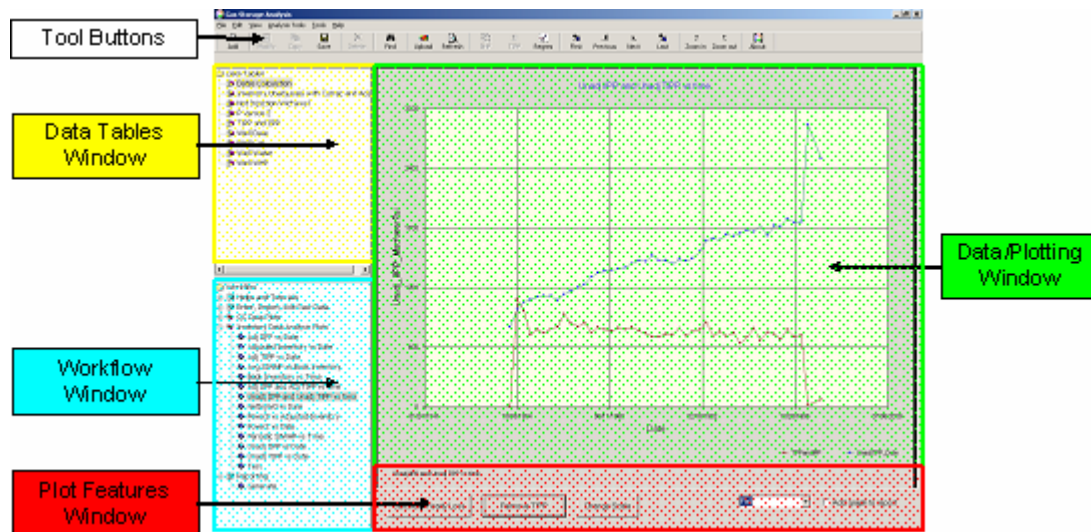


Figure 1: Major windows in the software work area

The development of comprehensive HELP features was considered a critical part of this project. Several HELP tools are available in two locations to guide the users as they use this software. All help features are available using the “help” menu at the top of the software window, and the HELP features typically used during the inventory analysis process are also included in the Workflow Window, under “Helps and Tutorials.” The various HELP features include the following:

- **Inventory Analysis Primer:** This document provides a very concise summary of the objectives, theory, data required, diagnostic plots, and analyses techniques involved in inventory analysis. It also includes a sample dataset and the analysis of the sample dataset.
- **Summary of References:** This document summarizes various references and technical papers related to Underground Gas Storage. These references are not limited to inventory analysis, but cover a wide range of UGS topics including:
 - Introduction to Gas Storage
 - Gas Storage Field Design
 - Optimization
 - Migration and Monitoring
 - Inventory Verification
 - Deliverability Maintenance and Enhancement

- Simulation of UGS Reservoirs
- Top Twenty Technical Papers
- Inventory Analysis Toolbox: This is an EXCEL™ spreadsheet that summarizes and/or calculates various data useful in the process of inventory analysis, including:
 - Estimated line losses as per a U.S. Bureau of Mines publication
 - Estimated volume of gas vented during a wellbore blowdown
 - Estimated volume of gas vented during a multi-rate well test
 - Estimated volume of gas contained in a pipeline at specified inlet and outlet conditions.
 - Estimated shut-in pseudopressure vs time for assumed reservoir properties (to estimate time to stabilized shut-in pressure).
 - Estimate (first order) of minimum gas flow rate to continuously unload fluids from a wellbore of specified configuration.
 - Units Conversion Table
 - Chart of estimated residual gas saturation as a function of porosity
 - Chart estimating (HP)/(MMscf/D) required to compress typical storage gas at 100 degrees F to 1000 psi using single stage compression.
- Input Template Help Information: There is help information for each input sheet in the EXCEL™ input template, including a description of the data needed and an example data input set.
- Technical Help for Diagnostic Plot Analysis: This document summarizes how various diagnostic plots are used and analyzed. In most cases, the following information is presented for each diagnostic plot:
 - Example plot
 - Purpose of the plot
 - Assumptions inherent in construction/use of the plot
 - Applicability of the plot
 - Dangers associated with misuse of plot
 - References
- Gas Storage Terminology and Gas Storage Glossary: This document lists and describes/defines various terms used in UGS, and includes a comprehensive glossary of terms.

The software tool has been tested using numerous actual field datasets to ensure the correct coding of all calculation processes. Nearly 20 datasets were loaded into the software and analyzed. These analysis results were compared to results previously obtained using manual analysis techniques to ensure the software gave consistent results.

2.3 Recommendations

We recommend that Gas Storage Technology Consortia (GSTC) members use this software for a period of time and provide the GSTC executive council with a list of additional features and upgrades the membership would like to incorporate into the software. Potential enhancements could include the following:

- Additional WHP-BHP correlations
- Additional Z-factor correlations
- Additional calculations/features in the “Toolbox”
- Additional diagnostic plots with associated calculations
- Enhanced interactive analysis features, such as
 - Enhanced data import features
 - Plot data points color-coded by date (e.g., P/Z vs Inventory plot)
 - Interactive selection of data point(s) to be included/excluded from analysis
 - Selection of *any* endpoints (not just actual data points) to draw plot lines
 - Expand the range of calculations made internally (e.g., have the software internally generate plot data required to construct the Cumulative Withdrawal vs Deliverability plot from raw input data instead of requiring the user to entering these calculated values in the input template).

3 EXPERIMENTAL

3.1 Introduction

Given the large number of useful diagnostic plots and techniques available for inventory analysis, we considered the ability of the software to automatically generate and interactively interpret inventory data to be of paramount importance in the development of the software.

Of nearly equal importance was the inclusion of HELP features that would allow storage engineers (especially inexperienced storage engineers) to more confidently employ the numerous graphical analysis techniques available, to fully appreciate the assumptions, limitations, and dangers associated with the application of these techniques to their specific reservoirs, and to provide the necessary technical references to more fully research the various inventory analysis methodologies.

All of this needed to be done in a software environment that allowed deployment of a product to users having a variety of types and versions of software available on their PC's. Therefore, careful consideration was given to the development platform used to develop the software, as well as any additional software requirements required for data importation into the software.

3.2 Software Development Platform and Layout

Given the above considerations, we decided to use Visual Basic™ as the software development platform, EXCEL™ to store raw inventory data for import into the software, and WORD™ to export reports.

Visual Basic™ was selected as the development platform to allow deployment of the software across a variety of platforms and minimizes the amount and type of specific software required to be installed on users' computer. EXCEL™ and WORD™ were selected because they are ubiquitous in the UGS industry.

There are five major areas or windows in the software work area (**Figure 2**):

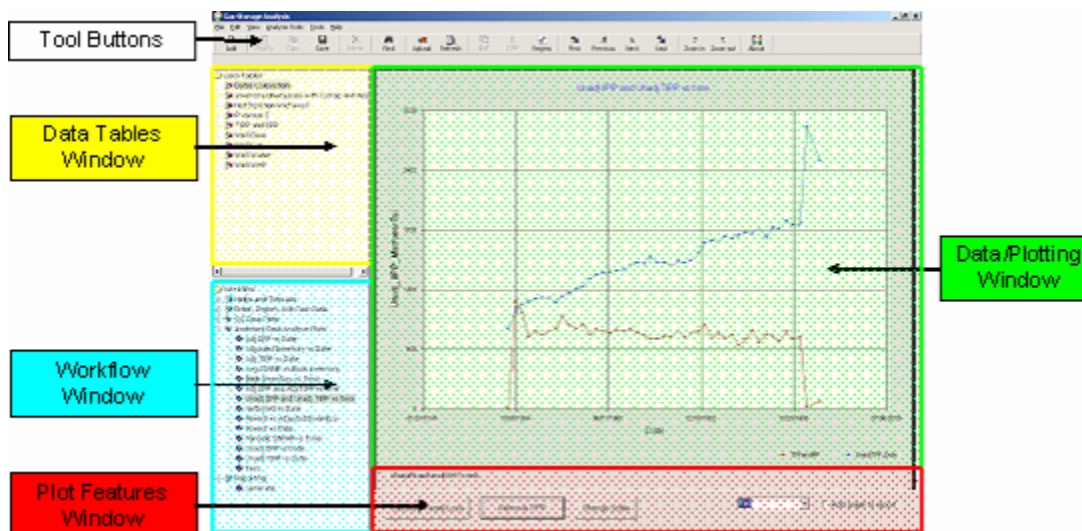


Figure 2: Major windows in the software work area

- At the extreme top of the work area (just below the various menus) are several toolbars associated with different aspects of inventory analysis calculations and workflow (e.g., BHP, BHP/Z, and Inventory Per Pound calculations, etc).
- On the top left portion of the screen is a window (highlighted in yellow) showing the tables containing input and calculated data.
- On the bottom left portion of the screen is a window (highlighted in blue) that shows an outline (in tree structure) of the workflow, including help options and reporting features.
- On the top right portion of the screen is a window (highlighted in green) that show table or plot information highlighted in the Data Table window or the Workflow window.
- On the bottom right portion of the screen is a window (highlighted in red) that contains various buttons that allow modification of various plot features.

The following sections provide a general description of software capabilities. For more comprehensive details and discussion of using this software can be found in the User's Manual (**Appendix I**).

3.3 Inventory Analysis Workflow

The general workflow followed for inventory analysis using this new software is summarized in **Figure 3**. This workflow is reflected in the structured order shown in the workflow window of the software, which was intentionally designed as such to promote use of proper inventory analysis workflow. For a more complete discussion of the inventory analysis process, see the Inventory Analysis Primer in **Appendix II**.

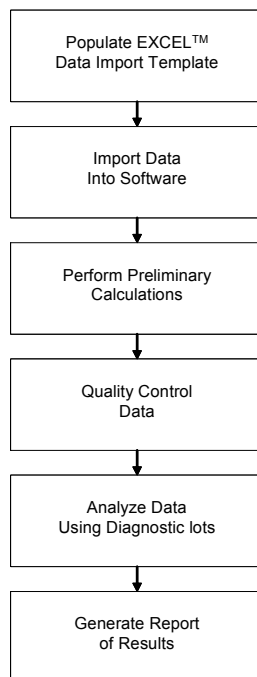


Figure 3: General workflow followed for inventory analysis using new software

The first step involves inputting raw inventory data into an EXCEL™ template. This data is then imported into the new software and stored in an ACCESS™ database for later manipulation. Next, basic calculations necessary to generate plots of historical operating parameters and specialized diagnostic plots are made. Several graphical control checks are then made of the data to identify any obvious errors in the raw and calculated data. Once the data QC process is completed, the user reviews and analyzes plots of historical operating data and interprets the specialized diagnostic plots that are pertinent to his specific field. Finally, the user constructs a draft report by selecting the specific plots to be included in the final report. Additional details of these processes are discussed below.

3.3.1 Populating Excel Input Template

Several potential options were available for data importation into the software. On the simplest end of the spectrum would be direct input of data into the software. Although this option would have been the easiest programming option, it was considered neither efficient nor user-friendly. On the complex end of the spectrum would be the interactive importation of data from *any* source (Access™, EXCEL™, ASCII, etc.) into the software. Although this would be the most user-friendly option, the level of programming effort to properly accomplish this was considered beyond the scope of this project.

Therefore, development of an EXCEL™ template which would act as an intermediate storage area for input data was considered a reasonable compromise, and was constructed. Selection of EXCEL™ for the template was strongly influenced by the fact that it is perhaps the most ubiquitous software used by storage engineers.

There are eight input sheets in the EXCEL™ template. Each input sheet includes a text box containing help information that 1) explains the type of data stored in the sheet, 2) describes the type, format, and units of the input items in the sheet (and whether they are required to be input by the user or if they are calculated by the program), and 3) and provides an example input data set. An example of an input sheet and the associated help information is shown in **Figure 4**.

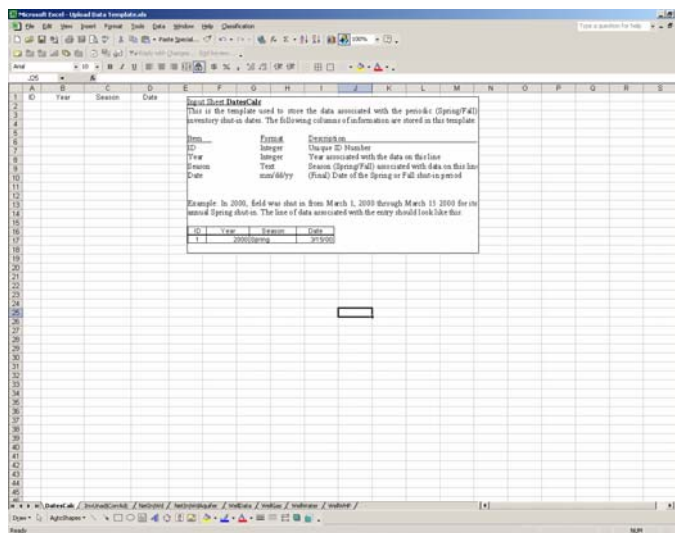


Figure 4: Example input sheet in EXCEL™ template and associated help information.

The first input sheet in the EXCEL™ input template contains information related to the periodic (Spring/Fall) inventory shut-in dates. Four columns of information are stored in this sheet of the input template:

<u>Item</u>	<u>Format</u>	<u>Description</u>
StorageField	Text	Name of the Storage Field
Year	Integer	Year associated with the data on this line
Season	Text	Season (Spring/Fall) associated with data on this line
Date	mm/dd/yy	(Final) Date of the Spring or Fall shut-in period

Example data provided was as follows: In 2000, The Heap Big storage field was shut in from March 1, 2000 through March 15, 2000 for its annual Spring shut-in. In this case, the line of data associated with the entry should look like this:

StorageField	Year	Season	Date
Heap Big	2000	Spring	3/15/00

The second input sheet in the EXCEL™ input template contains information related to book inventory and ADJUSTMENTS to the book inventory data. An ADJUSTMENT to book inventory is any modification to book inventory, including adjustments made for unknown losses, as well as known and quantified losses (e.g., well test in which gas was flared to atmosphere).

For example, if inventory analyses identify a total gas loss of 1 BCF between 2000 and 2003, but no specific cause of the loss can be identified, then an adjustment to the inventory necessary to correct the books is input here. Similarly, if a well is tested and flow rates and flow times are accurately measured during the test, then the volumes flared during the test would be considered an adjustment, since we know the date on which the test occurred and we measured the produced volumes.

The following columns of information are stored in this sheet of the input template:

<u>Item</u>	<u>Format</u>	<u>Description</u>
ID	Integer	Unique ID Number
Date	mm/dd/yy	Date
Unadjusted_Inventory_Bscf	Number	Unadjusted Book Inventory Volume, BCF
Corr_Vol	Number	Correction Vol – IGNORE THIS COLUMN
Cum_Corr	Number	Cumulative Correction Volume, BCF
Adj_Vol	Number	Adjustment Volume, BCF
Cum_Adj	Number	Cumulative Adjustment Volume, BCF
Inventory_Corrected_Adjusted (Calc'd)	Number	Unadjusted Book Inventory Vol BCF

Note that “Corr_Vol” and “Cum_Corr” values are NOT used in the software at this time, and should be entered as zeros. These were included because we anticipate using these columns in future software upgrades.

Example data provided was as follows: Inventory analysis identified a total gas loss of 1 BCF between 1/1/2000 and 12/31/2003, which was booked on 12/31/2003. The Unadjusted Book Inventory on this date was 0.5 BCF. In this case, the entry should look like this (NOTE: the value in column Inventory_Corrected_Adjusted is calculated by the spreadsheet – it is not necessary to input this calculated number):

ID	Date	Unadjusted_Inventory_Bscf	Corr_Vol	Cum_Corr	Adj_Vol	Cum_Adj	Inventory_Corrected_Adjusted
1	12/31/03	0.500	-	-	1.000	1.000	1.500

The third input sheet in the EXCEL™ input template contains information related to daily net injection/withdrawal volumes for the field. The following columns of information are stored in this sheet of the input template:

<u>Item</u>	<u>Format</u>	<u>Description</u>
ID	Integer	Unique ID Number
Date	mm/dd/yy	Date of recorded net INJ/WD for field
Net_InjWd_Mscf	number	Mscf of INJ(+) or WD(-) occurring on date

Example data might look as follows:

1	11/8/76	-4580
2	11/9/76	-5000
3	11/10/76	-5000
4	11/11/76	-5000
5	11/12/76	-728
6	11/13/76	0
7	11/14/76	0
8	11/15/76	0
9	11/16/76	0

The fourth input sheet in the EXCEL™ input template contains information necessary to generate the plot most frequently used to assess inventory in aquifer storage fields (i.e., the deliverability versus cumulative withdrawal plot, sometimes displayed as the deliverability versus inventory plot). The following columns of information are stored in this sheet of the input template:

<u>Item</u>	<u>Format</u>	<u>Description</u>
ID	Integer	Unique ID Number
Date	mm/dd/yy	Date of recorded net INJ/WD for field
Net_InjWd_Mscf	Number	Mscf of INJ(+) or WD(-) occurring on date
Inventory	Number	Unadjusted Book Inventory Volume, BCF
CumWD	Number	Cum withdrawal since last Spring/Fall shut-in date
Abs_Q	Number	Absolute value of injection or withdrawal rate

Typical input data might look like the following:

ID	Date	Net InjWd Mscf	Inventory	CumWD	Abs Q
8	08-Nov-76	-4580	1525420	4580	4580
9	09-Nov-76	-5000	1520420	9580	5000
10	10-Nov-76	-5000	1515420	14580	5000
11	11-Nov-76	-5000	1510420	19580	5000
12	12-Nov-76	-728	1509692	20308	728
13	13-Nov-76	0	1509692	20308	0
14	14-Nov-76	0	1509692	20308	0
15	15-Nov-76	0	1509692	20308	0
16	16-Nov-76	0	1509692	20308	0

The fifth input sheet in the EXCEL™ input template contains individual well data. The following columns of information are stored in this sheet of the input template:

<u>Item</u>	<u>Format</u>	<u>Description</u>
Well ID	Text	Name of the Storage Well
Well Type	Text	Well Type (IW, OB, ...)
Well Wt Fact	Number	Well Weighting Factor for BHP calculation
Resv Depth	Number	True Vertical Depth to Reservoir in Well
X	Number	X-Coordinate of Well Location
Y	Number	Y-Coordinate of Well Location

Data for a field having two IW wells and one OBS well might look like this:

Well ID	Well Type	Well Wt Fact	Resv Depth	X	Y
3625	IW	1	2982	1	7
3667	IW	1	3092	1	8
3684	OB	1	3088.5	1	9

The sixth input sheet in the EXCEL™ input template contains information related to individual well net gas Injection/Withdrawal volumes (e.g., flow rates measured at individual wellheads, if available). Four columns of information are stored in this sheet of the input template:

<u>Item</u>	<u>Format</u>	<u>Description</u>
ID	Integer	Unique Identifier
Date	Date	Date of recorded net injection for well
Well ID	Text	Name of the Storage Well
Net_Vol_Gas	Number	Net INJ(+) or WD(-) gas vol for well (Mscf)

Data for Field XYZ having has two IW wells might look like this:

ID	Date	Well_ID	Net_Vol_Gas
1	3/15/01	1	-2000
2	3/15/01	2	-1800
3	3/16/01	1	-1990
4	3/16/01	2	1780
5	3/17/01	1	1500
6	3/17/01	2	1200

The seventh input sheet in the EXCEL™ input template contains information related to individual well produced water volumes (if available). Four columns of information are stored in this sheet of the input template:

Item	Format	Description
ID	Integer	Unique Identifier
Date	Date	Date of recorded net injection for well
Well ID	Text	Name of the Storage Well
Net_Vol_Wtr	Number	Net INJ(+) or WD(-) water vol (Bbls)

Data for a field XYZ having has two IW wells might look like this:

ID	Date	Well_ID	Net_Vol_Wtr
1	3/15/01	1	1
2	3/15/01	2	2
3	3/16/01	1	1
4	3/16/01	2	2
5	3/17/01	1	0.5
6	3/17/01	2	0.3

The last input sheet in the EXCEL™ input template contains information related to individual wellhead pressure data. The following columns of information are stored in this sheet of the input template:

The following columns of information are stored in this template:

Item	Format	Description
ID	Integer	Unique Identifier
Well ID	Text	Name of the Storage Well
Date	mm/dd/yy	Date of recorded wellhead pressure
WHP_psig	Number	Measured wellhead pressure in psig
Comment	Text	Comment
Given_BHP*	Number	Given BHP (if given)
Calc_BHP	Number	Calc'd BHP (if BHP not given, enter zeros)

Example: Field has four IW wells. In this case, the entry might look like this (for one shut-in date):

ID	Well_ID	Date	WHP_psig	Comments	Given_BHP	Calc_BHP
1	1	9/15/50	55		0	0
2	2	9/15/50	67		0	0
3	3	9/15/50	49		0	0
4	4	9/15/50	50		0	0

* Note: Given_BHP values are NOT used in the software at this time, and should be entered as zeros. These were included because we anticipate using this column in future software upgrades.

3.3.2 Importing Data to Software

Use of the EXCELTM input template ensures uniformity of data type and format, which allows direct uploading of this data into the software. This process is completely automated, and required no user-intervention. Although this process may take several seconds, depending on the dataset size, it only needs to be performed once.

3.3.3 Performing Preliminary Calculations

Several preliminary calculations are necessary before starting the inventory analysis process, including calculation of BHP's, Z-factors, and Inventory-Per-Pound (IPP) values. Numerous methodologies are available for these calculations. For the initial release of the software, we decided to include only the most popular calculations/correlations.

For conversion of WHP to BHP, the user can choose between the exponential equation and Cullender and Smith. For the Z-factor calculation, the user can choose between Abou-Kassem and Hall-Yarborough correlations. There are certainly more rigorous (and arguably more technically correct) methods for making BHP and Z-factor calculations. However, in the authors' experience, these seem to be the most popular methods employed by storage operators today. Understandably, they likely continue to use older calculation methodologies to maintain continuity with historical inventory calculations.

The IPP calculations (both Total IPP and Incremental IPP) were calculated based on the definition of these variables.

The total inventory per pound is defined as follows:

$$TIPP = \frac{G_b}{p/z}$$

where:

TIPP = Total inventory per pound (total inventory per pressure unit)
 G_b = Book inventory

p/z = Average pressure divided by real gas deviation factor

The incremental inventory per pound is defined as:

$$IIPP = \frac{(G_{bf} - G_{bs})}{\left(\left(\frac{p}{z}\right)_f - \left(\frac{p}{z}\right)_s\right)}$$

where

IIPP = Incremental inventory per pound (pressure unit)
 G_b = Book inventory
 P/z = Average pressure divided by real gas deviation factor
 s = Spring, following withdrawal season
 f = Fall, following injection season

3.3.4 Quality Controlling Input/Calculated Data

Several plots can be generated and reviewed to ensure calculations made within the software were performed properly. These QC plots include:

- SIWHP vs SIBHP for All Wells
- Average Field SIWHP vs Avg Field SIBHP
- Average Field BHP vs Field Z-Factor
- Average Field BHP vs Field BHP/Z-Factor

None of the correlations currently employed in the software should exhibit discontinuities. Therefore, all of these plots should exhibit smooth trends with no outlying data points. The presence of any outlying data points on the QC plots may indicate that calculations have not been performed properly, and should be brought to the attention of the software developers.

3.3.5 Analyzing Data Using Diagnostic Plots

There are a very large number of plots available in the software to allow for comprehensive analysis of available inventory data. These are discussed below:

3.3.5.1 *Plots to review trends in basic operating data*

Several plots are used to review and assess trends in basic operating data, including:

- Net Injection/Withdrawal Rates vs Time
- Unadjusted Book Inventory vs Time
- Adjustments to Book Inventory vs Time
- Adjusted Book Inventory vs Time
- SIWHP vs Time

Since most approaches to inventory analysis implicitly assume that the storage facility has been operated in a fairly consistent manner over time, it is important to verify

operational consistency using the above plots. Look for consistency in the pressures and inventory levels from year to year.

During this process, several very basic trends may be identified in the raw operational data that tip off the analyst concerning possible inventory problems. For example, if the historical plots of Spring/Fall inventory and pressure indicate that the same maximum pressure is reached at the end of each injection cycle, but the corresponding inventory levels are increasing over time, you can be sure the IPP plots will indicate ongoing losses (or perhaps increases in the non-effective gas volumes).

3.3.5.2 Diagnostic plots to identify/quantify gas losses

There are several diagnostic plots used to identify and quantify gas losses, including:

- Unadjusted Book Inventory vs Time
- Average SIWHP vs Time
- P/Z vs Time
- Avg SIWHP vs Unadjusted Book Inventory
- Avg P/Z vs Unadjusted Book Inventory
- Unadjusted TIPP vs Time
- Unadjusted IIPP vs Time
- Deliverability vs Cumulative Withdrawal
- Deliverability vs Unadjusted Inventory

By using all of the plots above to assess potential inventory problems, the analyst will have a much higher confidence level in his conclusions, since those conclusions will be supported by the character of *all* the plots used in his analysis – not just one or two commonly used analysis plots.

3.3.5.3 Plots to verify that adjustments resolve discrepancies

After completing an inventory analysis and estimating loss rates and volumes, it is beneficial to generate the various diagnostic plots used in the analysis using post-analysis adjusted inventory volumes. If the diagnostic plots generated using the adjusted volumes (i.e., adjusted as per the results of your inventory analysis) indicate no ongoing losses, the analyst can be confident the appropriate adjustments have been determined.

These plots would include the following:

- Avg SIWHP vs Adjusted Book Inventory
- Avg P/Z vs Adjusted Book Inventory
- Adjusted TIPP vs Time
- Adjusted IIPP vs Time
- Deliverability vs Adjusted Inventory

3.3.6 Generating Reports

In order to enhance the software's user-friendliness and practicality, we incorporated an option to automatically generate reports from within the software. This feature allows the user to check a box on each plot they wish to include in the report. After these boxes are

checked on all the plots the user wishes included in a report, the software will export to WORD™ the reservoir input data and all of the plots having the “add graph to report” box checked.

Once exported to WORD™, the user can enhance the report by the addition of text to further document the input, processing, or analysis results. The final result will be a report in WORD™ which summarizes the reservoir input data, all pertinent plots used in the analysis, and the analyst’s comments and/or conclusions.

3.4 On-Line Help and References

Incorporation of extensive on-line help was considered a critical component of the project. Consequently, a considerable amount of time and effort was dedicated to making help options complete, informative, and useful to new or inexperienced engineers.

Help modules were constructed to help the user in the data input process, interpret the various diagnostic plots, perform on-the-fly calculations useful in inventory analysis, explain software features in detail, provide example inventory analysis problems and tutorials, explain commonly used gas storage terms and phases, and provide a comprehensive list of gas storage references and technical papers.

3.4.1.1 Help: Input Screens

Help is available for each sheet in the EXCEL™ input template. This help provides a general description of the type of data requested on the sheet, the specific data items required, a brief description (including the data format) of each input data item, and an example input data set.

3.4.1.2 Help: Analysis Plots

Help is also available for the interpretation and analysis of each plot used in the inventory analysis process. Included is an example plot of typical data, a description of the purpose of the plot, a discussion of the assumptions that are inherent in the use of the particular plot, the applicability of the plot, the dangers of using the specific plot, and any pertinent technical references related to the diagnostic plot.

Also included for the diagnostic plots are typical “type curves” showing what the diagnostic plot might look like for the cases of gas losses, gas gains, gas bubble growth, and/or gas bubble shrinkage.

3.4.1.3 Help: Toolbox

A “toolbox” was developed to perform various calculations that may be useful in the process of inventory verification. EXCEL™ was selected as the development platform for this toolbox due to the ease of performing calculations and generating graphics and because it is ubiquitous in the UGS industry. The tools in this toolbox include the following:

- Estimated line losses as per a U.S. Bureau of Mines publication
- Estimated volume of gas vented during a wellbore blowdown
- Estimated volume of gas vented during a multi-rate well test

- Estimated volume of gas contained in a pipeline at specified inlet and outlet conditions.
- Estimated shut-in pseudopressure vs time for assumed reservoir properties (to estimate time to stabilized shut-in pressure).
- Estimate (first order) of minimum gas flow rate to continuously unload fluids from a wellbore of specified configuration.
- Units Conversion Table
- Chart of estimated residual gas saturation as a function of porosity
- Chart estimating (HP)/(MMscf/D) required to compress typical storage gas at 100 degrees F to 1000 psi using single stage compression.

3.4.1.4 Help: Users Manual With Example Problem Tutorial

A comprehensive Users Manual has been written that describes the various features available in the software and how to use them. This Users Manual is included in **Appendix I**.

3.4.1.5 Help: Inventory Verification Primer

This document provides a very concise summary of the objectives, theory, data requirements, diagnostic plots, and analyses techniques involved in inventory analysis. It also includes a sample dataset and the analysis of the sample dataset. This Primer is included in **Appendix II**.

3.4.1.6 Help: References

A comprehensive list of references and technical papers (organized by topic) pertaining to the various aspects of underground natural gas storage have been prepared. These references are included in **Appendix III**.

3.4.1.7 Help: Storage Inventory and Deliverability Terminology

A list of the most common underground gas storage inventory and deliverability terms have been compiled and defined. These definitions are included in **Appendix IV**.

3.4.1.8 Help: Underground Gas Storage Glossary

A comprehensive glossary of the various terms used in the underground gas storage industry has been compiled, and is included in **Appendix V**.

4 RESULTS AND DISCUSSION

4.1 Software Developed

Work performed under contract DE-FC26-03NT41779 has resulted in the development of a comprehensive inventory analysis software tool that allows easy importation of typical storage inventory data, automatically generates pertinent raw data plots and analysis plots for the analysts review and processing, provides on-line help that provides an overview of the inventory analysis process and explains the assumptions, applications, limitations, and processes used to analyze specific diagnostic plots, and provide a “toolbox” application that would perform calculations useful in the process of inventory analysis.

This new tool significantly improves operators’ ability to effectively monitor inventory and resolve gas loss issues by making inventory analysis processes much more automated and much more comprehensive. It also enhances the analysis process by guiding the engineer to the appropriate analysis techniques and away from the inappropriate analysis techniques via the on-line help tools.

4.2 Cost Benefit Assessment

In an effort to estimate the efficiency gains achievable using this newly developed software, we re-analyzed several sets of inventory data that we had already analyzed for previous clients. By recording the time required to re-analyze the inventory data and generate a draft report using the new software and comparing this to the estimated time it took us to manually analyze the data without the new software, we could quantify efficiency gains.

Based on the results of this testing, it is estimated that the time required to perform a “typical” comprehensive inventory analysis was reduced by at least 50%. In several cases, the time required to go from raw data to a finished report was reduced very significantly, and resulted in completion of a finished report in a matter of 1-2 man-days, whereas previous analysis of the same data without the newly developed software required 1-2 man-weeks.

Although these represent significant gains in efficiency for the practicing storage engineer, the real value of the product is derived from enabling storage engineers to more confidently quantify ongoing storage losses earlier than if traditional methods alone were employed. This would allow earlier deployment of loss mitigation efforts and reduce the amount of losses incurred by storage operators.

Assuming that the average UGS operator has only 1/2 of one percent annual loss rate, the ability to detect and mitigate these losses just 2 years earlier would save operators over \$300 million at 2007 gas prices. Thus, even assuming the comprehensive inventory analysis software developed during this study has only a modest impact on inventory management, the financial impact to the industry is significant.

5 CONCLUSIONS

The development of a comprehensive inventory analysis software tool was completed and tested under contract DE-FC26-03NT41779. Benchmark testing suggests that operators' ability to efficiently analyze inventory data and resolve gas loss issues have been significantly improved.

Typical reductions in manpower requirements on the order of 50% were observed when the new software was used to perform typical comprehensive inventory analyses. The software also enhances the analysis process by helping the storage engineer use only the appropriate analysis techniques and avoid inappropriate techniques via the on-line help tools.

Deployment of this software in the UGS industry is expected to significantly reduce the time required to conduct inventory analysis and promote more accurate interpretation of inventory data, especially amongst young and/or inexperienced Gas Storage engineers.

Although the gains in efficiency for the practicing storage engineer are significant, the real value of the product is derived from enabling storage engineers to more confidently identify ongoing storage loss rates and volumes earlier than if traditional methods alone were employed. Conservative estimates suggest the economic impact could easily exceed \$300 million.

6 REFERENCES

1. Piper, L.D., McCain, W.D. Jr., Corredor, J.H.: "Compressibility Factors for Naturally Occurring Petroleum Gases," paper SPE 26668 presented at the 1993 SPE Annual Technical Conference and Exhibition, Houston, Texas, 3-6 October.
2. McCain, W.D. Jr.: *The Properties of Petroleum Fluids*, 2nd ed., Pennwell, 1990.
3. Al-Hussainy, R., Ramey, H.J., Jr., and Crawford, P.B.: "The Flow of Real Gases Through Porous Media," JPT (May 1966) 624; Trans. AIME 237.
4. Cullendar, N.H. and Smith, R.V.: "Practical Solution of Gas Flow Equations for Wells and Pipelines With Large Temperature Gradients," Trans. AIME 207 (1956) 281-287.
5. Young, K.L.: "Effect of Assumptions Used to Calculate Bottom-Hole Pressures in Gas Wells," JPT (April 1967) 547-550.
6. Dranchuk, P.M., and McFarland, J.D.: "The Effect of the Time Rate of Change of Momentum on Bottom-Hole Pressure in Flowing Gas Wells," J. Cdn. Pet. Tech. (April-June 1974) 34-38.
7. Lee, W.J., Rollins, J.B., and Spivey, J.P.: *Pressure Transient Testing*, p. ???
8. Goode, P.A., and Thambanayagam, R.K.M.: "Pressure Drawdown and Buildup Analysis of Horizontal Wells in Anisotropic Media," SPEFE (December 1987) 683-697.
9. Odeh, A.S, and Babu, D.K.: "Transient Flow Behavior of Horizontal Wells: Pressure Drawdown and Buildup Analysis," SPEFE (March 1990) 7-15.

7 LIST OF ACRONYMS AND ABBREVIATIONS

AVG	=	Average
BHP	=	Bottom Hole Pressure
Deg F	=	Degrees Fahrenheit
Gb	=	Book Inventory
IIPP	=	Incremental Inventory Per Pound
MMSCF/D	=	Thousand Mscf/D
P/Z	=	Pressure divided by Z-factor
Psi	=	Pressure per square inch
SIBHP	=	Shut-In Bottom Hole Pressure
SIWHP	=	Shut-In Wellhead Pressure
SW	=	Software
TIPP	=	Total Inventory Per Pound
UGS	=	Underground Gas Storage
VBA	=	Visual Basic Application
WHP	=	Wellhead Pressure
Z	=	Z-Factor

8 NOMENCLATURE

Symbols

- IPP = Inventory per “pound” (i.e., per p/z)
TIPP = Total Inventory per “pound” (i.e., per p/z)
IIPP = Incremental Inventory per “pound” (i.e., per p/z)
G = Inventory (Gas In Place)
p/z = pressure/z-factor
q = flow rate, Mscf/D

Subscripts

- b = book
f = Fall
s = Spring

Appendix I

Comprehensive Inventory Analysis Software - Users Manual

Table of Contents

1	Overview.....	4
1.1	Background.....	4
1.2	Software Windows Layout	4
1.3	Help Available	5
1.3.1	Inventory Analysis Primer	6
1.3.2	Summery of References and Papers	6
1.3.3	Inventory Analysis Toolbox	6
1.3.4	Input Template Help Information	6
1.3.5	Technical Help for Diagnostic Plot Analysis.....	7
1.3.6	Gas Storage Terminology and Gas Storage Glossary.....	7
2	Workflow	8
2.1	Data Importing.....	8
2.1.1	DatesCalc InputTemplate.....	9
2.1.2	InvUnadjCorrAdj Input Template.....	10
2.1.3	NetInjWd Input Template	11
2.1.4	WellData Input Template.....	12
2.1.5	WellGas Input Template	13
2.1.6	WellWater Input.....	14
2.1.7	WellWHP Input Template	15
2.1.8	Importing Data Into Software	16
2.2	Data QC Process	16
2.2.1	Avg SIWHP vs Avg SIBHP QC Plot	17
2.2.2	Avg BHP vs Avg Z-Factor Plot.....	17
2.2.3	Plot of SIWHP vs SIBHP For All Wells	18
2.3	Data Analysis Process.....	18
2.3.1	Analysis of Unadjusted Inventory and Avg SIBHP/z vs Time Plots.....	18
2.3.2	Analysis of P/z vs Unadjusted Book Inventory Plots	21

2.3.3 Analysis of Inventory Per Pound (IPP) Plots.....	21
2.4 Reporting.....	23
2.4.1 Including Interpreted Plots in a Report.....	23
2.4.2 Compiling Contents of a Report	24
2.4.3 Exporting and Editing a Report	24
3 Software Windows Layout and Summary of Features	25
3.1 Overall Window Layout	25
3.2 Tool Button Window	25
3.3 Data Tables Window.....	26
3.4 Workflow Window	26
3.5 Data/Plotting Window	27
3.6 Plot Feature Window	28
4 Example Problem.....	29
4.1 Loading Data Into EXCEL™ Template	32
4.2 Uploading Data into Software	37
4.3 Browsing Data Tables and Performing BHP, p/z, and IPP Calculations.....	41
4.4 Perusing HELP features and Using the ToolBox	44
4.5 Performing Inventory Analysis and Generating Reports.....	51
4.6 Generating Reports	57

1 Overview

1.1 Background

This manual explains how to use the software developed under contract DE-FC26-03NT41779. The primary objective of the project was to develop a comprehensive inventory analysis software tool that would:

- Allow easy importation of typical storage inventory data,
- Automatically generate pertinent raw data plots and analysis plots for the analysts review and processing,
- Provide on-line help that provides an overview of the inventory analysis process and explains the assumptions, applications, limitations, and processes used to analyze specific diagnostic plots, and
- Provide a “toolbox” application that would perform calculations useful in the process of inventory analysis.

The software development and design is briefly reviewed, including a summary of the major components of the software and online help features. An example dataset and analysis is presented.

This software was developed in the VisualBasic™ programming environment, uses Microsoft ACCESS™ for data storage, employs Microsoft EXCEL™ as a “bridge” between users’ data and the ACCESS™ database, and exports reports to WORD™. EXCEL™ was chosen for use as a template to hold data due to the ubiquitous use of EXCEL™ in the UGS industry. ACCESS™ was chosen due to its excellent data handling and data manipulation capabilities. Use of this software requires the installation of EXCEL™ and WORD™ on the user’s computer, but not ACCESS™.

1.2 Software Windows Layout

There are five major areas or windows in the software work area (**Figure 1**): 1) At the extreme top of the work area (just below the various menus) are several toolbars associated with different aspects of inventory analysis calculations and workflow (e.g., BHP and BHP/Z calculations, Inventory Per Pound calculations, etc). 2) On the top left portion of the screen is a window that show the tables containing the input and calculated data, 3) On the bottom left portion of the screen is a window that shows an outline (in tree structure) of the workflow, including help options and reporting features, 4) On the top right portion of the screen is a window that show table or plot information highlighted in the Data Table window or the Workflow window, and 5) On the bottom right portion of the screen is a window that contains various buttons that allow modification of various plot features.

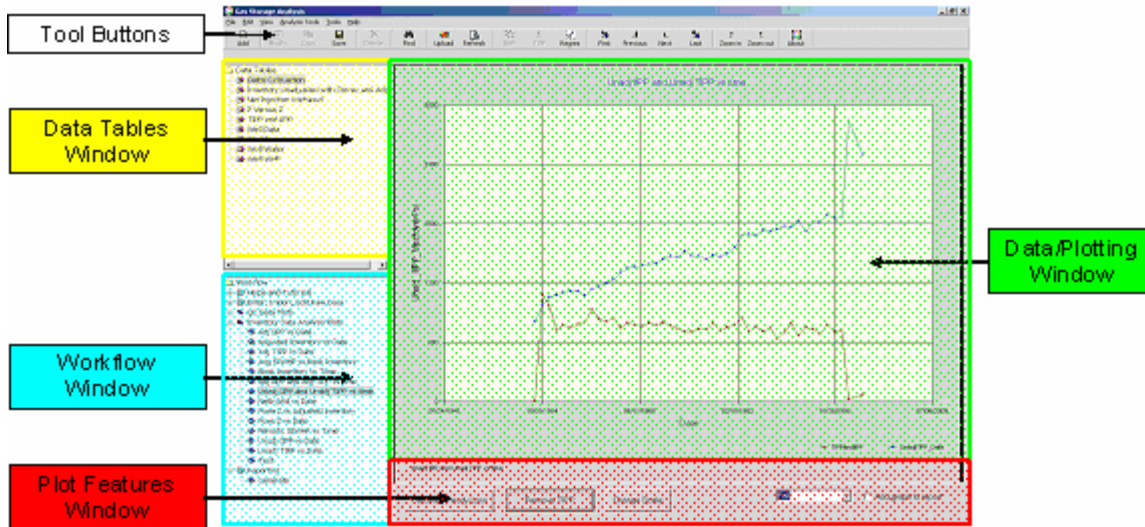


Figure 1: Major windows in the software work area

1.3 Help Available

HELP tools are available to guide the users as they use this software. All of the HELP features are accessible from the HELP menu located at the top of the software screen. Select HELP items (those HELP items the user is likely to use during the inventory analysis process) are also located in the Workflow Window of the work area, under “Helps and Tutorials.”

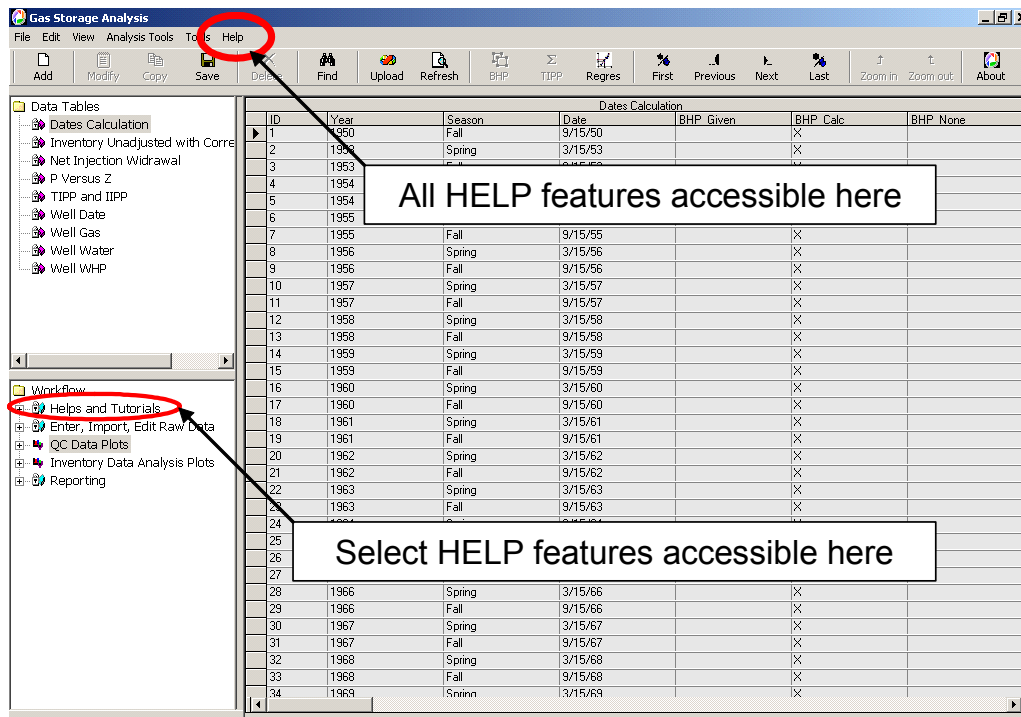


Figure 2: Location of Help Items

1.3.1 *Inventory Analysis Primer*

This is a document that summarizes the objectives, theory, data required, diagnostic plots, and analyses techniques involved in inventory analysis. It also includes a sample dataset and the analysis of the sample dataset.

1.3.2 *Summery of References and Papers*

This document summarizes references and technical papers related to Underground Gas Storage (these are not limited to inventory analysis, but cover a wide range of UGS topics) including:

- Introduction to Gas Storage
- Gas Storage Field Design
- Optimization
- Migration and Monitoring
- Inventory Verification
- Deliverability Maintenance and Enhancement
- Simulation of UGS Reservoirs
- Top Twenty Technical Papers

1.3.3 *Inventory Analysis Toolbox*

This is an EXCEL™ spreadsheet that summarized and/or calculates various data useful in the process of inventory analysis, including:

- Estimated line loss rates/volumes as per a Bureau of Mines Publication
- Estimated volume of gas vented during a wellbore blowdown
- Estimated volume of gas vented during a multi-rate well test
- Estimated volume of gas contained in a pipeline at specified inlet and outlet conditions.
- Estimated shut-in pseudopressure vs time for assumed reservoir properties (to estimate time to stabilized shut-in pressure).
- Estimate (first order) of minimum gas flow rate to continuously unload fluids from a wellbore of specified configuration.
- Units Conversion Table
- Chart of estimated residual gas saturation as a function of porosity
- Chart estimating (HP)/(MMscf/D) required to compress typical storage gas at 100 degrees F to 1000 psi using single stage compression.

1.3.4 *Input Template Help Information*

There is help information, including a description of the data needed and an example data input set, for each input sheet in the EXCEL™ input template.

1.3.5 *Technical Help for Diagnostic Plot Analysis*

This document summarizes how various diagnostic plots are used and analyzed. In most cases, the following information is presented for each diagnostic plot:

- Example plot
- Purpose of the plot
- Assumptions inherent in construction/use of the plot
- Applicability of the plot
- Dangers associated with misuse of plot
- References

1.3.6 *Gas Storage Inventory and Deliverability Terminology*

This document lists and describes/defines various inventory and deliverability terms.

1.3.7 *Underground Gas Storage Glossary*

This document lists and describes/defines various terms used in UGS industry, and is much broader in scope than the “Gas Storage Inventory and Deliverability Terminology: document above

2 Workflow

Figure 3 summarizes the basic workflow followed for inventory analysis using the new software.

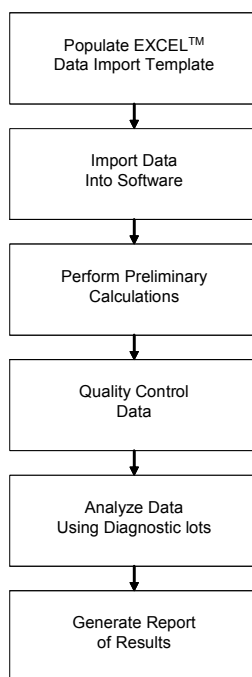


Figure 3: General workflow followed for inventory analysis using new software

The first step involves inputting the raw inventory data into an EXCEL™ template. This data is then imported into the new software and stored in an ACCESS™ database for later manipulation. Next, basic calculations necessary to generate plots of historical operating parameters and specialized diagnostic plots are made. Several graphical control checks are then made of the data to identify any obvious errors in the raw and calculated data. Once the data QC process is completed, the user reviews and analyzes plots of historical operating data and interprets the specialized diagnostic plots that are pertinent to his specific field. Finally, the user constructs a report by selecting the specific plots to be included in a final report. Additional details of this process will be discussed in more detail later in this report.

2.1 Data Importing

An EXCEL™ spreadsheet was created to facilitate transfer of data necessary for inventory analysis from the user to the software. This spreadsheet acts as a “template” to ensure the data types, order, and content are consistent with what the software expects upon import of the data. This template consists of an EXCEL™ spreadsheet containing several worksheets, each containing similar data types.

Each sheet in the EXCEL™ data template, and the input data contained in each of these sheets, is summarized below. Sample datasets for each sheet in the data template are also provided in the sheets and/or in the help screens shown on the right side of each sheet.

2.1.1 DatesCalc InputTemplate

This is the template used to store the data associated with the periodic (Spring/Fall) inventory shut-in dates and is shown with example data in **Figure 4**.

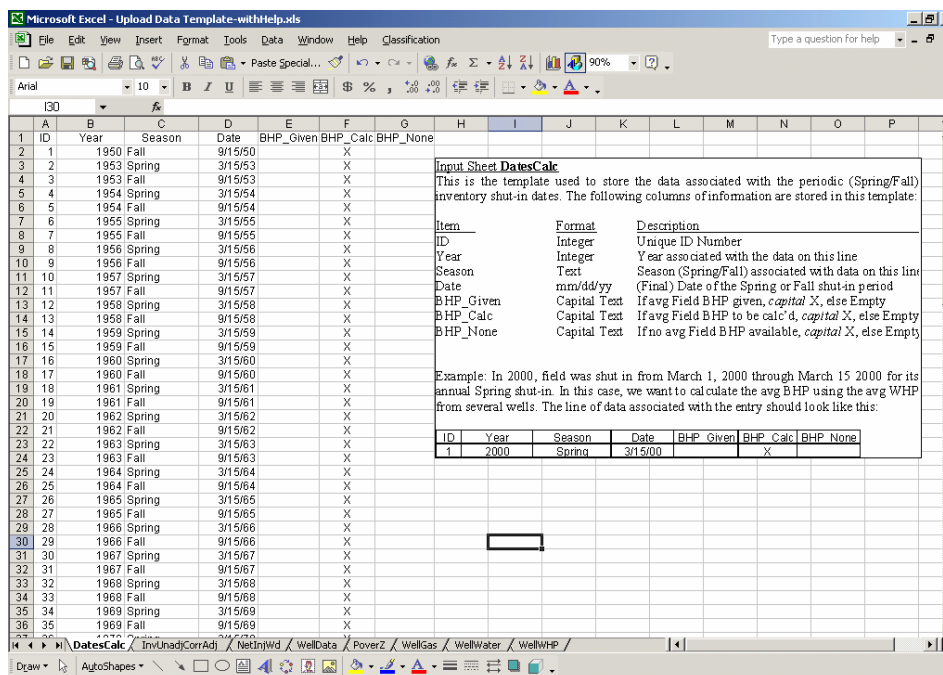


Figure 4: Template used to store the data associated with the periodic (Spring/Fall) inventory shut-in dates

The following columns of information are stored in this template:

<u>Item</u>	<u>Format</u>	<u>Description</u>
ID	Integer	Unique ID Number
Year	Integer	Year associated with the data on this line
Season	Text	Season (Spring/Fall) associated with data on this line
Date	mm/dd/yy	(Final) Date of the Spring or Fall shut-in period
BHP_Given	Capital Text	If avg Field BHP given, <i>capital X</i> , else Empty
BHP_Calc	Capital Text	If avg Field BHP to be calc'd, <i>capital X</i> , else Empty
BHP_None	Capital Text	If no avg Field BHP available, <i>capital X</i> , else Empty

Example: In 2000, field was shut in from March 1, 2000 through March 15 2000 for its annual Spring shut-in. In this case, we want to calculate the avg BHP using the avg WHP from several wells. The line of data associated with the entry should look like this:

ID	Year	Season	Date	BHP_Given	BHP_Calc	BHP_None
1	2000	Spring	3/15/00		X	

2.1.2 InvUnadjCorrAdj Input Template

This is the template used to store book inventory and ADJUSTMENTS to the book inventory data and is shown with example data in **Figure 5**.

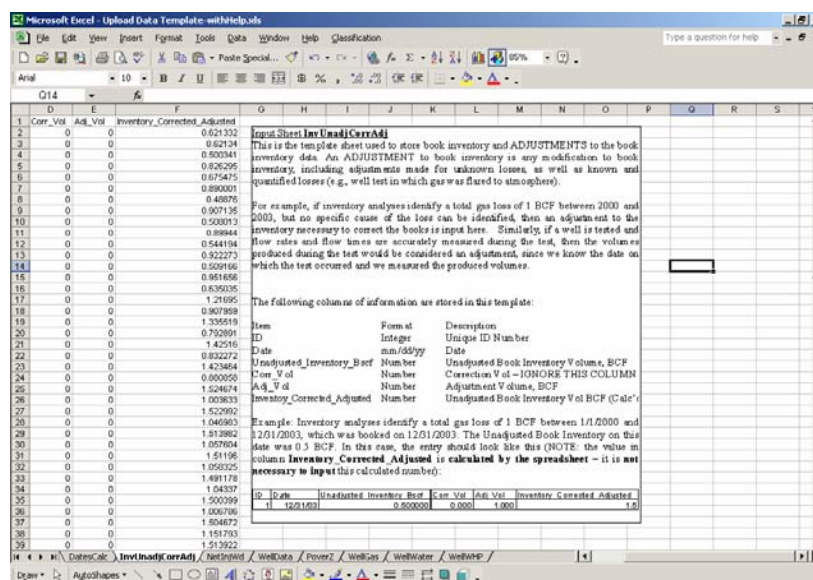


Figure 5: Template used to store book inventory and adjustments to the book inventory data

An ADJUSTMENT to book inventory is any modification to book inventory, including adjustments made for unknown losses, as well as known and quantified losses (e.g., well test in which gas was flared to atmosphere). For example, if inventory analyses identify a total gas loss of 1 BCF between 2000 and 2003, but no specific cause of the loss can be identified, then an adjustment to the inventory necessary to correct the books is input here. Similarly, if a well is tested and flow rates and flow times are accurately measured during the test, then the volumes produced during the test would be considered an adjustment, since we know the date on which the test occurred and we measured the produced volumes. The following columns of information are stored in this template:

<u>Item</u>	<u>Format</u>	<u>Description</u>
ID	Integer	Unique ID Number
Date	mm/dd/yy	Date
Unadjusted_Inventory_Bscf	Number	Unadjusted Book Inventory Volume, BCF
Corr_Vol	Number	Correction Vol – IGNORE THIS COLUMN
Adj_Vol	Number	Adjustment Volume, BCF
Inventory_Corrected_Adjusted	Number	Unadjusted Book Inventory Vol BCF (Calc'd)

Example: Inventory analyses identify a total gas loss of 1 BCF between 1/1/2000 and 12/31/2003, which was booked on 12/31/2003. The Unadjusted Book Inventory on this date was 0.5 BCF. In this case, the entry should look like this (NOTE: the value in column **Inventory_Corrected_Adjusted** is **calculated by the spreadsheet** – it is **not necessary to input** this calculated number):

ID	Date	Unadjusted_Inventory_Bscf	Corr_Vol	Adj_Vol	Inventory_Corrected_Adjusted
1	12/31/03	0.500000	0.000	1.000	1.5

2.1.3 NetInjWd Input Template

This is the input template used to store daily net injection/withdrawal volumes for the field, and is shown with example data in **Figure 6**.

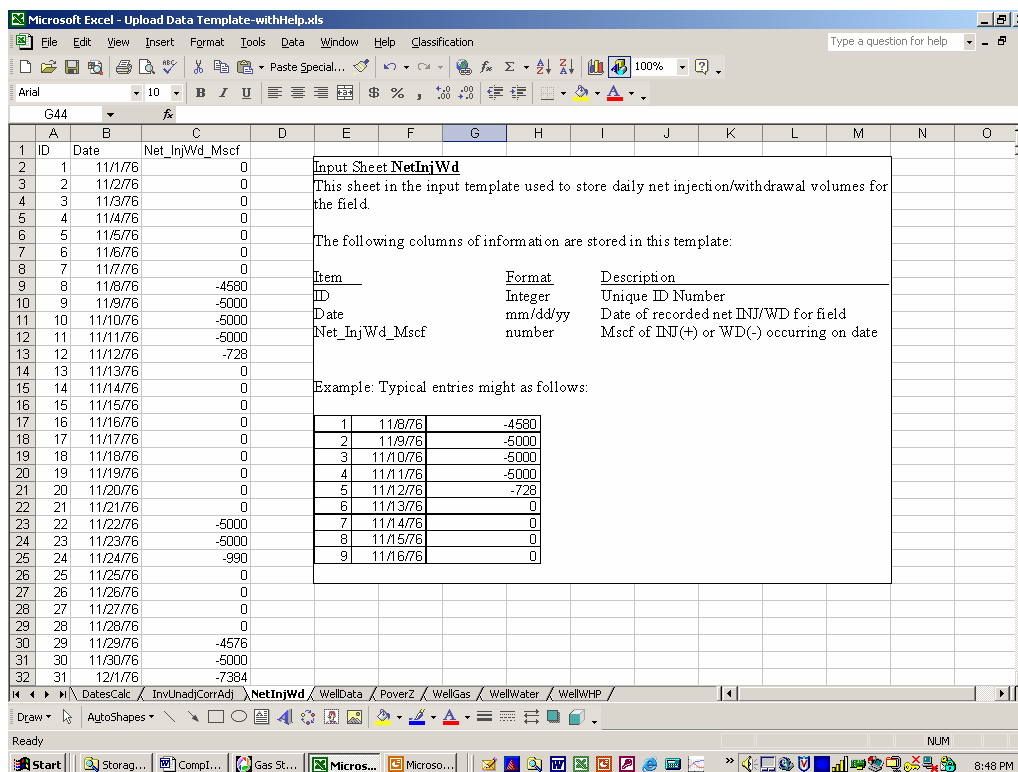


Figure 6: Template used to store daily net injection/withdrawal volumes for the field

The following columns of information are stored in this template:

<u>Item</u>	<u>Format</u>	<u>Description</u>
ID	Integer	Unique ID Number
Date	mm/dd/yy	Date of recorded net INJ/WD for field
Net_InjWd_Mscf	number	Mscf of INJ(+) or WD(-) occurring on date

Example: Typical entries might as follows:

1	11/8/76	-4580
2	11/9/76	-5000
3	11/10/76	-5000
4	11/11/76	-5000
5	11/12/76	-728
6	11/13/76	0
7	11/14/76	0
8	11/15/76	0
9	11/16/76	0

2.1.4 WellData Input Template

This template is used to store individual well data, and is shown with example data in **Figure 7**.

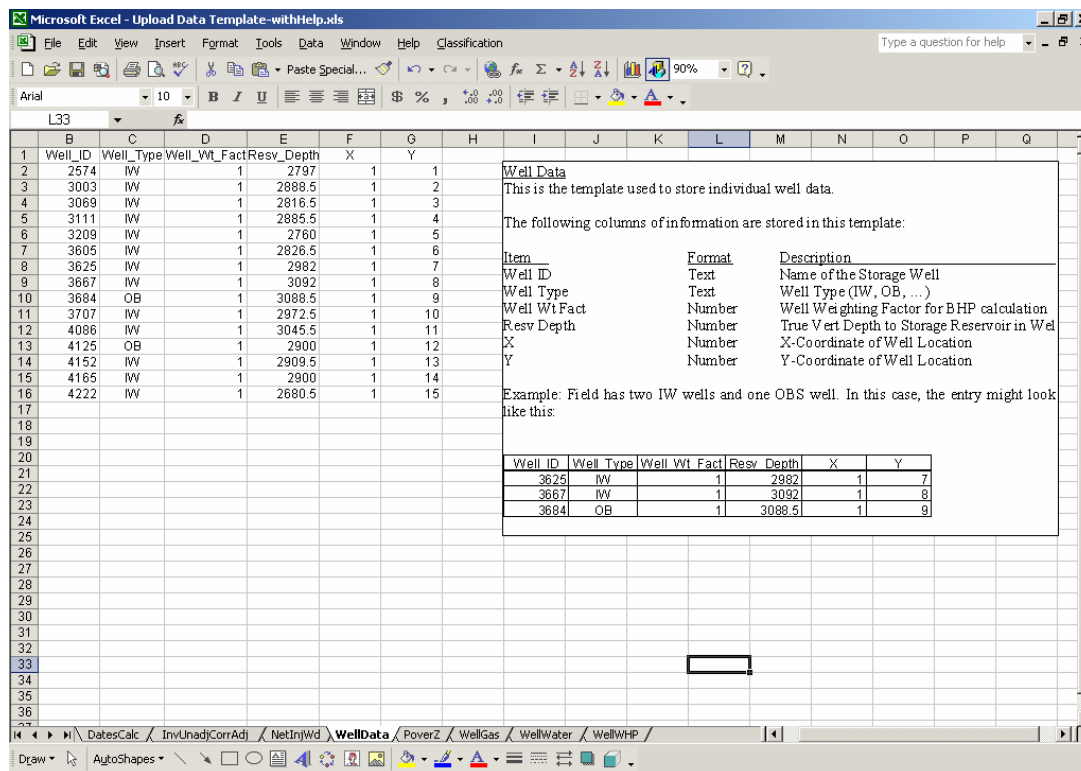


Figure 7: Template used to store individual well data

The following columns of information are stored in this template:

<u>Item</u>	<u>Format</u>	<u>Description</u>
Well ID	Text	Name of the Storage Well
Well Type	Text	Well Type (IW, OB, ...)
Well Wt Fact	Number	Well Weighting Factor for BHP calculation
Resv Depth	Number	True Vert Depth to Storage Reservoir in Well
X	Number	X-Coordinate of Well Location
Y	Number	Y-Coordinate of Well Location

Example: Field has two IW wells and one OBS well. In this case, the entry might look like this:

Well_ID	Well_Type	Well_Wt_Fact	Resv_Depth	X	Y
3625	IW	1	2982	1	7
3667	IW	1	3092	1	8
3684	OB	1	3088.5	1	9

2.1.5 WellGas Input Template

This is the template used to store individual well net gas Injection/Withdrawal volumes (if available), and is shown in Figure 8.

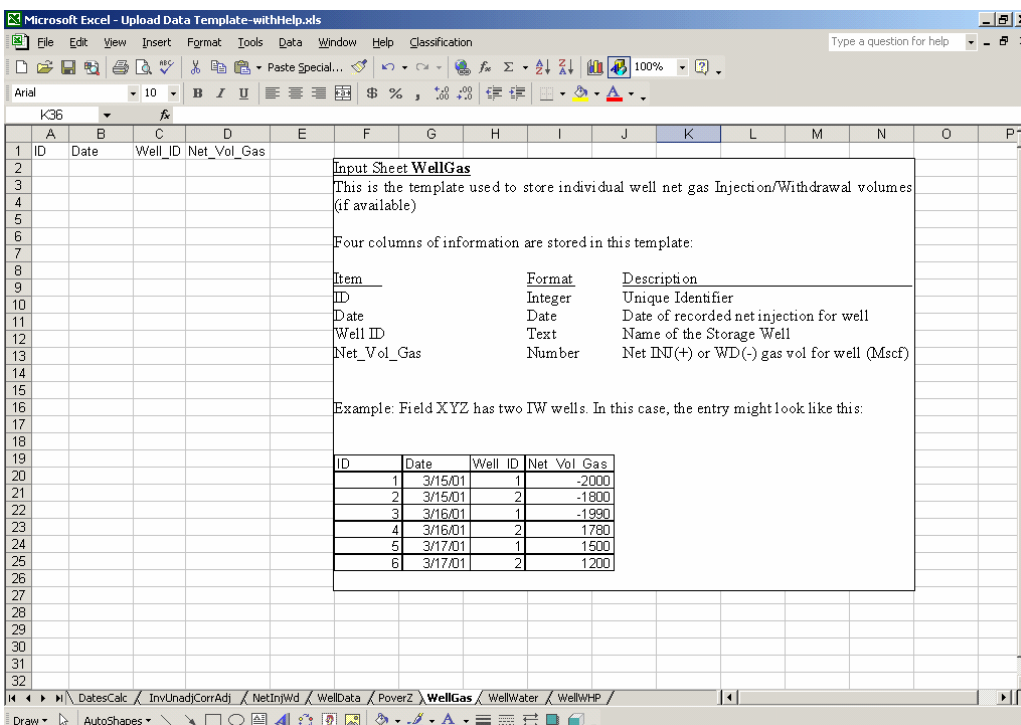


Figure 8: Template used to store individual well net gas Injection/Withdrawal volumes (if available)

Four columns of information are stored in this template:

<u>Item</u>	<u>Format</u>	<u>Description</u>
ID	Integer	Unique Identifier
Date	Date	Date of recorded net injection for well
Well ID	Text	Name of the Storage Well
Net_Vol_Gas	Number	Net INJ(+) or WD(-) gas vol for well (Mscf)

Example: Field XYZ has two IW wells. In this case, the entry might look like this:

ID	Date	Well ID	Net Vol Gas
1	3/15/01	1	-2000
2	3/15/01	2	-1800
3	3/16/01	1	-1990
4	3/16/01	2	1780
5	3/17/01	1	1500
6	3/17/01	2	1200

2.1.6 WellWater Input

This is the template used to store individual well produced water volumes (if available), and is shown in

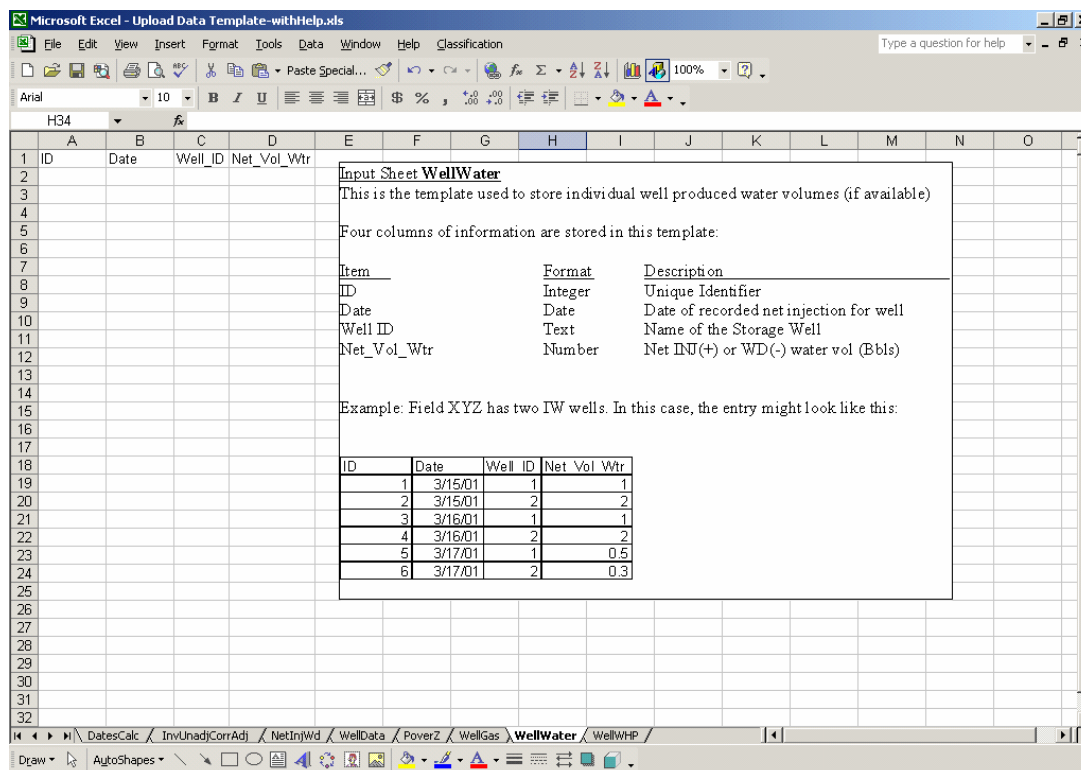


Figure 9: Template used to store individual well produced water volumes (if available)

Four columns of information are stored in this template:

<u>Item</u>	<u>Format</u>	<u>Description</u>
ID	Integer	Unique Identifier
Date	Date	Date of recorded net injection for well
Well ID	Text	Name of the Storage Well
Net_Vol_Wtr	Number	Net INJ(+) or WD(-) water vol (Bbls)

Example: Field XYZ has two IW wells. In this case, the entry might look like this:

ID	Date	Well_ID	Net_Vol_Wtr
1	3/15/01	1	1
2	3/15/01	2	2
3	3/16/01	1	1
4	3/16/01	2	2
5	3/17/01	1	0.5
6	3/17/01	2	0.3

2.1.7 WellWHP Input Template

This is the template used to store individual wellhead pressure data, and is shown with example data in **Figure 10**.

Input Sheet: WellWHP
This is the template used to store individual wellhead pressure data.
The following columns of information are stored in this template:

Item	Format	Description
ID	Integer	Unique Identifier
Well ID	Text	Name of the Storage Well
Date	mm/dd/yy	Date of recorded wellhead pressure
WHP_psig	Number	Measured wellhead pressure in psig
Comment	Text	Comment
Calc_BHP	Number	Calc'd BHP (if given)

Example: Field has four IW wells. In this case, the entry might look like this (for one shut-in date):

ID	Well ID	Date	WHP_psig	Comments	Calc_BHP
1	3003	9/15/50	44		0
2	3209	9/15/50	35		0
3	3605	9/15/50	36		0
4	3667	9/15/50	164		0

Figure 10: Template used to store individual wellhead pressure data

The following columns of information are stored in this template:

<u>Item</u>	<u>Format</u>	<u>Description</u>
ID	Integer	Unique Identifier
Well ID	Text	Name of the Storage Well
Date	mm/dd/yy	Date of recorded wellhead pressure
WHP_psig	Number	Measured wellhead pressure in psig
Comment	Text	Comment
Calc_BHP	Number	Calc'd BHP (if given)

Example: Field has four IW wells. In this case, the entry might look like this for one shut-in date:

ID	Well ID	Date	WHP_psig	Comments	Calc_BHP
1	3003	9/15/50	44		0
2	3209	9/15/50	35		0
3	3605	9/15/50	36		0
4	3667	9/15/50	164		0

2.1.8 Importing Data Into Software

Once all necessary data is input into the data input template, we can import this data into the software. This is done using the **upload tool button**, or executing the “Upload to Database” command on the Tools Menu. This process may take a minute or so, so please be patient. This importing process is only necessary the first time data is uploaded to the software.

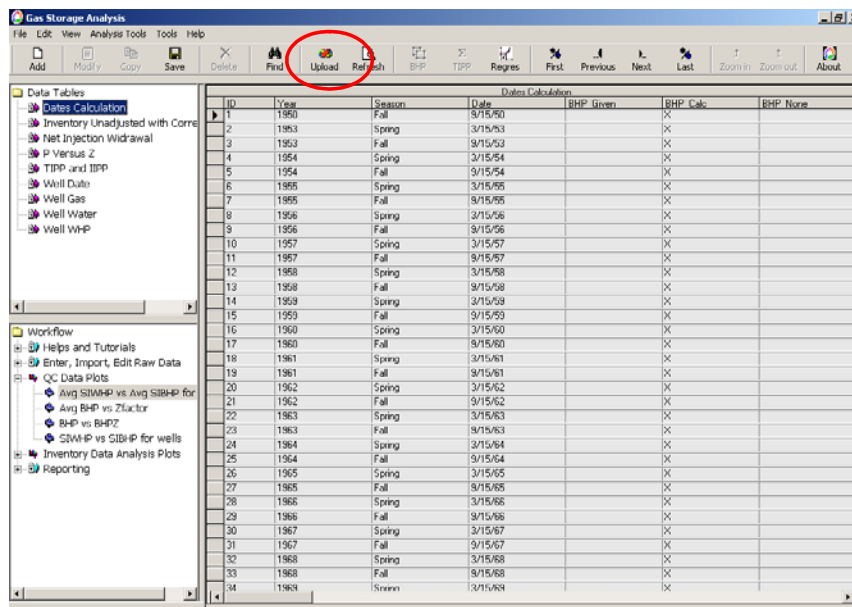


Figure 11: Location of Data Upload Tool Button

2.2 Data QC Process

There are several basic plots useful in identifying problems in input data and/or calculation results. These plots are shown in the Workflow Window, under the heading of **QC Data Plots**.

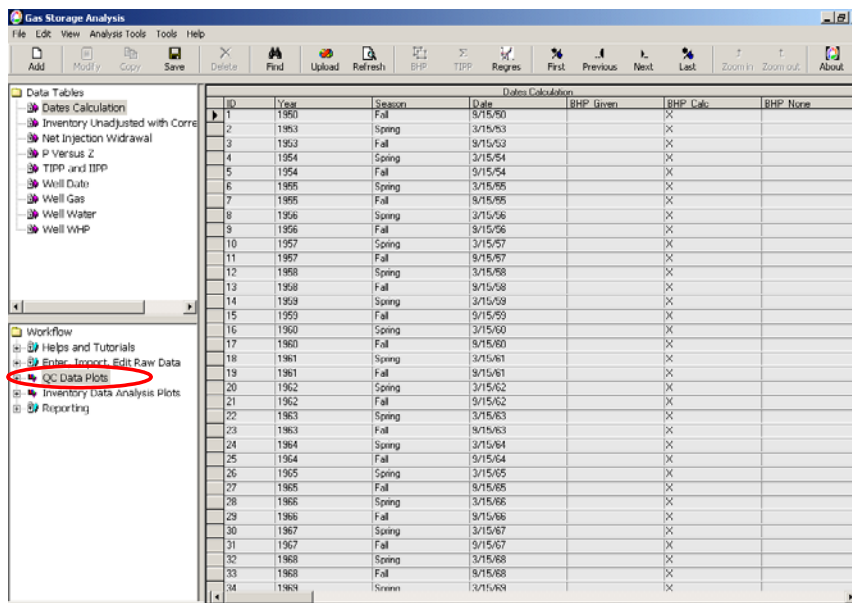


Figure 12: Location of QC Plots in Workflow Window

2.2.1 Avg SIWHP vs Avg SIBHP QC Plot

A plot of Avg SIWHP vs Avg SIBHP is shown in **Figure 13**. This plot should be a rather smooth line with no significant outlying points. Points that significantly deviate from the trend should be checked to ensure there are no errors in the calculation procedure.

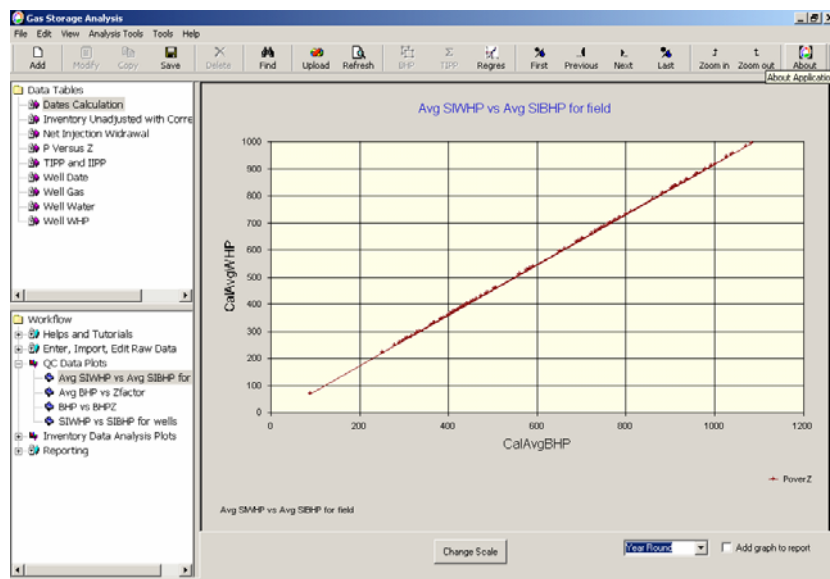


Figure 13: Example plot of Avg SIWHP vs Avg SIBHP

2.2.2 Avg BHP vs Avg Z-Factor Plot

A plot of Avg BHP vs Avg Z-Factor is shown in **Figure 15**. This plot should be a rather smooth line with no significant outlying points. Points that significantly deviate from the trend should be checked to ensure there are no errors in the calculation procedure.

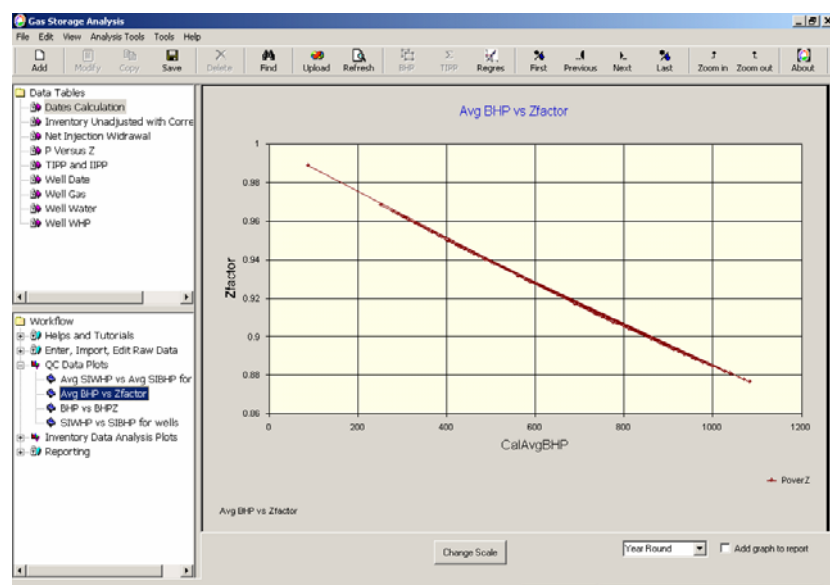


Figure 14: Example plot of Avg BHP vs Avg Z-Factor

2.2.3 Plot of SIWHP vs SIBHP For All Wells

A plot of SIWHP vs SIBHP For All Wells is shown in **Figure 15**. This plot should be a rather smooth line with no significant outlying points. Points that significantly deviate from the trend should be checked to ensure there are no errors in the calculation procedure.

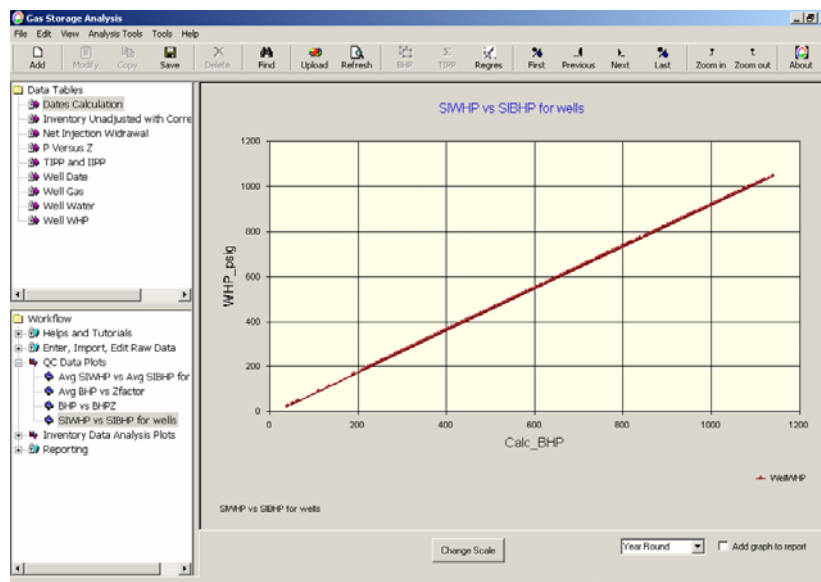


Figure 15: Example plot of SIWHP vs SIBHP For All Wells

2.3 Data Analysis Process

The inventory analysis (IA) process involves examining plots of historical operating data and other specialized diagnostic plots to identify trends indicative of gas losses, gas gains, gas bubble growth, and/or gas bubble shrinkage, and using graphical techniques to quantify the rates and volumes associated with these phenomena over time.

2.3.1 Analysis of Unadjusted Inventory and Avg SIBHP/z vs Time Plots

Typically, the first step in IA is to plot and review basic operating data. This usually involves looking for trends in the unadjusted inventory vs time plot, and the pressure (or P/z) vs time plot. If a volumetric reservoir is filled to the same inventory level each Fall, then we would expect the stabilized Fall shut-in pressure to be the same from year to year. We examine these two plots to look for deviations from this expected trend.

Examples of these two plots are shown in **Figure 16** and **Figure 17** below. The unadjusted inventory vs time plot shows that, since the 1960's, the reservoir has been filled to roughly the same inventory level at the end of each injection season. However, the BHP/z vs time plot shows that, since the 1960's, the BHP/z at the end of each injection season has been dropping.

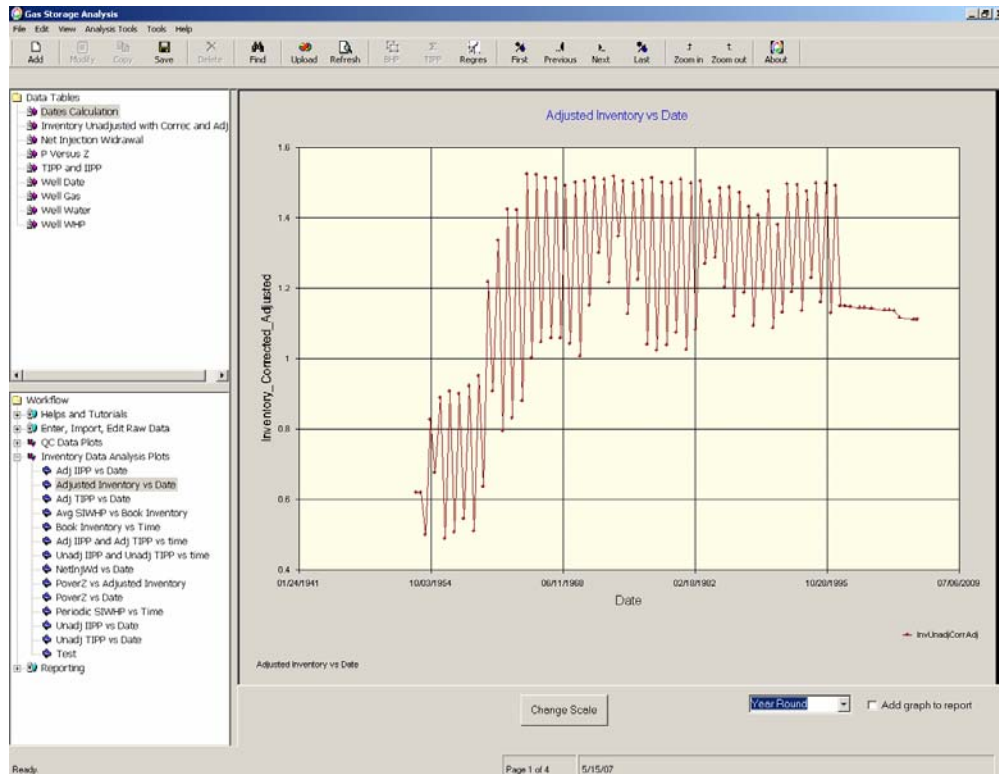


Figure 16: Unadjusted inventory vs time plot

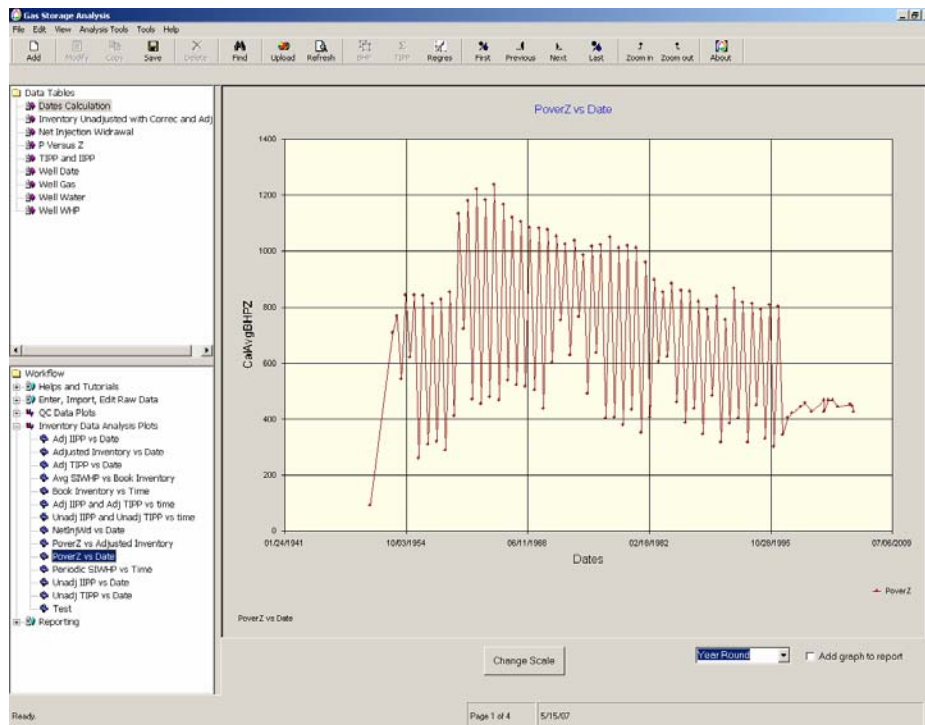


Figure 17: BHP/z vs time plot

Fall data points are considered by many storage engineers to be more reliable than Spring data points (due to the nature of injection vs withdrawal operations), and often times these plots are constructed using Fall points only. Examples of these two plots constructed using only Fall data points are shown in **Figure 18** and **Figure 19** below.

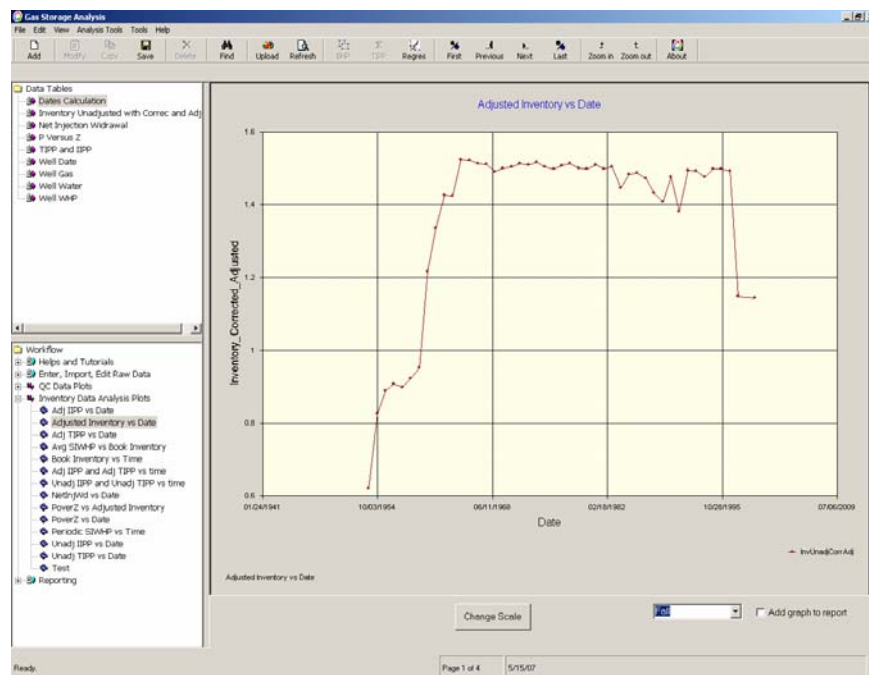


Figure 18: Unadjusted inventory vs time plot - Fall points only

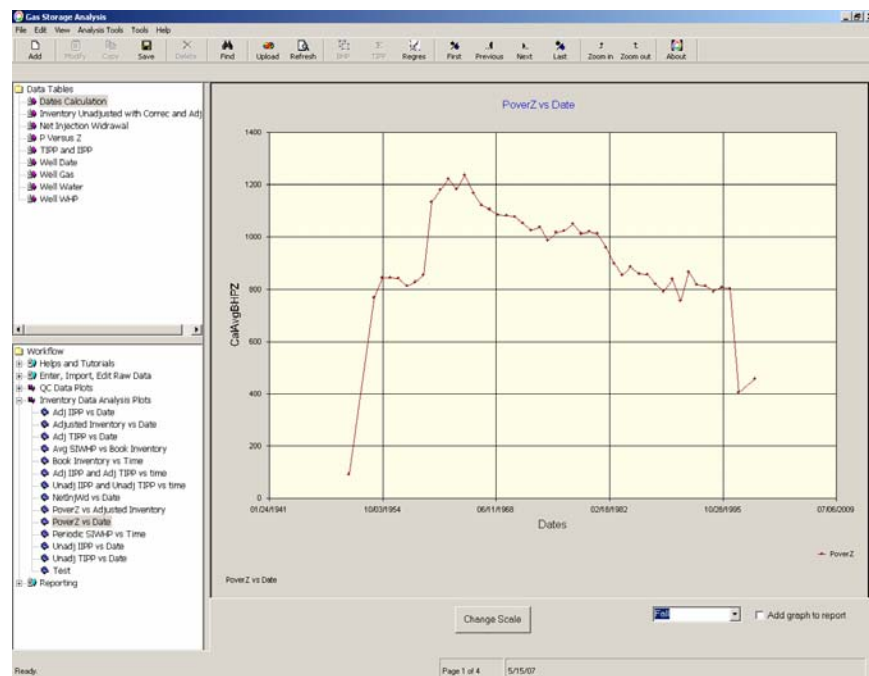


Figure 19: BHP/z vs time plot - Fall points only

2.3.2 Analysis of P/z vs Unadjusted Book Inventory Plots

A plot of P/z vs Unadjusted Inventory is very similar to what is typically referred to as a material balance plot (BHP/z vs Cumulative Production), often used to determine total GIP from primary production data in a volumetric gas reservoir. The difference is that the x-axis on this plot is the total unadjusted book inventory.

Theoretically, if a gas reservoir is volumetric, this plot should have the same slope (but different sign) as the material balance plot and pass through the origin. However, due to non-ideal conditions existing in most “volumetric” gas reservoirs reservoir, this is not the case, and deviations for ideal behavior can be used to estimate gas losses and changes in bubble size over time.

An example P/z vs Inventory plot is shown in **Figure 20**. The slope of the line on this plot remains roughly constant, but the position is changes (moves right) over time. This is indicative of ongoing gas losses.

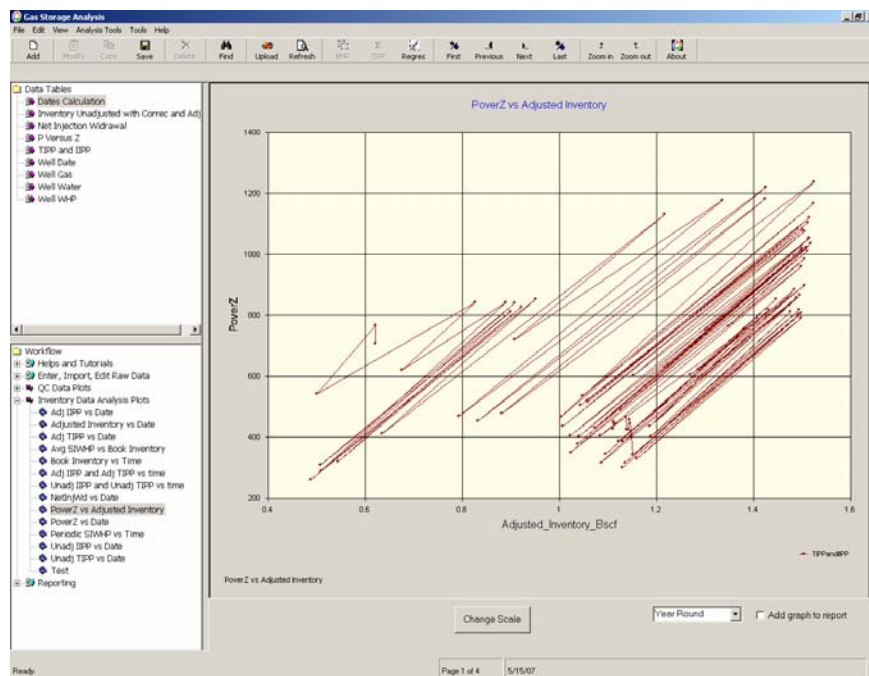


Figure 20: Example P/z vs Inventory plot

2.3.3 Analysis of Inventory Per Pound (IPP) Plots

Inventory Per Pound (IPP) plots are also used to estimate gas losses and/or gains as well as gas bubble growth and/or shrinkage (see the Inventory Primer for additional details on interpreting these diagnostic plots).

Two types of IPP plots are used. The Total IPP (TIPP) is defined as the total unadjusted book inventory divided by the BHP/z value corresponding to that inventory value. The Incremental IPP (IIPP) is defined as the *change* in the total unadjusted book inventory divided by the *change* in BHP/z value for a given injection or withdrawal cycle.

Examples of historical TIPP and IIPP values (using Fall data points only) are shown in **Figure 21**, and suggest that the subject field is experiencing ongoing gas losses. Note that we have the option of displaying or not displaying the TIPP curve (controlled using the Add/Remove TIPP button in the Plot Features window).

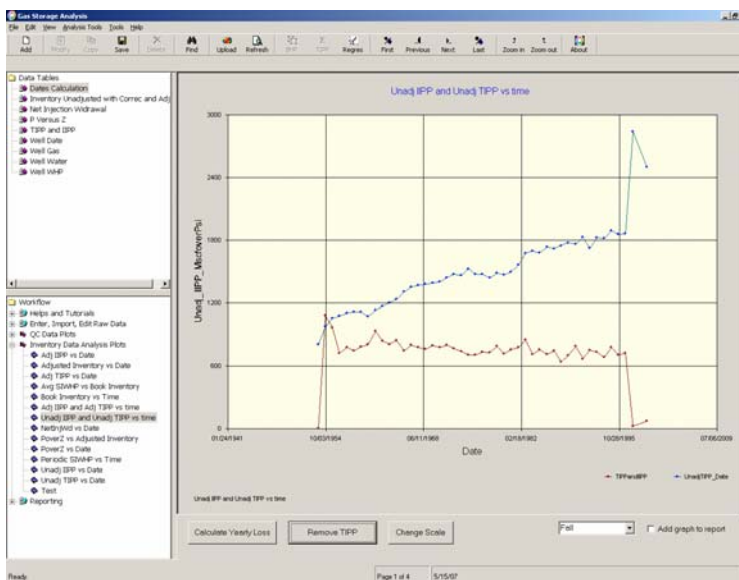


Figure 21: Examples of historical TIPP and IIPP values (using Fall data points only)

We can calculate the gas loss rate and total lost volume from this plot using the interactive analysis feature. In order to do this we first filter on Fall data only using the appropriate button in the plot feature window, then activate the TIPP graph (superimposed on the IIPP plot) using the appropriate button in the plot feature window (**Figure 22**). The resulting plot is what was shown in **Figure 21** above.

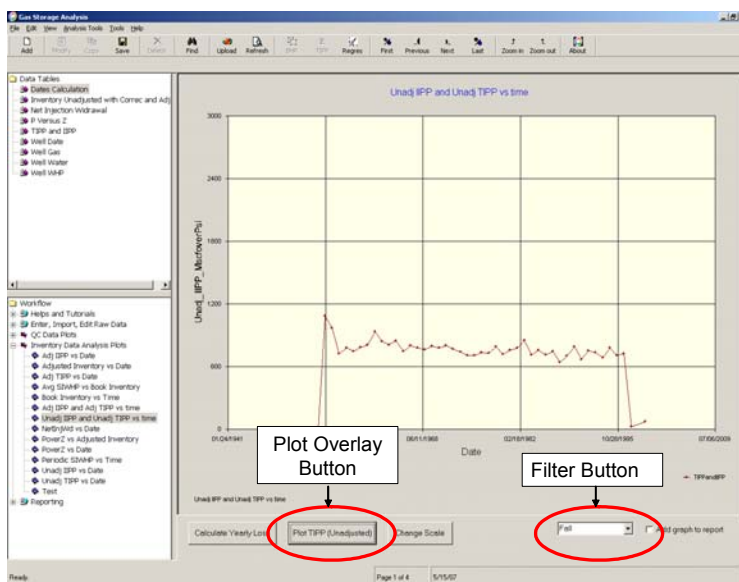


Figure 22: Location of Filter and Plot Overlay Buttons

Interpretation of this plot is initiated by clicking on the **Calculate Yearly Loss** in the plot feature window, which initially brings up a short description of the slope placement process. This

process consists of selecting a starting data point and an ending data point from the data points plotted on the TIPP plot.

After selecting the starting data point on the plot a calculation window will appear at the bottom of the plot. After selecting the ending data point, all of the calculation input data and the calculated loss rate and volume will be displayed in the calculation window at located at the bottom of the plot. Note that up to five separate lines can be used to determine five loss rates/volumes over the history of the storage field.

An example analysis of this data using 4 separate timeframes is shown in **Figure 23**.

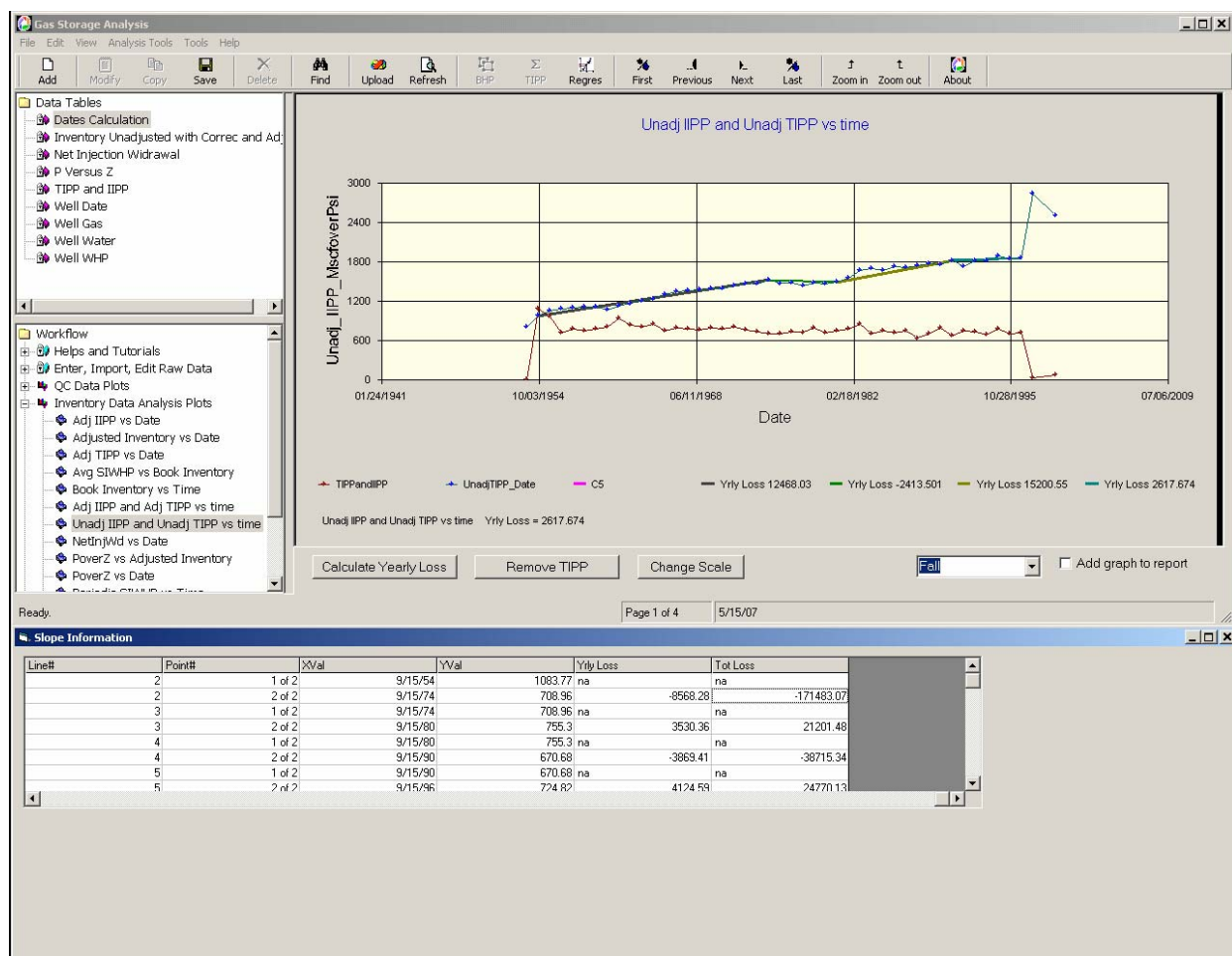


Figure 23: Example of graphical gas loss analysis and loss rate/volume calculations

2.4 Reporting

The reporting feature allows the user to easily capture the pertinent input data, IA plots, and analysis results, and export these data to a word processor for additional editing and formatting.

2.4.1 Including Interpreted Plots in a Report

An “Add graph to report” checkbox is located in right hand side of the plot features window. Checking this box while any particular plot is displayed will add the plot graphics (and any

analyses made using that plot) to a list of information to be included in an Inventory Analysis report. Every chart for which this box is checked will be included in a final report.

2.4.2 *Compiling Contents of a Report*

By simply checking the “Add graph to report” checkbox located in right hand side of the plot features window, the user can included all if the plots (and analyses) he wants to be included in the final report compiled by the software.

2.4.3 *Exporting and Editing a Report*

After checking the “Add graph to report” checkbox for all of the plots and analyses results the user wants to include in the final report, the user must click on “Generate” in the workflow window (under Reporting”) to compile the report and export it to WORD™ for further editing and inclusion of additional comments, text, and/or graphics not generated by the software.

3 Summary of Features in the Software Windows

3.1 Overall Window Layout

As noted earlier, there are five major areas or windows in the software work area (**Figure 1**): 1) At the extreme top of the work area (just below the various menus) are several toolbars associated with different aspects of inventory analysis calculations and workflow (e.g., BHP and BHP/Z calculations, Inventory Per Pound calculations, etc). 2) On the top left portion of the screen is a window that show the tables containing the input and calculated data, 3) On the bottom left portion of the screen is a window that shows an outline (in tree structure) of the workflow, including help options and reporting features, 4) On the top right portion of the screen is a window that show table or plot information highlighted in the Data Table window or the Workflow window, and 5) On the bottom right portion of the screen is a window that contains various buttons that allow modification of various plot features.

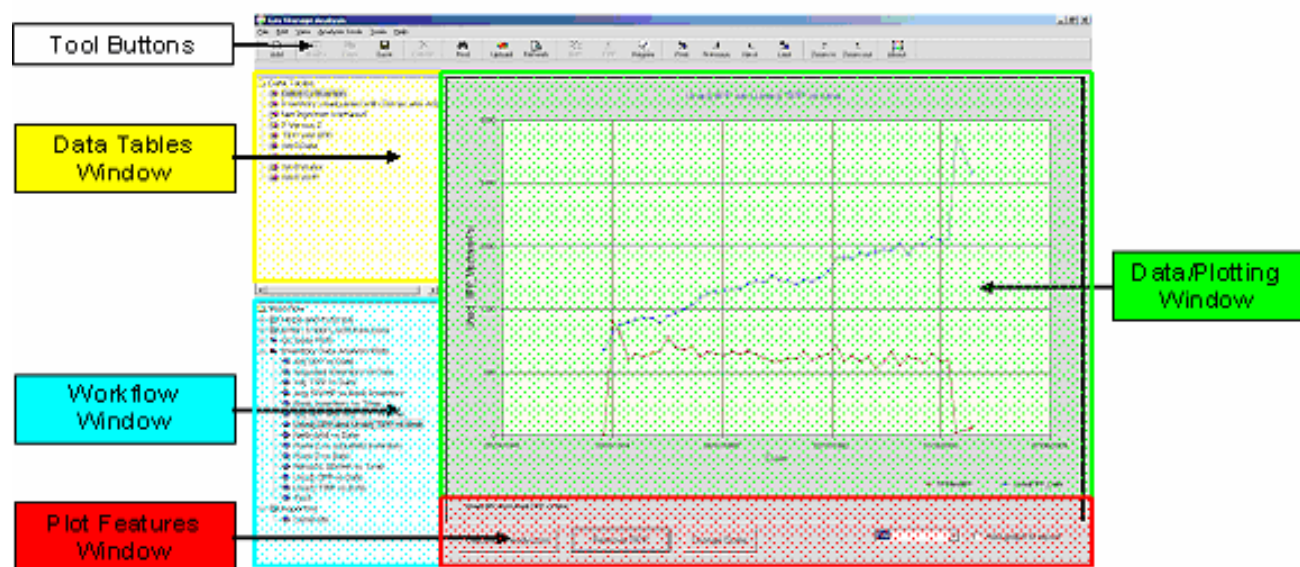


Figure 24: Major windows in the software work area

3.2 Tool Button Window

The tool button window is in the top of the software workspace, and contains all of the tool buttons, including tool buttons used to:

- Upload Data from the data input template
- Refresh the display in the active window
- Add, Delete, Modify, Save, and Copy data in tables
- Calculate the avg WHP, Avg BHP, avg BHP/Z and IPP values (TIPP and IIPP)
- Place a regression line on a plot
- Record navigation tool buttons for navigating data in tables:

- Go to first record in the table
- Go to next record in the table
- Go to previous record in the table
- Go to last record in the table
- Find data in the data tables
- Zoom into an area on a plot
- Zoom out of an area on a plot

3.3 Data Tables Window

The data table window contains all of the tables of data included in the database, including:

- Dates Calculation Table
- Unadjusted Book Inventory and Adjustments to Book Inventory
- Net Injection/Withdrawal Table
- P/z Table
- IIPP Table, which includes calculated values of TIPP and IIPP
- Well Data Table
- Well Water Table
- Well WHP Table

3.4 Workflow Window

The workflow window is arranged to reflect the order in which the various historical and diagnostic inventory analysis plots are analyzed, and includes the following selections:

- Various Helps, including
 - Inventory Primer
 - Inventory Analysis Toolbox
 - Technical References and Papers (grouped by Storage topic)
 - Glossary of Storage Terminology
 - Software Tutorial
- Data Manipulation features, including:
 - Data Importing (from EXCEL™ template)
 - Manual Data Entry
 - Data Editing
- QC Data Plots, including:

- Avg SIWHP vs Avg SIBHP
 - Avg SIBHP vs Avg Z-factor
 - Avg SIBHP vs Avg SIBHP/z
 - SIWHP vs SIBHP for all wells
- Inventory Analysis Plots of Historical Data, including:
 - Date vs Unadjusted Total Field Book Inventory
 - Date vs Adjustments to Total Field Book Inventory
 - Date vs Adjusted Total Book Inventory
 - Date vs Average Field Wellhead Pressure
 - Date vs Average Field Bottom Hole Pressure
 - Date vs Average Field (BHP/Z)
- Inventory Analysis Plots of Diagnostic Data, including:
 - Field Avg BHP/Z vs Unadjusted Total Field Book Inventory
 - Date vs UTIPP ([Unadjusted Total Inv]/[BHP/Z])
 - Date vs UIIPP ([Unadjusted Incremental Inv]/[Incremental BHP/Z])
 - Field Avg BHP/Z vs Adjusted Total Field Book Inventory
 - Date vs ATIPP ([Adjusted Total Inv]/[BHP/Z])
 - Date vs AIIPP ([Adjusted Total Inventory]/[BHP/Z])
 - Non-Effective Gas vs Time
 - Gas Loss Rate vs Time
 - Total Lost Gas Volume vs Time
- Reporting
 - Selection of this option will result in copies of reservoir input data and all plots selected for inclusion in the report to be compiled and sent to WORD™ for additional editing.

3.5 Data/Plotting Window

If the user clicks on a data table in the Data/Plotting window, the data in the selected table is displayed. Once displayed in the Data/Plotting window, data can be added, deleted, and edited, as appropriate.

If the user clicks on a plot in the Workflow window, the selected plot will be displayed. Once displayed in the Data/Plotting window, the plot can be analyzed using the appropriate tools in the Plot Features window.

3.6 Plot Feature Window

Once displayed in the Data/Plotting window, the plot display can be modified and the plot data can be analyzed using the appropriate tools in the Plot Features window, which include:

- **Change Scale Button:** This button allows the user to modify the x-axis or y-axis scale limits and number of scale divisions.
- **Filter Button:** This button allows the user to display Spring, Fall, or All data points on the selected plot.
- **Calculate Loss Button:** This button allows the user to select the starting and ending points for up to 5 trend lines on the TIPP chart, which are then used to and calculate the loss rate(s) and volume(s) associated with each of the specified lines.
- **Add Graph to Report Button:** This button allows the user to add the graph – as displayed at the time button is activated – to an automatically generated report.

4 Example Problem

In this section of the manual, we will walk the user through a typical Inventory Analysis (IA) process using the example data below.

The Big Boy Field is a single-well dry gas field that produced from 1925 to 1940. The field remained shut-in from 1940-1949, at which time it was converted to storage (no additional wells were drilled). It has been an active storage facility since 1950. The storage reservoir is known to have a small layer of lower permeability formation within the storage interval.

Historically, the storage field has operated between a minimum shut-in wellhead pressure of 650 psig and a maximum shut-in wellhead pressure of 1000 psig. Each Spring and Fall during storage operations, the operator measured the shut-in wellhead pressure in one IW well (Well ID 1) that is completed in the storage reservoir. The depth to the reservoir in this well is 5000 ft. The average wellhead temperature is 60 degrees F and the average reservoir temperature is 110 degrees F. Gas gravity is 0.58.

There is 1 mile of new (at conversion) 3" ID gathering line in the field. This line has custody transfer measurement facilities where it connects to a sales line that operates at 500 psi. From 1990 to 2000, separate measurement devices were "temporarily" installed at the sales lines to measure injected volumes. In 2000, this temporary injection measurement facility was removed.

Each year, when the wellhead pressures reach 700 psi, the one IW well is tested. During this test, the gas is vented into the atmosphere. These annual tests consist of three 15-minute flow periods (100 mscf/d, 200 mscd/d and 300 mscf/d) followed by a 45 minute extended flow (400 mscf/D).

At the end of withdrawal each year, a downhole camera is run in the IW well. Prior to running the camera, a bridge plug is set just above the bottom of the tubing (3" ID). There is a sealing packer at the bottom of the tubing, which is run inside casing (6" ID). Also at the end of withdrawal each year, the gathering line is blown down and pigged.

The Spring and Fall shut-in wellhead pressures recorded at the IW well and the corresponding unadjusted book inventory values are shown in the table on the following page.

Example Problem
Inventory Assessment Data

Date	Unadjusted Inventory (Bscf)	SIWHP psig
3/15/50	10.000000	650
9/15/50	15.000000	1000
3/15/51	10.100000	650
9/15/51	15.100000	1000
3/15/52	10.190000	650
9/15/52	15.190000	1000
3/15/53	10.270000	650
9/15/53	15.270000	1000
3/15/54	10.340000	650
9/15/54	15.340000	1000
3/15/55	10.400000	650
9/15/55	15.400000	1000
3/15/56	10.450000	650
9/15/56	15.450000	1000
3/15/57	10.490000	650
9/15/57	15.490000	1000
3/15/58	10.520000	650
9/15/58	15.520000	1000
3/15/59	10.540000	650
9/15/59	15.540000	1000
3/15/60	10.550000	650
9/15/60	15.550000	1000
3/15/61	10.550000	650
9/15/61	15.550000	1000
3/15/62	10.550000	650
9/15/62	15.550000	1000
3/15/63	10.550000	650
9/15/63	15.550000	1000
3/15/64	10.550000	650
9/15/64	15.550000	1000
3/15/65	10.550000	650
9/15/65	15.550000	1000
3/15/66	10.550000	650
9/15/66	15.550000	1000
3/15/67	10.550000	650
9/15/67	15.550000	1000
3/15/68	10.550000	650
9/15/68	15.550000	1000
3/15/69	10.550000	650
9/15/69	15.550000	1000
3/15/70	10.600000	650
9/15/70	15.600000	1000
3/15/71	10.650000	650
9/15/71	15.650000	1000
3/15/72	10.700000	650
9/15/72	15.700000	1000
3/15/73	10.750000	650
9/15/73	15.750000	1000
3/15/74	10.800000	650
9/15/74	15.800000	1000
3/15/75	10.850000	650
9/15/75	15.850000	1000
3/15/76	10.900000	650
9/15/76	15.900000	1000
3/15/77	10.950000	650
9/15/77	15.950000	1000
3/15/78	11.000000	650
9/15/78	16.000000	1000
3/15/79	11.050000	650
9/15/79	16.050000	1000
3/15/80	11.050000	650
9/15/80	16.050000	1000
3/15/81	11.050000	650
9/15/81	16.050000	1000
3/15/82	11.050000	650
9/15/82	16.050000	1000
3/15/83	11.050000	650
9/15/83	16.050000	1000
3/15/84	11.050000	650
9/15/84	16.050000	1000
3/15/85	11.050000	650
9/15/85	16.050000	1000
3/15/86	11.050000	650

Using the example data provided above:

- Load pertinent data into the EXCEL template
- Upload this data into the software
- Browse the data tables using the software
- Calculate BHP and BHP/Z values using the software
- Calculate TIPP and IIPP values using the software
- Peruse the various help features:
 - Open the Inventory Analysis Primer and peruse the document.
 - Open the Toolbox peruse the spreadsheet
 - Open the Help for input document and peruse the document.
 - Open the Help for analysis plots document and peruse the document.
 - Open the Storage Terms and peruse the document.
 - Open the Glossary and peruse the document.
 - Open the Summary of References and peruse the document.
- Browse the available analysis plots
- Review/Analyze appropriate diagnostic plots to calculate the inventory loss rates and volumes where appropriate
- Comment on the nature of the losses.
- Use the toolbox to determine if the losses can be reasonably explained by:
 - Line losses
 - Annual pigging of gathering lines
 - Annual well testing operations
 - Downhole camera Operations
- Select several plots for inclusion in a report and generate a draft report

4.1 Loading Data Into EXCEL™ Template

The first thing that needs to be done in any inventory analysis that utilizes the newly developed software is to reformat/reorganize the inventory data supplied by the operator. Generally, this is a fairly straightforward process, and simply involves cut/copy and paste commands within EXCEL, and perhaps some simple calculations within EXCEL to fill in necessary columns of input data.

We have installed the inventory analysis software on the D Drive, under the subdirectory called “Program Files.” During the installation process, a subdirectory is created under the “Program Files” subdirectory called “EXCEL Template.” In this subdirectory are several EXCEL files, including one named “Ex_Prob_Raw_Data.xls” in which is stored the raw data as collected by the operator. This file consists of a single sheet of data as shown above (see page with heading Example Problem Inventory Assessment Data). Open this file.

The EXCEL template used to import data into the software is in the same location, and is named “Upload Data Template.xls.” Open this file also. The first sheet in the file (“DatesCalc”) looks like this:

Input Sheet DatesCalc

This is the template used to store the data associated with the periods (Spring/Fall) inventory shut-in dates. The following columns of information are stored in this template:

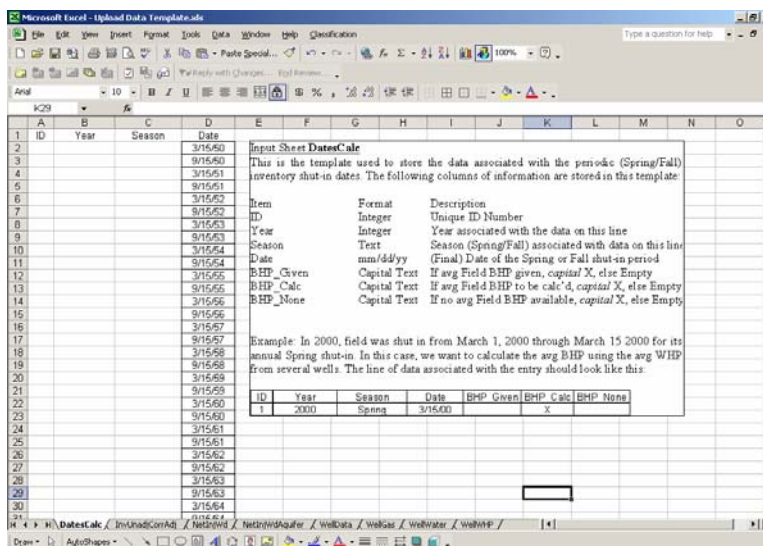
Item	Format	Description
ID	Integer	Unique ID Number
Year	Integer	Year associated with the data on this line
Season	Text	Season (Spring/Fall) associated with data on this line
Date	mm/dd/yy	(Final) Date of the Spring or Fall shut-in period
BHP_Given	Capital Text	If avg Field BHP to be calc'd, <i>capital X</i> , else Empty
BHP_Calc	Capital Text	If avg Field BHP to be calc'd, <i>capital X</i> , else Empty
BHP_None	Capital Text	If no avg Field BHP available, <i>capital X</i> , else Empty

Example: In 2000, field was shut in from March 1, 2000 through March 15, 2000 for its annual Spring shut-in. In this case, we want to calculate the avg BHP using the avg WHP from several wells. The line of data associated with the entry should look like this:

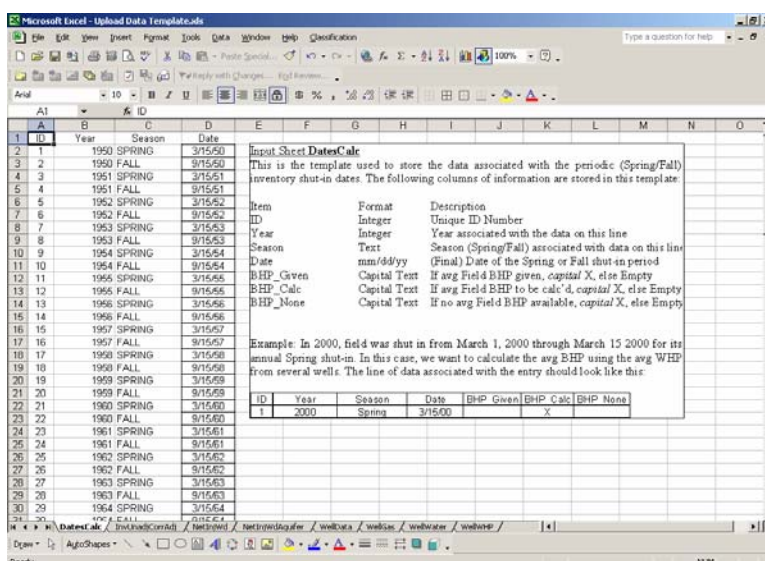
ID	Year	Season	Date	BHP_Given	BHP_Calc	BHP_None
1	2000	Spring	3/15/00		X	

To populate this sheet, we will perform the following steps:

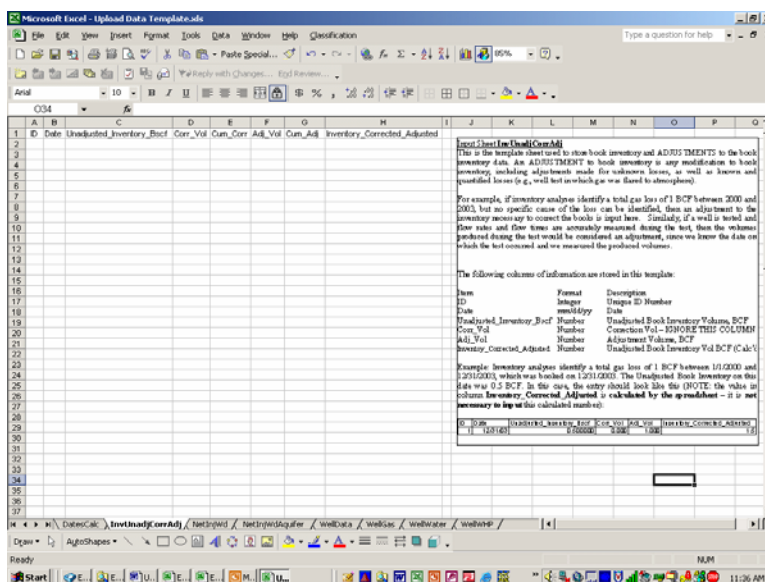
1. Copy data from cells A2–A113 in the raw data file (Ex_Prob_Raw_Data.xls) and past these values into Cells B2 – B113 in Sheet DatesCalc, in Excel template file (Upload Data Template.xls). Sheet DatesCalc in the “Upload Data Template.xls” should now look like this:



- The **ID** column in this spreadsheet is simply a unique integer, or “auto-number,” which we can populate by inputting a 1 in cell A2 and copying a formula in cells A3-A113 that adds one to the integer directly above it.
- The **Year** column in this spreadsheet can be calculated using the YEAR function in EXCEL, using the date in column D as the input. For example cell B2 would contain the formula “Year(D2).” This formula can then be copied to D3-D113 to populate the remaining cells.
- The **Season** column in this spreadsheet can be calculated using a conditional statement in EXCEL, using the date in column D as the input. For example cell C2 would contain the formula “IF(MONTH(D2)<6,“SPRING”,“FALL”).” This formula can then be copied to D3-D113 to populate the remaining cells. Sheet DatesCalc in the “Upload Data Template.xls” is now populated and should now look like this:



The second sheet in “Upload Data Template.xls” file (“InvUnadjCorrAdj”) looks like this:



To populate this sheet, we will perform the following steps:

1. Copy the date and book inventory values from cells A2–B113 in the raw data file (*Ex_Prob_Raw_Data.xls*) and past these values into Cells B2–C113 in Sheet “*InvUnadjCorrAdj*”, in Excel template file (*Upload Data Template.xls*).
2. The **ID** column in this spreadsheet is simply a unique integer, or “auto-number,” which we can populate by inputting a 1 in cell A2 and copying a formula in cells A3-A113 that adds one to the integer directly above it.
3. **Corr_Vol**, **Cum_Corr**, **Adj_Vol**, **Cum_Adj**, and **Inventory_Corrected_Adjusted** columns in this spreadsheet are used to store corrections and/or adjustments and store the calculated values of cum corrections, cum adjustments, and corrected adjusted book inventory. In this example, there are no corrections or adjustments to the book inventory, so all of these columns can be populated with zero’s. Note the following about this input sheet:
 - a. Although there are columns to input both “corrections” and “adjustments,” the “corrections” columns are included in anticipation of a software upgrade wherein a distinction between a correction and an adjustment can be made. When using the current version of the software, input all changes made to the book inventory as adjustment.
 - b. The values in columns labeled **Cum_Corr**, **Cum_Adj**, and **Inventory_Corrected_Adjusted**, are calculated within the software, and therefore zeros can be entered at this point
4. Sheet **InvUnadjCorrAdj** in the “*Upload Data Template.xls*” is now populated with data and should look like this:

A	B	C	D	E	F	G	H	I	J	K	L
1	ID	Date	Unadjusted_Inventory_Bscf	Corr_Vol	Cum_Corr_Adj_Vol	Cum_Adj	Inventory_Corrected	Adjusted			
2	1	3/15/60	8.500000	0	0	0	8.500				
3	2	9/15/60	13.500000	0	0	0	13.500				
4	3	3/15/61	8.600000	0	0	0	8.600				
5	4	9/15/61	13.600000	0	0	0	13.600				
6	5	3/15/62	8.690000	0	0	0	8.690				
7	6	9/15/62	13.690000	0	0	0	13.690				
8	7	3/15/63	8.770000	0	0	0	8.770				
9	8	9/15/63	13.770000	0	0	0	13.770				
10	9	3/15/64	8.840000	0	0	0	8.840				
11	10	9/15/64	13.840000	0	0	0	13.840				
12	11	3/15/65	8.900000	0	0	0	8.900				
13	12	9/15/65	13.900000	0	0	0	13.900				
14	13	3/15/66	8.950000	0	0	0	8.950				
15	14	9/15/66	13.950000	0	0	0	13.950				
16	15	3/15/67	8.990000	0	0	0	8.990				
17	16	9/15/67	13.990000	0	0	0	13.990				
18	17	3/15/68	9.020000	0	0	0	9.020				
19	18	9/15/68	14.020000	0	0	0	14.020				
20	19	3/15/69	9.040000	0	0	0	9.040				
21	20	9/15/69	14.040000	0	0	0	14.040				
22	21	3/15/60	9.050000	0	0	0	9.050				
23	22	9/15/60	14.050000	0	0	0	14.050				
24	23	3/15/61	9.050000	0	0	0	9.050				
25	24	9/15/61	14.050000	0	0	0	14.050				
26	25	3/15/62	9.050000	0	0	0	9.050				
27	26	9/15/62	14.050000	0	0	0	14.050				
28	27	3/15/63	9.050000	0	0	0	9.050				
29	28	9/15/63	14.050000	0	0	0	14.050				
30	29	3/15/64	9.050000	0	0	0	9.050				
31	30	9/15/64	14.050000	0	0	0	14.050				

No data was supplied in the example problem for the next two Sheets in the input template (**NetInjWd** and **NetInjWdAquifer**), so these will remain blank.

The **WellData** sheet contains information related to the one IW well. To populate this sheet, we will perform the following steps:

1. The **ID** column in this spreadsheet is simply a unique integer, or “auto-number,” which we can populate by inputting a 1 in cell A2 and copying a formula in cells A3-A113 that adds one to the integer directly above it.
2. The **Well_ID** column contains a unique identifier for each well, and has the format of an integer. We identified the well in which the shut-in wellhead pressure is measured each spring and Fall as Well 1, so we will use a **Well_ID** of 1 to identify the well.
3. The **Resv_Depth** column contains the depth (TVD) to the reservoir in the well, which was given as 5000 ft.
4. The **X** and **Y** columns contains well location information for use in future upgrades and is not used in this version of the software. You can enter any number in these columns you want, as they are not used.

The **WellData** sheet is now populated with data and should look like this:

Well ID	Well Type	Well Wt Fact	Resv Depth	X	Y
3625	IW	1	2982	1	7
3667	IW	1	3092	1	8
3684	OB	1	3088.5	1	9

No data was supplied in the example problem for the next two Sheets in the input template (**WellGas** and **WellWater**), so these will remain blank.

The last sheet in “Upload Data Template.xls file (“WellWHP”) looks like this:

ID	Well ID	Date	WHP_psig	Comments	Calc_BHP
1	3003	9/15/50	44		0
2	3209	9/15/50	35		0
3	3605	9/15/50	36		0
4	3667	9/15/50	164		0

To populate this sheet, we will perform the following steps:

1. Copy the Date and SIWHP in cells A2–A113 and cells C2–C113 in the raw data file (Ex_Prob_Raw_Data.xls) and past these values into cells C2–C113 and cells D2–D113 respectively in Sheet “SIWHP”, in Excel template file (Upload Data Template.xls).
2. The **ID** column in this spreadsheet is simply a unique integer, or “auto-number,” which we can populate by inputting a 1 in cell A2 and copying a formula in cells A3–A113 that adds one to the integer directly above it.
3. The **Well_ID** column should contain the Well_ID from the single well shown in sheet “WellID”
4. The **Comments** column can contain any text you wish to input. We will not input any comments in our file, so all rows under the header row in this sheet should be left blank.
5. The **Given_BHP** column is not used in this version of the software, and should be populated with zeros.
6. The **CalcBHP** column contains output calculated by the software after data is imported and should therefore contain all zeros at this point.
7. Sheet **SIWHP** in the “Upload Data Template.xls” is now populated with data and should look like this:

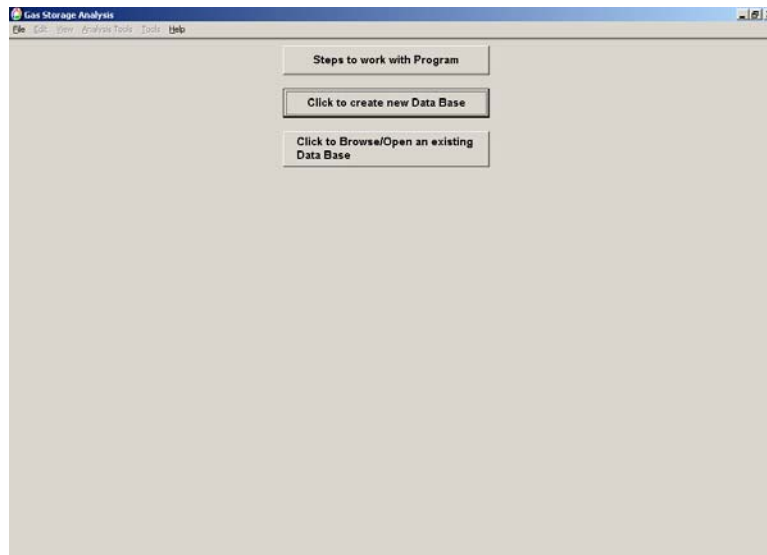
Item	Format	Description
ID	Integer	Unique Identifier
Well ID	Text	Name of the Storage Well
Date	mm/dd/yy	Date of recorded wellhead pressure
WHP_psig	Number	Measured wellhead pressure
Comment	Text	Comment
Calc_BHP	Number	Calc'd BHP (if given)

ID	Well ID	Date	WHP_psig	Comments	Calc_BHP
1	1000	9/15/60	44		0
2	3200	9/15/60	36		0
3	3605	9/15/60	36		0
4	3667	9/15/60	164		0

4.2 Uploading Data into Software

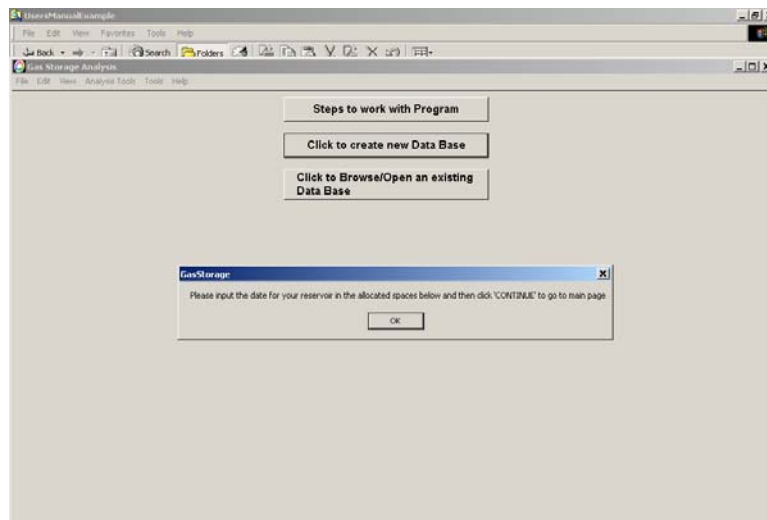
You have now completed populating the EXCEL file originally named, “Upload Data Template.xls.” It is now time to save this file using a different name, in a location you will remember. In this example, we will save the file in the same subdirectory as the Input Data Template was located (i.e., the subdirectory created on the D drive upon installation of the software, D:\Program Files\Gas Storage Software\Excel Template\)) and name it KGB_EXAMPLE_Data Template-2.xls.

To upload this data into the IAS, open/start the software. The first screen you will see looks as follows:



Select the button **Click to create New Database**, and use the dialogue box that appears to name the ACCESS file that will be created to contain your uploaded data, in a location of your choice. In this example, we will create an ACCESS file named “KGB_Example-2.mdb” in the same subdirectory that the Input Data Template was located (i.e., the subdirectory created on the D drive upon installation of the software (D:\Program Files\Gas Storage Software\Excel Template\)) and name it KGB_EXAMPLE_Data Template-2.xls.

After inputting the name you wish for the ACCESS database to be created, you will see the following dialogue box:



After you click OK, you will proceed to the reservoir data input screen, which looks as follows:

The screenshot shows the 'Reservoir Data' form in the 'Gas Storage Analysis' software. The form contains the following fields and controls:

- Name Of Storage Field:
- Field Type:
- Average Reservoir Depth:
- Average Reservoir Temperature:
- Wellhead Temperature:
- Reservoir Top Pressure:
- Reservoir Base Pressure:
- Gas Specific Gravity:
- Water Specific Gravity:
- Total Number of Wells:
- BHP Correlation:
- Z Factor:

Buttons: Done, Save, Continue

Populate the fields as shown in the following slide:

The screenshot shows the 'Reservoir Data' form in the 'Gas Storage Analysis' software with the following values entered:

- Name Of Storage Field: Big Eddy
- Field Type: Dry Gas
- Average Reservoir Depth: 5000
- Average Reservoir Temperature: 110
- Wellhead Temperature: 60
- Reservoir Top Pressure: 1000
- Reservoir Base Pressure: 650
- Gas Specific Gravity: 0.58
- Water Specific Gravity: 1.05
- Total Number of Wells: 1
- BHP Correlation: Cullender and Smith
- Z Factor: Hall-Verboorogh

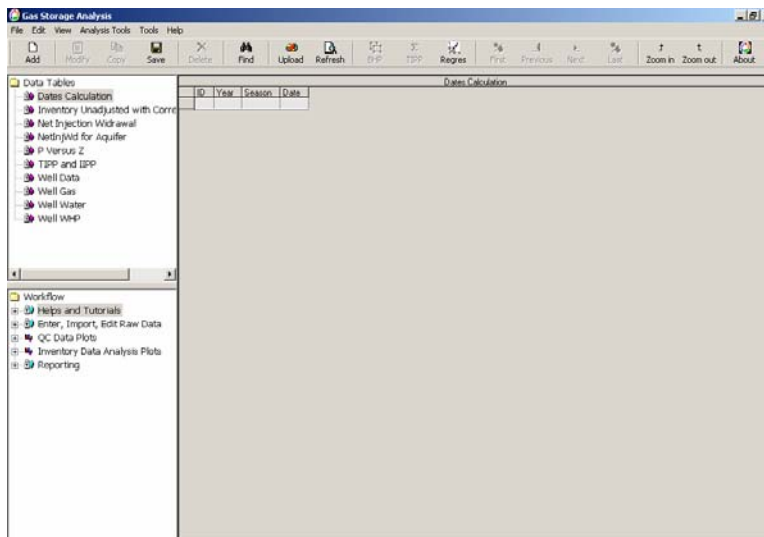
Buttons: Done, Save, Continue

Note the following:

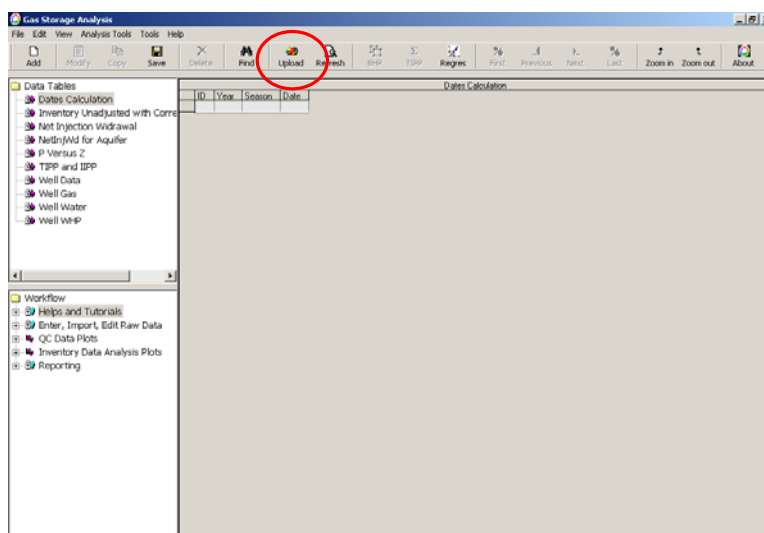
1. The average reservoir depth entered here is NOT the depth used to calculate SIBHP's from SIWHP's. We anticipate using this field in a later version of the software (allowing the user calculate all BHP's at the average reservoir depth or at the reservoir depth in each individual well). The depth associated with each individual well (entered on **WellData** sheet) is used to calculate BHP's from WHP's in each well.
2. Values entered for Reservoir Top and Base pressures are not used in this software version. We anticipate using them in later versions of the software. Values should be entered, but will not be used in the current software version.

3. Water specific gravity should be entered, but it is not used in dry gas wells.
4. When you click on the continue button, you will be asked if you want to save the changes – respond “yes.”

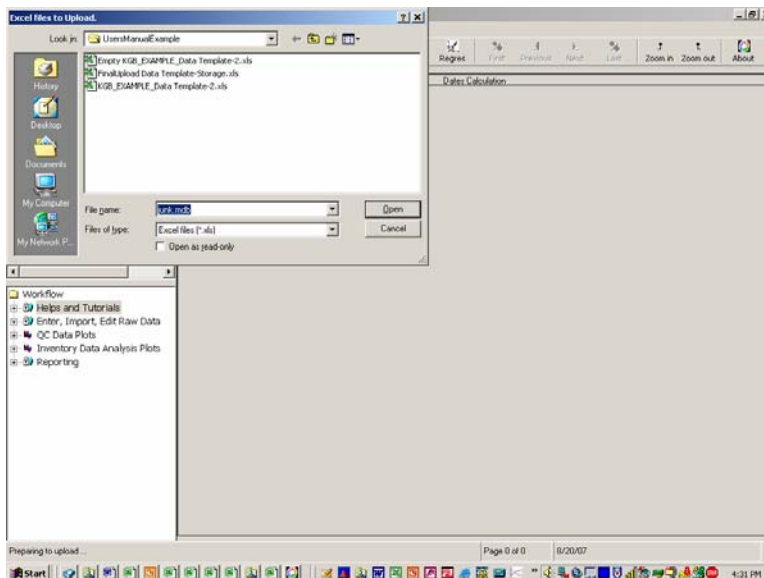
At this point, you will be in the software, but nothing other than the reservoir data has been entered. You will see the following screen at this point:



It is now time to import the data from the EXCEL template file we created, “KGB_EXAMPLE_Data Template-2.xls.” To do this, click on the “UPLOAD” tool button shown below:



You will then see the dialogue box below. Using this dialogue box, select the EXCEL input template file we created, (“KGB_EXAMPLE_Data Template-2.xls”) from the location in which we stored it (D:\Program Files\Gas Storage Software\Excel Template\), and select “OPEN.”



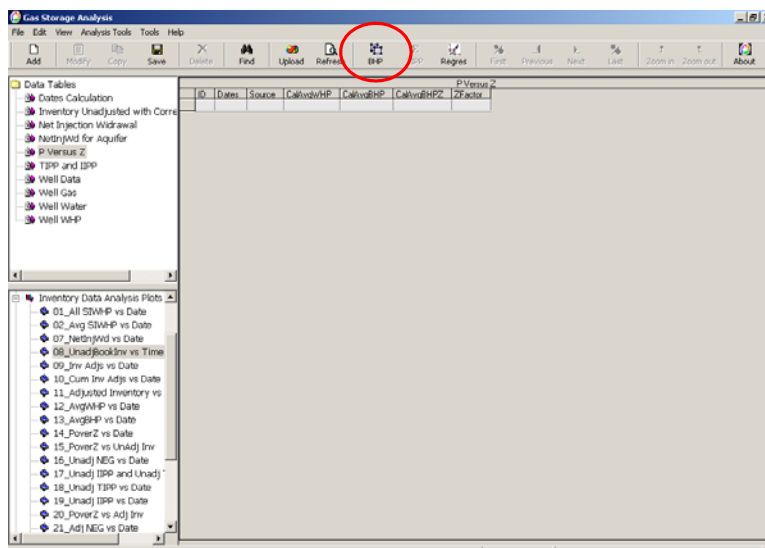
It will take a few moments to import the information from the EXCEL file, so be patient (this process is only required once). Upon completion of the import process, your screen should look as follows:

ID	Year	Season	Date
1	1950	Spring	3/15/50
2	1950	Fall	9/15/50
3	1951	Spring	3/15/51
4	1951	Fall	9/15/51
5	1952	Spring	3/15/52
6	1952	Fall	9/15/52
7	1953	Spring	3/15/53
8	1953	Fall	9/15/53
9	1954	Spring	3/15/54
10	1954	Fall	9/15/54
11	1955	Spring	3/15/55
12	1955	Fall	9/15/55
13	1956	Spring	3/15/56
14	1956	Fall	9/15/56
15	1957	Spring	3/15/57
16	1957	Fall	9/15/57
17	1958	Spring	3/15/58
18	1958	Fall	9/15/58
19	1959	Spring	3/15/59
20	1959	Fall	9/15/59
21	1960	Spring	3/15/60
22	1960	Fall	9/15/60
23	1961	Spring	3/15/61
24	1961	Fall	9/15/61
25	1962	Spring	3/15/62
26	1962	Fall	9/15/62
27	1962	Spring	3/15/63
28	1963	Fall	9/15/63
29	1964	Spring	3/15/64
30	1964	Fall	9/15/64
31	1965	Spring	3/15/65
32	1965	Fall	9/15/65
33	1966	Spring	3/15/66
34	1966	Fall	9/15/66
35	1967	Spring	3/15/67
36	1967	Fall	9/15/67

4.3 Browsing Data Tables and Performing BHP, p/z, and IPP Calculations

You can now browse the information located in the various tables by clicking on the table names in the Data Tables Window (upper left tree structure). Notice the following at this point:

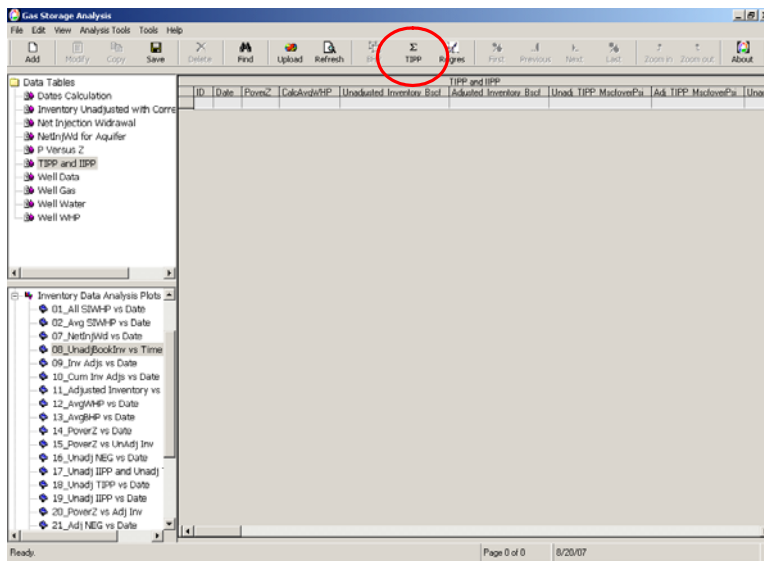
1. The first two data tables (“Dates Calculation” and “Inventory Unadjusted...”) contain data.
2. The third and fourth tables (“Net Injection Withdrawal” and “NetInjWdAquifer”) contain no data because we did not input any data in these tables.
3. The fifth table (“PoverZ”) contains no data because we have not yet calculated the BHP and Z values. To calculate the BHP and BHP/Z values, and populate this table with the calculated values, click on the “BHP” tool button shown below:



After clicking on the BHP tool button, the PoverZ table should look as follows:

ID	Dates	Source	CalcsvdBHP	CalcsvBHP	CalcsvBHPZ	P.Versus Z
1	3/15/50	650	740.52	792.67	0.9342	
2	3/15/50	1000	1135.11	1253.56	0.9055	
3	3/15/51	650	740.52	792.67	0.9342	
4	3/15/51	1000	1135.11	1253.56	0.9055	
5	3/15/52	650	740.52	792.67	0.9342	
6	3/15/52	1000	1135.11	1253.56	0.9055	
7	3/15/53	650	740.52	792.67	0.9342	
8	3/15/53	1000	1135.11	1253.56	0.9055	
9	3/15/54	650	740.52	792.67	0.9342	
10	3/15/54	1000	1135.11	1253.56	0.9055	
11	3/15/56	650	740.52	792.67	0.9342	
12	3/15/56	1000	1135.11	1253.56	0.9055	
13	3/15/56	650	740.52	792.67	0.9342	
14	3/15/56	1000	1135.11	1253.56	0.9055	
15	3/15/57	650	740.52	792.67	0.9342	
16	3/15/57	1000	1135.11	1253.56	0.9055	
17	3/15/58	650	740.52	792.67	0.9342	
18	3/15/58	1000	1135.11	1253.56	0.9055	
19	3/15/59	650	740.52	792.67	0.9342	
20	3/15/59	1000	1135.11	1253.56	0.9055	
21	3/15/60	650	740.52	792.67	0.9342	
22	3/15/60	1000	1135.11	1253.56	0.9055	
23	3/15/61	650	740.52	792.67	0.9342	
24	3/15/61	1000	1135.11	1253.56	0.9055	
25	3/15/62	650	740.52	792.67	0.9342	
26	3/15/62	1000	1135.11	1253.56	0.9055	
27	3/15/63	650	740.52	792.67	0.9342	
28	3/15/63	1000	1135.11	1253.56	0.9055	
29	3/15/64	650	740.52	792.67	0.9342	
30	3/15/64	1000	1135.11	1253.56	0.9055	
31	3/15/65	650	740.52	792.67	0.9342	
32	3/15/65	1000	1135.11	1253.56	0.9055	
33	3/15/66	650	740.52	792.67	0.9342	
34	3/15/66	1000	1135.11	1253.56	0.9055	
35	3/15/67	650	740.52	792.67	0.9342	

4. The Sixth table (“TIPP and IIPP”) contains no data because we have not yet calculated these values. To calculate TIPP and IIPP values and populate this table with the calculated values, click on the “TIPP” tool button shown below:

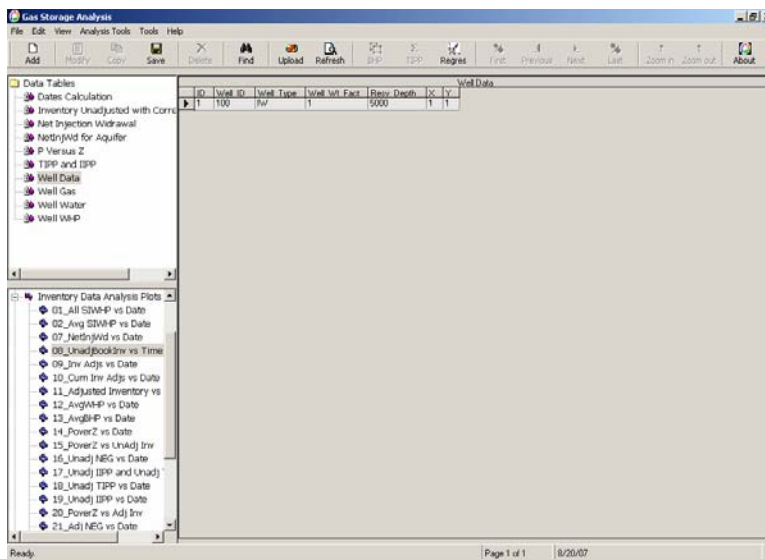


After clicking on the TIPP tool button, the “TIPP and IIPP table should look as follows:

The screenshot shows the 'Gas Storage Analysis' software interface with the 'TIPP and IIPP' table populated. The table has 8 columns: ID, Date, Power2, CalcAvrgHP, Unadjusted Inventory Bcfl, Adjusted Inventory Bcfl, Unadj. TIPP: MclowerePa, and Adj. TIPP: MclowerePa. The data is as follows:

ID	Date	Power2	CalcAvrgHP	Unadjusted Inventory Bcfl	Adjusted Inventory Bcfl	Unadj. TIPP: MclowerePa	Adj. TIPP: MclowerePa
1	3/15/50	792.67	650	8.5	8.5	10723.2518	10723.2518
2	3/15/50	1253.56	1000	13.5	13.5	10769.329	10769.329
3	3/15/51	792.67	650	8.6	8.6	10943.4077	10943.4077
4	3/15/51	1253.56	1000	13.6	13.6	10943.1018	10943.1018
5	3/15/52	792.67	650	8.63	8.63	10962.540	10962.540
6	3/15/52	1253.56	1000	13.63	13.63	10920.6973	10920.6973
7	3/15/53	792.67	650	8.77	8.77	11063.8727	11063.8727
8	3/15/53	1253.56	1000	13.77	13.77	10994.7195	10994.7195
9	3/15/54	792.67	650	8.84	8.84	11152.1819	11152.1819
10	3/15/54	1253.56	1000	13.84	13.84	11040.5565	11040.5565
11	3/15/55	792.67	650	8.9	8.9	11227.8754	11227.8754
12	3/15/55	1253.56	1000	13.9	13.9	11088.4202	11088.4202
13	3/15/56	792.67	650	8.95	8.95	11290.9534	11290.9534
14	3/15/56	1253.56	1000	13.95	13.95	11126.3066	11126.3066
15	3/15/57	792.67	650	8.99	8.99	11341.4167	11341.4167
16	3/15/57	1253.56	1000	13.99	13.99	11160.2167	11160.2167
17	3/15/58	792.67	650	9.02	9.02	11379.2625	11379.2625
18	3/15/58	1253.56	1000	14.02	14.02	11184.1475	11184.1475
19	3/15/59	792.67	650	9.04	9.04	11404.4837	11404.4837
20	3/15/59	1253.56	1000	14.04	14.04	11200.1021	11200.1021
21	3/15/60	792.67	650	9.05	9.05	11417.1063	11417.1063
22	3/15/60	1253.56	1000	14.05	14.05	11206.0794	11206.0794
23	3/15/61	792.67	650	9.05	9.05	11417.1093	11417.1093
24	3/15/61	1253.56	1000	14.05	14.05	11206.0794	11206.0794
25	3/15/62	792.67	650	9.05	9.05	11417.1093	11417.1093
26	3/15/62	1253.56	1000	14.05	14.05	11206.0794	11206.0794
27	3/15/63	792.67	650	9.05	9.05	11417.1093	11417.1093
28	3/15/63	1253.56	1000	14.05	14.05	11206.0794	11206.0794
29	3/15/64	792.67	650	9.05	9.05	11417.1093	11417.1093
30	3/15/64	1253.56	1000	14.05	14.05	11206.0794	11206.0794
31	3/15/65	792.67	650	9.05	9.05	11417.1093	11417.1093
32	3/15/65	1253.56	1000	14.05	14.05	11206.0794	11206.0794
33	3/15/66	792.67	650	9.05	9.05	11417.1093	11417.1093
34	3/15/66	1253.56	1000	14.05	14.05	11206.0794	11206.0794

5. The seventh table contains the well data we entered, and should look as follows:

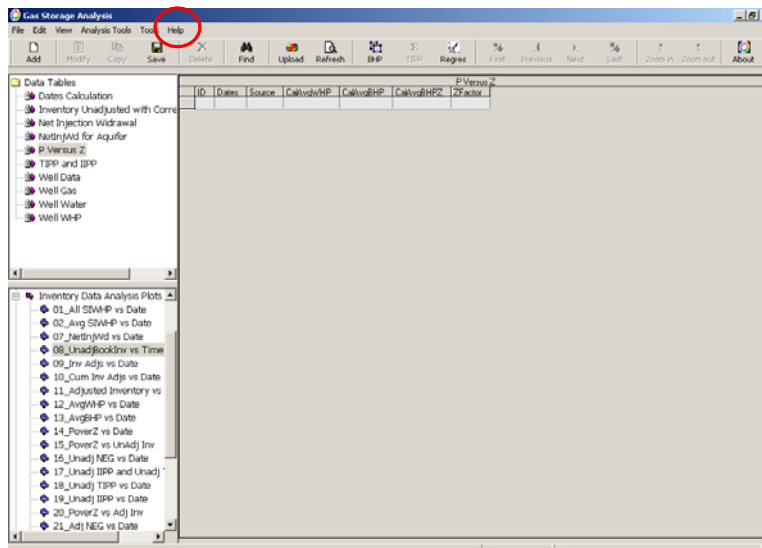


- The eighth and ninth tables (“Well Gas” and “Well Water”) contain no data because we did not input any data in these tables.
- The tenth table (“WellWHP”) contains the SIWHP’s input and the SIBHP’s calculated from these SIWHP’s, and should look as follows:

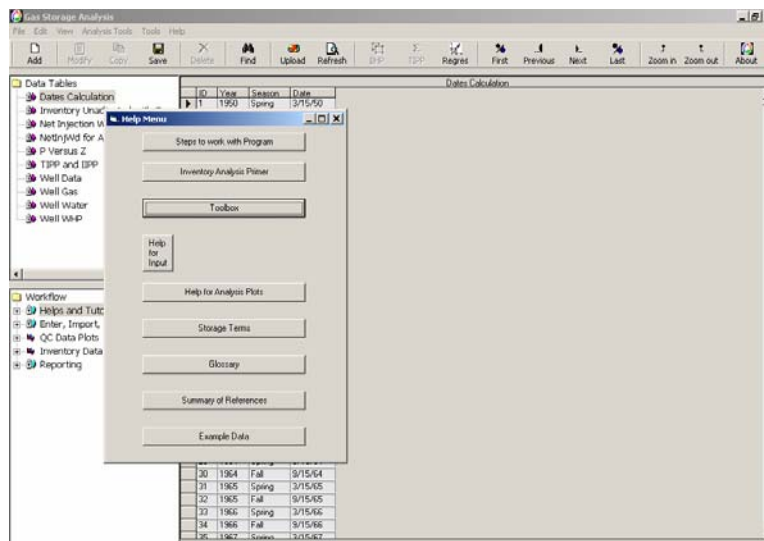
Well ID	Date	SIWHP	Comments	SIBHP	Calc. SIBHP
100	3/15/50	650		0	740.52
100	3/15/51	1000		0	1135.11
100	3/15/51	850		0	740.52
100	3/15/52	850		0	740.52
100	3/15/52	1000		0	1135.11
100	3/15/53	850		0	740.52
100	3/15/53	1000		0	1135.11
100	3/15/54	650		0	740.52
100	3/15/54	1000		0	1135.11
100	3/15/55	850		0	740.52
100	3/15/55	1000		0	1135.11
100	3/15/56	850		0	740.52
100	3/15/56	1000		0	1135.11
100	3/15/57	850		0	740.52
100	3/15/57	1000		0	1135.11
100	3/15/58	850		0	740.52
100	3/15/58	1000		0	1135.11
100	3/15/59	850		0	740.52
100	3/15/59	1000		0	1135.11
100	3/15/60	1000		0	1135.11
100	3/15/61	850		0	740.52
100	3/15/61	1000		0	1135.11
100	3/15/62	850		0	740.52
100	3/15/62	1000		0	1135.11
100	3/15/63	850		0	740.52
100	3/15/63	1000		0	1135.11
100	3/15/64	650		0	740.52
100	3/15/64	1000		0	1135.11
100	3/15/65	850		0	740.52
100	3/15/65	1000		0	1135.11
100	3/15/66	650		0	740.52
100	3/15/66	1000		0	1135.11
100	3/15/67	850		0	740.52

4.4 Perusing HELP features and Using the Toolbox

At this point, we will take a moment to briefly peruse the various HELP features in the software. To access the various HELP features of the software, go to the help menu at the top of the screen, as shown below:



This help button will bring up a menu of help items as shown below:



The various HELP menu items shown include the following:

Steps to work with Program

This is a very abbreviated Users' Manual compiled by the programmer that provides only the most essential information required to use the software.

Inventory Analysis Primer

This is a fairly complete introduction to inventory analysis, and includes discussions on the theory behind inventory analysis, the uses of various inventory analysis diagnostic plots, and references. The table of contents for this document is shown below.

1.	Introduction to Inventory Verification.....	3
1.1.	Objectives	3
1.2.	Theory.....	3
1.3.	Data Required	4
1.4.	Key or Indicator Wells.....	5
1.4.1.	Calculated Average Reservoir Pressure from Keywell SIWHP's	5
1.4.2.	Calculated Average Reservoir Pressures from IW Well SIWHP's	5
2.	Inventory Analysis Plots	6
2.1.	Plot of Basic Operational Data	6
2.2.	Gas Material Balance Plots: BHP/z vs Cum Production	7
2.3.	Pressure Content Plots – p/Z vs Inventory.....	8
2.4.	Inventory Per Pounds Plots.....	13
2.5.	Non-Effective Gas	17
2.6.	Pore Volume Ratio.....	18
2.7.	Inventory Variance From Material Balance	20
2.8.	Inventory Analysis in Aquifer Storage	20
2.9.	Inventory Analysis Nomenclature	22
3.	Example Problem.....	24
3.1.	Loading Data Into EXCEL™ Template	27
3.2.	Uploading Data into Software	32
3.3.	Browsing Data & Calculating BHP, p/z, and IPP Values	37
3.4.	Perusing HELP features and Using the Toolbox	40
3.5.	Performing Inventory Analysis.....	46
3.6.	Generating Reports	53
4.	REFERENCES	57

Toolbox

Selecting this option opens a HELP document related to the EXCEL “Toolbox” that was developed as part of this software. The EXCEL Toolbox is accessed from within the workflow window, and will be discussed in more detail later.

Help for Input

Selecting this option activates a drop-down box to the right, which allows the user to select the input screen for which he needs help. Upon selection of an item in the drop-down box, a WORD file is opened that provides HELP information related to the selected input screen. A description of the data entered on this screen, including data names and formats are summarized.

Help for Analysis Plots

Selecting this option opens a WORD document that provides detailed help for each of the various data QC plots and the diagnostic plots used to estimate loss rates and volumes. The each plot, the purpose, assumptions, applicability, dangers of mis-use, examples, and references are discussed.

Storage Terms

Selecting this option opens a WORD document that provides a description of the various terms used in inventory analysis.

Glossary

Selecting this option opens a WORD document that provides a description of the various terms used in the underground gas storage industry. It is similar in purpose to the “Storage Terms” help above, but much broader in scope.

Summary of References

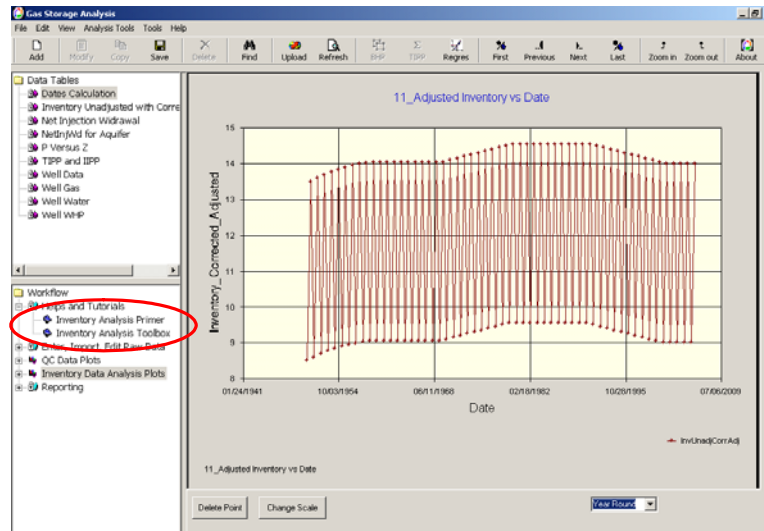
Selecting this option opens a WORD document that provides a list of various references and technical papers related to the gas storage industry. These references are listed by topic, and should look something like this:

Table of Contents	
1. Introduction to Gas Storage	
2. Gas Storage Field Design	
3. Optimization	
4. Migration and Monitoring	
5. Inventory Verification	
6. Deliverability Maintenance and Enhancement	
7. Simulation of UGS Reservoirs	
8. Special Topics	
9. Top Twenty Papers	

Example Data

Selecting this option opens an EXCEL document containing the Spring/Fall pressure and inventory example data.

Select HELP features are also accessible for the Workflow window, since we anticipate they will commonly be referenced during the inventory analysis process. In the Workflow Window, there are two Help items listed, the Inventory Primer and the Toolbox, as shown below:



Inventory Analysis Primer

As noted above, this is a fairly complete introduction to inventory analysis, and includes discussions on the theory behind inventory analysis, the uses of various inventory analysis diagnostic plots, and references.

Toolbox

Select this option and open the EXCEL “Toolbox.”

After opening the EXCEL Toolbox, go to sheet **Bureau-of-Mines Est Line Losses**, and enter the data given in the example problem data set above to estimate the annual line losses each year we might expect from the 1 mile long gathering line carrying gas from the wellhead to the sales point.

After inputting the example data, your sheet should look like the following:

Pipeline Losses		
1	Pipeline Losses	
2	Gathering lines and wells recommended leakage factor	0.00010 (Mscf/yr-ft psi)
3	Transmission lines recommended leakage factor	0.00010 (Mscf/yr-ft psi)
4	Gathering line length	6200 ft
5	Gathering line ID	3 in
6	Transmission line length	0 ft
7	Transmission line ID	24 in
8	Time	1 year
9	Average Pressure	000 psi
10	Total Loss	34 Mscf

Obviously, the annual loss rate/volume calculated using the Bureau of Mines data is minimal, and we would not expect that potential losses in the gathering lines to contribute significant to any overall losses from the field.

Next, go to sheet **Est Wellbore Blowdown Volume**, and enter the data given in the example problem data set above to estimate the annual line losses each year we might expect from blowing down the well each year prior to running the camera. After inputting the example data, your sheet should look like the following:

Wellbore Blowdown Volume Calculation		
2	Tubing ID	3 in
3	Tubing Depth	5000 ft
4	Casing ID	6 in
5	Casing Depth	5000 ft
6	Packer on Tubing	Yes
7	Packer Depth	4950 ft
8	Gas Gravity	0.68
9	Wellhead Pressure	650 psia
10	Wellhead Temperature	60 °F
11	Bottomhole Temperature	110 °F
12	Bottomhole Pressure	724.0 psia
13	Wellbore Blowdown Volume (Final WHP=0 psi)	12 Mscf

Obviously, the annual lost volume due to blowing down the well prior to running a camera is minimal, and we would not expect that these losses contribute significant to any overall losses from the field.

Next, go to sheet **Est Well Test Volumes**, and enter the data given in the example problem data set above to estimate the annual losses associated with running the well test each year. After inputting the example data, your sheet should look like the following:

Well Testing Volume	Rate (Mscf/day)	Duration (hours)	Cum Production (Mscf)
	100	0.25	1.0
	200	0.25	3.1
	300	0.25	6.3
	400	0.75	19.8
	500	0	19.8
	600	0	19.8
	700	0	19.8
	800	0	19.8

Obviously, the annual lost volume due to testing the well each year is minimal, and we would not expect that these losses contribute significant to any overall losses from the field.

Next, go to sheet **Est Pipeline Volumes**, and enter the data given in the example problem data set above to estimate the annual losses associated with blowing down the gathering line to run the pig each year. After inputting the example data, your sheet should look like the following:

Pipeline Volume	Pipe ID	Pipe Length	Gas Gravity	Inlet Pressure	Inlet Temperature	Outlet Pressure	Outlet Temperature	Pipeline volume
	3 in	5,280 ft	0.58	800 psia	100 °F	500 psia	100 °F	17 Mscf

Obviously, the annual lost volume due to pigging the gathering line each year is minimal, and we would not expect that these losses contribute significant to any overall losses from the field.

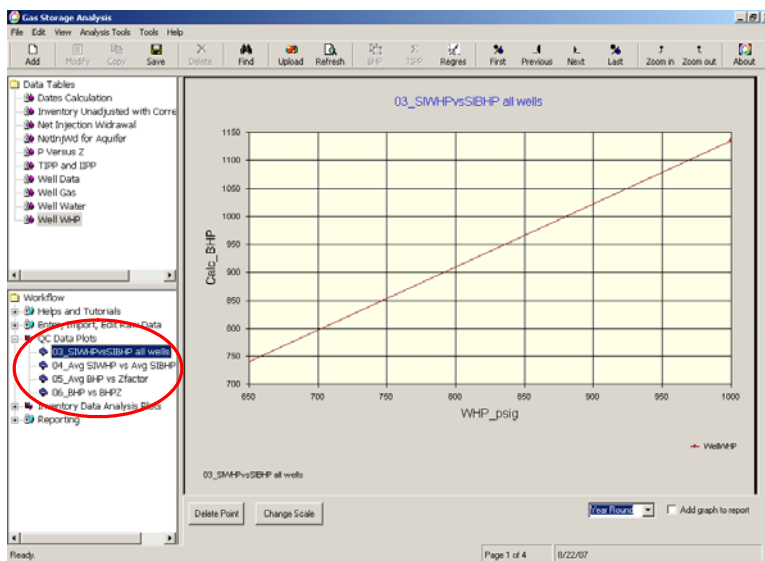
Note that not all of the calculations that can be made in this EXCEL Toolbox have been demonstrated here.

4.5 Performing Inventory Analysis and Generating Reports

At this point, all of the data from the example problem has been input/uploaded. We have perused the data tables and the help options, and we used the Toolbox feature to estimate any inventory losses due to field operations. The next step is to use the various plots to analyze loss rates and volumes over the entire life of storage operations.

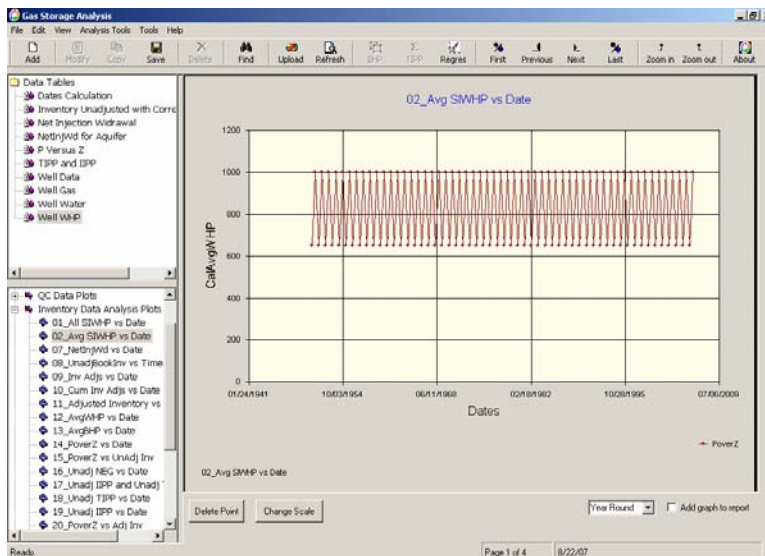
At this point, it is recommended that you open a word processing document to keep notes about the trends observed during the inventory analysis process. These notes will prove to be extremely valuable after your analysis is complete and you generate a draft report.

We start by reviewing the data QC plots shown in the Workflow Window, under QC Data Plots (see below). Since none of these plots show any irregularities, it is safe to assume that no problems were encountered during the calculation processes we performed earlier.



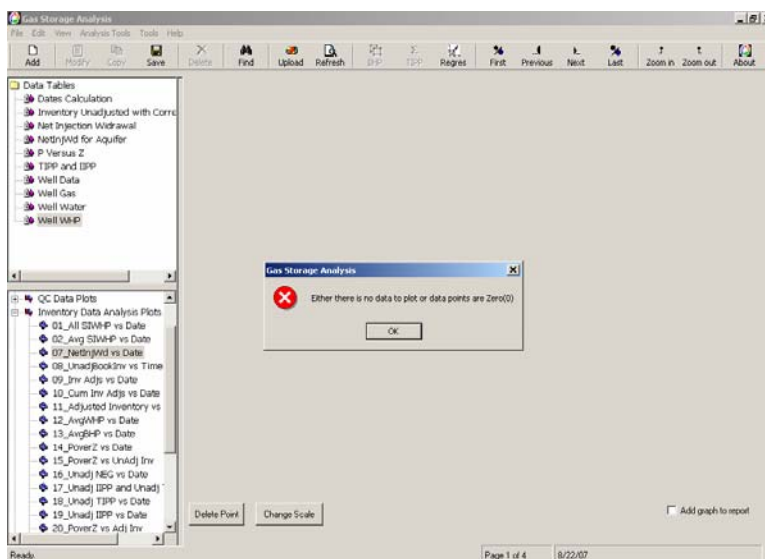
After reviewing the data QC plots, we review plots of operational data to identify any operational trends that may provide preliminary, qualitative indications of ongoing losses and show timeframes wherein we need to be careful analyzing data due to widely varying operational practices.

The first two plots (**All SIWHP vs Date** and **Avg SIWHP vs Date**) are identical, since there is only one well in the field. For the purpose of this example, look at the **Avg SIWHP vs Date**, which should look like this (you may have to change the scale on the plot):



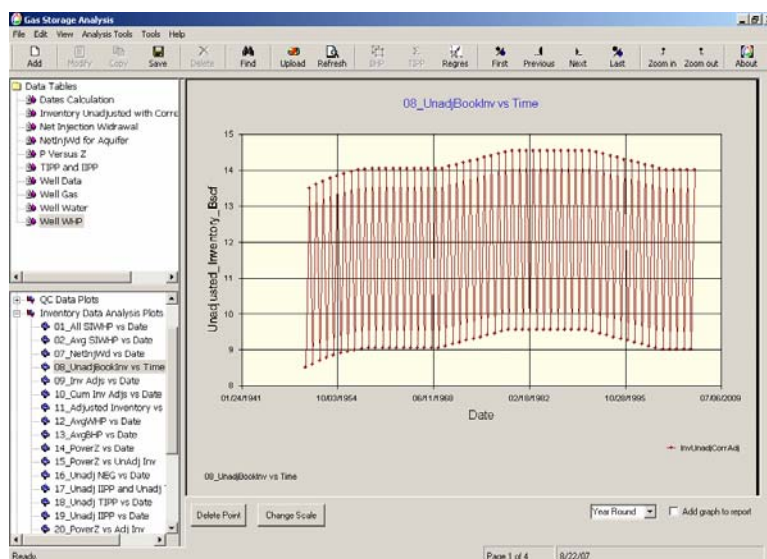
We observe from this plot that the field has consistently been operated between 650 psi and 1000 psi throughout its life. Therefore, we do not have to worry about wide fluctuations in minimum and maximum operating pressures skewing trends in other diagnostic plots.

We did not load any daily or monthly Net Injection information, so the next plot shows nothing:



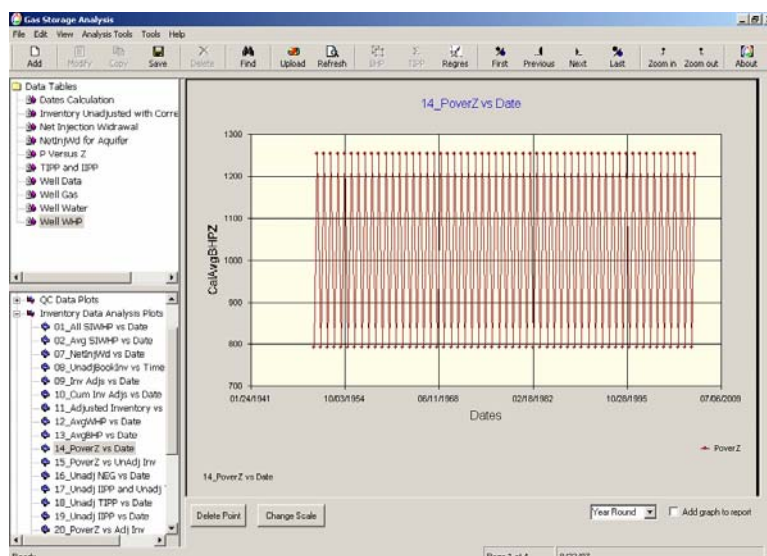
The next plot in the workflow is the **UnadjBookInv vs Time**, which shows the book inventory prior to any adjustments as a function of time. This plot is revealing, especially in light of how

regularly the field was operated from a pressure perspective. This plot shows that various levels of inventory were required over the field life to achieve the same Spring and Fall shut-in pressures. This trend is a strong indicator, albeit qualitative indicator, that there have been losses and gains occurring during storage operations.



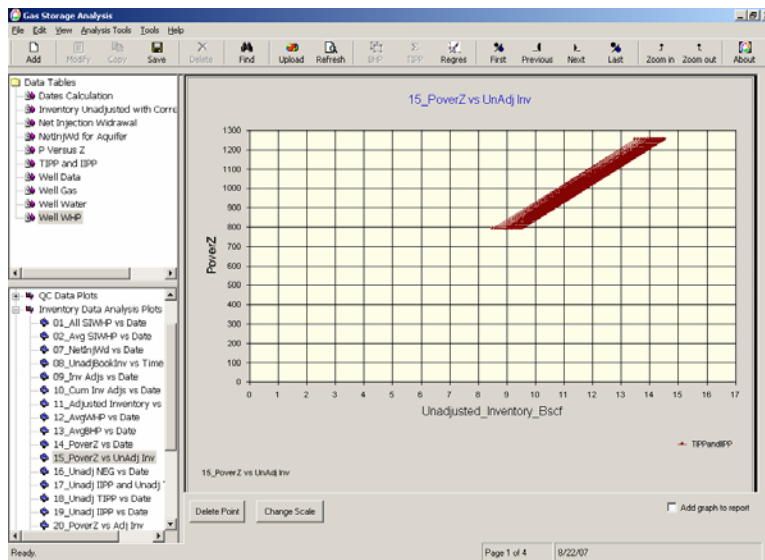
The next three plots, **Inv Adjs vs Date**, **Cum Inv Adjs vs Date**, and **Adjusted Inventory vs Date** are trivial, as no inventory adjustments have been booked during the life of the field. In addition, the two plots after these, **Avg WHP vs Date** and **Avg BHP vs Date**, are not noteworthy.

The next plot, **PoverZ vs Date**, reflects the same trends as the SIWHP vs time, and further demonstrates the uniformity of operations over the life of the storage field from a pressure perspective.

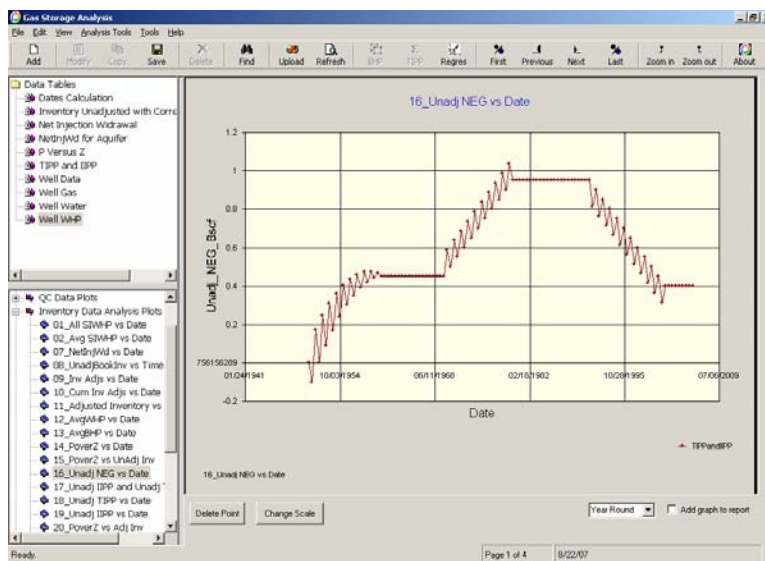


The next plot, **PoverZ vs UnadjInv**, is a plot of the unadjusted book inventory vs the BHP/Z. This plot shows movement to the right and left at various points during the life of storage

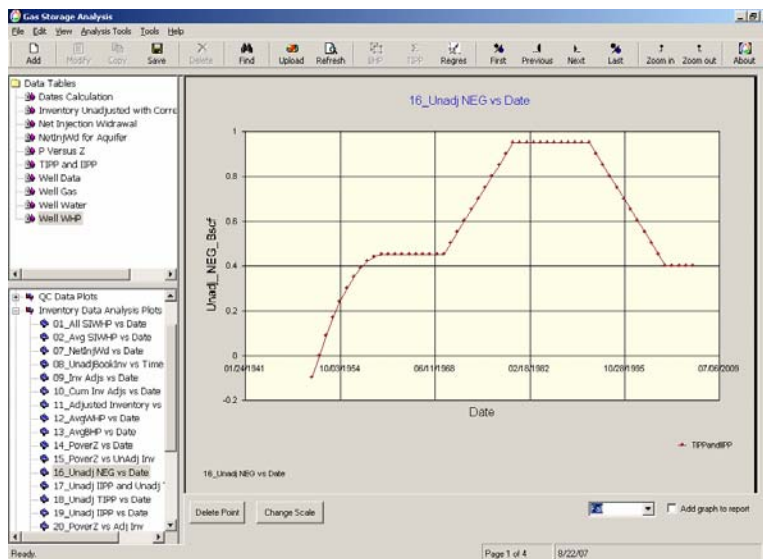
operations, which leads us to the conclusion the losses and gains have occurred during storage operations. This is consistent with the qualitative conclusions drawn from a review of the the operational plots (SIWHP vs Time and Unadjusted Book Inventory vs Time).



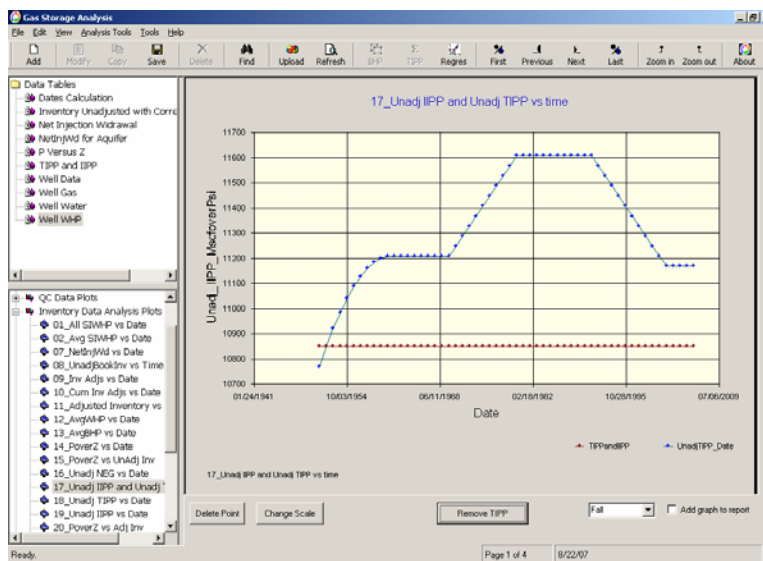
The next plot, Unadj NEG vs Date, shows the non-effective gas (NEG) calculated for each cycle by back-extrapolating the BHP/Z vs Unadjusted Book Inventory plot for that cycle to a BHP/Z value of zero (i.e., the x-intercept of the plot). This plot clearly indicates the time periods experiencing losses, gains, and stability:



Note that the relative uniformity of injection operations compared to withdrawal operations lead some storage engineers to use only fall data to analyze NEG vs time plots and IPP vs time plots. By applying the FALL filter on this plot, we can generate the plot using only Fall data points:



The next plot is the Unadjusted TIPP vs time and Unadjusted IIPP vs time. These are perhaps the most widely used inventory analysis plots in the storage industry. Usually, these plots are generated using Fall only data points, since injection operations are relatively more uniform than withdrawal operations. Therefore, the Fall data points are generally thought to be less operationally influenced. A plot of IPP values vs time generated using Fall only data points is shown below:

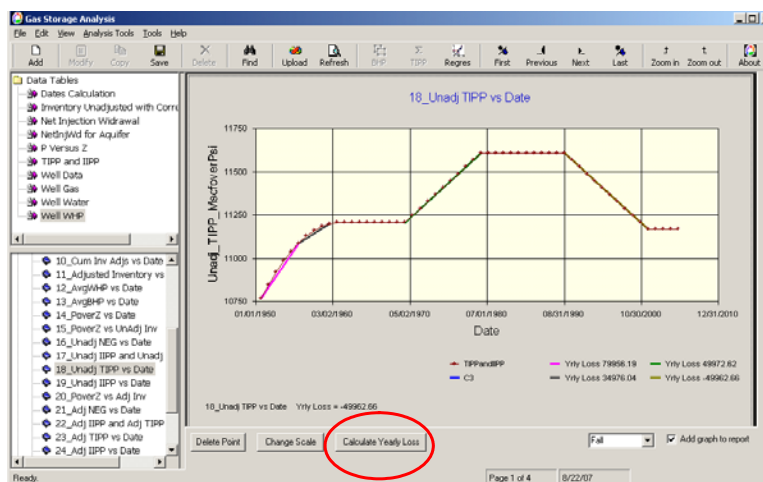


This plot clearly shows the following:

1. Non-linear increase in the TIPP w/Flat IIPP in 1950's (GAIN)

2. Flat TIPP and IIPP during 1960's (NO LOSS or GAIN)
3. Linear increase in the TIPP w/Flat IIPP in 1970's (LOSS)
4. Flat TIPP and IIPP during 1980's (NO LOSS or GAIN)
5. Non-linear decrease in the TIPP w/Flat IIPP in 1990's (GAIN)
6. Flat TIPP and IIPP from 2000-2005 (NO LOSS or GAIN)
- 7.

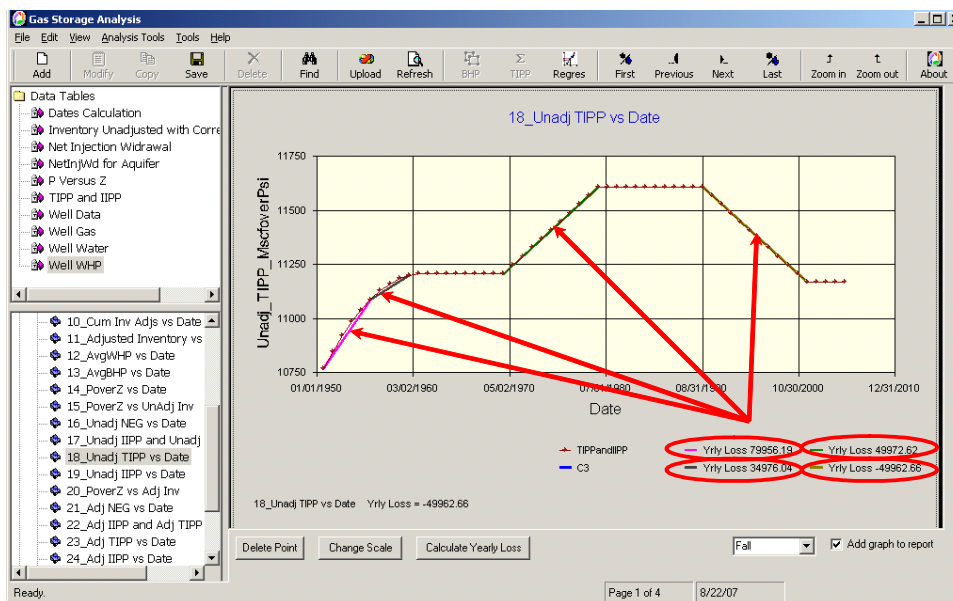
In order to calculate the loss rates and volumes, we will use the TIPP plot generated with Fall only data points. This is accomplished by clicking on the UnadjTIPP vs Date plot in the Workflow window, filtering on Fall data points, and clicking on the “Calculate Yearly Loss” button (see below).



You can calculate losses for up to 5 time periods using the “Calculate Yearly Loss” button. Simply click the button, read the pop-up directions, and click OK to close the directions. Click on the data point closest to the start of the loss period, then click on the data point closest to the end of the loss period.

The software will automatically calculate annual loss rates for each period and display results on the plot. Using this information, we can calculate the total gains/losses by multiplying the gain/loss rate for each loss period by the number of years the gain/loss occurred, and summing the volumes for each period.

For this example, the TIPP vs Date used to calculate the loss rate looks like the following after loss analysis was performed:



The losses calculated using this plot can be summarized as follows:

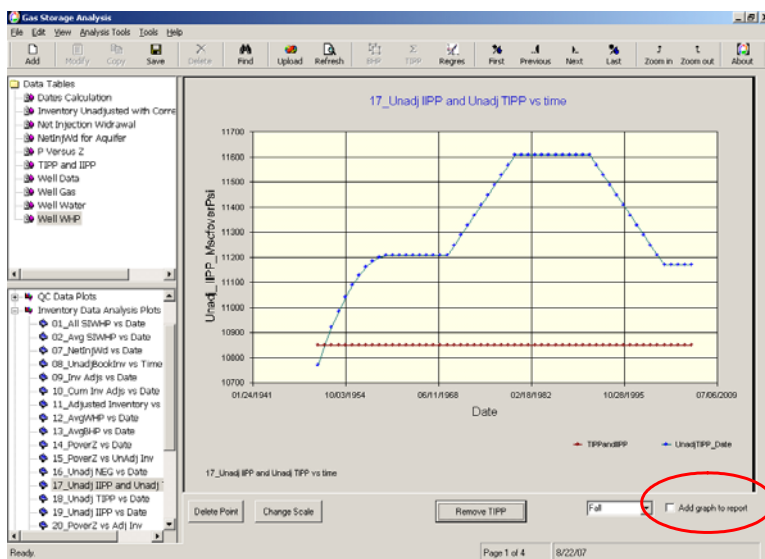
- 80 MMscf/yr loss 1950-1955 (Lost Volume = 400 MMscf)
- 35 MMscf/yr loss 1955-1960 (Lost Volume = 175 MMscf)
- No Losses 1960-1970 (Lost Volume = 0 MMscf)
- 50 MMscf/yr loss 1970-1980 (Lost Volume = 500 MMscf)
- No Losses 1980-1990 (Lost Volume = 0 MMscf)
- 50 MMscf/yr *gain* 1990-2000 (Lost Volume = -500 MMscf)
- No Losses 2000-2005 (Lost Volume = 0 MMscf)

Therefore, based on this analysis, the total net inventory lost over the time period 1950-2005 is 575 MMscf

4.6 Generating Reports

At the bottom right of each plot, there is a check box for the user to indicate if he wants that particular plot to be included in the report. By simply checking this box for the plots of interest, we can “collect” the plots we would like to include in this report.

For the purpose of this example, we will include all non-trivial plots in the report, so we will need to make sure each of these plots has the “Add Graph to Report” box checked. This would also be a good time to make sure all of the axes ranges are set appropriately. The figure below shows the location of the check box used to include plots in the report.



In addition, if the user has taken a few notes in a word processing document during the inventory analysis process (as recommended above), it is quite easy to merge the two documents into a final report that includes all of the pertinent plots used in the inventory analysis process. For the example problems, notes collected during the inventory analysis process might look something like the following:

QC Plots
None of the QC plots show any irregularities, so it is safe to assume that no problems were encountered during the calculation processes performed.

SIWHP vs Date Plots
The field has consistently been operated between 650 psi and 1000 psi throughout its life. Therefore, we do not have to worry about wide fluctuations in minimum and maximum operating pressures skewing trends in other diagnostic plots.

Unadjusted Inventory History
A plot of unadjusted inventory vs time is revealing, especially in light of how regularly the field was operated from a pressure perspective. This plot shows that various levels of inventory were required over the life of the field to achieve the same Spring and Fall shut-in pressures. This type of trend is a strong indicator, albeit a qualitative indicator, that there have been losses and gains occurring during over the life of storage operations

BHP/Z vs Unadj Book Inv
A plot of the unadjusted book inventory vs the BHP/Z shows movement to the right and left at various points during the life of storage operations, which leads us to the conclusion the losses and gains have occurred during storage operations. This is consistent with the qualitative conclusions drawn from a review of the operational plots (SIWHP vs Time and Unadjusted Book Inventory vs Time).

NEG History
The plot of Unadjusted NEG vs Date clearly indicates the time periods experiencing losses, gains, and stability.

IPP History Plots
A plot of IPP values vs time generated with Fall data points clearly shows the following:

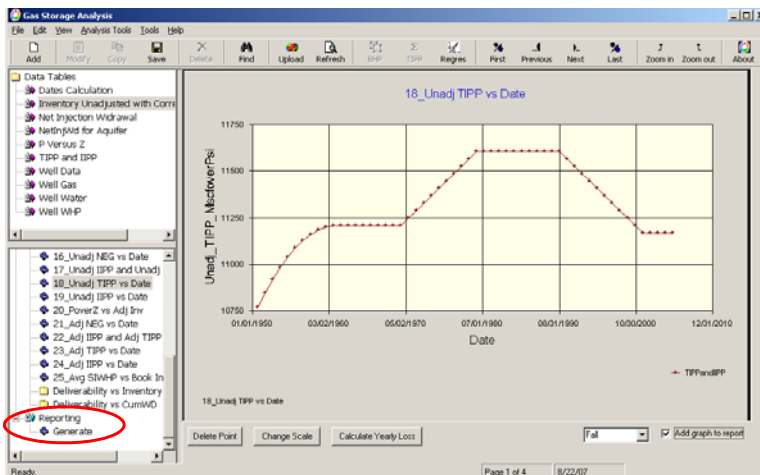
1. Non-linear increase in the TIPP w/Flat IIPP in 1950's (GAIN)
2. Flat TIPP and IIPP during 1960's (NO LOSS or GAIN)
3. Linear increase in the TIPP w/Flat IIPP in 1970's (LOSS)
4. Flat TIPP and IIPP during 1980's (NO LOSS or GAIN)
5. Non-linear decrease in the TIPP w/Flat IIPP in 1990's (GAIN)
6. Flat TIPP and IIPP from 2000-2005 (NO LOSS or GAIN)

Loss Calculations using the TIPP Plot
Loss rates and volumes were calculated using the TIPP plot generated with Fall only data points. The losses calculated using this plot can be summarized as follows:

- 80 MMscf/yr loss 1950-1955 (Lost Volume = 400 MMscf)
- 35 MMscf/yr loss 1955-1960 (Lost Volume = 175 MMscf)
- No Losses 1960-1970 (Lost Volume = 0 MMscf)
- 50 MMscf/yr loss 1970-1980 (Lost Volume = 500 MMscf)
- No Losses 1980-1990 (Lost Volume = 0 MMscf)
- 50 MMscf/yr gain 1990-2000 (Lost Volume = -500 MMscf)
- No Losses 2000-2005 (Lost Volume = 0 MMscf)

Therefore, based on this analysis, the total net inventory lost over the time period 1950-2005 is 575 MMscf

After checking the boxes on all of the charts you would like to be included in the report, go to the Workflow Window, expand the “Reporting” portion of tree directory to see the “Generate” option and click on the Generate option:



This will bring up a document preview window that will show all of the plots you have selected in thumbnail view. By clicking on the “Generate Report” button (see below), the information shown in thumbnail view will be exported to a WORD document for further editing.



After the report information was dumped to WORD and this file was opened, we opened the comments file we compiled during the analysis procedure (shown earlier). We then cut/pasted the information from the comments document into the WORD document, rearranged some information, added a report cover page.

The result is a first draft (or final draft, depending on requirements of the client) of an Inventory Analysis Report (see below):

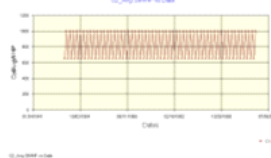
Gas Storage Inventory Analysis
Big Boy Field

Summary of Reservoir Information

Field Name	Example
Field Type	Dry Gas
Average Reservoir Depth (ft)	5000
Average Reservoir Temperature (F)	110
Wellhead Temperature (F)	60
Reservoir Top Pressure (psia)	1000
Reservoir Base Pressure (psia)	630
Gas specific gravity	0.38
Water specific gravity	1.05
Total Number of wells	1
BHP correlation	Cullender and Smith
z-factor correlation	Hall-Yarborough

Review of Data QC Plots
None of the QC plots show any irregularities, so it is safe to assume that no problems were encountered during the calculation process performed.

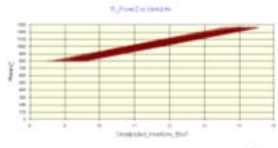
Review of Operational Plots
Based on a review of the SIWHP vs Date Plots, it is apparent that the field has consistently been operated between 630 psi and 1000 psi throughout its life. Therefore, we do not have to worry about wide fluctuations in minimum and maximum operating pressures skewing trends in other diagnostic plots.



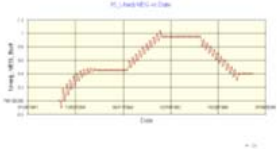
Based on a review of the unadjusted book inventory vs time, it is apparent that various levels of inventory were required over the life of the field to achieve the same Spring and Fall shut-in pressures. This type of trend is a strong indicator, albeit a qualitative indicator, that there have been losses and gains occurring during over the life of storage operations.



Review of Diagnostic Plots
Based on a review of the unadjusted book inventory vs the BHP/Z plot, it is apparent that movement has occurred to the right and left at various points during the life of storage operations. This suggests that losses and gains have occurred during storage operations. This is consistent with the qualitative conclusions drawn from a review of the operational plots (SIWHP vs Time and Unadjusted Book Inventory vs Time).

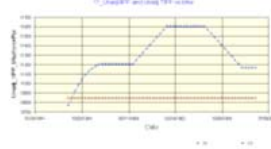


The plot of Unadjusted NEG vs Date clearly indicates the time periods experiencing losses, gains, and stability.



IPP History Plots
A plot of IPP values vs time generated with Fall data points clearly shows the following:

1. Non-linear increase in the TIPP w/Fall IPP in 1950's (GAIN)
2. Flat TIPP and IPP during 1960's (NO LOSS or GAIN)
3. Linear increase in the TIPP w/Fall IPP in 1970's (LOSS)
4. Flat TIPP and IPP during 1980's (NO LOSS or GAIN)
5. Non-linear decrease in the TIPP w/Fall IPP in 1990's (GAIN)
6. Flat TIPP and IPP from 2000-2005 (NO LOSS or GAIN)



Loss Calculations using the TIEPP Plot
Loss rates and volumes were calculated using the TIEPP plot generated with Fall only data points. The losses calculated using this plot can be summarized as follows:

- 80 MMcf/yr loss 1950-1955 (Lost Volume = 400 MMcf)
- 35 MMcf/yr loss 1955-1960 (Lost Volume = 175 MMcf)
- No Losses 1960-1970 (Lost Volume = 0 MMcf)
- 50 MMcf/yr loss 1970-1980 (Lost Volume = 500 MMcf)
- No Losses 1980-1990 (Lost Volume = 0 MMcf)
- 50 MMcf/yr gain 1990-2000 (Lost Volume = -500 MMcf)
- No Losses 2000-2005 (Lost Volume = 0 MMcf)



Based on this analysis, the total net inventory lost between 1950-2005 is 575 MMcf.

Appendix II
UGS Inventory Verification Primer

Table of Contents

1.	Introduction to Inventory Verification	3
1.1.	Objectives.....	3
1.2.	Theory	3
1.3.	Data Required	4
1.4.	Key or Indicator Wells	5
1.4.1.	Calculated Average Reservoir Pressure from Keywell SIWHP's	5
1.4.2.	Calculated Average Reservoir Pressures from IW Well SIWHP's	5
2.	Inventory Analysis Plots	6
2.1.	Plot of Basic Operational Data.....	6
2.2.	Gas Material Balance Plots: BHP/z vs Cum Production	7
2.3.	Pressure Content Plots – p/Z vs Inventory	8
2.4.	Inventory Per Pounds Plots	13
2.5.	Non-Effective Gas.....	17
2.6.	Pore Volume Ratio.....	18
2.7.	Inventory Variance From Material Balance.....	20
2.8.	Inventory Analysis in Aquifer Storage	20
2.9.	Inventory Analysis Nomenclature	22
3.	Example Problem.....	24
3.1.	Loading Data Into EXCEL™ Template	27
3.2.	Uploading Data into Software.....	32
3.3.	Browsing Data & Calculating BHP, p/z, and IPP Values.....	37
3.4.	Perusing HELP features and Using the ToolBox.....	40
3.5.	Performing Inventory Analysis.....	46
3.6.	Generating Reports.....	53
4.	References	57

1. Introduction to Inventory Verification

Inventory verification is a way to keep track of amount of gas in storage through analysis of shut-in well pressures and injection and withdrawal volumes

1.1. Objectives

The objectives of inventory verification include the following:

- To verify book inventory is actually present in the reservoir and available for withdrawal
- If gas has been lost, to determine its magnitude
- To monitor growth or shrinkage of gas bubble in aquifer storage

1.2. Theory

Traditional inventory verification techniques are based on the real gas law (note: aquifer storage fields may require different analysis techniques – see section 4 below)

$$p V = znRT$$

If pressure varies from point to point within the reservoir, may need to calculate average pressure from individual well pressures

$$p_{avg} = \frac{\sum p_i h_i A_i}{\sum h_i A_i}$$

Where

A_i	=	Drainage area of well i
h_i	=	Thickness of reservoir in drainage area of well i
p_i	=	Pressure of well i
p_{avg}	=	Average reservoir pressure

It is important to note that virtually all of the industry-standard inventory analysis techniques (except reservoir simulation) assume that the storage field is operated in a similar manner from year to year, and that shut-in pressures used in the calculations are stabilized. The results of these industry-standard inventory analysis techniques should be interpreted with caution if significant changes in operations occur from year to year and/or shut-in periods are not of sufficient length to ensure stable shut-in if pressures.

1.3. Data Required

The amount and types of data required for the inventory analysis process will vary, depending on the type of reservoir being analyzed (dry gas or aquifer). Generally, the primary types of data used in the inventory analysis process include:

- Static field/reservoir data, including:
 - Field Name
 - Field Type (Dry Gas or Strong Aquifer)
 - Reservoir Depth
 - Reservoir Temperature
 - Reservoir Pressures (Base Pressure and Top Pressure)
 - Specific Gravity (Gas and Water)
- Static well data, including:
 - Well ID
 - Well Name
 - Well Type
 - Weighting Factor used in average pressure calculations
 - Depth to reservoir at well location
- Dynamic well data, including
 - Shut-in Pressure for each well, for each shut-in event
- Dynamic field inventory data, including
 - Book Inventory (Uncorrected and Unadjusted) vs date
 - Historical Inventory Corrections vs date
 - Historical Inventory Adjustments vs date

1.4. Key or Indicator Wells

Often, one or more wells are designated as key wells

- Typically they remain shut-in
- No injection or withdrawal from these wells
- Best if not even tied into surface header, to avoid erroneous pressures:
 - Cannot leak from header into well
 - Cannot leak from well into header

The next best thing to a key well as described above is pseudo-key well:

- Typically shut-in for a period of time only *periodically* (e.g., weekly)
 - Injection or withdrawal from these wells occur between shut-in's
 - Must be tied into surface header

Selection of key well locations should be such that pressures are representative of average reservoir pressure. If no key wells are available in a field, the operator usually shuts-in all I/W wells each spring and fall for a period of time sufficient for pressure stabilization

The number and types of calculations made during the inventory analysis process will vary, depending on the type of reservoir being analyzed (dry gas or aquifer). In nearly all analyses, however, it is necessary to calculate the average reservoir pressure from raw wellhead pressure data. The two most common calculation methods used are discussed below.

1.4.1. *Calculated Average Reservoir Pressure from Keywell SIWHP's*

Usually, a keywell is located such that the bottom hole pressure calculated from the pressure observed in this well is considered representative of the average reservoir pressure. In the rare instances where an operator has more than one keywell, it may be necessary to calculate an average bottom hole pressure.

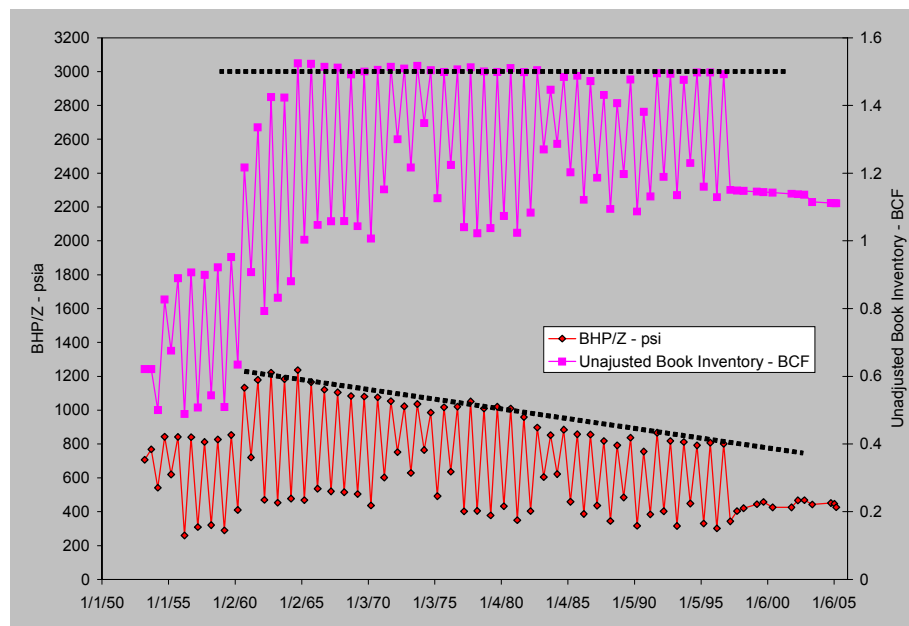
1.4.2. *Calculated Average Reservoir Pressures from IW Well SIWHP's*

In most storage fields, operators use wellhead pressures collected from IW wells at the end of spring and fall shut-in periods to estimate average reservoir pressure. In this case, an average shut-in wellhead pressure is calculated using individual well SIWHP values at the end of the shut-in period. This average shut-in wellhead pressure is then converted to a bottom hole pressure assumed to be representative of the average reservoir pressure. Either an arithmetic or a weighted average technique can be used, depending on the characteristics of the reservoir.

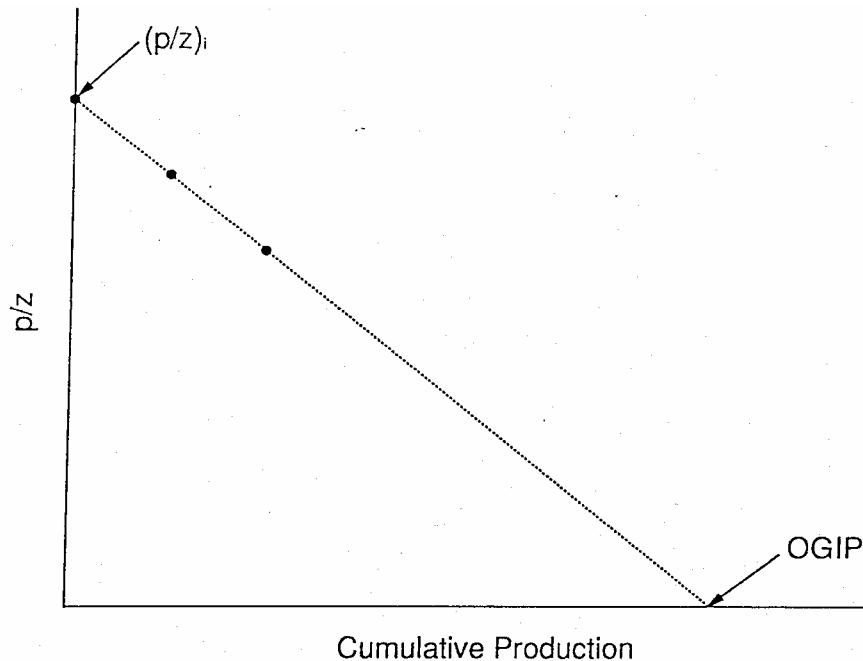
2. Inventory Analysis Plots

2.1. Plot of Basic Operational Data

- Review plots of operational data to
 - Identify any operational trends that may provide preliminary, qualitative indications of ongoing losses and
 - Show timeframes wherein we need to be careful analyzing data due to widely varying operational practices.
- Example of such a plot is the BHP/z vs Time and Unadjusted Book inventory vs time plots shown below. In this example plot, we see that:
 - Unadjusted book inventory is remaining relatively steady over time while
 - BHP/Z values are declining over time
- The trends in this example suggest that losses may be occurring.



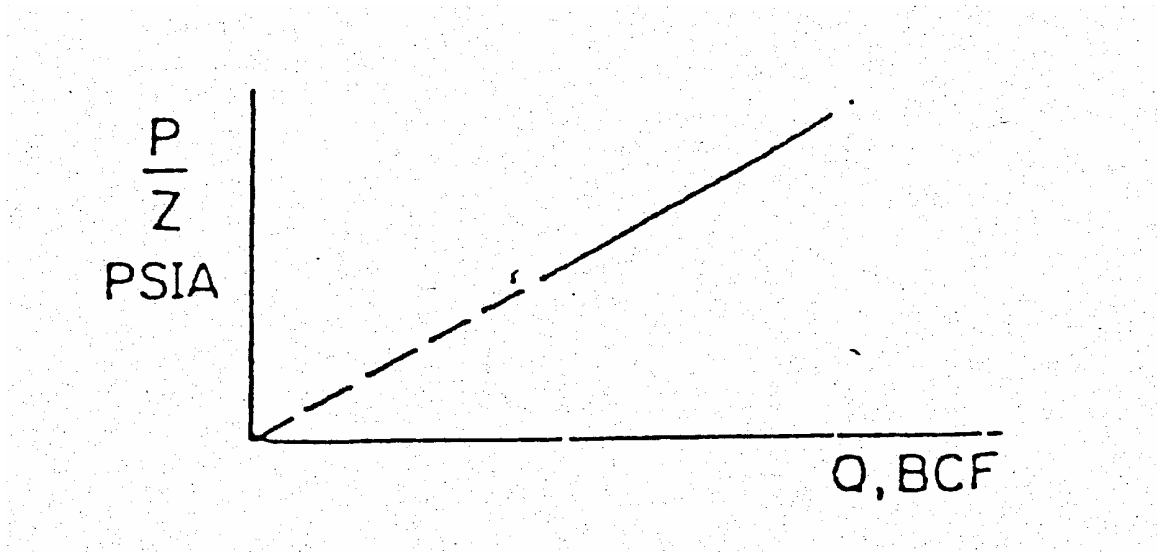
2.2. Gas Material Balance Plots: BHP/z vs Cum Production



Gas material balance performance during primary depletion of volumetric gas reservoir.

- Graph
 - p/Z from
 - Pressure survey
 - One or more key wells
 - Vs. Cumulative production
- Often used during primary production to
 - Determine drive mechanism
 - Estimate original gas-in-place (prior to conversion to storage, this estimated GIP volume is often presumed to be a reasonable estimate of the total top gas in storage at initial reservoir pressure)

2.3. Pressure Content Plots – p/Z vs Inventory



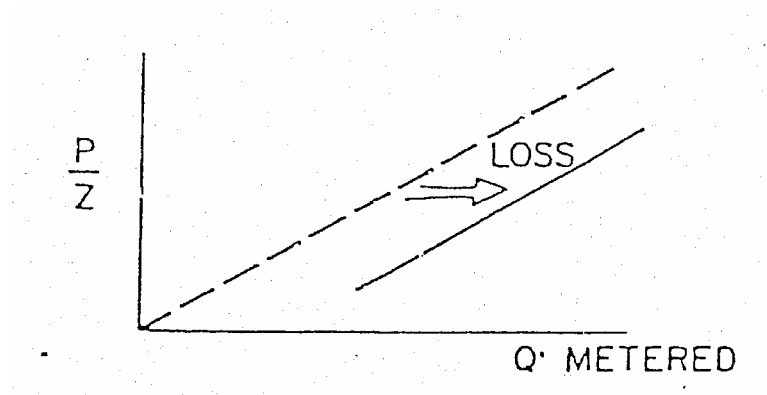
Pressure-content curve for a constant volume reservoir.

From Tek (1987).

- Graph
 - p/Z from
 - Pressure survey
 - One or more key wells
 - Vs. Inventory calculated from injection and withdrawal records (book inventory)

- Detection of Gas Loss

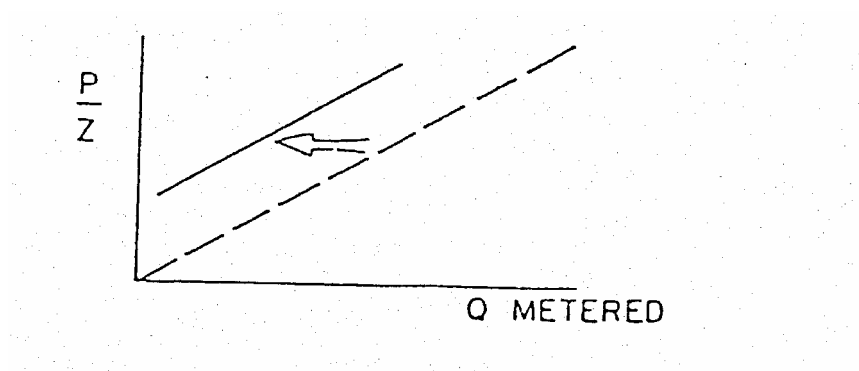
- Line moves to the right with time
- Changes in x-intercept indicate the amount of loss



Effect of finite gas loss. From Tek (1987).

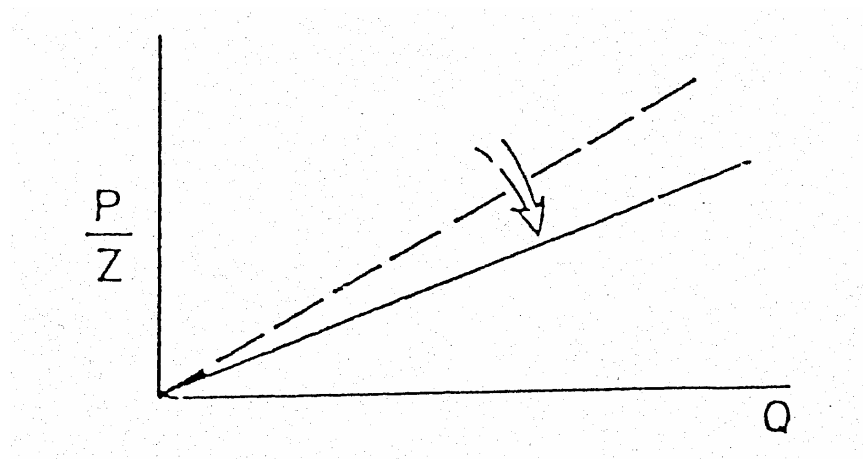
- Detection of Gas Gain

- This might occur for a collector zone
- Line moves to the left with time
- Changes in x-intercept indicate the amount of gain



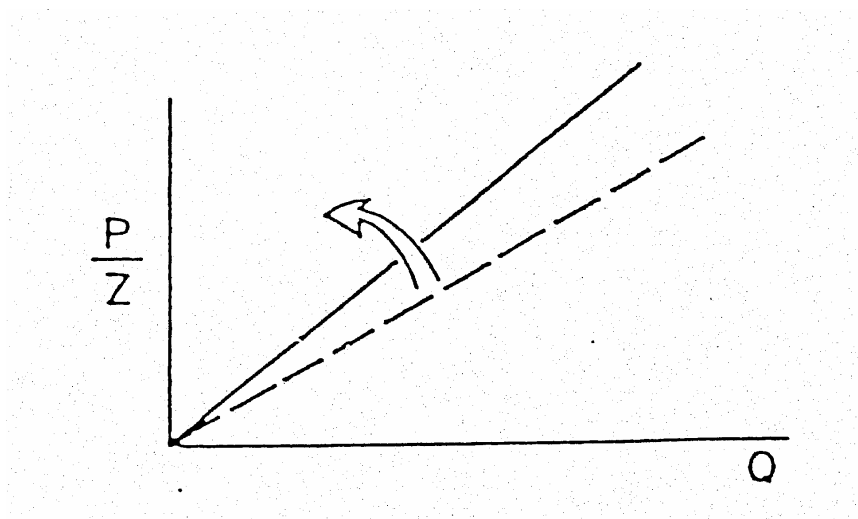
Effect of finite gas gain. From Tek (1987).

- Detection of Gas Bubble Growth
 - Slope of line decreases
 - x-intercept does not change



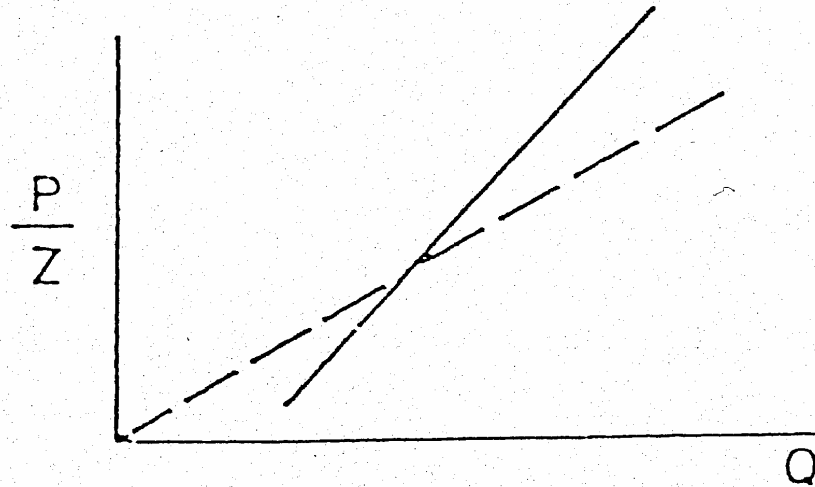
**Pressure-content curve for a reservoir subject to a volume increase.
From Tek (1987).**

- Detection of Gas Bubble Shrinkage
 - Slope of line increases
 - x-intercept does not change

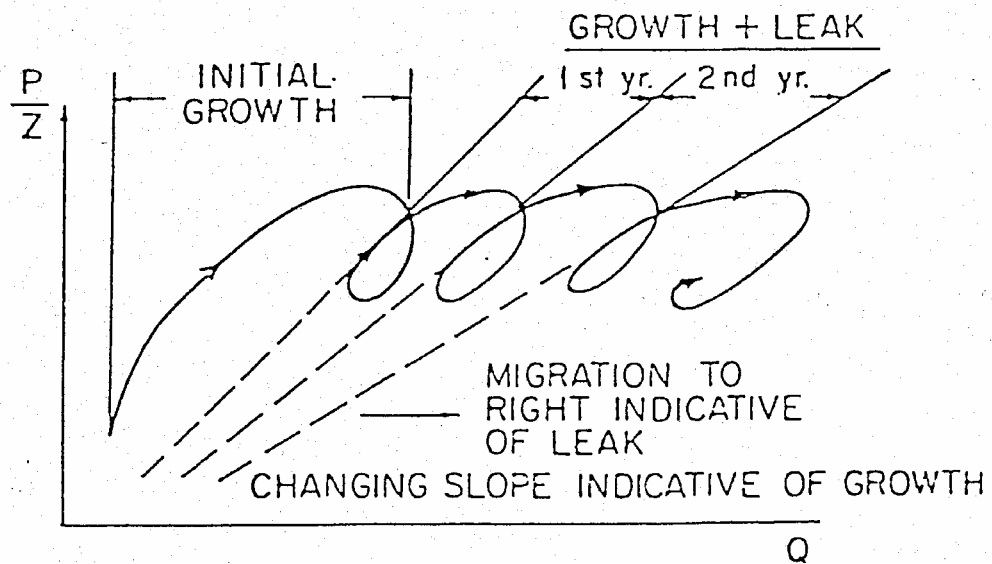


**Pressure-content curve for a reservoir subject to a volume decrease.
From Tek (1987).**

- Detection of Combinations: Gas loss or gain and gas bubble growth or shrinkage

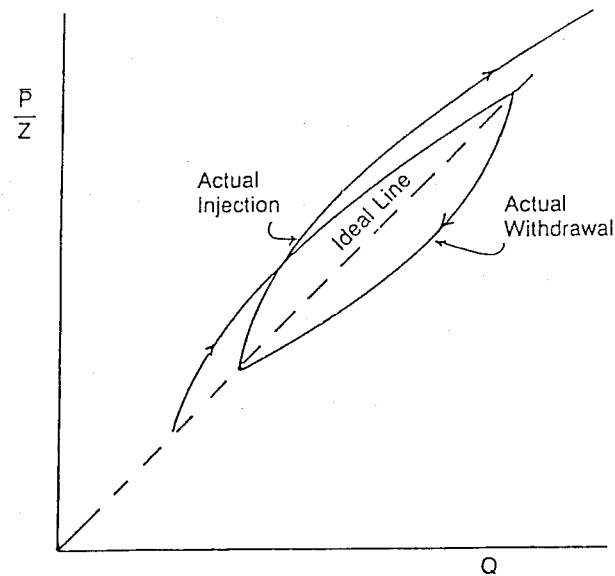


Pressure-content curve for a reservoir subject to a volume decrease and finite loss. From Tek (1987).



Pressure-content performance in an aquifer storage subject to growth and leak. From Tek (1987).

- Hysteresis Curves



Pressure-content pattern on a volumetric storage reservoir showing hysteresis.

From Tek (1987).

- Often, p/Z vs inventory plots exhibit higher pressures at a given inventory level during injection than at the same inventory level during withdrawal
 - This is caused by not having full pressure equilibrium in the reservoir
 - Following injection, measured wellbore pressure may still be higher than average reservoir pressure, even after 7 day shut-in
 - Following withdrawal, measured wellbore pressure likely to be lower than average reservoir pressure
- Contributing factors
 - Low permeability
 - Layering - presence of layers may require one or two orders of magnitude longer to reach equilibrium than homogeneous system with same average permeability
 - Water movement in the aquifer.

- Ways to minimize the effect
 - Allow adequate time for pressure to stabilize (may not be feasible)
 - Use pressures measured at observation wells which are not used for production
 - Use methods from pressure transient analysis to extrapolate pressure measurements to current average drainage area pressure

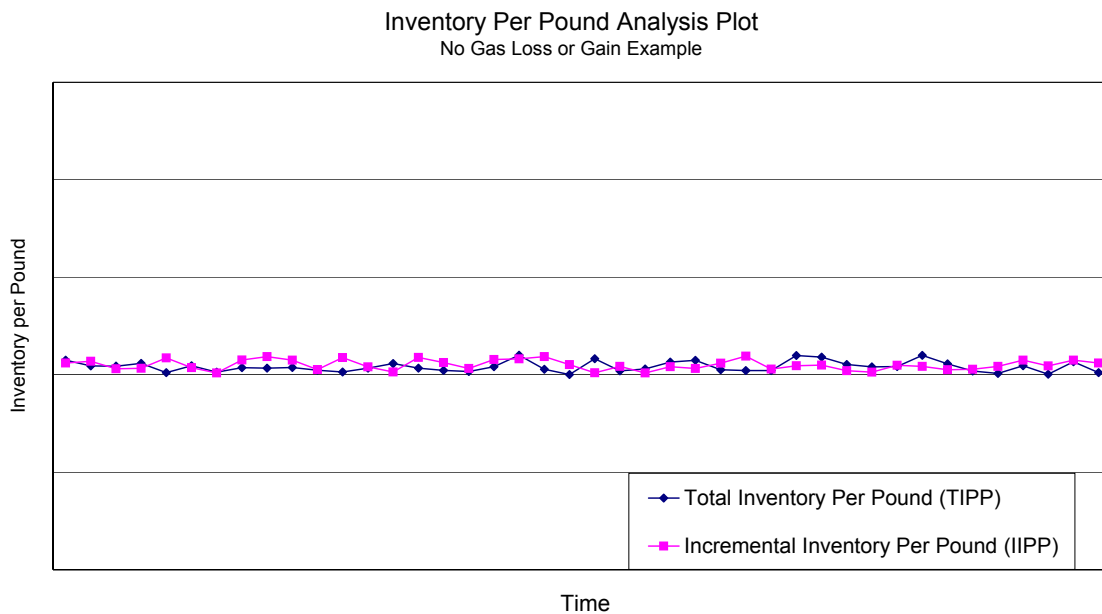
2.4. Inventory Per Pounds Plots

- Graph
 - Total inventory per pound: [(Book inventory) / (P/Z)] vs. Time
- $$TIPP = \frac{G_b}{p/z}$$
- where
 - TIPP = Total inventory per pound (total inventory per pressure unit)
 - G_b = Book inventory
 - p/z = Average pressure divided by real gas deviation factor
-
- Graph
 - Incremental inventory per pound vs. Time
 - (Change in book inventory) / (Change in p/z for INJ or WD season)] vs. Time

$$IIPP = \frac{(G_{bf} - G_{bs})}{\left(\left(\frac{p}{z} \right)_f - \left(\frac{p}{z} \right)_s \right)}$$

- where
 - IIPP = Incremental inventory per pound (pressure unit)
 - G_b = Book inventory
 - P/z = Average pressure divided by real gas deviation factor
 - s = Spring, following withdrawal season
 - f = Fall, following injection season

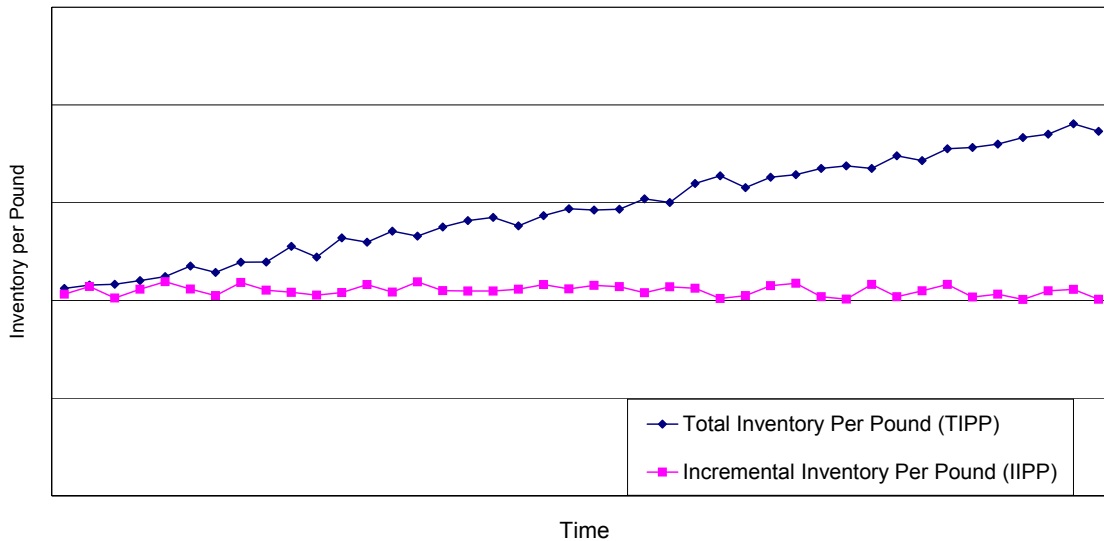
- Detection of constant volume reservoir
 - Total inventory per pound is constant with time
 - Incremental inventory per pound is also constant with time, and is approximately equal to the total inventory per pound



Example plot indicating no gas gains/losses

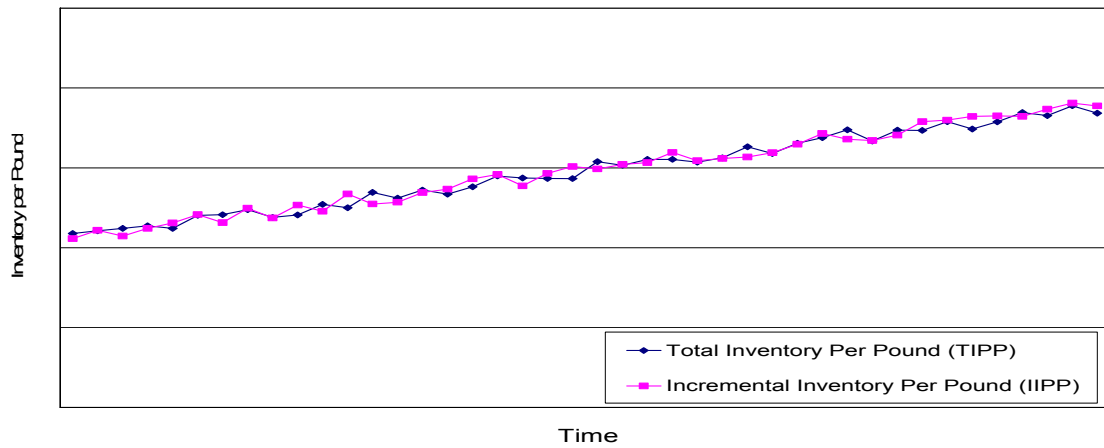
- Detection of gas bubble growth/gas loss
 - Total inventory per pound increases with time
 - Incremental inventory per pound
 - Constant with time indicates an on-going gas loss
 - Increasing with time indicates a growing gas bubble

Inventory Per Pound Analysis Plot
Ongoing Gas Loss Example



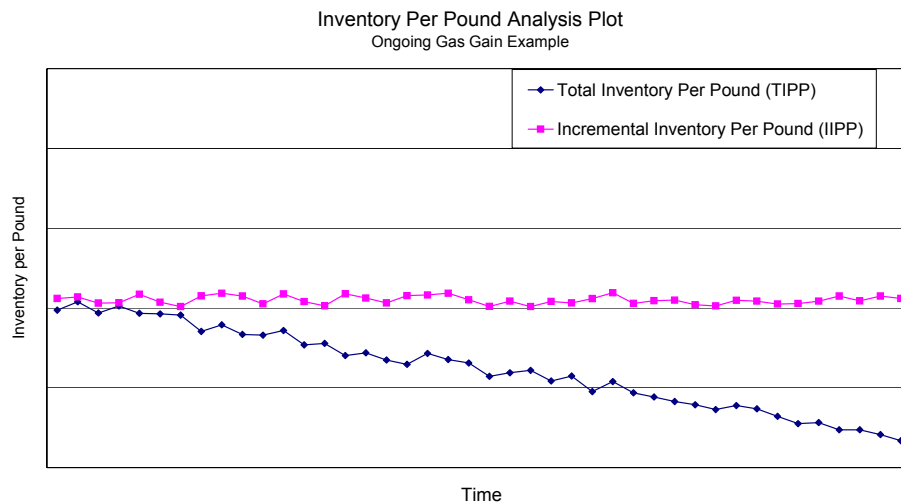
Example plot indicating ongoing gas losses

Inventory Per Pound Analysis Plot
Bubble Growth Example

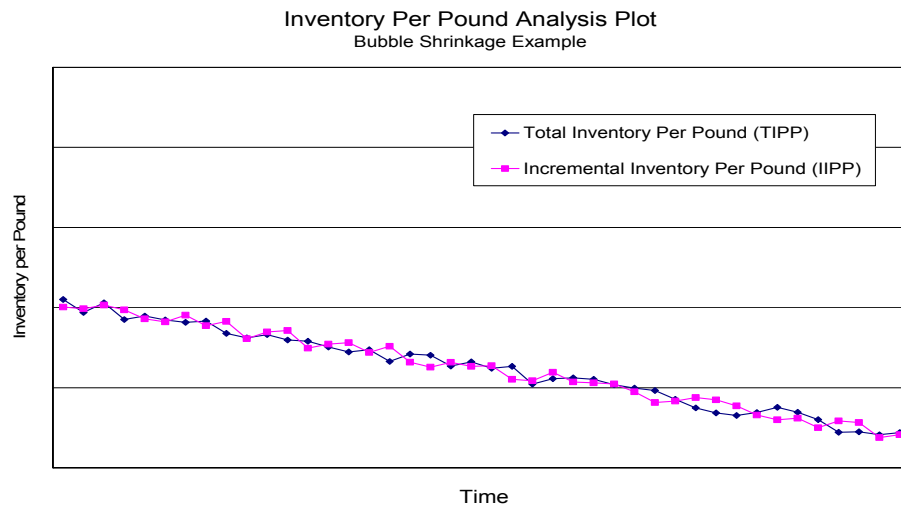


Example plot indicating bubble growth

- Detection of Gas bubble shrinkage/gas gain
 - Total inventory per pound decreases with time
 - Incremental inventory per pound
 - Constant with time indicates an on-going gas gain
 - Increasing with time indicates a shrinking gas bubble

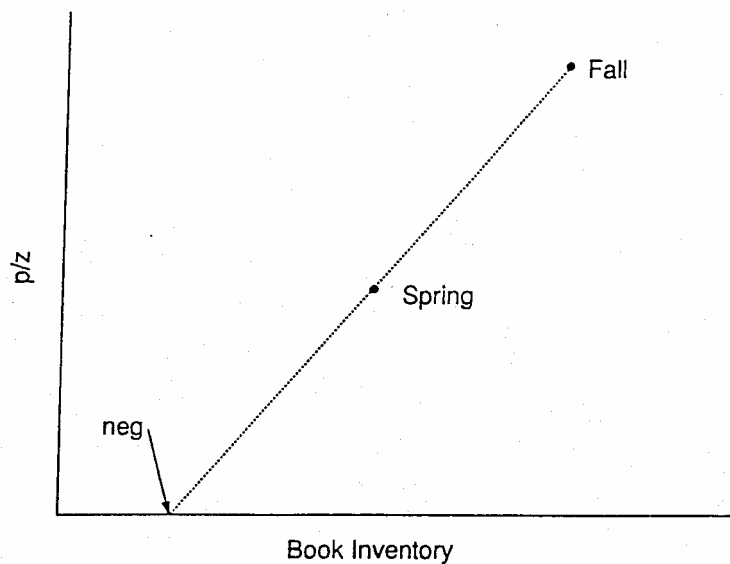


Example plot indicating ongoing gas gains



Example plot indicating bubble shrinkage

2.5. Non-Effective Gas



Extrapolation of fall-spring pressure content graph to zero p/z.

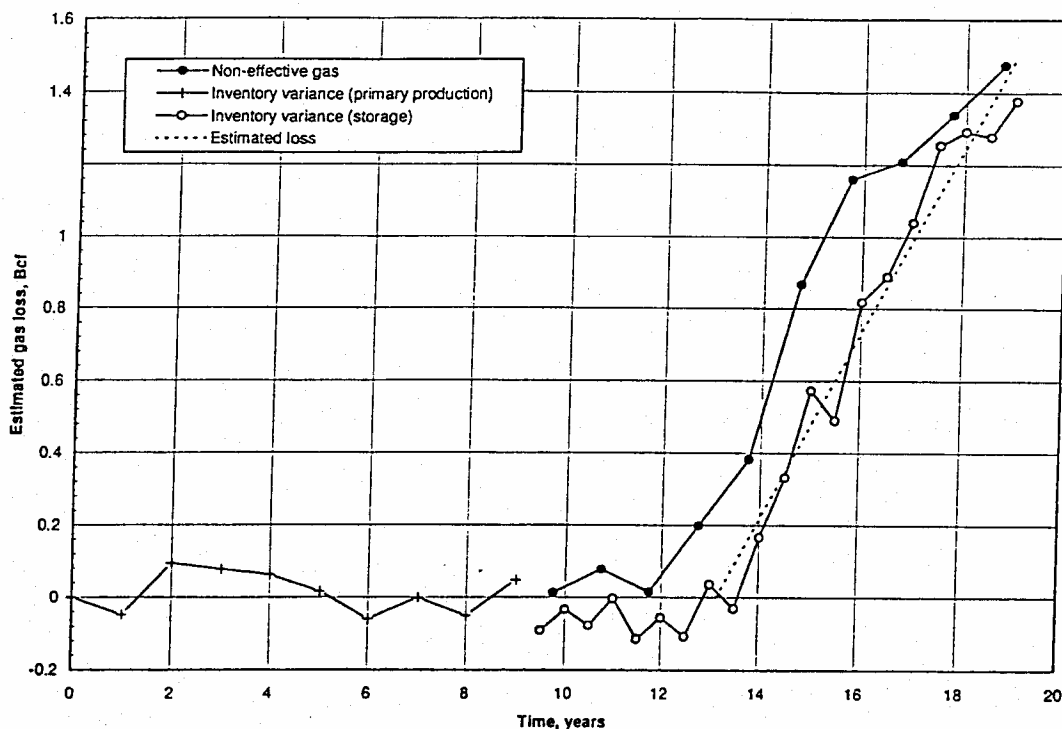
- Extrapolate fall-spring p/z vs. book inventory to p/z = 0

$$NEG = GIP_f - \left(\frac{p}{z}\right)_f \frac{(GIP_f - GIP_s)}{\left(\left(\frac{p}{z}\right)_f - \left(\frac{p}{z}\right)_s\right)}$$

where

- NEG = "Non-effective gas"
- GIP = Gas in place
- p/z = Average reservoir pressure divided by real gas deviation factor
- f = Fall conditions, at end of injection season
- s = Spring conditions, at end of withdrawal season

- Graph
 - Non-effective gas
 - vs. Time
- Gives direct estimate of total gas lost as a function of time



2.6. Pore Volume Ratio

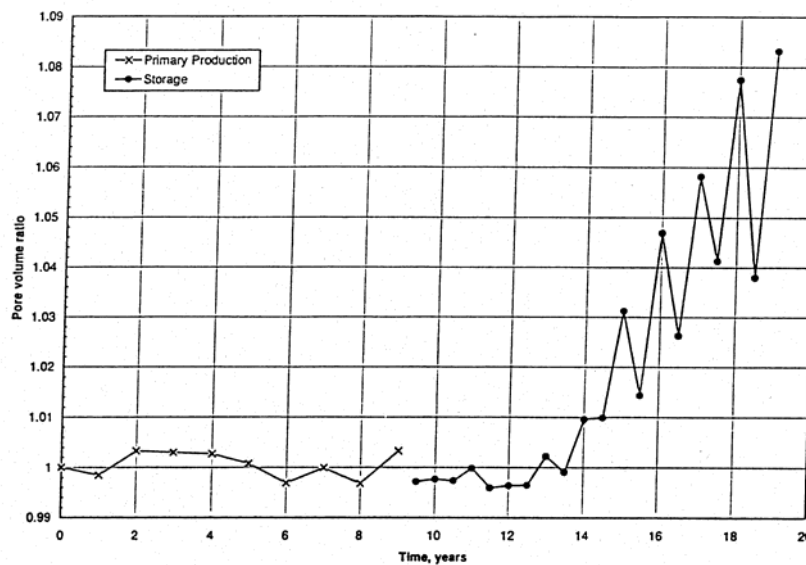
- Ratio of reservoir volume occupied by book inventory to original gas pore volume

$$PVR = \frac{\left(G_b / \left(\frac{P}{z} \right) \right)}{\left(G / \left(\frac{P}{z} \right)_i \right)}$$

Where

- PVR = Pore volume ratio
- G = Original gas in place
- G_b = Book inventory
- (p/z) = Conditions at time of Book inventory
- $(p/z)_i$ = Initial conditions

- Graph Pore volume ratio vs. Time
- Trends in the calculated PVR from unity indicate
 - Constant pore volume (PVR = 1)
 - Pore volume growth (PVR > 1.0)
 - Pore Volume shrinkage (PVR < 1.0)



Pore volume ratio.

Plot of pore volume ratio showing pore volume growth

2.7. *Inventory Variance From Material Balance*

- Difference between book gas-in-place and gas-in-place from material balance calculation

$$\text{Variance} = G_b - G \frac{(p/z)}{(p/z)_i}$$

where

G = Original gas in place

G_b = Book inventory

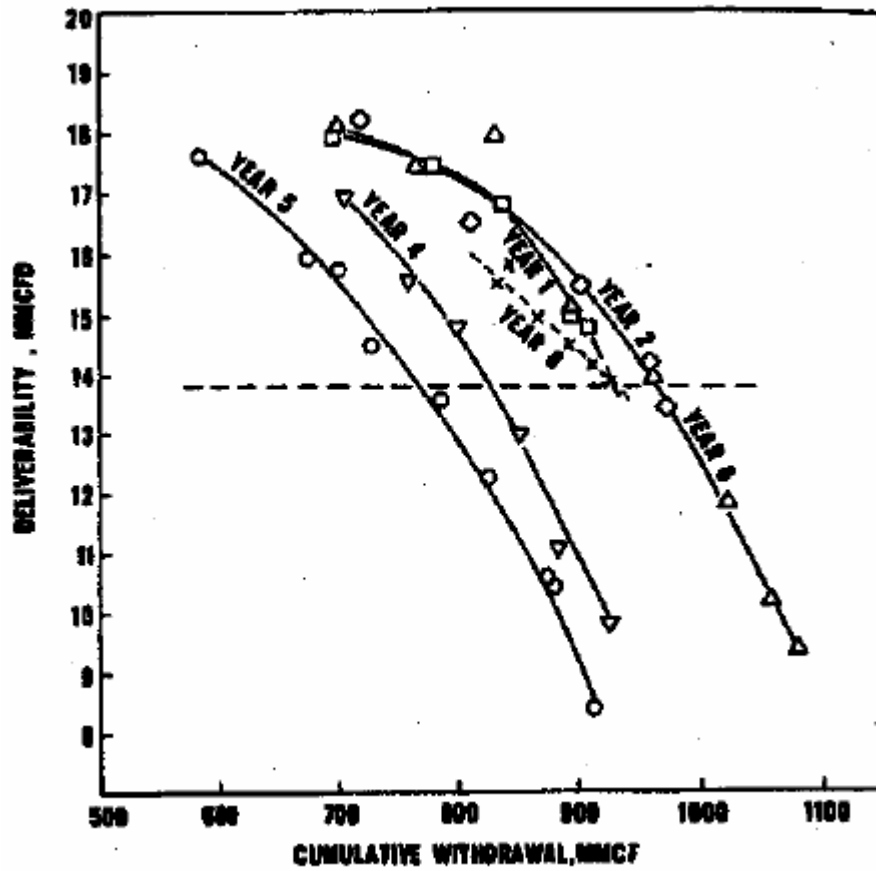
(p/z) = Conditions at time of Book inventory

$(p/z)_i$ = Initial conditions

- Graph Variance vs. Time
 - Gives direct estimate of total gas lost as a function of time
 - Very similar shape to non-effective gas graph

2.8. *Inventory Analysis in Aquifer Storage*

- A strong aquifer may provide enough pressure support that pressure content and inventory per pound plots cannot be used
- Graph Field deliverability vs. Cumulative seasonal withdrawal
 - If no loss is occurring, curves for consecutive seasons with overly each other
 - If there is loss, field deliverability will decrease at a given cumulative withdrawal with subsequent season



Plot of field deliverability vs. cumulative seasonal withdrawal indicating gas losses from Mayfield 1981

2.9. *Inventory Analysis Nomenclature*

For purposes of analysis techniques used in this software, we define the following terms:

Book Inventory

The book inventory at any point in time equals the estimated volume of gas in the reservoir at the time of conversion to storage, plus the cumulative net injected volume (cumulative net injected volume = total injections - total withdrawals). Caution should be exercised when evaluating data from storage operators, as the reporting of inventory is not standard between (and sometimes within) companies. For example, some report “Total **Injected** Book Inventory” (exclusive of native gas inventory), some report “Total **Working Gas** Inventory,” and others report “**Total Gas in Place** Inventory” (using estimated native gas volumes).

Book Inventory Adjustment

Book inventory adjustments represent corrections to inventory volumes, and are usually taken/booked at a discrete point in time on storage company ledgers. These adjustments could be taken to correct for lost volumes due to known causes (e.g., gas produced from a well initially thought to be isolated from the storage reservoir which is later determined to be in communication with the storage reservoir), or unknown causes (e.g., the inventory analysis process may indicate ongoing losses are occurring from an undetermined cause). In both cases a book inventory adjustment is typically made by the storage operator.

It should be noted that adjustments to book inventory are not typically spread over the timeframe of the loss, but usually show up at a specific point in time on the storage company’s ledger. A storage engineer performing inventory analysis may want to spread these adjustments over the time period during which the inferred losses are estimated to have occurred, in order to make the trends of the diagnostic plots used in inventory analysis consistent with the timing of the lost rates/volumes.

Non-Effective Gas

Non-Effective Gas (NEG) is gas inventory which has no observable impact on storage operations. The NEG volume usually manifests itself as an x-intercept on a plot of (Total GIP) vs (P/Z), where the Total GIP is plotted on the x-axis and the P/z is plotted on the y-axis. Non-effective gas may or may not be recoverable at the conclusion of storage operations, and therefore may or may not represent lost gas.

An example of *recoverable* non-effective gas may clarify the concept. There will often be a volume of gas that, over a \pm 50-yr primary production life of a gas field, can be removed from portions of the reservoir having lower permeability than the portion of the reservoir volume with higher permeability (containing most of the storage working gas volume during storage operations).

After conversion of the producing gas field to storage, it will take several cycles of higher average operating pressures to replace gas volumes depleted from tighter portions of the field during primary production. During this time period, gas that is initially injected into the high perm

portion of the reservoir during early storage operations can “leak” into the lower perm portion of the reservoir and be “stored” in the lower perm reservoir volumes. Because these volumes have lower permeabilities, the gas cannot be effectively removed within the very short withdrawal periods associated with storage operations. Hence, from a P/z-analysis standpoint, it appears that these gas volumes are not present in the reservoir. Hence the term, “Non-Effective.”

Note that not all NEG is recoverable, as lost gas is also non-effective during storage operations.

3. Example Problem

In this section of the manual, we will walk the user through a typical Inventory Analysis (IA) process using the example data below.

The Big Boy Field is a single-well dry gas field that produced from 1925 to 1940. The field remained shut-in from 1940-1949, at which time it was converted to storage (no additional wells were drilled). It has been an active storage facility since 1950. The storage reservoir is known to have a small layer of lower permeability formation within the storage interval.

Historically, the storage field has operated between a minimum shut-in wellhead pressure of 650 psig and a maximum shut-in wellhead pressure of 1000 psig. Each Spring and Fall during storage operations, the operator measured the shut-in wellhead pressure in one IW well (Well ID 1) that is completed in the storage reservoir. The depth to the reservoir in this well is 5000 ft. The average wellhead temperature is 60 degrees F and the average reservoir temperature is 110 degrees F. Gas gravity is 0.58.

There is 1 mile of new (at conversion) 3" ID gathering line in the field. This line has custody transfer measurement facilities where it connects to a sales line that operates at 500 psi. From 1990 to 2000, separate measurement devices were "temporarily" installed at the sales lines to measure injected volumes. In 2000, this temporary injection measurement facility was removed.

Each year, when the wellhead pressures reach 700 psi, the one IW well is tested. During this test, the gas is vented into the atmosphere. These annual tests consist of three 15-minute flow periods (100 mscf/d, 200 mscf/d and 300 mscf/d) followed by a 45 minute extended flow (400 mscf/D).

At the end of withdrawal each year, a downhole camera is run in the IW well. Prior to running the camera, a bridge plug is set just above the bottom of the tubing (3" ID). There is a sealing packer at the bottom of the tubing, which is run inside casing (6" ID). Also at the end of withdrawal each year, the gathering line is blown down and pigged.

The Spring and Fall shut-in wellhead pressures recorded at the IW well and the corresponding unadjusted book inventory values are shown in the table on the following page.

Example Problem
Inventory Assessment Data

Date	Unadjusted Inventory (Bscf)	SIWHP psig
3/15/50	10.000000	650
9/15/50	15.000000	1000
3/15/51	10.100000	650
9/15/51	15.100000	1000
3/15/52	10.190000	650
9/15/52	15.190000	1000
3/15/53	10.270000	650
9/15/53	15.270000	1000
3/15/54	10.340000	650
9/15/54	15.340000	1000
3/15/55	10.400000	650
9/15/55	15.400000	1000
3/15/56	10.450000	650
9/15/56	15.450000	1000
3/15/57	10.490000	650
9/15/57	15.490000	1000
3/15/58	10.520000	650
9/15/58	15.520000	1000
3/15/59	10.540000	650
9/15/59	15.540000	1000
3/15/60	10.550000	650
9/15/60	15.550000	1000
3/15/61	10.550000	650
9/15/61	15.550000	1000
3/15/62	10.550000	650
9/15/62	15.550000	1000
3/15/63	10.550000	650
9/15/63	15.550000	1000
3/15/64	10.550000	650
9/15/64	15.550000	1000
3/15/65	10.550000	650
9/15/65	15.550000	1000
3/15/66	10.550000	650
9/15/66	15.550000	1000
3/15/67	10.550000	650
9/15/67	15.550000	1000
3/15/68	10.550000	650
9/15/68	15.550000	1000
3/15/69	10.550000	650
9/15/69	15.550000	1000
3/15/70	10.600000	650
9/15/70	15.600000	1000
3/15/71	10.650000	650
9/15/71	15.650000	1000
3/15/72	10.700000	650
9/15/72	15.700000	1000
3/15/73	10.750000	650
9/15/73	15.750000	1000
3/15/74	10.800000	650
9/15/74	15.800000	1000
3/15/75	10.850000	650
9/15/75	15.850000	1000
3/15/76	10.900000	650
9/15/76	15.900000	1000
3/15/77	10.950000	650
9/15/77	15.950000	1000
3/15/78	11.000000	650
9/15/78	16.000000	1000
3/15/79	11.050000	650
9/15/79	16.050000	1000
3/15/80	11.050000	650
9/15/80	16.050000	1000
3/15/81	11.050000	650
9/15/81	16.050000	1000
3/15/82	11.050000	650
9/15/82	16.050000	1000
3/15/83	11.050000	650
9/15/83	16.050000	1000
3/15/84	11.050000	650
9/15/84	16.050000	1000
3/15/85	11.050000	650
9/15/85	16.050000	1000
3/15/86	11.050000	650

Using the example data provided above:

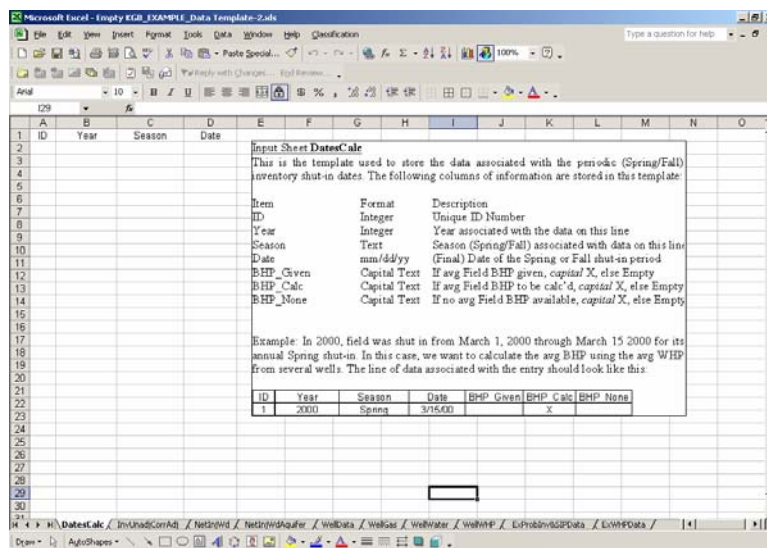
- Load pertinent data into the EXCEL template
- Upload this data into the software
- Browse the data tables using the software
- Calculate BHP and BHP/Z values using the software
- Calculate TIPP and IIPP values using the software
- Peruse the various help features:
 - Open the Inventory Analysis Primer and peruse the document.
 - Open the Toolbox peruse the spreadsheet
 - Open the Help for input document and peruse the document.
 - Open the Help for analysis plots document and peruse the document.
 - Open the Storage Terms and peruse the document.
 - Open the Glossary and peruse the document.
 - Open the Summary of References and peruse the document.
- Browse the available analysis plots
- Review/Analyze appropriate diagnostic plots to calculate the inventory loss rates and volumes where appropriate
- Comment on the nature of the losses.
- Use the toolbox to determine if the losses can be reasonably explained by:
 - Line losses
 - Annual pigging of gathering lines
 - Annual well testing operations
 - Downhole camera Operations
- Select several plots for inclusion in a report and generate a draft report

3.1. Loading Data Into EXCEL™ Template

The first thing that needs to be done in any inventory analysis that utilizes the newly developed software is to reformat/reorganize the inventory data supplied by the operator. Generally, this is a fairly straightforward process, and simply involves cut/copy and paste commands within EXCEL, and perhaps some simple calculations within EXCEL to fill in necessary columns of input data.

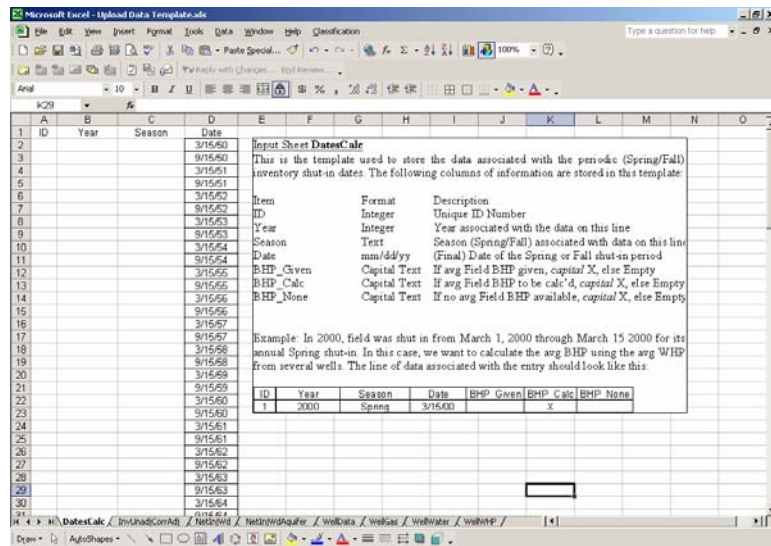
We have installed the inventory analysis software on the D Drive, under the subdirectory called “Program Files.” During the installation process, a subdirectory is created under the “Program Files” subdirectory called “EXCEL Template.” In this subdirectory are several EXCEL files, including one named “Ex_Prob_Raw_Data.xls” in which is stored the raw data as collected by the operator. This file consists of a single sheet of data as shown above (see page with heading Example Problem Inventory Assessment Data). Open this file.

The EXCEL template used to import data into the software is in the same location, and is named “Upload Data Template.xls.” Open this file also. The first sheet in the file (“DatesCalc”) looks like this:

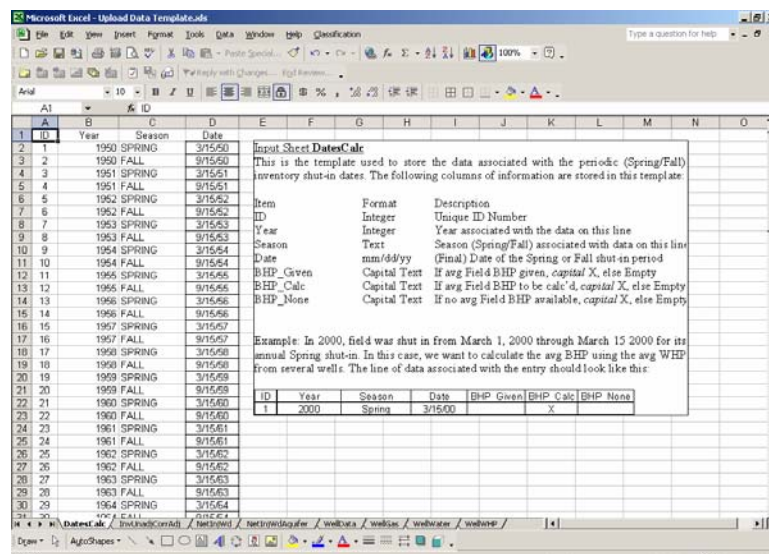


To populate this sheet, we will perform the following steps:

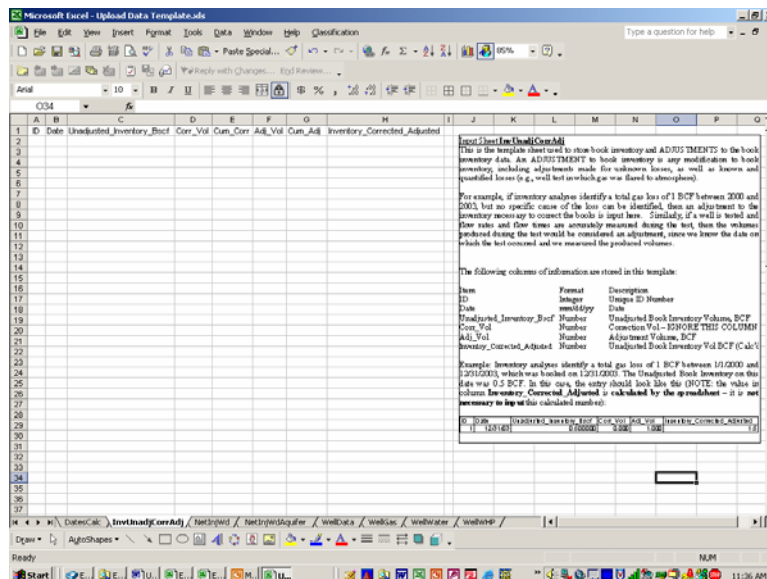
1. Copy data from cells A2–A113 in the raw data file (Ex_Prob_Raw_Data.xls) and past these values into Cells B2 – B113 in Sheet DatesCalc, in Excel template file (Upload Data Template.xls). Sheet DatesCalc in the “Upload Data Template.xls” should now look like this:



- The **ID** column in this spreadsheet is simply a unique integer, or “auto-number,” which we can populate by inputting a 1 in cell A2 and copying a formula in cells A3-A113 that adds one to the integer directly above it.
- The **Year** column in this spreadsheet can be calculated using the YEAR function in EXCEL, using the date in column D as the input. For example cell B2 would contain the formula “Year(D2).” This formula can then be copied to D3-D113 to populate the remaining cells.
- The **Season** column in this spreadsheet can be calculated using a conditional statement in EXCEL, using the date in column D as the input. For example cell C2 would contain the formula “IF(MONTH(D2)<6,"SPRING","FALL").” This formula can then be copied to D3-D113 to populate the remaining cells. Sheet DatesCalc in the “Upload Data Template.xls” is now populated and should now look like this:



The second sheet in “Upload Data Template.xls file (“InvUnadjCorrAdj”) looks like this:



To populate this sheet, we will perform the following steps:

1. Copy the date and book inventory values from cells A2–B113 in the raw data file (Ex_Prob_Raw_Data.xls) and past these values into Cells B2–C113 in Sheet “InvUnadjCorrAdj”, in Excel template file (Upload Data Template.xls).
2. The **ID** column in this spreadsheet is simply a unique integer, or “auto-number,” which we can populate by inputting a 1 in cell A2 and copying a formula in cells A3–A113 that adds one to the integer directly above it.
3. **Corr_Vol, Cum_Corr, Adj_Vol, Cum_Adj, and Inventory_Corrected_Adjusted** columns in this spreadsheet are used to store corrections and/or adjustments and store the calculated values of cum corrections, cum adjustments, and corrected adjusted book inventory. In this example, there are no corrections or adjustments to the book inventory, so all of these columns can be populated with zero’s. Note the following about this input sheet:
 - a. Although there are columns to input both “corrections” and “adjustments,” the “corrections” columns are included in anticipation of a software upgrade wherein a distinction between a correction and an adjustment can be made. When using the current version of the software, input all changes made to the book inventory as adjustment.
 - b. The values in columns labeled **Cum_Corr, Cum_Adj, and Inventory_Corrected_Adjusted**, are calculated within the software, and therefore zeros can be entered at this point

4. Sheet **InvUnadjCorrAdj** in the “Upload Data Template.xls” is now populated with data and should look like this:

A	B	C	D	E	F	G	H	I	J	K	L
1	ID	Date	Unadjusted_Inventory_Bscf	Corr_Val	Cum_Corr_Adj_Val	Cum_Adj	Inventory_Corrected	Adjusted			
2	1	3/15/50	8.500000	0	0	0	8.500				
3	2	9/15/50	13.500000	0	0	0	13.500				
4	3	3/15/51	8.600000	0	0	0	8.600				
5	4	9/15/51	13.600000	0	0	0	13.600				
6	5	3/15/52	8.690000	0	0	0	8.690				
7	6	9/15/52	13.690000	0	0	0	13.690				
8	7	3/15/53	8.770000	0	0	0	8.770				
9	8	9/15/53	13.770000	0	0	0	13.770				
10	9	3/15/54	8.840000	0	0	0	8.840				
11	10	9/15/54	13.840000	0	0	0	13.840				
12	11	3/15/55	8.900000	0	0	0	8.900				
13	12	9/15/55	13.900000	0	0	0	13.900				
14	13	3/15/56	8.990000	0	0	0	8.990				
15	14	9/15/56	13.990000	0	0	0	13.990				
16	15	3/15/57	8.990000	0	0	0	8.990				
17	16	9/15/57	13.990000	0	0	0	13.990				
18	17	3/15/58	9.020000	0	0	0	9.020				
19	18	9/15/58	14.020000	0	0	0	14.020				
20	19	3/15/59	9.040000	0	0	0	9.040				
21	20	9/15/59	14.040000	0	0	0	14.040				
22	21	3/15/60	9.050000	0	0	0	9.050				
23	22	9/15/60	14.050000	0	0	0	14.050				
24	23	3/15/61	9.050000	0	0	0	9.050				
25	24	9/15/61	14.050000	0	0	0	14.050				
26	25	3/15/62	9.050000	0	0	0	9.050				
27	26	9/15/62	14.050000	0	0	0	14.050				
28	27	3/15/63	9.050000	0	0	0	9.050				
29	28	9/15/63	14.050000	0	0	0	14.050				
30	29	3/15/64	9.050000	0	0	0	9.050				
31	30	9/15/64	14.050000	0	0	0	14.050				

No data was supplied in the example problem for the next two Sheets in the input template (**NetInjWd** and **NetInjWdAquifer**), so these will remain blank.

The **WellData** sheet contains information related to the one IW well. To populate this sheet, we will perform the following steps:

1. The **ID** column in this spreadsheet is simply a unique integer, or “auto-number,” which we can populate by inputting a 1 in cell A2 and copying a formula in cells A3-A113 that adds one to the integer directly above it.
2. The **Well_ID** column contains a unique identifier for each well, and has the format of an integer. We identified the well in which the shut-in wellhead pressure is measured each spring and Fall as Well 1, so we will use a **Well_ID** of 1 to identify the well.
3. The **Resv_Depth** column contains the depth (TVD) to the reservoir in the well, which was given as 5000 ft.
4. The **X** and **Y** columns contains well location information for use in future upgrades and is not used in this version of the software. You can enter any number in these columns you want, as they are not used.

The **WellData** sheet is now populated with data and should look like this:

Item	Format	Description
Well ID	Text	Name of the Storage Well
Well Type	Text	Well Type (IW, OB, ...)
Well Wt Fact	Number	Well Weighting Factor for
Resv Depth	Number	True Vert Depth to Storage
X	Number	X-Coordinate of Well Loc.
Y	Number	Y-Coordinate of Well Loc.

Well ID	Well Type	Well Wt Fact	Resv Depth	X	Y
3625	IW	1	2082	1	7
3667	IW	1	3092	1	8
3684	OB	1	3088.5	1	8

No data was supplied in the example problem for the next two Sheets in the input template (**WellGas** and **WellWater**), so these will remain blank.

The last sheet in “Upload Data Template.xls file (“WellWHP”) looks like this:

Item	Format	Description
ID	Integer	Unique Identifier
Well ID	Text	Name of the Storage Well
Date	mm/dd/yy	Date of recorded wellhead pr
WHP_psig	Number	Measured wellhead pressure
Comment	Text	Comment
Calc_BHP	Number	Calc'd BHP (if given)

ID	Well ID	Date	WHP_psig	Comments	Calc_BHP
1	3003	9/15/50	44		0
2	3209	9/15/50	35		0
3	3605	9/15/50	36		0
4	3667	9/15/50	164		0

To populate this sheet, we will perform the following steps:

1. Copy the Date and SIWHP in cells A2–A113 and cells C2–C113 in the raw data file (Ex_Prob_Raw_Data.xls) and past these values into cells C2–C113 and cells D2–D113 respectively in Sheet “SIWHP”, in Excel template file (Upload Data Template.xls).

- The **ID** column in this spreadsheet is simply a unique integer, or “auto-number,” which we can populate by inputting a 1 in cell A2 and copying a formula in cells A3-A113 that adds one to the integer directly above it.
- The **Well_ID** column should contain the Well_ID from the single well shown in sheet “WellID”
- The **Comments** column can contain any text you wish to input. We will not input any comments in our file, so all rows under the header row in this sheet should be left blank.
- The **Given_BHP** column is not used in this version of the software, and should be populated with zeros.
- The **CalcBHP** column contains output calculated by the software after data is imported and should therefore contain all zeros at this point.
- Sheet **SIWHP** in the “Upload Data Template.xls” is now populated with data and should look like this:

Input Sheet WellWHP

This is the template used to store individual wellhead pressure data.

The following columns of information are stored in this template:

Item	Format	Description
ID	Integer	Unique Identifier
Well ID	Text	Name of the Storage Well
Date	mm/dd/yy	Date of recorded wellhead pr
WHP_psig	Number	Measured wellhead pressure
Comment	Text	Comment
Calc_BHP	Number	Calc'd BHP (if given)

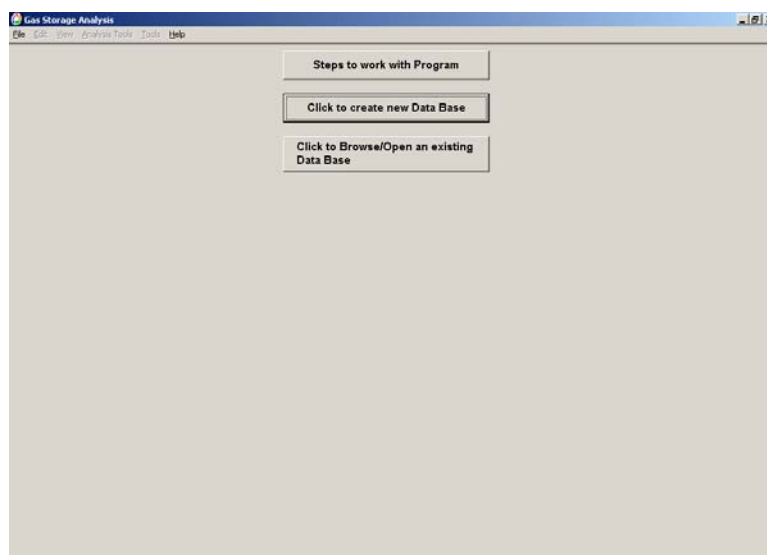
Example: Field has four IW wells. In this case, the entry might look like this (in date):

ID	Well ID	Date	WHP_psig	Comments	Calc_BHP
1	3003	9/15/50	44		0
2	3002	9/15/50	35		0
3	3665	9/15/50	38		0
4	3667	9/15/50	164		0

3.2. Uploading Data into Software

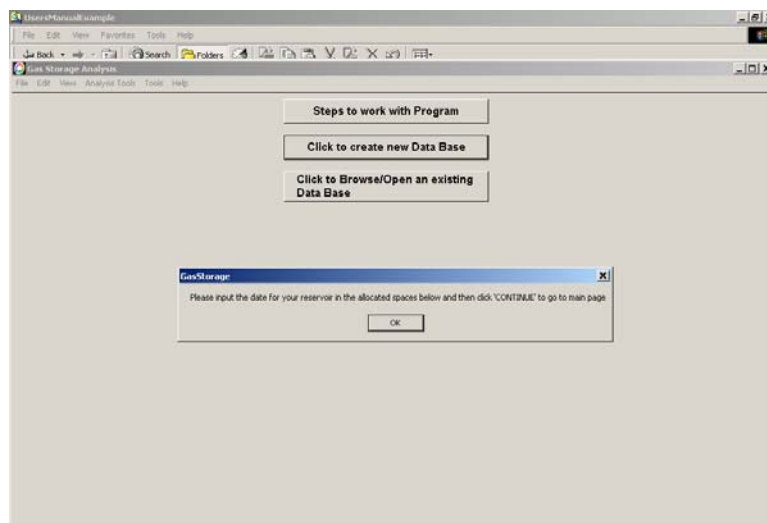
You have now completed populating the EXCEL file originally named, “Upload Data Template.xls.” It is now time to save this file using a different name, in a location you will remember. In this example, we will save the file in the same subdirectory as the Input Data Template was located (i.e., the subdirectory created on the D drive upon installation of the software, D:\Program Files\Gas Storage Software\Excel Template\) and name it KGB_EXAMPLE_Data Template-2.xls.

To upload this data into the IAS, open/start the software. The first screen you will see looks as follows:



Select the button **Click to create New Database**, and use the dialogue box that appears to name the ACCESS file that will be created to contain your uploaded data, in a location of your choice. In this example, we will create an ACCESS file named “KGB_Example-2.mdb” in the same subdirectory that the Input Data Template was located (i.e., the subdirectory created on the D drive upon installation of the software (D:\Program Files\Gas Storage Software\Excel Template\)) and name it KGB_EXAMPLE_Data Template-2.xls.

After inputting the name you wish for the ACCESS database to be created, you will see the following dialogue box:



After you click OK, you will proceed to the reservoir data input screen, which looks as follows:

Reservoir Data

Name Of Storage Field:

Field Type:

Average Reservoir Depth:

Average Reservoir Temperature:

Wellhead Temperature:

Reservoir Top Pressure:

Reservoir Base Pressure:

Gas Specific Gravity:

Water Specific Gravity:

Total Number of Wells:

BHP Correlation:

Z Factor:

Buttons:

Populate the fields as shown in the following slide:

Reservoir Data

Name Of Storage Field:

Field Type:

Average Reservoir Depth:

Average Reservoir Temperature:

Wellhead Temperature:

Reservoir Top Pressure:

Reservoir Base Pressure:

Gas Specific Gravity:

Water Specific Gravity:

Total Number of Wells:

BHP Correlation:

Z Factor:

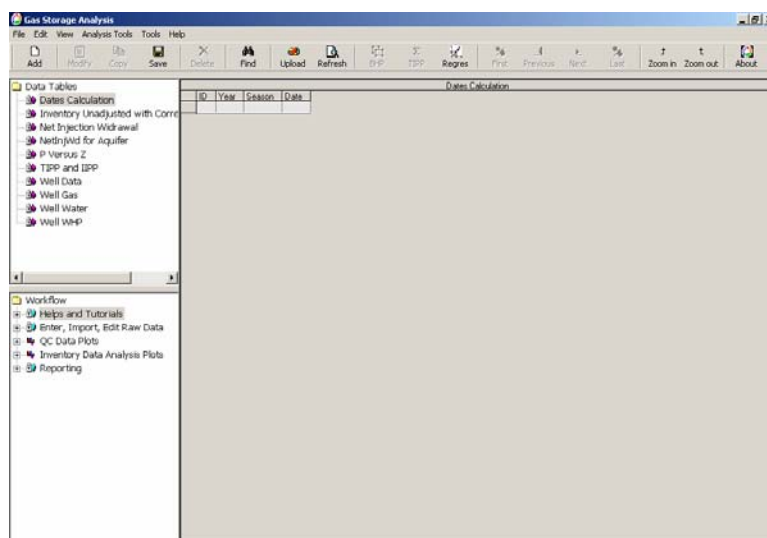
Buttons:

Note the following:

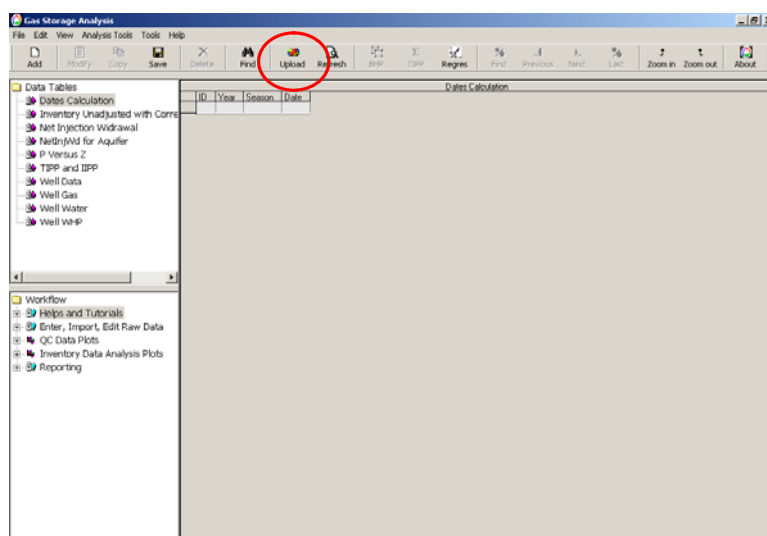
1. The average reservoir depth entered here is NOT the depth used to calculate SIBHP's from SIWHP's. We anticipate using this field in a later version of the software (allowing the user calculate all BHP's at the average reservoir depth or at the reservoir depth in each individual well). The depth associated with each individual well (entered on **WellData** sheet) is used to calculate BHP's from WHP's in each well.

2. Values entered for Reservoir Top and Base pressures are not used in this software version. We anticipate using them in later versions of the software. Values should be entered, but will not be used in the current software version.
3. Water specific gravity should be entered, but it is not used in dry gas wells.
4. When you click on the continue button, you will be asked if you want to save the changes – respond “yes.”

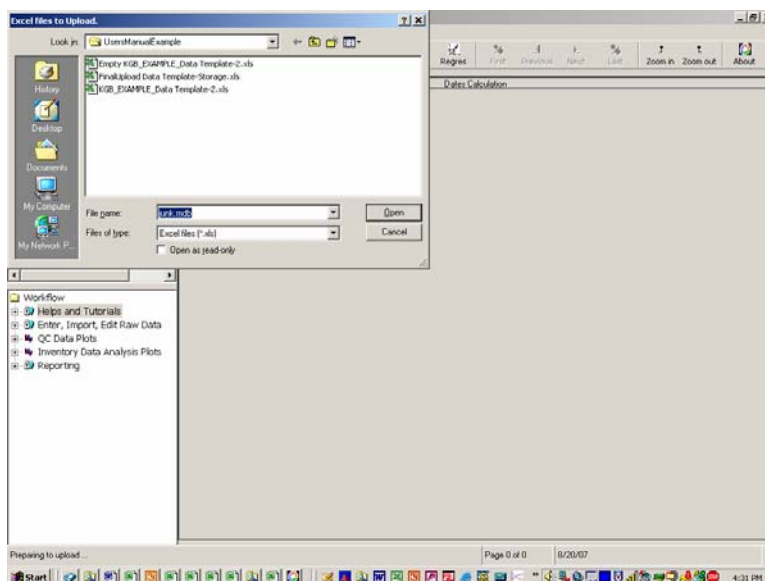
At this point, you will be in the software, but nothing other than the reservoir data has been entered. You will see the following screen at this point:



It is now time to import the data from the EXCEL template file we created, “KGB_EXAMPLE_Data Template-2.xls.” To do this, click on the “UPLOAD” tool button shown below:



You will then see the dialogue box below. Using this dialogue box, select the EXCEL input template file we created, (“KGB_EXAMPLE_Data Template-2.xls”) from the location in which we stored it (D:\Program Files\Gas Storage Software\Excel Template\), and select “OPEN.”



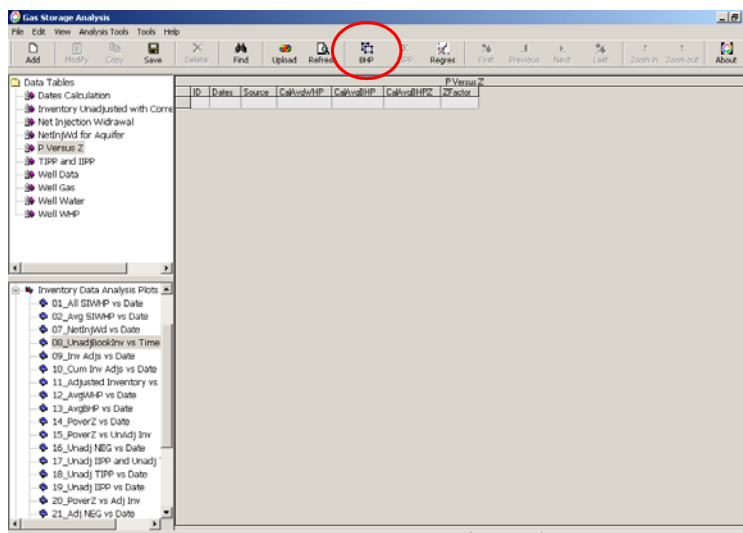
It will take a few moments to import the information from the EXCEL file, so be patient (this process is only required once). Upon completion of the import process, your screen should look as follows:

ID	Year	Season	Date
1	1950	Spring	3/15/50
2	1950	Fall	9/15/50
3	1951	Spring	3/15/51
4	1951	Fall	9/15/51
5	1952	Spring	3/15/52
6	1952	Fall	9/15/52
7	1953	Spring	3/15/53
8	1953	Fall	9/15/53
9	1954	Spring	3/15/54
10	1954	Fall	9/15/54
11	1955	Spring	3/15/55
12	1955	Fall	9/15/55
13	1956	Spring	3/15/56
14	1956	Fall	9/15/56
15	1957	Spring	3/15/57
16	1957	Fall	9/15/57
17	1958	Spring	3/15/58
18	1958	Fall	9/15/58
19	1959	Spring	3/15/59
20	1959	Fall	9/15/59
21	1960	Spring	3/15/60
22	1960	Fall	9/15/60
23	1961	Spring	3/15/61
24	1961	Fall	9/15/61
25	1962	Spring	3/15/62
26	1962	Fall	9/15/62
27	1963	Spring	3/15/63
28	1963	Fall	9/15/63
29	1964	Spring	3/15/64
30	1964	Fall	9/15/64
31	1965	Spring	3/15/65
32	1965	Fall	9/15/65
33	1966	Spring	3/15/66
34	1966	Fall	9/15/66
35	1967	Spring	3/15/67

3.3. Browsing Data & Calculating BHP, p/z, and IPP Values

You can now browse the information located in the various tables by clicking on the table names in the Data Tables Window (upper left tree structure). Notice the following at this point:

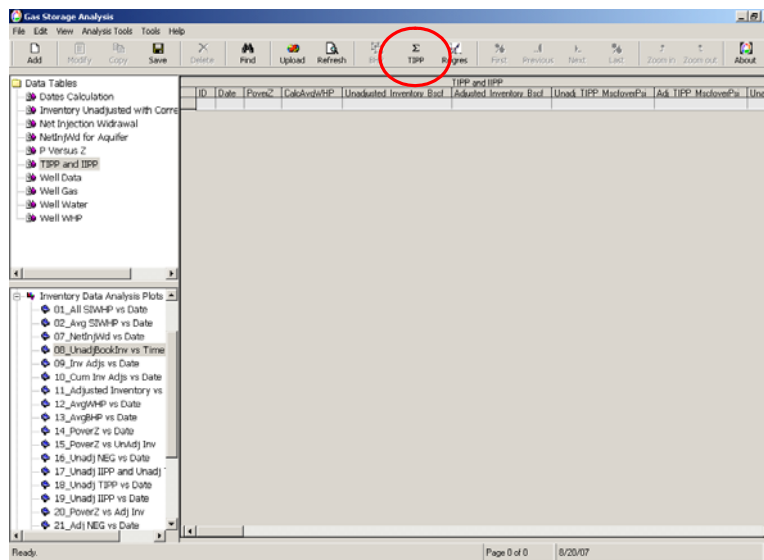
1. The first two data tables (“Dates Calculation” & “Inventory Unadjusted...”) contain data.
2. The third and fourth tables (“Net Injection Withdrawal” and “NetInjWdAquifer”) contain no data because we did not input any data in these tables.
3. The fifth table (“PoverZ”) contains no data because we have not yet calculated the BHP and Z values. To calculate the BHP and BHP/Z values, and populate this table with the calculated values, click on the “BHP” tool button shown below:



After clicking on the BHP tool button, the PoverZ table should look as follows:

ID	Dates	Source	CalcInvBHP	CalcWdBHP	CalcWdIPPZ	PoverZ
1	3/15/50	650	740.52	792.67	0.9342	
2	3/15/50	1000	1135.11	1253.56	0.9055	
3	3/15/51	650	740.52	792.67	0.9342	
4	3/15/51	1000	1135.11	1253.56	0.9055	
5	3/15/52	650	740.52	792.67	0.9342	
6	3/15/52	1000	1135.11	1253.56	0.9055	
7	3/15/53	650	740.52	792.67	0.9342	
8	3/15/53	1000	1135.11	1253.56	0.9055	
9	3/15/54	650	740.52	792.67	0.9342	
10	3/15/54	1000	1135.11	1253.56	0.9055	
11	3/15/55	650	740.52	792.67	0.9342	
12	3/15/55	1000	1135.11	1253.56	0.9055	
13	3/15/56	650	740.52	792.67	0.9342	
14	3/15/56	1000	1135.11	1253.56	0.9055	
15	3/15/57	650	740.52	792.67	0.9342	
16	3/15/57	1000	1135.11	1253.56	0.9055	
17	3/15/58	650	740.52	792.67	0.9342	
18	3/15/58	1000	1135.11	1253.56	0.9055	
19	3/15/59	650	740.52	792.67	0.9342	
20	3/15/59	1000	1135.11	1253.56	0.9055	
21	3/15/60	650	740.52	792.67	0.9342	
22	3/15/60	1000	1135.11	1253.56	0.9055	
23	3/15/61	650	740.52	792.67	0.9342	
24	3/15/61	1000	1135.11	1253.56	0.9055	
25	3/15/62	650	740.52	792.67	0.9342	
26	3/15/62	1000	1135.11	1253.56	0.9055	
27	3/15/63	650	740.52	792.67	0.9342	
28	3/15/63	1000	1135.11	1253.56	0.9055	
29	3/15/64	650	740.52	792.67	0.9342	
30	3/15/64	1000	1135.11	1253.56	0.9055	
31	3/15/65	650	740.52	792.67	0.9342	
32	3/15/65	1000	1135.11	1253.56	0.9055	
33	3/15/66	650	740.52	792.67	0.9342	
34	3/15/66	1000	1135.11	1253.56	0.9055	
35	3/15/67	650	740.52	792.67	0.9342	

- The Sixth table (“TIPP and IIPP”) contains no data because we have not yet calculated these values. To calculate TIPP and IIPP values and populate this table with the calculated values, click on the “TIPP” tool button shown below:
-

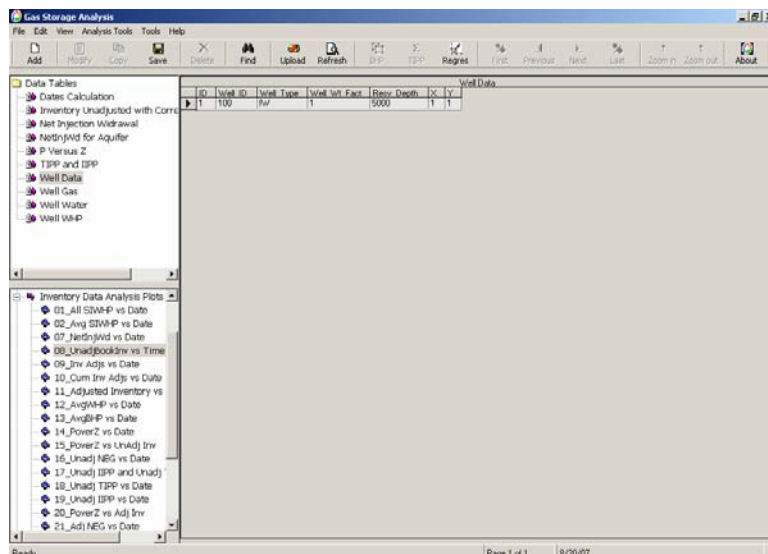


After clicking on the TIPP tool button, the “TIPP and IIPP table should look as follows:

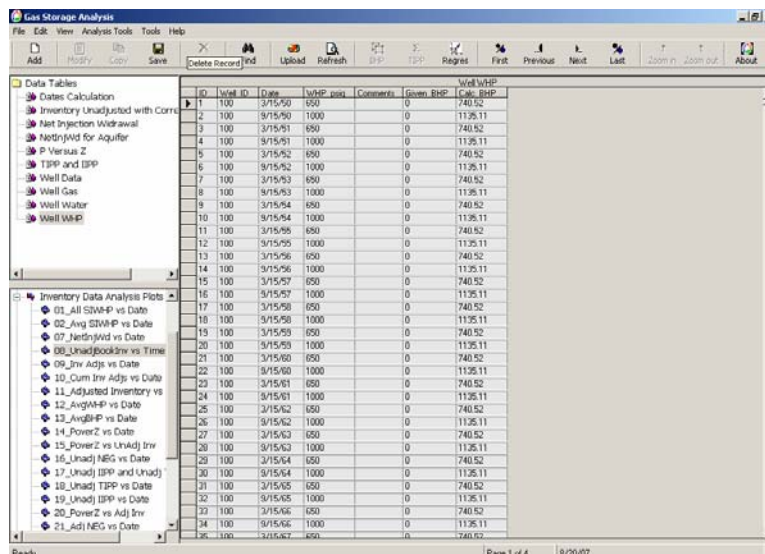
The screenshot shows the same software interface, but the 'TIPP and IIPP' table is now populated with data. The table has columns for ID, Date, PowerZ, CalcAvdwhP, Unadjusted Inventory_Bal, Adjusted Inventory_Bal, Unadj_TIPP_MclovePa, and Adj_TIPP_MclovePa.

ID	Date	PowerZ	CalcAvdwhP	Unadjusted Inventory_Bal	Adjusted Inventory_Bal	Unadj_TIPP_MclovePa	Adj_TIPP_MclovePa
1	3/15/60	792.67	650	8.5	8.5	10723.2518	10723.2518
2	3/15/60	1263.56	1000	13.5	13.5	10989.428	10989.428
3	3/15/61	792.67	650	8.6	8.6	10843.4077	10843.4077
4	3/15/61	1263.56	1000	13.6	13.6	10843.1018	10843.1018
5	3/15/62	792.67	650	8.69	8.69	10982.548	10982.548
6	3/15/62	1263.56	1000	13.69	13.69	10920.8973	10920.8973
7	3/15/63	792.67	650	8.77	8.77	11063.9727	11063.9727
8	3/15/63	1263.56	1000	13.77	13.77	10984.7155	10984.7155
9	3/15/64	792.67	650	8.84	8.84	11152.1819	11152.1819
10	3/15/64	1263.56	1000	13.84	13.84	11040.9585	11040.9585
11	3/15/65	792.67	650	8.9	8.9	11227.8754	11227.8754
12	3/15/65	1263.56	1000	13.9	13.9	11080.4202	11080.4202
13	3/15/66	792.67	650	8.95	8.95	11290.9634	11290.9634
14	3/15/66	1263.56	1000	13.95	13.95	11126.3666	11126.3666
15	3/15/67	792.67	650	8.99	8.99	11341.4157	11341.4157
16	3/15/67	1263.56	1000	13.99	13.99	11160.2157	11160.2157
17	3/15/68	792.67	650	9.02	9.02	11379.3625	11379.3625
18	3/15/68	1263.56	1000	14.02	14.02	11184.1425	11184.1425
19	3/15/69	792.67	650	9.04	9.04	11404.4937	11404.4937
20	3/15/69	1263.56	1000	14.04	14.04	11200.1021	11200.1021
21	3/15/60	792.67	650	9.05	9.05	11417.1093	11417.1093
22	3/15/60	1263.56	1000	14.05	14.05	11208.0794	11208.0794
23	3/15/61	792.67	650	9.05	9.05	11417.1093	11417.1093
24	3/15/61	1263.56	1000	14.05	14.05	11208.0794	11208.0794
25	3/15/62	792.67	650	9.05	9.05	11417.1093	11417.1093
26	3/15/62	1263.56	1000	14.05	14.05	11208.0794	11208.0794
27	3/15/63	792.67	650	9.05	9.05	11417.1093	11417.1093
28	3/15/63	1263.56	1000	14.05	14.05	11208.0794	11208.0794
29	3/15/64	792.67	650	9.05	9.05	11417.1093	11417.1093
30	3/15/64	1263.56	1000	14.05	14.05	11208.0794	11208.0794
31	3/15/65	792.67	650	9.05	9.05	11417.1093	11417.1093
32	3/15/65	1263.56	1000	14.05	14.05	11208.0794	11208.0794
33	3/15/66	792.67	650	9.05	9.05	11417.1093	11417.1093
34	3/15/66	1263.56	1000	14.05	14.05	11208.0794	11208.0794

- The seventh table contains the well data we entered, and should look as follows:

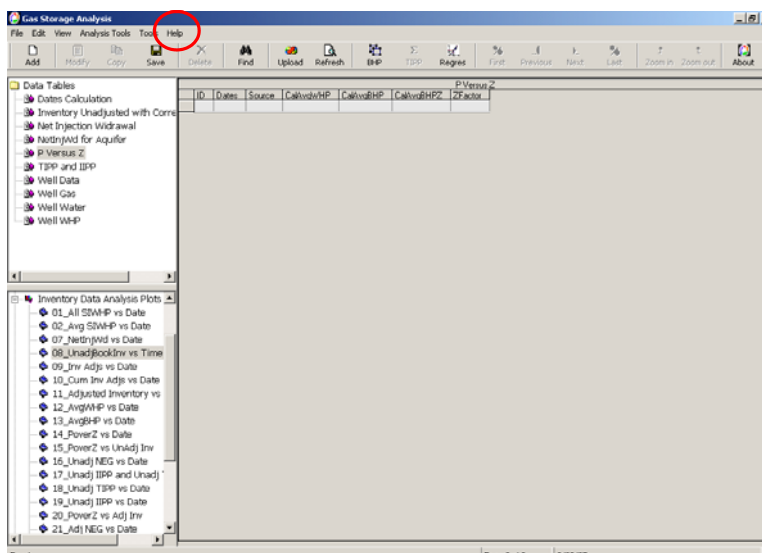


7. The eighth and ninth tables (“Well Gas” and “Well Water”) contain no data because we did not input any data in these tables.
8. The tenth table (“WellWHP”) contains the SIWHP’s input and the SIBHP’s calculated from these SIWHP’s, and should look as follows:

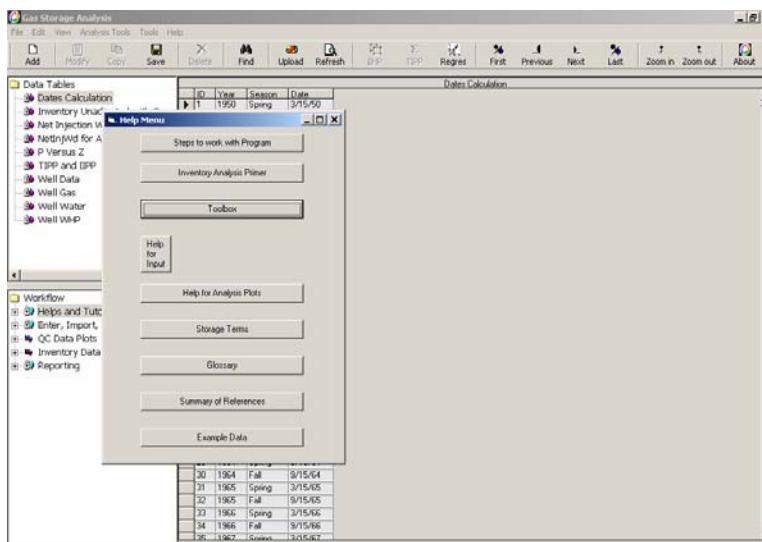


3.4. Perusing HELP features and Using the ToolBox

At this point, we will take a moment to briefly peruse the various HELP features in the software. To access the various HELP features of the software, go to the help menu at the top of the screen, as shown below:



This help button will bring up a menu of help items as shown below:



The various HELP menu items shown include the following:

Steps to work with Program

This is a very abbreviated Users' Manual compiled by the programmer that provides only the most essential information required to use the software.

Inventory Analysis Primer

This is a fairly complete introduction to inventory analysis, and includes discussions on the theory behind inventory analysis, the uses of various inventory analysis diagnostic plots, and references. The table of contents for this document is shown below.

Table of Contents

1. Introduction to Inventory Verification.....	2
1.1. Objectives.....	2
1.2. Theory.....	2
1.3. Data Required.....	2
2. Key or Indicator Wells.....	2
2.1. Background.....	2
2.2. Average Reservoir Pressure from Keywells.....	2
2.3. Average Reservoir Pressures from IW Well SIWHP's.....	2
3. Inventory Analysis Plots.....	2
3.1. Gas Material Balance Plots – p/Z vs Cumulative Production.....	2
3.2. Pressure Content Plots – p/Z vs Inventory.....	2
3.3. Inventory Per Pounds Plots.....	2
3.4. Non-Effective Gas.....	2
3.5. Pore Volume Ratio.....	2
3.6. Inventory Variance From Material Balance.....	2
3.7. Inventory Analysis in Aquifer Storage.....	2
4. Example Problem.....	2
5. Example Problem Solution.....	2
6. PAPERS.....	2
7. REFERENCES.....	2

Toolbox

Selecting this option opens a HELP document related to the EXCEL “Toolbox” that was developed as part of this software. The EXCEL Toolbox is accessed from within the workflow window, and will be discussed in more detail later.

Help for Input

Selecting this option activates a drop-down box to the right, which allows the user to select the input screen for which he needs help. Upon selection of an item in the drop-down box, a WORD file is opened that provides HELP information related to the selected input screen. A description of the data entered on this screen, including data names and formats are summarized.

Help for Analysis Plots

Selecting this option opens a WORD document that provides detailed help for each of the various data QC plots and the diagnostic plots used to estimate loss rates and volumes. The each plot, the purpose, assumptions, applicability, dangers of mis-use, examples, and references are discussed.

Storage Terms

Selecting this option opens a WORD document that provides a description of the various terms used in inventory analysis.

Glossary

Selecting this option opens a WORD document that provides a description of the various terms used in the underground gas storage industry. It is similar in purpose to the “Storage Terms” help above, but much broader in scope.

Summary of References

Selecting this option opens a WORD document that provides a list of various references and technical papers related to the gas storage industry. These references are listed by topic, and should look something like this:

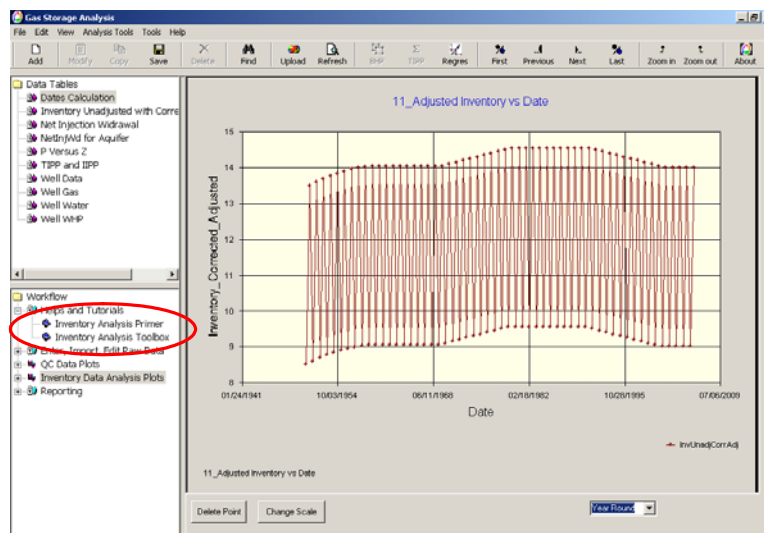
Table of Contents

1. Introduction to Gas Storage	4
2. Gas Storage Field Design	5
3. Optimization	8
4. Migration and Monitoring	10
5. Inventory Verification	12
6. Deliverability Maintenance and Enhancement	13
7. Simulation of UGS Reservoirs	14
8. NEW Papers	15
9. Top Twenty Papers	18

Example Data

Selecting this option opens an EXCEL document containing the Spring/Fall pressure and inventory example data.

Select HELP features are also accessible for the Workflow window, since we anticipate they will commonly be referenced during the inventory analysis process. In the Workflow Window, there are two Help items listed, the Inventory Primer and the Toolbox, as shown below:



Inventory Analysis Primer

As noted above, this is a fairly complete introduction to inventory analysis, and includes discussions on the theory behind inventory analysis, the uses of various inventory analysis diagnostic plots, and references.

Toolbox

Select this option and open the EXCEL “Toolbox.”

After opening the EXCEL Toolbox, go to sheet **Bureau-of-Mines Est Line Losses**, and enter the data given in the example problem data set above to estimate the annual line losses each year we might expect from the 1 mile long gathering line carrying gas from the wellhead to the sales point.

After inputting the example data, your sheet should look like the following:

	A	B	C	E	F	G	H	I	J	
1	Pipeline Losses									
2	Gathering lines and wells recommended leakage factor			0.00010	(Mcscf/yr-ft-ps)					
3	Transmission lines recommended leakage factor			0.000010	(Mcscf/yr-ft-ps)					
4	Gathering line length			5200	ft					
5	Gathering line ID			3	in.					
6	Transmission line length			0	ft					
7	Transmission line ID			24	in.					
8	Time			1	year					
9	Average Pressure			800	psi					
10	Total Loss									85
11										
12										
13										
14										
15										
16										
17										
18										
19										
20										
21										
22										
23										
24										
25										
26										
27										
28										
29										
30										
31										

Obviously, the annual loss rate/volume calculated using the Bureau of Mines data is minimal, and we would not expect that potential losses in the gathering lines to contribute significant to any overall losses from the field.

Next, go to sheet **Est Wellbore Blowdown Volume**, and enter the data given in the example problem data set above to estimate the annual line losses each year we might expect from blowing down the well each year prior to running the camera.

After inputting the example data, your sheet should look like the following:

	A	B	C	D	E	F	G	H	I	
1	Wellbore Blowdown Volume Calculation									
2	Tubing ID		3	in						
3	Tubing Depth		6000	ft						
4	Casing ID		6	in						
5	Casing Depth		5000	ft						
6	Packer on Tubing		Yes							
7	Packer Depth		4950	ft						
8	Gas Gravity		0.58							
9	Wellhead Pressure		650	psia						
10	Wellhead Temperature		90	°F						
11	Bottomhole Temperature		110	°F						
12	Bottomhole Pressure		724.0	psia						
13	Wellbore Blowdown Volume (Final WIHP=0 psi)		12	bbcf						

Obviously, the annual lost volume due to blowing down the well prior to running a camera is minimal, and we would not expect that these losses contribute significant to any overall losses from the field.

Next, go to sheet **Est Well Test Volumes**, and enter the data given in the example problem data set above to estimate the annual losses associated with running the well test each year. After inputting the example data, your sheet should look like the following:

	A	B	C	D	E	F	G	H	I	J
1	Well Testing Volume									
2	Rate (bbcf/day)	Duration (hours)	Cum Production (bbcf)							
3	100	0.25	1.0							
4	200	0.25	3.1							
5	300	0.25	6.3							
6	400	0.75	18.8							
7	500	0	18.8							
8	600	0	18.8							
9	700	0	18.8							
10	800	0	18.8							

Obviously, the annual lost volume due to testing the well each year is minimal, and we would not expect that these losses contribute significant to any overall losses from the field.

Next, go to sheet **Est Pipeline Volumes**, and enter the data given in the example problem data set above to estimate the annual losses associated with blowing down the gathering line to run the pig each year. After inputting the example data, your sheet should look like the following:

	A	B	C	E	F	G	H	I	J	
1	Est Pipeline Volumes									
2	Pipe ID		3 in							
3	Pipe Length		5280 ft							
4	Gas Gravity		0.88							
5	Inlet Pressure		500 psia							
6	Inlet Temperature		100 °F							
7	Outlet Pressure		500 psia							
8	Outlet Temperature		100 °F							
9	Pipeline volume									17 Mscl
10										
11										
12										
13										
14										
15										
16										
17										
18										
19										
20										
21										
22										
23										
24										
25										
26										
27										
28										
29										
30										

Obviously, the annual lost volume due to pigging the gathering line each year is minimal, and we would not expect that these losses contribute significant to any overall losses from the field.

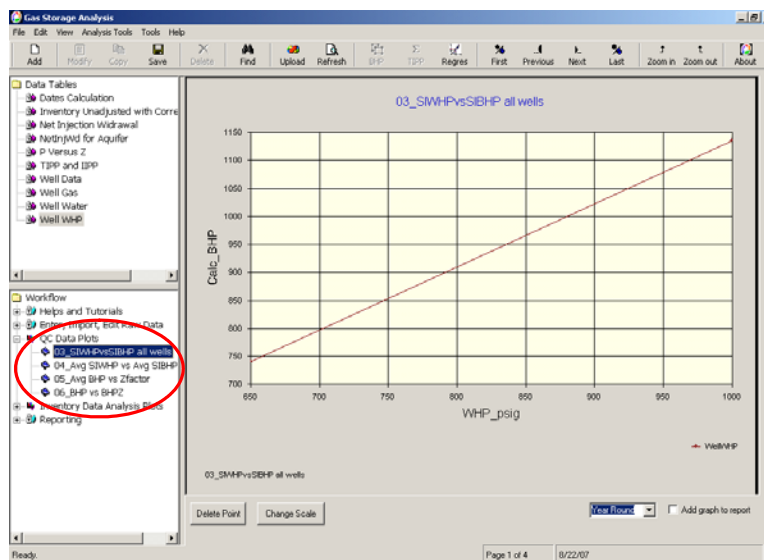
Note that not all of the calculations that can be made in this EXCEL Toolbox have been demonstrated here.

3.5. Performing Inventory Analysis

At this point, all of the data from the example problem has been input/uploaded. We have perused the data tables and the help options, and we used the Toolbox feature to estimate any inventory losses due to field operations. The next step is to use the various plots to analyze loss rates and volumes over the entire life of storage operations.

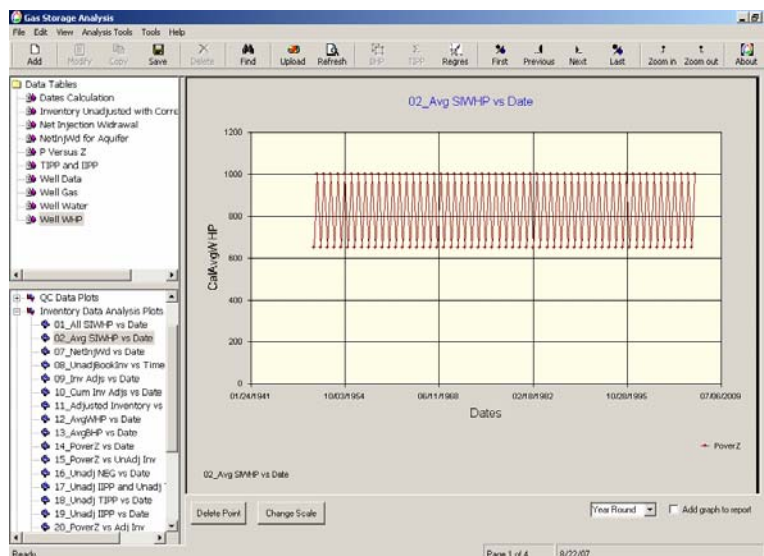
At this point, it is recommended that you open a word processing document to keep notes about the trends observed during the inventory analysis process. These notes will prove to be extremely valuable after your analysis is complete and you generate a draft report.

We start by reviewing the data QC plots shown in the Workflow Window, under QC Data Plots (see below). Since none of these plots show any irregularities, it is safe to assume that no problems were encountered during the calculation processes we performed earlier.



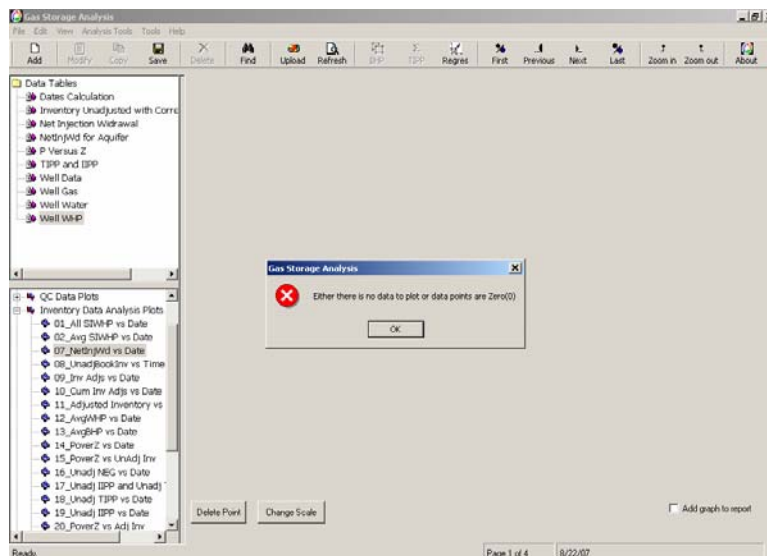
After reviewing the data QC plots, we review plots of operational data to identify any operational trends that may provide preliminary, qualitative indications of ongoing losses and show timeframes wherein we need to be careful analyzing data due to widely varying operational practices.

The first two plots (**All SIWHP vs Date** and **Avg SIWHP vs Date**) are identical, since there is only one well in the field. For the purpose of this example, look at the **Avg SIWHP vs Date**, which should look like this (you may have to change the scale on the plot):

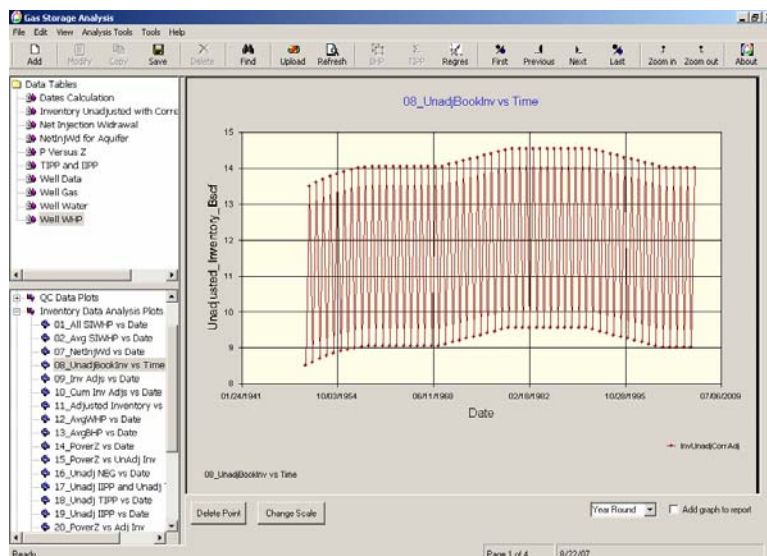


We observe from this plot that the field has consistently been operated between 650 psi and 1000 psi throughout its life. Therefore, we do not have to worry about wide fluctuations in minimum and maximum operating pressures skewing trends in other diagnostic plots.

We did not load any daily or monthly Net Injection information, so the next plot shows nothing:

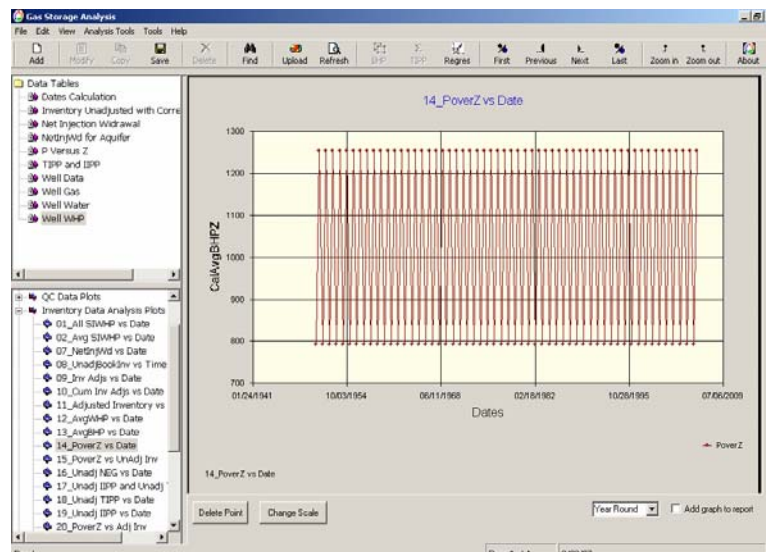


The next plot in the workflow is the **UnadjBookInv vs Time**, which shows the book inventory prior to any adjustments as a function of time. This plot is revealing, especially in light of how regularly the field was operated from a pressure perspective. This plot shows that various levels of inventory were required over the field life to achieve the same Spring and Fall shut-in pressures. This trend is a strong indicator, albeit qualitative indicator, that there have been losses and gains occurring during storage operations.

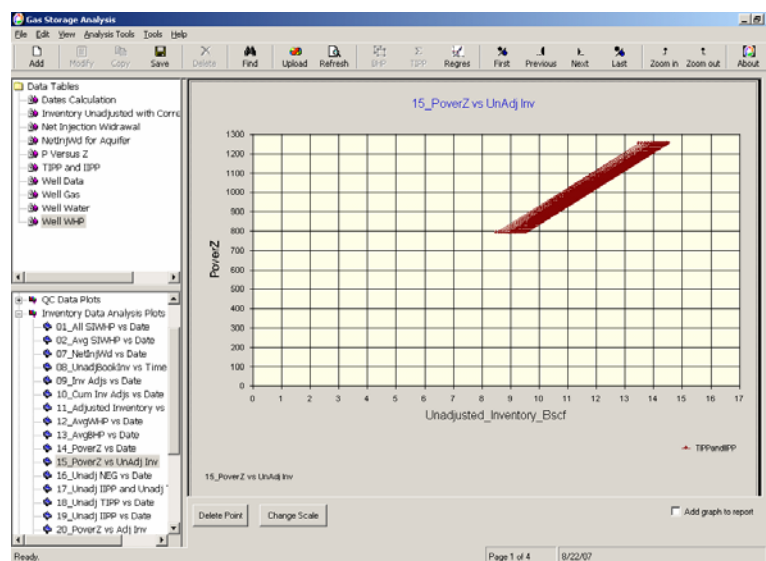


The next three plots, **Inv Adjs vs Date**, **Cum Inv Adjs vs Date**, and **Adjusted Inventory vs Date** are trivial, as no inventory adjustments have been booked during the life of the field. In addition, the two plots after these, **Avg WHP vs Date** and **Avg BHP vs Date**, are not noteworthy.

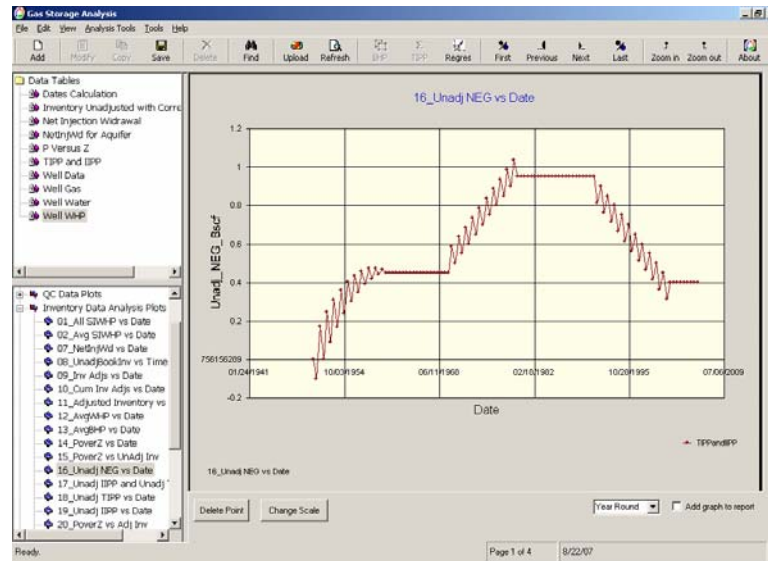
The next plot, **PoverZ vs Date**, reflects the same trends as the SIWHP vs time, and further demonstrates the uniformity of operations over the life of the storage field from a pressure perspective.



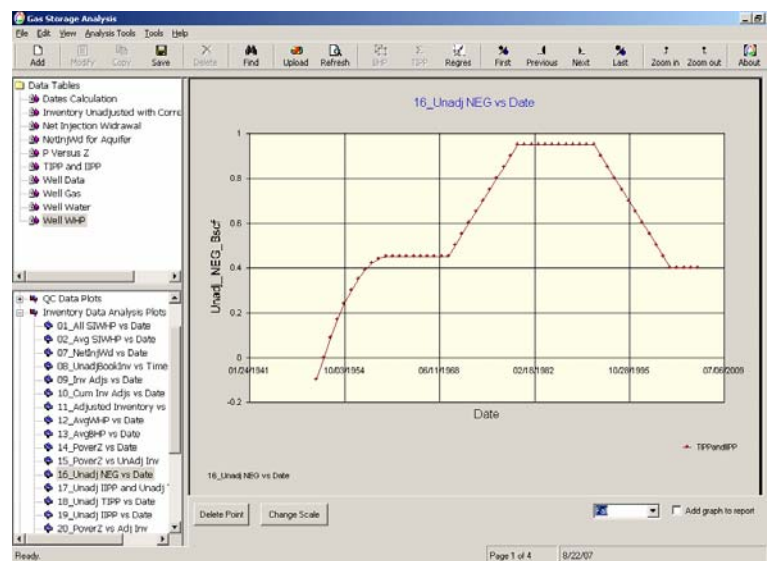
The next plot, **PoverZ vs UnadjInv**, is a plot of the unadjusted book inventory vs the BHP/Z. This plot shows movement to the right and left at various points during the life of storage operations, which leads us to the conclusion the losses and gains have occurred during storage operations. This is consistent with the qualitative conclusions drawn from a review of the the operational plots (SIWHP vs Time and Unadjusted Book Inventory vs Time).



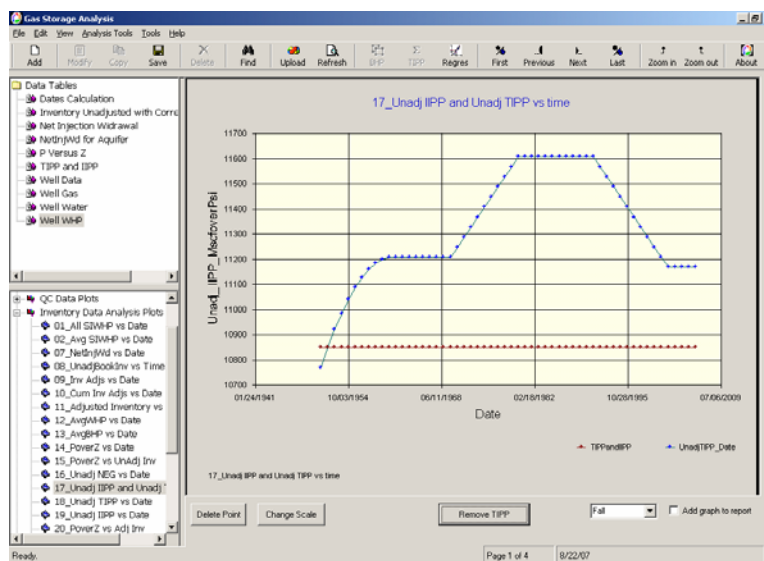
The next plot, Unadj NEG vs Date, shows the non-effective gas (NEG) calculated for each cycle by back-extrapolating the BHP/Z vs Unadjusted Book Inventory plot for that cycle to a BHP/Z value of zero (i.e., the x-intercept of the plot). This plot clearly indicates the time periods experiencing losses, gains, and stability:



Note that the relative uniformity of injection operations compared to withdrawal operations lead some storage engineers to use only fall data to analyze NEG vs time plots and IPP vs time plots. By applying the FALL filter on this plot, we can generate the plot using only Fall data points:



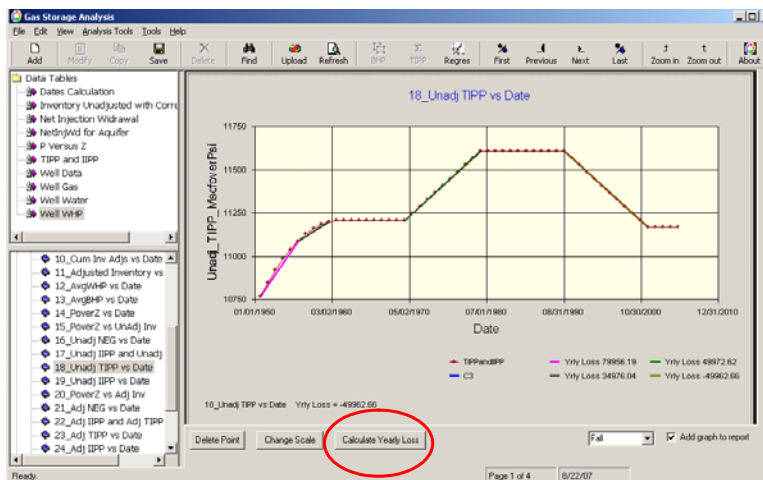
The next plot is the Unadjusted TIPP vs time and Unadjusted IIPP vs time. These are perhaps the most widely used inventory analysis plots in the storage industry. Usually, these plots are generated using Fall only data points, since injection operations are relatively more uniform than withdrawal operations. Therefore, the Fall data points are generally thought to be less operationally influenced. A plot of IPP values vs time generated using Fall only data points is shown below:



This plot clearly shows the following:

1. Non-linear increase in the TIPP w/Flat IIPP in 1950's (GAIN)
2. Flat TIPP and IIPP during 1960's (NO LOSS or GAIN)
3. Linear increase in the TIPP w/Flat IIPP in 1970's (LOSS)
4. Flat TIPP and IIPP during 1980's (NO LOSS or GAIN)
5. Non-linear decrease in the TIPP w/Flat IIPP in 1990's (GAIN)
6. Flat TIPP and IIPP from 2000-2005 (NO LOSS or GAIN)

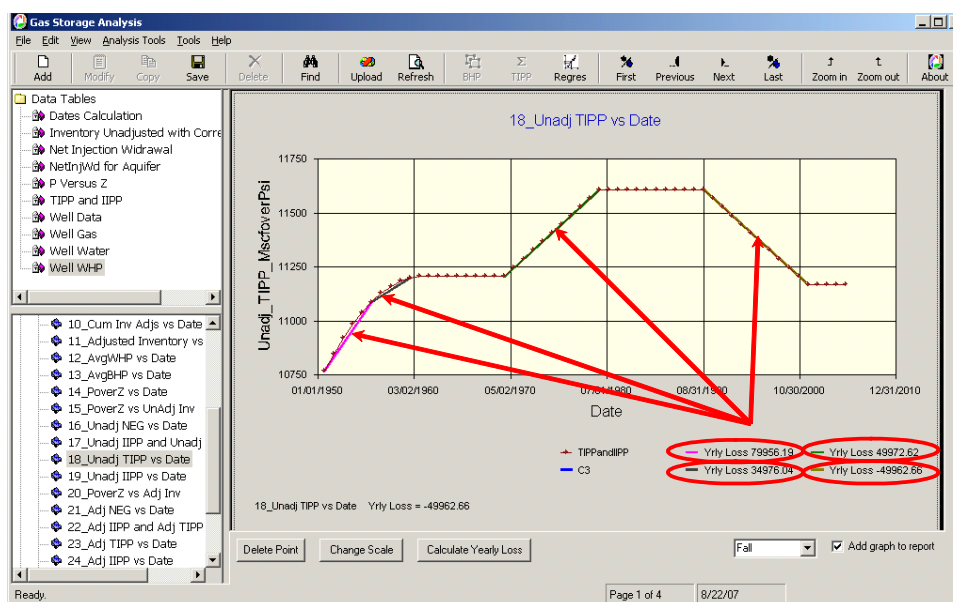
In order to calculate the loss rates and volumes, we will use the TIPP plot generated with Fall only data points. This is accomplished by clicking on the UnadjTIPP vs Date plot in the Workflow window, filtering on Fall data points, and clicking on the "Calculate Yearly Loss" button (see below).



You can calculate losses for up to 5 time periods using the “Calculate Yearly Loss” button. Simply click the button, read the pop-up directions, and click OK to close the directions. Click on the data point closest to the start of the loss period, then click on the data point closest to the end of the loss period.

The software will automatically calculate annual loss rates for each period and display results on the plot. Using this information, we can calculate the total gains/losses by multiplying the gain/loss rate for each loss period by the number of years the gain/loss occurred, and summing the volumes for each period.

For this example, the TIPP vs Date used to calculate the loss rate looks like the following after loss analysis was performed:



The losses calculated using this plot can be summarized as follows:

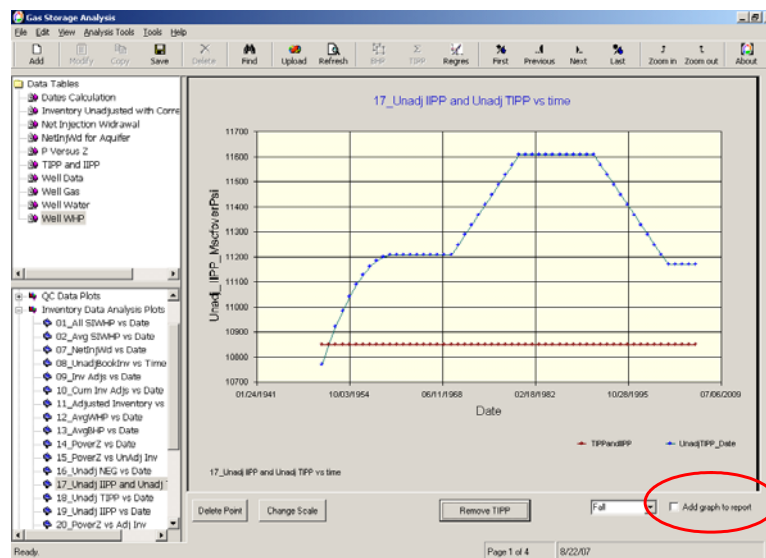
- 80 MMscf/yr loss 1950-1955 (Lost Volume = 400 MMscf)
- 35 MMscf/yr loss 1955-1960 (Lost Volume = 175 MMscf)
- No Losses 1960-1970 (Lost Volume = 0 MMscf)
- 50 MMscf/yr loss 1970-1980 (Lost Volume = 500 MMscf)
- No Losses 1980-1990 (Lost Volume = 0 MMscf)
- 50 MMscf/yr *gain* 1990-2000 (Lost Volume = -500 MMscf)
- No Losses 2000-2005 (Lost Volume = 0 MMscf)

Therefore, based on this analysis, the total net inventory lost from 1950 to 2005 is 575 MMscf

3.6. Generating Reports

At the bottom right of each plot, there is a check box for the user to indicate if he wants that particular plot to be included in the report. By simply checking this box for the plots of interest, we can “collect” the plots we would like to include in this report.

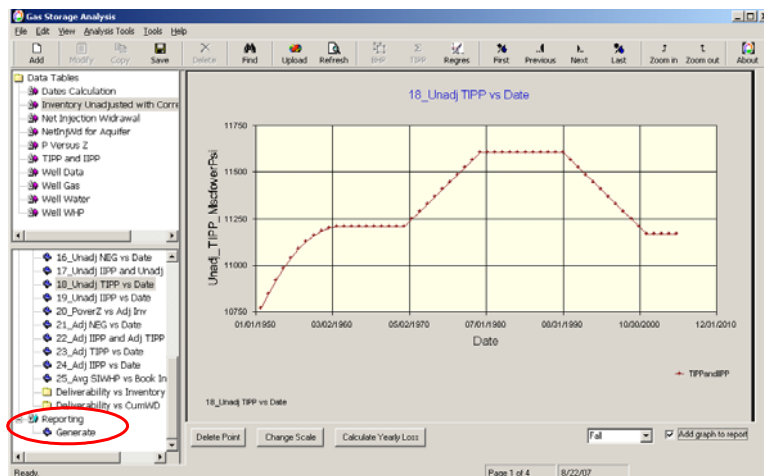
For the purpose of this example, we will include all non-trivial plots in the report, so we will need to make sure each of these plots has the “Add Graph to Report” box checked. This would also be a good time to make sure all of the axes ranges are set appropriately. The figure below shows the location of the check box used to include plots in the report.



In addition, if the user has taken a few notes in a word processing document during the inventory analysis process (as recommended above), it is quite easy to merge the two documents into a final report that includes all of the pertinent plots used in the inventory analysis process. For the example problems, notes collected during the inventory analysis process might look something like the following:

<p><u>QC Plots</u> None of the QC plots show any irregularities, so it is safe to assume that no problems were encountered during the calculation processes performed.</p> <p><u>SIWHP vs Date Plots</u> The field has consistently been operated between 650 psi and 1000 psi throughout its life. Therefore, we do not have to worry about wide fluctuations in minimum and maximum operating pressures skewing trends in other diagnostic plots.</p> <p><u>Unadjusted Inventory History</u> A plot of unadjusted inventory vs time is revealing, especially in light of how regularly the field was operated from a pressure perspective. This plot shows that various levels of inventory were required over the life of the field to achieve the same Spring and Fall shut-in pressures. This type of trend is a strong indicator, albeit a qualitative indicator, that there have been losses and gains occurring during over the life of storage operations.</p> <p><u>BHP/Z vs Unadj Book Inv</u> A plot of the unadjusted book inventory vs the BHP/Z shows movement to the right and left at various points during the life of storage operations, which leads us to the conclusion the losses and gains have occurred during storage operations. This is consistent with the qualitative conclusions drawn from a review of the operational plots (SIWHP vs Time and Unadjusted Book Inventory vs Time).</p> <p><u>NEG History</u> The plot of Unadjusted NEG vs Date clearly indicates the time periods experiencing losses, gains, and stability.</p> <p><u>IPP History Plots</u> A plot of IPP values vs time generated with Fall data points clearly shows the following:</p> <ol style="list-style-type: none"> 1. Non-linear increase in the TIPP w/Flat IIPP in 1950's (GAIN) 2. Flat TIPP and IIPP during 1960's (NO LOSS or GAIN) 3. Linear increase in the TIPP w/Flat IIPP in 1970's (LOSS) 4. Flat TIPP and IIPP during 1980's (NO LOSS or GAIN) 5. Non-linear decrease in the TIPP w/Flat IIPP in 1990's (GAIN) 6. Flat TIPP and IIPP from 2000-2005 (NO LOSS or GAIN) <p><u>Loss Calculations using the TIPP Plot</u> Loss rates and volumes were calculated using the TIPP plot generated with Fall only data points. The losses calculated using this plot can be summarized as follows:</p> <ul style="list-style-type: none"> • 80 MMscf/yr loss 1950-1955 (Lost Volume = 400 MMscf) • 35 MMscf/yr loss 1955-1960 (Lost Volume = 175 MMscf) • No Losses 1960-1970 (Lost Volume = 0 MMscf) • 50 MMscf/yr loss 1970-1980 (Lost Volume = 500 MMscf) • No Losses 1980-1990 (Lost Volume = 0 MMscf) • 50 MMscf/yr <i>gain</i> 1990-2000 (Lost Volume = -500 MMscf) • No Losses 2000-2005 (Lost Volume = 0 MMscf) <p>Therefore, based on this analysis, the total net inventory lost over the time period 1950-2005 is 575 MMscf</p>
--

After checking the boxes on all of the charts you would like to be included in the report, go to the Workflow Window, expand the “Reporting” portion of tree directory to see the “Generate” option and click on the Generate option:



This will bring up a document preview window that will show all of the plots you have selected in thumbnail view. By clicking on the “Generate Report” button (see below), the information shown in thumbnail view will be exported to a WORD document for further editing.



After the report information was dumped to WORD and this file was opened, we opened the comments file we compiled during the analysis procedure (shown earlier). We then cut/pasted the information from the comments document into the WORD document, rearranged some information, added a report cover page.

The result is a first draft (or final draft, depending on requirements of the client) of an Inventory Analysis Report (see below):

Gas Storage Inventory Analysis

Big Boy Field

Summary of Reservoir Information

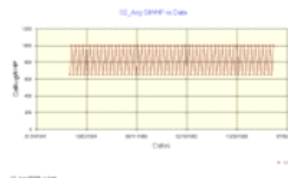
Field Name	Example
Field Type	Dry Gas
Average Reservoir Depth (ft)	5000
Average Reservoir Temperature (F)	110
Wellhead Temperature (F)	60
Reservoir Top Pressure (psia)	1000
Reservoir Base Pressure (psia)	630
Gas specific gravity	0.58
Water specific gravity	1.05
Total Number of wells	1
BHP correlation	Cullender and Smith
z-factor correlation	Hall-Yarborough

Review of Data QCPlots

None of the QC plots show any irregularities, so it is safe to assume that no problems were encountered during the calculation processes performed.

Review of Operational Plots

Based on a review of the SIMHP vs Date Plots, it is apparent that the field has consistently been operated between 630 psi and 1000 psi throughout its life. Therefore, we do not have to worry about wide fluctuations in minimum and maximum operating pressures skewing trends in other diagnostic plots.

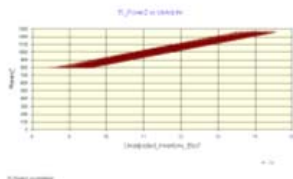


Based on a review of the unadjusted inventory vs time, it is apparent that various levels of inventory were required over the life of the field to achieve the same Spring and Fall shut-in pressures. This type of trend is a strong indicator, albeit a qualitative indicator, that there have been losses and gains occurring during over the life of storage operations.

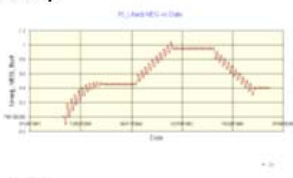


Review of Diagnostic Plots

Based on a review of the unadjusted book inventory vs the EHP/Z plot, it is apparent that movement has occurred to the right and left at various points during the life of storage operations. This suggests that losses and gains have occurred during storage operations. This is consistent with the qualitative conclusions drawn from a review of the operational plots (SIMHP vs Time and Unadjusted Book Inventory vs Time).



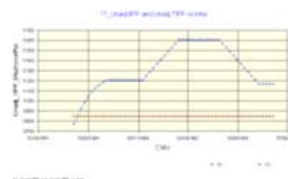
The plot of Unadjusted NEG vs Date clearly indicates the time periods experiencing losses, gains, and stability.



IPP History Plots

A plot of IPP values vs time generated with Fall data points clearly shows the following:

1. Non-linear increase in the TPP w/Flat IPP in 1950's (GAIN)
2. Flat TPP and IPP during 1960's (NO LOSS or GAIN)
3. Linear increase in the TPP w/Flat IPP in 1970's (LOSS)
4. Flat TPP and IPP during 1980's (NO LOSS or GAIN)
5. Non-linear decrease in the TPP w/Flat IPP in 1990's (GAIN)
6. Flat TPP and IPP from 2000-2005 (NO LOSS or GAIN)



Loss Calculations using the TIPP Plot

Loss rates and volumes were calculated using the TIPP plot generated with Fall only data points. The losses calculated using this plot can be summarized as follows:

- 80 MMcf/yr loss 1950-1955 (Lost Volume = 400 MMcf)
- 25 MMcf/yr loss 1955-1960 (Lost Volume = 175 MMcf)
- No Losses 1960-1970 (Lost Volume = 0 MMcf)
- 50 MMcf/yr loss 1970-1980 (Lost Volume = 500 MMcf)
- No Losses 1980-1990 (Lost Volume = 0 MMcf)
- 50 MMcf/yr gain 1990-2000 (Lost Volume = -500 MMcf)
- No Losses 2000-2005 (Lost Volume = 0 MMcf)



Based on this analysis, the total net inventory lost between 1950-2005 is 575 MMcf.

4. References

- Chierici, G. L., Gottardi, G. A., and Guidorzi, R. P. "Identified Models for Gas Storage Dynamics," *SPEJ* (April 1981) 151-159.
- Dowdle, W.: "Inventory Verification in Gas Storage Reservoirs," presentation at the Gas Daily and Gas Storage Report Gas Storage Technical Seminar, April 14, 1994, Houston, Texas.
- Hubbard, R. M., and Eienbaas, J. R." "Determining Gas-Filled Pore Volume in a Water-Drive Gas-Storage Reservoir," *JPT* (April 1964) 383-,388 •
- Mayfield, "Inventory Verification of Gas Storage Fields," SPE 9391, *JPT* (Sept. 1981) 1730-34.
- Molinard, J. E., Le Bitoux, P., Peice, V. and Tek, M. R. "Practical Model for Predicting Pressure in Gas-Storage Reservoirs," *SPEE* (Nov. 1 990) 576-580.
- Tek, M. R.: *Underground Storage of Natural Gas*, Gulf, 1987.
- Tutt, C. J" "A Practical Regression Model of Pressure/Inventory Hysteresis in Natural Gas Storage Fields," *JPT* (June 1978) 885-889.
- Tutt, Charles, Jr." "Natural Gas Storage Field Inventory Verification by Statistical Analysis of Observation Well Pressures," AGA paper 84-DT-89, 1984 Operating Section Proceedings.

Appendix III
Underground Gas Storage References

Table of Contents

1.	INTRODUCTION TO GAS STORAGE.....	3
2.	GAS STORAGE FIELD DESIGN.....	4
3.	OPTIMIZATION	6
4.	MIGRATION AND MONITORING	7
5.	INVENTORY VERIFICATION	8
6.	DELIVERABILITY MAINTENANCE AND ENHANCEMENT	9
7.	SIMULATION OF UGS RESERVOIRS	10
8.	SPECIAL TOPICS	11
9.	TOP TWENTY PAPERS	12

1. Introduction to Gas Storage

Coats, K. H.: "Some Technical and Economic Aspects of Underground Gas Storage," JPT (Dec. 1966) 1561-66.

Katz, D. L., and Tek, M. R.: "Overview on Underground Storage of Natural Gas," JPT (June 1981) 943-951.

Katz, D. L., et. al., Handbook of Natural Gas Engineering, McGraw-Hill, 1959.

Katz, D. L.: "Making Good Use of Observation Wells," Proc. AGA Transmission Conference, St. Louis (1977) T-251.

Katz, D. L.: "Monitoring Gas Storage Reservoirs," paper SPE 3287 presented at the 1971 Midwest Oil and Gas Industry Symposium, Chicago, April 1-2.

Tek, M. R.: Underground Storage of Natural Gas, Gulf, 1987.

The Potential for Natural Gas in the United States, National Petroleum Council, 1992.

Underground Storage, American Gas Association, 1990.

2. Gas Storage Field Design

Beyea, R. O. and Pinckney, K. D.: "Optimization of Cathodic Protection of Well Casing in the Texas Panhandle," paper SPE 24299, presented at the 1992 Mid-Continent Gas Symposium, Amarillo, TX, April 13-14.

Briggs, J. E. Jr., and Katz, D. L.: "Drainage of Water from Sand in Developing Aquifer Storage," paper SPE 1501 presented at the 1966 Annual Fall Meeting, Dallas, Oct. 2-5.

Coleman, S. B., Clay, H. B., McCurdy, D. G., and Norris, H. L. III: "A New Look at Predicting Gas-Well Load-Up," JPT (March 1991) 329-333.

Evernos, A. I., and Comer, A. G.: "On the Feasibility of Pressure Relief by Water Removal During Development and Operation of Gas Storage in Aquifers," paper SPE 4038 presented at the 1972 Annual Fall Meeting, San Antonio, Oct. 8-11.

Griffith, Howard D. Jr. and Rinehart, Richard D.: "Early Planning for Gas Storage Pays Off - A Case History of Kentucky's Largest Gas Field," paper SPE 3434 presented at the 46th Annual Fall Meeting of the Society of Petroleum Engineers, New Orleans, October 3-6, 1971.

Gober, W. H.: "Factors Influencing the Performance of Gas Storage Reservoirs Developed in Aquifers," paper SPE 1346 presented at the 1965 Gas Technology Symposium, Liberal, Kansas, November 18-19.

Hamlin, A. W.: "Cathodic Protection of Gas Storage Well Casings," AGA paper 91-DT-72, AGA 1991 Operating System Proceedings.

Henry, William A. and Fix, Frank F.: "Development of Aquifer Gas Storage Field with Minimum Environmental Impact," paper SPE 5139 presented at the 49th Annual Fall Meeting of the Society of Petroleum Engineers, Houston, October 6-9, 1974.

Katz, D. L., et. al., Handbook of Natural Gas Engineering, McGraw-Hill, 1959.

Katz, D. L., Vary, J. A., and Elenbaas, J. R.: "Design of Gas Storage Fields," Trans. AIME (1959) 216, 44-48.

Katz, D. L.: "Monitoring Gas Storage Reservoirs," paper SPE 3287 presented at the 1971 Midwest Oil and Gas Symposium, Chicago, April 1-2.

McMinn, R. E.: "Production Techniques for Aquifer-Type Storage Fields," paper SPE 1635 presented at the Gas Technology Symposium, Omaha, Nebraska, September 15-16, 1966.

Oden, R. D., and Jennings, J. W.: "Modification of the Cullender and Smith Equation for More Accurate Bottomhole Pressure Calculations in Gas Wells," SPE 17306

presented at the 1988 Permian Basin Oil and Gas Recovery Conference, Midland, Texas, March 10-11.

Peffer, J. W., Miller, M. A., and Hill, A. D.: "An Improved Method for Calculating Bottomhole Pressures in Flowing Gas Wells With Liquid Present," SPE 15655 presented at the 1986 Annual Technical Conference and Exhibition, New Orleans, Oct 5-8.

Smith, R. V.: "Determining Friction Factors for Measuring Productivity of Gas Wells," Trans. AIME (1950) 189, 73-82.

Stiff, H. A.: "The Interpretation of Chemical Water Analysis by Means of Patterns," Technical Note 84, Trans. AIME (1951) 192, 376-379.

Sukkar, Y. K., and Cornell, D.: "Direct Calculation of Bottom-Hole Pressures in Natural Gas Wells," Trans AIME (1955)204,43-48.

Tek, M. R.: Underground Storage of Natural Gas, Gulf, 1987. The Potential for Natural Gas in the United States, National Petroleum Council, 1992.

Turner, R. G., Hubbard, M. G., and Dukler, A. E.: "Analysis and Prediction of Minimum Flow Rate for the Continuous Removal of Liquids from Gas Wells," JPT (Nov. 1969) 1475-82.

U.S. Natural Gas Availability - Gas Supply Through the Year 2000, Office of Technology Assessment, 1985.

Wingerter, J. R.: "The Use of Inert Gas to Test Potential Gas Storage Aquifers," paper SPE 2770, 1969.

Witherspoon, P. A., Mueller, T. D., and Donovan, R. W.: "Evaluation of Underground Gas-Storage Conditions In Aquifers Through Investigations of Groundwater Hydrology," JPT (May 1962) 555-561.

Young, K. L.: "Effect of Assumptions Used to Calculate Bottom-Hole Pressures in Gas Wells," JPT (April 1967) 547-550.

3. Optimization

Coats, K. H.: "An Approach to Locating New Wells in Heterogeneous, Gas Producing Fields," JPT (May 1969) 549-558.

Duane, J. W.: "Gas Storage Field Development Optimization," JPT (March 1967) 323-330.

Henderson, J. H., Dempsey, J. R., and Tyler, J. C.: "Use of Numerical Models to Develop and Operate Gas Storage Reservoirs," JPT (Nov. 1968) 1239-1246.

Katz, D. L., et. al., Handbook of Natural Gas Engineering, McGraw-Hill, 1959.

McVay, D. A., and Spivey, J. P.: "Optimizing Gas Storage Reservoir Performance," SPE 28639 presented at the 1994 Annual Technical Conference and Exhibition, New Orleans, Sept. 25-28.

Misra, B. R.: "Graphical Design of Underground Gas Storage Developed From a Depleted Gas Field," SPE 7105, unsolicited paper, 1978.

Tek, M. R., Elenbaas, J. R., Whims, M. and Roberts, J. L.: "Design of Storage Fields With Minimum Temperature and Pressure Control at the Surface," paper SPE 8413 presented at the 1979 Annual Fall Technical Conference and Exhibition, Las Vegas, Sept. 23-26.

Van Horn, H. G., and Wienecke, D. R.: "A Method for Optimizing the Design of Gas Storage Systems," SPE 2966 presented at the 1970 Annual Fall Meeting, Houston, Oct. 4-7.

4. Migration and Monitoring

Araktingi, R. E., Benefield, M. E., Bessenyei, Z., Coats, K. H., and Tek, M. R.: "Leroy Storage Facility, Uinta County, Wyoming: A Case History of Attempted Gas-Migration Control," JPT (Jan. 1984) 132-140.

Chierici, G. L., Gottardi, G. A., and Guidorzi, R. P.: "Identified Models for Gas Storage Dynamics," SPEJ (April 1981) 151-159.

Coleman, D. D.: "The Use of Geochemical Fingerprinting To Identify Migrated Gas at the Epps Underground Gas Storage Field," paper SPE 24926 presented at the 1992 Annual Technical Conference and Exhibition, Washington, D.C., Oct. 4-7.

Coleman, D. D., Meents, W. F., Liu, Chao-Li, and Keough, R. A.: "Isotopic Identification of Leakage Gas from Underground Storage Reservoirs – A Progress Report," paper SPE 6491 presented at the 1977 Midwest Gas Storage and Production Symposium, Indianapolis, April 13-15.

Dake, L. P.: Fundamentals of Reservoir Engineering, Elsevier, 1978.

Gentges, Richard J.: "Monitoring Casing Corrosion in Natural Gas Storage Fields," AGA paper 85-DT-65, 1985 Operating Section Proceedings.

Katz, D. L.: "Containment of Gas in Storage Fields," AGA paper 78-T-79, 1978 Operating Section Proceedings.

Katz, D. L.: "Monitoring Gas Storage Reservoirs," paper SPE 3287 presented at the 1971 Midwest Oil and Gas Industry Symposium, Chicago, April 1-2.

Knepper, G. A., and Cuthbert, J. F.: "Gas Storage Problems and Detection Methods," paper SPE 8412 presented at the 1979 Annual Fall Technical Conference and Exhibition, Las Vegas, Sept. 23-26.

Tutt, C. J.: "A Practical Regression Model of Pressure/Inventory Hysteresis in Natural Gas Storage Fields," JPT (June 1978) 885-889.

Tutt, Charles, Jr.: "Natural Gas Storage Field Inventory Verification by Statistical Analysis of Observation Well Pressures," AGA paper 84-DT-89, 1984 Operating Section Proceedings.

5. Inventory Verification

Dowdle, W.: "Inventory Verification in Gas Storage Reservoirs," presentation at the Gas Daily and Gas Storage Report Gas Storage Technical Seminar, April 14, 1994, Houston Texas.

Hubbard, R. M., and Elenbaas, J. R.: "Determining Gas-Filled Pore Volume in a Water-Drive Gas-Storage Reservoir," JPT (April 1964) 383-388.

Mayfield, "Inventory Verification of Gas Storage Fields," SPE 9391, JPT (Sept. 1981) 1730-34.

Tek, M. R.: Underground Storage of Natural Gas, Gulf, 1987.

Mayfield, J. F.: "Inventory Verification of Gas Storage Fields," JPT (Sept. 1981) 1730-1734.

Hubbard, R. M., and Elenbaas, J. R.: "Determining Gas-Filled Pore Volume in a Water-Drive Gas-Storage Reservoir," JPT (April 1964) 383-388.

6. Deliverability Maintenance and Enhancement

Babu, D. K., and Odeh, A. S.: "Productivity of a Horizontal Well," SPERE (Nov. 1989) 417-421.

Bergin, S. R., and Shikari, Y. A.: "A Horizontal Well in Gas Storage: A Case Study," paper SPE 26165 presented at the 1993 Gas Technology Symposium, Calgary, June 28-30.

Cinco-Ley, H., and Samaniego-V., F.: "Transient Pressure Analysis for Fractured Wells," JPT (Sept. 1981) 1749-66.

Dereniewski, Edward; Hekim, Yusuf; and Roberts, Joseph L.: "Deliverability Interference in Gas Storage Reservoirs," AGA paper 82-T-20, 1982 Operating Section Proceedings.

Hall, J. Kevin, and Shikari, Yusuf: "Critical Parameters for Optimizing Horizontal Well Performance in Gas Storage Reservoirs," AGA paper 93-DT-50, 1993 Operating Section Proceedings.

Gredell, Mark E., and Benson, Mark A.: "Slim-hole Horizontal Well Improves Gas Storage Deliverability," OGJ (December 11, 1995) 66-70. Lee, W. J., Rollins, J. B., and Spivey, J. P.: Pressure Transient Testing, SPE Textbook Series, in progress.

State-of-Technology Assessment and Evaluation of Gas Storage Well Productivity Enhancement Techniques, GRI Topical Report GRI-93/0001.

7. Simulation of UGS Reservoirs

Wells & Evans, "Engineering Evaluation and Performance Analysis of the Loop Gas Storage Field," paper SPE 24922 presented at the 1992 Annual Technical Conference and Exhibition, Washington, D.C., Oct. 4-7.

8. Special Topics

Barron, Thomas F.: "Regulatory, Technical Pressures Prompt More U.S. Salt-cavern Gas Storage," OGJ Special, (September 12, 1994) 55-67.

Misrah, B. R., Foh, S. E., Shikari, Y. A., Berry, R. M., and Labaune, F.: "The Use of Inert Base Gas in Underground Natural Gas Storage," paper SPE 17741 presented at the 1988 Gas Technology Symposium, Dallas, June 13-15.

Herzog, R. A.: "Retrograde Vaporization of Residual Condensation in Storage Field Development," AGA paper 80-T-54, 1980 Operating Section Proceedings.

Weibel, Rudolph W.: "Gas Storage Enhances Oil Production," OGJ (January 21, 1991) 33-36.

9. Top Twenty Papers

Katz, Donald L., and Tek, M. Rasin: "Overview on Underground Storage of Natural Gas," JPT (June 1981) 943-951.

Griffith, Howard D. Jr. and Rinehart, Richard D.: "Early Planning for Gas Storage Pays Off - A Case History of Kentucky's Largest Gas Field," paper SPE 3434 presented at the 46th Annual Fall Meeting of the Society of Petroleum Engineers, New Orleans, October 3-6, 1971.

Katz, Donald L.: "Containment of Gas in Storage Fields," AGA paper 78-T-79, 1978 Operating Section Proceedings

Mayfield, J. F.: "Inventory Verification of Gas Storage Fields," JPT (Sept. 1981) 1730-1734.

Wells & Evans, "Engineering Evaluation and Performance Analysis of the Loop Gas Storage Field," paper SPE 24922 presented at the 1992 Annual Technical Conference and Exhibition, Washington, D.C., Oct. 4-7.

Knepper, G. A., and Cuthbert, J. F.: "Gas Storage Problems and Detection Methods," paper SPE 8412 presented at the 1979 Annual Fall Technical Conference and Exhibition, Las Vegas, Sept. 23-26.

Coleman, D. D.: "The Use of Geochemical Fingerprinting To Identify Migrated Gas at the Epps Underground Gas Storage Field," paper SPE 24926 presented at the 1992 Annual Technical Conference and Exhibition, Washington, D.C., Oct. 4-7.

Araktingi, R. E., Benefield, M. E., Bessenyei, Z., Coats, K. H., and Tek, M. R.: "Leroy Storage Facility, Uinta County, Wyoming: A Case History of Attempted Gas-Migration Control," JPT (Jan. 1984) 132-140.

Gober, W. H.: "Factors Influencing the Performance of Gas Storage Reservoirs Developed in Aquifers," paper SPE 1346 presented at the 1965 Gas Technology Symposium, Liberal, Kansas, November 18-19.

Hubbard, R. M., and Elenbaas, J. R.: "Determining Gas-Filled Pore Volume in a Water-Drive Gas-Storage Reservoir," JPT (April 1964) 383-388.

Henry, William A. and Fix, Frank F.: "Development of Aquifer Gas Storage Field with Minimum Environmental Impact," paper SPE 5139 presented at the 49th Annual Fall Meeting of the Society of Petroleum Engineers, Houston, October 6-9, 1974.

McMinn, R. E.: "Production Techniques for Aquifer-Type Storage Fields," paper SPE 1635 presented at the Gas Technology Symposium, Omaha, Nebraska, September 15-16, 1966.

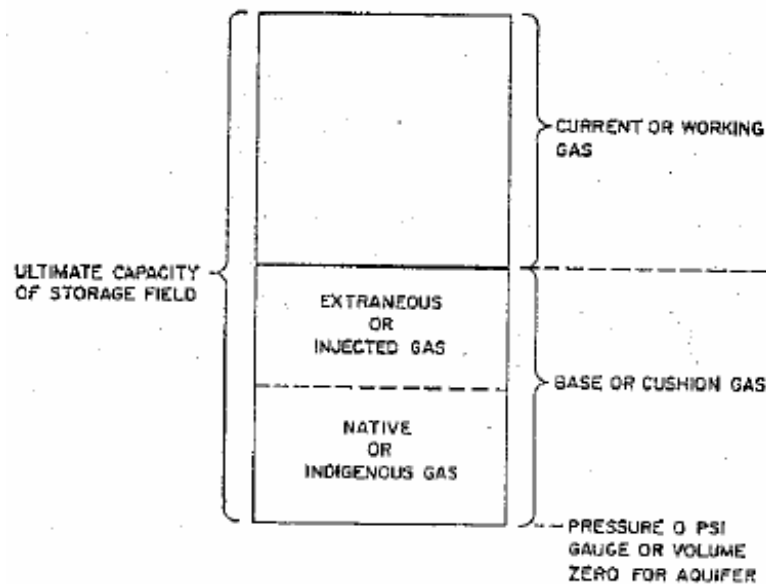
- Weibel, Rudolph W.: "Gas Storage Enhances Oil Production," OGJ (January 21, 1991) 33-36.
- Herzog, R. A.: "Retrograde Vaporization of Residual Condensation in Storage Field Development," AGA paper 80-T-54, 1980 Operating Section Proceedings.
- Dereniewski, Edward; Hekim, Yusuf; and Roberts, Joseph L.: "Deliverability Interference in Gas Storage Reservoirs," AGA paper 82-T-20, 1982 Operating Section Proceedings.
- Hall, J. Kevin, and Shikari, Yusuf: "Critical Parameters for Optimizing Horizontal Well Performance in Gas Storage Reservoirs," AGA paper 93-DT-50, 1993 Operating Section Proceedings.
- Gredell, Mark E., and Benson, Mark A.: "Slim-hole Horizontal Well Improves Gas Storage Deliverability," OGJ (December 11, 1995) 66-70.
- Gentges, Richard J.: "Monitoring Casing Corrosion in Natural Gas Storage Fields," AGA paper 85-DT-65, 1985 Operating Section Proceedings.
- Misrah, B. R., Foh, S. E., Shikari, Y. A., Berry, R. M., and Labaune, F.: "The Use of Inert Base Gas in Underground Natural Gas Storage," paper SPE 17741 presented at the 1988 Gas Technology Symposium, Dallas, June 13-15.
- Barron, Thomas F.: "Regulatory, Technical Pressures Prompt More U. S. Salt-cavern Gas Storage," OGJ Special, (September 12, 1994) 55-67.

Appendix IV

Underground Gas Storage Inventory & Deliverability Terminology

Gas Storage Terminology

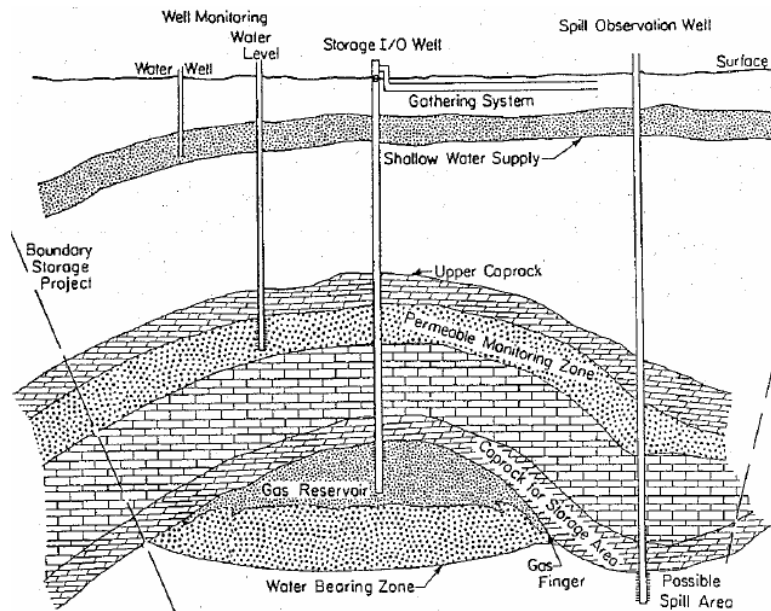
Inventory



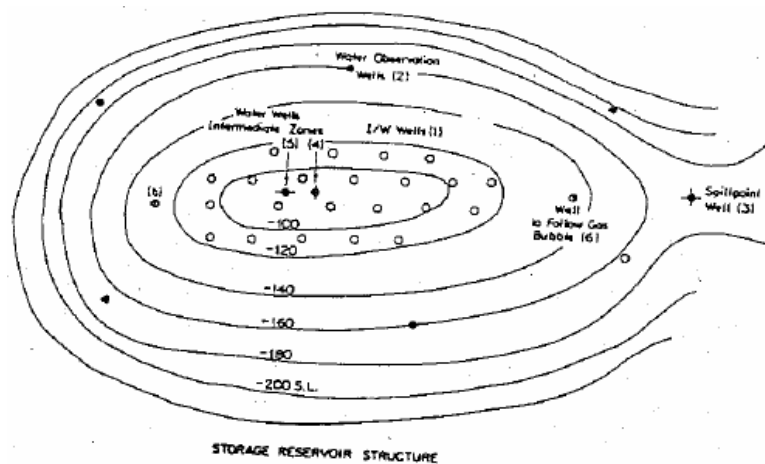
Gas volumes in storage fields. From Katz, *et. al.*, 1959.

- Cushion gas (base gas)
 - The volume of gas that must remain in the storage field to maintain an adequate deliverability rate throughout the withdrawal season
- Working gas (top gas)
 - The volume of gas in reservoir above the designed level of the cushion gas
 - May or may not be completely withdrawn during any particular output season
 - Conditions may permit the total working capacity to be used more than once during any season
- Native gas
 - Gas originally present in a depleted gas or oil field
 - After a reservoir is converted to storage, remaining gas becomes part of the cushion gas volume
- Injected gas

- Gas injected into a storage reservoir
- Likely to be different in composition from native gas



Cross section of gas storage field. From Katz, 1971.



**Generalized structure map of gas storage field.
From Katz, 1977.**

- Spill point
 - Point on structure at which gas is most likely to escape
- Delta pressure
 - Operating pressure for a gas storage reservoir which is higher than original reservoir pressure
 - Aquifer storage reservoirs always have some delta pressure
 - Depleted gas and oil reservoirs may or may not be operated under delta pressure conditions
- Migration
 - Movement of storage gas beyond the storage area, so that it cannot be recovered through the wells completed in the storage zone
- Cycling
 - The process of injecting or withdrawing a percentage or all of a storage reservoir's working gas capacity during a particular season

Deliverability

- Deliverability
 - The maximum rate at which gas can be withdrawn from an underground reservoir under a given set of conditions
 - Deliverability depends on rock characteristics, reservoir pressure, and facilities such as wells, pipelines, and compressors
- Pipeline load factor
 - The ratio of the average annual pipeline flow rate to the design capacity
- Degree-day deficiency
 - Measure of space heating requirement for a given climate
 - Sum over a year or other time period of 65 °F - the mean daily temperature
 - On a graph of temperature vs. time in days, area between a horizontal line corresponding to a temperature of 65 °F and the mean daily temperature
- Sendout
 - Gas volume delivered to the transmission line or consumer
- Peak day
 - The day of maximum demand for natural gas service
 - Usually occurs on the coldest day of the year, when demand for natural gas for heating is at its highest
 - May occur on the hottest day of the year, when demand for space cooling drives electric generation demand to its highest levels
- Peak day deliverability
 - Deliverability required to meet peak day demand
- Design day deliverability
 - The rate of delivery at which a storage facility is designed to be used when storage withdrawals are at their maximum levels
 - Controls design of surface equipment capacity

- Peak-day sendout
 - Gas actually delivered to the transmission line or consumer on the peak day
- Base load
 - Average withdrawal rate during the withdrawal season
 - Obtained by dividing the working gas capacity by the number of days in the withdrawal season
- Peak shaving
 - Practice of providing for short-term (hours-days) demands using specially designed facilities

Appendix V
UGS Glossary

The following definitions were selected from a larger list published by the U.S. National Petroleum Council in 1992

American Gas Association (AGA) - The US gas utility industry trade association.

Base Gas - See “Cushion Gas”.

BCF - Billion Cubic Feet. A volumetric unit of measurement for natural gas.

Certification Capacity - The maximum volume of gas that may be stored in an underground storage facility certificated by the Federal Energy Regulatory Commission. Absent a certificate, a reservoir’s present developed operating capacity is considered to be its “certified” capacity.

Citygate - A point or measuring station at which a gas distribution company receives gas from a pipeline company or transmission system.

Citygate Sales Services - Interstate pipeline natural gas sales service where the title to gas sold changes at the pipeline’s interconnection with the purchasing local distribution company.

Commercial Consumption - Gas consumed by non-manufacturing establishments or agencies primarily engaged in the sale of goods or services. Included are such establishments as hotels, restaurants, wholesale and retail stores, and other service enterprises; gas consumed by establishments engaged in agriculture, forestry, and fishers; and gas consumed by local, state, and federal agencies engaged in non-manufacturing activities.

Curtailments - The rationing of natural gas supplies to an end user when gas is in short supply, or when demand for service exceeds a pipeline’s capacity, usually to an industrial user and/or power generator.

Cushion Gas - The volume of gas, including native gas, that must remain in the storage field to maintain an adequate reservoir pressure and deliverability rate throughout the withdrawal season.

Cycling - The process of injecting or withdrawing a percentage or all of a storage reservoir’s working gas capacity during a particular season.

Deliverability - The rate at which gas can be withdrawn from an underground reservoir. Actual rates depend on rock characteristics, reservoir pressure, and facilities such as wells, pipelines, and compressors.

Delivered - The physical transfer of natural, synthetic, and/or supplemental gas from facilities operated by the responding company to facilities operated by others or to consumers.

Demand Charge - A charge levied in a contract between a pipeline and local distribution company, electric generator, or industrial user for firm gas pipeline transportation service. The demand charge must be paid whether or not gas is used up to the volume covered by the charge.

Demand Side Management - Programs designed to encourage customers to use less natural gas or other fuels or less electricity and to use it more efficiently (i.e., conservation) or to reduce peak demand (i.e., load management).

Demand Day Capacity - The volume of natural gas that a pipeline facility is designed to transport during one day, given the assumptions used in the design process, such as pressures, pipeline efficiency, and peak hourly rates.

Design Day Deliverability - The rate of delivery at which a storage facility is designed to be used when storage withdrawals are at their maximum levels.

Developed Operating Capacity - That portion of operating capacity which is currently available for storage use.

End User - Anyone who purchases and consumes natural gas.

Field - A single pool or multiple pools of hydrocarbons grouped on, or related to, a single structural or stratigraphic feature.

Firm Gas - Gas sold on a continuous and generally long-term contract.

Firm Service - Service offered to customers (regardless of class or service) under schedules or contracts that anticipate no interruptions. The period of service may be for only a specified part of the year as in off-peak service. Certain firm service contracts may contain clauses that permit unexpected interruption in case the supply to residential customers is threatened during an emergency.

Fracturing - Improvement of the flow continuity between gas-bearing reservoir rock and the wellbore by creating fractures which extend some distance into the reservoir.

Gas Condensate Well - A gas well producing from a gas reservoir containing considerable quantities of liquid hydrocarbons in the pentane and heavier range, generally describes as "condensate".

Gas Research Institute (GRI) - A US organization which funds research efforts in all phases of the natural gas industry, including exploration and production, transmission, storage, and end-use application.

Gas Well - A gas well completed for the production of natural gas from one or more gas zones or reservoir.

Gathering System - Facilities constructed and operated to receive natural gas from the wellhead and transport, process, compress, and deliver that gas to a pipeline, LDC, or end user. The construction and operation of gathering systems is not a federally regulated business, and in some states is not regulated by the state.

Hub - A hub is a location where gas sellers and gas purchasers can arrange transactions. The location of the hub can be anywhere multiple supplies, pipelines, or purchasers interconnect. “Market centers” are hubs located near central market areas. “Pooling points” are hubs located near center supply production areas. Physical hubs are found at processing plants, offshore platforms, pipeline interconnects, and storage fields. “Paper” hubs may be located anywhere parties arrange title transfers (changes in ownership) of natural gas.

Hydrates - Gas hydrates are physical combinations of gas and water in which the gas molecules fit into a crystalline structure similar to that of ice. Gas hydrates are considered a speculative source of gas.

Industrial Consumption - Natural gas consumed by manufacturing and mining establishments for heat, power, and chemical feedstock.

Interruptible Gas - Gas sold to customers with a provision that permits curtailment or cessation of service at the discretion of the distributing company or pipeline under certain circumstances, as specified in the service contract.

Local Distribution Company (LDC) - A company that distributes natural gas at retail to individual residential, commercial, and industrial consumers. LDCs are typically granted an exclusive franchise to serve a geographic area by state or local governments, subject to some requirement to provide universal service. Rates and terms and conditions of service are typically (but not always) subject to regulation.

Market Center - A place, located near natural gas market areas, where many gas sellers and gas buyers may arrange to buy/sell natural gas. See “Hub”.

MCF/D - “Thousand cubic feet of natural gas per day”. A volume unit of measurements for natural gas.

MMCF/D - “Million cubic feet of natural gas per day”. A volume unit of measurement for natural gas.

Native Gas -The gas remaining in a reservoir at the end of a reservoir’s producing life. After a reservoir is converted to storage, remaining gas becomes part of the cushion gas volume.

Off-Peak - Periods of time when natural gas pipeline facilities are typically not flowing natural gas at design capacity.

Operating Capacity - The maximum volume of gas an underground storage field can store. This quantity is limited by such factors as facilities, operational procedure, confinement, and geological and engineering properties.

Peak Day - The day of maximum demand for natural gas service. In any given area, the “peak day” usually occurs on the coldest day of the year, when demand for natural gas for heating is at its highest/ Because each part of the country experiences different weather conditions, the peak day for each region or area is usually different. In some parts of the country, such as the Southeast and the Southwest Central regions, the peak day may occur on the hottest day of the year, when demand for space cooling drives electric generation demand to its highest levels.

Peak-Day Deliverability - The rate of delivery at which a storage facility is designed to be used for peak days.

Pipeline - A continuous pipe conduit, complete with such equipment as valves, compressor stations, communications systems, and meters, for transporting natural and/or supplemental gas from one point to another, usually from a point in or beyond the producing field or processing plant to another pipeline or to points of use. Also refers to a company operating such facilities.

Reservoir Pressure - The force within a reservoir that causes the gas and/or oil to flow through the geological formation to the wells.

Residential Consumption - Gas consumed in private dwellings, including apartments, for heating, air conditioning, cooking, water heating, and other household uses.

Storage Additions - Volumes of gas injected or otherwise added to underground natural gas reservoirs or liquefied natural gas storage.

Storage Field - A facility where natural gas is stored for later use. A natural gas storage field is usually a depleted oil- or gas-producing field (but can also be an underground aquifer or salt cavern). The wells in these depleted fields are used to either inject or withdraw gas from the reservoir as circumstances require.

Storage Volume - The total volume of gas in a reservoir. It is comprised of the cushion and working gas volumes.

Storage Withdrawals - Volumes of gas withdrawn from underground storage or liquefied natural gas storage.

Top Gas - See “Working Gas”.

Underground Storage - The storage of natural gas in underground reservoirs at a different location from which it was produced.

Underground Storage Injections - Gas from external sources put into underground storage reservoirs.

Underground Storage Withdrawals - Gas removed from underground storage reservoirs.

Vented - Gas released into the air on the base site or at processing plants.

Well Workover - Work done on a well that improves the mechanical condition of the well or work that treats the reservoir in order to improve gas flow.

Working Gas - The volume of gas in reservoir above the designed level of the cushion gas. It may or may not be completely withdrawn during any particular output season. Conditions may permit the total working capacity to be used more than once during any season.

Appendix H
2005, Cement Evaluation in Gas Filled Boreholes,
Baker Atlas Final Report

CEMENT EVALUATION IN GAS FILLED BOREHOLES FINAL REPORT

Reporting Period Start Date: 05/01/2005

Reporting Period End Date: 12/31/2006

Edward Domangue

February 2007

DE-FC26-03NT41779

Baker Hughes Oilfield Operations, Inc.

Baker Atlas

2001 Rankin Road

Houston, TX 77073

DISCLAIMER

“This report was prepared as an account of work sponsored by an agency of the United States Government. Neither the United States Government nor any agency thereof, nor any of their employees, makes any warranty, express or implied, or assumes any legal liability or responsibility for the accuracy, completeness, or usefulness of any information, apparatus, product, or process disclosed, or represents that its use would not infringe privately owned rights. Reference herein to any specific commercial product, process, or service by trade name, trademark, manufacturer, or otherwise does not necessarily constitute or imply its endorsement, recommendation, or favoring by the United States Government or any agency thereof. The views and opinions of authors expressed herein do not necessarily state or reflect those of the United States Government or any agency thereof.”

ABSTRACT

Contained in this report is a description of efforts at determining the suitability of a new technology (EMATs) to perform cement evaluation in gas filled boreholes (e.g. gas storage wells). Also addressed is the issue of casing to cement microannulus using EMAT technology.

Included in the report are the following:

- Background/relevancy.
- Fundamentals of the new technology.
- Results of analytical modeling to establish feasibility.
- Experimental setup and data results.
- Conclusions

Findings of the investigation are that the technology will be suitable for the intended applications.

TABLE OF CONTENTS

1.0 EXECUTIVE SUMMARY	5
2.0 BACKGROUND	6
3.0 EXPERIMENTAL.....	7
3.1 OVERVIEW	7
3.2 CEMENT MODELS FOR TESTING LAB INSTRUMENTS.....	7
3.3 MICRO-ANNULUS STUDY	8
3.4 TRANSDUCERS	11
3.5 TRANSDUCER CONFIGURATION	12
3.6 MODELING	13
4.0 RESULTS AND DISCUSSION.....	14
5.0 CONCLUSIONS	20
6.0 REFERENCES	20

1.0 EXECUTIVE SUMMARY

Beginning in 2002, Baker Atlas began looking at methods of improving cement evaluation in the new, lighter weight cements being introduced to the oil and gas industry. One avenue of investigation included the use of new acoustic sensors that broadened the type and frequency of acoustic signals that could be induced into the casing. A benefit of this sensor technology was that it did not rely on acoustic coupling of the signal through the borehole fluid, thus having the potential to work in gas-filled boreholes. Although such an application was not needed in conventional oil and gas development, Baker Atlas recognized the potential interest of the gas storage industry in such an application.

With the support of the Gas Storage Technology Consortium, Baker Atlas conducted a series of tests to determine whether this technology could indeed run cement evaluation logs in gas-filled boreholes. These additional tests were performed at Baker Atlas' Houston facility in conjunction with ongoing development of the new sensors. Furthermore, an additional evaluation of the ability of this technology to differentiate between uncemented pipe and a 'micro-annulus' was undertaken as such conditions are thought to be prevalent in older gas storage wells. The following report details these tests and their results.

The testing conducted under this program has shown that these new sensors are indeed capable of providing cement evaluation services in gas-filled boreholes. Although exact sensor response varied somewhat from the responses in liquid-filled boreholes, these differences are not material in terms of identifying a cement sheath around the casing. Finally, additional tests clearly show a method of differentiating between uncemented pipe and a micro-annulus.

Much work remains to be done to field an instrument and service usable in field work. Baker Atlas continues to work on this technology, however, and expects to conduct field trials of the new measurements in the future.

2.0 BACKGROUND

According to the Department of Energy, Office of Fossil Energy, there are approximately 110 operators maintaining more than 17,000 gas storage wells in over 415 underground storage facilities across the United States. [1]

In virtually every application, steel casing, cemented into place, serves to isolate the well from the underground formations forming part of the downhole completion hardware through which storage gas is injected and withdrawn under pressure.

The process of cementing wellbore casing in place provides two major benefits in gas storage wells. First, cement provides zonal isolation, preventing gas migration up the well bore between the formation and the casing. Second, cement transfers stress from the casing to the formation, increasing the effective strength and working pressure of the casing. [2] Unfortunately, reliable cement evaluation data does not exist on many wells in use for gas storage today.

Current cement evaluation techniques are designed to operate in fluid-filled holes typically on newly drilled but uncompleted wells. These techniques typically use an acoustic wave generated and then received by a logging tool within the wellbore to detect cement placed outside the casing and quantify several simple properties of this cement. A major restriction of all these services with respect to the gas storage industry, however, is their reliance on fluid in the casing to provide acoustic coupling between the logging tool and the casing. These tools are therefore unable to operate in gas-filled boreholes.

This report details the progress of efforts to confirm the validity of a new technique as well as the applicability of the technique for evaluating cement in gas-filled boreholes. The effort is part of a much larger project primarily intended to address the current shortfall within the industry for evaluation of highly modified, light-weight cements which normally have fluid-filled casings.

The ultimate benefit to the gas storage industry of a cement evaluation service capable of operating in a gas filled borehole is significant. First, it could provide direct proof of cement placement and zonal isolation in older gas wells (today, such a determination requires filling the well with fluid before logging). Second, the presence of cement between casing and the formation provides a method of transferring pressure-induced stress from the casing to the formation, greatly increasing the effective burst strength of the casing. Verification of cement placement should allow more realistic assessment of remaining casing burst strength, eliminating significant cost associated with unneeded

workovers. Finally, it is generally accepted that a sheath of competent cement on the exterior of the casing is beneficial in reducing the effects of corrosion on the casing wall.

3.0 EXPERIMENTAL

3.1 Overview

Prior generation cement evaluation techniques are fully capable of evaluating the placement of conventional cements in newly drilled wells. The most widely accepted technique uses a compressional acoustic wave generated and then received by a logging tool within the wellbore to detect cement placed outside the casing and quantify several simple properties of this cement. Due to the acoustic impedance mismatch between gas and steel, however, these instruments can not couple sufficient acoustic energy into the casing and cement to effectively make these measurements in gas filled boreholes. Prior to the effort contracted for and reported upon herein, Baker Atlas had identified that Electro Magnetic Acoustic Transducers (EMAT) were capable of generating controlled guided acoustic waves in electrically conductive material. Among these guided waves are Shear Horizontal (SH) and Lamb waves of both the symmetric and asymmetric types. SH waves are sometimes referred to as transversely polarized waves. In a steel plate, SH particle displacement is tangential to the plate while direction of propagation is normal to the particle displacement. Lamb waves in a steel plate have particle displacement normal to the plate and again propagation is normal to the particle displacement. Because of these wave properties, Baker Atlas felt that EMATs would be able to provide capabilities beyond those of conventional cement evaluation devices. Subsequent analytical modeling further indicated those capabilities were probable.

Making use of EMATs, Baker Atlas is currently in the design phase of a new acoustic instrument intended for evaluation of light-weight cements. Because 100% of the current market for cement bond measurements is in fluid-filled boreholes, this effort is primarily directed towards those applications. Our work thus far indicates the instruments could be developed into a viable cement evaluation service for gas-filled boreholes.

This report provides certain details of our investigation techniques, observations, and conclusions as to the applicability of these concepts in gas-filled boreholes.

3.2 Cement models for testing lab instruments

Baker Atlas has applied for and has been granted a patent on several of these candidate techniques that could be used in gas-filled boreholes. [3] We are confident that these techniques will yield a suitable technique for eventual incorporation into a field measurement.

After initial evaluation for suitability, the selected measurement technologies have been built into test articles suitable for lab use only. Measurements with these devices have been made in several specially constructed cement test models (see Figures 1 and 2). These cement models were constructed with various cement formulations, casing thickness, and in a very special case, a controlled micro-annular condition.

Measurements were performed with both water and air in the borehole for direct comparison. Models were constructed so that they may be pressured internally to 1,000 psi to further simulate downhole conditions if needed (need was not demonstrated in the process of making measurements).

3.3 Micro-annulus study

When the first step was completed, the next required step in determining the feasibility of making cement evaluation measurements was to evaluate the effect of any potential 'microannulus' on the measurement. A microannulus is a very small gap between the cement and the casing. In typical completions, this gap is often caused by thermal casing expansion during cement curing and by wellbore pressure fluctuations (reduction of casing fluid weight, for example) subsequent to cement setting. Under conditions normally experienced during well completion, the size of the microannulus is typically no more than a few thousandths of an inch and is temporarily reversed for bond logging by increasing the fluid pressure within the well. In the case of gas storage wells, however, normal field operations imply that the thermal and pressure cycles may be large and last for months. It is thought that large microannuli are therefore possible in the gas storage well environment.

Prior to the effort contracted for and reported on herein, Baker Atlas was seeking new methods for evaluating cement in the presence of a microannulus without need for the conventional approach of pressuring up on the casing to swell the casing and close the microannulus. In the course of our search, we discovered that EMATs were capable of generating guided acoustic waves of several types in electrically conductive material. Further, our analytical modeling also indicated that one or a combination of two or more of these guided waves would be useful in the said cement evaluation.

In the case of a typical gas storage well simply increasing the borehole pressure, as is done in conventional wells, it is normally not possible since these wells usually have open perforations.

In order to fully understand this effect, a physical model was built so that actual transducer response in a microannulus can be studied. This model required a special "tapered" casing, which can be raised or lowered by means of a hydraulic jack, varying the size of the microannulus. A schematic of the model is shown in Figure 2.

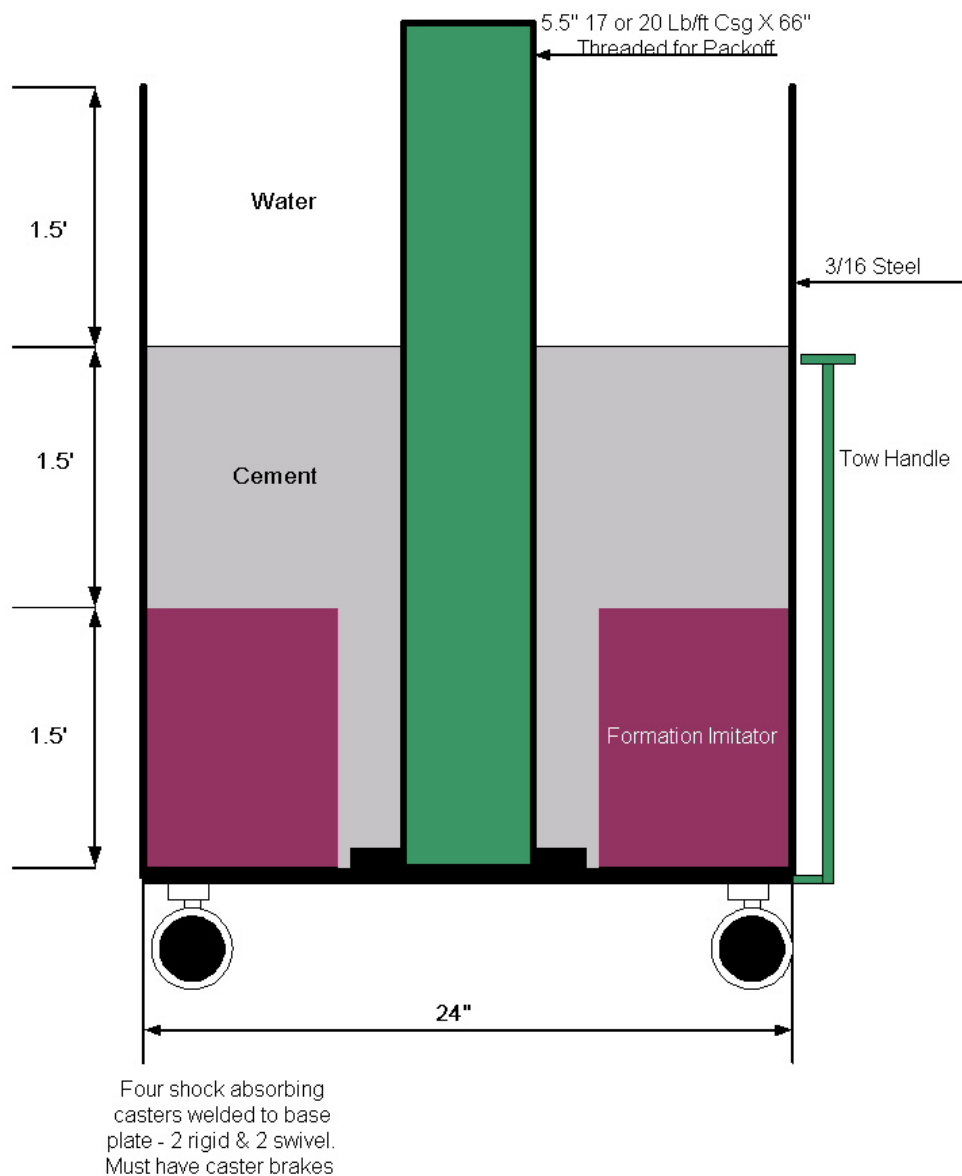


Figure 1

Drawing of a typical cement model for evaluation of new cement evaluation technology. Note central casing is welded to the bottom plate of the fixture during fabrication. The next step is to install the formation imitator which is actually a highly dense synthetic, cementitious material. The formation imitator was placed in all models save the microannulus fixture and the single free pipe model.

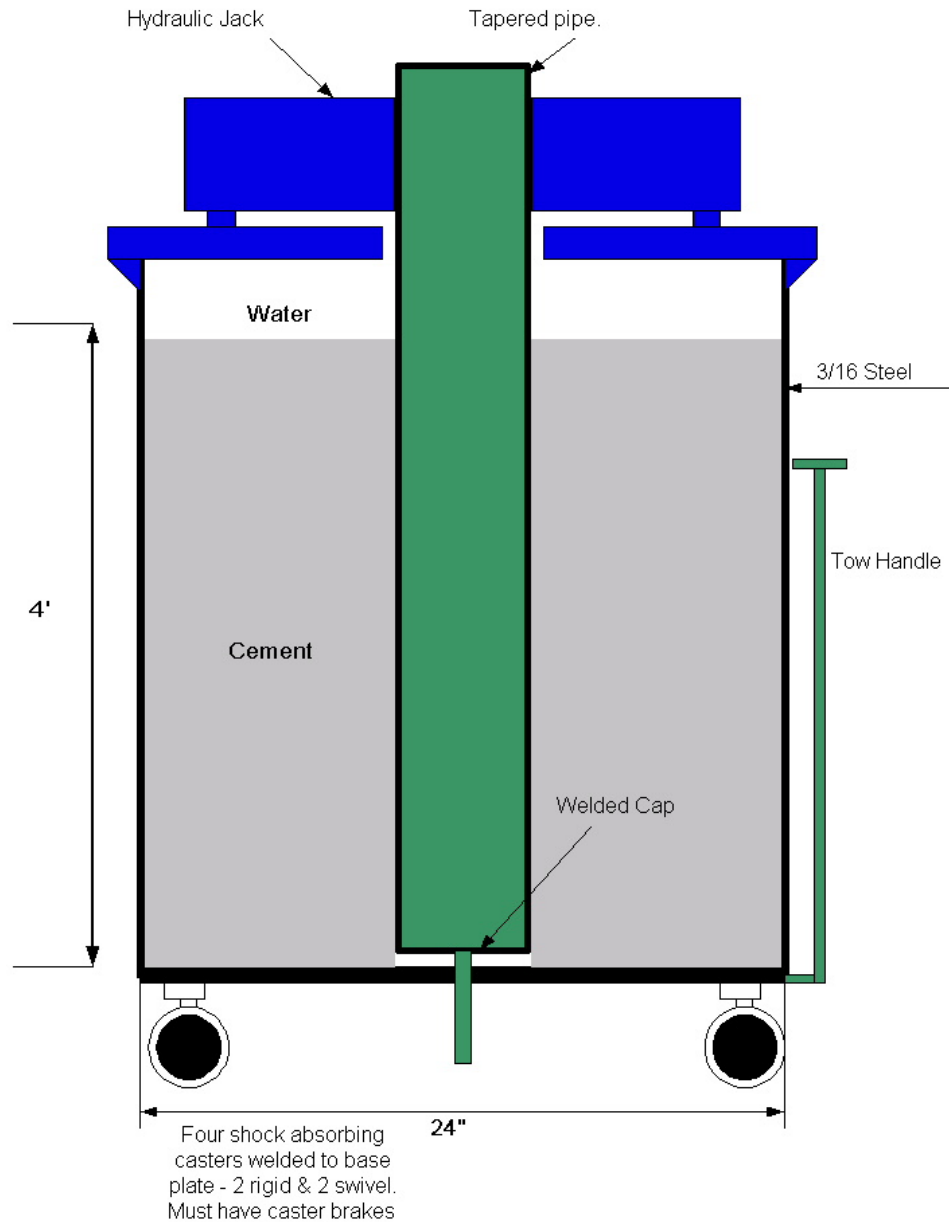


Figure 2

Drawing of a highly specialized version of cement model which permits investigation of microannular effects on the new cement evaluation techniques. The center casing is not attached to the bottom plate, but rather can be moved up and down in the cement column. The center casing is additionally tapered (smaller at the bottom), so that moving the casing up creates a controlled and progressively larger microannulus.

It should be pointed out that great care was exercised in the formulation, mixing, and placement of cement in the models. Nevertheless, the resulting specimens were not always of uniform quality and certain discontinuities in the cement column were present

as observed from the resulting data. More on this subject is offered later in the results and discussion section.

Eight cement models in total are constructed, but for purposes of this report, we will show data taken in three of the models.

3.4 Transducers

A review of the previously mentioned patent will reveal that our choice of transducer type is the Electro Magnetic Acoustic Transducer, or EMAT as they are known in the world of NDT. This transducer type was chosen for three principle reasons:

- By selection of the magnet and coil configuration and dimensions, the transducers are able to send and receive acoustic energy at different wavelengths as well as different modes of propagation.
- By excitation of multiple frequencies, the transducers are able to send and receive acoustic energy at different velocities and demonstrate varying degrees of sensitivity to casing and cement properties.
- The transducers do not require a liquid couplant to send and receive acoustic signals.

A simplified schematic of an EMAT can be observed in Fig. 3.

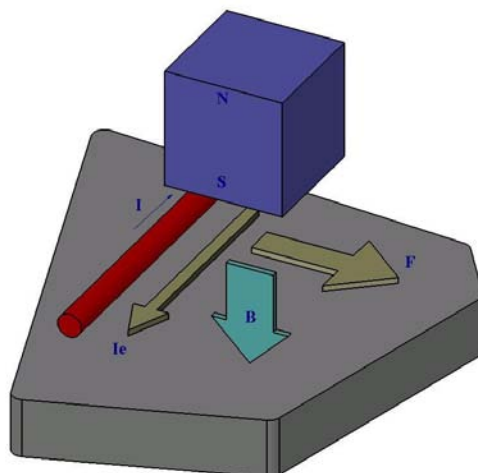


Figure 3

An EMAT uses non-contact electromagnetic transduction to impart physical stress to a conductive medium. A current I , in a wire near a conductive surface induces an equal and opposite eddy current I_e in the surface of the material. When a magnetic field is present, a force is created in the conductive surface known as a Lorentz force. This basic effect is the same as used in an electric motor to convert electrical energy into mechanical energy.

$$F = I_e \times B$$

This force generates particle displacement resulting in elastic waves. Selection of magnet and wire (coil) configuration and dimension controls a resulting Ultrasonic Guided wave. Common types of guided waves are Shear Horizontal (SH), also known as tangentially opposed, and Lamb waves of both symmetric and asymmetric type. Further information is available in published literature. [4]

3.5 Transducer configuration

For purposes of this study, a simple arrangement of transmitter and receivers was used consisting of only one transmitter and two receivers placed at equal distance radially. The arc between each transducer covers 120 Deg of the casing inner surface. Schematic of this arrangement can be observed in Figure 4.

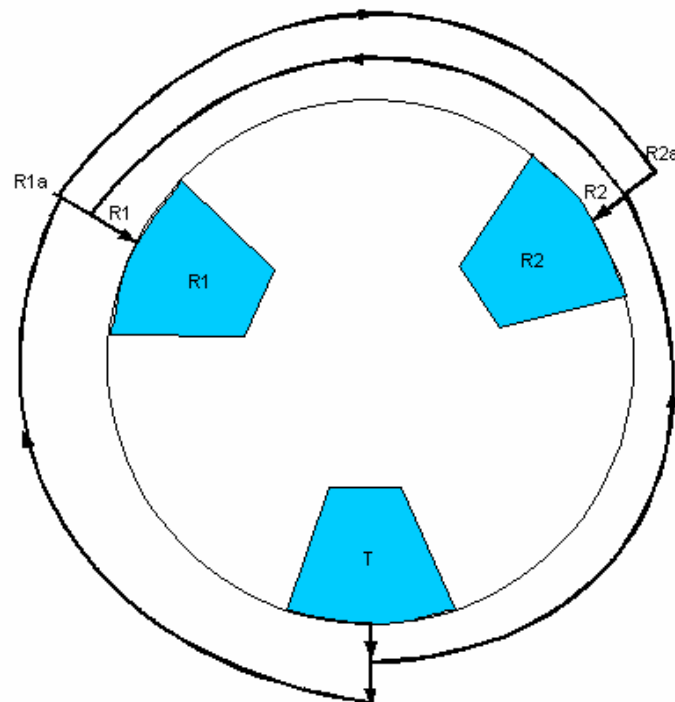


Figure 4

Using the above simple configuration, a single compensated measurement of attenuation can be made between Receivers One and Two using all three transducers. The calculation is made as follows using amplitudes from four arrivals. R1 and R2 measurements are made when the signals from the transmitter travel in one direction, and R1a and R2a are made as a result of signals traveling in the opposite direction.

$$Attn = \frac{-10}{\Delta} * \text{Log} \frac{R1}{R2} * \frac{R2a}{R1a}$$

This calculation approach provides an attenuation measurement compensated for transducer differences and is already widely accepted in the industry.

3.6 Modeling

Prior to entering the empirical phase of this project, a considerable amount of modeling was conducted in hopes of establishing the feasibility of going ahead with the larger effort. The results of one such model are presented in Figure 5. The intent of this model is to depict expected attenuation results for SH transducers from two specific cement density formulations across multiple casing wall thicknesses. Please keep in mind that the model assumes ideal contact with the cement as well as absolutely uniform placement and density. The results served as justification to commence with the experiments.

As will be evident from the results and discussion section, there is good numerical agreement with the case of low density cement. However, the model predicts much higher attenuation in the conventional 14 lb/gal cement slurry than was actually measured. Again, the model represents an ideal environment as well as an ideal instrument. In practice, measurements made with our transducers encountered signals in the far receivers that were below the threshold of noise. The resulting data therefore understates the actual acoustic attenuation rates present. It is our intention that further development will make use of improved technology which will permit us to more accurately measure actual attenuation rates.

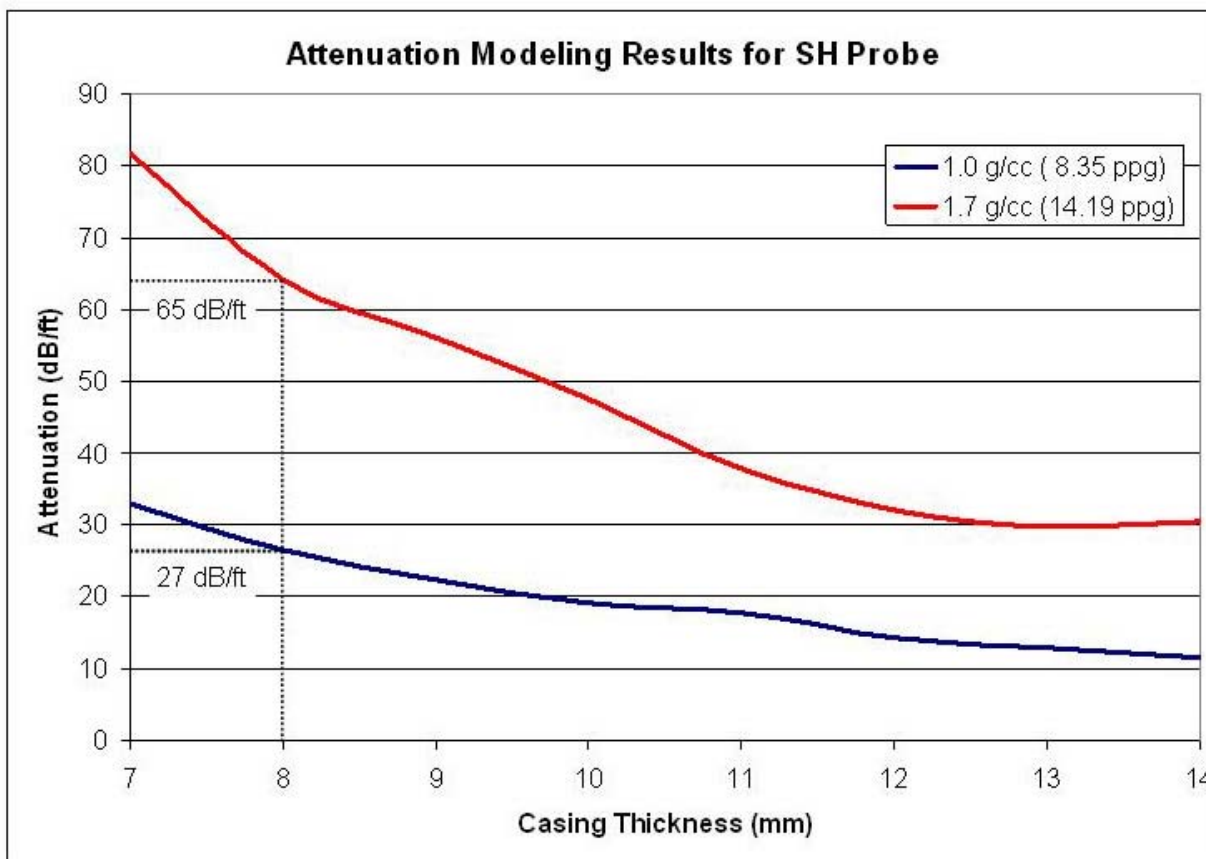


Figure 5

Modeled attenuation obtained for SH waves for 2 different slurry densities for the case of ideal contact between the pipe and cement. Highlighted results correspond to physical configuration of model data presented in Figures 6 and 7.

4.0 RESULTS AND DISCUSSION

In all cases, the following data was obtained beginning with the test instrument starting at the bottom of all three cement models and then pulled at an approximately constant rate to the top of the model. We would therefore expect that the instrument would detect cement in the lower sections and free pipe near the top (left to right on the data figures).

Figure 6 depicts a Shear Horizontal (SH) EMAT instrument response in terms of acoustic attenuation in the cement model with a fairly conventional 14 lb/gal extended slurry. Data is taken with and without fluid in the center casing. As previously mentioned, you will note that the quality of the cement is not as uniform and continuous as might be expected. Even so, a maximum attenuation rate of more than 40 dB/ft is observed in the cement with a contrasting attenuation of near 5 dB/ft in the free pipe section or a net 35 dB/ft contrast. By comparison, conventional cement evaluation systems demonstrate a net contrast of only approximately 10-12 dB/ft in a similar environment.

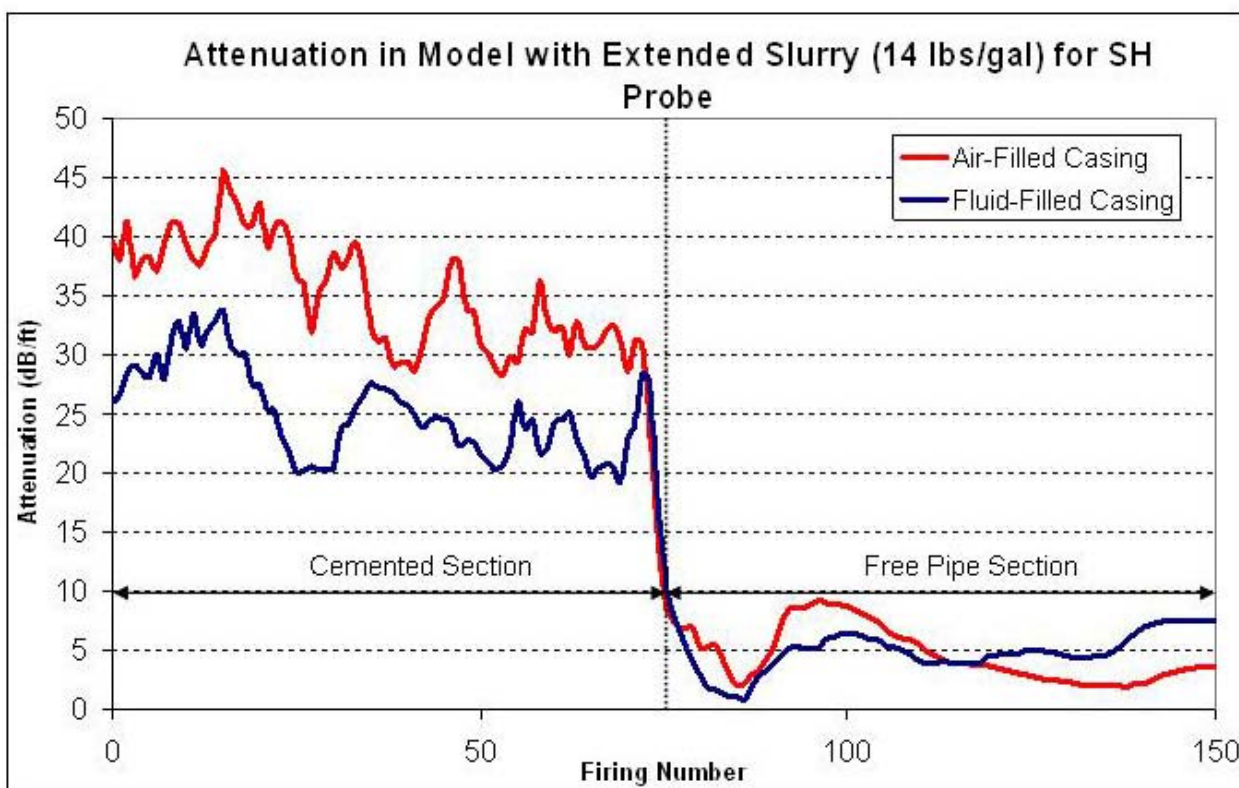


Figure 6

Attenuations obtained in experiments with SH probe for model with extended cement slurry contrasting air filled vs. fluid filled center casing.

Figure 7 depicts the data from the SH instrument in the cement model which contains extreme low density 7 lb/gal cement, again with and without fluid in the center casing. While the contrast between cemented and free pipe is not as high as in the prior example, the contrast still remains significant in terms of being able to identify the presence of cement. In this case, approximately 25 dB/ft maximum net contrast.

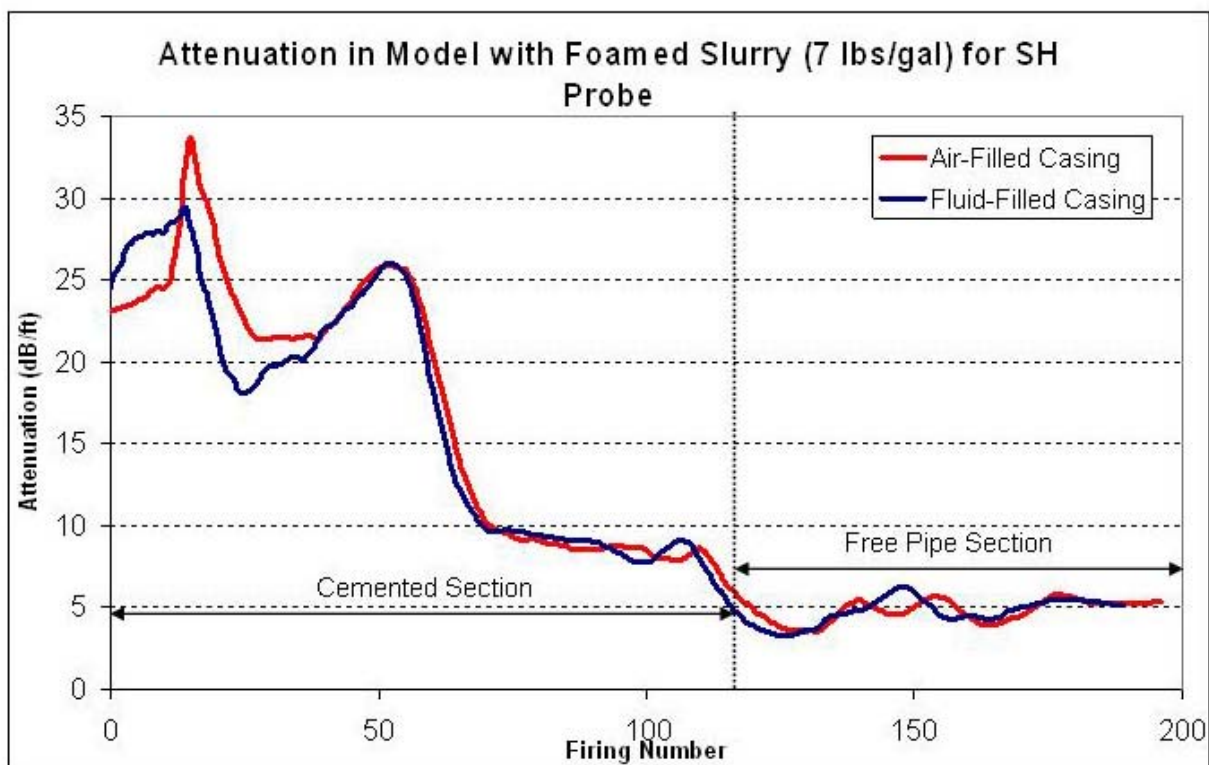


Figure 7

Attenuation obtained in experiments with SH probe for model with foamed cement slurry contrasting air filled vs. fluid filled center casing.

Figure 8 shows the data taken with the SH instrument from the microannulus cement model with fluid inside the center casing. Recall that the microannulus model has the additional capability over all the other models to move a tapered center casing up and down in the cement column creating a controlled microannulus of greater size as the pipe is moved up. In this model, the best cement encountered is just about halfway up the cement column. The black curve depicts cement conditions after cementing and before the casing was ever moved. All other curves represent varying degrees of microannulus size.

You will note that all the other curves are essentially equal-valued without regard to size of the microannulus present.

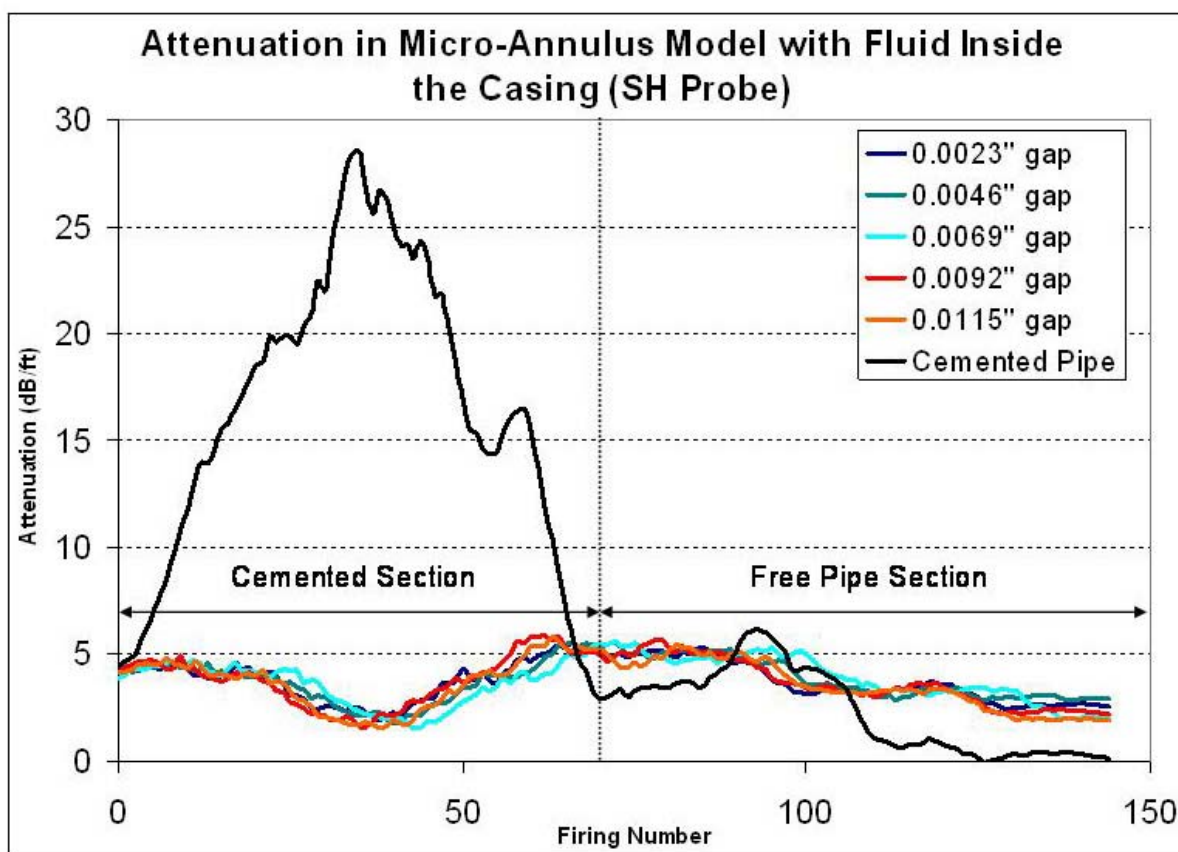


Figure 8

SH Probe results in the microannulus fixture with fluid inside the center casing first with fully cemented casing and then with varying microannulus size. Note that once a microannulus is present, all SH data is essentially equal valued.

Figure 9 displays the data results in the microannulus fixture over the same microannulus conditions as in the previous example, however in this case there is no fluid in the casing. In Figures 9 and 10, the first introduction of a microannulus results in free pipe readings. Please also note that there is essentially no difference in results from the air-filled and fluid-filled experiments.

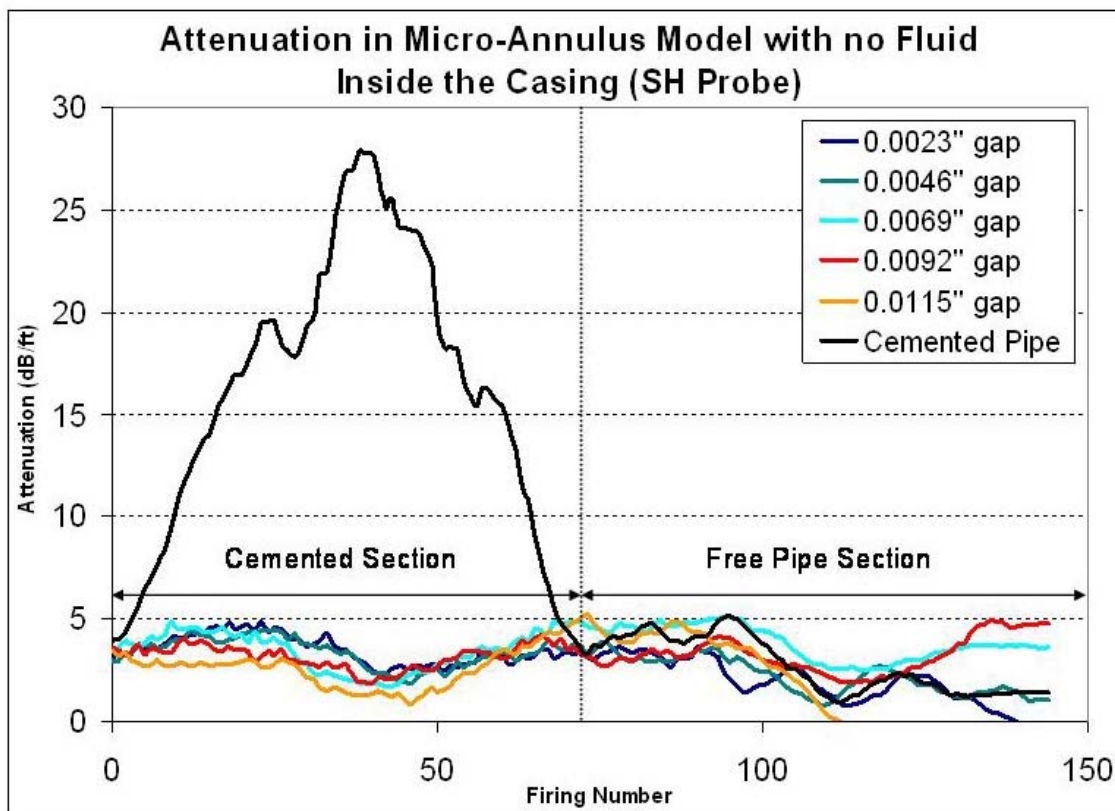


Figure 9

SH Probe results in the microannulus fixture with no fluid inside the center casing first with fully cemented casing and then with varying microannulus size. Note that once a microannulus is present, all SH data is essentially equal valued.

Figure 10 displays data taken with a flexural mode (LAMB) EMAT instrument in the microannulus model with the same microannulus conditions as in the prior two examples. Only data with no fluid inside the casing is presented. Again, the black curve represents data in the model after cementing and before the casing was ever moved. You will note that attenuation is present in all positions, even with a microannulus of 0.0115". You may also notice that the data appears to be offset from curve to curve. This is due to the apparatus used to transport the instrument up the casing. It was not possible to control the exact start time and velocity during the experiments. There is a nevertheless a high degree of similarity between all curves.

The attenuations observed tend to get larger as the microannulus also gets larger. The last two stations, however (0.0092" and 0.0115") seem to converge. The last station (0.0115") is the largest microannulus we can create with this model.

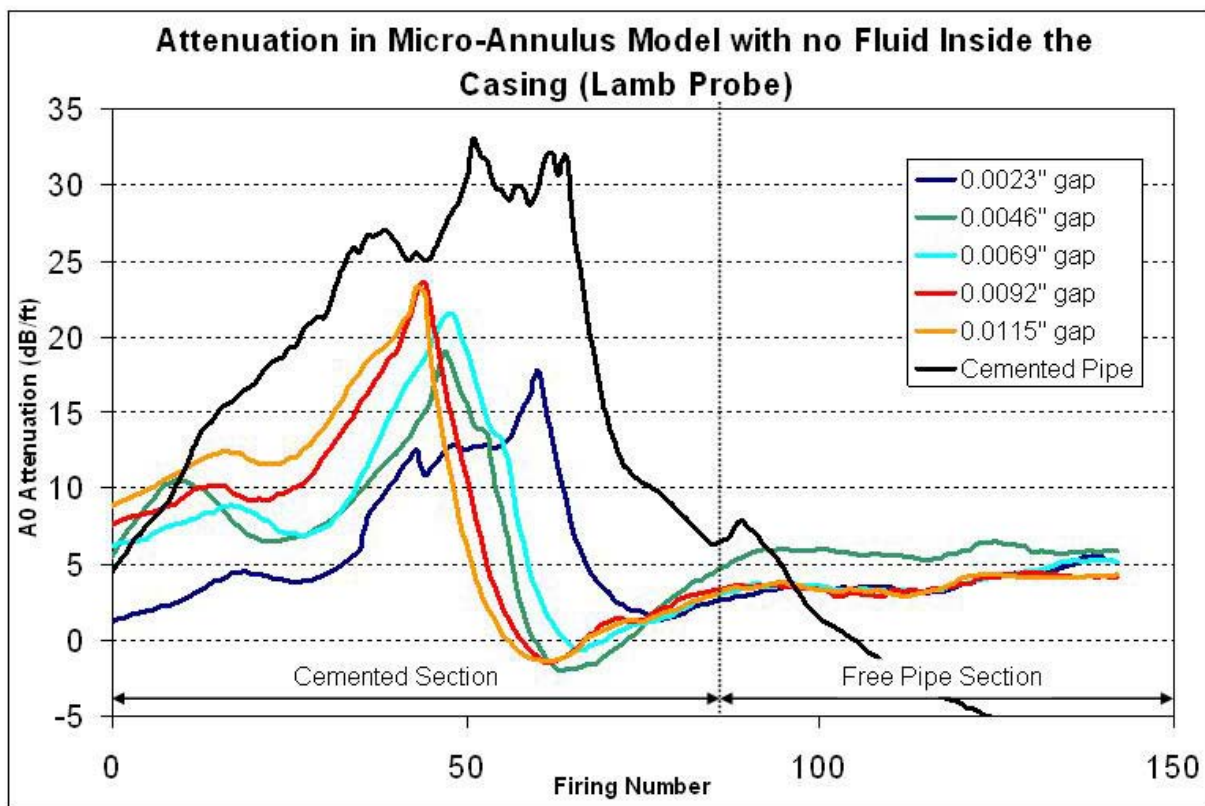


Figure 10

5.0 CONCLUSIONS

The data indicates that the SH EMAT instrument is clearly able to distinguish cemented pipe from free pipe without regard to whether there is fluid inside the measured casing. This is true even in the presence of extremely light weight (7 lb/gal) foamed cement.

As was predicted early on in the project, the SH EMAT instrument displays free pipe value whenever a microannulus is also present.

As was hoped at the outset of the project, the LAMB EMAT instrument is able to distinguish cemented pipe from free pipe even in the presence of a sizable microannulus (0.0115”).

A combination of SH and LAMB EMAT sensors permits detection of cement presence even when a microannulus is also present. The condition is detectable without regard to whether there is fluid or air inside the casing.

6.0 REFERENCES

[1] Department of Energy, Office of Fossil Fuels; Website: *Gas Storage and Liquefied Natural Gas*, February 16,2004

[2] Fleckenstein, Eustes, & Miller, SPE 62596

[3] United States Patent 7,150,317 Barolak, et al. December 19, 2006

[4] NDT Resource Center website

United States Patent Application 20050190648 Method and apparatus for cement bond evaluation using transversely polarized shear waves

United States Patent Application 20060198243 Use of lamb waves in cement bond logging

Appendix I
2005, Smart Gas: Using Chemicals to Improve Gas Deliverability,
Correlations Company Final Report

Smart Gas: Using Chemicals to Improve Gas Deliverability

Final Report

Reporting Period Start Date:

May 1, 2005

Reporting Period End Date:

December 31, 2006

Principal Authors:

William W. Weiss

Xina Xie, Ph.D.

DOE Award No.

DE-FC26-03NT41779

Subaward No. 2909-CC-DOE-1779

Report Issue Date:

June 30, 2006

Prime Awardee

The Pennsylvania State University

110 Technology Center Building

University Park, PA 16802

Subawardee

Correlations Company

P.O. Box 730

115 Court Street

Socorro, NM 87801

Disclaimer

“This report was prepared as an account of work sponsored by an agency of the United States Government. Neither the United States Government nor any agency thereof, nor any of their employees, makes any warranty, express or implied, or assumes any legal liability or responsibility for the accuracy, completeness, or usefulness of any information, apparatus, product, or process disclosed, or represents that its use would not infringe privately owned rights. Reference herein to any specific commercial product, process, or service by trade name, trademark, manufacture, or otherwise does not necessarily constitute or imply its endorsement, recommendation, or favoring by the United States Government or any agency thereof. The views and opinions of authors expressed herein do not necessarily state or reflect those of the United States Government or any agency thereof.”

Table of Contents

	Page Number
List of Tables	3
List of Figures	3
Abstract	5
Executive Summary	5
Introduction	6
Experimental Results	11
Laboratory Screening Tests	11
Capillary rise	11
Critical micelle concentration	15
Contact angle (water drop)/core	16
Core imbibition	19
Deliverability	23
Sandstone	23
Dolomite	25
Engineering	25
Production history analysis	26
Waverly St. Peter aquifer storage facility	26
Bell River Mills Niagaran reef storage facility	33
Discussion	36
Conclusions	38
References	38
Appendix	40

List of Tables

Page Number

Table 1. Potential gas wetting agents	6
Table 2. Synthetic seawater composition	11
Table 3. Capillary rise tests results	12
Table 4. CMC test results	16
Table 5. Surfactant prices	36

List of Figures

Figure 1. Capillary tube test.	7
Figure 2. Surfactant drop screening method.	8
Figure 3. Representation of an imbibition test	9
Figure 4. Demonstration of the dry/wet gas concept where the constant-flow rate pressure drop is measured independently in the first and second half of the core.	10
Figure 5. Deliverability history of the Waverly well #91 during the 2004 season.	11
Figure 6. Capillary rise of surfactants at 10,000 ppm in water.	13
Figure 7. Capillary rise of surfactants at 1,000 ppm in water.	13
Figure 8. Capillary rise of surfactants at 100 ppm in water.	14
Figure 9. Capillary rise of surfactants at 10,000 ppm in methanol.	14
Figure 10. Capillary rise of surfactants at 1,000 ppm in methanol.	15
Figure 11. Capillary rise of surfactants at 100 ppm in methanol.	15
Figure 12. Critical micelle concentration test results.	16
Figure 13. Water drop on St. Peter sandstone.	17
Figure 14. Water drops on untreated Niagaran dolomite core plugs.	17
Figure 15. Water drop contact angle on treated sandstone is less than 90°.	18
Figure 16. Water drops on treated dolomite are similar to contact angles shown in Fig. 15.	19
Figure 17. Forty-two percent less water was imbibed into the surfactant-treated core (17).	20
Figure 18. Seventeen percent less water was imbibed into surfactant-treated core (3).	21
Figure 19. Imbibition test results with Niagaran dolomite core # 2428.	22
Figure 20. Bell River Mills core 2396 imbibition test result.	23
Figure 21. Gas deliverability through St. Peter 109-md sandstone.	24
Figure 22. Deliverability test results through 68-md St. Peter sandstone.	24
Figure 23. Marginal increase in deliverability with surfactant-treated dolomite core.	25
Figure 24. Waverly # 5 performance history.	26
Figure 25. Well 5 flow rate vs. pressure.	27
Figure 26. Rate, flowing pressure, deliverability, and observation well pressure of Well 5.	28
Figure 27. Core porosity vs. the average of the short normal log over 1' intervals.	29
Figure 28. Core porosity vs. the average of the short normal log over 3' intervals.	30
Figure 29. Core porosity vs. the average of the SP log over 3' intervals.	31
Figure 30. Core porosity vs. the 1 st derivative of the average of the SP log over 3' intervals.	32
Figure 31. Fuzzified core porosity vs. the average of the short normal log over 1' intervals.	33
Figure 32. Fill and withdrawal rate-pressure history.	34

Figure 33. Deliverability vs. cumulative withdrawal.	35
Figure 34. Injectivity vs. cumulative fill volume.	35
Figure 35. Potential deliverability increase with Well 91 surfactant treatment.	37
Figure A1. Summary of capillary rise tests.	40
Figure A2. Krg in St. Peter sandstone core "A" with brine or Tomadry N-4.	41
Figure A3. Krg in St. Peter Sandstone "M" with brine or Stepenquat 300.	41
Figure A4. Krg in dolomite core #2428 with brine or N-4 Surfactant.	42
Figure A5. Krg in dolomite core #2396 with brine or Tomadry N-4.	42
Figure A6. Performance history of Waverly well # 21.	43
Figure A7. Performance history of Waverly well # 88.	44
Figure A8. Performance history of Waverly well #99.	45

Abstract

Each year, more than 17,000 gas storage wells in the United States lose from 3–5% of their storage capacity and deliverability. In addition, the gas storage industry spends \$80–100 million annually to revitalize existing wells; thus, there is an economic incentive to develop new stimulation methods. Limited laboratory information suggests that using surfactants to alter the wettability of the reservoir rock could increase deliverability of gas storage wells. The objective of this project was to develop new technology to improve deliverability from gas storage wells. Two cost-effective surfactants were selected from 11 candidates through preliminary screening tests for additional reservoir core tests. Reservoir cores from three gas storage facilities including sandstone and dolomite reservoirs were used to evaluate surfactant-gas-core systems. The imbibition and core flood tests showed that gas deliverability and storage capacity were improved in surfactant-treated sandstone cores. However, the surfactants had a very limited effect on dolomite cores. An engineering analysis was conducted to develop an analytical method to evaluate future field tests of the new technology. The aquifer storage facilities are candidates for field testing.

Executive Summary

The objective of this project was to develop new technology to improve deliverability from gas storage wells. The laboratory effort included preliminary surfactant-screening tests and work with reservoir cores to evaluate surfactant-gas-core systems. In addition to the use of capillary tubes to screen surfactants, a novel method based on the contact angle of water drops on reservoir cores was investigated. Concurrently, an engineering analysis was conducted to provide an inventory of storage facility reservoirs that are candidates for field testing and establish baseline metrics. Initially the potential fields included sandstone and dolomite reservoirs in dry gas fields and water aquifers. However, the laboratory tests failed to support the application of surfactants in dolomite gas storage reservoirs because the cores were not water-wet.

It is known that water-wet porous media imbibe water in a fashion similar to water rising in a glass capillary tube. In gas storage reservoirs, the imbibition force promotes the retention of water in the pore space, which curtails the deliverability of gas to the wellbore during periods of high demand. In a similar manner, the injection of gas during the fill cycle is restricted. The pore space occupied by irreducible water is also not available for gas storage. Adding surfactants to the well during the fill cycle could decrease the capillary pressure by changing the rock surface wettability.

Results from this project provide the foundation for a possible continuation project that would focus on field demonstrations of the new technology. Many variables could affect changes in well deliverability. New smart technology based on fuzzy logic and neural networks would be used to analyze the field test results and generate correlations that would optimize commercial applications.

Introduction

Each year, more than 17,000 gas storage wells in the United States lose from 3–5% of their storage capacity and deliverability. The gas storage industry spends \$80–100 million annually to revitalize existing wells with methods such as mechanically removing debris, washing, injecting acids, and creating new perforations in the well pipe.¹ Improvements are limited and temporary. A principal cause of the loss of deliverability problem is the retention of water in the reservoir matrix, also known as relative permeability effects.² A solution to the reduced deliverability due to capillary forces is the subject of this final report. Here flow performance is characterized with a gas deliverability index defined as the quotient of flow rate divided by pressure drop, $q/\Delta P$, across a core plug or into/out of the wellbore.

Many gas storage reservoirs are thought to be water-wet, which promotes the retention of water around the near-wellbore formation via capillary forces, or $P_c = \frac{2\sigma \cos \theta}{r}$, where P_c is the capillary pressure, σ is the gas-water surface tension, θ is the contact angle, and r is the equivalent capillary radius. The greater the capillary pressure, the more water retained. The problem becomes increasingly serious with decreased formation permeability due to the smaller pore sizes generating stronger capillary action. The retained water curtails the gas deliverability to the wellbores of gas storage wells during periods of high demand and in a similar manner restricts the injection of gas during the fill cycle. Notice that P_c is dependent on both the interfacial tension and the contact angle. Altering the interfacial tension depends on the presence of a fluid, whereas continuous presence of a fluid is not necessary when altering the contact angle. This is important if increased well deliverability is to remain following stimulation.

Others have investigated the effect of using surfactants and alcohol to reduce the interfacial tension in the laboratory and tested the effect in the field.^{3–6} In fact, Fahes and Firoozabadi⁶ used an expensive fluorochemical surfactant to permanently alter the wettability of water-wet sandstone core to intermediate wettability. A number of chemicals shown in Table 1 have been evaluated in gas deliverability laboratory studies.

Chemical	Description	Vendor
WITCO 1276	Ammonium alkyl ether sulfate (hard acid)	Akzo Nobel
WITCO 1298	Alkylbenzenesulfonic acid (soft acid)	Akzo Nobel
Arquad 2HT-75	Quaternary ammonium cationic	Akzo Nobel
Stepanquat 300	Dicodimethyl ammonium Chloride	Stepan Chemical
Accosoft 808	Methyl tallow amidoethyl tallow imidazolin sulphate	Stepan Chemical
Octyl Palmite	Palmitic acid-2-ethylhexyl alcohol ester	Stepan Chemical
FC 4430	Fluorosurfactant fluoroaliphatic polymeric esters	3M Corp
FC 4432	Fluorosurfactant fluoroaliphatic polymeric esters	3M Corp
FC 4434	Fluorosurfactant fluoroaliphatic polymeric esters	3M Corp
T91-8	Ethoxylated alcohol	Tomah Products
TomaDry N-4	Formulated cationic surfactant	Tomah Products
OSA	Oil-soluble amine	Oil-Chem
REDICOTE CS 392S	Fatty polyamine derivative–Sandstones	Akzo Nobel
REDICOTE CS 393L	Fatty polyamine derivative–Limestone & dolomites	Akzo Nobel
Quilon	Tetradecanoato chromic chloride hydroxide	DuPont

In the present study inexpensive methods were investigated to screen the chemicals prior to testing with field cores. The capillary rise method was developed to screen chemicals for sandstone reservoirs. The principle is demonstrated in Fig. 1 with water and food dye: the greater the rise, the more water-wet the system.



Figure 1. Capillary tube test.

A drop method illustrated with Fig. 2 from Fahes and Firoozabadi shows promise as an inexpensive surfactant-screening protocol. The spreading drop with a contact angle greater than 90° indicates a water-wet rock surface, while the beaded drop with a contact angle less than 90° indicates a non-water-wet surface.

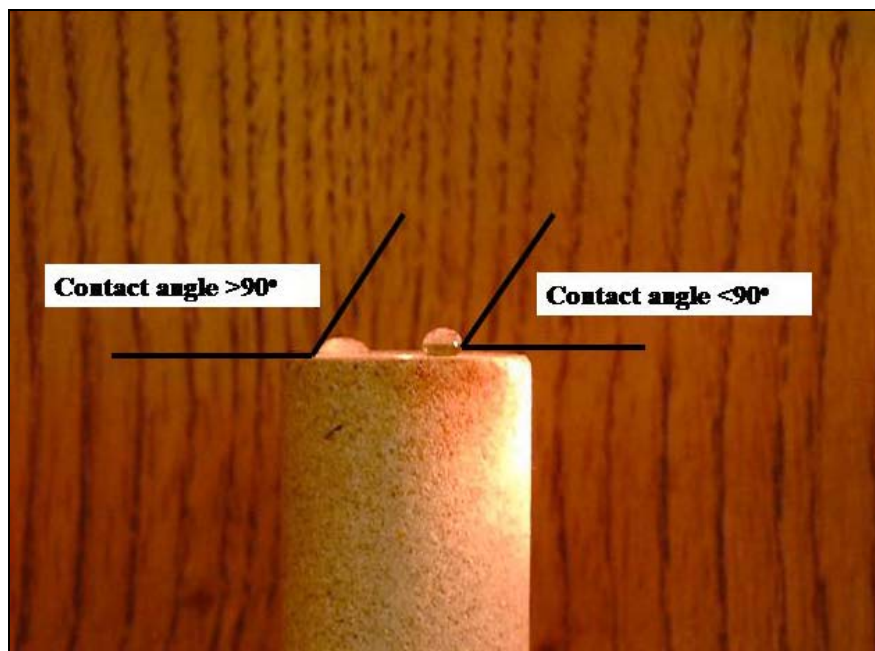


Figure 2. Surfactant drop screening method.⁶

After the surfactant screening with capillary tubes, surfactants were selected for imbibition tests with reservoir cores, followed by flow testing with reservoir cores and wet gas.

The imbibition of water into dry reservoir cores was determined by measuring the weight gain in cores with and without surfactant treatment as represented in Fig. 3.

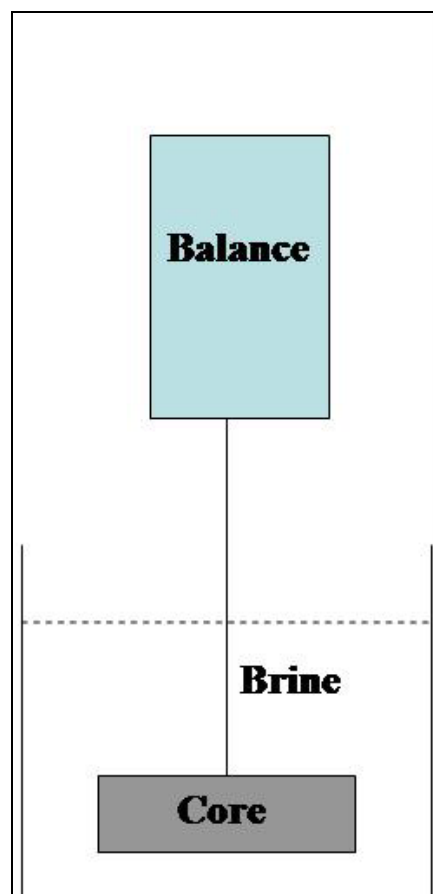


Figure 3. Representation of an imbibition test.

Constant pressure and temperature conditions were maintained during the laboratory imbibition experiments; therefore, the difference in weight gain of the treated vs. non-treated cores represents the change in the storage capacity of the core. Changes in the deliverability index of each core were measured with flow tests conducted with treated and non-treated cores. Since dry gas can volatilize the residual water trapped in the cores, wet-gas was used for all flow experiments. The dry/wet gas concept⁷ is shown in Fig. 4 where the constant-flow rate pressure drop was measured independently in the first and second half of the core. Note that the pressure drop doubled in the area of the core where water had not yet vaporized.

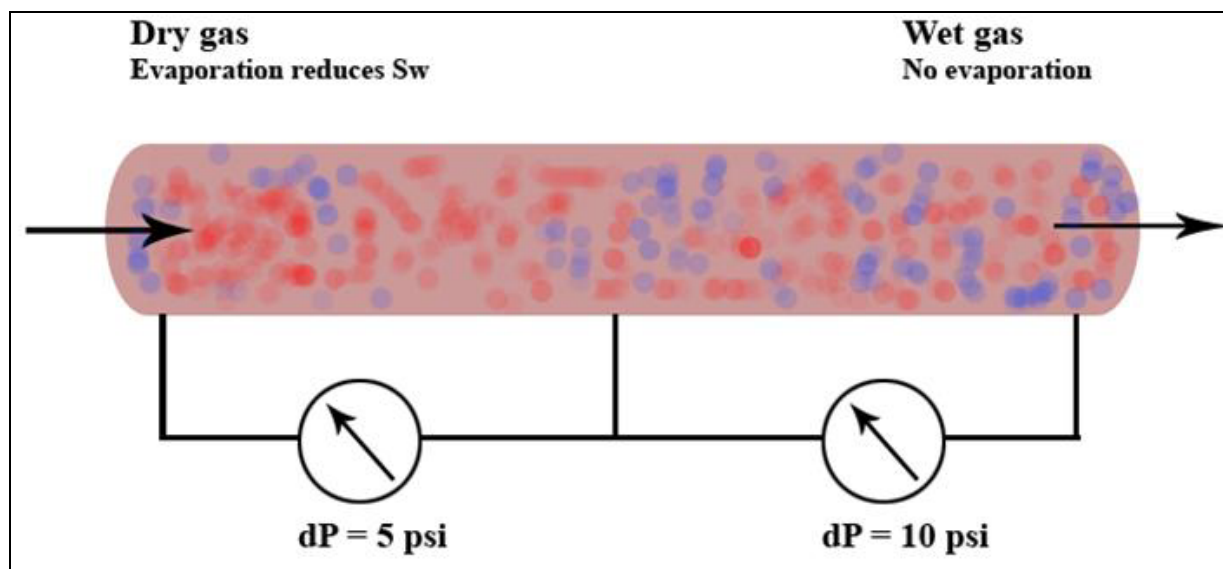


Figure 4. Demonstration of the dry/wet gas concept where the constant-flow rate pressure drop was measured independently in the first and second half of the core. Note that dP in wet-gas half of the core is twice that of the dry gas area.

Three operators offered data and cores for this project. Panhandle Energy provided sandstone cores and water analyses from their Waverly, St. Peter aquifer, storage facility along with production history of the withdrawal and fill cycles. Ameren Corp. provided sandstone sidewall cores and water analyses from their Mt. Simon sandstone aquifer, Sciota storage facility. Michigan Consolidated Gas provided dolomite cores (courtesy of William Harrison, Michigan Basin Core Research Laboratory, Western Michigan University) and production history from their Bell River Mills Niagaran reef storage facility. It was determined that field deliverability expressed as the wellhead flow rate divided by the difference in bottom hole pressure measured at an observation well and the flowing wellhead pressure generated trends that could be used to evaluate a field test of using surfactants to increase deliverability. Shown in Fig. 5 is a plot of the historical deliverability vs. cumulative withdrawals from Waverly well #91 during the 2004 season. Constructing the plot with cumulative withdrawals rather than time reduces the noise seen in time plots.

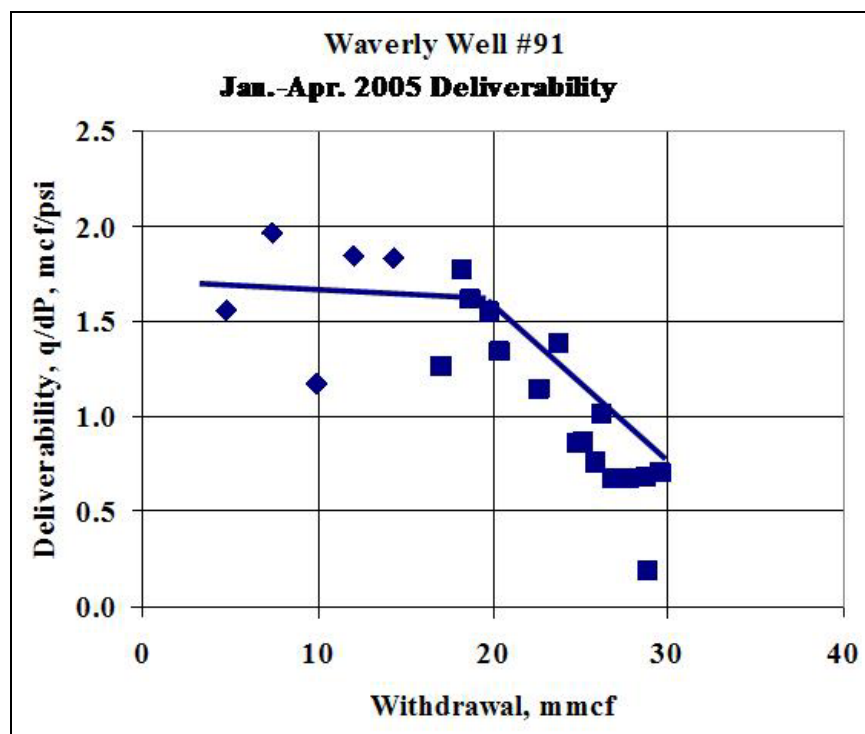


Figure 5. Deliverability history of the Waverly well #91 during the 2004 season.

Experimental Results

Laboratory Screening Tests

Capillary rise

Capillary rise tests (Fig. 1) were the first step in the laboratory surfactant-screening procedure. Each surfactant was diluted with either methanol or water to prepare solutions of various concentrations. Clean capillary tubes with a diameter of about 1 mm were first soaked in surfactant solutions, drained, and then inserted in synthetic seawater. The greater the rise of water in the capillary tube, the greater the water-wetness of the testing system. The seawater composition is listed in Table 2.

Composition	Na ⁺	K ⁺	Mg ²⁺	Ca ²⁺	Cl ⁻	HCO ₃ ⁻	SO ₄ ²⁻	TDS
Concentration, ppm	10890	490	1368	428	19700	124	2960	35960

The capillary rise of seawater and dilute solutions of surfactants in seawater and methanol against air was measured with a cathetometer. The results obtained with 11 of the 14 surfactants are presented in Table 3. Vendors were not able to provide samples of three of the potential samples listed in Table 1.

Table 3. Capillary rise tests results			
Surfactants (bar chart code)	Capillary rises (cm) after soaking by different solutions (Methanol)	Capillary rises (cm) after soaking by different solutions (Water)	Observation
Stepanquat 300 (1)	1% ---0.76 0.1% ---0.79 0.01%--1.86	1% ---0.73 0.1% ---0.74 0.01% ---0.75 0.002%---0.83	
Witcolate 1276 (3)	1% ---1.63 0.1% ---2.18 0.01%---2.25	1% ---0.9 0.1% ---2.14 0.01% ---2.23	
Octyl Palmitate (5)	1% ---1.9 0.1% ---1.92 0.01%---1.99		Not soluble in water
Witconic 1298 (7)	1% ---0.77 0.1% ---1.04 0.01%---1.07	1% ---0.8 0.1% ---0.94 0.01%---2.08	
FC-4430 (9)	1% ---0.75 0.1% ---1.08 0.01%---2.25	1% ---0.89 0.1% ---1.67 0.01%---2.32	
FC-4432 (11)	1% ---0.83 0.1% ---1.2 0.01%---2.22	1% ---0.72 0.1% ---2.01 0.01%---2.28	
FC-4434 (13)	1% ---0.74 0.1% ---2.25 0.01%---2.33	1% ---1.38 0.1% ---1.79 0.01%---1.86	
Tomadol 91-8 (15)	1% ---0.78 0.1% ---0.98 0.01%---2.23	1% ---1.03 0.1% ---1.58 0.01%---2.42	
Tomadry N-4 (17)	1% ---0.7 0.1% ---0.72 0.01%---2.17	1% ---0.7 0.1% ---0.71 0.01%---0.71	
Accosoft 808 (90%) (19)	1% ---0.83 0.1% ---0.93 0.01%---2.2	1% ---0.72 0.1% ---0.76 0.01%---2.12	Dispersed in water
Arquad 2HT-75 (21)	1% ---0.82 0.1% ---1.09 0.01%---2.01		Not soluble in water
Capillary rise of clean tube: in (23) sea water = 2.51 cm, in (25) methanol = 0.87 cm			

The capillary rise experimental results with water as the diluent are presented graphically as bar charts in Figs. 6–10 (see Table 3 for reference code). The results are normalized with water as 1.0 and shown in Figs. 6–8 with water as the solvent and surfactant concentrations of 10,000, 1,000, and 100 ppm. Notice that the capillary rise of all surfactants is less than water indicating that the water-wetness of glass tubes was reduced.

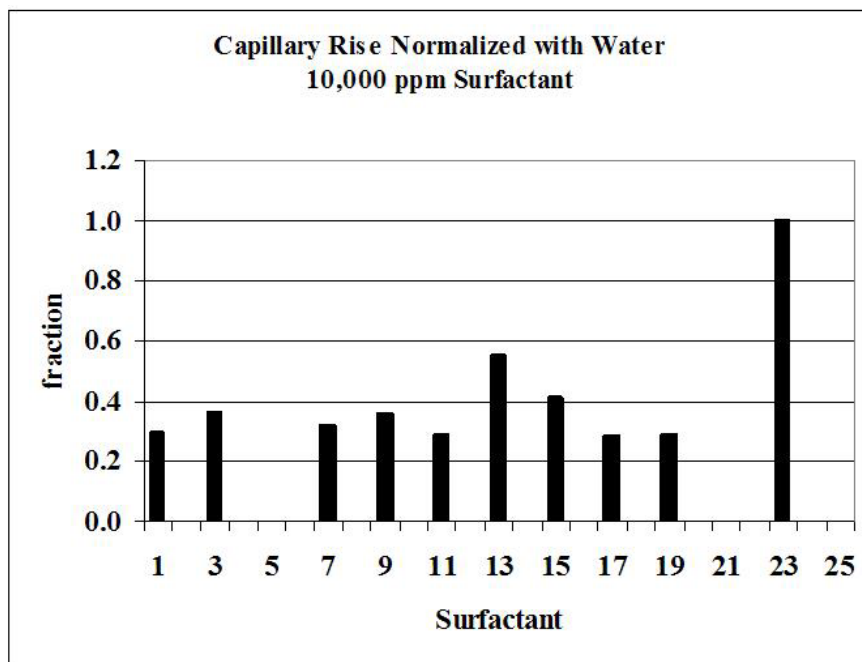


Figure 6. Capillary rise of surfactants at 10,000 ppm in water.

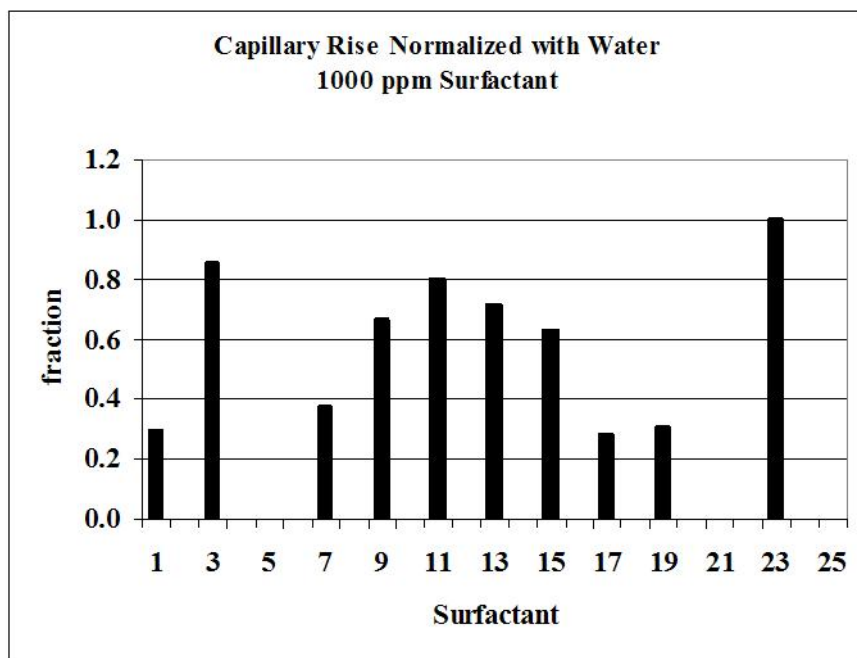


Figure 7. Capillary rise of surfactants at 1,000 ppm in water.

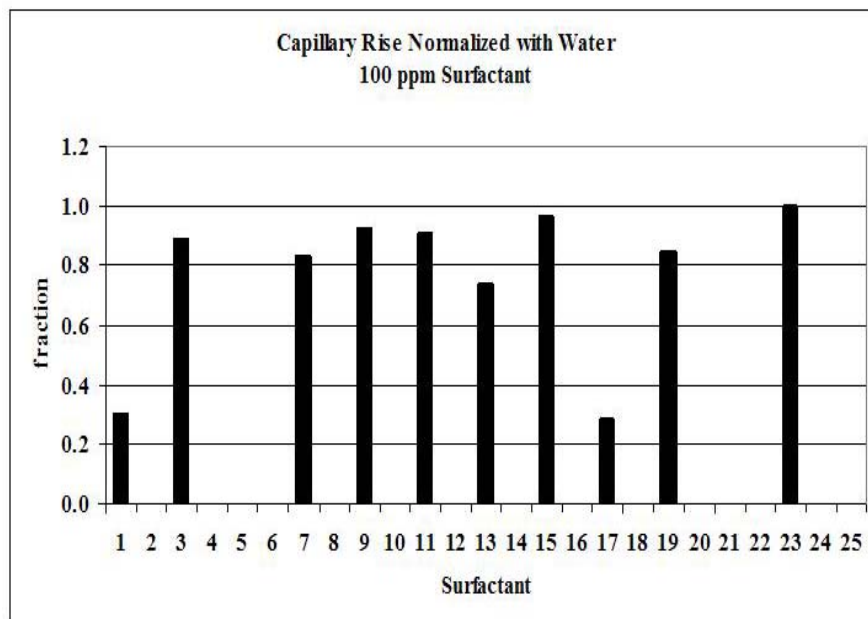


Figure 8. Capillary rise of surfactants at 100 ppm in water.

Shown in Figs. 9–11 are results of the capillary rise experiments using methanol as the diluent to ensure solubility of the surfactants. Surfactants dissolved in methanol do not significantly reduce the tube wettability as shown in Figs. 9–11. The capillary rise tests are summarized in the appendix (Fig. A1).

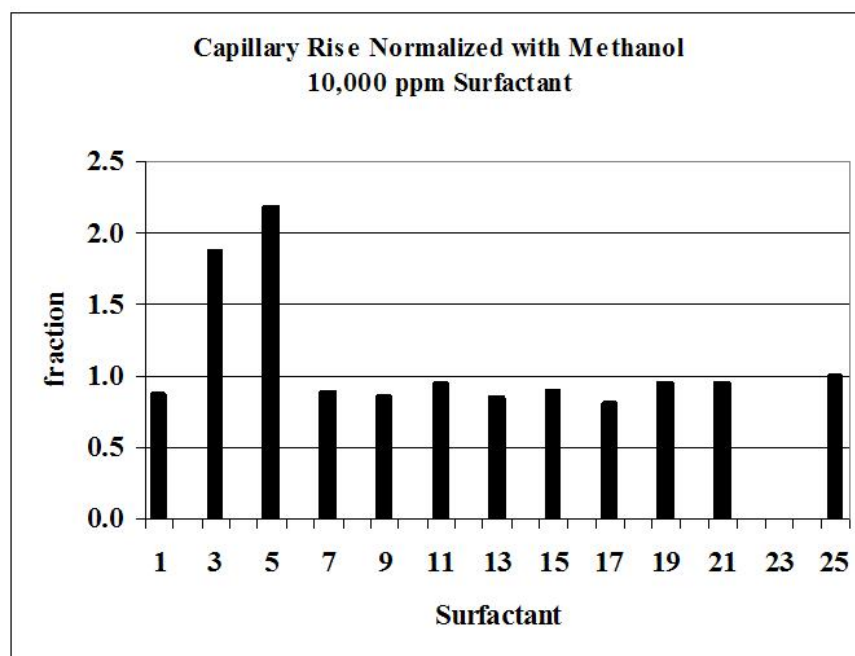


Figure 9. Capillary rise of surfactants at 10,000 ppm in methanol.

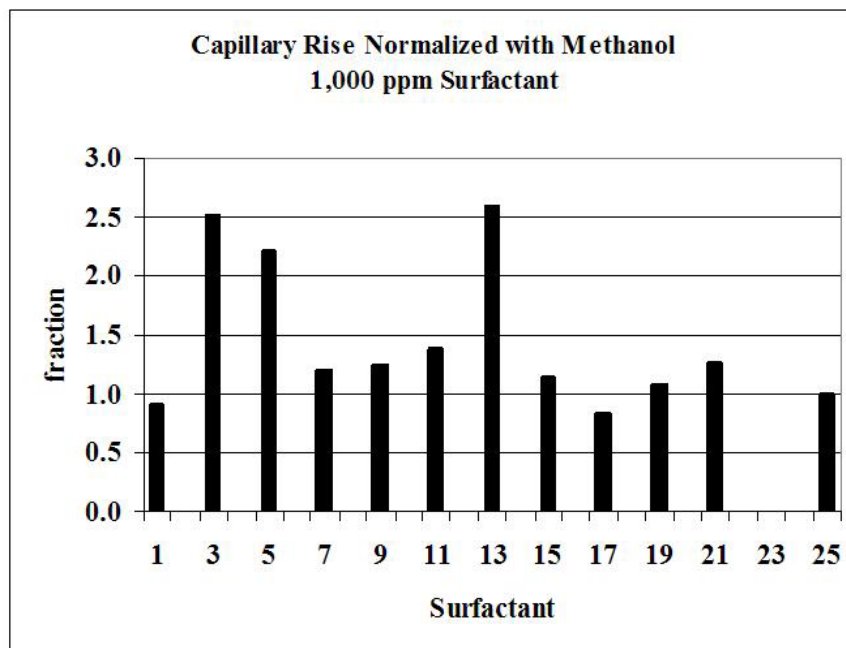


Figure 10. Capillary rise of surfactants at 1,000 ppm in methanol.

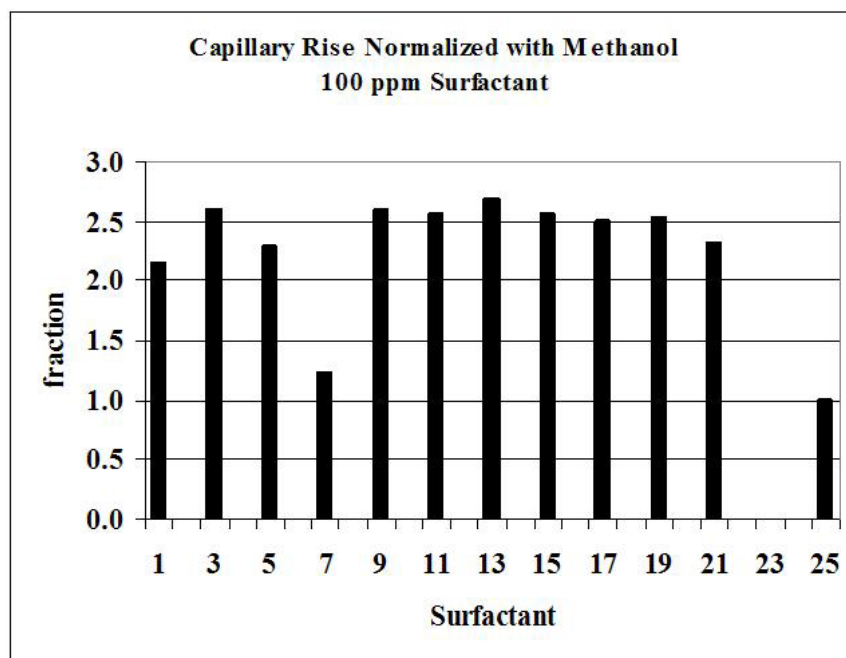


Figure 11. Capillary rise of surfactants at 100 ppm in methanol.

Critical micelle concentration

The critical micelle concentration (CMC) of both Stepanquat 300 and Tom adry N-4 was measured. CMC is the stabilized surface tension value measured at increasing surfactant concentrations in seawater using a DuNouy ring tensiometer. Fig. 12 shows that the CMC of both surfactants is about 10,000 ppm (1.0%). The surface tension of Stepanquat 300 (1) is 30.5

dyne/cm and Tomadry N-4 (17) is 41.7 at the CMC as shown in Table 4. The CMC is used to determine the application concentration.

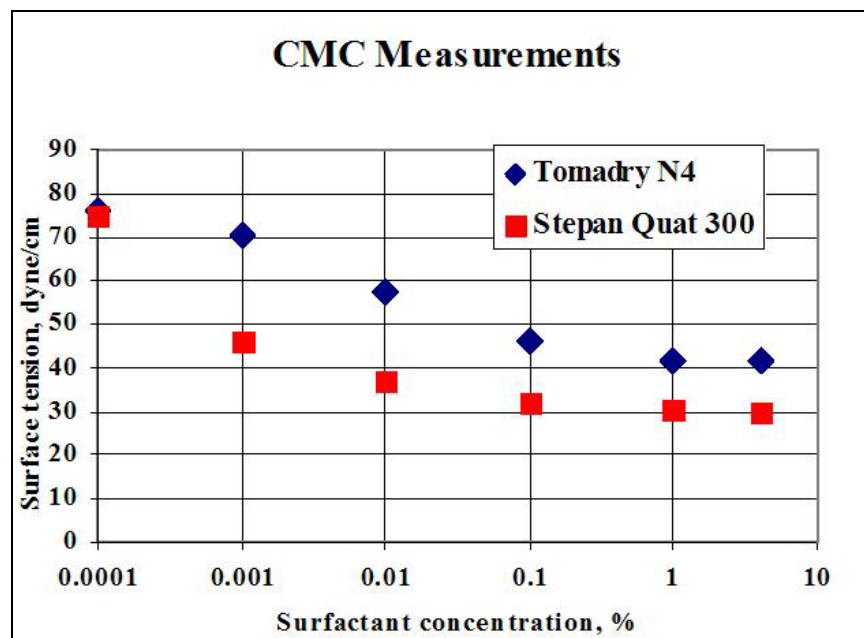


Figure 12. Critical micelle concentration test results.

Tomadry N-4		Stepanquat 300	
Concentration, %	IFT, mN/m	Concentration, %	IFT, mN/m
4	41.6	4	29.8
1	41.7	1	30.5
0.1	46.3	0.1	32.3
0.01	57.5	0.01	37.1
0.001	70.2	0.001	46.4
0.0001	76	0.0001	74.9
0	76.7	0	76.7

Contact angle (water drop)/core

A potential screening test consisting of observing the imbibition properties of a drop of water or dilute surfactant on the surface of reservoir core material was investigated. As shown in Fig. 2, a drop of water that beads on the surface of a treated Berea core suggests that the core is not water-wet. In a similar manner core plugs were cut from the St. Peter sandstone (Waverly field), the Mt. Simon sandstone (Sciota field sidewall plugs), and the Niagaran dolomite (Bell River Mills field).

Shown in Fig. 13 is a drop of water (red food dye added) placed on the surface of the St. Peter sandstone. The drop immediately spreads and is imbibed into the core; thus, the contact angle is 180° indicating a strongly water-wet surface. Rapid imbibition was also noted with the Mt. Simon sidewall core. Recall that both the Waverly and the Sciota storage facilities were developed in water aquifers.

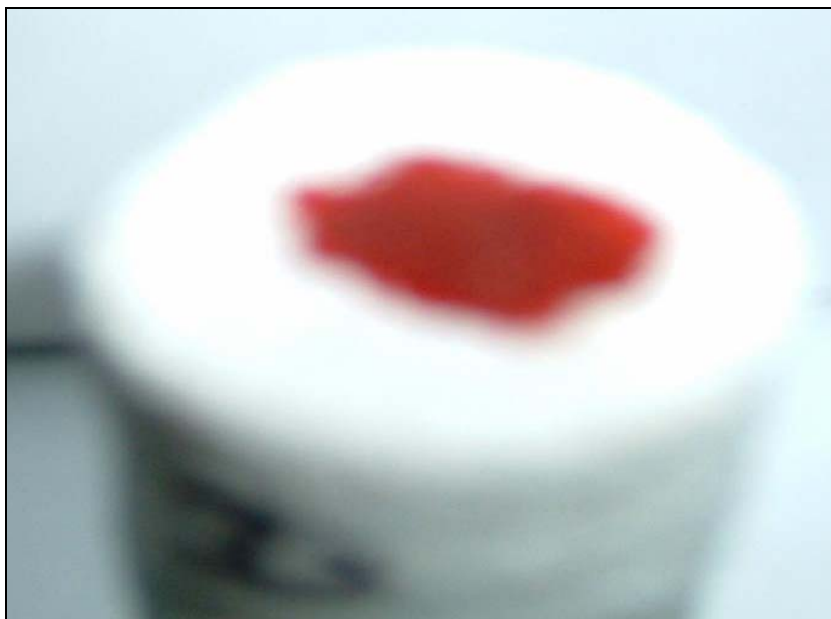


Figure 13. Water drop on St. Peter sandstone.

A water drop on the Bell River Mills dolomite core as shown in Fig. 14 is not imbibed as rapidly. Note that the drops on the first and third cores indicate that the dolomite is not water-wet. The permeability of the sandstone cores was ~ 100 md, while the dolomite cores were about 1000 md.

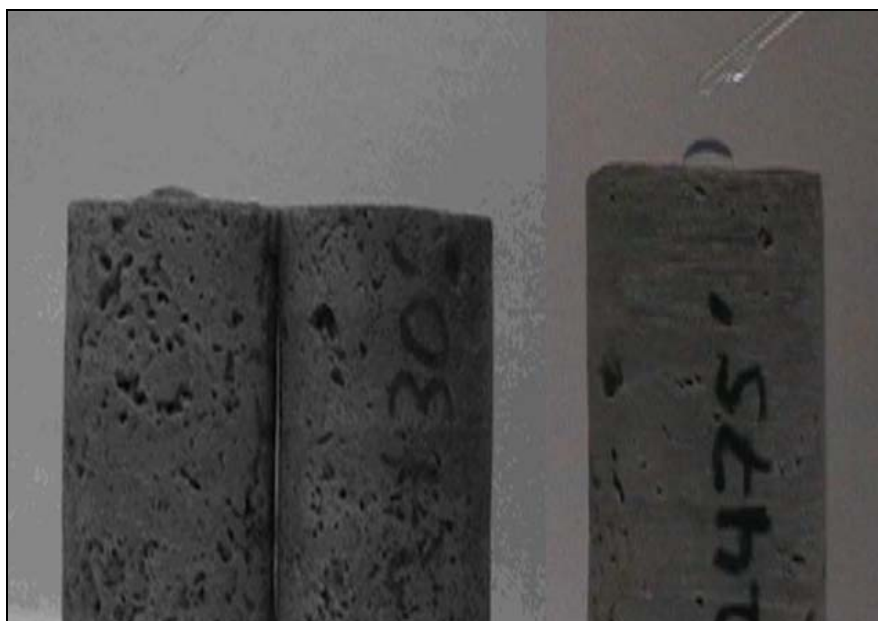


Figure 14. Water drops on untreated Niagaran dolomite core plugs.

The sandstone cores were flooded with 2% surfactant solutions (Tomadry N-4); the dolomite cores were treated with Arquad 2HT-75 and Stepanquat 300. As shown in Fig. 15 the contact angle of the water drop was less than 90° , and the water was not imbibed.



Figure 15. Water drop contact angle on treated sandstone is less than 90° .

Treating the dolomite cores with 1% surfactant solutions had little effect on the natural wettability of the core, judging by the similarity of the untreated core contact angle shown in Fig. 16.



Figure 16. Water drops on treated dolomite are similar to contact angles shown in Fig. 14.

Core Imbibition

The imbibition of reservoir water into dry reservoir cores was measured by the weight method described earlier. The St. Peter sandstone and the Niagaran reef dolomite were tested in this manner after which they were treated with surfactant solutions, and the imbibition properties were again measured.

The initial weight of the dry sandstone core was 54.750 g. Porosity was 12% and k_g was 109 md. The core was submerged in reservoir synthetic brine, and the weight of the core was measured periodically as water was imbibed. Once imbibition ceased, the core was flooded with a 2% surfactant solution of Tomadry N-4 and allowed to equilibrate overnight. The surfactant-saturated core was then flooded with dry gas to residual saturation. The initial weight of the surfactant-treated core was 54.766 g, very close to the initial dry core weight. The final weight of the surfactant-treated core increased by 1.654 g (3%), while the final weight of the non-surfactant core increased by 2.830 g (5.2%). The results are shown with a bar graph in Fig. 17. It is clear that the storage volume of the core was increased by 42% following treatment with a 2% solution of Tomadry N4.

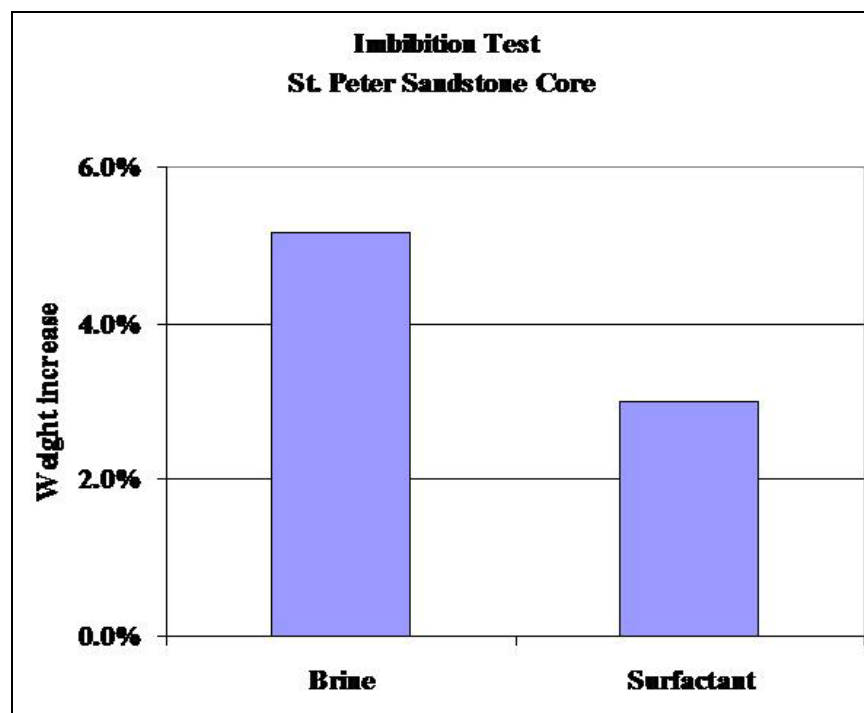


Figure 17. Forty-two percent less water was imbibed into the surfactant-treated core (17).

The imbibition-altering properties of a 1% solution of Stepanquat 300 were determined with a St. Peter Sandstone core M. The porosity was 11.2 %, and k_g was 68 md. The surfactant-treated core imbibed 0.4 g less water (2.0 g vs. 2.4 g) than the dry core. Based on an initial core weight of 54 g, the increase in storage capacity was 0.7%. The results are shown graphically in Fig. 18.

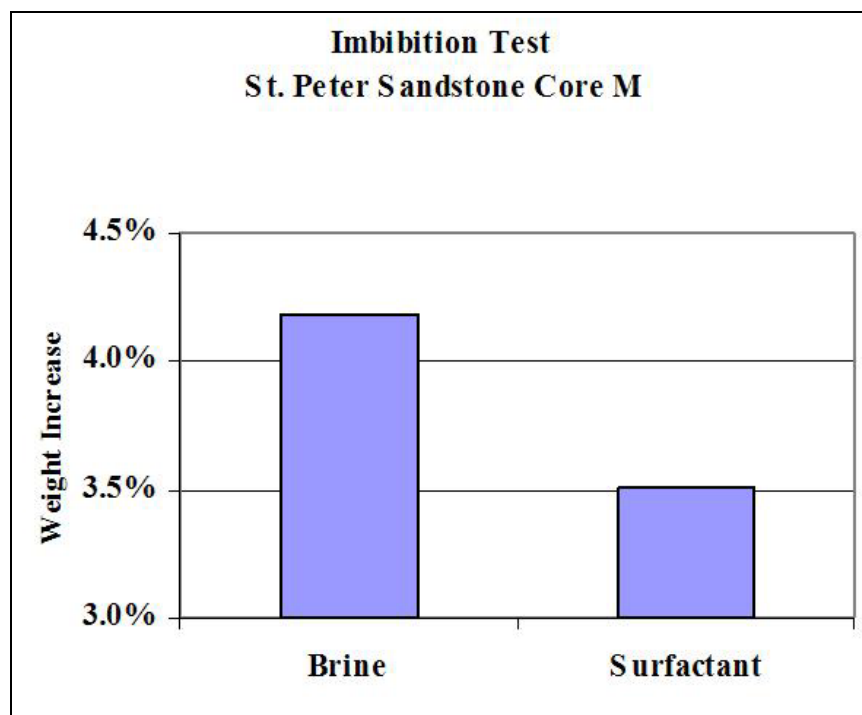


Figure 18. Seventeen percent less water was imbibed into surfactant-treated core (3).

Shown in Fig. 19 are the imbibition test results with the Niagaran reef dolomite core #2428. Pertinent core properties are 750-m d k_g and 24% porosity. The surfactant was Tomadry N-4 (17). Note that the storage capacity of the core decreased suggesting that the core was not naturally water-wet.

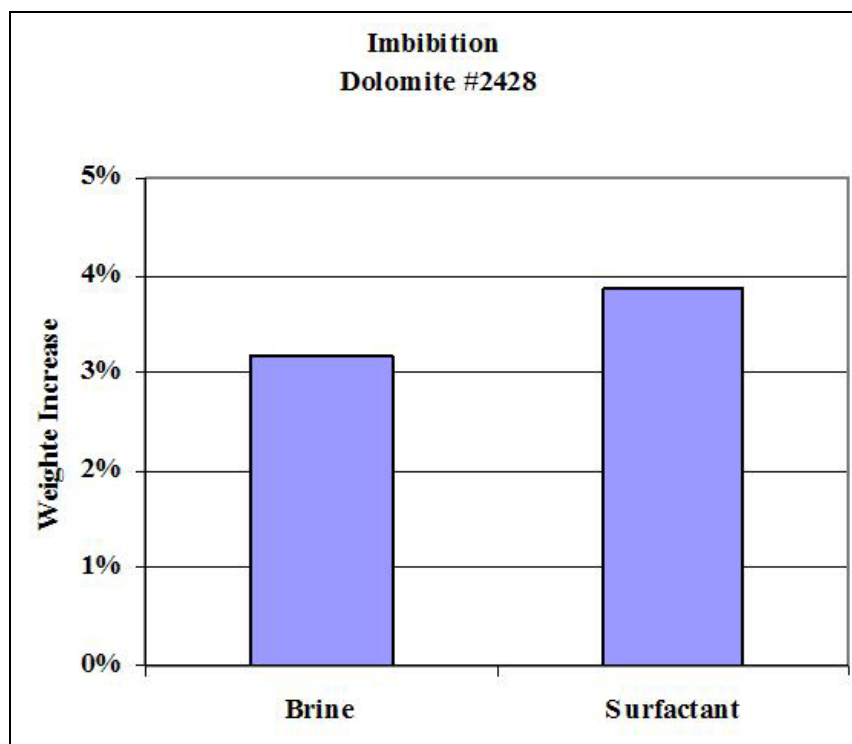


Figure 19. Imbibition test results with Niagaran dolomite core # 2428.

Since the Bell River Mills reservoir was originally a dry gas Niagaran reef field and most dry gas fields are believed to be water-wet, the imbibition test was repeated. The core properties of dolomite core #2396 are 620-m d k_g and 28% porosity. The imbibition test results are quite similar to the core #2428 as shown in Fig. 20. Again, the unexpected result suggests that that the reservoir is not water-wet.

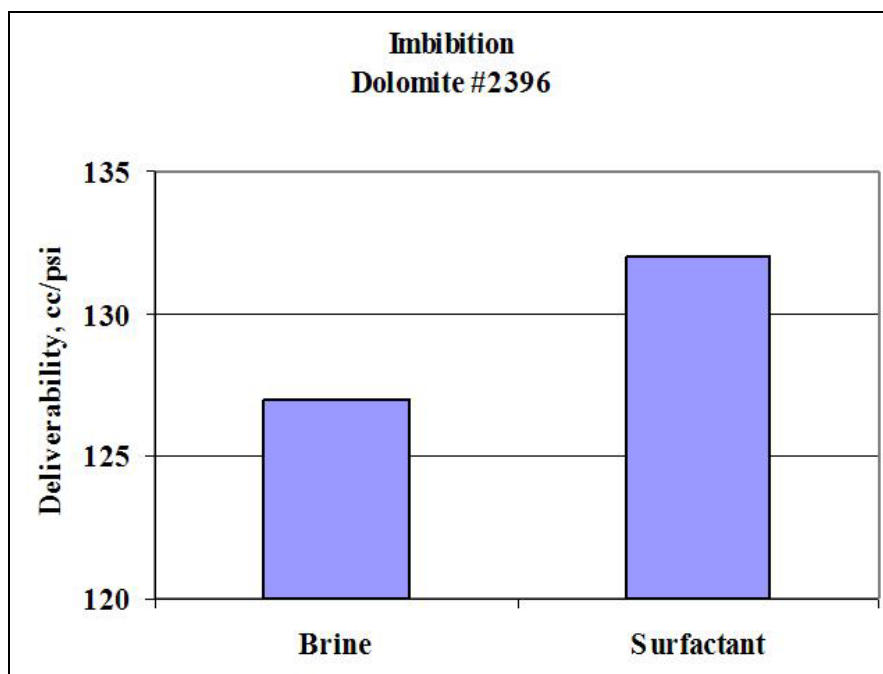


Figure 20. Bell River Mills core 2396 imbibition test result.

The core imbibition tests indicate that the aquifer storage reservoirs are water-wet. Treatment with low concentrations of surfactants, either #3 or #17, increased the storage capacity of the sandstone cores. Surfactant treatments did not increase the storage capacity of the dolomite cores.

Deliverability

Sandstone

The effect of surfactants on the deliverability index, $q/\Delta P$, was determined with a series of flow tests. The dimensions of the cores used for the deliverability (flow) test were ~4" long with a 1" diameter. Wet gas was injected until a stable flow rate was reached. The core was then saturated with 2% surfactant solution and again flooded with wet gas until the rate stabilized. All gas volumes were at standard conditions. The surfactant was Tomadry N-4 (17).

St. Peter sandstone core plugs were cut for testing. The Mt. Simon sidewall cores were not suitable for flow testing experiments. Results of the deliverability tests of St. Peter core A with a 109-md permeability and 12% porosity are shown in Fig. 21. A 2% solution of Tomadry N-4 was used to treat the core. The treatment improved deliverability by 59%.

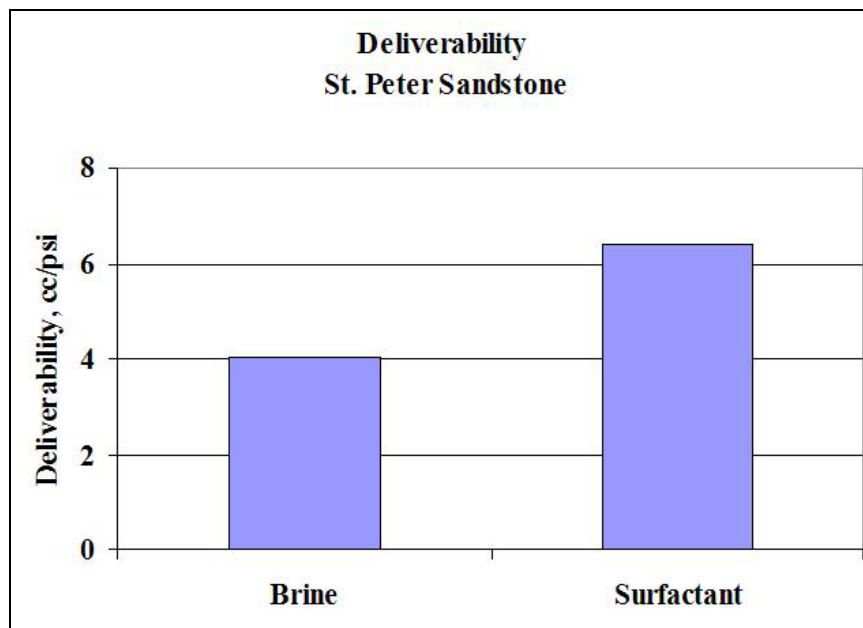


Figure 21. Gas deliverability through St. Peter 109-md sandstone.

A sandstone deliverability test was conducted with a 1% solution of Stepanquat 300 (1) using St. Peter core M with a 68-md k_g and 11.2 % porosity. The surfactant increased deliverability by 20% as shown in Fig. 22.

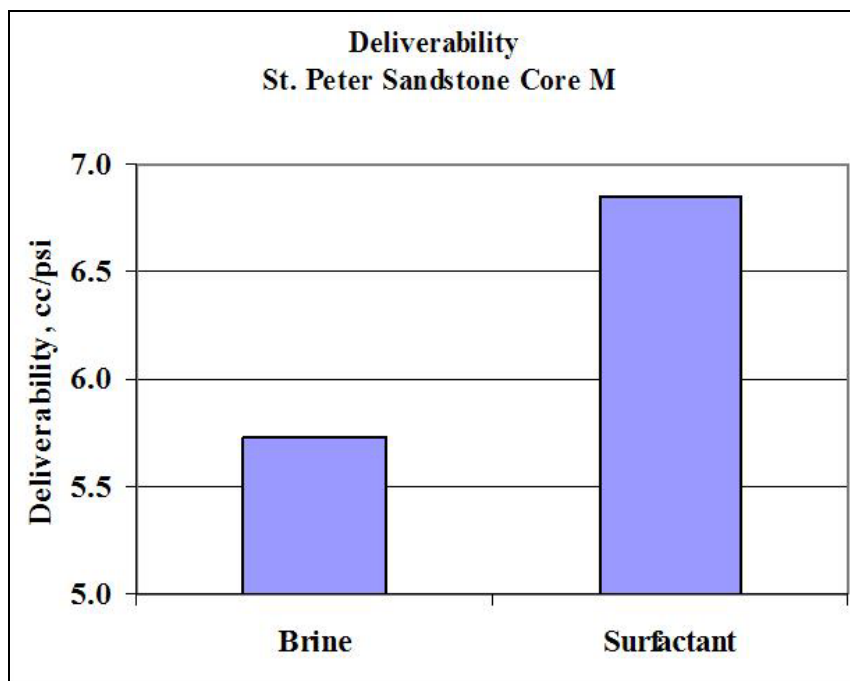


Figure 22. Deliverability test results through 68-md St. Peter sandstone.

Dolomite

Despite the adverse effect on storage capacity, the performance of surfactant treatment on the Niagaran reef dolomite cores on gas deliverability was measured. Dolomite core # 2428 with a 750-md k_g and 24% porosity was treated with a 2% solution of Tomadry N-4. The effect on deliverability was positive with a 1.7% increase as shown in Fig. 23.

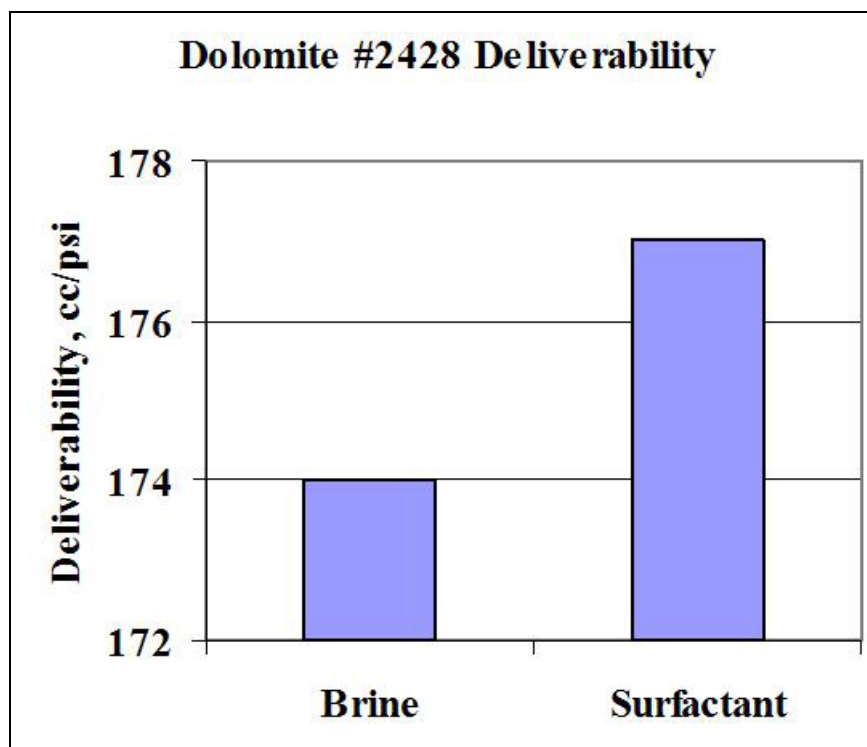


Figure 23. Marginal increase in deliverability with surfactant-treated dolomite core.

The deliverability test performed on dolomite core #2396 generated a 4% increase in this 810-md sample with 28% porosity. The marginal increase in deliverability with surfactant treatment of dolomite cores complements the dolomite imbibition test results.

The deliverability tests are presented as a function of cumulative gas injection in the appendix (Figs. A2–A5).

Engineering

A key to successful interpretation of field applications of remedial techniques is the performance history. Evaluation of the benefits of the surfactant stimulation technique requires that deliverability prior to treatment be compared to post-treatment results. The pressure-rate history of the Waverly St. Peter aquifer storage facility provided by Panhandle Energy and similar data from Bell River Mills Niagaran reef storage facility operated by Michigan Consolidated Gas was evaluated for prior-treatment trends.

Production history analysis

Waverly St. Peter aquifer storage facility

The Waverly storage facility monthly production history (December 2004–April 20 05) served as a 25-well dataset including the withdrawal rate, flowing wellhead pressure, shut-in observation well pressure, and delta P defined as shut-in pressure squared minus flowing pressure squared. Four wells (Nos. 5, 21, 88, 91) with lengthy, continuous production records were selected for analysis to generate baseline information for potential field tests. Conventional plots of flow rate vs. time were developed. The noise in these plots was somewhat reduced by substituting cumulative gas produced for time.

Waverly is an aquifer storage facility as evident in the various production curves. The rate deteriorates until it is essentially flat when the bottom water encroaches on the perforations. This is seen with data from well 5 as shown in Fig. 24. If the withdrawal rate following the surfactant treatment is greater than the withdrawal rate without surfactant, the economics of fieldwide treatment could be investigated.

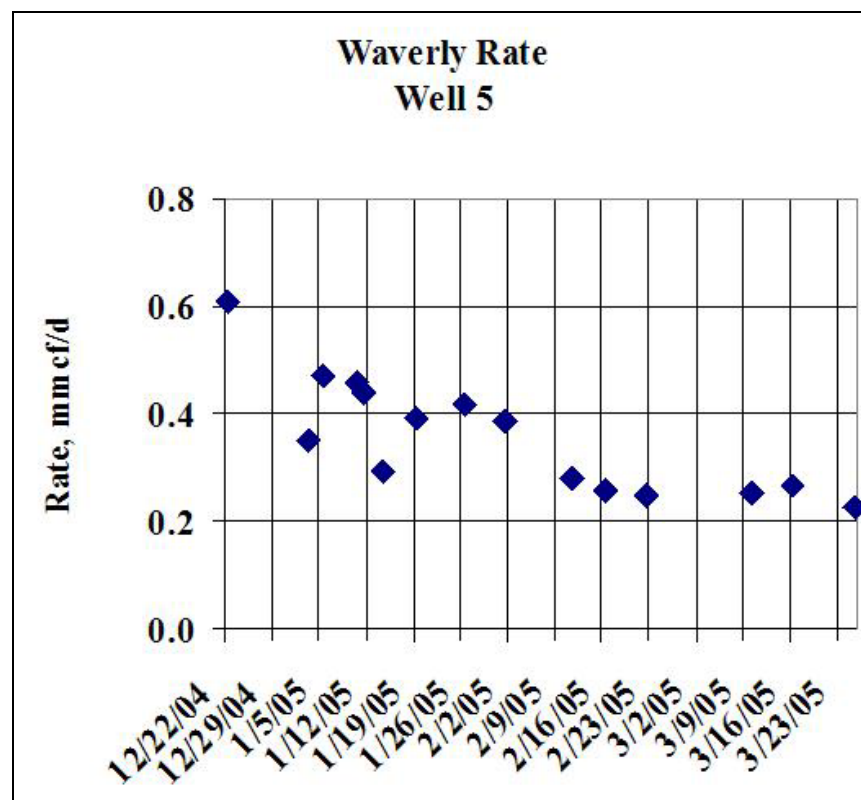


Figure 24. Waverly # 5 performance history.

The relationship between flow rate and pressure should be a continuous function with the condition of non-turbulent flow as expected at the pressure measurement points. However, two distinct trends in the rate are evident in Fig. 25. The two distinct linear trends are the result of bottom water encroachment. The fact that the trends are linear facilitates a before/after analysis.

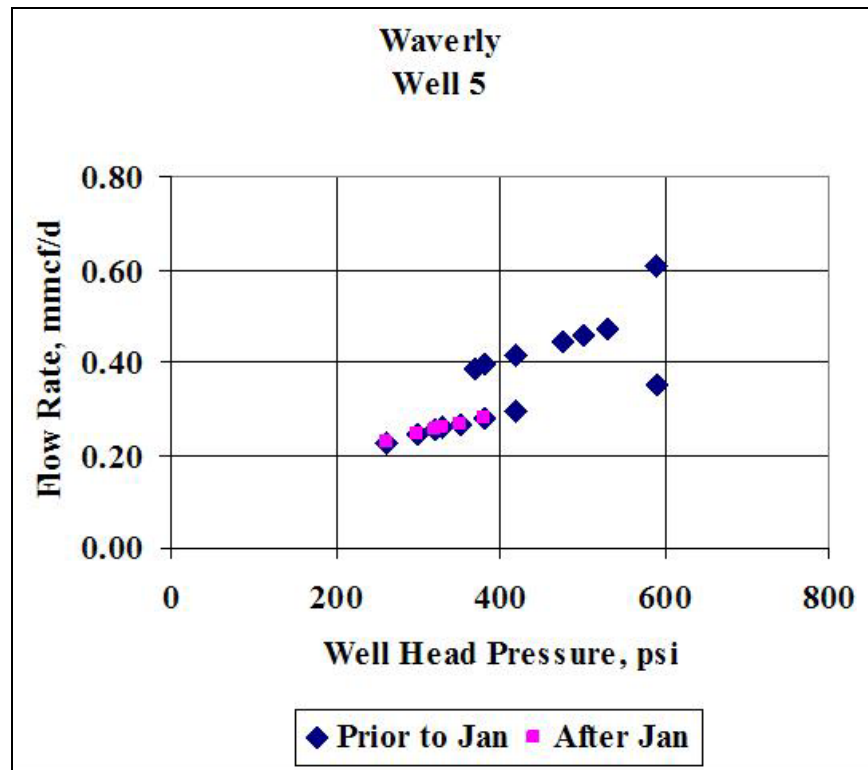


Figure 25. Well 5 flow rate vs. pressure.

Cumulative gas withdrawn was substituted for time in Fig. 26 that shows the relationship between rate, wellhead flowing pressure, deliverability defined as rate/dP, and observation well shut-in pressure. It is evident that as the reservoir pressure approaches 500 psi, the rate tends to stabilize. The same phenomenon occurs in wells 21, 88, and 91, shown in the appendix (Figs. A6–A8).

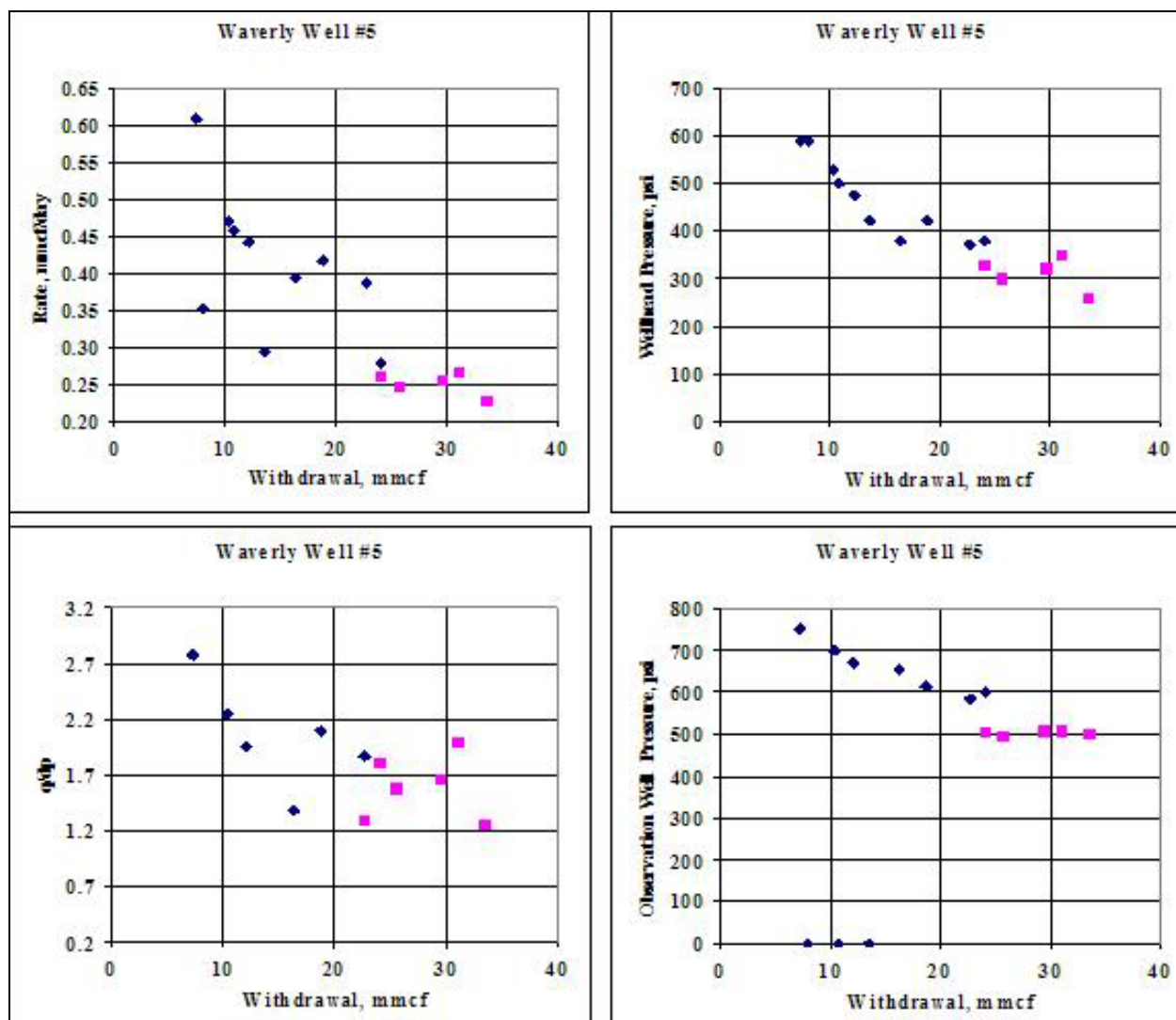


Figure 26. Rate, flowing pressure, deliverability, and observation well pressure of Well 5.

Waverly field logs were obtained to estimate porosity in the even to pore volume calculations are included in the design of the surfactant volumes required for field application. Both core and log information was available from the Doolin 1-16 well. Since all wells were not cored, the Doolin 1-16 well information was used to adjust the constants in log interpretation equations to match the core-measured porosity. These tuned equations could be applied to non-cored wells.

Waverly field core cut from the stored gas interval (top @ 1821 ft; base @ 1898 ft) in the St. Peter formation Doolin 1-16 well was received along with resistivity logs and the SP log. Core plugs were drilled from core sections from 1833-34 and 1855-61 ft to obtain material for the laboratory work described earlier. The log interval was 1800–2010 ft and consisted of the ShortNormal, LongNormal, MicroInverse, and MicroNormal electrical logs, plus the SP log.

The reported core measurements are at 1-ft intervals, while the log measurements are at ½-ft intervals. The log values were averaged over 1-ft intervals and plotted vs. the core values as shown in Fig. 27. Others⁸ recognized the existence of a relationship between the short normal log and porosity. However, Fig. 27 shows that the correlation is not strong. Similar correlations are observed in Figs. 28–31.

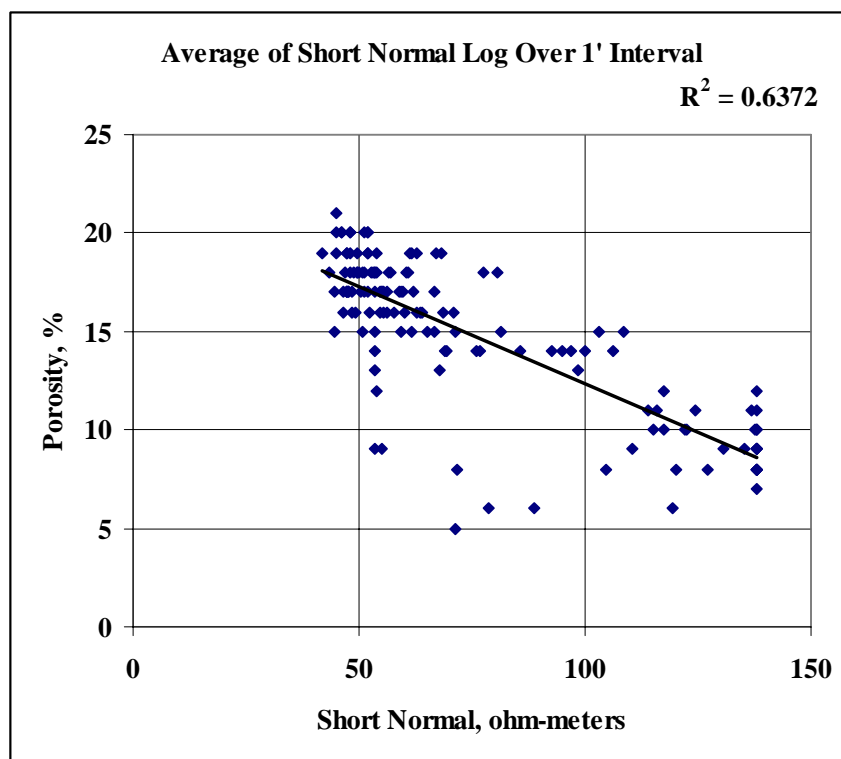


Figure 27. Core porosity vs. the average of the short normal log over 1' intervals.

Increasing the log averaging interval to 3 ft had very little effect on the correlation coefficient in Fig. 26 coefficient as shown in Fig. 27.

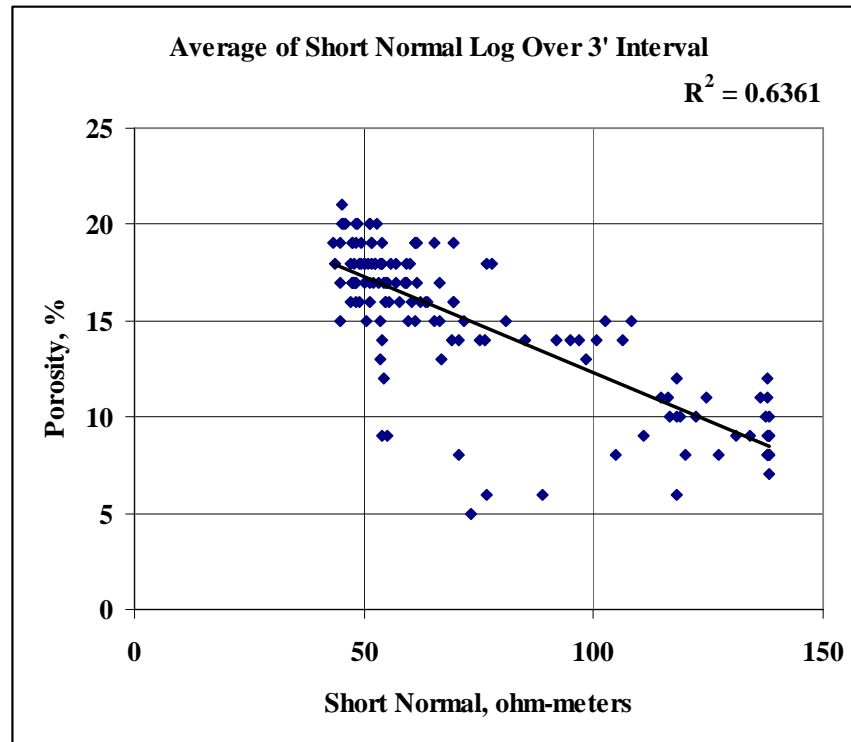


Figure 28. Core porosity vs. the average of the short normal log over 3' intervals.

The correlation between the SP log averaged over a 3-ft interval and core porosity was poor as shown in Fig. 29.

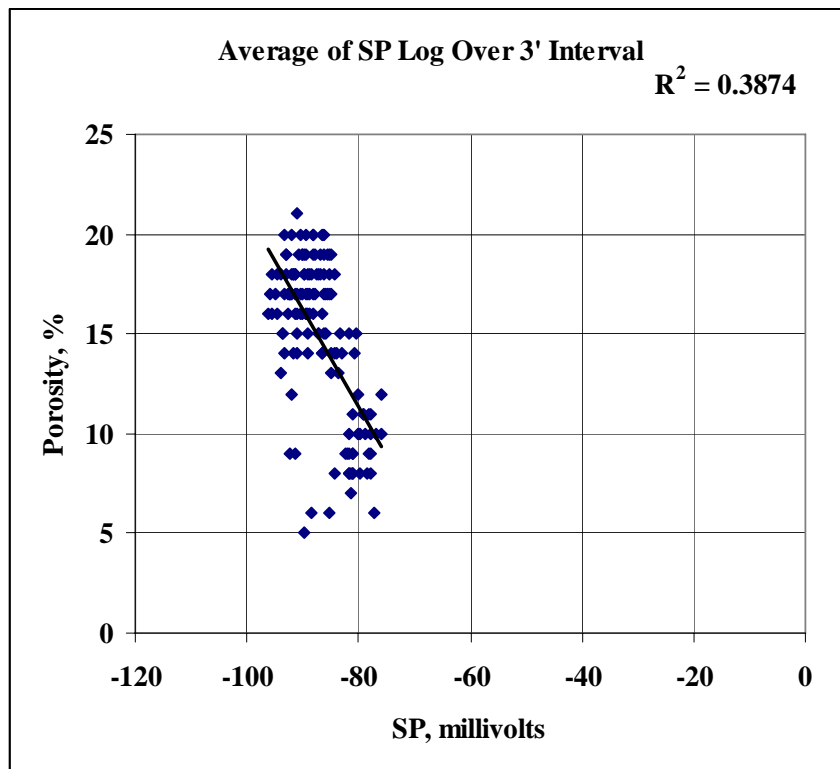


Figure 29. Core porosity vs. the average of the SP log over 3' intervals.

Derivatives of the log values have been demonstrated to be better correlating variables than measured log values.⁹ The first derivative of the SP log was calculated and plotted vs. the core porosity as shown in Fig. 30. No correlation exists.

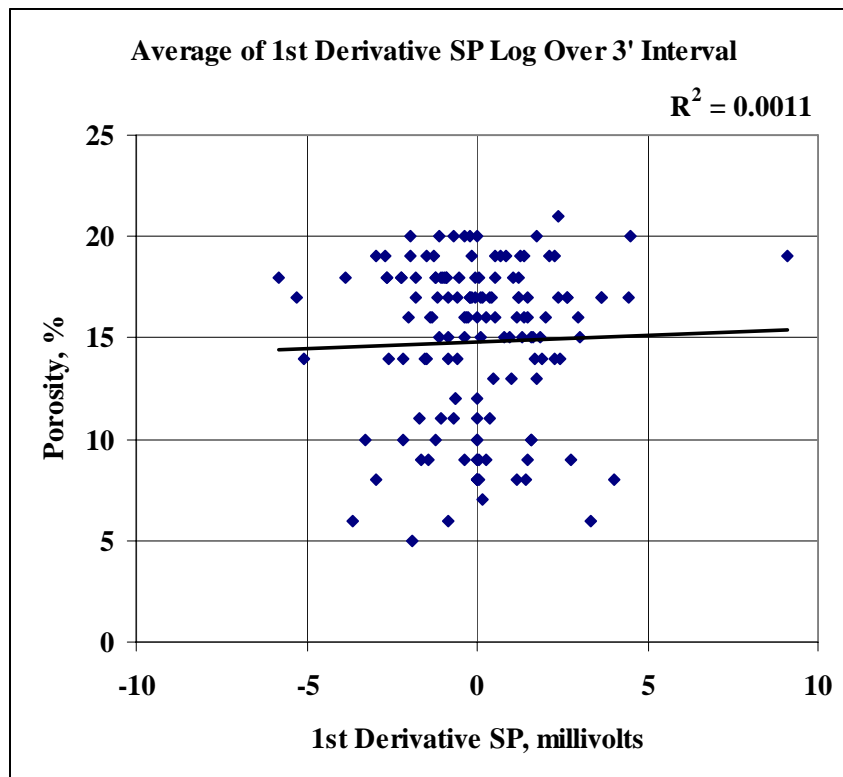


Figure 30. Core porosity vs. the 1st derivative of the average of the SP log over 3' intervals.

Datasets of the Doolin 1-16 type have been successfully correlated using fuzzy logic. The core porosity was fuzzified and plotted vs. the values of the short normal curve averaged over a 1-ft interval. The resulting fuzzy curve as shown in Fig. 31 (continuous curve) has sufficient range to be used as a tool to calculate porosity given the short normal curve. The actual core values are also shown in Fig. 31 to provide a sense for the effect of generating a fuzzy curve.

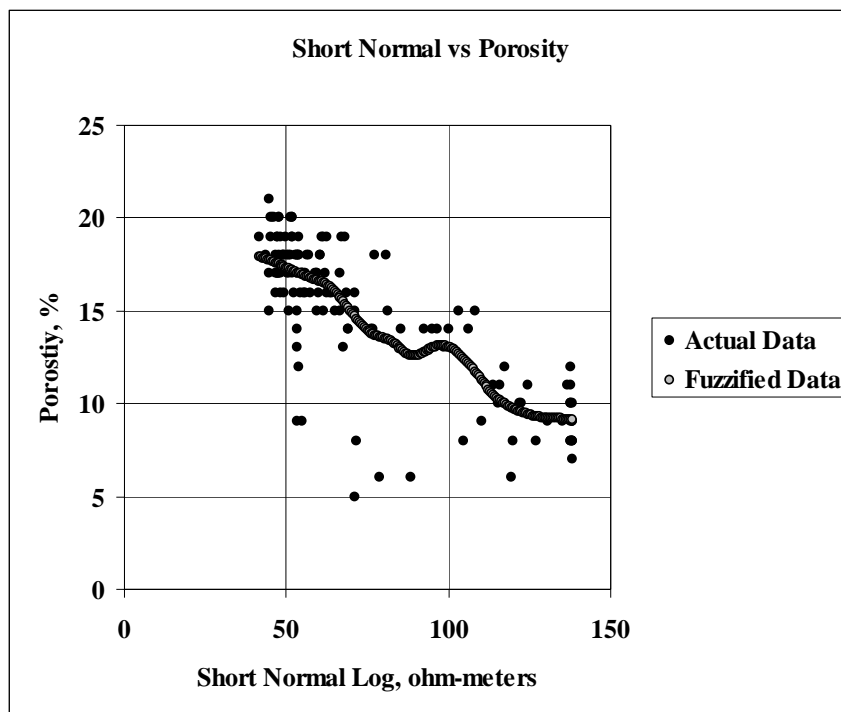


Figure 31. Fuzzified core porosity vs. the average of the short normal log over 1' intervals.

The intent of the core/log analysis was to develop a neural network to generate porosity and permeability models given log measurements. Fuzzy curves are useful when selecting input variables for neural networks. Fuzzy curves similar to Fig. 31 were generated for the ShortNormal, LongNormal, MicroInverse, and MicroNormal electrical logs, plus the SP log vs. the core porosity values. The fuzzy curves suggested that all of the resistivity curves were appropriate variables for multivariate analysis. The abundance of measured core porosity values suggested that significant multivariable correlations would result with neural network correlations. Unfortunately none of the neural network architectures generated correlations greater than the fuzzy resistivity curves alone. The SP values did not improve the neural networks based solely on the resistivity logs as inputs.

Bell River Mills Niagaran reef storage facility

Michigan Consolidated Gas provided about 7000 rate-pressure measurements collected during a 1-year period (Oct. 1996 to Oct. 1997). Observation well pressure data accompanied the Diekland #2 well rate-pressure history. This history was reduced to daily averages and graphed in manner similar to the format used to examine the Waverly facility information analyzed last quarter. The purpose of the analysis was to determine if stabilized trends existed that could be easily used to measure improved well deliverability should laboratory core tests support a field test.

The fill rate, withdrawal rate, fill pressure, and withdrawal pressure vs. time are plotted in Fig. 32.

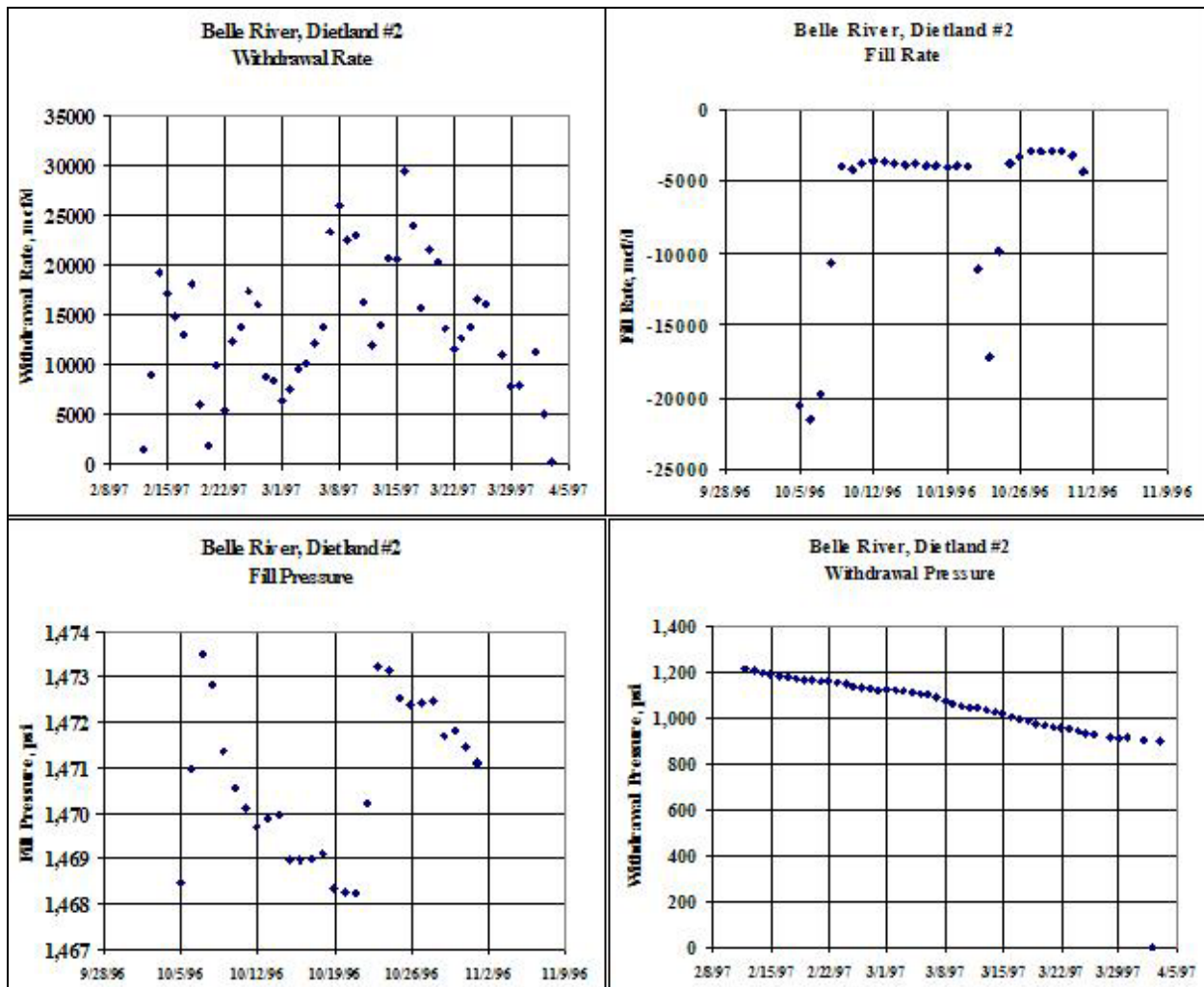


Figure 32. Fill and withdrawal rate-pressure history.

Obvious trends are evident in the fill rate and pressure plots along with the withdrawal pressure. Observation well pressure is assumed to represent static reservoir pressure in the deliverability index calculation of flow rate divided by pressure drop. Temperature and depth corrections were not applied to the wellhead pressure and rate measurements. Cumulative withdrawal volumes were substituted for time to smooth the deliverability data as shown in Fig. 33. Cumulative injection volume was substituted for time in Fig. 34. The trend in the deliverability data shown in Fig. 33 is more readily evident than the injectivity plot (Fig. 34).

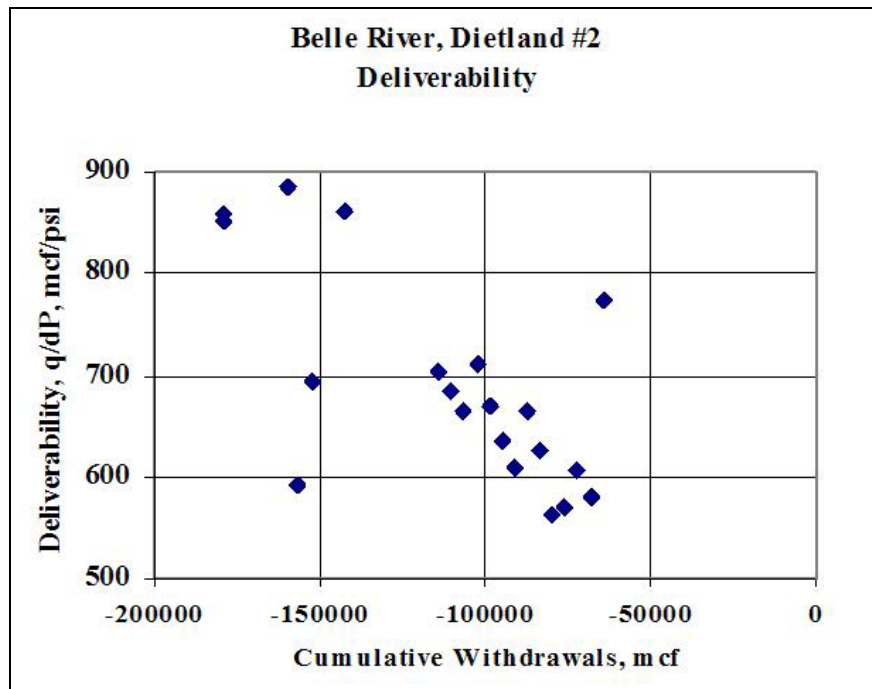


Figure 33. Deliverability vs. cumulative withdrawal.

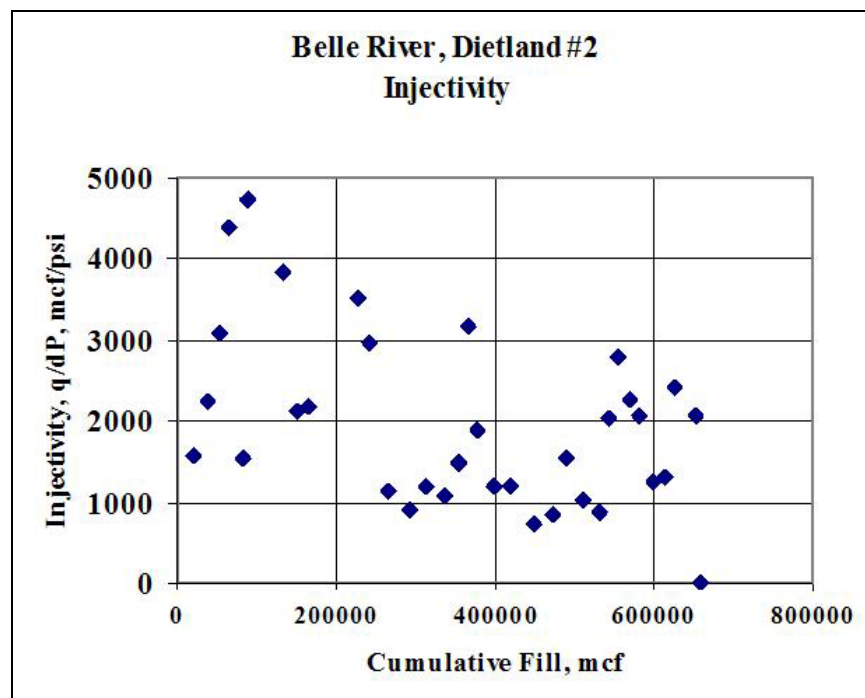


Figure 34. Injectivity vs. cumulative fill volume.

The linearity of the deliverability vs. withdrawals presentation of the pressure-rate historical data provides a baseline suitable for measuring the effect of surfactant on gas deliverability from either water-wet sandstone or non-water-wet dolomite storage facilities.

Discussion

This project evolved from an unpublished experiment conducted with a known water-wet limestone core from a Central Texas outcrop. It was observed that treating the core with an oil-soluble surfactant and then displacing the oil solution with water followed by displacement with gas doubled the gas flow rate over that at residual water saturation. Dry gas reservoirs and hence gas storage reservoirs were assumed to be water-wet, especially with the repeated fill/withdrawal cycles. After discussions concerning suitable surfactants with four vendors, requests were made for 14 surfactants that might make rocks less water-wet. The vendors supplied 11 samples. The costs of the surfactants varied from \$1.50–\$45.00 per lb as shown in Table 5.

Table 5. Surfactant prices*		
Chemical	Vendor	Cost \$/lb
Tomadry N-4	Tomah Products	\$1.47
Stepanquat 300	Stepan	\$1.86
Witconic 1298	Akzo Nobel	\$3.22
FC 4430	3M distributor	\$44.84

*Price quotes of four potential surfactants were obtained during August 2005.

Since core tests involving preparation, precise weights, and monitoring of flow experiments require time and expense, additional methods were developed to screen the wetting properties of dilute solutions of the surfactants. Capillary tubes were used to measure the rise of water in dry tubes vs. the rise of water in tubes treated with surfactants. Another test consisted of observing a drop of water on reservoir core material. Drops that spread (contact angle to air $>90^\circ$) were imbibed into the core. Drops that beaded on the core surface (contact angle to air $<90^\circ$) did so at a much slower rate or not at all.

Stepanquat 300 and Tomadry N-4 suppressed the capillary rise of water in tubes treated with surfactant to a greater degree than the other surfactants. Both are formulated compounds of quaternary ammonium cationic surfactants. The IFT measurements (Stepanquat ~ 30 dyne/cm and Tomadry ~ 40 dyne/cm) demonstrate that IFT and contact angle are separate components in the capillary pressure equation. Both generated a 0.7 cm rise in capillary tubes treated with 1% solutions of surfactant. Young's equation (see appendix) generates a contact angle of 75.4° for Stepanquat 300 and 76.0° for Tomadry N-4 suggesting that the difference in the performance of the two products in the core tests is the result of slight variations in their formulations. Since the cost effectiveness in suppressing capillary rise of the two surfactants is less than the other surfactants, they were selected for additional laboratory tests.

Generally the water-drop/contact angle on treated and untreated cores supports the precise capillary rise measurements. Both sandstone cores were water-wet, and the wetness was reduced with surfactants. However, the wetness of the dolomite appeared to be essentially constant with or without surfactant. Glass (quartz) capillary tubes are available, but availability of other materials such as dolomite or limestone is not known. Hence the advantage to using the

water-drop/contact angle tests on reservoir core material is attractive; however, additional work is required to improve the accuracy of the procedure.

The imbibition tests with reservoir cores are designed to test the effectiveness of surfactants in reducing the imbibition of water into the cores, thus increasing the volume available to store gas. The experimental results with the St. Peter core-water system demonstrate that a 2% solution of Tomadry N-4 increased the storage capacity of the core by 42%, while a 1% solution of Stepanquat 300 generated a 0.7% increase. Surfactants marginally affected the storage capacity of the dolomite cores in an adverse manner. This could be interpreted as the reservoir dolomite being naturally oil-wet.¹⁰

Core flow tests with reservoir cores were conducted to measure the deliverability defined as the flow rate divided by the pressure drop across the core. Laboratory experiments with a St. Peter sandstone core treated with a 2% solution of Tomadry N-4 resulted in a 59% increase in gas deliverability. A 40% less permeable St. Peter sandstone core treated with a 1% solution of Stepanquat 300 resulted in a 20% increase in gas deliverability. The gas deliverability through dolomite cores was only marginally increased.

While the Mt. Simon sandstone sidewall cores were not used in the flow tests due to size problems, the similarity in contact angle/core drop test observations suggests that the Mt. Simon sandstone would generate increased deliverability and storage capacity similar to St. Peter sandstone.

The rate-pressure history available from both the Waverly and Bell River Mills fields is adequate for field test baseline purposes. The laboratory data support a Waverly field test of the use of surfactants to increase gas deliverability from storage wells. If a field test could be scaled to the laboratory results, the deliverability of well 91 would increase as shown in Fig. 35.

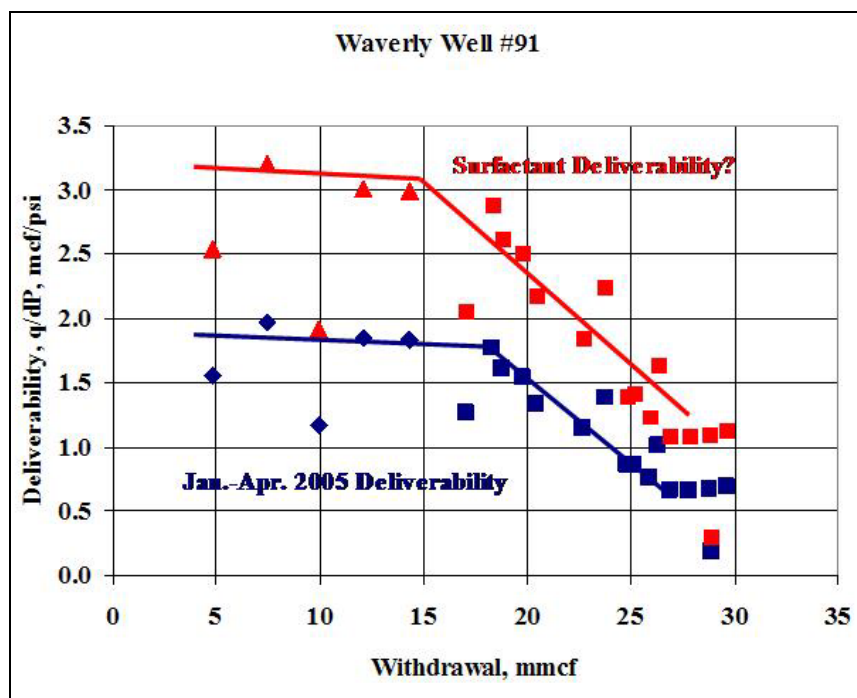


Figure 35. Potential deliverability increase with Well 91 surfactant treatment.

The laboratory data do not support a Bell River Mills field test. However, the rate-pressure history may prove useful for a salt inhibitor field test should the current laboratory work generate supporting information.

Conclusions

This project demonstrates that the wettability of gas storage reservoirs plays an important role in the void space available for storage. The deliverability of gas from a storage well is also dependent on rock wettability. It was determined through laboratory tests with cores from aquifer storage sites that some surfactants can decrease the natural water-wetness of sandstone thereby increasing gas deliverability and gas storage volume. This was not the case with dolomite cores from a storage facility that was formerly a dry gas reservoir. Transferring this new concept from the laboratory to the field should be of interest during times of limited storage capacity.

The value of laboratory testing with cores as a guide for field sites was confirmed with the surprising results obtained with dolomite cores from a storage facility that was formerly a dry gas reservoir. The notion that all dry gas reservoirs are strongly water-wet was erroneous.

References

1. Yeager, V.J., Blaush, M.E., Behenna, F.R., and Foh, S.E.: "Damage Mechanisms in Gas Storage Wells," SPE 38863 presented at the SPE Annual Technical Conference and Exhibition, San Antonio, TX (October 5–8, 1997).
2. Ammer, J.R. and Sames, G.P.: "Advances for Improved Storage: Deliverability Enhancement and New Storage Facilities," Paper SPE 65638 presented at the 2000 SPE Eastern Regional Meeting, Morgantown, WV (October 17–19, 2000).
3. Penny, G.S., Soliman, M.Y., Conway, M.W., and Briscoe, J.E.: "Enhanced Load Water-recovery Technique Improves Stimulation Results," paper SPE12149 presented at the 58th Annual Technical Conference and Exhibition, San Francisco, CA (October 5–8, 1983).
4. Al-Anazi, H.A., Walker, J.G., Pope, G.A., Sharma, M.M., and Hackney, D.F.: "A Successful Methanol Treatment in a Gas-Condensate Reservoir: Field Application," paper 80901-PA, February 2005 SPE Production & Facilities.
5. Mahadevan, J. and Sharma, M.M.: "Clean-up of Water Blocks in Low Permeability Formations," SPE 84216 presented at the SPE Annual Technical Conference and Exhibition, Denver, CO (October 5–8, 2003).
6. Fahes, M. and Firoozabadi, A.: "Wettability Alteration to Intermediate Gas-Wetting for Gas-Water Systems at Reservoir Condition," presented at the 8th International Symposium on Reservoir Wettability, Rice University, Houston, TX (May 16–18, 2004).

7. Du, L., Walker, J., Pope, G., Sharma, M., and Wang, P.: "Use of Solvents to Improve the Productivity of Gas Condensate Wells," SPE 62935 presented at the 2000 SPE Annual Technical Conference and Exhibition, Dallas, TX (October 1–4, 2000).
8. Hilchie, D.W. : *Old Electrical Log Interpretation*, IED Exploration, Inc., Tulsa OK, (1979) 118-120.
9. Weiss, W .W., Xie, X., Weiss, J.W., Subramanian, V., Taylor, A., and Edens, F.: "Artificial Intelligence Used to Evaluate 23 Single-Well Surfactant Soak Treatments," SPE Paper 89457 presented at the 14th Symposium on Improved Oil Recovery, Tulsa, OK (April 17–21, 2004).
10. Wardlaw, N.C. and McKellar, M.: "Wettability and Connate Water Saturations in Hydrocarbon Reservoirs with Bitumen Deposits." *Journal of Petroleum Science and Engineering* 20 (1998) 141-146.

Appendix

Additional laboratory results and Waverly production histories

Additional figures have been constructed from the laboratory test results and the Waverly production histories. Young's equation was utilized.

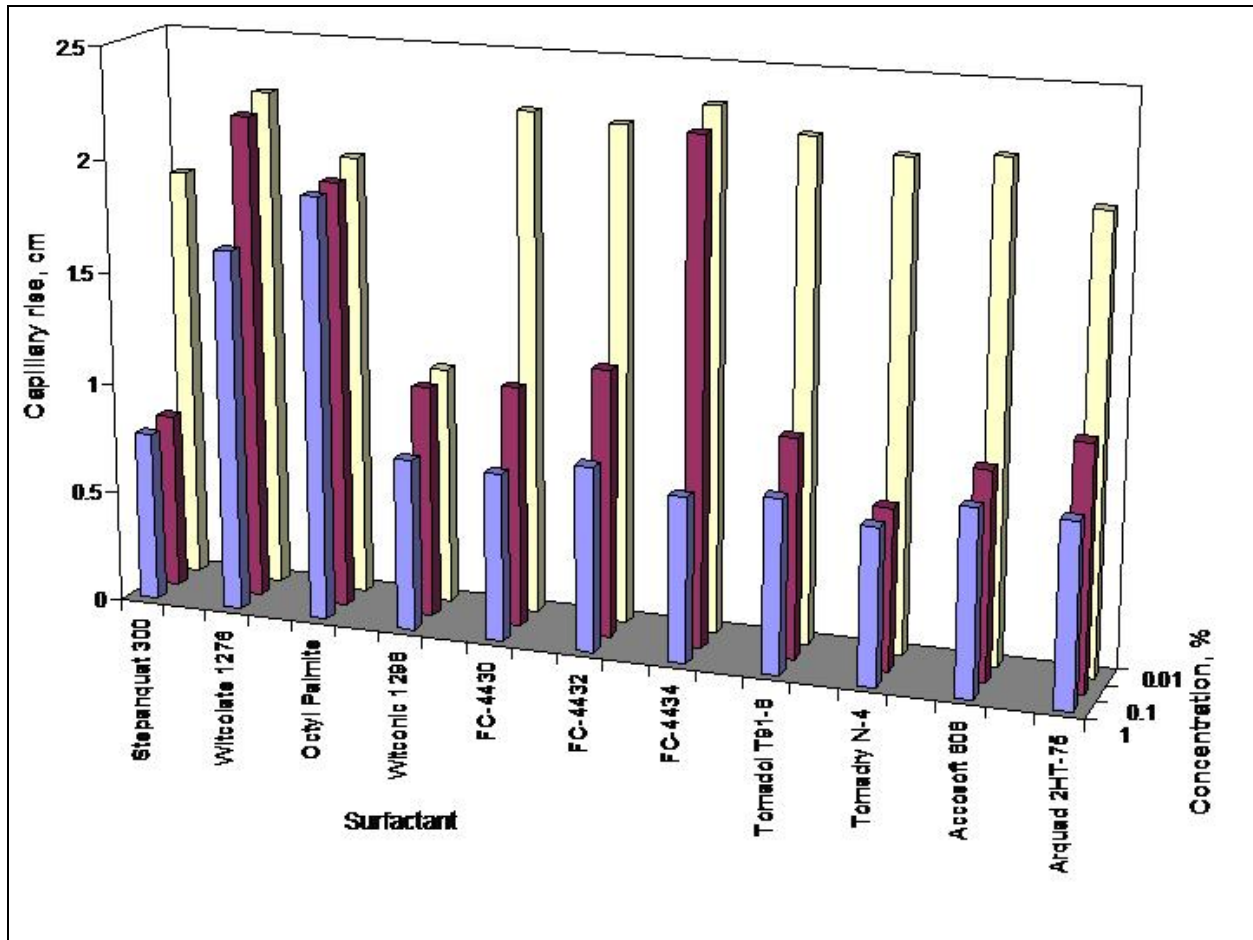


Figure A6. Summary of capillary rise tests.

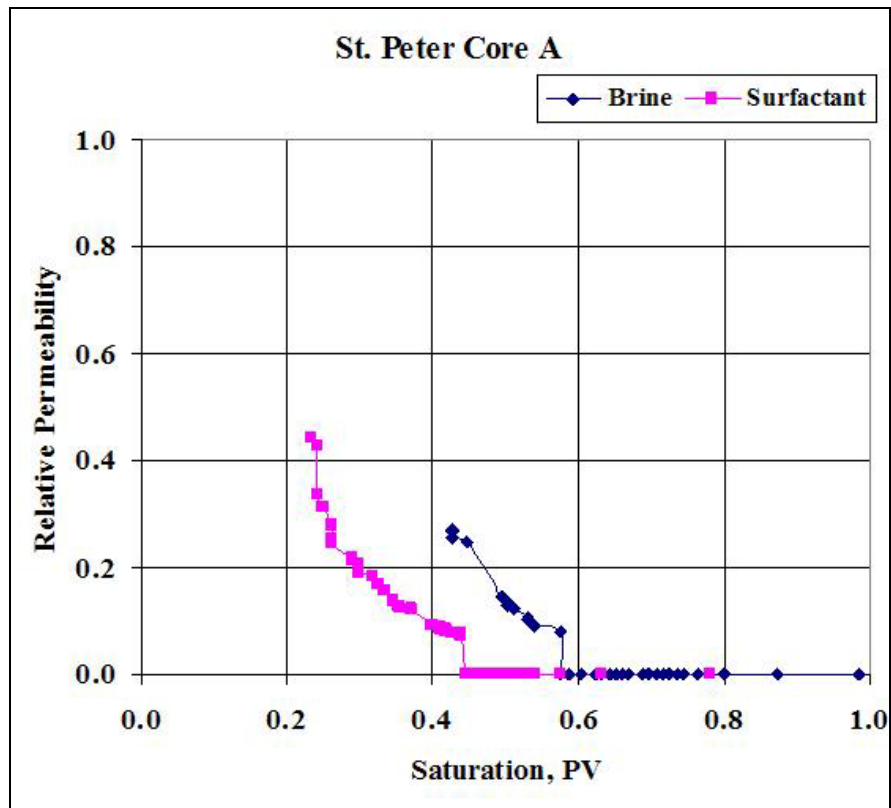


Figure A7. K_{rg} in St. Peter sandstone core “A” with brine or Tomadry N-4.

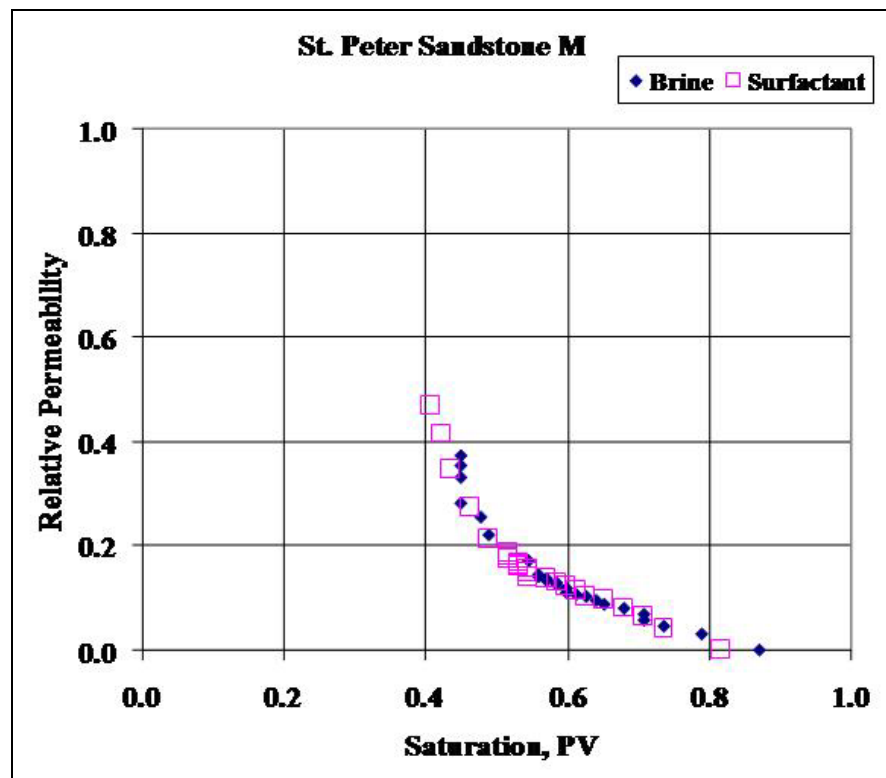


Figure A8. K_{rg} in St. Peter Sandstone “M” with brine or Stepanquat 300.

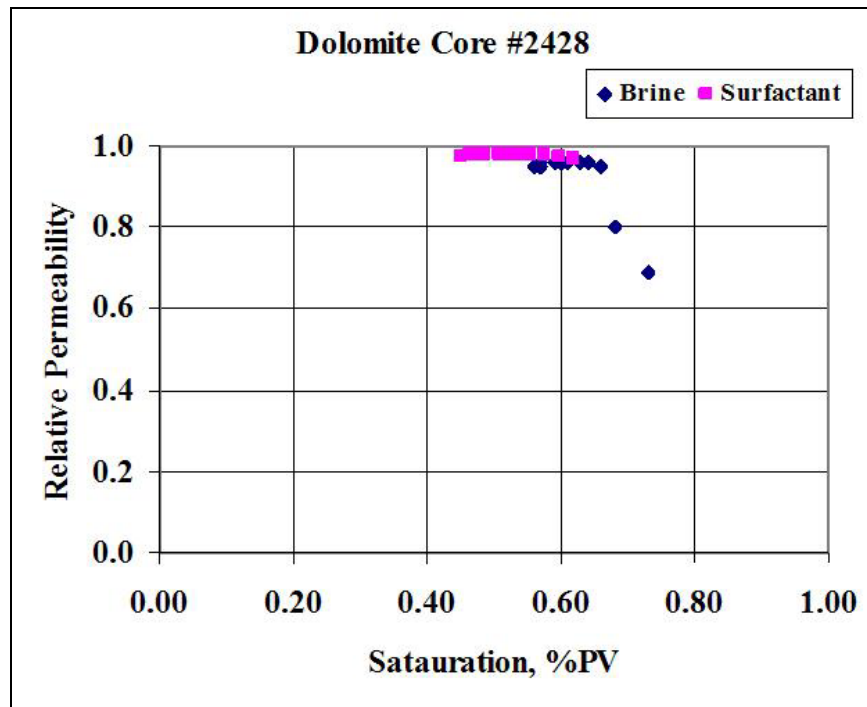


Figure A9. K_{rg} in dolomite core #2428 with brine or N-4 Surfactant.

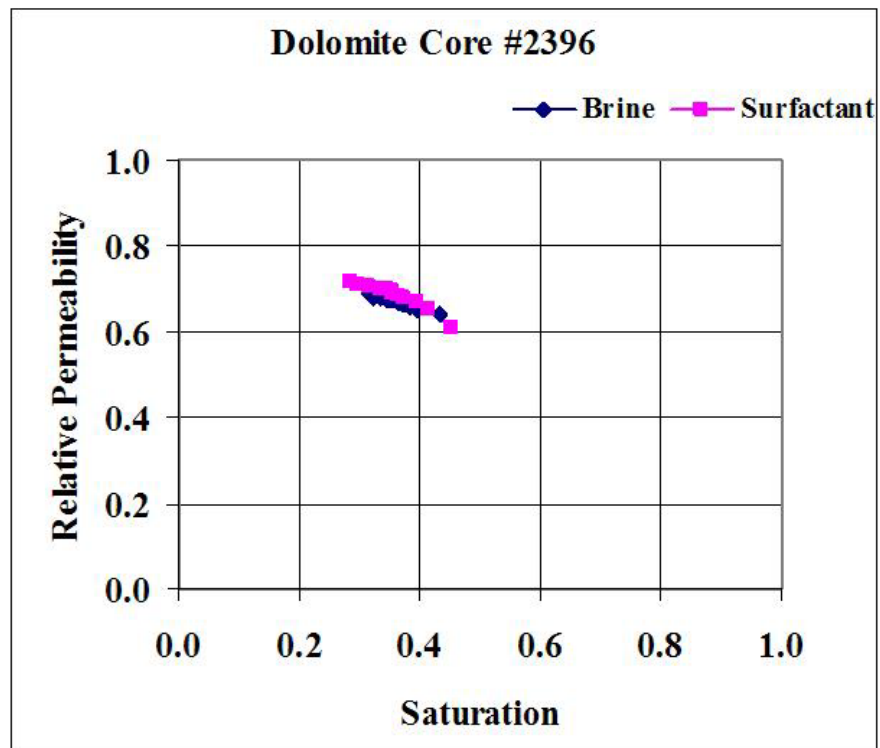


Figure A10. K_{rg} in dolomite core #2396 with brine or Tomadry N-4.

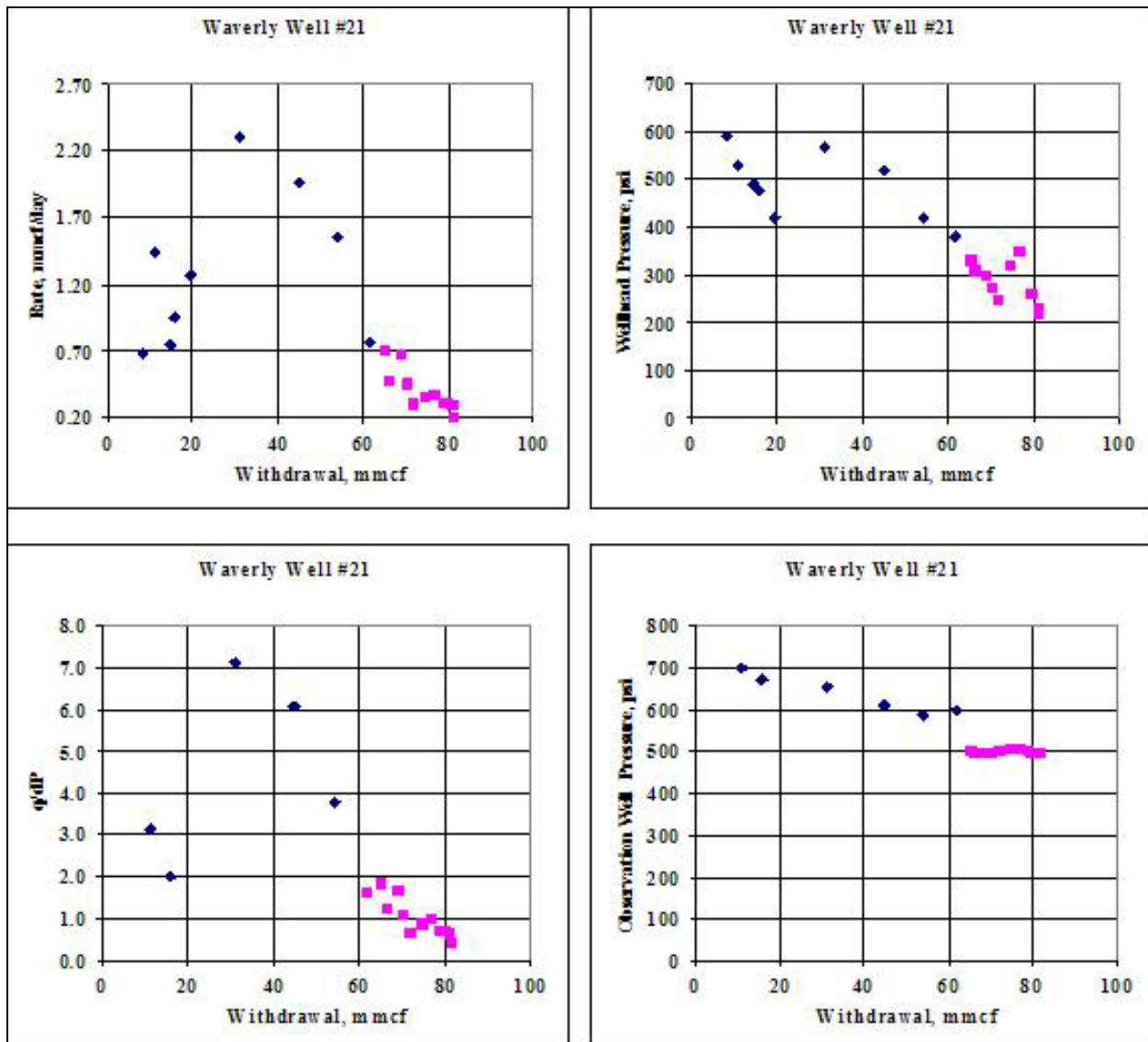


Figure A11. Performance history of Waverly well # 21 during the 2004 season.

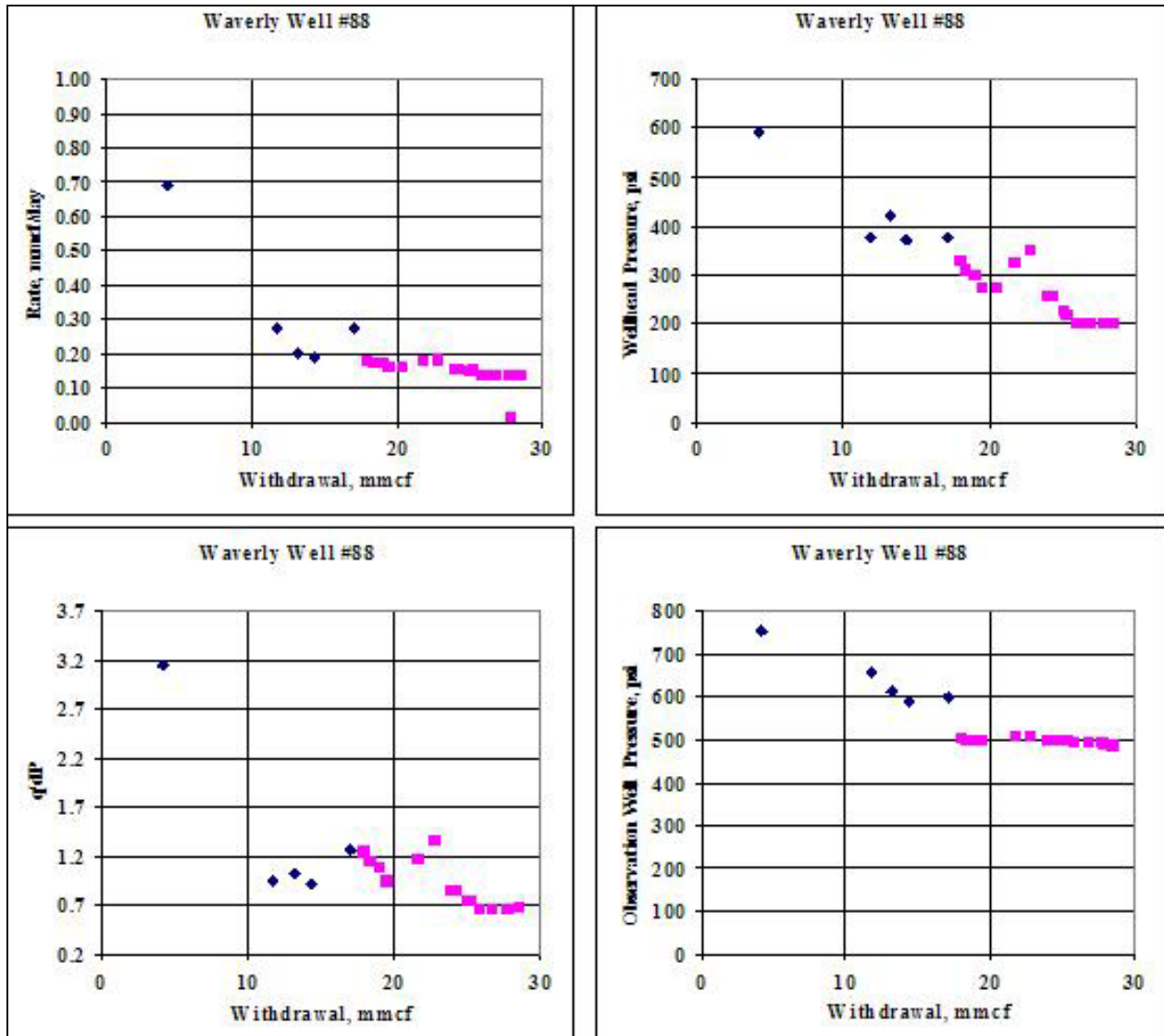


Figure A12. Performance history of Waverly well # 88 during the 2004 season.

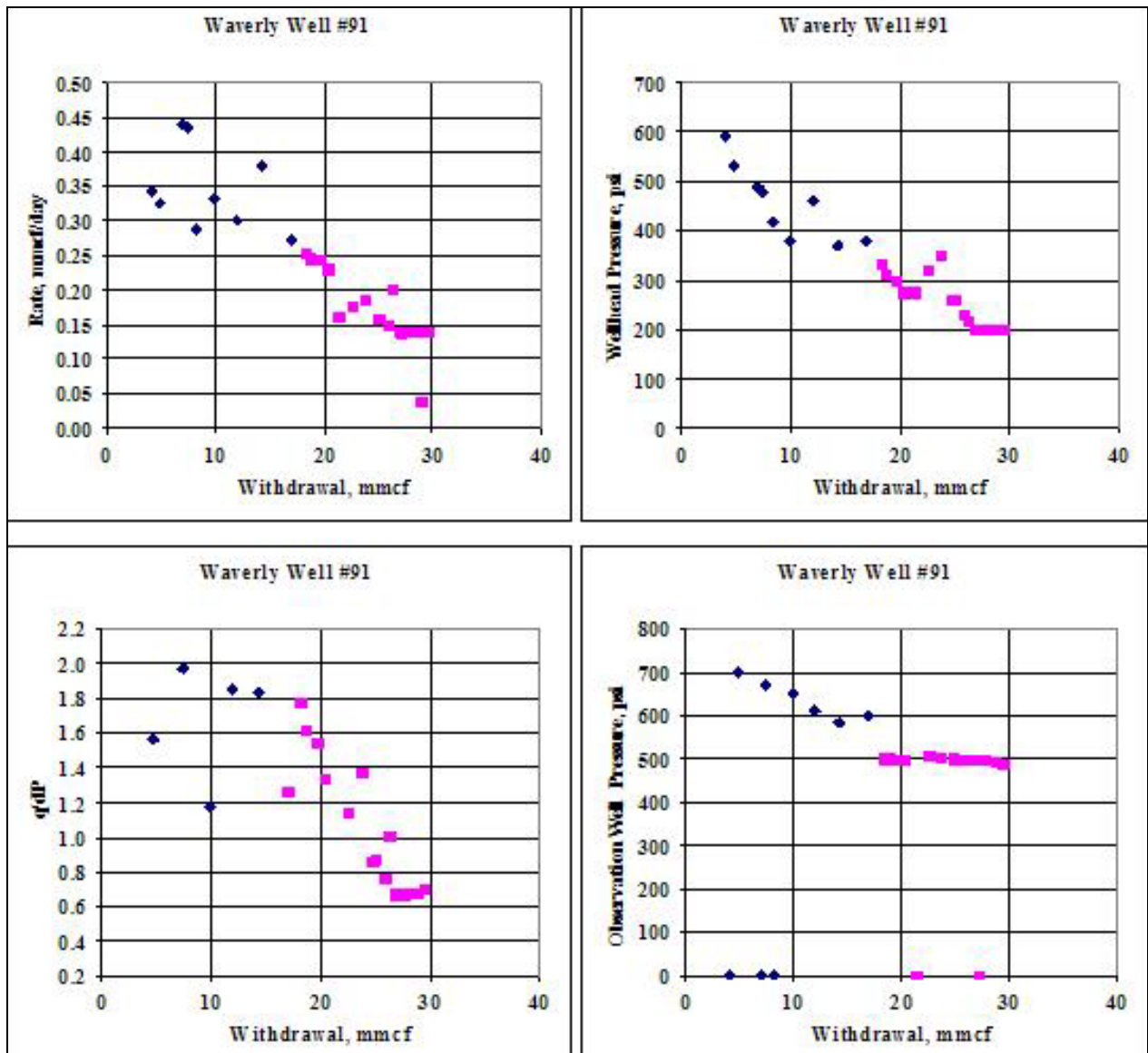


Figure A13. Performance history of Waverly well #99 during the 2004 season.

Young's Equation

Young's equation is $P_c = \frac{2\sigma \cos \theta}{r} = \rho gh$, where density, ρ = water density; gravity, $g = 981$ cm/s²; h = capillary rise, cm; r = capillary radius, cm; θ = contact angle, and deg; σ = water surface tension.

The application to the laboratory data results in practically identical contact angles.

Appendix J
2005, Wellbore Cement Bond Integrity,
University of Texas Final Report

GAS STORAGE TECHNOLOGY CONSORTIUM

Research Project

WELLBORE CEMENT BOND INTEGRITY

Final Report

Reporting Period: May 1, 2005 - December 31, 2006

Award Number DE-FC26-03NT41779 (2910-UT-DOE-1779)

Final Technical Report, Issued April 2007

Reporting Period May 1, 2005 – December 31, 2006

The University of Texas at Austin

Prepared and Submitted by K. E Gray

Phone (512) 471-3242 Fax (512) 471-9605

DISCLAIMER

This report was prepared as an account of work sponsored by an agency of the United States Government. Neither the United States Government nor any agency thereof, nor any of their employees, makes any warranty, express or implied, or assumes any legal liability or responsibility for the accuracy, completeness, or usefulness of any information, apparatus, product or process disclosed, or represents that its use would not infringe privately owned rights. Reference herein to any specific commercial product, process, or service by trade name, trademark, manufacturer, or otherwise does not necessarily constitute or imply its endorsement, recommendation, or favoring by the United States Government or constitute or imply its endorsement, recommendation, or favoring by the United States Government or any agency thereof. The views and opinions of authors expressed herein do not necessarily state or reflect those of the United States Government or any agency thereof.

WELLBORE CEMENT BOND INTEGRITY

ABSTRACT

This program of studies combines laboratory experimental measurements and numerical simulations to investigate bonding between cement and casing, and effects of mechanical stress on cement and bond. P-waves are detected immediately upon pouring the slurry into the chamber. A dramatic increase in velocity during curing reflects the initial solidification of the slurry. Static deformation behavior was assessed by measurements of changes in wave propagation, static deformation, and failure during curing. Variations in axial stress with axial strain during triaxial deformations differ significantly for repeated deformation cycles on the same specimen. For single deformation cycles carried out on different specimens, deformation behavior follows the same trend as the dynamic moduli and the trend indicated for the unloading modulus for the multiple-deformation tests. Results for the multiple deformations on the same specimen show a trend towards lower values than those found for the multiple deformations, which is compatible with large surface-related strains in the multiple deformation tests. Permanent strains for the multiple deformations on Mix 2 (cement plus moisture-absorbing additives) indicate the presence of a non-recoverable surface deformation during the first deformation cycle, which is absent for the subsequent cycles. The amount of free water at the beginning of curing appears to significantly affect the strength of the cured cement. Numerical simulation of wave propagation in the cement-casing environment were also carried out, based on a two-dimensional discrete particle method. The simulations are compared with experimental tests in test assemblies configured to replicate bond indexing behavior. Simulations investigated wave propagation along the casing, and effects of changes in cement-casing bonds on the propagation. Non-uniform bonding affected wave amplitude in the same manner as percentage of the surface area bonded and, in some cases, completely obscured variations due to bond quality. Changes in the mechanical properties also affect amplitude. Amplitude variations scale roughly with the cumulative effect of fractional changes in bond stiffness times bond fraction, but variations in non-uniform distributions can lead to substantial deviations from this general trend. The placement of bonds with altered mechanical properties has more of an effect on wave amplitude than placement of unbonded zones. Simulations the influence of sand and porosity on cement behavior leads to attenuation of high-frequency components in the waves.

WELLBORE CEMENT BOND INTEGRITY

TABLE OF CONTENTS

Disclaimer	2
Abstract	3
Table of Contents	4
Executive Summary	5
Introduction	8
Experimental	10
Results and Discussion	14
1. Wave Propagation	14
2. Static Deformation Behavior	16
3. Discrete Element Modeling	24
Conclusions	37
References	40
Figures	41

WELLBORE CEMENT BOND INTEGRITY

EXECUTIVE SUMMARY

This program of studies combines laboratory measurements and numerical simulations to investigate bonding between cement and casing, and effects of mechanical stress on cement and bond. New apparatus and test procedures were developed for the study of cement-boundary interactions during curing and stress cycling. Systems were fabricated and used for studies of wave propagation through cement and traveling vertically along the side boundaries of the chamber. Compressional and shear wave velocities were monitored during curing periods. P-waves are detected immediately upon pouring the slurry into the chamber, and travel times during the initial 6-10 hours of curing are almost constant. A dramatic increase in velocity between 11 and 23 hours of curing reflects the initial solidification of the slurry. The earliest evidence for shear waves is seen after curing for more than 9 hours, which is consistent with the p-wave evidence that prior to this time the specimen is still a liquid. Subsequent shear waves can be identified by longer travel times. Poisson's ratios were determined from the set of shear and compressional mode velocities, and ratios were found to vary from initial values of 0.5, representative of a fluid at curing time near zero, to about 0.25, typical of intact rock, as the cement cures.

Static deformation behavior was assessed by measurements of changes in wave propagation, static deformation, and failure carried out on specimens of Type H cement during curing from slurry to rigid solids. CT images were acquired for three of the post-test specimens, to assess possible differences in cement texture. For at least one of each of the cement mixtures cured under ambient and 1 kpsi confining pressure, excess water was removed from the top of the poured specimen as it was produced. At least one specimen of each cement mixture cured under ambient and 1 kpsi confining pressures was pressurized and cured without removing the water layer.

Variations in axial stress with axial strain during triaxial deformations differ significantly for repeated deformation cycles on the same specimen. Behavior for specimens that did not retain excess water during initial curing showed a gradual decrease in slope (yielding) but no evidence of failure. Specimens that retained substantial amounts of water during curing showed an initial positive curvature at low stresses, gradual yielding and failure. Wave velocities measured at the end of each of the deformation cycles were not affected appreciably by deformation, but increased systematically with curing time. CT scan images indicated in these images are the large voids

associated with absorption of free water into the cement crystal structure during curing, and deformation-related fractures.

In other tests, tri-axial single deformation cycles were carried out on different specimens of the two types of cement, after curing. Deformation behavior follows the same trend as the dynamic moduli and the trend indicated for the unloading modulus for the multiple-deformation tests. The data for the Series III tests do show a trend towards lower values than those found for the multiple deformations, which is compatible with large surface-related strains in the multiple deformation tests, suggesting that the surface effects are largely eliminated during the first loading cycle of the multiple-deformation tests, but are present for each of the single deformation cycles in the multiple deformations. Permanent strains for the multiple deformations on Mix 2 (cement plus moisture-absorbing additives) indicate the presence of a non-recoverable surface deformation during the first deformation cycle, which is absent for the subsequent cycles. The variations of the observations show a smoother and more gradual decrease in non-recoverable strain in single deformations than the multiple-cycle deformational cycles. Generally, the multiple-deformation tests show permanent strains below those for the single deformation tests. Non-recoverable strains for Mix 1 and Mix 2 specimens are all significantly smaller than corresponding values for Mix 1 tests. The amount of free water at the beginning of curing appears to significantly affect the strength of the cured cement.

The third area of studies in this program is the numerical simulation of wave propagation in the cement-casing environment. The simulations are based on a two-dimensional discrete particle method (DPM). This numerical code is designed to simulate mechanical properties using an assembly of small finite particles. Macroscopic behavior is derived from first-principal micromechanical processes, coupled with a graphical user interface for the visualization of the waves. The simulations are compared with experimental tests conducted in a separate study in test assemblies configured to replicate bond indexing behavior.

The numerical simulations provide for detailed analysis of the experimental observations of wave propagation, using well-defined test conditions. The DEM simulation used in this study models the mechanical properties by treating the sample as a collection of spherical particles interacting via Newton's second law. The interaction of particles is treated as a series of springs, arising from overlap between the particles, and by elastic forces developed by deformation of inter-particle bonds. The model input parameters were determined by comparing computed wave velocities with published values, and altering the spring stiffness of the particles to match the measured wave velocities.

The first simulations investigated wave propagation along the casing, and effects of changes in cement-casing bonds on the propagation. Simulations of changes in the fraction of intact bonds, which is equivalent to variations in the fraction of contact area bonded in this 2D simulation, confirmed a direct relationship between wave amplitude and the percentage of intact bonds which is the essential basis for cement bond log interpretation. Examination of the effects of non-uniform bonding on wave amplitude showed that energy loss into the cement depends not only on the total percentage of the surface area bonded, but also the location of the bonds relative to the receiver. Computed amplitude variations for non-uniform distribution could, in some cases, completely obscure variations due to bond quality. Simulations of the effects of a weakening of the mechanical bond material stiffness on wave propagation showed that changes in the mechanical properties have the same effect on amplitude as fractional changes in the fraction of the bonded contact area. The results show that amplitude variations scale roughly with the cumulative effect of fractional changes in bond stiffness times bond fraction. However, variations in non-uniform distributions can lead to substantial deviations from this general trend. Simulations of the combined effect of non-uniform distribution of bonds with different stiffness shows that changes in mechanical behavior near the receiver have less effect on wave amplitude than changes further from the receiver. This behavior is similar to that observed for changes in the percentage of the contacts. The placement of bonds with altered mechanical properties has more of an effect on wave amplitude than placement of unbonded zones.

Simulations of wave propagation within the cement analyzed the influence of sand and porosity on cement behavior. Both types of inclusions alter the acoustic impedance of the cement, which will complicate bond quality evaluations, but the most important process was the attenuation of high-frequency components in the waves by scattering by void inclusions.

WELLBORE CEMENT BOND INTEGRITY

INTRODUCTION

This final report summarizes activities in the project, *Wellbore Cement Bond Integrity*. Technical, economic, environmental, and safety considerations underscore the pressing need by gas storage operators to understand the ways in which elements of a well bore and cement sheath interact during drilling, completion, and production operations. Better understanding of cement hardening, cement adhesion, and the effects of cyclic pressure and temperature-related stresses on these processes are needed for development of improvements in cement/casing/formation seals, and better techniques for assessments of seal quality with down-hole logging tools.

The components of a well-bore are physically coupled. While pressures inside the casing are easily measured and mechanical behavior of casing is well documented, little is known about the stresses, displacements, and behavioral features of the casing/cement interface outward through the cement, mud cake, plastic zone, and formation. Interface stresses, displacements, and coupling conditions change continually as well-bore pressures, pore pressures, and temperatures fluctuate. An understanding of the 3-D, time-dependent changes through all of the system components is necessary for addressing the well-bore cement bond integrity problem, especially in gas storage operations.

Concerns about cementation fall into two broad categories: 1) development of a satisfactory cement/casing/formation seal; and 2) quantitative assessments of the quality of the seal with down-hole logging tools. A better understanding of cement hardening, cement adhesion, and effects of cyclic pressure and temperature-related stresses on these processes is useful for addressing both of these concerns.

Laboratory assessments of wave propagation and deformational behavior of the cement-casing environment are especially useful in connection with these concerns. The most widely used tools for evaluating the quality of cement are based on acoustic measurements. The concept of an acoustical bond logging tool first appeared in the literature in 1959 (Tixier et al). Extensive results of laboratory and field testing of tools were published in 1961 by Grosmanin et al.; and Anderson and Walkers, and by 1962, a working tool was in use in the field. This configuration, the Cement Bond Log, is still in wide use. These tools transmit a 20 kHz spherical acoustic signal into the cased borehole. The amount of this signal lost into the formation is proportional to the acoustic coupling

between cement and formation, so that the amplitude of the propagated casing wave is inversely proportional to the integrity of the cement-casing bond. A more recent configuration, the Cement Evaluation Tool (Froelich et al., 1981), is based on ultrasonic pulse-echo technology originally developed for the Borehole Televiwer. An array of ultrasonic (nominal 0.5 MHz) transmitter/receivers placed around the circumference of the cylindrical sonde samples the relative amplitude of the echo train from approximately one square inch of the casing/cement/formation system adjacent to the transducer. Waveform amplitude is sampled during several gating windows, the latest of which provides a measure of coupling of sound energy into the formation (and a consequent loss of reflected amplitude).

Suites of laboratory tests were carried out in existing triaxial testing apparatus, and in bench-top apparatus custom designed to evaluate wave propagation in cement and along the cement-casing interface, as freshly-poured cement cures over minutes through one week. The GSTC project has been carried out in conjunction with and co-funded by a University of Texas Industrial Affiliates Research Program, *Life-Of-Well Rock, Fluid, and Stress Systems*. This program consists of three topical areas: I. Soft Sediment Systems; II. Wellbore and Near-Wellbore Casing, Cement, and Formation Interactions; and III. Pressure Management Operations. These programs overlap many concerns with the GSTC project..

In Soft Sediment Systems, the overall goal is to quantify subsurface processes and behavior of rock, fluid, and stress systems in soft, friable, poorly consolidated, weak formations. The analytical formulations of classical continuum mechanics are demonstrably inadequate for such systems, and understanding of complex, interrelated processes in very weak, granular materials is needed to develop relevant behavioral 'laws', guidelines, and correlations for field applications. Laboratory data on non-elastic rock behavior at elevated effective stresses are included in this report.

In Wellbore, Near-Wellbore, and Formation Interactions, the overall goal is to quantify the numerous stresses, strains, displacements, and interacting conditions around the wellbore region. Three, four, or more mechanical components in series (such as casing, cement, mud cake, gravel packs, liners, screens, formation) exhibit coupled interactions during drilling, completion, and production operations. Quantifications of cement shrinkage and stress transfers in wellbore and near-wellbore constituent components are the subject of the project, "Casing, Cement, and Formation Interactions During Drilling, Completion, and Production Operations". Results and

conclusions from that work useful in evaluating the cement/casing bond integrity are included in this report.

In Pressure Management Operations, the overall goal is to quantify combined static and dynamic stresses and displacements at strategic locations within and around the well bore 'U-tube' for applications such as Managed Pressure Drilling, Underbalance/Balance/Overbalance Drilling, Mud Cap Drilling, Measurements While Drilling, and Logging While Drilling. Critical pressure magnitudes and small pressure tolerances have large economic, technical, safety, and environmental consequences. Cement sheath integrity and its critical role in zonal isolation is one of several pressure/flow limiting items of concern in that work and will provide useful information to cement bond log technology.

Leverage to the Wellbore Cement Bond Integrity project from the Life-Of-Well Program has been and will continue to be substantial, owing to the large resource and support system (test facilities, data systems) utilized in Simultaneous Property System capabilities, other preparation/testing facilities on hand, and the proactive collaboration of industrial colleagues participating in the Life-Of-Well project indicated above.

The following section of this report discusses measurements of wave propagation during cement curing, and the equipment developed in the study to investigate the behavior. The next section is a detailed discussion of the deformation and wave propagation measurements carried out in the SPS system, during curing of two cement mixtures. The next section discusses the developments of numerical simulations based on the DEM techniques, and the final section is a discussion of conclusions developed on the basis of the current measurements.

EXPERIMENTAL

A preliminary sequence of graduated cylinder tests were carried out to assess the evolution of a layer of free water during curing, and to evaluate its effect on wave propagation. Photographs of the top surface of a freshly-poured specimen were taken over a period of several hours after pouring.

A bench-top experiment was then carried out. In this experiment, a 4-inch diameter by 4-inch long PVC tube was placed between end platens containing s- and p-wave transducers, and the chamber was filled with cement slurry. In this geometry, the 2-inch diameter end platens extend

into the cement, and the aqueous layer should be above the bottom surface of the top pedestal (and out of the wave propagation pathway).

The next test was carried out in the same bench-top apparatus, but using 3 sets of 0.17" shims placed on top of the PVC tube. These shims increased the distance between the end platens, and hence the length of the cement between the platens. By progressively removing the shims one set at a time at various times during the initial 12-hour curing stage – while the cement was still in a liquid state - the top platen was progressively pressed into the cement. In this way we hoped to force out the aqueous layer between the top platen and the specimen.

In these benchtop tests, the presence of the water layer and associated chemical interaction between the fluid and the aluminum platens effectively prevented detection of ultrasonic waves traveling through the cement during the early stages of curing. The difficulties in measuring wave propagation led to the design of a new apparatus for investigation of curing behavior and corresponding changes in propagation behavior. A primary concern was the development of techniques for measuring waves propagating through cement during the very earliest curing times.

The basic approach was to mount transducers well below a top surface, in an apparatus in which waves travel horizontally through the cement. The 4" x 4" apparatus shown in Figure 1 was designed and fabricated. A larger (4" x 8" chamber; Figure 2) was also constructed, to investigate features of waves traveling along different path-ways representative of the down-hole casing/cement environment. It provides for measurements of waves traveling vertically along the side boundaries of the chamber – but still well removed from the specimen top and the accompanying layer of free water. Side panels were either plexiglass (as in Figure 2) or steel (not shown).

A large suite of wave propagation measurements was carried out with these test assemblies, using the initial cement mixture (only Type H Portland cement). Cement slurry was mixed according to API #10 procedures, and poured immediately into the test box. Travel times for p-waves across the sample were monitored for the entire duration of the tests. Shear waves were not observed until after curing times of approximately 10 hours, and were generally not monitored until after curing overnight. Waveforms of waves propagating across the chambers (for 4"x4" and 4"x8" boxes) and along the chamber side walls (for the 4"x8" box) were captured and stored at nominal 1-day intervals as the specimens cured.

Suites of mechanical deformation and failure measurements and simultaneous changes in wave propagation were carried out over a nominal one-week time period, during which specimens

prepared from slurry at time zero cured to a rigid solid. The investigation was carried out using triaxial measurements in the Simultaneous Property System (SPS) shown in Figure 3. This test system has been developed and refined over four decades of operation at the UT Center for Earth Science and Engineering. A jacketed cylindrical test specimen is subjected to lateral stresses from a confining fluid and an independent axial load. Simultaneous measurements of axial and radial displacements, and ultrasonic shear and compressional wave propagation were carried out during loading and unloading deformations. Deformation parameters are measured by load and displacement transducers, and stored in digital files in the computer-based data acquisition system.

The specimen for these tests were cement slurry, poured immediately after mixing into the jacket attached to the bottom platen. Two cement mixtures were used. The first mixture, Mix 1, was composed only of Class H Portland cement. The second mixture, Mix 2, was a recipe provided by one of the Life-of-Well sponsors. It contained bentonite and BA-90, both of which absorb excess water and thereby reduce the amount of free water present during early stages of curing. Both mixtures were prepared according to API 10A.

After filling the jacket with the cement slurry (and removing excess water from the top of the specimen), the top platen was inserted into the jacket, and the three alignment rods were secured to the bottom and top end platens. At this point the sample-end platen assembly was a continuous column, and - except for specimens #2, #3, and #4 - axial specimen length was determined directly by measurement of the spacing between the platens. The reference axial displacement transducer output corresponding to this initial state was measured and recorded. No subsequent adjustments of the axial displacement transducer position were made, and all subsequent changes in length were relative to this initial position.

The sample assembly was placed in the pressure vessel and the confining pressure (200 psi or 1 kpsi) was applied. Shear wave propagation measurements proved to be problematic for this series of measurements. No s-wave propagation is possible prior to solidification of the cement, and the lead shims used for isolation of platens and specimen led to a degradation of signal quality, so that determinations of first arrival times for velocity determinations was not reliable. No shear wave velocity measurements are reported for these tests.

Also, no lateral displacement measurements were carried out for this series of tests. The lateral displacement transducers in the SPS are spring loaded on to the specimen, and the stress exerted by the springs led to significant (permanent) deformation of the slurry specimens. Out of

concern for spurious behavior introduced by such changes in cross-section geometry, the lateral transducers were not attached for this series of tests.

For each of the specimens, the test sequence was as follows.

1. Freshly poured cement was cured for 24 hours under various confining pressures.
2. Hydrostatic confining pressure was increased to 1kpsi, and a triaxial loading cycle up to a deviatoric axial stress of 1kpsi was carried out, and the specimen was unloaded to the hydrostatic 1kpsi stress.
3. For some of the specimens, p-wave velocities were measured at several points during the loading /unloading cycle.
4. The p-wave velocity was measured in all specimens after the initial triaxial loading cycle (at 1kpsi hydrostatic confining pressure).
5. Additional 1 kpsi triaxial loading cycles were carried out for some of the specimens at 24 – 48 hour intervals. P-wave velocities were measured after each of these loading cycles, at a hydrostatic confining pressure of 1kpsi.

The specimens were cured for 24 hours under ambient, 200 psi, and 1 kpsi confining pressures. Within minutes after pouring each of the specimens, a layer of free water was observed on the top surface. Left alone, this free water was re-absorbed into the specimen over the next 24 hours. For at least one of each of the cement mixtures cured under ambient and 1kpsi confining pressure, this water layer was removed from the top of the poured specimen as it was produced, for approximately 30 minutes prior to the application of confining pressure. At least one specimen of each cement mixture cured under ambient and 1 kpsi confining pressures was pressurized and cured without removing the water layer. The water layer was not removed for any of the specimens cured under 200 psi confining pressure.

After the sequence of deformations, three of the specimens (#11, a Mix 1 specimen with no adjustment of water content; #9, a Mix 1 specimen in which excess free water was removed prior to curing; and #6, a Mix 2 specimen) were examined in the UT Geology Computerized Axial Tomography (CT) scanner. This provides a high resolution (nominal 100 micron) view of porosity within the specimen. This porosity includes initial pore space as well as fractures associated with deformation-induced failure. Results from this series of multiple-deformation tests are designated as Series II tests.

Uncertainties in observed behavior in this series of tests led to a modification of the test sequence, carried out in the final series of static deformation tests. In these tests fresh Mix 1 and

Mix 2 specimens were poured at the beginning of the test sequence, and the specimen was allowed to cure – undisturbed – for a time period of 14, 24, 36, 48, or 168 hours. After the curing period, the specimen was deformed by carrying out a loading cycle, and the sample was removed. A new specimen was poured into the specimen chamber, and the sequence was repeated for a different curing time. The revised sequence was repeated for Mix 2 specimens. These tests are designated as Series III and Series IV tests, for Mix 1 and Mix 2 slurries, respectively.

RESULTS AND DISCUSSION

1. Wave Propagation

Observations during the preliminary shakedown tests of wave propagation demonstrated that the quality of waveforms is generally poor during the first 24 hours of curing. A photograph of the top layer of free water after curing for 24 hours is shown in Figure 4. Four representative images over a 24 hour period are shown in Figure 5. Subsequent to 24 hours of curing, waveforms were still of poor quality until the specimens were axially loaded. A primary source of difficulties in wave propagation measurements is the development of a small layer of water at the top end of cement slurry. This water is re-absorbed during the first 18 hours of curing. This aqueous layer can have significant impact on wave propagation – especially shear waves – along such a vertical column.

One consequence of this water layer is corrosion of the aluminum end platen in testing systems, and deposition of cement minerals from the aqueous layer. This behavior is shown in Figures 6 and 7. These photographs show the upper and lower end platens and specimen surfaces. There is considerable residue on the top platen, while the bottom platen remains flat and relatively clean.

The quality of wave-forms shown in Figure 8 illustrates the problem with the aqueous layer. Post test observations of the end platens revealed that the bottom specimen surface and end platen were clearly damaged, consistent with the poor wave-forms. Water in the aqueous layer in this test was apparently trapped by the low permeability of the partially cured specimen.

The use of shims during cement curing was clearly effective in improving coupling for the later-stage curing for p-waves, shown in Figure 9. Computed velocities for these waveforms are shown in Figure 10. Post-test observation of the top platen and test specimen surfaces were much cleaner and flatter than those in the previous bench-top tests. However, none of the wave-forms shown were captured during the initial 12 hours of curing, as the cement cured from slurry to solid. The signal

qualities during these early stages were too poor to provide useable measures of travel times. Coupling across the free water layer is apparently insufficient to provide useable waveforms.

These observations led to the design of the new 4" x 4" test chamber shown in Figure 1. The illustration of compressional waveforms in the 4" x 4" chamber shown in Figure 11 shows the success of the chamber design for monitoring wave propagation during curing. Well-defined p-waves are detected immediately upon pouring the slurry into the chamber. Travel times during the initial 6-10 hours of curing are almost constant, indicating that the slurry remains in a predominately liquid state during this period. The dramatic increase in velocity between 11 and 23 hours of curing – reflecting the initial solidification of the slurry – is clearly reflected in the decrease in corresponding arrival times. Additional, more gradual increases in velocity are observed through curing times of 100 hours, but subsequent changes (out to 167 hours) are small.

Measurements of shear waveforms are more problematic, but can still be clearly detected in this apparatus. An example of signals measured and detected by a shear wave transducer is shown in Figure 12. Initial signals detected for travel times of about 20 microseconds are p-wave precursors, created by mode conversions at the specimen-surface boundary. The earliest evidence for shear waves is seen after curing for more than 9 hours, which is consistent with the p-wave evidence that prior to this time the specimen is still a liquid. After 9 hours of curing, a shear wave can be identified by its longer travel time and the similarity of waveforms moving to progressively shorter travel times. Again, large changes in travel times - reflecting increases in velocity - are evident in travel times observed for signals which have cured between 9 and 24 hours.

Wave velocities for these tests were determined by procedures in which waveforms were shifted in time until a best-fit overlap between waveforms captured at different times was obtained (Figures 5, 6, 13, and 14). Aligned waveforms for the p-waves in Figure 11 are shown in Figure 13, and those for aligned shear wave-forms from Figure 12 are shown in Figure 14. An initial velocity was determined, based on the first arrival for the un-shifted wave for a curing time at which there is a well-defined arrival (arrow in Figure 12, vertical line in Figure 13). Subsequent travel times – and, hence, velocities – were determined by shift times necessary to align the waveforms. The waveform changes significantly, so only the initial portion (the first break for the signal) is aligned. The same procedure was used for both compressional and shear waves, except that the precursor signal in the shear wave-forms (presumably from mode conversion into p-waves) at short travel times was ignored.

Summaries of variations in p- and s-wave velocities with curing time are shown in Figures 15 and 16, respectively. Note that these data are taken from several different test specimens. The results for both p- and s-waves are very reproducible, supporting the reliability of the measurement methodology and the reproducibility of the curing process. The results are re-plotted on a common scale in Figure 17, along with variations in computed dynamic Poisson's ratio.

Further evidence for the reliability of the measurements – and, in this case, specimen uniformity - is provided by wave propagation measurements in the second new apparatus (4"x 8" assembly; Figure 2). This system is configured with 4 compound (ie., s- and p-wave) transducers, so that waves propagating across the top of the poured specimen (which is left open to the atmosphere) could be compared with those traversing the specimen bottom. Results for shear waves traveling across the top and bottom of the specimen are shown in Figures 18 and 19, respectively. In both cases, the waveforms for equivalent pathways are virtually identical.

The behavior of p-waves is also similar for waves generated and detected by transducers on the same sides of the chamber (Figures 20 and 21), indicating similarities of cement-sidewall adhesion. Corresponding waveforms generated and detected by s-wave transducers are shown in Figures 22 and 23. The s-waves for different faces differ by a 180° phase shift, but are otherwise the same.

2. Static Deformation Behavior

The studies described in this section were designed to assess the evolution of static and dynamic mechanical behavior of cement slurry as it cured. Plots of stress - strain behavior for each of the Mix 1 test specimens are shown in Figures 24-37. Figure 24 includes a graphical illustration of yield, failure, Young's modulus, and permanent strain. All strains are shown positive for shortening, and, except for specimens 2, 3, and 4 (as noted above), were computed relative to the initial axial length of poured slurry. For all specimens, stress-strain behavior during the first deformation cycle was significantly different than that for all subsequent deformation cycles. Variations in the first cycle are generally non-linear and exhibit substantial permanent axial strains. Subsequent cycles are almost linear, and result in almost no permanent strain. Deformation behavior in this first cycle is similar for all specimens except #7, #8, #11, and #12 (Figures 24, 27-29):

1. an initial linear region of increasing stress with strain;
2. a gradual decrease in slope (yielding) at approximately 1.4 to 1.8 kpsi.

3. at the end of axial loading where the load ram was stopped to re-configure the apparatus for unloading (nominally 5 minutes), axial stress decreased and axial strain (shortening) increased, linearly; and
4. during unloading, deviatoric axial stress decreased in a linear fashion, down to the hydrostatic confining pressure.

Loading behavior for the Mix 1 specimens that were not wicked (#7, #8, #11, and #12; Figures 27, 24, 28, and 29, respectively) is qualitatively and quantitatively different from that for the other specimens. The initial loading, also non-linear, has an initial positive curvature at low stresses, gradual yielding at intermediate stresses (1.5-1.8 kpsi), and failure at approximately 1.8 kpsi.

Non-recoverable strain (NRS, defined as the difference between axial strain before and after the first deformation cycle) provides a quantitative measure of non-elastic behavior. The largest NRS's were observed for Specimens #7, #8, #11, and #12, all of which were Mix 1 samples with no removal of excess water. These specimens all show evidence of failure (Figures 27, 24, 28, and 29, respectively) at a deviatoric axial stress of approximately 1.7 kpsi. However, specimen #10 (Figure 30; also a Mix 1 sample with no removal of excess water) did not give an indication of failure during deformation. None of the Mix 2 specimens or Mix 1 specimens with excess water removed, showed evidence of failure during the triaxial deformations.

The linear unloading behavior is generally considered to represent elastic material behavior, and the slope of the unloading curve is designated as the elastic Young's modulus. (Note that not all the deformation cycles are included in the plots, because after 2 or 3 cycles the stress-strain data are virtually identical for each subsequent cycle. However, unloading slopes (Young's moduli) for all the deformations are included in the tabular summations below).

Several test parameters derived from these plots are summarized in Table 1 for the Mix 1 specimens, and Table 2 for the Mix 2 specimens. Wave velocities measured at the end of each of the deformation cycles are also included in the tables. The tabulated parameters, in the order they appear in the tables are

1. Specimen ID;
2. WRI (water removal interval) - Length of time, in hours, free water on the top of the poured slurry was removed by wicking;
3. P_{CUR} (curing pressure, psi) – confining pressure during initial 24 hour cure;

4. NRS (non-recoverable strain, milli-strain) – permanent shortening of the specimen after the first triaxial stress cycle (immediately after 24 hour cure);
5. SS (stress-strain cycle) – ID for the loading / unloading cycles carried out over the total duration of testing for the specimen;
6. E (static Young's modulus) – slope of the linear portion of unloading stress-strain variations for the triaxial deformation designated by the SS ID;
7. V_p (p-wave velocity) – measured p-wave velocity for the indicated measurement ID; and
8. C_p (dynamic constrained modulus, kpsi) – computed from V_p and a density of 2.85 gm/cc.

Table 1. Mechanical properties of Mix 1 cement specimens, measured during curing and deformation.

Test #	El Time (hr)	Wick-t(hr)	P(cure)	NRS(milli)	SS #	E (kpsi)	Vp (ft/sec)	Cp(kpsi)	
2	25.1	2	0	2	b	1553	10042	3872	
	25.8					1553	10314	4084	
	26					1553	10332	4098	
	49.6					c	3661	11223	4835
	72.3					d	5759	11680	5238
	95.6					e	6154	12049	5573
	167.9					f	6929	12387	5891
9	23.9	0.5	1000	2	b	1120	8674	2889	
	24.6					b	2148	8867	3018
	49.1					c	2149	10880	4545
	78.8					d	3838	11619	5183
	122.4					e	4685	11967	5498
16	22.5	0.5	0	3	a	1330	8004	2460	
	23.0					a	1330	9112	3187
	23.8					a	1330	9552	3503
	24.1					a	1330	9805	3691
	24.4					a	1330	9805	3691
7	23.2	0	1000	5	b	1006	8328	2662	
	24.1					b	1006	8506	2778
	25.4					b	1006	8629	2859
	25.5					b	1007	8629	2859
8	23.7	0	1000	10	b	1537	8569	2819	
	25.8					b	1537	9384	3381
	48.8					c	1537	11153	4776
	73.5					d	3038	11705	5260
11	23.8	0	1000	9	b	995	9384	3381	
	25.6					b	995	9845	3721
	27.0					b	996	10354	4116
	27.4					b	996	10354	4116
12	22.6	0	200	10	b	848	8060	2494	
	24.5					b	848	8436	2732
	25.8					b	849	8644	2869
	27.3					b	849	8707	2911
10	24.2	0	0	1	b	1115	8269	2625	
	48.2					c	2822	10463	4203
	72.2					d	2969	11049	4687
	72.5					d	2970	11111	4740

Table 2. Mechanical properties of Mix 2 cement specimens, measured during curing and deformation.

Test #	EITime (hr)	WickTim(hr)	P(cure)	NRS(milli)	SS #	E (kpsi)	Vp (ft/sec)	Cp (kpsi)
4	24.4	0.5	0	1	a	1340	9257	3290
	25				a	1340	9410	3400
	25.2				a	1340	9504	3468
	48.4				b	2657	11736	5288
	72.5				c	3363	12373	5878
	144				d	5055	12935	6424
15	23.6	0.5	0	1	a	1538	8403	2711
	24.1				a	1538	8718	2918
	24.6				a	1538	8989	3102
	25.0				a	1538	9030	3131
	25.4				a	1538	9059	3150
5	0.2	0.5	1000	1	a		6085	1422
	24				b	2001	9077	3163
	25.3				b	2001	9223	3266
	26.1				b	2001	9374	3374
	26.3				b	2001	9374	3374
	49.2				c	4561	10788	4468
	121.6				d	4880	11668	5226
	145.6				e	5042	11668	5226
13	22.6	0	200	1	b	913	8004	2460
	24.0				b	913	8226	2598
	24.7				b	913	8401	2710
	25.2				b	913	8401	2710
3	25.6	0	0	3	a	1170	7765	2315
	26.2				a	1170	8093	2514
	26.5				a	1170	8116	2529
	26.8				a	1170	8116	2529
	48.2				b	2701	10079	3900
	71.7				c	3843	10638	4345
	95.6				d	4396	10942	4597
	167.7				e	4914	11263	4871
14	21.3	0	0	2	a	1273	9107	3184
	21.6				a	1273	9326	3339
	22.1				a	1273	9634	3563
	22.5				a	1273	9714	3623
	23.4				a	1273	9730	3635
6	24.9	0	1000	1	b	1683	9221	3265
	48.2				c	3927	9221	3265
	97.2				d	5029	10729	4419
	144.3				e	5259	11347	4943

CT Images of one slice of scans for Specimens #11, #6, and #9 are shown in Figures 38-40. The images are from approximately midway along the axis of the specimens. The principal features indicated in these images are the large voids associated with absorption of free water into the cement crystal structure during curing, and deformation-related fractures. The image of the failed

specimen #11 (Figure 38), shows considerable internal fracturing, consistent with the failure seen in the stress-strain plot (Figure 28). Scans of a Mix 2 specimen (#6, Figure 39) and a Mix 1 specimen with water removal (#9, Figure 40) showed no evidence of internal fracturing. Neither of these specimens, nor any other Mix 1 wicked specimens or Mix 2 specimen, wicked or unwicked, showed evidence of failure during the triaxial deformation.

Water content appears to affect the strength of the cured cement, as evidenced by the observation of failure (and larger values of NRS) during deformation of Mix 1 specimens for which excess free water was removed by wicking. However, this may not be related to the strength of the cement matrix. Specimen #10, also a Mix 1 sample with no wicking, gave no indication of failure, either in the stress-strain behavior (Figure 30) or from visual inspection of the post-deformation specimen. The principal difference between curing in Specimen #10 and all the other un-wicked Mix 1 specimens is that only Specimen #10 was cured while unconfined.

No CT scan was carried out for Specimen #10. However, a visual comparison of Specimen #10 with Specimen #11, shown in Figure 41, does suggest a possible mechanism for the difference in failure behavior: differences in effective stress. Few of the large vugs seen in CT images were visible on the visual observation of specimen surfaces in, but the ones that are visible for Specimen #10 appear to be significantly larger than those for Specimen #11. The un-wicked Mix 1 specimens have the greatest volume of free water prior to deformation, and post test observations (several days after mixing) still show remnant free water. This would indicate that specimens still have significant quantities of pore water during the initial deformation cycle. If this were the case, pore pressure could be created during the early stage of the triaxial loading, leading to a lowering of effective stress and a corresponding decrease in compressive strength. On the other hand, the larger pore volume created in Specimen #10 during unconfined curing, would accommodate a greater volume of pore water without a significant decrease in effective stress, and an apparent increase in compressive strength.

Variations in p-wave velocities with curing time are shown in Figure 42, for all test specimens. There is more scatter in these data than for velocities determined in the 4"x4" Box Tests (Figure 8), reflecting the greater loss of signal strength for the SPS transducers, propagation through longer test specimens (nominal 2 1/2 inches in the SPS versus 1 inch in the box), and the well documented (Chapter 1) presence of water and an associated top specimen roughness in the SPS configuration. Nevertheless, the pattern of variations and asymptotic values is the same for both test series (Figures 14 and 42).

Variations in static Young's moduli with curing time are summarized in Figure 43. The overall behavior indicates that static deformation behavior of these cement mixtures are similar to those in the dynamic moduli (Figure 42). Again, no systematic relationship between Young's moduli and curing pressure is evident.

The magnitudes of the non-recoverable strains for this series of tests are significantly larger, and the unloading moduli are significantly smaller, for the first deformational cycles than those for subsequent deformations. Differences between loading and unloading slopes, and the magnitudes of non-recoverable strains, decrease with subsequent deformations, becoming negligible by the third cycle. Loading behavior for the un-wicked Mix 1 specimens after 24 hours (#7, 8, 11, and 12; Figures 24, 27 – 29) shows a large positive curvature at low stresses, gradual yielding at intermediate stresses (1.5 kpsi), and failure at approximately 1.8 kpsi. These specimens have the largest non-recoverable strain of all multiple-deformation specimens. Deformation of the Mix 2 specimen #6 and the wicked Mix 1 specimen #9 are initially more linear than deformations of specimen #8, and show a gradual decrease in slope (yielding) at 1.4 to 1.8 kpsi. None of the Mix 2 or wicked Mix 1 specimens show evidence of failure.

However, the variations in behavior observed for this series of tests may be related to two different processes: 1) deformation and failure of the cement surface at the end(s) of the specimen; and 2) hardening and strengthening of the cement as it cures. Clear evidence for the development of surface irregularities is visible on the top of the specimens at the ends of the tests, and the deformation of small-scale surface features could lead to additional strain, and obscure behavior due to the curing process. In order to assess this surface-related behavior, a modified sequence of curing and deformation measurements were carried out.

Deformation behavior for the Series III tests are shown in Figures 44 - 48. Variations in computed Young's moduli with curing time are shown in Figure 49. The modulus variations again show the large scatter associated with determinations of static Young's moduli, but the behavior follows the same trend as the dynamic moduli (Figure 16) and the trend indicated for the unloading moduli for the Series II tests (Figure 43): a rapid increase after curing for about 14 hours, slowing rate of increase through the next few days, and settling to an asymptotic value after 5 – 7 days. In spite of the large scatter the data for the Series III tests do show a trend towards lower values than those found for the Series II results, which is compatible with larger surface-related strains in the Series III tests. The data support the hypothesis that the surface effects are largely eliminated

during the first loading cycle of the Series II tests, but are present for each of the (single) deformation cycles in the Series III tests.

Non-recoverable strains for the Series III tests at different curing times are shown in Figure 50. Also shown in the plot are results from the Series II Mix 1 tests, with and without removal of the initial free water by wicking. The permanent strains for the Series II Mix 2 tests, on both wicked and un-wicked specimens, again indicate the presence of a non-recoverable surface deformation during the first deformation cycle, which is absent for the subsequent cycles. The variations of the Series III strains, all of which include the first-cycle surface strains, show a smoother and more gradual decrease in non-recoverable strain than the multiple-cycle deformational cycles of the Series II tests. Except for the initial deformation cycle after curing for 24 hours, all the Series II tests have permanent strains below those for the Series III tests.

Measured behavior during deformation cycles of Mix 2 specimens (Series IV tests) is shown in Figures 51-55. The amount of permanent strain is clearly smaller, and the stress-strain slopes are clearly larger, for all the Mix 2 tests. Results from the Series III and Series IV are compared in Figure 57. They exhibit the same type of behavior as Mix 1 specimens (Figure 43; data is re-plotted on Figure 58 for comparison), but all Mix 2 values of Young's modulus are larger than corresponding Mix 1 values. Results from the repeat deformations are re-plotted in Figure 59.

As noted, permanent strains for Mix 2 (Series IV) specimens are all significantly smaller than corresponding values for Mix 1 (Series III). In fact, all permanent strains for Mix 2 are effectively zero, except for the single test for the 14-hour curing time. Note that two different specimens were tested for curing times of 24 hours; results for the two tests were approximately identical.

The Series III and IV tests again show a weakening effect of excess water on deformational behavior, and confirm the presence of surface-related deformations in addition to the deformations related to material hardening with curing time. Test results from the previous test sequence, in which a cement specimen was repeatedly deformed at various intervals of curing, showed that the magnitudes of the non-recoverable strains are significantly larger, and the unloading moduli are significantly smaller, for the first deformational cycle than those for subsequent deformations. The separate test specimens aged for time periods of 14, 24, 36, 48, or 168 hours before deformation show lower values of non-recoverable strain, and larger values of unloading moduli than those found for the Series II results in support of the hypothesis that the surface effects are largely eliminated during the first loading cycle of the Series II tests, but are present for each of the (single)

deformation cycles in the Series III tests. The amount of permanent strain is clearly smaller for Series III tests, and the stress-strain slopes are clearly larger, than for all the Series IV (Mix 2) tests.

3. Discrete Element Modeling

The third area of investigation in the program of studies was a numerical simulation of wave propagation in the well-bore/casing/cement environment, using a simulator which is based on micromechanical deformational processes. In work through this program year, formalism for such a treatment of wave propagation has been established. In the following discussion of activities to date, several examples of simulated behavior are presented, to demonstrate the utility of the approach in understanding behavior observed in the experimental program. The numerical simulations are based on a two-dimensional discrete particle method PFC2D, (Potunday and Cundal, 2004), a commercial discrete element model (DEM). PFC2D is designed to simulate mechanical properties using an assembly of small finite particles. Macroscopic deformational and wave propagation behavior are derived from first-principal micromechanical processes, coupled with a graphical user interface for the visualization of the waves.

The DEM simulation used in this study models the mechanical properties by treating the sample as a collection of spherical particles interacting via Newton's second law. The interaction of particles is treated as a series of springs, arising from overlap between the particles, and by elastic forces developed by deformation of inter-particle bonds. The inter-particle bonds represent cement with a finite volume, and are designated here as cement bonds. These bonds are also referred to as parallel bonds, because they contributed forces in addition to – or in parallel with – contact forces arising from overlap between particles. The various particle-particle interactions are shown schematically in Figure 60. In this study, mechanical properties of the particles and of the cement bonds are the same.

The particles in this simulation represent a basic cell of cement or steel, into which porosity will be introduced later. The sample consists of a two-dimensional assembly with hexagonal packing of circular particles, for which the aerial porosity between the particles is 9%. In order to reduce the porosity to zero, cement (parallel bond material) between the particles is assigned a mass and size to completely fill the void space. The particles are treated as a collection of spheres whose centroids all lie within the same plane.

The inter-particle bonds in the cement and in the steel are uniform within the assembly, but the bonds at the steel-cement interface have mechanical properties which are adjusted or removed to

simulate variations in bonding. The properties and position of each bond were set individually, allowing for conditions such as channeling and poor cement bonding to be simulated. The particles and the cement have both shear and normal stiffness.

Waves in PFC2D are modeled by imposing a velocity to a subset of the particles (transmitters). The imposed particle velocities propagate through the assembly via inter-particle forces, in the same manner as elastic disturbances in a physical system. Waves are detected at another subset of designated particles (receivers). Wave forms are determined by the time dependence of particle velocities at specified positions.

A portion (approximately half of the total length) of the model assembly is shown in Figure 61. The total assembly contains about 20,000 particles. Selected groups of particles are configured to act as wave transmitters or receivers. The ‘transducer’ groups are placed in the same positions in the model assembly as in the laboratory assembly discussed in the previous chapter. Additional transmitters and receivers are placed within the assembly to record the wave behavior as it propagates in the assembly. The gray particles in assemblies represent the cement, the yellow particles steel, and the reddish-brown lines between the steel and the cement are the parallel bonds at that interface. The purple particles are wave transmitters in the assembly, and the other colors represent wave receivers.

The receivers in the steel as depicted in Figure 61 are spaced 5 centimeters apart. Transmitters and receivers were also placed in the cement, with the receivers shown in Figure 61 placed 5 centimeters apart in position to measure wave propagation vertically in cement. The transmitters and receivers which measure horizontal wave propagation from left to right through the cement are 5.08 centimeters apart. Additional receivers, not shown in Figure 61, were placed in the cement along the left to right propagation path. Waves are created by specification of particle velocities.

Figure 62 illustrates the process of p-wave generation, by imposing a sinusoidal particle velocity in the horizontal direction, shown in red, onto the red-colored transmitter particles on the left-hand surface. Figure 63 shows the distribution of particle velocities after the initial particle oscillations have propagated across the width of the assembly. The p-wave velocity is given by the assembly width divided by the elapsed time for the detection of motions of particles in the right-hand receiver (purple balls).

The model input parameters for the model were determined by comparing computed wave velocities with published values, and altering the spring stiffness of the particles to match the

measured wave velocities. Initial values of normal and shear stiffness values for the particles were determined by the relationship between the particle stiffness, (spring constant), k^n and k^s , and the corresponding elastic constant (E_C ; Itasca, 2002):

$$k^n = \frac{AE_c}{L} \quad (3.1)$$

$$k^s = \frac{12IE_c}{L^3} \quad (3.2)$$

In equation 3.1, k^n and k^s are the normal and shear stiffness of the particle, A is the cross-sectional area at the contact, E_c is the contact Young's modulus, E_c , and L is the length between the particle centers. I is the moment of inertia of the particles. The contact Young's modulus is found to be related to the material Young's modulus by a factor of four (Park, 2006). The relation between the mechanical properties of the bonding to the input properties of the parallel bonds is (Itasca, 2002):

$$\bar{k}^n = \frac{\bar{E}_c}{L} \quad (3.3)$$

$$\bar{k}^s = \frac{3\bar{R}\bar{E}_c}{4\tilde{R}L} \quad (3.4)$$

where \bar{R} is the radius of the parallel bond and \tilde{R} is the particle radius.

Two particle assemblies were used for the model calibrations. Each of these assemblies contained 20,000 particles of only one material (steel or cement). The model contained a transmitter and two receivers and the wave velocity was measured between the first and second receivers. The velocities were considered matched if they were within 30 m/s of the actual velocity of the materials.

A comparison of actual wave velocities for cement (Gray, 2006 a,b), steel (Rose, 1999), and quartz (Best, 1997) to wave velocities determined from the PFC simulation are shown in Table 3. From the tabulation, the wave velocity for the modeled steel and cement is within an acceptable margin of error. Quartz particles, which are used later in the study, were also modeled.

Table 3. Wave velocities of assembly materials for model calibration

Material	V_p (m/s)	V_s (m/s)	V_p modeled (m/s)	V_s modeled (m/s)
Steel	5820	2950	5836	2939
Class H Cement	3386	1924	3361	1895
Quartz, Solid	6047	4092	6048	4304
Quartz, un-Consolidated	1000		981	

This calibrated DEM model was then used to carry out several simulations to characterize different aspects of wave propagation behavior in detail. Variations in bond quality, fraction of intact bonds, and bond stiffness at the steel-cement interface were introduced to investigate the effects on wave behavior in the model. The simulations were fashioned to replicate wave paths used in the experimental tests in Section b.

WAVE PROPAGATION IN CASING - VARIATIONS IN FRACTION OF BONDS

Figure 64 shows the initial portion of waveforms for simulated p-waves traveling vertically through the steel portion of the assembly, for three different fractions of intact bonds between cement and steel particles at the interface. Figure 65 plots the normalized amplitude as a function of the fractions of intact bonds (equivalent to the percentage of contact area bonded in this 2D simulation). The plot clearly displays a linear relationship between wave amplitude and the percentage of intact bonds. Hence, wave propagation simulated by PFC confirms the essential aspect of cement bond log theory: the amplitude of waves propagating in the steel ‘casing’ should decrease as the percentage of the bonds between cement and steel at the cement-steel interface increases (Pardue et al., 1963).

In the above simulation the unbonded particles were uniformly distributed along the interface between transmitter and receiver. The effects of non-uniform bonding on wave amplitude were also examined. For this simulation, two non-uniform distributions of bonds were used, in which the density of cement-steel bonds adjacent to the receiver differs from the average bond density between the transmitter and receiver. In Case 1 (Figure 66), all bonds between transmitter and receiver are intact. In Case 2 (Figure 67) only half the bonds along the interface between transmitter and receiver, and none of the bonds adjacent to the transmitter are intact. In both non-uniform distributions a total of 66% of all bonds along the left hand interface are intact. The locations of the bonds are displayed as blue lines in Figures 66 and 67 for the two different distributions. Note that the assemblies in Figures 66 and 67 show only a portion (approximately half) the total assembly of particles. Computed waveforms for these distributions are shown in Figure 68.

For non-uniform bonding Case 1, the computed wave amplitude is indistinguishable from that for the 100 percent uniformly bonded case (in which all touching particles are bonded). The measured energy loss into the cement depends not only on the total percentage of the surface area

bonded, but also the location of the bonds relative to the receiver. Computed amplitude variations for non-uniform distribution Case 1 are indistinguishable from the 100 percent (uniform) bonded case (all touching particles are bonded). In this example, 66% of the total number of touching particles over the cement-steel interface on the left side of the sample were bonded, but all of the touching particles on the surface area between the transmitter and the receiver were bonded.

In the next example 50 percent of the touching particles in the steel-cement interface between the transmitter and the receiver were bonded. There are no bonds in the zone adjacent to the transmitter in this case; all of the bonds between the transmitter and the receiver are located near the receiver. Again, 66% of the total number of touching particles on the left side steel-cement interface were bonded.

These simulations indicate that non-uniform bonding leads to significant uncertainty in bond index determinations. The results show that the bond index measures the percentage of the steel-cement interface bonded between the transmitter and receiver, but it is especially sensitive to changes in bonding near the receiver. This is supported by Table 4, which gives the bond index measurement compared to the percentage of the surface area at the steel-cement bonded between the transmitter and the receiver. The large error of the bond index measurement in non-uniform case 2 was also found in several other non-uniform bonding cases (not shown). The simulations indicate that bonding in the region adjacent to the receiver has a greater effect on the amplitude of the recorded wave than bonds located away from the receiver.

Table 4. Bond Index determinations for distributions in which 66% percent of the total steel-cement interface is bonded. These values were calculated from the simulations shown in Figure 68.

Case	Bond Index	Actual Percent Bonded Between Receivers
66% uniform	0.68	0.66
66% non-uniform 1	1.00	1.00
66% non-uniform 2	0.37	0.50

WAVE PROPAGATION IN STEEL, VARIATION IN BOND STIFFNESS

The next simulations were carried out to investigate the effects of a weakening of the mechanical properties of the bond material on wave propagation. For this simulation the stiffness of the bonds at the steel-cement interface was reduced. Only the bonds at the steel-cement interface were altered. Figure 69 illustrates the changes in wave amplitude due to changes in the mechanical bonding at the steel-cement interface. The samples in Figure 70 were completely bonded at the steel-cement interface, while the bond stiffnesses of the interface bonds were varied. The summary

of results in Table 5 shows that changes in the mechanical properties have the same effect on amplitude as fractional changes in the fraction of the bonded contact area.

Table 5. Bond index measurement for a fully bonded steel-cement interface; with changes to the mechanical properties of the bonds. The measurement was calculated using the amplitudes from the simulations shown in Figure 69.

Case	Bond Index
10% Stiffness	0.118
50% Stiffness	0.587
90% Stiffness	0.901
100% Stiffness	1.000

WAVE PROPAGATION IN STEEL, VARIATIONS IN MECHANICAL PROPERTIES AND BONDING FRACTION.

The next simulations were carried out for cases in which both the mechanical properties of the bonds (bond stiffnesses) and the percentage of the intact bonds at the steel-cement interface were varied. A value for the percentage of bonds was first selected, and for each value, simulations were carried out for four different values of stiffness. A new value of bond fraction was then selected, and the simulations were again carried out for the four stiffness values. Simulations were carried out for stiffness values of 100%, 90%, 50% and 10% of the cement bond stiffness value, and for fractions of intact bonds of 100%, 90%, 50% and 10% percent of the total value. Figure 71 shows amplitudes of p-wave traveling in steel, for the case of a uniform distribution of 90 percent of intact bonds along the interface, with the indicated stiffnesses.

Table 6. Bond Index simulations on samples with various mechanical properties, for 90% uniformly bonded contact area. Values were calculated from the simulations shown in Figure 70.

Percent of Contact area Bonded	Bond Mechanical Properties	Bond Index
90%	10%	.118
90%	50%	.447
90%	90%	.874

The results in Table 6 show that these bond index measurements can be approximated by the product of contact area bonded multiplied by the percentage of the mechanical properties of the cement present in the bond mechanical properties. For instance, when 90 percent of the contact area of the steel-cement interface was bonded, and the bond mechanical properties were 90 percent of the cement mechanical properties, the bond index measurement was 0.874, close to the value of 0.81 expected for 90% bonding fraction with bond material with 90% stiffness. Table 7 shows the

variations in p-wave amplitude with variations in bond stiffness, for a specimen with 50% bonding fraction. Again, computed bond index roughly scales with the product of bond fraction and percentage of bond stiffness. Additional simulations with different bond fractions and stiffnesses all showed the cumulative effect on amplitude.

Table 7. Bond index measurement on modeled sample with altered bond mechanical properties and 50% of contact area bonded uniformly

Percent of Contact area Bonded	Bond Mechanical Properties	Bond Index
50%	10%	0.076
50%	50%	0.356
50%	90%	0.461

Simulations were next carried out for specimens in which half (50%) of the bonds are intact, but are not uniformly distributed along the cement- steel interface. Intact bonds shown in Table 8 were clustered at three locations along the steel- cement interface. In the first case, there were two clusters of bonds at the interface: one located between the transmitter and the receiver, with no bonds immediately before the transmitter or after the receiver; a second cluster of bonds that started just before the receiver; and a the third case for which bonding at the interface started at the base of the sample and continued to the midpoint of the sample height where the receiver is located. These results show that amplitude variations scale roughly with the cumulative effect of conditions at the steel-cement interface, but variations in non-uniform distributions can lead to substantial deviations from the general trend.

Table 8. Bond index determinations in a simulation of variations in bond mechanical properties, for an average of 50% area bonded non-uniformly. The bonding in the first case was clustered between the transmitter and the receiver, with no bonding just before the transmitter and after the receiver. In the second case the bonding between the transmitter and the receiver was just before the receiver. The majority of the bonding in this case was not located between the transmitter and the receiver. In the third case the interface was fully bonded between the transmitter and the receiver.

Total Percentage of surface area bonded	Bond Mechanical Properties	Percent of Surface area between Receivers Bonded	Bond Index
50%	10%	100%	0.181
50%	10%	5%	0.034
50%	10%	100%	0.138

WAVE PROPAGATION IN STEEL: DISTRIBUTION OF MECHANICAL PROPERTIES

From the foregoing discussion, alteration of the mechanical properties of bond material at the steel-cement interface affects the amplitude of waves propagating in the steel in the same

manner as the percent of the interface bonded. It has also been shown that placement of unbonded and bonded zones affects the p-wave amplitude. The next series of simulations were carried out to investigate the combined effect of non-uniform distribution of properties and bonds on wave amplitudes. This simulation was carried out on a sample with 90 percent of the bonds between the transmitter and the receiver bonded. The mechanical properties for half of the distance between the transmitter and the receiver were decreased to 10 percent of the cement mechanical properties. The results of these simulations were compared to the same sample with bond mechanical properties that were 10 percent and 100 percent of the cement mechanical properties for all bonds at the steel-cement interface. Figure 71 shows that changes in the steel-cement interface near the receiver have less effect on wave amplitude than changes further from the receiver. This behavior is similar to that observed when testing the percentage of the contact area bonding. Changes in the mechanical properties near the receiver have less effect on the recorded amplitude.

The results shown in Table 9 indicate that placement of altered bond mechanical properties at the interface have more of an effect on wave amplitude than placement of unbonded zones. The method of estimating the bond index measurement by multiplying the percent of the contact area bonded by the percentage of the original mechanical properties present between the transmitter and the receiver is not accurate enough to be used with any confidence. Similar behavior was found for other simulations.

Table 9. Effect of Placement of altered bond properties between transmitter and receiver. Half of the length (referenced in the Case description) has altered properties. The other half has of the mechanical properties of the cement.

Case	Bond Stiffness	Bond Index
Near transmitter	10%	0.735
Near receiver	10%	0.375
reference	10%	0.118
reference	100%	0.921

WAVE PROPAGATION THROUGH CEMENT; VARIATIONS OF BONDING FRACTION

The discussion thus far has considered the effects of bonding and mechanical properties on p-wave transmission through the steel 'casing'. In the next discussion, consider horizontal p-wave propagation within the cement zone. The experimental study clearly demonstrated that the quality of the bonding at the steel-cement interface significantly affects wave behavior through the cement. In the simulations of this behavior, the percentage of the steel-cement interface bonds on the left side of the sample were altered, while the bonding at the steel-cement interface on the right side of

the sample was fixed at 100% of the steel-cement interface bonds. Waves were input at a transducer on the left edge of the sample and detected at a receiver located on the right edge. The effects of varying mechanical properties of the bond were also investigated by altering the bond stiffnesses at the steel-cement interface on the left side of the sample.

Results of simulations for different distributions of interface bonds are shown in Figure 72. The amplitudes decrease as the percentage of intact bonds at the steel-cement interface on the left side of the sample decreases, although the amplitude is not reduced to zero with 0% bonding (wave energy is still transmitted across the interface by physical contacts between steel and cement particles). Simulations of the effects of altered bond mechanical properties (not shown here) also show a decrease in amplitude with decreasing stiffness of the bonds.

Figure 73 presents results from the same simulations plotted on an expanded time scale, which shows high frequency (nominal 1MHz) oscillations caused by multiple reflections of the wave at the surfaces of the steel plate. Similar behavior was observed in some of the measured waveforms in the experimental study (see Figure 17 or 18). These high-frequency oscillations are not attenuated in the same manner as the main pulse (see below). The oscillations probably arise from multiple reflections within the steel on the left side of the specimen. They have potential as a means for more precise determination of the quality of bonding between cement and casing, and will be treated in some detail in the following discussion.

WAVE PROPAGATION IN CEMENT: EFFECTS OF QUARTZ CONTENT

The next simulations were carried out to investigate the effects of inclusions in the cement. Two types of inclusion were investigated: quartz and void space (porosity). The inclusions were introduced by replacing cement particles at randomly selected positions. Cement bonds were used to bond the cement to the quartz. The steel-cement interface in this sample was 100% bonded for both the left and the right interface. The waves were introduced into the sample on the left side and detected on the right side.

Both types of inclusions alter the acoustic impedance of the cement. Figure 74 shows that the inclusion of quartz into the cement generally increases the amplitude. However, an upper limit is reached at a concentration of about 10 percent quartz, and the computed amplitude of the waveform for a quartz concentration of 10 percent was higher than that for 15 percent quartz. From visual inspection of the assembly, it appears that this anomaly was caused by the placement of the

quartz grains. The sample with 10% quartz had a higher percentage of quartz between the transmitter and receiver than the sample with 15% quartz.

The addition of quartz to the sample increases the propagation velocity in the sample, as shown by the decreases in arrival times in Figure 75. The effect of the addition of quartz on the acoustic impedance of the cement is displayed in Table 10. The inclusion of quartz in the model assembly increased the impedance. The high-frequency oscillations in this simulation are not significantly affected by quartz content.

Table 10. Acoustic impedance in the cement with the addition of quartz in the cement.

Percent Quartz in Cement	Z_o (kg/m ² s)
0.00%	6.40E+06
1.00%	6.42E+06
5.00%	6.53E+06
10.00%	6.67E+06
15.00%	6.87E+06
20.00%	7.06E+06

WAVE PROPAGATION THROUGH THE CEMENT; EFFECTS OF VOIDS

In the next simulations, void spaces were introduced by removing cement particles at randomly selected locations. The additional porosity reduces propagation speed, as shown in Figure 76. The variation in acoustic impedance with inclusions of voids is listed in Table 11.

In addition to the changes in acoustic impedance, the introduction of voids into the assembly leads to waveform scattering. The large discontinuity in mechanical behavior at the void locations leads to local reflections, and this scattering leads to a corresponding decrease in signal amplitude. The scattering is sensitive to wavelength, and should be greatest when the wavelength is on the same order as the size of the voids. Wavelengths in this simulation are not this small, but scattering should be greater for the higher-frequency waves created by the multiple-reflection within the steel, than for the lower frequencies input directly. This is the behavior exhibited for signals shown in Figure 76.

The decrease in high-frequency content is clearly shown in Figure 76 for specimens with void content. At a concentration of 5 percent the high frequency oscillations are still present, but they have almost completely disappeared for a void concentration of 10%. At the same time, the amplitudes of the lower-frequency waveforms increase with void concentration, as energy from the high-frequency signals is converted by the scattering into the lower-frequency signals.

Table 11. Variations in acoustic impedance in cement with the addition of voids.

Void Concentration in Cement	Z_o (kg/m ² s)
0.00%	6.40E+06
1.00%	6.31E+06
5.00%	5.83E+06
10.00%	5.30E+06
15.00%	4.74E+06
20.00%	4.27E+06

WAVE PROPAGATION THROUGH THE CEMENT: COMBINED EFFECTS OF QUARTZ AND VOIDS

In the next simulations both quartz and voids were added to the cement. The steel-cement interfaces were fully bonded for these simulations. A wave was introduced at a transmitter on the left edge of the assembly, and detected by the receiver on the right edge.

The computed waveforms in Figure 77 show effects from variations in void concentration for a fixed (5%) quartz concentration. The observed behavior is similar to that in Figure 76 for the addition of voids only, except that the high-frequency oscillations are still present to some degree for 15 percent void concentration in the sample.

Figure 78 shows the variations in p-waveforms with void concentration, for waves in samples with fixed 10% quartz content. The waveforms differ only slightly from those for 5% quartz content. This is shown in greater detail in Figure 79, which shows variations with quartz content for fixed (15%) void content. This plot is very similar to the plot of amplitude variations shown in Figure 74. The addition of quartz has little impact on computed waveform amplitudes.

Three cases without high frequency oscillations, as determined by the graphical display of particle velocity, are compared to the case with no quartz in the cement, in which the high frequency oscillations did occur. In cases where destructive scattering occurred, an increase in quartz caused the amplitude to decrease and the smoothness of the waveform to increase. All cases of destructive scattering had significant increases in amplitude compared to the reference case.

EVOLUTION OF HIGH-FREQUENCY SIGNALS

The final set of simulations looks at the evolution of the high-frequency waves, presumably generated by the multiple reflections in the steel plates, and attenuated by scattering of the waves by voids in the cement. These waves may – or may not - impact interpretations of signals in bond quality tools. Analysis of their behavior illustrates the utility of PFC simulations, in which wave

behavior within the interior of material. Such observations are completely outside the realm of possibility for experimental measurements in the laboratory.

One of the concerns about wave propagation in the bore-hole environment is whether the observed behavior is due to interface processes, or due to changes within the body of cement. For this investigation direct observations of particle motion of cement particles during wave propagation are combined with ‘virtual’ receivers (designated particles used for detecting wave behavior). This approach permits the viewing of waveforms at any stage of their generation and propagation, and to completely isolate interface behavior from changes during wave propagation.

Figure 80 shows waves detected from such a receiver located just beyond the steel-cement interface on the left side of the sample. It shows an initial half cycle of the high-frequency introduced on the left side of the specimen, and several cycles of the high-frequency signal from multiple reflections in the steel on the left side. None of these high-frequency signals ultimately reach the external receiver on the right side of the assembly (cf., Figure 79). The plot shows graphically that the disappearance of the high frequency signal is not from inadequate coupling of the signal into the specimen.

Figure 81 the wave-form detected at a receiver placed midway along the path within the cement. It shows that the high-frequency waveforms were still present midway through the cement, although at reduced amplitudes resulting from scattering within the cement. All the signal wavelengths have increased in Figure 81, also due to the scattering.

The wave-forms detected at the external receiver on the right side of the model assembly was shown in Figure 79. None of the high-frequency waveforms are evident in this figure. The apparent wavelength of the measured wave has increased significantly, due to overlapping scattering fields recorded at the receiver. Much of the high-frequency attenuation was due to scattering (Figure 81), but some of the losses were at the right side interface (Figure 82).

Using PFC’s graphical display, effects of cement inclusions on wave propagation can be visually assessed. The following series of simulations tracks waveforms by the locations and magnitudes of particle velocities (red arrows) associated with wave propagation. The first set of figures, Figures 83 through 85, show particle displacements during wave propagation in a cement sample with no voids (no scattering). The high-frequency cycles are clearly evident in all three plots, as the wave travels across the cement and as it is reflected back by the interface on the right (Figure 85).

The next set of simulations show the propagation of the same wave-form introduced in the previous figures, into cement with a small (5%) void content. Some wave-form degradation is evident from the beginning (Figure 86), but the wave front (first arrival) is still clearly defined. After traversing the cement, much of the high-frequency content is absent (Figure 87), while the distinct wave front persists. Some evidence for the presence of the high-frequency signal still exists in Figure 88, after reflection from the right side interface, but the wave-form has been substantially dispersed by the scattering.

The last set of simulations show the wave behavior in the cement with 15% voids. The wave-form is already dispersed by the first cycle of input signal (Figure 89). After the wave-front has almost traversed the cement (Figure 90) almost all high-frequency content has disappeared, and the wave-form is reduced to a uniform distribution of particle motions behind a distinct wave-front (Figure 91). Further dispersion of the wave-form, and a less-well defined wave-front are evident in the wave reflected from the right side (Figure 92). The simulation results clearly show that the attenuation of the high-frequency signal is due to scattering from voids within the cement, and not from coupling the signals at the steel-cement interface.

CONCLUSIONS

It has been more than ten years since the last significant advances in commercial cement evaluation tools. In this time, significant changes have taken place in the nature of wells and the requirements of the cement that is used. The increase in the popularity of gas storage wells and the prospect of large numbers of carbon dioxide storage or sequestration wells presents new problems. The cost of logging must be balanced by the fact that even a good log is not a guarantee of a good seal. In many cases the operator's judgment is based on the understandings of older economic calculations. This may require rethinking to fully utilize newer technology and adapt to the changes that are taking place in the industry. It is our belief that coordinated laboratory testing and numerical simulations can best address these needs. This study has demonstrated the viability of this approach in several test sequences.

New test procedures and apparatus were developed for the study of cement-boundary interactions during curing and deformation. Compressional and shear wave velocities were monitored during nominal one-week curing periods. P-waves are detected immediately upon pouring the slurry into the chamber, and travel times during the initial 6-10 hours of curing are almost constant. A dramatic increase in velocity between 11 and 23 hours of curing reflects the initial solidification of the slurry. The earliest evidence for shear waves is seen after curing for more than 9 hours, consistent with the p-wave evidence that prior to this time the specimen is still a liquid. Measured behaviors for both p- and s-waves are highly reproducible. Dynamic Poisson's ratios determined from the set of shear and compressional mode velocities were found to vary from initial values of 0.5, representative of a fluid at curing time near zero, to about 0.25, typical of intact rock, as the cement cures. A second assembly was also developed, which provides for simulations of wave propagation along a casing-cement interface.

Experiments carried out in an in-house triaxial testing system, during curing of cements from slurry to rigid solid, provide further information on cement-casing bonding, and simultaneous wave velocity measurements correlate with the static behavior. Variations in axial stress with axial strain after overnight curing are generally non-linear and exhibit substantial permanent axial strains. Subsequent cycles are almost linear, with almost no permanent strain. Stress-strain variations are strongly affected by the amount of water retained in the cement during curing. The observed variations suggest that the variations of strength with water content are the consequence of excess

pore pressure. The strong dependence of cement mechanical behavior on water content will be a concern of subsequent studies.

Test results from test in which cement was repeatedly deformed at various intervals of curing, showed that the magnitudes of the non-recoverable strains are significantly larger, and the unloading moduli are significantly smaller, for the first deformational cycle than those for subsequent deformations. In the present research separate test specimens aged for different time periods before deformation show lower values of non-recoverable strain, and larger values of unloading moduli than those found for the multiple-deformation results. The results suggest that the surface effects are largely eliminated during the first of several repeated loading cycle, but are present for each of the (single) deformation cycles in the single-cycle tests. The amount of permanent strain is clearly smaller for single-cycle tests on Mix 1 (cement only) material, and the stress-strain slopes are clearly larger, than for all the single-cycle tests on Mix 2 (cement plus moisture-absorbents) specimens.

The companion numerical simulation tests were able to reproduce central features of the experimental tests, and illustrate the potential for utilizing the simulations to better understand cement bond quality. The study achieved two goals: 1) It has provided a numerical framework, based on a discrete particle computation, to quantitatively analyze details of the propagation of waves in the well-bore – cement environment; and 2) Preliminary analysis using the simulation has provided information that is directly useful for interpreting bond quality in log tools. Computed changes in the fraction of the area bonded at the steel-cement interface (bond quality) are consistent with those predicted by cement bond log theory. However, the simulations show quantitatively that changes in the mechanical properties of material at the interface lead to behavior which can be indistinguishable from that of poor bonding. This can be an important cause of error when interpreting the quality of the bond between the cement and casing from the bond index measurement.

Simulations of wave propagation within the cement show details of wave-particle interactions, and demonstrate that interactions within the cement are as important as behavior at the cement-casing interface. This behavior has direct application to measurements using the variable density log. Additional simulation of wave propagation in a casing coupled, with varying degrees of bond quality, to cement with varying degrees of material properties (porosity, bond and particle stiffness) provide for comprehensive evaluation of the existing wireline tools.

This preliminary analysis of wave propagation with a discrete particle simulation indicates that the behavior can be predicted in considerable detail. Further activity, with more rigorous material properties and boundary conditions, could lead to significant improvements in bond log interpretation. The wave propagation model in PFC2D can be expanded to the bond between the cement and the formation. Ultimately, simulations of wave propagation in full three-dimensional models should be carried out.

REFERENCES

- Best, A. I., Sams, M.S., 1997, Compressional Wave Velocity and Attenuation at Ultrasonic and Sonic Frequencies in Near-Surface Sedimentary Rocks, *Geophysical Prospecting*, Vol. 45, No. 2, pp. 327-344.
- Froelich, B., Pittman, D., and Seeman, B.: Cement Evaluation Tool - A New Approach to Cement Evaluation, *Journal of Petroleum Technology*, Aug., 1982, pp. 1835-41.
- Gray, K. E., 2006a, Acoustic Signatures During Cement Slurry Hardening: Part 2, GSTC Quarterly Report #1, June 1, 2006 - August 31, 2006. DE-FC26-03NT41779 (3139-UT-DOE-1779).
- Gray, K. E., 2006b, Acoustic Signatures During Cement Slurry Hardening: Part 3, GSTC Quarterly Report #2, September 1, 2006 - November 30, 2006 (DE-FC26-03NT41779 (3139-UT-DOE-1779)).
- Grosman, M., Kokesh, F.P., and Majani, P.: A Sonic Method of Analyzing The Quality of Cementation of Borehole Casings, *Journal of Petroleum Technology*, Feb., 1961, pg 165.
- Itasca Consulting Group, Inc., 2002, PFC^{2D} (Particle Flow Code in 2 Dimensions), Minneapolis, MN.3
- Pardue, G.H., Morris, R., Gollwitzer, L.W., and Moran, J. H., 1963, Cement Bond Log - A Study of Cement and Casing Variables, *Journal of Petroleum Technology*, May, pp. 545-555.
- Park, N., 2006, *Discrete Element Modeling of Rock Fracture Behavior: Fracture Toughness, and Time Dependent Fracture Growth*, Dissertation, University of Texas at Austin.
- Potyondy, D. O. and Cundall, P. A., 2004, A Bonded-Particle for Rock, *International Journal of Rock Mechanics and Mining Sciences*, Vol. 41, No. 8, pp. 1329-1364.
- Rose, J. L., 1999, *Ultrasonic Waves in Solid Media*, Cambridge University Press, New York.
- Tixier, M. P., et al.: Sonic Logging, *Journal of Petroleum Technology*, Vol. 216, 1959, p. 106.

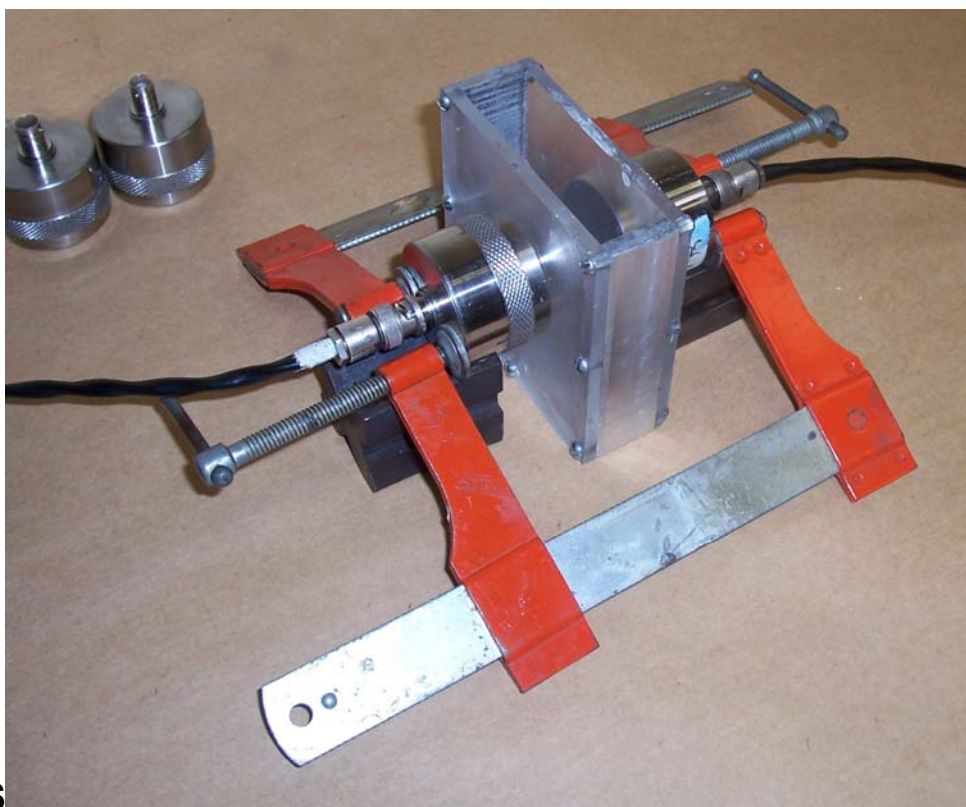
**FIGURES**

Figure 1. Chamber for measurements of wave propagation during curing. Cement slurry is poured into 1" thick chamber between 4" x 4" side walls (plexiglass in this figure). Transducers clamped to the side walls, as shown for the bottom transducer, are used for transmitting and receiving both shear and compressional mode waves travelling through the cement.

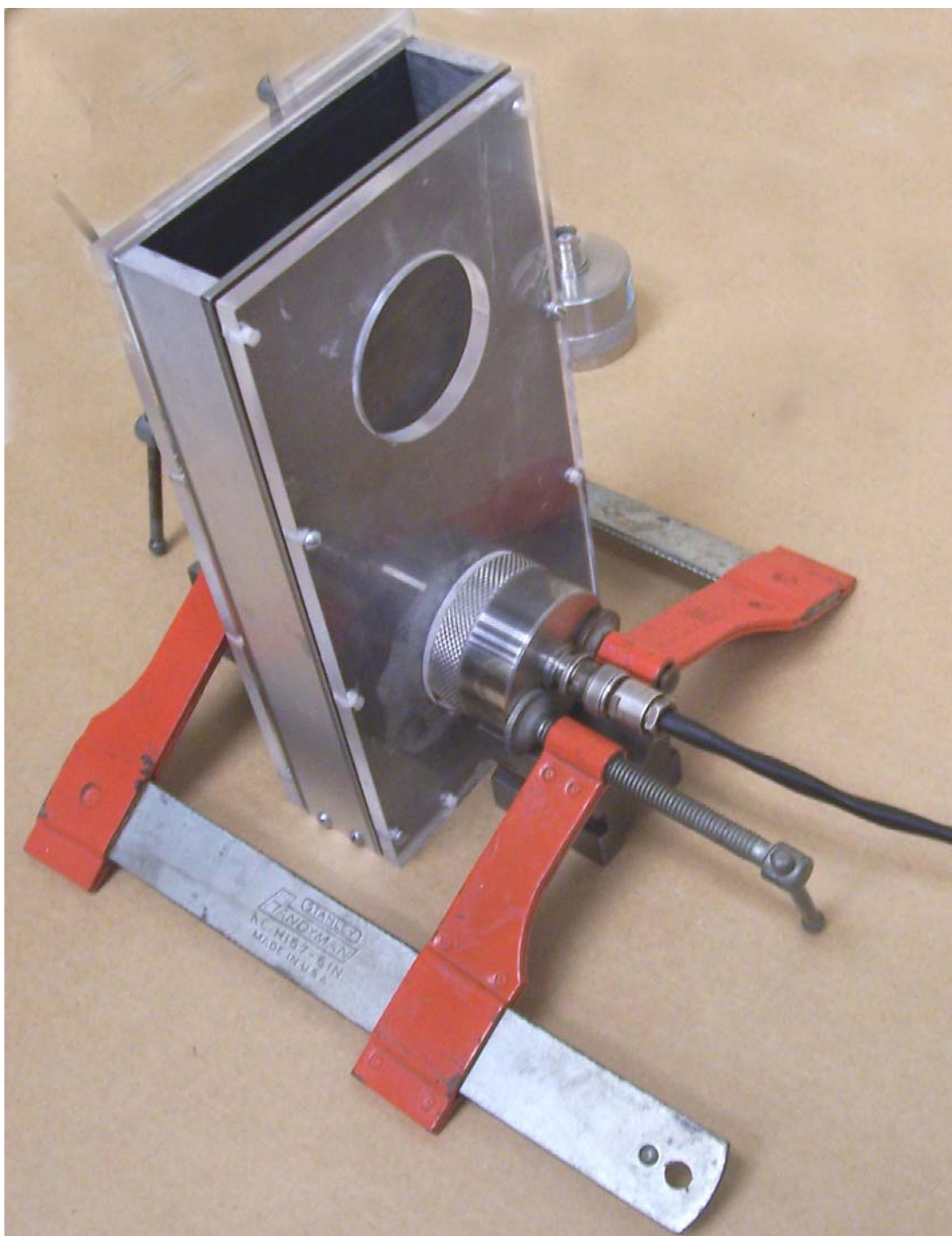
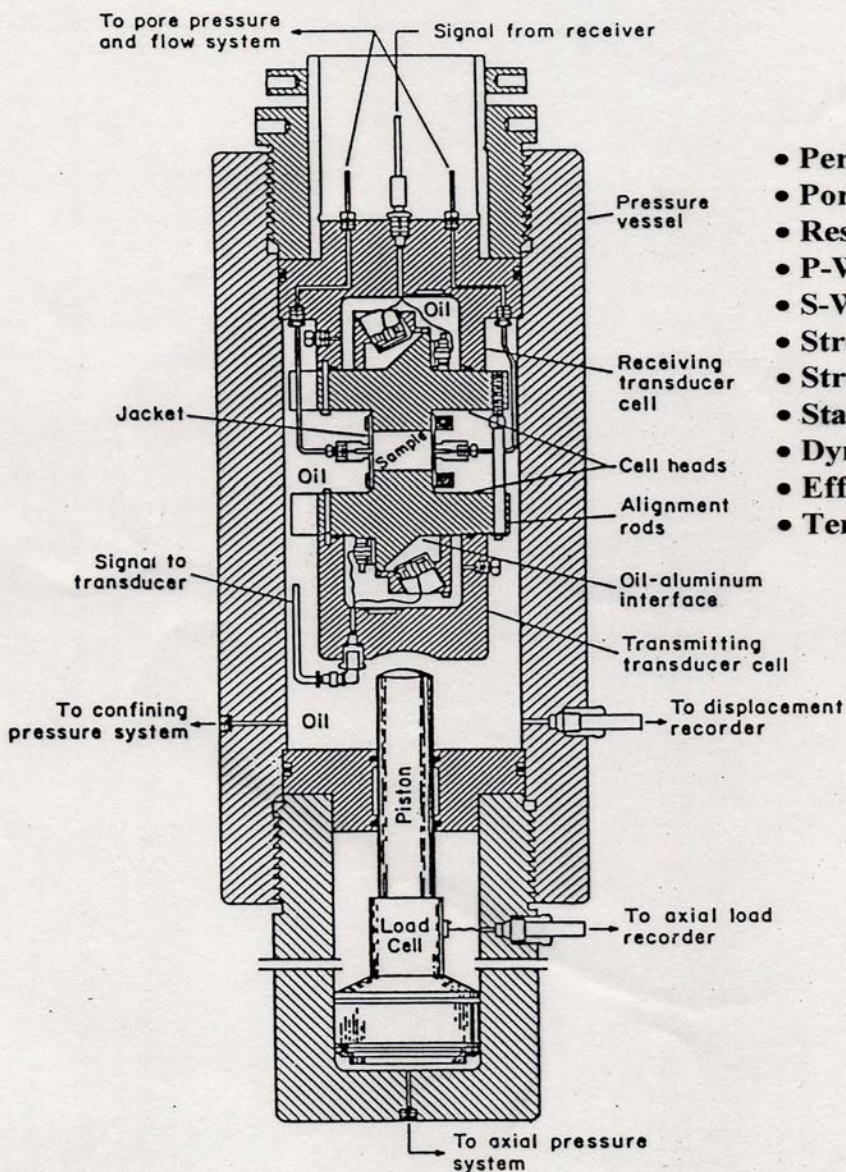


Figure 2. Large test assembly for wave propagation measurements using 4 ultrasonic transducers clamped to the 4" x 8" side walls. Different locations of the transducers provide for s- and -p waves traveling through the cement and along the side faces the specimen.

Simultaneous Property System

Computer-Controlled:

- Overburden
- Confining Pressure
- Pore Pressure
- Load Path
- Load Rate
- Flow Rate
- Pressure Drop
- Data Access
- Data Handling
- Servo-Controlled Feedback Looping



- Permeability
- Porosity
- Resistivity
- P-Wave Velocity
- S-Wave Velocity
- Stress-Strain (Vertical)
- Stress-Strain (Lateral)
- Static Moduli
- Dynamic Moduli
- Effective Stress: 60,000 Ft.
- Temperature: 550 °F

Figure 3. Schematic diagram of Simultaneous Property System, for testing of borehole components under simulated downhole conditions. (Life-Of-Well Rock, Fluid, and Stress Systems, University of Texas at Austin, July 1, 2004).



Figure 4. Side view of a graduated cylinder (250 ml) filled with cement slurry, after curing overnight. The white line around the circumference at the top of the cement column delineates the zone initially occupied by water expelled from the cement, and later re-absorbed

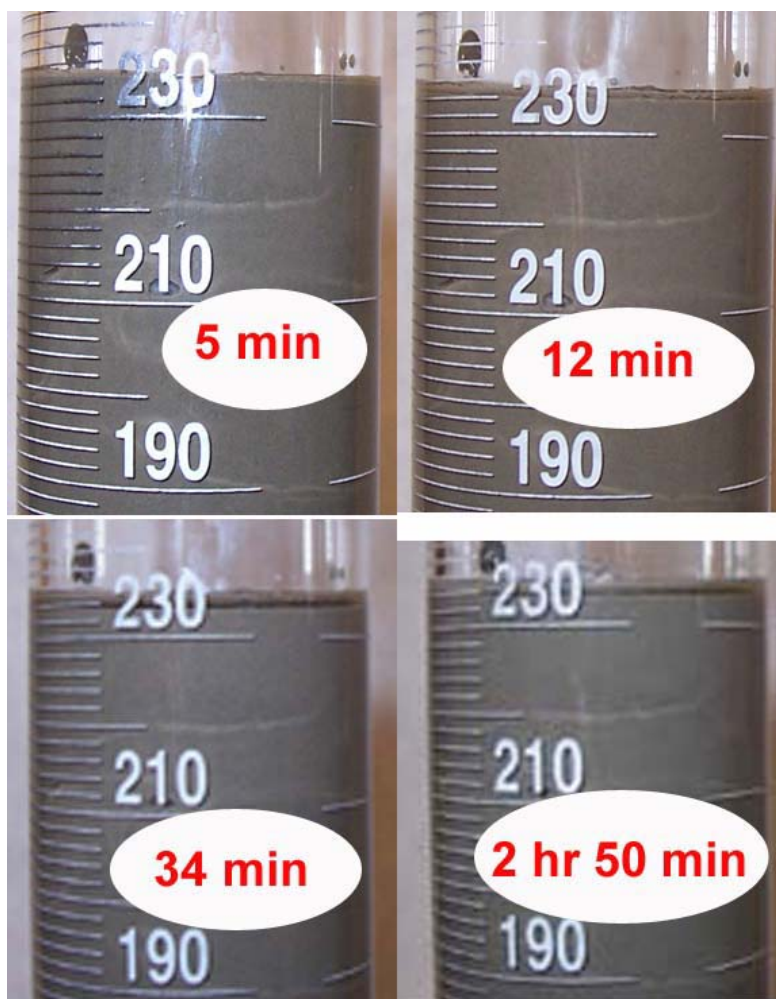


Figure 5. Photographs of a graduated cylinder filled with a freshly mixed cement slurry at time zero. Note the formation of the water layer at the top of the specimen, which persists throughout the sequence. The water layer was absent on the following day, but no shrinkage or expansion of the cement column was observed.



Figure 6. Particulate material deposited on the upper end platen, presumably from within an aqueous layer during several days in which the cement specimen was in the vessel.



Figure 7. Post test photographs of top (right side) and bottom (left side) surfaces of test specimen (top) and end platens (bottom).

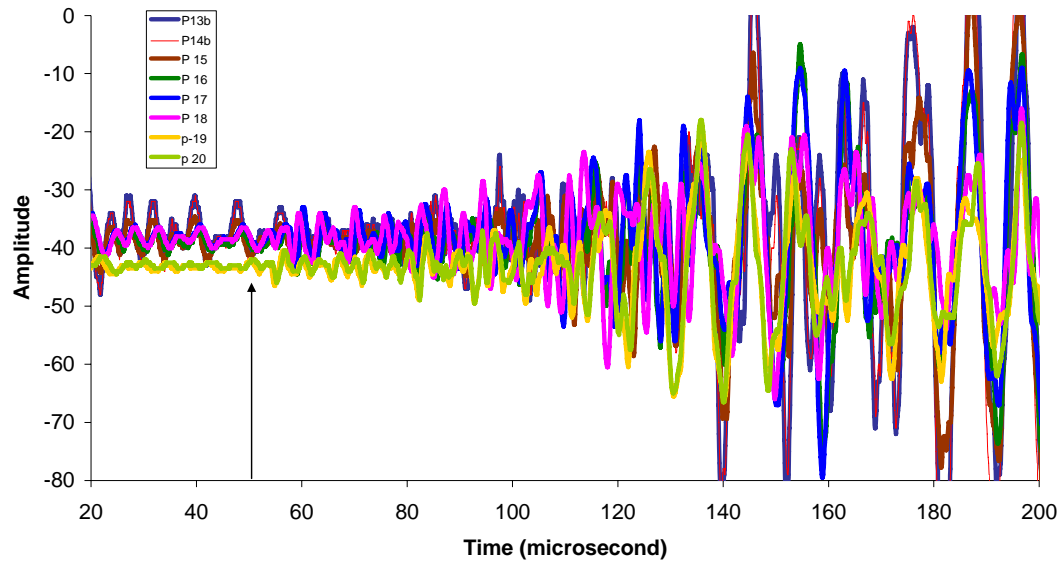


Figure 8. Waveforms for *p*-waves in the bench-top configuration with a rigid separation between end platens.

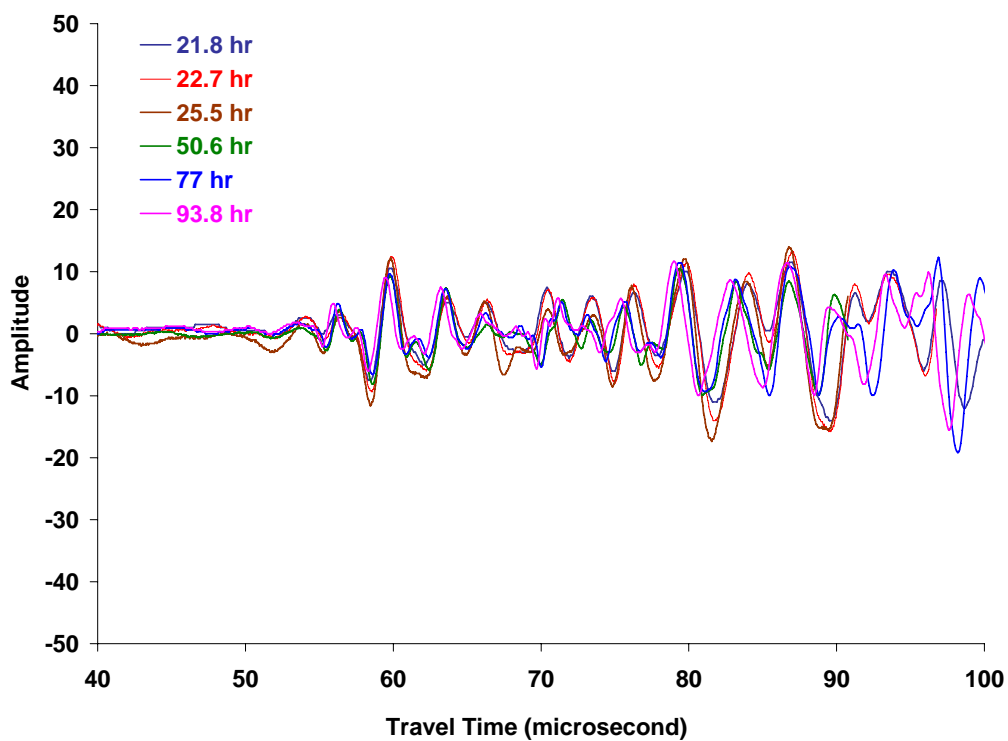


Figure 9. *P*-wave waveforms observed at elapsed times indicated in legend, in which the end platens were progressively pressed into the cement during curing of the still-liquid cement (not shown). The signals have been offset in time to provide optimum overlap. Wave forms offset to provide approximate overlap and estimated common first arrival (arrow) used to compute *p*-wave velocities (Figure 10).

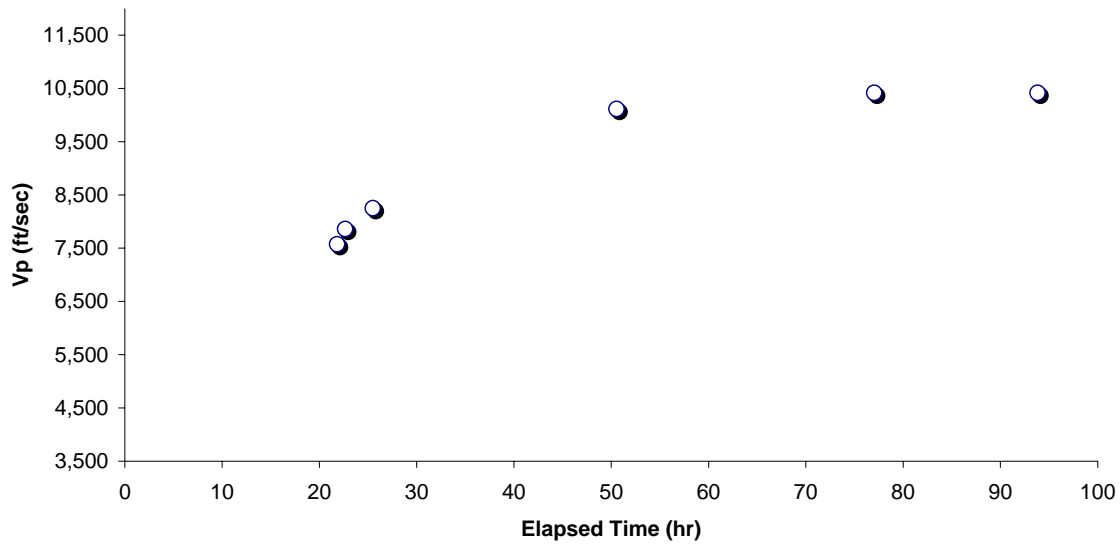


Figure 10. P-wave velocities computed from offsets used in Figure 9, during later stages of curing.

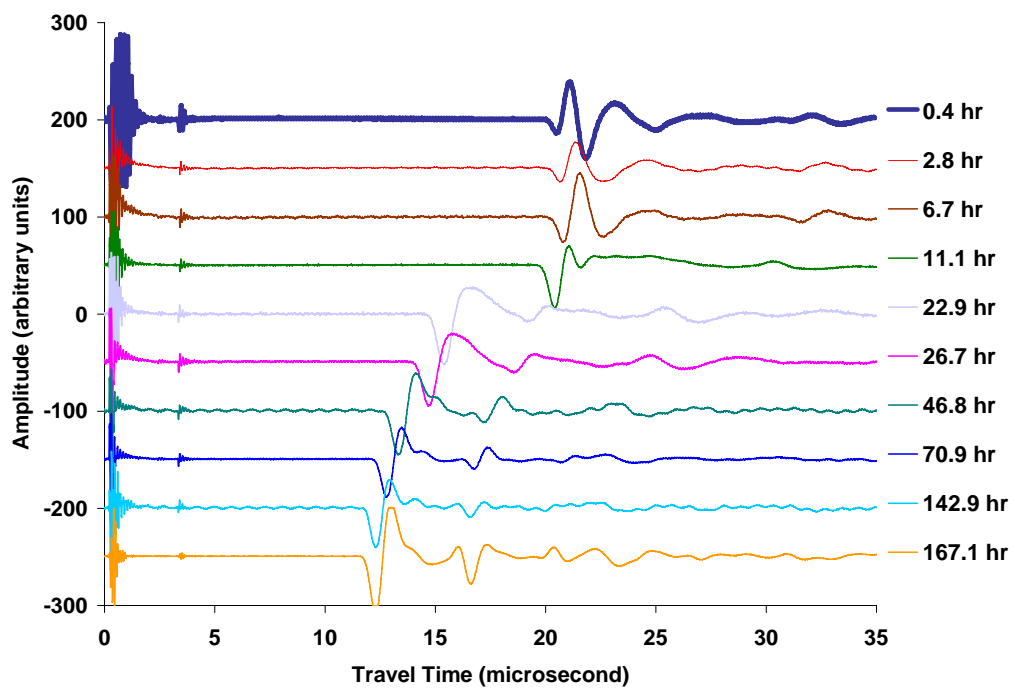


Figure 11. Compressional waveforms traveling through a cement slurry poured into the 4" x 4" chamber (Figure 1) from time 0, after successively greater curing times shown on the right side of the plot.

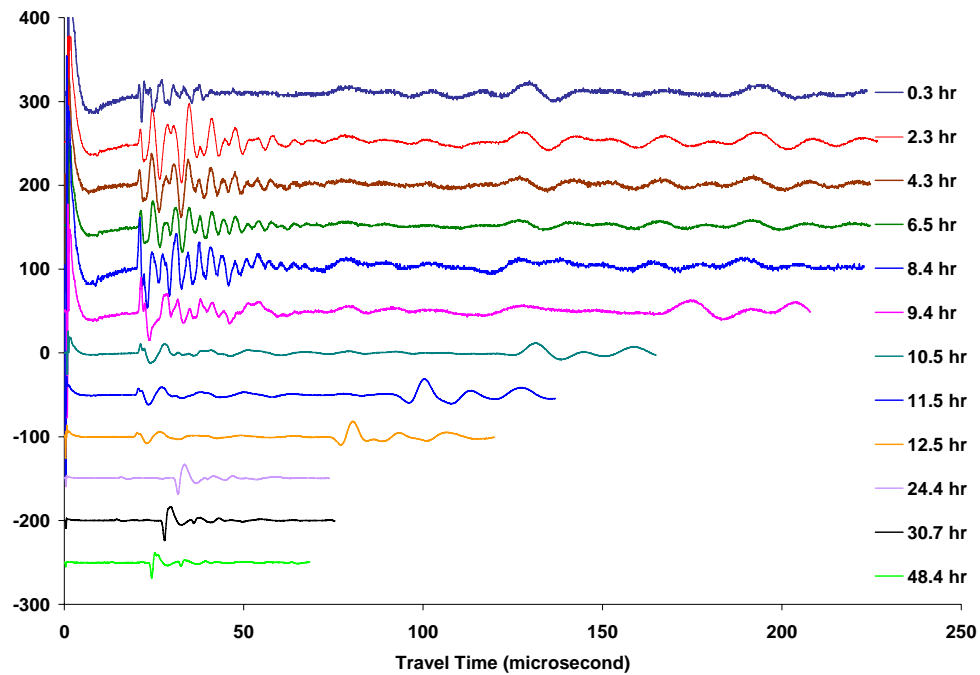


Figure 12. Shear waveforms traveling through a cement slurry poured into the 4" x 4" chamber (Figure 1) from time 0, with curing times shown on the right side of the plot.

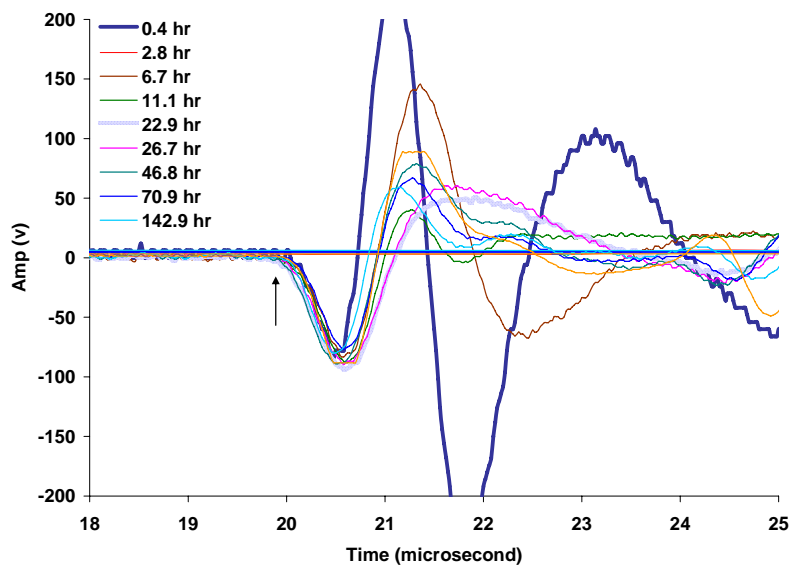


Figure 13. Shifted compressional mode waveforms for different curing times in the 4x4" apparatus (Figure 1), aligned for velocity computations.

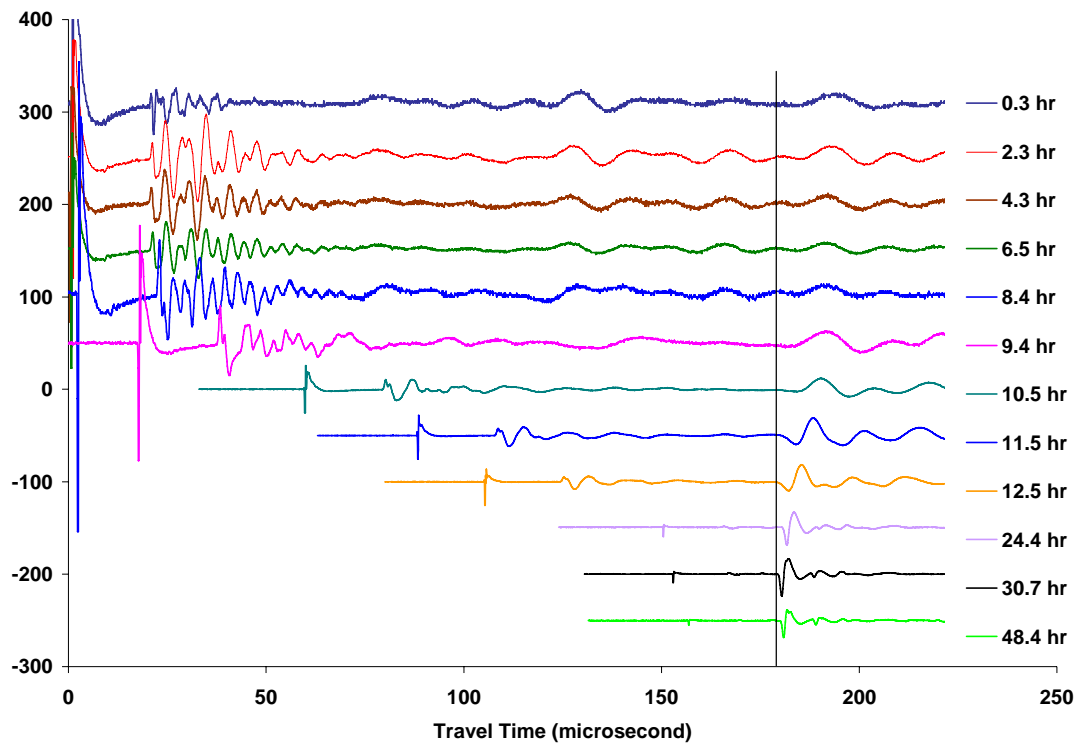


Figure 14. Aligned shear mode waveforms in 4x4" chamber (Figure 1) for velocity computations. Signal for early travel times is a p-wave precursor, which is ignored in waveform shifting.

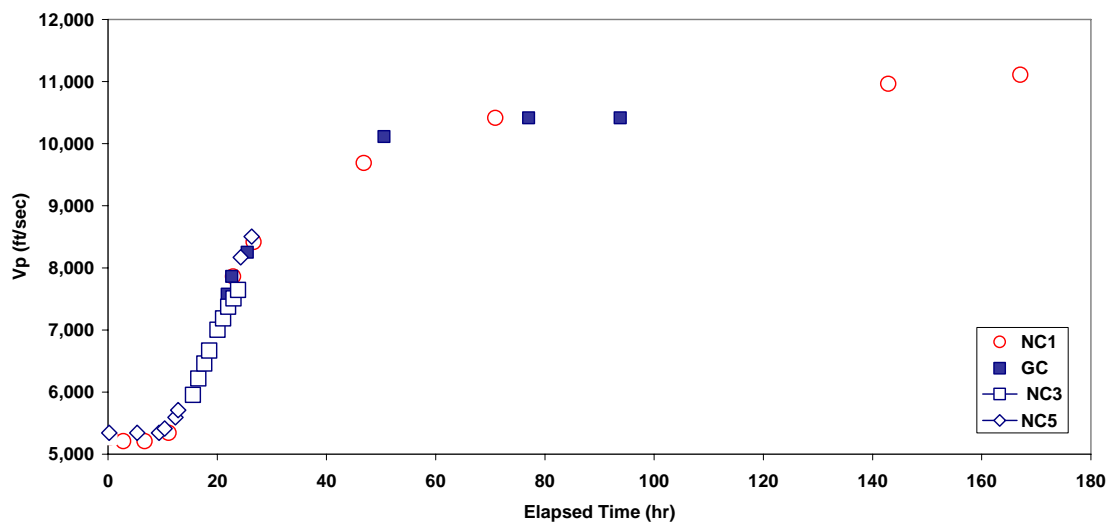


Figure 15. Cumulative plot of p-wave velocity variations during curing of cement. Data taken from measurements on 4 different specimens: one in the Gulf Cell (GC), and 3 different specimens in the new 4" x 4" cell (NC1, 3, and 5, apparatus shown in Figure 1).

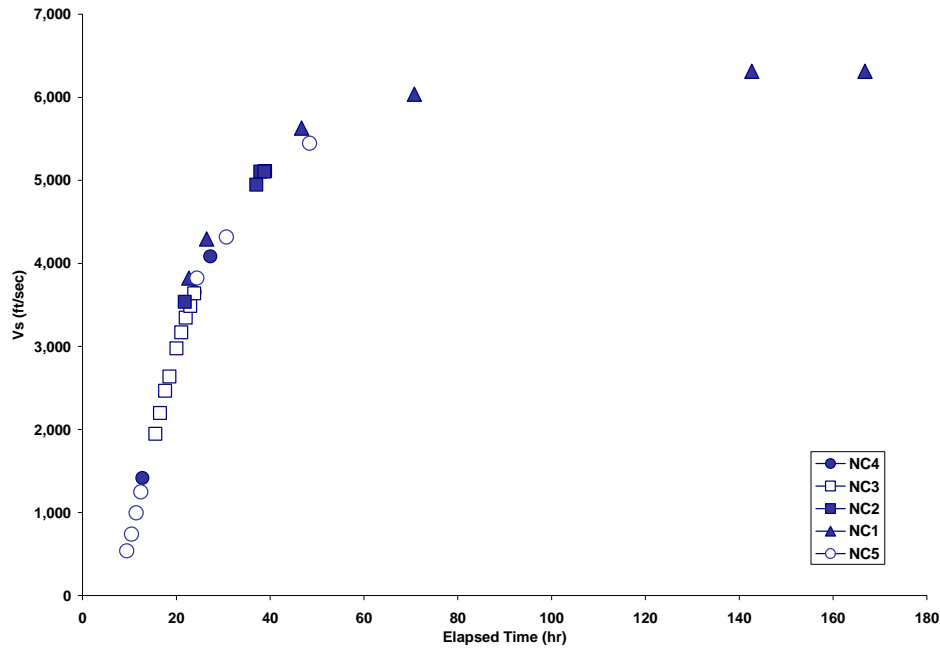


Figure 16. Cumulative plot of *s*-wave velocity variations during curing of cement. Data taken from measurements on 5 different specimens in the new 4”x4” apparatus (NC1-5; Figure 1).

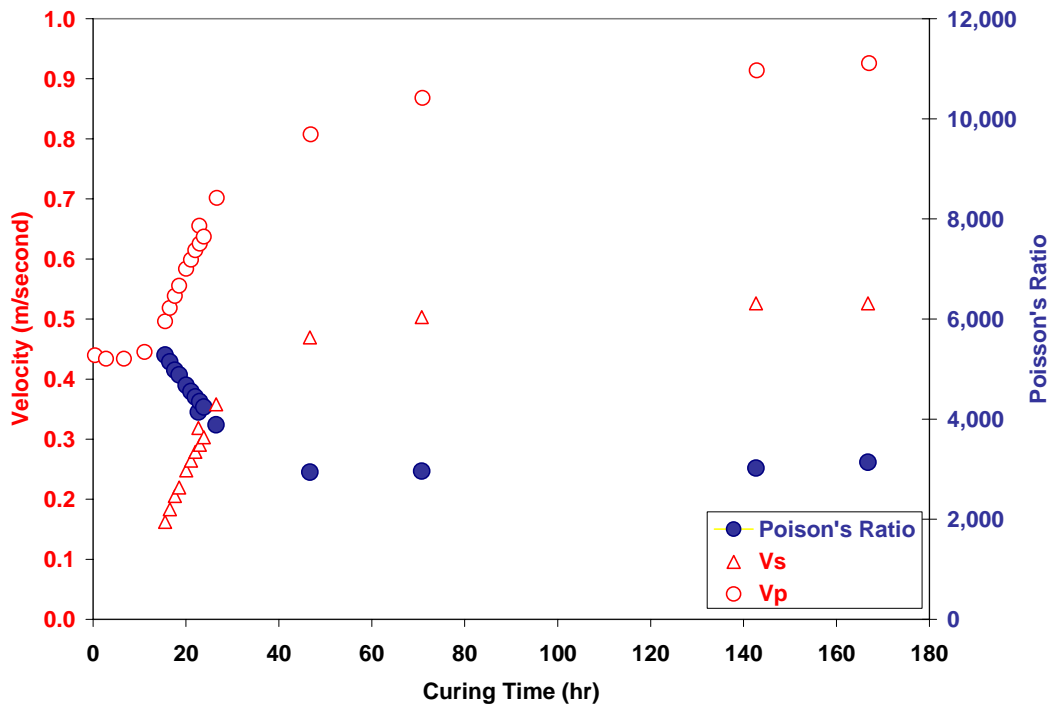


Figure 17. Variations in dynamic Poisson's ratio with curing time. *S*- and *P*-wave velocity variations from Figures 15 and 16 are repeated for comparison.

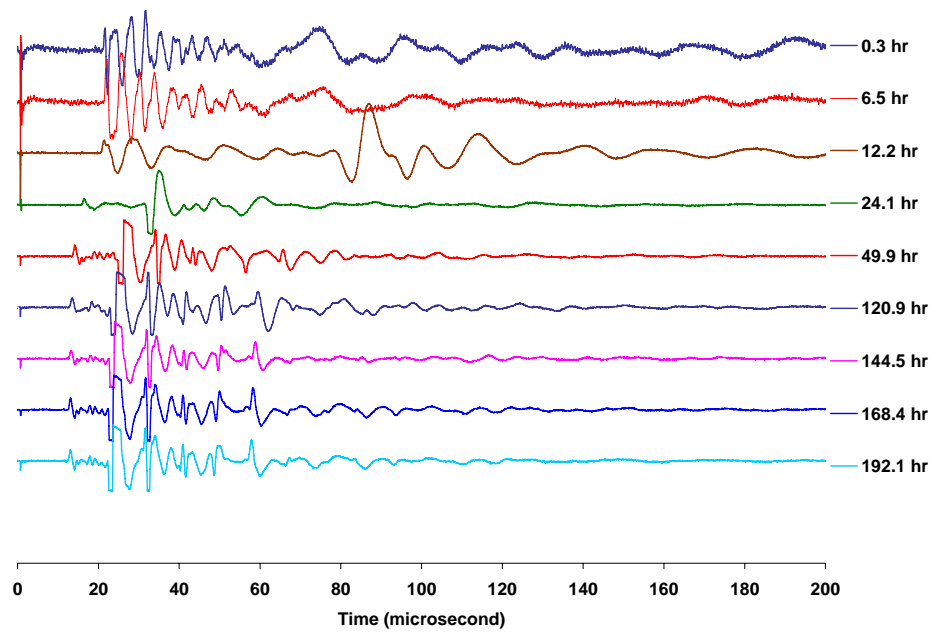


Figure 18. Waveforms for shear waves traveling across the bottom of a cement specimen in the 4'' x 8'' chamber (Figure 2), for different curing times shown on the right side.

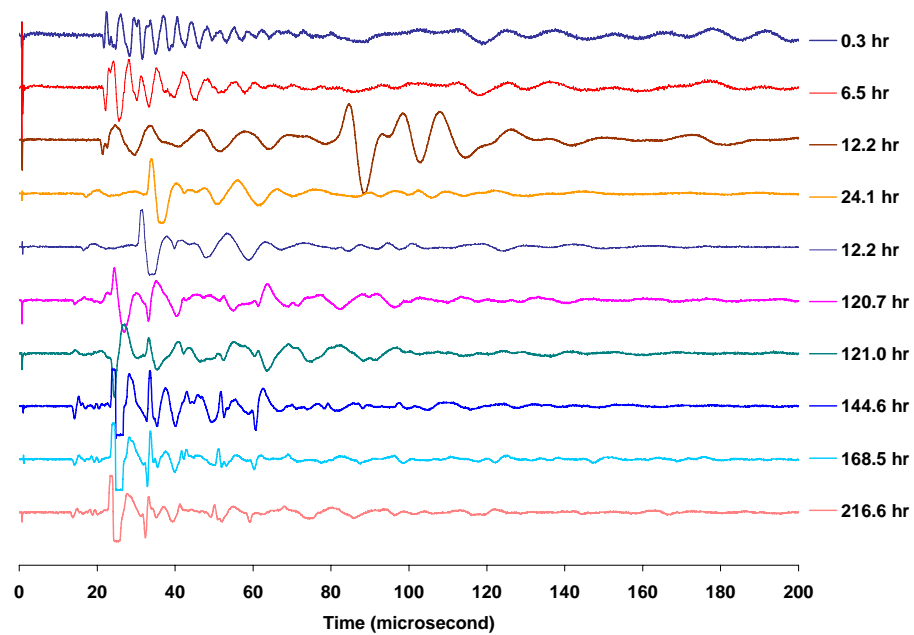


Figure 19. Corresponding plot for shear waves traveling across top end of specimen in 4'' x 8'' chamber (Figure 2).

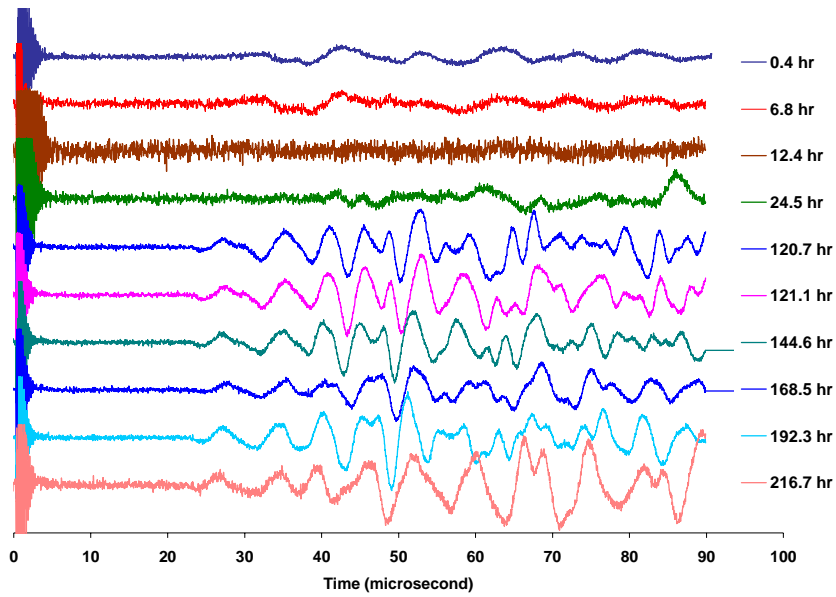


Figure 20. Wave patterns for propagation of signals generated and detected by p-wave transducers on the right face of the apparatus shown in Figure 2.

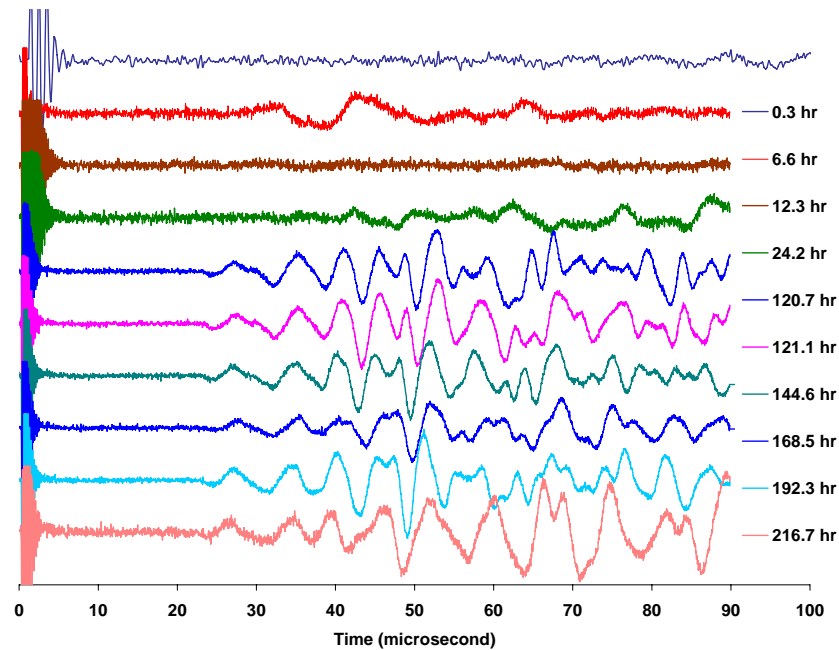


Figure 21. Corresponding plot for waves generated by p-wave transducers, traveling along the left face of the 4" x 8" apparatus (Figure 2).

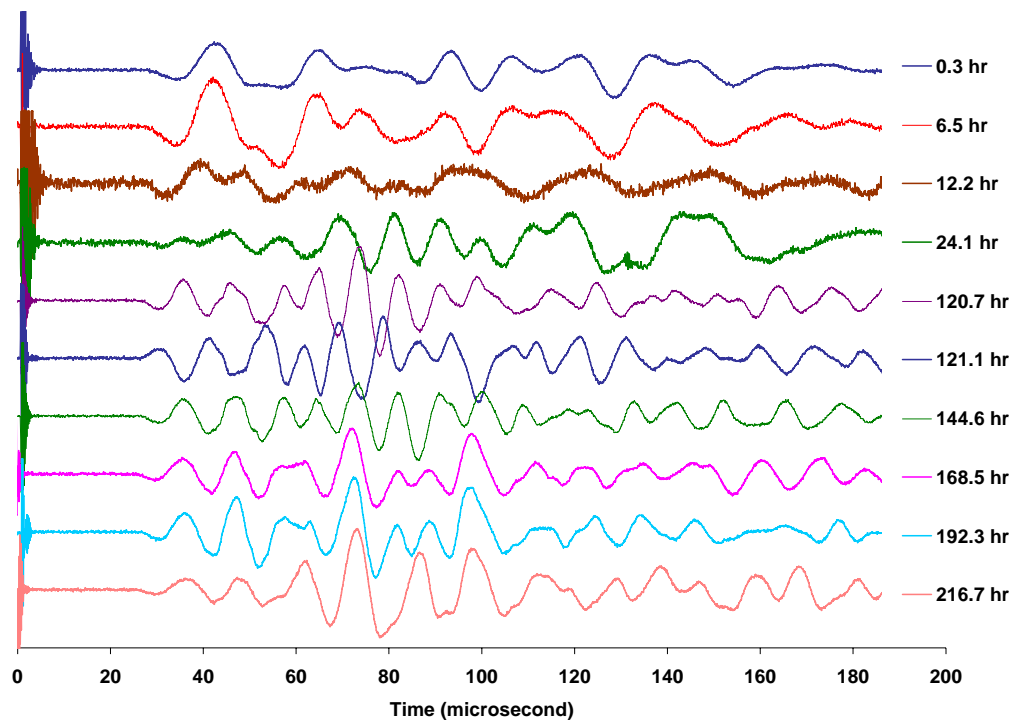


Figure 22. Wave forms for waves generated and detected by shear transducers mounted on the right side of the 4" x 8" chamber (Figure 2).

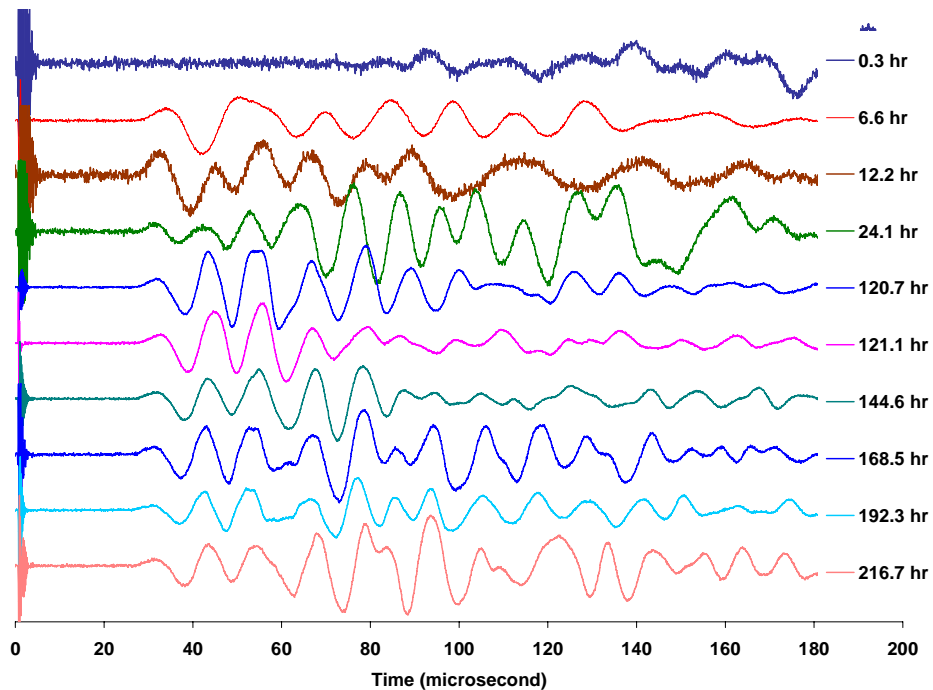


Figure 23. Wave forms for waves generated and detected by shear transducers mounted on the left side of the 4" x 8" chamber (Figure 2)

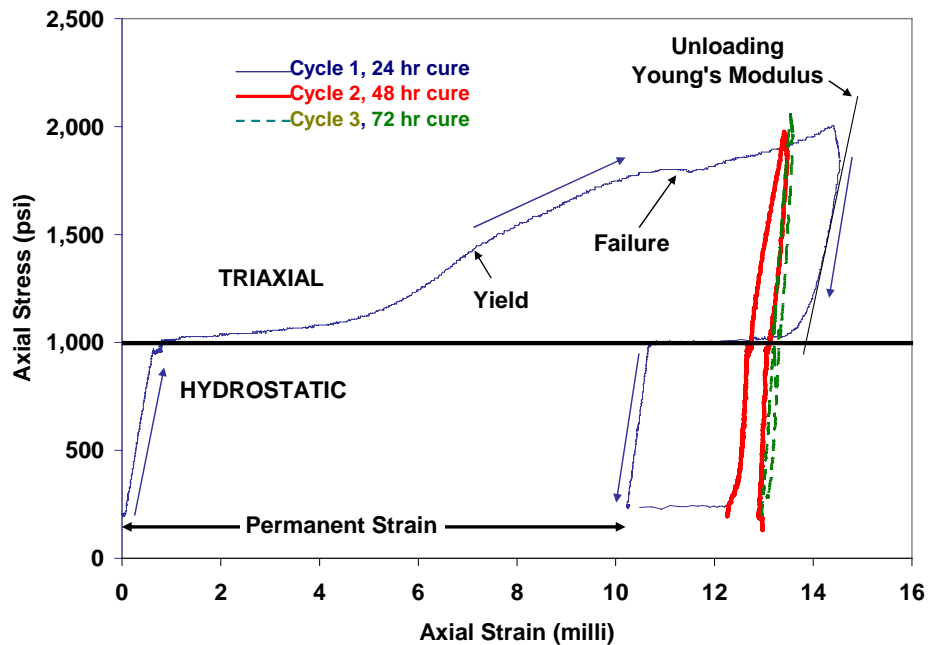


Figure 24. Axial stress - strain behavior of Mix 1 Specimen #8 after deformations at indicated times. Graphical definitions of yield, failure, Young's modulus, and permanent strain are also shown.

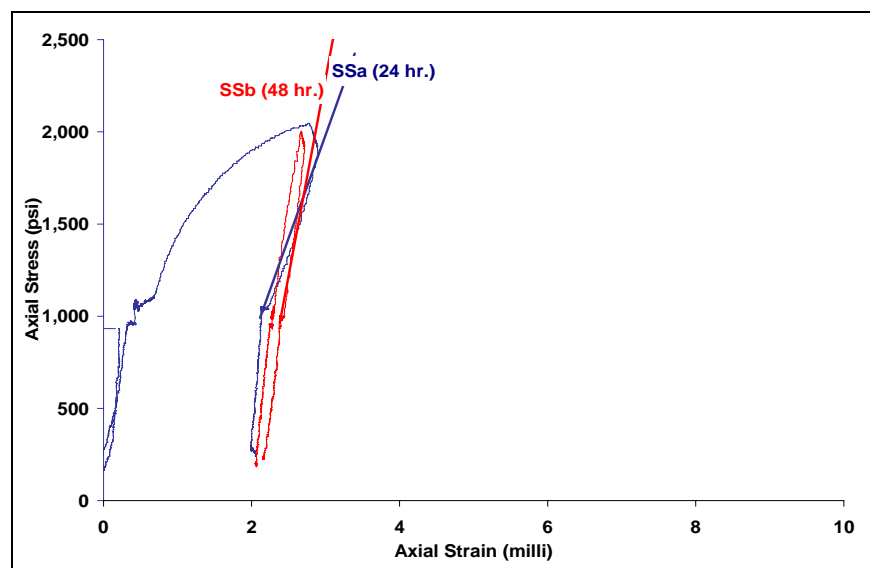


Figure 25. Axial stress - strain behavior of Mix 1 specimen #9 during curing and deformations at indicated times. Young's moduli computed from linear stress strain slopes are listed in Table 1.

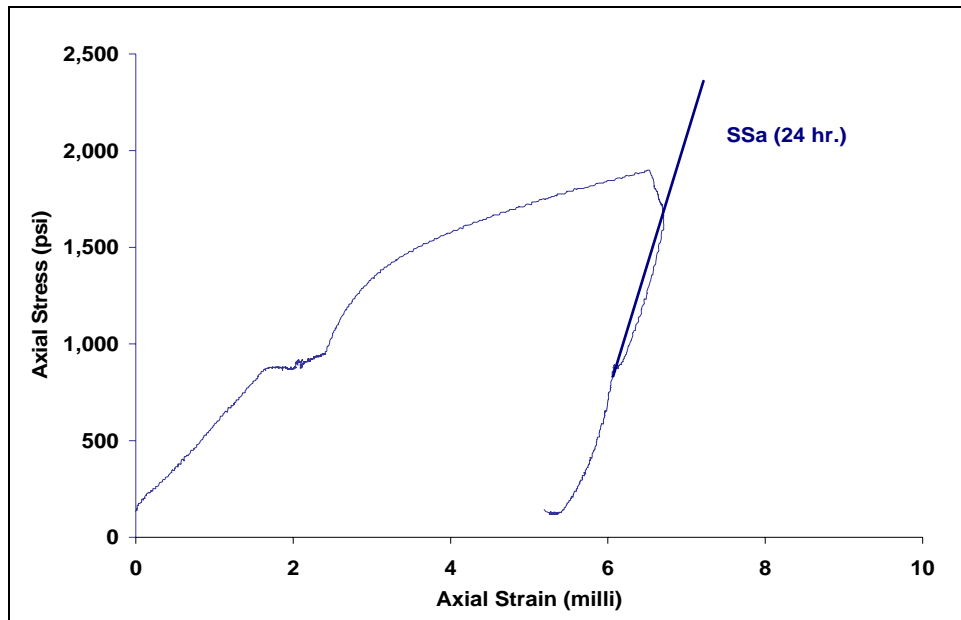


Figure 26. Axial stress-strain behavior in Mix 1 specimen #16 after curing ($P_c = 0$) and deformation. Young's modulus computed from linear stress-strain slope is listed in Table 1.

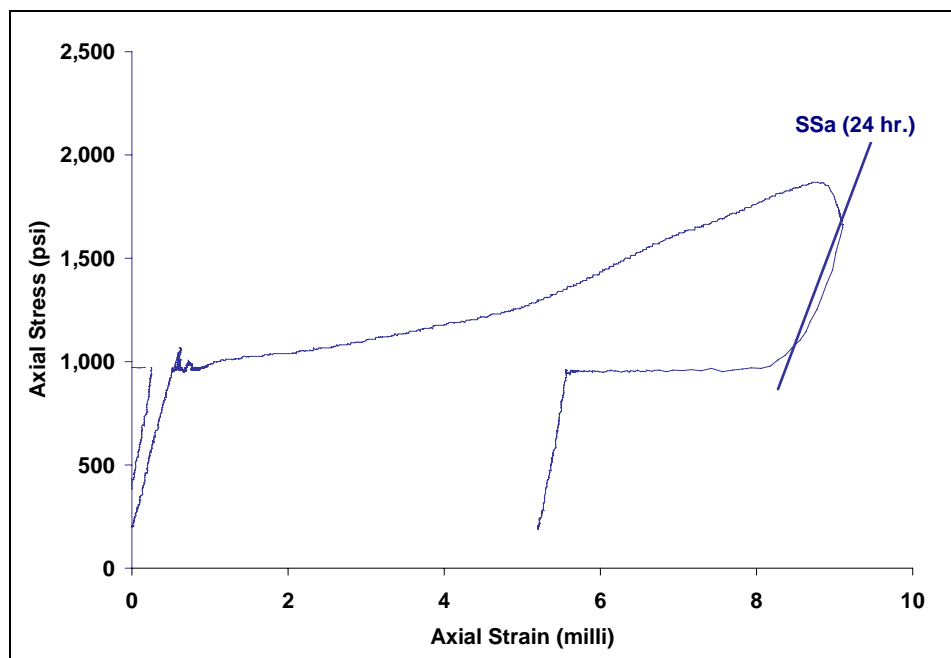


Figure 27. Axial stress-strain behavior during curing and deformation of Mix 1 specimen #7. Some evidence of failure is indicated by break in slope at an axial stress of approximately 1.7 kpsi. Young's modulus computed from linear stress-strain slope is listed in Table 1.

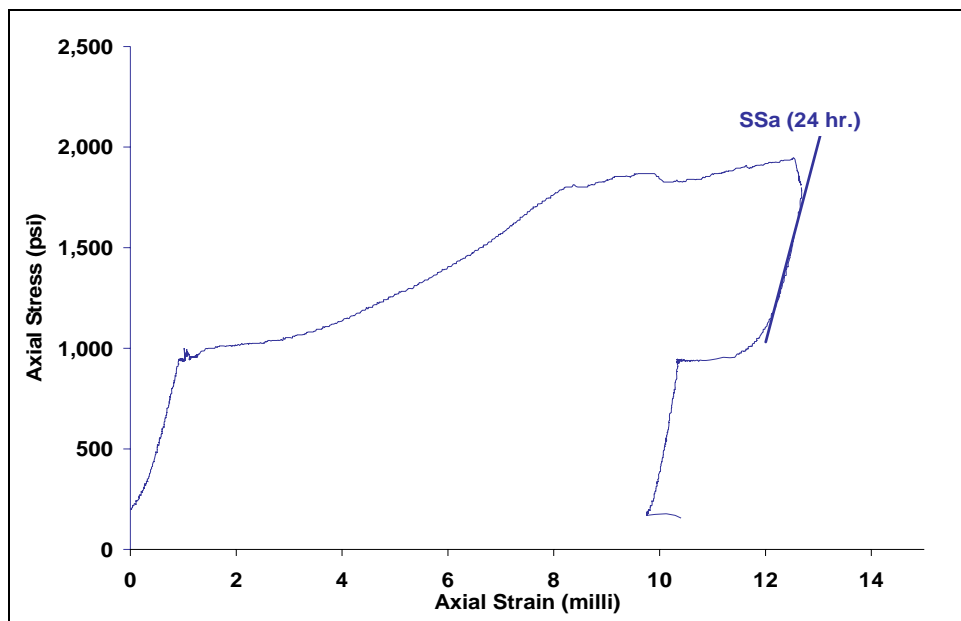


Figure 28. Axial stress - strain behavior of Mix 1 specimen #11 during curing and deformation. Note clear evidence of failure at an axial stress of approximately 1.8 kpsi. Young's modulus computed from linear stress-strain slope is listed in Table 1.

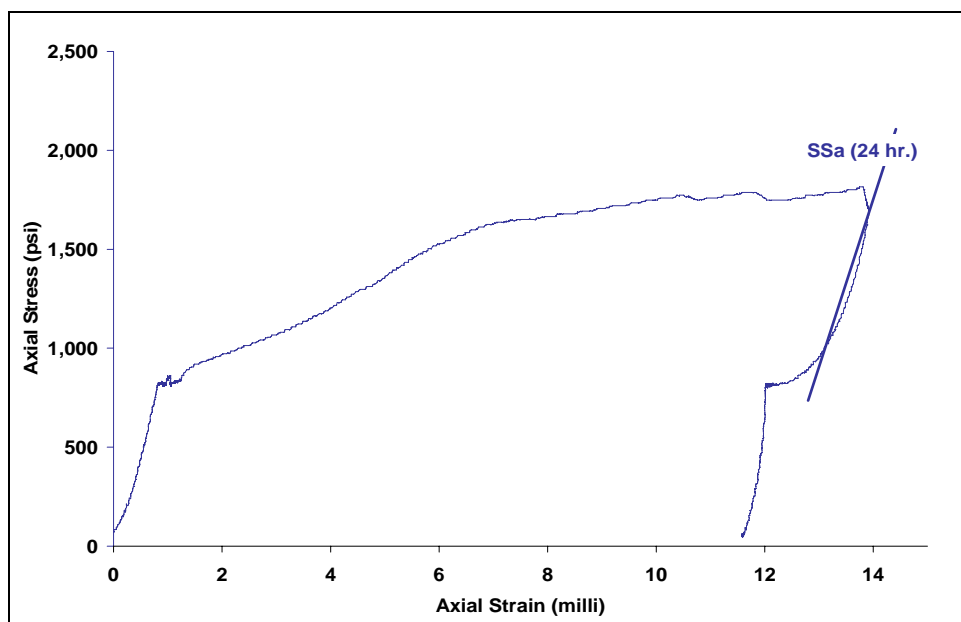


Figure 29. Axial stress - strain behavior during curing ($P_c = 200$ psi) and deformation of Mix 1 specimen #12. Note clear evidence of specimen failure at an axial stress of approximately 1.7 kpsi. Young's modulus computed from linear stress-strain slope is listed in Table 1.

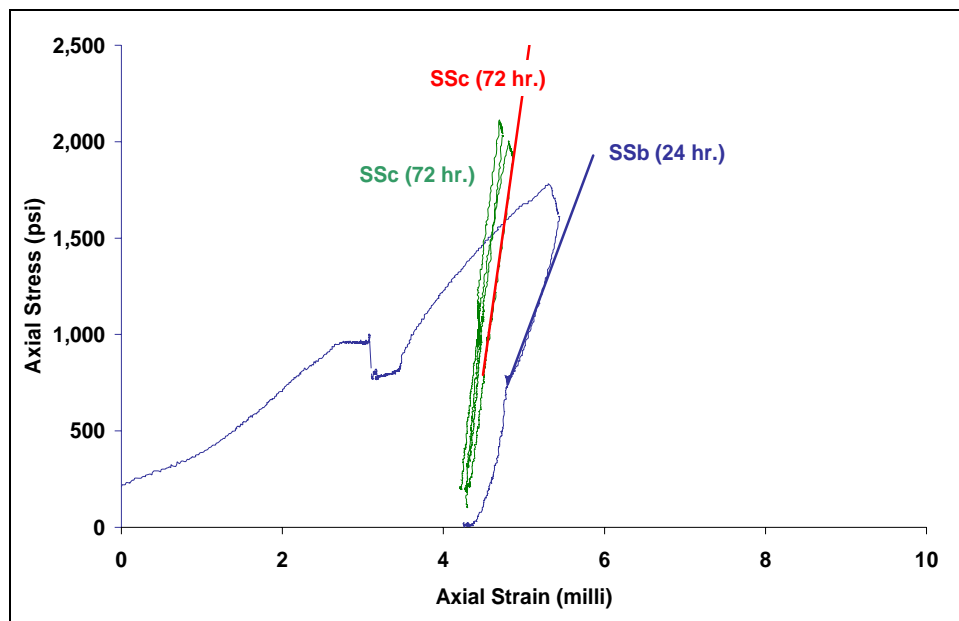


Figure 30 Axial stress - strain behavior of Mix 1 specimen #10 during curing ($P_c = 0$; apparent drift in axial stress during initial curing was due to load cell drift) and deformation at indicated times. Young's moduli computed from linear stress-strain slopes are listed in Table 1.

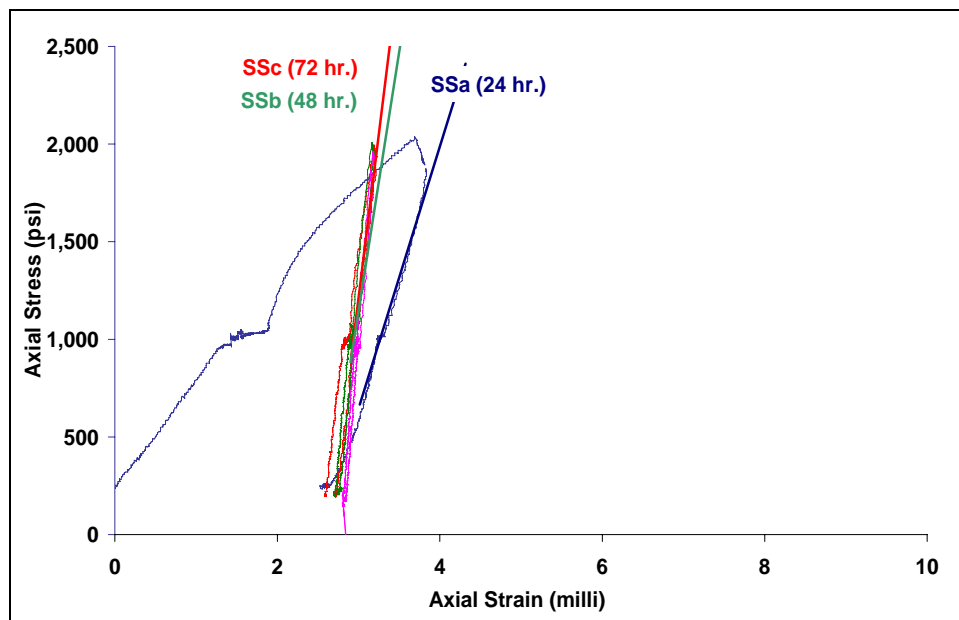


Figure 31. Axial stress-strain behavior in Mix 2 specimen # 4 after curing and deformation at indicated times. Young's moduli computed from linear stress-strain slopes are listed in Table 2.

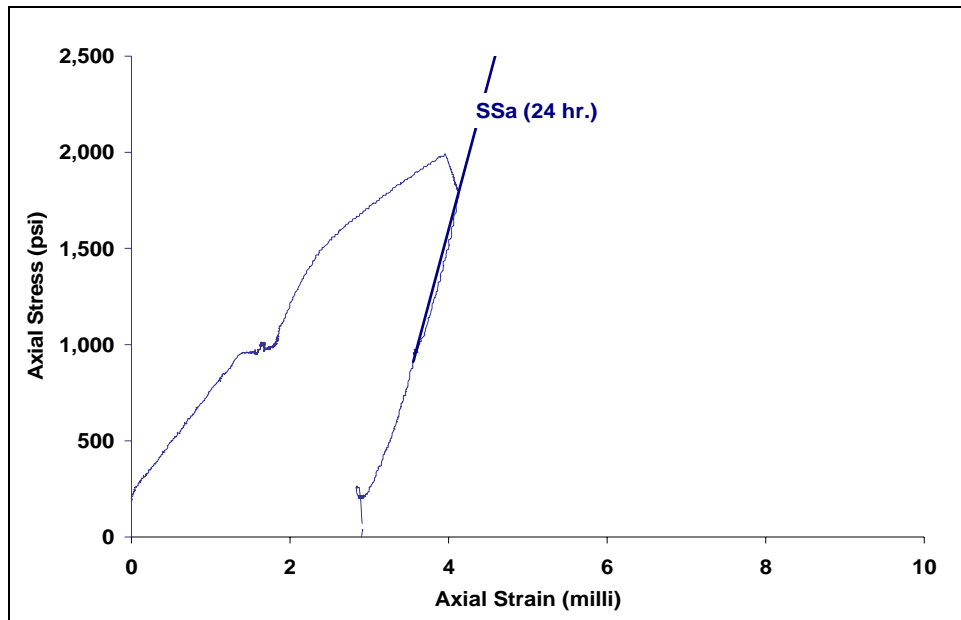


Figure 32. Axial stress-strain behavior in Mix 2 specimen #15 during curing ($P_c = 0$) and deformation. Young's modulus computed from linear stress-strain slope is listed in Table 2.

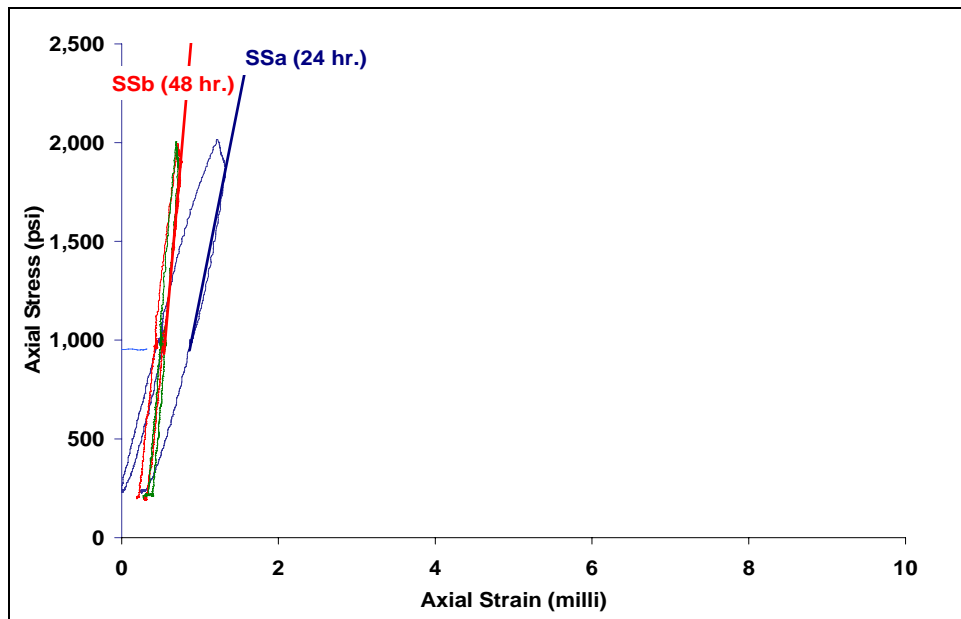


Figure 33. Axial stress-strain behavior of Mix 2 specimen #5 during curing and deformation at indicated times,. Young's moduli computed from linear stress strain slopes are listed in Table 2.

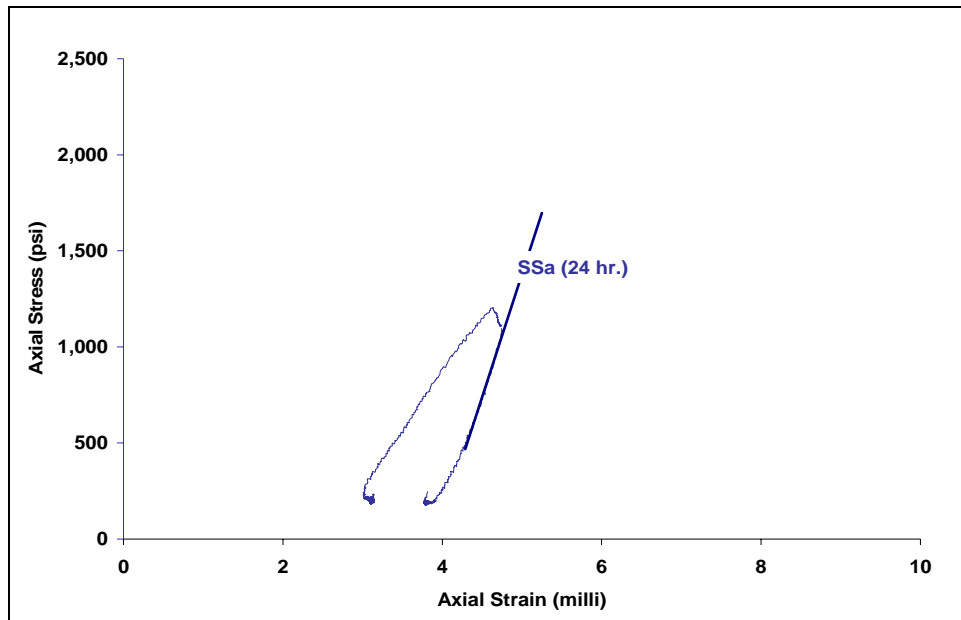


Figure 34. Axial stress-strain behavior of Mix 2 specimen #13 during curing ($P_c = 1$ kpsi) and deformation at indicated times. Young's moduli computed from linear stress strain slopes are listed in Table 2. Note lower confining pressure (200 psi) for this deformation

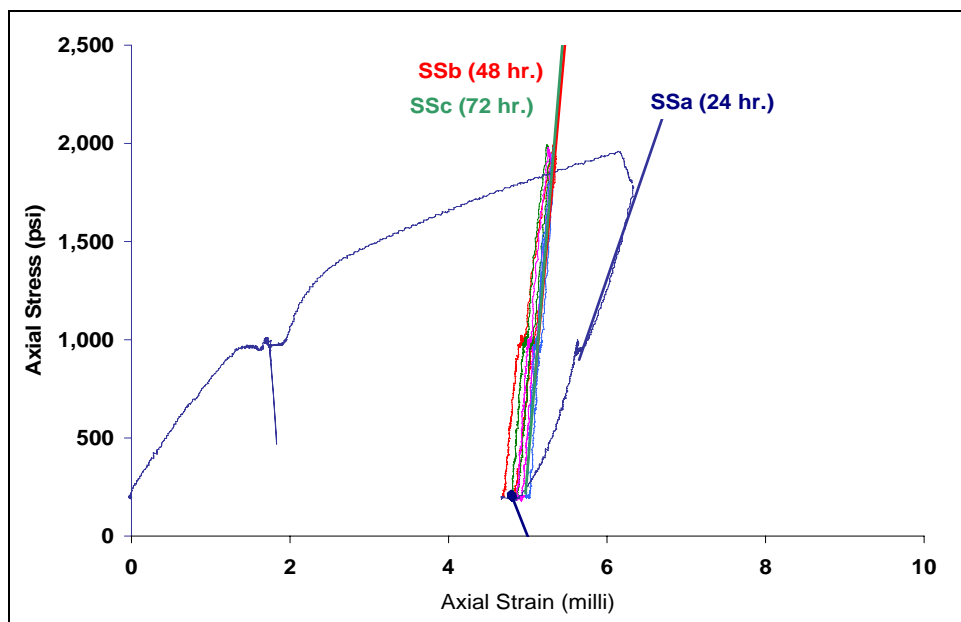


Figure 35. Axial stress-strain behavior in Mix 2 specimen #3 after curing and deformation at indicated times. Young's moduli computed from linear stress-strain slopes are listed in Table 2.

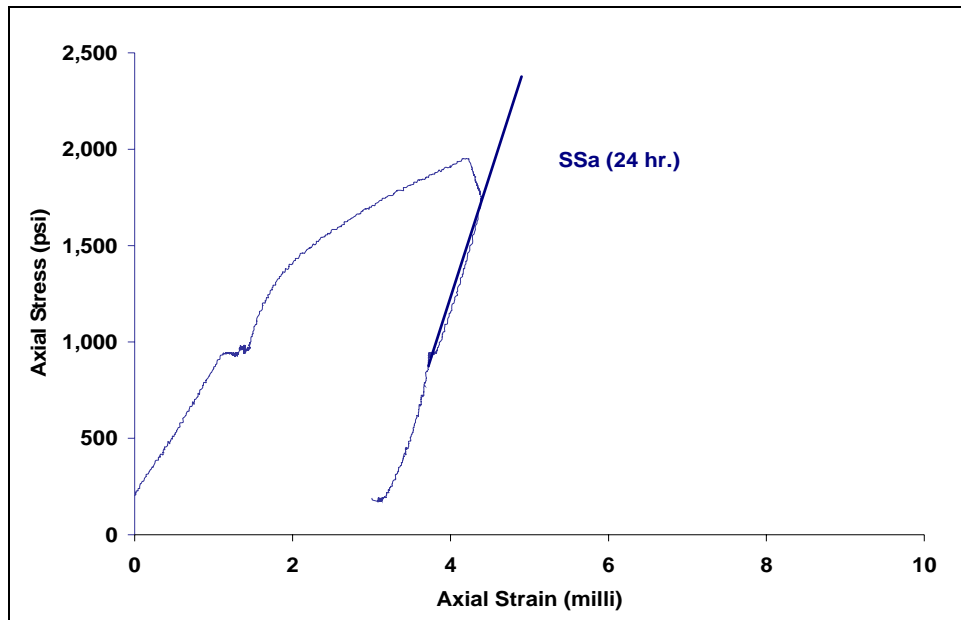


Figure 36. Axial stress-strain behavior in Mix 2 specimen #14 during curing and deformation. Young's modulus computed from linear stress-strain slopes is listed in Table 24.

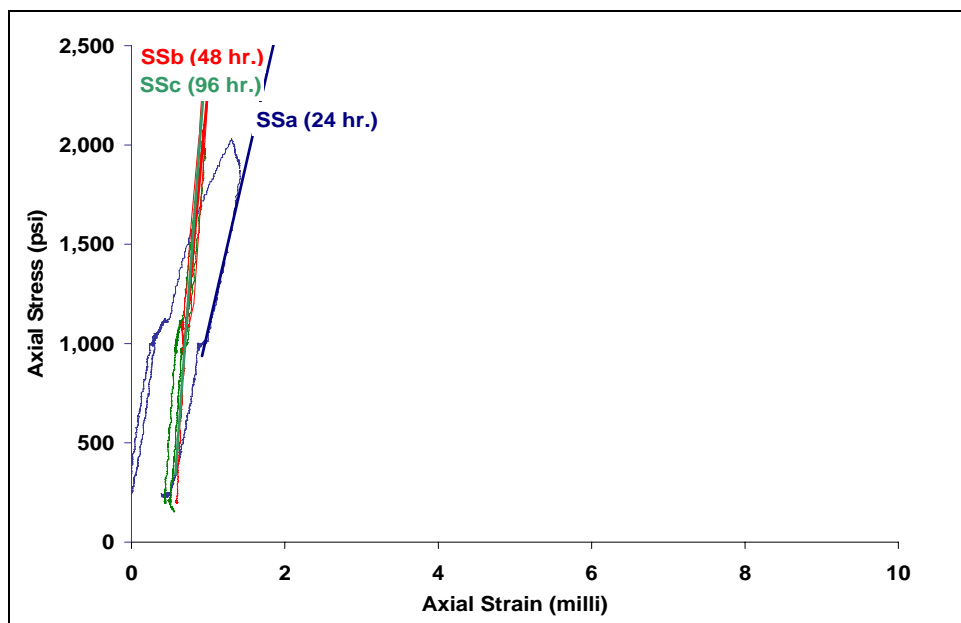


Figure 37. Axial stress-strain behavior in Mix 2 specimen #6 after curing and deformation at indicated times. Young's moduli computed from linear stress-strain slopes are listed in Table 2.

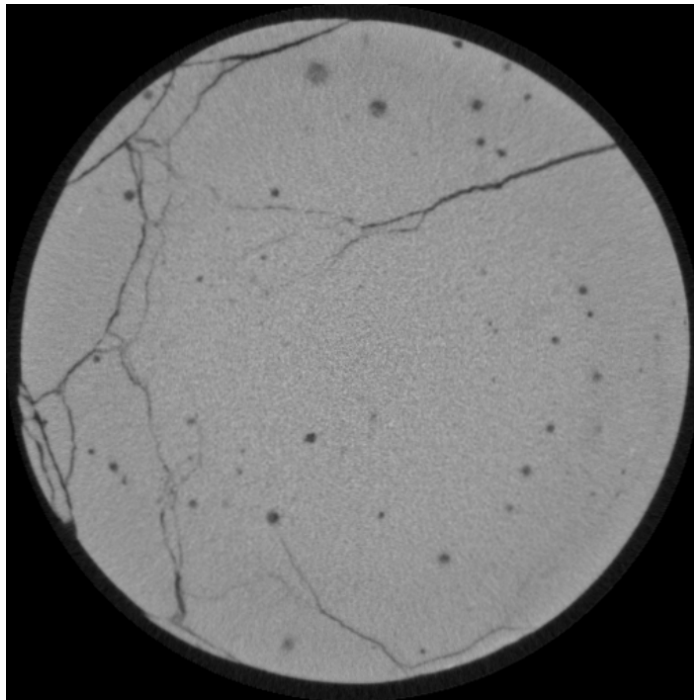


Figure 38. Single slice, approximately midway along cylinder axis, of post-test CT image of specimen #11 (Mix 1, excess water not removed), showing extensive internal fracturing from failure during triaxial deformation (Figure 28).

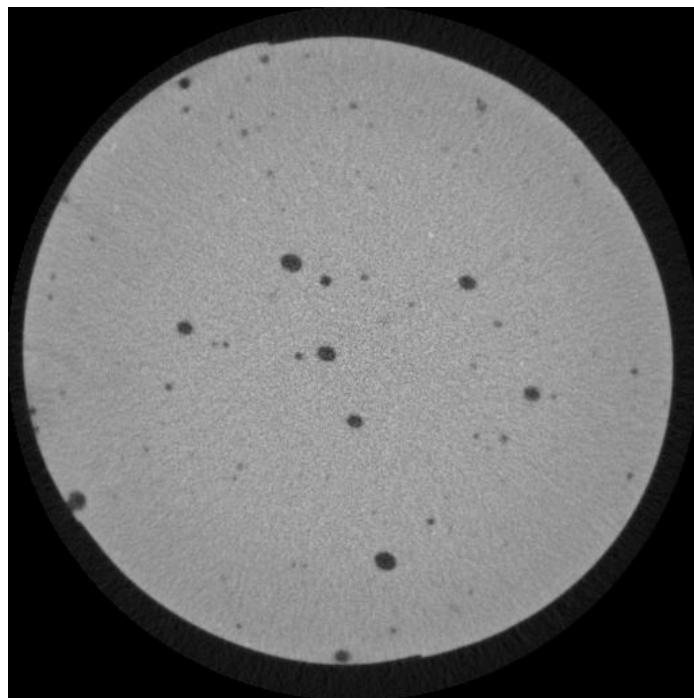


Figure 39. Single slice, approximately midway along cylinder axis, of post-test CT image of specimen #6 (Mix 2, excess water not removed), showing lack of internal fracturing after triaxial deformation. Deformation gives no indication of failure (Figure 37).

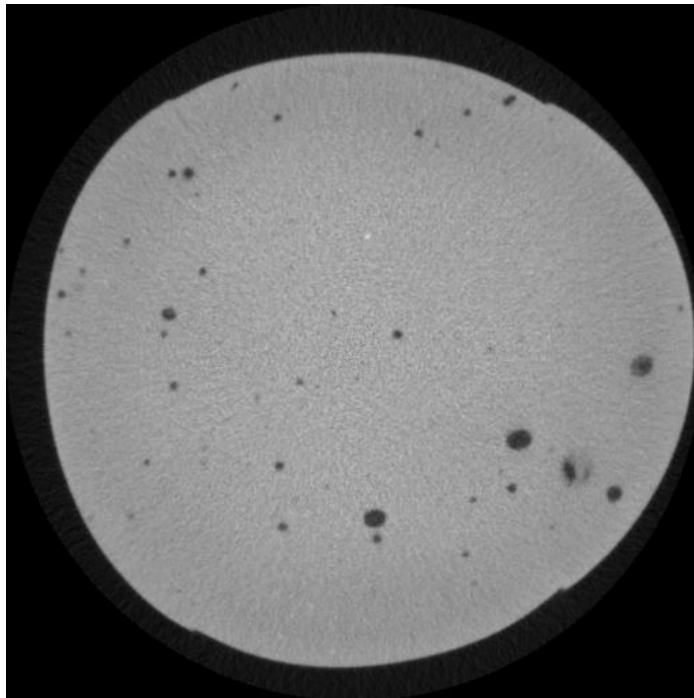


Figure 40. Single slice, approximately midway along cylinder axis, of post-test CT image of specimen #9 (Mix 1, excess water removed by wicking), showing lack of internal fracturing after triaxial deformation. Specimen gives no indication of failure (Figure 25).



Figure 41. Photographic comparison of post-test Specimen 10 (left side) and 11 (right side), showing greater porosity in Specimen 10.

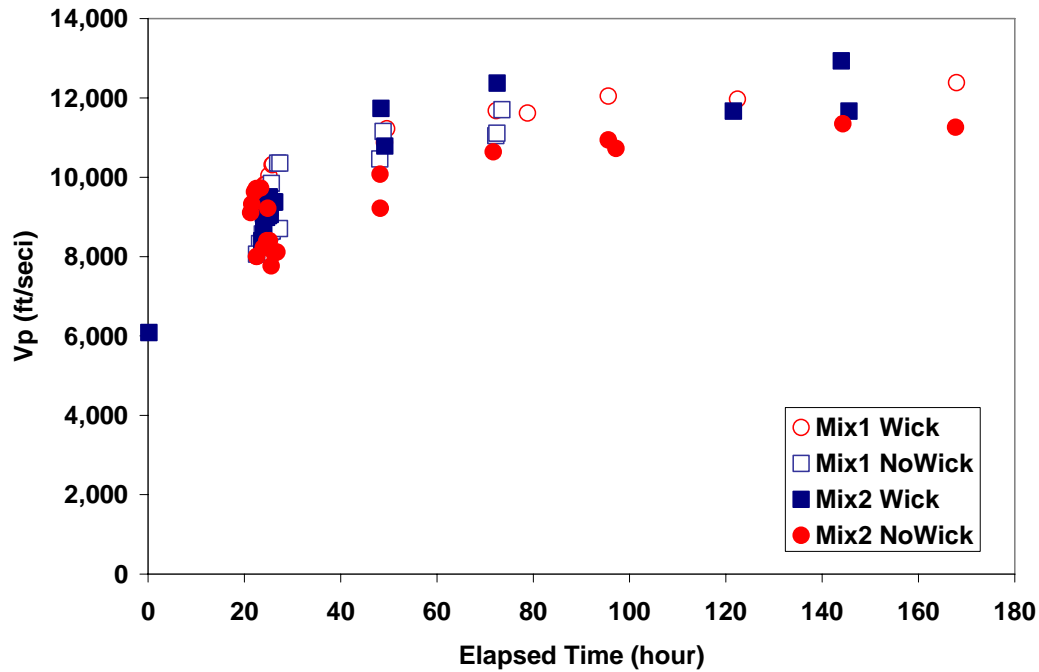


Figure 42. Variations in p -wave velocity for all specimens.

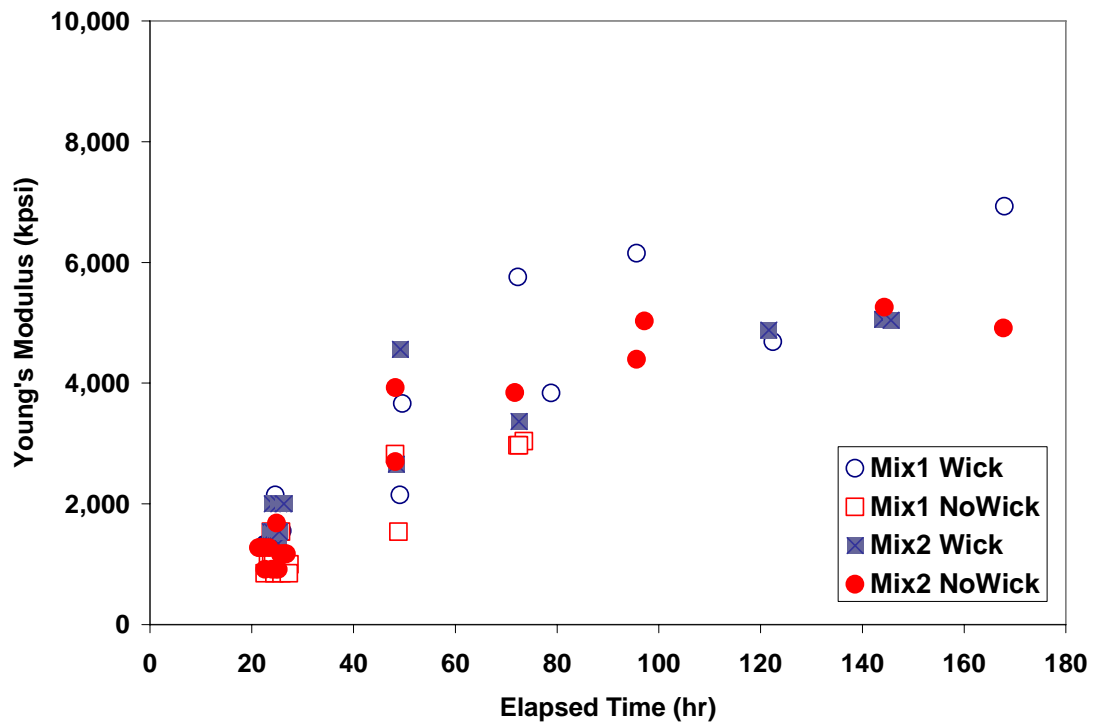


Figure 43. Variations of static Young's moduli with curing time.

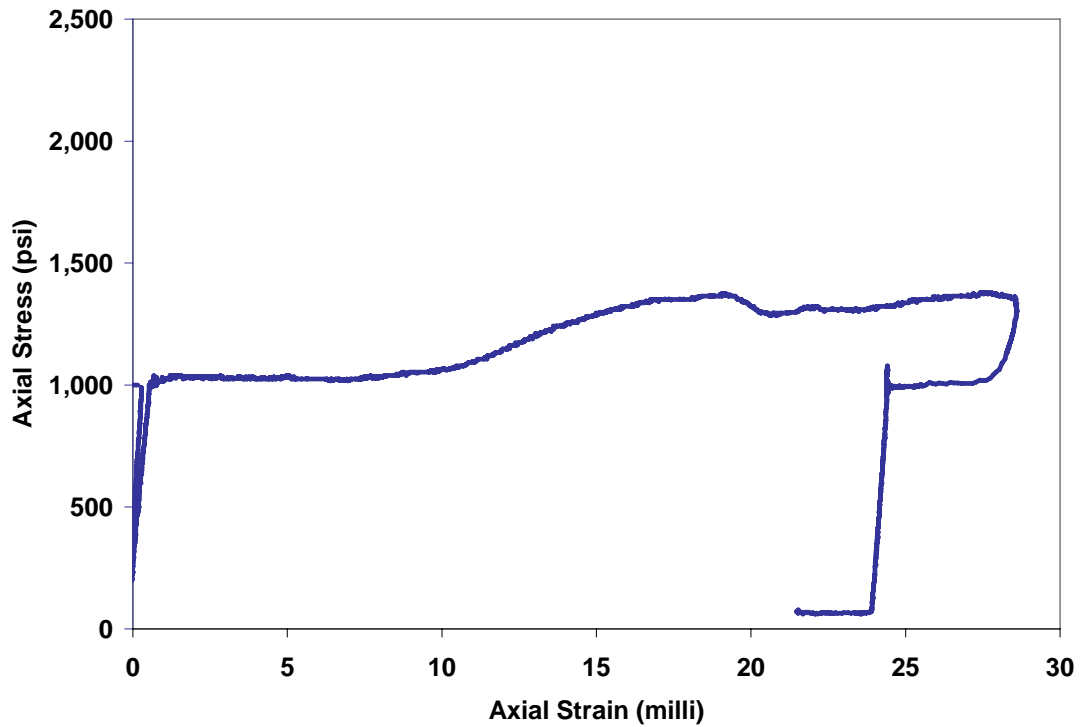


Figure 44. Stress-strain behavior of Mix 1 specimen #III-2 after curing for 14 hours.

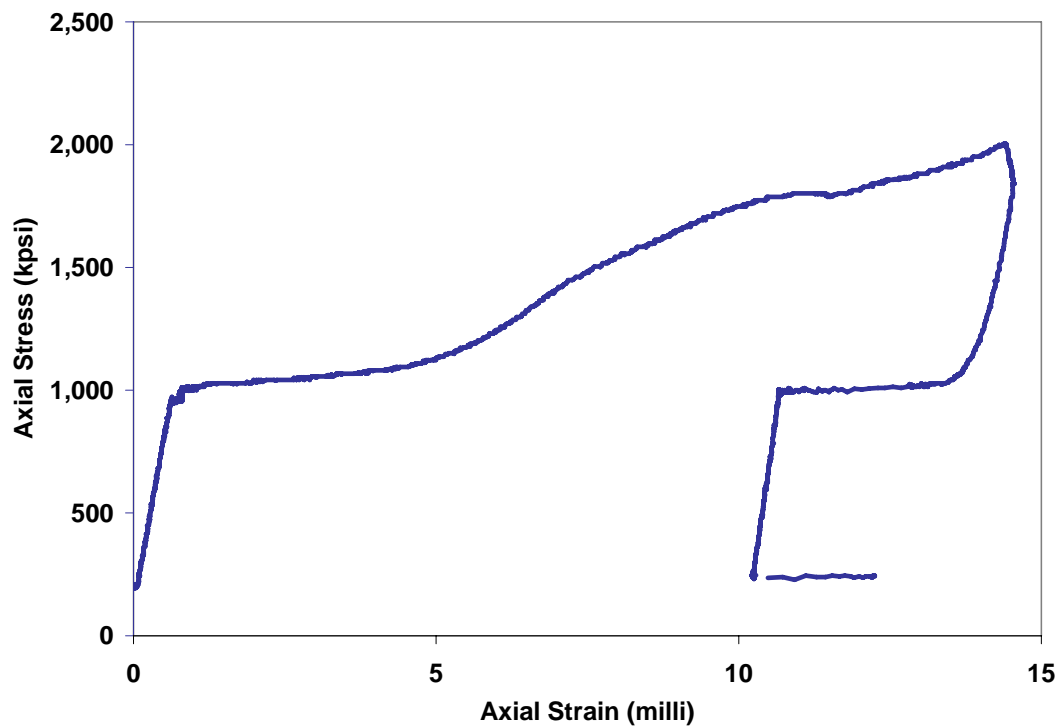


Figure 45. Stress strain behavior of Mix 1 specimen # II-8 (data from Figure 24) after curing for 24 hours.

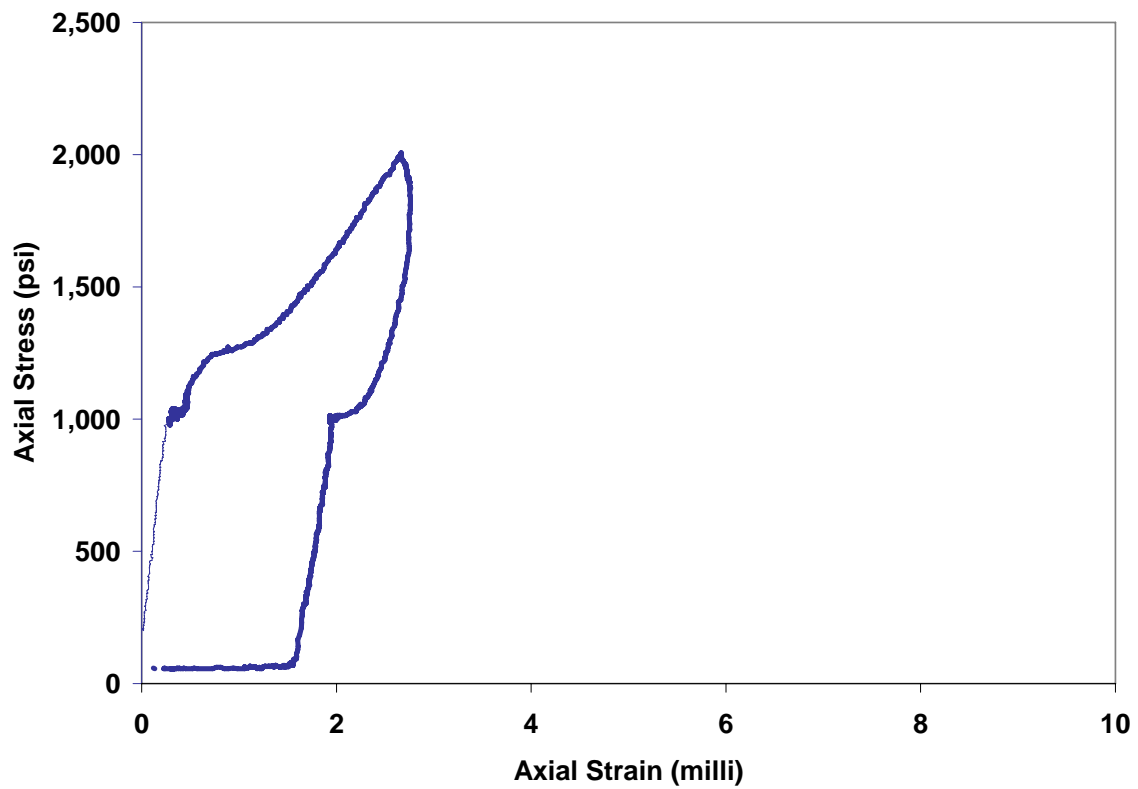


Figure 46. Stress strain behavior of Mix 1 Specimen #III-1 after curing for 36 hours.

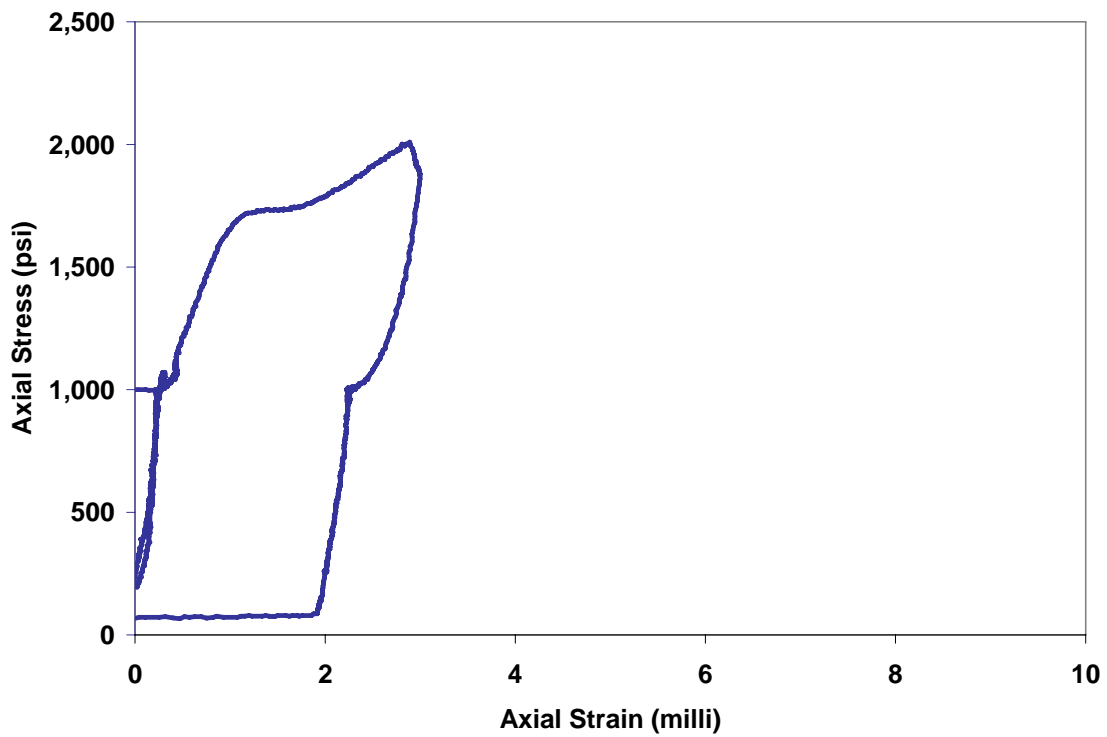


Figure 47. Stress strain behavior of Mix 1 specimen #III-3, after curing for 48 hours.

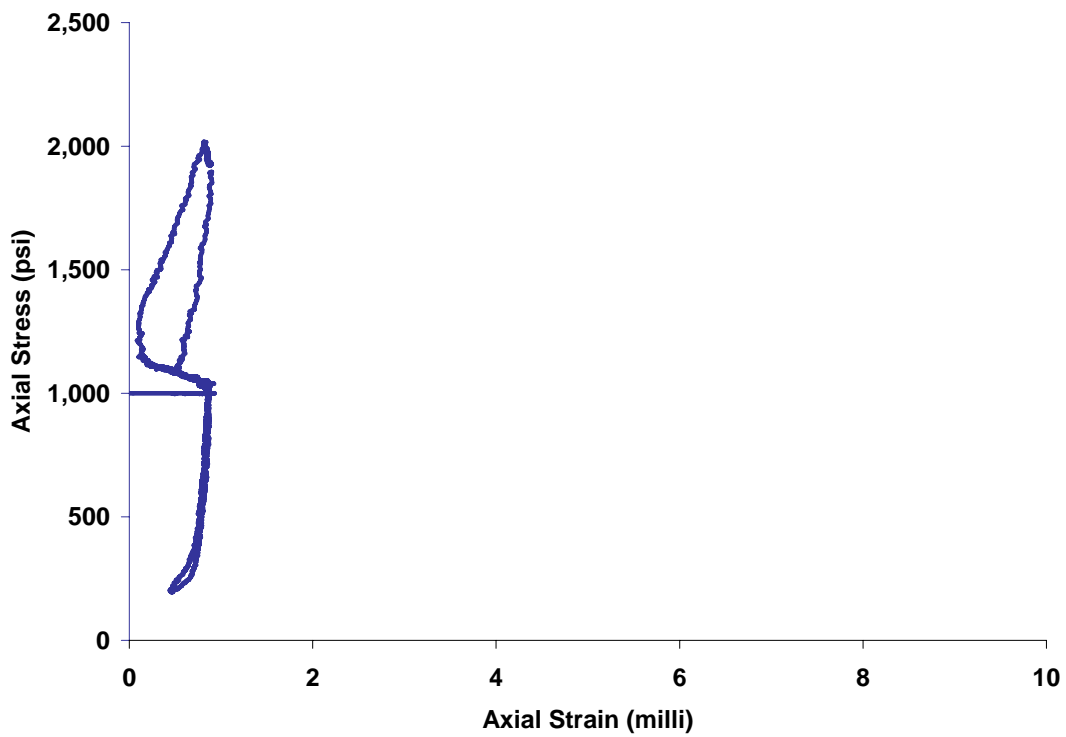


Figure 48. Stress strain behavior of Mix 1 specimen #III-4 after curing for 5 days.

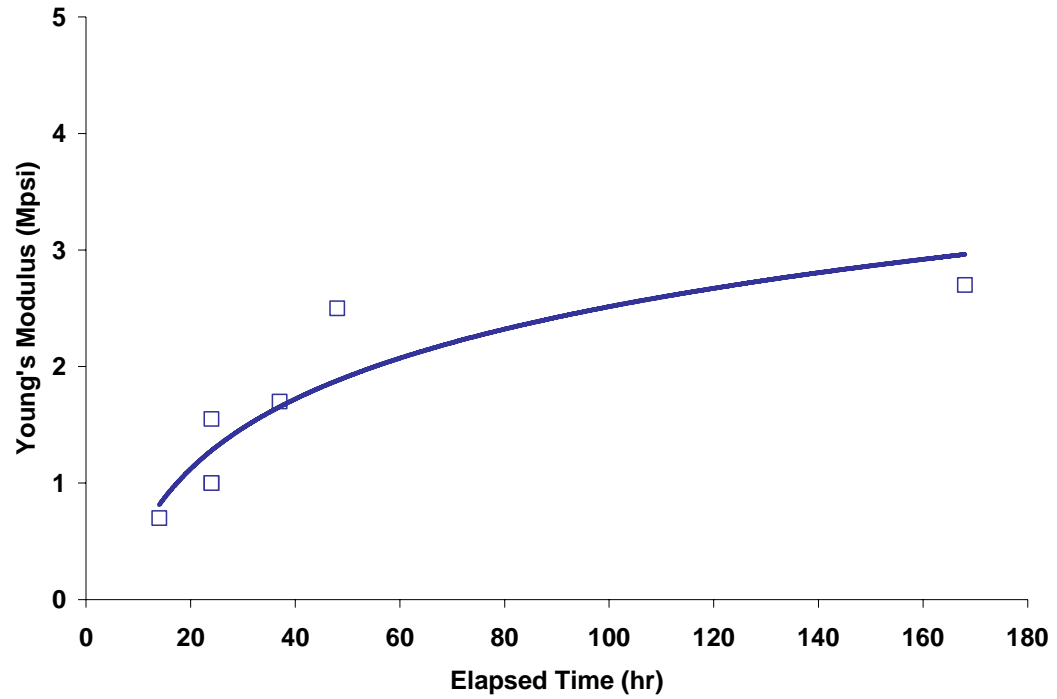


Figure 49. Variations in Young's modulus for Series III tests (data from Figures 44-48), for indicated curing times.

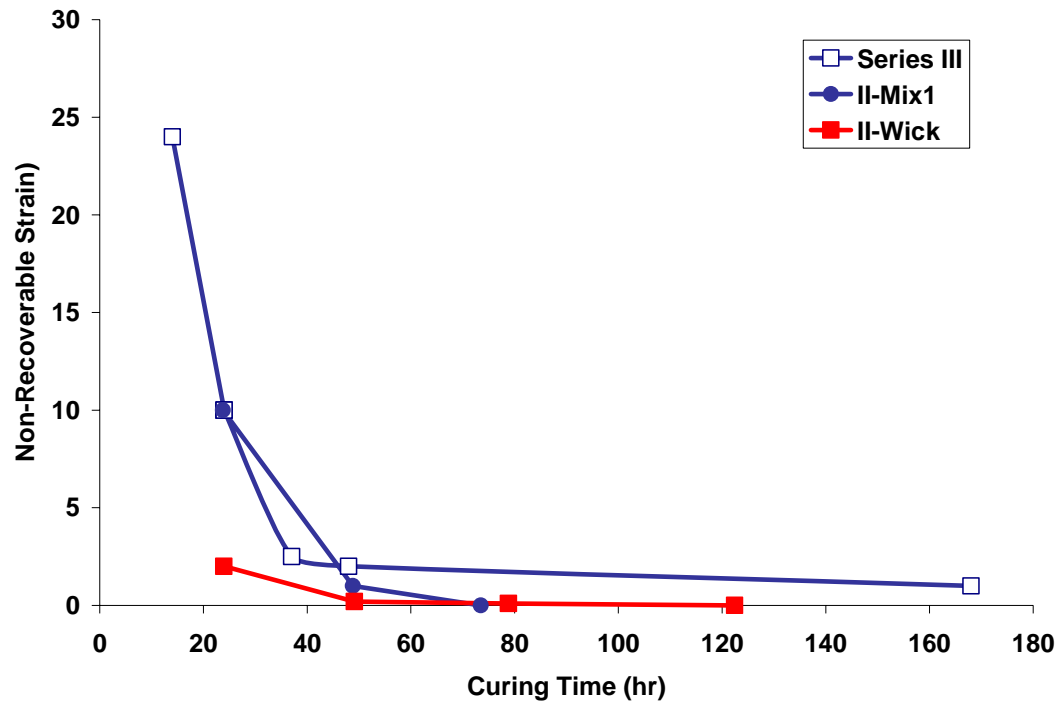


Figure 50. Non-recoverable strain from Series III tests (open squares; data shown in Figures 44 – 48) for indicated curing times. Mix 1 (filled circles) and wicked (filled squares) results from Series II tests shown for comparison.

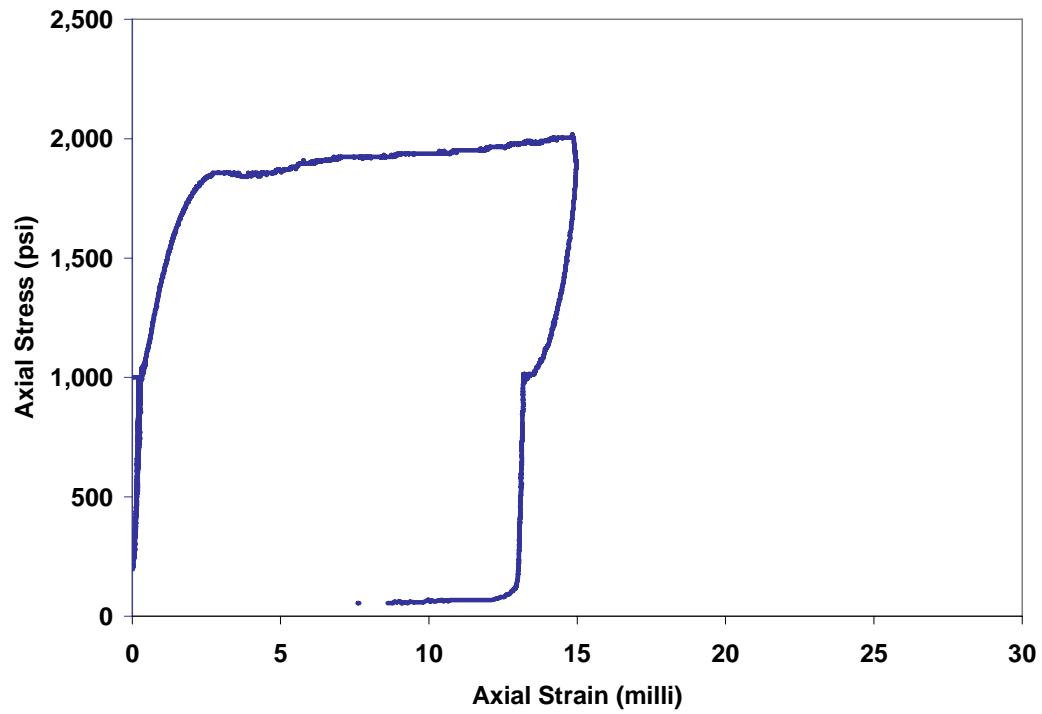


Figure 51. Stress – strain behavior for Mix 2 Specimen #IV-5, after curing for 14 hours.

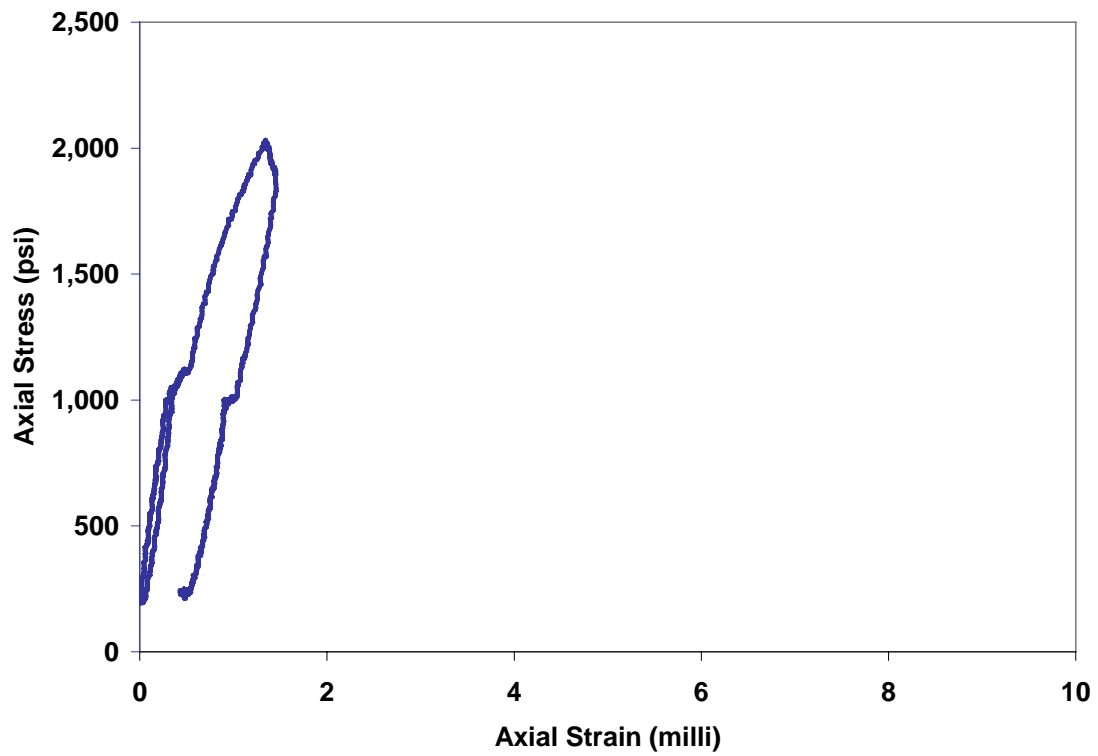


Figure 52. Stress – strain behavior for Mix 2 Specimen #II-6, after curing for 24 hours.

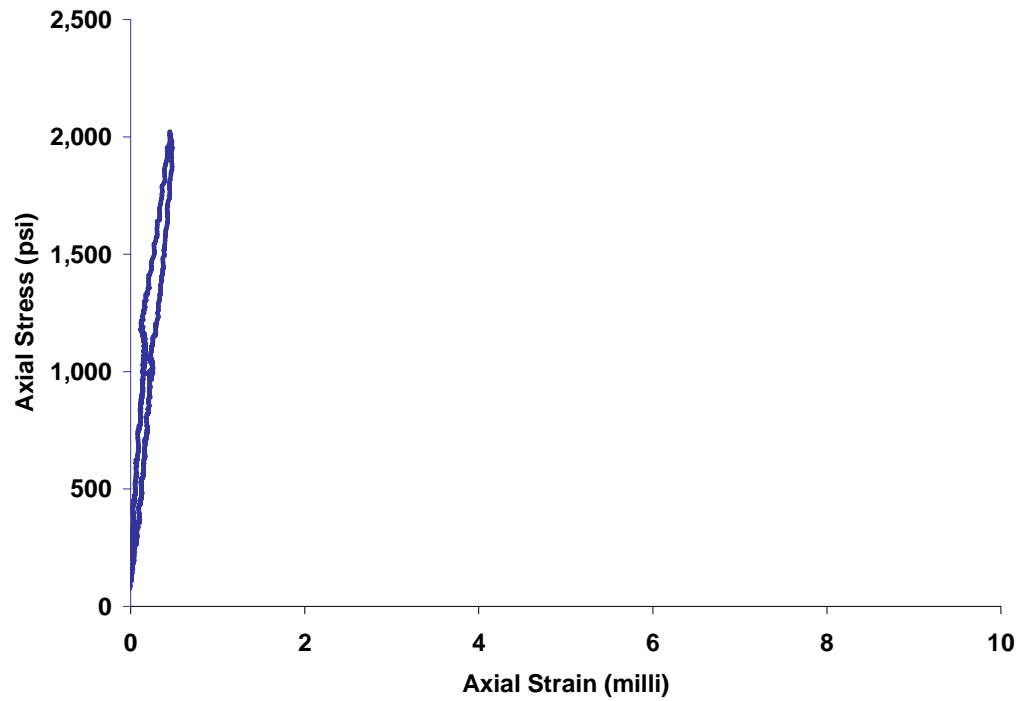


Figure 53. Stress – strain behavior for Mix 2 Specimen #IV-2, after curing for 36 hours

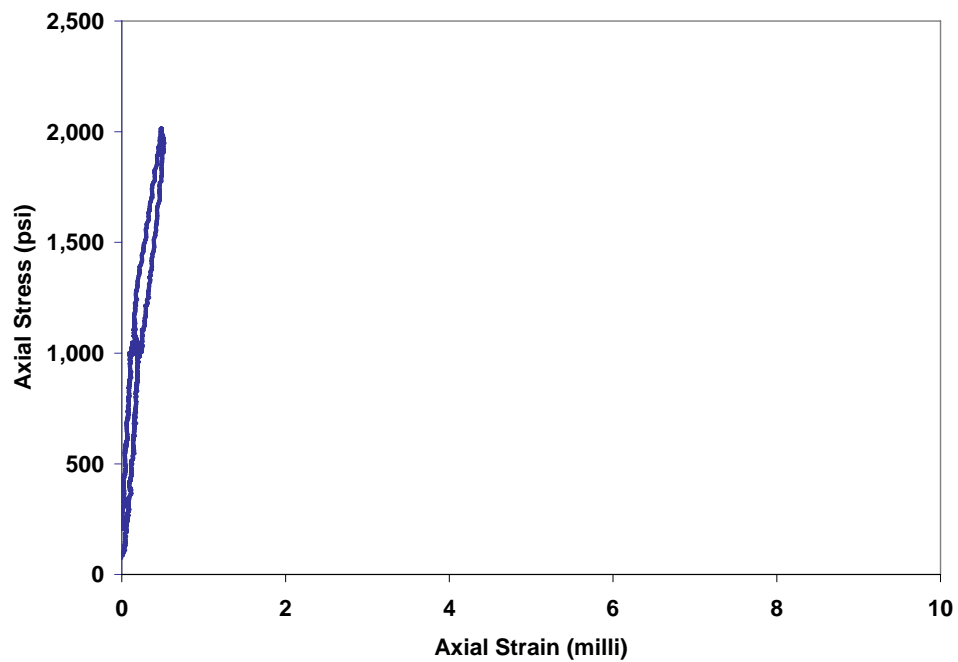


Figure 54. Stress – strain behavior for Mix 2 Specimen #IV-3, after curing for 48 hours

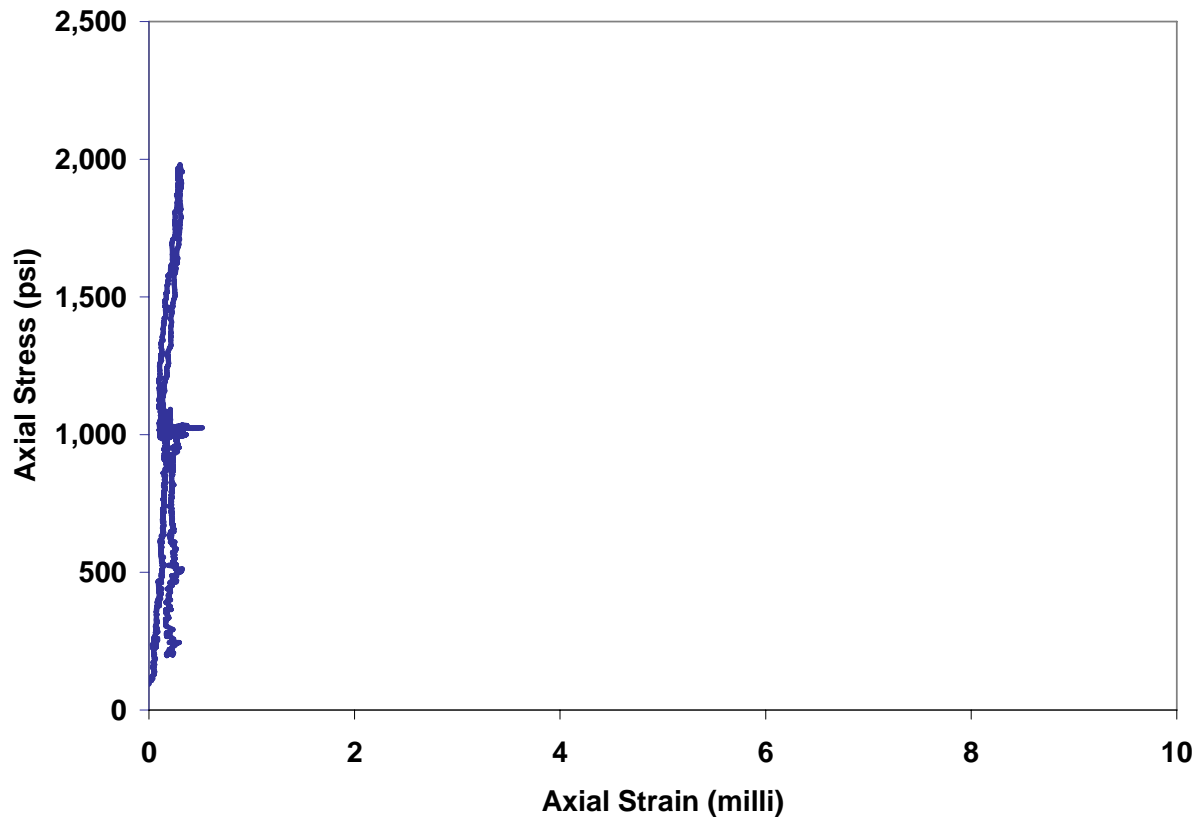


Figure 55. Stress – strain behavior for Mix 2 Specimen #IV-3, after curing for 48 hours.

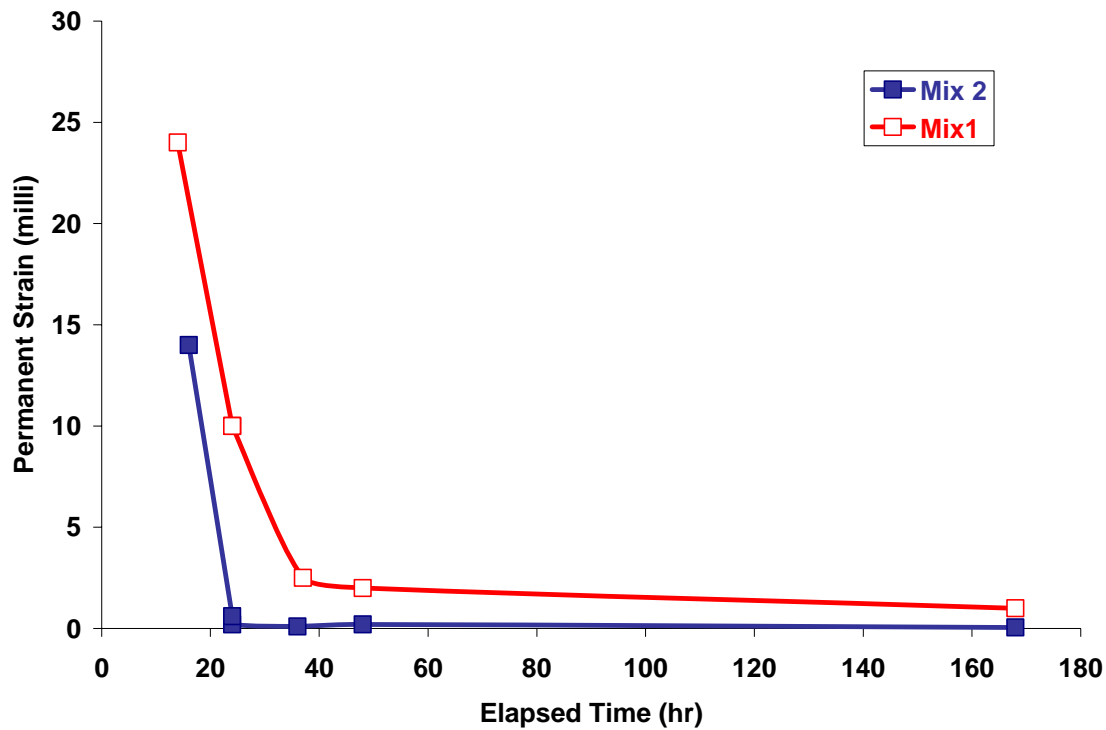


Figure 56. Variations in non-recoverable strain with curing time Series IV tests (Mix 2) specimen (filled squares). Series III test results (Mix 1, open squares) shown for comparison.

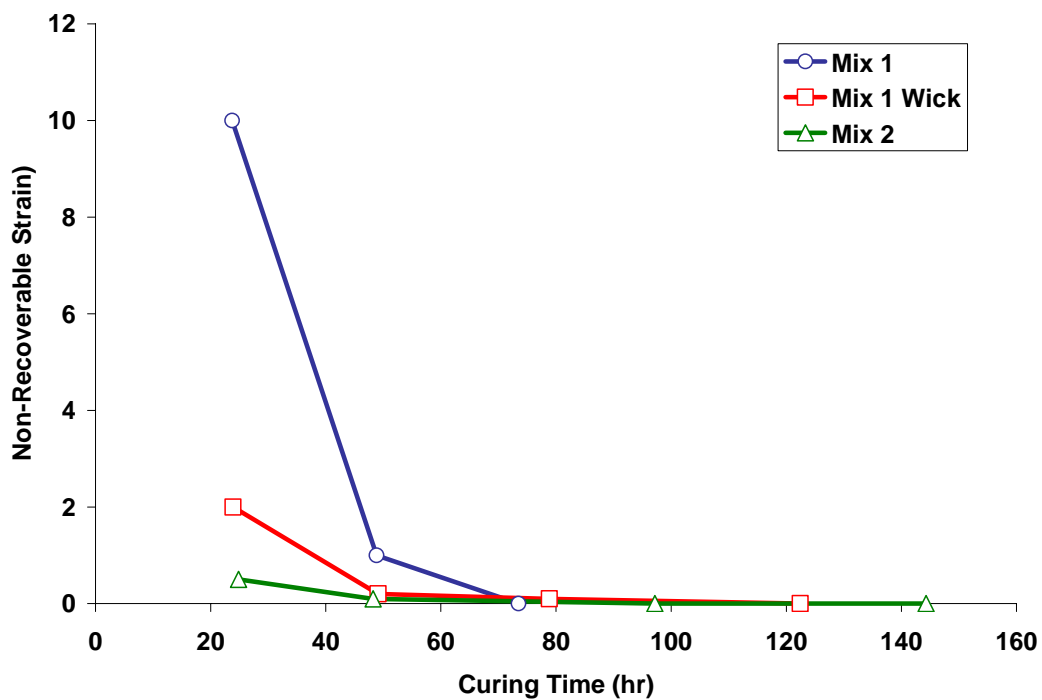


Figure 57. Non-recoverable strain for repeated deformations as functions of curing times,, from data shown in Figures 44-48.

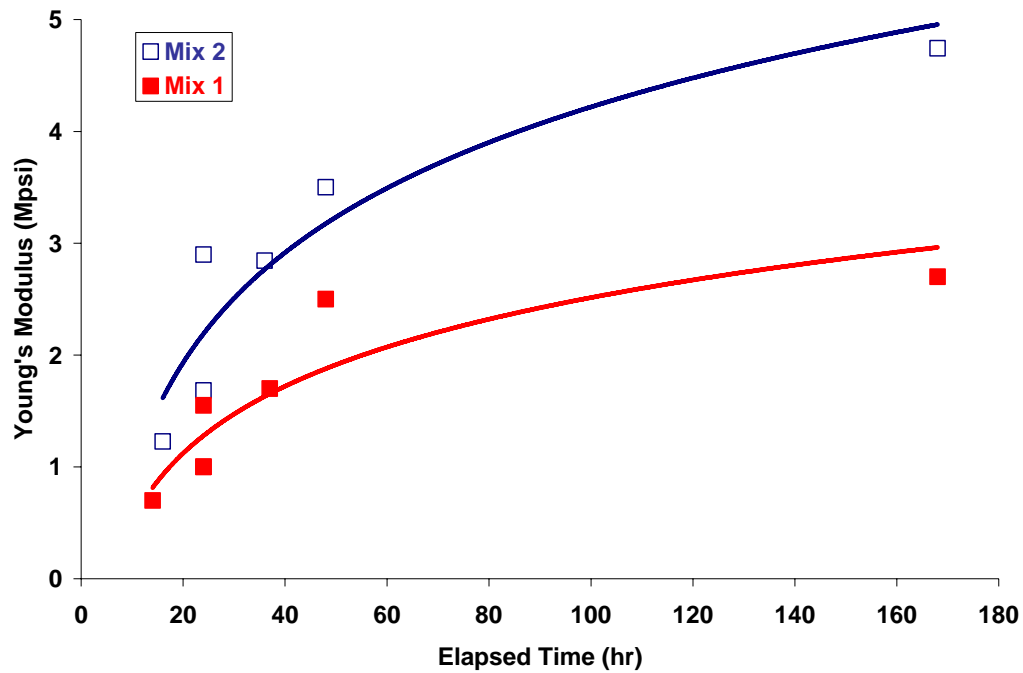


Figure 58. Variations in Young's modulus with curing time for Series IV tests (Mix 2) specimen (open squares). Series III test results (Mix1, filled squares) shown for comparison.

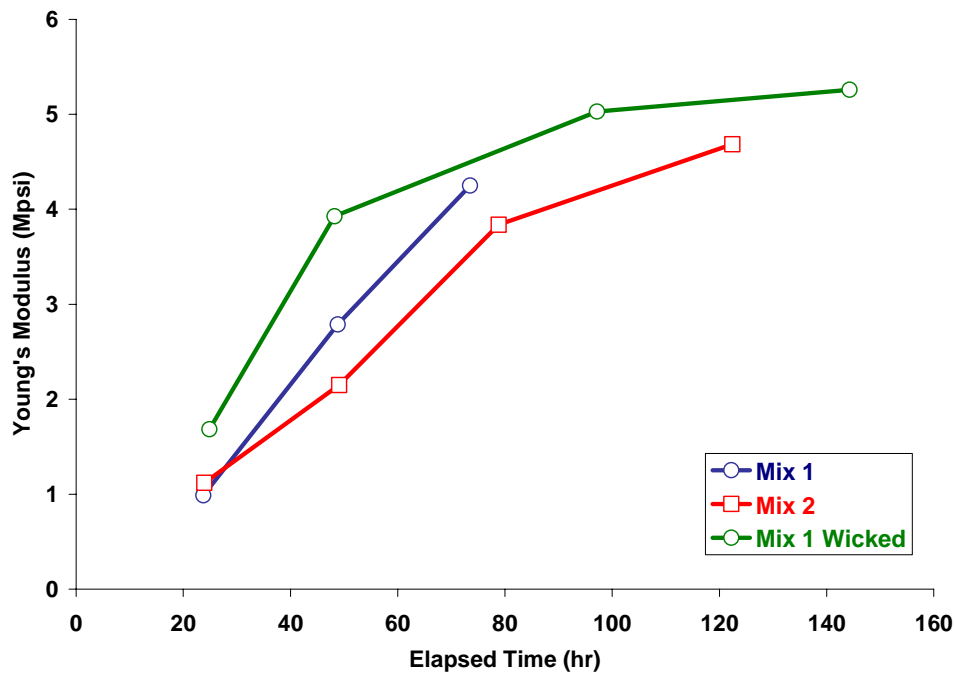


Figure 59. Variations in Young's modulus from unloading data of repeat tests on specimens as function of curing time, from data shown in Figures 44-48.

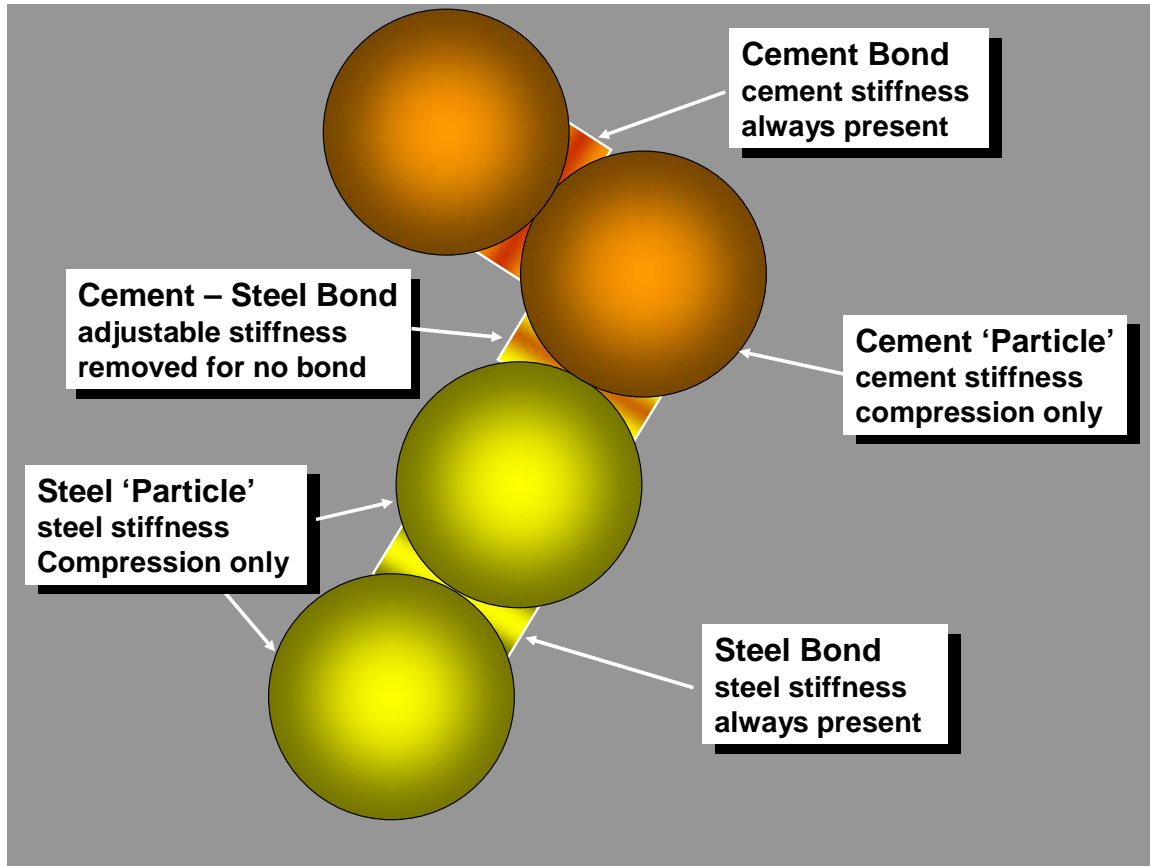


Figure 60. Particle interaction in PFC2D assembly.

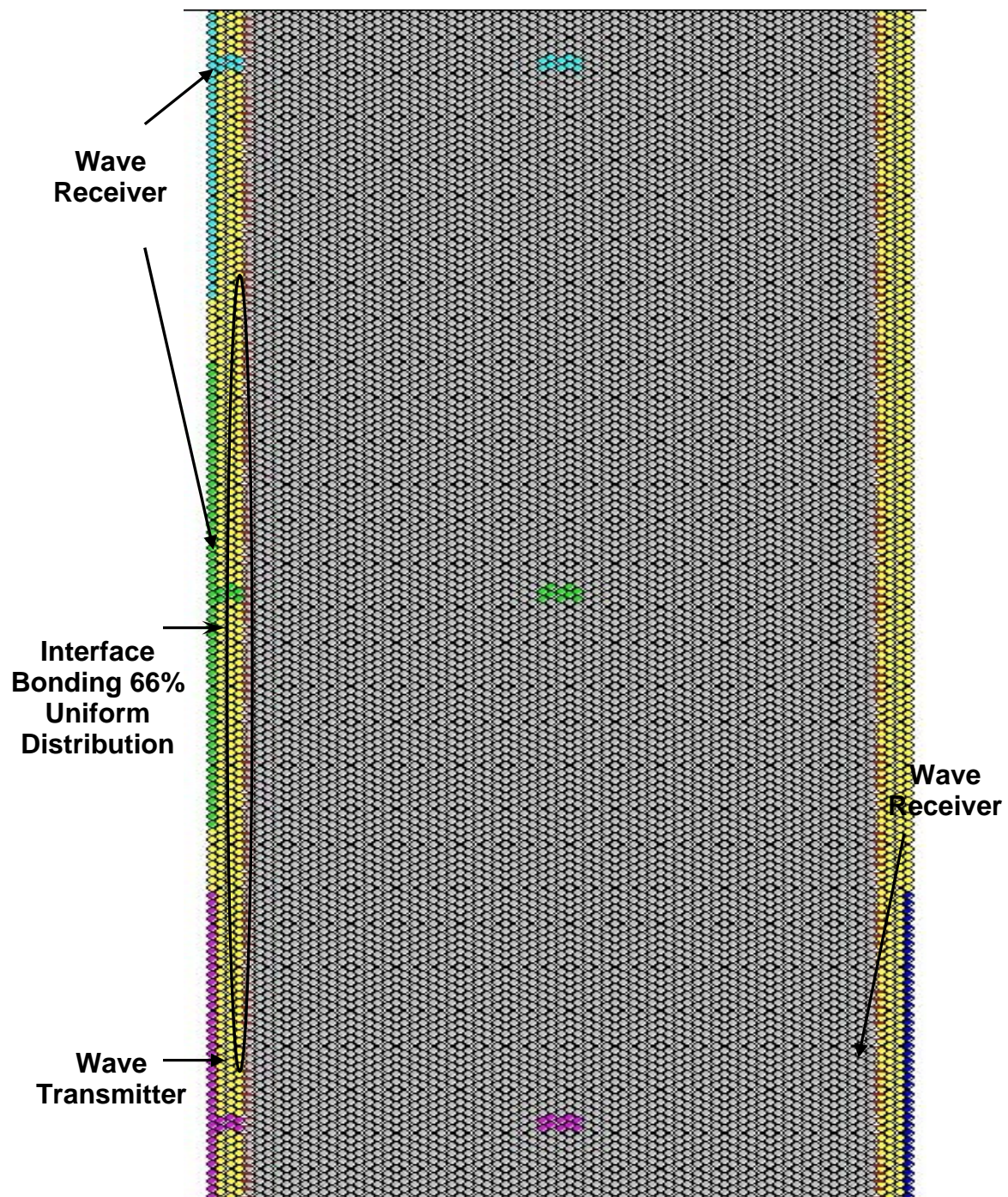


Figure 61. Model assembly in PFC2D with imbedded wave transmitter and receivers. The figure has been enlarged slightly to provide more detail; not all of the assembly is shown.

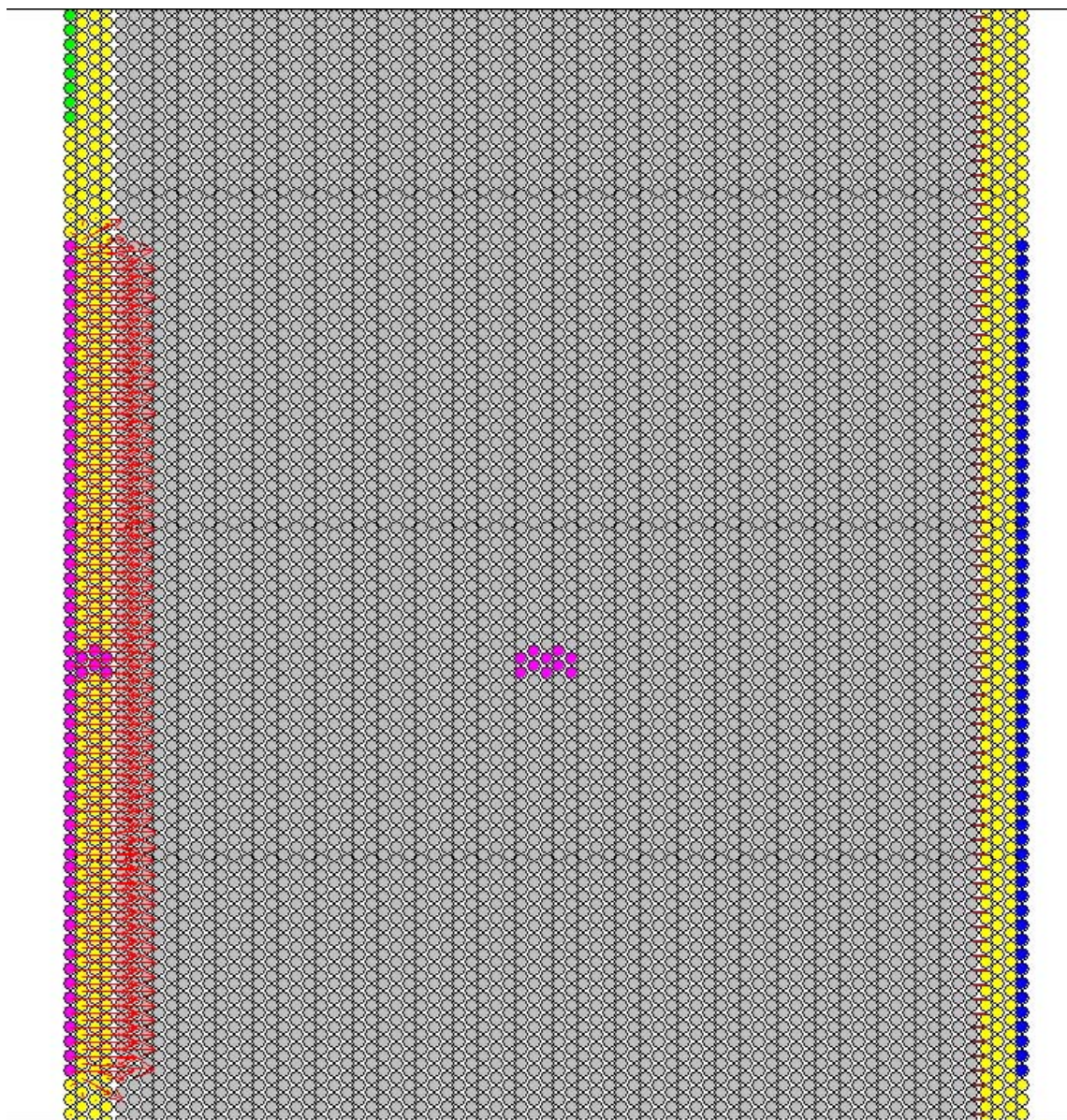


Figure 62. Wave input in modeled assembly. Red arrows, which represent the velocity of the particles, designate the location of wave in the sample

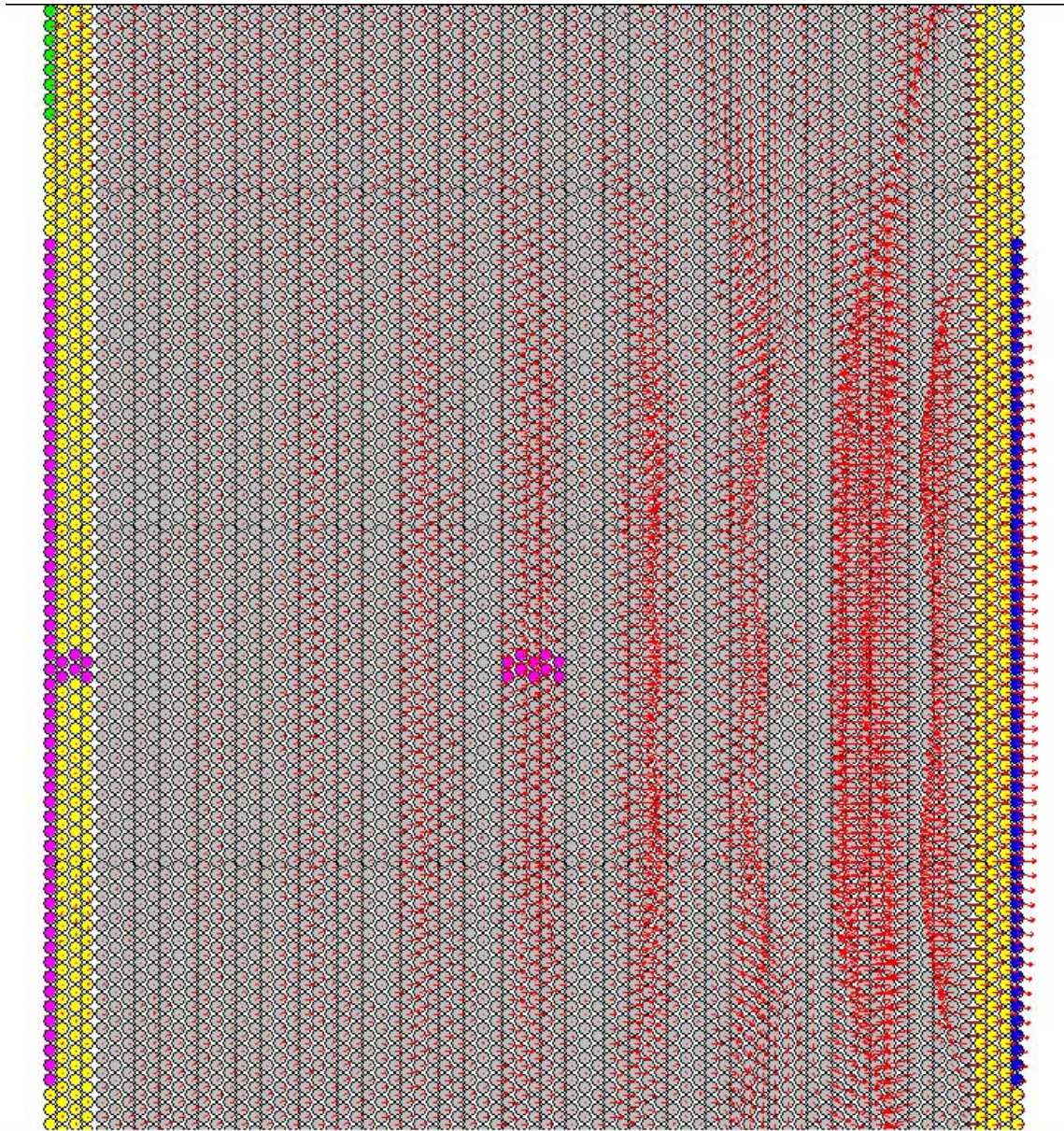


Figure 63. Wave input in model assembly after a lapse in time.

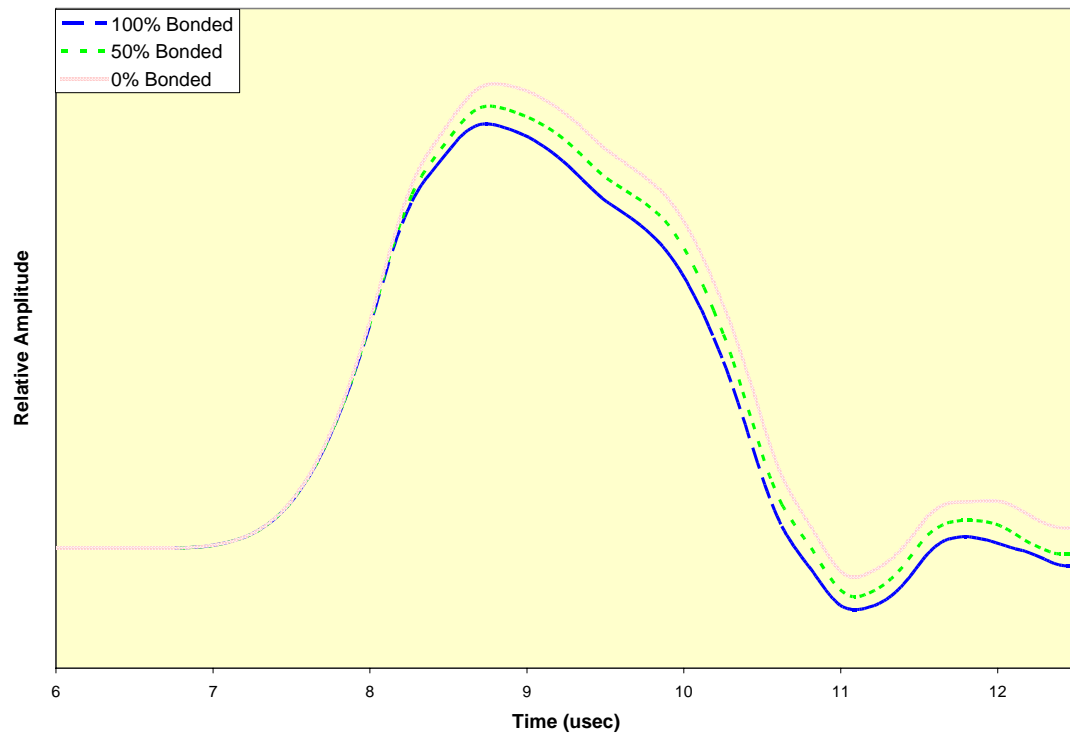


Figure 64. Effects of incomplete bonding on wave amplitude. The wave propagation propagates through the steel parallel to the steel-cement interface. The percentage of the steel-cement interface that is bonded is specified in the legend.

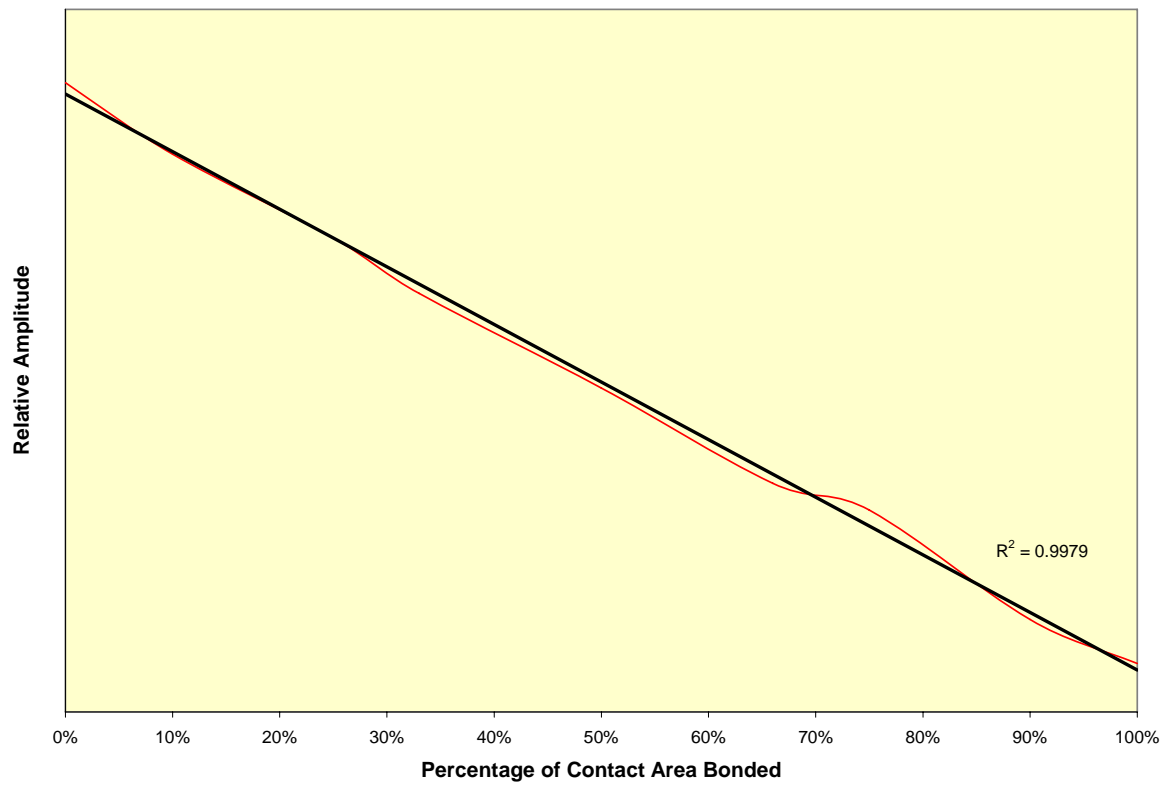


Figure 65. Relationship between p-wave amplitude and the fraction of intact bonds between the steel and the cement.

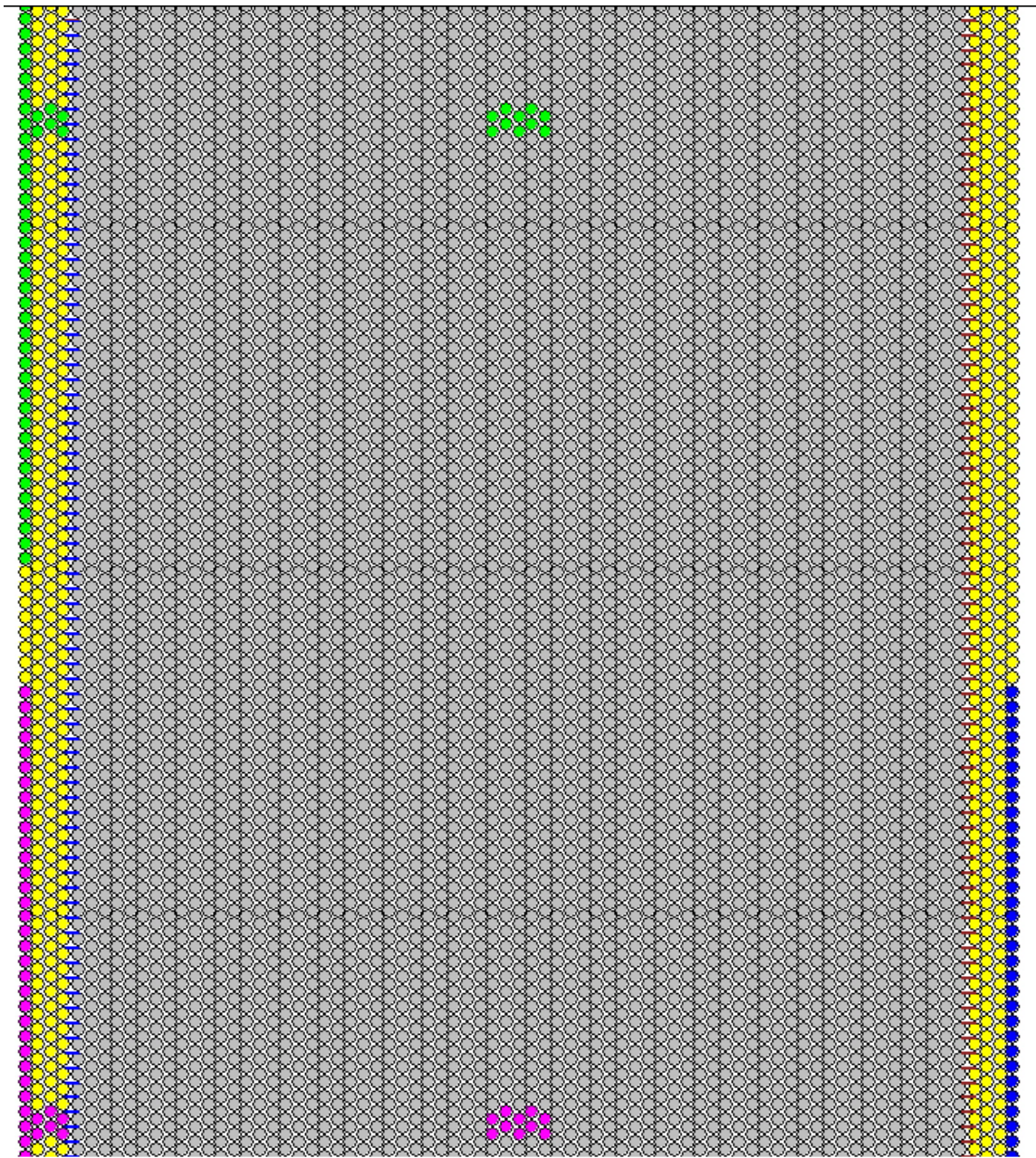


Figure 66. Model assembly with non-uniform distribution of intact bonds (blue lines) across the steel-cement interface on the left side of the assembly. Although all bonds in the portion of the interface shown are intact, only 66% of the total number of interface bonds on the left side of the assembly are intact. This distribution of interface bonds is designated as non-uniform Case 1 in Figure 68.

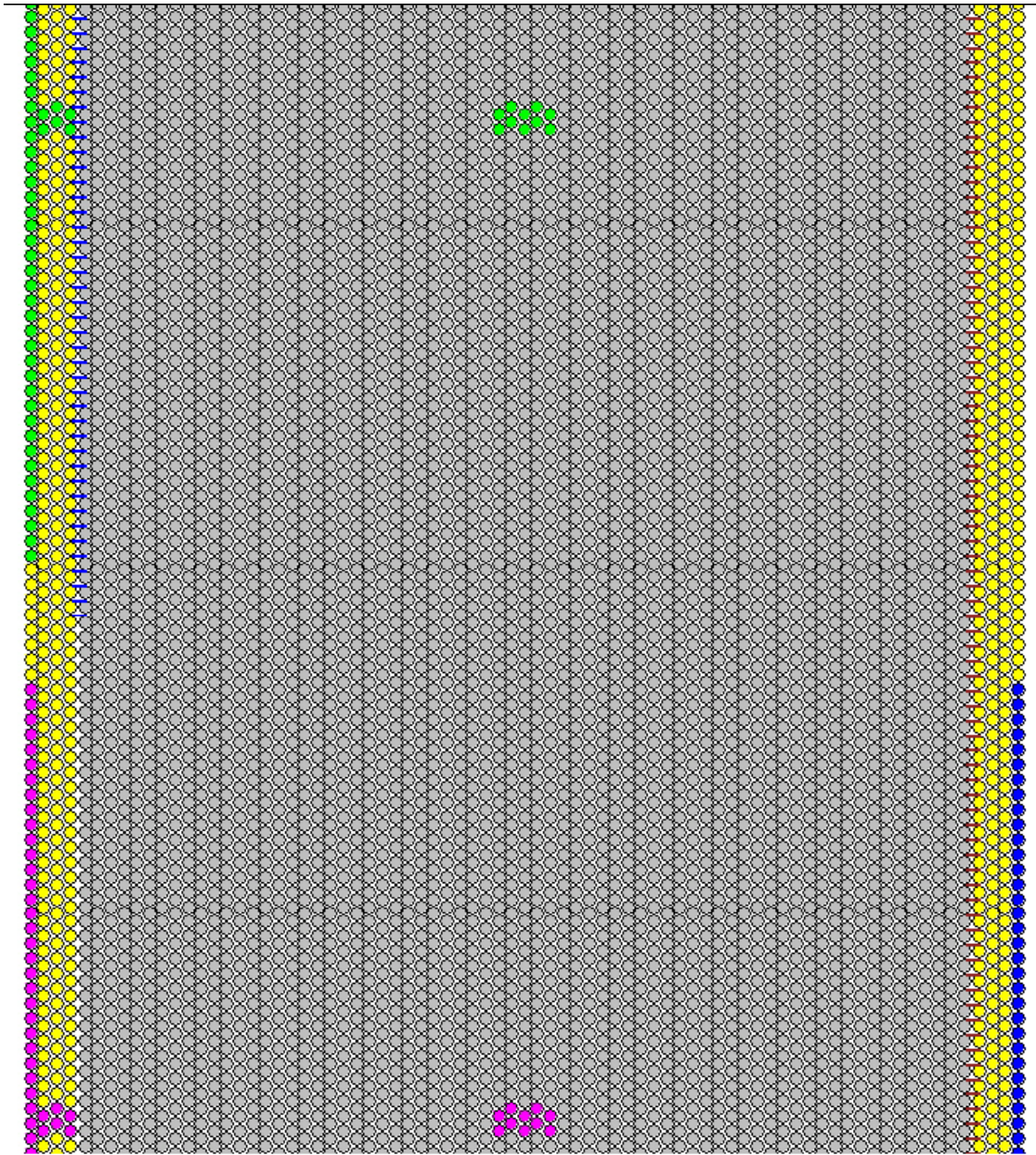


Figure 67. Model assembly with non-uniform distribution of intact bonds (blue lines) across the steel-cement interface on the left side of the assembly. Bonds in this assembly are clustered in the top half of the sample; 66% of total particle pairs along the left side interface are bonded, whereas the steel-cement interface is bonded for only half of the distance between the transmitter and the receiver, and totally un-bonded along the transmitter region. This distribution is labeled as non-uniform Case 2 in Figure 68.

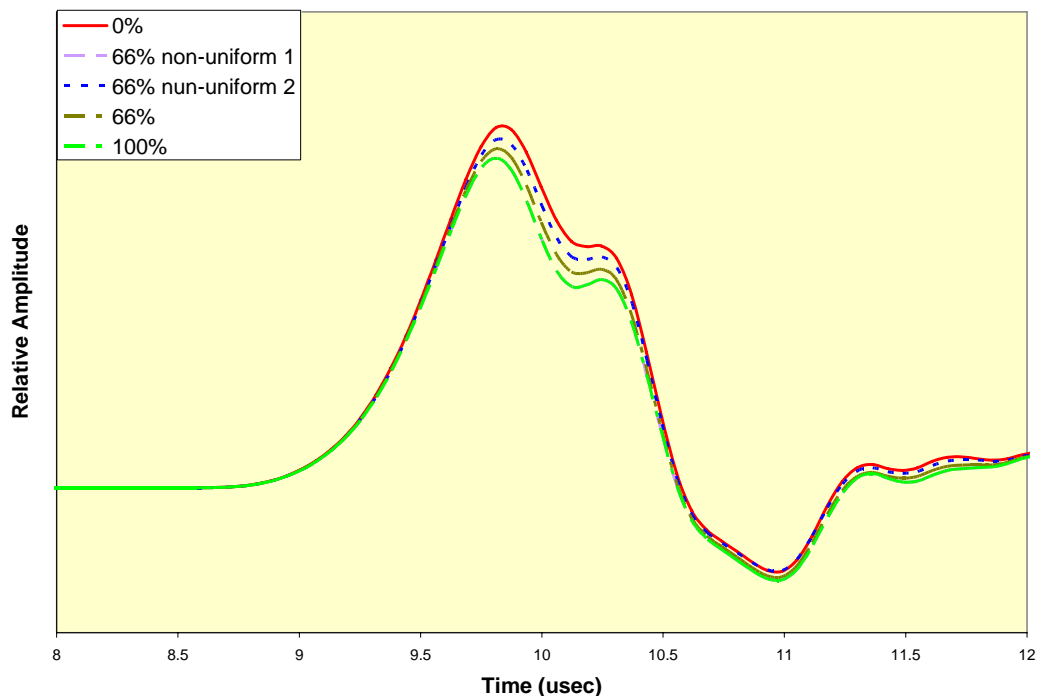


Figure 68. Non-Uniform bonding with uniform bonding waveforms as a reference. Waves propagated through the steel, parallel to the steel-cement interface on the left side of the sample. The bonding at the steel-cement interface is indicated in the legend. Non-uniform 1 and non-uniform 2 refer to the bonding states depicted in Figures 66 and 67, respectively.

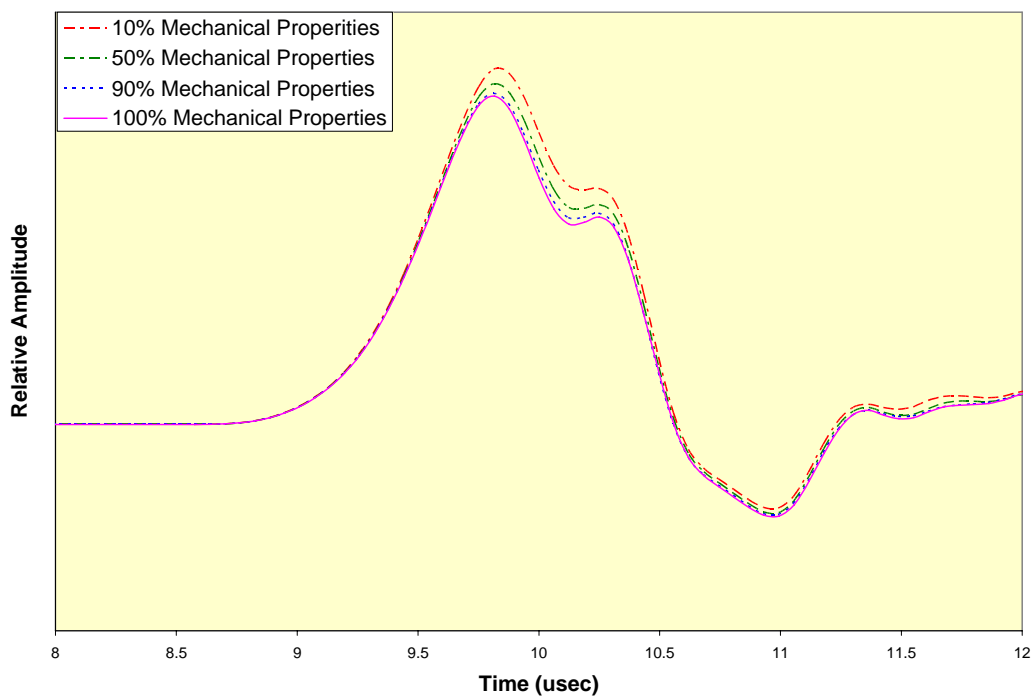


Figure 69. Wave propagation in steel, with 100% of contact area bonded at the steel-cement interface. Mechanical Properties of the bonds for each waveform is given in the legend, as a percentage of the mechanical properties of the cement.

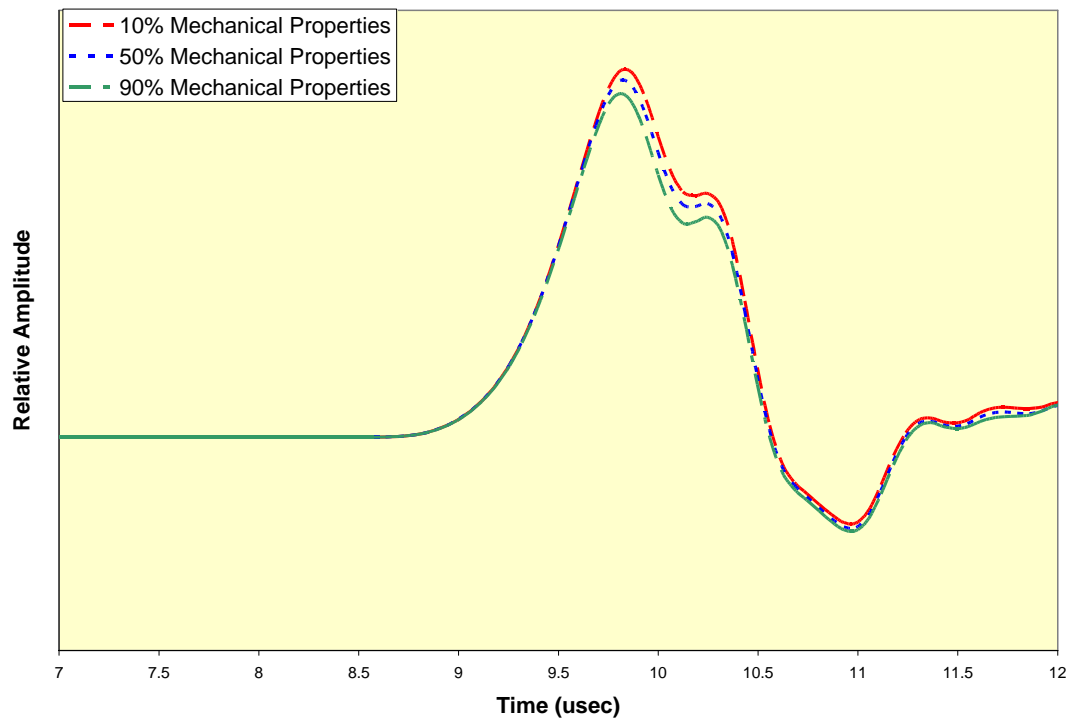


Figure 70. Wave propagation in steel 90% of contact area bonded uniformly, with changing mechanical properties of the bonding at the steel-cement interface

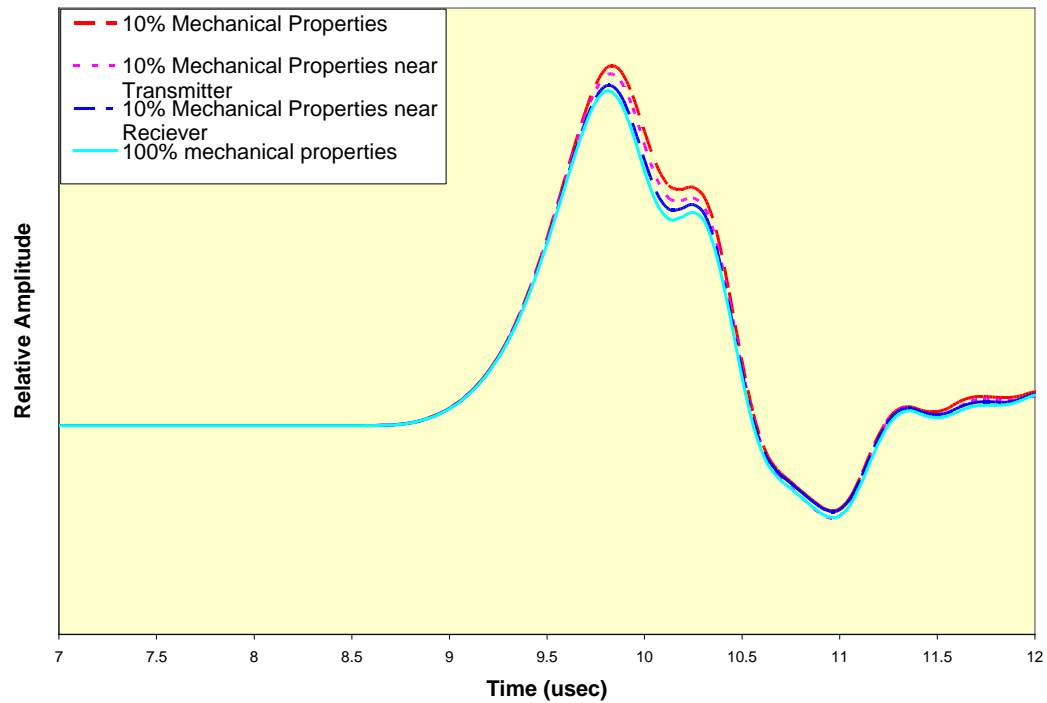


Figure 71. Effects of placement of zones of altered mechanical properties between the receivers. In these simulations 90% of the bonds at the steel-cement interface are intact. The simulations were carried out with altered mechanical properties for half the distance between the transmitter and receiver, in a region located either near the transmitter or the receiver. The behavior for these distributions are compared with that of uniformly distributed bonds with altered properties.

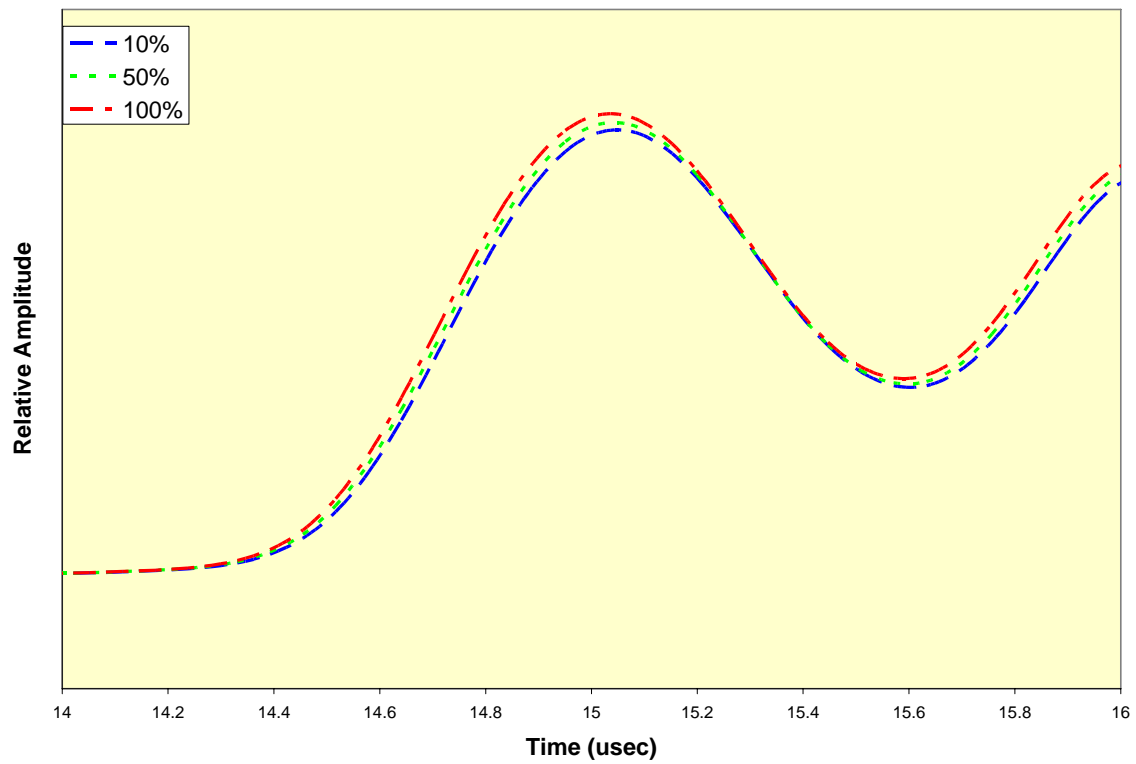


Figure 72. Amplitudes of detected p-waves propagating through the assembly from left to right, through steel, cement and then steel, with changing fractions of intact bonds at the steel-cement interface on the left side of the sample.

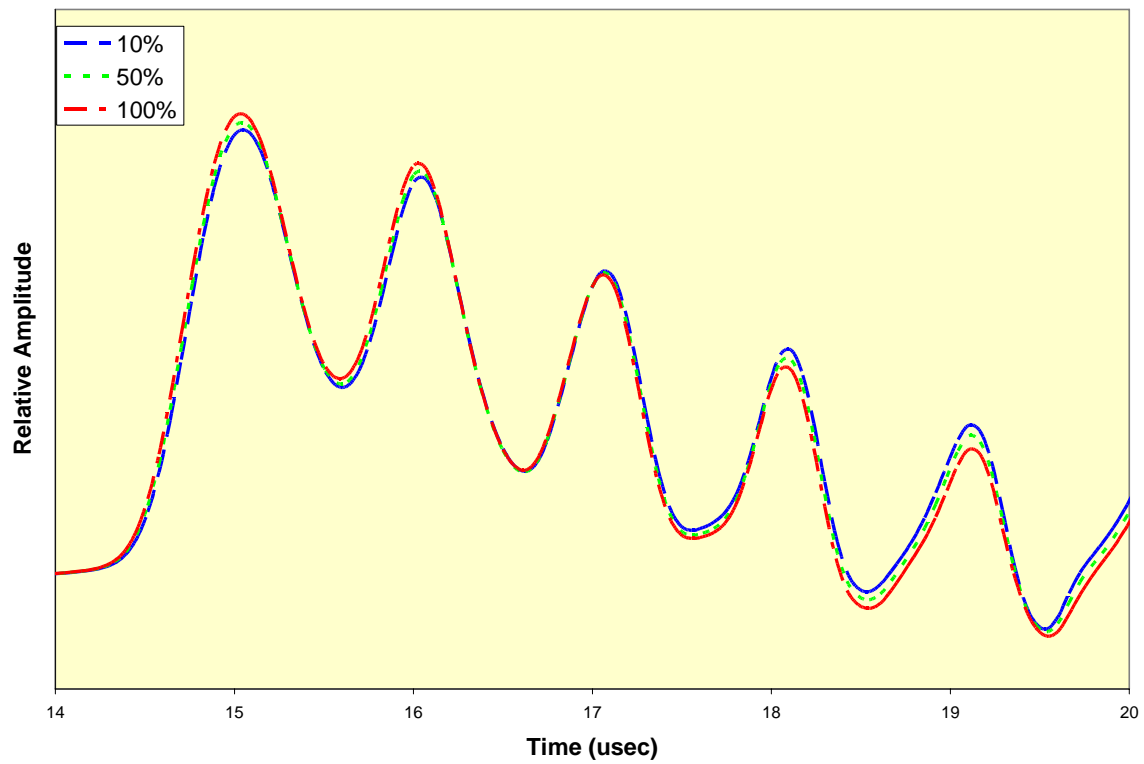


Figure 73. Same *p*-wave as in Figure 72, with expanded time scale to show high-frequency oscillations from multiple reflections within the steel 'casing'.

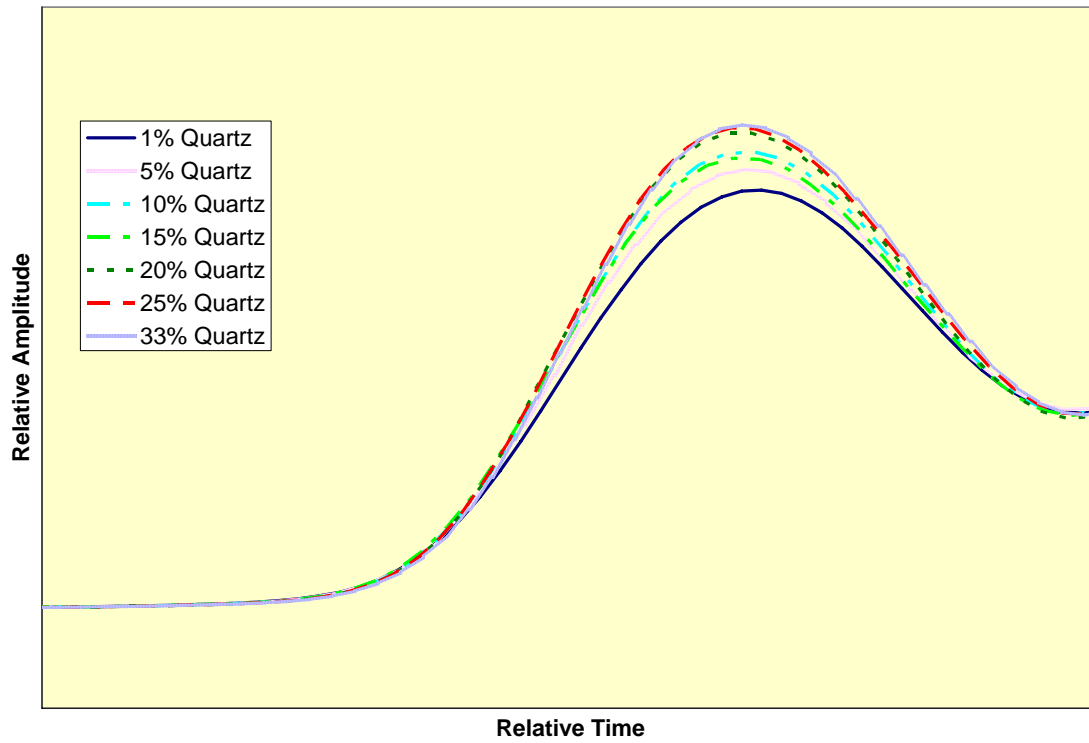


Figure 74. Propagation through assembly with the inclusion of quartz. The time scale has been altered so that the first arrival time of each waveform is the same. Arrival times were between 14 and 14.2 microseconds.

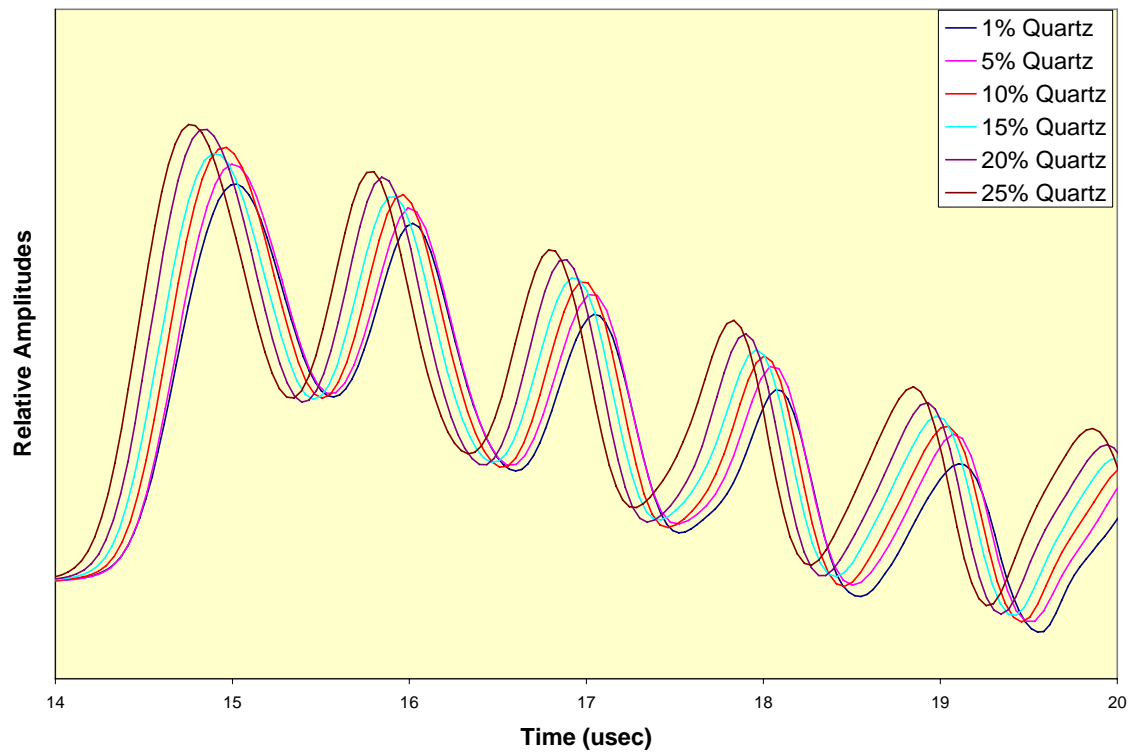


Figure 75. P-wave propagation through sample with added quartz, with expanded timescale to show high-frequency reflected waveforms.

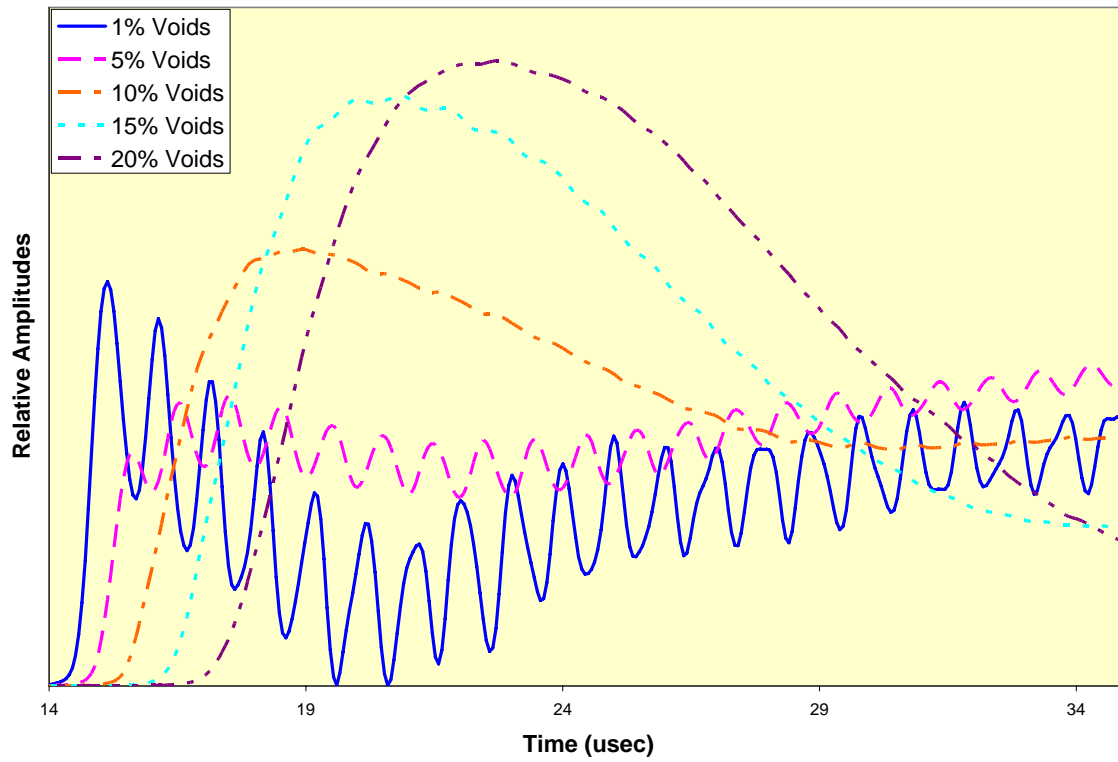


Figure 76. Propagation through the sample with void spaces added to the cement. Steel-cement interfaces are 100 % bonded with no quartz inclusions.

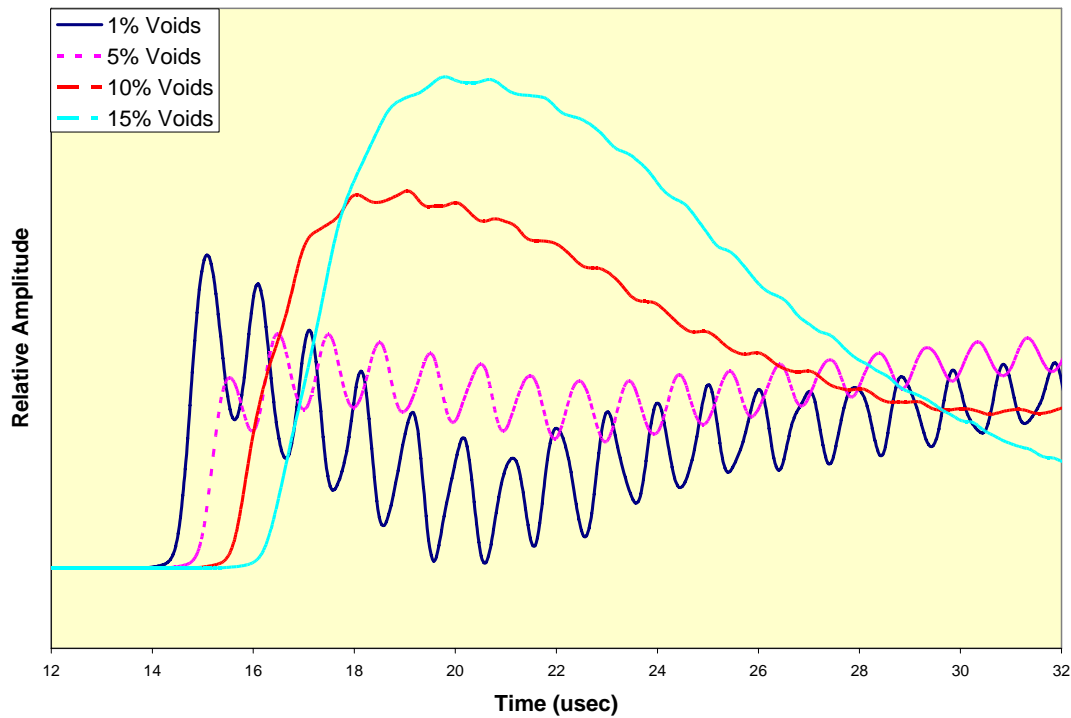


Figure 77. Detected *p*-waveforms for horizontal propagation through sample with a fixed 5% quartz and the indicated voids contents. All of the steel cement interface was bonded and the wave was propagated from a transducer on the left side of the sample to a receiver on the right side of the sample.

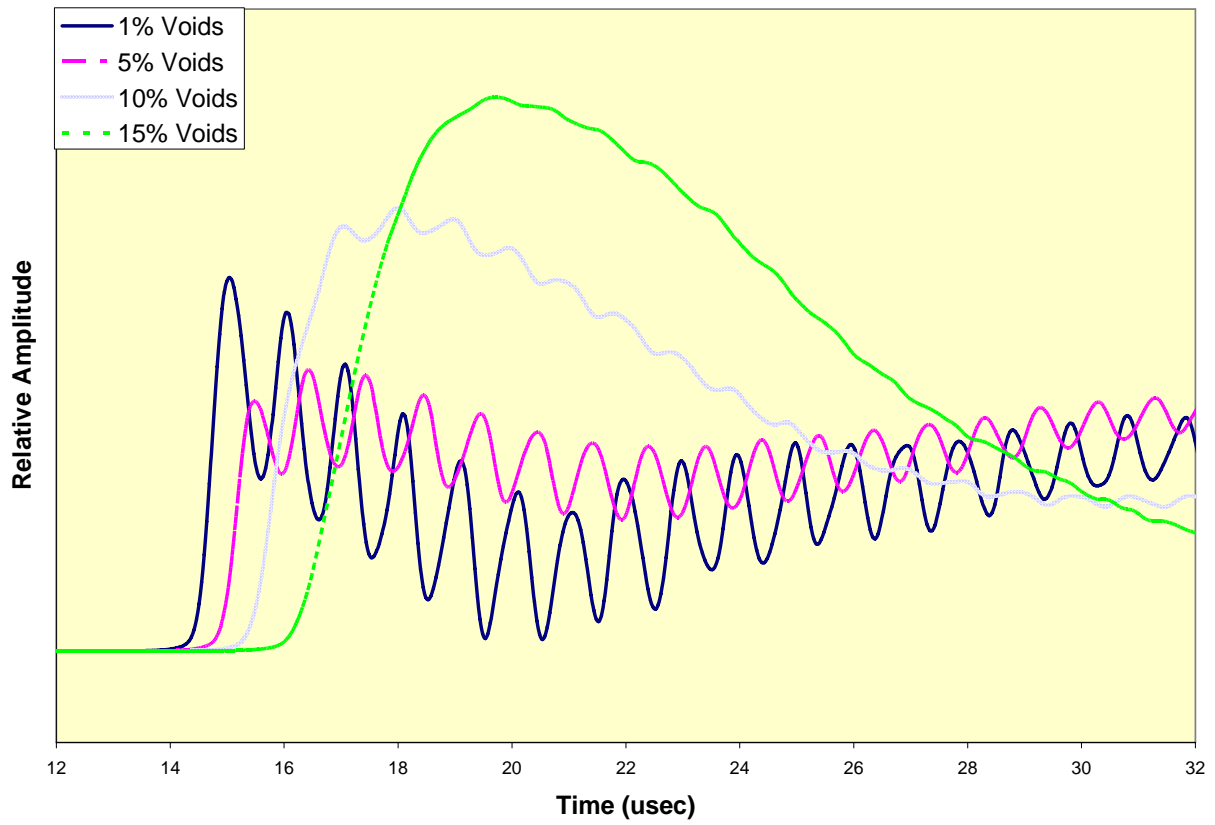


Figure 78. Horizontal propagation through assembly with 10% quartz.

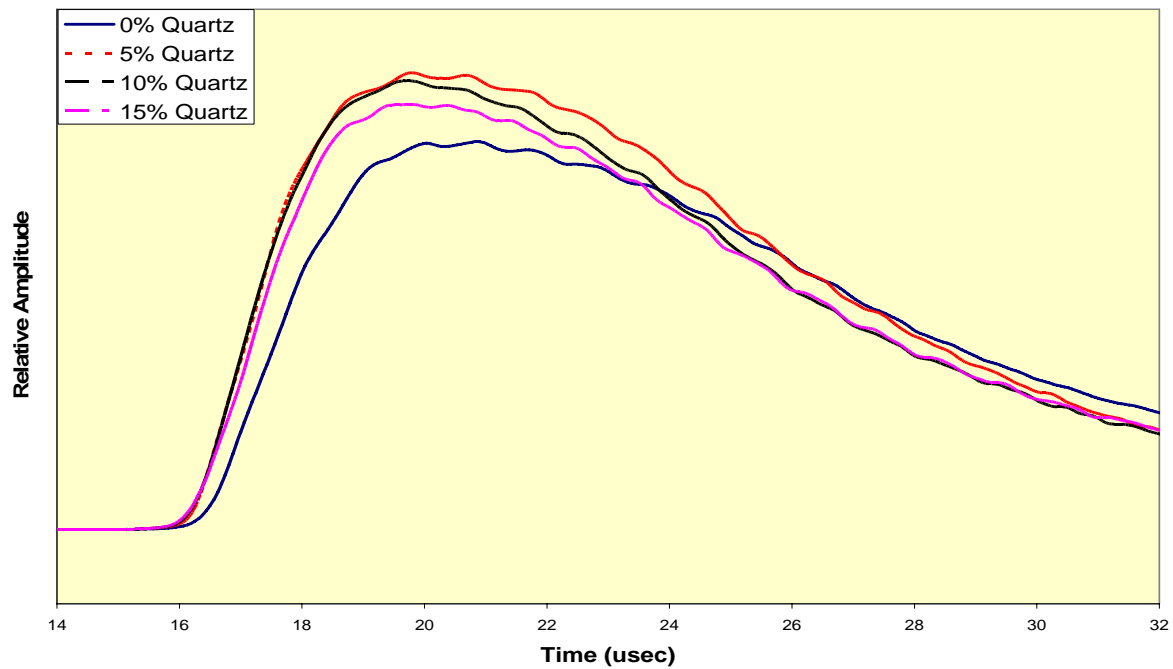


Figure 79. Horizontal propagation through cement with 15% voids. 100% of the steel cement interface was bonded and the wave was propagated from a transducer on the left side of the sample to a receiver on the right side of the sample

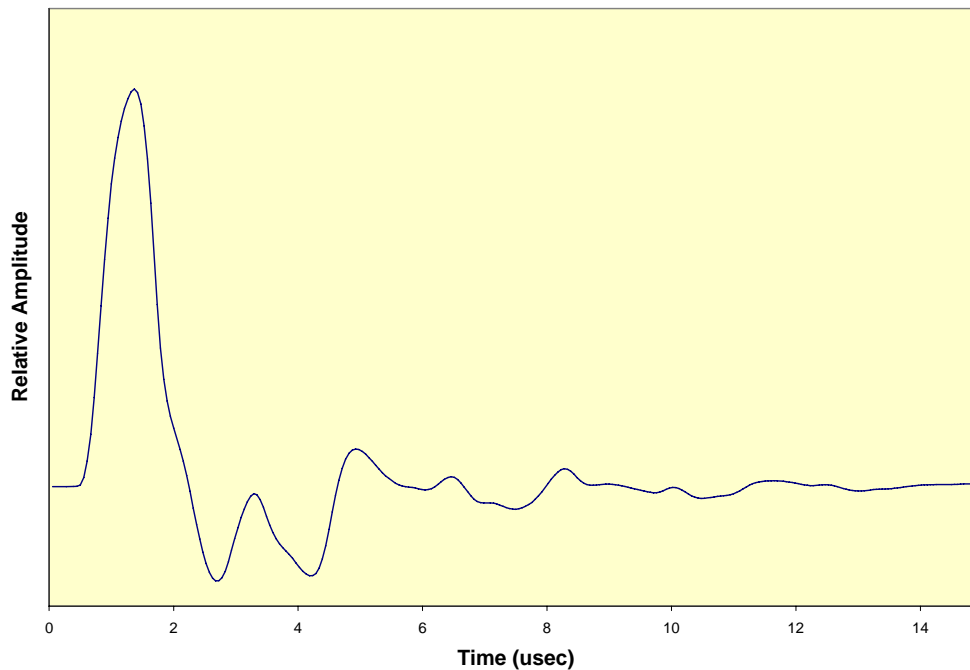


Figure 80. Horizontal p-wave in a sample with 5% quartz and 15% voids. Waveforms detected at a receiver near the steel-cement interface on the left side of the sample.

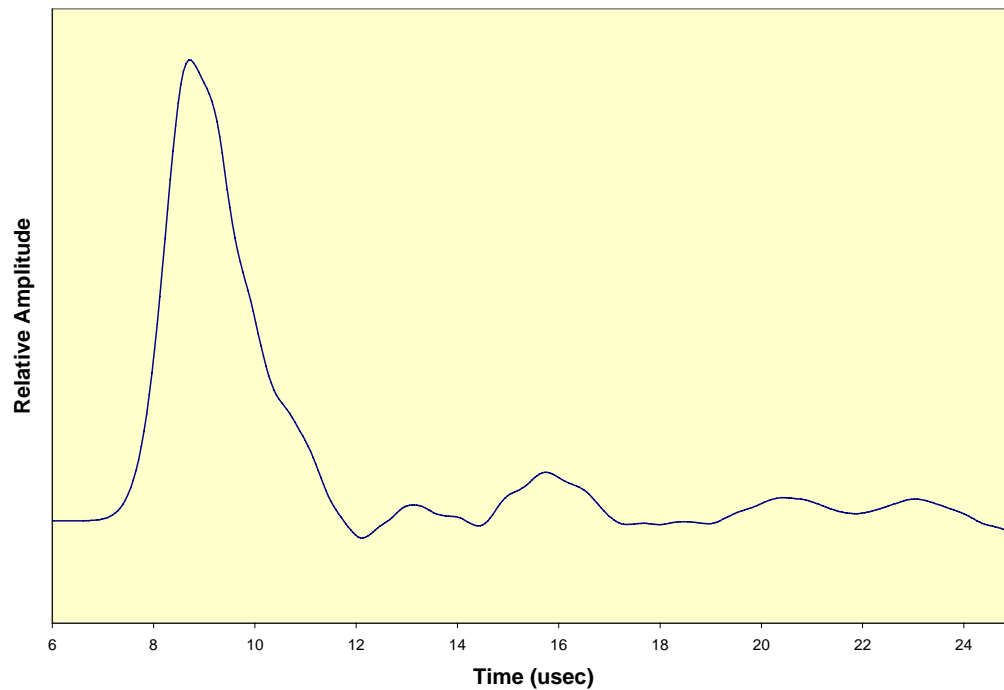


Figure 81. Horizontal wave in sample with 5% quartz and 15% voids. Waveforms detected midway through the cement.

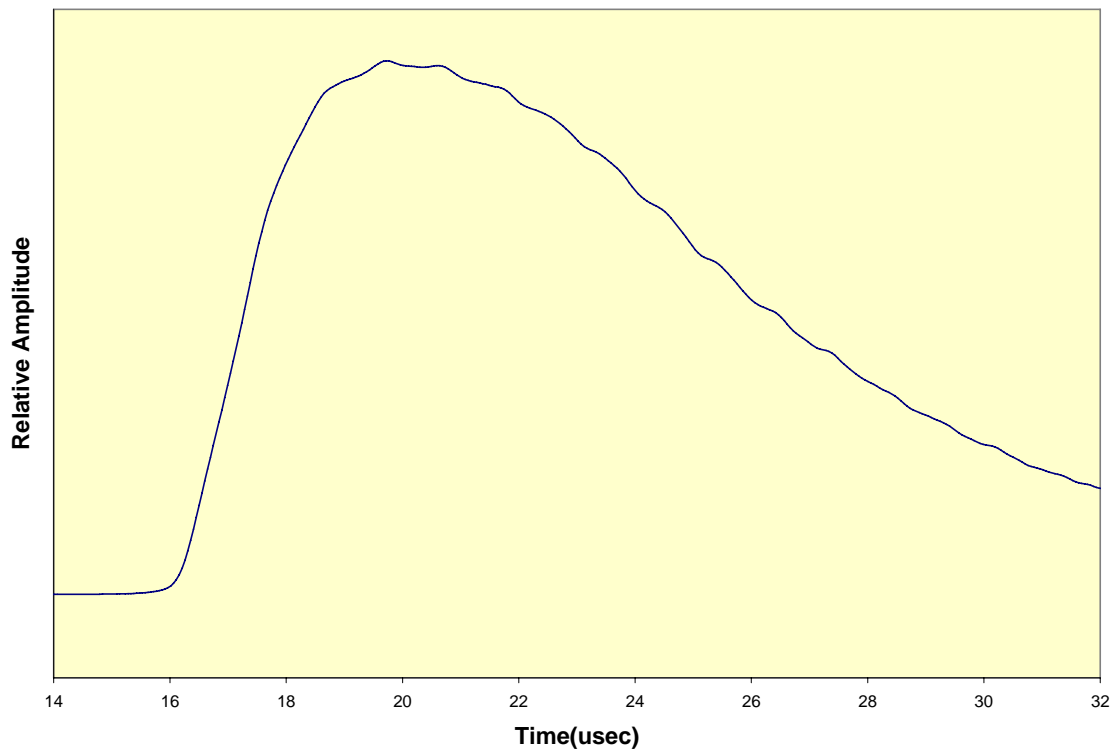


Figure 82. Horizontal wave input in sample with 5% quartz and 15% voids. Waveforms measured at steel receiver on right hand side of the sample.

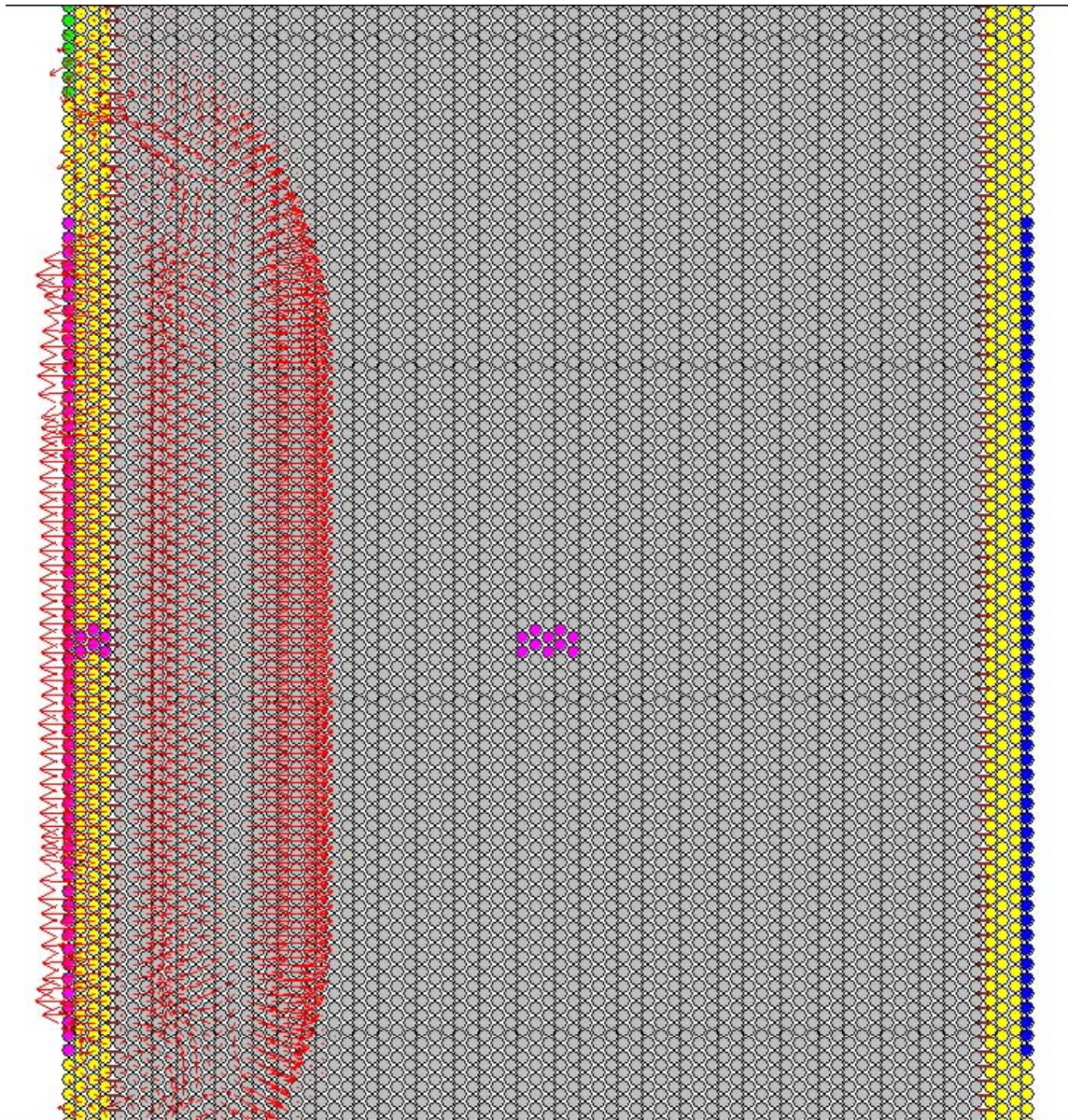


Figure 83. Waveforms in cement with no voids. Red arrows indicate particle velocities associated with propagating wave.

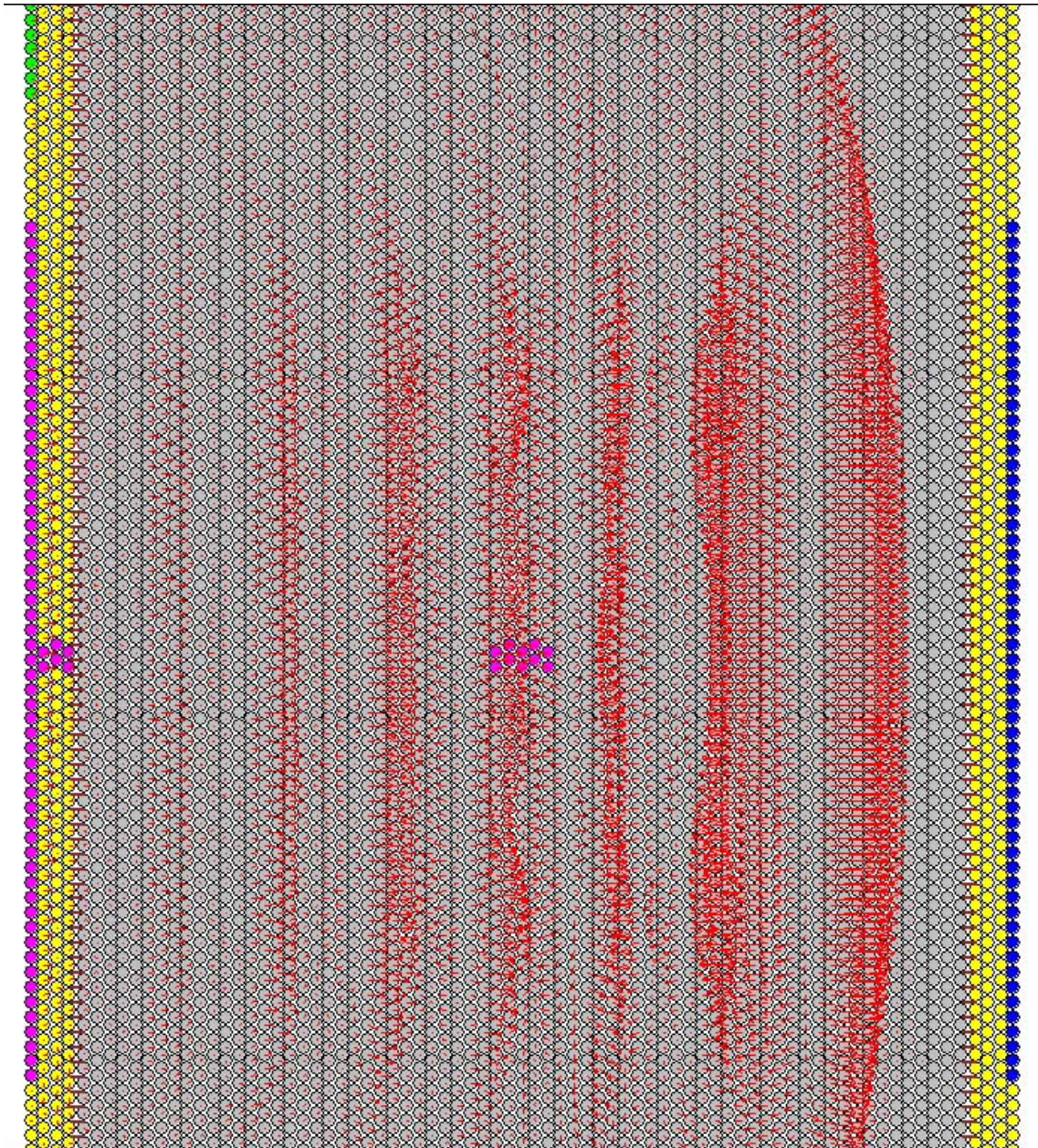


Figure 84. Waveforms in assembly with no voids, after propagation across cement.

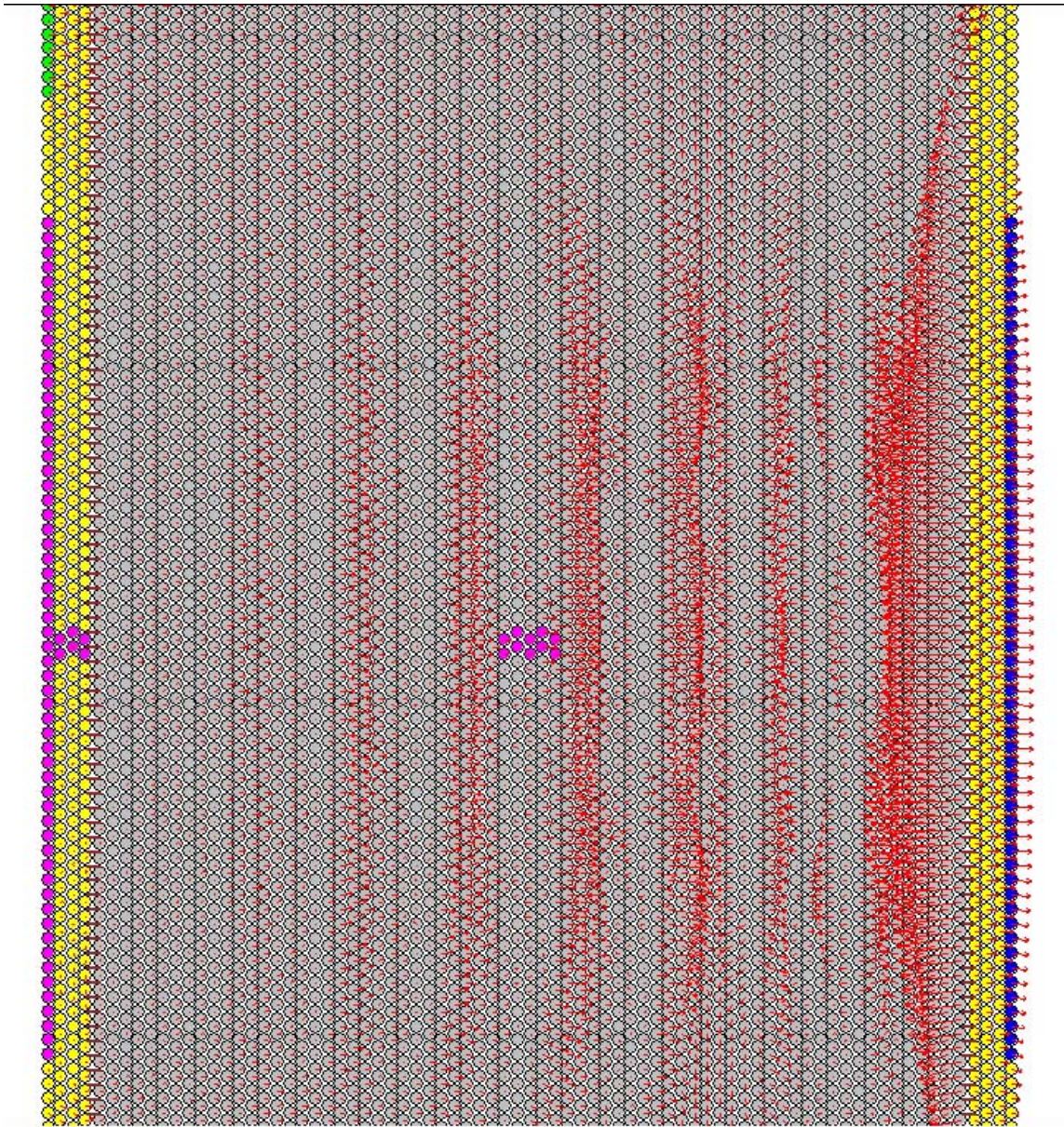


Figure 85. P-waveforms in sample with no voids (no scattering), after transit across the cement and reflecting from the right interface.

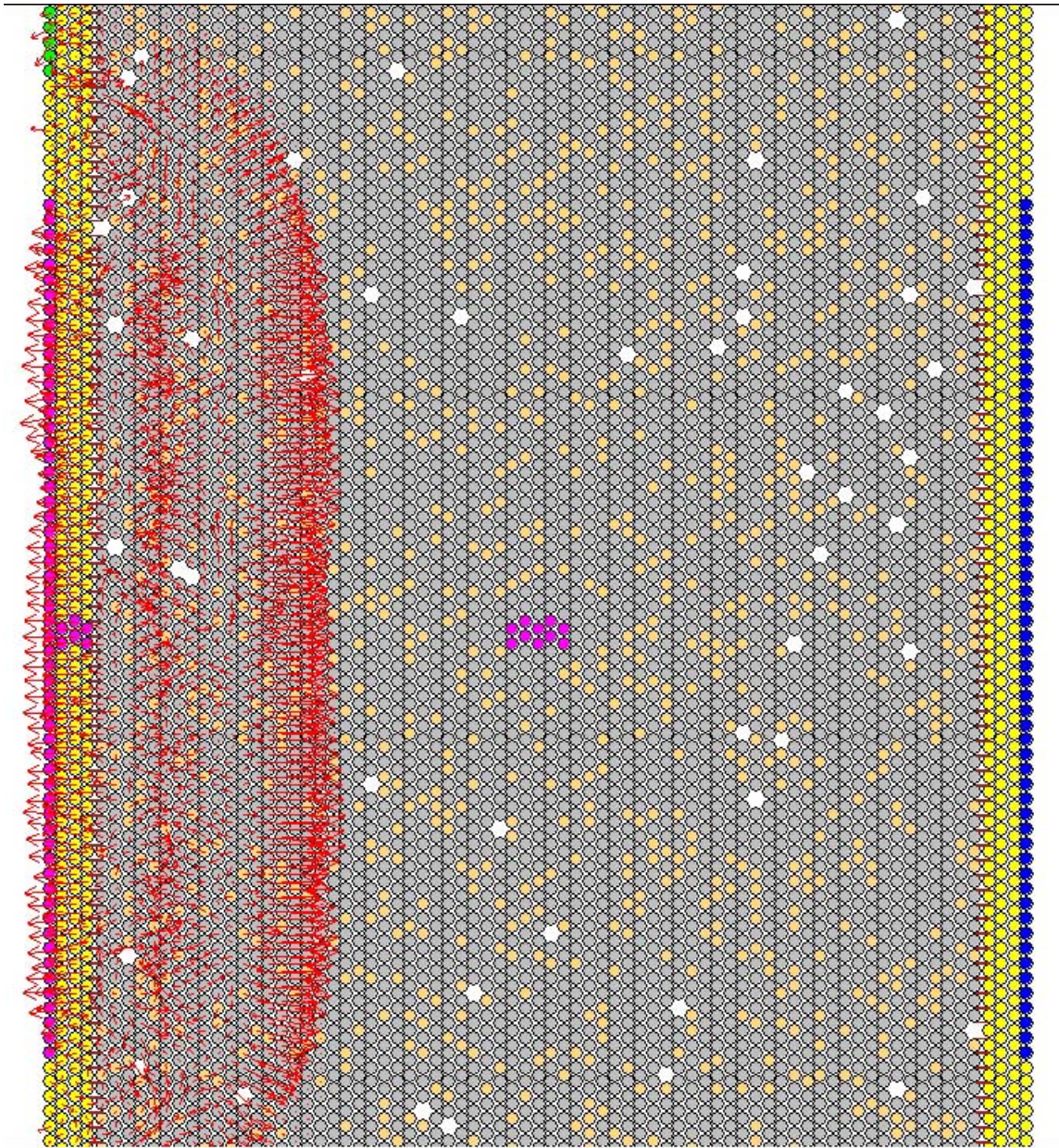


Figure 86. P-wave propagation in cement with 5% voids, after introducing the first wave-form cycle.

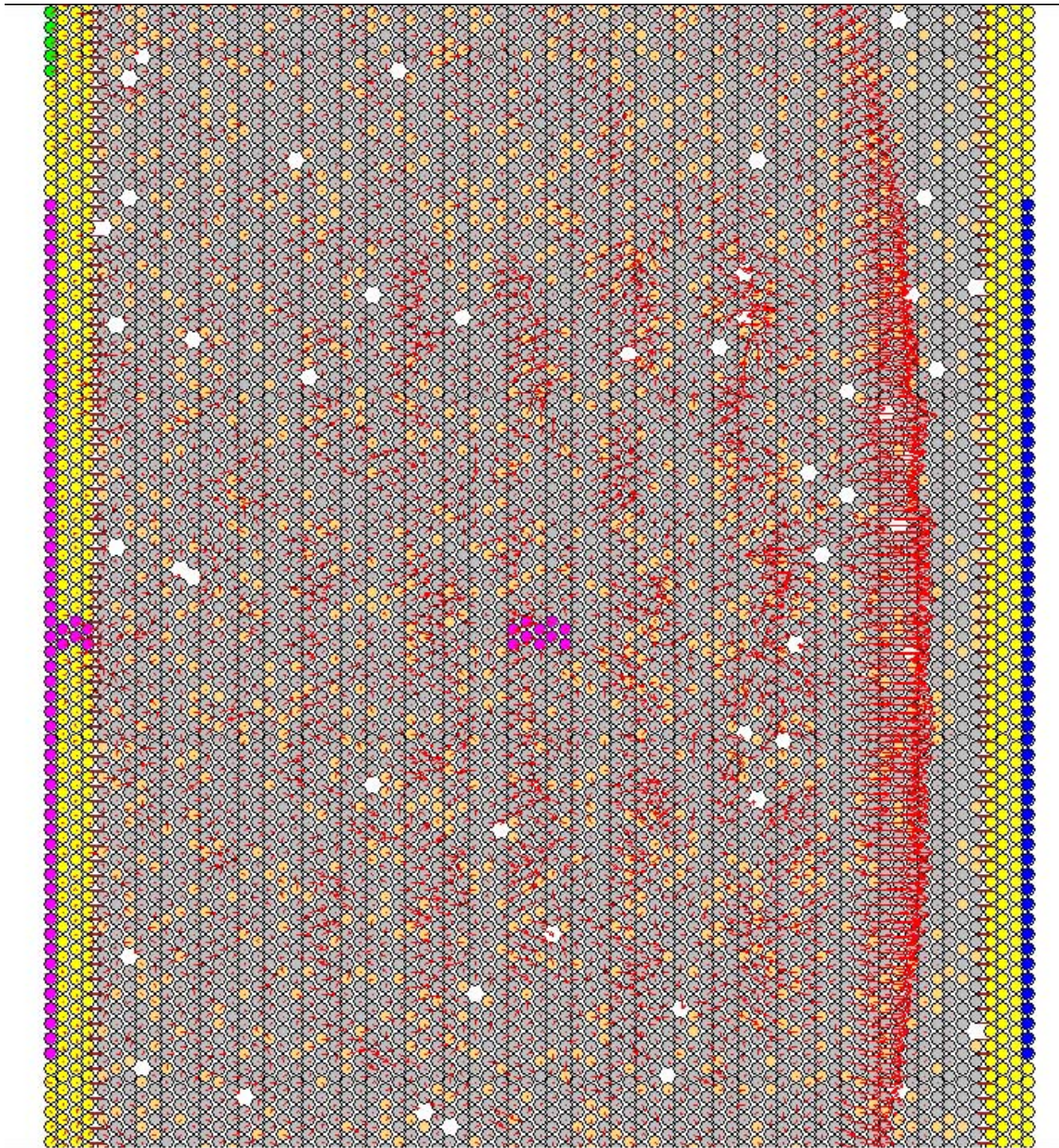


Figure 87. P-wave propagation in cement with 5% voids, after transit through the cement zone.

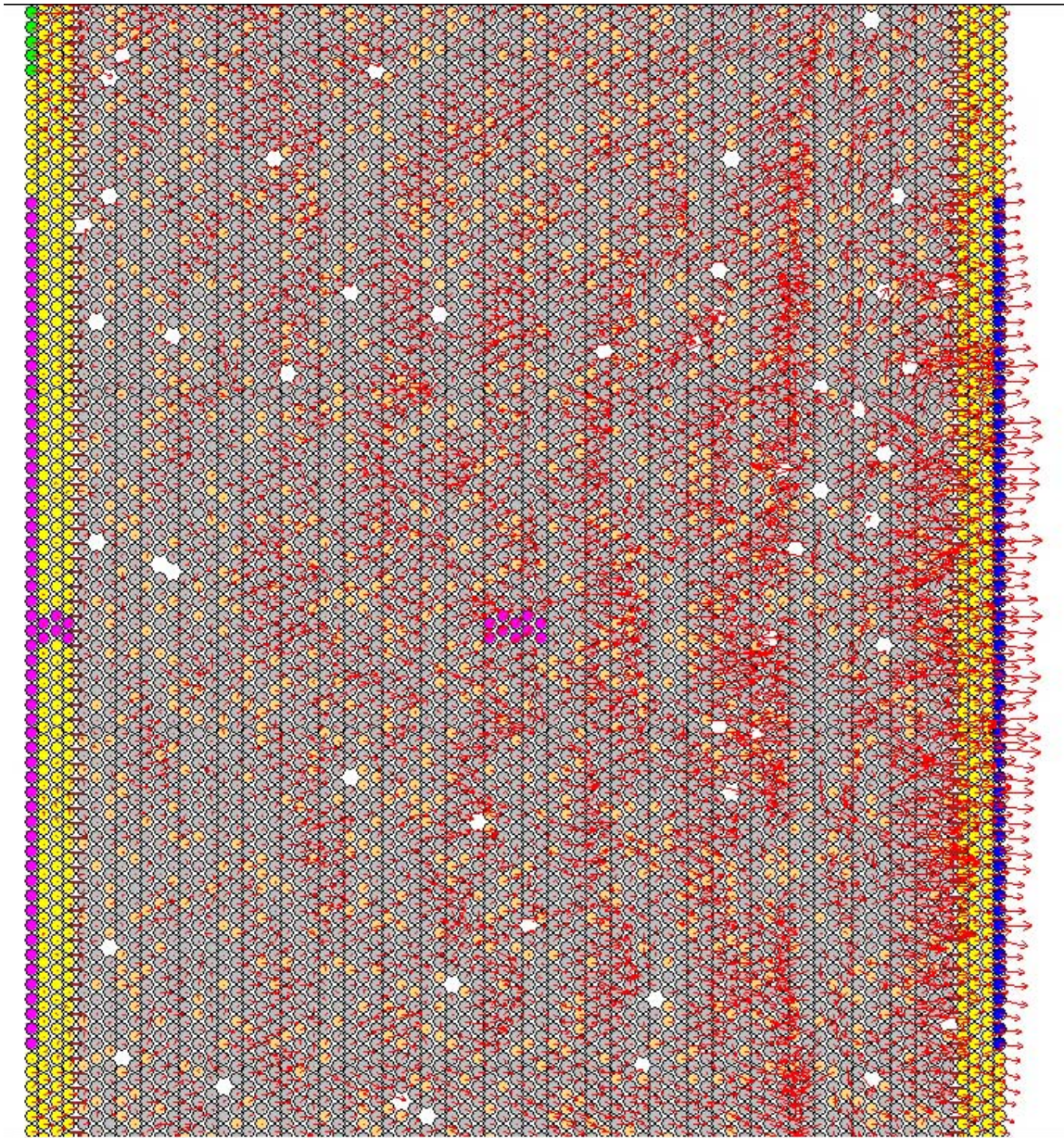


Figure 88. P-wave propagation in cement with 5% voids, after passage through the cement zone and reflection at the right side interface.

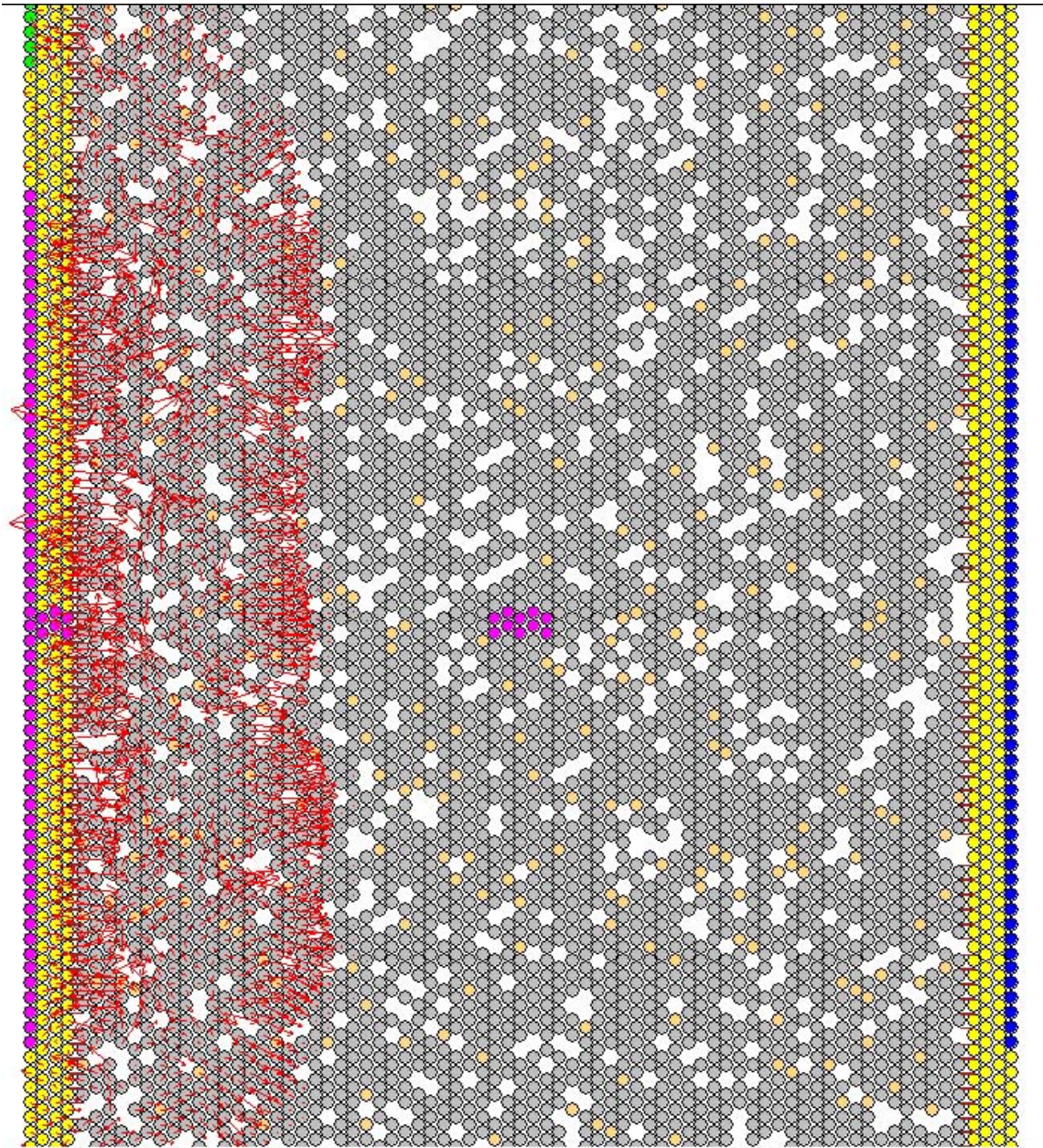


Figure 89. P-wave propagation in cement with 15% voids, after introduction of one cycle of the waveform.

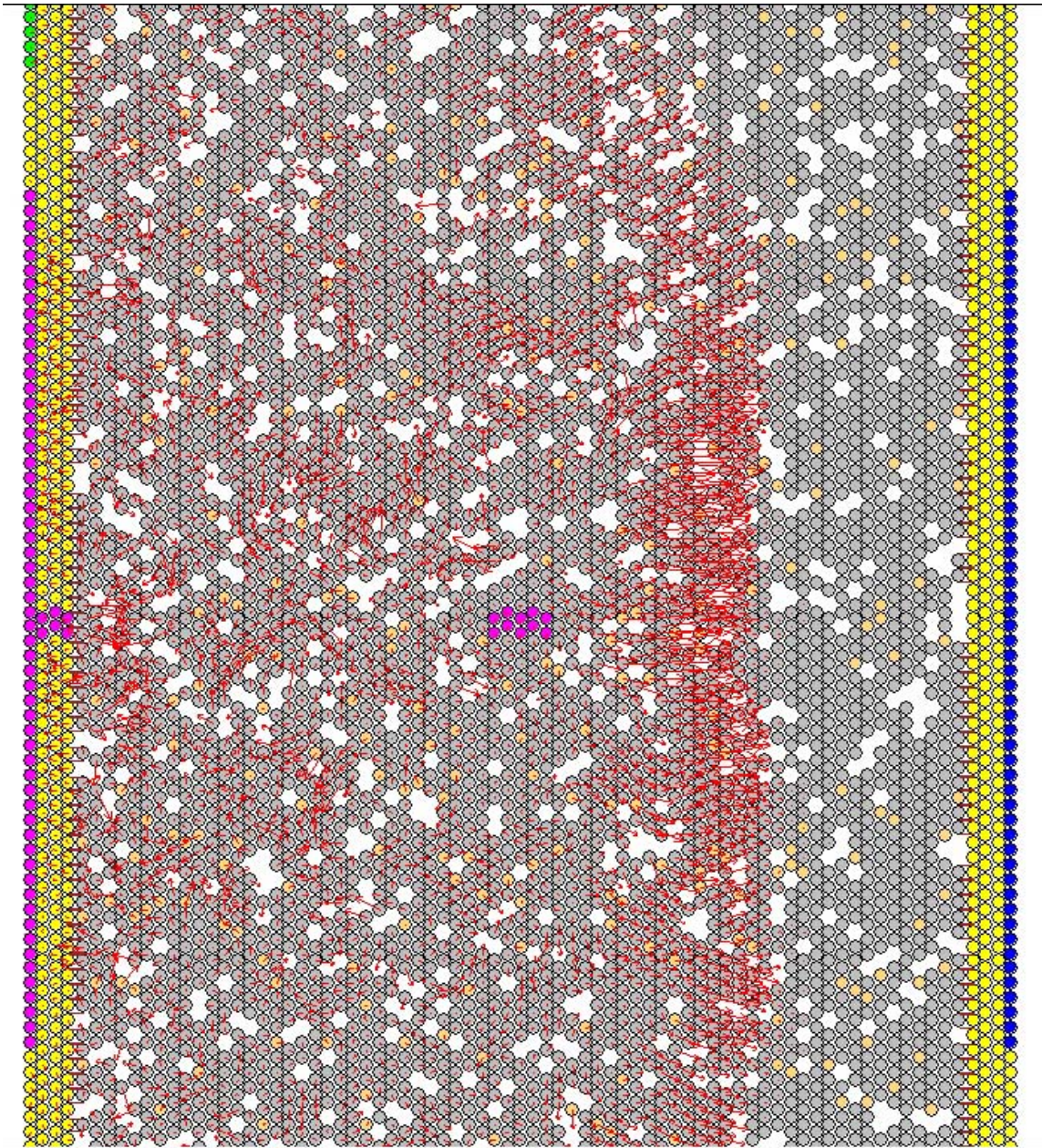


Figure 90. P-wave propagation in cement with 15% voids, after passage through most of the cement zone.

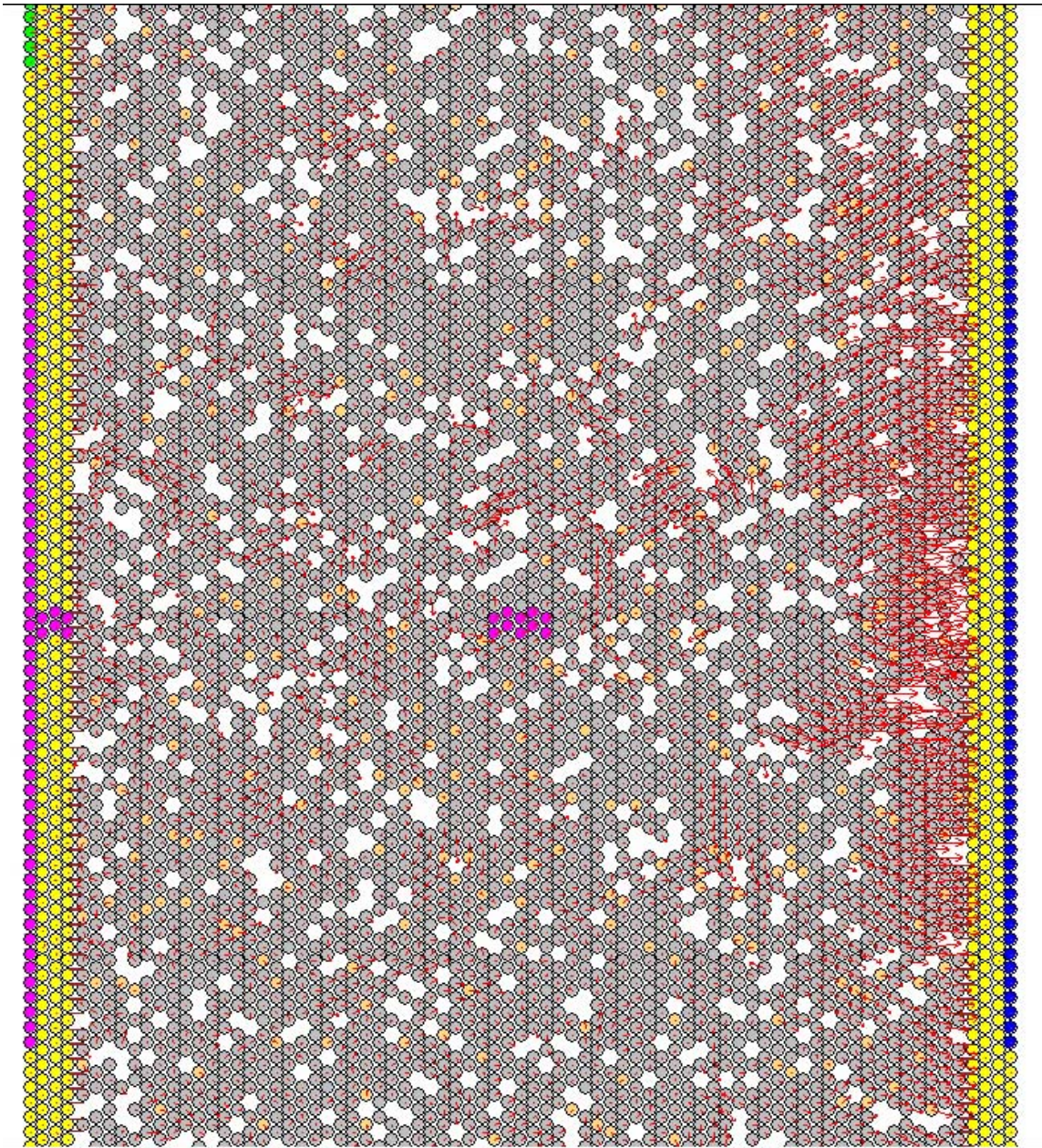


Figure 91. P-wave propagation in cement with 15% voids, after passing through the cement zone.

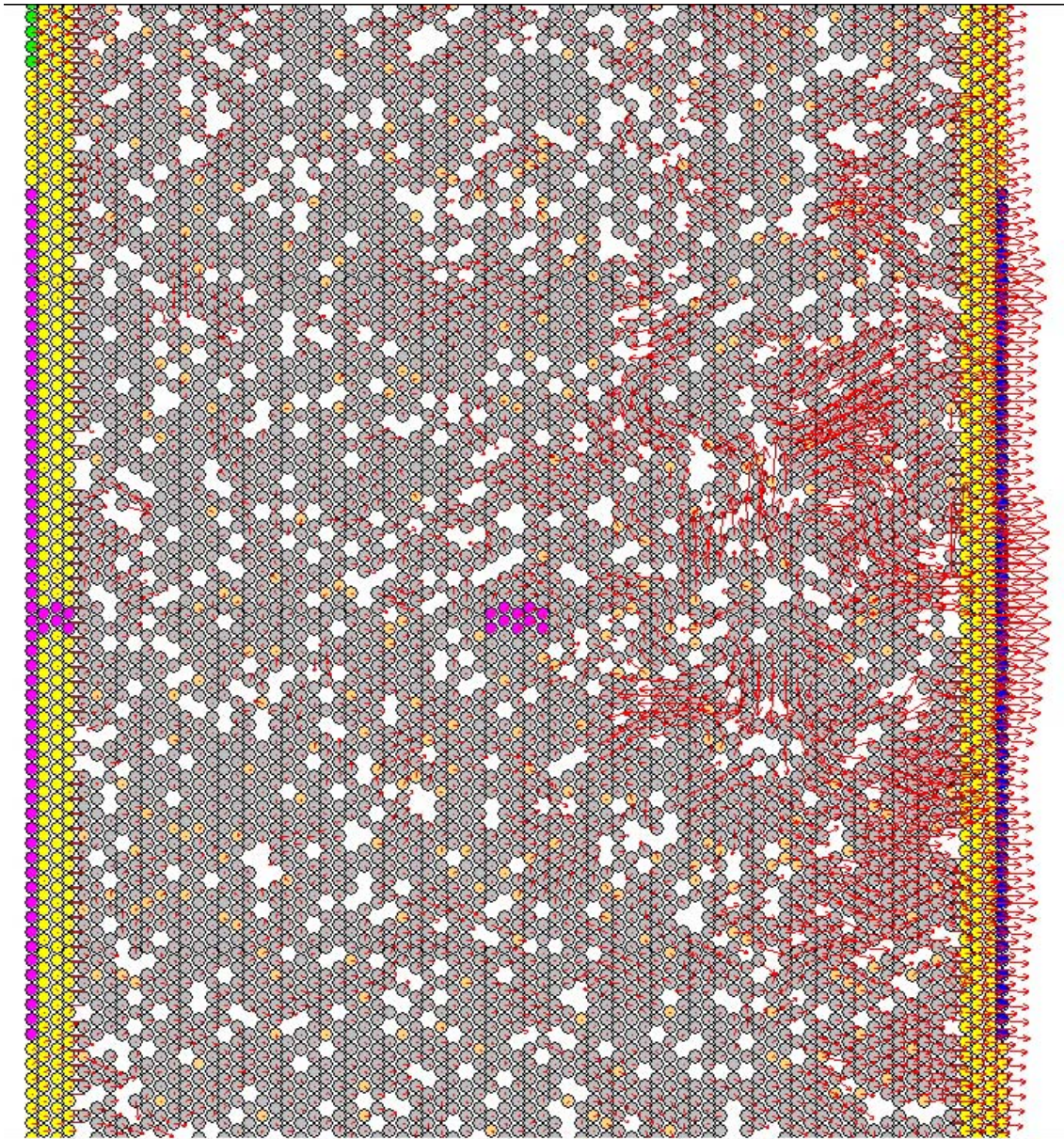


Figure 92. P-wave propagation in cement with 15% voids, after passage through the cement zone and reflection at the right side boundary.

Appendix K
2005, Demonstration-Scale Constructed Wetland System for Treatment
of Produced Waters from Underground Gas Storage,
Clemson University Final Report

**Demonstration-Scale Constructed Wetland System for
Treatment of Produced Waters from Underground Gas Storage**

**Final Technical Report
October 1, 2005 – March 31, 2007**

Submitted by:

**James W. Castle (PI), Ph.D., Associate Professor, Clemson University
John H. Rodgers Jr. (Co-PI), Ph.D., Professor, Clemson University
Evan H. Cross, Graduate Research Assistant, Clemson University
Brenda M. Johnson, Graduate Research Assistant, Clemson University
Scott E. Brame, Research Associate, Clemson University
George M. Huddleston, Ph.D., Senior Staff Scientist, ENTRIX
Cynthia Murray-Gulde, Ph.D., Senior Staff Scientist, ENTRIX
Doug Mooney, P.E., Senior Project Engineer, ENTRIX**

May 30, 2007

**Gas Storage Technology Consortium
Subaward #3039-CU-DOE-1779**

**Clemson University
340 Brackett Hall
Box 340919
Clemson, SC 29634**

Disclaimer

“This report was prepared as an account of work sponsored by an agency of the United States Government. Neither the United States Government nor any agency thereof, nor any of their employees, makes any warranty, express or implied, or assumes any legal liability or responsibility for the accuracy, completeness, or usefulness of any information, apparatus, product, or process disclosed, or represents that its use would not infringe privately owned rights. Reference herein to any specific commercial product, process, or service by trade name, trademark, manufacturer, or otherwise does not necessarily constitute or imply its endorsement, recommendation, or favoring by the United States Government or any agency thereof. The views and opinions of authors expressed herein do not necessarily state or reflect those of the United States Government or any agency thereof.”

Abstract

The purpose of this investigation was to demonstrate the utility of a constructed wetland treatment system to effectively and consistently treat waters produced from an underground gas storage field. To ensure efficient disposal or reuse of waters produced from gas storage facilities, effective and reliable water treatment systems are needed. Presently, treatment or disposal of produced waters adds substantial operational costs to many gas storage facilities.

During the first quarter of this investigation, a demonstration-scale constructed wetland system was designed and constructed for onsite treatment of targeted constituents in water produced from a gas storage field. Design criteria for the demonstration-scale constructed wetland treatment system were developed based on a site visit and on data collected from the pilot-scale system constructed and evaluated during our previous GSTC-sponsored project. In the second quarter of this investigation, design schematics were finalized, and data regarding costs of treatment were analyzed. In the third quarter of the project, the demonstration-scale system was constructed. After construction of the system and planting, the wetland plants acclimated to storm water and produced water from the gas storage site.

Three experiments involving flow through the demonstration-scale constructed wetland treatment system were performed. In the first experiment, onsite storm water was used for flow through the system. For the second experiment, produced water was co-managed with storm water to create low-ionic strength water. The third experiment, which involved storm water co-managed with a larger fraction of produced water to create high-ionic strength water, showed successful treatment in terms of metal removal. Measurements from the constructed wetland indicated that the plants are healthy and that redox potential of the hydrosol is within targeted levels.

Results demonstrate the utility of constructed wetland systems for onsite treatment of gas storage produced waters. The demonstration-scale treatment system was designed and constructed successfully, and treatment was confirmed.

TABLE OF CONTENTS

DISCLAIMER.....	ii
ABSTRACT.....	iii
INTRODUCTION	1
EXECUTIVE SUMMARY	3
EXPERIMENTAL.....	4
Task 1: Design the Demonstration-Scale Constructed Wetland Treatment System.....	4
Task 2: Obtain Permits to Construct.....	4
Task 3: Construct the Demonstration-Scale System.....	4
Task 4: Monitor Treatment	5
Task 5: Evaluate Performance	5
Task 6: Document Results and Prepare Reports.....	5
RESULTS AND DISCUSSION.....	6
Task 1: Design the Demonstration-Scale Constructed Wetland Treatment System.....	6
Task 2: Obtain Permits to Construct.....	7
Task 3: Construct the Demonstration Scale System.....	7
Task 4: Monitor Treatment	9
Task 5: Evaluate Performance.....	10
Task 6: Document Results and Prepare Reports.....	10
CONCLUSION.....	11
REFERENCES CITED.....	30
OTHER PERTINENT PUBLICATIONS.....	30

List of Figures

Figure 1. Process schematic diagram.....	12
Figure 2. Produced water treatment system layout.....	13
Figure 3. Greenhouse wetland plan.....	14
Figure 4. Frame anchor layout plan	15
Figure 5. Greenhouse wetland, truss anchor, and liner anchor sections.....	16
Figure 6. Tank connection details and wetland discharge section.....	17
Figure 7. Exterior of greenhouse and tanks.....	18

Figure 8. Interior of greenhouse.....	18
Figure 9. Planting of <i>S. californicus</i> and <i>T. latifolia</i>	19
Figure 10. Components of the treatment system.....	19
Figure 11. Redox potential in the wetland with time.....	19
Figure 12. Wetland one month after planting.....	20
Figure 13. Wetland three months after planting.....	20
Figure 14. Wetland six months after planting.....	21
Figure 15. Wetland ten months after planting.....	21
Figure 16. Plant and shoot densities in the wetland with time.....	22
Figure 17. PVC frame (1 m ²) used for plant and shoot density measurements.....	22
Figure 18. Schematic diagram showing measurement locations in wetland.....	23

List of Tables

Table 1. Analytical methods for parameters monitored from the demonstration-scale constructed wetland treatment system.....	24
Table 2. Cost/barrel (Minimum-Maximum) for treatment of produced waters.....	25
Table 3. Simulated natural gas storage produced waters by category based on chloride concentration	26
Table 4. Average inflow/outflow, % removal, and estimated rate coefficients for cadmium, copper, lead, and zinc using a pilot-scale system.....	27
Table 5. Chemical composition of storm water currently within the wetland	28
Table 6. Acclimation monitoring data from experiment 1.....	29
Table 7. Acclimation monitoring data from experiment 2.....	29
Table 8. Acclimation monitoring data from experiment 3.....	29

Introduction

Produced waters pose a challenge for treatment because they vary greatly in their composition. High costs associated with existing produced water treatment and disposal methods limit the expansion of existing gas storage fields as well as development of new fields. Currently, there are two common methods for handling produced water. The first method involves the transport of produced water to specialized treatment facilities followed by surface discharge of the treated water, and the second method is to reinject the water into the subsurface. While volumes of produced water increase, the cost of conventional treatment methods are escalating exponentially due to increasingly stringent surface discharge and re-injection regulations under the Clean Water Act (CWA) through the National Pollutant Discharge Elimination System (NPDES), and Safe Drinking Water Act through the Underground Injection Control (UIC). Development of new approaches for treatment of produced water is essential for continued operation of existing storage fields and construction of new facilities.

Water produced from gas storage facilities is often generated in relatively high volumes and can contain a variety of constituents that limit disposal or reuse of the water. Constituents such as chlorides, hydrocarbons, and metals are of concern in these waters. Although salinity of some produced waters may be low enough to meet NPDES discharge limits, concentrations of other constituents in these waters may preclude discharge, resulting in a need for treatment or disposal. Specifically designed constructed wetland treatment systems (CWTS) have been used to treat various constituents independently. However, these systems have yet to be applied at full scale to waters produced from gas storage fields. Wetlands facilitate unique reactions not occurring in other aquatic or terrestrial systems. Constructed wetlands can be poised or buffered to ensure that desired reactions (transfers and transformations) affecting the constituents targeted for treatment proceed at predictable rates over long periods of time (decades). The use of constructed wetland treatment systems offers the following specific advantages:

1. low construction cost;
2. low operational and maintenance costs;
3. reliability; and
4. flexibility in design, so the approach is applicable to a wide range of water quality and quantity.

In the previous Gas Storage Technology Consortium (GSTC) sponsored investigation that we recently completed, a pilot-scale CWTS was designed, constructed, and found to effectively treat simulated produced water. The approach is applicable to waters with a range of chloride concentrations, as well as varying concentrations of cadmium, copper, lead, zinc, and oil. The pilot-scale study provided data regarding the feasibility of this approach for treating gas storage produced waters of varied composition. Results from the pilot-scale study served to decrease uncertainties and confirm design features for the

demonstration-scale constructed wetland treatment system.

The purpose of our investigation is to develop a readily implemented method for treating produced water that can be integrated with surface facilities of gas storage fields while maintaining low costs. The goal of this phase of the project was to design and construct a demonstration-scale CWTS that effectively treats produced water from a field site.

Specific tasks of this demonstration study were:

1. Design the demonstration-scale constructed wetland treatment system;
2. Obtain permits to construct;
3. Construct the demonstration-scale system;
4. Monitor treatment;
5. Evaluate performance; and
6. Document results and prepare reports.

The major expected benefit of investigating CWTS technology for handling water produced from gas storage is significantly decreased costs for produced water management, which could potentially lead to expansion of existing storage fields. In addition, new geographic areas may be opened for development of gas storage fields in light of the anticipated economic advantages.

Executive Summary

The goal of this investigation is to demonstrate the utility of a constructed wetland treatment system to treat waters produced from an underground gas storage field. To ensure efficient disposal or reuse of waters produced from gas storage, effective and reliable water treatment systems are needed. Produced waters are often generated in relatively high volumes and contain a variety of constituents that limit disposal or reuse. Presently, treatment or disposal of produced waters adds substantial operational costs to many gas storage fields. The purpose of this investigation by Clemson University in partnership with Dominion Transmission, Inc., and the Gas Storage Technology Consortium was to demonstrate a low cost and readily implemented method for treating produced water as part of a system integrated with surface facilities of a gas storage field. This approach is applicable to a range of produced waters, since the composition (including salinity) and volume of water produced from one gas storage field to another can vary greatly. The approach involves identifying and confirming targeted constituents, designing constructed wetlands for treatment based on biogeochemistry and macrofeatures (hydroperiod, hydrosol, and vegetation), and conducting carefully designed pilot and demonstration-scale studies to confirm performance and function of the constructed systems. The current investigation utilized a demonstration-scale constructed wetland treatment system to confirm operation and performance under field conditions. The demonstration-scale system was designed and built specifically to treat targeted constituents in water produced from a gas storage facility. Produced water and storm water from the facility were co-managed and treated using the system, and performance was determined through comparison of inflow to outflow concentrations of targeted constituents in the water.

The approach of this investigation incorporated the use of sound theory and fundamental principles, such as the Laws of Thermodynamics and basic biogeochemistry. A major expected benefit of this investigation is that the results will contribute to reduced cost of water management, which will potentially lead to expansion of existing storage fields. In addition, new geographic areas may be opened for development of gas storage fields due to the anticipated economic advantages.

Experimental

Task 1: Design the Demonstration-Scale Constructed Wetland Treatment System

The purpose of Task 1 was to design a demonstration-scale CWTS at a field site so that the results will be applicable for designing future full-scale systems at additional sites. The comprehensive engineering report and schematic diagrams for the demonstration-scale CWTS were completed by ENTRIX (Figures 1-6).

Storm water collected within the gas storage facility often contains dilute concentrations of constituents found in natural gas storage produced water (NGSPW) as well as constituents from wastewater delivery trucks (e.g. oil and grease) that require treatment prior to discharge to receiving aquatic systems. NGSPW and storm water were co-managed in a 10,000 gallon storage tank to reduce chloride concentrations. For waters with chloride concentrations exceeding 4,000 mg/L, a reverse osmosis system can be used to reduce chloride concentrations to levels that can be tolerated by the wetland plants.

Produced water treatment costs were compiled in order to compare the treatment costs of several common conventional treatment methods to costs associated with produced water treatment utilizing a CWTS. This was done in order to demonstrate the potential economic benefits derived from use of a CWTS in comparison with conventional treatment methods.

Additional experiments were conducted utilizing the pilot-scale CWTS in order to obtain additional data which can be incorporated into the design of the demonstration-scale system to achieve optimal treatment performance.

Task 2: Obtain Permits to Construct

The objective of this task was to obtain any permits needed for construction of the demonstration-scale CWTS, including the greenhouse. This objective was omitted because outflow water from the CWTS is collected and treated by conventional methods.

Task 3: Construct the Demonstration-Scale System

This task involved construction of the demonstration-scale CWTS at a site in West Virginia. The first phase of construction included surveying the site. Site preparation, excavation, and plumbing were completed by Ryan Environmental. A HDPE liner was included to prevent leaching of water into or out of the CWTS. A 28 by 45 foot greenhouse was constructed to enable year-round monitoring of the demonstration-scale CWTS. The greenhouse and its support systems were installed by Jaderloon (Irmo, SC) at the excavated and lined site. Local topsoil was amended with gypsum, iron, and slow release fertilizer to prepare it for use as hydrosol in the constructed wetland. The planted

area of the greenhouse was 20 by 33 feet (660 square feet). The first 330 square foot section of the wetland was planted with *Schoenoplectus californicus* (California bulrush) in order to support a reducing aquatic environment. The second 330 square foot section was planted with *Typha latifolia* (cattail) in order to support an oxidizing aquatic environment.

Task 4: Monitor Treatment

Samples were collected from inflow and outflow water of the CWTS. These samples were analyzed for concentrations of targeted constituents. The analyses were performed in laboratories at Clemson University using standard methods (*Standard Methods for the Examination of Water and Wastewater*, APHA et al., 1998). Sampling frequency was based on the hydraulic retention time of water in the system.

Task 5: Evaluate Performance

Performance of the CWTS was evaluated by comparing the concentrations of constituents of concern (e.g., metals) in the inflow to concentrations in the outflow. Analytical methods for the parameters monitored are listed in Table 1.

Task 6: Document Results and Prepare Reports

The reports included data collected during the various tasks, including composition of the produced water and monitoring data.

Results and Discussion

Task 1: Design the Demonstration-Scale Constructed Wetland Treatment System

The demonstration-scale CWTS was built at Dominion Transmission's Lightburn facility near Bridgeport, WV. In October, 2005, investigators from Clemson University along with collaborators from Dominion and ENTRIX visited the site. The specific location was selected, and field measurements were obtained for use in designing the system. Engineering drawings were produced by engineers at ENTRIX, and computer-assisted drafting of the design was completed.

Cost Comparison

The overall goal of this research is to find a cost effective means for handling NGSPW. Common treatment methods for NGSPW include deep-well injection and transport to specialized treatment facilities (Nakels et al., 2003). Depending on water composition, other treatment methods may be utilized to dispose of NGSPW. Examples of alternative disposal methods include evaporation ponds, treatment by publicly owned treatment works, road-spread, and surface discharge. Each of these methods has associated costs and restrictions depending on the composition, volume, and location of the water. A cost summary of these disposal/treatment methods and costs for operation and management of constructed wetland treatment systems are listed in Table 2.

Operating costs for CWTS are significantly less than conventional treatment methods. If a CWTS can be installed on site, the transport of produced water may be reduced or eliminated.

Additional Experimental Data for Design

Results from the previous pilot-scale study served to decrease uncertainties and confirm design features for the current demonstration-scale CWTS. To obtain additional data for scaling to a demonstration project, a second, simulated fresh produced water (freshwater 2) was investigated during the second quarter of the current project. Simulated produced waters were formulated according to the constituents and concentrations listed in Table 3. The metal concentration data aided in determining accurate rate coefficients (Table 4) for design of the demonstration-scale project.

Percent metal removal was calculated by:

$$\% \text{ removal} = \left(\frac{[A_0] - [A]}{[A_0]} \right) 100 \quad \text{Equation 1}$$

where [A] is the final outflow metal concentration (mg/L), and [A₀] is the initial inflow metal concentration (mg/L).

Rate coefficients for removal of metals from the water column were estimated by assuming a first-order reaction rate:

$$k = \frac{-\ln([A]/[A_0])}{t} \quad \text{Equation 2}$$

where k is the rate coefficient (day^{-1}), $[A]$ is the final outflow metal concentration (mg/L), $[A_0]$ is the initial inflow metal concentration (mg/L), and t is hydraulic retention time (days) of the entire system.

The pilot-scale experiments provide data concerning the biogeochemical conditions within the system during simulated NGSPW treatment. These data may be used for making adjustments and/or adding amendments to a demonstration-scale or field-scale CWTS in order to establish similar biogeochemical conditions for treating NGSPW. Also, improvements can be made to obtain optimal treatment performance at the pilot scale, which can be applied to the design of the demonstration- and field-scale systems to maximize performance.

Engineering Design

ENTRIX completed a very thorough engineering design and report for the demonstration-scale CWTS. The design covered all facets of construction, and the report described all components required for effective treatment of produced water at the demonstration scale including individual component description, specifications, manufacturer, and cost. Engineering design drawings are shown in Figures 1 through 6.

Task 2: Obtain Permits to Construct

Permitting needs have been investigated. Because the demonstration-scale CWTS was contained in a temporary greenhouse located on industrial property, building permits were not required for this project. Also, because outflow water from the demonstration-scale CWTS was monitored and then commingled with the existing produced water waste stream rather than released as surface discharge, NPDES permits were not needed.

Task 3: Construct the Demonstration-Scale System

The demonstration-scale CWTS is contained in an 8.5 by 13.7 m (28 by 45 foot) freestanding poly cover greenhouse. Jaderloon Greenhouse Company of Irmo, SC delivered and assembled the greenhouse on site. The site was cleared, leveled, and excavated to a depth of about 1 m (3 feet) by Ryan Environmental prior to covering by the greenhouse. The excavated area was lined with an HDPE liner, and approximately 45 cm (18 inches) of topsoil from the excavation was placed on top of the liner as hydrosoil for the CWTS. The remaining excavated soil was used to berm and slope storm water away from the greenhouse and the CWTS. The greenhouse includes a propane heater and an evaporative cooler. Following construction of the greenhouse and associated support systems (i.e. plumbing and electrical), pumps, an oil/water separator, and a reverse

osmosis system were installed. Soil amendments and plants were added. Construction photos are shown in Figures 7 and 8, and photographs of the planting process are shown in Figure 9.

Local soils were used as hydrosol. The hydrosol was analyzed and amended with gypsum, iron, and slow release fertilizer to achieve the appropriate redox conditions and promote plant growth. The demonstration-scale CWTS was densely planted (24 cm centers) with *S. californicus* and *T. latifolia*. Storm water was added to the wetland and maintained at a suitable depth during the wetland acclimation period.

The plants chosen for this project, *S. californicus* (Bulrush) and *T. latifolia* (Cattail), behave differently after transplanting. Cattails typically maintain a deep green color after transplanting and begin to show signs of growth within approximately two to three weeks after planting. Commonly, bulrush brown as the roots develop within new hydrosol and begin to show signs of growth four to five weeks after planting. The bulrush eventually establish roots, and after a period of time, they too show extensive growth.

Enclosure of the demonstration-scale CWTS in a greenhouse facilitated year-round monitoring of the wetland during this investigation. Conditions within the greenhouse can be regulated for assessment of the demonstration-scale system. Although enclosure within a greenhouse contributed to investigation of the demonstration-scale CWTS, the greenhouse may not be necessary for successful operation of the system at this site and at other sites in a similar climatic zone.

Construction included installing a metering pump, oil/water separator, reverse osmosis system, and inflow spreader pipe (Figure 10).

After initial construction of the demonstration-scale CWTS, the configuration of inflow to the wetland was modified to manage flow between the metering pump and the reverse osmosis (RO) system. The RO system includes an external charge pump that supplies water to the main RO pump and membranes. We recognized that reconfiguration was needed to control and maintain flow rate between the pumps. Overflow could cause loss of system performance, and underflow could cause pumps to burn up and possibly damage the RO membranes. The new control system includes multiple, water-level float devices in a tank between the metering pump and RO system. These float devices actuate relays that can turn the metering pump on and off as needed to maintain steady flow for the RO charge pump. The RO system is equipped with pressure sensors that shut down the RO system if pressure becomes too high or too low. The outputs from the RO pressure sensors are wired to relays so that a shutoff condition at the RO will turn off both the metering pump and charge pump. Additionally, if the float devices fail and the float tank overflows, a backup float sensor in an overflow tank will shut down the entire system. As a final safeguard, the overflow tank was plumbed to transfer excess overflow water directly to the waste tank.

Task 4: Monitor Treatment

Treatment was investigated by sampling the inflow and outflow water from the CWTS. The samples were analyzed to determine concentrations of targeted constituents including Zn, Cu, Cd, Pb, Fe, Se, oil & grease. The analysis was performed in laboratories at Clemson University using standard methods (*Standard Methods for the Examination of Water and Wastewater*, APHA et al., 1998). Sampling frequency was based on the hydraulic retention time of the water in the system, which was 7 days. Samples were collected from the wetland inflow on days 1 and 7 to monitor any compositional changes in inflow water throughout the retention time. Wetland outflow samples were collected on day 7.

Redox and plant density were measured at specific locations 3, 6, 8, and 10 months after planting. These data were used to assess both the biogeochemical conditions and plant health and vigor within the system. Redox (reduction/oxidation potential), which is a measure of the ability to donate or accept electrons, strongly influences the biogeochemical reactions occurring within the wetland. These measurements were taken using a platinum-tipped, insulated copper wire inserted several centimeters into the hydrosol. Using a milli-volt reader, a reference electrode was connected to the negative pole of the meter and placed in the water column. The exposed copper wire was attached to an electrode connected to the positive pole of the meter. This measured the electrical potential in milli-volts between the platinum-tipped insulated copper wire and the reference probe. Redox values in the wetland changed favorably during the acclimation period (Figure 11).

Plant and shoot density values indicated strong growth and reproduction of both bulrush and cattails (Figures 12, 13, 14, 15, and 16). Plant and shoot density was measured by counting all individuals within the boundaries of a 1 m² PVC frame placed within the wetland at each data collection site (Figures 17 and 18). Shoots are defined as new plants that developed post-planting and were separated from the “plant” count by size and appearance. There were approximately 16 bulrush and 11 cattails per m² on the day of planting.

To promote reducing conditions, organic matter was added to the area of the wetland planted with bulrush. Redox in the bulrush half of the wetland continued to move toward targeted values less than -150 mV. The cattail half of the wetland progressed toward targeted redox values greater than -50 mV.

For the first six months after construction, plants acclimated to storm water in the wetland. This storm water contained many constituents found in NGSPW in very low concentrations and was therefore well suited for acclimation. A sample of this storm water was collected and analyzed (Table 5). The results of the storm water compositional analysis were used to simulate storm water introduced to a pilot-scale CWTS system at Clemson University for treatment assessment.

Three experiments involving flow through the system were performed to assess the wetland system. For the first experiment, storm water was delivered for flow through the system. Samples were collected from inflow and outflow, and the samples were analyzed (Table 6). Inflow concentrations of Cu, Se, and Oil & Grease were reduced from 0.04, 0.04, and 84 mg/L to 0.02, 0.01, and 53 mg/L respectively. For the second experiment, produced water was co-managed with the storm water to create low-ionic strength water containing slightly higher concentrations of chlorides, metals, metalloids, and organics. Results of sample analysis are shown in Table 7. Inflow concentrations of Zn and Oil & Grease were reduced from 3.53 and 23 mg/L to 1.8 and 13 mg/L respectively. The third experiment involved co-management of produced water with storm water to create a matrix of high ionic strength containing higher concentrations of chlorides, metals, metalloids, and organics. Results of sample analysis are shown in Table 8. Inflow concentrations of Cu, Zn, Cd, and Pb were reduced from 0.2, 8.78, 0.08, and 0.05 mg/L to non-detect, 1.37, 0.05, and 0.03 mg/L respectively.

Task 5: Evaluate Performance

Performance of the CWTS was evaluated by comparing the concentrations of constituents of concern in the inflow to concentrations in the outflow. For the first experiment, storm water containing ~500 mg/L chlorides was delivered to the wetland for treatment. Removal of Zn, Cu, Pb, Fe, Se, and oil & grease was achieved in varying degrees (Table 6). For the second experiment, 7,900 gallons of storm water collected from the wetland outflow during experiment 1 was mixed with 300 gallons of NGSPW to achieve a chloride concentration of ~1,500 mg/L. In this experiment, only zinc and oil & grease concentrations were reduced, and the remaining constituents were either non-detect in both inflow and outflow waters or were discharged at higher concentrations than in the inflow waters (Table 7). The higher discharge concentrations in experiment 2 may be the result of evapotranspiration (ET), as average ambient air temperatures for this experiment were higher than those measured during experiment 1. Low removal percentage of some constituents of concern during experiments 1 and 2 may be attributed to the system not yet being fully acclimated to conditions (e.g., redox potential) necessary to achieve targeted treatment performance. The third and final experiment utilized ~8,650 gallons of storm water and 350 gallons of produced water to achieve a chloride concentration of ~2,500 mg/L. Concentrations of Cu, Cd, Pb, and Zn were reduced during flow through the constructed wetland system (Table 8). Treatment effectiveness achieved during experiment 3 is attributed to the system being acclimated, as indicated by stable values of redox potential within the targeted range.

Task 6: Document Results and Prepare Reports

All quarterly technical reports were prepared and transmitted to GSTC on time in accordance with project reporting requirements.

Conclusion

Design criteria for the demonstration-scale CWTS were developed based on a site visit and on data from the pilot-scale CWTS evaluated during our previous GSTC-sponsored project. A design report completed by ENTRIX provided specifications for construction of the demonstration-scale CWTS. The CWTS was constructed and is enclosed in a greenhouse. Because outflow water from the CWTS is commingled into the existing produced water waste stream rather than released as surface discharge, a NPDES permit was not required. This allowed the project to proceed without waiting for regulatory action.

Information compiled concerning operating costs of produced water treatment using conventional methods and CWTS illustrates the economic benefit gained by utilizing a CWTS in the treatment of gas storage produced waters. Experimental data obtained from additional pilot-scale research support previous findings and provide data concerning specific biogeochemical conditions observed in an operating CWTS for treating NGSPW.

Storm water was introduced to the CWTS for acclimation of hydrosol conditions and plants. This wastewater contained many constituents found in NGSPW in very low concentrations and was therefore well suited for acclimation. Both bulrush and cattails grew well during acclimation of the constructed wetland. Measurements confirmed the increase in plant and shoot densities. To promote reducing conditions, organic matter was added to the area of the wetland planted with bulrush. Redox potential in the wetland reached targeted values for treatment.

Three experiments involving flow through the demonstration-scale CWTS were performed. For the first experiment, storm water was used for flow through the system. In the second experiment, produced water was co-managed with storm water to create low-ionic strength water. For the third and final experiment, storm water was co-managed with a larger fraction of produced water to create high-ionic strength water. Samples were collected from inflow and outflow for each experiment. Treatment effectiveness was indicated by decreasing concentrations of constituents of concern during the third experiment.

Results demonstrate the utility of constructed wetland systems for onsite treatment of gas storage produced waters. The demonstration-scale treatment system was designed and constructed successfully, and treatment was confirmed.

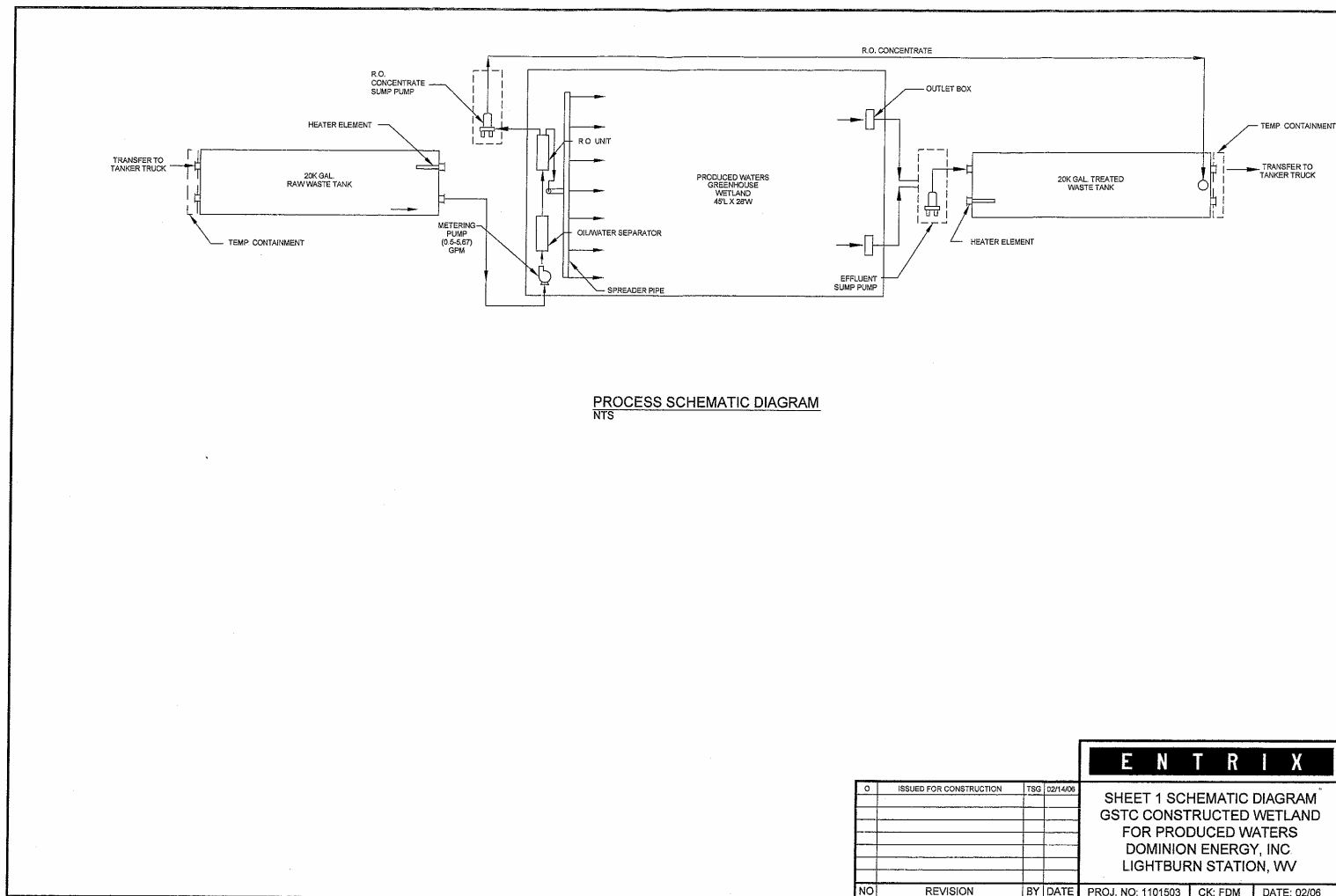


Figure 1. Process schematic diagram

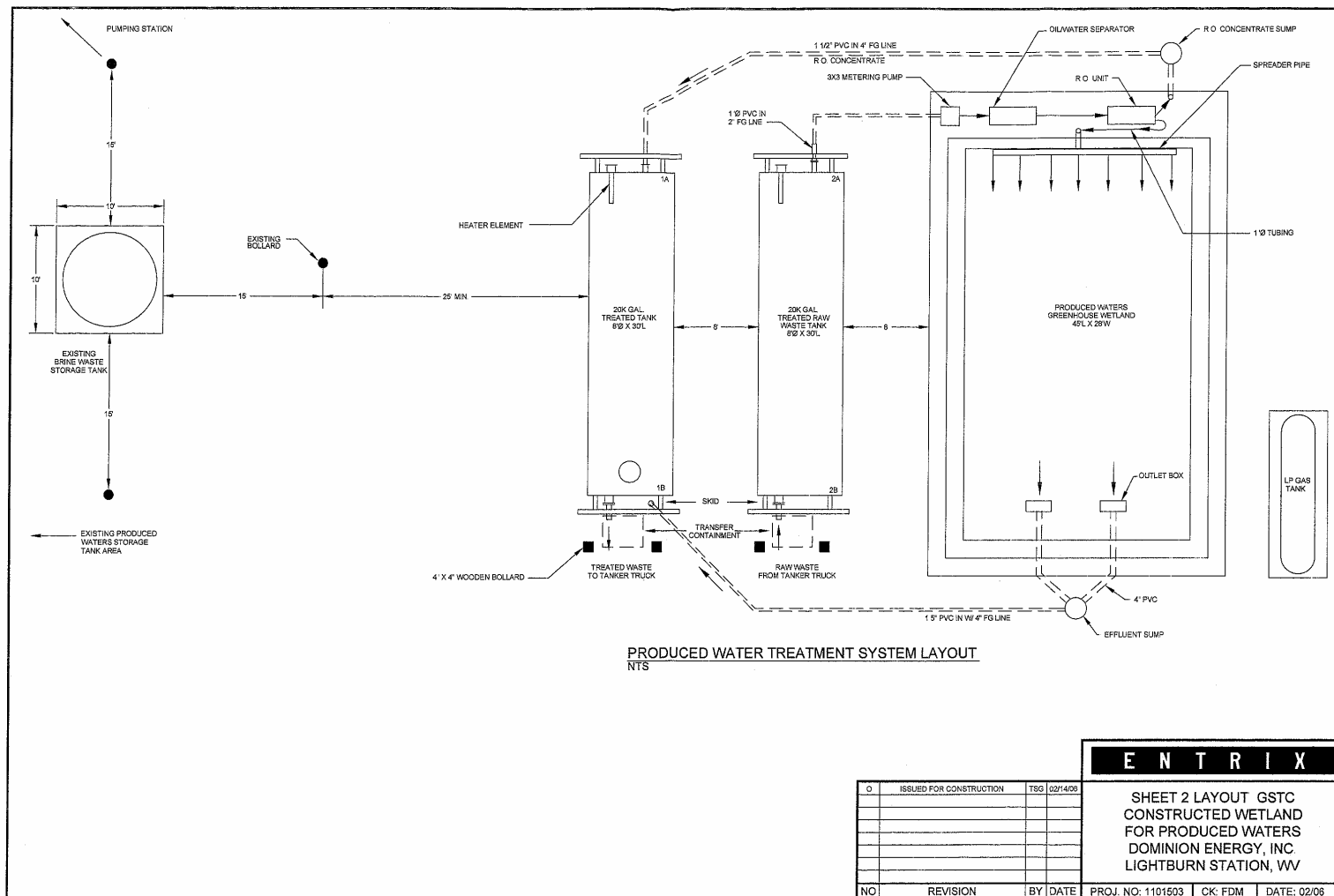
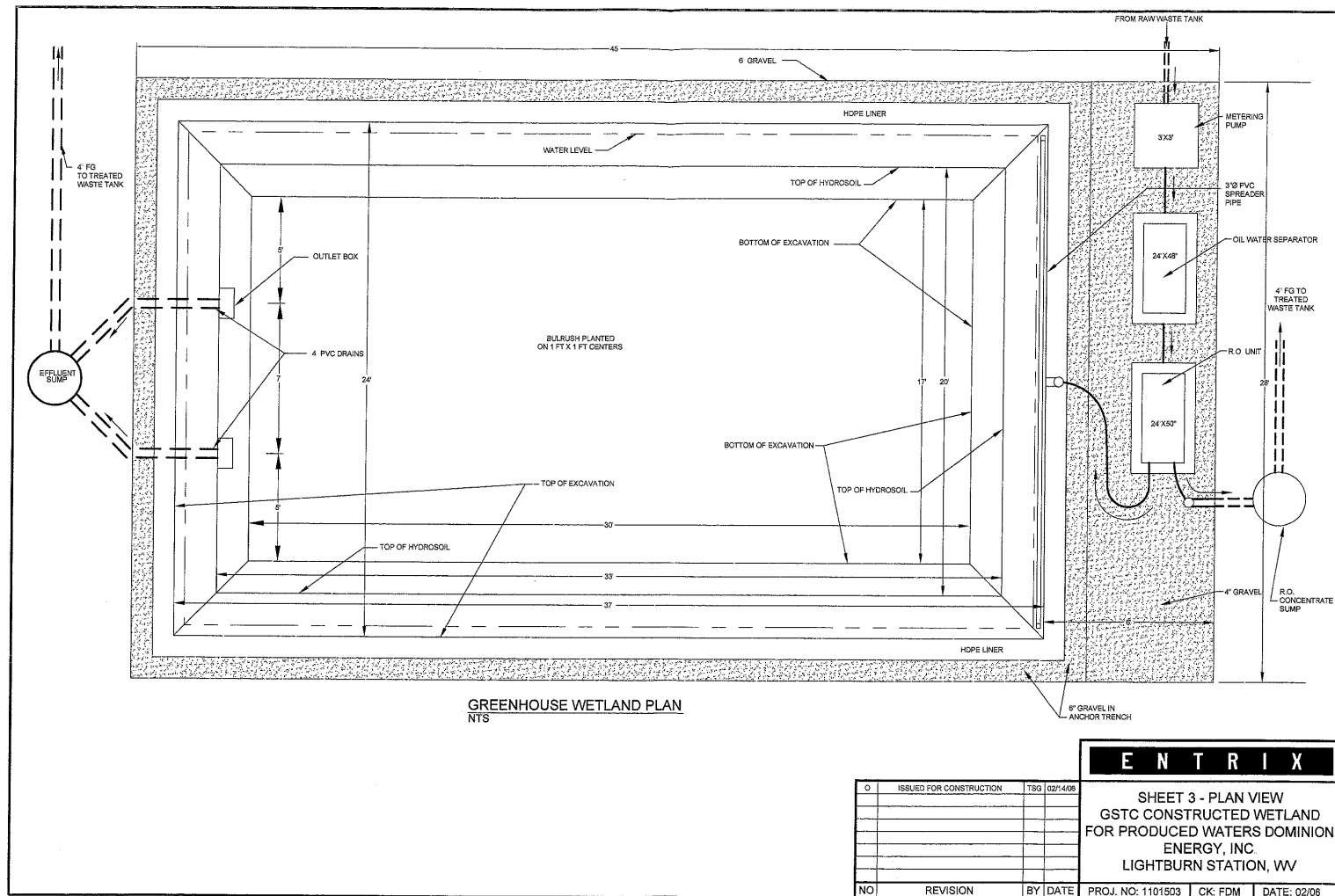


Figure 2. Produced water treatment system layout.



NO	REVISION	BY	DATE

ENTRIX			
SHEET 3 - PLAN VIEW GSTC CONSTRUCTED WETLAND FOR PRODUCED WATERS DOMINION ENERGY, INC. LIGHTBURN STATION, WV			
PROJ. NO:	1101503	CK:	FDM
DATE:	02/06		

Figure 3. Greenhouse wetland plan.

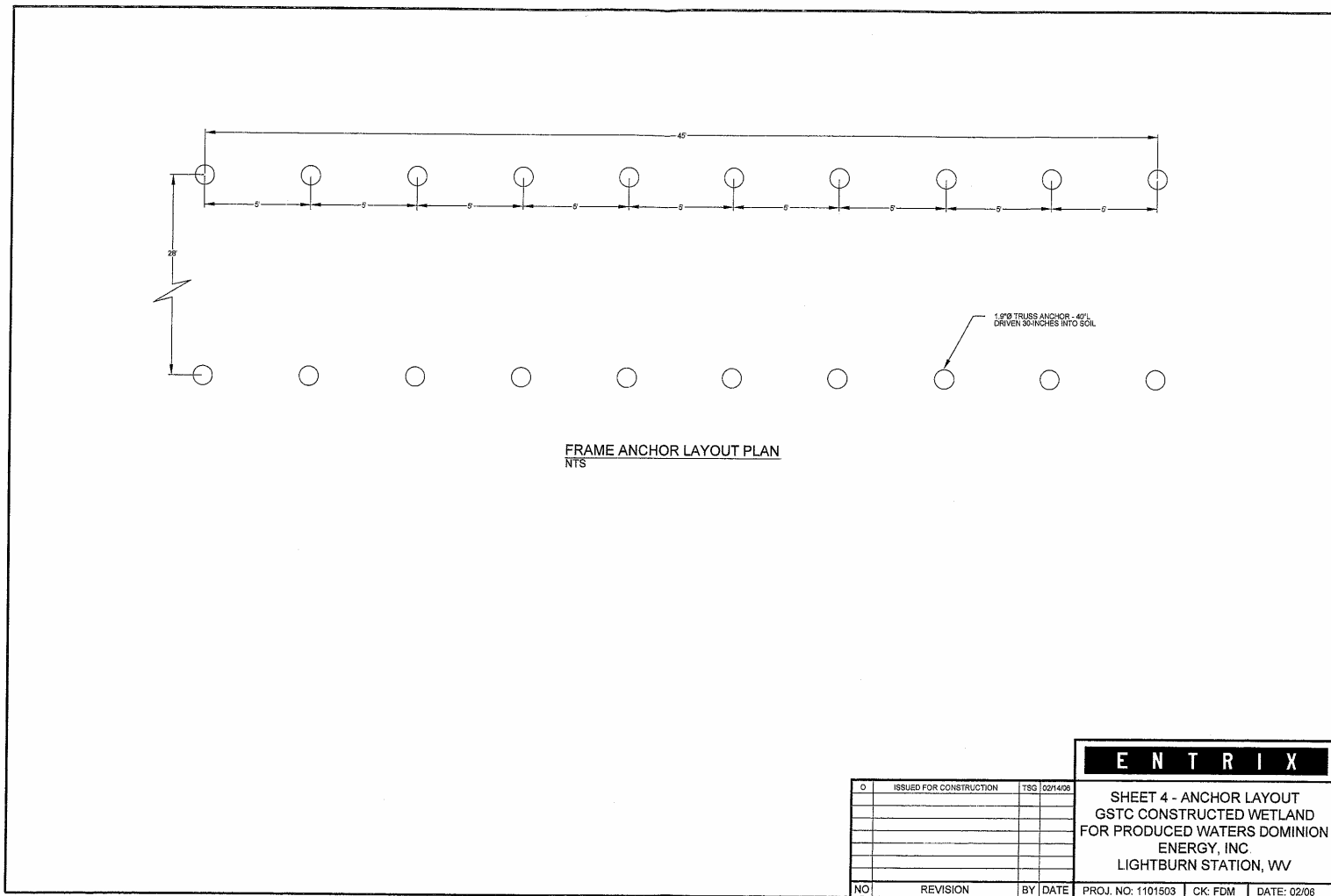


Figure 4. Frame anchor layout plan.

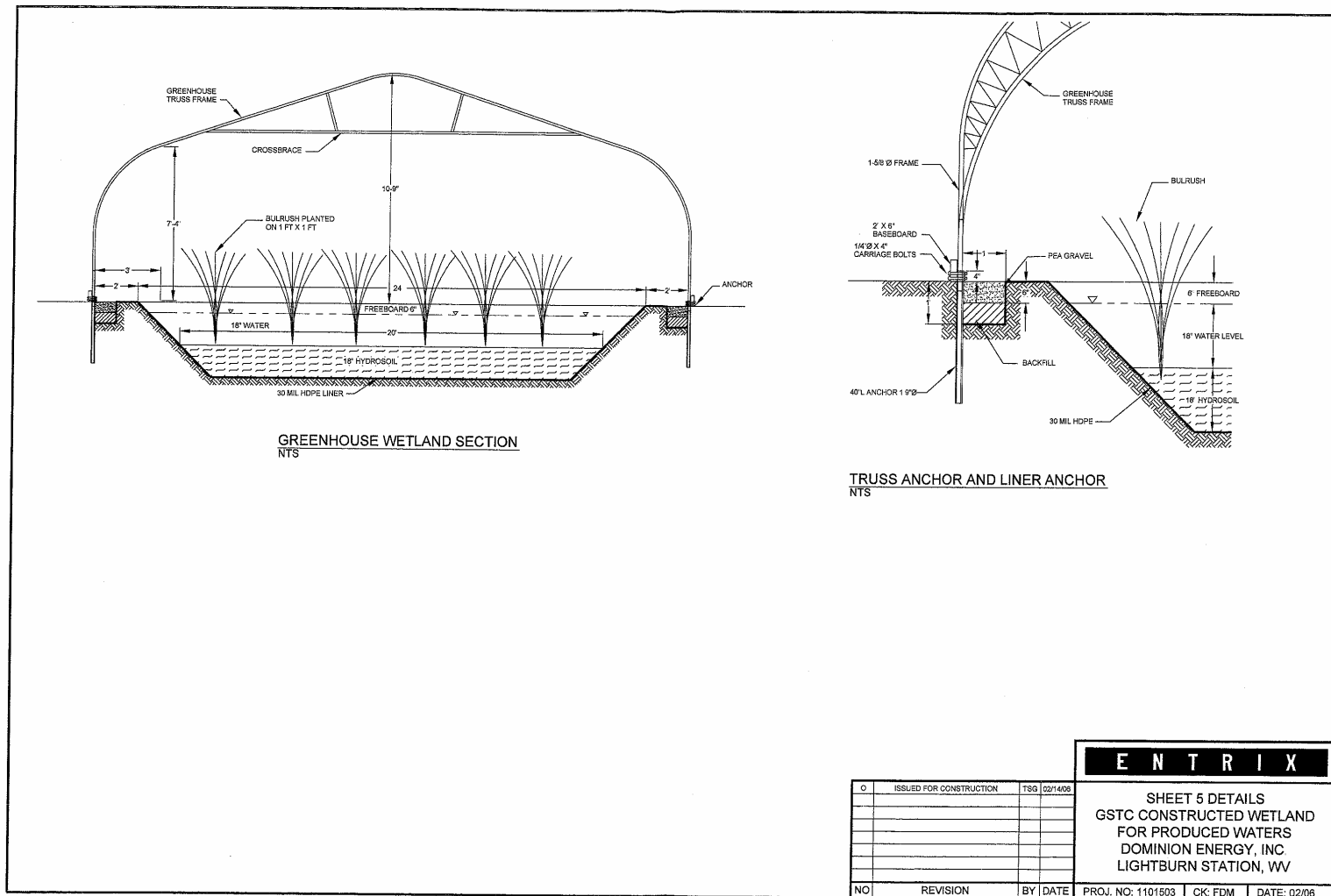


Figure 5. Greenhouse wetland, truss anchor, and liner anchor sections.

ENTRIX			
0	ISSUED FOR CONSTRUCTION	TSG	02/14/06
NO	REVISION	BY	DATE
		PROJ. NO:	1101503
		CK:	FDM
		DATE:	02/06

SHEET 5 DETAILS
 GSTC CONSTRUCTED WETLAND
 FOR PRODUCED WATERS
 DOMINION ENERGY, INC
 LIGHTBURN STATION, WV

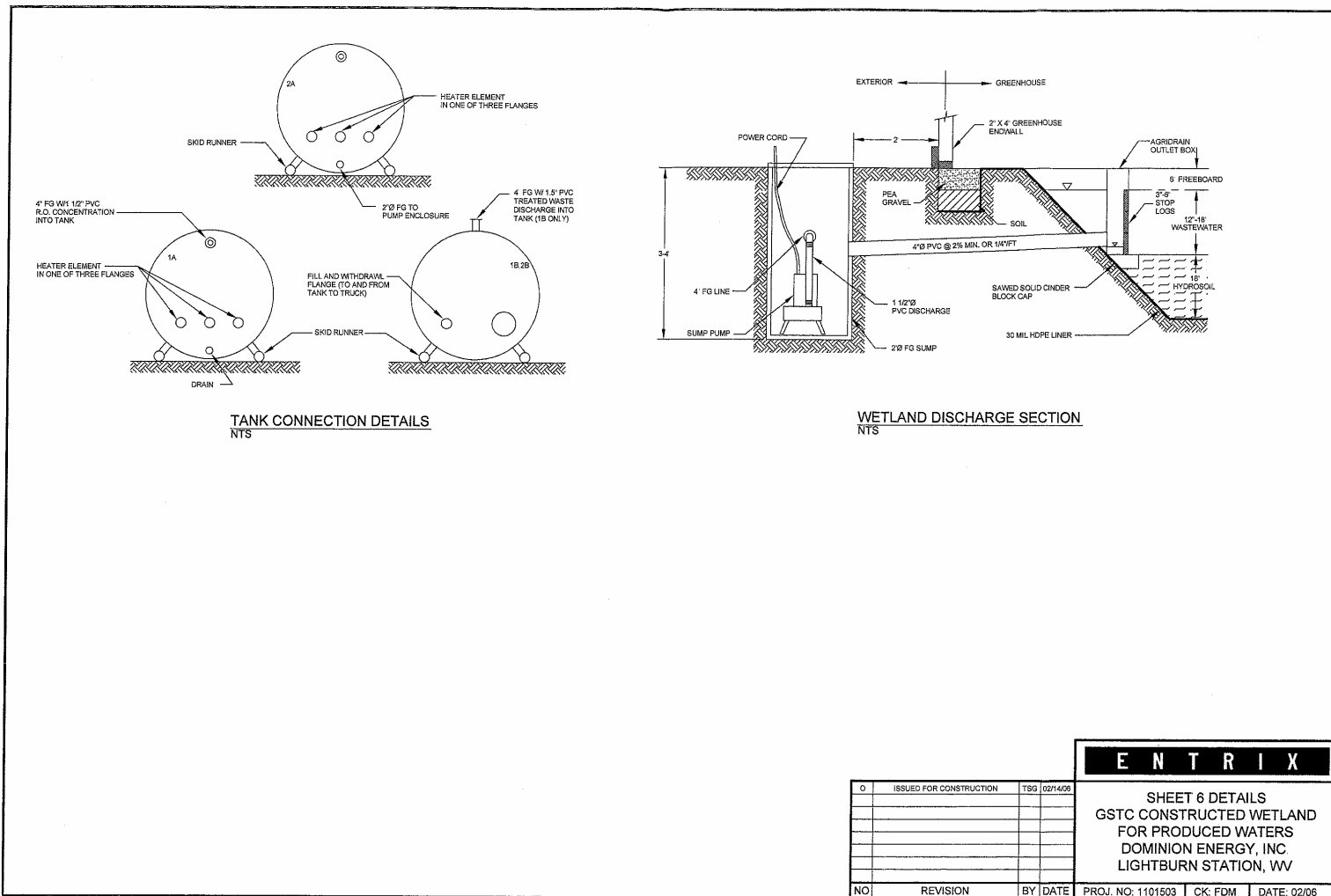


Figure 6. Tank connection details and wetland discharge section.

ENTRIX

SHEET 6 DETAILS
GSTC CONSTRUCTED WETLAND
FOR PRODUCED WATERS
DOMINION ENERGY, INC
LIGHTBURN STATION, WV

0	ISSUED FOR CONSTRUCTION	TSG	02/14/06
NO	REVISION	BY	DATE

PROJ. NO. 1101503 CK: FDM DATE: 02/06



Figure 7. Exterior of greenhouse and tanks. Inflow tank is to the right, effluent tank is to the left.

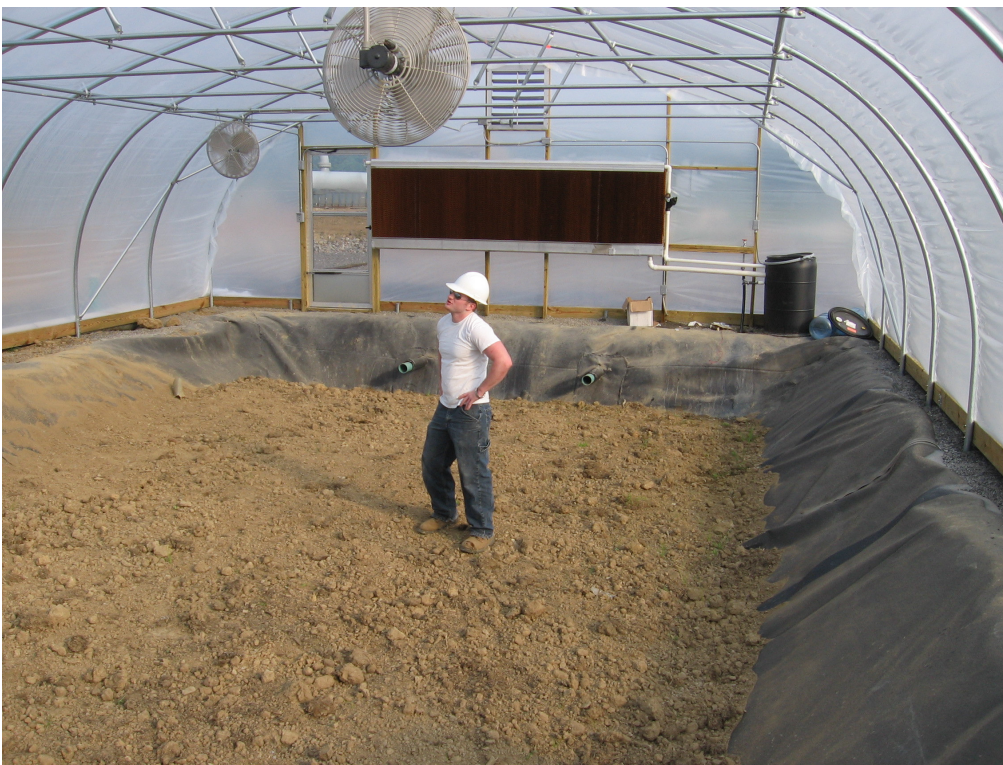


Figure 8. Interior of greenhouse including HDPE liner, hydrosoil and a graduate student.

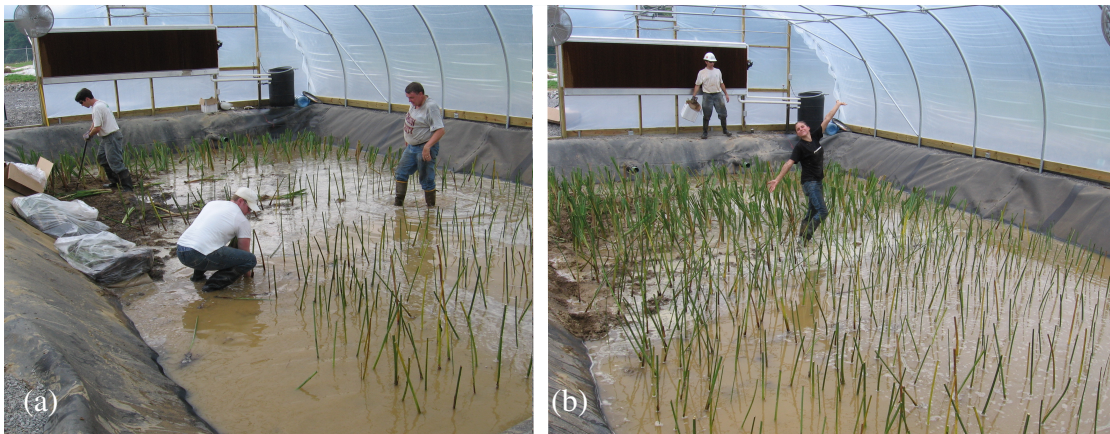


Figure 9. Planting of *S. californicus* and *T. latifolia*: (a) planting process (b) completed planting.

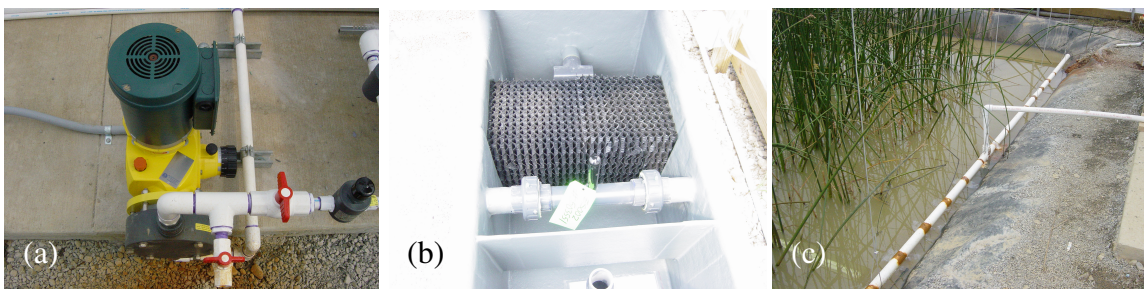


Figure 10. Components of the treatment system. (a) metering pump (b) oil-water separator (c) inflow spreader pipe.

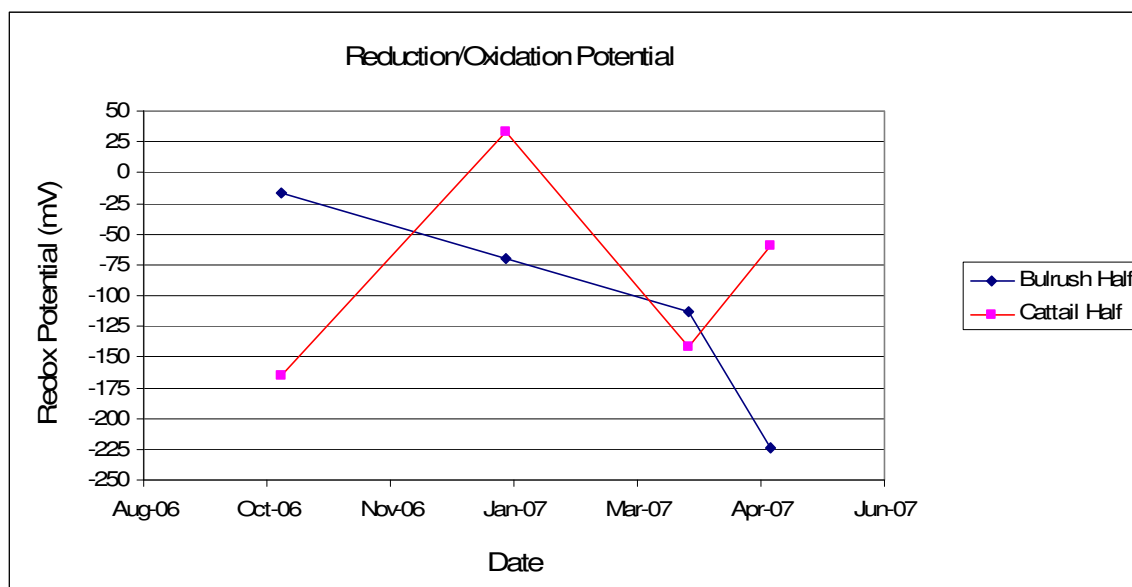


Figure 11. Redox potential in the wetland with time.

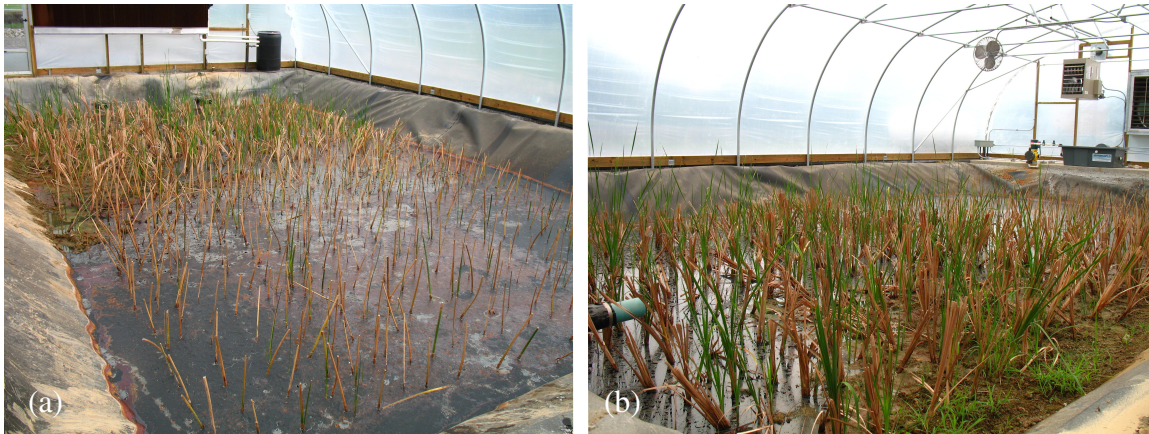


Figure 12. Wetland one month after planting: (a) bulrush side of wetland (b) cattail side of wetland

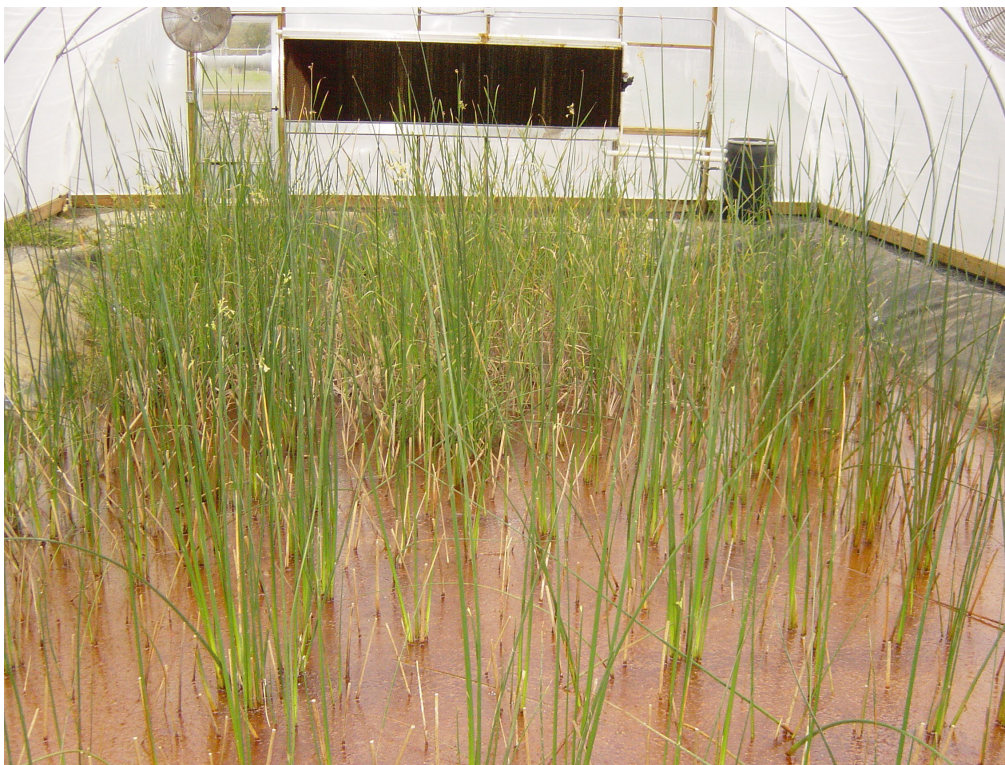


Figure 13. Wetland three months after planting. Bulrush are in the front, and cattails are in the back.



Figure 14. Wetland six months after planting. Bulrush are in the front and cattails are in the back. The mature bulrush have developed seed heads.

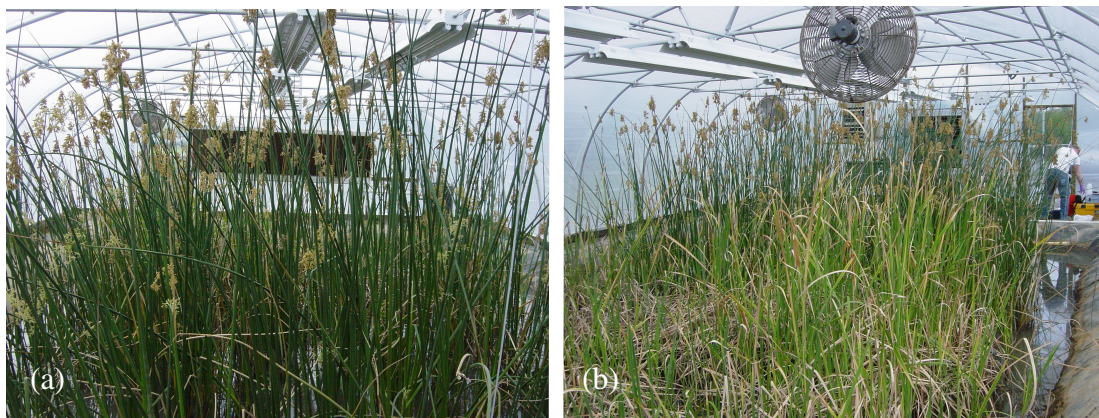


Figure 15. Wetland ten months after planting: (a) bulrush side of wetland (b) cattail side of wetland

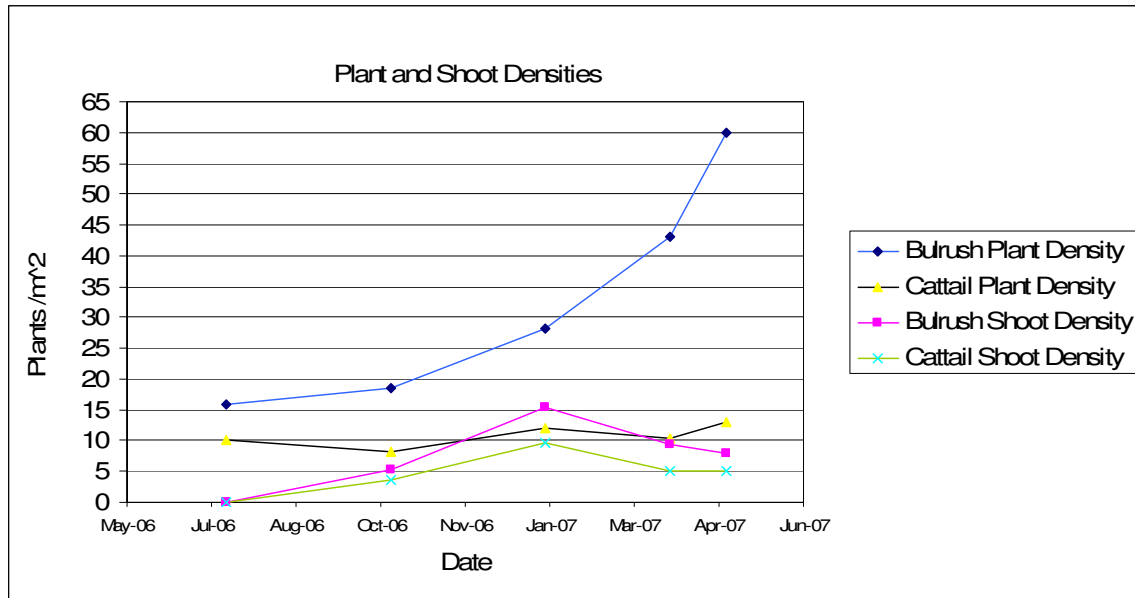


Figure 16. Plant and shoot densities in the wetland with time.

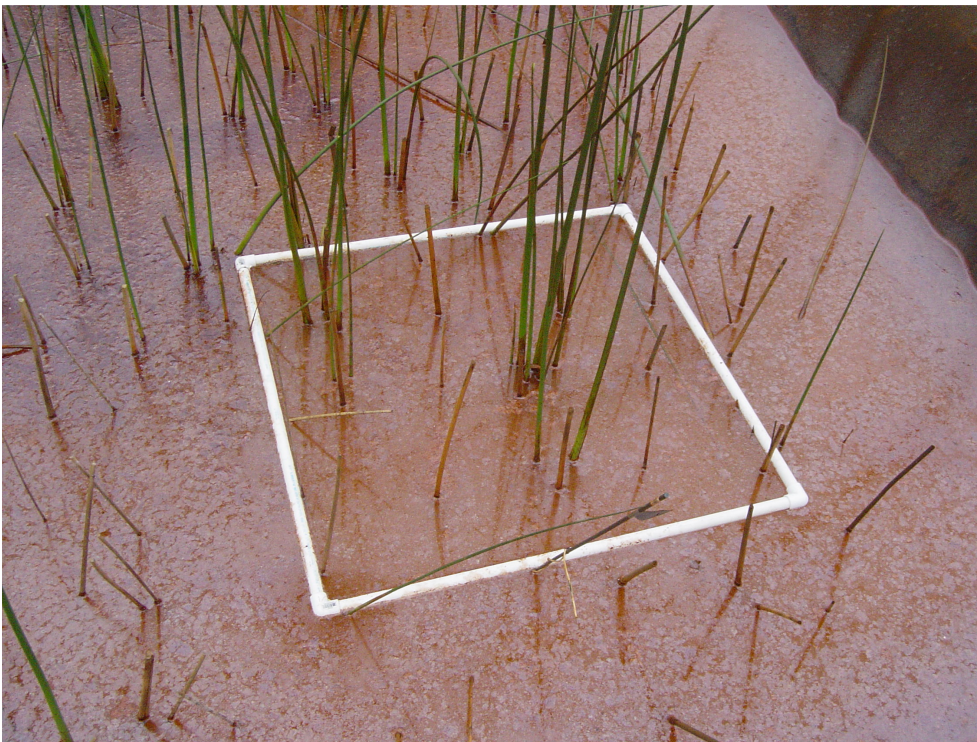


Figure 17. PVC frame (1 m²) used for plant and shoot density measurements.

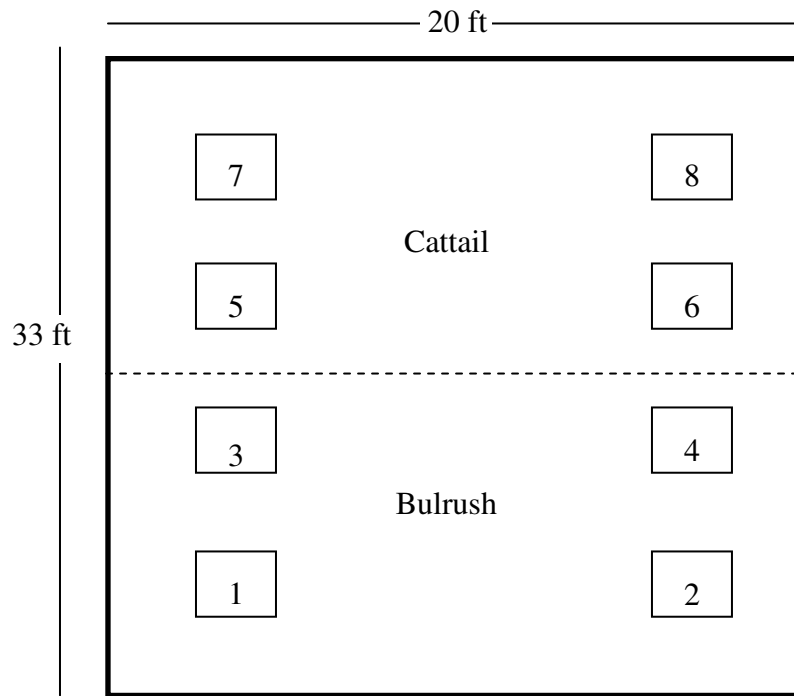


Figure 18. Schematic diagram showing measurement locations in wetland.

Table 1: Analytical methods for parameters monitored from the demonstration-scale constructed wetland treatment system.

Parameter	Method	Method Detection Limit
Temperature	Direct Instrumentation: YSI Model 52	0.5°C
pH	Direct Instrumentation: Orion Model 420A	0.01
Conductivity	Direct Instrumentation: YSI 30	0.1 µS/cm
Alkalinity	Standard Methods: 2320 B (APHA, 1998)	2 mg/L as CaCO ₃
Hardness	Standard Methods: 2340 C (APHA, 1998)	2 mg/L as CaCO ₃
DO ¹	Direct Instrumentation: YSI Model 52	0.1 mg/L
COD ²	Closed reflux colorimetry (HACH- modified from Standard Methods: 5220 D) (APHA, 1998)	3 mg/L
BOD ³	Standard Methods: 5210 B (APHA, 1998)	0.1 mg/L
Chloride	High: HACH Drop Count Titration Method	500 mg/L
	Low: HACH colorimetric method 8207	25 mg/L
Sulfate	Standard Methods: 4500 E (APHA, 1998)	1 mg/L
Metals	Atomic Absorption Spectrometry (AA) (U.S. EPA, 1991)	Cd-0.002 mg/L Cu-0.010 mg/L Pb-0.050 mg/L Zn-0.005 mg/L
	Inductively Coupled Plasma-Atomic Emissions Spectrometry (ICP-AES): 200.8 (U.S. EPA, 1991)	Cd-0.010 mg/L Cu-0.005 mg/L Pb-0.015 mg/L Zn-0.010 mg/L
TDS ⁴	Standard Methods: 2540 C (APHA, 1998)	0.1 mg/L
TSS ⁵	Standard Methods: 2540 D (APHA, 1998)	0.1 mg/L
Oil and Grease	TOC ⁶ & TPH ⁷	Undetermined
Bulk Redox	Standard Voltmeter, Accumet® calomel reference electrode, and <i>in situ</i> platinum-tipped electrodes (Faulkner et al., 1989).	±10mV
Toxicity	<i>Ceriodaphnia dubia</i> , (U.S. EPA, 2002)	

¹ Dissolved Oxygen² Chemical Oxygen Demand⁷ Total Petroleum Hydrocarbons³ Biological Oxygen Demand⁴ Total Dissolved Solids⁵ Total Suspended Solid⁶ Total Organic Carbons

Table 2: Cost/barrel (Minimum-Maximum) for treatment of produced waters

Treatment Method	Cost (\$/barrel)	State	Reference
Evaporation/injection	\$0.01-\$0.09	CA	(Veil, 1997)
Injection	\$1.00	KY	(Veil, 1997)
Injection	\$0.20-\$4.50	LA	(Veil, 1997)
Evaporation	\$0.25-\$0.81	NM	(Veil, 1997)
Evaporation/injection	\$0.69	NM	(Veil, 1997)
Injection	\$0.69	NM	(Veil, 1997)
Injection	\$0.30	OK	(Veil, 1997)
POTW	\$0.65-\$1.50	PA	(Veil, 1997)
POTW/Road Spread	\$1.30-\$4.20	PA	(Veil, 1997)
Treat/Discharge	\$1.00-\$2.10	PA	(Veil, 1997)
Treat/NPDES	\$1.00-\$2.10	PA	(Veil, 1997)
Treat/POTW	\$1.25-\$1.80	PA	(Veil, 1997)
Injection	\$0.23-\$4.50	TX	(Veil, 1997)
Evaporation	\$0.50-\$0.75	UT	(Veil, 1997)
Evaporation	\$0.50-\$2.50	WY	(Veil, 1997)
Injection	\$0.60-\$8.00	WY	(Veil, 1997)
Treat/injection or discharge	\$0.96	WY	(Veil, 1997)
Treat/injection or NPDES	\$0.96	WY	(Veil, 1997)
1.4 Acre CWTS	\$0.007		(Mooney, 2006)
6.25 Acre CWTS	\$0.034		(Mooney, 2006)
8 Acre CWTS	\$0.015		(Mooney, 2006)
12.5 Acre CWTS	\$0.019		(Mooney, 2006)
15 Acre CWTS	\$0.022		(Mooney, 2006)
15 Acre CWTS	\$0.017		(Mooney, 2006)

Table 3: Formulations of simulated natural gas storage produced waters by category based on chloride concentration. All waters except fresh water 2 were investigated in the previous pilot-scale project; freshwater 2 was investigated in the current demonstration-scale project.

Constituent (mg/L)	Simulated Source	Fresh Water Target Inflow		Brackish Water Target Inflow		Saline Water Target Inflow	Hyper-Saline Water Target Inflow
		1	2	1	2		
Cadmium	CdCl ₂	0.02	0.4	0.04	0.40	0.8	1.21
Copper	CuCl ₂ ·2H ₂ O	0.02	0.8	0.67	1.0	3.34	5
Lead	PbCl ₂	0.1	1	0.67	2.6	6.84	10.2
Zinc	ZnCl ₂	0.1	5	1.31	21	45.9	69
Oil/Grease	Motor Oil	3	20	15	23	49	78
Chlorides	CaCl ₂ , NaCl, MgCl ₂ ·6H ₂ O	400		2,500		15,000	40,000

* Cadmium is not regulated by any reviewed NPDES permits

Table 4: Average inflow/outflow, % removal, and estimated rate coefficients (k, units = d^{-1} = 1/days) for cadmium, copper, lead, and zinc using a pilot-scale CWTS. (Averages do not include non-detect values.)

Water Type	Sampling Point	Cadmium mg/L	Copper mg/L	Lead mg/L	Zinc mg/L
Simulated Fresh Produced Water 1	In	0.0212	ND	ND	0.635
	Out	0.0157	ND	ND	0.022
	% Removal	27%	NA	NA	97%
	k (d^{-1})	0.093	NA	NA	0.749
Simulated Fresh Produced Water 2	In	0.312	0.703	0.744	5.18
	Out	0.008	ND	ND	0.367
	% Removal	98%	>99.1%	>99%	93%
	k (d^{-1})	0.733	0.953	0.964	0.529
Simulated Brackish Produced Water 1	In	0.039	0.67	0.671	1.318
	Out	0.034	0.106	0.051	1.493
	% Removal	14%	84%	92%	-13%
	k (d^{-1})	0.03	0.37	0.514	-0.025
Simulated Brackish Produced Water 2	In	0.409	1.052	2.557	21.63
	Out	0.252	0.099	0.176	12.985
	% Removal	39%	91%	94%	41%
	k (d^{-1})	0.137	0.675	0.94	0.152
Simulated Saline Produced Water	In	1.008	5.012	6.096	44.734
	Out	0.004	0.063	0.136	0.374
	% Removal	>99%	99%	98%	99%
	k (d^{-1})	0.842	0.638	0.547	0.704
Simulated Hyper-Saline Produced Water	In	1.958	1.056	12.23	70.5
	Out	0.008	ND	0.095	0.185
	% Removal	>99%	>99%	99%	>99%
	k (d^{-1})	0.81	0.886	0.706	0.865
NA-Not Available ND-Non Detect					

Table 5: Chemical composition of storm water in wetland during initial acclimation.

Constituent	Concentration (mg/L)	EPA Method
Aluminum	0.098*	200.7
Antimony	ND	200.7
Arsenic	ND	200.7
Barium	0.047	200.7
Beryllium	ND	200.7
Cadmium	ND	200.7
Calcium	44.1	200.7
Chromium	ND	200.7
Cobalt	ND	200.7
Copper	ND	200.7
Iron	51.6*	200.7
Lead	0.0028	200.7
Magnesium	5.5	200.7
Manganese	0.52*	200.7
Nickel	ND	200.7
Potassium	15.8	200.7
Selenium	0.013	200.7
Silver	ND	200.7
Sodium	19.6	200.7
Thallium	ND	200.7
Tin	0.013	200.7
Vanadium	ND	200.7
Zinc	1.6*	200.7
Mercury	ND	245.1
Oil & Grease	8.4*	413.1
Total Petroleum Hydrocarbons	7.4*	413.1M
* Concentration exceeds EPA drinking water standards		ND-Non Detect

Table 6: Acclimation monitoring data from experiment 1, consisting of storm water with a chloride concentration of 500 mg/L.

Sample Location	Sample Concentrations (mg/L)						
	Cu	Zn	Cd	Pb	Fe	Se	Oil and Grease
Wetland Inflow	0.04	0.47	0.01	0.11	101.08	0.04	84.90
Wetland Outflow	0.02	0.41	0.01	0.01	94.24	0.01	51.85
% Removal	52	12	NR	8	7	75	39
NR - No Removal							

Table 7: Acclimation monitoring data from experiment 2, consisting of 7,900 gallons of storm water mixed with 300 gallons of NGSPW and a chloride concentration of 1,500 mg/L.

Sample Location	Sample Concentrations (mg/L)						
	Cu	Zn	Cd	Pb	Fe	Se	Oil and Grease
Wetland Inflow	ND	3.53	0.01	0.09	156.20	ND	23.00
Wetland Outflow	ND	1.80	0.01	0.12	194.23	ND	12.65
% Removal	ND	49	NR	NR	NR	ND	45
ND - Non-Detect							
NR - No Removal							

Table 8: Acclimation monitoring data from experiment 3, consisting of 8,600 gallons of storm water mixed with 350 gallons of NGSPW and a chloride concentration of 2,500 mg/L.

Sample Location	Sample Concentrations (mg/L)						
	Cu	Zn	Cd	Pb	Fe	Se	Oil and Grease
Wetland Inflow	0.20	8.78	0.08	0.05	443.39	ND	NA
Wetland Outflow	ND	1.37	0.05	0.03	438.64	ND	NA
% Removal	100	84	39	44	1	ND	NA
ND - Non-Detect							
NR - No Removal							

References Cited

American Public Health Association (APHA), American Water Works Association, and Water Pollution Control Federation. 1998. Standard methods for examination of water and wastewater, 20th Ed. American Public Health Association, Washington, D.C.

Faulkner, S.P., W.H. Patrick, Jr., R.P. Gambrell. 1989. Field techniques for measuring wetland soil parameters. *Soil Sci. Soc. Am. J.* 53: 883-890.

Mooney, Doug. 2006. Typical constructed wetlands operating costs. E-mail to Evan Cross, March 13, 2006.

Nakels, D.V., I. Oritx, and J. R. Frank. 2003. An analysis of management strategies for produced waters from natural gas production. *Produced Water: Technological /Environmental Issues and Solutions*. J. P. Ray, F.R. Engelhardt eds. Plenum Press. New York. Pp 151-162.

United States Environmental Protection Agency (U.S. EPA). 1991. *Methods for the Determination of Metals in Environmental Samples*, EPA/600/4-91/010. Cincinnati, OH.

United States Environmental Protection Agency (U.S. EPA). 2002. *Short-term Methods for Estimating Chronic Toxicity of Effluents and Receiving Water to Freshwater Organisms*, EPA/600/4-91/002. Cincinnati, OH.

Veil, John A.. 1997. Costs for off-site disposal of nonhazardous oil field wastes: salt caverns versus other disposal methods. U.S. Department of Energy, Assistant Secretary for Fossil Energy. W-31-109-Eng-38

Other Pertinent Publications

Gillespie, Jr., W.B., W.B. Hawkins, J.H. Rodgers, Jr., M.L. Cano, and P.B. Dorn. 2000. Transfer and transformations of zinc in constructed wetlands: Mitigation of a refinery effluent. *Ecological Engineering* 14: 279-292.

Hawkins, W.B., J.H. Rodgers, Jr., A.W. Dunn, P.B. Dorn, and M.L. Cano. 1997. Design and construction of wetlands for aqueous transfers and transformations of selected metals. *Ecotoxicology and Environmental Safety* 36: 238-248.

Huddleston, G.M. III and J.H. Rodgers, Jr. *in press*. Integrated design of a constructed wetland system for treatment of copper-contaminated wastewater. *Water Environment Research*.

Huddleston, G.M. III, W.B. Gillespie, Jr., and J.H. Rodgers, Jr. 2000. Using constructed wetlands to treat biochemical oxygen demand and ammonia associated with a refinery effluent. *Ecotoxicology and Environmental Safety* 45:188-193.

Knight, R.L., R.H. Kadlec, and H.M. Ohlendorf. 1999. The use of treatment wetlands for petroleum industry effluents. *Environmental Science & Tech.* 33: 973-980.

Mastin, B.J., J.H. Rodgers, Jr. and Y.T. Shah. 2001. Hybrid cavitation/constructed wetland reactors for treatment of chlorinated and non-chlorinated organics. *Chemical Engineering Tech.* 24: 97A-105A.

Moore, M.T., J.H. Rodgers, Jr., S. Smith, Jr. and C.M. Cooper. 2001. Mitigation of metolachlor-associated agriculture runoff using constructed wetlands in Mississippi, USA. *Agric. Ecosystems and Environ.* 84: 169-176.

Moshiri, G.A. (ed.). 1993. *Construction wetlands for water quality improvement*: Lewis Publishers, Ann Arbor, Michigan.

Murray-Gulde, C., J.E. Heatley, T. Karanfil, J.H. Rodgers, Jr., and J.E. Myers. 2003. Performance of a hybrid reverse osmosis-constructed wetland treatment system for brackish water. *Water Research* 37: 705-713.

Murray-Gulde, C.L., J. Bearr, and J.H. Rodgers, Jr. 2005. Evaluation of a constructed wetland treatment system specifically designed to decrease bioavailable copper in a wastestream. *Ecotoxicology and Environmental Safety* 61: 60-73.

Myers, J.E. 2000. Constructed wetland overview for the petroleum industry. Society of Petroleum Engineers E&P Environmental Conference, Stavanger, Norway (SPE 61181).

Myers, J.E., L.M. Jackson, R.F. Bernier, and D.A. Miles. 2001. An evaluation of the Department of Energy naval petroleum reserve No. 3 produced water biotreatment facility. Society of Petroleum Engineers E&P Environmental Conference, San Antonio, TX (SPE 66522).

Pope, D. H., and R.M. Pope. 1999. Diagnosis, treatment, and monitoring of microbiologically influenced productivity in natural gas storage facilities. Gas Research Institute, Report GRI-00-0056.

SAS Institute. 2002. *Statistical Analysis System. Version 9*. SAS Institute Inc., Cary, North Carolina.

United States Environmental Protection Agency (USEPA). 2000. EPA Office of Compliance Sector Notebook Project: Profile of the Oil and Gas Extraction Industry. EPA/310-R-99-006.

United States Environmental Protection Agency (USEPA). 2002. ECOTOX User Guide: ECOTOXicology Database System. Version 3.0. Available: <<http://www.epa.gov/ecotox/>>.

United States Environmental Protection Agency (USEPA). 2004. National Pollutant Discharge Elimination System: View NPDES Individual and General Permits. Available: <<http://cfpub.epa.gov/npdes/permitissuance/genpermits.cfm>>.

Veil, A., M.G. Puder, D. Elcock, and R.J. Redweik, Jr. 2004. A white paper describing produced water from production of crude oil, natural gas, and coal bed methane. United States Department of Energy, National Energy Technology Laboratory. Contract W-31-109-Eng-38.

Appendix L
2005, Gas Storage Field Deliverability Enhancement and Maintenance:
An Intelligent Portfolio Management Approach,
West Virginia University Final Report

Gas Storage Field Deliverability Enhancement and Maintenance: An Intelligent Portfolio Management Approach.

Final Report

Reporting Start Date: September 1, 2004

Reporting End Date: December 31, 2006

Report prepared by:

Shahab D. Mohaghegh, Ph.D.
Principal Investigator

Razi Gaskari, Ph.D.
Co-Principal Investigator

And Mr. Kazim Malik

Petroleum & Natural Gas Engineering
West Virginia University
Morgantown, WV 26506
Telephone: 304.293.7682
Fax: 304.293.5708

Reporting Issue Date: January 2007

Subcontract No. 3040-WVRC-DOE-1779

Report prepared for:

GSCT Consortium Director
PSU/Energy Institute
The Pennsylvania State University
C211 Coal Utilization Laboratory
University Park, PA 16802-2309
Telephone: 814.865.0531
Fax: 814.685.3248
Email: jlm9@psu.edu

DISCLAIMER

This report was prepared as an account of work sponsored by an agency of the United States Government. Neither the United States Government nor any agency thereof, nor any of their employees, makes any warranty, expressed or implied, or assumes no legal liability or responsibility for the accuracy, completeness, or usefulness of any information, apparatus, product, or process disclosed, or represents that its use would not infringe privately owned rights. Reference herein to any specific commercial product, process, or service by trade name, trademark, manufacturer, or otherwise does not necessarily constitute or imply its endorsement, recommendation, or favoring by the United States Government or any agency thereof. The views and opinions of authors expressed herein do not necessarily state or reflect those of the United States Government or any agency thereof.

ABSTRACT

Portfolio management, a common practice in the financial market, is essentially an optimization problem that attempts to increase return on investment. The objective of this project is to apply the state-of-the-art in optimum portfolio management to the gas storage field in order to optimize the return on investment associated with well remedial operations.

Each year gas storage operators spend hundreds of thousands of dollars on workovers, re-completions, and re-stimulations of storage wells in order to battle the decline in deliverability due to well damage with time. A typical storage field has tens if not hundreds of production wells. Each well will respond to remedial operations in its own unique way. The well's response to the remedial operation is a function of a set of uncontrollable reservoir characteristics such as porosity and permeability and a set of controllable parameters such as completion and stimulation practices.

The objective of this project is to identify the combination of best candidate wells for the remedial operations that will result in the most successful program each year, and consequently provides the highest return on investment. The project deliverable is a Windows-based software application that would perform the analysis and provide the list of wells and their corresponding remedial operation for each year based on the budget constraints identified by the user.

The state-of-the-art in intelligent systems application that is currently being used extensively in the Wall Street is the methodology to achieve the objectives of this proposed project. This methodology includes a hybrid form of artificial neural networks, genetic algorithms and fuzzy logic. Columbia Gas Transmission Corporation is the industry partner of this project and cooperated with the research and development team in order to ensure successful completion of the project.

The software application that is the deliverable of this project and is explained in much detail in this report is available to public free of charge. One important note about the software is that the current, publicly available version of the software includes a neural network model that has been developed for our industry partner based on the data that they made available. Once a storage operator decides to implement this software, they should contact the principal investigator of this project (*Shahab D. Mohaghegh, Professor, Petroleum & Natural Gas Engineering, West Virginia University, Email: shahab@wvu.edu - Tel; 304-293-7682 ext. 3405 – Web Site: <http://shahab.pe.wvu.edu>*) and arrange for development of a neural network model for their specific storage field. In order to make the best use of capabilities of the software package, it is recommended that the storage field have a minimum of 75 wells (wells with data that can be used for analysis).

TABLE OF CONTENTS

Abstract	3
Table of Content	4
List of Figures	5
List of Figures	7
Introduction	8
Executive Summary	9
Experimental	10
Results & Discussions	11
Conclusions	102
References	103

LIST OF FIGURES

Figure 1. Well-bore data retrieved from a file	14
Figure 2. Correction of Wrong API number in data	15
Figure 3. Data addition and refinement for Well-bore Data	16
Figure 4. Multiple Data Entries in Completion Table	18
Figure 5. Well-bore data retrieved from a file	20
Figure 6. Data addition and refinement for Completion Data	19
Figure 7. Perforation data retrieved from a file	22
Figure 8. Data addition and refinement for Perforation Data	23
Figure 9. Perforation data retrieved from a file	25
Figure 10. Microfiche to Database process	26
Figure 11. Different formats of Nitrogen Amount	27
Figure 12. Data addition and refinement for Stimulation Data	29
Figure 13. Tubing head pressure profile for multi-point test	33
Figure 14. Bottom-hole pressure profile for multi-point test	33
Figure 15. Flow test 1 – Delta pressure squared vs. time	34
Figure 16. Flow test 2 – Delta pressure squared vs. time	34
Figure 17. Extended flow test – Delta pressure squared vs. time	35
Figure 18. Log-log graph	35
Figure 19. Gas properties simulator	36
Figure 20. Calculation of true skin	37
Figure 21. Calculation of true skin from build up test	38
Figure 22. Retrieving flow rate of an open flow test	40
Figure 23. Flow Diagram of Well Test Analysis procedure	42
Figure 24. Neural Network Inputs and their source	44
Figure 25. Accuracy of training data for the Neural Net	45
Figure 26. Accuracy of calibration data for the Neural Net	45
Figure 27. Accuracy of verification data for the Neural Net	46
Figure 28. Different option in the software that make it versatile	48
Figure 29. Data addition and refinement for well test data	49
Figure 30. Screen shot of database showing different tables	50
Figure 31. Main Screen of software	51
Figure 32. File Main options	52
Figure 33. Screen shot of Template file	53
Figure 34. Comment that shows format of some cells in Template Excel file.....	53
Figure 35. Import data from filled-out Template	54
Figure 36. Remove all data from database.....	54
Figure 37. Exit from file menu.....	55
Figure 38. Help menu options.....	55
Figure 39. “about” screen from help menu.....	56
Figure 40. Browsing through the well-bore data	57
Figure 41. Well-bore tab	59
Figure 42. Completion tab	60
Figure 43. Perforation tab	61
Figure 44. Stimulation tab	62
Figure 45. Well-test tab	63
Figure 46. Adding a complete new Well – well-bore tab	64
Figure 47. Adding a complete new Well - completion tab.....	65
Figure 48. Adding a complete new Well – entering data for wellbore	66

Figure 49. Adding a complete new Well – entering data for perforation	66
Figure 50. Adding a complete new Well – entering data for stimulation	67
Figure 51. Adding a complete new Well – entering data for well test	67
Figure 52. Result of adding a complete new well	68
Figure 53. Editing well data	71
Figure 54. Editing completion data	72
Figure 55. Saving completion data	73
Figure 56. Saved completion data	74
Figure 57. Deleting perforation record	75
Figure 58. Finding a well	76
Figure 59. Well-test Analysis Option in well-test tab	77
Figure 60. Show Chart – Peak Day Rate	77
Figure 61. Show Chart – Absolute Open Flow	78
Figure 62. Show Chart – Skin	78
Figure 63. Show Chart – All Well Tests	79
Figure 64. Well Test Analysis button	80
Figure 65. Well Test Analysis module	80
Figure 66. Well Test Analysis tool	82
Figure 67. Draw a line and calculate the slope	83
Figure 68. Simplified well test analysis tool	83
Figure 69. Simplified well test with one well test before or after stimulation.....	84
Figure 70. LIT well test analysis.....	85
Figure 71. Multi point well test analysis	86
Figure 72. Well extended pressure profile	87
Figure 73. Selecting the build-up selection from pressure profile	89
Figure 74. Diagnostic plot analysis	90
Figure 75. Calculating skin from Horner plot	91
Figure 76. Selecting Ohio County	91
Figure 77. Selecting wells according to stimulation year	92
Figure 78. Offset wells	92
Figure 79. Selecting Well Parameters	93
Figure 80. Result of the wells & parameters selected	94
Figure 81. Start Candidate Selection from main screen	95
Figure 82. Candidate Selection main screen	95
Figure 83. Selecting a well for candidate selection	99
Figure 84. Options to control Candidate Selection process	97
Figure 85. Cost analysis Module.....	99
Figure 86. Inputs that used to train the Neural Network	99
Figure 87. Select the controllable parameters in optimization process	100
Figure 88. Setup GA parameters	100
Figure 89. If one of the Neural Net input is well test before stimulation it could setup here.	100
Figure 90. Optimization process for one well.....	101
Figure 91. Optimization result for selected wells.....	101
Figure 92. Rank the optimization result based on delta skin in order to find the best candidate	101

LIST OF TABLES

Table 1. Draw down Test Results	37
Table 2. Build-up test results	39
Table 3. Average Results	39
Table 4. Calculation to determine the length of chromosome	47
Table 5. CA characteristic	47

INTRODUCTION

Each year Gas Storage operators spend hundreds of thousands of dollars to combat the inevitable decline in the deliverability of their production wells. The decline in deliverability with time has two major contributors. The first contributor is geology and reservoir characteristics that are uncontrollable parameters. The second sets of parameters that contribute to the decline are associated with well damage that is addressed by well remedial operations such as workovers, re-completions, and re-stimulation of the producing wells. The parameters associated with these remedial operations can be controlled by the operator.

It is a fact that every well will respond to a specific remedial operation in a unique way. For example, the deliverability of well “A” will increase two folds if a proper restimulation is performed on it while the same operation performed on well “B” will result in little or no deliverability enhancement. Same is true for workovers. Finding the best candidate for restimulation or workover, each year, among the tens or hundreds of wells is a challenging task. Consider another situation where well “C” will have a 70% increase if a restimulation is performed but it would have a 65% increase if a far less expensive workover is performed. Obviously performing a workover instead of a restimulation on well “C” would be more economical this year.

EXECUTIVE SUMMARY

Portfolio management, a common practice in the financial market, is essentially an optimization problem that attempts to increase return on investment. The objective of this project is to apply the state-of-the-art in optimum portfolio management to the gas storage field in order to optimize the return on investment associated with well remedial operations.

Each year gas storage operators spend hundreds of thousands of dollars on workovers, re-completions, and re-stimulations of storage wells in order to battle the decline in deliverability due to well damage with time. A typical storage field has tens if not hundreds of production wells. Each well will respond to remedial operations in its own unique way. The well's response to the remedial operation is a function of a set of uncontrollable reservoir characteristics such as porosity and permeability and a set of controllable parameters such as completion and stimulation practices.

The objective of this project is to identify the combination of best candidate wells for the remedial operations that will result in the most successful program each year, and consequently provides the highest return on investment. The project deliverable is a Windows-based software application that would perform the analysis and provide the list of wells and their corresponding remedial operation for each year based on the budget constraints identified by the user.

The state-of-the-art in intelligent systems application that is currently being used extensively in the Wall Street is the methodology to achieve the objectives of this proposed project. This methodology includes a hybrid form of artificial neural networks, genetic algorithms and fuzzy logic. Columbia Gas Transmission Corporation is the industry partner of this project and cooperated with the research and development team in order to ensure successful completion of the project.

The software application that is the deliverable of this project and is explained in much detail in this report is available to public free of charge. One important note about the software is that the current, publicly available version of the software includes a neural network model that has been developed for our industry partner based on the data that they made available. Once a storage operator decides to implement this software, they should contact the principal investigator of this project (*Shahab D. Mohaghegh, Professor, Petroleum & Natural Gas Engineering, West Virginia University, Email: shahab@wvu.edu - Tel; 304-293-7682 ext. 3405 – Web Site: <http://shahab.pe.wvu.edu>*) and arrange for development of a neural network model for their specific storage field. In order to make the best use of capabilities of the software package, it is recommended that the storage field have a minimum of 75 wells (wells with data that can be used for analysis).

EXPERIMENTAL

No experimental work was performed during this project.

RESULTS & DISCUSSIONS

This is the detail report of the progress made so far in the above mentioned project, which consists of following components:

- 1- Project Overview
- 2- Data made available and its format
- 3- Neural Network Model
- 4- Genetic Optimization Model
- 5- Database & Software

PROJECT OVERVIEW

The objective of this project is to apply state-of-the-art intelligent, optimum portfolio management to the gas storage field in order to optimize the return on investment associated with well remedial operations. Columbia Gas Transmission Corporation is the industry partner in this project and provided us with very valuable data and in-depth knowledge about their gas storage field operations.

The data in very crude form was provided to the research and development team in the last week of March, 2005. The team extracted valuable data and organized it in a form of database, with generic make up in order to be reusable. Windows-based software was developed which can help the user in viewing and later populating the data with easy to use interface. One of its modules provides the user with all the valid stimulations required as an input for Neural Network. A Neural Network was trained in order to predict skin for different stimulation parameters. A Genetic Optimization tool was developed and associated with the trained Neural Network in order to find the optimum stimulation parameters. The software ranks the well according to maximum change in skin value or/and stimulation cost for a well. Then a decision is made to re-stimulate a well or not accordingly.

DATA MADE AVAILABLE AND ITS FORMAT

The research and development (R & D) team was initially provided data in MS excel worksheets. On further request, some pdf files with well schematics, well test files and well summary files were provided but still the required data especially relating to stimulations and well-tests was so scarce that the team in July, 2005 went to the Columbia Transmission Corporation Office in Charleston, WV to get more information. Retrieval of data from different files and thousands of microfiche was taking so long at the office that it was decided that West Virginia University lab facilities will be used to read thousands of microfiche. So, for the next few weeks the team concentrated its efforts on data collection. That data could be segregated into five main tables, each relating to specific characteristic features of the gas storage wells. The five characteristic features are as below:

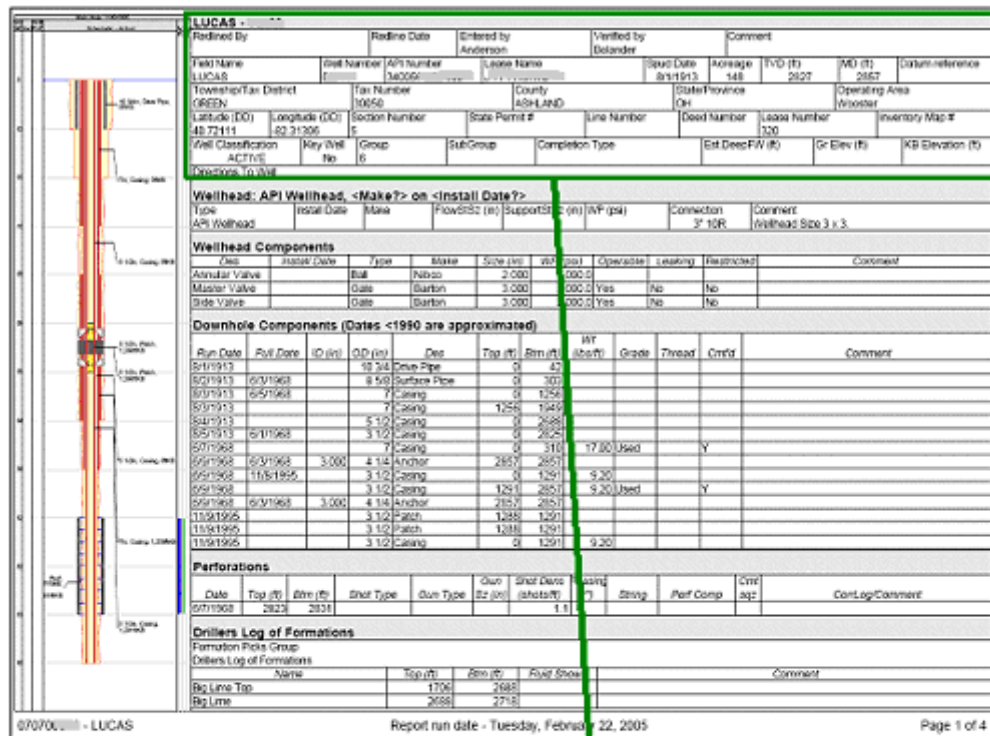
- 1- Well-bore data
- 2- Completion Data
- 3- Perforation Data
- 4- Stimulation Data
- 5- Well-Test Data
- 6- Reservoir Characteristic Data

WELL BORE DATA

It includes basic features of the well like location, depth, well name ... etc. Data about well-bore was retrieved mostly from well schematics and well summary reports. The data already provided by Columbia Transmission Corporation was also verified. The complete list of the data type retrieved is as below:

1. API Number
2. Field Name
3. Well
4. Lease Name
5. Classification
6. Latitude (Lat)
7. Longitude (Long)
8. Section
9. Township
10. County
11. State
12. Operator
13. Total Vertical Depth
14. Formation

Picture of one of the forms from which this data was retrieved is on next page



LUCAS - 000000									
Redlined By		Redline Date		Entered by		Verified by		Comment	
Anderson				Anderson		Bolander			
Field Name		Well Number		API Number		Lease Name		Spud Date	
LUCAS		340056		340056				8/1/1913	
Township/Tax District		Tax Number		County		State/Province		Acreage	
GREEN		30050		ASHLAND		OH		148	
Latitude (DD)		Longitude (DD)		Section Number		State Permit #		Line Number	
40.72111		-82.31306		5					
Well Classification		Key Well		Group		SubGroup		Completion Type	
ACTIVE		No		6					
								Est. DeepFW (ft)	

Fig1. Well-bore data retrieved from a file

The tables contained many minor mistakes like wrong Well API number, length, and many spelling mistakes. A picture of this correction is shown below:

1	A	B	C	D	E	F	G	H	I	J	K
	Field Name	Well	Lease Name	API	Classification	Latitude	Longitude	Section	Township	County	State
32	LUCAS	03897	*SYLVIA C. KROUT, ET AL*	34-005-93897	ACTIVE	40.6961	-82.3058	17	GREEN	ASHLAND	OH
33	LUCAS	03912	P. SHAFFER #1	34-005-602660000	SPECIAL	40.7133	-82.24	1	GREEN	ASHLAND	OH
34	LUCAS	03921	G. W. HINER #2	34-005-93921	ACTIVE	40.7383	-82.2719	34	VERMILLION	ASHLAND	OH
35	LUCAS	03926	JOHN BUSLER #1	34-005-602650000	ACTIVE	40.7106	-82.2358	12	GREEN	ASHLAND	OH
36	LUCAS	03929	D. KICK #1	34-005-93929	ACTIVE	40.7103	-82.2611	10	GREEN	ASHLAND	OH
37	LUCAS	03931	W. E. GUTHRIE #1	34-005-93931	ACTIVE	40.6889	-82.3047	17	GREEN	ASHLAND	OH
38	LUCAS	03932	H. J. TRUMPOWER #1	34139601180000	ACTIVE				MONROE	RICHLAND	OH
39	LUCAS	03935	J. O. ANDREWS #2	34-005-93935	ACTIVE				GREEN	ASHLAND	OH
40	LUCAS	03939	M. A. MAURER #1	34-005-93939	ACTIVE				VERMILLION	ASHLAND	OH
41	LUCAS	03945	*RUSSEL J. LIFER, ET UX*	34-005-93945	ACTIVE				GREEN	ASHLAND	OH
42	LUCAS	03946	C. SMITH #1	34005602420000	ACTIVE	40.6703	-82.3339	19	GREEN	ASHLAND	OH
43	LUCAS	03950	G. W. PURVINE #1	34139601230000	ACTIVE	40.6736	-82.3453	24	MONROE	RICHLAND	OH
44	LUCAS	03953	J. H. ROWE #1	34139201590000	ACTIVE	40.6761	-82.3417	24	MONROE	RICHLAND	OH
45	LUCAS	03963	WM. & MARY BRENNSTUHL #1	34-005-93963	ACTIVE	40.6228	-82.2925	9	HANOVER	ASHLAND	OH
46	LUCAS	03967	J. F. MANG #1	34005602590000	ACTIVE	40.6983	-82.3061	8	GREEN	ASHLAND	OH
47	LUCAS	03969	J. & E. PARR #1	34-005-93969	ACTIVE	40.6739	-82.3375	19	GREEN	ASHLAND	OH
48	LUCAS	03972	J. H. ROWE #2	34-139-93972	ACTIVE	40.6797	-82.3408	24	MONROE	RICHLAND	OH
49	LUCAS	03976	W. & M. APPLGATE #1	34-139-93976	ACTIVE	40.6836	-82.3494	13	MONROE	RICHLAND	OH
50	LUCAS	03978	A. & C. GUTHRIE #1	34-005-93978	ACTIVE	40.6806	-82.3356	19	GREEN	ASHLAND	OH
51	LUCAS	03983	E. & M. OSWALD #1	34139601590000	ACTIVE	40.6836	-82.345	13	MONROE	RICHLAND	OH
52	LUCAS	03995	S. E. MCKENLEY #1	34-005-93995	ACTIVE	40.7378	-82.2231	36	VERMILLION	ASHLAND	OH
53	LUCAS	03997	W. & M. APPLGATE #2	34-139-93997	ACTIVE	40.6856	-82.3536	13	MONROE	RICHLAND	OH
54	LUCAS	04008	H. & M. MCGUIRE #1	34005216200000	ACTIVE	40.6983	-82.2614	10	GREEN	ASHLAND	OH

Wrong API Number length

1	Field Name	Well	API	Classification	Latitude	Longitude	Section	Township	County	State	Operator
32	LUCAS	03897	34-005-93897	ACTIVE	40.6961	-82.3058	17	GREEN	ASHLAND	OH	Columbia Gas Transmissi
33	LUCAS	03912	34-005-60266	SPECIAL	40.7133	-82.24	1	GREEN	ASHLAND	OH	Columbia Gas Transmissi
34	LUCAS	03921	34-005-93921	ACTIVE	40.7383	-82.2719	34	VERMILLION	ASHLAND	OH	Columbia Gas Transmissi
35	LUCAS	03926	34-005-60265	ACTIVE	40.7106	-82.2358	12	GREEN	ASHLAND	OH	Columbia Gas Transmissi
36	LUCAS	03929	34-005-93929	ACTIVE	40.7103	-82.2611	10	GREEN	ASHLAND	OH	Columbia Gas Transmissi
37	LUCAS	03931	34-005-93931	ACTIVE	40.6889	-82.3047	17	GREEN	ASHLAND	OH	Columbia Gas Transmissi
38	LUCAS	03932	34-139-60118	ACTIVE	40.6736	-82.3478	24	MONROE	RICHLAND	OH	Columbia Gas Transmissi
39	LUCAS	03935	34-005-93935	ACTIVE		-82.247	2	GREEN	ASHLAND	OH	Columbia Gas Transmissi
40	LUCAS	03939	34-005-93939	ACTIVE		-82.2375	25	VERMILLION	ASHLAND	OH	Columbia Gas Transmissi
41	LUCAS	03945	34-005-93945	ACTIVE		-82.3017	17	GREEN	ASHLAND	OH	Columbia Gas Transmissi
42	LUCAS	03946	34-005-60242	ACTIVE	40.6703	-82.3339	19	GREEN	ASHLAND	OH	Columbia Gas Transmissi
43	LUCAS	03950	34-139-60123	ACTIVE	40.6736	-82.3453	24	MONROE	RICHLAND	OH	Columbia Gas Transmissi
44	LUCAS	03953	34-139-20159	ACTIVE	40.6761	-82.3417	24	MONROE	RICHLAND	OH	Columbia Gas Transmissi
45	LUCAS	03963	34-005-93963	ACTIVE	40.6228	-82.2925	9	HANOVER	ASHLAND	OH	Columbia Gas Transmissi
46	LUCAS	03967	34-005-60259	ACTIVE	40.6983	-82.3061	8	GREEN	ASHLAND	OH	Columbia Gas Transmissi
47	LUCAS	03969	34-005-93969	ACTIVE	40.6739	-82.3375	19	GREEN	ASHLAND	OH	Columbia Gas Transmissi
48	LUCAS	03972	34-139-93972	ACTIVE	40.6797	-82.3408	24	MONROE	RICHLAND	OH	Columbia Gas Transmissi
49	LUCAS	03976	34-139-93976	ACTIVE	40.6836	-82.3494	13	MONROE	RICHLAND	OH	Columbia Gas Transmissi
50	LUCAS	03978	34-005-93978	ACTIVE	40.6806	-82.3356	19	GREEN	ASHLAND	OH	Columbia Gas Transmissi
51	LUCAS	03983	34-139-60159	ACTIVE	40.6836	-82.345	13	MONROE	RICHLAND	OH	Columbia Gas Transmissi
52	LUCAS	03995	34-005-93995	ACTIVE	40.7378	-82.2231	36	VERMILLION	ASHLAND	OH	Columbia Gas Transmissi
53	LUCAS	03997	34-139-93997	ACTIVE	40.6856	-82.3536	13	MONROE	RICHLAND	OH	Columbia Gas Transmissi
54	LUCAS	04008	34-005-21620	ACTIVE	40.6983	-82.2614	10	GREEN	ASHLAND	OH	Columbia Gas Transmissi

Corrected API Number

Fig2. Correction of Wrong API number in data

Analysis of raw data vs. refined data:

WELLBORE DATA														
DATA FIELDS	API Number	Field Name	Well	Lease Name	Classification	Lat	Long	Section	Township	County	State	Operator	Total Vertical Depth	Formation
INITIAL DATA AVAILABLE	430	427	430	430	427	429	430	430	430	430	430	430	425	430
FINAL DATA AVAILABLE	430	430	430	430	430	430	430	430	430	430	430	430	430	430

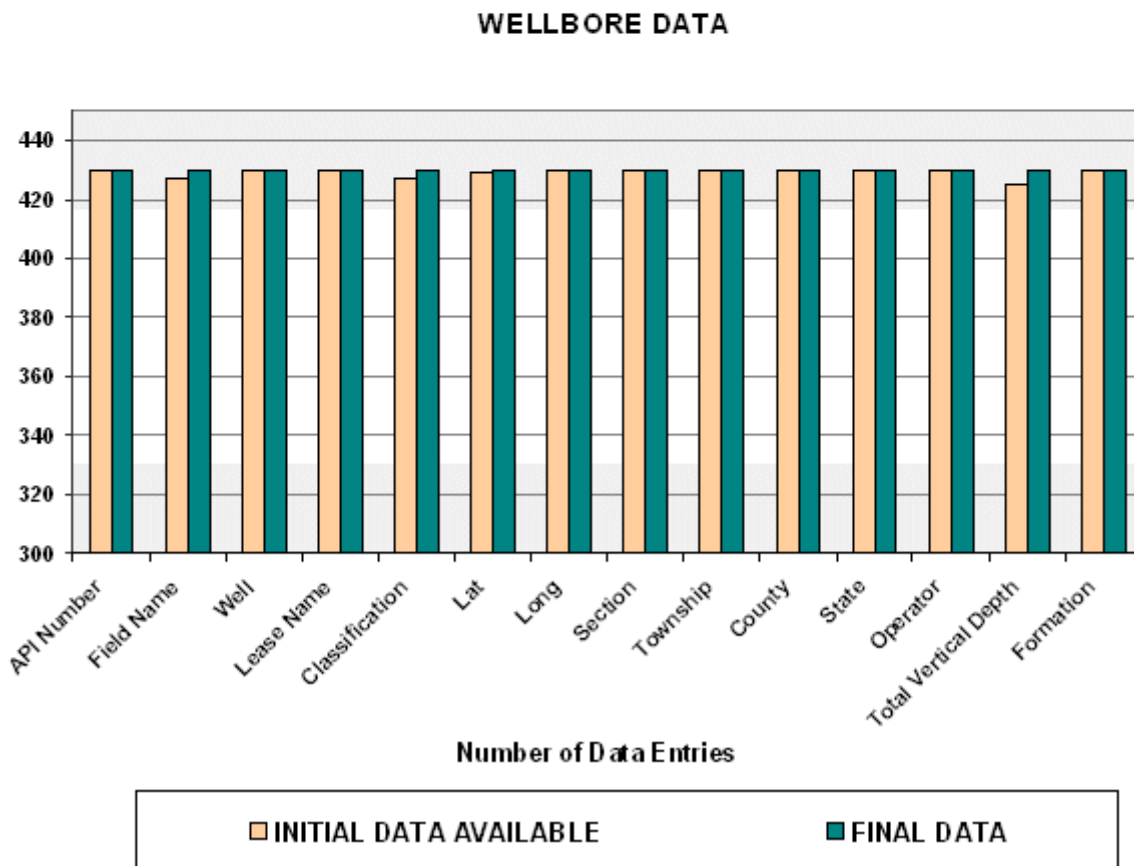


Fig3. Data addition and refinement for Well-bore Data

COMPLETION DATA

Completion data mostly relates to the type and depth of casing/liner/tubing run in the gas storage wells. The data type retained for the database includes the following:

1. API Number
2. Field Name
3. Well Name (Well)
4. Completion Description (Des)
5. Date Tubing Run (Dt Tm Rn)
6. Outer Diameter (OD)
7. Top of Casing
8. Bottom of Casing(Bot)
9. Casing Weight (Weight)
10. Casing Grade (Grade)

Unfortunately the data was mostly in an excel file and had to be verified with well schematic drawings. This led to the most unusual step in this project as it lead to reduction of valuable data available to us. This was due to the erroneous and multiple data entry originally in the completion table. Identification of the multiple entries and their removal from table was the most focused act of cleaning the data, as omission of desirable records was unacceptable. Following pictures show one of such flawed multiple data entries which were removed.

	A	B	C	D	E	F	G	H	I	J	K	L
1	Field Name	Well	API	Des	DTmRun	OD	Top	Bot	Weight	Grade		
71	LUCAS	00873	34-005-90873	Casing	03-Oct-17	7.00	0	2043	20.00			
72	LUCAS	00873	34-005-90873	Casing	02-Mar-64	5.50	0	2908	17.00	Seamless		
73	LUCAS	01981	34-005-91981	Drive Pipe	01-Nov-24	10.75	0	33	40.00			
74	LUCAS	01981	34-005-91981	Surface Pipe	02-Nov-24	8.63	0	299	24.00			
75	LUCAS	01981	34-005-91981	Casing	03-Nov-24	7.00	1893	1931	20.00			
76	LUCAS	01981	34-005-91981	Casing	04-Nov-24	5.50	0	2681	17.00			
77	LUCAS	01981	34-005-91981	Casing	02-Nov-63	3.50	0	2694	9.20	Used		
78	LUCAS	01981	34-005-91981	Packer	03-Nov-63	5.50	2684	2694		Straight Anchor		
79	LUCAS	01981	34-005-91981	Packer	03-Nov-63							
80	LUCAS	01981	34-005-91981	Packer	03-Nov-63							
81	LUCAS	02008	34-005-92008	Drive Pipe	01-Jul-25							
82	LUCAS	02008	34-005-92008	Surface Pipe	02-Jul-25							
83	LUCAS	02008	34-005-92008	Packer	03-Jul-25	8.63	1829	1839		Larkin Lead B.H.		
84	LUCAS	02008	34-005-92008	Packer	03-Jul-25	8.63	1829	1839				
85	LUCAS	02008	34-005-92008	Casing	03-Jul-25	7.00	1793	1839	20.00			
86	LUCAS	02008	34-005-92008	Packer	04-Jul-25	7.00	2500	2510				
87	LUCAS	02008	34-005-92008	Packer	04-Jul-25	7.00	2500	2510		OVS Midget		
88	LUCAS	02008	34-005-92008	Casing	04-Jul-25	5.50	0	2510	17.00			
89	LUCAS	02008	34-005-92008	Casing	02-Oct-63	5.50	0	2654				
90	LUCAS	02008	34-005-92008	Packer	02-Oct-63	5.50	2551	2561				
91	LUCAS	02008	34-005-92008	Anchor	02-Oct-63	5.50	2561	2571				
92	LUCAS	02008	34-005-92008	Packer	02-Oct-63	5.50	2551	2561				
93	LUCAS	02008	34-005-92008	Anchor	02-Oct-63	5.50	2561	2571				
94	LUCAS	02060	34-005-92060	Casing	01-Oct-25	10.75	0	64	40.00			

Fig4. Multiple Data Entries in Completion Table

In the completion table, the following notations used as casing description were replaced in place of different notations being used to have a standard definition

NOTATION KEPT IN DATABASE	Surface casing
NOTATIONS DISCARDED	Drive pipe
	Driver Pipe
	Swedge
	Two stage

Completion data was mostly re- checked for accuracy from the documents, picture of which is shown below for a Well.

LUCAS

Redlined By: _____ Redline Date: _____ Entered by: Anderson Verified by: Bolander Comment: _____

Field Name: LUCAS Well Number: 06... API Number: 340056... Lease Name: ... Spud Date: 8/1/1913 Acreage: 148 TVD (ft): 2827 MD (ft): 2857 Datum reference: _____

Township/Tax District: GREEN Tax Number: 30050 County: ASHLAND State/Province: OH Operating Area: Wooster

Latitude (DD): 42.72111 Longitude (DD): -81.1306 Section Number: 5 State Permit #: _____ Line Number: _____ Deed Number: _____ Lease Number: _____ Inventory Map #: _____

Well Classification: ACTIVE Key Well: No Group: _____ SubGroup: _____ Completion Type: _____ Est. DeepFW (ft): _____ Gr Elev (ft): _____ KB Elevation (ft): _____

Directions To Well: _____

Wellhead: API Wellhead, <Make?> on <Install Date?>

Type	Install Date	Make	FlowStSz (in)	SupportStSz (in)	WP (psi)	Connection	Comment
API Wellhead						3" 10R	Wellhead Size 3 x 3.

Wellhead Components

Des	Install Date	Type	Make	Size (in)	WP (psi)	Operate	Leaking	Restricted	Comment
Annular Valve		Ball	Nibco	2.000	2,000.0				
Master Valve		Gate	Barton	3.000	2,000.0	Yes	No	No	
Side Valve		Gate	Barton	3.000	2,000.0	Yes	No	No	

Downhole Components (Dates <1990 are approximated)

Run Date	Pull Date	ID (in)	OD (in)	Des	Top (ft)	Btn (ft)	Wt (lbs/ft)	Grade	Thread	Cmt'd	Comment
8/1/1913			10 3/4	Drive Pipe	0	42					
8/2/1913	6/3/1968		8 5/8	Surface Pipe	0	303					
8/3/1913	6/5/1968		7	Casing	0	1256					
8/3/1913			7	Casing	1256	1949					
8/4/1913			5 1/2	Casing	0	2688					
8/5/1913	6/1/1968		3 1/2	Casing	0	2825					
6/7/1968			7	Casing	0	310	17.00			Used	
6/9/1968	6/3/1968	3.000	4 1/4	Anchor	2857	2857					
6/9/1968	11/8/1995		3 1/2	Casing	0	1291	9.20				
6/9/1968			3 1/2	Casing	1291	2857	9.20			Used	
6/9/1968	6/3/1968	3.000	4 1/4	Anchor	2857	2857					
11/9/1995			3 1/2	Patch	1288	1291					
11/9/1995			3 1/2	Patch	1288	1291					
11/9/1995			3 1/2	Casing	0	1291	9.20				

↓

Downhole Components (Dates <1990 are approximated)											
Run Date	Pull Date	ID (in)	OD (in)	Des	Top (ft)	Btn (ft)	Wt (lbs/ft)	Grade	Thread	Cmt'd	Comment
8/1/1913			10 3/4	Drive Pipe	0	42					
8/2/1913	6/3/1968		8 5/8	Surface Pipe	0	303					
8/3/1913	6/5/1968		7	Casing	0	1256					
8/3/1913			7	Casing	1256	1949					
8/4/1913			5 1/2	Casing	0	2688					
8/5/1913	6/1/1968		3 1/2	Casing	0	2825					
6/7/1968			7	Casing	0	310	17.00			Used	
6/9/1968	6/3/1968	3.000	4 1/4	Anchor	2857	2857					
6/9/1968	11/8/1995		3 1/2	Casing	0	1291	9.20				
6/9/1968			3 1/2	Casing	1291	2857	9.20			Used	
6/9/1968	6/3/1968	3.000	4 1/4	Anchor	2857	2857					
11/9/1995			3 1/2	Patch	1288	1291					
11/9/1995			3 1/2	Patch	1288	1291					
11/9/1995			3 1/2	Casing	0	1291	9.20				

Fig5. Well-bore data retrieved from a file

Analysis of raw data vs. refined data:

Please note that multiple data entry was the major reason for the reduction in the refined data from the initial data.

COMPLETION DATA											
DATA FIELDS	Total Completions Run	API Number	Field Name	Well	Description	Date Tubing Run	OD	Top Casing	Bot	Weight	Grade
INITIAL DATA AVAILABLE	2910	431	431	431	2909	2909	2909	2909	2909	1781	1607
FINAL DATA AVAILABLE	2413	430	431	431	2413	2413	2413	2413	2413	1723	1607

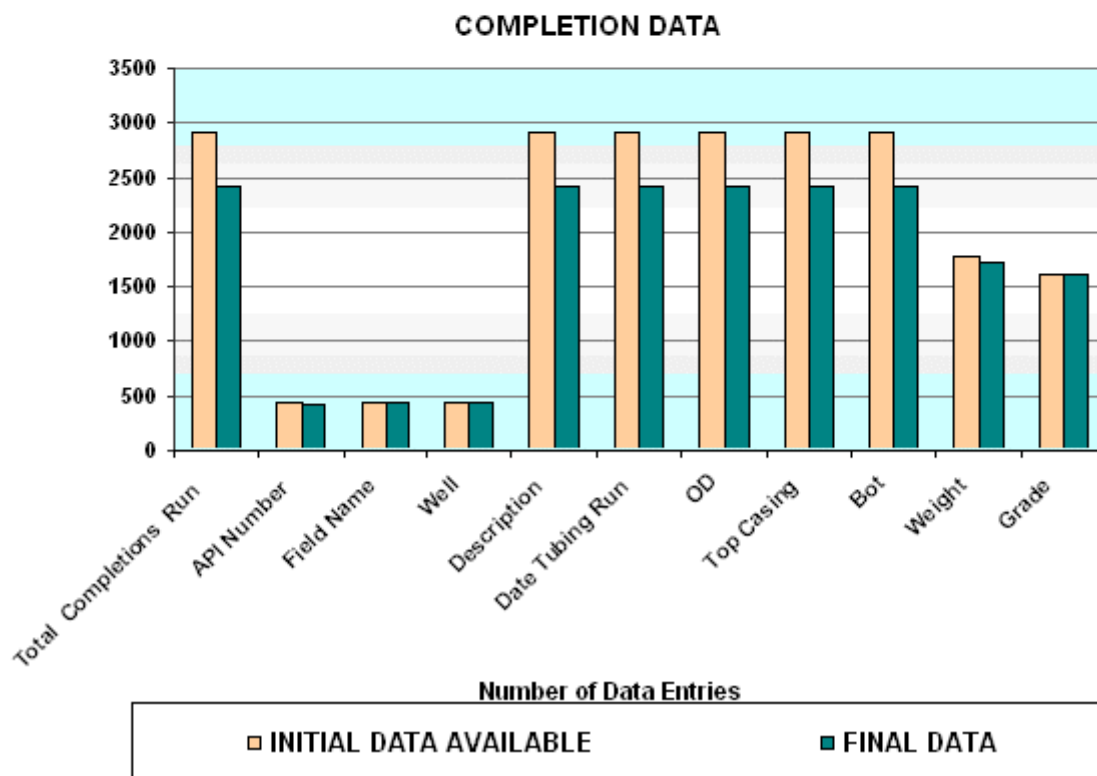


Fig6. Data addition and refinement for Completion Data

PERFORATION DATA

This data set contains all the information relating to the perforations done on the gas storage well like perforation top & bottom depth and shots per foot. Following are the data types included in this type of data set:

1. Well API Number
2. Field Name
3. Well Name
4. Completion Type
5. Perforation Date (Perf Date)
6. Perforation Top (Perf Top)
7. Perforation Bottom (Perf Btm)
8. Shot Type
9. Shot Per foot (Shot Per ft)

The picture of a document showing this information is shown below.

LUCAS - 00											
Redlined By		Redline Date		Entered by Anderson		Verified by Bolander		Comment			
Field Name LUCAS	Well Number 00...	API Number 340056	Lease Name			Spud Date 8/1/1913	Acreage 148	TVD (ft) 2827	MD (ft) 2857	Datum reference	
Township/Tax District GREEN		Tax Number 30050	County ASHLAND			State/Province OH		Operating Area Wooster			
Latitude (DD) 42111	Longitude (DD) 81306	Section Number 5	State Permit #	Line Number	Deed Number	Lease Number	Inventory Map #				
Well Classification ACTIVE	Key Well No	Group 8	SubGroup	Completion Type		Est DeepFW (ft)	Gr Elev (ft)	KB Elevation (ft)			
Directions To Well											
Wellhead: API Wellhead, <Make?> on <Install Date?>											
Type API Wellhead	Install Date	Make	FlowStSz (in)	SupportStSz (in)	WP (psi)	Connection 3" 10R	Comment Wellhead Size 3 x 3.				
Wellhead Components											
Des	Instal Date	Type	Make	Size (in)	WP (psi)	Operable	Leaking	Restricted	Comment		
Annular Valve		Ball	Nibco	2.000	2,000.0						
Master Valve		Gate	Barton	3.000	2,000.0	Yes	No	No			
Side Valve		Gate	Barton	3.000	2,000.0	Yes	No	No			
Downhole Components (Dates <1990 are approximated)											
Run Date	Full Date	ID (in)	OD (in)	Des	Top (ft)	Btm (ft)	WT (lbs/ft)	Grade	Thread	Cmt/ft	Comment
8/1/1913			10.34	Drive Pipe	0	42					
8/2/1913	8/3/1968		8.5/8	Surface Pipe	0	303					
8/3/1913	8/5/1968		7	Casing	0	1256					
8/3/1913			7	Casing	1256	1949					
8/4/1913			5.1/2	Casing	0	2638					
8/5/1913	8/1/1968		3.1/2	Casing	0	2625					
8/7/1968			7	Casing	0	310	17.00	Used		Y	
8/9/1968	8/3/1968	3.000	4.1/4	Anchor	2857	2857					
8/9/1968	11/8/1995		3.1/2	Casing	0	1291	9.20				
8/9/1968			3.1/2	Casing	1291	2857	9.20	Used		Y	
8/9/1968	8/3/1968	3.000	4.1/4	Anchor	2857	2857					
11/9/1955			3.1/2	Patch	1288	1291					
11/9/1955			3.1/2	Patch	1288	1291					
11/9/1955			3.1/2	Casing	0	1291	9.20				
Perforations											
Date	Top (ft)	Btm (ft)	Shot Type	Gun Type	Gun Sz (in)	Shot Dens (shots/ft)	Phasing (°)	String	Perf Comp	Cmt sqz	Comment
8/7/1968	2823	2831				1.1					
Drillers Log of Formations											
Formation Picks Group											
Drillers Log of Formations											
Name	Top (ft)	B	Fluid Shows	Comment							
Big Lime Top	1706										
Big Lime	2658										

070700323 - LUCAS

Report run date

y, February 22, 2005

Page 1 of 4

Perforations											
Date	Top (ft)	Btm (ft)	Shot Type	Gun Type	Gun Sz (in)	Shot Dens (shots/ft)	Phasing (°)	String	Perf Comp	Cmt sqz	Comment
8/7/1968	2823	2831				1.1					

Fig7. Perforation data retrieved from a file

Analysis of raw data vs. refined data:

PERFORATION DATA										
DATA FIELDS	Total Perforations	API Number	Field Name	Well Name	Completion Type	Perf Date	Perf Top	Perf Bottom	Shot Type	Shot Per ft
INITIAL DATA AVAILABLE	392	57	57	57	48	392	392	392	209	383
FINAL DATA AVAILABLE	392	57	57	57	48	392	392	392	209	383

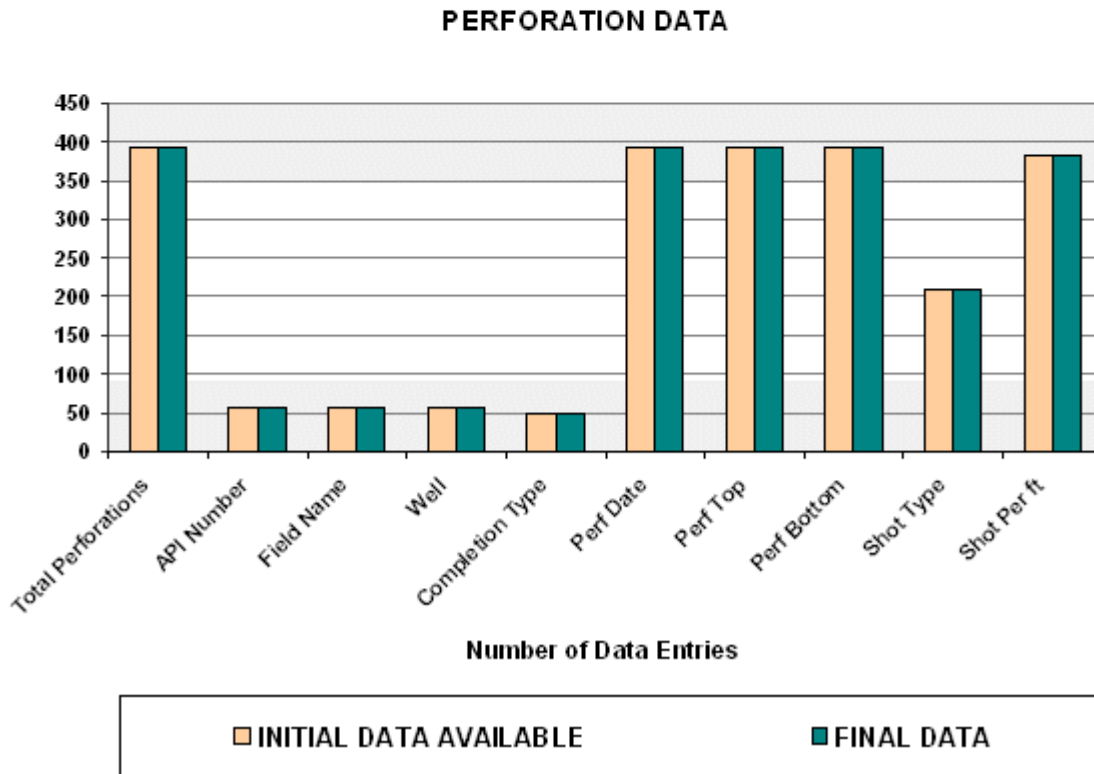


Fig8. Data addition and refinement for Perforation Data

STIMULATION DATA

Stimulation data is one of the most significant datasets about the storage wells. Because of this, it was very important that we have maximum records of valid stimulations. Following data type is used to represent stimulation:

1. API Well Number
2. Well Name
3. Size of String
4. Stimulation From
5. Stimulation To
6. No Of Shots
7. Fractured by
8. Stimulation Type
9. Stimulation Date
10. Water
11. Acid
12. Gel
13. Foam
14. Nitrogen
15. Alcohol
16. Cushion
17. Flush
18. Sand Quantity
19. Sand Type
20. Injection Rate
21. Total Fluid
22. Breakdown Pressure
23. ISIP

Unfortunately, initially we didn't have much data about the stimulations being done in this Lucas field. With this in mind, every record with Columbia Transmission Corporation was carefully examined. The largest source of stimulation data came from the thousands of microfiche with some data being found in well summary reports. Following is a picture of data in well summary reports.

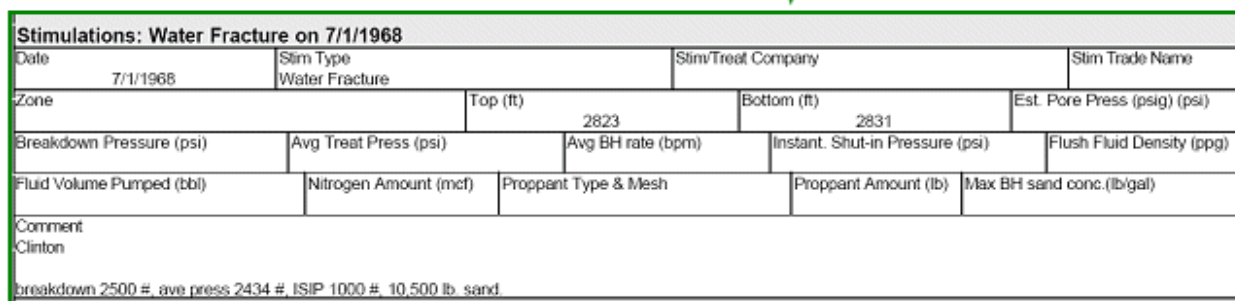
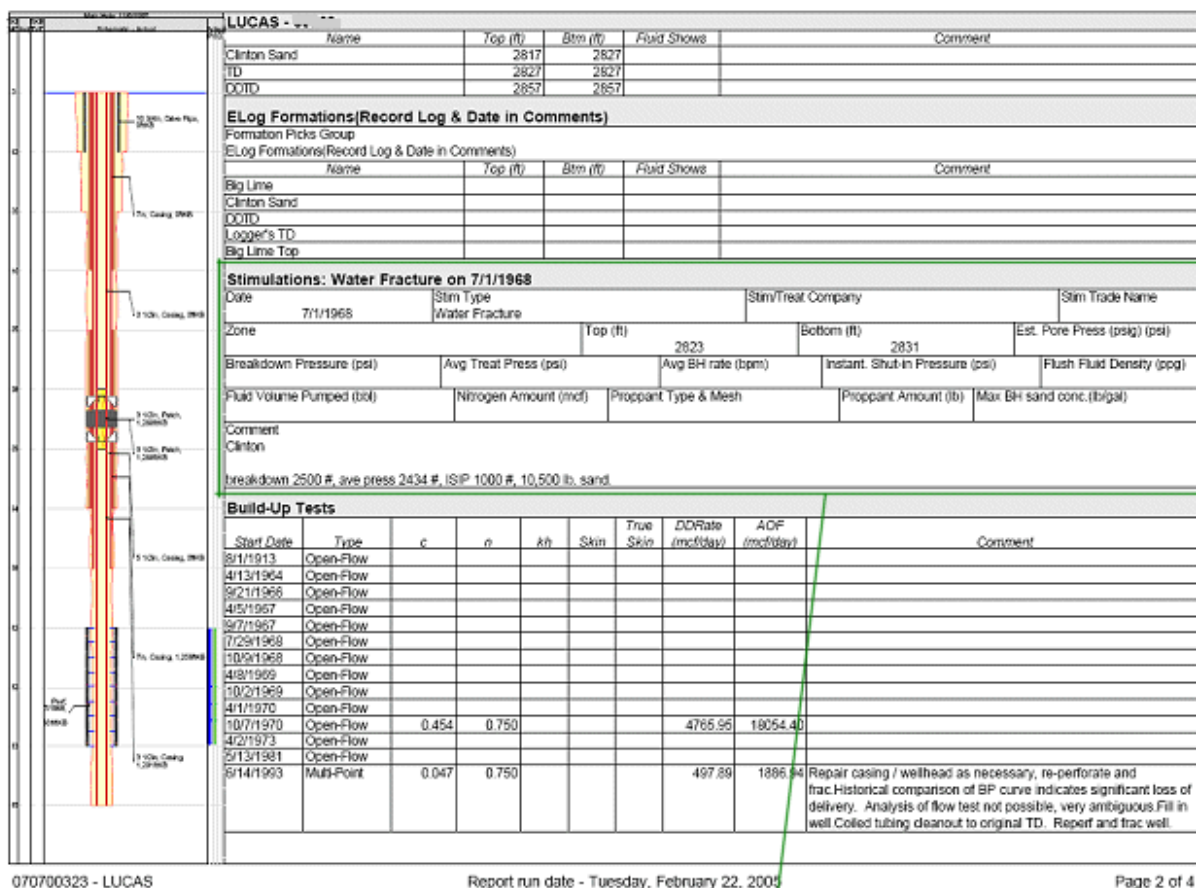
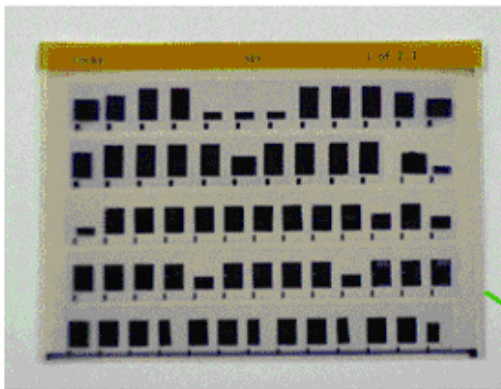
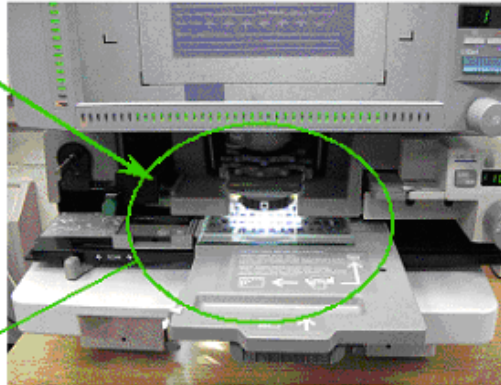


Fig9. Stimulation data retrieved from a file



Each Microfiche contained dozens of documents from invoices to valuable stimulation and well-test data

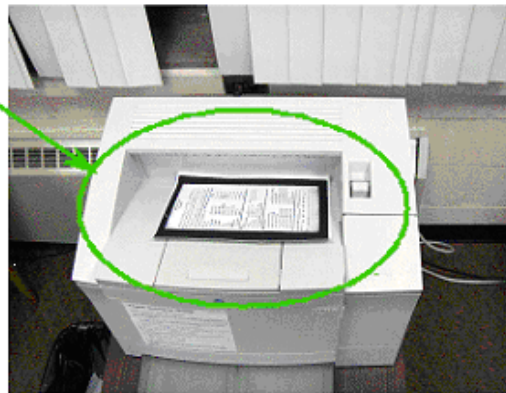
Microfiche were read by digital Microfilm scanners



Each scanned image of the microfiche was searched and read for valuable data



Prints were taken of the documents containing data



Data was entered in the database

API Number	SizeOfString	StartFrom	SamTo	NoOfGhosts	Fracturedby	Type	Sta
34-005-01272	4.5	2962	2906 9		Oswell Inc.	Water-Gel	11
34-005-01420	4.5	2799	2764 11		Oswell Inc.	Water-Gel	12
34-005-02087	4.5	2804	2810 13		Oswell Inc.	Water-N2	6
34-005-02089	4.5	2838	2845 12		Oswell Inc.	Water-N2	7
34-005-02089	4.5	2820	2826 10		Oswell Inc.	Water-N2	6
34-005-02087	4.5	2863	2860 12		Haliburton Co.	Water-Gel	7
34-005-02001	4.5	2723	2748 12		Haliburton Co.	Water-Gel	6
34-005-02907	3.5	2023	2045 13		Haliburton Co.	Water-Gel	7
34-005-02009	4.5	2796	2814 5		Haliburton Co.	Water-Gel	7
34-005-02909	4.5	2809	2814 5		Haliburton Co.	Water-Gel	7
34-005-02911	4.5	2785	2806 13		Haliburton Co.	Water-Gel	9
34-005-02960	4.5	2911	2921 13		Oswell Inc.	Water-Gel	10
34-005-10516	5.5	2568	2608		Haliburton Co.	Visa-Frac	12
34-005-10517	5.5	2555	2590		Oswell Inc.	Water-N2	5
34-005-10518	5.5	2580	2622		Oswell Inc.	Petro-Gel	12
34-005-10519	5.5	2574	2652		Haliburton Co.	Water-N2	9
34-005-10520	5.0	2505	2964		Oswell Inc.	Water-Gel	1
34-005-10527	5.5	2866	2901		Oswell Inc.	Water-N2	5
34-005-10533	5.5	2627	2653		Oswell Inc.	Petro-Gel	12
34-005-10538	5.5	2804	2844		Oswell Inc.	Petro-Gel	12
34-005-10540	5.5	2860	2905		Oswell Inc.	Water-N2	6

Fig10. Microfiche to Database process

Following are pictures of some types of data formats for fracture jobs found in the records

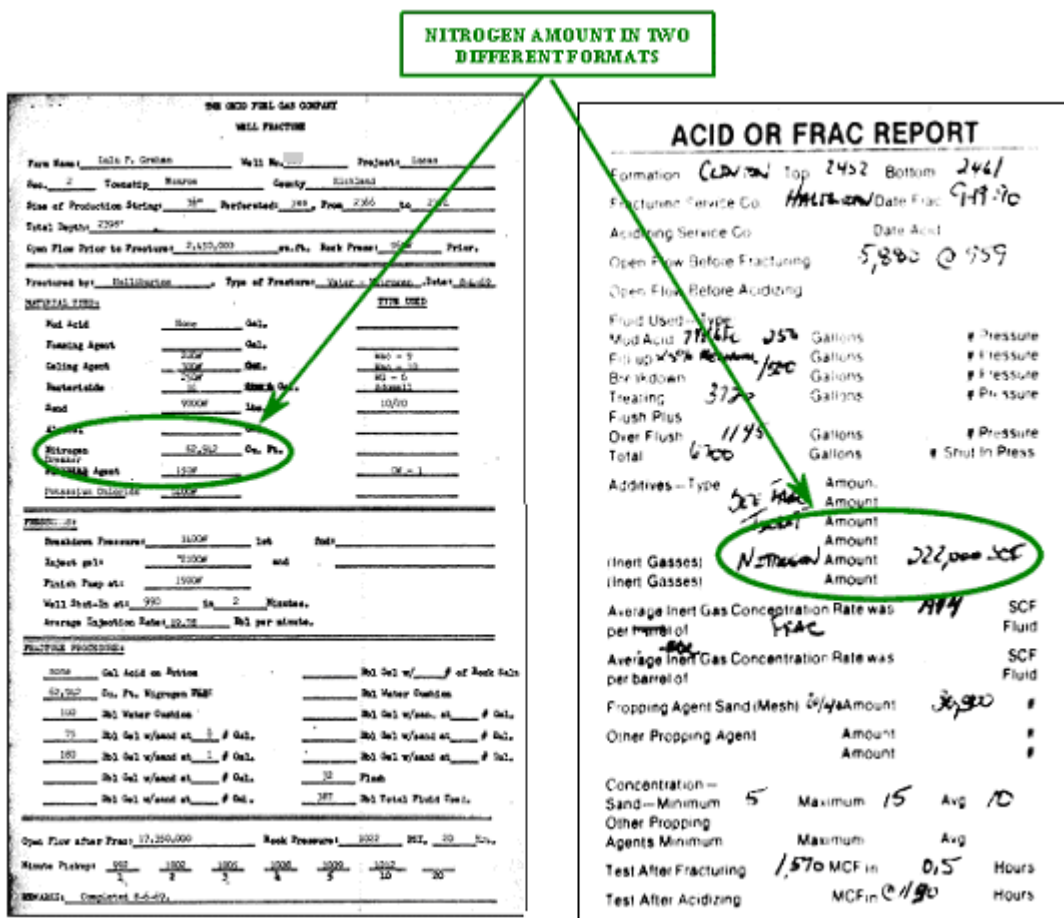


Fig11. Different formats of Nitrogen Amount

During the data entry different sign conventions and unit conversions were carried out as follows:

MEASURED QUANTITY	UNITS IN RECORDS	UNITS USED IN DATABASE
SAND	1 sack 1 sks	100 lbs
NITROGEN	52M	52,000 SCF
LIQUID PERFORATIONS	1 bbl 2000-2005 ft, 10 shots 10/5	42 gal 2 shots /ft

The following notations were used in place of different notations being used in the tables:

NOTATIONS USED IN DATABASE	WATER GEL FRAC	PETRO GEL FRAC	FOAM FRAC	NITRO SHOT	WATER/N2 FRAC	WATER FRAC	10/20 SAND
NOTATIONS THAT WERE REPLACED	Gelled water frac	Petro gel	Foam	Shot	Water / N2	water	10/20
	Water Gel	Petro Gel Petro gel fracture	foam Frac foam fracture		Water N2 Fracture Water nitrogen		Sand 10/20
					Water/N2 assist Water Fracture w/N2 assist		

All records of Nitro-shots were discarded for this database as they have no stimulation parameters on record and are part of history now plus they also damage the well. Above all, they will tend to degrade the Neural Network.

Analysis of raw data vs. refined data:

STIMULATION DATA																								
DATA FIELDS	Total Stimulations	API Number	Well	Size Of String	Stim From	Stim To	No Of Shots	Fractured by	Type	Stim Date	Water	Acid	Gel	Foam	N2	Alcohol	Cushion	Flush	Sand Quantity	Sand Type	Injection Rate	Total Fluid	Breakdown Pressure	ISIP
INITIAL DATA AVAILABLE	32	32	32	32	32	32	32	32	32	32	0	0	0	0	0	0	0	0	32	32	25	0	27	24
FINAL DATA AVAILABLE	390	430	430	308	388	388	156	354	370	391	85	293	294	157	249	21	277	302	368	266	263	317	181	346

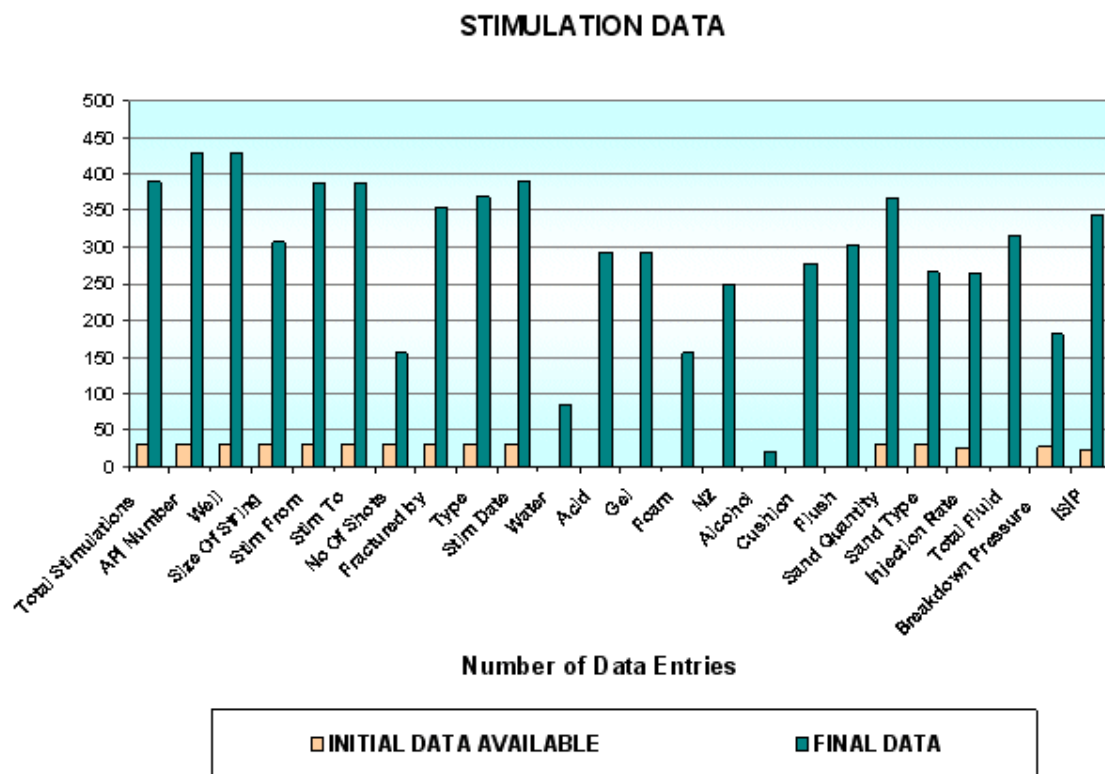


Fig12. Data addition and refinement for Stimulation Data.

WELL TEST DATA

Well-test data is the most extensive dataset that our R & D team worked on. It has the maximum amount of records nearly 3365 and 29 data types that control every aspect of a well-test. The data type selected for a well-test representation consists of following:

1. Well API Number
2. Field Name
3. Test Date
4. Test Type
5. Time 1
6. Field Pressure 1
7. Flowing Pressure 1
8. Rate 1
9. Time 2
10. Field Pressure 2
11. Flowing Pressure 2
12. Rate 2
13. Time 3
14. Field Pressure 3
15. Flowing Pressure 3
16. Rate 3
17. Time Extended
18. Field Pressure Extended
19. Flowing Pressure Extended
20. Rate Extended
21. kh
22. Skin
23. True Skin
24. Non Darcy Co-efficient
25. n Value
26. C Value
27. Delta Pressure Squared
28. Peak Day Rate
29. Absolute Open Flow

Estimation of n, C, peak day rate & absolute open flow

Single/Open flow Tests:

The values used for point 1 and 2 are from different well-tests

1- Find ΔP^2

3-
$$\frac{1}{n} = \frac{\log(\bar{p}^2 - p_{wf}^2)_2 - \log(\bar{p}^2 - p_{wf}^2)_1}{\log q_2 - \log q_1}$$
 (Where q is in MMcfD)

4-
$$C = \frac{q_g}{(\bar{p}^2 - p_{wf}^2)^n}$$
 (Where q is in McfD)

5-
$$AOF = C(1150^2 - 0^2)^n$$
 McfD

6-
$$PDRate = (C \times 250,000)^n$$
 McfD

Multi-Point Tests:

Estimation of n, C, PD rate & AOF:

Same as above except that the points used are from the same test

NOTE: The n, C, PD rate & AOF values for more than 400 well-tests were manually calculated

Estimation of kh, skin, true skin, non--darcy coefficient

- 1- From extended draw-down test plot ($P_i - P_{wf}$) vs. time on log-log paper. Draw unit-line for un-stimulated wells and half-slope line for Stimulated wells. Find end of well-bore storage effects after 1-1/2 log time cycle
- 2- Find values of viscosity, z-factor, compressibility of storage gas at different pressure assuming Gas gravity = 0.585 & temperature = 75 F = 535 R

Draw-Down Test:

- 1- Plot P_{wf}^2 vs. time
- 2- Draw straight line after pseudo-steady state starts
- 3- Find slope m and P^2 1hr
- 4-
$$kh = \frac{1637qTzu}{m}$$
- 5-
$$S = 1.151 \left[\frac{p^2 - p^2_{1hr}}{m} - \log \left(\frac{k}{\phi \mu c r_w^2} \right) + 3.23 \right]$$
- 6- Plot skin vs. flow-rate. It should be a straight line
- 7- Slope of this line is D
- 8- Find True Skin (S') at $q=0$.

Build-Up Test:

- 1- Plot P_{wf}^2 vs. $(tp+dt)/dt$ on semi-log paper
- 2- Draw straight line after well-bore storage effects diminishes
- 3- Find slope m and P^2 1hr
- 4-
$$kh = \frac{1637qTzu}{m}$$
- 5-
$$S = 1.151 \left[\frac{p^2_{1hr} - p^2}{m} - \log \left(\frac{k}{\phi \mu c r_w^2} \right) + 3.23 \right]$$
- 6- Plot skin vs. flow-rate. It should be a straight line
- 7- Slope of this line is D
- 8- Find True Skin (S') at $q=0$.

We require time, flow-rate & Bottom hole pressure from the data which are present in two txt files as bottom hole & surface recording files. The flow rates are at Wellhead so we match the BHP & THP with time.

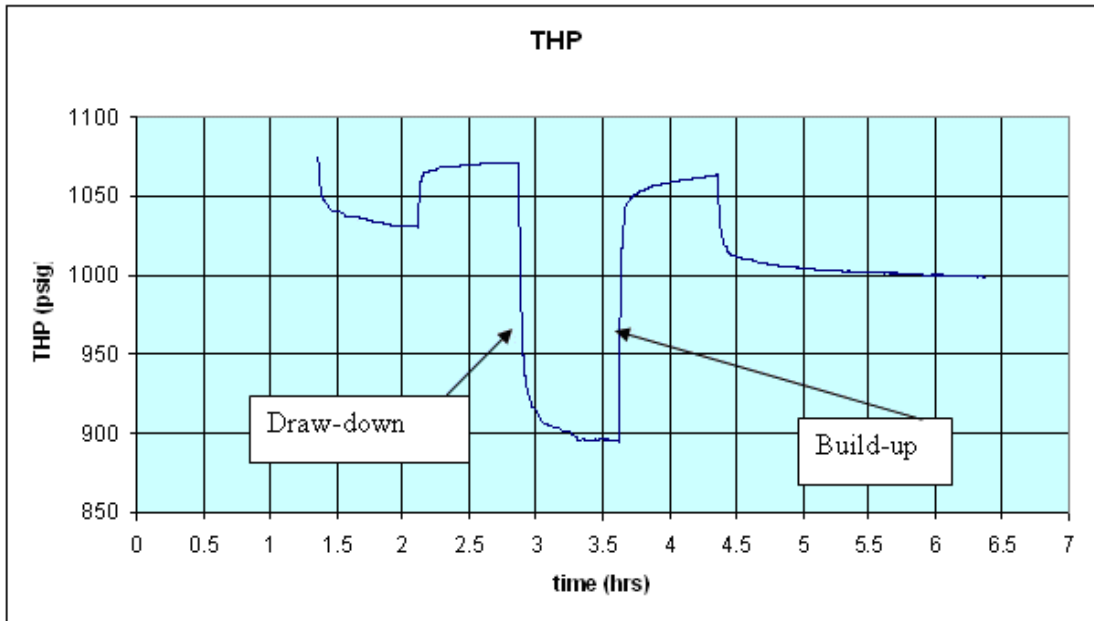


Fig13. Tubing Head Pressure profile for Multi-Point test

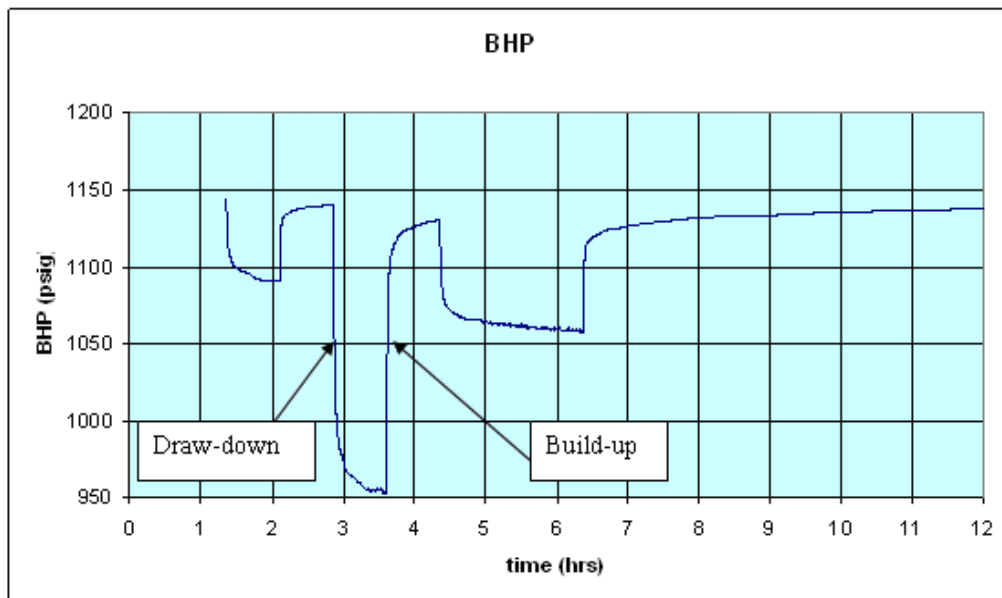


Fig14. Bottom Hole Pressure profile for Multi-Point test

The multipoint-test data is divided into Draw-down & build-up test and each one is analyzed separately.

Draw-down test

Analysis of drawdown tests was done as described above and following graphs were obtained

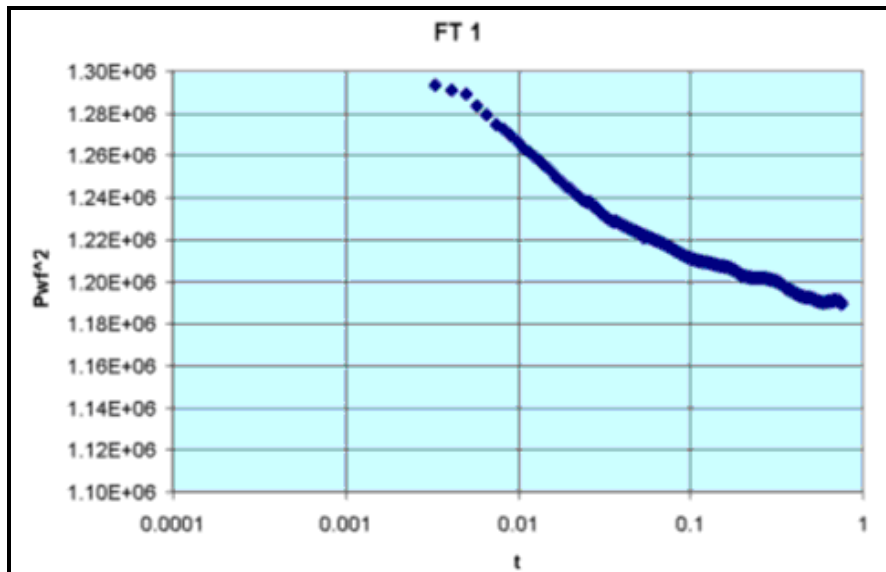


Fig15. Flow Test 1 – Delta pressure squared vs. time

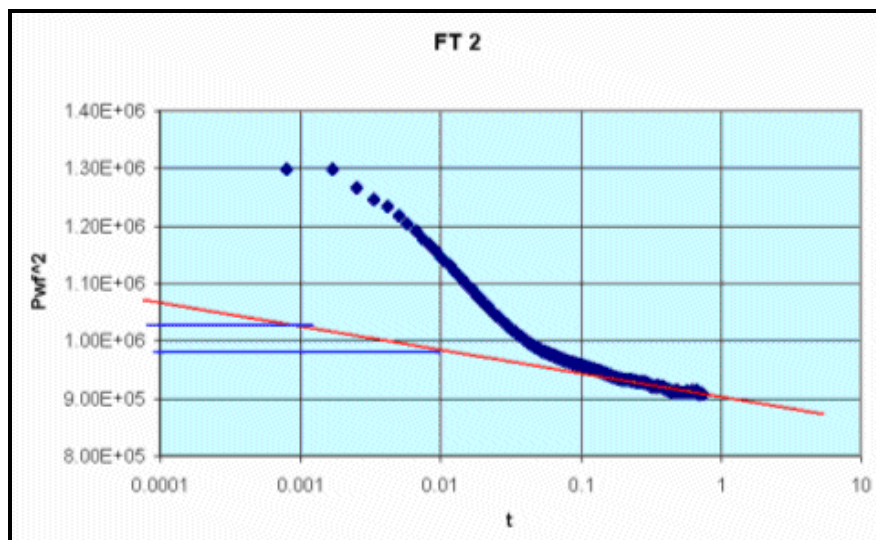


Fig16. Flow Test 2 – Delta pressure squared vs. time

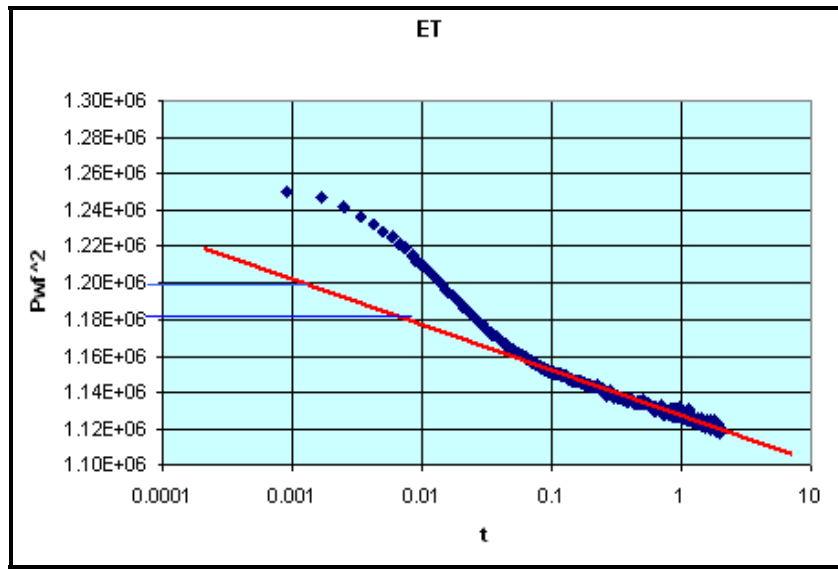


Fig17. Extended Flow Test – Delta pressure squared vs. time

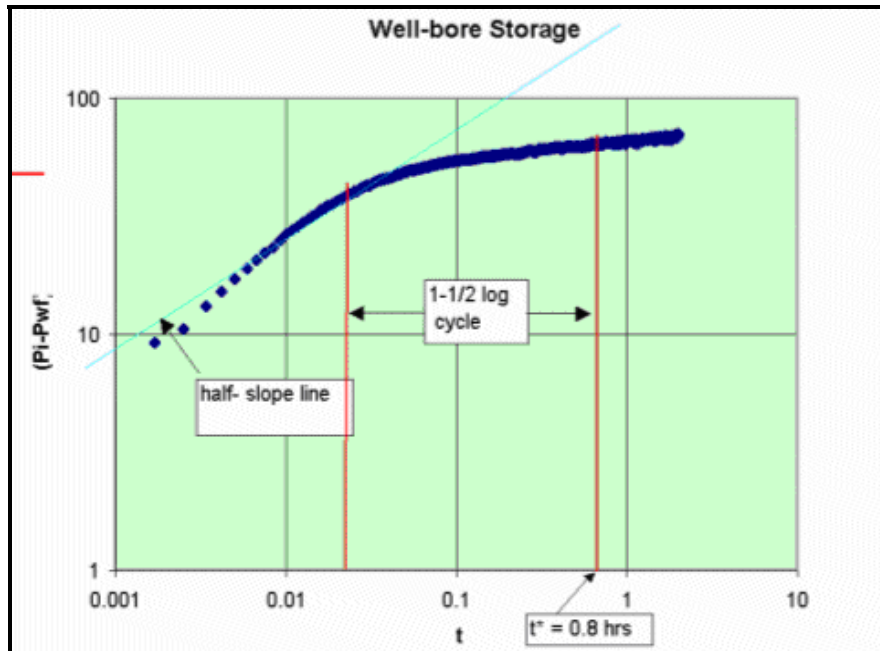


Fig18. Log-log graph

For well-tests after fracture half-slope line is drawn and for un-simulated wells unit slope line is drawn to find end of well-bore effects and start of pseudo-steady state.

Gas production Simulator was used to find the values of viscosity, z-factor and compressibility of storage gas at different pressure assuming Gas gravity = 0.585 & Temperature = 75 F = 535 R that are also used by Columbia Trans.

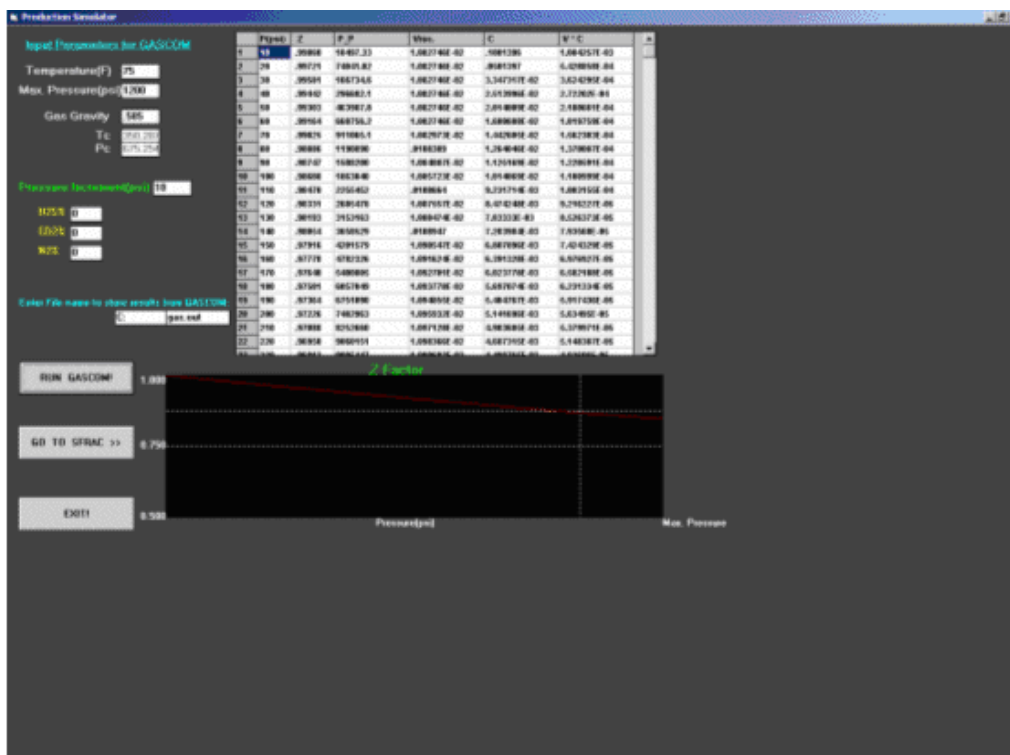


Fig19. Gas Properties Simulator

The slope from P_{wf}^2 vs. time on semi-log graph was used to find kh & then skin. The three values of skin were plotted on Q vs. S graph and extrapolated to $Q = 0$ to get True skin ($S^?$).

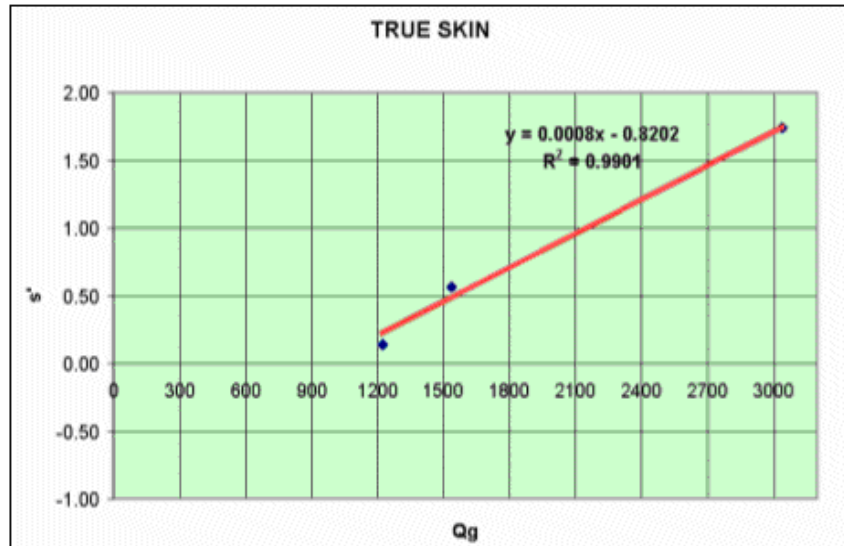


Fig20. Calculation of True skin

	FLOW TEST 1	FLOW TEST T2	EXTENDED TEST
porosity	0.14	0.14	0.14
rw	0.1458333	0.1458333	0.1458333
Ct	1.02E-03	1.08E-03	1.04E-03
Uav	1.28E-02	1.26E-02	1.27E-02
Zav	0.8558691	0.8635354	0.859119
P	1143	1140	1127.3
Qav	1223.8668	3038.7039	1536.1134
Tav	533	533	533
h	10	10	10
m	2.00E+04	5.40E+04	2.20E+04
kh	5.86E+02	5.36E+02	6.67E+02
k	5.86E+01	5.36E+01	6.67E+01
plhr²	1.185E+06	9.000E+05	1.128E+06
S	0.14	1.74	0.57
S'	-0.8202		
D	0.0008		

Table 1. Draw down Test Results

Build-up test

In build-up tests, the slope drawn for Horner plot is after the time when well-bore storage effects were found to be minimizing from previous draw-down test. This slope is then used to find the values of kh & skin. The True skin is found the similar way as in draw-down test.

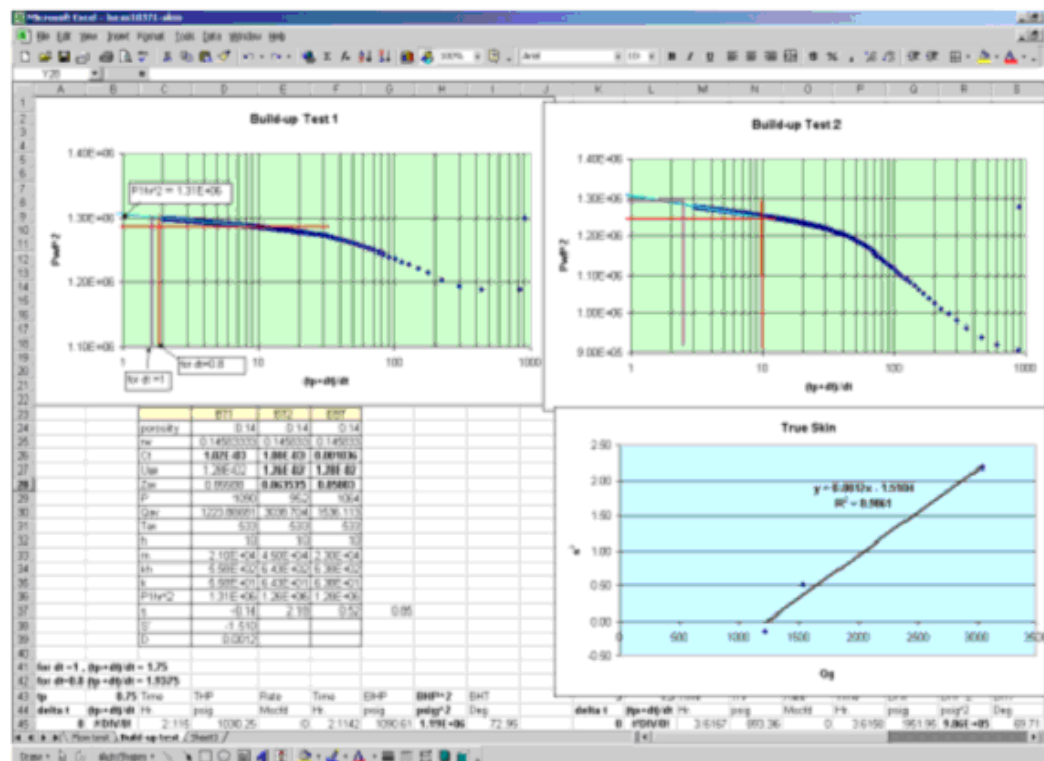


Fig21. Calculation of True skin Build-up test

	BUILD-UP TEST 1	BUILD-UP TEST 2	EXTENDED BUILD-UP TEST
porosity	0.14	0.14	0.14
rw	0.14583333	0.145833	0.145833
Ct	1.02E-03	1.08E-03	0.001036
Uav	1.28E-02	1.26E-02	1.28E-02
Zav	0.85588	0.863535	0.85803
P	1090	952	1064
Qav	1223.86681	3038.704	1536.113
Tav	533	533	533
h	10	10	10
m	2.10E+04	4.50E+04	2.30E+04
kh	5.58E+02	6.43E+02	6.38E+02
k	5.58E+01	6.43E+01	6.38E+01
Plhr ²	1.31E+06	1.26E+06	1.28E+06
s	-0.14	2.18	0.52
S'	-1.510		
D	0.0012		

Table 2. Build-up test results

	DRAW-DOWN	BUILD-UP	AVERAGE	ACTUAL
S'	-0.8202	-1.510	-1.165	-1.17
D	0.0008	0.0012	0.0010	.00126

Table 3. Average Results

Due to large errors corresponding to estimating skin and kh values manually, it was decided that for time being these values will not be entered in the database.

Following are some pictures of the documents to show the different format in which the data was presented in files and microfiche.

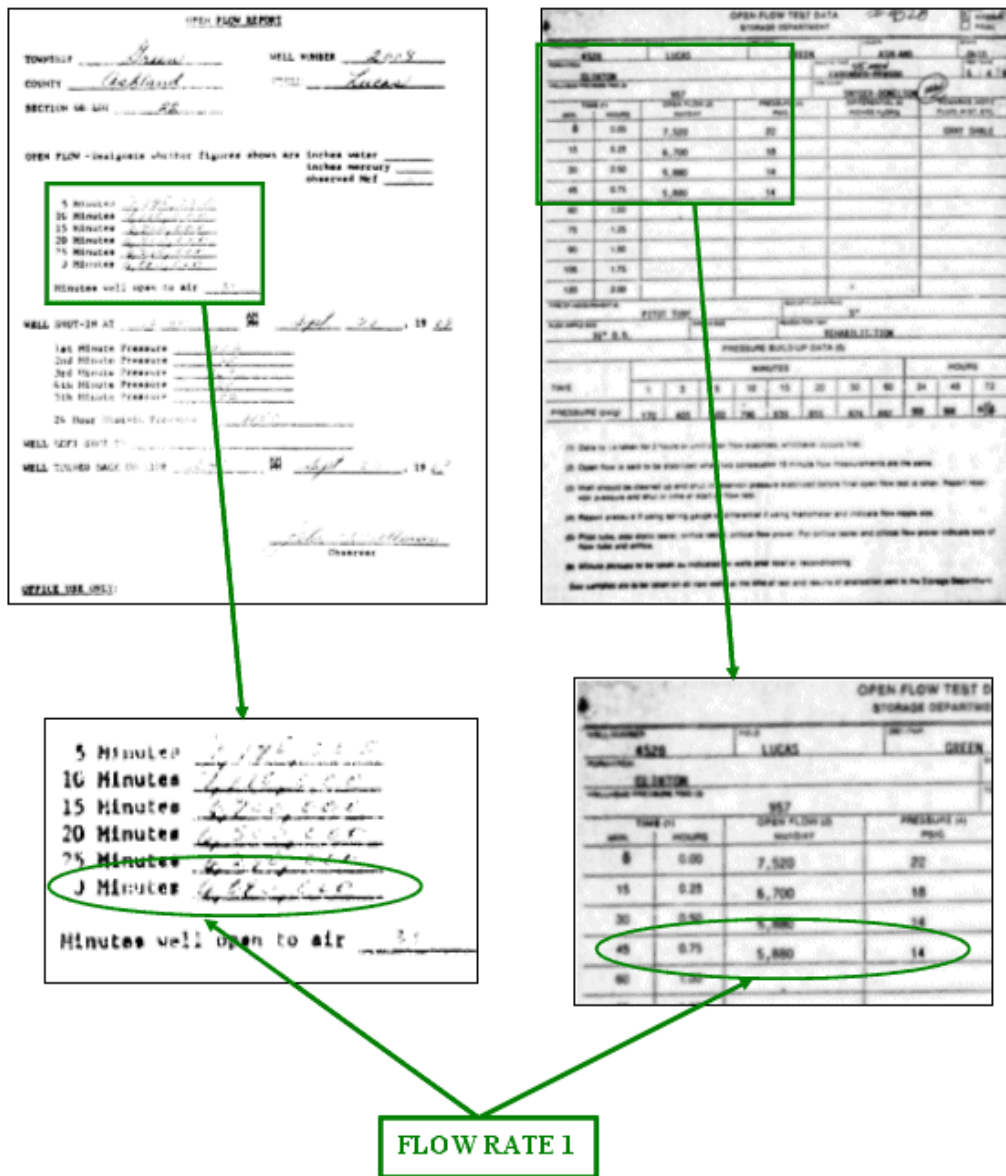
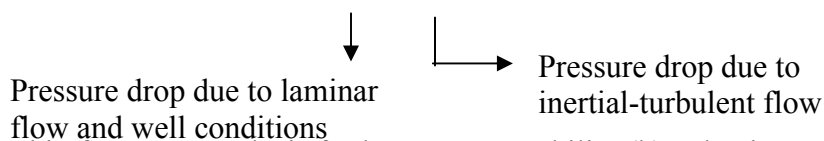


Fig22. Retrieving flow-rate of an open-flow test

Laminar Inertial Turbulent (LIT) Test

Analysis of data from isochronal type test using Laminar Inertial Turbulent (LIT) flow equation will yield considerable data. This method can also be used to find skin of a well from single-point test when the value of permeability of reservoir is known from prior multi-point test. The LIT equation is written as:

$$\Delta\psi = \bar{\psi}_R - \psi_{wf} = a_t q_{sc} + b q_{sc}^2$$



Procedure for calculating Skin from LIT analysis for known permeability (k) value is as shown below:

1. Calculate a_t and b from equations below:

$$a_t = \frac{\sum \frac{\Delta\Psi}{q_{sc}} \sum q_{sc}^2 - \sum q_{sc} \sum \Delta\Psi}{N \sum q_{sc}^2 - \sum q_{sc} \sum q_{sc}}$$

N= Number of data points

$$b = \frac{N \sum \Delta\Psi - \sum q_{sc} \sum \frac{\Delta\Psi}{q_{sc}}}{N \sum q_{sc}^2 - \sum q_{sc} \sum q_{sc}}$$

2. Plot $(\Delta\Psi - b q_{sc}^2)$ vs. q_{sc} on a logarithmic scale. The transient data points should form a straight line. If they don't form a straight line, calculate a_t and b again with the data which forms the straight line.
3. Calculate Skin (S) with the formula.

$$S = \frac{1}{0.869} \left[a_t \times 10^6 \frac{kh}{1.632 \times 10^6 T} - \log \left(\frac{kt}{\phi \mu_i c_i r_w^2} \right) + 3.23 \right]$$

Where:

- $\Delta\Psi$: Delta Pseudo Pressure
- k : Effective permeability to gas, md
- h : Net pay thickness, ft
- t : Flow time, hrs
- ϕ : Porosity, %
- μ_i : Initial Viscosity, cp
- c_i : Initial compressibility, psi-1
- T : Temperature of the reservoir, °R
- r_w : Well-bore radius, ft
- S : Skin, dimensionless

Flow Diagram of Well Test Analysis procedure

Following is the flow diagram of the well test analysis procedure and the type of values that we get from the data.

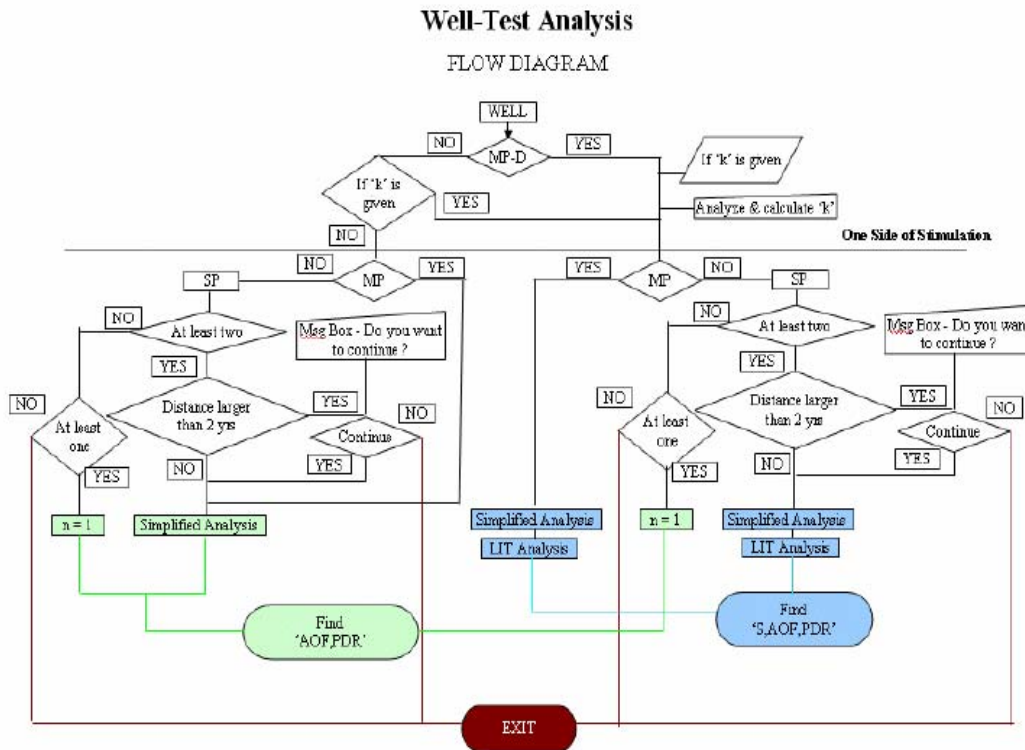


Fig23. Flow Diagram of Well Test Analysis procedure

RESERVIOR CHARACTERISTIC

It includes some reservoir properties. The complete list of the data type retrieved is shown below:

1. API Number
2. Well Radius
3. Reservoir Porosity
4. Reservoir Temperature
5. Gas Specific Gravity
6. Reservoir Thickness

NEURAL NETWORK MODULE

The Neural nets are very powerful in predicting non-linear relationships. As the relationship between skin and stimulation parameters is non-linear and very complicated, thus neural nets are used which are very good at it. With skin values before and after the stimulation calculated and stimulation parameters known, we can now use these valid stimulations to train the Neural Network to use it as a prediction tool. Intelligent Data Evaluation and Artificial Network IDEA® software by Intelligent Solutions Inc. was used to design the neural network. This software is very versatile in making different nets with different training algorithms. Generalized Regression Neural Net (GRNN) was used to train the neural net. The net had 11 inputs and 1 output as skin. The source of data for the neural net is given in Figure 24.

	Inputs	Source
1	Lat	Database
2	Long	Database
3	Sum Fluids	Sum of item 5,6,7,8
4	Prior-Ich	Database
5	Water (bbls)	GA
6	Acid (bbls)	GA
7	Gel (bbls)	GA
8	Foam (bbls)	GA
9	N2(Mcf)	GA
10	Sand Quantity (lbs)	GA
11	After-Test Type 3- Multi-Point 2- Single-Point 1- Open-Flow	GA

Fig24. Neural Network Inputs and their source

Out of the 78 valid stimulations available, the Neural net was trained on 60 data items while 14 were used as calibration data and 4 as verification data. The Neural network showed very good results for all three types of data. The screen shot taken from the IDEA software for training of the neural net is shown in Figure 25.

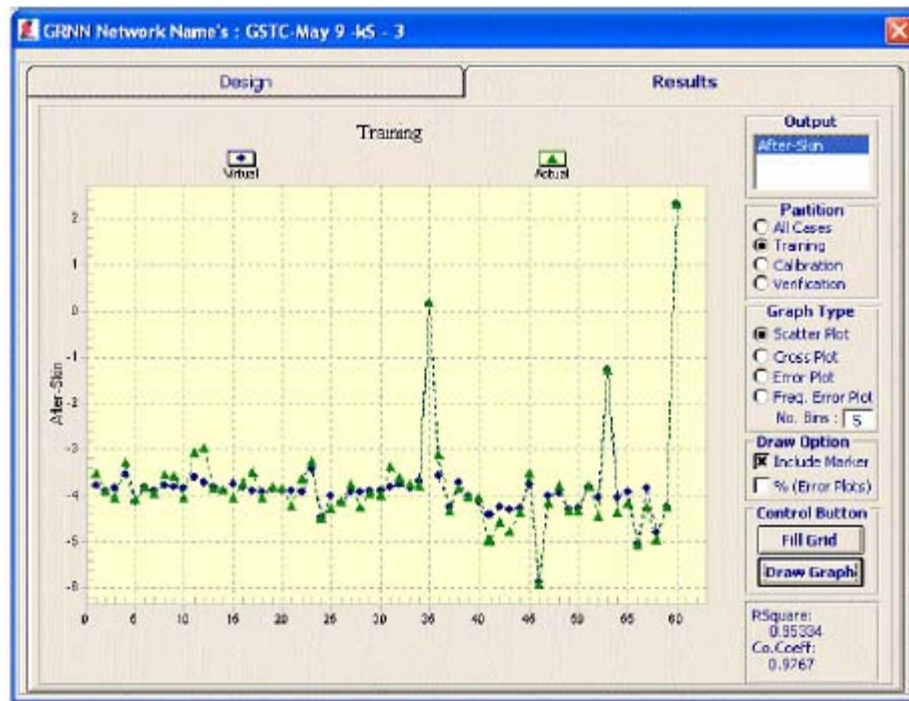


Fig25. Accuracy of training data for the Neural Net

The calibration and verification of the Neural net is shown in Figure 26 and Figure 27 respectively. After the accurate results of this GRNN, the software was updated to use the GRNN generated files to be used in the Genetic algorithm.

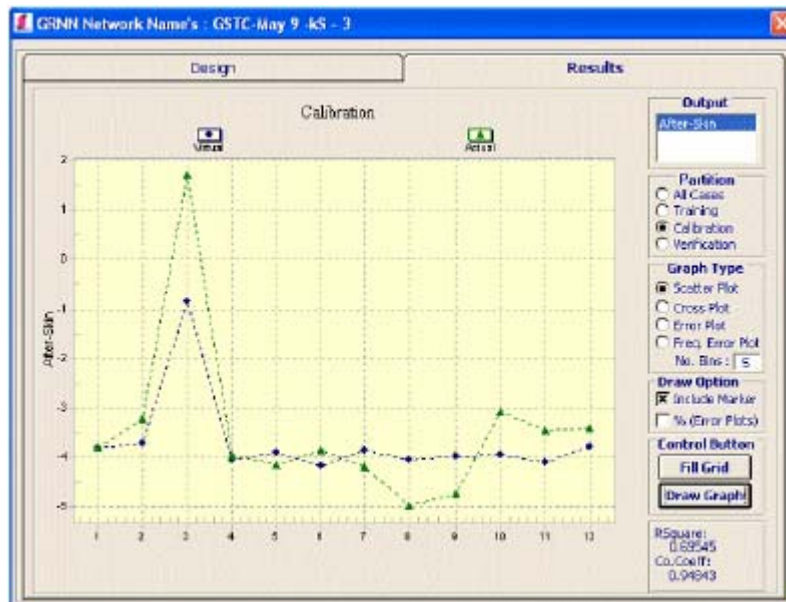


Fig26. Accuracy of calibration data for the Neural net

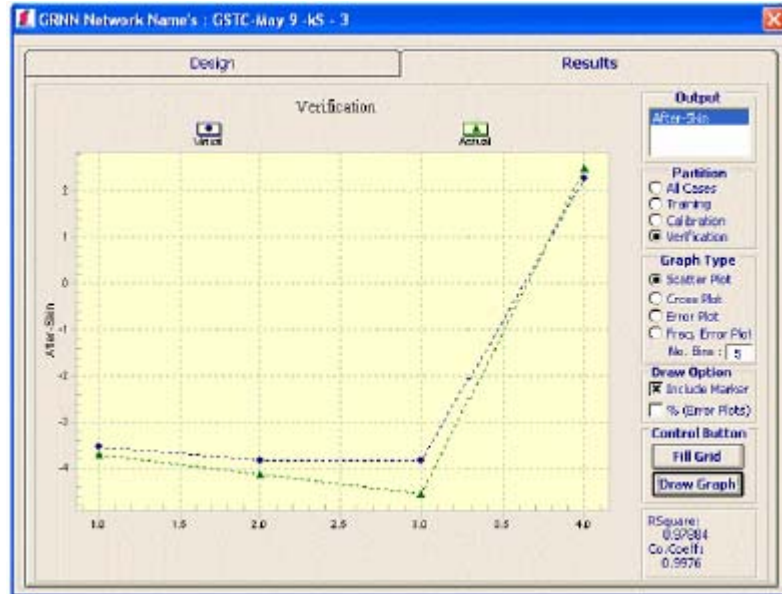


Fig27. Accuracy of verification data for the Neural net

GENETIC OPTIMIZATION MODEL

Genetic Algorithm was written to optimize the stimulation parameters used in the neural net. Out of the 11 input parameters, 7 can be varied to obtain optimum skin. The range of these variables was calculated and accuracy desired was determined to design the length of the chromosome of Genetic Algorithm (GA) that will be required. The calculation is shown in the table 4. for the chromosome length if all the parameters are selected.

	GA Input Parameter	Min	Max	Range	Accuracy Required	Accuracy Size	Range Size	Chromosome Size	Min Byte size	Max Byte size
1	Water (lbs)	0	345	345	1	1	345	9	$2^9=256$	$2^9=512$
2	Acid (lbs)	0	11.9	11.9	0.01	100	1190	11	$2^{11}=1024$	$2^{11}=2048$
3	Gel (lbs)	0	535	535	1	1	535	10	$2^{10}=512$	$2^{10}=1024$
4	Foam (lbs)	0	1.7	1.7	0.01	100	170	8	$2^8=128$	$2^8=256$
5	N2(Mcf)	0	368	368	1	1	368	9	$2^9=256$	$2^9=512$
6	Samt. Quantity (lbs)	0	30000	30000	100	0.01	300	9	$2^9=256$	$2^9=512$
7	After Test Type 3- Multi Point 2- Single Point 1- Open Flow	1	3	3	1	1	3	2	$2^2=2$	$2^2=4$

Table 4. Calculation to determine the length of chromosome

The length of chromosome came out to be $9 + 11 + 10 + 8 + 9 + 9 + 2 = 58$.

The GA characteristics that were used are shown in Table 5. These were the best but can be changed as desired to suit other neural nets in the future.

GA CHARACTERISTICS	VALUE
Crossover rate	60 %
Mutation rate	10 %
Population size	500
No of Generations	10
Next Generation criteria	Top 30 % ranked from previous generation
Crossover criteria	Top 25 % has 75 % chance of Crossover

Table 5. CA characteristic

There are two optimization methods made available in this software. One is optimization just based on skin and other, based on both skin and cost. The optimization objective function is calculated using the following formula and GA minimizes this optimization objective function.

$$\text{Optimization Objective Function} = \frac{Skin - Skin_{min}}{Skin_{max} - Skin_{min}} \times Skin \text{ weight} + \frac{Cost - Cost_{min}}{Cost_{max} - Cost_{min}} \times Cost \text{ weight}$$

Software compatibility and variability:

In the software user has been given many options to accommodate the particular situation that he has and data availability if different from the data that we have used to verify the results from this software.

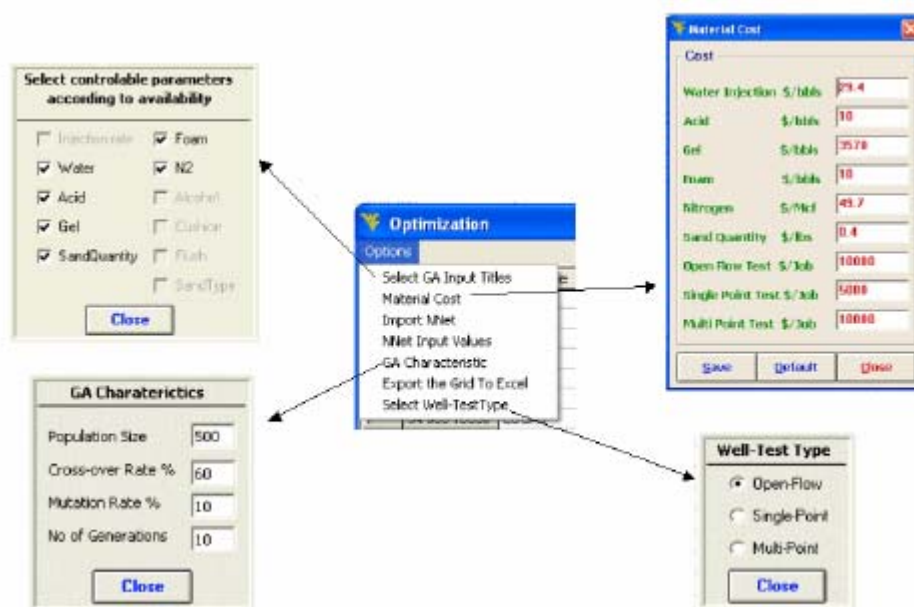


Fig28. Different options in the software that makes it versatile.

One of such variability introduced is that the software can use any other neural net if it is required. The option menu of the optimization screen has the option to import any other neural network. Plus, there is an option to select the available controllable parameters for the GA. For example, if the user does not want to use or does not have foam and nitrogen, then he can unselect them as shown in Figure 3.18. The length of GA will change according to the selection.

As the Neural Net has ‘Well-Test Type’ as its input, so the ‘Select Well-Test Type’ menu option gives the user an option to choose the test the user wants the neural net to interpret the well-test. With changing price of hydro-carbons, the petroleum industry is going through fluctuating material cost. The stimulation material prices change frequently and are a factor of demand and supply in that region. The software has the option to change the price of the stimulation material before applying the GA to the available data.

Analysis of raw data vs. refined data:

WELL TEST DATA																															
DATA FIELDS	Total Well-Tests	API Number	Field Name	Well	Test Date	Test Type	Time 1	Field Pressure 1	Flowing Pressure 1	Rate 1	Time 2	Field Pressure 2	Flowing Pressure 2	Rate 2	Time 3	Field Pressure 3	Flowing Pressure 3	Rate 3	Time Extended	Field Pressure Ext	Flowing Pressure Ext	Rate Ext	kh	skin	True skin	Non Darcy Coefficient	n-Value	C-Value	Delta P Squared	Peak Day Rate	Absolute Open Flow
INITIAL DATA AVAILABLE	3223	431	431	431	3223	3223	3223	3223	3223	3223	347	347	347	347	292	292	292	292	345	345	345	345	191	182	163	163	916	916	916	916	916
FINAL DATA AVAILABLE	3365	431	431	431	3365	3365	3365	3365	3365	3365	347	347	347	347	292	292	292	292	345	345	345	345	194	185	166	166	1362	1362	1362	1362	1362

WELL TEST DATA

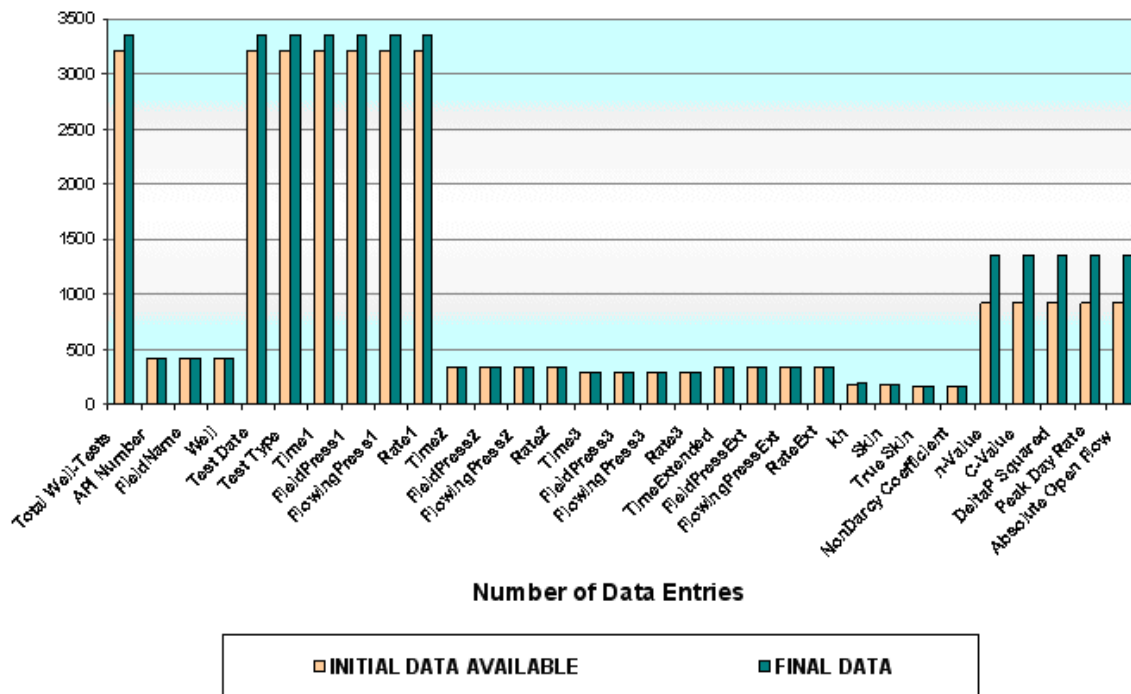


Fig29. Data addition and refinement for well test data

DATABASE & SOFTWARE

SOFTWARE BASICS

This software allows you to add/edit well data in the database and choose the data that you want to look at, for a selected well. It also has a Well Test Analysis tool which calculates the well deliverability parameters like n , C , Peak Day rate & Absolute Open Flow

The database for this software consists of five main tables

1. Well bore Data
2. Completion Data
3. Perforation Data
4. Stimulation Data
5. Well Test Data
6. Reservoir Characteristic Data

The **API number** of a well is the primary key in this database so it must be known before adding a record and cannot be duplicated

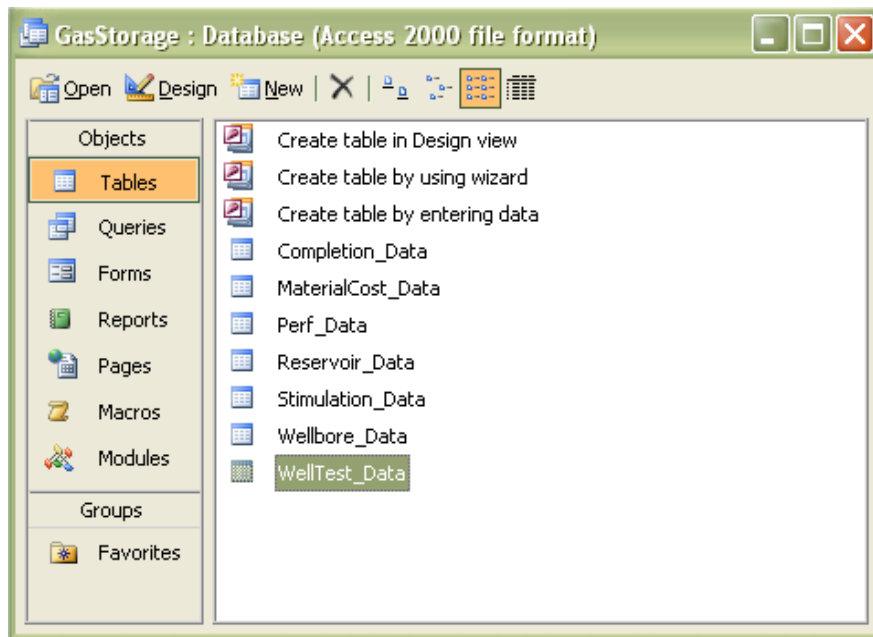


Fig30. Screen shot of database showing different tables

The software starts with the main menu screen with six options



Fig31. Main Screen of software

Complete list of items and sub-items in the above command buttons is shown below:

File

- o Create Template
- o Import Data from filled-out Template
- o Remove all data from database
- o Exit

Help

- o User Manual
- o Formulas
- o About

Edit Well Data

- o Well bore
- o Completion
- o Stimulation
- o Perforation
- o Stimulation
- o Well Test
 - Well Test Analysis Tool
- o Reservoir
- o Find a Well

View Well Data

- o Select State & county
- o Select Wells
- o Selection Options
- o Select Well Data

Candidate Selection

File

The file menu can be accessed from the top left corner of menu bar. It contains four options.

- o Create Template
- o Import Data from filled-out Template
- o Remove all data from database
- o Exit

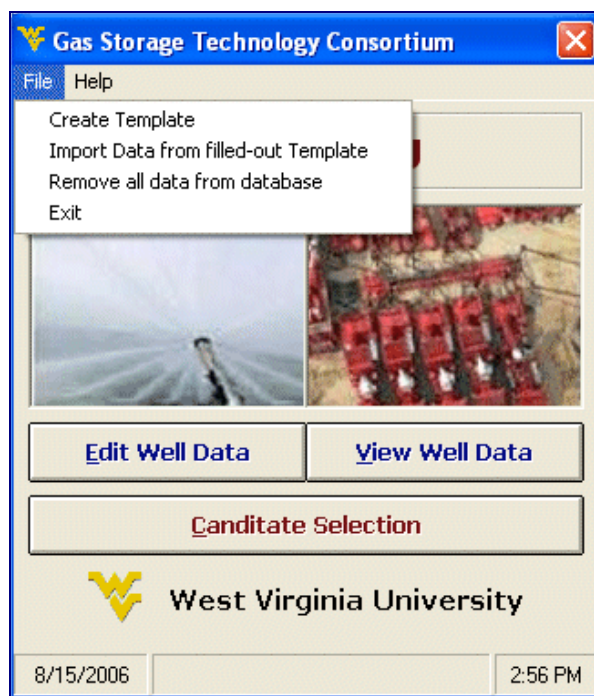


Fig32. File Menu options

Create Template

By executing this option first the user need to select a location in hard drive in order to save Template file.

Once the Template is successfully created in the hard drive, a message will appear indicating the user that the template file has been created.

Following is the screen shot of the Template file showing the Well bore data.

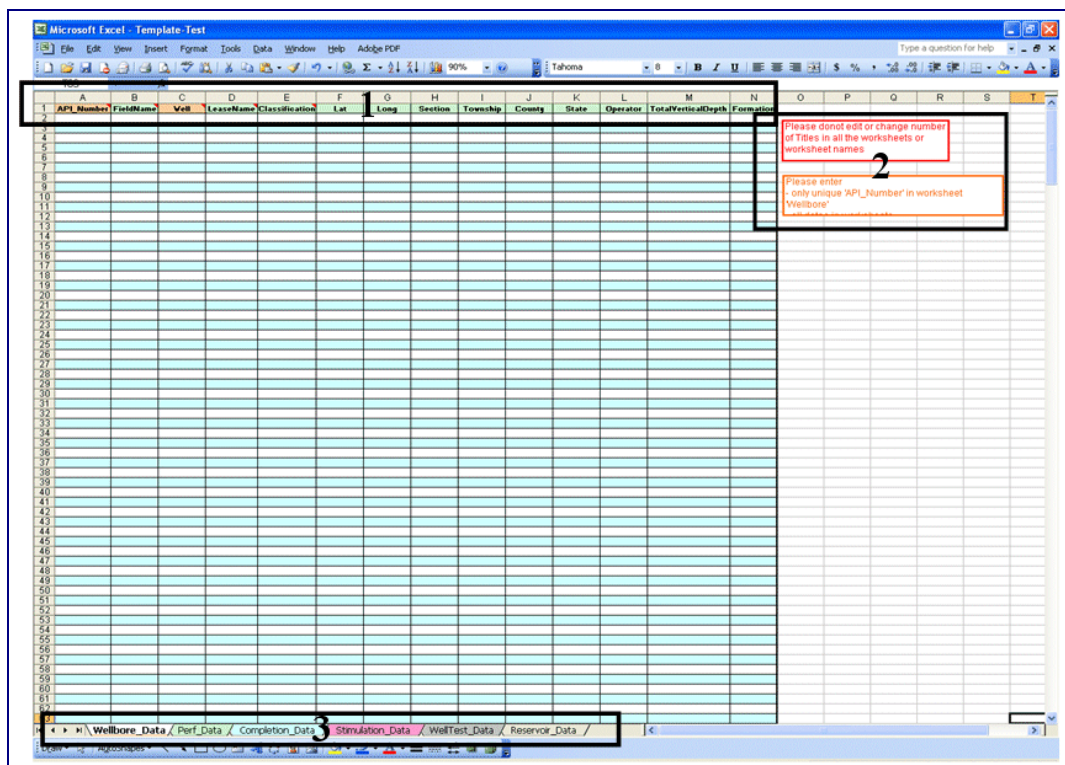


Fig33. Screen shot of Template file

It has six worksheets, each representing the table in the database of the software.

- Well bore Data
- Completion Data
- Stimulation Data
- Perforation Data
- Stimulation Data
- Well Test Data
- Reservoir Characteristic

1. These are the fields of the table. Each field represents one characteristic of the table and each row is one record. If the user is not clear about any field, then he/she can drag the screen cursor to that field name and the comment will appear like in the picture below where it will give a little explanation, its format and an example so that the user understands what sort of data to enter in each field

	A	B	C	D
1	API_Number	Field Name	Kazim:	
2			Unique API number of the well	
3			Format: ##-###-####	
4			Example: 12-345-67890	

Fig34. Comments that shows format of some cells in Template Excel file

2. This section has two sets of warnings for the user entering data. One is to not edit or change number of Titles in all the worksheets or worksheet names and the other is to add only unique 'API Number' in worksheet 'Well bore Data' and all dates in worksheets where required.
This has been done as the data is retrieved from the template according to some specific format and non presence of any data in elementary field might stop program from using that record. All the elementary fields' background is orange/red while others are in green.
3. This section shows all the worksheets in the Template file.

Import Data from filled-out Template

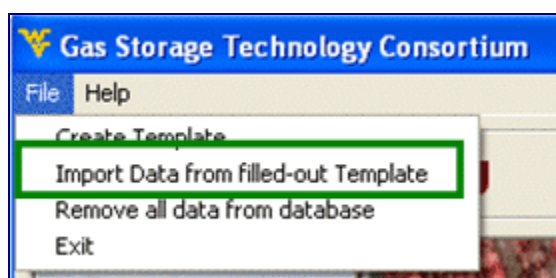


Fig35. Import data from filled-out Template

If this option is selected from the file menu, then the program will ask the user to select the filled Template file from the location. The new data will be appended to the existing data.

Remove all data from database

If the user doesn't want to append the data to the previous database but instead wants to up-load a whole new data, then there is an option in file menu as highlighted in the snapshot below. This option will remove all data in the previous database. After removing the data from previous database, the user can up-load the updated data from the template or enter it in the software.

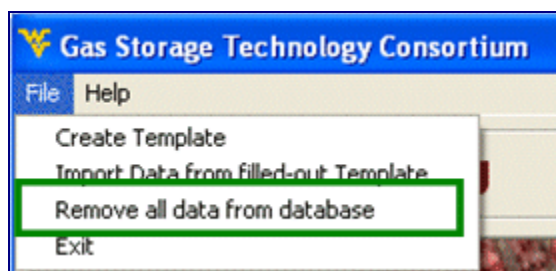


Fig36. Remove all data from database

Exit

The program can be exited by two options. One is to exit by using the file menu and selecting 'Exit' while the other is to select the cross on the top right corner as in normal windows based applications.

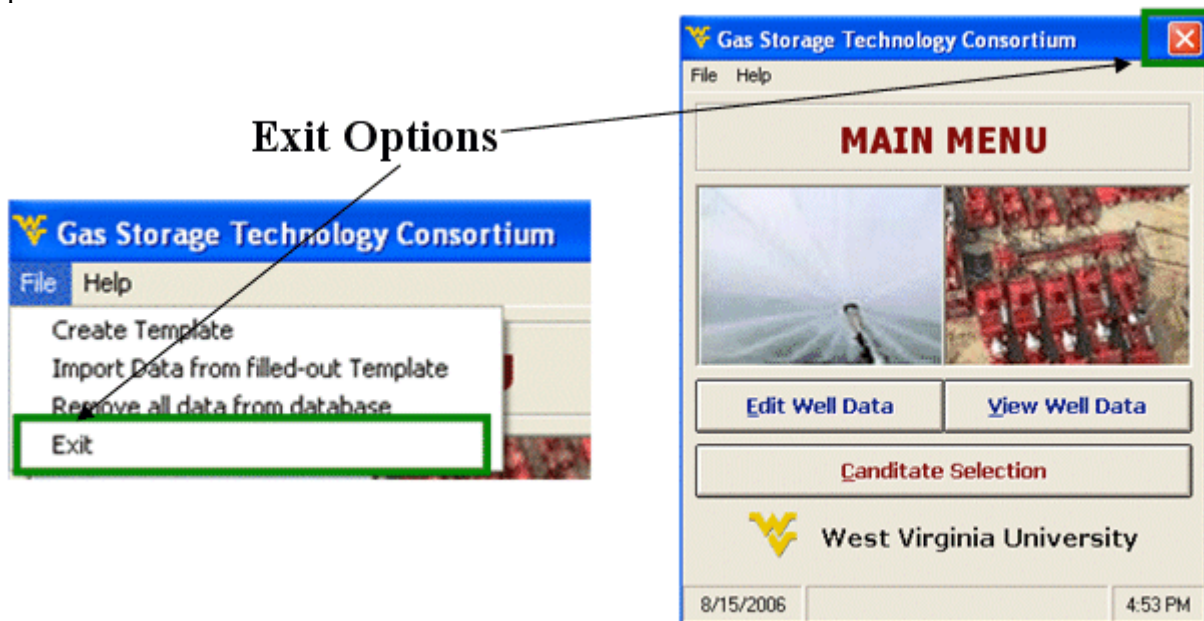


Fig37. Exit form file menu

Help

Another option that can be accessed from the menu bar on top of the main menu screen is the Help menu option.

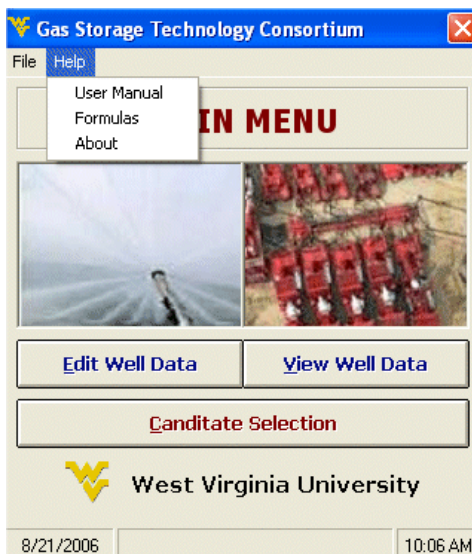


Fig38. Help menu options

It contains three types of information one is the User Manual for this software and second is the Formulas used in this software and third 'About' form which shows the system information and software contributors.

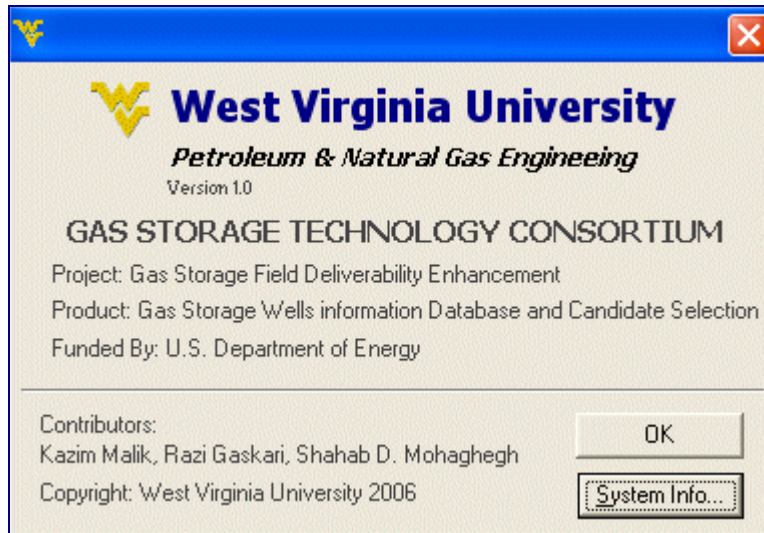


Fig39. "about" screen form help menu

Edit/View Well Data

This screen has all the well data in the form of five tabs (for five database tables) that can be edited / viewed or a Well Test Analysis can be performed in the Well Test tab.

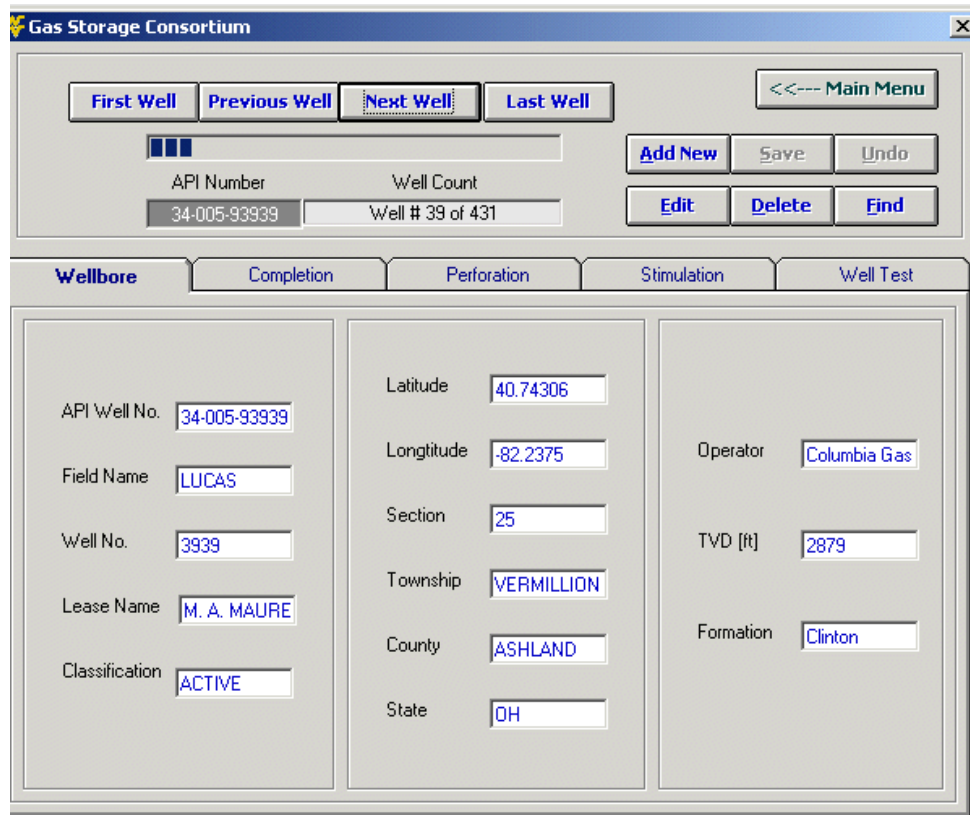


Fig40. Browsing through the well-bore data

To browse between different wells



To move to the first well, previous well, next well & the last well in the record, click on the button assigned to it. The records are sorted in ascending order according to well number

API Number & Well Count



The progress bar shows the relative position of the record and well count shows the current well position in the well bore database out of the total records. The API number of the current well is also displayed

Back to main menu



Takes you back to the very first screen of the program

Editing Tools



These buttons will help you to add a new record, edit or delete it or find a well for which you want the data to be retrieved if you know its API number.

Different Tabs

WELL BORE:

Wellbore	Completion	Perforation	Stimulation	Well Test
API Well No. <input type="text" value="34-005-93939"/>		Latitude <input type="text" value="40.74306"/>		
Field Name <input type="text" value="LUCAS"/>		Longitude <input type="text" value="-82.2375"/>		Operator <input type="text" value="Columbia Gas"/>
Well No. <input type="text" value="3939"/>		Section <input type="text" value="25"/>		TVD [ft] <input type="text" value="2879"/>
Lease Name <input type="text" value="M. A. MAURE"/>		Township <input type="text" value="VERMILLION"/>		Formation <input type="text" value="Clinton"/>
Classification <input type="text" value="ACTIVE"/>		County <input type="text" value="ASHLAND"/>		
		State <input type="text" value="OH"/>		

Fig41. Well-bore tab

This tab contains all the data pertaining to the name, location & some main features of the current well.

COMPLETION:

Wellbore	Completion	Perforation	Stimulation	Well Test
Completion # 4 of 6				
Field Name	LUCAS	OD (in)	7	
Well No.	326	Top (ft)	0	
Description	Casing	Bottom (ft)	75	
Date Tubing Run	11/2/1969 MM/DD/YYYY	Weight (lbs/ft)	17.00	
		Grade	SMLS USED	
First Completion Previous Completion Next Completion Last Completion				

Fig42. Completion tab

This tab contains all the data relating to different completion run in the well.

To browse between different Completions

First Completion	Previous Completion	Next Completion	Last Completion
-------------------------	----------------------------	------------------------	------------------------

To move to the first completion, previous completion, next completion & the last completion in the record, click on the button assigned to it. The completions are assorted in ascending order according to date tubing run for current well.

PERFORATION:

Wellbore	Completion	Perforation	Stimulation	Well Test
Perforation # 2 of 3				
Field Name	LUCAS	Perforation Top [ft]	2,371	
Well No.	12058	Perforation Bottom [ft]	2,407	
Perforation Type	Set-Thru	Shot Type	size. 50 / Glass	
Perforation Date	5-Sep-1981 MM/DD/YYYY	Shots Per foot	1.0	
First perforation Previous Perforation Next Perforation Last Perforation				

Fig43. Perforation tab

To browse between different Perforations



To move to the first perforation, previous perforation, next perforation & the last perforation in the record, click on the button assigned to it. The perforations are sorted in ascending order according to perforation date for current well.

STIMULATION:

Wellbore	Completion	Perforation	Stimulation	Well Test	
Stimulation # 1 of 1					
Well No.	3932	Type	Water-N2	Flush [bbls]	30
Size of String (in)	3.5	Water [bbls]	50	Sand Quantity [lbs]	8000
Stim From [ft]	2906	Acid [bbls]	2.4	Sand Type	20/40
Stim To [ft]	2928	Gel [bbls]	125	Injection Rate [bbls/min]	13
No of Shots	44	Foam [bbls]	0.07	Total Fluid [bbls]	229.87
Fractured by	Dowell Inc.	N2 [Mcf]	50	Summary Total [bbls]	175
Date	8/2/1966	Alcohol [bbls]	2.4	Break-down Pr. [psi]	2000
	MM/DD/YYYY	Cushion [bbls]	20	ISIP [psi]	1000
First Stimulation Previous Stimualtion Next Stimulation Last Stimualtion					

Fig44. Stimulation tab

To browse between different Stimulations

First Stimulation	Previous Stimualtion	Next Stimulation	Last Stimualtion
--------------------------	-----------------------------	-------------------------	-------------------------

To move to the first stimulation, previous stimulation, next stimulation & the last stimulation in the record, click on the button assigned to it. The stimulations are sorted in ascending order according to stimulation date for current well.

WELL TEST:

WellTest # 3 of 9				
Well Test	Time [hrs]	Field Pr. [psi]	Flow Pr. [psi]	Rate [McfD]
First Reading	0.75	1030	860	2029
Second Reading	0.75	1020	955	1129
Third Reading	0.75	1015	926	1420
Extended Time	2	1015	924	1416

Field Name	LUCAS
Well No.	10913
Test Date	12/28/1999
Test Type	Multi-Point

kh [md-ft]	446	NonDarcyCo-eff	3	DeltaP ² [psi ²]	250000
Skin	3.65	n Value	0.630	PD Rate [McfD]	1743
True Skin	-2.5	C Value	0.68641	ADF [McfD]	5063

Well Test Analysis

PD Rate
 ADF
 Skin
 All Well Tests

Show

[First WellTest](#)
[Previous WellTest](#)
[Next WellTest](#)
[Last Welltest](#)

Fig45. Well-test tab

To browse between different Well Tests



To move to the first well test, previous well test, next well test & the last well test in the record, click on the button assigned to it. The well tests are sorted in ascending order according to well test date for current well.

Adding a new data

One can add a complete new well or just only a new well-bore/completion/perforation/stimulation/well-test data by following method

Adding a complete new well data

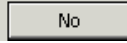
- 1- Click on the Add New button  while keeping your well bore tab as active.

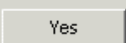
The screenshot shows a software window titled "Gas Storage Consortium". At the top, there are navigation buttons: "First Well", "Previous Well", "Next Well", "Last Well", and "<<--- Main Menu". Below these are input fields for "API Number" (containing "34-005-60183") and "Well Count" (containing "Adding New Well-bore data"). To the right are buttons for "Add New", "Save", "Undo", "Edit", "Delete", and "Find".

The main area has five tabs: "Wellbore" (selected), "Completion", "Perforation", "Stimulation", and "Well Test". The "Wellbore" tab contains three columns of input fields:

- Column 1: API Well No., Field Name, Well No., Lease Name, Classification.
- Column 2: Latitude, Longitude, Section, Township, County, State.
- Column 3: Operator, TVD [ft], Formation.

Fig46. Adding a complete new Well – well-bore tab

The following messages will pop-up. If you want to add the complete new well-bore data then click No button .

If you don't have the dates of Stimulation, Completion, Perforation & Well-Test data, then click Yes  and then add them one-by one.

The dialog box is titled "Gas Consortium" and contains a question mark icon. The text reads: "Do you want to Add only Wellbore Data ? Otherwise you must know the dates of Stimulation,Completion,Perforation & Well-Test". At the bottom are "Yes" and "No" buttons.

Following screen appears if No is clicked:

The screenshot shows a software window titled "Gas Storage Consortium". At the top, there are navigation buttons: "First Well", "Previous Well", "Next Well", "Last Well", and "<<--- Main Menu". Below these are input fields for "API Number" (containing "34-005-60183") and "Well Count" (containing "Adding New Well-bore data"). To the right are buttons for "Add New", "Save", "Undo", "Edit", "Delete", and "Find".

The main area has a tabbed interface with five tabs: "Wellbore", "Completion", "Perforation", "Stimulation", and "Well Test". The "Completion" tab is selected and highlighted with a yellow border. Below the tabs is a sub-header "Adding New Completion".

The "Adding New Completion" section contains two columns of input fields:

- Field Name
- Well No.
- Description
- Date Tubing Run (format: MM/DD/YYYY)
- OD [in]
- Top [ft]
- Bottom [ft]
- Weight [lbs/ft]
- Grade

At the bottom of the "Adding New Completion" section are four buttons: "First Completion", "Previous Completion", "Next Completion", and "Last Completion".

Fig47. Adding a complete new Well - completion tab

The background color of text boxes of all tabs including well-bore tab will be yellow indicating that they are ready for entering data.

- 2- Enter the data in all the tabs. The dates for completion, perforation, stimulation & well test job should be known.

Fig48. Adding a complete new Well – entering data for wellbore

Fig49. Adding a complete new Well – entering data for perforation

Gas Storage Consortium

First Well Previous Well Next Well Last Well <<--- Main Menu

API Number Well Count
34-005-60183 Adding New Well-bore data

Add New Save Undo
Edit Delete Find

Wellbore Completion Perforation **Stimulation** Well Test

Adding New Stimulation

Well No. Type Flush [bbls]
Size of String (in) 3 Water [bbls] Sand Quantity [lbs]
Stim From (ft) 1670 Acid [bbls] Sand Type
Stim To (ft) 1680 Gel [bbls] Injection Rate [bbls/min]
No of Shots 20 Foam [bbls] Total Fluid [bbls]
Fractured by KAM N2 [Mcf] Summary Total [bbls]
Date 09/26/2004 Alcohol [bbls] Break-down Pr. [psi]
MM/DD/YYYY Cushion [bbls] ISIP [psi]

First Stimulation Previous Stimulation Next Stimulation Last Stimulation

Fig50. Adding a complete new Well – entering data for stimulation

Gas Storage Consortium

First Well Previous Well Next Well Last Well <<--- Main Menu

API Number Well Count
34-005-60183 Adding New Well-bore data

Add New Save Undo
Edit Delete Find

Wellbore Completion Perforation Stimulation **Well Test**

Adding New Well Test

Well Test

	Time [hrs]	Field Pr. [psi]	Flow Pr. [psi]	Rate [McfD]
First Reading				
Second Reading				
Third Reading				
Extended Time				

Field Name
Well No.
Test Date 09/26/2005
Test Type

Well Test
 PD Rate
 ADF

Show Chart
Well Test Analysis

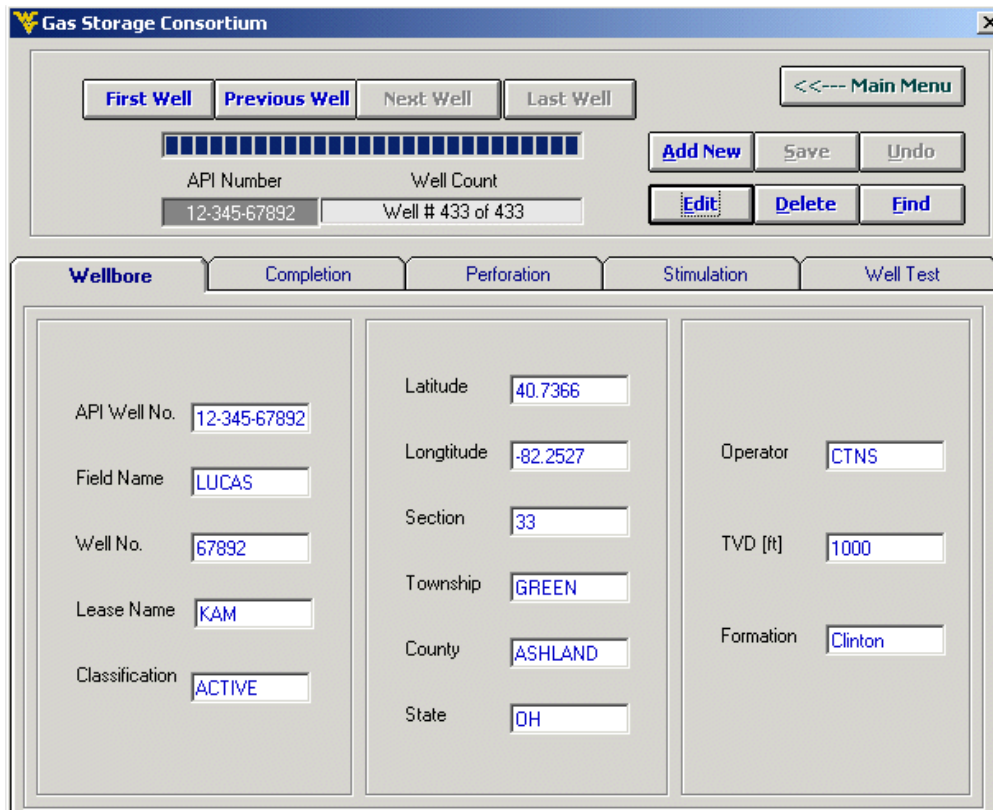
kh [md-ft] NonDarcyCo-eff DeltaP² [psi²]
Skin n Value PD Rate [McfD]
True Skin C Value ADF [McfD]

First WellTest Previous WellTest Next WellTest Last WellTest

Fig51. Adding a complete new Well – entering data for well test

3- Click the Save button 

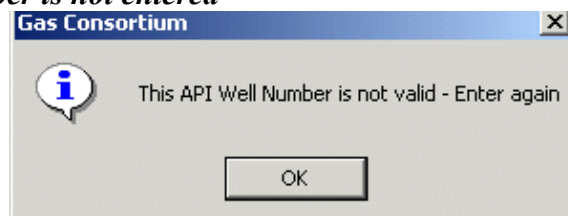
Result of adding of complete well data



The screenshot shows the 'Gas Storage Consortium' software window. At the top, there are navigation buttons: 'First Well', 'Previous Well', 'Next Well', 'Last Well', and '<<--- Main Menu'. Below these is a progress bar and a list of buttons: 'Add New', 'Save', 'Undo', 'Edit', 'Delete', and 'Find'. The 'API Number' field contains '12-345-67892' and the 'Well Count' field shows 'Well # 433 of 433'. The main data entry area is divided into three columns: 'Wellbore', 'Perforation', and 'Well Test'. The 'Wellbore' column contains fields for 'API Well No.' (12-345-67892), 'Field Name' (LUCAS), 'Well No.' (67892), 'Lease Name' (KAM), and 'Classification' (ACTIVE). The 'Perforation' column contains fields for 'Latitude' (40.7366), 'Longitude' (-82.2527), 'Section' (33), 'Township' (GREEN), 'County' (ASHLAND), and 'State' (OH). The 'Well Test' column contains fields for 'Operator' (CTNS), 'TVD [ft]' (1000), and 'Formation' (Clinton).

Fig52. Result of adding a complete new well

Warnings – If API Number is not entered



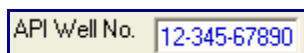
Warnings – If API Number entered is already in the database



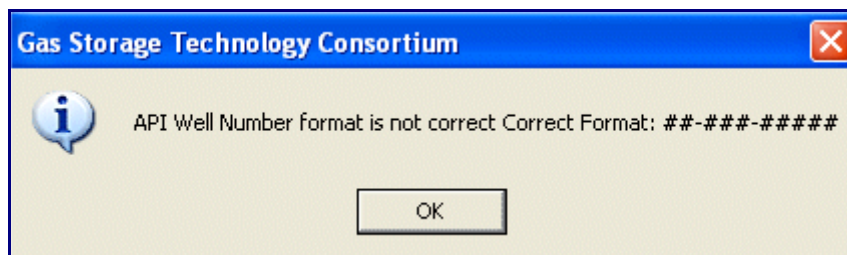
Note: The dates for completion, perforation, stimulation & well test should always be entered as the output of the software is directly dependent on the chronology of events. The format of date is also specified for the user where required. A close picture of that format is below:



You need to enter API well number only once in the well-bore tab and it will be automatically copied in the rest of tabs and procedure is the same for editing. The format for entering well API Number is:



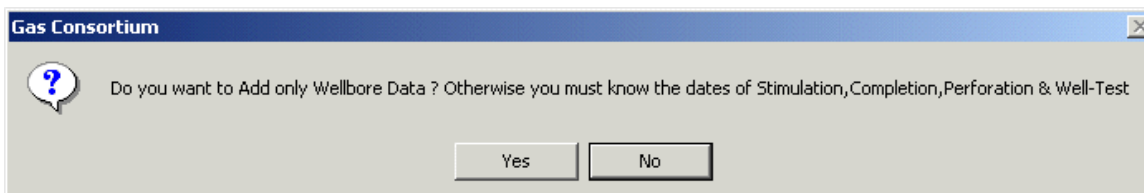
If wrong format or well API number is entered for a new well, then you will be greeted with the following message



Adding only well-bore/completion/perforation/stimulation/well-test data

- 1- Click on the Add New button  while keeping that tab active for which you want to add the data.

Only for well-bore tab following message pops up:



Click Yes  button to add only Well-bore data.

The background color of all text boxes of that tab will be yellow indicating that they are ready for entering data.

2- Enter the data. The dates for completion, perforation, stimulation & well test job should be known.

3- Click the Save button .

Editing data

One can edit complete well or just only a new well-bore/completion/perforation/stimulation/well-test data by following methods:

Editing a complete well data

1- Click on the Edit button  while keeping your well bore tab as active.

Following screen pops up:



Select accordingly.

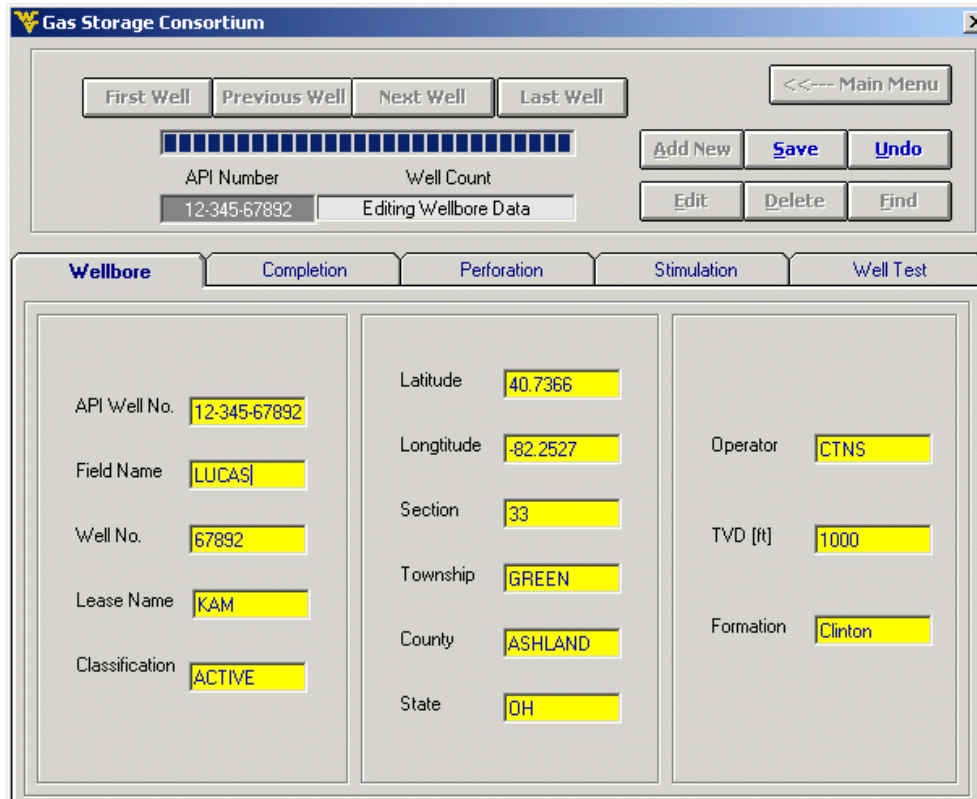


Fig53. Editing well data

The screenshot shows a software window titled "Gas Storage Consortium". At the top, there are navigation buttons: "First Well", "Previous Well", "Next Well", "Last Well", and "<<--- Main Menu". Below these is a progress bar and a "Well Count" field. The "API Number" field contains "12-345-67892" and the "Well Count" field contains "Editing Wellbore Data". There are also "Add New", "Save", "Undo", "Edit", "Delete", and "Find" buttons. Below the navigation is a tabbed interface with tabs for "Wellbore", "Completion", "Perforation", "Stimulation", and "Well Test". The "Completion" tab is active, showing a form titled "Editing Completion Data". The form has two columns of input fields. The left column includes "Field Name" (LUCAS), "Well No." (67892), "Description" (yellow), and "Date Tubing Run" (9/26/2005). The right column includes "OD (in)", "Top (ft)", "Bottom (ft)", "Weight (lbs/ft)", and "Grade", all of which are yellow. At the bottom of the form are buttons for "First Completion", "Previous Completion", "Next Completion", and "Last Completion".

Fig54. Editing completion data

The background color of text boxes of all tabs including well-bore tab will be yellow indicating that they are ready for entering data.

2- Enter the data in all the active tabs. The dates for completion, perforation, stimulation & well test job should be known.

3- Click the Save button .

Editing only completion/perforation/stimulation/well-test data

- 1- Click on the Edit button  while keeping that tab active for which you want to edit the data except well bore tab.

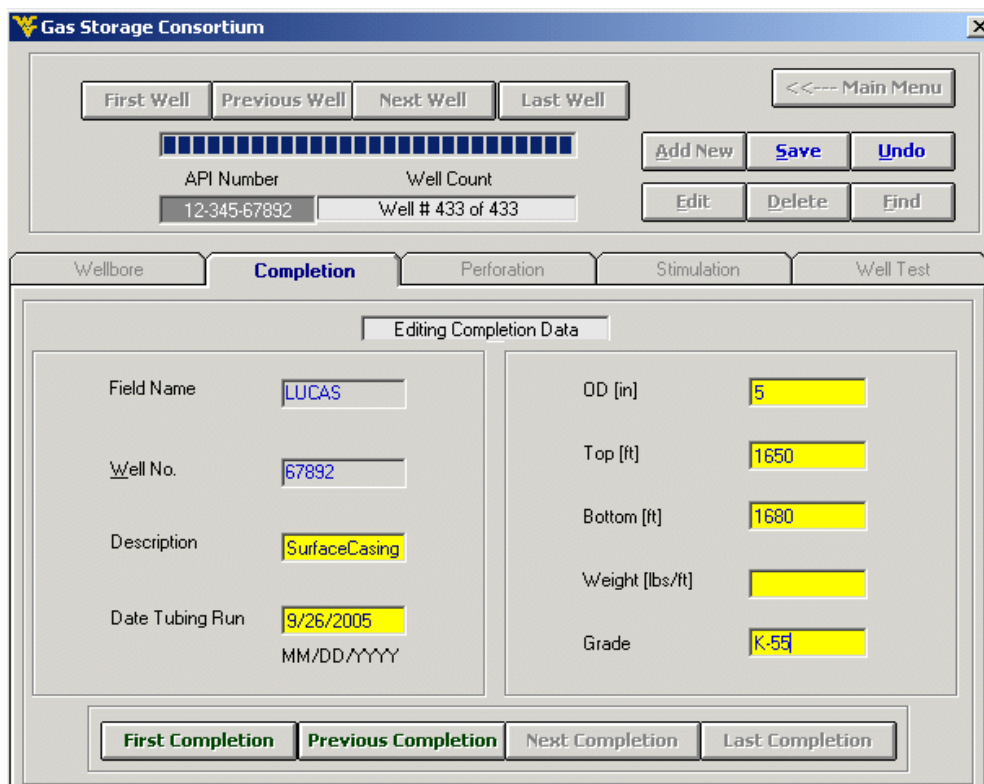


Fig55. Saving completion data

The background color of all text boxes of that tab will be yellow indicating that they are ready for entering data.

Enter the data. The dates for completion, perforation, stimulation & well test job should be known.

Click the Save button .

Result of editing only completion data

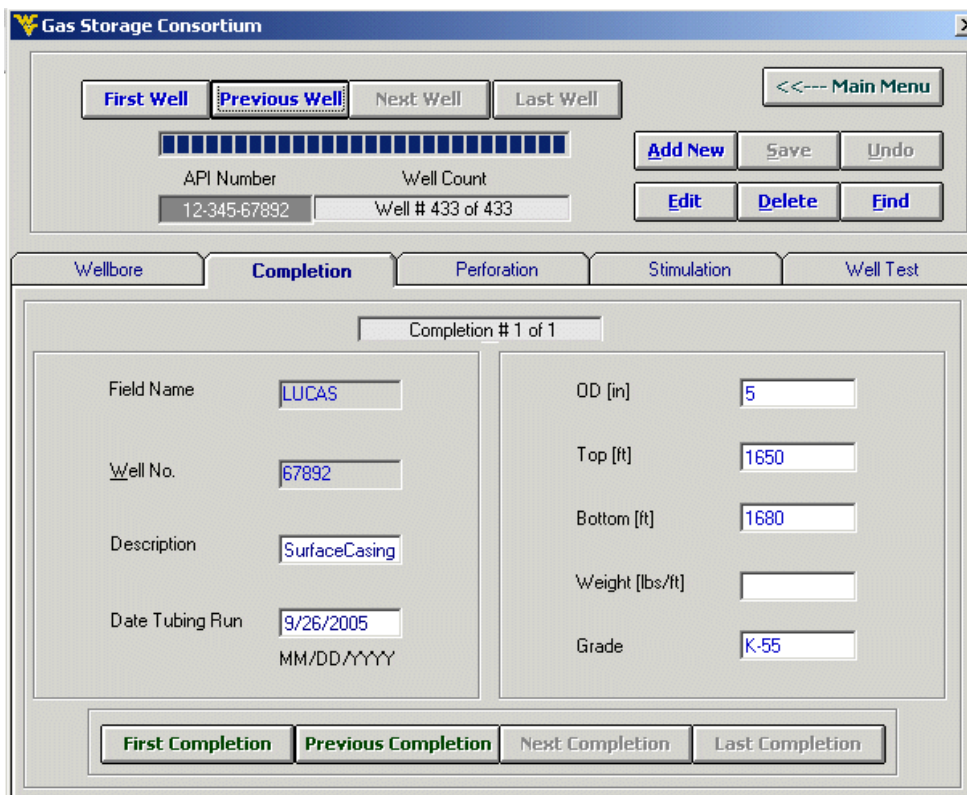


Fig56. Saved completion data

Deleting data

One can delete complete well or just only delete completion/perforation/ stimulation/well-test data by following methods:

Deleting a complete well data

- 1- Click on Delete button  while keeping your well bore tab as active

Editing only completion/perforation/ stimulation/well-test data

- 1- Click on Delete button  while keeping that tab active of which you want to delete the data except well bore tab.

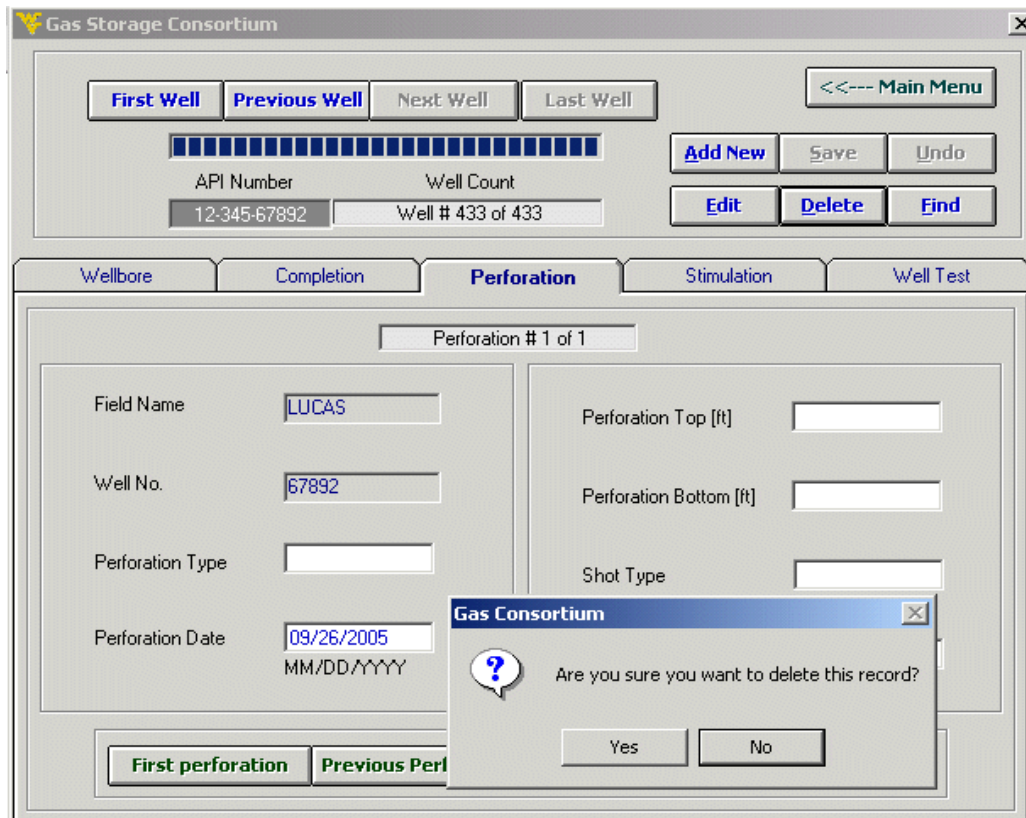


Fig57. Deleting perforation record

You will be greeted with the above message to make sure that delete button is not accidentally pressed.

- 2- Click on yes if you want the selected record to be deleted.

Undo the edit/add operation:

To undo the edit or add operation before they can be saved click undo button



Finding a well

Follow the following procedure to find a well for which you have some idea of its API well number:

Click on Find button



The following screen is displayed:

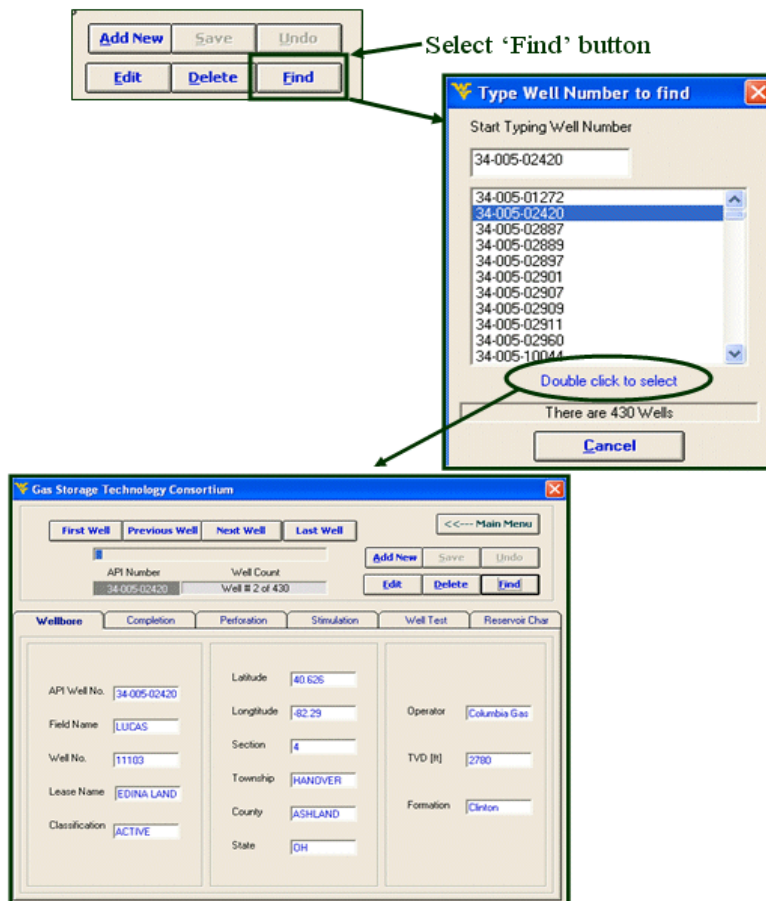


Fig58. Finding a well

WELL TEST ANALYSIS

To perform well test analysis on a well and draw graph of Peak day rate and Absolute open flow, use the option / command buttons below:



Fig59. Well-test Analysis Option in well-test tab

Peak day, AOF, Skin, and all well test graph

Select **PD rate**, **AOF**, **Skin** or **All well Tests** option button and then click on the **Show** button . The following screens will appear according to the option selected:



Fig60. Show Chart – Peak Day Rate

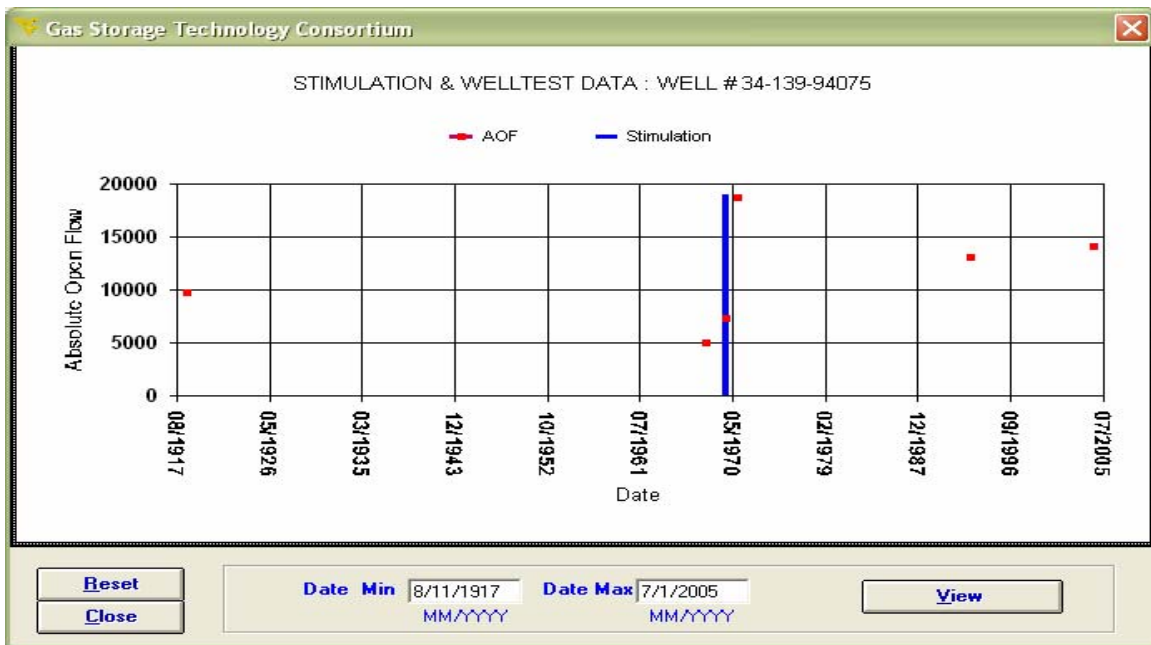


Fig61. Show Chart – Absolute Open Flow

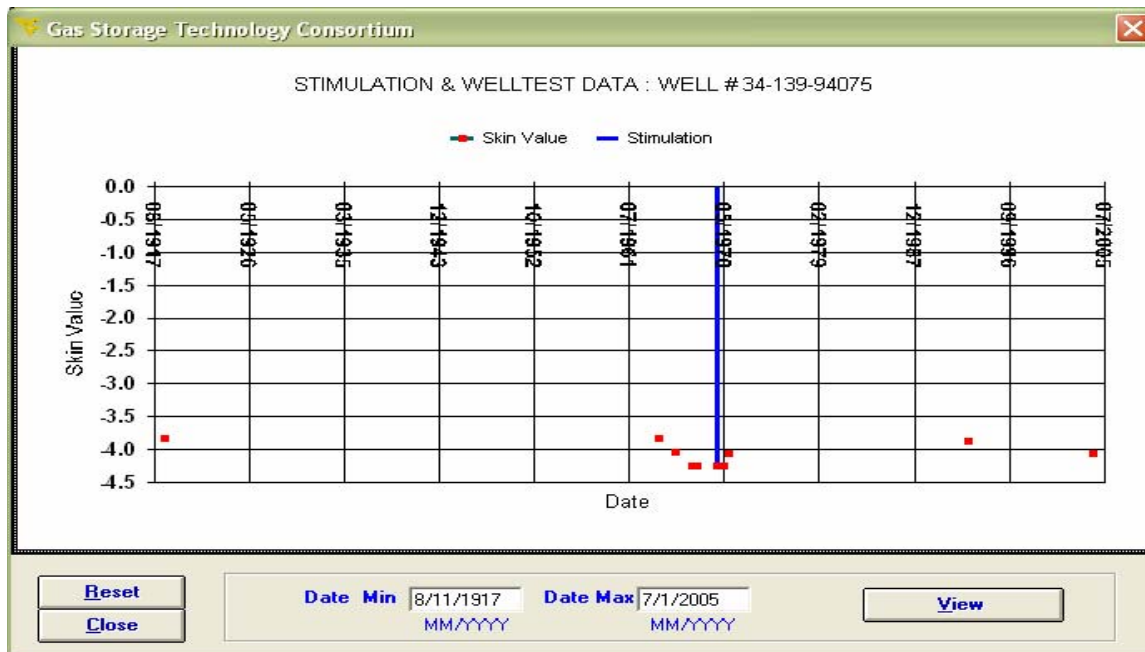


Fig62. Show Chart – Skin

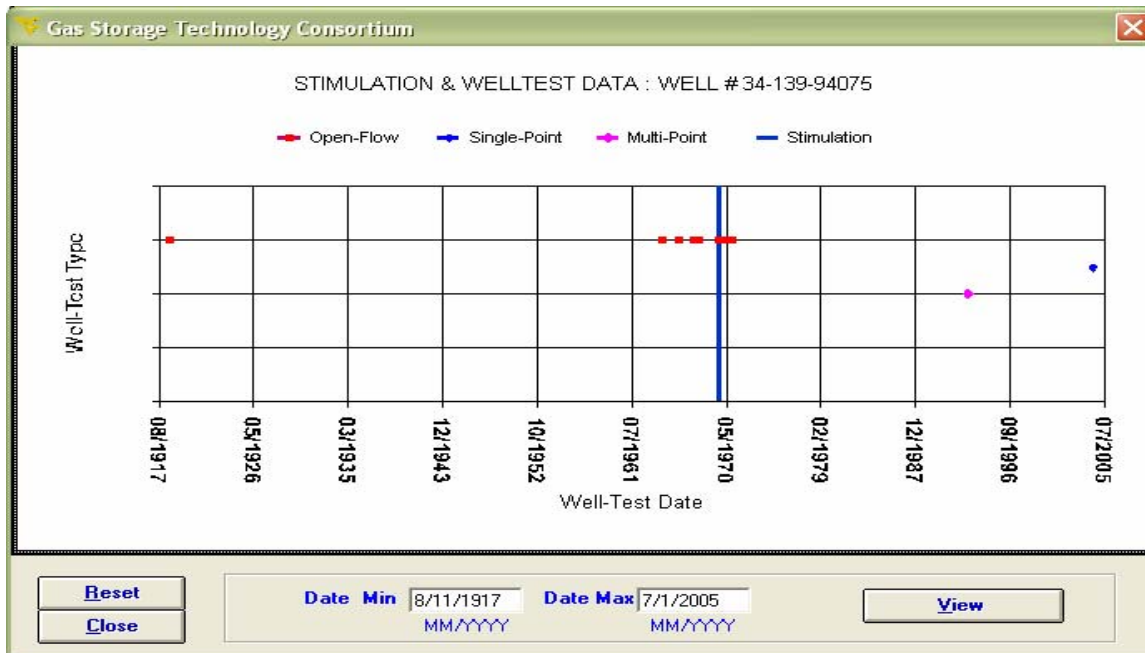


Fig63. Show Chart – All Well Tests

WELL TEST ANALYSIS TOOL

The user can do three types of Well Test Analysis in this software:

- 1- Simplified Analysis (for calculating n , C , PD rate & AOF)
- 2- LIT Analysis (for calculating Skin if 'k' is known)
- 3- Build-up Test Analysis (If Detailed Multi-Point Test data is available)

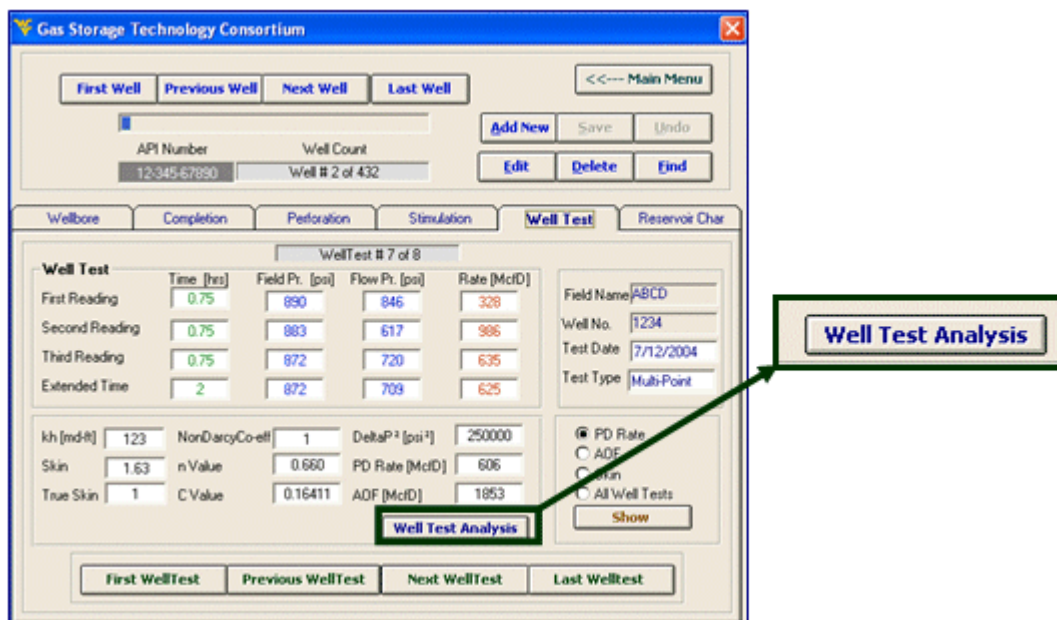


Fig64. Well Test Analysis button

The analysis tools are very similar for Simplified and LIT Analysis except where mentioned. The interface below will appear when you select 'Well Test Analysis' button. It will give you a glimpse of what has happened on the well since it was drilled.

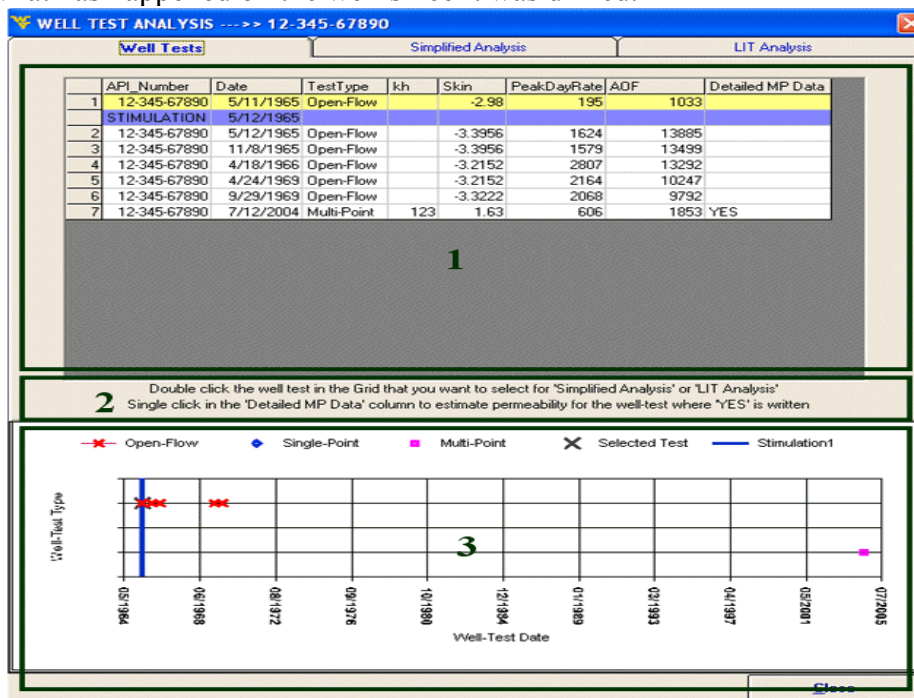


Fig65. Well Test Analysis Module

1. This section contains all the data in a grid form API Number, Date of well test, Test Type, kh value, Skin value, Peak Day rate, Absolute Open Flow and information in 'YES' or 'NO' form if the Detailed Multi-point data (Pressure profile & flow-rate vs.

time) is available for a given test or not. The back color of selected well-test is yellow while of stimulation is purple. The first well-test is selected by default.

2. This section contains instructions as how to select well-tests for analysis. Single click on any well-test will make it the current well-test with background changed to yellow and by double click; it will be selected for Simplified and LIT Analysis. If the Detailed MP Data for a well-test is given, then it can be selected for permeability analysis (build-up test) by single click on the cell where 'YES' is written. This way the build-up test analysis module will show up.
3. This section shows the time of different well tests which are indicated by three types of markers and stimulations on a well which are represented by straight blue vertical lines. The selected well have the similar marker according to its test-type but its color is dark green.

Once any well-test is double clicked, it is selected and added in the list box of simplified and LIT Analysis.

Simplified Analysis:

The screen shot of Simplified Analysis tab is below with Well-test # 2 to # 7 selected for analysis.

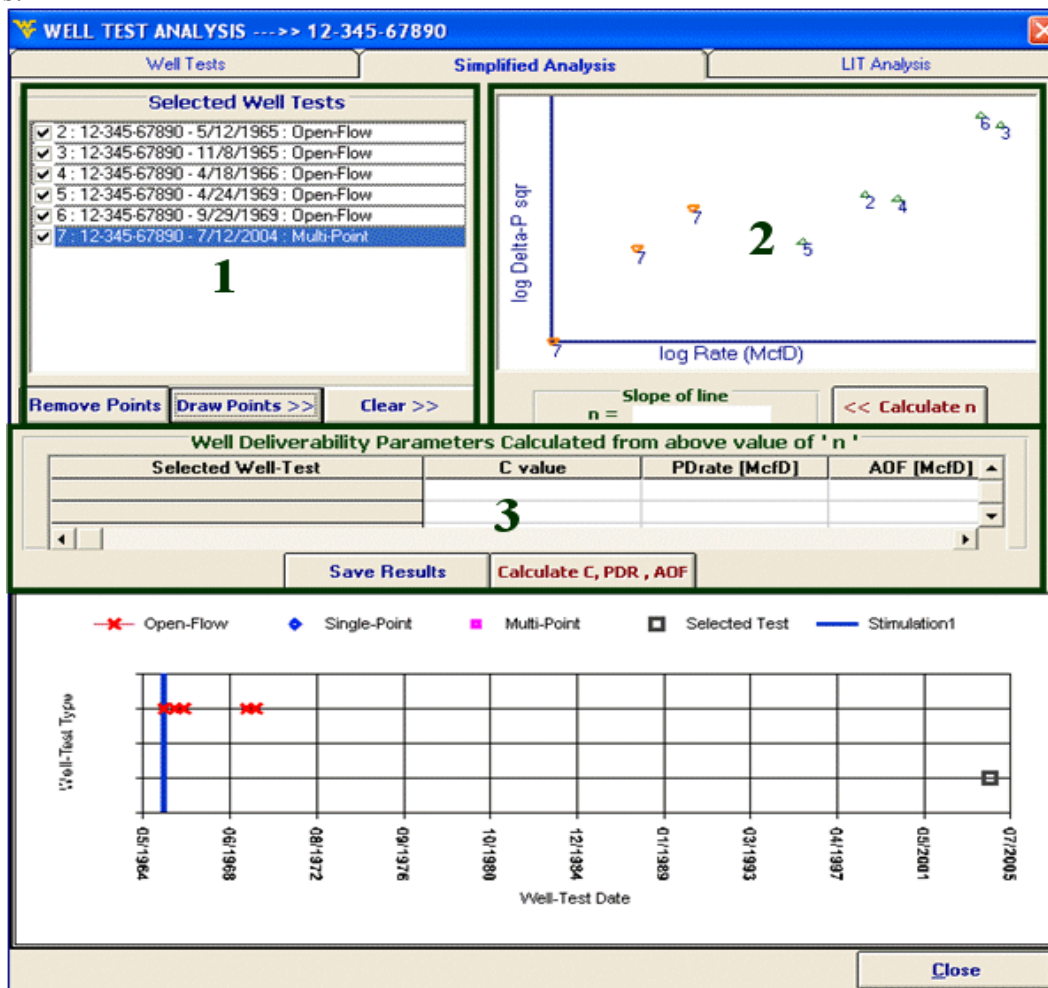


Fig66. Well Test analysis tool

1. This section contains the list box which has the entire well-tests selected for an analysis. Any test now again can be selected or de-selected by using the check-box in front of it. Once the well-tests are selected, then they can be drawn on log-log graph of Flow-rate (McfD) vs. Delta Pressure Square (Delta P sqr) by selecting the 'Draw Points' button. This graph can be cleared by selecting the 'Clear>>' button also if the well-tests drawn need to be changed.
2. Once the data points have been drawn, the user can draw a line in the picture box keeping left mouse button held down like shown below:

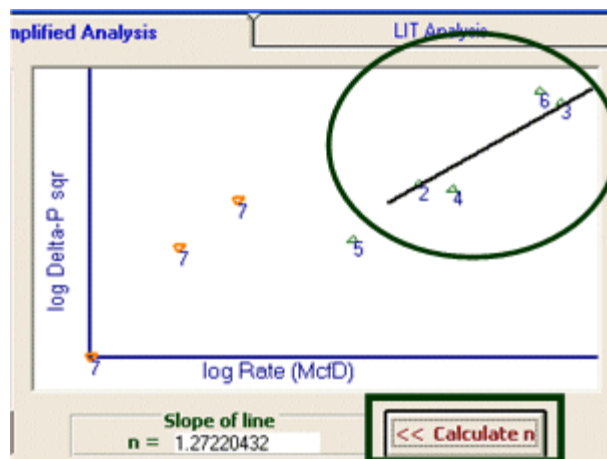


Fig67. Draw a line and calculate the slope

Select 'Calculate n' button to find the slope of the drawn line. The slope will be calculated in front of 'n' text box.

1. Now the user can select the well-tests that he/she intended to the simplified analysis on them. Then a line should draw based on the selected well tests in the picture box (Figure 68). The slope (n) will be calculated by mouse clicking on the "Calculate n" Button. The values of C, Peak Day Rate and Absolute Open Flow will be calculated and shown in the grid as shown in the picture shot on next page. These results can be saved in the database by selecting the 'Save' button.

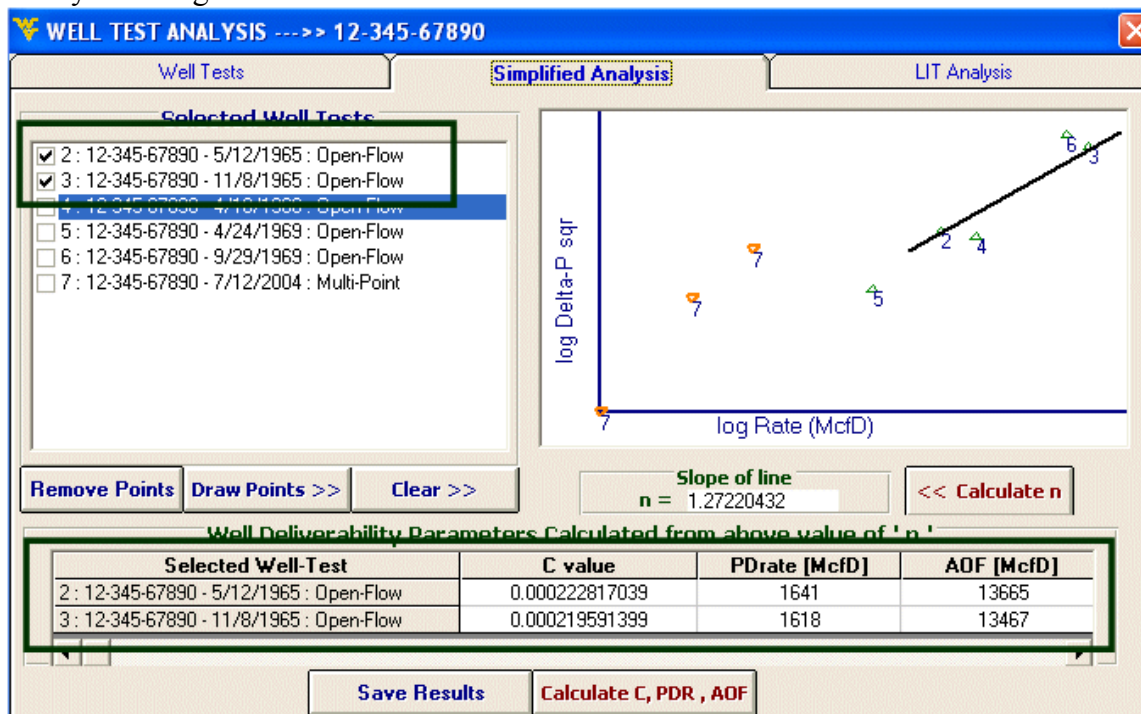


Fig68. Simplified well test analysis tool

Note: If there is only one well-test before or after the stimulation, then the value of n can be assumed and written in the textbox in front of label 'n' as shown in the picture below. The value of 'n' cannot be assumed for more than one well at a time so if there is more than one well-test for which the value of 'n' has to be assumed, then they should be selected one by one.

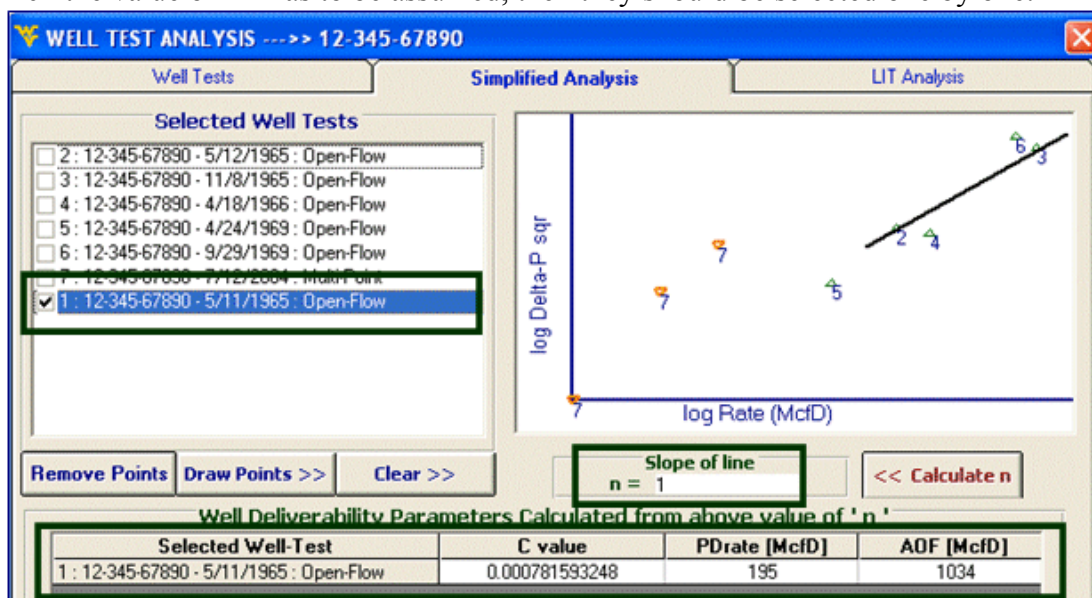


Fig69. Simplified well test with one well test before or after stimulation

Laminar Inertial Turbulent (LIT) test Analysis:

The screen shot of the LIT analysis is below:

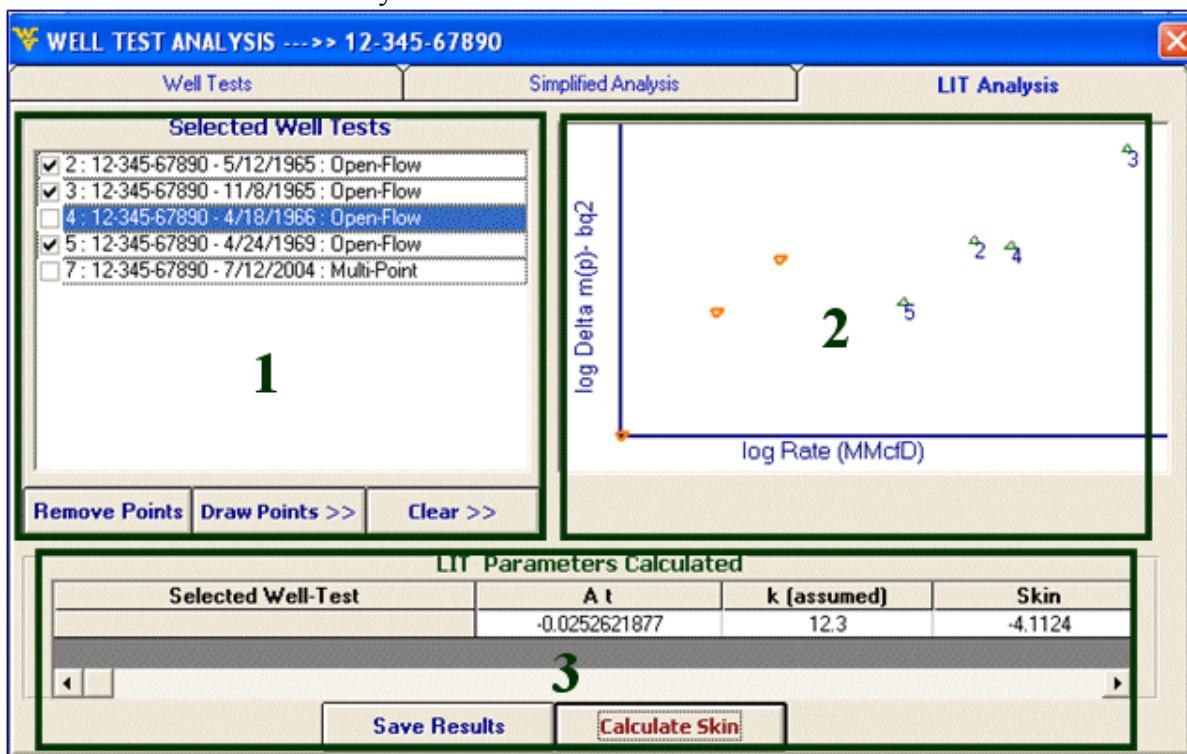
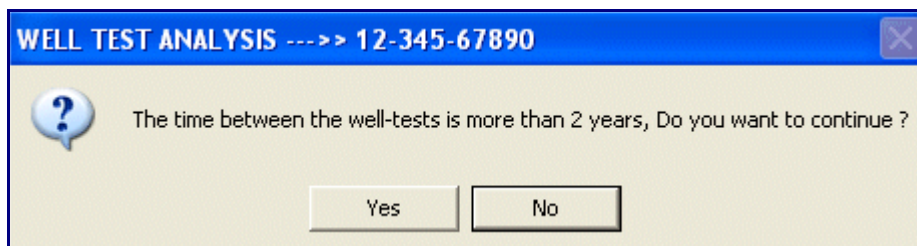


Fig70. LIT well test analysis

1. This section is the same as for Simplified Analysis.
2. In this section, the well-test points are drawn on log – log plot of ‘Flow rate (MMcFD) vs. Delta pseudo pressure – bq^2 ’. There is no need to draw a slope line in this plot. Instead, the points can be selected by visual inspection that they form a straight line and that they were conducted preferably within 2 years. In the snapshot above, well test points 2,3 and 5 have been selected to calculate Skin.
3. When the ‘Calculate’ button is pressed, the program uses the permeability value ‘k’ from the nearest well-test and calculates skin. The new value of skin can be saved in the database by selecting ‘Save Results’ button.

Note: Multi-point test points give erroneous calculations if selected with other well-tests as they are recorded one flow after another simultaneously, not like Open Flow and single point tests, which are recorded once a year.

If the selected well-tests are not within 2 years, then the following message will appear giving the user choice either to select other well-tests or continue with the well-tests selected.



Build-up test Analysis:

If any Multi-point well test has a detailed data (pressure and flow-rate profile vs. time), then the 'Detailed MP Data' column in front of that test will show 'YES'. It means that the data for this well-test can be analyzed to estimate a value of permeability.

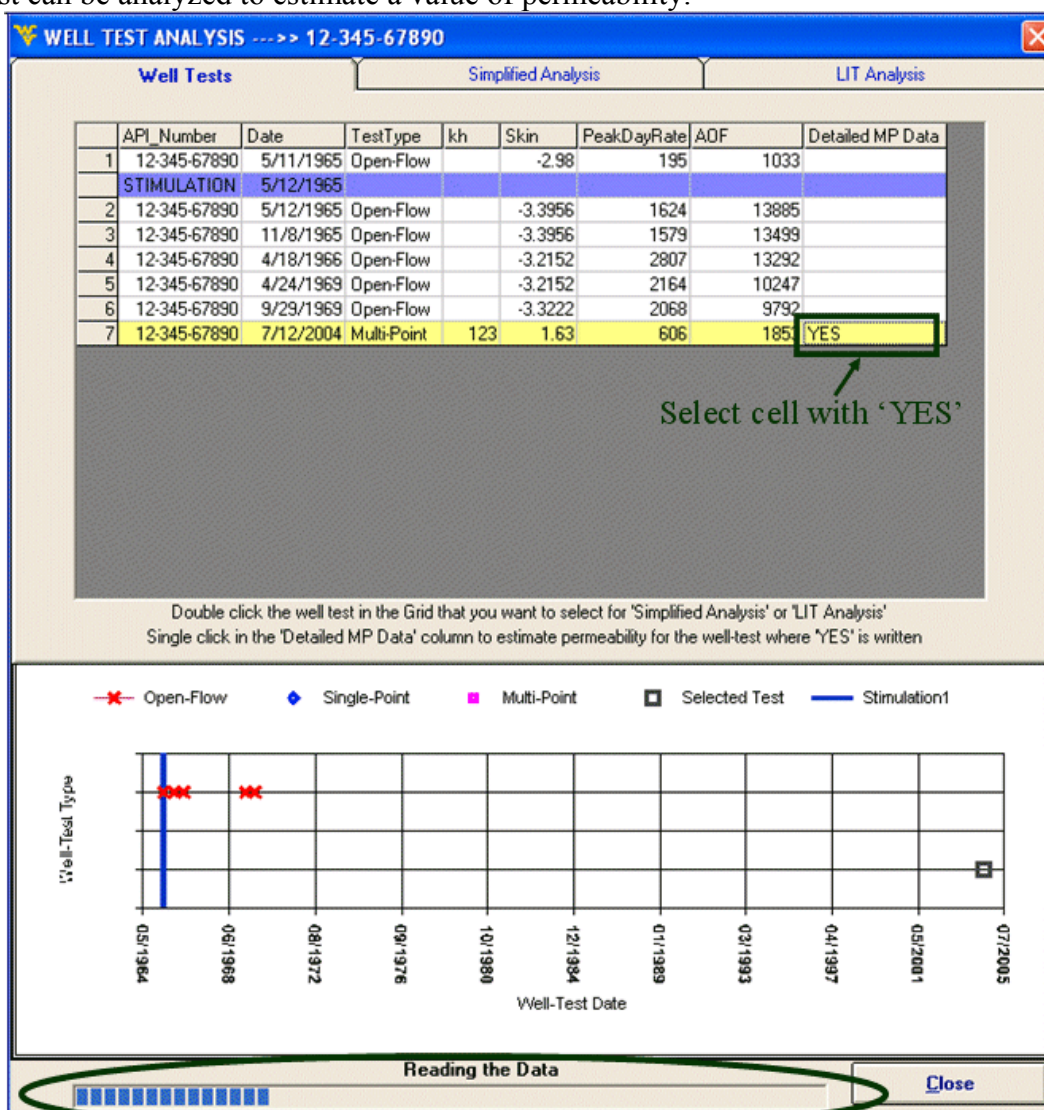


Fig71. Multi point well test analysis

If the cell with value 'YES' is selected the software will read the data from the excel file and progress bar will become visible like in the picture shot above showing that the data is being read.

After the complete data has been read by the software, the following screen will appear showing the pressure profile of the well-test.

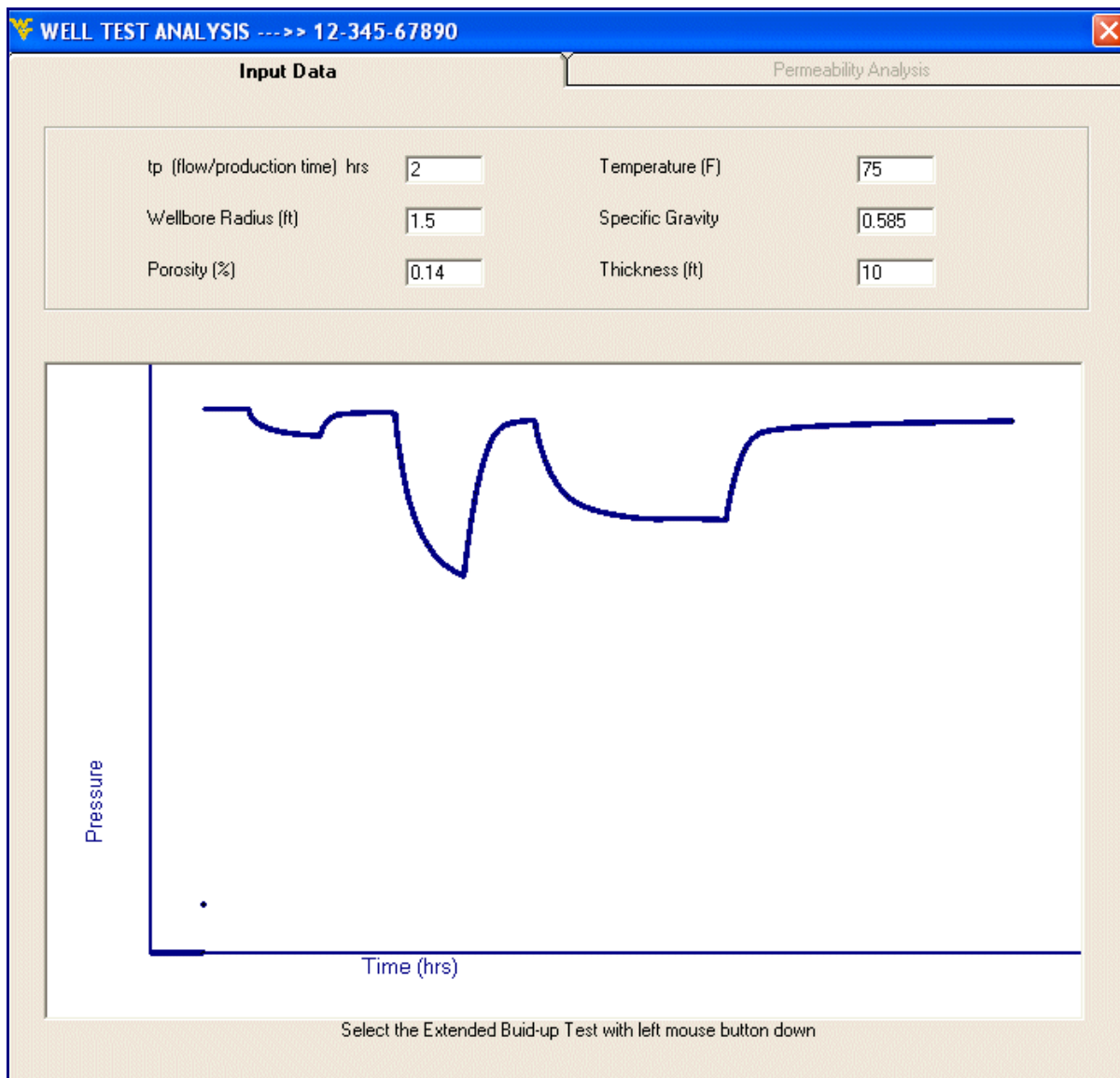


Fig72. Well extended pressure profile

All the Input data is retrieved from the database and if it is not found, then default values are inserted. The value 'tp (flow/production time)' is 2 hrs by default but can be changed by the user. The Extended build-up test for 2 or more hours should be selected by keeping the left mouse button down. The green lines will indicate portion of build-up test selected.

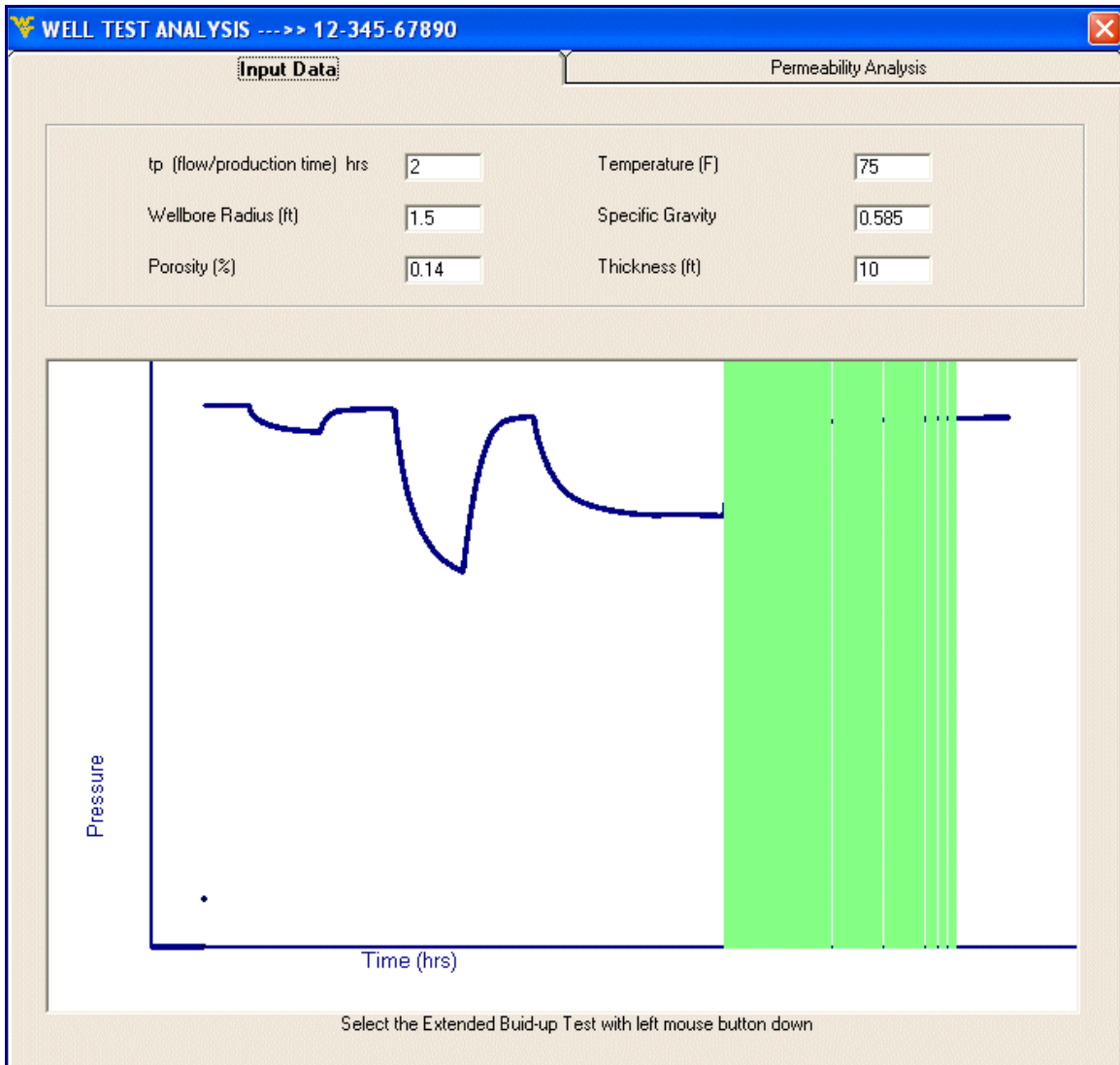
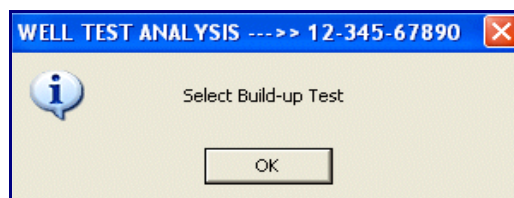


Fig73. Selecting the build-up section from pressure profile

If by mistake draw-down data is selected, then the following message will appear informing the user to select build-up data again.



After the portion of build-up data has been correctly selected, the permeability analysis tab will show following graphs. The first one is the log-log diagnostic plot between 'Del Pressure' and 'Del Time'. The user should select the first point which does not fall on the unit slope line drawn by holding the left mouse button down. The initial pressure 'Pi' and flow rate text box values will be selected from the build-up portion of the extended well-test selected. The graphs will be drawn again with a green line drawn on the Horner plot indicating The End of Well-Bore Storage (tewbs).

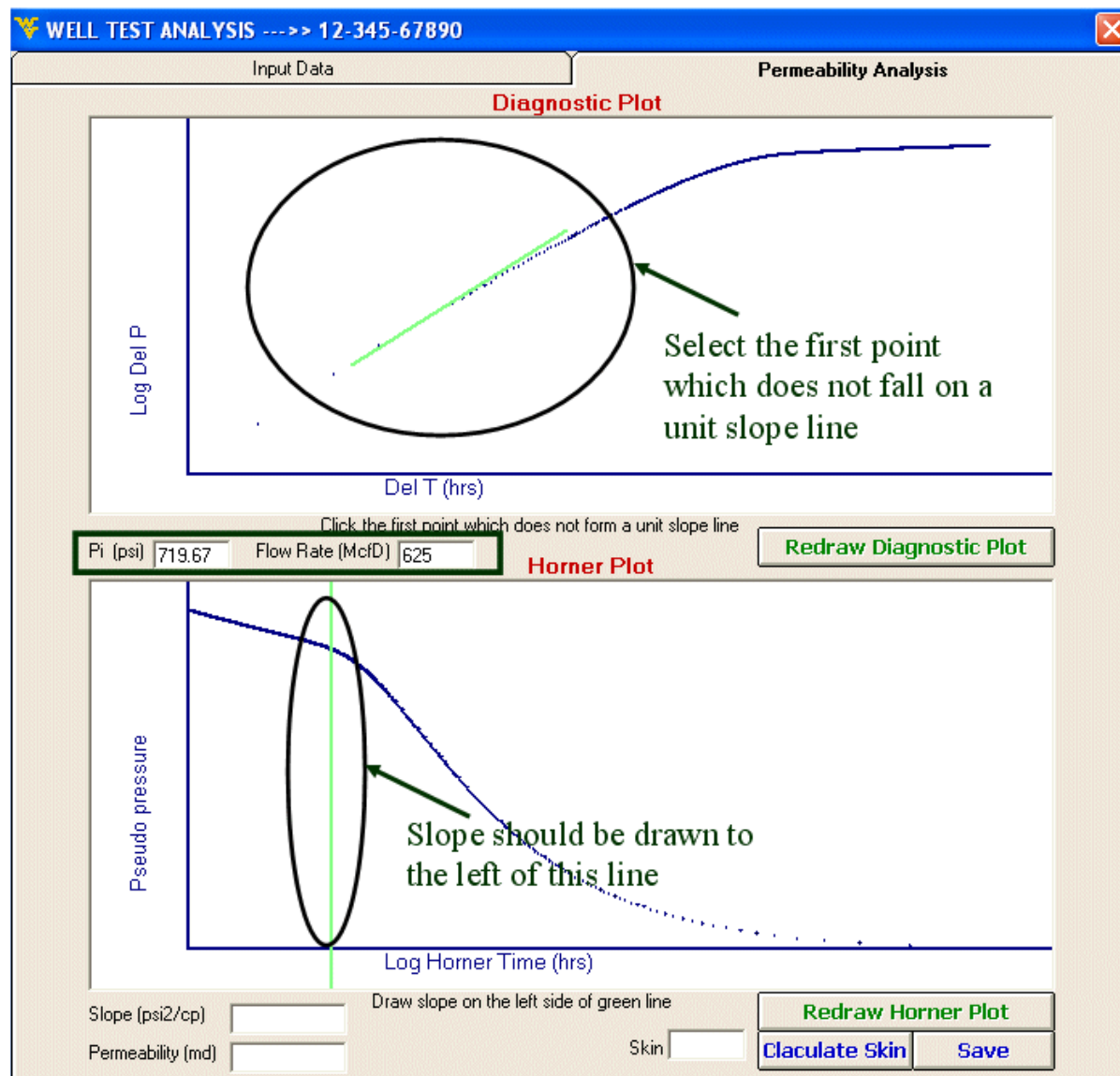


Fig74. Diagnostic plot analysis

The slope should be drawn on the Horner plot on the left side of the end of well bore storage line shown in green on Horner plot.

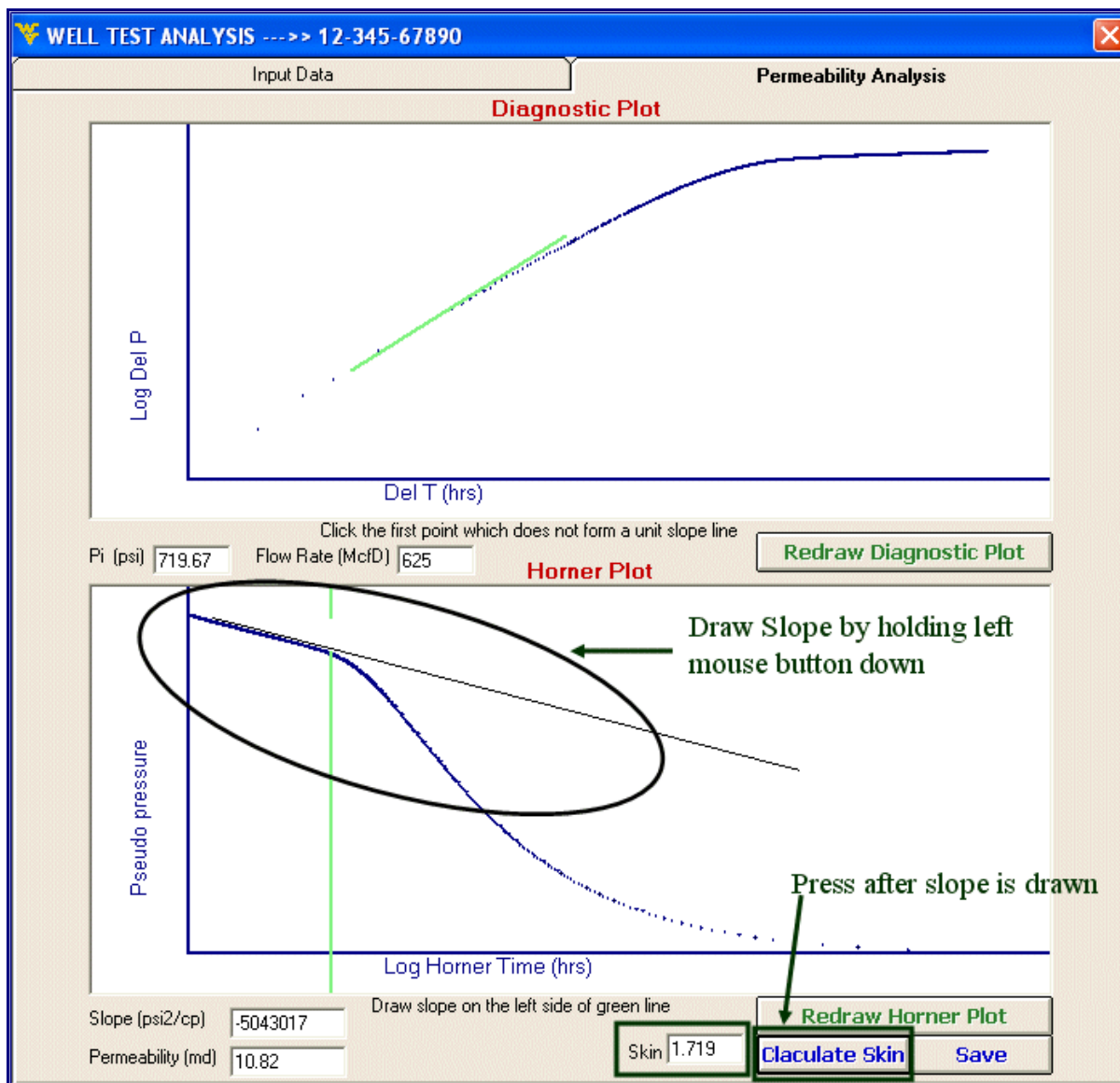


Fig75. Calculating skin from Horner plot

After the slope is drawn, the user can select 'Calculate Skin' button to find the skin of the well. The respective graphs can be redrawn any time by selecting the 'Redraw Diagnostic Plot' or 'Redraw Horner Plot'. The value of permeability and Skin can be saved in the database by selecting 'Save' button.

SELECT WELL DATA

In this form the user can choose to select the data of the wells that he wants to look at. Following are a few ways he can choose the data:

Selecting a well by State/County:

The user selects the state first and then the county. All the wells will be selected for that county in the selected wells list box:

The screenshot shows a software interface with two main panels. The left panel, titled 'SELECT', has two sub-sections: 'OHIO' and 'COUNTY'. Under 'OHIO', the text 'OH' is highlighted in a blue selection box. Under 'COUNTY', the text 'ASHLAND' and 'RICHLAND' is listed. Below these sections is a 'Reset' button. The right panel, titled 'SELECTED WELLS', has a sub-section 'API Well Number' containing a list of well numbers with checkboxes: 34-005-01272 (checked), 34-005-02420, 34-005-02887, 34-005-02889, 34-005-02897, 34-005-02901, 34-005-02907, 34-005-02909, 34-005-02911, 34-005-02960, 34-005-10044, 34-005-10516, and 34-005-10517. Below this list is a 'Select All' button.

Fig76. Selecting Ohio County

Selecting wells by stimulation year:

The user can select the option button for stimulated year and input the year values. If Select Wells button is clicked, then all the wells that have been stimulated between these years will be shown in the selected wells list box

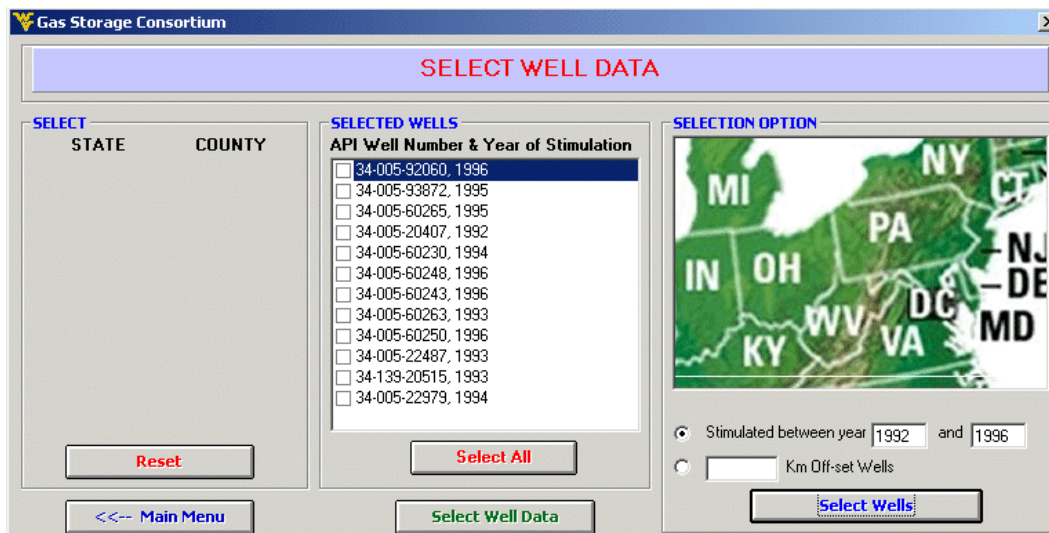


Fig77. Selecting wells according to stimulation year

Selecting offsets wells form a well:

The user selects the offset option and the well near which he wants to find the off-set wells, and then enters the distance of off-set in kilometers. If Select Wells button is clicked, then all the wells that are off-set of the selected well will be shown in the selected wells list box

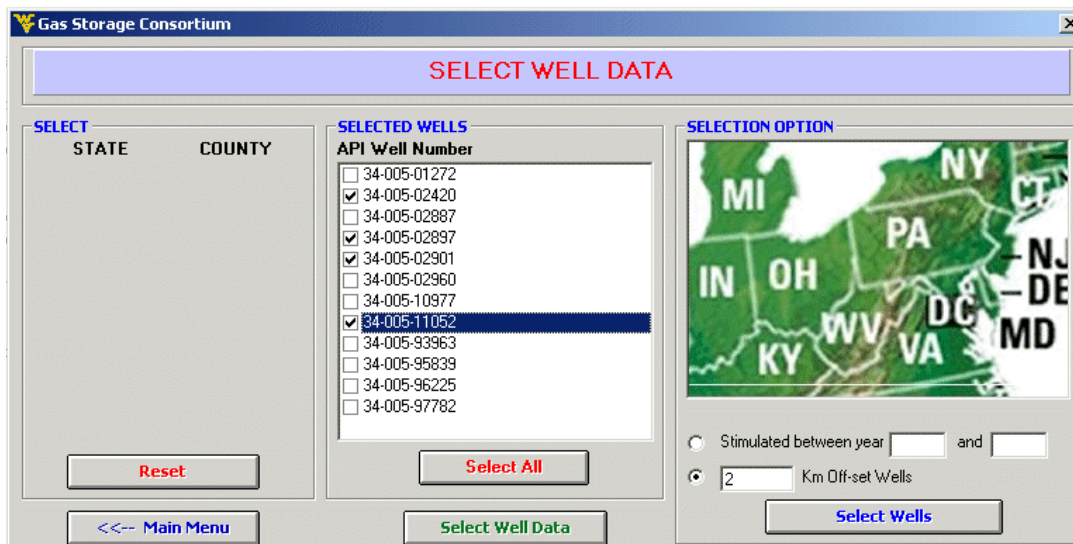


Fig78. Offset wells

Display the selected wells data:

When the wells for which the user want the data to be retrieved have been selected, click the Select Well Data button  and select the parameters.

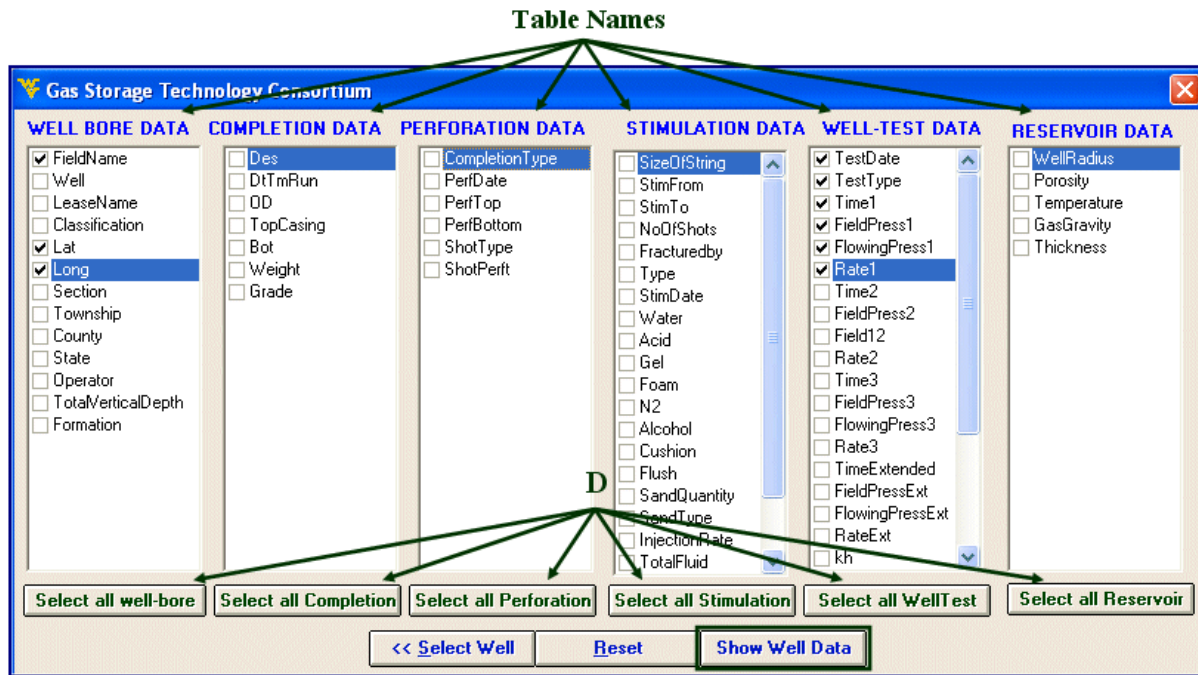


Fig79. Selecting Well Parameters

Click Show Well Data  to retrieve the data.

API_Number	FieldName	Lat	Long	TestDate	TestType	Time1	FieldPress1	FlowingPres	Rate1
12-345-67890	ABCD	20.62222	-62.27472	9/29/1969	Open-Flow		1138	0	9602
12-345-67890	ABCD	20.62222	-62.27472	4/18/1966	Open-Flow		679	0	4970
12-345-67890	ABCD	20.62222	-62.27472	11/8/1965	Open-Flow		1070	0	11210
12-345-67890	ABCD	20.62222	-62.27472	5/12/1965	Open-Flow		699	0	3850
12-345-67890	ABCD	20.62222	-62.27472	5/11/1965	Open-Flow		465	0	169
12-345-67890	ABCD	20.62222	-62.27472	4/24/1969	Open-Flow		522	0	2345
12-345-67890	ABCD	20.62222	-62.27472	7/12/2004	Multi-Point	0.75	890	846	328

Fig80. Result of the wells & parameters selected

CANDIDATE SELECTION

This module will appear on selecting the ‘Candidate Selection’ button from Main Menu.

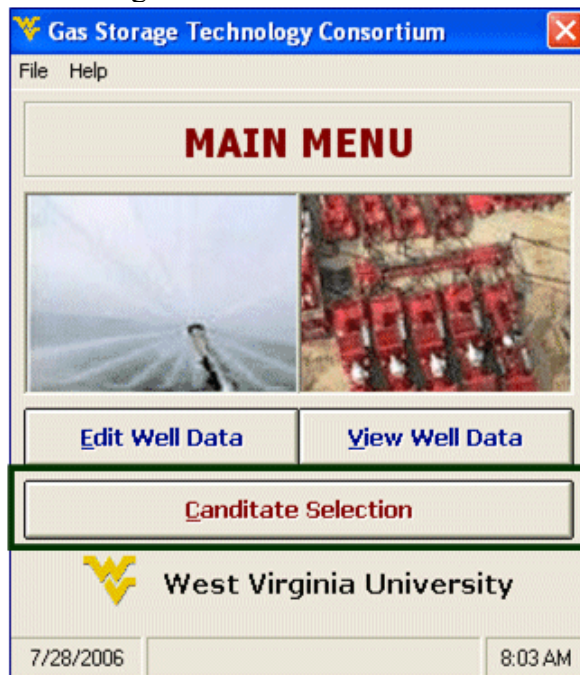


Fig81. Start Candidate Selection form main screen

For intelligent candidate selection of wells, it is very important that only valid data is given to the Neural Network (NN) for training. Valid data is one which will not degrade the performance of the NN and is useful in NN training.

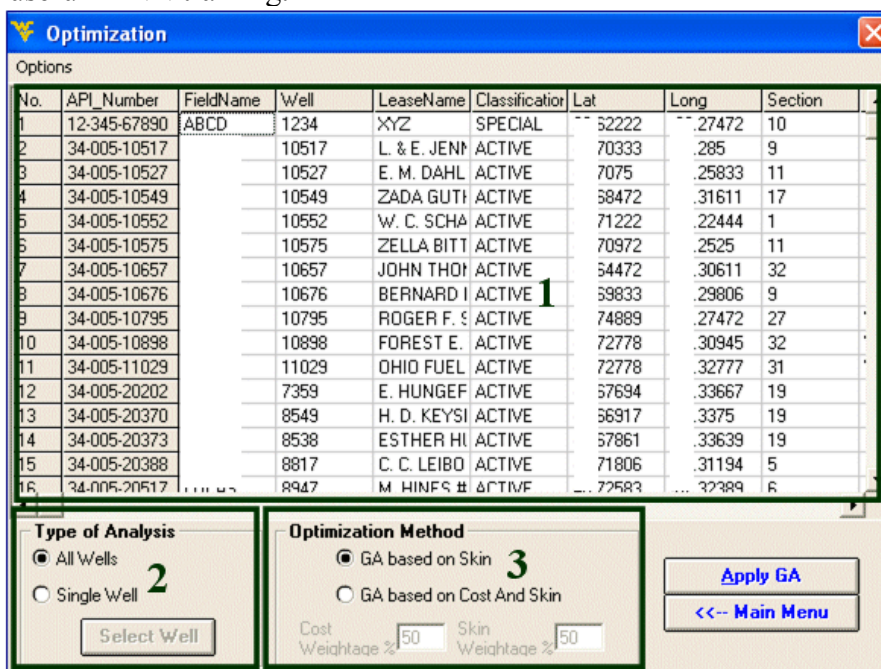


Fig82. Candidate Selection main screen

1. When this module is loaded, each row in this section of the grid represents a valid stimulation as shown in figure above. Following, is the criteria for valid stimulation selection:

Valid Stimulation – It should have skin value before & after stimulation.

Valid Perforation – Perforation just before the stimulation.

Valid Completion – The smallest size completion run before stimulation.

Valid Well-test – Well-test having skin value just before or after the well-test.

2. Two types of analysis can be done on the wells: One option is to apply Genetic optimization on wells one at a time and the other is to apply it on all wells. If the ‘All Wells’ option is selected, then the ‘Select Well’ button will be enabled and the user can select the well the same way as shown in the previous section of the user Manual for – Find a well.

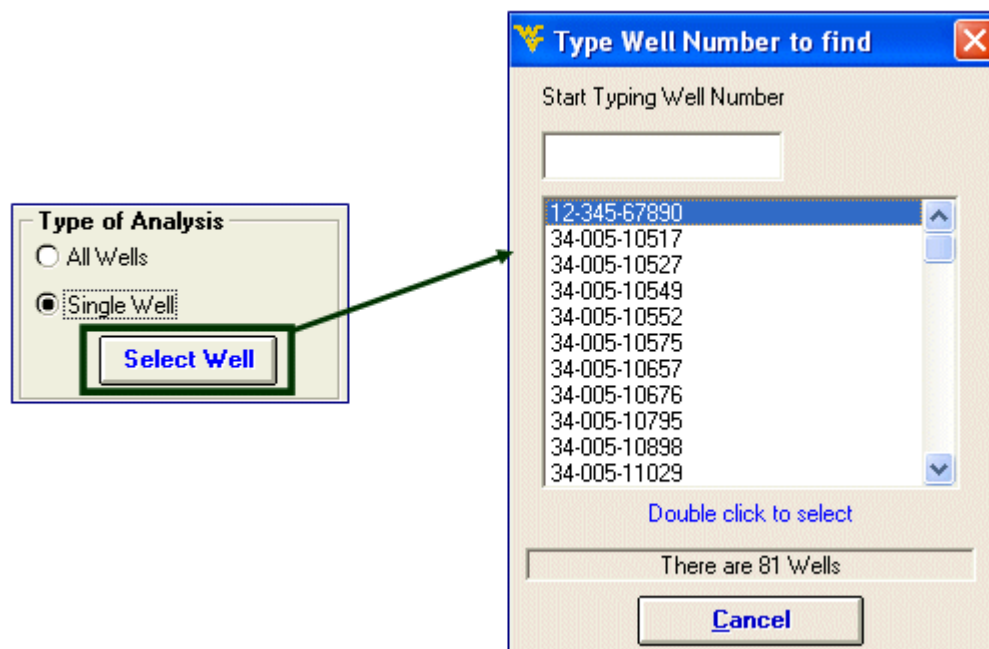
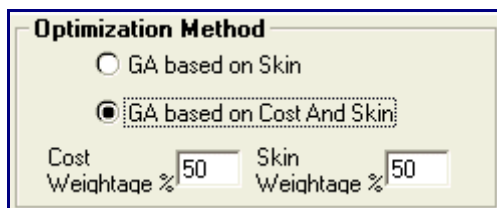


Fig83. Selecting a well for candidate selection process

3. This section of module relates to the Optimization methods available. User can optimize the stimulations according to only change in skin criteria or may choose to select the ‘GA based on cost and skin’ option where he/she can give different weight ages to cost and skin.



Optimization Method

GA based on Skin

GA based on Cost And Skin

Cost Weightage % Skin Weightage %

Options Menu:

This software can cater for many varied situations. These options can be selected from the 'options' menu bar on the top of the form. It contains following items:

- Select controllable parameters
- Material cost
- Import NNet
- NNet Input values
- GA characteristic
- Export the Grid to Excel
- Select Well-Test Type

Following is a screen shot of the items in the Options menu tool bar.

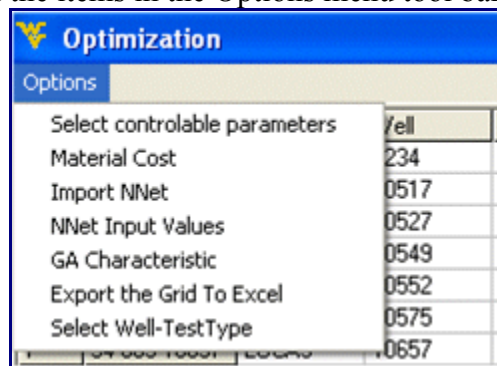


Fig84. Options to control Candidate Selection process

Material cost can be changed by the user as the prices fluctuate. These prices can be saved in the database by selecting 'Save' button and Default values can be retrieved by selecting 'Default' button. The screen shot of material cost is shown below and price is just an estimate and can be changed by user.

Material Cost

Cost

Water Injection \$/bbbls 29.4

Acid \$/bbbls 10

Gel \$/bbbls 3570

Foam \$/bbbls 10

Nitrogen \$/Mcf 49.7

Sand Quantity \$/lbs 0.4

Open Flow Test \$/Job 10000

Single Point Test \$/Job 5000

Multi Point Test \$/Job 10000

Save Default Close

Fig85. Cost analysis module

NNet Input

No.	API Number	Lat	Long	Water	Acid	Gel	Foam	N2	SumFluids	SandQuantil	Prior-kh	After-TestTy
1	12-345-	222	472	255	1.2	131	0	50		12100	123	Open-Flow
2	34-005-	333	5	255	1.2	131	0	50		12100	123	Open-Flow
3	34-005-	75	333	255	2.4	136	1.6	80		13600	395	Open-Flow
4	34-005-	472	511	0	1.2	75	0	0		6000	378	Open-Flow
5	34-005-	222	444	265	2.4	140	0.2	85		13650	100	Open-Flow
6	34-005-	372	25	255	1.2	130	0	45		9500	523.3	Open-Flow
7	34-005-	472	511	0	4.8	375	0.1	125		13100	362	Open-Flow
8	34-005-	333	306	234	2.4	129	0.2	60		11000	210	Open-Flow
9	34-005-	389	472	0	4.8	155	0.3	83.7		13900	557	Open-Flow
10	34-005-	778	345	0	2.4	435	0.1	75		24400	1374	Open-Flow
11	34-005-	778	777	0	6	435	0.1	75		20000	288	Open-Flow
12	34-005-	594	367	0	0	0	0	0		2000	793	Open-Flow
13	34-005-	317	75	0	1.2	24	0	0		2000	134	Open-Flow
14	34-005-	361	339	0	0	0	0	0		2000	120	Open-Flow
15	34-005-	306	194	0	0	0	0	0		1700	141	Open-Flow
16	34-005-	583	389	0	0	150	0	0		2000	1210	Open-Flow

Close

Fig86. Inputs that used to train the Neural Network

If the user wants to look at the Neural Network inputs being used, then ‘NNet Input’ option will take the user to a new form as shown above where all the inputs are shown. Keep in mind that this grid can only be seen once and that only after the Genetic optimization has been applied.

If some material is not available for stimulation, then still the user can optimize the stimulation by de-selecting that material from the ‘Select controllable parameters’ option. The materials not enabled are the ones that are not being used by the Neural Network in use.

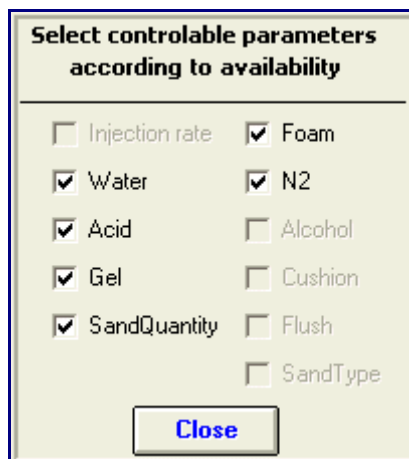


Fig87. Select the controllable parameters in optimization process

A new Neural Network can be used if the data is changed or appended by importing its 'ida' file. When a new Neural Network is imported, it might change the optimum GA parameters. The user can change them from 'GA characteristic' option. The default values are always loaded at startup as shown in figure below but can be changed by user.

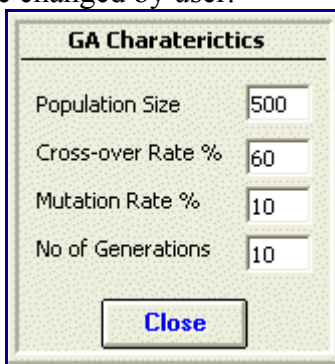


Fig88. Setup GA parameters

If one of the Neural Net inputs is well test before stimulation, the type of the wells test in optimization process should specify here.

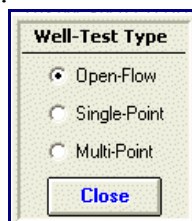


Fig89. Type of the wells test in optimization process.

When all the parameters for GA have been selected and user selects the ‘Apply GA’ button, then the screen below will appear showing the values of optimized stimulation slurry and change in skin due to this stimulation. The picture below shows the GA optimization done on well # 12-345-67890.

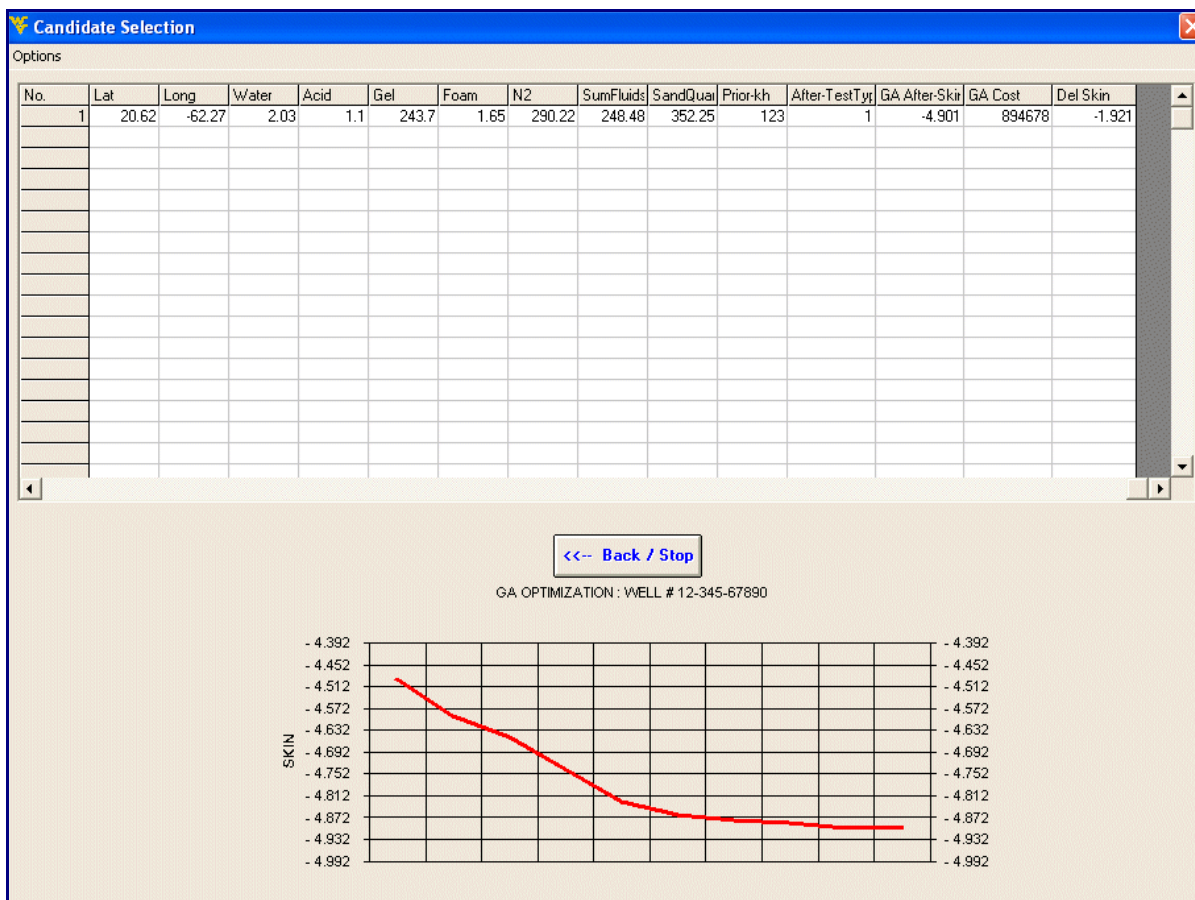


Fig90. Optimization process for one well

If the optimization is applied to all the wells, then we can rank the wells according to the change in skin by selecting 'Rank the wells' from Options menu bar on the top left corner of the form as shown in snapshot below.

	Water	Acid	Gel	Foam	N2	SumFluids	SandQual	Prior-kh	After-TestTyr	GA After-Skir	GA Cost	Del Skin	
2	6.75	11.34	121.85	1.63	252.77	141.57	469.67	123	1	-5.024	458092	-2.044	
3	0.68	10.52	161.08	1.7	162.04	173.97	5107.63	395	1	-4.959	595277	-1.1013	
4	3.38	6.17	153.75	1.66	272.94	164.96	6340.51	378	1	-5.048	575179	-1.3871	
5	4.05	11.21	103.03	0.03	46.09	118.32	23835.62	100	1	-4.457	389857	-1.7965	
6	10.8	5.71	78.45	1.7	205.96	96.66	3287.67	523.3	1	-4.882	301995	-1.2657	
7	0	9.67	124.47	1.7	315.43	135.84	880.63	362	1	-5.048	470491	-0.9724	
8	2.3	12.15	6.46	234.81	1.63	137.55	255.06	117.42	210	1	-5.04	855608	-1.4872
9	0.75	2.7	8.14	102.5	1.67	163.48	115.02	7866.93	557	1	-4.797	387383	-0.5144
10	0.73	272.08	11.89	434.59	0.03	356.48	718.6	28649.71	1374	1	-5.782	1598780	-0.859
11	0.73	2.7	11.35	132.83	1.69	227.57	148.58	1115.46	288	1	-5.042	496186	-1.0263
12	0.68	10.8	2.45	189.32	1.7	247.01	204.27	2407.05	793	1	-5.05	699456	-0.7801
13	0.67	5.4	2.57	211.28	1.7	195.16	220.95	1819.96	134	1	-5.049	774901	-1.5019
14	0.68	11.48	3.78	218.08	1.7	41.05	235.04	5107.63	120	1	-5.049	793018	-1.654
15	0.72	8.1	7.01	211.28	1.69	109.46	228.07	2172.21	141	1	-5.039	770906	-1.0117
16	0.73	103.97	11.88	446.62	0.4	364.4	562.87	29647.75	1210	1	-5.699	1637575	-2.6374
17	0.72	8.78	9.56	144.34	1.64	177.88	164.32	5988.26	233	1	-5.043	536900	-1.4835
18	0.73	2.7	7.75	182.52	1.67	223.25	194.63	1467.71	401	1	-5.026	673442	-1.1274

Fig91. Optimization result for selected wells

The wells are ranked according to change in skin as shown in the figure below. These ranked wells and the optimized stimulation data now can be exported to excel by selecting 'Export to Excel' in the Option menu of Candidate Selection module.

Wells Ranked according to Change in Skin

No.	Lat	Long	Water	Acid	Gel	Foam	N2	SumFluids	SandQual	Prior-kh	After-TestTyr	GA After-Skir	GA Cost	Del Skin
64	1.71	.36	0	3.03	243.7	1.67	26.65	248.41	3698.63	957	1	-5.049	882877	-6.459
35	1.67	2.3	1.35	5.84	164.21	1.7	234.77	173.1	6810.18	105	1	-5.046	610748	-2.8672
15	1.73	.32	103.97	11.88	446.62	0.4	364.4	562.87	29647.75	1210	1	-5.699	1637575	-2.6374
43	1.66	2.3	2.03	1.65	192.45	1.69	333.43	197.82	176.13	308.7	1	-5.048	713794	-2.2202
65	1.71	.37	204.57	11.87	471.2	0.19	342.79	687.82	29941.29	1712	1	-5.879	1727323	-2.1033
1	10.7	.28	6.75	11.34	121.85	1.63	252.77	141.57	469.67	123	1	-5.024	458092	-2.044
61	1.71	.36	142.46	11.75	507.81	0.07	347.12	662.09	28356.16	1880	1	-5.894	1855768	-2.0423
69	1.71	.35	7.43	9.26	222.79	1.69	72.02	241.16	410.96	576	1	-5.048	809417	-2.0098
79	1.71	.34	0	6.52	234.81	1.7	150.51	243.04	1467.71	100	1	-5.047	856437	-1.9297
24	10.7	.29	7.43	2.69	212.33	1.65	84.98	224.09	3992.17	100	1	-5.027	774088	-1.8304
18	1.74	.31	180.26	11.33	448.71	0.53	362.96	640.83	29060.67	1770	1	-5.872	1646975	-1.8082
4	1.71	.22	4.05	11.21	103.03	0.03	46.09	118.32	23835.62	100	1	-4.457	389857	-1.7965
66	1.72	.36	261.28	11.85	456.03	1.1	353.6	730.27	26125.24	1317	1	-5.747	1673867	-1.7729
59	1.74	.31	3.38	8.82	172.06	1.65	295.98	185.9	2289.63	117	1	-5	640076	-1.7104
19	1.72	2.3	1.35	3.71	205.53	1.67	272.22	212.26	0	122	1	-5.024	757357	-1.6857
13	1.68	.34	11.48	3.78	218.08	1.7	41.05	235.04	5107.63	120	1	-5.049	793018	-1.654
37	1.69	2.3	3.38	2.44	265.15	1.67	141.87	272.63	117.42	209	1	-5.045	963812	-1.6262
70	1.68	.36	0.68	0.08	343.59	1.7	65.53	346.04	234.83	206	1	-5.049	1240013	-1.6002

Fig92. Rank the optimization result based on delta skin in order to find the best candidates

CONCLUSION

The main aim of this study was to find the re-stimulation candidate wells with the given data without trying to spend thousands of dollars on well-test and gas reservoir simulators. Detailed analysis of well-tests performed on the storage field was done and intelligent tools like Neural networks to predict the Skin and Genetic Algorithms were used to optimize the stimulation and to select the best stimulations for a well. The following conclusions can be drawn from this research:

1. The Artificial Intelligence Tool can predict Skin with high degree of confidence.
2. The Portfolio Management for re-stimulation candidate selection provides a cost effective method for taking full advantage of annual budget for remedial operations.
3. This software is the first successful attempt to combine Data editing, Well-Test analysis and Artificial Intelligence in one software package.

REFERENCES

NONE

Appendix M
2009, Ultrasonic Guided Wave Integrity Analysis Tool for Well Casing,
The Pennsylvania State University Final Report

ULTRASONIC GUIDED WAVE INTEGRITY ANALYSIS TOOL FOR WELL CASING

FINAL REPORT

Report Start Date: 1 January 2009

Report End Date: 31 December 2009

Principal Authors:

Cliff J. Lissenden

Joseph L. Rose

Report Issue Date: November 2010

DOE Award Number: DE-FC26-03NT41779 (subaward number 3809-TPSU-DOE-1779)

Submitting Organization:

The Pennsylvania State University

212 EES Building

University Park, PA 16802

Disclaimer:

This report was prepared as an account of work sponsored by an agency of the United States Government. Neither the United States Government nor any agency thereof, nor any of their employees, makes any warranty, express or implied, or assumes any legal liability or responsibility for the accuracy, completeness, or usefulness of any information, apparatus, product, or process disclosed, or represents that its use would not infringe privately owned rights. Reference herein to any specific commercial product, process, or service by trade name, trademark, manufacturer, or otherwise does not necessarily constitute or imply its endorsement, recommendation, or favoring by the United States Government or any agency thereof. The views and opinions of authors expressed herein do not necessarily state or reflect those of the United States Government or any agency thereof.

ABSTRACT

Underground natural gas storage requires wells for access. The steel well casing is in a harsh environment and is susceptible to corrosion and cracking, which compromise its structural integrity. To ensure the safety of the public and the environment, and to protect the investment in the storage facility, it is necessary to monitor the integrity of these mechanical systems. Magnetic flux leakage (MFL) probes are used to diagnose the mechanical integrity of well casings. This technology is well suited for damage detection but less so for classification and sizing of defects.

Guided wave ultrasonic technology (GWUT) is emerging as an excellent way to inspect over long distances from a single point and has applications in the oil, gas, and power generation industries. One of the first commercial applications has been long range guided wave inspection of unpiggable pipeline sections such as cased crossings and compressor stations. Improvements to these systems continue to enhance performance and expand areas of use. Through the proper application of theoretical wave mechanics, numerical modeling, and physically-based experimentation, guided waves can be optimized by selecting the modes and frequencies with the ideal dispersion characteristics and wave structures for a particular task.

A synergistic approach would combine the advantages of MFL with those of GWUT and, in the process, overcome many of the disadvantages of the two traditionally independent methodologies. The result would be a more decisive, robust, and information-rich inspection system for detecting and sizing corrosion that neither of the individual technologies is capable of on their own. The strengths and weaknesses of MFL and GWUT for detection and sizing of corrosion anomalies will guide modeling and sensor development for integrity analysis of well casing. Since MFL tools exist, the focus of this project is GWUT. A multi-sensor down-hole fixture is designed and fabricated that transmits and receives axial guided waves as well as circumferential guided waves in order to detect, locate, classify, and size defects that reduce the mechanical integrity of the casing. The design is based on theoretically driven experimentation and computational modeling.

To provide the best defect characterization capabilities the tool is designed to generate shear-horizontal waves both circumferentially around the well casing as well as longitudinally. Electromagnetic acoustic transducers are constructed with Neodymium magnets and electrical coils. The noncontact nature of the transducers makes them both durable and practical for operating inside a well casing. A 270 kHz excitation frequency is selected to excite only the fundamental shear-horizontal mode and therefore enhance signal processing and data analysis. Transducers are positioned by pneumatics and protected by enclosures.

In addition to a proof-of-concept demonstration system, two generations of in-line tools are designed, built, and tested. The final design is shown to accurately detect surface defects in 4" schedule 40 pipe in a laboratory setting. It is also demonstrated to function well in a field trial, where data were acquired over a 50 ft length of an observation well in North Akron, Ohio. Strong signals were received in the field trial despite the fact that no cleaning of the well casing was performed and much scale and moisture accumulated on the transducer heads during operation. Further efforts to introduce this technology to practice are encouraged.

ULTRASONIC GUIDED WAVE INTEGRITY ANALYSIS TOOL FOR WELL CASING**TABLE OF CONTENTS**

ABSTRACT.....	i
TABLE OF CONTENTS.....	ii
LIST OF GRAPHICAL MATERIALS	iii
INTRODUCTION	1
EXECUTIVE SUMMARY	2
METHODS	3
RESULTS AND DISCUSSION.....	19
CONCLUSION.....	40
REFERENCES	41

LIST OF GRAPHICAL MATERIALS

Figure 1 Phase velocity dispersion curves for circumferential SH-waves in a 4 in. Schedule 40 pipe showing an example activation line for EMAT-type loading	3
Figure 2 Group velocity dispersion curves for circumferential SH-waves in a 4 in. Schedule 40 pipe.....	4
Figure 3 Lorentz EMAT transducer principle	5
Figure 4 Design of an SH-wave EMAT transducer for use with an ILI tool.....	5
Figure 5 Illustration showing inspection using (a) circumferential waves and (b) axial waves.....	6
Figure 6 Phase velocity (top) and group velocity (bottom) dispersion curves for a 20-in Schedule 10 pipe with no wall loss, 30% wall loss, 50% wall loss, and 70% wall loss	8
Figure 7 Finite element model of a 20-in Schedule 10 pipe with no defect (top) and with a 70% through wall notch with a radius of 0.25” (bottom). In the top plot, it is seen that both the S0 and A0 modes are excited at 175 kHz. In the bottom plot, it is seen the defect causes wave reflection as well as mode conversion from S0 to A0.....	10
Figure 8 Analytic envelopes of the wave packages received at (a) the receiving node 22.5° to the left of the defect and (b) the receiving node 22.5° to the right of the defect	11
Figure 9 Gated view of the transmitted S0 (TS0) mode seen in Figure 8b showing the change in time-of-flight (TOF) with increasing defect depth. The plot on the right summarizes the actual change in TOF as referenced from the defect-free case	11
Figure 10 Transmission, reflection, and mode conversion factors as a function of through-wall defect depth.....	12
Figure 11 Finite element model of a defect with circumferential extent.....	13
Figure 12 Example RF waveforms and analytic envelopes for U_r and U_θ displacement components. Plot (a) corresponds to the top receiving node and (b) to the bottom receiving node. Data corresponds to the case of 70% TW circumferential defect.....	13
Figure 13 Analytic envelopes of waveforms for the (a) top receiving node and (b) bottom receiving node showing differences for different TW depths of circumferential defect.....	14
Figure 14 Transmission, reflection, and mode conversion factors as a function of through-wall depth of circumferential defect	14
Figure 15 Finite element model showing original thickness (left) and with gradual wall loss to 70% of the original thickness.....	15
Figure 16 Example RF waveform and analytic envelopes for U_r and U_θ displacement. The transmitted S0 and A0 modes are clearly seen	16
Figure 17 (a) Time gated view of the analytic envelopes of the S0 and A0 waves for the different gradual wall thickness reduction models. (b) Graphical representation of the change in TOF of the S0 and A0 modes	17
Figure 18 FFT of S0 wave packet for different wall thicknesses; as the thickness decreases, the frequency increases.....	17
Figure 19 Comparison of signals obtained from a pipe with damage. Signal amplitude is plotted for no damage, 1/16 th in. deep defect, and 3/16 th in. deep defect respectively. The second column shows the same signal, but zoomed in to see small changes in the signals more clearly. The right column shows photographs of the specimen corresponding to each defect. The red ellipses denote the reflected signal as a result of the defect in the specimen	19

Figure 20 3.5 in. prototype tool skeleton with 4 in. couplers on each end and diametrically opposing holes to accommodate EMAT sensors	20
Figure 21 4-layer MDF block inserted into the prototype skeleton to provide a mild force to keep the EMAT sensors against the pipe wall.....	21
Figure 22 Left: 1 st generation tool with sensors installed. Right: after installation of the wear-resistant coating	21
Figure 23 Reflection from a 3/16 th in. deep drilled hole of 3/8 th in. diameter. The reflection appears between 120 and 140 microseconds on the oscilloscope.....	22
Figure 24 Phase velocity dispersion curves for circumferential SH guided waves in a 4-in. diameter Schedule 40 pipe and activation lines for an EMAT transducer	23
Figure 25 The EMAT concept; magnets poled in the vertical direction are placed over a conducting coil, which produces a Lorentz force perpendicular to the eddy current J and static magnetic field B	24
Figure 26 Trial EMAT configuration on casing coupling. Pipe donated by EQT Midstream	25
Figure 27 EMAT operating at 475 kHz on schedule 40 pipe with and without defects was not effective for defect detection	26
Figure 28 EMAT operating at 280 kHz on schedule 40 pipe with and without defects. The defect was easily detected because only one mode was generated	26
Figure 29 The <i>needs matrix</i> used in the final prototype design.....	27
Figure 30 Preliminary design of well casing ILI tool.....	28
Figure 31 Final EMAT head design.....	29
Figure 32 Tool level design with circumferential EMAT set up.....	30
Figure 33 Fully assembled ILI tool without protective covers on the circumferential guided wave part of the tool	30
Figure 34 3D model of the circumferential subassembly. Suspension capability in the nose cone can be seen in the upper right	31
Figure 35 EMAT head 3D drawing (on left) and photograph of the EMAT head (on right).....	31
Figure 36 Encoder position shown on the left and the internal pre-amps mounted internally on the right.....	32
Figure 37 Magnet geometry for longitudinal wave subassembly, half of the magnets have the opposite polarity.....	32
Figure 38 Experimental setup at Penn State for tests on 4" schedule 40 well casing.....	35
Figure 39 Received 270 kHz circumferential SH wave signals from regions of well casing pipe with no defects, and regions having side-by-side partial holes 30, 50, and 70 percent through wall (TW) thickness.....	35
Figure 40 Reduction in the wrap-around signal peak amplitude due to the presence of a defect. The defect is a cluster of two holes of various depths. The excitation frequency is 270 kHz.....	36
Figure 41 Reduction in the ratio of transmitted-to-reflected wave amplitude for the first three wrap-around signal peaks due to the defect. The defect is a cluster of two holes of various depths. The excitation frequency is 270 kHz.....	36
Figure 42 Launching the ILI tool into an observation well in North Canton, Ohio	37
Figure 43 A-scan sequence of circumferential SH wave signals for depths of 30-38 feet (9.1-11.6 m). Up to 8 wrap-around signals are visible for the 270 kHz tone burst.....	38
Figure 44 Signals from axially propagating SH waves acquired from the observation well at different depths are shown for a 270 kHz excitation frequency	38

Table 1 Nomenclature used in figures.....	9
Table 2 Bill of materials for circumferential wave subassembly.....	33
Table 3 Bill of materials for longitudinal wave subassembly.....	34

INTRODUCTION

Safety is a significant concern in the storage and distribution of natural gas. Thus, the integrity of steel well casing is periodically evaluated. Nondestructive inspections are commonly performed using in-line magnetic flux leakage (MFL) probes. However, the ability of MFL technology to accurately characterize the extent of material loss due to corrosion is not always as good as decision makers would like. Herein, the use of guided ultrasonic waves (GUW) to characterize the extent of corrosion is investigated, with the intent to eventually create a dual GUW/MFL tool. An in-line tool that generates circumferential propagating and longitudinally propagating shear-horizontal waves is designed, built, and tested. At the heart of the tool are electromagnetic acoustic transducers that generate and receive shear-horizontal waves. The capability of the tool to detect defects in 4" schedule 40 steel casing is established in the laboratory. Finally, the tool is tested in a well field to demonstrate its functionality in real well casing.

EXECUTIVE SUMMARY

Underground natural gas storage requires wells for access. The steel well casing is in a harsh environment and is susceptible to corrosion and cracking, which compromise its structural integrity. To ensure the safety of the public and the environment, and to protect the investment in the storage facility, it is necessary to monitor the integrity of these mechanical systems. Magnetic flux leakage (MFL) probes are used to diagnose the mechanical integrity of well casings. This technology is well suited for damage detection but less so for classification and sizing of defects.

Guided wave ultrasonic technology (GWUT) is emerging as an excellent way to inspect over long distances from a single point and has applications in the oil, gas, and power generation industries. One of the first commercial applications has been long range guided wave inspection of unpiggable pipeline sections such as cased crossings and compressor stations. Improvements to these systems continue to enhance performance and expand areas of use. Through the proper application of theoretical wave mechanics, numerical modeling, and physically-based experimentation, guided waves can be optimized by selecting the modes and frequencies with the ideal dispersion characteristics and wave structures for a particular task.

A synergistic approach would combine the advantages of MFL with those of GWUT and, in the process, overcome many of the disadvantages of the two traditionally independent methodologies. The result would be a more decisive, robust, and information-rich inspection system for detecting and sizing corrosion that neither of the individual technologies is capable of on their own. The strengths and weaknesses of MFL and GWUT for detection and sizing of corrosion anomalies will guide modeling and sensor development for integrity analysis of well casing. Since MFL tools exist, the focus of this proposal is GWUT. A multi-sensor down-hole fixture is envisioned that transmits and receives axial guided waves as well as circumferential guided waves in order to detect, locate, classify, and size defects that reduce the mechanical integrity of the casing. The objective of the project is to design an optimal sensory tool for sizing corrosion and crack defects in steel casing. Here, optimal refers to defect sensitivity, reliability, cost, and ease of use. The design will leverage findings regarding axial guided waves from a previous GSTC-funded project, as well as ongoing research and development of circumferential guided wave methodology.

The methods proposed herein include analytical modeling, numerical simulations, sensor and equipment design, laboratory experiments, and field studies. The unique aspect of the project is that it is fundamentally driven by theoretical considerations. Study of guided wave propagation and interaction with defects will enable optimal design of sensors, fixtures, data acquisition, signal processing, and pattern recognition algorithms.

The in-line inspection tool is comprised of two assemblies that are tethered together. Each assembly houses two EMATs (electromagnetic acoustic transducers), one generates shear-horizontal waves and the other receives them. Wave propagation is circumferential in one assembly and longitudinal in the other. Defect detection capability is demonstrated in the laboratory and field tests show that the tool operates well in the intended environment and is sufficiently rugged and robust.

METHODS

Background

Guided waves arise when traditional ultrasonic longitudinal- and shear- waves interact with the boundaries of the structure in which they travel. This interaction results in complex interference patterns that form propagating guided-wave modes. Unlike traditional ultrasonic bulk-waves, which have frequency-independent velocities, guided-wave velocity is a function of frequency. As seen in Figure 1, phase velocity dispersion curves provide a graphical representation of the frequency-dependent velocity for different wave modes. The particular curves shown in Figure 1 are for Shear-Horizontal (SH) waves propagating in the circumferential direction of a 4 in. Schedule 40 pipe. A sample activation line is shown for loading with an Electromagnetic Acoustic Transducer (EMAT) and indicates which modes can be excited and at what frequency using an EMAT with a specific wavelength. This type of loading is significant for this project and will be discussed in more depth in the next subsection. Another difference between guided waves and bulk waves is that a packet of guided waves travel at a velocity that is different than the phase velocity. The velocity of a group of guided waves is referred to as the “group” velocity and is the velocity that is measured in experiment. The group velocity dispersion curves can be calculated from the phase velocity curves and are shown in Figure 2 for circumferential SH-waves in a 4 in. Schedule 40 pipe.

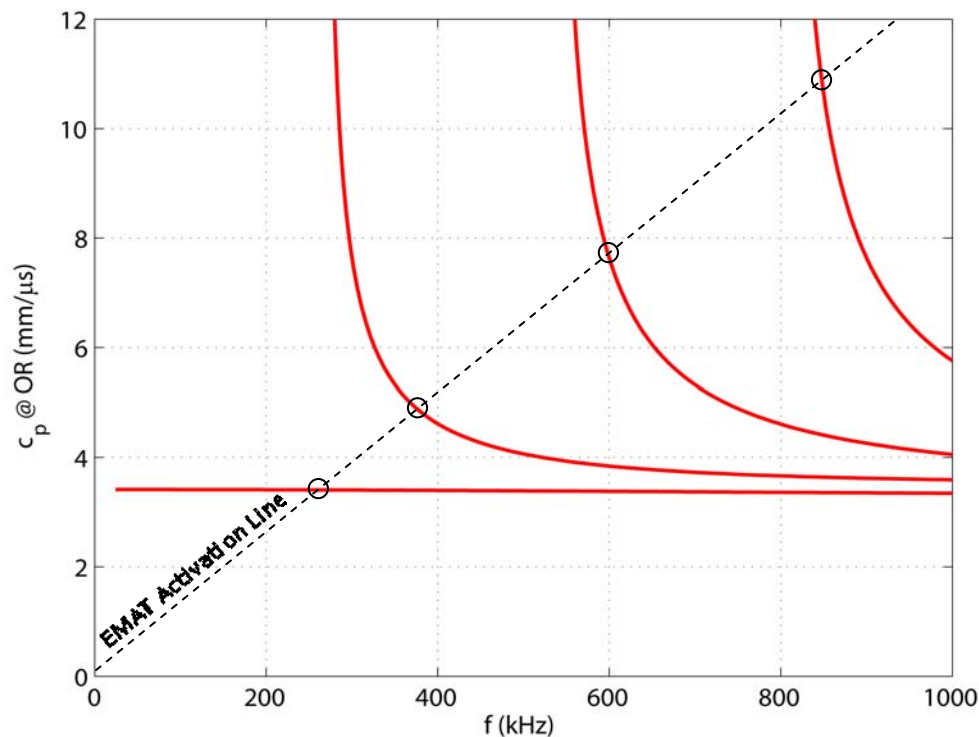


Figure 1 Phase velocity dispersion curves for circumferential SH-waves in a 4 in. Schedule 40 pipe showing an example activation line for EMAT-type loading.

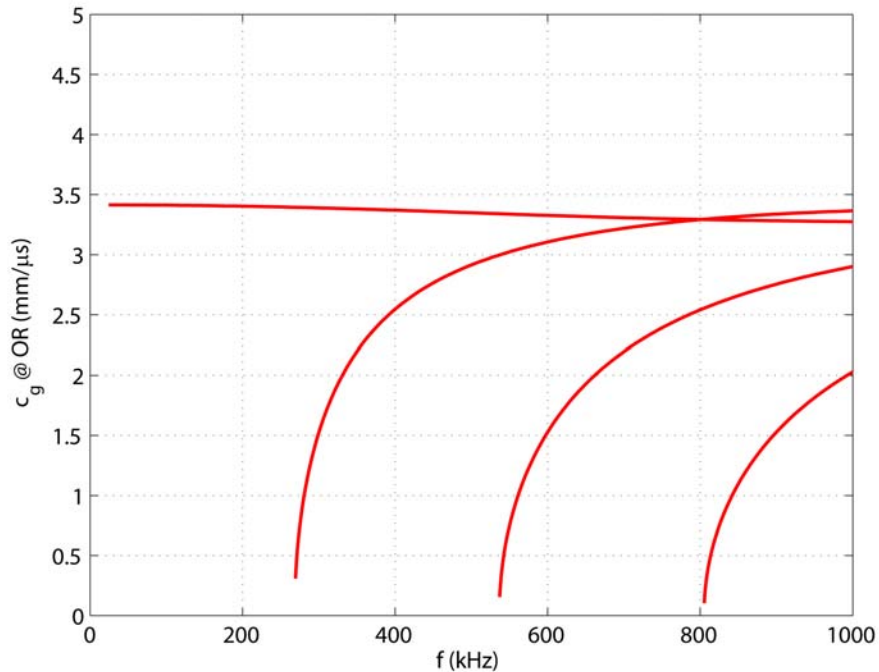


Figure 2 Group velocity dispersion curves for circumferential SH-waves in a 4 in. Schedule 40 pipe.

Electromagnetic Acoustic Transducers

Electromagnetic acoustic transducers (EMATs) generate and receive ultrasound by coupling magnetic fields to the flow of current within a specimen. EMATs can be non-contact, operate at elevated temperatures, work on rough or oxidized surfaces, and operate at high speeds, making them ideal for application with In-Line inspection (ILI) tools. Depending on the configuration of the magnetic field and eddy currents, Lamb and shear horizontal (SH) guided waves can both be generated and received.

The EMATs used in this project are Lorentz force EMATs. Figure 3 illustrates the Lorentz concept. The first component to the Lorentz force transduction mechanism is an eddy current. An eddy current (J) is induced in the part by passing a current (I) through a wire or trace in close proximity to the specimen. The part to be inspected must be conductive for this to occur. In addition to the eddy current, a static magnetic field (B) must be present. When the current is pulsed in the presence of the magnetic field a force (F) is induced in the specimen. The direction of the force can be determined by the right hand rule. The magnitude and direction of the force are given by Equation 1, where F is the force per unit volume, J is the induced dynamic current density, and B is the static magnetic induction.

$$\mathbf{F} = \mathbf{J} \times \mathbf{B} \quad [1]$$

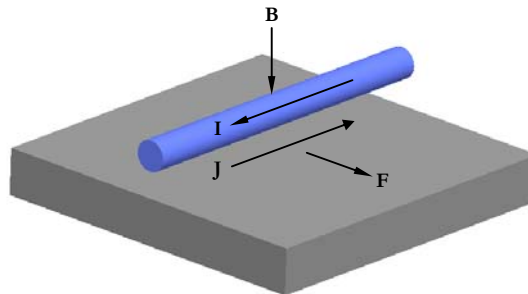


Figure 3 Lorentz EMAT transducer principle.

The two most typical Lorentz force EMAT configurations are for the generation of Lamb- and SH-waves. Figure 4 shows the typical configuration of an SH-wave EMAT. The wavelength of the induced wave for an SH EMAT can be changed by altering the thickness of the magnets. For both the Lamb-wave and SH-wave EMATs, changing the wavelength of the sensor allows the designer to sweep through the dispersion curve space. A given wavelength activates a line in the dispersion curve plane that originates at the origin and has a slope corresponding to a fixed wavelength, as was shown in Figure 1. The slope of the line can be altered by changing the magnet spacing. A specific mode can then be activated by exciting the transducer at a set frequency.

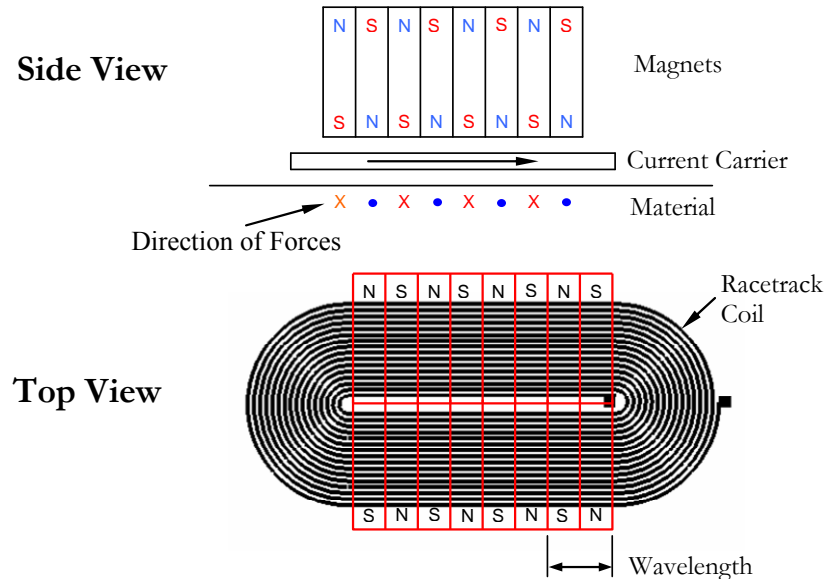


Figure 4 Design of an SH-wave EMAT transducer for use with an ILI tool.

Lamb-type and SH-wave EMATs are both excellent candidates for the inspection of well casings. Using these two configurations it is possible to generate a large range of mode-frequency combinations. The lower limit to the mode-frequency combination will be dictated by the physical size of the transducer that can be effectively incorporated into the In-Line Inspection (ILI) tool design. As wavelengths become large, so does the size of the transducer. The upper

limit of the mode-frequency combination will be dictated by the relative attenuation caused by absorption into the cement casing.

In addition to the two general types of guided waves, Lamb and SH, each type can be excited in either the circumferential direction or the axial direction, as illustrated in Figure 5. Figure 5(b) shows inspection from the outside of the pipe, although it is equally applicable to inspection using sensors situated on the inside diameter of the pipe. Both circumferential and longitudinal waves are explored in this research project.

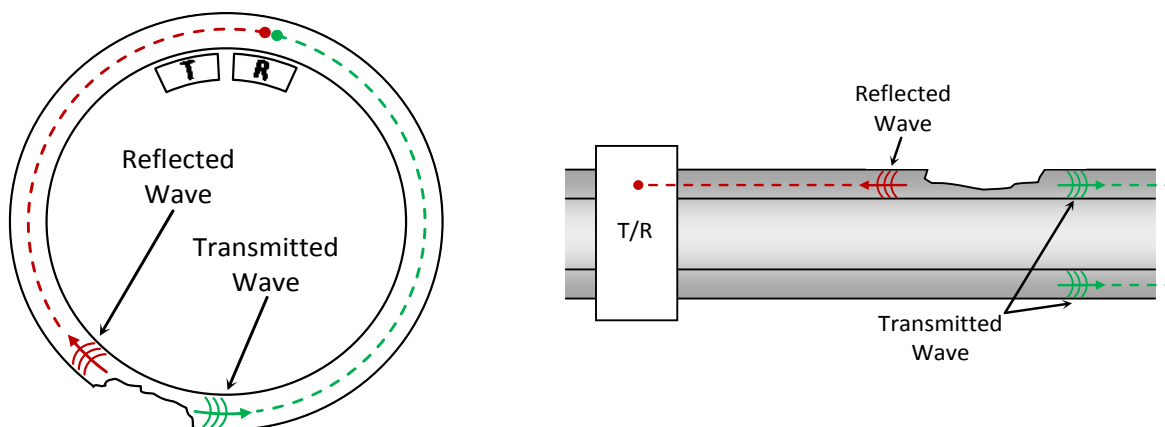


Figure 5 Illustration showing inspection using (a) circumferential waves and (b) axial waves.

Analytical Modeling

Guided wave signals will be analyzed for indications of damage with the help of signal processing. Wave packets acquired after propagation through normal and defected material will be compared using pattern recognition algorithms. The capability and accuracy of a pattern recognition sizing approach will depend greatly on the number of features available for the analysis of a particular anomaly and it is therefore critical to select inspection parameters that will result in information-rich data. Thus it is important to carefully select the transducer arrangement and methods used. We concentrate on the selection of a guided wave mode and frequency with potential to provide this information-rich data. A Lamb-type mode was selected for this task. The zeroth order symmetric mode (S0) at a frequency of approximately 175 kHz is desirable as there is only one other mode in this region to which energy can be converted, the zeroth order antisymmetric mode (A0). By remaining in this region of the dispersion space, it is assured that only these two modes will exist in the pipe wall.

Figure 6 shows the phase and group velocity dispersion curves for circumferential Lamb-type waves in an example structure; a 20-in Schedule 10 pipe. A large diameter pipe was used for modeling purposes so that clear visualization of the mode conversion phenomenon could be observed. The results are scalable to 4-in diameter pipe. The dispersion curves are plotted for

different wall thicknesses to show the general trends in the curves as wall thickness is lost. This will be beneficial in the selection of sizing parameters.

As seen in the phase velocity dispersion curves, the S0 mode at 175 kHz is relatively non-dispersive, meaning all frequencies near this center frequency will propagate at approximately the same phase velocity and therefore distortion of the wave packet over time is minimized. Another interesting phenomenon observed at this frequency is seen in the group velocity dispersion curves. As the pipe wall becomes thinner, the group velocity of the S0 mode increases and the group velocity of the A0 mode, in the same frequency regime, decreases. The group velocity of the A0 mode changes more drastically with thickness and therefore is expected to provide better resolution.

Several defect geometries are considered by using finite element analysis (FEA). Both 2D- and 3D- finite-element analyses were conducted, though refinement of the 3D- models is required before a comprehensive analysis can be reported. For this reason, emphasis here will be placed on the 2D- models and on the development of the fundamental characteristics of Lamb-type wave interaction with material defects, including the identification of sizing features that have the greatest potential to be extended to three-dimensional analysis. The modeling introduced here applies to the approximate sizing of defect types such as axial grooves and slots, general corrosion, and circumferential grooves and slots. It also serves as a starting point for the sizing of pitting corrosion.

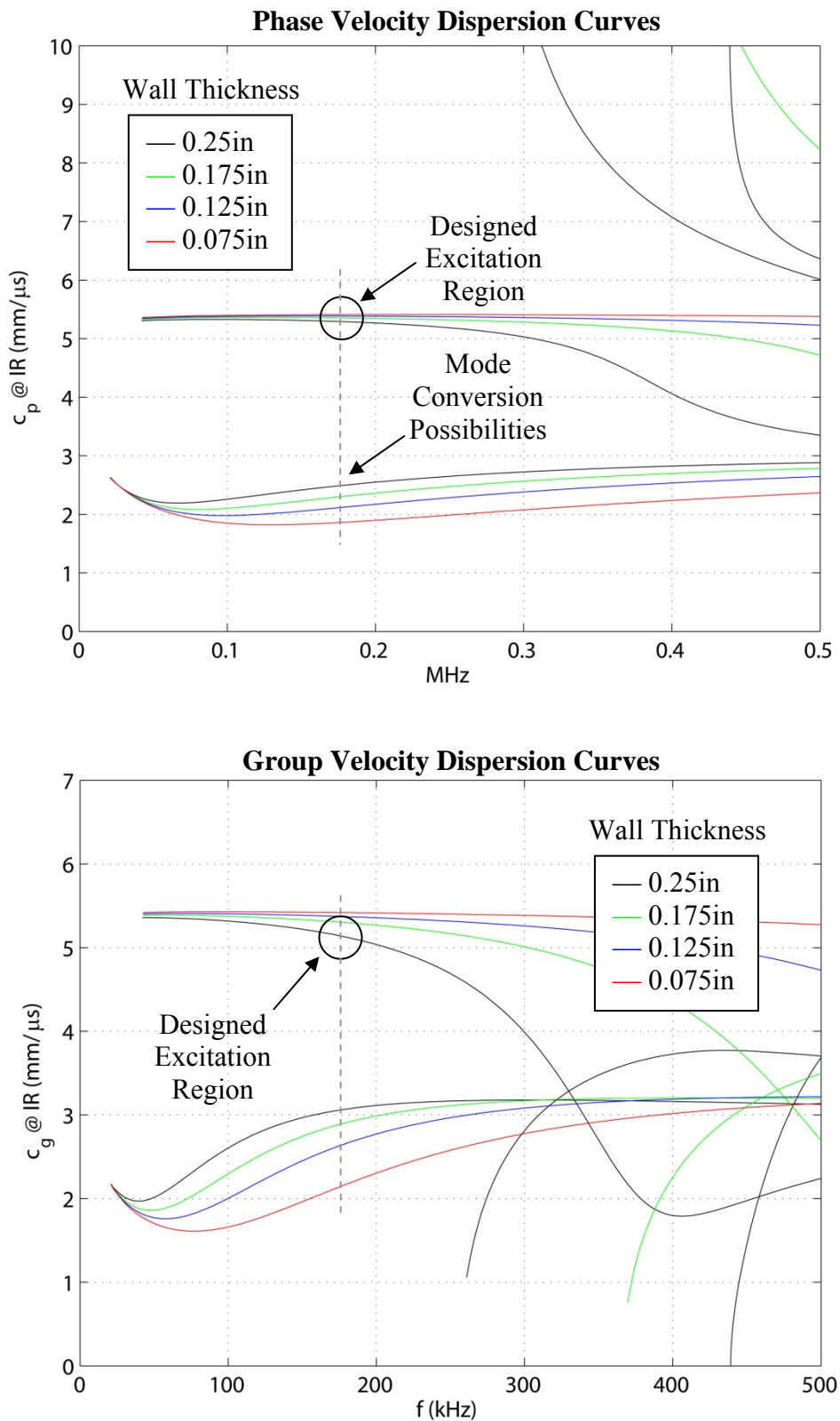


Figure 6 Phase velocity (top) and group velocity (bottom) dispersion curves for a 20-in Schedule 10 pipe with no wall loss, 30% wall loss, 50% wall loss, and 70% wall loss.

Axial Grooves/Slots and Pitting Defects – FEA

To study the interaction of the S0 and A0 Lamb-type waves with an axial groove, a 2D plane strain model was generated. This also represents a simplified pitting problem, as certain aspects of the analysis can be extended to the sizing of pits in three dimensions. Four cases were studied, a defect free pipe, and three 0.25" radius spherical defects with 30%, 50%, and 70% through-wall (TW) depths. In order to clearly see the interaction of the wave with the defects, the pipe circumference was modeled with a small gap at the 3 o'clock position. The open edges of the gap were modeled using infinite elements in order to nearly eliminate reflections from the boundary. From a practical standpoint, this is equivalent to saying that a wave will be absorbed by the coating/product before completely traversing the pipe. Experience has shown that this can be a realistic assumption. Figure 7 shows the modeled cross section of a pipe with no defect and a pipe with a 70% TW notch at the 6 o'clock position.

Wave propagation was induced using comb-type loading; a fixed wavelength technique which approximates the loading of an electromagnetic acoustic transducer (EMAT). Excitation occurred at the 12 o'clock position with receiving nodes placed 22.5° to each side of the defect so to collect transmission and reflection information. Figure 8 shows the analytic envelopes obtained by taking the Hilbert transform of the wave packages received at the two receiving nodes. Table 1 defines the nomenclature seen in the figure and in figures that follow.

Table 1 Nomenclature used in figures

IS0/IA0	Incident S0/A0 Mode
TS0/RS0	Transmitted/Reflected S0 Mode
TA0/RA0	Transmitted/Reflected A0 Mode
MCA0	Mode Converted A0 Mode

In Figure 8a it is seen that the amount of reflected S0 energy and mode converted A0 energy increases markedly with increasing defect depth. Additionally, it is seen in Figure 3b that the transmitted S0 energy experiences a slight shift in time, corresponding to the depth of the defect. A gated view of the time shift as well as a plot of the actual differences in the time-of-flight (TOF) can be seen in Figure 9. For the 70% TW defect, there is approximately an 11 μs shift in the TOF. This large of a difference is easily resolved in with instrumentation in the field.

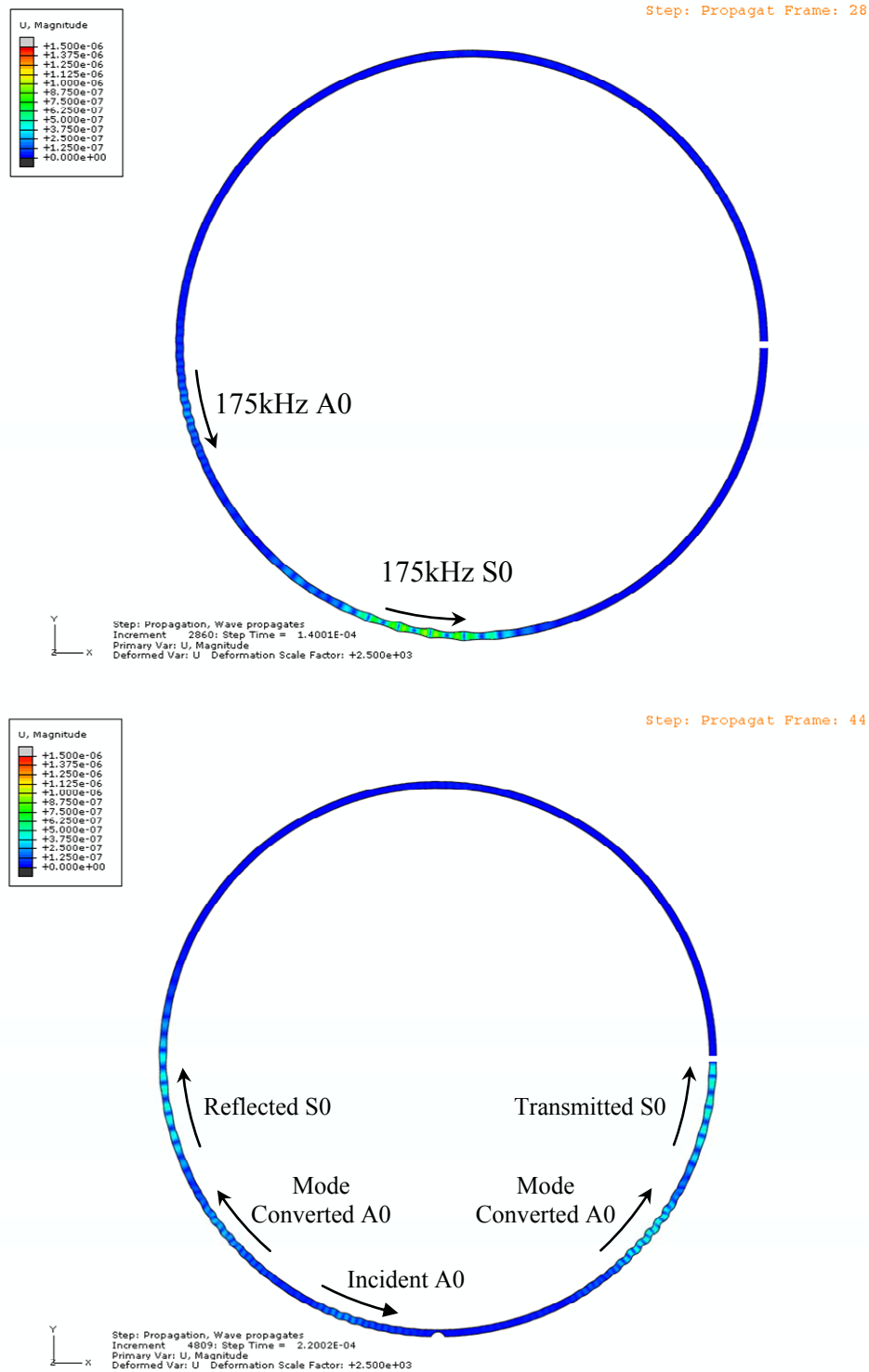


Figure 7 Finite element model of a 20-in Schedule 10 pipe with no defect (top) and with a 70% through wall notch with a radius of 0.25” (bottom). In the top plot, it is seen that both the S0 and A0 modes are excited at 175 kHz. In the bottom plot, it is seen the defect causes wave reflection as well as mode conversion from S0 to A0.

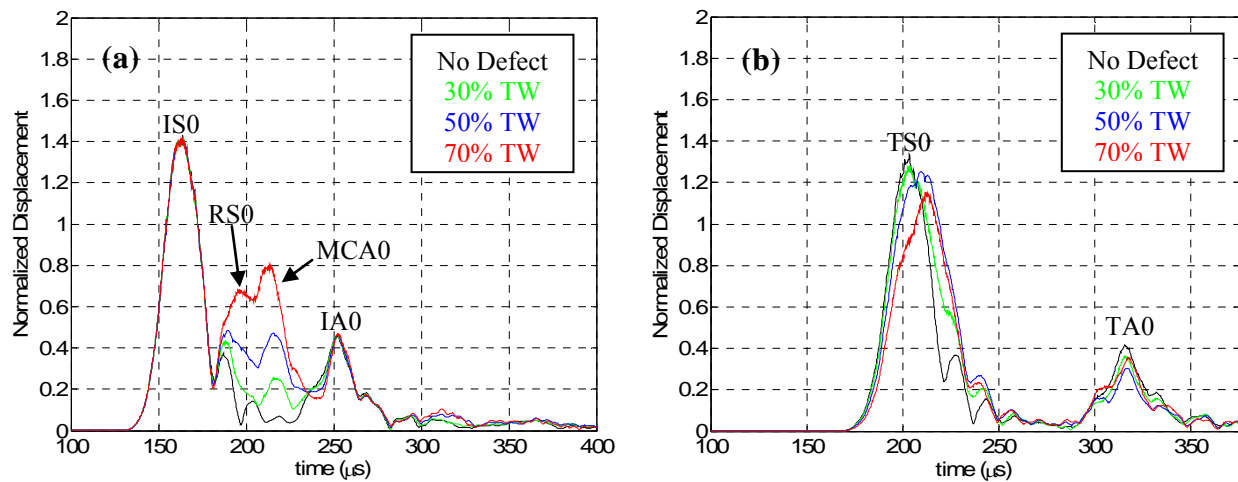


Figure 8 Analytic envelopes of the wave packages received at (a) the receiving node 22.5° to the left of the defect and (b) the receiving node 22.5° to the right of the defect.

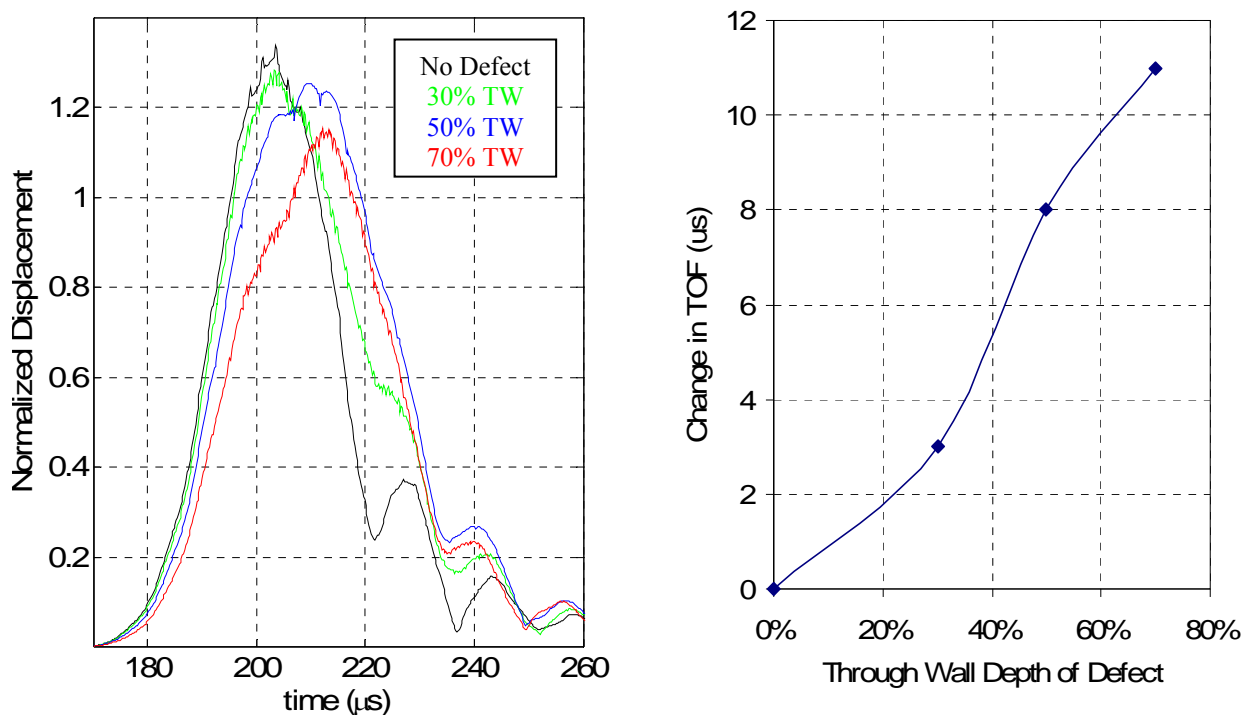


Figure 9 Gated view of the transmitted S_0 (TS_0) mode seen in Figure 8b showing the change in time-of-flight (TOF) with increasing defect depth. The plot on the right summarizes the actual change in TOF as referenced from the defect-free case.

Figure 10 summarizes the transmission, reflection, and mode conversion factors in graphical form. From this plot it is seen that two very promising sizing features include the mode converted A_0 (MCA_0) content and the reflected S_0 (RS_0) content. The transmitted S_0 (TS_0)

content decreases with increasing through-wall depth but at a less significant rate than the MCA0 and RS0 are increasing. All three features are valid inputs for a pattern recognition algorithm. The transmitted A0 (TA0) content is not entirely decreasing with TW depth and more modeling will be needed to understand this trend.

While raw amplitude is not always a reliable feature, ratios of transmitted/reflected/converted energy can often be used reliably. One of the benefits of utilizing the Lamb-type modes is that the inter-mode comparisons or ratios can be formed. The type of analysis presented here can be practically implemented by populating the circumference of the pipe with multiple sensors pairs. By nesting a transmitting sensor between two receivers, a signal reference can be obtained and both the reflected and transmitted energy can be analyzed.

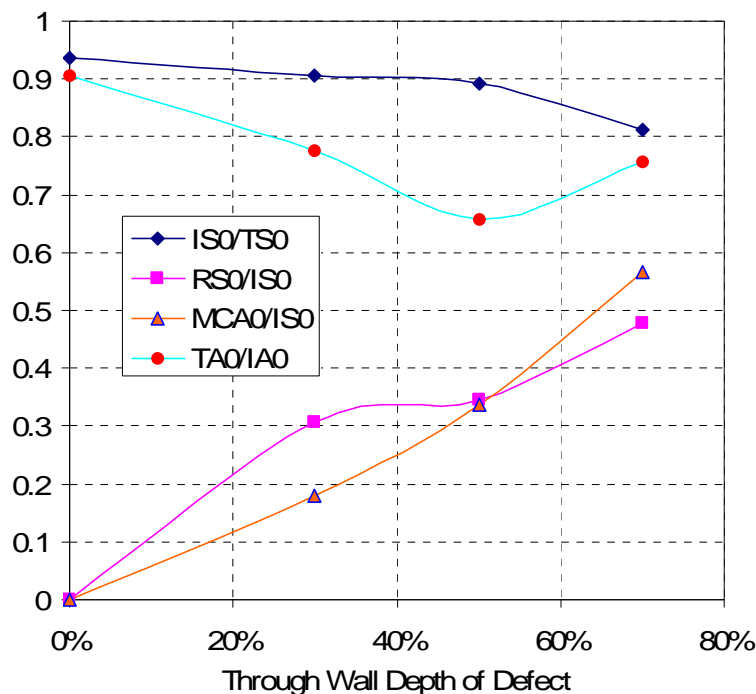


Figure 10 Transmission, reflection, and mode conversion factors as a function of through-wall defect depth.

Circumferential Grooves/Slots and Global Corrosion Defects - FEA

Another type of defect of practical interest is the circumferential groove. While magnetic flux leakage (MFL) tools can estimate the axial length of the defect with relatively good accuracy, it is more difficult to determine the circumferential extent. With an accurate axial length and circumferential width measurement, it is possible to obtain a more accurate depth estimate, especially through the fusion of the MFL and guided-wave data.

Figure 11 shows the finite element model used to study the effects of a circumferential defect on Lamb-type wave propagation. The defect occurs over a 15° portion of the circumference and, as before, through-wall depths of 30%, 50%, and 70% were studied in addition to the defect-free

case. A multiple transmitter arrangement was adopted for this study to show how the circumferential extent of a defect can be measured using guided waves in a practical manner. Receiving nodes were placed adjacent to the transmitting regions as indicated in Figure 11a. Figure 11b shows some of the transmitted, reflected, and converted energy that results from the interaction of the Lamb-type wave with the defect. Figure 12 shows some sample RF waveforms and their corresponding analytic envelopes for the 70% TW depth circumferential defect.

Figure 13 shows a comparison of the analytic envelopes of the different TW depth defects for the top (Fig 13a) and bottom (Fig 13b) receiving nodes. Again it is seen that TS0, RS0, and MCA0 energy provide a reliable means for estimating TW depth. The reflection, transmission, and mode converted amplitudes are summarized graphically in Figure 14. Any of these features can be plotted relative to one another.

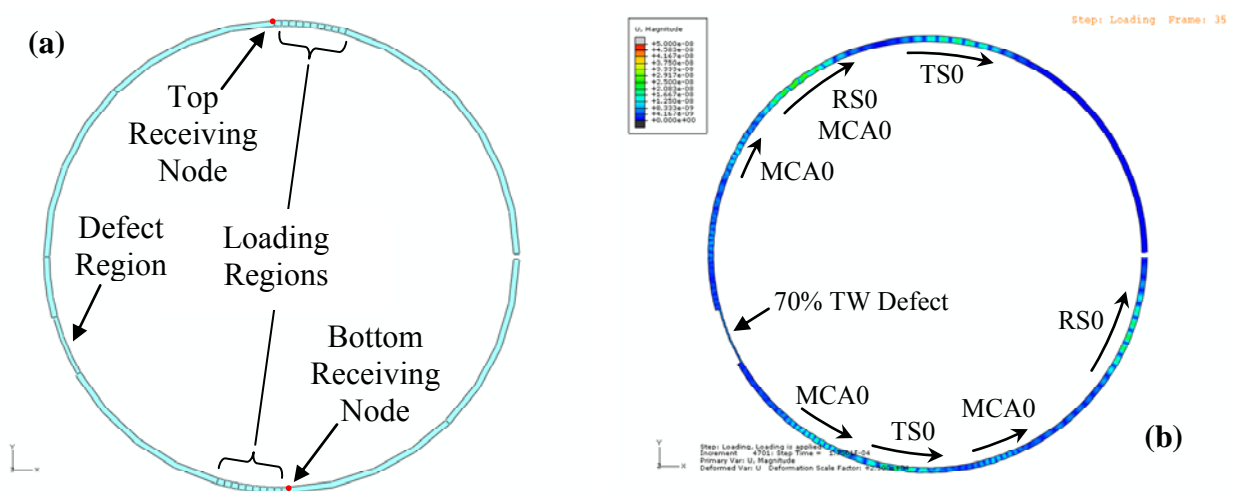


Figure 11 Finite element model of a defect with circumferential extent.

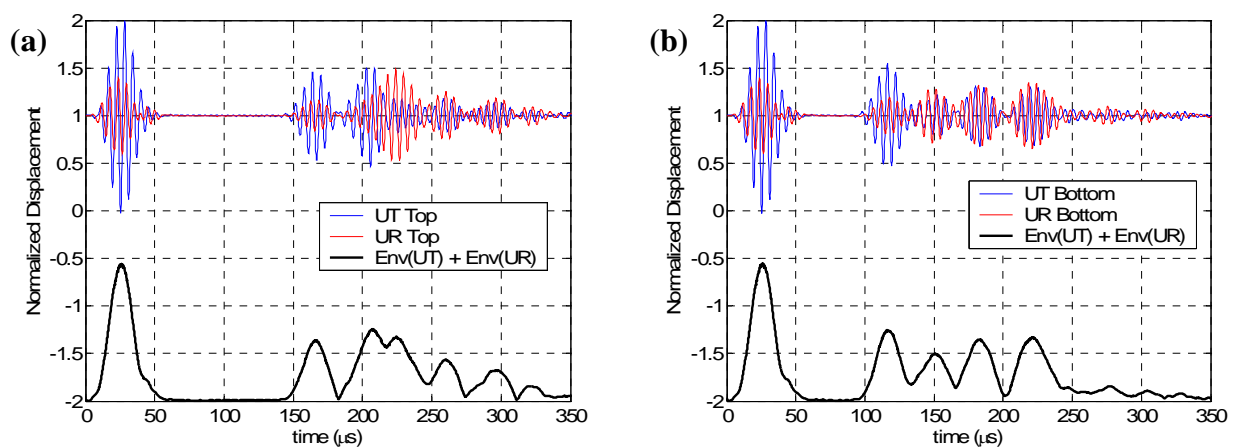


Figure 12 Example RF waveforms and analytic envelopes for U_r and U_θ displacement components. Plot (a) corresponds to the top receiving node and (b) to the bottom receiving node. Data corresponds to the case of 70% TW circumferential defect.

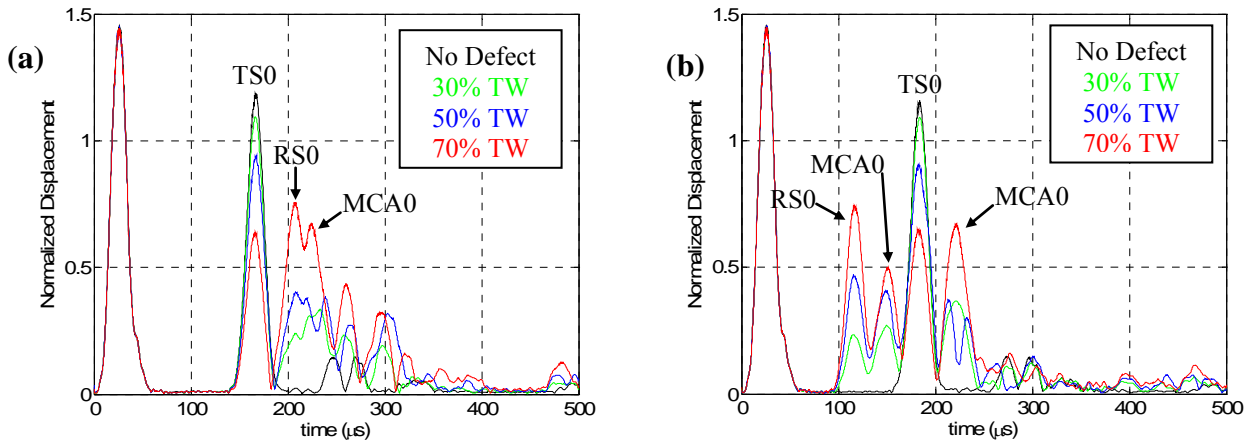


Figure 13 Analytic envelopes of waveforms for the (a) top receiving node and (b) bottom receiving node showing differences for different TW depths of circumferential defect.

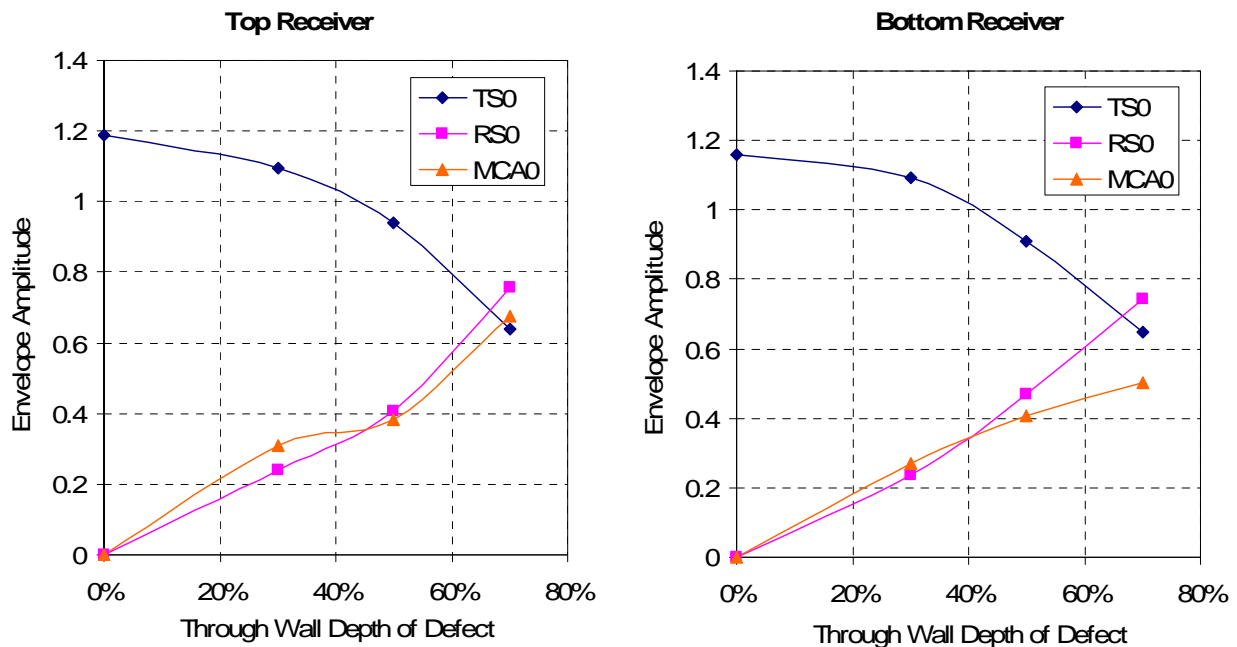


Figure 14 Transmission, reflection, and mode conversion factors as a function of through-wall depth of circumferential defect.

Estimating the depth of the circumferential defect would actually be the second step in sizing of a circumferential defect. In order to obtain a unique solution, first the circumferential extent should be determined. This is easily done by measuring the TOF of the RS0 signals on each side of the defect. For example, the TOF of the RS0 for the top receiving node is $\sim 181 \mu\text{s}$ and the TOF of the RS0 for the bottom node is $\sim 107 \mu\text{s}$. Assuming a group velocity for the S0 mode of $5\text{mm}/\mu\text{s}$ (as measured from model), the distance to the top edge of the defect is $\sim 454 \text{ mm}$ and the distance to the bottom edge of the defect is $\sim 267 \text{ mm}$. Since the receiving nodes are precisely opposed to each other, circumferential extent is half the circumference minus the distance to the defect on each side, or $(778 - 454 - 267 = 57\text{mm})$. So the estimated circumferential extent of the

defect is 57 mm and the actual extent based on 15° of the circumference is 65mm, a difference of 8 mm. This error could be reduced by employing more accurate TOF measurement algorithms such as a correlation routine.

Gradual Wall Thinning Defects - FEA

In some cases a corrosion region may not have distinct edges but instead may have gradual thinning over a large area. In these situations MFL can estimate the axial length relatively well but has difficulty estimating the circumferential extent. While guided waves may also have difficulty estimating the circumferential extent, because there will be not edge reflections, this issue can be circumvented by performing a direct thickness estimate over segmented circumferential regions. A model was created to demonstrate this capability.

As seen in Figure 15, the model consisted of a pipe cross section with gradual wall loss over a region slightly less than 180° . Four models were generated; a full thickness model and models with 30%, 50%, and 70% TW depth at the thinnest point (9 o'clock).

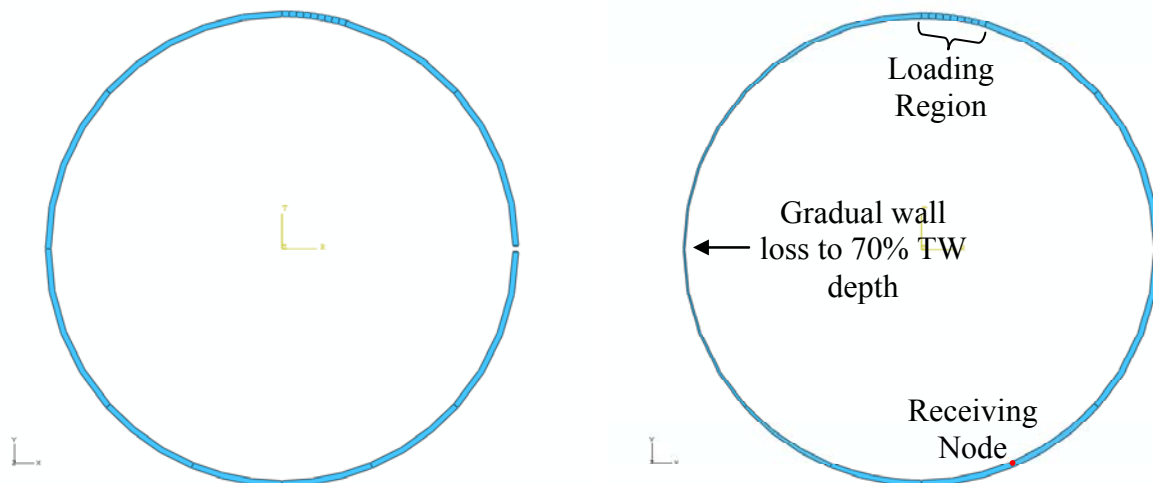


Figure 15 Finite element model showing original thickness (left) and with gradual wall loss to 70% of the original thickness.

Figure 16 shows the r - and θ - displacement RF waveforms and combined analytic envelope for the pipe with the full remaining wall thickness. Seen clearly are the transmitted S_0 and A_0 wave modes. Figure 17 shows the envelopes for the full-thickness model as well as the 30%, 50%, and 70% gradual wall loss models. From Figure 17, an obvious shift in the TOF of both the S_0 and A_0 modes is seen. As the wall thickness reduces the velocity of the S_0 mode increases and the velocity of the A_0 mode decreases. The decrease in velocity of the A_0 mode is more significant. This agrees with the trends seen in the dispersion curves shown in Figure 6. A simple way to estimate the remaining thickness would be to monitor the TOF between the peaks of the S_0 and A_0 modes. An increasing TOF would be indicative of wall thinning. The estimated wall thickness would be comparable to an average over the region between the two sensors.

Because the modeled “transducer” is designed to generate the S_0 mode and has a fixed wavelength as such, an increase in wave velocity should be accompanied by an increase in

frequency to maintain the proper wavelength. This phenomenon is illustrated in Figure 18, which shows the FFTs of the S0 wave packet for the different wall thickness models. It is observed that there is a slight increase in the frequency content of the wave packet as the pipe wall becomes thinner. This frequency shifting effect could potentially be magnified by decreasing wavelength, effectively moving into a dispersion space with more drastic velocity variations. Another option may be to design the optimal loading condition for the A0 mode at 175 kHz.

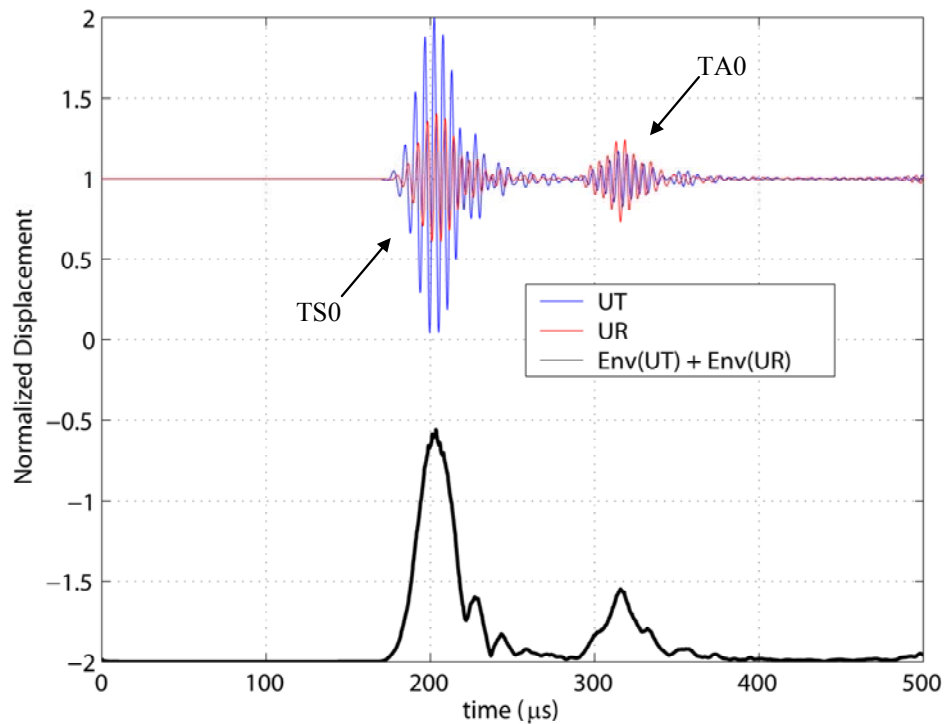


Figure 16 Example RF waveform and analytic envelopes for U_r and U_θ displacement. The transmitted S0 and A0 modes are clearly seen.

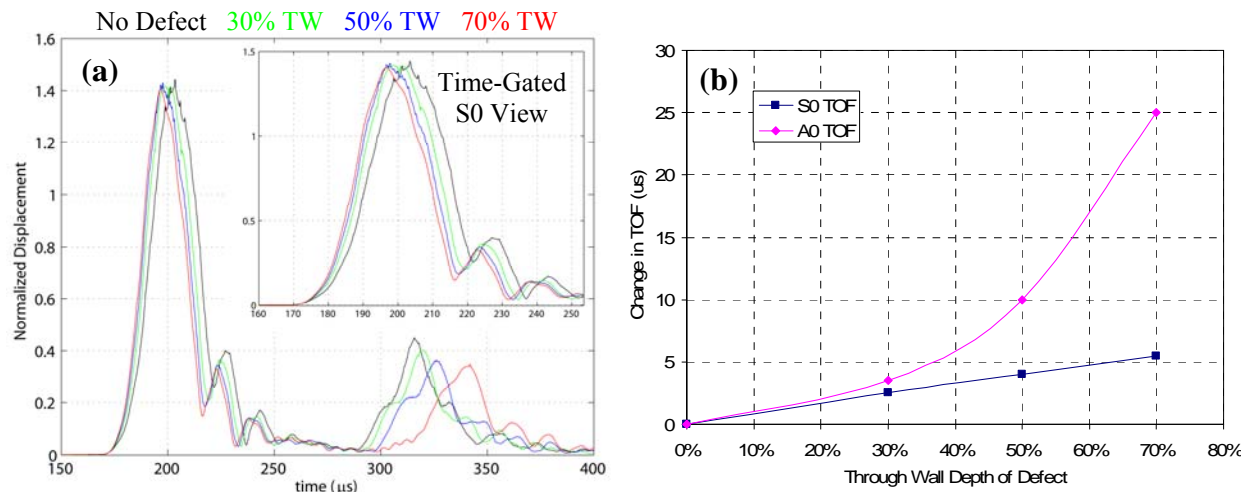


Figure 17 (a) Time gated view of the analytic envelopes of the S0 and A0 waves for the different gradual wall thickness reduction models. (b) Graphical representation of the change in TOF of the S0 and A0 modes.

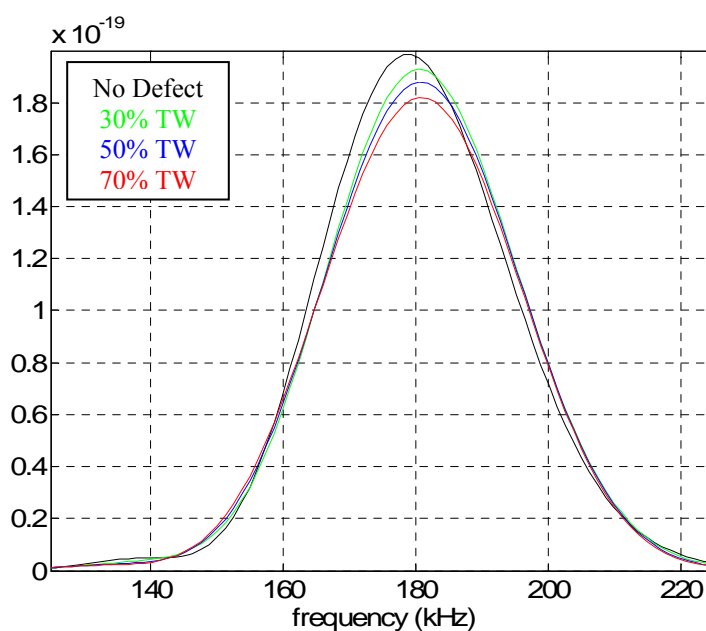


Figure 18 FFT of S0 wave packet for different wall thicknesses; as the thickness decreases, the frequency increases.

The analytical modeling identifies the development of a pattern recognition feature vector for the sizing estimation of different types of defect. Two-dimensional finite-element models were created for defect types representative of axial grooves/slots, general corrosion, and circumferential grooves/slots. Many of the identified features will be directly applicable to the sizing of other defect geometries, such as pitting, with modification. At present, seven features and/or methods have been identified for the approximate sizing of the aforementioned defect types. Additional features and methods may be added later so to create an extensive information-

rich pattern recognition feature vector. Also presented was a technique for estimating the remaining wall thickness of a corrosion region with gradual wall loss. The model results just shown indicate that fabrication of an in-line inspection tool has strong merit.

RESULTS AND DISCUSSION

Proof of Concept

Some initial laboratory experimentation was done in order to provide a proof-of-concept test. A 4 in. Schedule 40 steel pipe was obtained and a pair of 530 kHz EMAT sensors were placed on the specimen in a circumferential configuration. It was observed that the amplitude of the received wave depended significantly on the position of the receiver transducer relative to the transmitting transducer. This behavior is expected because of constructive and destructive wave interference due to the bi-directional wave propagation characteristics of the EMAT transmitter. To test the EMAT sensors for sensitivity to damage in the specimen, a 3/8th in. drill bit was used to remove a small amount of material from the pipe. This was done by drilling a hole about 1/16th of an inch deep with the drill bit. Guided waves were sent around this damage location and the resulting signals were compared to the signals obtained when there was no damage in the pipe. A reflection from this damage was observed in the waveform. The hole was deepened to about 3/16th of an inch deep and the procedure was repeated. The reflection from the damaged region was again observed with even greater amplitude. Figure 19 shows a comparison of the signals obtained for the specimen with no damage, as compared to the signals obtained on the specimen with the two stages of damage. The first column of plots represents the amplitude of the received signal as a function of time for the cases of no damage, 1/16th inch deep damage, and 3/16th inch deep damage respectively in order from top to bottom. The second column consists of the same plots but with less amplitude range in order to show small changes in the signal. The third column shows a photograph of the specimen for each level of damage. The red ellipses on the plots show the reflection from the damage.

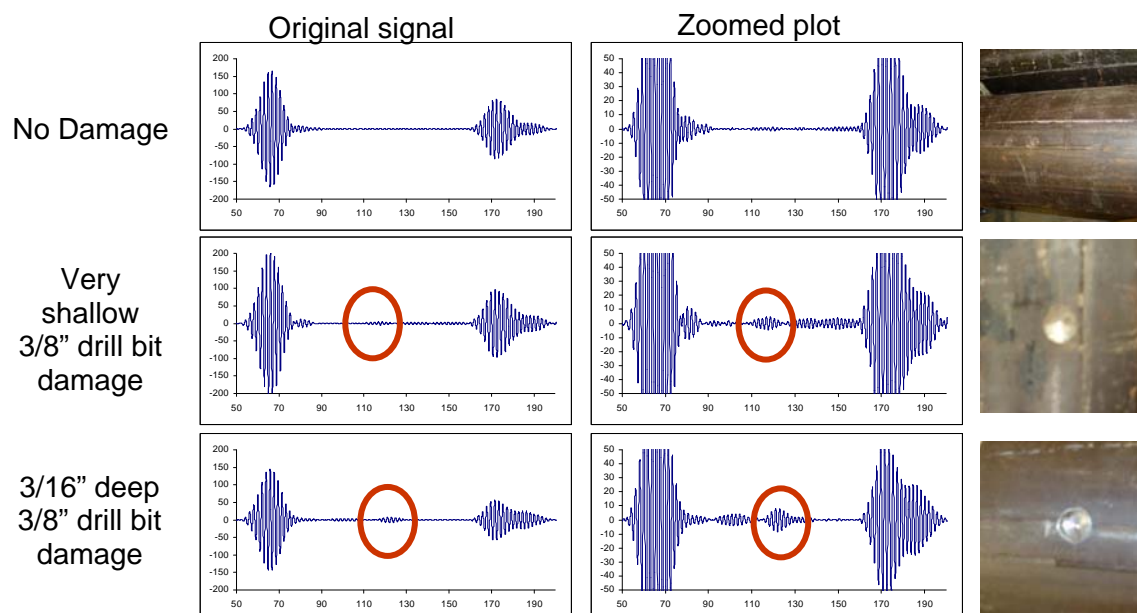


Figure 19 Comparison of signals obtained from a pipe with damage. Signal amplitude is plotted for no damage, 1/16th in. deep defect, and 3/16th in. deep defect respectively. The second column shows the same signal, but zoomed in to see small changes in the signals more clearly. The right column shows photographs of the specimen corresponding to each defect. The red ellipses denote the reflected signal as a result of the defect in the specimen.

It can be seen that the EMATs are sensitive to this type of damage in the pipe. Even with a small amount of damage ($1/16^{\text{th}}$ inch deep), the waveform detects damage through a reflection. With increasing amount of damage, the reflection from the damage increases. In order to prove the concept inside the pipe, a 1st generation prototype tool was constructed to hold the sensors accurately in place. This is discussed in the next section.

1st Generation Tool

In order to precisely orient the EMAT sensors on the inside of the 4 in. diameter pipe specimens, a prototype ILI tool was conceived and fabricated. Due to the high sensitivity of the EMAT receiver to its circumferential position relative to the transmitter, a rigid prototype design was selected for the 1st generation tool. An 8 in. long section of 3.5 in. diameter PVC pipe was used for the skeleton of the tool. A straight collar-type coupler that fit snugly into the 4 in. specimen was placed on each end of this pipe section to keep the longitudinal axis of the tool concentric with the longitudinal axis of the steel specimen. Square holes were cut into the sides of the tool to allow a pocket for the magnet packs of the sensors to recess into the tool and to provide the force on the magnets needed to move them through the pipe. The holes were placed diametrically opposite to each other in order to achieve constructive wave interference at the receiver. Figure 20 shows a photograph of the prototype tool skeleton consisting of the 3.5 in. PVC pipe section and the two collars. The square holes for the magnets are also shown in this picture.



Figure 20 3.5 in. prototype tool skeleton with 4 in. couplers on each end and diametrically opposing holes to accommodate EMAT sensors.

Additionally, a four-layer block of Medium Density Fiber-board (MDF) was constructed to fit inside the tool and provide additional support for the EMAT magnets. Figure 21 shows a photograph of this block. The center two layers of the block were notched to allow the necessary space for the magnets to recess into the tool. The outer two layers of MDF were intended to keep the two center layers in place behind the magnet packs. Finally, foam was placed in the recessions of the MDF block to provide a force on the sensors in order to keep them in contact with the pipe specimen wall.

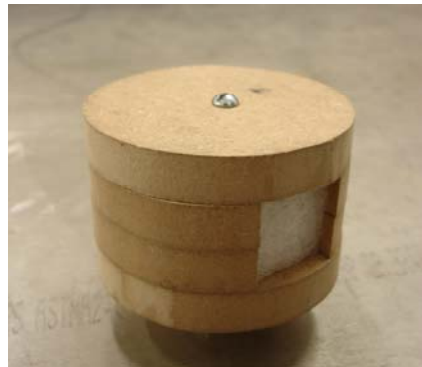


Figure 21 4-layer MDF block inserted into the prototype skeleton to provide a mild force to keep the EMAT sensors against the pipe wall.

The area between the two couplers was filled out with several layers of an abrasion-resistant polymer. Square holes were cut out of each layer to match the holes in the tool skeleton. The EMAT sensors were inserted into the designated spaces and held in place with Mylar tape. Holes were drilled into the tool to allow the wires to be routed inside the tool and the sensors were covered with a final layer of the abrasion-resistant polymer. Figure 22 shows the tool with the sensors installed as well as the final prototype.



Figure 22 Left: 1st generation tool with sensors installed. Right: after installation of the wear-resistant coating.

The prototype tool was successfully used to collect data from inside a 4 in. pipe specimen. Figure 23 shows the waveform envelope obtained from the prototype tool inside a pipe with a 3/8th in. diameter drilled hole that was approximately 3/16th in. deep. The reflection from this hole is clearly seen between 120 and 140 microseconds on the oscilloscope. Other types of simulated damage will also be examined. The tool performed very well and provided the basic design for a more rugged tool.

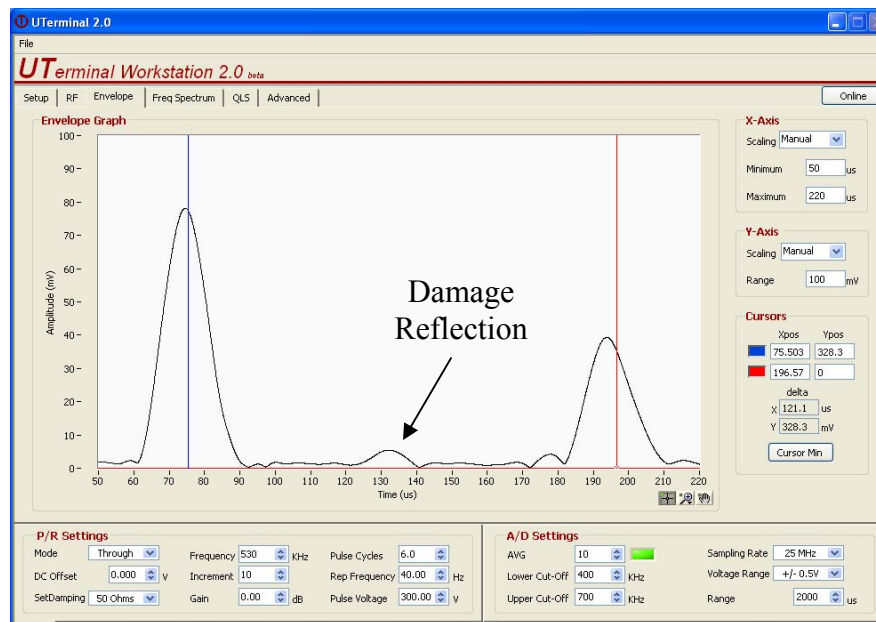


Figure 23 Reflection from a 3/16th in. deep drilled hole of 3/8th in. diameter. The reflection appears between 120 and 140 microseconds on the oscilloscope.

2nd Generation Tool

Traditional ultrasonic bulk waves are commonly used in nondestructive testing (NDT) applications. When these waves interact with the boundaries of the material in which they propagate, they become 'guided waves'. Guided waves are an extremely valuable tool for various NDT and structural health monitoring applications. As demonstrated earlier, the velocity of guided waves is a frequency dependent entity, which allows for flexibility in the sensor design, and makes theoretically driven experimentation very important. The foundation of guided wave theoretical analysis is phase velocity and group velocity dispersion curves. The shear-horizontal (SH) wave mode phase velocity dispersion curves for a 4-in. schedule 40 pipe are shown in Figure 24. By generating a dispersion curve for a particular geometry, the frequency dependence of guided waves can be seen. This enables intelligent selection of wave modes and transducer designs, which greatly reduces experimentation time.

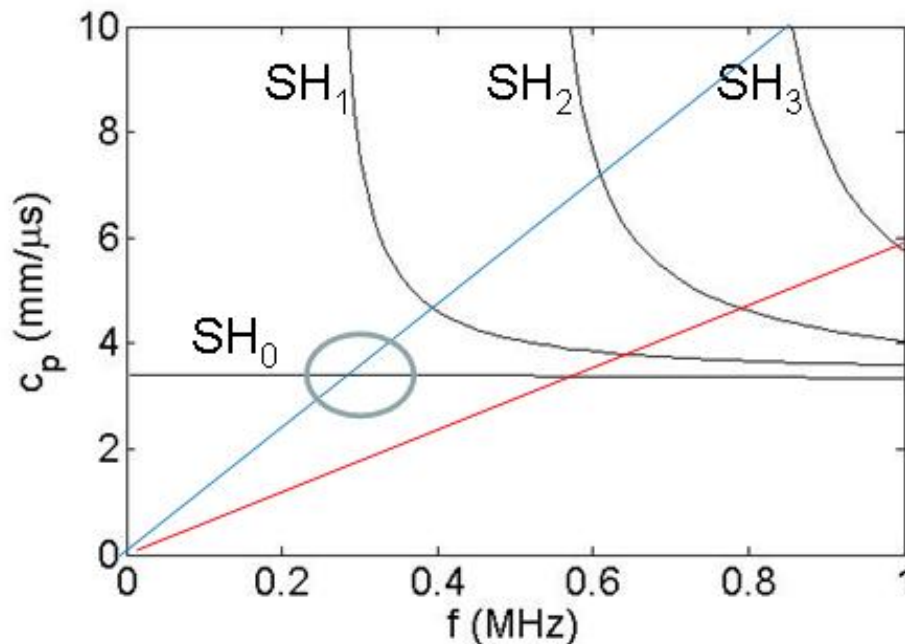


Figure 24 Phase velocity dispersion curves for circumferential SH guided waves in a 4-in. diameter Schedule 40 pipe and activation lines for an EMAT transducer.

Activation lines are shown on the dispersion curves in Figure 24; these lines correspond to the wavelength generated by an EMAT transducer, which in turn is dictated by the thickness of the magnets that are used in the EMAT. The blue ellipse on the upper activation line represents the frequency that was chosen for our application. SH_0 is the name for the fundamental mode; the zero-th order shear horizontal mode. This mode was chosen at the frequency 275 kHz because it is nearly non-dispersive and since it is below the cutoffs of higher order modes, it has little chance of creating confusing mode conversions. This means that the signals received will primarily consist of a single mode, which allows for a greatly simplified signal analysis. The shear horizontal circumferential guided wave at the SH_0 mode should also allow for greater defect detection sensitivity and make defect sizing an attainable feature of the inspection tool.

Electromagnetic Acoustic Transducer (EMAT) Design

Electromagnetic Acoustic Transducers (EMATs) were selected in order to generate shear horizontal circumferential guided waves in the steel well casing. The EMAT induces eddy currents in the pipe, whereupon the magnetic field creates a Lorentz Force. The Lorentz force causes the particles in the material to vibrate in the direction of the force, causing a wave to propagate in the circumferential direction of the pipe. Another benefit of using EMATs is that they are non-contact transducers; they do not need to physically touch the pipe. It is very easy to generate SH waves with EMAT transducers. For these reasons they are excellent transducers for conducting materials and for this application. The EMAT concept of operation is shown in Figure 25.

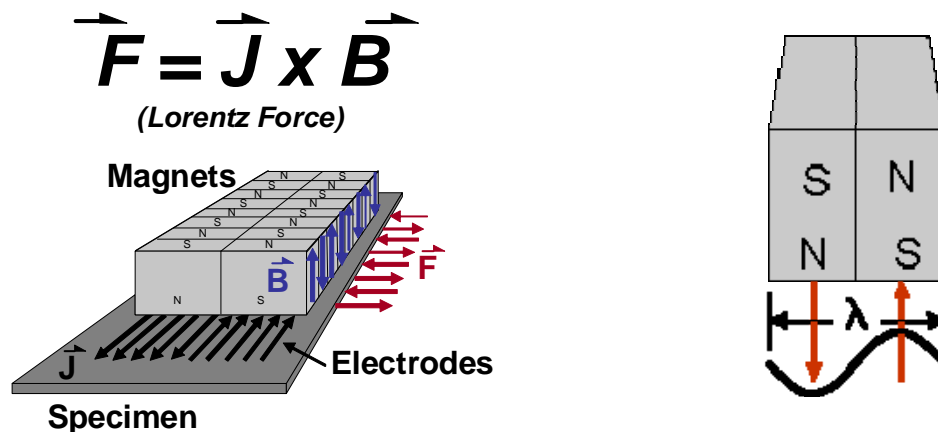


Figure 25 The EMAT concept; magnets poled in the vertical direction are placed over a conducting coil, which produces a Lorentz force perpendicular to the eddy current \mathbf{J} and static magnetic field \mathbf{B} .

In earlier work, several techniques were evaluated, including high energy excitation methods, in order to maximize the penetration depth of guided waves. Guided waves were generated by mechanical excitation, such as a pneumatic BB gun and a spring-loaded center hole-punch. While the excitation worked well, the method did not enable top-down inspection of an entire well casing. In addition, the method did not lend itself to defect sizing. The circumferential guided wave approach has much greater defect detection, classification, and sizing potential. Figure 26 shows an EMAT located on the outside of a threaded coupling on well casing donated by EQT Midstream for this project. In this case the EMATs are located on the outer surface of the casing because, much to our surprise, the 1st generation tool would not fit through the coupling or the casing due to ovalization of the casing. This demonstrated the need for a more robust tool with larger tolerances.

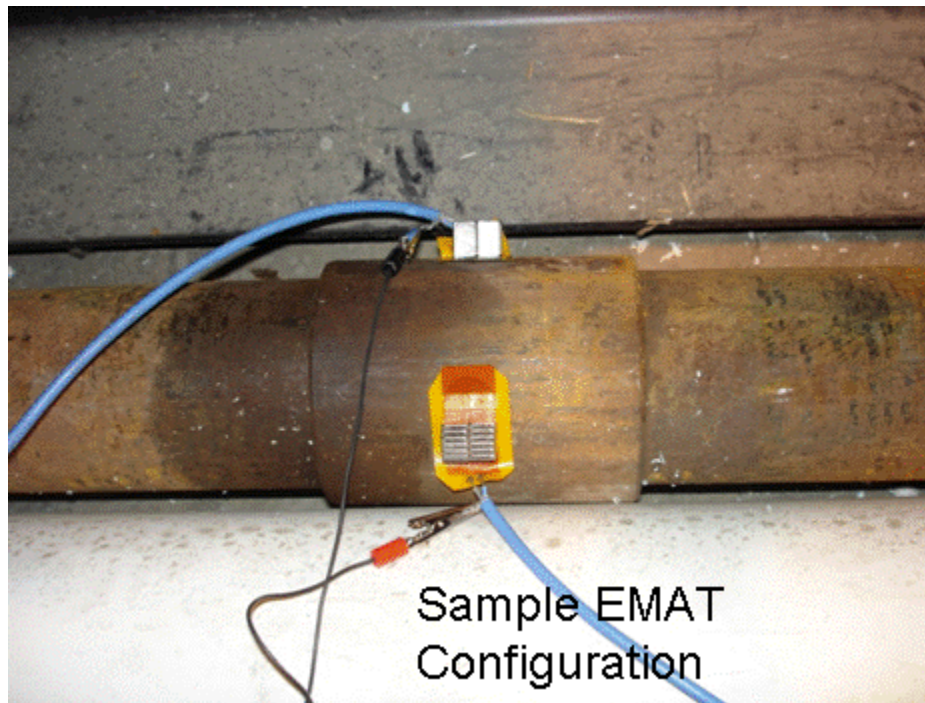
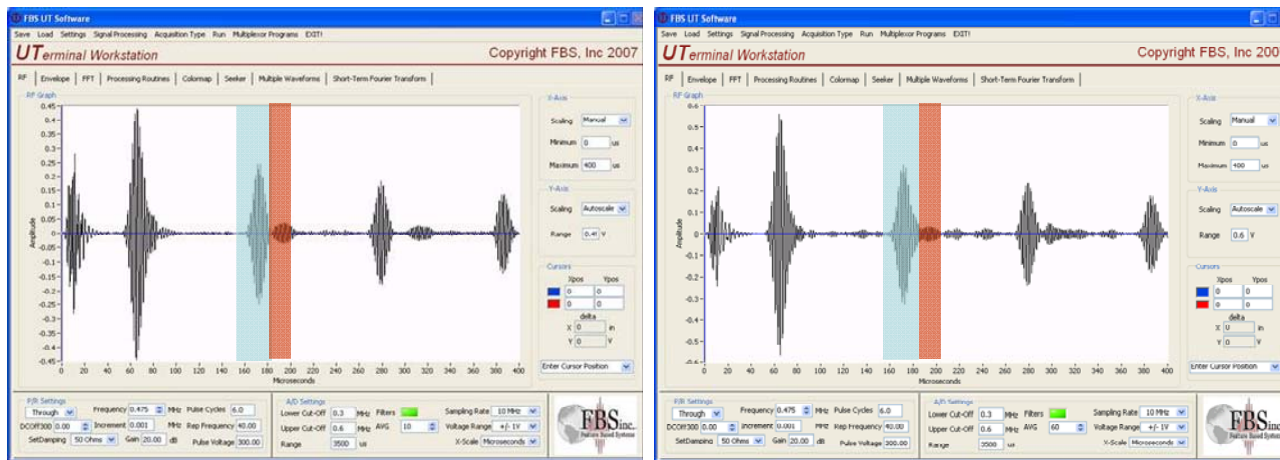


Figure 26 Trial EMAT configuration on casing coupling. Pipe donated by EQT Midstream.

The first step in the design of the tool is to optimize the EMATs. The goal of the tool is to use both circumferential and longitudinal guided waves to detect and characterize defects (primarily corrosion). The idea is employ data fusion from circumferential and longitudinal ultrasonic guided waves and MFL to help locate, classify, and size anomalies. A cluster defect was used in data collection with both circumferential and longitudinal wave test setups. Various magnets with different thicknesses were used, as well as curved and flat magnets. Magnet thickness corresponds to wavelength, which allows activation of different SH modes at different frequencies. The original prototype tool used a frequency of 475 kHz. Data was collected at 475 kHz in the circumferential direction around a defect-free section of 4-in. schedule 40 pipe, as well as a section of pipe with a cluster defect. The results are shown in Figure 27. The defect is not apparent in these results because there is a higher order mode present at this frequency that masks the signal from the defect. Much better results were obtained when a 280 kHz frequency was used, as is shown in Figure 28. At this frequency no other modes are present, making defect detection more reliable. At both frequencies (475 and 280 kHz) wrap-around signals are detected. These occur for each revolution of wave propagation around the circumference of the pipe. These wrap-around signals will be shown to be quite useful for defect detection.

475 kHz through transmission (defect not easily defined)



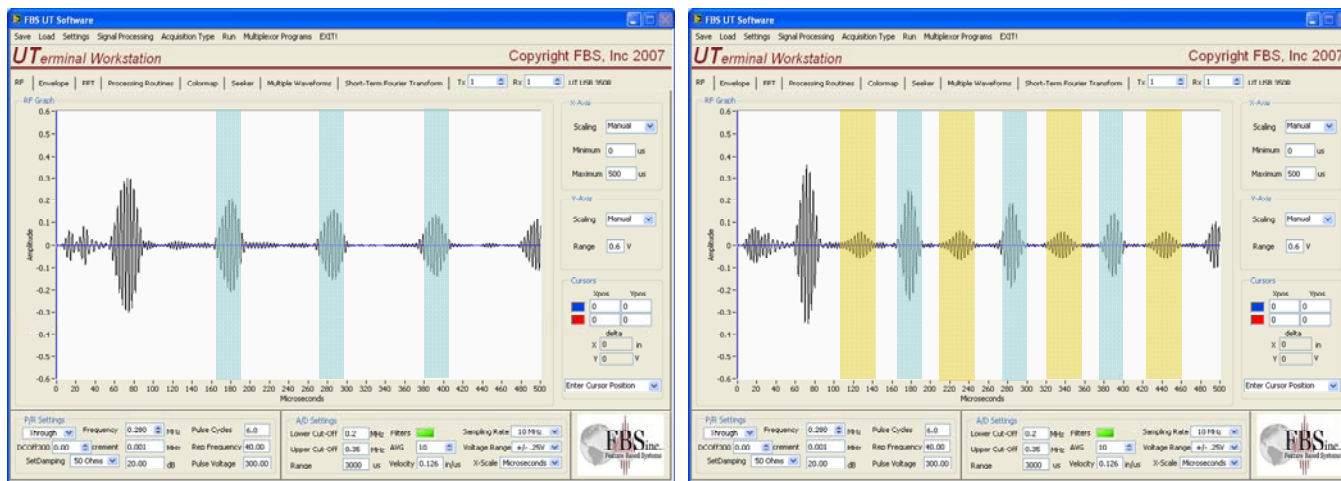
No defects

Cluster defect

- Pipe wrap around
- Higher order mode

Figure 27 EMAT operating at 475 kHz on schedule 40 pipe with and without defects was not effective for defect detection.

280 kHz through transmission



No defects

Cluster defect

- Pipe wrap around
- cluster defect

Figure 28 EMAT operating at 280 kHz on schedule 40 pipe with and without defects. The defect was easily detected because only one mode was generated.

The 1st generation tool is used as a feasibility test of circumferential EMAT's inside a 4 in. schedule 40 pipe. There were a few issues that had to be addressed. If there was pipe size inconsistency the tool would not fit. This was due to the tool outer diameter tolerance being too small, and as a result the tool would not fit inside a gas storage test well casing. A new tool that utilizes circumferential and longitudinal waves was designed. First, a 'needs matrix' was constructed to aid in the design process, and is shown in Figure 29.

	Metric	1" diameter variability	Circumferential waves	Axial waves	Coil surface protection	EMAT to pipe Contact minimized	Minimize electronics housed in tool	Tool encasement	Pneumatic operation suspension	Aluminum construction	Facilitate waterjet capabilities
Need											
Variable pipe size		X									
Detect corrosion			X	X							
Detect axial defects			X								
Detect longitudinal defects				X							
Identify loose joints				X							
Robust					X	X	X	X	X		
Home position must be retracted									X		
Tool always centered									X		
lightweight										X	
Reliable data collection					X	X		X			
prototype cost effective											X

Figure 29 The *needs matrix* used in the final prototype design.

A spring loaded, waterproof, and dustproof packaged encoder is to be used in the final design. This will ensure accurate data collection as the tool is pulled up through a well casing. An abrasion resistant urethane sheet proved very robust when used in the initial prototype and will be used to protect the electrical coil. Board mounted Lemo connectors will be utilized to connect coils to the electrical cable. This is a nice feature and will eliminate the need to solder directly to a solder pad on the coil. The solder joint is often a point of failure for EMAT coils. A coil was designed that uses this Lemo connector.

The planned basic operation of the tool is simple. This tool should be lowered down into a gas storage well, then once in place, expand, to have the EMAT's properly positioned. Finally, the

tool will be pulled up out of the well, taking data at predetermined increments. The preliminary 3D design drawings and comments are shown in Figure 30.

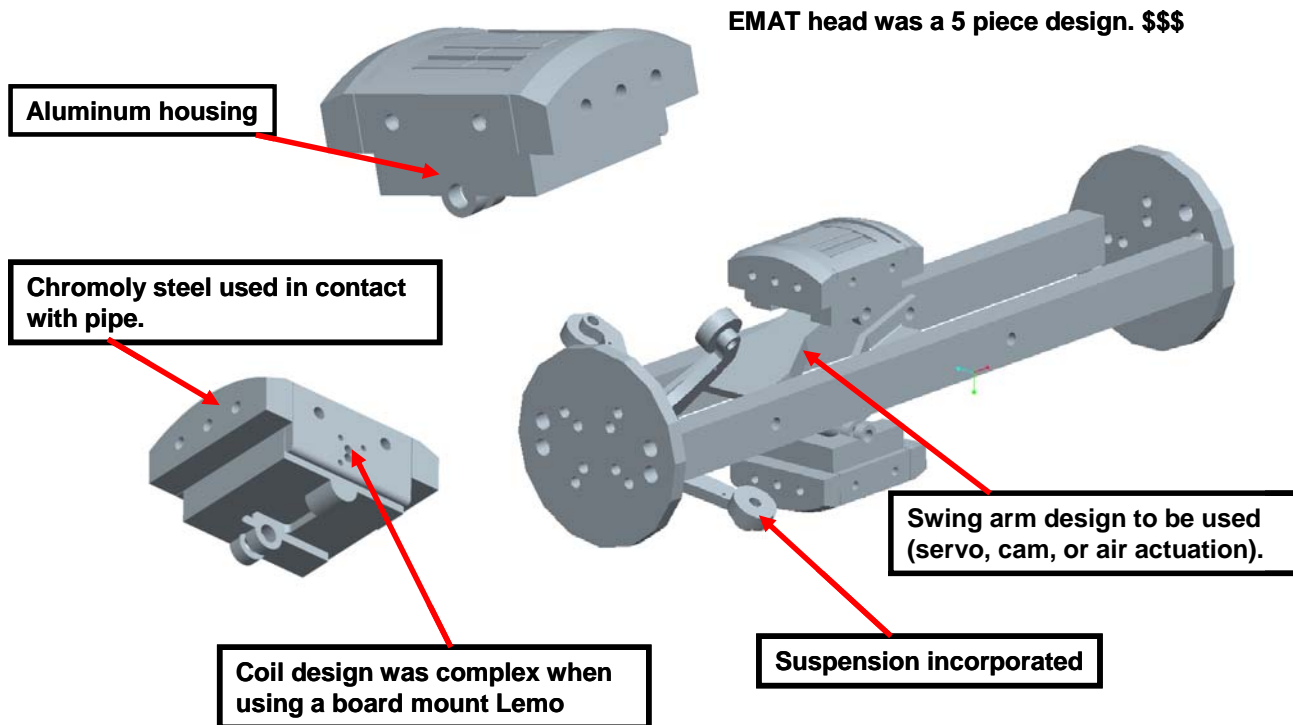


Figure 30 Preliminary design of well casing ILI tool.

The preliminary design was improved upon in many ways. Originally, the EMAT housing was a five piece design. Chromoly was used as the wear surface to be in contact with the pipe. These pieces would bolt to the aluminum housing that would hold the magnets, coil, and urethane. This many pieces would be expensive to manufacture. The design was not easily adaptable to create longitudinally aligned EMATs. In Figure 30 only circumferential EMAT heads are shown. The coil design would be complicated as well in order to wrap back around a chromoly side piece. Due to the limited space, swingarms were used from a different direction for each EMAT head. This had the potential for the heads to be misaligned while taking data. A suspension was used to keep the tool centered in the pipe. In a perfect world, the tool might ride in the center. The design had potential for over 1/4" misalignment. That is just enough misalignment to produce unreliable results. Also, cam or servo actuation would have been used. This is not a preferred way to actuate the EMAT heads. If there was an electrical problem, the EMATs could be stuck in the outward position. On the contrary, with pneumatic actuation, in the event of a malfunction the EMATs would lose contact and return to the inward position.

The final design of the EMAT heads utilizes an air cylinder with a wedge that pushes the two heads directly apart from each other. The two heads ride in the same groove. All of these design considerations ensure that each head moves outward the same amount, and misalignment is not an issue because the tool is self centering. As shown in Figure 31, springs are used to return the heads to the inward position. A coil with a board mounted Lemo is used, and is attached to another plate to extend the connector beyond the guide rails. The final design is cost effective to manufacture as well. Furthermore, the housing is easily modified to enclose a coil and magnets for either circumferential or longitudinal guided wave generation/reception. Urethane is used to protect the coil from wear. This head design does not have a wear surface. Small bearings are employed to be in contact with the well casing and have a small amount of liftoff for the coil. The 3D component level design of the EMAT heads is detailed in Figure 32.

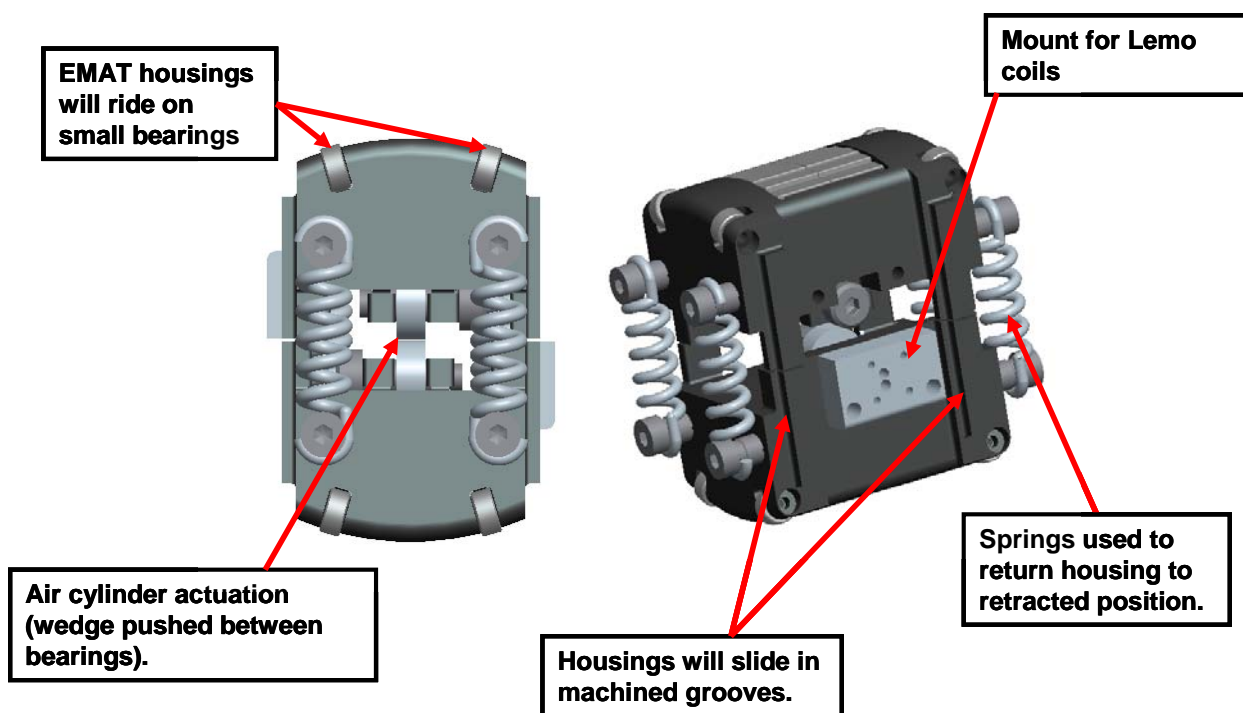


Figure 31 Final EMAT head design.

The system level design of the final prototype includes a frame that doubles as guide rails for the EMAT heads. A cover encloses the entire assembly. A suspension is also included, and all electronics are neatly housed inside. The only open sections are for the EMAT heads, suspension, and encoder to protrude and make contact with the inside of the well casing. Again, circumferential EMAT heads are slightly modified and a second, very similar, section of the tool will house a longitudinal EMAT set up. 3D drawings are shown in Figure 32.

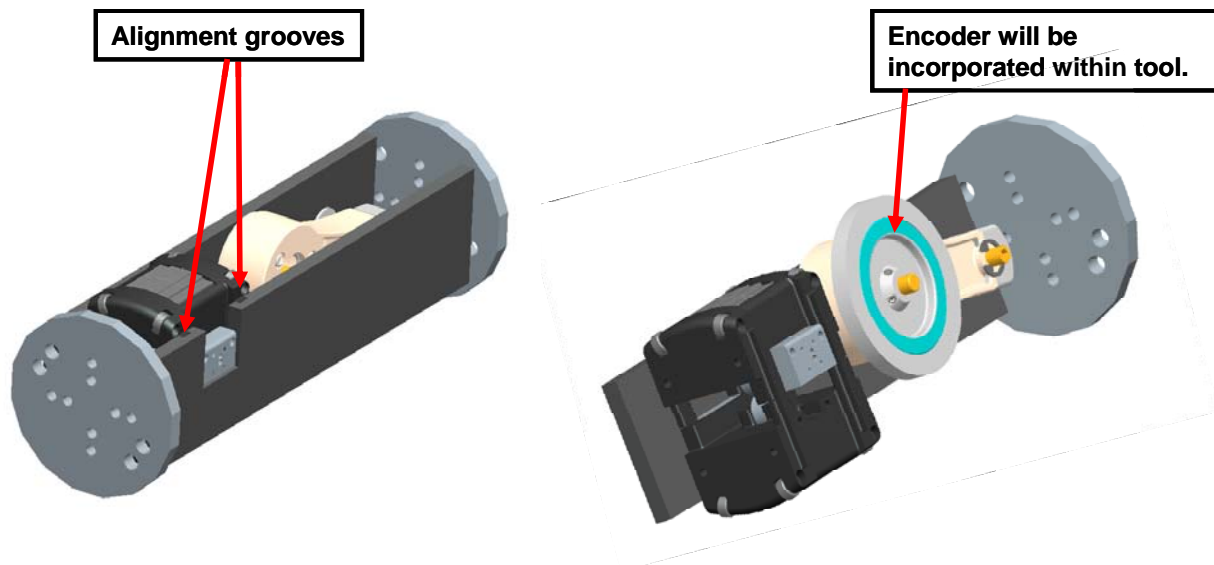


Figure 32 Tool level design with circumferential EMAT set up.

The in-line inspection (ILI) tool generates and receives circumferential and longitudinal shear horizontal waves within well casing. The tool is comprised of two subassemblies as shown in Figure 33. They are able to be used together and can generate both circumferential and longitudinal guided waves, or based on the user and detectability preference they can be separated and generate guided waves in only one direction.

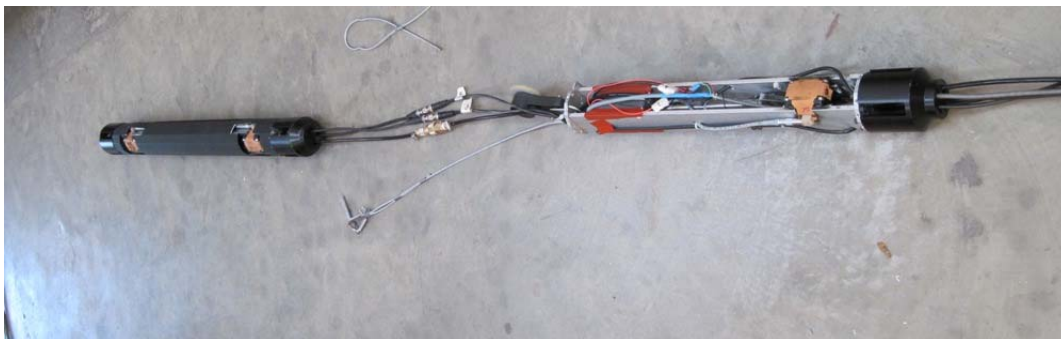


Figure 33 Fully assembled ILI tool without protective covers on the circumferential guided wave part of the tool.

Two separate pre-amps are used. One was isolated to each tool. Both pre-amps are housed in the circumferential portion of the tool. Both subassemblies were pulsed simultaneously. This allowed for one external matching network to be used. The same matching network could be used for one subassembly or both.

There was concern that alignment within the pipe would be a problem. So each subassembly was designed to have a suspension on both ends, which can be seen on one end in Figure 34. There were no alignment issues so the suspension was not utilized as seen in Figure 33.



Figure 34 3D model of the circumferential subassembly. Suspension capability in the nose cone can be seen in the upper right.

The ILI tool utilizes air cylinders to actuate the EMAT heads outward to make contact with the pipe wall. A graphite aerosol spray was the lubricant of choice to keep the heads moving inward and outward. The heads can be seen in Figure 35. Each head had an orange protective urethane sheet over the electrical coil.

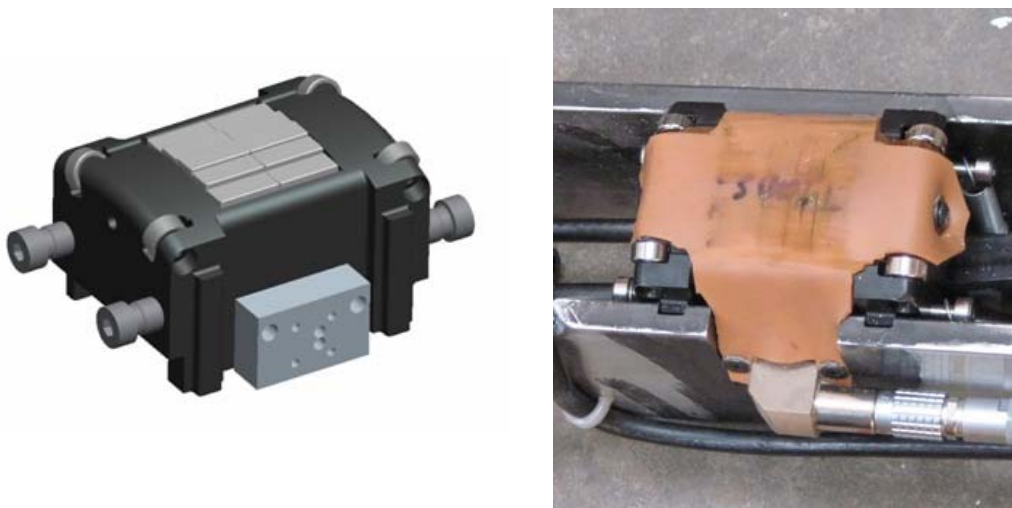


Figure 35 EMAT head 3D drawing (on left) and photograph of the EMAT head (on right).

All of the components are tightly packed within the ILI tool, so it was decided to mount the encoder outside the enclosures between them as shown in Figure 36. This had been anticipated; therefore a robust encoder was selected. The side-by-side pre-amps with the circumferential subassembly can also be seen in Figure 36.

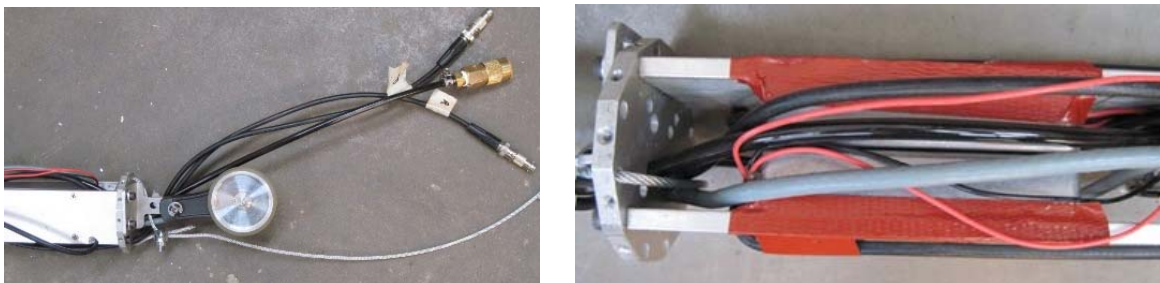


Figure 36 Encoder position shown on the left and the internal pre-amps mounted internally on the right.

The magnets in the EMAT are Neodymium and 0.20 in. thick. Magnets for the longitudinal wave EMATs have a radius as shown in Figure 37 to fit inside the head. The magnets for the circumferential wave EMAT are 0.80" x 0.50" x 0.20".

The bill of materials for each the circumferential wave and the longitudinal wave subsystems are given in Table 2 and 3 respectively. The material cost of the 2nd generation tool, including parts and machining is approximately \$8,000.

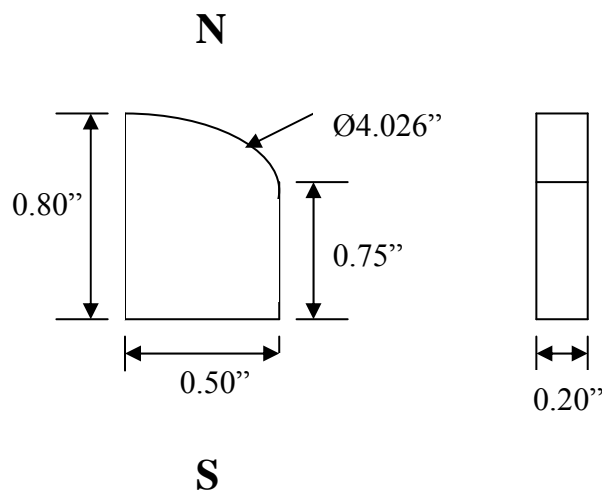


Figure 37 Magnet geometry for longitudinal wave subassembly, half of the magnets have the opposite polarity.

amplitude to the reflected wave amplitude decreases as expected for increasing larger defects, as shown in Figure 41 for the first 3 wrap-around signals. This ratio, and its inverse, combine the effects of reduced transmission and increased reflection into one feature.



Figure 38 Experimental setup at Penn State for tests on 4" schedule 40 well casing.

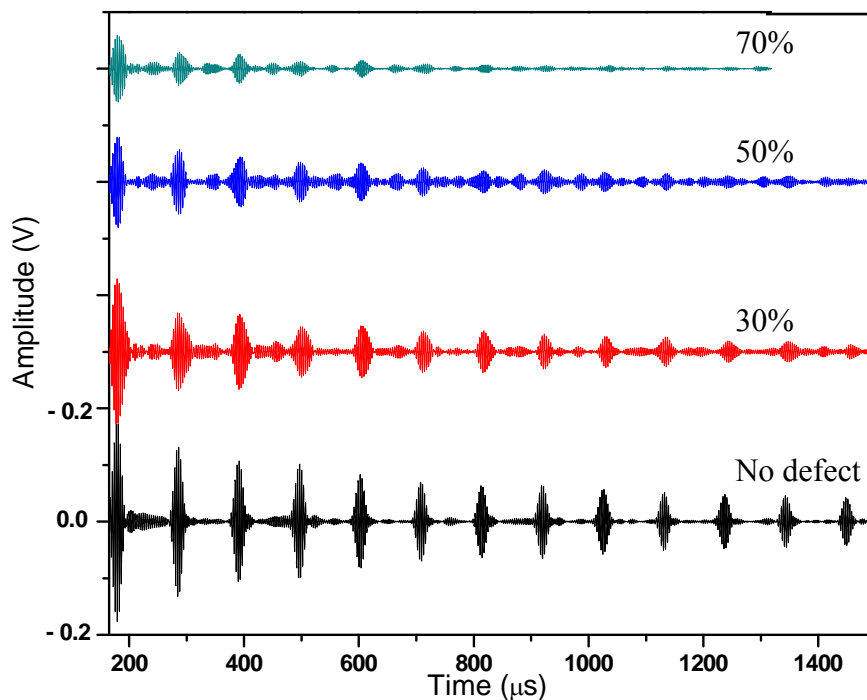


Figure 39 Received 270 kHz circumferential SH wave signals from regions of well casing pipe with no defects, and regions having side-by-side partial holes 30, 50, and 70 percent through wall (TW) thickness.

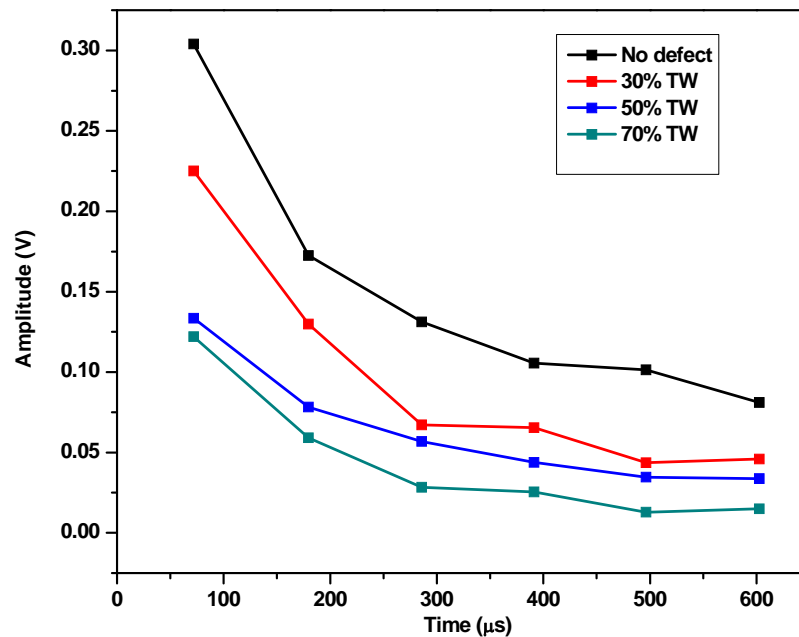


Figure 40 Reduction in the wrap-around signal peak amplitude due to the presence of a defect. The defect is a cluster of two holes of various depths. The excitation frequency is 270 kHz.

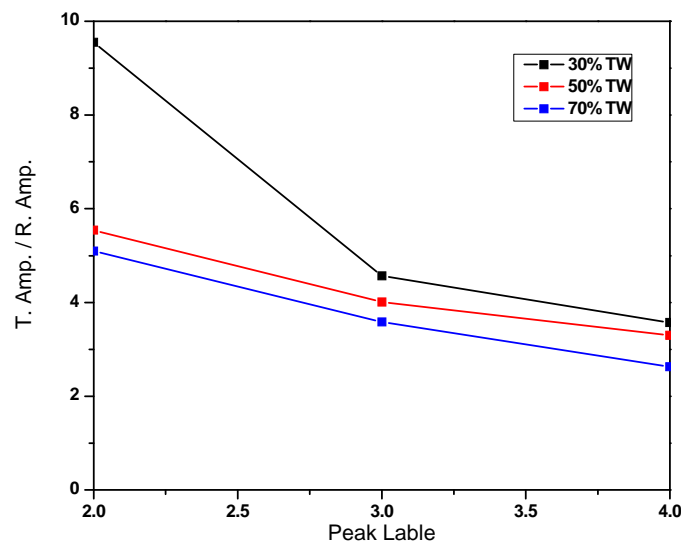


Figure 41 Reduction in the ratio of transmitted-to-reflected wave amplitude for the first three wrap-around signal peaks due to the defect. The defect is a cluster of two holes of various depths. The excitation frequency is 270 kHz.

Field Trials

The 2nd generation in-line inspection tool was tested in an observation well operated by Dominion Resources in North Canton, OH. The test was performed to evaluate operation of the tool in service conditions and assess the quality of the received signals. There was no expectation that damage was present.

The well cap was removed and the tool was lowered into the well (see Figure 42) to a depth of approximately 50 ft (15 m), which is well above the water line. Pneumatic pressure was applied to position the EMAT heads for transmitting and receiving both circumferential and longitudinal SH waves. Signals were sent and received as the in-line tool was pulled back up through the well casing. The encoder had a persistent issue that blew a fuse, so the tool was advanced in increments of 1 ft (0.3 m) to facilitate uniform data acquisition. A sequence of received circumferential SH wave signals is shown in Figure 43 for an excitation frequency of 270 kHz. Based on the group velocity of the SH₀ mode, the time for a wave to traverse the circumference is 106 μ s. Up to 8 wrap-around signals are clearly visible. Samples of the longitudinally propagating SH waves are shown in Figure 44. The intermittent signals that appear at different times are probably reflections from nearby threaded couplings.



Figure 42 Launching the ILI tool into an observation well in North Canton, Ohio

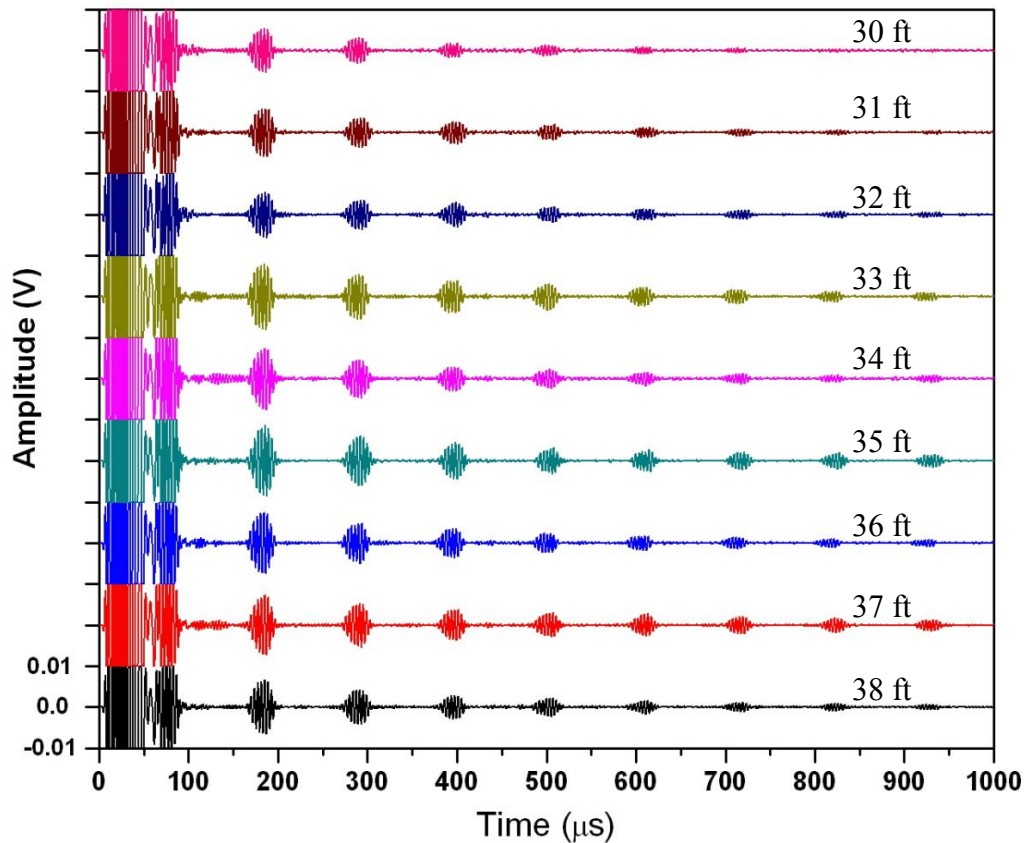


Figure 43 A-scan sequence of circumferential SH wave signals for depths of 30-38 feet (9.1-11.6 m). Up to 8 wrap-around signals are visible for the 270 kHz tone burst.

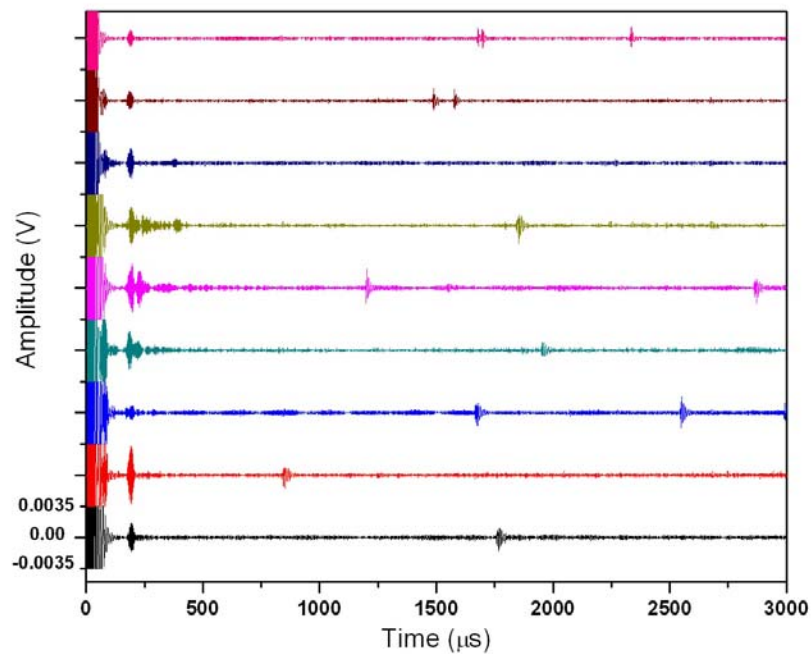


Figure 44 Signals from axially propagating SH waves acquired from the observation well at different depths are shown for a 270 kHz excitation frequency.

During the field tests the tool proved to be very rugged. Conditions were very unfavorable because the inside of the well casing was not cleaned in any way. The ILI tool came out with very worn urethane wear covers. Much scale and moisture built up on the EMAT heads during use, but the tool continued to acquire clean signals because it is a noncontact sensor. Additional improvements can be made before a commercial product is created. Results of the field trial indicate that the final design should be easier to take apart and clean. The tool should be environmentally sealed better. The protective urethane cover size should be adjusted to account for wear. To prevent misalignment of the EMAT heads, and ensure smooth operation, the heads could be mounted on sliders with a Teflon sleeve.

Results from this project were presented at the Review of Progress in Nondestructive Evaluation conference in San Diego, CA 18-23 July 2010 [Lindsey et al, 2011] as well as at the Gas Storage Technology Consortium meeting in Kansas City, MO 22 September 2010.

CONCLUSION

A multi-sensor down-hole fixture is designed and fabricated that transmits and receives axial guided waves as well as circumferential guided waves in order to detect, locate, classify, and size defects that reduce the mechanical integrity of the steel well casing. The design is based on theoretically driven experimentation and computational modeling.

To provide the best defect characterization capabilities the tool is designed to generate shear-horizontal waves both circumferentially around the well casing as well as longitudinally. Electromagnetic acoustic transducers are constructed with Neodymium magnets and electrical coils. The noncontact nature of the transducers makes them both durable and practical for operating inside a well casing. A 270 kHz excitation frequency is selected, based on the phase velocity dispersion curves, to excite only the fundamental shear-horizontal mode and therefore enhance signal processing and data analysis. Transducers are positioned by pneumatics and protected by enclosures.

In addition to a proof-of-concept demonstration system, two generations of in-line tools are designed, built, and tested. The final design is shown to accurately detect surface defects in 4" schedule 40 pipe in a laboratory setting. It is also demonstrated to function well in a field trial, where data were acquired over a 50 ft length of an observation well in North Akron, Ohio. Strong signals were received in the field trial despite the fact that no cleaning of the well casing was performed and much scale and moisture accumulated on the transducer heads during operation. The circumferential guided waves were detectable for up to 8 revolutions around the casing. The presence of a defect creates a detectable reflection and reduces the wrap-around transmitted waves. Further efforts to introduce this technology to practice are encouraged.

REFERENCES

M.S. Lindsey, E. Khajeh, J.K. Van Velsor, C.J. Lissenden, J.L. Rose, 2011, "In-line corrosion inspection using circumferential and longitudinal ultrasonic guided waves," In: *Review of Progress in Quantitative Nondestructive Evaluation*, Vol. 30, D.O. Thompson and D.E. Chimenti, Eds., American Institute of Physics Proc., In-press.

Appendix N
2009, RGD X-Ray Technology Well Bore Inspection and Assessment -
A Feasibility Study,
Gas Technology Institute Final Report

FINAL REPORT

RSD X-Ray Technology: Well Bore Inspection and Assessment – A Feasibility Study

Award Number: 3888-GTI-DOE-1779

Submission Date: November 15, 2010

Prepared For:

The Pennsylvania State University
110 Technology Center Building
University Park, PA

Prepared By:

Mr. Andy Hammerschmidt, GTI
Team Project Manager/Principal Investigator
1700 South Mt. Prospect Rd
Des Plaines, IL 60018
andrew.hammerschmidt@gastechnology.org
847-768-0686

Daniel Shedlock, Ph. D., NuSAFE
Co-Principal Investigator
601 Oak Ridge Turnpike
Oak Ridge, TN 37830
dshedlock@nucsafe.com
865-220-5050

Gas Technology Institute
1700 S. Mount Prospect Rd.
Des Plaines, Illinois 60018
www.gastechnology.org

DISCLAIMER

“This report was prepared as an account of work sponsored by an agency of the United States government. Neither the United States Government nor any agency thereof, nor any of their employees, makes any warranty, express or implied, or assumes any legal liability or responsibility for the accuracy, completeness, or usefulness of any information, apparatus, product, or process disclosed, or represents that its use would not infringe privately owned rights. Reference herein to any specific commercial product, process, or service by trade name, trademark, manufacturer, or otherwise does not necessarily constitute or imply its endorsement, recommendation, or favoring by the United States Government or any agency thereof. The views and opinions of authors expressed herein do not necessarily state or reflect those of the United States Government or any agency thereof.”

ABSTRACT

Through a partnership development with Gas Technology Institute (GTI) and NuSAFE, Inc., the goal of this project is to package patented RSD technology (“Radiography by Selective Detection of Scatter Field Velocity Components,” U.S. Patent 7,224,772, May, 29, 2007) and through integration of commercial off the shelf (COTS) components ascertain the feasibility of developing a package profile to meet the demanding down-hole and transmission non-destructive evaluation (NDE) environment. The following report includes results of the feasibility analysis, experimental data, conceptual engineering design of prototypes, and recommendations for future prototype development.

TABLE OF CONTENTS

	Page
DISCLAIMER	ii
ABSTRACT	iii
TABLE OF CONTENTS	iv
TABLE OF FIGURES	5
LIST OF TABLES	7
INTRODUCTION	8
EXECUTIVE SUMMARY	9
EXPERIMENTAL	11
<i>Operational Specifications</i>	11
Physical Specifications	11
Environmental Specifications	12
General Capability Specifications	12
<i>RSD System Component Review</i>	12
Detector Review	12
Power, Cabling and Communication Review	15
RSD System Housing Material Review	16
RESULTS AND DISCUSSION	31
<i>Pipeline Inspection Experimental Results</i>	31
Introduction	31
Steel Pipe (Casing and Transmission Applications)	32
Poly Pipe	36
<i>Scale and Corrosion Identification Analysis</i>	46
<i>Conceptual Prototype Design</i>	48
Design for Wellbore Casing Tool	48
Design for Transmission Pipeline Tool	55
CONCLUSION	60
REFERENCES	61

TABLE OF FIGURES

Figure 1. Images for the 12 inch diameter yellow Driscoplex pipe with different thicknesses of aluminum plate overlays.	18
Figure 2. Line profile 12 inch diameter yellow Driscoplex pipe for baseline case (no overlay). ...	19
Figure 3. Line profile for 12 inch diameter Driscoplex pipe case with 0.125" thick Al plate overlay.	19
Figure 4. Line profile for 12 inch diameter Driscoplex pipe case with 0.1875" thick Al plate overlay.	20
Figure 5. Line profile for 12 inch diameter Driscoplex pipe case with 0.250" thick Al plate overlay.	20
Figure 6. Images for the 24 inch diameter steel pipe with different thicknesses of aluminum plate overlays.	21
Figure 7. Line profile for the 24 inch diameter steel pipe baseline case (no overlay).	22
Figure 8. Line profile for the 24 inch diameter steel pipe case with 0.125" thick Al plate overlay.	22
Figure 9. Line profile for the 24 inch diameter steel pipe case with 0.1875" thick Al plate overlay.	23
Figure 10. Line profile for the 24 inch diameter steel pipe case with 0.250" thick Al plate overlay.	23
Figure 11. Images for the 12 inch diameter yellow Driscoplex pipe with different thicknesses of carbon composite overlays.....	24
Figure 12. Line profile for 12 inch diameter yellow Driscoplex pipe baseline case (no overlay). ...	25
Figure 13. Line profile for 12 inch diameter Driscoplex pipe case with 0.03125" thick C composite overlay.	25
Figure 14. Line profile for 12 inch diameter Driscoplex pipe case with 0.0625" thick C composite overlay.	26
Figure 15. Line profile for 12 inch diameter Driscoplex pipe case with 0.125" thick C composite overlay.	26
Figure 16. Images for the 24 inch diameter steel pipe with different thicknesses of carbon composite overlays.	27
Figure 17. Line profile for the 24 inch diameter steel pipe baseline case (no overlay).	28
Figure 18. Line profile for the 24 inch diameter steel pipe case with 0.03125" thick C composite overlay.	28
Figure 19. Line profile for the 24 inch diameter steel pipe case with 0.0625" thick C composite overlay.	29
Figure 20. Line profile for the 24 inch diameter steel pipe case with 0.125" thick C composite overlay.	29

Figure 21. Poly pipes include a combination of polyethylene and polyamide pipes: (left) 8 inch diameter Polypipe, HDPE, 3408; (center) 6 inch diameter, Polyamide 12, SDR 11;.....	31
Figure 22. 24 inch diameter steel pipe (left) sample 1, internal defects; (right) sample 2, external defects.	32
Figure 23. Experimental setup for preliminary scanning. The x-ray beam sweeps across the sample and scatters back to the detectors.	33
Figure 24. Sample scan of ¼ inch wall steel pipe, external defects, 160 kV. Note the pipe was imaged from inside out so the defects are mirror imaged.	34
Figure 25. Sample scan of ¼ inch wall steel pipe, external defects, 160 kV. Note the pipe was imaged from inside out so the defects are mirror imaged.	34
Figure 26. Sample scan of ¼ inch wall steel pipe, 160 kV; similar to Figure 7-4 with additional optimization.....	35
Figure 27. Sample scan of ¼ inch wall steel pipe, internal defects, 160 kV.....	36
Figure 28. Sample RSD scan of polyamide 12, SDR11, 6 inch diameter pipe.	37
Figure 29. Sample RSD scan of MDPE, 12 inch diameter, DriscoPlex 6500 PE 2406.....	38
Figure 30. Sample RSD scan of MDPE, 12 inch diameter, DriscoPlex 6500 PE 2406.....	38
Figure 31. Sample RSD scan of 8 inch diameter Polypipe, HDPE, 3408.....	39
Figure 32. Experimental setup for future scanning through water stack-up.	40
Figure 33. Acceptable butt fusion welds – proper alignment and double roll-back bead.....	41
Figure 34. Unacceptable butt fusion welds.....	41
Figure 35. Unacceptable fusion butt welds.....	42
Figure 36. Yellow stripe, 6 inch diameter PE3408 polyethylene pipe sample and SXI images.	43
Figure 37. Yellowstripe, 6 inch diameter PE3408 Polypipe sample and some additional SXI images.	44
Figure 38. Yellowstripe, 6 inch diameter PE3408 Polypipe sample and SXI images with debris on the inside of the sample. Tiny stones on the inside of the weld seam (left) and sand on the inside of the pipe (center and right).	45
Figure 39. Calculated spectral shift from two different salts and Iron, NaCl, and K ₂ CO ₃	46
Figure 40. Measured x-ray backscatter spectrum using NaI detectors	47
Figure 41. Calculated backscatter spectral shift from two common scale deposits containing barium sulfate and calcium carbonate.....	48
Figure 42. Downhole x-ray backscatter tool.	50
Figure 43. Detail of scanning head for downhole tool.	50
Figure 44. Bisected cylindrical detector with two illumination beams.....	52
Figure 45. Tri-sected cylindrical detector with three illumination beams.	53
Figure 46. Specifications for a 2.75 inch diameter Panoramic RTW x-ray generator	54
Figure 47. Transmission line x-ray backscatter tool.....	56

Figure 48. Multiple smart pig transmission pipeline scanning system with centering standoffs for larger diameter pipes:	56
Figure 49. Conceptual smart pig that includes the x-ray backscatter tool components	57

LIST OF TABLES

Table 1. Rochester Wire Company Optical Tow Wire.....	15
Table 2. Load Power Estimates for Rochester Wire at 15,000 feet.....	15

INTRODUCTION

Scaling, corrosion, precipitates, and casing defects are all issues storage operators face on a continual basis in managing the integrity of their gas storage assets. These issues often lead to diminished deliverability (5 to 20%), as well as casing integrity issues requiring costly remediation. The mineral scale formation and material defect assessment process in well bores is complicated, time consuming, and costly due to the range of storage conditions and existing technologies.

This research project assessed the feasibility and developed a conceptual model of a real-time digital x-ray tool for in-situ compositional identification and quantification of scale in gas storage wells and pipelines. The tool will also assess and quantify material defects, pitting, and penetrations in casings and associated piping. Included in this final report are also results from efforts focused on transmission pipeline NDE as well as the technology's effectiveness in evaluating non-metallic materials such as high density polyethylene and polyamides.

Scatter X-ray Imaging (SXI) is a new type of x-ray backscatter imaging referred to as radiography by selective detection (RSD). It has been successfully employed in the non-destructive evaluation (NDE) of a wide variety of interrogation applications. This enhanced Compton backscatter imaging (CBI) technique, and the various RSD modalities being used today, has been under development since 1986 at the University of Florida when it was first used for detection of buried land mines. Since being commercialized at NuSAFE, this technology has been deployed in the government and commercial aerospace programs including NASA, Boeing, and Lockheed Martin.

Radiography by selective detection allows for preferential detection of backscatter components that are responsible for improving image contrast. This is accomplished through a set of specially designed detectors and both fixed and movable detector collimators. The SXI system is a proven technology that has been tested on a wide variety of materials and applications. The focus of RSD has been one-sided detection for applications where conventional non-destructive examination methods either will not work or give poor results. Acquired images have clearly shown, for a variety of conditions, that proper selection of x-ray field scatter components leads to a significant improvement in image quality and contrast. Improvements are significant enough in some cases that objects not visible to conventional x-ray backscatter imaging or transmission radiography become clearly discernable.

The gas storage industry will benefit from this innovative technology as it can provide real time data and analysis on both scale formation inside the well bore as well as assess the well bore casing integrity itself. The proposed technology can provide this information in a single scan, creating an ideal application for determining pre and post remedial treatment effectiveness. The assessment process will be significantly streamlined, eliminating the delay for lab analysis and reducing rig time considerably. Cost savings will potentially be in the tens of thousands on an annual basis for a typical integrity management program.

EXECUTIVE SUMMARY

As indicated in the introduction, the purpose of this research effort was to determine the feasibility of utilizing the RSD technology for effective non-destructive evaluation (NDE) of wellbore casings including material defects, pitting, penetrations as well as scaling mechanisms. Based on stakeholder input, the feasibility analysis was extended to transmission pipeline NDE as well as its effectiveness in assessing non-metallic materials commonly used for distribution and emerging transmission pipeline applications. Investigative analysis, experimental data capture, transport modeling, and prototype conceptual engineering design were performed under this research effort to conclusively determine feasibility of the RSD system for the intended applications. Results of these efforts are included in this report.

A survey of currently available well bore assessment technologies was conducted and information collected from Gas Storage Operators. Specifically, the type of tools, mode of deployment, pressure and temperature conditions, data collection and analysis protocol, if any, and well bore assessment procedures were compared. Current neutron and gamma Compton scatter techniques were evaluated to determine if the types of detectors and electronics used for these existing techniques are compatible with the backscatter radiography imaging technique that is going to be developed. Conducted concurrently was an overall information gathering process to find any current commercial off-the-shelf (COTS) components that can be integrated into a fully functional system. This included:

- Evaluation of existing down-hole radiation and detection measurement devices. The detection devices included neutron, gamma, and x-ray devices. The device detectors included solid state detectors, gas filled detectors, and scintillators.
- Evaluation of existing down-hole packages to help define required operational parameters as well as challenging environmental conditions.
- Materials required for packaging/housing were investigated such as carbon or polymer based materials that would allow the interrogating beam to exit, scatter, return, and be measured in the device.
- Existing high-temperature, long-distance communication media was investigated for down-hole applications.
- Investigation into Gamma and neutron sources that are typically used for profile logging. Gamma sources are typically used to determine porosity and bulk density mapping, while neutron sources are used for hydrocarbon mapping and elemental analysis through neutron activation analysis (NAA).

Experimental data capture efforts focused on identifying and testing individual components of x-ray backscatter systems in a variety of scenarios reflective of the targeted applications. This included:

- Evaluation and integration of a linear detector array into the x-ray backscatter system to evaluate the performance and image quality for general non-destructive evaluation (NDE) applications.
- Water is a high scattering material. It was determined that x-rays can easily image through a few cm of water. Resolution and contrast as a function of water thickness was determined to a depth of 6 cm.

- Utilization of existing components and technologies to collect images of samples on an experimental basis for conceptual design and engineering models was executed. X-ray backscatter systems existed to perform this work. The goal was to collect sample images that would be characteristic of the actual device without having the significant expense of building the actual prototype. To the extent possible, this was accomplished through the use of detailed radiation transport calculations that were used to correlate experimental data to actual expected system performance.

Because the scope of work in this feasibility analysis does not include building an actual prototype, it was necessary to develop detailed radiation transport calculations. These radiation transport models were used to correlate experimental results and generate a conceptual design. Radiation transport modeling was also used to evaluate the effectiveness of many different parameters without having to actually build a device. Parameters included:

- Evaluation of radiation detectors
- Evaluation of packaging materials
- Evaluation of the source and its correlation to imaging speed
- Evaluation of mechanical design and layout

Based on a combination of radiation transport models and experimental results, 3-D solid conceptual designs of the expected devices (wellbore casing and transmission applications) were developed using the components identified as optimal in the previous activities. Several factors influenced the overall design:

- Detectors
- Source
- Housing material
- Space constraints

With a combination of the experimental results, radiation transport models and mechanical design, it was possible to define a set of expected operational specifications and determine that RSD is a feasible technology platform for effective assessment and NDE of wellbore casings, transmission pipelines, and non-metallic distribution and transmission piping systems.

EXPERIMENTAL

This section of the report focuses on the investigation and development of general specifications of the potential prototype device. These specifications provided the baseline for analysis and investigation of individual components of the RSD system for optimization of a prototype design. A brief survey and investigation of currently available well bore assessment technologies was conducted and information collected from Gas Storage Operators. Specifically, the type of tools, mode of deployment, pressure and temperature conditions, data collection and analysis protocol, if any, and well bore assessment procedures were compared. Current neutron and gamma Compton scatter techniques were evaluated to determine if the types of detectors and electronics used for these existing techniques are compatible with the backscatter radiography imaging technique that is to be developed as a result of this feasibility study. Conducted concurrently was an overall information gathering process to find any current commercial off-the-shelf (COTS) components that can be integrated into a fully functional system. The section below details general specifications developed to which a conceptual engineering design must meet for both down-hole and transmission applications.

Operational Specifications

Physical Specifications

Small Diameter Down-hole:

- One system should have physical dimension less than 4 inches in diameter.
- Length not to exceed 20 feet; ideally tandem or component segments no greater than around 8-10 feet in length.
- Imaging and detector end to be about 4-6 feet.
- HV and controller to be about 4-6 feet.
- Explosion proof specifications Class 1 Division 1. Heavier is better.
- Check power requirements.

Large Diameter Transmission Line Specifications:

- A larger system will be developed simultaneously for operation in larger diameter pipe. This system should not exceed 20 inches in diameter.
- Scalable tool size of 11 to 40 inches by adjusting model dimensions without significant redesign.
- Explosion proof specifications Class 1 Division 1
- Weight restrictions to be determined (TDW)
- Preference for untethered system
 - Possibly a generator
 - Battery operator
 - Power for a mile or two of pipeline
 - Location device for an untethered system

Environmental Specifications

Small Diameter Down-hole:

- Small diameter pipe temperature design to 60 C to 100 C.

Large Diameter Transmission Line Specifications:

- Large diameter pipe temperature design to 100 C.

General Capability Specifications

Small Diameter Down-hole:

- Tethered, with real time feedback.

Large Diameter Transmission Line Specifications:

- No real time feedback needed if device is un-tethered.
- General transmission line buried anywhere from 5 feet down to 12 feet.

With basic design specifications established, research efforts focused on investigation and analysis of individual components of the RSD system for optimization of a prototype design.

RSD System Component Review

Detector Review

Detector Introduction

Radiation detection and measurement in well logging is focused on learning more about the surrounding structure of the bore hole and its surrounding geophysical characteristics. The goal of this research effort is to use radiation detectors for imaging and potential elemental analysis.

For typical transmission radiography, standard film has been around for over 100 years. Today these films are being replaced with phosphor imaging plates that can be read in a laser scanner. This technique is referred to as computed radiography (CR). Digital radiography (DR) can use a variety of devices that include: a charge coupled device (CCD) array, 2-D array or a translating linear array to capture a two dimensional imaging. Digital radiography completely removes the film and imaging plates from the process and converts the x-ray image directly to a digital image that can be transmitted real-time. This in-situ process allows anyone performing NDI to make near real-time decisions about the data being received. For example, if you are taking a quick pass, low resolution scan, a trained user can immediately identify problem areas; stop the scan; and obtain a high resolution scan of the region of interest (ROI) before proceeding. For this technique to work, the quick pass scan must meet resolution specifications for things such as wall loss, scale buildup, and corrosion. The high-speed real-time method can save a tremendous amount time in trying to relocate a ROI and collect information after the scan is complete. This is often the case when data is logged and reviewed at a later date.

This review of detectors is limited to detectors with potential for specific project applications. The underlying physical principles of all radiation detectors are the same. Radiation passing through the detector interacts with some material within the detector. Neutral particles, such as gamma rays, x-rays, and neutrons have relatively large ranges in materials, depositing their energy in some type of detection material. The detector converts this energy into an electrical signal that can be analyzed and recorded. For example, scintillating materials convert the amount of gamma or x-ray energy into light via electron transitions. The light is then collected with a photo-sensitive device such as a photo-multiplier tube (PMT), avalanche photo-diode (APD), complementary metal-oxide-semiconductor (CMOS) or solid state pin-diode detectors. Each of these conversion processes has its pros and cons as will be discussed later in this report. Scintillators come in both organic and inorganic forms, solid and liquids, amorphous and crystalline structures. One of the most commonly used scintillators is NaI(Tl). Many scintillators property are compared to NaI which is used as a reference standard.

Gas filled detectors use a gas that is dissociated by ionizing radiation. The dissociated ions and electrons are collected over a charged field between an anode and cathode. Geiger Mueller (GM) tubes and proportional counters are examples of gas filled detectors. High pressure xenon detectors are often used in down-hole applications for gross gamma mapping. Other types of gas filled detectors, typically for neutrons, can be filled with ^3He , or lined with isotopes such as ^{10}B or ^6Li . Once the neutron is absorbed in these materials the resulting particles again cause ionization in gas and charge is similarly collected.

For solid state detectors, such high purity germanium (HPGe), as a charge particle passes through a semiconductor, many electron-hole pairs are produced as the radiation loses energy. The amount of energy required to create one electron-hole pair is the ionization energy ($\bar{\epsilon}$) of the semiconductor. The ionization energies for semiconductors are typically on the order of electron volts (eV) whereas for gas ionization detectors values are tens of electron volts. The low band gap gives the detector higher resolution, but typically requires the detector to be cooled to cryogenic temperatures. The number of electron hole pairs is simply the energy lost (E) divided by the ionization energy. Also, thermal noise of the detector is based on the rate of electron-hole pairs generated due to the band gap of the semiconductor (E_g). The electron drift mobility (μ) will affect the diffusion of electrons in the semiconductor, also a significant indicator of the noise of the detector. The density (\bar{n}) of the semiconductor will affect the interaction of radiation with the semiconductor, in both the production of electron-hole pairs as well as radiation damage. The displacement energy (E_d) is an indication of sensitivity to semiconductor damage from incoming radiation. Highly desired semiconductors should have low drift mobility and wide band-gap to reduce the noise from thermal temperature fluctuations. [6]

Current Detector Technology

For gamma ray detection, NaI(Tl) and HPGe are the primary detectors used. HPGe is a solid state high resolution spectroscopy detector that is primarily used to analyze the gamma signature induced by activation from a neutron source. Analysis of these gamma lines can be used to perform isotopic identification. HPGe requires temperatures below 77 K for optimal performance. This low temperature is maintained with different techniques. The first and most common technique is submersing the crystal in liquid nitrogen. Some down-hole equipment manufacturers have also used liquid methane. A third technique is to provide mechanical

cooling through a Stirling engine type of device. Electronic cooling using a Peltier device is possible, but the process is inefficient and typically does not achieve cryogenic temperatures.

NaI is more commonly used for gamma counting and lower resolution spectroscopy. While HPGe detectors have a 661 keV resolution of about 0.7 %, NaI has a resolution of about 8 %. NaI is very commonly employed due to its inherently high efficiency and a long operating history with known performance. Although deployed in a variety of tools, NaI is a fragile crystal that is also hygroscopic. Other crystal scintillator detector options being investigated include CsI, YSO, and LYSO.

Another issue that needs to be addressed for any detector system is stability and signal-to-noise ratio (SNR) as a function of temperature. Two approaches have been taken in the field to stabilize the SNR. One option is to provide cooling. Cooling could be of the Peltier type or a mechanical Stirling engine.

A second option used by many of the logging devices is to preheat the system to a temperature higher than will be seen in the down-hole operation. The system is held at this temperature for about 30 minutes before being logging begins. Since the device is maintaining a constant temperature, no temperature drift occurs.

A third option is to characterize the detector system response as function of temperature. A smart sensor can then compensate or gain stabilize as a function of temperature. NuSAFE employs active gain stabilization for all of its fielded systems. This gain stabilization maintains the detector's calibration as function of temperature. Commercially deployed systems are stable over a temperature of -40 C (-40 ° F) to +50 C (122 ° F). Commercial NuSAFE x-ray backscatter systems are currently designed for operation from 0 C (-32° F) to 40 C (104° F)

Detector Materials Evaluated

- There is a line of PVT [11, 12] detectors that are temperature rated up to 212 °F (100 C). These detectors were evaluated for both large diameter bore pipe (12 inches and larger) and for small (around 3 or 4 inch diameter) down-hole detector applications. PVT is the cheapest and most rugged of the detector materials being evaluated. However, it does not have any relevant down-hole operating history. This material can be cast and machined to nearly any size and shape. PVT does however begin to oxidize over time at high temperatures. It expected to have 3-5 years operating life in the field before having to be replaced. The PVT scintillators being considered are Eljen Technologies' EJ-240, EJ-244, and EJ-248, and Saint Gobain's BC-440, and BC-448.
- LYSO and YSO were evaluated for 3 inch diameter detector application for down-hole use. LYSO has only recently become commercially available in the past 18 months. These are very expensive detector materials, however they are the most rugged and have the most stable temperature profile. LYSO and YSO are expected to have a 5-7 year field operating life before having to be replaced.
- NaI is currently the down-hole staple for porosity and gamma field mapping and was evaluated for detector applications up to four inches in diameter. NaI is the most fragile detector material being considered, and is also hygroscopic. However because of the

long operating history, most of these problems have been overcome in the field. NaI is more expensive than PVT and less expensive than LYSO and YSO. It is also available in larger sizes than the YSO and LYSO. NaI currently has 3-5 years field operating life before having to be replaced.

Power, Cabling and Communication Review

As a starting point for beginning of conceptual design, the scanning system (including all ancillary systems) is expected to draw at least 2000 watts of power. The current NuSAFE x-ray backscatter system draws approximately 4000 watts of power for the entire system. Cabling that can meet this minimum requirement was evaluated.

Because real-time control and feedback is a highly desirable specification, it was necessary to find down-hole wire fiber optic and power ratings of greater than 2000 watts. The optical tow wire in Table 1 has both fiber optics and high power density. One of the limitations of this cable is a temperature rating of 175 °F (80 °C). This temperature of 175 °F also pushes the limits of today's x-ray technology. Table 2 presents load power estimates for two of the wires in Table 1 at 15000 feet.

Table 1. Rochester Wire Company Optical Tow Wire

Part #	Diameter		Breaking Strength		Weight in Water		Cdrs.	dc Resistance		Fibers
	Mm	in	kN	lbf	kg/km	lbs/kft		ohm/km	ohm/kft	
A302351	17.30	0.681	204.6	46,000	905	608	3	4.9	1.5	3smf
A303950	11.07	0.436	64.5	14,500	332	223	3	23.5	7.2	3mmf
A303954	11.07	0.436	64.5	14,500	338	227	3	23.5	7.2	4mmf
A305382	9.98	.393	71.0	16,000	322	217	2	82.0	25.0	2smf

Table 2. Load Power Estimates for Rochester Wire at 15,000 feet

Part	Power Conductor	Resistance Ohms/ Kft	Total Resistance for 15,000ft	Conductor Voltage (V)	Assumed Load Voltage (V)	Load max current (A)	Load Power (W)
A302351	3 (11AWG)	1.5	22.5	2,800	200	115.6	23,120
A303950	3 (18AWG)	7.2	108	600	200	3.7	740

RSD System Housing Material Review

The down-hole and/or pipe transmission line inspection tool vessel is an absolutely critical component. Most down-hole tools are currently made from stainless steel, and a few from titanium alloys. Clearly, the tool vessel material needs to withstand the pressure, temperature and other environmental conditions required for down-hole applications or transmission pipeline conditions. However, it is also essential that the tool vessel allow the imaging x-ray radiation from the source to exit the vessel, scatter from the pipe wall and then return through the tool vessel to the detectors. Stainless steel will not meet this requirement and titanium alloys are questionable. For x-rays, ideal materials are low z materials. Beryllium is often used as windows for x-ray tubes because it is relatively transparent to x-rays; however, beryllium is extremely expensive and machining of beryllium represents a severe health hazard. Carbon fiber composites are a good candidate because they allow x-rays to exit the vessel and return. Aluminum is also a candidate if it can withstand the required pressures and corrosive environment. Aluminum may work well for the pipe transmission line tool, but is doubtful for any down-hole tool because of the severity of environmental conditions. Aluminum is less expensive than the carbon composites and replacement of a damaged aluminum vessel should be quite simple. In order to examine the potential performance of aluminum and carbon fiber composites as tool vessel materials, imaging was performed for both the 12 inch diameter Driscoplex Pipe and for the 24 inch diameter steel pipe using different overlay thicknesses of aluminum and carbon fiber composites to determine the effect of these candidate vessel materials on image quality.

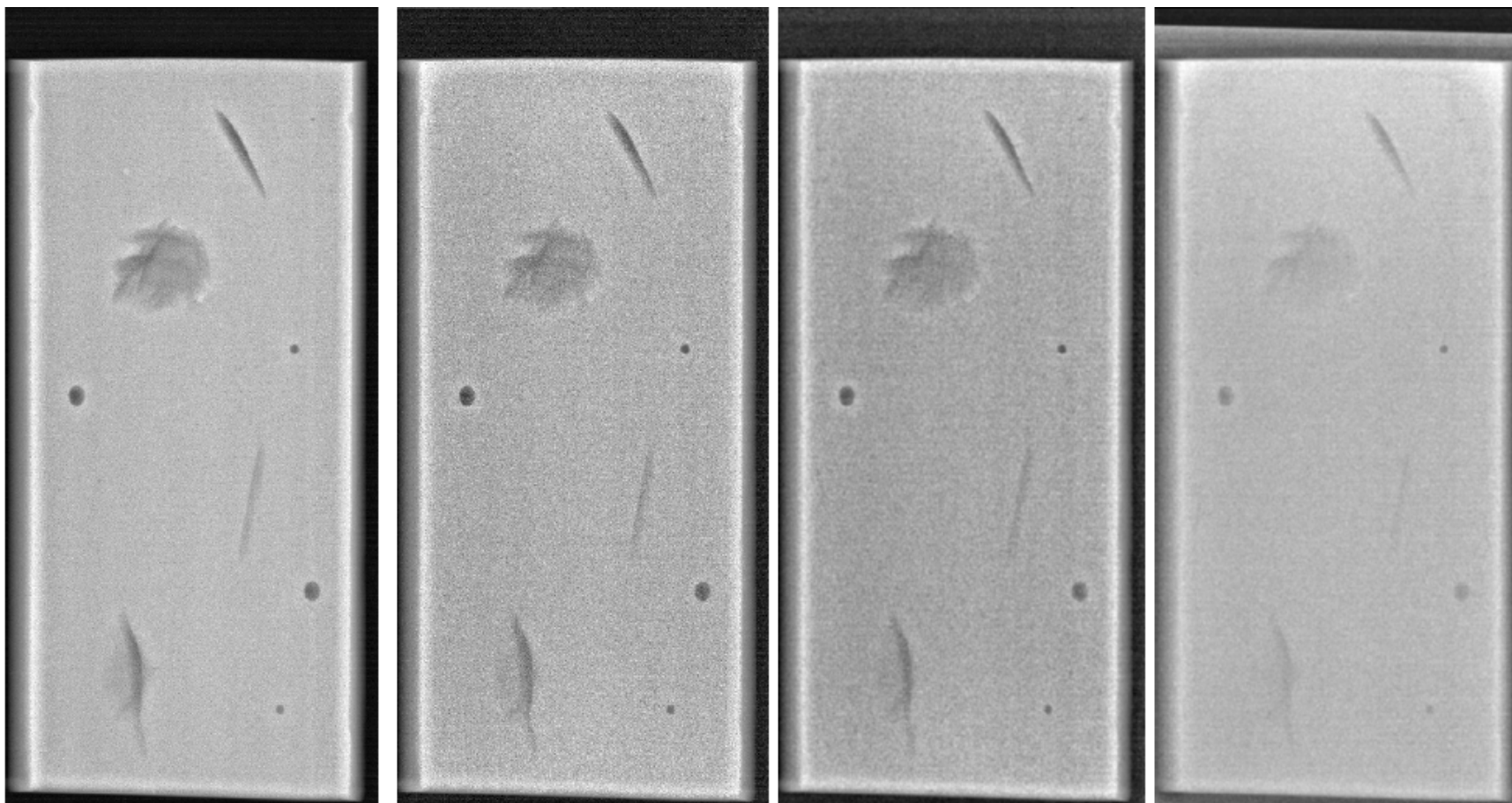
Figure 1 shows images for the 12 inch diameter Driscoplex pipe for a baseline case with no overlay and for aluminum plate overlays with thicknesses of 0.125", 0.1875" and 0.250", respectively. Figure 2 through Figure 5 present line profiles for these four cases. The line profile is for the cut shown by the dashed line in Figure 30 which crosses through two defects. From the images in Figure 1 and the line profiles in Figure 2 through Figure 5, the image results remain quite good up through 0.1875" (3/16") thick aluminum. At 1/4" thick aluminum, there is significant degradation in image quality.

Figure 6 shows images for the 24 inch diameter steel pipe for a baseline case with no overlay and for aluminum plate overlays with thicknesses of 0.125", 0.1875" and 0.250", respectively. Figure 7 through Figure 10 present line profiles for these four cases. The line profile is for the cut shown by the dashed line in Figure 25 and Figure 6 which crosses through one defect. From the images in Figure 6 the image results remain good up through 0.1875" (3/16") thick aluminum. At 1/4" thick aluminum, there is significant degradation in image quality. From the line profiles, this significant defect is clearly visible even through 1/4" aluminum. However, the fractional decrease in contrast for this defect falls almost in half in going from 0.1875" to 0.250" thick aluminum.

Figure 11 shows images for the 12 inch diameter Driscoplex pipe for a baseline case with no overlay and for carbon composite plate overlays with thicknesses of 0.03125", 0.0625" and 0.125", respectively. Figure 12 through Figure 15 present line profiles for these four cases. The line profile is for the cut shown by the dashed line in Figure 30 and Figure 11 which crosses through two defects. From the images in Figure 11 and the line profiles in Figure 12 through Figure 15, although there is a small, gradual decrease in image quality with increasing composite

overlay thickness, the overall image results remain quite good throughout, including for the 0.125" thick composite overlay.

Figure 16 shows images for the 24 inch diameter steel pipe for a baseline case with no overlay and for carbon composite plate overlays with thicknesses of 0.03125", 0.0625" and 0.125", respectively. Figure 17 through Figure 20 present line profiles for these four cases. The line profile is for the cut shown by the dashed line in Figure 25 and Figure 6 which crosses through one defect. From Figure 16, the image quality begins to decrease at around the 0.125" thick composite overlay. From the line profiles, this significant defect is clearly visible even through the 0.125" thick composite. However, the fractional decrease in contrast for this defect falls almost in half while going from 0.0625" to 0.125" thick composite.



Baseline – no overlay

0.125" Al plate overlay

0.1875" Al plate overlay

0.250" Al plate overlay

Figure 1. Images for the 12 inch diameter yellow Driscoplex pipe with different thicknesses of aluminum plate overlays.

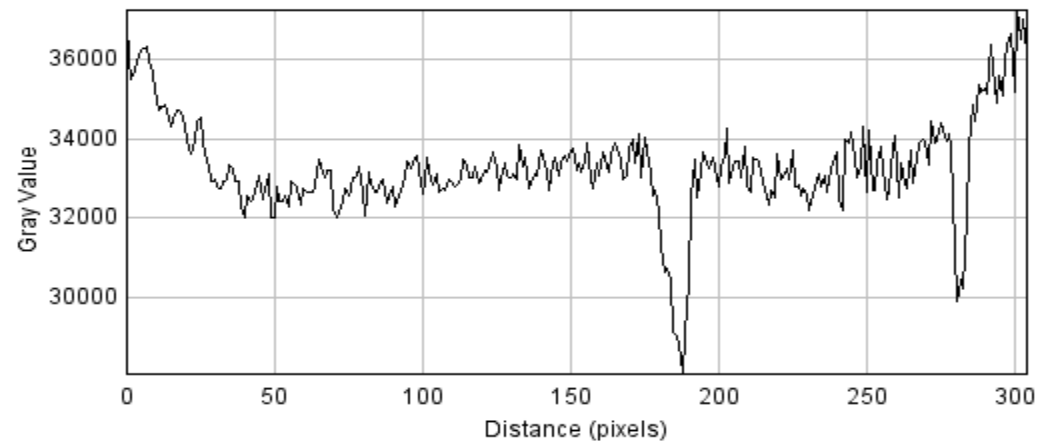


Figure 2. Line profile 12 inch diameter yellow Driscopex pipe for baseline case (no overlay).

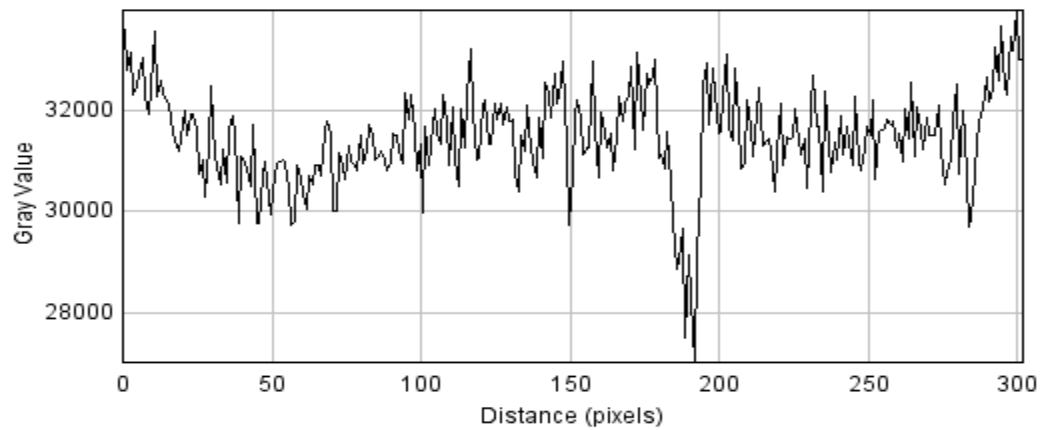


Figure 3. Line profile for 12 inch diameter Driscopex pipe case with 0.125" thick Al plate overlay.

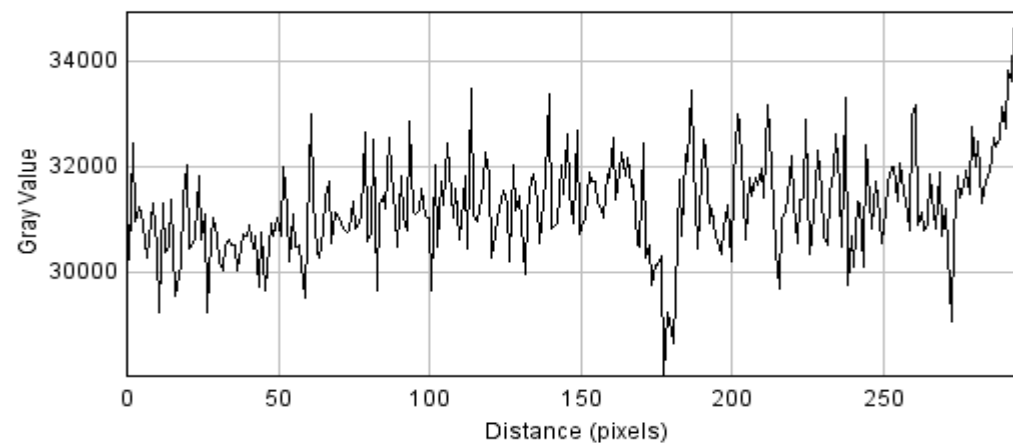


Figure 4. Line profile for 12 inch diameter Driscoplex pipe case with 0.1875" thick Al plate overlay.

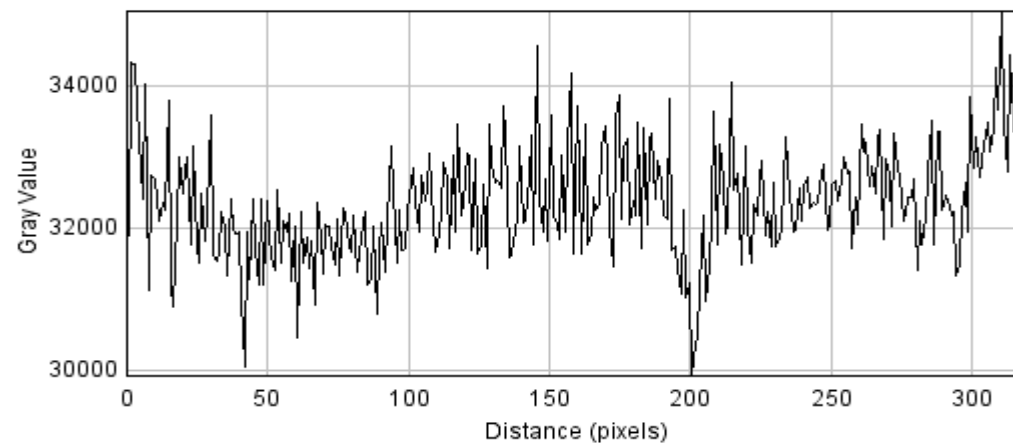
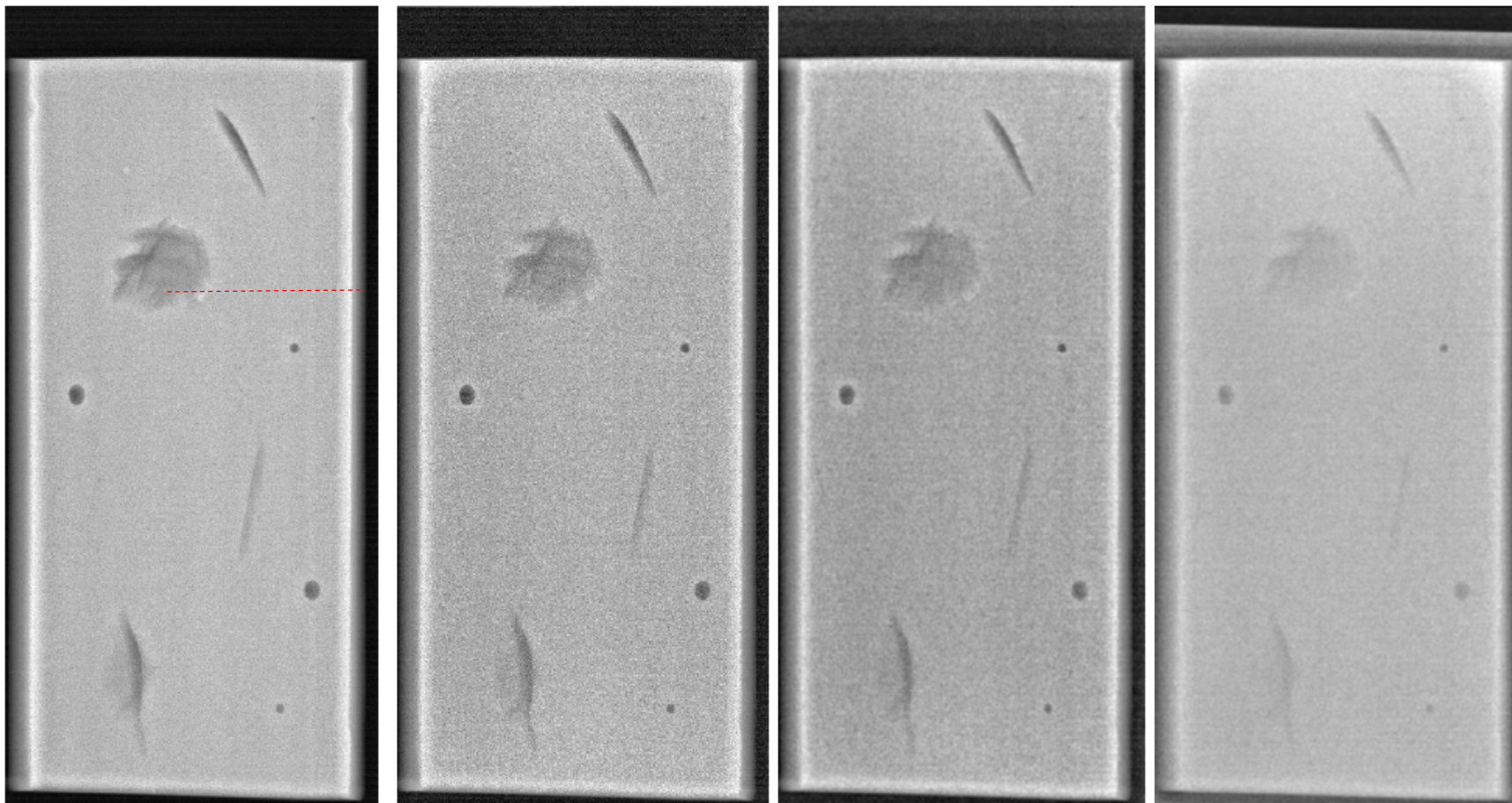


Figure 5. Line profile for 12 inch diameter Driscoplex pipe case with 0.250" thick Al plate overlay.



Baseline – no overlay

0.125" Al plate overlay

0.1875" Al plate overlay

0.250" Al plate overlay

Figure 6. Images for the 24 inch diameter steel pipe with different thicknesses of aluminum plate overlays.

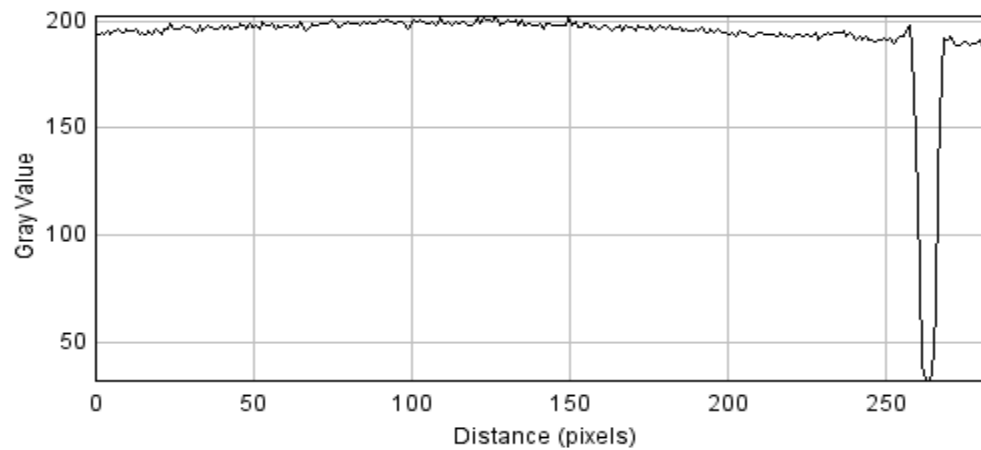


Figure 7. Line profile for the 24 inch diameter steel pipe baseline case (no overlay).

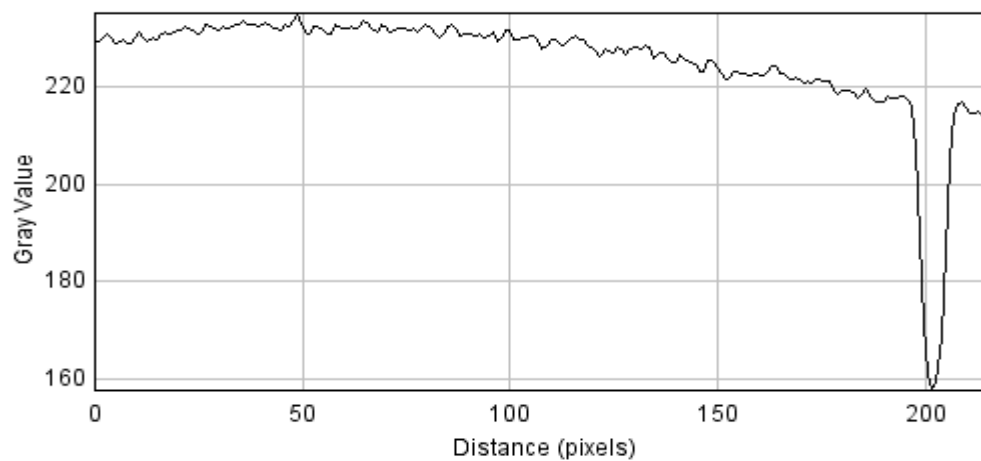


Figure 8. Line profile for the 24 inch diameter steel pipe case with 0.125" thick Al plate overlay.

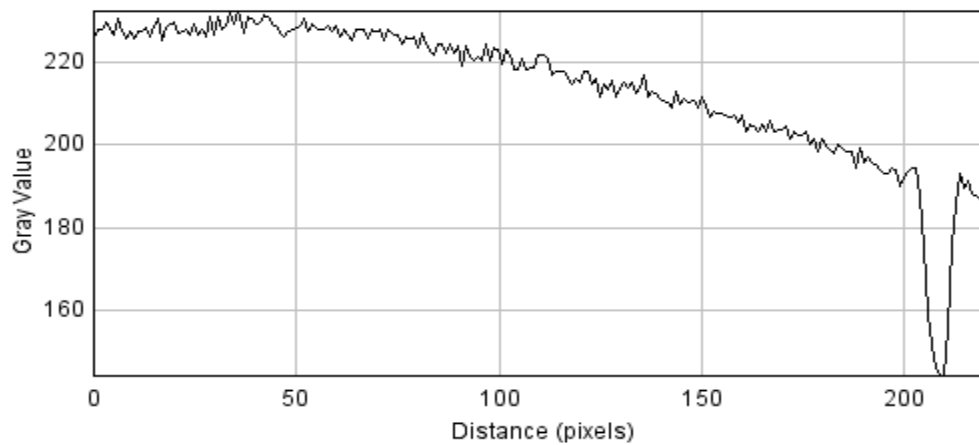


Figure 9. Line profile for the 24 inch diameter steel pipe case with 0.1875" thick Al plate overlay.

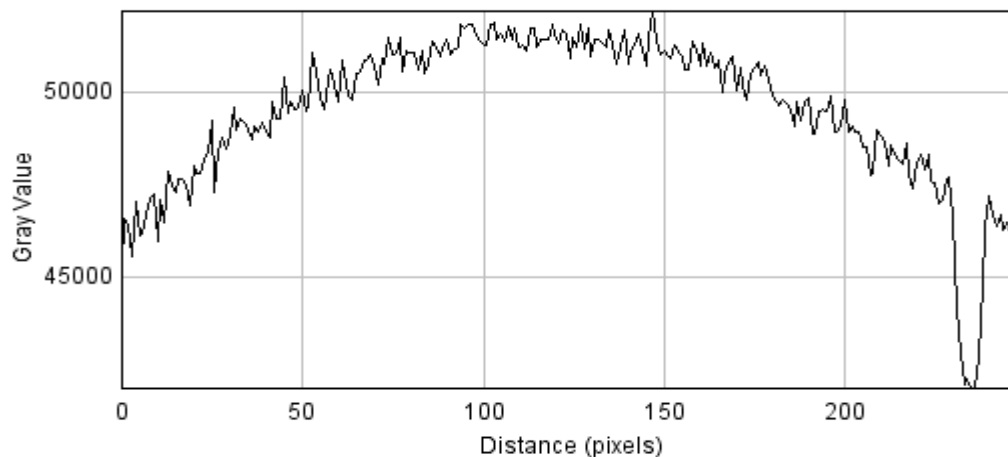
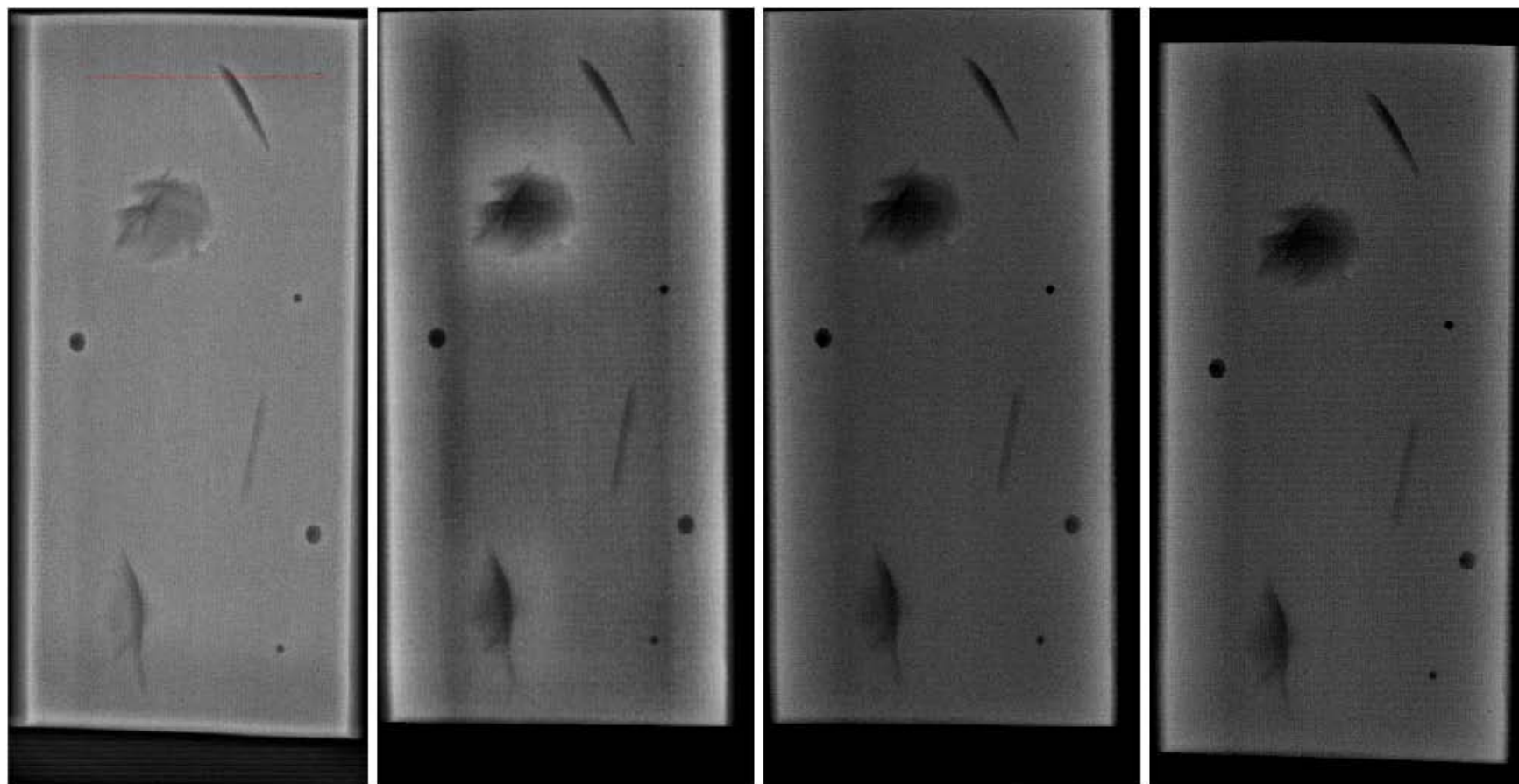


Figure 10. Line profile for the 24 inch diameter steel pipe case with 0.250" thick Al plate overlay.



Baseline – no overlay 0.03125" C composite overlay 0.0625" C composite overlay 0.125" C composite overlay
Figure 11. Images for the 12 inch diameter yellow Driscoplex pipe with different thicknesses of carbon composite overlays.

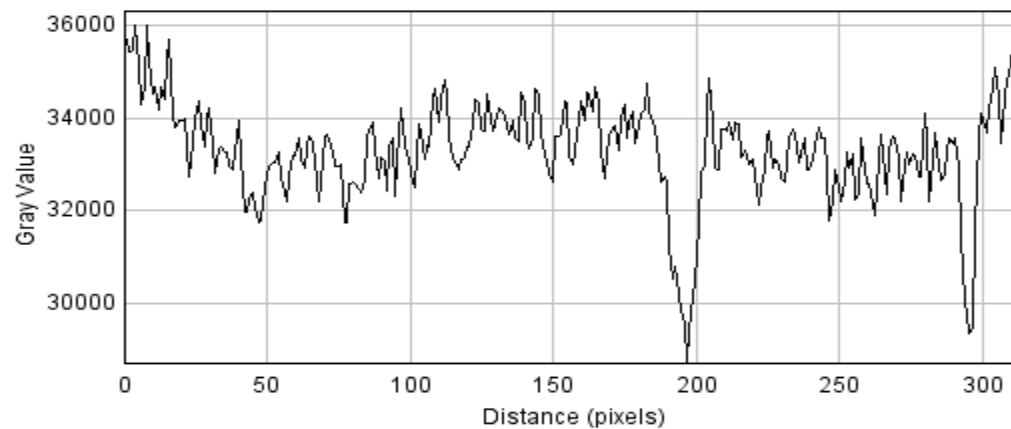


Figure 12. Line profile for 12 inch diameter yellow Driscoplex pipe baseline case (no overlay).

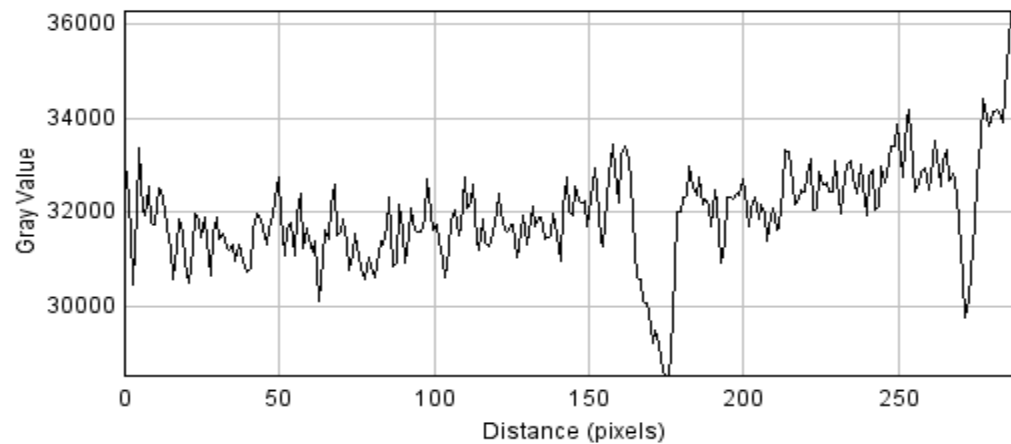


Figure 13. Line profile for 12 inch diameter Driscoplex pipe case with 0.03125" thick C composite overlay.

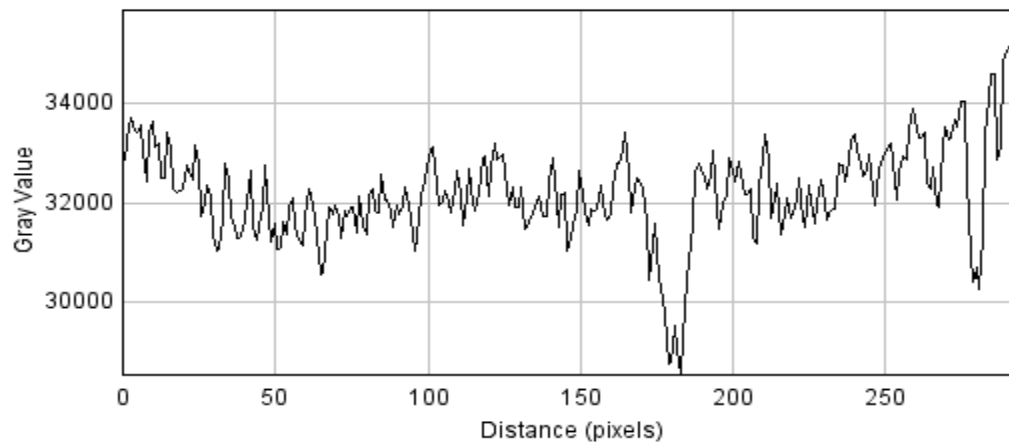


Figure 14. Line profile for 12 inch diameter Driscoplex pipe case with 0.0625" thick C composite overlay.

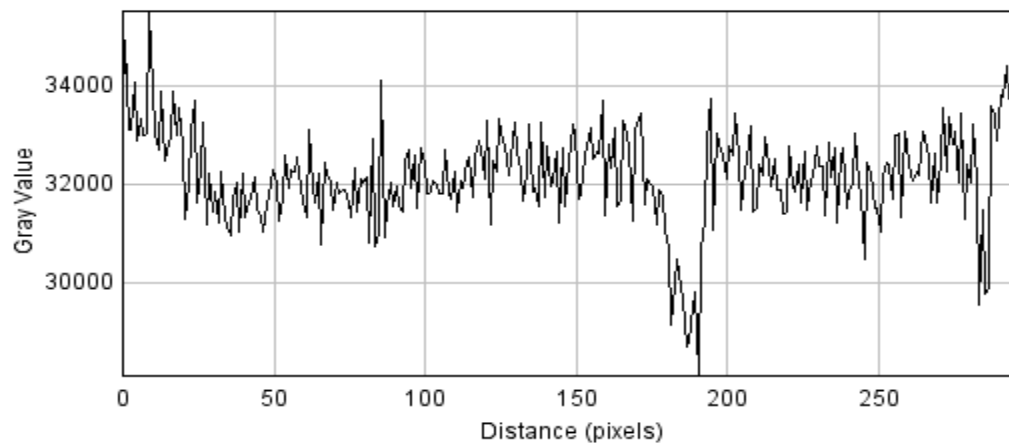
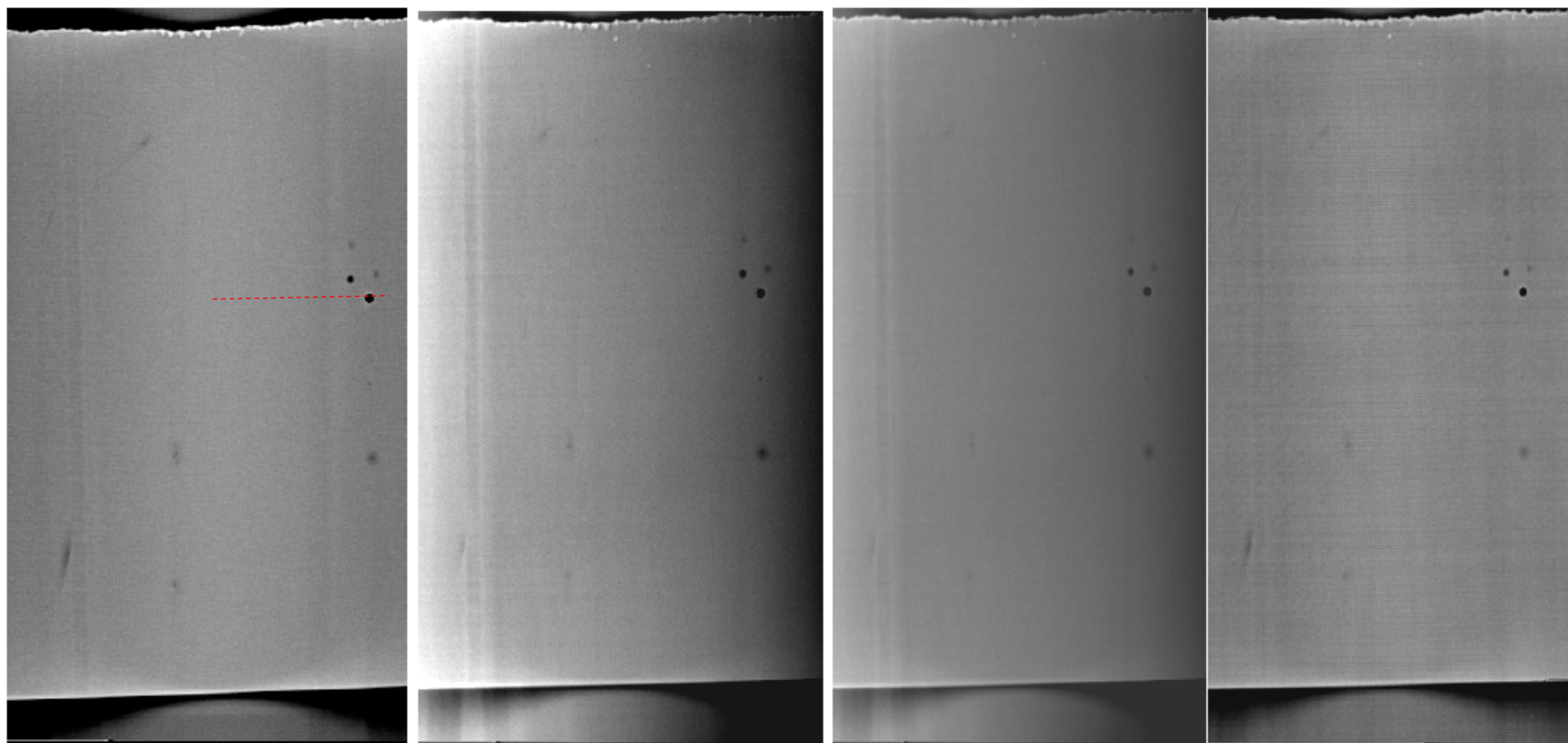


Figure 15. Line profile for 12 inch diameter Driscoplex pipe case with 0.125" thick C composite overlay.



Baseline – no overlay

0.03125" C composite overlay

0.0625" C composite overlay

0.125" C composite overlay

Figure 16. Images for the 24 inch diameter steel pipe with different thicknesses of carbon composite overlays.

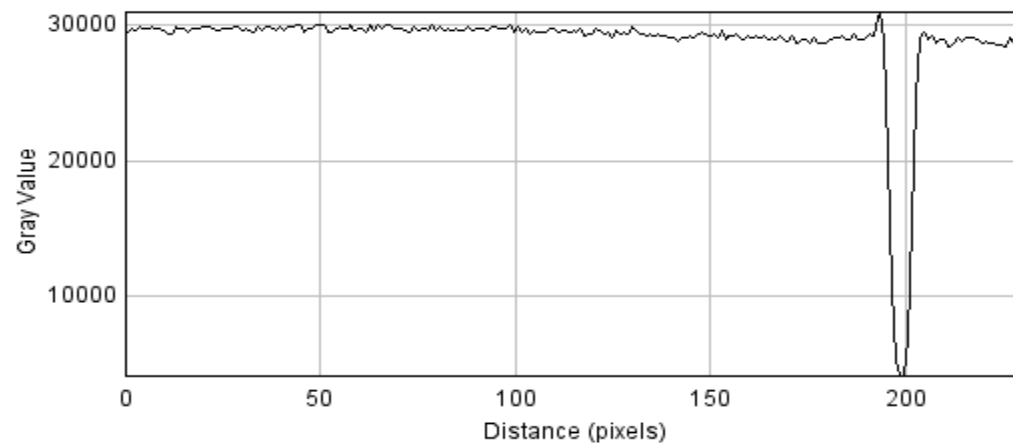


Figure 17. Line profile for the 24 inch diameter steel pipe baseline case (no overlay).

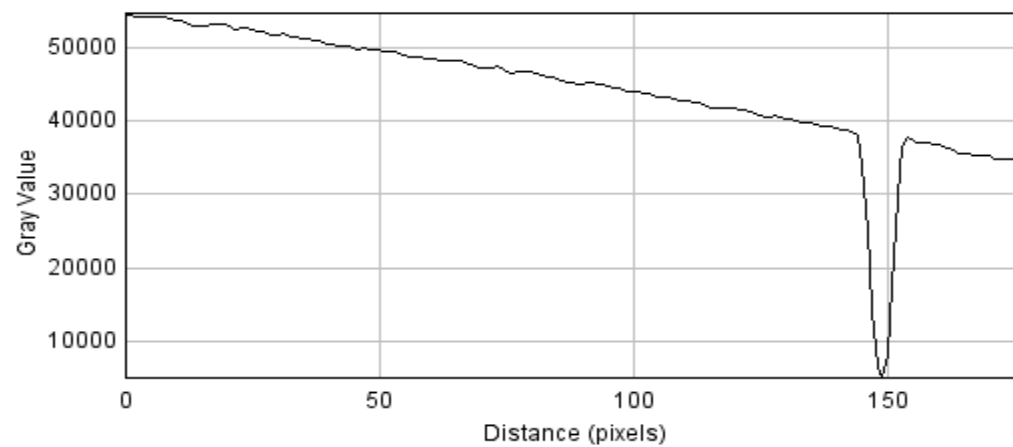


Figure 18. Line profile for the 24 inch diameter steel pipe case with 0.03125" thick C composite overlay.

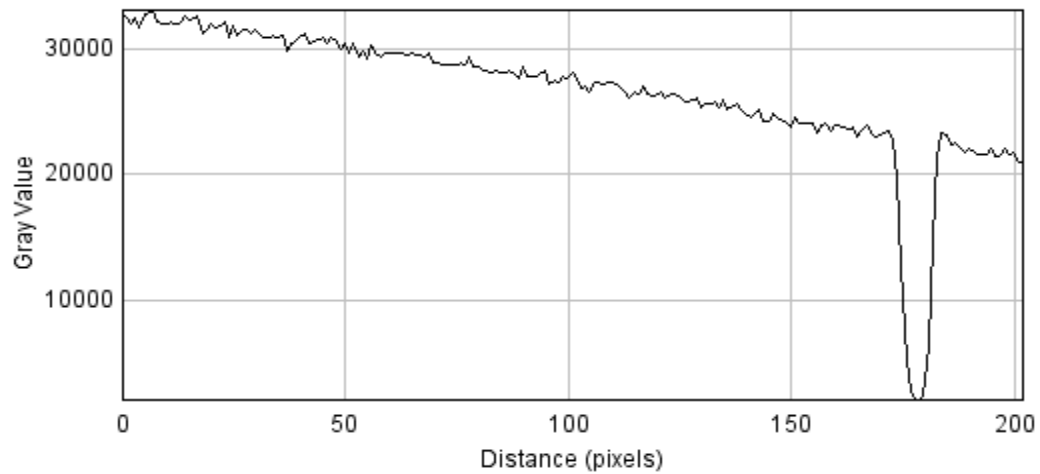


Figure 19. Line profile for the 24 inch diameter steel pipe case with 0.0625" thick C composite overlay.

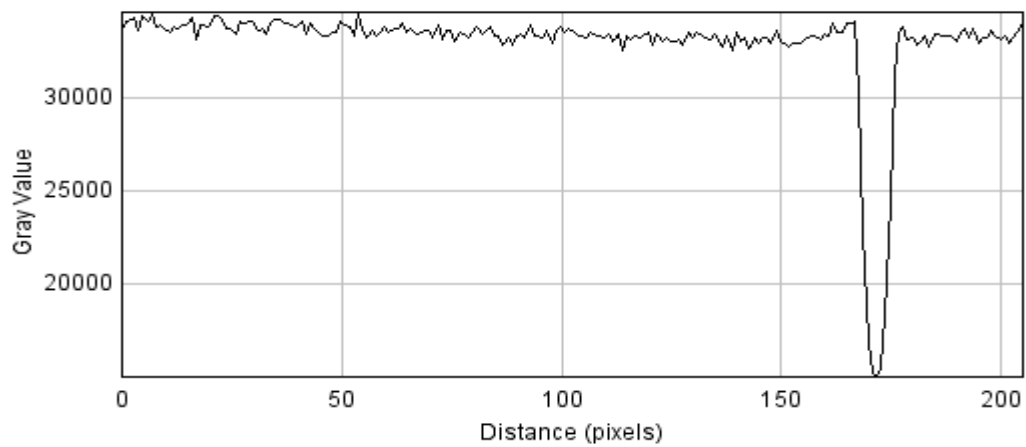


Figure 20. Line profile for the 24 inch diameter steel pipe case with 0.125" thick C composite overlay.

Housing Review Summary

The tool housing study evaluated the affects of two different types of potential housing materials, carbon fiber composite and aluminum. Either material would make a good housing for the device. The housing material type should be selected based upon tool application considering the following pros and cons.

The carbon fiber thicknesses of 1/32, 1/16, and 1/8 inch were evaluated. The actual thickness required for the housing would depend upon the application for which the tool was developed. The carbon fiber composite is a good candidate for housing material because it attenuates the backscatter signal less, provides better signal to noise for large flaws, and has good thermal and strength properties for housing in comparison to aluminum. It should noted the carbon fiber composite (CFC) used for the analysis was an off the shelf, relatively large weave CFC. The large weave pattern does become visible in the images especially at wall thicknesses approaching 1/8 inch. The weave pattern may make it difficult to resolve very small defects, however this may not be an issue for many applications. The CFC housing is more complex to design and will cost more than an aluminum housing even in large scale production.

Aluminum of 1/16, 1/8 and 1/4 inch was tested as potential housing material. A housing made from aluminum would have to be thicker than a comparable housing made from CFC. While the aluminum attenuated the signal from defects in the pipe about 10 percent more than aluminum for the same given thickness, the aluminum is smooth and does not superimpose a pattern on the image, reducing the background noise in the image. This would be very useful for analyzing small flaws and defects.

RESULTS AND DISCUSSION

Pipeline Inspection Experimental Results

Introduction

The previous section of the report focused on development of specifications and analysis of individual components for optimization of the RSD system. This section of the report will focus on summarizing the results utilizing the RSD system in scanning numerous pipeline samples of both metallic and non-metallic materials. These scans using optimized parameters and commercial off the shelf components are critical in determining the baseline feasibility of utilizing the RSD system for wellbore casing inspection and transmission pipeline NDE applications. These baseline results, in conjunction with the individual system component analysis and housing material analysis, were utilized to develop the conceptual engineering models discussed later in this section.

A variety of pipe samples were obtained for baseline imaging, both metallic and non-metallic. Figure 21 shows three different types of poly pipe. The samples consist of 8 inch diameter high density polyethylene (HDPE) pipe (left), 6 inch diameter polyamide 12 (PA12) (center), and 12 inch diameter medium density polyethylene (MDPE) pipe (right). These samples were used to determine the effectiveness of x-ray backscatter imaging on different types of poly pipe. Unlike transmission radiography that generates image contrast from photoelectric absorption and x-ray attenuation, x-ray backscatter imaging relies on Compton scatter to generate the images. Compton scatter causes blurring and loss of contrast and resolution for transmission radiography, but the low molecular weight materials used in poly actually enhance the x-ray backscatter images. These types of poly pipe are ideally suited for x-ray backscatter imaging.



Figure 21. Poly pipes include a combination of polyethylene and polyamide pipes: (left) 8 inch diameter Polypipe, HDPE, 3408; (center) 6 inch diameter, Polyamide 12, SDR 11; (right) 12 inch diameter, DriscoPlex 6500 PE 2406, MDPE.

Steel Pipe (Casing and Transmission Applications)

Figure 22 shows a sample of 24 inch diameter, ¼ inch thick steel piping. Both the poly pipe and steel pipe samples have defects. These samples are used for preliminary scans to demonstrate x-ray backscatter imaging capability. Corrosion byproduct and other materials can also be placed on the pipe surfaces to demonstrate x-ray backscatter capabilities of indentifying different types of corrosion. Higher energy will be required to penetrate the steel to find defects, corrosion and pipe loss. The current x-ray backscatter system is limited to 160 kV. A 225 kV system will be required to image through heavier gauge pipe than shown in Figure 22.



Figure 22. 24 inch diameter steel pipe (left) sample 1, internal defects; (right) sample 2, external defects.

Figure 23 shows the experimental setup for x-ray backscatter images in Figure 24. These are preliminary scans to determine the x-ray energy required for imaging defects through ¼ inch of steel. The x-ray backscatter used for generating the images has the following system specifications:

- Comet 160 kV MXR160HP/11 x-ray tube
- Spellman 160 kV high voltage generator
- 1 mm illumination beam tube apertures
- Rotating collimator with maximum rotational speed of 200 RPM
- Linear rail travel system with a maximum linear translation speed of 7 feet per minute
- PVT detectors 18" x 2" x 12" inches

The ID of the pipe section was positioned about 18 to 20 inches from the x-ray backscatter system. Several scans were taken at different generator kV settings. Defects on the outside diameter of the steel pipe begin to have significant contrast at 160 kV. Some of the smaller and shallow defects are not visible; Figure 24 shows a few of the external pipe defects. Figure 25 and Figure 26 show the steel pipe external defects after further optimization. All but the two

smallest holes imaging from the inside out on the 24 inch diameter steel pipe are now visible. Figure 27 shows imaging results for the 24 inch diameter pipe with internal defects. Increasing the x-ray source to 225 kV over the current 160 kV may increase the probability of the detection on the smallest defects.

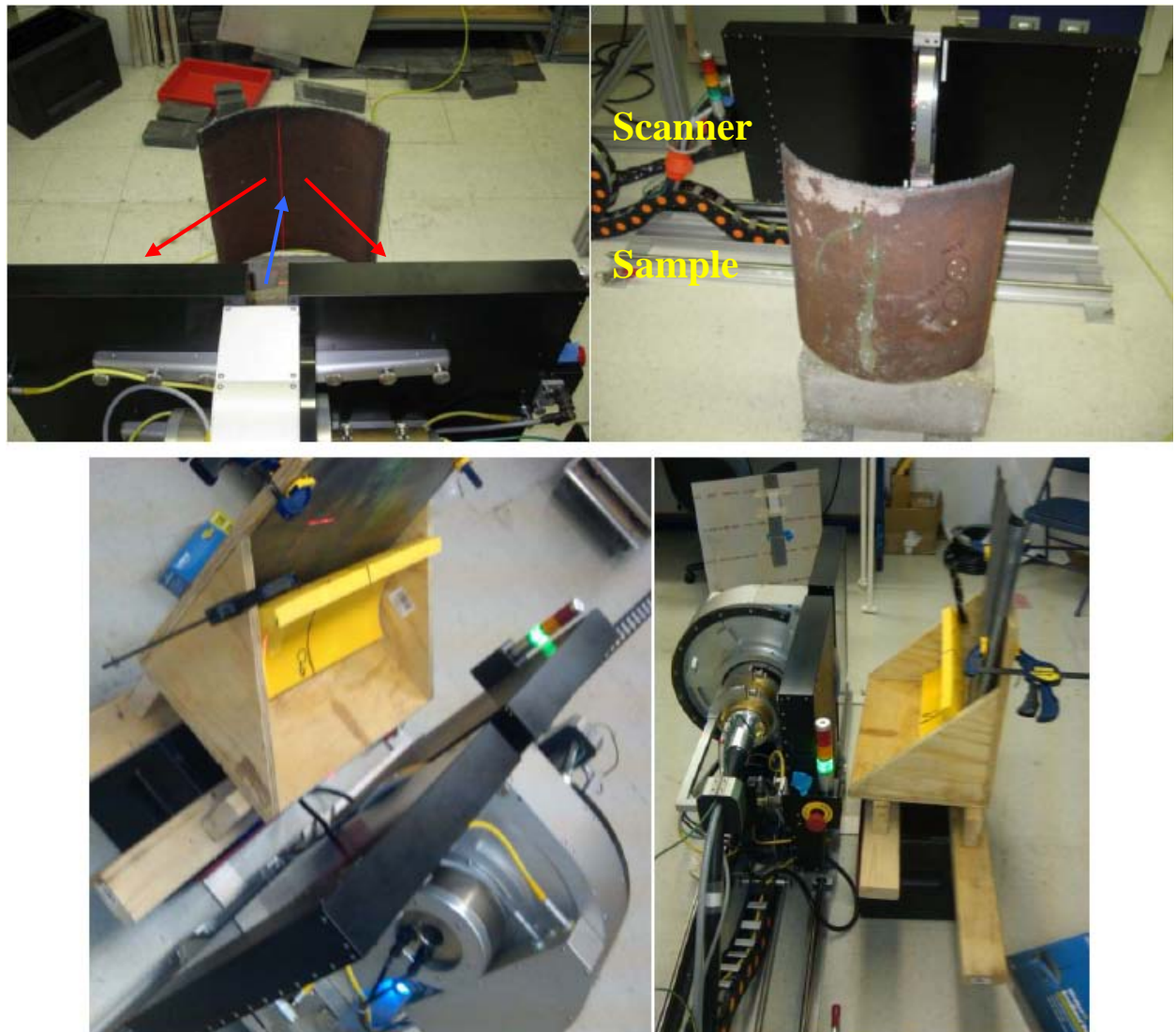


Figure 23. Experimental setup for preliminary scanning. The x-ray beam sweeps across the sample and scatters back to the detectors.

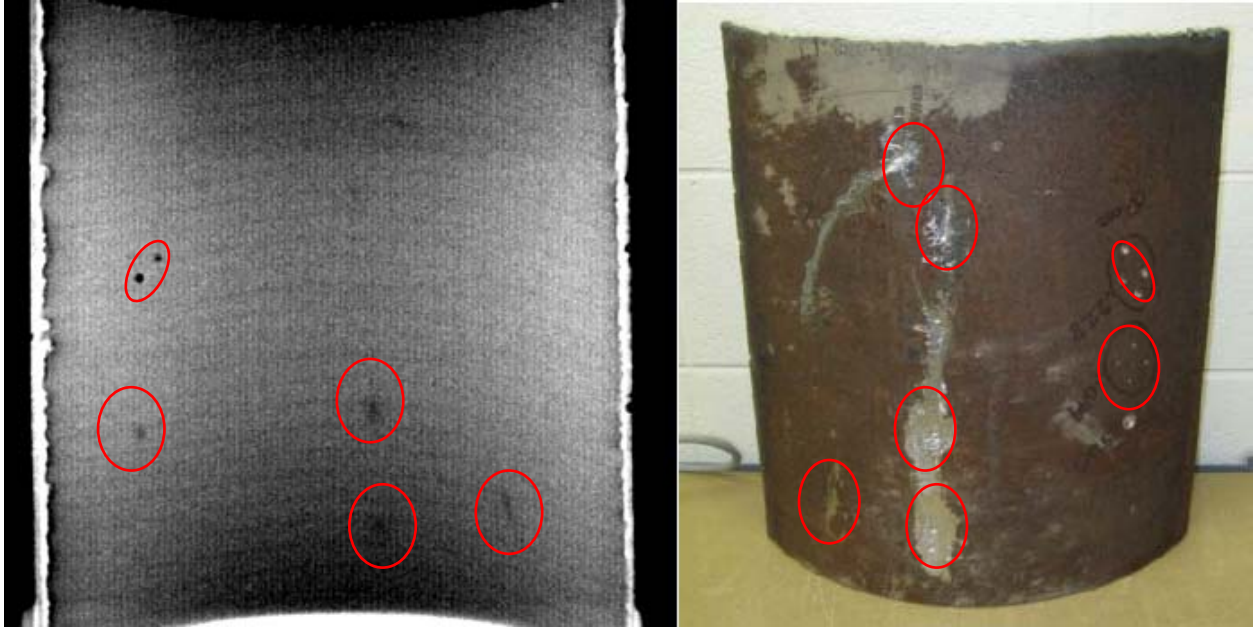


Figure 24. Sample scan of $\frac{1}{4}$ inch wall steel pipe, external defects, 160 kV. Note the pipe was imaged from inside out so the defects are mirror imaged.



Figure 25. Sample scan of $\frac{1}{4}$ inch wall steel pipe, external defects, 160 kV. Note the pipe was imaged from inside out so the defects are mirror imaged.

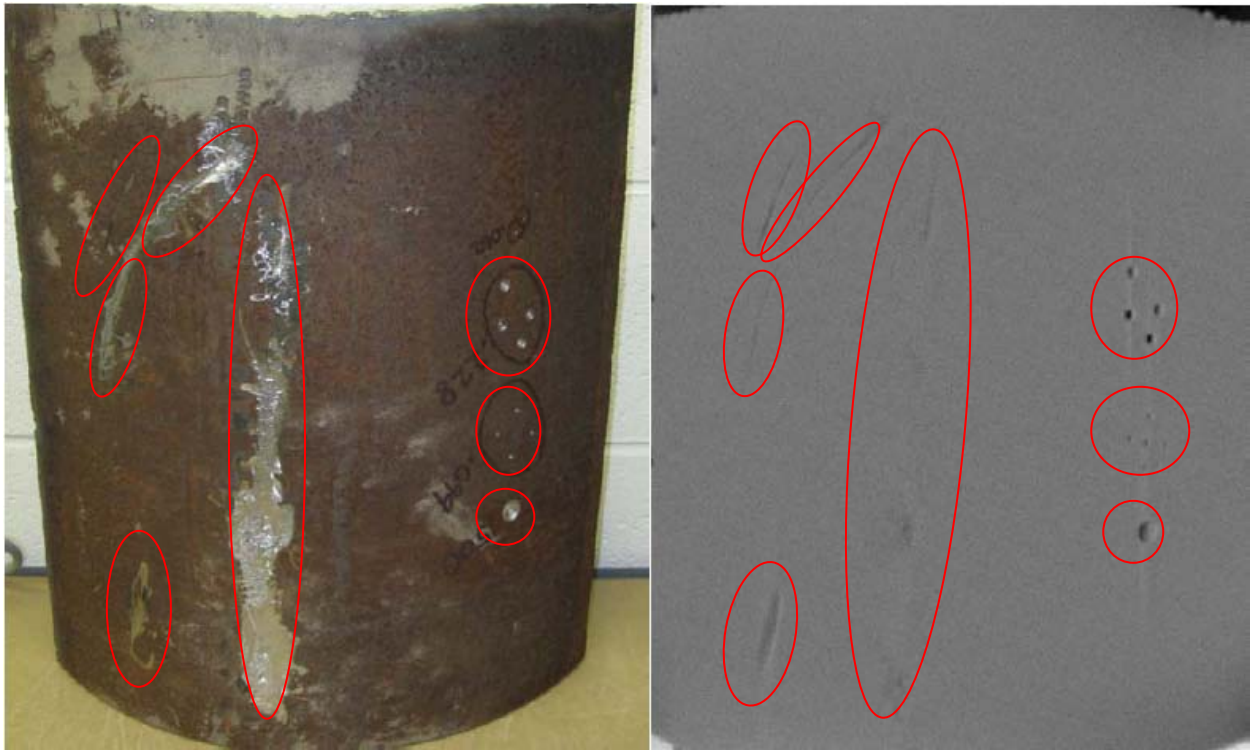


Figure 26. Sample scan of 1/4 inch wall steel pipe, 160 kV; similar to Figure 7-4 with additional optimization.

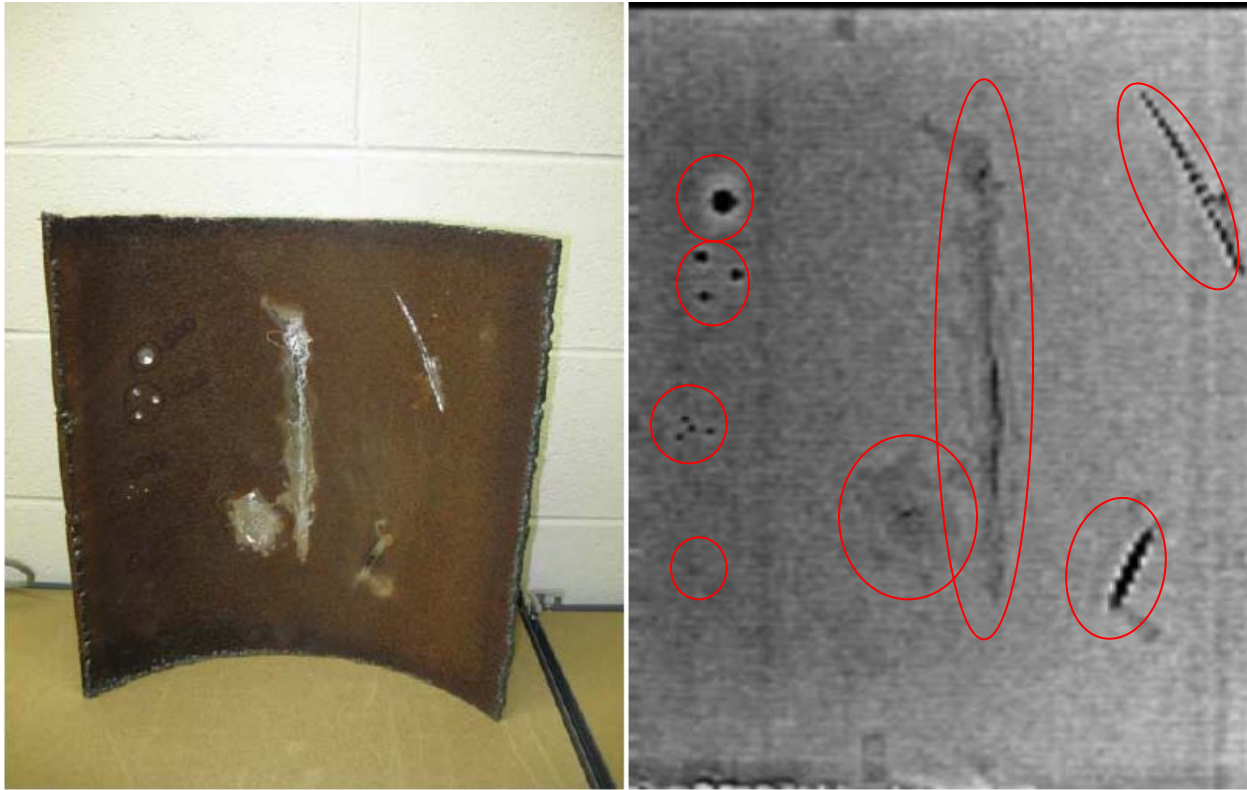


Figure 27. Sample scan of 1/4 inch wall steel pipe, internal defects, 160 kV.

Poly Pipe

Poly Pipe Material Testing

Figure 28 shows the sample and imaging results for 6 inch diameter polyamide pipe. The sample was imaged from the inside out, and anomalies on both sides of the pipe can easily be seen. This means an instrument can be run down the center of a pipe and detect anomalies on both the inside and outside of a pipe. Poly pipes are highly favorable for x-ray backscatter imaging because x-ray backscatter images are generated predominately by Compton scattered x-rays. The polymer hydrocarbon chains are easily penetrated by x-rays and generate a very strong x-ray backscatter signal. All anomalies on both the inside and outside of the pipe are easily seen. One of the great of advantages of having fully digital x-ray images is the ability to adjust window, level, contrast, change lookup tables or any other combination of digital image processing that is available on the open market.

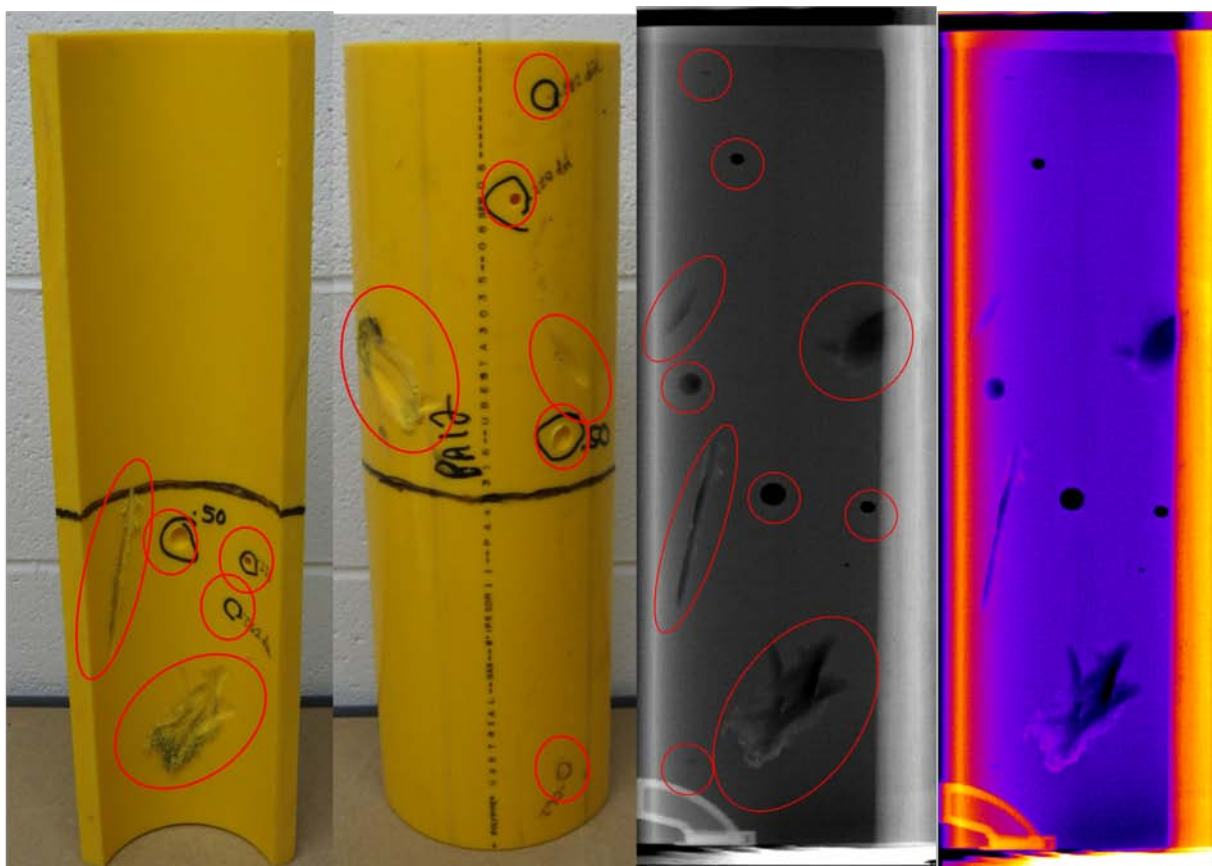


Figure 28. Sample RSD scan of polyamide 12, SDR11, 6 inch diameter pipe.

Figure 29 shows the sample and imaging results for a 12 inch diameter medium density polyethylene pipe. The sample was imaged from the inside out, and anomalies on both sides of the pipe can easily be seen. The gash on the outside of the pipe is estimated to be less than 10 percent wall loss and is easily visible by imaging from the inside of the pipe. The standoff for the imaging of the pipe was approximately 20 inches. Because the instrument is going to be designed to run down the center of the pipes, the standoff is expected to be less than 20 inches in the majority of scenarios. Figure 30 shows a scan of the same pipe performed at a higher speed, but at a smaller pixel size.

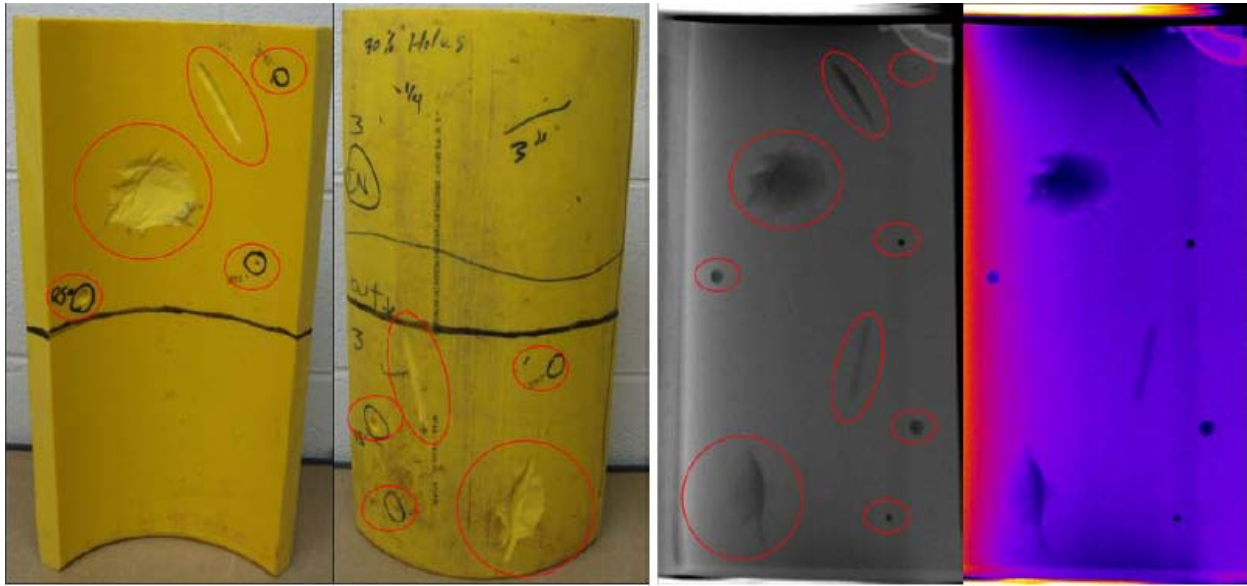


Figure 29. Sample RSD scan of MDPE, 12 inch diameter, DriscoPlex 6500 PE 2406 (1 mm pixels and 2.469 ms/pixel).

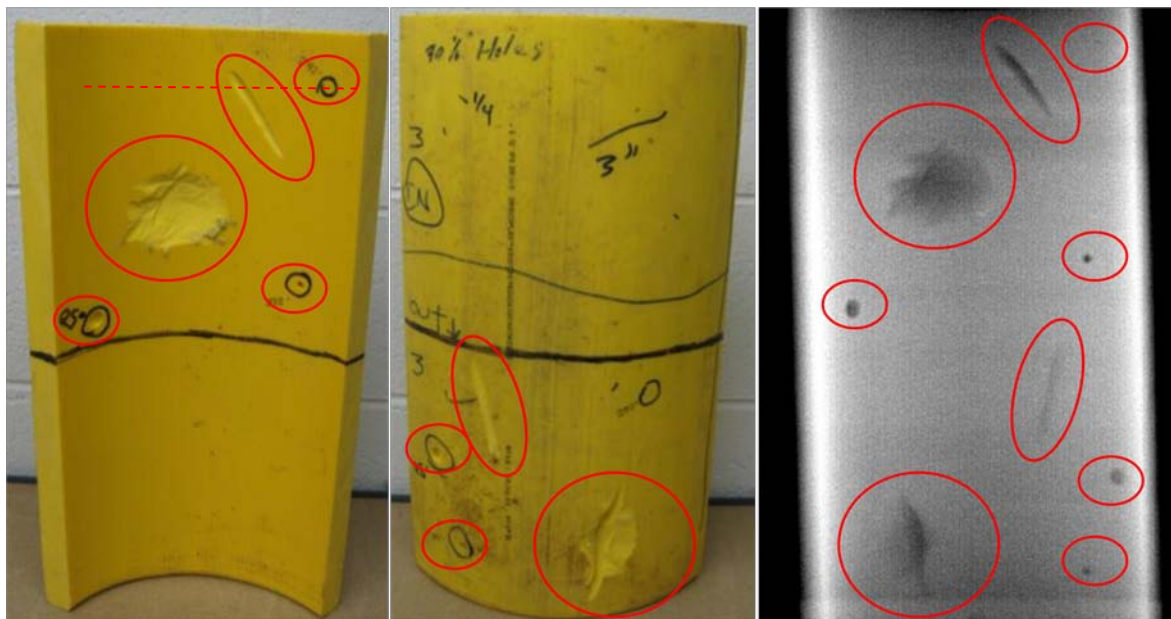


Figure 30. Sample RSD scan of MDPE, 12 inch diameter, DriscoPlex 6500 PE 2406 (0.5 mm pixels and 0.2778 ms/pixel).

Figure 31 shows the sample and imaging results for an 8 inch diameter HDPE pipe. All defects are easily detected even in the HDPE polyethylene pipe.



Figure 31. Sample RSD scan of 8 inch diameter Polypipe, HDPE, 3408.

The preliminary scans were performed with a rotating collimator on a linear track. The samples of pipe stood on end. The distance between the sample and the scanner was changed by sliding the samples closer to and further away from the system. Many of the future optimization scans were performed with the same scanner, but with a different motion profile setup (as shown in Figure 32). In this configuration the scanner is mounted on an x-y scan table. The distance to the sample on the lift table can easily be controlled. This configuration is also favorable because corrosion byproduct and water can easily be placed between the scanner and sample being analyzed.



Figure 32. Experimental setup for future scanning through water stack-up.

Butt Fusion Weld Inspection

An integral part of any non-metallic pipe system is the method used to join the system components. Proper engineering design of a system will take into consideration the type and effectiveness of the techniques used to join the piping components and appurtenances as well as the durability of the resulting joints. The integrity and versatility of the joining techniques used for polyethylene pipe allow the designer to take advantage of the performance benefits of polyethylene in a wide variety of applications. The butt weld fusion procedures have been proven to consistently produce sound fusion joints when used correctly and are recommended for the joining of polymer pipe products.

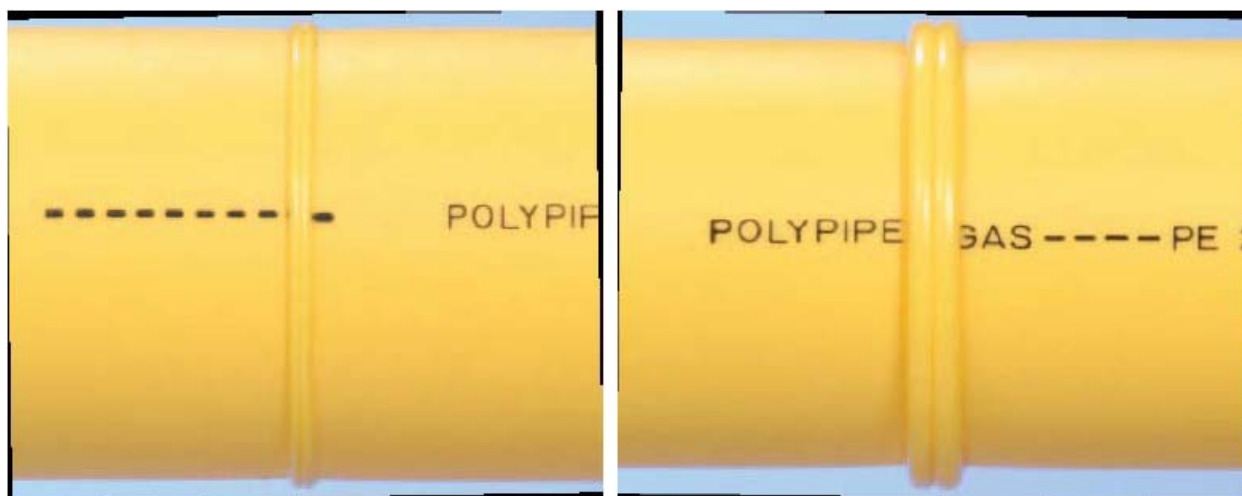
The principle behind heat fusion is to heat two surfaces to a designated temperature, and then fuse them together by application of a sufficient force. This applied force causes the melted materials to flow and mix, resulting in a permanent, monolithic fusion joint. When fused according to the recommended procedures, the fusion or joint becomes as strong as or stronger than the pipe itself in both tensile and pressure properties. Fusion procedures require specific

tools and equipment for the fusion process and pipe material and for the sizes of pipe and fittings to be joined.

The butt fusion weld technique consists of heating the squared ends of two pipes, a pipe and fitting, or two fittings by holding them against a heated plate, removing the plate when the proper melt temperature is obtained, promptly bringing the ends together and allowing the joint to cool while maintaining the appropriate applied force. Properly fused polyethylene joints do not leak. If a leak is detected during hydrostatic testing, it is possible for a system failure to occur. Figure 33 shows examples of acceptable fusion butt welds and Figure 35 shows examples of unacceptable fusion butt welds. Another issue, especially with welds performed in the field, is dust, sand, etc. penetrating into the heated pipe ends and ending up in the weld joint.



Figure 33. Acceptable butt fusion welds – proper alignment and double roll-back bead



Melt bead too small due to insufficient heat time

Melt bead too large due to excessive heating and/or over-pressurizing of joint

Figure 34. Unacceptable butt fusion welds

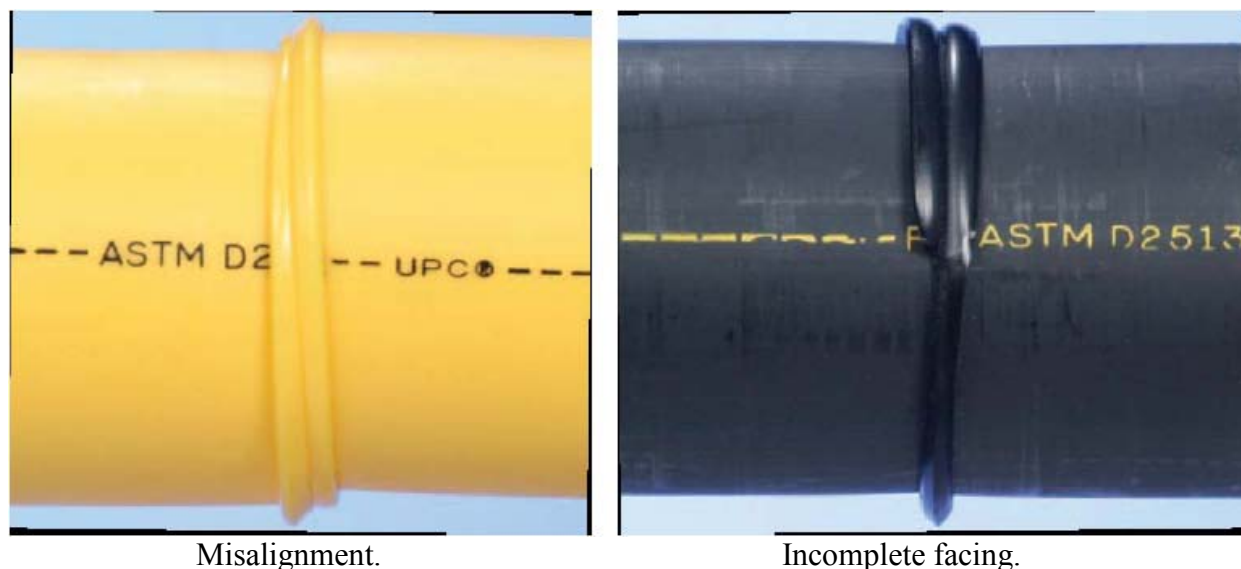


Figure 35. Unacceptable fusion butt welds.

Figure 36 shows the yellow stripe, 6 inch diameter PE3408 polyethylene sample and some SXI images. The photo shows that the fusion butt weld has a bad facing. The two pieces of pipe are also not properly aligned. The images in Figure 36 not only show that there are surface problems with the butt weld facing, but that there are also internal issues with this weld. The red circles in the images also identify the presence of some type of impurity within the weld; this feature is not visible on either the inside or outside of the weld.

The top two SXI images in Figure 37 show the same Yellowstripe, 6 inch diameter PE3408 Poly pipe sample but with a large grain of sand inserted in the inside seam of the butt weld. This grain is clearly visible in the images. The bottom image in Figure 37 shows the same impurity within the butt weld that was noted in Figure 36.

Figure 38 shows SXI images of the Yellowstripe, 6 inch diameter PE3408 Poly pipe sample with debris located on the inside of the pipe. The image on the left shows two tiny stones located on the inside of the pipe in the weld seam. The center and right images show the pipe with sand located on the inside surface of the pipe.

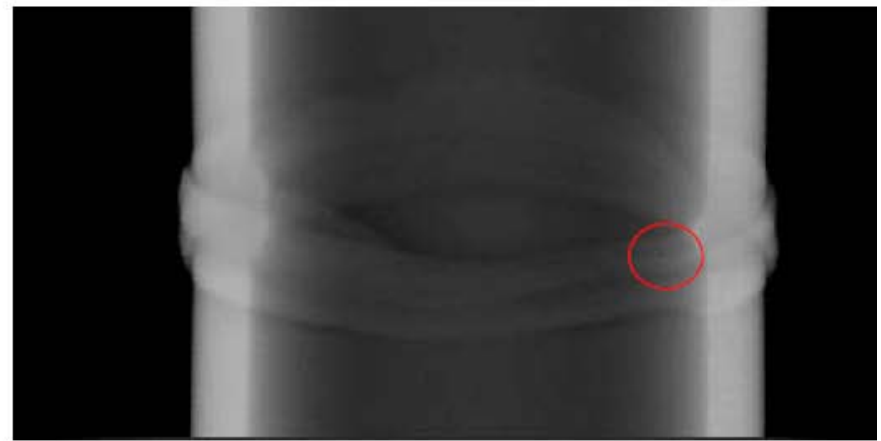
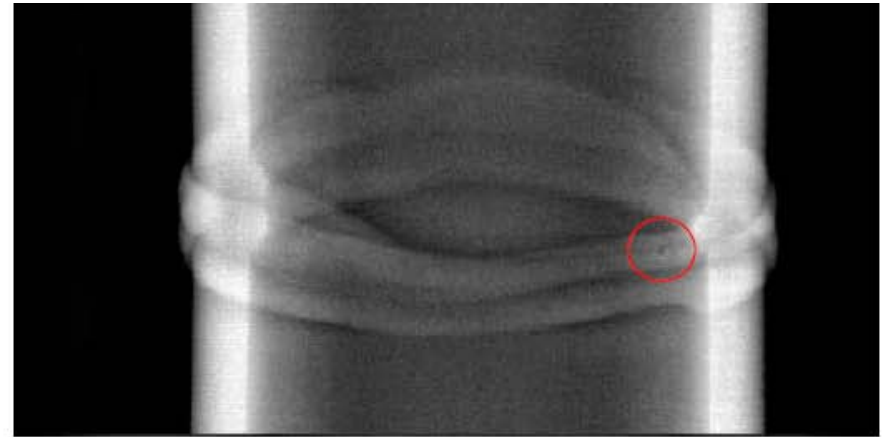


Figure 36. Yellow stripe, 6 inch diameter PE3408 polyethylene pipe sample and SXI images.

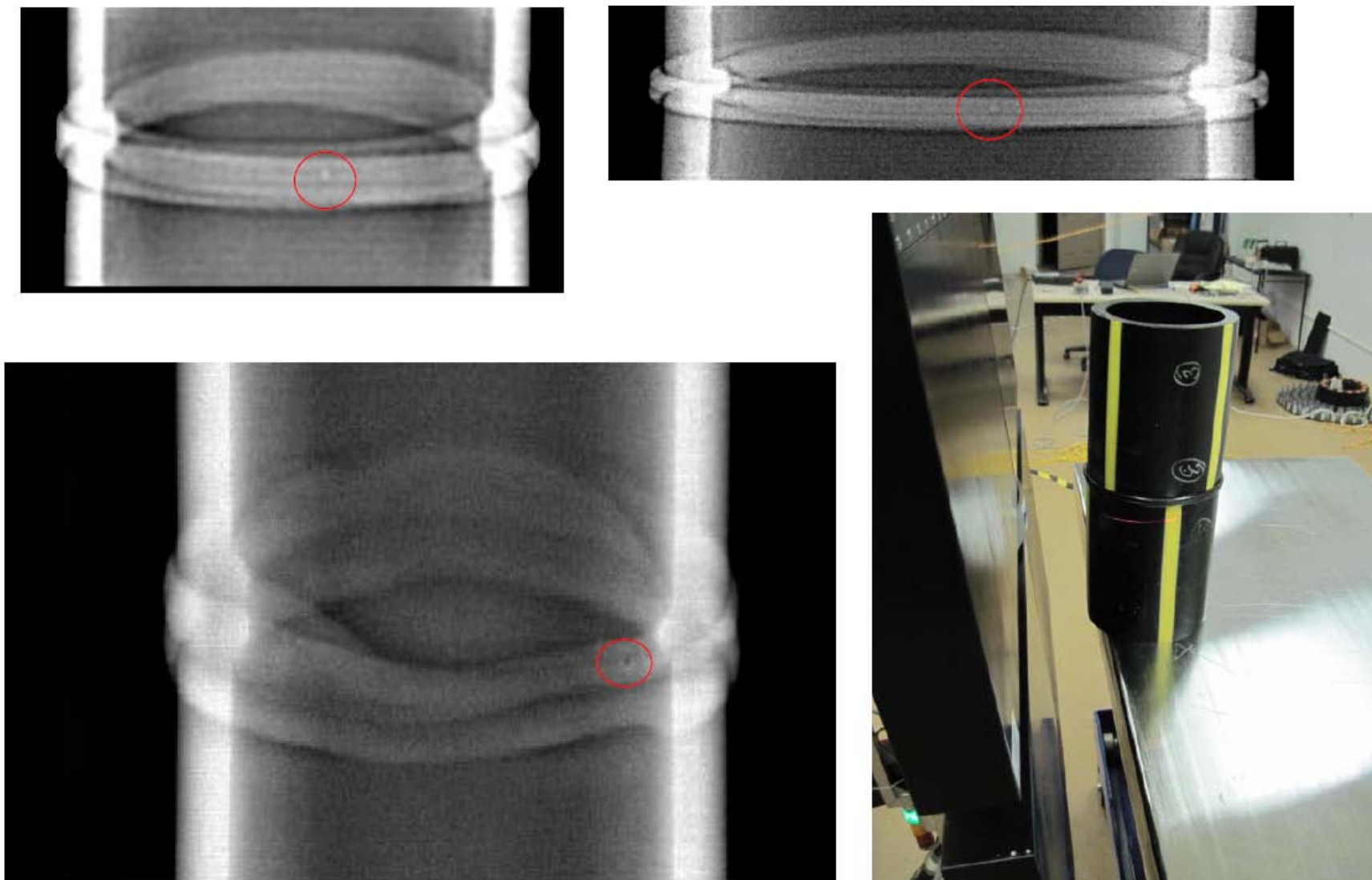


Figure 37. Yellowstripe, 6 inch diameter PE3408 Polypipe sample and some additional SXI images.

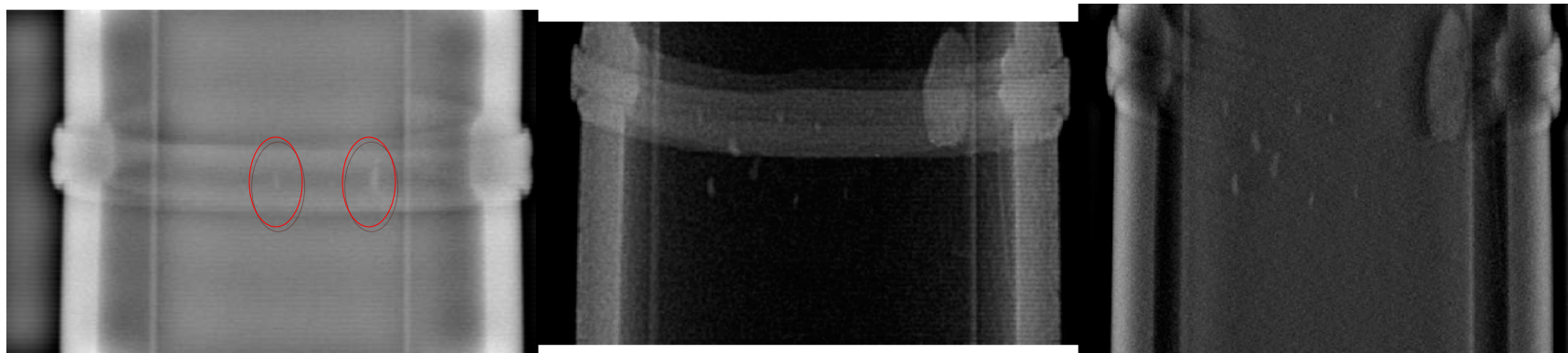


Figure 38. Yellowstripe, 6 inch diameter PE3408 Polypipe sample and SXI images with debris on the inside of the sample. Tiny stones on the inside of the weld seam (left) and sand on the inside of the pipe (center and right).

Scale and Corrosion Identification Analysis

An objective of this research effort was to analyze x-ray backscatter capabilities of performing compositional analysis of scale and corrosion, including microbial induced corrosion (MIC), on pipelines and wellbore casings. X-ray backscatter is sensitive to electron density, and scattering to absorption ratio. The scattering to absorption ratios are highly dependent upon the atomic number, Z , of each element. This means it may be possible to identify different types of scale and corrosion by the shift they induce in the x-ray backscatter spectra. In order for there to be a measured spectral shift, there needs to be an effective difference in the Z of the mixtures or compounds being identified. Figure 39 shows the spectral shift for sodium chloride, potassium carbonate, and iron. Potassium carbonate and NaCl only have an effective Z difference of about 4.4%, however, these salts were readily available for testing and calculation.

K₂CO₃ (Potassium Carbonate)

$Z_{\text{eff}} = 15.9$
 $\rho = 2.29 \text{ g/cc}$
 MW = 138.2
 $n_e = 1.586 \times 10^{23} \text{ electrons/cc}$

NaCl (common salt)

$Z_{\text{eff}} = 15.2$
 $\rho = 2.165 \text{ g/cc}$
 MW = 58.5
 $n_e = 3.388 \times 10^{23} \text{ electrons/cc}$

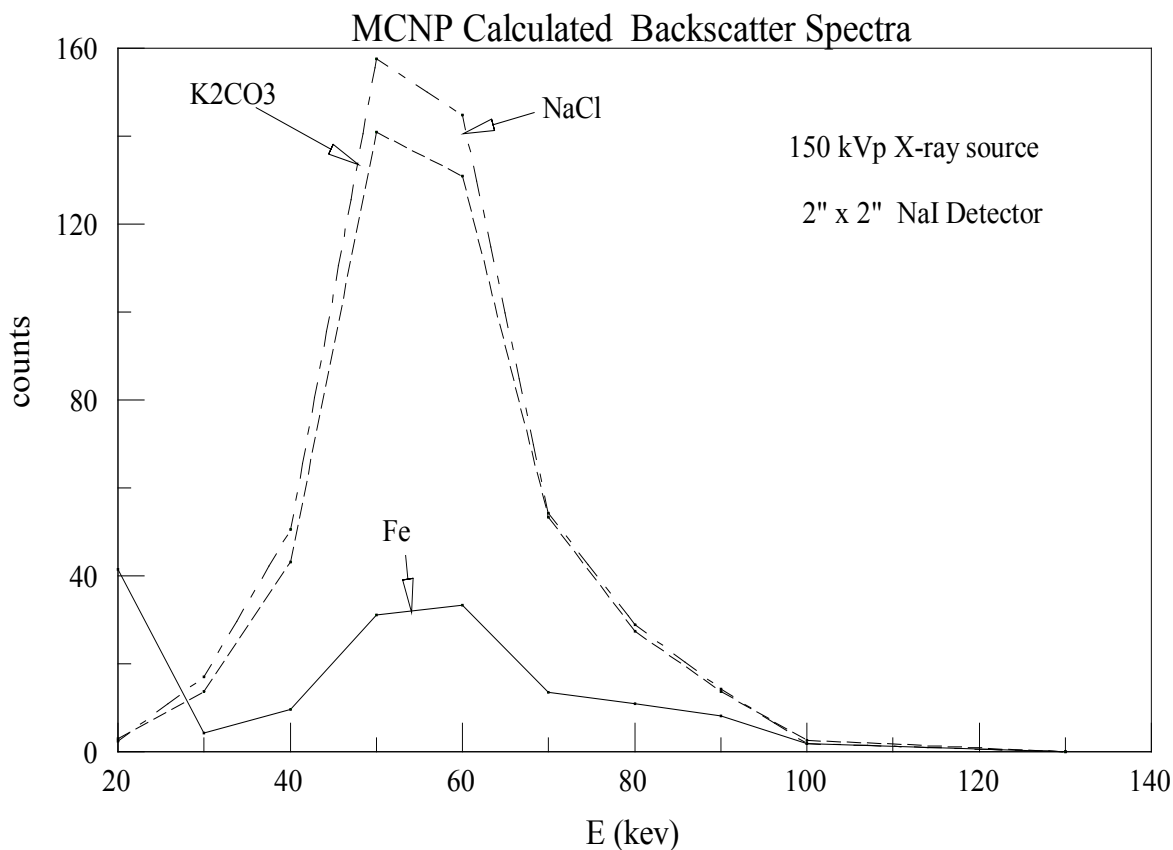


Figure 39. Calculated spectral shift from two different salts and Iron, NaCl, and K₂CO₃

Figure 40 shows the measured shift in the x-ray backscatter spectrum taken with a 2"x4" NaI detector. The backscatter spectrum is measured realtime while an x-ray backscatter image. The calculated results are confirmed with measured results, showing a total spectral shift of about 3%. It should be noted that these two salts would be difficult to separate in field measurements. However, many scale and corrosion deposits have vastly different effective Zs. Examples of common scale deposits with widely varying effective Zs are barium sulfate and calcium carbonate. Actual field samples of scale and corrosion where not made available during the project, so the values in Figure 41 are expected calculated values. It is expected that scales with different effect Z values will be disinguishabled during the image scannig processes by analysing the backscatter spectral shift.

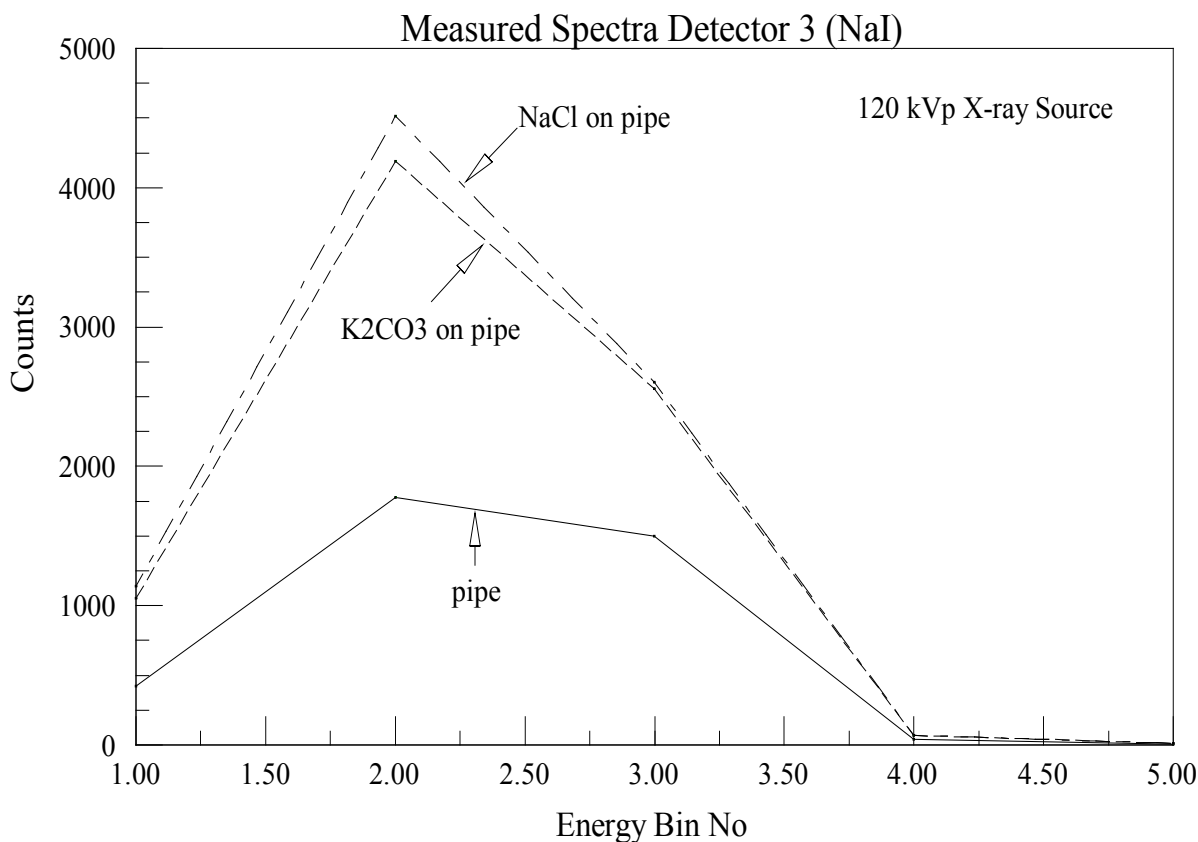


Figure 40. Measured x-ray backscatter spectrum using NaI detectors

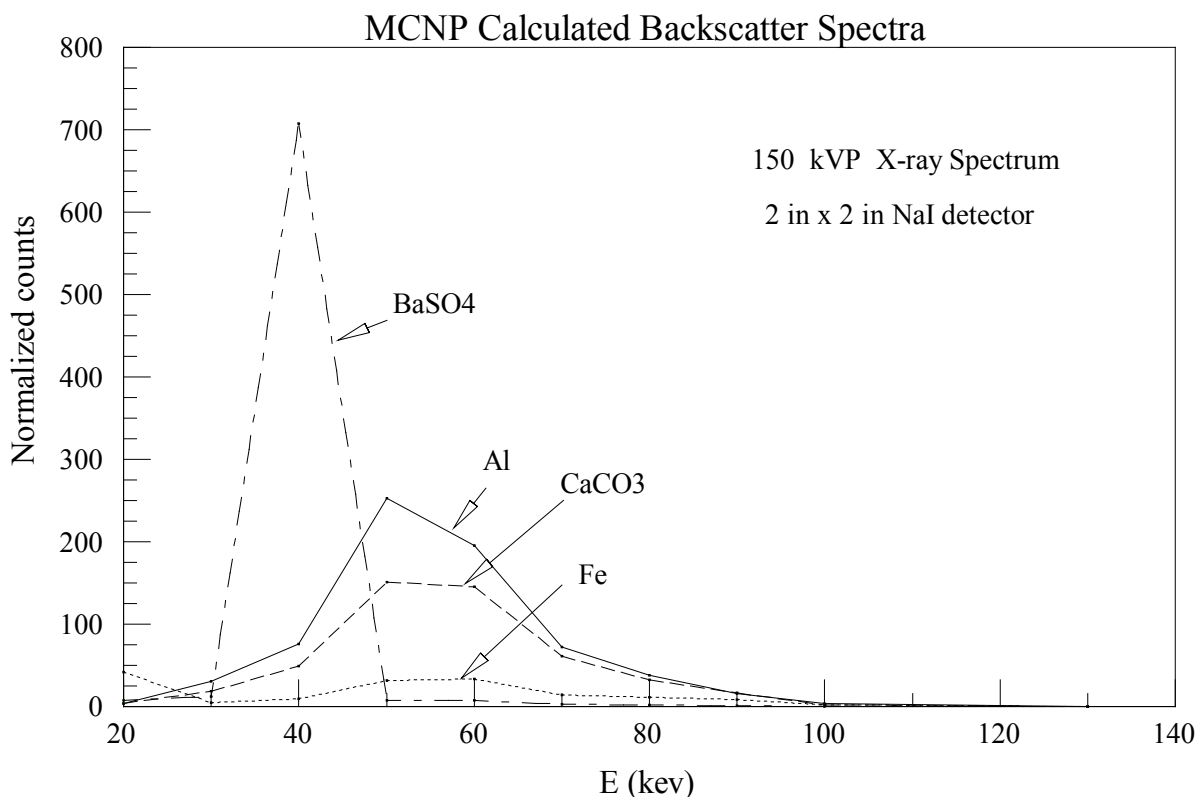


Figure 41. Calculated backscatter spectral shift from two common scale deposits containing barium sulfate and calcium carbonate.

Conceptual Prototype Design

In conjunction with developing operational parameters, experimental pipeline inspection scanning, and analysis for scale/corrosion identification described earlier in this section, a 3-D CAD conceptual design of both the down-hole and transmission pipeline instruments were developed. The 3-D conceptual design is being used to evaluate different materials for their mechanical properties. A conceptual design of the instruments is required to develop a detailed 3-D radiation transport model. The radiation transport models can then be used in conjunction with the experimental data to estimate the expected performance of the device.

Design for Wellbore Casing Tool

The down-hole tool is shown in Figure 42 and details of the scanning head are shown in Figure 43. The external housing for this application is approximately 4 inches in diameter. However, the tool can easily be scaled up for larger diameter pipe or used with centering standoff. As shown in Figure 42, the tool can be segmented, isolating the imaging components from the high voltage and power ends of the unit. A segmented unit would be useful for allowing the tool to navigate a small radius well casing used in horizontal drilling applications. Vertical well casing, similar to what is primarily used for gas storage, would probably not require a segmented unit.

Each segment would be approximately 4 inches in diameter with a segment length less than 10 feet. A single unit system (i.e. an unsegmented system) would have a total length less than 15 feet. Each system would require the following components:

Control System and Power Generation

- The recommended method for the imaging tool would be x-ray backscatter.
- High voltage generator – An x-ray high voltage (HV) tube would be used to generate x-rays. This HV generator would generate HV in the range of 80 to 160 kV. Higher energy systems can always be used to generate HV x-rays of 225 kV and more. In the realm of x-ray imaging, this HV X-ray generator power would have to be around 800 watts in order to obtain imaging speeds upwards of 3 to 6 feet per minute. Higher power systems or multiple imaging stages can be used to increase the imaging speed of the system.
- System power management - The system would have a power management and control module. This module would filter the power coming down the tethered line and deliver power to both the scanning head detector electronics and HV generator.
- System cooling – A portion of the tool would be required for cooling the x-ray tube if an x-ray source were used. The cooling can be delivered as a refrigerant, mechanical cooling such as with a Stirling engine, or electro-mechanical cooling such as a Peltier cooler. The cooling system would provide adequate heat removal to dissipate the excess heat generated in the x-ray tube. The amount of cooling required would be approximately equal to the amount of power consumed by the HV X-ray generator, because better than 99% of the power used to make x-rays is dumped into the system as heat. Another potential option for fixed duration cooling would be the use of a heat dump reservoir that contained low temperature refrigerant such as liquid nitrogen. A liquid nitrogen reservoir could cool the system for a few hours of operation.

Scanning Head

The scanning end of the instrument consists of an x-ray tube, a direct-drive motor to turn the rotating source collimator and a radiation detector with the associated electronics. In this current design, the detector is a 3 inch diameter, 6 inch long NaI detector. The vessel wall thickness of the carbon fiber composite is about ¼ inch thick. Stress, strain and deformation calculations were performed using the CMOS tool (finite element analysis) in Solid Works (3-D modeling and design CAD tool) to determine the final material thickness and necessary reinforcement structures to withstand pressures up to 4500 psi.

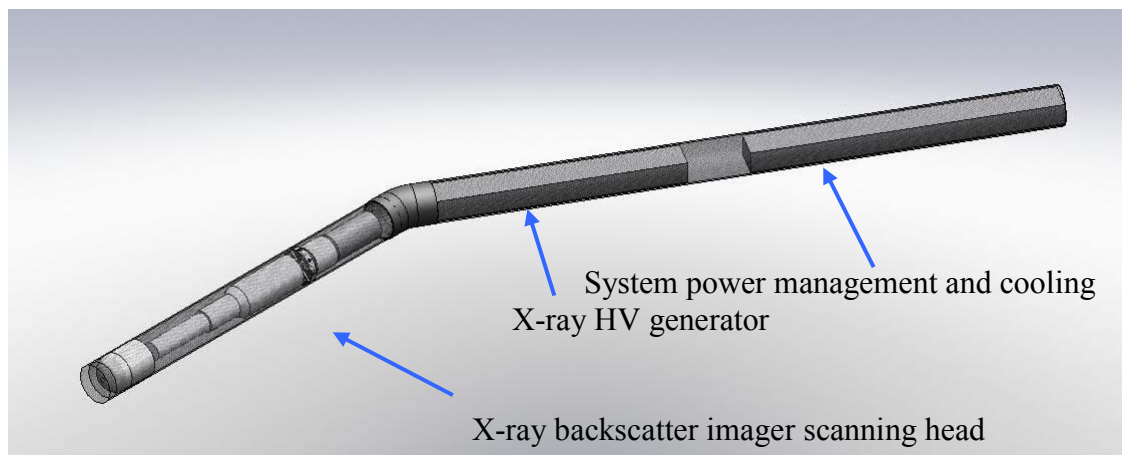


Figure 42. Downhole x-ray backscatter tool.

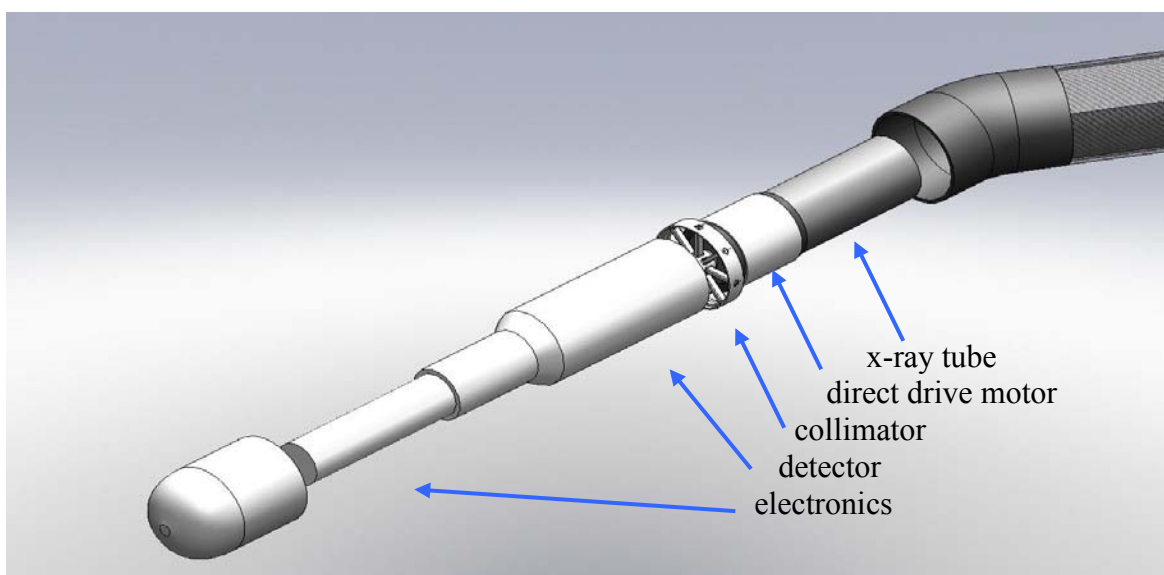


Figure 43. Detail of scanning head for downhole tool.

Conceptual Prototype System Operation

The general theory of operation is that a pencil beam of radiation is generated by restricting the illumination field with a rotating collimator. The pencil beam of radiation exits the housing, and penetrates the surrounding well casing. It then backscatters toward the inspection tool and the signal is detected by a radiation detector. Each pixel of the image is directly related to the backscatter signal from the pencil beam of emitted radiation. In order to generate an image, the pencil beam is rotated by use of a mechanical rotating collimator. This moves the pencil beam circumferentially around the pipe. When this circumferential rotation is combined with a linear translation, the pencil beam can sweep over the entire internal area of the pipe. It would cover the entire area of the pipe with a helix pattern. Each area of the pipe is mapped to a pixel value in the image based upon the location of the pencil beam when the measurement is taken, essentially generating an x-ray backscatter radiograph of the entire inside of the pipe. For the

down-hole tool, the tool will most likely be lowered into the casing. It will then be drawn out of the casing at constant velocity using the tether (wireline).

The overall length of the tool in the conceptual design is approximately 9 feet long with a flexing segment at 3 feet as shown in Figure 42. The packaging for this instrument must be made from a carbon fiber composite or other low Z material that will not significantly hinder the x-ray backscatter field. System power management and cooling are located at the tethered end of the instrument. Moving down the string to the next section is the HV generator for the x-ray tube. The x-ray tube is coupled to the HV generator with a flex HV cable. Decoupling the x-ray tube from HV generator simplifies the design, manufacturing and maintenance of the x-ray system.

- X-ray Source: The x-ray source is panoramic x-ray source allowing x-rays to leave the x-ray tube in a 360 degree field. This field is then restricted with an illumination beam tube collimator.
- Illumination beam tube collimator: This restricts the illumination beam to a pencil beam, allowing the inside of the pipe to be imaged with backscatter one pixel at a time. The illumination beam tube would provide at least one single exit point where the beam would exit the tool, scatter off the surrounding casing, and be detected by the radiation detector. It is possible to use more than one illumination beam tube and image multiple sections of the pipe simultaneously as long as cross-talk between the simultaneous beams can be eliminated. A method for measuring the backscatter signal from simultaneous beams is discussed in the detector description.
- Direct drive motor: A direct drive motor can be used to rotate the illumination beam tube collimator.
- Radiation detector: The radiation detector is a sensor for converting the penetrating radiation into a measured electrical signal. There are many different varieties of radiation detectors. For this system we will use scintillators such as NaI or PVT (polyvinyltoluene). For a single illumination beam tube collimator, the detector may be a single crystal NaI detector. The x-ray backscatter signal is detected and recorded as a pixel value dependent upon the position of the rotating collimator wheel.

If the x-ray source collimator has two exiting illumination beams, then a method is needed to measure the backscatter from each of the illumination beam tubes independently and simultaneously without significant cross-talk. This can be accomplished by using a segmented cylindrical detector as shown in Figure 44 and Figure 45. For the system in Figure 44, the bisected cylindrical detector would actually rotate with the illumination beam tube collimator. This would result in each half of the detector imaging (looking) at the same beam tube. In the case of the bisected detector and dual beam collimator, a double helix image of the pipe wall would be traced out as the tool traverses the pipe sections.

This concept can be expanded to N number of beam tubes where the detector is N-sectored as long as the section does not become so small that the cross-talk between illumination beam tubes becomes an issue. With a small 5 inch diameter pipe, this is probably limited to 2 or 3 segments and beam tubes. Larger diameter pipe can have more segments as the distance between the beams increases with increasing circumference.

The radiation detector also has a set of electronics. The electronics are a NuSAFE smart sensor. This sensor converts transducer signal from the radiation detector and builds the image of the pipe wall. The analog signal is immediately converted to a digital signal that can be either stored locally or transmitted real time back to a control area on the surface.

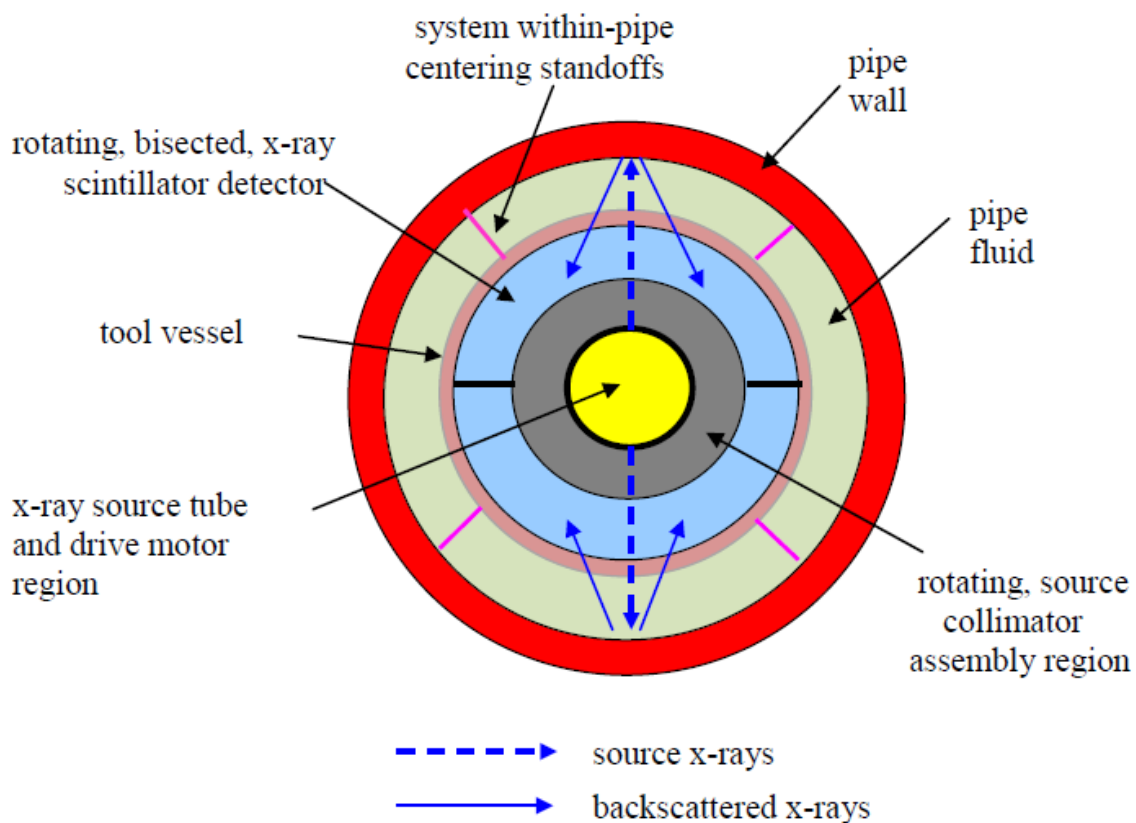


Figure 44. Bisected cylindrical detector with two illumination beams.

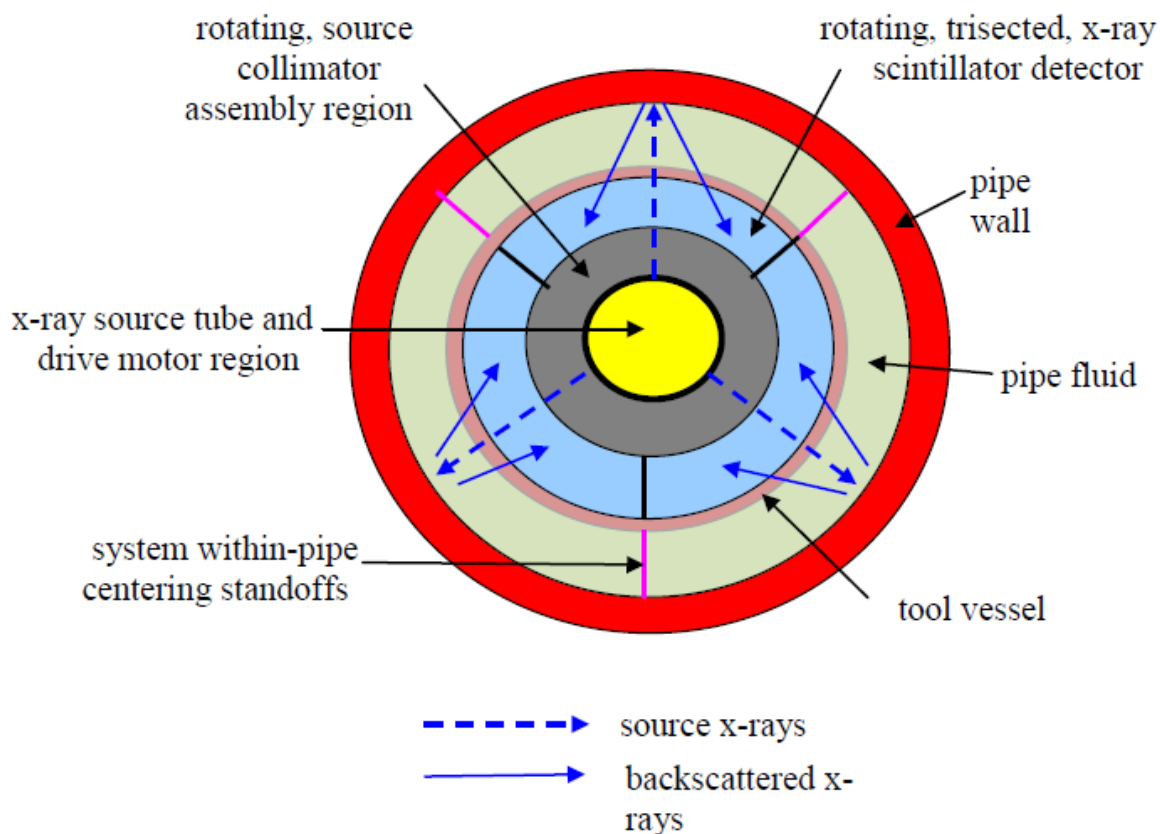


Figure 45. Tri-sected cylindrical detector with three illumination beams.

Initial radiation transport models have been developed for this conceptual design instrument. Using a NaI 3x3 inch detector and imaging a 6 inch diameter pipe with an 80 μ s pixel dwell time, the estimated gamma source strength would have to be approximately 170,000 Ci. Because a gamma source of this strength is difficult to license and nearly impossible to transport, it is recommended that consideration of a gamma source for the application be completely abandoned for imaging purposes. Most typical gamma sources used for compensated density logs are around 1.6 to 2.0 curies. A gamma source for imaging would be 100,000 times more radioactive than typical sources. Even increasing the detector size to 3 x 6 inches as shown in the conceptual design model would not decrease the source to a reasonable strength

A review of existing x-ray sources has been performed. The most interesting off-the-shelf x-ray tube is from RTW. It is a metal ceramic x-ray tube. The tube is a panoramic tube that is about 2.75 inches in diameter (see Figure 46). This tube would actually fit into a 4 inch diameter package and allow wires to be routed by the tube. Discussions have also been held with some current x-ray tube manufactures regarding the option of a custom x-ray tube and generator being developed for the application. Some potential tube and generator manufactures include Spellman, Gulmay, Comet, Varian and Source Ray.

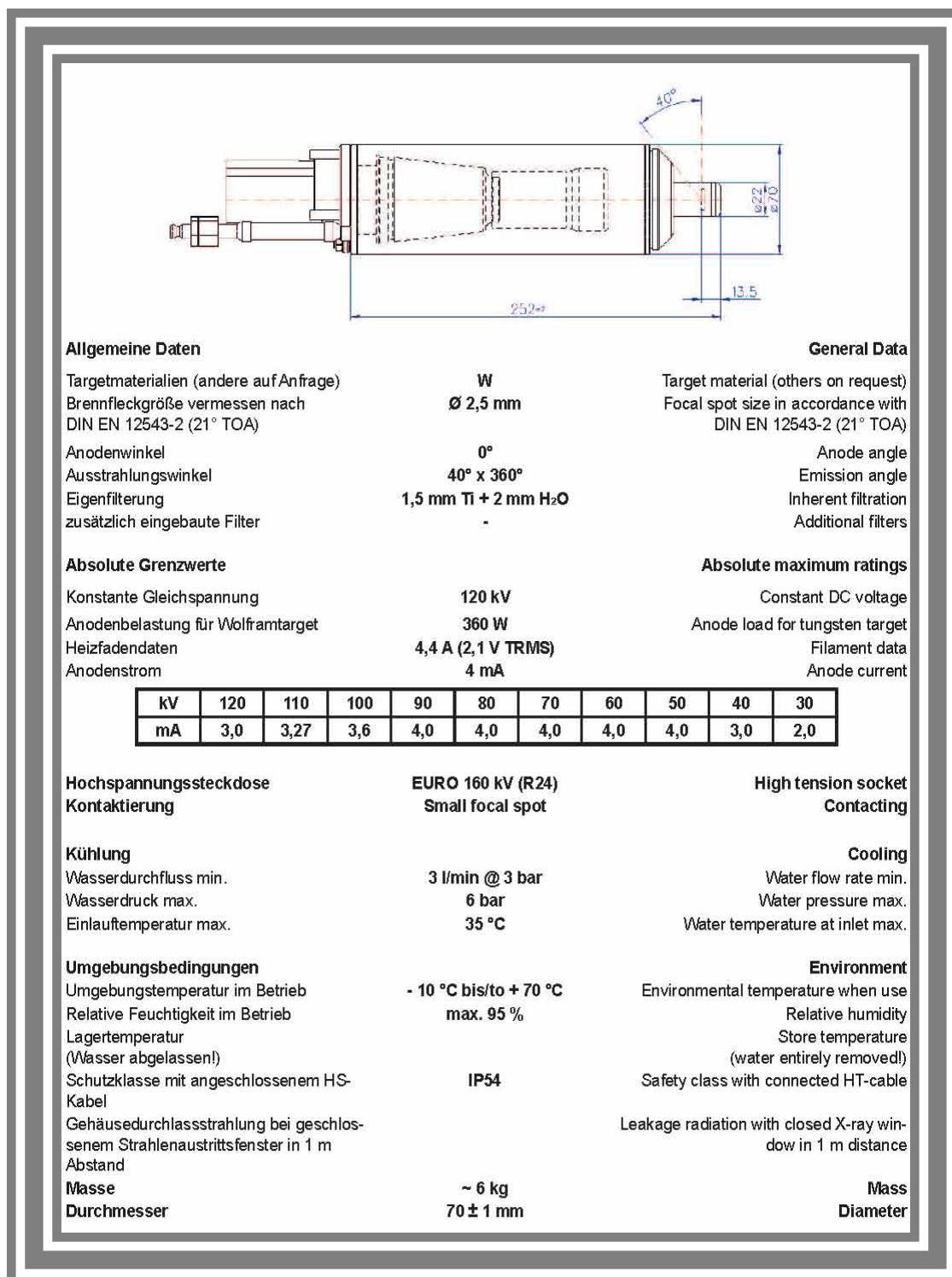


Figure 46. Specifications for a 2.75 inch diameter Panoramic RTW x-ray generator

Design for Transmission Pipeline Tool

A sketch of the transmission pipeline inspection tool scanning head's internal features is shown in Figure 47. (With reference to Figure 44 and Figure 45, Figure 47 shows the portion of the tool located inside of the scanning head vessel.) This tool can range anywhere in size from 12 inches in diameter to 36 inches in diameter depending upon the diameter of the pipe being inspected. The scanning head shown in Figure 47 would be housed in a smart pig application. There are several concepts for the smart pig design. The smart pig can either be all-in-one, or chained together in a string of consecutive smart pigs. The all-in-one smart pig would contain everything required for the system to function including: x-ray tube, HV generator, control system, battery power and detectors.

A segmented smart pig concept is similar to the down-hole tool where the scanning head shown in Figure 47 would be located in one smart pig, and generator and control would be located in a second smart pig, tethered to the first smart pig. This multiple smart pig design also allows for multiple scanning heads to be controlled by a single controller. An example of a multiple scanning head smart pig is shown in Figure 48. The length of each smart pig is approximately equal to diameter of the smart pig. Figure 49 shows a conceptual smart pig that includes the x-ray backscatter tool components shown in Figure 47. Centering devices are used to center the smart pig inside the pipe. An 18 inch diameter transmission pipe x-ray backscatter scanner can theoretically scan pipes from 20 inches in diameter up to 36 inches in diameter. Imaging resolution and contrast will decrease as the standoff distance from the inside diameter of the pipe increases. This means that for optimum scanning speed, resolution and contrast, the diameter of the tool should be closely matched to the inside diameter of the pipe.

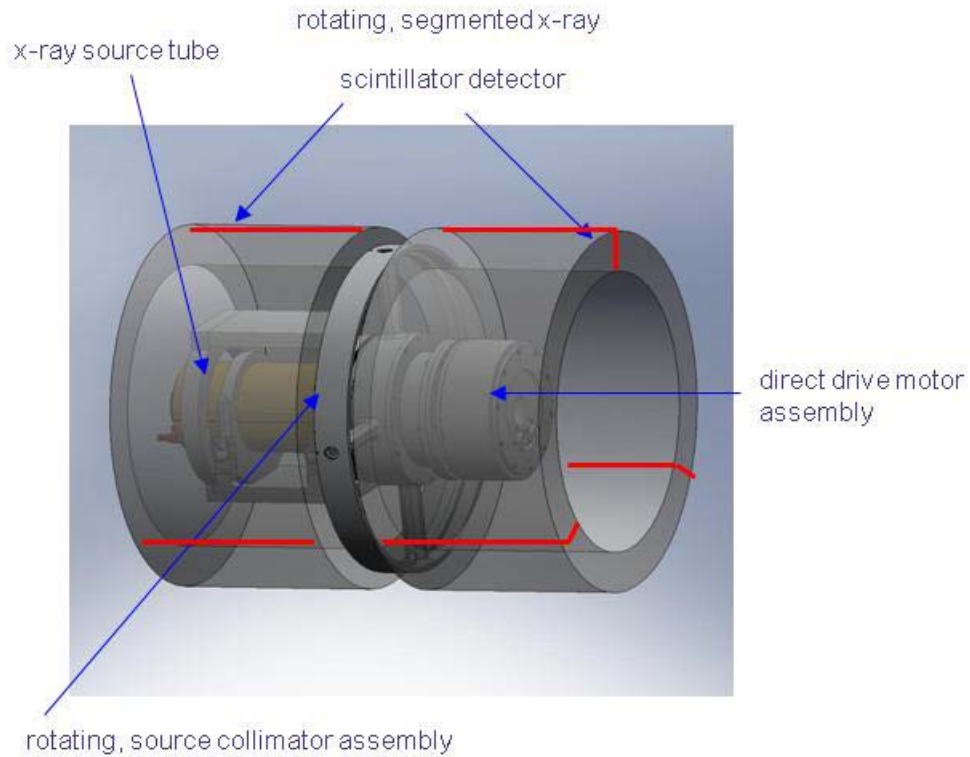


Figure 47. Transmission line x-ray backscatter tool.

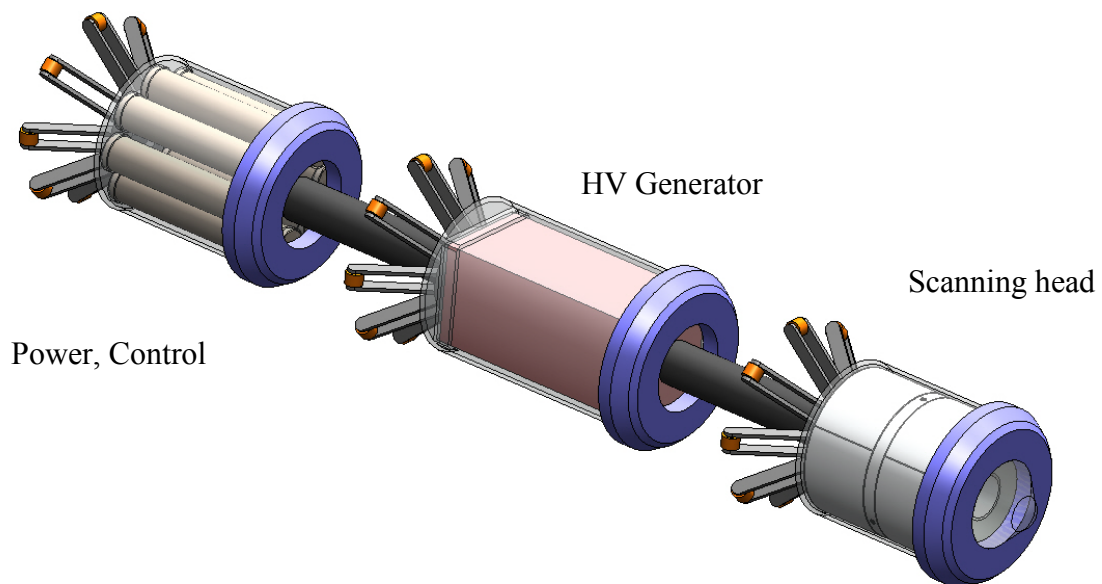


Figure 48. Multiple smart pig transmission pipeline scanning system with centering standoffs for larger diameter pipes:

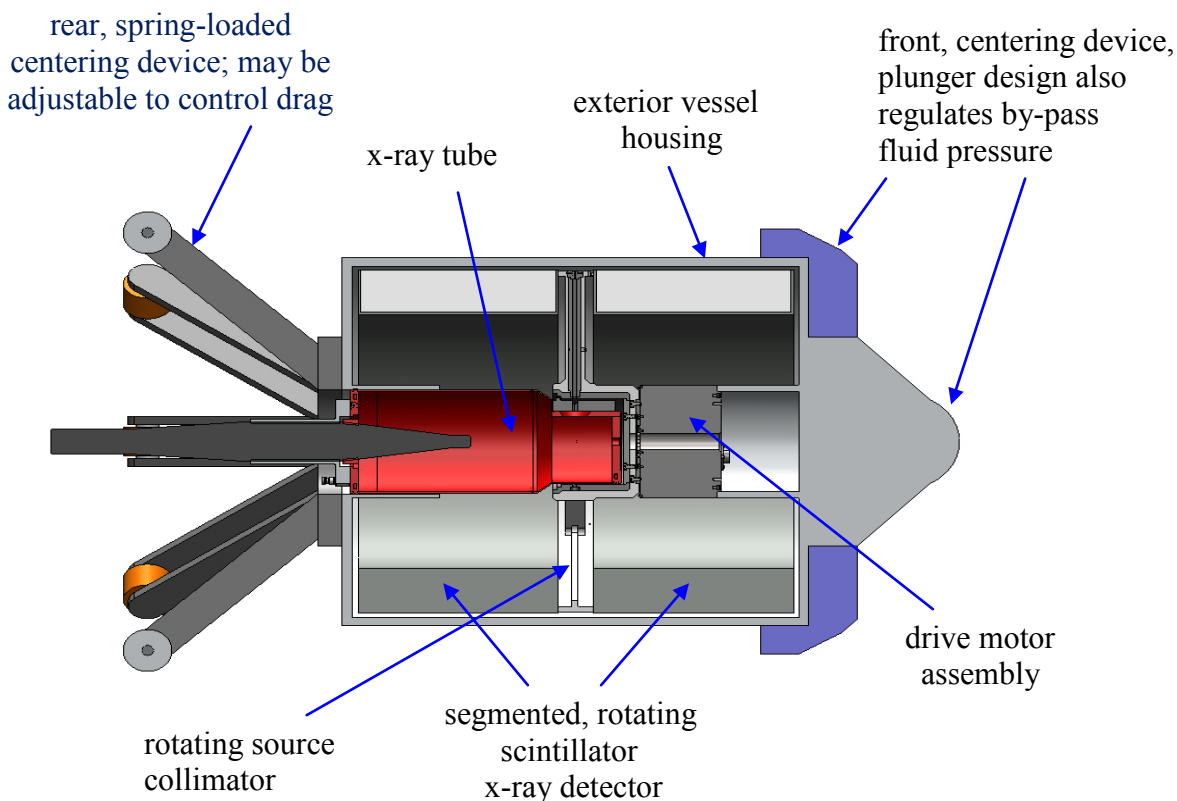


Figure 49. Conceptual smart pig that includes the x-ray backscatter tool components shown in Figure 47.

A standoff of up to 6 inches will not significantly reduce the image quality. With standoffs greater than 6 inches on the radius, the same imaging tool can be used, however, the imaging speed will have to be decreased to be able to maintain close to the same image quality.

Control System and Power Generation

- The recommended method for the imaging tool would be x-ray backscatter.
- High voltage generator: For transmission piping it is recommended that a 225 kV HV generator be used for imaging. This will allow the system to easily penetrate through at least 6 mm of steel.
- System power management: The system would have a power management and control module. This module would filter the power coming down the tethered line and deliver power to both the scanning head detector electronics and HV generator. The system power management can be either integral to a single smart pig or tethered across multiple smart pigs. The system will be battery operated. One of the smart pigs may contain a turbine-generator to power the batteries. Because the system will probably scan at a maximum of 1 to 3 meters per minute, and the “fluid” in the system can be moving at up

to 30 meters per second, the pressure head generated behind the smart pig will not only be used to push the system through the pipe, but may also be used for power generation to charge the batteries.

- System cooling: Because the system is not expected to encounter temperature as high as in the down hole application, the system will use water cooling. A closed loop water radiator cooling system will be used to cool the x-ray tube and HV electronics. This cooling system will transfer its heat to the pipe's fluid, liquid or gas. A water-to-air radiator will be used for gaseous fluids, while a water-water radiator will be used for liquid fluids. It is not anticipated that mechanical cooling or refrigeration will be needed for this system.

Scanning Head

The scanning head will use a close to off-the-shelf 225 kV x-ray source, and be nearly identical to that of the down-hole conceptual design.

Conceptual Prototype System Operation

The theory of operation for the transmission pipe line tool is identical to the theory of operation for the down-hole tool, except the form factor is different and the system is not tethered to a power supply. The general theory of operation is that a pencil beam of radiation is generated by restricting the illumination field with a rotating collimator. The pencil beam of radiation exits the housing, and penetrates the surrounding transmission piping. It then backscatters toward the inspection tool and the signal is detected by a radiation detector. Each pixel of the image is directly related to the backscatter signal from the pencil beam of radiation. In order to generate an image, the pencil beam is rotated by use of a mechanical rotating collimator. This moves the pencil beam circumferentially around the pipe. When this circumferential rotation is combined with a linear translation, the pencil beam can sweep over the entire internal area of the pipe. It would cover the entire area of the pipe with a helix pattern. Each area of the pipe is mapped to a pixel value in the image based upon location of the pencil when the measurement is taken, essentially generating an x-ray backscatter radiograph of the entire inside of the pipe. Rather than be drawn at a constant velocity by a tether, the smart pig will be forced to linearly traverse the pipe because of the pressure differential. The speed at which the system moves through the pipe will be controlled by the pressure the standoffs exert on the inside diameter of the pipe.

- X-ray source: The x-ray source is a panoramic x-ray source allowing x-rays to leave the x-ray tube in a 360 degree field. This field is then restricted with an illumination beam tube collimator. This tube will be a 225 kV x-ray source.
- Illumination beam tube collimator: Restricts the illumination beam to a pencil beam, allowing the inside of the pipe to be imaged with backscatter imaging one pixel at a time. The illumination beam tube would provide at least one single exit point where the beam would exit the tool, scatter off the surrounding pipe wall and be detected by the radiation detector. It is possible to use more than one illumination beam tube and image multiple sections of the pipe simultaneously as long as cross-talk between the simultaneous beams

can be eliminated. A method for measuring the backscatter signal from simultaneous beams is discussed in the detector description. The diameter of the rotating collimator for this application will be approximately 16 inches.

- Direct drive motor: A direct drive motor will be used to rotate the illumination beam tube collimator. In this system it is also possible to drive the rotating collimator with a belt drive, worm gear, or any other type of mechanical rotation drive mechanism.
- Radiation detector: The radiation detector is the sensor for converting the penetrating radiation into a measured electrical signal. For this system, because of the size of the detector required to produce the desired imaging speed and quality, a cylindrical shell of PVT will be used as the scintillator detector. This type of PVT detector can be made very large, machined and finished to a variety of different shapes. The x-ray backscatter signal is detected and recorded as a pixel value dependent upon the position of the rotating collimator wheel.

If the illumination beam tube collimator has two illumination beams exiting the collimator, then a method is needed to measure the backscatter from each of the illumination beam tubes independently and simultaneously without significant cross-talk. This can be accomplished by using a segmented cylindrical detector as shown in Figure 6-3a. For this system, the bisected cylindrical detector would actually rotate with the illumination beam tube collimator. This would result in each half of the detector imaging (looking) at the same beam tube. In the case of the bisected detector and dual beam collimator, a double helix image of the pipe wall would be traced out as the tool traverses the pipe sections.

This concept can be expanded to N number of beam tubes where the detector is N-sected as long as the sections do not become so small that the cross-talk between illumination beam tubes becomes an issue (see Figure 6-3b for a trisected configuration). With small diameter piping, this is most likely 2 to 3 segments and beam tubes. Larger diameter pipe can have more segments as the distance between the beams increases with increasing circumference.

The radiation detector also has a set of electronics. The electronics are a NuSAFE smart sensor. This sensor converts transducer signal from the radiation detector and builds the image of the pipe wall. The analog signal is immediately converted to a digital signal that can be either stored locally or transmitted real time back to a control area.

CONCLUSION

The purpose of this research effort was to determine the feasibility of utilizing the RSD technology for effective non-destructive evaluation (NDE) of wellbore casings including material defects, pitting, penetrations as well as scaling mechanisms. Based on stakeholder input, the feasibility analysis was extended to transmission pipeline NDE as well as its effectiveness in assessing non-metallic materials commonly used for distribution and emerging transmission pipeline applications. Investigative analysis, experimental data capture, transport modeling, and prototype conceptual engineering design were performed under this research effort to conclusively determine feasibility of the RSD system for the intended applications.

Comprehensive reviews of available components, material accessibility, and known accuracy of radiation transport models indicate that the proposed RSD system is potentially a viable tool for NDE evaluation of wellbore casings as well as transmission and distribution pipelines, both metallic and non-metallic. Its inherent capabilities, such as real time results, digital images of defects and potential compositional analysis of corrosion features makes this an attractive tool for further prototype development.

All work contained in this research effort are logical and incremental steps leading to the development of an alpha prototype NDE tool. Two conceptual designs and 3-D models have been developed in preparation of further advancement of the technology for both down-hole and transmission applications.

The recommended next step is to proceed with alpha prototype development of the tool. Guidance from the stakeholder community will be required to determine the intended application and targeted industry, ultimately deciding whether to focus initial technology development efforts on down-hole or pipeline applications.

REFERENCES

Useful links and references:

1. RADIATION SOURCE Use and Replacement, ABBREVIATED VERSION, Committee on Radiation Source Use and Replacement, Nuclear and Radiation Studies Board, Division on Earth and Life Studies, NATIONAL RESEARCH COUNCIL OF THE NATIONAL ACADEMIES, THE NATIONAL ACADEMIES PRESS, Copyright 2008, http://books.nap.edu/openbook.php?record_id=11976&page=R1
2. Saint Gobain, Standard Geophysical Detectors, Ruggedized Assemblies, Copyright 2001, http://www.detectors.saint-gobain.com/Media/Documents/S000000000000001004/SGC_Standard_geophysical.pdf
3. Saint Gobain, Spectra Series Integrated Geophysical Detectors, High Performance Design, Copyright 2001, http://www.detectors.saint-gobain.com/Media/Documents/S000000000000001004/SGC_Spectra_Series.pdf
4. Saint Gobain, Next Generation Geophysical Detectors for Increased Scintillation Performance, Copyright 2004-6, http://www.detectors.saint-gobain.com/Media/Documents/S000000000000001004/SGC_NxGenTi_Detectors_Information_Sheet.pdf
5. Saint Gobain, nplus Integrated Geophysical Detector Thermal Neutron Application, Copyright 2001, http://www.detectors.saint-gobain.com/Media/Documents/S000000000000001004/SGC_Nplus.pdf
6. Rosza C. M. et al. Bicon Corporation, "Characteristics of Scintillators for Well Logging to 225 C" IEEE Nuclear Science Symposium, Poster No. 5E4, Oct 1989, http://www.detectors.saint-gobain.com/Media/Documents/S000000000000001004/SGC_Technical_Paper_Characteristics_of_Scintillators_to_225_deg_C_Doc509.pdf
7. Saint Gobain, Oil & Gas Group, Copyright 2007, http://www.detectors.saint-gobain.com/Media/Documents/S000000000000001004/SG_Oil_Gas_Group_brochure.pdf
8. NETL, Oil & Gas Projects, Harsh-Environment Solid-State Gamma Detectors for Down-hole Gas and Oil Exploration, DE-FC26-04NT42107, August 2007, http://www.netl.doe.gov/technologies/oil-gas/NaturalGas/Projects_n/EP/DCS/DCS_42107GammaDetect.html
9. Hamamatsu, Oil well logging, Ruggedized Photomultiplier Tubes, June 2006, http://sales.hamamatsu.com/assets/pdf/catsandguides/PMT_ruggedized.pdf
10. Scionix, LaCl₃: Ce Scintillation Crystal (0.9 % Ce) <http://www.scionixusa.com/pages/pdf/LaCl3%20literature.pdf>

National Energy Technology Laboratory

626 Cochrans Mill Road
P.O. Box 10940
Pittsburgh, PA 15236-0940

3610 Collins Ferry Road
P.O. Box 880
Morgantown, WV 26507-0880

One West Third Street, Suite 1400
Tulsa, OK 74103-3519

1450 Queen Avenue SW
Albany, OR 97321-2198

2175 University Ave. South
Suite 201
Fairbanks, AK 99709

Visit the NETL website at:
www.netl.doe.gov

Customer Service:
1-800-553-7681

